

Lecture Notes in Electrical Engineering 195

Society of Automotive Engineers  
of China (SAE-China)  
International Federation  
of Automotive Engineering Societies (FISITA)  
*Editors*

# Proceedings of the FISITA 2012 World Automotive Congress

Volume 7: Vehicle Design  
and Testing (I)



 Springer

The Springer logo, which consists of a stylized white chess knight (horse) facing left, positioned to the left of the word "Springer" in a serif font.

# Lecture Notes in Electrical Engineering

Volume 195

For further volumes:  
<http://www.springer.com/series/7818>



Society of Automotive Engineers of China  
(SAE-China) · International Federation of  
Automotive Engineering Societies (FISITA)  
Editors

# Proceedings of the FISITA 2012 World Automotive Congress

Volume 7: Vehicle Design  
and Testing (I)



 Springer

The Springer logo, consisting of a stylized white chess knight piece on a black square, followed by the word "Springer" in a black serif font.

*Editors*  
SAE-China  
Beijing  
People's Republic of China

FISITA  
London  
UK

ISSN 1876-1100  
ISBN 978-3-642-33834-2  
DOI 10.1007/978-3-642-33835-9  
Springer Heidelberg New York Dordrecht London

ISSN 1876-1119 (electronic)  
ISBN 978-3-642-33835-9 (eBook)

Library of Congress Control Number: 2012948289

© Springer-Verlag Berlin Heidelberg 2013

This work is subject to copyright. All rights are reserved by the Publisher, whether the whole or part of the material is concerned, specifically the rights of translation, reprinting, reuse of illustrations, recitation, broadcasting, reproduction on microfilms or in any other physical way, and transmission or information storage and retrieval, electronic adaptation, computer software, or by similar or dissimilar methodology now known or hereafter developed. Exempted from this legal reservation are brief excerpts in connection with reviews or scholarly analysis or material supplied specifically for the purpose of being entered and executed on a computer system, for exclusive use by the purchaser of the work. Duplication of this publication or parts thereof is permitted only under the provisions of the Copyright Law of the Publisher's location, in its current version, and permission for use must always be obtained from Springer. Permissions for use may be obtained through RightsLink at the Copyright Clearance Center. Violations are liable to prosecution under the respective Copyright Law.

The use of general descriptive names, registered names, trademarks, service marks, etc. in this publication does not imply, even in the absence of a specific statement, that such names are exempt from the relevant protective laws and regulations and therefore free for general use.

While the advice and information in this book are believed to be true and accurate at the date of publication, neither the authors nor the editors nor the publisher can accept any legal responsibility for any errors or omissions that may be made. The publisher makes no warranty, express or implied, with respect to the material contained herein.

Printed on acid-free paper

Springer is part of Springer Science+Business Media ([www.springer.com](http://www.springer.com))

# Contents

## Part I Vehicle Performance Development

<b>A New Approach to Improve the Design Quality of Chinese National Brand Vehicle</b> . . . . .	3
F2012-E01-004 Du Cao, Jing Deng and Fengfei Fu	
<b>The Process of Vehicle Dynamics Development</b> . . . . .	13
F2012-E01-011 Zhanglin Cai, Stephen Chan, Xiaofeng Tang and Jiang Xin	
<b>Development of Methodologies for Evaluation, Simulation and Improvement of Cross-Wind Sensitivity.</b> . . . . .	23
F2012-E01-014 Guido Tosolin, Jonathan Webb, Alex Català, Alfonso Escuer and Young Jin Hyun	
<b>Maneuvering Experiment of Personal Mobility Vehicle with CVT-Type Steering Mechanism</b> . . . . .	35
F2012-E01-016 Yoshihiro Suda, Hirayama Yuki, Masahiko Aki and Takafumi Takagi	
<b>Vehicle Performance Objective Management in Automotive R&amp;D</b> . . .	45
F2012-E01-018 Xuezhen Wu, Haiqiang Han, Liqiang Dai, Linghua Zou and Fuquan Zhao	
<b>Improving Energy Efficiency of Heavy-Duty Vehicles: A Systemic Perspective and Some Case Studies</b> . . . . .	51
F2012-E01-024 Juhani Laurikko, Kimmo Erkkilä, Petri Laine and Nils-Olof Nylund	

<b>Study on the Active Front Steering System with Steady Gain . . . . .</b>	<b>65</b>
F2012-E01-025	
Youkun Zhang and Baohui Liu	
<b>Design Optimization of Full Vehicle Suspension Based on Ride and Handling Performance . . . . .</b>	<b>75</b>
F2012-E01-026	
Tey Jing Yuen, Ramli Rahizar, Zainul Abidin Mohd Azman, Alias Anuar and Dzakaria Afandi	
<b>Improve Fuel Economy of Commercial Vehicles Through the Correct Driving . . . . .</b>	<b>87</b>
F2012-E01-029	
Ping Guo, Zhenlei Li, Zhiwu Zhang, Jun Chi, Shuai Lu, Ye Lin, Zhengfa Shi and Jingcai Shi	
<b>Research on Test Method of Off-road Vehicle Trafficability . . . . .</b>	<b>97</b>
F2012-E01-031	
Wenhu Qin, Zhanjun Guo and Weigong Zhang	
<b>Part II Vehicle Integration Platformized and Universal Design</b>	
<b>A Design Method for Future Automobiles . . . . .</b>	<b>109</b>
F2012-E02-003	
Zhifeng Wang, Wu Yang, Zhiguo Le and Fuquan Zhao	
<b>Effect of Engineering Materials for Vehicle Collision Simulation. . . . .</b>	<b>123</b>
F2012-E02-005	
Yanling Huang, Gaoji Yin, Zhitao Wang, Juanli Ni, Li Li, Qiang Liu, Anzhi Yang and Fuquan Zhao	
<b>Part III Development of CAD/CAE/CAM and CF Methods in Automotive Practice</b>	
<b>Simulation of Leaf Spring Balanced Suspension Based on Virtual Test-Rig . . . . .</b>	<b>135</b>
F2012-E03-002	
Xinpeng Tang and Kun Liu	
<b>A Simulation Analysis and Optimization of Mode and Stiffness of BIW . . . . .</b>	<b>145</b>
F2012-E03-004	
Qiuxia Zhang, Leyi Zhang and Mingtao Guo	

**Vehicle Wading Simulation with STRA-CCM+ . . . . .** 157  
 F2012-E03-005  
 Xin Zheng, Xin Qiao and Fanhua Kong

**Developing Low-Noise Low Back Pressure Intake System  
 by CAE Technology . . . . .** 167  
 F2012-E03-006  
 Yue Chang Chen, Haotian Shi and Yang Guang

**Study on Vehicle Modeling and Steering Performance . . . . .** 177  
 F2012-E03-009  
 Minglun Cao and Cai Yang

**Surrogate Model for Aerodynamic and Handling Stability  
 Optimization of a Tractor-Trailer in Crosswinds . . . . .** 189  
 F2012-E03-010  
 Xu Gong, Zhengqi Gu, Jian Ye, Xu Yan and Zhiming Zhao

**Calculation of Drum Brake Temperatures in Ten-Cycle Braking . . . . .** 201  
 F2012-E03-013  
 Kun Zhang and Cai Yang

**Solution of the Glare Risk in Vehicle Inner Trim Designing . . . . .** 209  
 F2012-E03-014  
 Mengdong Mi, Yongqing Liu, Congwen Yu, Sujuan Peng, Bin Feng,  
 Jian Shi and Pin Wang

**Topology Optimization Design of a Heavy Truck Frame. . . . .** 219  
 F2012-E03-015  
 Jingxin Wang, Tie Wang, Yanchao Yang, Zhaohui Peng,  
 Zhi Li and Na Wang

**Bridging the Gap Between CAD and CAE in Composite  
 Structures Development Process for the Automotive Industry. . . . .** 229  
 F2012-E03-016  
 Samouil Saltiel, Michalis Giannakidis and Nikos Toulas

**Ensuring Reliability of Automotive Electronics  
 by Using Thermal Analysis . . . . .** 241  
 F2012-E03-019  
 Boris Marovic and Alexandra Francois-Saint-Cyr

<b>Effects of Frequency Response Spacing on Vibration Fatigue Analysis</b> .....	253
F2012-E03-020	
Jasuk Koo	
<b>CAE Supported ESC Development/Release Process</b> .....	267
F2012-E03-021	
Yiqin Mao, Johannes Wiessalla, Jan Meier, Wolfgang Risse, Guy Mathot and Manfred Blum	
<b>Application of Optimization Algorithm to HVAC Configuration Design</b> .....	277
F2012-E03-023	
Tatsuro Kyuto, Motohiro Kitada and Hideo Asano	
<b>Research of Flow Field Simulation for Lubrication System and Effect Evaluation on a 7-Speed Dual Clutch Transmission</b> .....	285
F2012-E03-033	
Yinhui Lin, Zhihua Hu, Chaoqiang Xiong, Mengyan Zang, Yuan Jia, Yong Chen, Daguo Luo and Fuquan Zhao	
<b>Application of Stiffness Estimation and Structure Optimization in Rubber Component Development.</b> .....	299
F2012-E03-036	
Min Sun, Yuan Qu, Youfeng Qiu and Shenrong Wu	
<b>Brake Cooling Simulation: A Combined Procedure of CFD, Thermal and 1D Software</b> .....	309
F2012-E03-037	
Enric Aramburu and Roger Calvo	
<b>BIW Optimization by Means of an Automated CAE Process for the Reduction of Welding Points</b> .....	321
F2012-E03-038	
Pérez Mario, Calvo Roger and Hirschbeck Bernhard	
<b>Establishing a Carbon Fiber Material Database for Crashworthiness Structural Development</b> .....	329
F2012-E03-039	
Pablo Cruz and Raúl Ureña	
<b>Full Vehicle Durability Analysis by Means of the IDIADA Virtual Proving Ground</b> .....	337
F2012-E03-040	
Jordi Arbiol, José Antonio Muñoz, Xavierl Armengo and Enric Aramburu	

**The Parametrical Design and Optimization of Body Frame Based on Crashworthiness and Lightweight** . . . . . 349  
 F2012-E03-042  
 Yongxin Men, Guojun Zheng, Huicai Zelong Lu and Zelong Wang

**Development of Concept Analysis and Multi-Objective Optimization Platform for Body-In-White Structure** . . . . . 361  
 F2012-E03-046  
 Yiwen Li, Hongjian Li, Zuofeng Pan and Tao Xu

**Fatigue Life Prediction of Spot-Weld for Auto Body Based on Multiple Load Cases** . . . . . 373  
 F2012-E03-049  
 Liling Zhang, Qing Jiang, Xuefeng Chen and Xu Wang

**Acoustic Isolation Analysis of Weatherstrip Considering Door Opening Condition** . . . . . 383  
 F2012-E03-050  
 Tae Hyung Kim, Hak Jin Kim, Heon Young Kim, Joon Chul Park, Byung-Kwon Min and Chang-Kuk Yim

**Assessment of Modeling Individual Physiological Differences when Predicting Thermal Comfort** . . . . . 393  
 F2012-E03-053  
 Curran Allen and Hepokoski Mark

**The Multi-Physics Coupling Analysis Based on Electro-Magnetic, Structural and Acoustic Characters for a Drive Motor in EV** . . . . . 399  
 F2012-E03-057  
 Jinling Zeng, Yingzi Piao, Bingwu Lu, Fuxiang Huo and Qun Zhang

**Modular Car Body Design and Optimization by an Implicit Parameterization Technique via SFE CONCEPT** . . . . . 413  
 F2012-E03-058  
 Fabian Duddeck and Hans Zimmer

**A New Approach for Vibro-Acoustic Optimization Using Discrete and Continuous Shape Variables Applied to a Car Body** . . . . . 425  
 F2012-E03-059  
 Hans Zimmer, Arnold Gross-Thebing, Manohar Prabhu and Fabian Duddeck

## **Part IV Advanced Chassis, Body Structure and Design**

<b>Integrated Architectures for Third Generation Electric Vehicles: Technical Challenges Meeting Customer Requirements . . . . .</b>	<b>437</b>
F2012-E04-001 Micha Lesemann, Leif Ickert, Lutz Eckstein, Sven Faßbender, Michael Funcke and Jac Wismans	
<b>The Ring-Shaped Route Body Structure Design and Evaluation Method . . . . .</b>	<b>447</b>
F2012-E04-002 Feng Xiao and XinHua Gao	
<b>The Study of Wheeled Semi-trailer Design and Development Based on Scale Model . . . . .</b>	<b>463</b>
F2012-E04-003 Xiong Xin, Xuexun Guo and Libo Wang	
<b>The Concept and Methodology of Creating the Universal Life-Saver with Rotary-Screw Mover . . . . .</b>	<b>477</b>
F2012-E04-004 Maxim Krashennikov, Anatoly Kulashov, Viktor Shapkin and Alla Koshurina	
<b>Research on the Development Procedure of Light-Weight New Body Architecture . . . . .</b>	<b>491</b>
F2012-E04-005 Xiangyang Fu, Guohong Shi, Xin Jiang, Yunhui Duan and Zhengchao Song	
<b>Control and Simulation of Regenerative Suspension Using Permanent Magnetic Synchronous Motor . . . . .</b>	<b>505</b>
F2012-E04-007 Weihua Wang and Songshan Liu	
<b>The Application of Tolerance Analysis During Engineering Process. . .</b>	<b>515</b>
F2012-E04-009 Wei Wang and ZhiHan Zhou	
<b>Synchronized Design Optimization Method of Body Joints and Major Cross Sectional Members . . . . .</b>	<b>531</b>
F2012-E04-010 Jie Xiang, Yong Chen and Youmin Guo	



**Design and Development of Contractive Suspension in Hill-Climb Races** . . . . . 539  
 F2012-E04-014  
 Antonini Pierluigi and Cibrario Valerio

**Modularized Design of the Engine Compartment Design Based on the Theory of CBR** . . . . . 553  
 F2012-E04-016  
 Honghua Li, Wei Li and Fuquan Zhao

**Development of First Order Analysis for Torsion Beam Suspension (FOA/TB) Corresponding to Modular Design** . . . . . 561  
 F2012-E04-017  
 Kazuaki Chiku, Hideki Sugiura, Takaaki Uno and Toshiji Hirotani

**A Pillar Structure Optimization Design of Driving Safety** . . . . . 571  
 F2012-E04-018  
 Guolin Li, Jun Sui, Xiang Zheng, Honghua Li and Fuquan Zhao

**A New Body Concept for Electric Vehicle: PBC-EV** . . . . . 579  
 F2012-E04-020  
 Jaehyun Kim, Hongwoo Lee, Kyunghwan Chung, Hyounyoung Lee, Yeonsik Kang and Jaebok Nam

**The Study on Development of High Security and High Comfort Commercial Vehicle Cab** . . . . . 593  
 F2012-E04-021  
 Yuhai Chang and Xiaojun Yang

**The Design and Simulation Analysis of Electromagnetic Energy Regenerative Suspension System** . . . . . 601  
 F2012-E04-023  
 Hongbin Ren, Sizhong Chen and Zhanzong Feng

**Optimization of the Magnetic Property of a Magnetorheological Squeeze Mount** . . . . . 611  
 F2012-E04-024  
 Xinjie Zhang, Fangwu Ma, Fuquan Zhao, Konghui Guo and Mehdi Ahmadian

**Semi-Active Suspension Adaptive Control Strategy Based on Hybrid Control** . . . . . 625  
 F2012-E04-025  
 Xinjie Zhang, Wuhui Yu, Fangwu Ma, Fuquan Zhao and Konghui Guo

**Optibody Project: Optimizing Vehicle Structures for Electric Light Trucks and Vans . . . . . 633**  
 F2012-E04-026  
 Eduardo del Pozo de Dios, Arturo Dávila,  
 Juan José Alba and Massimiliano Avalor

**Linear Quadratic Gaussian Optimal Control Strategy for Four-Wheel Steering Vehicle . . . . . 641**  
 F2012-E04-028  
 Yan Chen, Wenqiang Chen, Xingmin Wei and Fuquan Zhao

**Design and Validation of a Race Car with Respect to Aerodynamics and Body Styling . . . . . 651**  
 F2012-E04-029  
 Abdul Vaseem Akram, M. Ajay Kumar,  
 K.C. Vora and Mohammad Rafiq

**Part V Automotive Ergonomic, Interior and Exterior Trim Design**

**Driver Accommodation Assessment Using Physics-Based Posture Prediction Model . . . . . 665**  
 F2012-E05-001  
 Ozsoy Burak and Jingzhou (James) Yang

**Design of the Adjustable Vehicle Seating Buck for Ergonomics Verification . . . . . 677**  
 F2012-E05-002  
 Hongfang Ling, Li Wu and Gang Li

**Study on Preventing Dazzle of Meter . . . . . 691**  
 F2012- E05-006  
 Luo Pan, Xiaolin Liao, Guozheng Luo, Jing Wang,  
 Dejian Cheng and Li Yu

**A Study and Application of Optimization on Console Development. . . 701**  
 F2012-E05-009  
 Ruiyan Zhang, Ni Cao and Miao Luo

**Enhancing Vehicle Ingress/Egress Ergonomics with Digital Human Models . . . . . 713**  
 F2012-E05-010  
 Nanxin Wang, Ksenia Kozak, Jian Wan,  
 Gianna Gomez-Levi and Gary Strumolo

**Preliminary Research on Muscle Activity in Driver’s Steering Maneuver for Driver’s Assistance System Evaluation . . . . .** 723  
 F2012-E05-011  
 Ryouhei Hayama, Yahui Liu, Xuewu Ji, Takahiro Mizuno, Tomoyasu Kada and Liming Lou

**Color TFT Instrument Clusters in the Chinese Market. . . . .** 737  
 F2012-E05-012  
 Huibin Li, Gerhard Mueller, Karl Reich and Leo Glasenhardt

**Color and Texture Design of Chinese Automobile Brand . . . . .** 747  
 F2012-E05-014  
 Yanhong Hao and Fuquan Zhao

**Development of Shock-Absorbing Grip-Handle Structures on the Headliner . . . . .** 761  
 F2012-E05-015  
 Hee Sang Park, Yongsu Chang and Jun Ho Jung

**SEMG Based Recognition for Lumbar Muscle Fatigue During Prolonged Driving . . . . .** 773  
 F2012-E05-017  
 Xin Tao, Bo Cheng, Bo Wang, Feiruo Zhang, Guofa Li and Chaoyang Chen

**Part VI Vehicle Style and Aerodynamic Design**

**Aerodynamic Investigations in Conceptual Vehicle Development Supported by Integrated Design and Simulation Methods. . . . .** 787  
 F2012-E06-004  
 Mario Hirz, Severin Stadler, Martin Prenner and Johannes Mayr

**Research on Drag Reduction of Commercial Vehicle Based on Aerodynamics. . . . .** 801  
 F2012-E06-007  
 Shijie Fan, Qiang Fu, Jialin Zhang, Jinying Ma, Jing Zhao and Kelong Lu

**The State of Equilibrium in Car Body Design: The Application of Asymmetry for Enhanced Harmony. . . . .** 811  
 F2012-E06-009  
 Liming Fu, Mingyang Sun and Alvin Chan

**Part VII New Materials and Structures**

**The Analysis of Composite Leaf Spring by Finite Element Method and Experimental Measurements . . . . .** 823  
 F2012-E07-004  
 Jiashi Wang, Zaike Li and Qibin Jiang

**Finite Element Analysis of Two Kinds of Dump Trunk. . . . .** 831  
 F2012-E07-005  
 Zhi Li, Tie Wang, Jingxin Wang, Zhaohui Peng and Na Wang

**Advanced Solid Lubricant Technology Improve Engine Performance . . . . .** 839  
 F2012-E07-006  
 Yupeng An, Kejin Zhang, Dan Wang, Junyan Zhang and Bin Zhang

**Wrought Magnesium Alloy AZ31 Grain Refinement by Predeformation . . . . .** 851  
 F2012-E07-007  
 Fei Xiong, Lichun Cui and Ping Wang

**Consideration of Biomimetics in Structural Design of Vehicle Side Intrusion Bars . . . . .** 859  
 F2012-E07-009  
 Yan Rui, Aleksandar Subic and Chunhui Wang

**Development of High Performance FRP Crush Box: A Report of JSAE FRP Working Group Activity. Numerical Analysis of Fracture Behavior of FRP Crush Box with Tapered Trigger . . . . .** 869  
 F2012-E07-012  
 Reika Akita, Atsushi Yokoyama, Asao Koike, Kouji Kawamura, Yoshihiro Sukegawa and Hiromichi Oohira

**Development of the High Performance FRP Crush Box: A Report of JSAE FRP Working Group Activity. Analysis of Collapse Mechanism of the Trigger Part of FRP Crush Box . . . . .** 879  
 F2012-E07-013  
 Asao Koike, Atsushi Yokoyama, Reika Akita, Yoshiro Sukegawa, Koji Kawamura and Hiromichi Oohira

**Research of Application of Crash Durable Adhesive on a Chinese Domestic Car Body . . . . . 889**  
 F2012-E07-020  
 Zhongying Yue, Xiukui Yuan, Chaoqian Gao, Liantai Yuan, Qiang Liu, Fuquan Zhao, Yufei Wang, Xiaojun Yang and Jie Xu

**The Study of Aluminum Alloy Application on Automotive Control Arm . . . . . 901**  
 F2012-E07-021  
 Juanli Ni, Li Li, Qiang Liu, Fuquan Zhao, Yi Xu, Shijie Guo and Bowen Changhai

**Using Shape Memory Alloys in Automotive Safety Systems . . . . . 909**  
 F2012-E07-023  
 Viorel Gheorghita, Paul Gumpel, Joachim Strittmatter, Chiru Anghel, Thomas Heitz and Mathias Senn

**Study on Electro Rheological Fluid Shock Damper and Adjustable Damping Performance . . . . . 919**  
 F2012-E07-024  
 Jianhua Wang, Fei Xie, Yuncheng Wang and Chunbao Guo

**Cyclic Tension–Compression Test of Mg Alloy Sheet at the Elevated Temperature . . . . . 927**  
 F2012-E07-029  
 Oh Suk Seo, Heon Young Kim, Myoung-Gyu Lee, Ji Hoon Kim and Dae Yong Kim

**The Third Generation Auto Sheet Steel: Theory and Practice. . . . . 933**  
 F2012-E07-030  
 Shanqiang Ying and Han Dong

**Part VIII Automotive Reliability Technology**

**Vehicle Usage Measurement and Analysis Based on the Random Retail Customer . . . . . 951**  
 F2012-E08-001  
 Yaozeng Pan, Feng Yang and Chenyang Li

**Part IX Lightweight Design Technology**

**Design, Evaluation Methods and Parameters of Automotive Lightweight** . . . . . 965  
 F2012-E09-001  
 Mingtu Ma and Hongzhou Lu

**Body Light Weight and Cost Control** . . . . . 977  
 F2012-E09-006  
 Dazhou Guo

**Lightweight Design and Formability Analysis of Auto Body Aluminum Trunk Lid** . . . . . 987  
 F2012-E09-007  
 Zhao Liu, Ping Zhu and Xiaojing Zhu

**Geometric Parameters Optimal Design of Variable Cross-Section Rim** . . . . . 1003  
 F2012-E09-009  
 Hongyu Wang

**Lightweight Design for a FSC Car Based on Modal and Stiffness Analysis** . . . . . 1009  
 F2012-E09-012  
 Liman Jiang, Guoquan Wang, Guoqing Gong and Ruiqian Zhang

**Application of Comprehensive Optimization into Bus Structure Lightweight Improvement in 3-Section Chassis Frame** . . . . . 1023  
 F2012-E09-014  
 Congcheng Ma and Fengchong Lan

**Applying Agile Software Principles and Practices for Fast Automotive Development** . . . . . 1033  
 F2012-E09-015  
 David Socha, Tyler C Folsom and Joe Justice

**Multi-Objective Evaluation Regulation Study of Automotive Lightweight** . . . . . 1047  
 F2012-E09-016  
 Hongzhou Lu, Zhiwen Wang, Ma Mingtu, Yilong Cheng and Guimin Lu

**Future Mobility Requires Advanced Car Concepts and Power Train** . . . . . 1057  
 F2012-E09-025  
 Sven Augustin

**A Lightweight Optimization Method of Vehicle Body Structure Design. . . . . 1063**  
 F2012-E09-026  
 Zhixiang Li and Jifa Mei

**Analysis of the Transient Thermomechanical Behaviour of a Lightweight Brake Disc for a Regenerative Braking System. . . . . 1075**  
 F2012-E09-028  
 S. Sarip, A. J. Day, P. Olley and H. S. Qi

**Concept Analysis of Automotive Aluminium Alloy Bumper . . . . . 1089**  
 F2012-E09-030  
 Xinming Wan, Xiao Zhi, Qingjiang Zhao, Guangyao Wang and Xiaofei Xu

**Study on Lightweight of Vehicle Body Structure Based on Implicit Parametric Model . . . . . 1101**  
 F2012-E09-031  
 Jiyou Zhang, Shudan Liu, Hong Peng, Yongxin Men and Fuquan Zhao

**Lightweight Design and Evaluation for Cab-in-White of Heavy-Duty Truck . . . . . 1109**  
 F2012-E09-034  
 Xinyu Wang, Dengfeng Wang, Wanlai Sun and Peiwu Liu

**Research on Parameterized Structural Modeling for Carbody Lightweighting. . . . . 1119**  
 F2012-E09-038  
 Xin Chen, Fangwu Ma, Dengfeng Wang, Yongxin Men, Qiang Liu, Zaiqi Yao, Junlong Zhou and Chen Xie

**Reliability-Based Topology Optimization of Control Arm of Suspension for Lightweight Design. . . . . 1129**  
 F2012-E09-039  
 Qinghai Zhao, Xiaokai Chen and Yi Lin

**Structural Lightweight Design of Engine Connecting Rod. . . . . 1139**  
 F2012-E09-042  
 Fuxiang Huo, Jun Li, Yu Xu, Bing Wu, Yepeng Han, Peng Li and Qun Zhang

**Part X Design for Recycling**

**Development of Environmental Assessment System of Vehicle . . . . . 1151**  
 F2012-E10-001  
 Moosang Yu and Yunjong Kim

**Research on Hydraulic Regenerative Braking System for Pure Electric Vehicle Based on AMESim . . . . . 1161**  
 F2012-E10-002

Junping Jiang, Xiaobin Ning, Yaoting Xu, Qiucheng Wang,  
 Wei Liu, Zhijie Pan and Fuquan Zhao

**Part XI Dynamic Modeling**

**Main Problems of Creating Surface Traction-Transport Vehicles with Mechatronic Systems . . . . . 1173**  
 F2012-E11-001

Belousov Boris and Ksenevich Tatiana

**Wheelbase Filtering Effect on Vehicle Ride Dynamics. . . . . 1183**  
 F2012-E11-007

Kang Song, Xiaokai Chen and Yi Lin

**Part XII Simulation and Experimental Validation**

**Modeling and Experimental Research About a New Type of Vehicle Active Suspension Electromagnetic Actuator . . . . . 1199**  
 F2012-E12-001

Lai Fei and Huang Chaoqun

**Research on Nonlinear Characteristics of Hydro-Pneumatic Spring and Impact to Ride Performance of Vehicles. . . . . 1211**  
 F2012-E12-002

Junwei Zhang, Sizhong Chen, Zhicheng Wu, Lin Yang and Bin Zhang

**Simulation Research on Car Suspension Durability Enhancement Test Based on Virtual Proving Ground . . . . . 1223**  
 F2012-E12-003

Zhenglin Cao, Jun Li and Konghui Guo

**Simulation Research on Strong Fluid–Solid Interaction of Hydraulic Engine Mount . . . . . 1235**  
 F2012-E12-004

Zhenglin Cao, Jun Li, Konghui Guo and Qun Zhang

**A Study on Battery Model Verification Using Battery HILS . . . . . 1249**  
 F2012-E12-008

Hyun-Sik Song, Tae-Hoon Kim, Jin-Beom Jeong, Byoung-Hoon Kim,  
 Dong-Hyun Shin, Baek-Haeng Lee and Hoon Heo



**Extended Flexible Environment and Vehicle Simulation for an Automated Validation . . . . .** 1263  
 F2012-E12-010  
 Albert Albers, Rolf Hettel, Matthias Behrendt, Tobias Düser and Alexander Schwarz

**Application of Energy Distribution Analysis During the Vehicle Development . . . . .** 1275  
 F2012-E12-012  
 Yongsheng Long, Jianpeng Shi, Li Xin, Xueen Zhang, Jun Wang and Shaoju Qu

**Simulation and Correlation of Commercial Axle Banjo Housing Fracture Under Braking Fatigue Test . . . . .** 1287  
 F2012-E12-013  
 Ajay Guddeti and Abhijit Nilangekar

**Development of a Vehicle Simulator Based on a Real Car for Research and Education Purposes . . . . .** 1301  
 F2012-E12-015  
 Zsolt Szalay, Péter Gáspár, Zoltán Kánya and Dávid Nagy

**Early Verification of Complex Distributed Systems Using Model Driven Development and Virtual Engineering . . . . .** 1313  
 F2012-E12-020  
 Lance Brooks, Jun Wu and Darrell Teegarden

**Research in the Impact of Curtain Airbag Deployment on Interior . . . . .** 1327  
 F2012-E12-021  
 Shuyuan Zhou, Liangming Xiang, Jie Lou, Wenwei Zhang and Min Xu

**Multi-Domain Modeling and Simulation of Automotive Air Conditioning System Based On Modelica . . . . .** 1337  
 F2012-E12-024  
 Jing Li, Yunqing Zhang and Wei Chen

**Predictive Energy Management Strategies in Virtual Driving Tests: Early Evaluation of Networked Controller Functions in Realistic Use Cases . . . . .** 1351  
 F2012-E12-027  
 Andreas Kunz, Bernhard Schick and Steffen Lange

<b>Evaluation of Video-Based Driver Assistance Systems with Sensor Data Fusion by Using Virtual Test Driving . . . . .</b>	1363
F2012-E12-028 Bernhard Schick and Steffen Schmidt	
<b>Vehicle Warm-Up Analysis with Experimental and Co-Simulation Methods. . . . .</b>	1377
F2012-E12-029 Daniel Ghebru, Christian Donn, Wolfgang Zulehner, Heiko Kubach, Uwe Wagner, Ulrich Spicher, Wolfgang Puntigam and Klaus Strasser	
<b>Modelling and Simulation of AMT Truck Clutch Actuating Mechanism . . . . .</b>	1391
F2012-E12-030 Yanying Guo, Xintian Lu, Tao Yan and Zhonghui Sun	
<b>Vibration Fatigue Analysis of Adaptive Front Lighting System. . . . .</b>	1401
F2012-E12-031 Yeon Gyoo Lee, Seungryul Choi and Tae Ryong Jeon	
<b>Application of Two-Chamber Muffler to Reduce Car Noise in Engine Intake System . . . . .</b>	1411
F2012-E12-040 Zhihong Tang, Zhenying Zhu, Yongxin Men and Fuquan Zhao	
<b>Ergonomic Simulation and Optimization During the Body Assembly . . . . .</b>	1419
F2012-E12-041 Yanjun Gao, Xianbo Wei, Beifang Ma, Yang Yu, Xingmin Wei and Fuquan Zhao	
<b>Test and Analysis of the Mechanical Properties for Laser-Welding Seams and Spot-Welding Joints . . . . .</b>	1429
F2012-E12-046 Liling Zhang, Xuefeng Chen, Qing Jiang and Xu Wang	
<b>Aerodynamic Design and Numerical Simulation Analysis of a Passenger Car's Defrosting Duct. . . . .</b>	1441
F2012-E12-048 Bo Yang, Li-na Huang and Fengtao Ren	

**An Operating System for the Optimization of Technical Systems Using the Example of Transmission Calibration . . . . .** 1449  
 F2012-E12-051  
 Albert Albers, Alexander Schwarz, Matthias Behrendt and Rolf Hettel

**Model Structure, Realization and Learning Process For a Driver Model Being Capable to Improve Performance with Learning by Itself . . . . .** 1461  
 F2012-E12-052  
 Kazuhide Togai and Hisashi Tamaki

**Part XIII Virtual Design, Testing and Validation**

**The Suspension Optimization of FSAE Racing Car Based on Virtual Prototyping Technology . . . . .** 1481  
 F2012-E13-002  
 Jun Ni, Sizhong Chen and Zhicheng Wu

**The Study of the Impact of Aluminum Formability Parameters on its Stamping Formability . . . . .** 1491  
 F2012-E13-003  
 Jian Zhang, Mingtu Ma and Hongzhou Lu

**Calculation of Shrinkage Rate for Injection Molding Based on Moldflow . . . . .** 1501  
 F2012-E13-007  
 Fangcheng Xiao, Lei Chen and Xiao Wang

**A Study of Contact Condition in Vehicle Transmission Virtual Assembly System . . . . .** 1511  
 F2012-E13-010  
 Yan Chen, Shouwen Yao and Fei Liu

**The Multi-Properties Modeling Technologies of Virtual Assembly for Vehicle Transmission Based on the Design . . . . .** 1521  
 F2012-E13-011  
 Fei Liu, Qingdong Yan, Shouwen Yao and Xin Zheng

**New Technologies in Driving Dynamics Performance Simulation . . .** 1531  
 F2012-E13-012  
 Cibrario Valerio and Cugnon Frederic

**Transmission System Design and Manufacture in FSC Racing Vehicle. . . . . 1551**  
 F2012-E13-014  
 Zhenpo Wang, Changfu Zou, Lei Yue and Lei Zhang

**Parallel Design Optimization of Articulated Heavy Vehicles with Active Safety Systems . . . . . 1563**  
 F2012-E13-015  
 Manjurul Md. Islam, Steve Mikaric, Yuping He and Thomas Hu

**The Application of Dual Limit Analysis Method in Physical Performance Characteristics Defining and Structural Designing . . . . 1577**  
 F2012-E13-016  
 Chi Luo

**Predicting Battery Pack Thermal and Electrical Performance in a Vehicle Using Realistic Drive Cycle Power Profiles . . . . . 1587**  
 F2012-E13-017  
 Allen Curran and Scott Peck

**Virtual Test Drive in the Application Process of ESP®-Systems to Ensure Performance and Robustness. . . . . 1595**  
 F2012-E13-019  
 Albert Lutz, Fabien Macaire and Walter My

**The Test and Analysis of Car’s Brake Noise. . . . . 1611**  
 F2012-E13-020  
 Qinghai Sui

**Thermal Management Simulation of Passenger Car with Naturally Aspirated and Turbocharged Gasoline Engine . . . . . 1621**  
 F2012-E13-021  
 Haie Chen, Hongzhou Li, Xinxin Dai, Qun Chen and Kang Li

**Part XIV Testing of Components, Systems and Full Vehicle**

**Research on User Vehicle Operation Regularity . . . . . 1643**  
 F2012-E14-008  
 Zhonggao Yu, Yutan Zhang, Yonghong Xu, Gan Chen, Jianguang Zhou, Jianxian Chen and Jie Bai

**Acoustic Mode and Structure Mode Analysis of Heavy Duty Truck Muffler** . . . . . 1655  
 F2012-E14-011  
 Guoquan Wang, Cheng Zhao, Liangcheng Zhang and Yong Chen

**Transient Thermal Measurement of Electronic Components and Radiometric Characterization of LEDs** . . . . . 1669  
 F2012-E14-013  
 Boris Marovic and Alexandra Francois-Saint-Cyr

**Maneuver-Based Testing of Integrated, Highly Interconnected Safety Systems** . . . . . 1677  
 F2012-E14-019  
 Kathrin Sattler, Andreas Raith, Thomas Brandmeier, Christian Schyr and Daouda Sadou

**Studying of Instantaneous Emissions Character for Hybrid Electric Vehicle** . . . . . 1691  
 F2012-E14-024  
 Yanxin Nie, Baocheng Du, Peng Wan and Jingsi Xie

**Effect of Cryogenic Treatment on Retained Austenite and Fatigue Life of Gcr15 Wheel-Hub Bearing** . . . . . 1701  
 F2012-E14-025  
 Qiucheng Wang, Xiaobin Ning, Qi Chen and Bintao Mao

**A Study on Analysis Method of Motion Characteristics in the Crash Test Based on Computer Vision** . . . . . 1709  
 F2012-E14-029  
 Guohua Cao, Gang Han, Weiguo Liu and Fuquan Zhao

**Study of Optimized Tuning in Full AFLS Head Lamps** . . . . . 1719  
 F2012-E14-031  
 Doohyun Kim

**Improvements in Test Protocols for Electric Vehicles to Determine Range and Total Energy Consumption** . . . . . 1733  
 F2012-E14-032  
 Juhani Laurikko, Jukka Nuottimäki and Nils-Olof Nylund

**New AMFM Test Method with Android Operation System** . . . . . 1745  
 F2012-E14-038  
 Yongqing Zhu, Kerun Xu, Lubing Zeng, Minjie Tian and Chendong Wang

**Part XV Subjective and Objective Evaluation of Performances**

**Ergonomic Evaluation System for Vehicle Package. . . . . 1755**

F2012-E15-001

Shihai Li, Yongqing Liu, Zhongxian Chen, Mengdong Mi, Hao Chen,  
Weiwei Du, Tingchuan Song and Huang Jian

**Subjective and Objective Vehicle Tests, Two Parallel**

**Vehicle Handling Evaluations . . . . . 1767**

F2012-E15-004

Eric Chabrier and Michel Grima

**Subjective Evaluation and Modeling of Human Ride Comfort of  
Electric Vehicle Using Tools Based on Artificial Neural Networks. . . 1777**

F2012-E15-005

Lerspalungsanti Sarawut, Albers Albert and Ott Sascha

**Torque Vectoring Control Design Based on Objective**

**Driving Dynamic Parameters. . . . . 1787**

F2012-E15-006

Michael Graf and Markus Lienkamp

**Integrated State Estimation with Driving Dynamic Sensors  
and GPS Data to Evaluate Driving Dynamics Control Functions. . . 1797**

F2012-E15-013

Markus Bauer, Carlo Ackermann and Rolf Isermann

**Evaluation Tool for Current and Future Powertrains. . . . . 1807**

F2012-E15-016

Barak Adam

**Part XVI Other**

**Wet Handling Track: Utilities, Water System, Coefficient  
of Adherence. . . . . 1825**

F2012-E16-005

Pinilla Marc, Carbonell Abel and Arango Luz A

**The Development of an Auxiliary Unloading Device  
for Dump Trucks . . . . . 1837**

F2012-E16-006

Guoxing Li and Tie Wang

**Part I**  
**Vehicle Performance Development**

# A New Approach to Improve the Design Quality of Chinese National Brand Vehicle

Du Cao, Jing Deng and Fengfei Fu

**Abstract** With the rapid development of China's automotive industry, improving the vehicle design quality has become a serious challenge to the Chinese OEM's. Using some effective quality analysis tools and methods, this paper demonstrates how to convert customers' subjective demands into feasible engineering design solutions; thereby improving vehicle design quality. The paper also explores how to predict achievable design quality targets for vehicle development. A new approach is proposed for design quality improvement of Chinese national brand vehicles. JD Power quality evaluation methods have identified the major differences subjectively between Chinese national brand vehicles and international (JV) brand vehicles. But, the identified issues need to be classified into specific engineering design quality problems. By means of a competitive benchmark analysis, specific customer issues can be analyzed and ranked. Then, DFMEA, QFD and other technical tools are used to prevent the occurrence of vehicle design quality defects. Furthermore, the solvable and unsolvable design quality problems are summarized and counted during early design stages. The vehicle design quality targets are accordingly predicted and precisely set up. Through the methods mentioned above, many design quality problems that have occurred in previous vehicle programs can be solved, and the quality targets for new vehicle development programs can be predicted at an early stage. This systematic approach minimizes potential shortcomings of a vehicle design and development process which is traditionally based on individual engineer's experience. Young and relatively inexperienced engineers are provided with a clear process for avoiding

---

F2012-E01-004

---

D. Cao (✉) · J. Deng · F. Fu  
Changan Auto Global R&D Center, Changan Automobile Co. Ltd., Chongqing, People's Republic of China  
e-mail: sunqiemail@163.com



future design quality problems. Implementation of such a product development process provides a new approach that can rapidly improve the design quality of Chinese national brand vehicles.

**Keywords** New approach · Vehicle design · Improvement · Quality problems · Quality assessment

## 1 The Development of Chinese Vehicles Market

By the end of 2011, there are over one billion vehicles in use all over the world, while over eighty million vehicles in use in China. Chinese vehicle sales has been keeping number one in sales marketing since 2009. It has reached over eighteen million vehicle sold in 2011. But the demands of thirty million vehicles sales needed and four hundred and five million vehicles in use for Chinese auto market are forecasted in 2011.

With a rapid expanding of Chinese vehicles market, the vehicles selling of the national brand name has grown quickly in last 10 years. It takes more and more shares in the percentage of Chinese auto market sales pie [1–3]. It is noticed that most Chinese national brand vehicles are sold in the low price area of this pie and the increase rate in sales slows down or even shrank in the last year (Fig. 1). How to improve its quality for the increase in value and customer satisfaction is a challenge to Chinese auto makers in recent years.

## 2 The Current Situation of Chinese National Brand Vehicle Quality

There are some evaluations of the vehicle quality directly from customers, for example, JD Power and consumer feedback report. It is well known that JD power is the good index for the customer opinion. IQS, as “things go wrong” index in the JD Power, reflects the quality issues of customer concerning [4–6].

There is the quality gap for the IQS between Chinese national brand vehicles and international (JV) brand vehicles (Fig. 2) and no improvement especially in recent years. How to improve the vehicle quality during the vehicle development? This paper intends to find a new approach to improve Chinese brand vehicle quality and narrow the gap between Chinese and international vehicle brands.

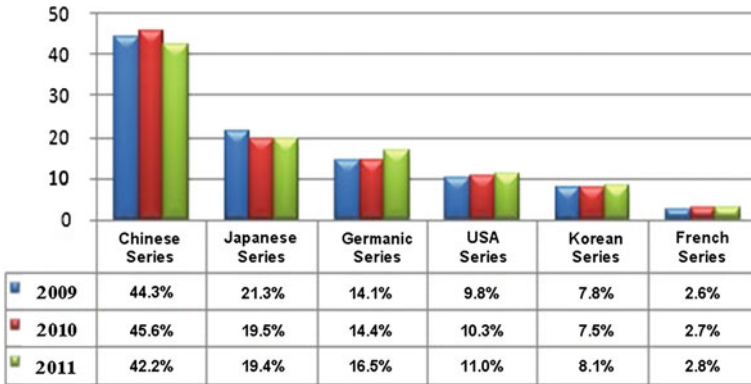


Fig. 1 The possession of vehicle market in last 3 years

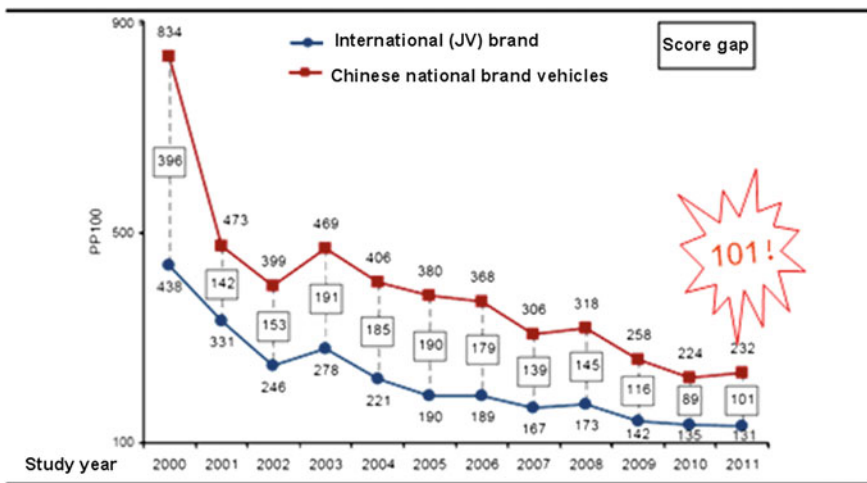


Fig. 2 The quality gap between Chinese national brand vehicles and international (JV) brand vehicles

### 3 Vehicle Quality Assessment

Generally speaking, there are two aspects for the vehicle design quality, subjective and objective qualities (Fig. 3). The objective quality includes material selection, design quality, and production control implemented by engineers. While the subjective quality normally is a describing issue for customer perception, such as convenience and comfort from four aspects: vision, touch, smell, and hearing, as described in Fig. 3. The evaluation of IQS comes from customer subjective demands.

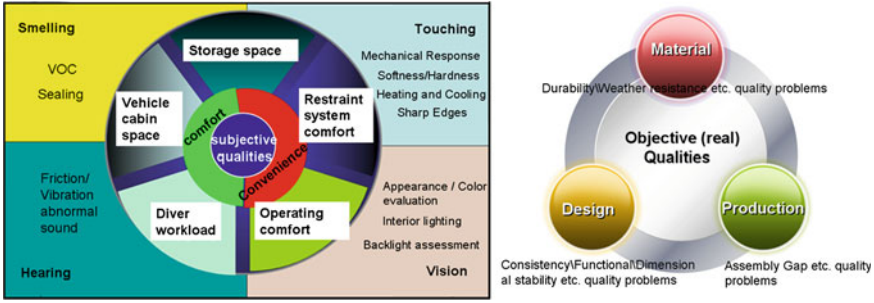


Fig. 3 The factors of subjective and objective qualities

First, we have to know what the customer demand or the quality from view of the customers are; Second, how to convert customers’ subjective demands into feasible engineering design solutions; Third, how to evade identified problems at the early design stage. Furthermore, we may predict what our new improved vehicle performance could be in the market quantitatively.

### 4 The Way to Convert Subjective Quality Demands Into Objective Solutions

With regard to the subjective quality, the identified issues collected from IQS can be unscrambled and classified into specific engineering design quality problems by engineers. Also, specific customer issues can be analyzed and ranked, so called “top issues”. Following flow chart (Fig. 4) describes the procedure of subjective evaluating classification for a “face-lifting” which means a re-design launched vehicle. The diamond frame in the flow chart is a feasible or balancing judgment for a technical execution based on the following factors: (1) Problem importance; (2) Cost; (3) Technical feasibility; (4) Timing; (5) Difficulty and so on. According to the flow chart, we can also re-evaluate and forecast the score of IQS for a new “face-lifting” vehicle performance before its launching. For a brand new vehicle development, we can collect IQS information from the similar vehicles and follow the same flow chart below for both a technical feasibility study and IQS score forecast of the simulation.

There are three aspects for a vehicle design quality: perceptive quality, functional quality, and reliability. The information from JD Power can cover most of these aspects (Fig. 5). In order to translate and break down the subjective evaluations into different systems, we have to identify each customer’s description for a specific engineering problem.

As an example, the following charts (Table 1) from JD Power show the statistical figures of the IQS (PP100) for rough problem classification, problem ranking, ranking comparison etc.

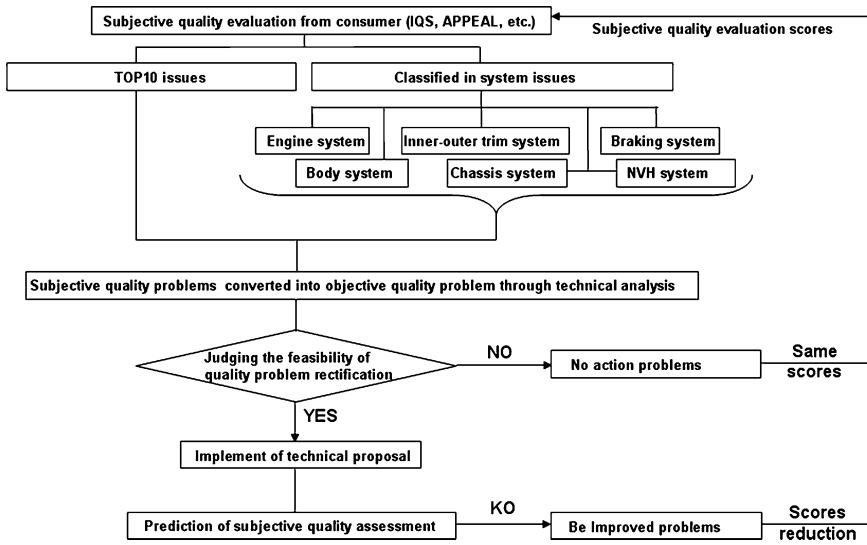


Fig. 4 The flow chart of the way to improve the quality of vehicle

Fig. 5 Three aspects for a vehicle design quality

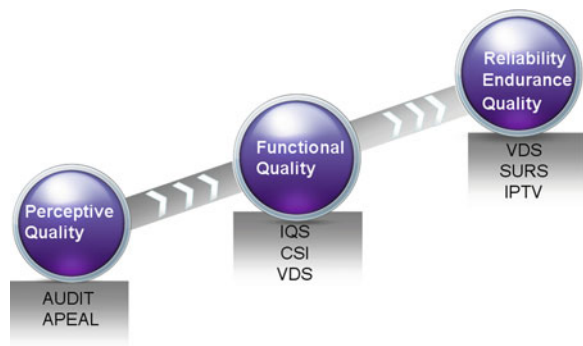











Table 2 ranks the top ten issues based on the scores shown in the last column of Table 1 for the national brand vehicle.




Each problem is further sorted out for a specific engineering system in the Table 1. Some description of problems, such as item 9, may be semantic ambiguity, which needs a further marketing investigation. Furthermore, different color marks are stamped for the technical execution. The solvable and unsolvable design quality problems are summarized and counted during early design process. The vehicle design quality targets for IQS score are accordingly predicted and precisely set up:

**Table 1** Classifying PP100 problem to system

	CHN_2011IQS	USA_2011IQS	IND_2010IQS	TH_2010IQS
The general situation	162	107	142	106
Fault & Hard operative	103	52	89	71
Design flaws	52	49	46	19
	<b>44</b>	15	<b>42</b>	18
Engine & transmission problems	36	12	26	22
Appearance of the vehicle outer trim	25	<b>17</b>	28	<b>28</b>
Driving experience	17	10	15	11
Vehicle inner trim	16	<b>17</b>	13	9
Automotive air conditioning systems	13	12	9	7
Control/instrumentation	6	15	<b>3</b>	7
Seat	<b>5</b>	<b>8</b>	7	<b>4</b>

**Table 2** The top ten issues

No.	Customer concerns	System	Maneuver ability	Current level	Average level	score change
1	Rough gear meshing	Engine/transmission		12.0	6.3	-4
2	Fuel consumption too high	Power train		7.4	3.1	-3
3	Less engine power as A/C on	Engine/transmission		8.9	4.1	0
4	Abnormal engine noise	Engine		6.2	3.4	-3
5	Braking noise	Braking		6.7	5.2	-1
6	Cooling un-satisfaction	A/C system		5.1	3.5	-2
7	A/C blowing noise	A/C system		5.7	4.1	-3
8	Vehicle pull and drift	Chassis		4.5	2.7	-2
9	Unpleasant driving experience			3.8	3.1	0
10	Wiper out of control	Electric		3.6	1.5	-2

-  Red: Technical difficulty or cost inflation—not to implement;
-  Yellow: Technical difficulty—partially improvement;
-  Green: To be solved

Then, DFMEA, QFD and other technical tools are used to prevent the occurrence of vehicle design quality defects. Here is an example, “8D”, one of an engineering analyzing technical tools, is used for the second item of the top ten issues (Table 3).

By means of a competitive benchmark analysis, other identified system issues from JD Power are also classified into specific engineering design quality problems. These problems can be analyzed and ranked accordingly. Following is the example of the problems for interior trims (Table 4).

**Table 3** 8D solves the quality problem

Work steps	Work content
1 Describe the problem	(1) According to the feedback of after-sale department, fuel consumption is too high (2) The score of problem is 7.4 from the IQS, which is much higher than the average score
2 Use a team	–
3 Implement and verify short-term corrective actions	(1) Improving engine performance through CAE simulation analysis (no obvious effect) (2) Engine speed ratio optimization (which relates to the vehicle system development, will cost a long research cycle and have a large difficulty in technical) (3) No temporary measures could be used to solve the problem.
4 Define and verify root causes	(1) Poor engine performance (2) Engine speed ratio matching unreasonable (3) Driving resistance is larger than competitive models (4) Electronically controlled matching is unreasonable
5 Verify corrective actions/implement and validate corrective actions	(1) Increasing engine load to improve engine speed ratio (cost: ¥1200)
6	(2) Replacing tires and reducing the weight of vehicle to improve the driving resistance (cost: ¥350–400) (3) Optimizing electronic control calibration through optimal driving resistance curve to improve electronically controlled matching (cost: ¥100–150)
7 Take preventive measures	(1) Research the way to improve engine performance (2) Control the weight of whole vehicle (3) Focus on wind resistance problem (4) Promoting the application of new technologies
8 Congratulate your team	(1) Reach the target of quality problem rectification (2) Obtained a set of analysis methods and workflow to solve the fuel consumption is too high

Some effective quality analysis tools and methods, such as DFMEA, Check list, DVPR, Fishbone analysis and so on, may be applied to convert customers' subjective concerns into feasible engineering design solutions, thereby improving vehicle design quality. DFMEA is used as following example (Table 5):

DFMEA, as a powerful technical tool, can convert a customer concern into possible engineering failure modes. It should consider failure causes from cycle usage, environmental exposure, and component/system interactions. Risk Priority Number (RPN) values should be analyzed. Actions to manage and/or mitigate the impact of failure modes should be implemented for high RPN and/or high severity failure modes. DFMEA action item closure should be implemented prior to the manufacturing. It has to prove that the problems have been eliminated through appropriate design controls for an improvement in the design under engineering

**Table 4** Classify system quality problems (inner trim)

No.	Customer concerns	System	Maneuverability	Current level	Average level	Confirm Rectification plan	score change
1	Interior easily dirty /	Inner trim system		7.2	3.9	Y	-5
2	Foot mats would be slip			3.75	2.6	Y	-3.75
3	Door trim panel - gap / unable to fit well			1.0	0.4	Y	-0.5
4	IP system : squeak and rattle			4.0	0.3	Y	-2
5	Console - damaged & abnormal sound			1.3	0.4	Y	-1

**Table 5** DFMEA of inner door trim (part)

No. SYSTEM		POTENTIAL FAILURE MODE AND EFFECTS ANALYSIS (DESIGN)										FMEA 编号: _____					
Inner & Outer trim COMPONENT		DESIGN RESPONSIBILITY										设计 审核 日期					
COMPONENT: Inner_door_trim		DESIGN RESPONSIBILITY										PREPARED BY: _____					
PART NUMBER: _____		REV DATE: _____										FMEA DATE: _____					
CORE TEAM												FMEA DATE (rev): _____					
FUNCTION /REQUIREMENT	POTENTIAL FAILURE MODE	POTENTIAL EFFECTS OF FAILURE	DEV	CLASS	POTENTIAL CAUSE(S) /MECHANISM(S) OF FAILURE	OCC	CURRENT DESIGN CONTROLS	DETECT DESIGN	DET	RPN	RECOMMENDED ACTION(S)	RESPONSIBILITY TARGET COMPLETION DATE	ACTION RESULTS				
													S	O	D	RPN	
1. Decorative effect of vehicle interior 2. A sense of vehicle quality	The gap between door trim and door is too large or non-uniform	1. Poor appearance 2. Customer dissatisfaction	5	I	The stiffness of door trim is low, door trim is easily to warp. The position of fixing point is not proper. The section of door trim connecting to the door is not proper. Due to the mistake on design of COMT, clips is not mounted properly.	5 3 4 6	Design review and benchmark	DMD	3	75							
	The stiffness of door trim is low		5		There is no connecting structure between door and door trim at the center of door, so the position of connecting struc is not proper. The rib of door trim takes no effect. The bending stiffness of material is low	5 3	Design review and benchmark Material approval	DMD DVP	7 3	175 45	Design department 2007.12.30	add ribs	5	2	2	20	

review. With the same procedure of the flow chart (Fig. 4), many design quality problems that have occurred in previous vehicle programs can be solved, and the quality targets for new vehicle development programs can be predicted at an early stage.

### 5 Prediction of Subjective Quality Assessment

Based on the flow chart (Fig. 4), a prediction of total improved IQS score for a new vehicle can be set as the following chart (Fig. 6). The major problems are shown with different color marks. The subtraction of IQS score for an improvement of each system is also shown in the chart. Thus, a new target score for IQS is forecasted.

As shown in Fig. 6, the original IQS score is 250 based on the average similar vehicle investigation; an improved IQS for a new vehicle could be 185 if the quality problems with green and yellow marks could be improved.

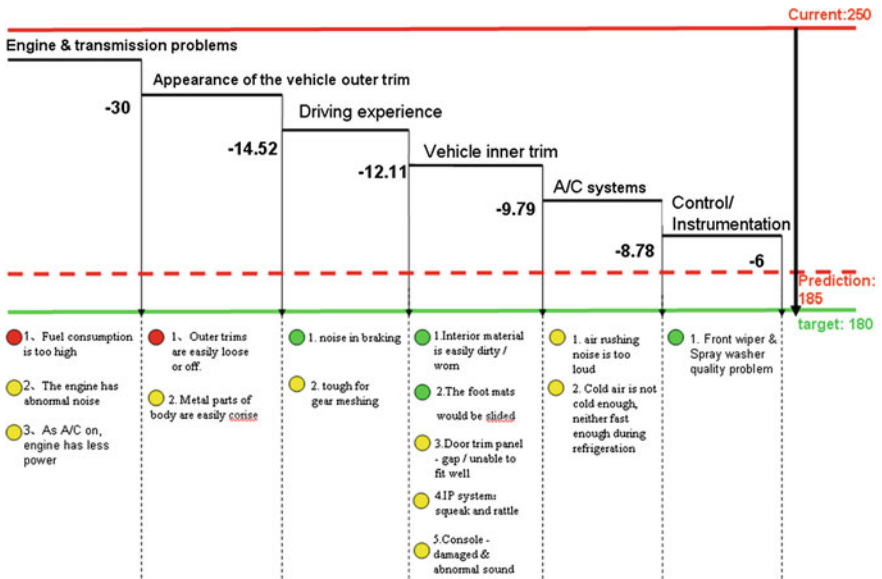


Fig. 6 Forecasting the subjective assessment

## 6 Improving the Design Quality is the Only to Develop Chinese Brand Vehicles

According to the quality improvement analysis path, with the help of technical tools, the main vehicle development problems can be solved in the early stage of the design process. This systematic approach minimizes potential shortcomings of a vehicle design and development process which is traditionally based on individual engineer’s experience. Young and relatively inexperienced engineers are provided with a clear process for avoiding future design quality problems. Therefore, the implementation of such a product development process provides a new approach that can rapidly improve the design quality of Chinese national brand vehicles.

### References

1. Weber J (2009) Automotive development process. Springer, Berlin, pp 80–100
2. JD Power Asia Pacific, Initial Quality Study Report, 2011.11
3. Liu D, Liu E (2011) Chinese local brand vehicles development status, brand and security, 2011.4



4. Li W (2011) Chinese auto market trend analysis, cooperative economic and technology, 2011.10
5. Qiu W (2011) A approach to solve early quality problems, Chinese automotive engineering annual meeting, 2011.10
6. Cao L (2011) A set survey about JD. Power, the home of automotive, 2011.8

# The Process of Vehicle Dynamics Development

Zhanglin Cai, Stephen Chan, Xiaofeng Tang and Jiang Xin

**Abstract** Automobile production in China is now ranked first in the world. As the market matures, vehicle users become more demanding on vehicle performance. Vehicle dynamics performance is directly related to drivers' ride and handling experience. The process of optimizing ride and handling has long been a challenge faced by chassis engineers. This article provides a comprehensive view of vehicle dynamics development for typical passenger vehicles. It focuses on the development work for suspension system before hardware is procured. The definition of vehicle dynamics is also explained in the first part of the article as background information.

**Keywords** Vehicle dynamics · Development process · Ride and handling · Simulation analysis · Suspension

Vehicle dynamics development is generally divided into three major phases:

- The first phase is to set the performance goals. Target setting is based on design experience of the vehicle development team as well as translating market requirements, or voice of the customers, into vehicle dynamics requirements. Typically vehicle dynamics specifications include ride, handling, and braking. During this phase of development, a lot of benchmark objective testing as well as subjective assessment are done to provide sufficient information for target setting.

---

F2012-E01-011

---

Z. Cai (✉) · S. Chan · X. Tang · J. Xin  
Pan Asia Technical Automotive Center Co., Ltd, Shanghai, China  
e-mail: zhanglin\_cai@patac.com.cn

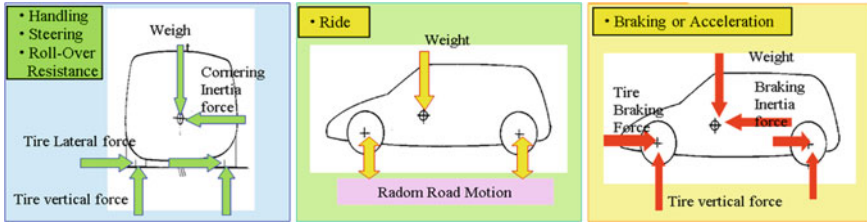


Fig. 1 Three aspects of vehicle dynamics

- The second phase is to develop the subsystem requirements from the vehicle dynamics specifications. The subsystem-level synthesis and performance tests are required in this stage to provide data to support subsystem target setting.
- The third phase is to transform the subsystem specification into component design parameters. This requires more precise simulation modelling tool for analysis in order to understand the design parameters of the key chassis components effect on overall vehicle dynamic performance. The result of this phase is to provide the component design requirements for the component level suppliers.

Once the hardware prototype is procured, in both vehicle level and component level, chassis tuning work begins. The goal is to refine the component specifications while balancing many chassis design parameters in order to meet the vehicle specifications. Although the second and third phases of the process are done early in the development, it is normal to iterate the process until an optimum design is completed. The specifications are occasionally modified as the vehicle program progresses, especially during the vehicle prototype phase of the development process. This can be caused by durability issues, simulation model discrepancy with actual performance, or marketing new trends.

In order to illustrate this process, roll dynamics is used as an example in this article. From determination of roll gradient to developing of front and rear roll stiffness, and roll stiffness to suspension component specifications.

## 1 What is Vehicle Dynamics?

Vehicle dynamics refers to the directional performance and dynamics of road vehicles, and typically vehicle dynamics is based on classical mechanics.

Vehicle motions are mostly due to the forces generated between the tires and road, and aerodynamics effects. In this article, the main focus is on suspension design and development, and aerodynamics effects are not considered. The tire forces can be divided into three directions: lateral, longitudinal, and vertical. Hence, vehicle dynamics performance can be divided into three aspects according to the force direction [1], see Fig. 1.

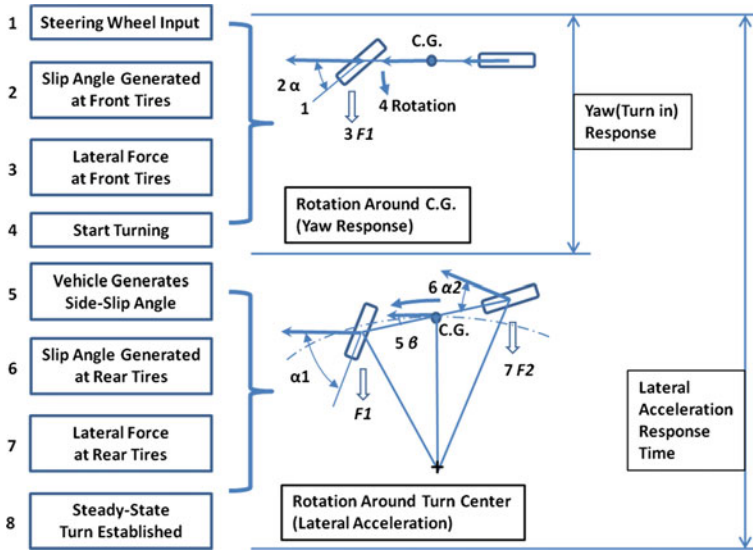


Fig. 2 Vehicle cornering sequence

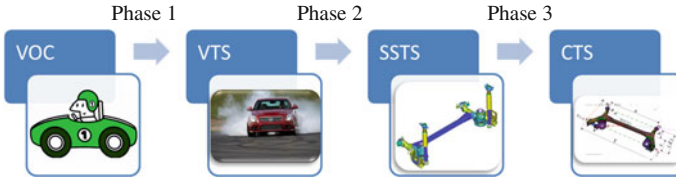
- Lateral dynamics: examples are handling, steering response, and roll-over resistance.
- Longitudinal dynamics: examples are acceleration and braking performance.
- Vertical dynamics: examples are ride and pitch performance.

Take lateral dynamics as an example, the response sequence from a step steering input can be broken down into steps as shown in Fig. 2.

## 2 Vehicle Dynamics Development Process

Vehicle dynamics development process generally defined as the development work done before the prototype vehicle is produced. It is generally divided into three phases as shown in Fig. 3:

- Phase 1: VOC to VTS (Voice of Customers to Vehicle Technical Specifications)  
The first phase is to set the performance goals. Target setting is based on design experience of the vehicle development team as well as translating market requirements into vehicle dynamics requirements. Typically vehicle dynamics specifications include as ride, handling, and braking. This phase requires a lot of benchmark objective testing as well as subjective assessment to support target setting.
- Phase 2: VTS to SSTS (Vehicle Technical Specifications to Subsystem Technical Specifications)



**Fig. 3** Vehicle dynamics development process

The second phase is to develop the subsystem requirements from the vehicle dynamics specifications. The subsystem-level synthesis and performance tests are required in this stage to provide data to support subsystem target setting.

- Phase 3: SSTS to CTS (Subsystem Technical Specification to Component Technical Specifications)

The third phase is to transform the subsystem specifications into component design parameters. This requires more precise simulation modelling tool for analysis in order to understand the design parameters of key chassis components effect on overall vehicle dynamic performance.

## 2.1 First Phase: From Voc to VTS

The first phase is the setting of performance goals. In addition to the development team visions and past experience on the vehicle performance targets, understanding of the voice of the customers and marketing trend are also key factors in setting vehicle performance targets. This is illustrated below in Table 1: VOC items regarding handling and ride are listed in the left column. VTS performance metrics are listed in the top row. Through the process of completing the Quality House table, the important VTS metrics can be identified.

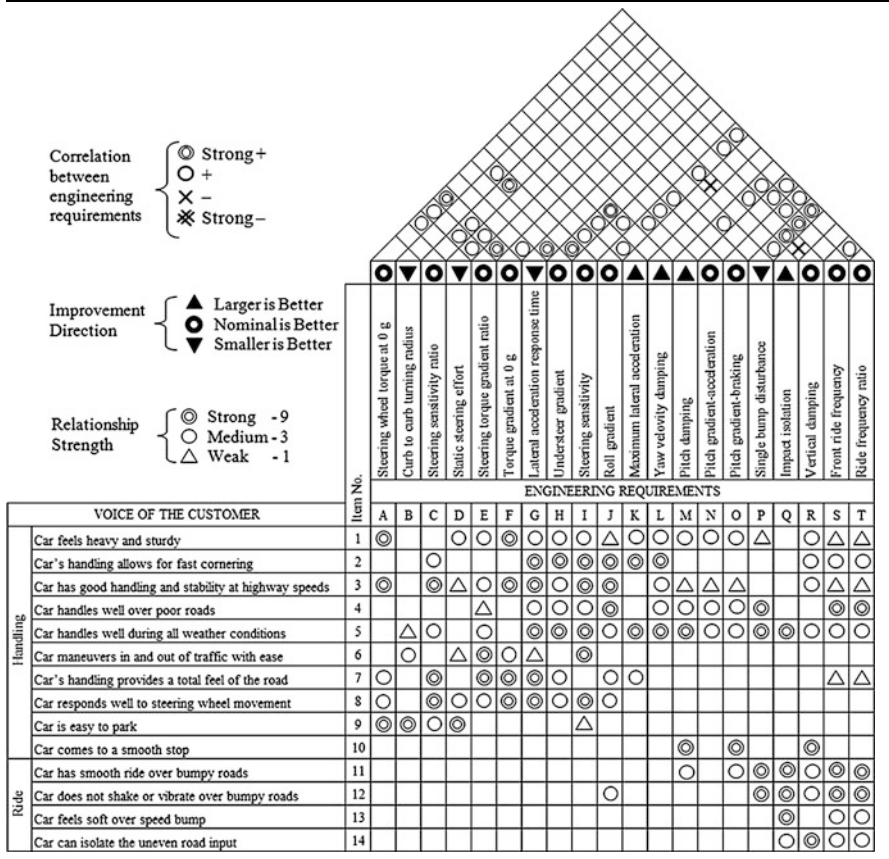
Based on the results above, some of the VTS metrics are more influential on VOC than others. However, it is important to select the representative VOC metrics and VTS metrics when using the Quality House analysis.

## 2.2 Second Phase: From VTS to SSTS

The second phase is to develop the subsystem requirements (SSTS) based on the vehicle dynamics specifications (VTS), see Fig. 4. The subsystem-level synthesis and performance tests are required in this stage to provide data to support subsystem target setting.

Roll gradient is used as an example here to illustrate the VTS flow down process.

**Table 1** Quality house showing the relationship between VOC and VTS



Based on input from benchmarking study and development team input, the VTS roll gradient target for a new compact passenger vehicle is  $\leq 5$  deg/g.

The roll gradient is contributed by the front and rear suspension roll stiffness. While achieving the roll gradient of  $\leq 5$  deg/g, the limit handling performance requirement has to be met. The stability at the limit handling condition (typically greater than 0.6 g lateral acceleration) is an important factor in vehicle handling. The front roll stiffness and rear roll stiffness have to be balanced correctly. This is typically done by selecting a Tire Lateral Load Transfer Distribution (TLLTD). In this case the TLLTD is selected to be 60 % to ensure stable cornering at the limit.

In this case, the basic vehicle information is listed below:

- Mass 1,040 kg
- Mass Distribution 61 % Front
- Roll-Center Height Front 55 mm, Rear 150 mm
- TLLTD Requirement 60 %
- Roll Gradient  $\leq 5$  deg/g

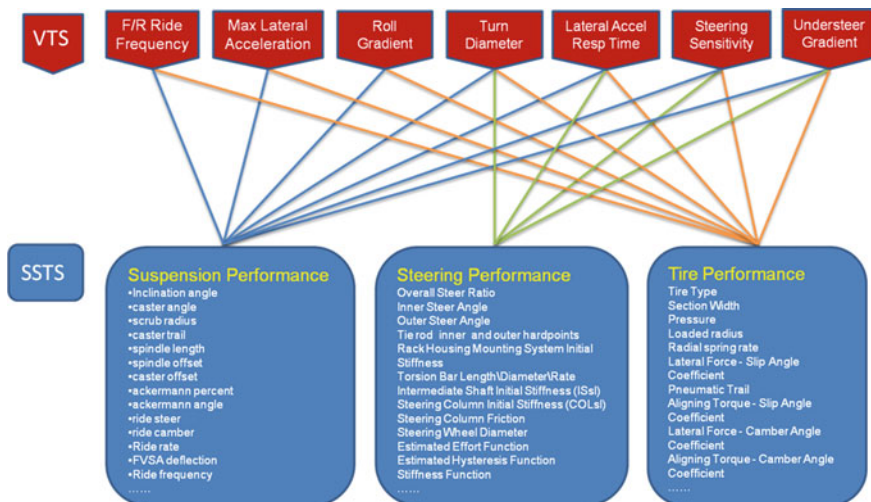


Fig. 4 Flow down from VTS to SSTS

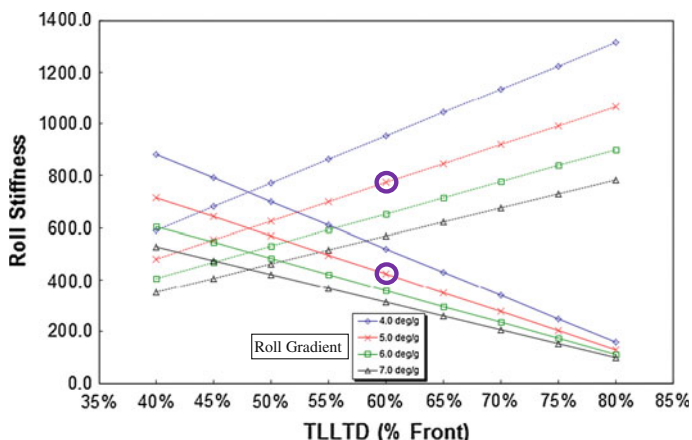


Fig. 5 Front and rear roll stiffness vs. TLLTD

Figure 5 shows the output from a synthesis tool showing relationship of the suspension roll and rear roll stiffness vs. TLLTD. In order to meet the design requirements: 780 and 410 Nm/deg are selected (the points with circle) for the front and rear roll stiffness respectively. The front roll stiffness and rear roll stiffness are the part of the suspension subsystem technical specifications.

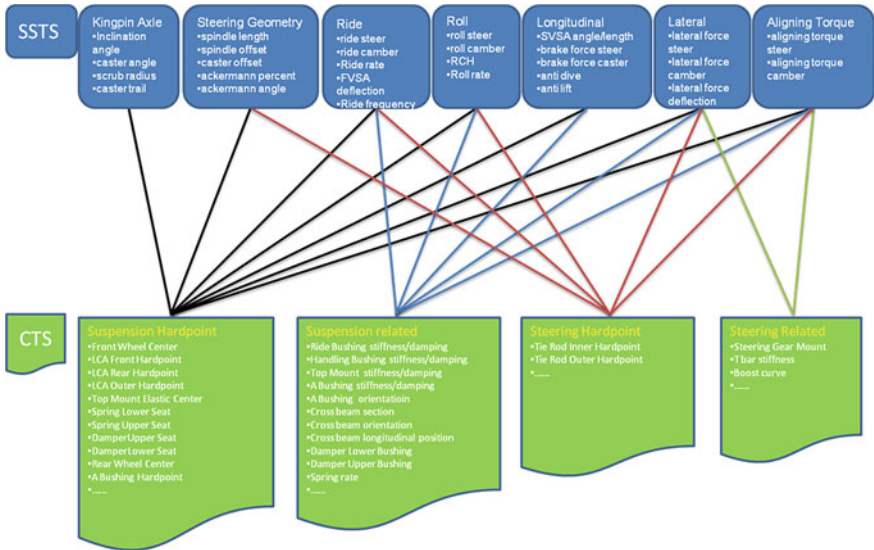


Fig. 6 Flow down from SSTS to CTS

### 2.3 Third Phase: From SSTS to CTS

The third phase of the process is to transform the subsystem specifications into component technical specifications, see Fig. 6. This requires more precise simulation modelling tools for analysis in order to understand the effects of design parameters on performance.

Roll performance is used as an example here to illustrate the SSTS to CTS flow down process.

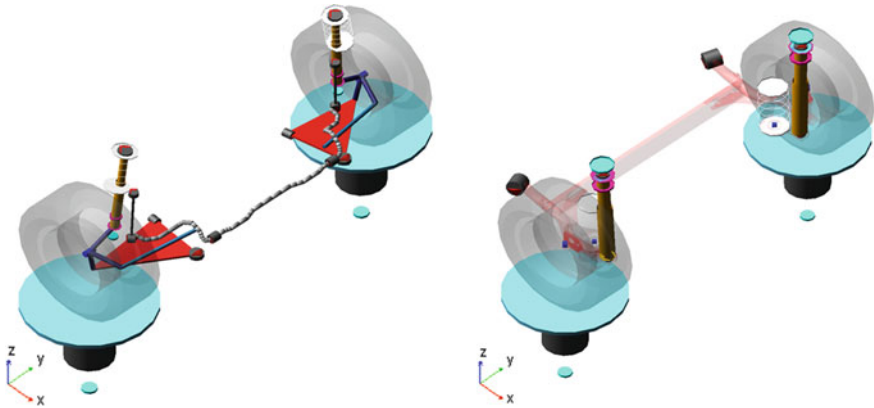
In the second process, the vehicle technical specification of body roll gradient of 5 deg/g is the design target. 780 Nm/deg front roll stiffness and 410 Nm/deg roll stiffness are set as part of front and rear suspension subsystem specifications.

The third phase of the process is to set the design parameters for the front and rear suspensions individual components in order to achieve the roll stiffness while meeting all the other subsystem specifications such as ride rate.

In order to meet the roll stiffness requirements, suspension key parameters such as spring rate, roll-center height, and stabilizer bar size are defined. In the process of defining these key parameters, suspension ride frequency and packaging requirements need to be balanced carefully to obtain an optimum chassis performance.

In order to determine the suspension components specification, suspension simulation model ADAMS [2] is used to determine the roll stiffness of the suspension from the suspension components. Figure 7 shows the ADAMS model of the front and rear suspension of a compact passenger vehicle.





**Fig. 7** Front and rear suspension model

### Suspension Component Specifications to Meet SSTS Requirements:

Spring Rate:	Front 19 N/mm	Rear 18 N/mm
Stab Bar Size:	Front 22 mm	Rear none (solid twist axle)

Once the stabilizer bar mounting point and stiffness are determined, the mount point stiffness requirements have to be provided to the body structure development team as a body structure design criteria.

The first round of the three phases of the vehicle dynamics development is completed. All the component design specifications are defined. Prototypes are then built followed by subjective evaluation and objective testing.

Once the hardware prototype is procured, subjective evaluation and tuning begin. The goal is to refine the component specifications while balancing chassis design parameters to meet the vehicle requirements. Subjective evaluation and objective testing work hand-in-hand with simulation analysis in the prototype development stage. Through this process, a well-balanced chassis performance can be achieved.

## 3 Summary

Due to limited space, only roll dynamics is discussed in detailed. The roll dynamics example is only a small portion of the suspension development based on vehicle dynamics performance. Other areas to be considered including lateral mode dynamic response which is mainly affected by front and rear cornering compliances, and steering response; vertical mode need to be considered including pitch dynamics and ride frequency of the front and rear suspension.

Although the second and third phases of the process are done early in the development before physical hardware is procured. The vehicle level specification, subsystem specification, and component technical specifications are occasionally modified as the vehicle development program proceeds. This can be caused by durability issues, government regulations such as fuel economy requirements, or marketing new trends. New balancing strategies are sometimes applied for the vehicle under development.

## References

Knable J, Leffert R (2008) Understanding vehicle dynamics for passenger cars and light trucks, a general motors vehicle system approach. Knable and Associates, Inc  
ADAMS/CAR user guide, MSC Inc

# Development of Methodologies for Evaluation, Simulation and Improvement of Cross-Wind Sensitivity

Guido Tosolin, Jonathan Webb, Alex Català, Alfonso Escuer and Young Jin Hyun

**Abstract** The sensitivity of a vehicle to cross-wind depends on many factors involving the design of the suspensions and the aerodynamics of the body [1, 2]. However, the knowledge about this phenomenon has still to be improved, in order to develop vehicles with optimum characteristics for cross-wind sensitivity and high-speed stability. Moreover, also the driver perception of the phenomenon is poorly understood. The object of the present study is to improve the global understanding of the vehicle response to cross-wind, focussing on testing procedures, objective/subjective correlation and simulation.

**Keywords** Cross-wind · Side-wind · Metrics · Sensitivity analysis · Simulation

## 1 Introduction

The study wanted to provide a complete knowledge of the cross-wind phenomenon, including assessment, investigation of the most relevant factors and development of design solutions and guidelines. To achieve this result, the following activities have been carried out:

---

F2012-E01-014

---

G. Tosolin (✉) · J. Webb · A. Català · A. Escuer  
IDIADA AT, Tarragona, Spain  
e-mail: guido.tosolin@idiada.com

Y. J. Hyun  
Hyundai Motor Company, Seoul, South Korea



**Fig. 1** IDIADA cross-wind facility

**Table 1** Cross-wind facility technical characteristics

Number of fans	10 units (2.6 height × 2.6 width each)
Length of cross-wind zone	30.5 m
Acceleration line	600 m
Wind speed	Up to 30 m/s
Number of anemometers	5

- Objective and Subjective full vehicle testing on three vehicles in the cross-wind facility of IDIADA.
- Correlation between subjective feeling and objective parameters, to validate specific metrics for evaluation.
- K and C bench testing, to obtain suspension characteristics.
- Creation of a full vehicle model validated with objective test results, specifically for simulation of vehicle response in cross-wind.
- Realization of a sensitivity analysis, with the simulation model, aimed at investigating the influence of several suspension and aerodynamic parameters on the cross-wind sensitivity of the vehicle.

## 2 Subjective Evaluation

The first activity of the project was the subjective evaluation of the three vehicles on the cross-wind facility of IDIADA (see Fig. 1). The characteristics of this facility are summarized in Table 1.

The subjective evaluation was conducted in two phases. During phase one a professional driver performed a preliminary test with the three vehicles on the cross-wind track, under several testing conditions. The objective of this preliminary work was to fix testing conditions and to prepare a simple evaluation sheet, with ratings aimed at capturing different aspects of the cross-wind perception. The evaluation sheet is visible in Fig. 2.

X-WIND EVALUATION SHEET		Date	Vehicle 1		Vehicle 2		Vehicle 3	
			rating	comments	rating	comments	rating	comments
Driver:								
1.1	Side wind sensitivity, over all	120 kph						
1.2	Yaw gain build up							
1.3	Body roll behavior (sudden, linear, surprising?)							
1.4	Steering (wheel) input from X-wind							
1.5	Steering correcting input							
2.1	Side wind sensitivity, over all	140 kph						
2.2	Yaw gain build up							
2.3	Body roll behavior (sudden, linear, surprising?)							
2.4	Steering (wheel) input from X-wind							
2.5	Steering correcting input							
3.1	Side wind sensitivity, over all	160 kph						
3.2	Yaw gain build up							
3.3	Body roll behavior (sudden, linear, surprising?)							
3.4	Steering (wheel) input from X-wind							
3.5	Steering correcting input							

Rating	Perception
1	
2	Safety risk, failure
3	
4	Objection
5	Poor
6	Acceptable
7	Good
8	Very good
9	Excellent
10	Exceptional

Fig. 2 Cross-wind evaluation sheet

During phase two, the cross-wind behaviour of the three vehicles has been evaluated by seven drivers with different levels of experience. The objective was to validate the ratings and to investigate how the phenomenon is perceived by a wide range of drivers.

The drivers had the possibility to drive the vehicles at three different speeds in the cross-wind track. Then they had to evaluate the vehicle response in terms of global side wind sensitivity, yaw rate build up (directional stability), body roll behaviour and reaction on the steering wheel. When passing through the fan areas, they had to actuate the steering handle, trying to maintain a straight line. The path was marked on the track with a line of cones. The speed of the lateral wind was kept constant at 20 m/s in all the repetitions. This speed is also the one suggested by the ISO 12021 [3].

The ratings assigned by all the drivers were then analysed and compared with the ratings of the professional driver. The data were organised in diagrams like the one in Fig. 3. In this figure it is possible to see the level of correlation between the ratings of the various drivers.

This activity proved the validity of the ratings used to assess the cross-wind sensitivity, because it was possible to capture the subjective impression of a wide range of drivers, with a satisfactory level of coherence. The ratings have been reused later, for the correlation between subjective feeling and objective measurement.

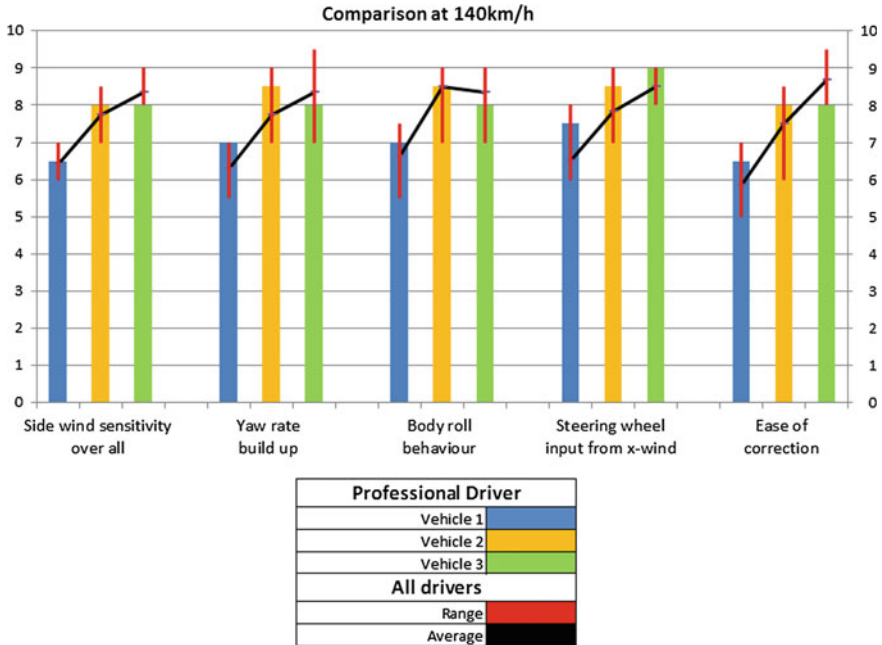


Fig. 3 Comparison diagram for cross-wind evaluation

Table 2 Instrumentation and signals recorded

Sensor	Brand	Signal
GPS platform (RT3100)	Oxford T.	Longitudinal speed
		Lateral speed
		Longitudinal acceleration
		Lateral acceleration
		Vertical acceleration
		Roll angle
		Pitch angle
		Yaw angle
		Roll rate
		Pitch rate
Steering wheel sensor	RMS	Yaw rate position
		Steering angle
		Steering torque

### 3 Objective Measurement

The three vehicles have been equipped for objective measurements with the instrumentation reported in Table 2. In the same it is also possible to see the signals recorded during the tests.

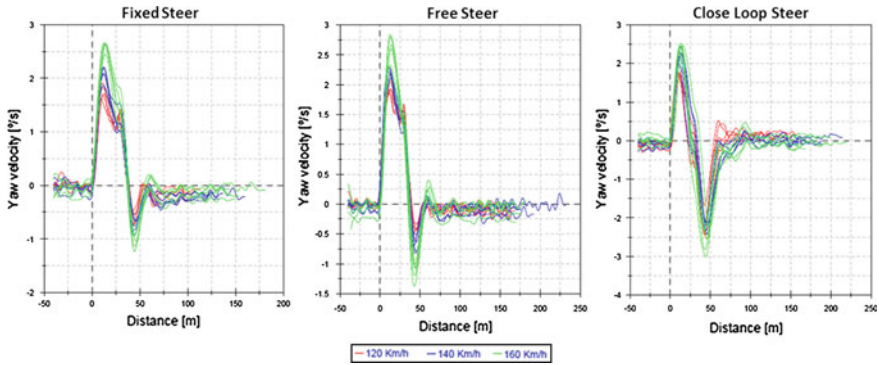
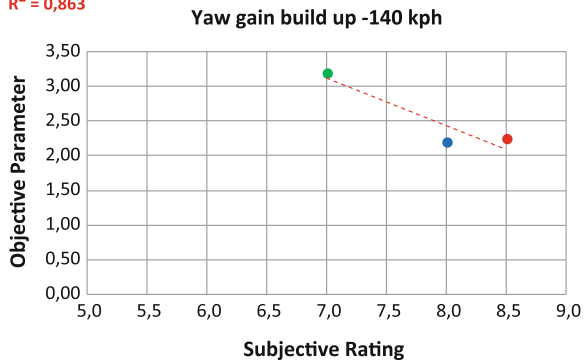


Fig. 4 Yaw Rate due to cross-wind: different runs at different speeds with the same vehicle

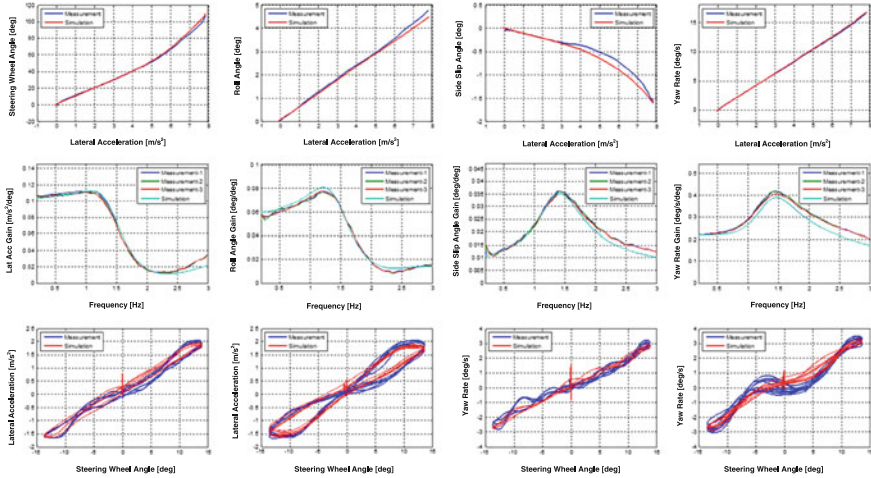
Fig. 5 Correlation diagram  $R^2 = 0,863$



The objective tests have been conducted with three different modalities, named, respectively, “fixed steering”, “free steering” and “close loop steering”. Each represents a different actuation of the steering handle when the vehicle is passing through the lateral wind. In the “fixed steering” test, the handle was kept fix in straight position (steering wheel angle equal to zero). In the “free steering” the handle was left free (steering wheel torque input from the driver equal to zero). Finally, in the “close loop steering” test the driver had to try to keep a straight trajectory marked by two lanes of cones.

The reason for trying many different test conditions was to verify which one had the highest level of correlation with the subjective evaluation. Furthermore, it was necessary to verify the best compromise between the close loop test, very similar to the subjective testing conditions, and the repeatability and objectivity of the open loop ones. As an example, Fig. 4 illustrates the diagrams of yaw rate obtained with the three different methodologies.

It is possible to see that the best repeatability is given by the fixed steer test. The open loop test is less repeatable and is also the one for which it is more difficult to see the influence of speed.



**Fig. 6** Model validation results: Steady state cornering (1st row), frequency response (2nd row) and on-centre weave at 0.2 and 0.4 Hz (3rd row). Tests performed at 100 km/h

## 4 Objective/Subjective Correlation

After the tests, the data have been post-processed in order to generate correlation metrics. A metric is defined as an established relationship between a subjective evaluation and an objective test parameter. For this, several parameters have been obtained from the objective data and then have been compared with the subjective ratings in diagrams like the one in Fig. 5. On the x-axis there are the ratings of the three vehicles tested, while on the y-axis there is the value of the objective parameter. With such kind of diagrams it is possible to verify the correlation between the rating and the parameter.

## 5 Simulation Model

Once the subjective/objective metrics were defined, the next goal was to perform a sensitivity analysis to investigate how these metrics were influenced by various vehicle parameters. For this, a simulation model of one of the vehicles was created with the commercial software IPG carmaker [4]. The main characteristics of the model are summarized in the following points:

- Suspensions are modelled as multi-dimensional look-up tables. In order to generate the look-up tables the vehicle has been tested on the Kinematics and Compliance bench. The test data have then been processed with a tool of IDIADA, which is able to automatically generate the maps.
- Aerodynamic forces and moments are modelled through equations with the following form:



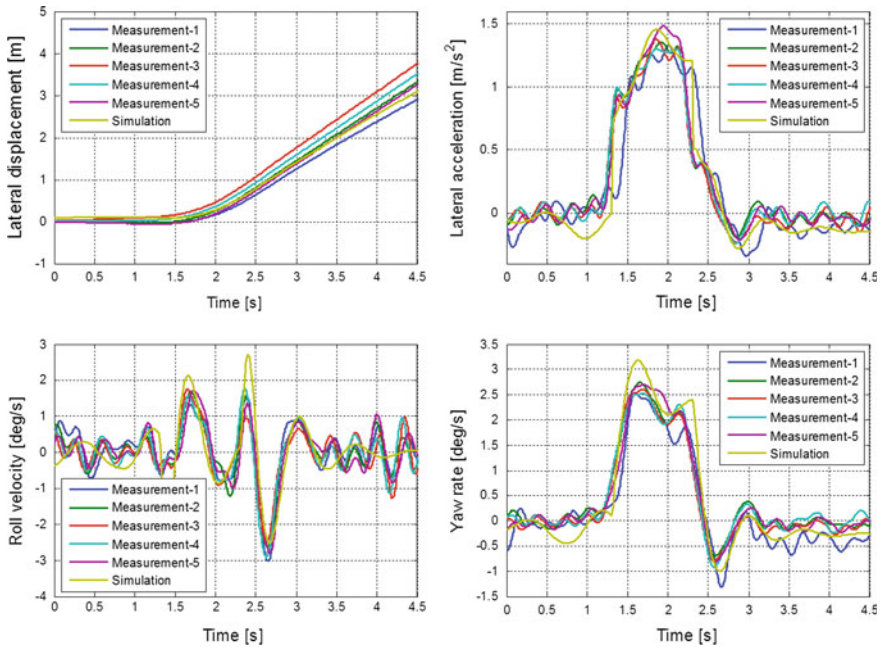


Fig. 7 Cross-wind validation results at 120 km/h

$$F_x = \frac{\rho}{2} c_x A v^2$$

$F_x$  represents one general component of force/moment applied on the vehicle body;  $\rho$  is the air density;  $c_x$  is the aerodynamic coefficient relative to the datum component of force/moment;  $v$  is the relative speed between the vehicle and the wind. The value of the aerodynamic coefficients is a function of the angle of attack of the wind. The coefficients have been obtained by Hyundai from tests in the wind tunnel.

- Springs, dampers, bump-stops, antiroll bars and all the others components have been obtained from measurement data.
- Inertia and COG position of the body have also been obtained from real data.
- Tyres are modelled as Magic Formulas.

Before undergoing cross-wind simulation, the model has been validated with several handling manoeuvres. A representative selection of the validation results is reported in Fig. 6, where it is possible to see the high level of correlation that was achieved.

After the validation of the handling manoeuvres, the model has been validated for the cross-wind test. The following signals have been considered: lateral displacement, lateral acceleration, yaw rate and roll rate. In fact, these are the most important to calculate the metrics. The simulations have been performed with three

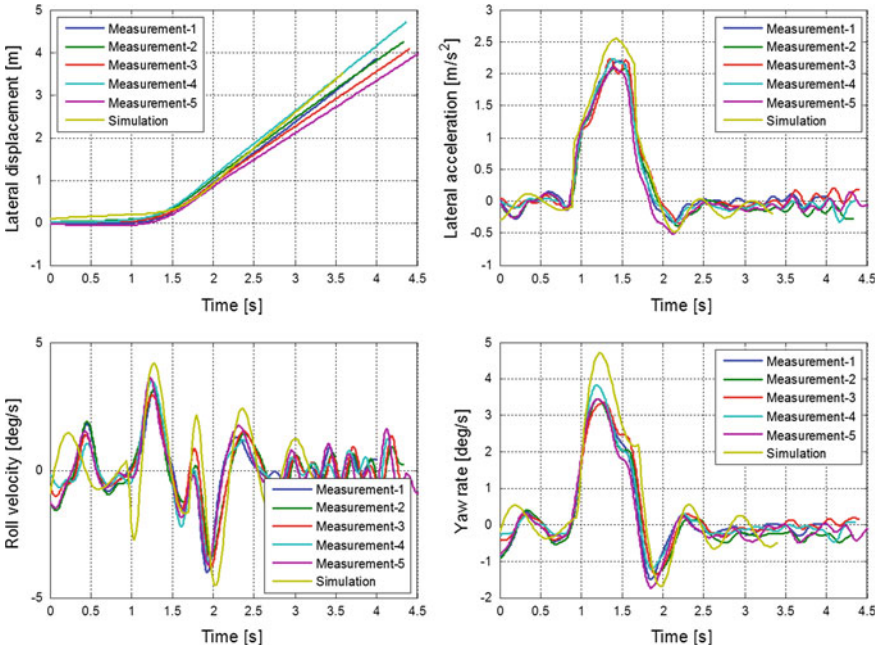


Fig. 8 Cross-wind validation results at 160 km/h

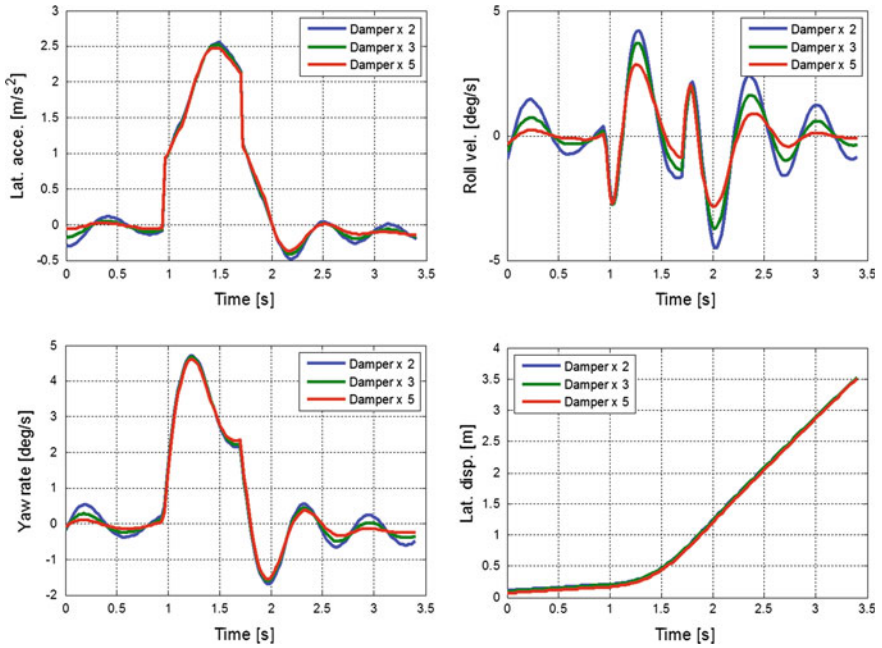
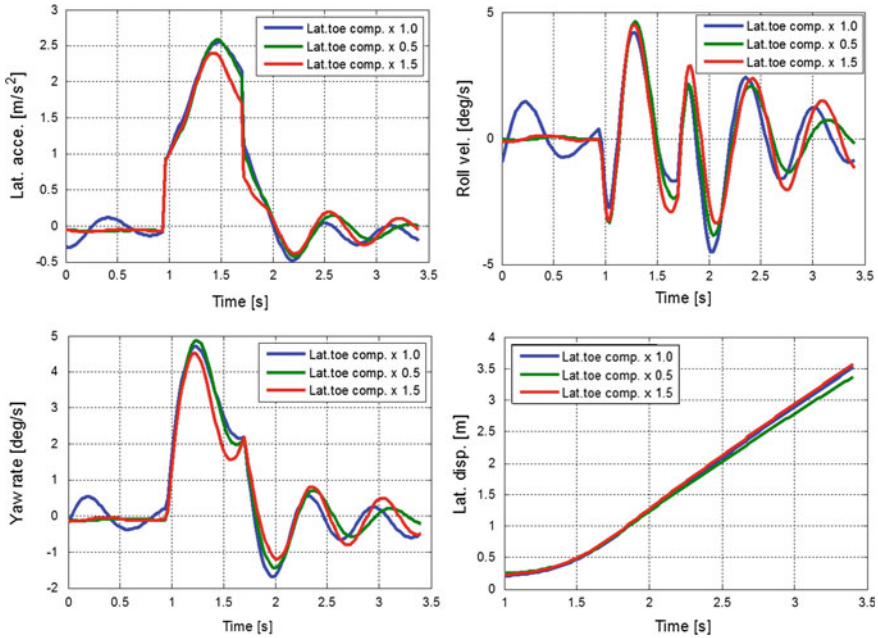


Fig. 9 Cross-wind simulation: influence of dampers



**Fig. 10** Cross-wind simulation: influence of rear toe compliance

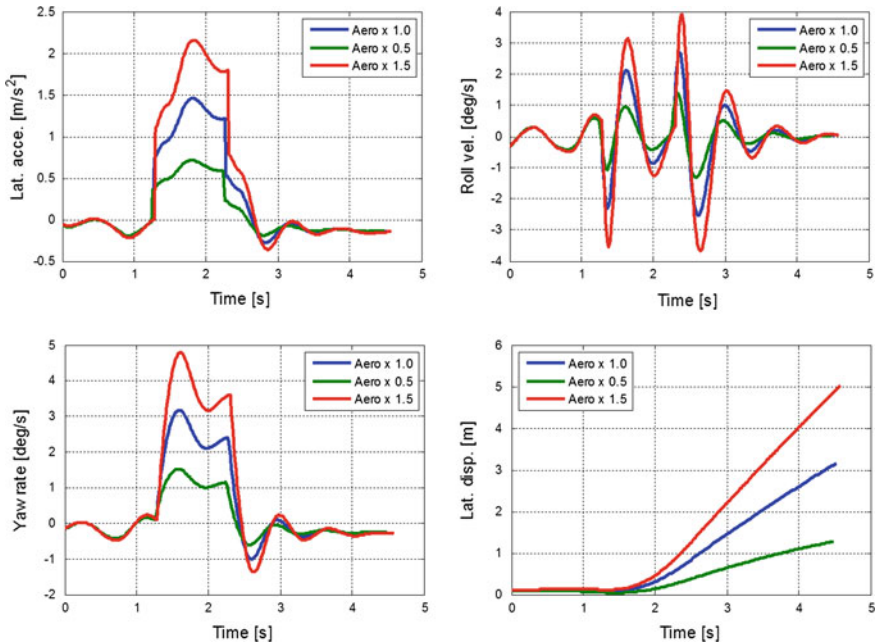
different vehicle speeds, while the wind speed is maintained constant at 20 m/s as in the real tests. In Figs. 7 and 8 the validation results are reported for the simulation at 120 and 160 km/h respectively. The simulations have been performed with the steering wheel fixed (angle equal to zero).

## 6 Sensitivity Analysis

The sensitivity analysis was aimed at investigating the impact of the following parameters on the cross-wind response:

- Damper forces
- Antiroll bar stiffness
- Kinematic and Compliance characteristics
- Vehicle mass and inertia characteristics
- Aerodynamic characteristics.

The diagrams below show some examples of the results. In Fig. 9 it is possible to see the effect of different dampers tuning. It is possible to see that this component has quite a strong impact on the roll velocity, which has demonstrated to be an important modifier of the driver subjective feeling.



**Fig. 11** Cross-wind simulation: influence of aerodynamic coefficients

In Fig. 10 it is possible to see the effect of a variation in the toe compliance under lateral force of the rear axle. The red line corresponds to more toe-in compliance and it is visible how this has a small influence on the peak of lateral acceleration.

Finally, in Fig. 11 is visible the effect of scaling the aerodynamic coefficients. It is possible to see the significant influence on the vehicle response which is possible to obtain through these parameters.

## 7 Conclusions

The study demonstrated that the combination of testing and simulation activities is able to provide a characterization of the cross-wind sensitivity, as well as to identify the design features which are able to improve vehicle performance. Specifically, test procedures for subjective and objective evaluation of cross-wind sensitivity have been developed and validated; the driver perception of cross-wind stability has been analysed and correlated with subjective/objective metrics; suspension and aerodynamic features impacting on the vehicle response has been investigated.

Moreover, it has been shown how simulation of cross-wind can be a valid tool to investigate cross-wind sensitivity and improve vehicle performance.

Although this project was focussed on luxury sedans where the highest performance requirements are desired, IDIADA and HMC are applying these technology process across the complete range of products to ensure a safe and desirable cross-wind performance. In the future, more test data, obtained from several vehicles, will improve the level of validation of the subjective/objective correlation metrics.

## References

1. ISO 12021:2010 (1996) Road vehicles—sensitivity to lateral wind—open-loop test method using wind generator input. Geneva
2. CarMaker Reference Manual (2010) IPG Automotive GmbH
3. Macadam CC et al (1990) Crosswind sensitivity of passenger cars and the influence of chassis and aerodynamic properties on driver preferences. *Veh Syst Dyn* 19:201–236
4. Wojciak J (2010) Experimental study of on-road aerodynamics during crosswind. *Gusts*, 8th MIRA international vehicle aerodynamics conference

# Maneuvering Experiment of Personal Mobility Vehicle with CVT-Type Steering Mechanism

Yoshihiro Suda, Hirayama Yuki, Masahiko Aki  
and Takafumi Takagi

**Abstract** This paper deals with maneuvering experiment of a tricycle-type personal mobility vehicle (PMV) with a new steering mechanism. The proposed steering mechanism has a continuously variable transmission (CVT) between rear two wheels. This feature of the PMV is steered by difference wheel speed between right and left wheels. In this paper, first the PMV mechanism is explained and then, steering characteristics is explained. Next, improved steering mechanism which makes easy to maneuver the PMV is suggested and the mechanism is explained. Finally, maneuvering experiment which was chosen as the slalom course was performed for a verification of the proposed mechanism effect. The result of the experiment shows that, due to adjusting left-side and right-side steering lever comparatively, steering characteristic has been improved. The data that has been used in this experiment are distance between tricycle and pole, usage time of riding, range of front wheel steering angle, and excessive number of steering times.

**Keywords** Personal mobility vehicle · CVT · Steering system · Experiment

---

F2012-E01-016

---

Y. Suda (✉) · H. Yuki · M. Aki  
Institute of Industrial Science, The University of Tokyo, Tokyo, Japan  
e-mail: suda@iis.u-tokyo.ac.jp

M. Aki  
e-mail: masaaki@iis.u-tokyo.ac.jp

T. Takagi  
JTEKT Corporation, Nagoya, Japan

## 1 Introduction

In recent years, a new transportation mode which is friendly to both environment and human is required as a solution for an aging society and an environmental conservation. A personal mobility vehicle (PMV) is focused by the recent social requirement. The PMV is an individual-sized small vehicle for a short-distance and a convenient move [1–6]. In our laboratory, a new concept PMV which has a combined characteristic of a bicycle and a parallel wheeled type vehicle was proposed. This PMV is able to be chosen of two modes by intended uses. The bicycle mode is appropriate for high speed riding in wide area. On the other hands, the parallel wheeled mode is expected to be used for low speed riding in crowded area.

At the moment, various PMVs which have characteristic functions have been developed. In this paper, a new steering type PMV is proposed. This PMV consists of one front wheel and two rear wheels. Its steering mechanism is different from the conventional tricycle (Fig. 1). By using the CVT, difference of the rotation speed of the rear wheels makes the CVT steer. The objective of this paper is to propose a new human machine interface (HMI) for steering operation. Firstly the steering characteristic of this PMV is mentioned, next the new steering interface method is proposed. Finally the verify experiment method and result are shown.

## 2 Proposed Steering Concept and Mechanism

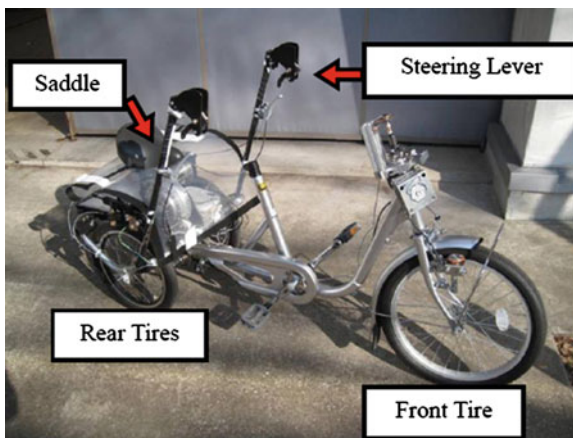
The PMV proposed in this paper has a different steering system from a conventional tricycle. The PMV is able to be steered by a different speed between rear two wheels which is controlled using a CVT. An overview of a PMV mechanism is shown in Fig. 1. A CVT output shaft is connected to a rear left wheel. A driving torque from pedals is transmitted to a rear right wheel and a CVT converted rear left wheel in travelling direction. The right wheel speed is treated as a reference wheel speed. When the left wheel speed increases by the CVT, the PMV turns to the right side. On the other hand, when the left wheel speed decreases by the CVT, the PMV turns to the left side. A driving torque difference by the CVT generates by a rotation angle of pulley which is operated by steering levers. The steering levers are connected through a wire to the pulley. A front wheel has a steering angle by a cornering force (Fig. 2).

## 3 Characteristics of Left and Right Turning Radius

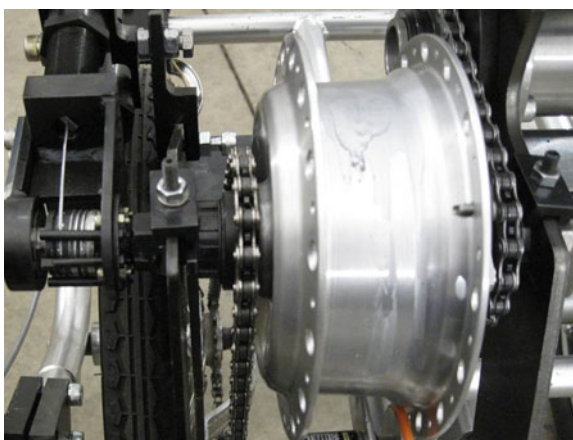
This steering mechanism is explained in Fig. 3. When the right wheel which is the reference rotates same speed, a turning radius is different between the right turn and the left turn.



**Fig. 1** Tricycle with new control mechanism



**Fig. 2** Continuously variable transmission



**Fig. 3** Steering lever and braking lever





**Fig. 4** Constant force spring at front wheel



Assume that the friction force between front wheel and the ground is small and vehicle attitude is determined by the difference in the rotational speed of the rear wheels, let CVT gear ratio is  $\alpha$ , the distance between two rear wheels is  $r$ , and turning radius is  $R$ . Then, following equations are obtained.

Assume that the friction force between front wheel and the ground is small and vehicle attitude is determined by the difference in the rotational speed of the rear wheels, let CVT gear ratio is  $\alpha$ , the distance between two rear wheels is  $r$ , and turning radius is  $R$ . Then, following equations are obtained.

$$R = \left| \frac{r}{\alpha - 1} + \frac{r}{2} \right| \quad (1)$$

Moreover, if we give the speed of the vehicle is  $V$  and right rear wheel speed is  $v$ , then, following equations are obtained.




$$V = \frac{\alpha + 1}{2} v \quad (2)$$

From the Eqs. (1), (2) this steering mechanism has the difference between turning left and turning right's turning radius and velocity.

To improve the degradation of operability due to differences in turning radius of turning left and right, the author pay attention on adjusting reaction force of the left and right steering lever. In order to adjust reaction force, reaction force adjusting device was installed at the wire which connecting the steering lever and CVT input pulley. The device composes of reaction force adjusting spring inside as shown in Fig. 4. Let's give the natural length is  $l$ , and the reaction force adjusting device total length is  $A + B$ , when  $A$  is the length of the screw which can be changed and  $B$  is constant value. A displacement generated from the lever action denotes  $x$ , and its stiffness denotes  $k_m$ . Then a lever reaction force  $F_m$  is obtained from Eq. (3).

$$F_m = k_m \{ l - (A + B) + x \} \quad (3)$$

**Table 1** Conditions of reaction force in experiment

Condition 1	Condition 2	Condition 3
		
Left Reaction Force = Right Reaction Force	Left Reaction Force > Right Reaction Force	Left Reaction Force < Right Reaction Force

Then, an actual lever reaction force  $F_L$  is expressed from sum of the reaction force adjusting device and a reaction force in the lever and a friction force of wire.

$$F_L = k_m \{l - (A + B) + x\} + k_L x + F_{friction} \tag{4}$$

In this paper, the length  $A$  is adjusted in the Eq. (4) which is adjustable as a studied parameter, in order to improve the steering operation. In the experiment, three reaction force conditions are set by adjusting of length  $A$ , shown in Table 1.

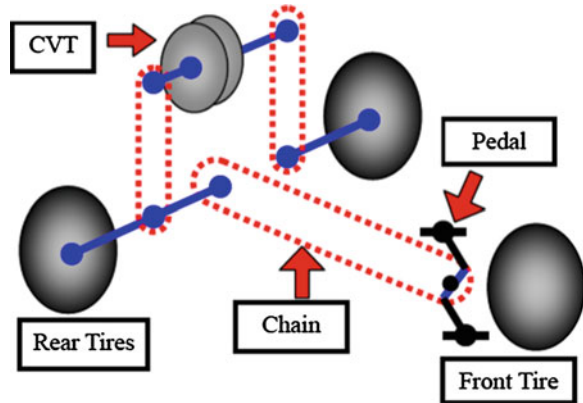
#### 4 Running Experiment: Overview of Experimental Procedure

In the experiment the reaction force of left–right steering lever are changed into three conditions. Let’s give the left hand side steering lever is  $F_l$  and the right hand side is  $F_r$ , condition 1, 2, 3 is  $F_l = F_r$ ,  $F_l > F_r$ ,  $F_l < F_r$  respectively (Table 1). The riding course which was used in the experiment is slalom course which composed of four poles. The distance between the poles is 7.5 m, the width of course is equal to 5 m and the length is 37.5 m. The forward tract starts from 0 point in Fig. 5, then goes the right side of the 1st pole, then passes 1st and 2nd pole to left side, then again to the right side until the end of the course respectively. The backward tract is similar to the forward tract but the tract begins from passing the 5th pole through to the left as seen in Fig. 5. In the experiment, 4 male examinees are 20–30 years old. The distance between the tricycle and the pole was measured by the video camera, at the same time the amount of operating lever and steering angle were measured by installed potential meters (Table 2).

#### 5 Running Experiment: Experimental Result

Time and distance between each pole and vehicle is measured by the camera (Figs. 6, 7). Let’s give the name to each pole, 1–4 for forward route, 5–8 for backward route, as shown in Fig. 8. Then we will get the result of the distance

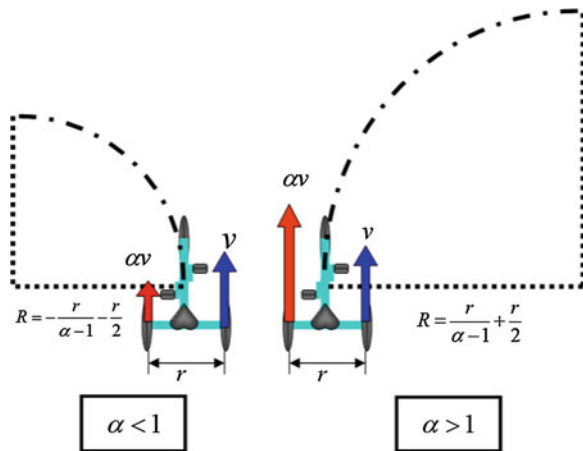
**Fig. 5** Mechanism of driving force transmission



**Table 2** Conditions of test course

	Length [m]
Course (traveling direction)	37.5
Interval (traveling direction)	7.5
Width (cross direction)	2.5

**Fig. 6** Difference of turning radius between right and left direction



between each pole and vehicle as shown in Fig. 9, which is the average result of 4 examinees. Plus value in the Fig. 6 means the vehicle is at the right side of traveling direction and oppositely minus value means the vehicle is at the left side.

For condition 1 which the left and right lever's reaction is equal, when the examinees passed the poles to the right hand side, the distance between pole and vehicle is bigger than when they passed to the left hand side. The average of the different distance is 0.31 m. Next comparing with condition 1, condition 2 which left lever reaction force is bigger than right lever, the different distance become bigger, and the average is 0.55 m



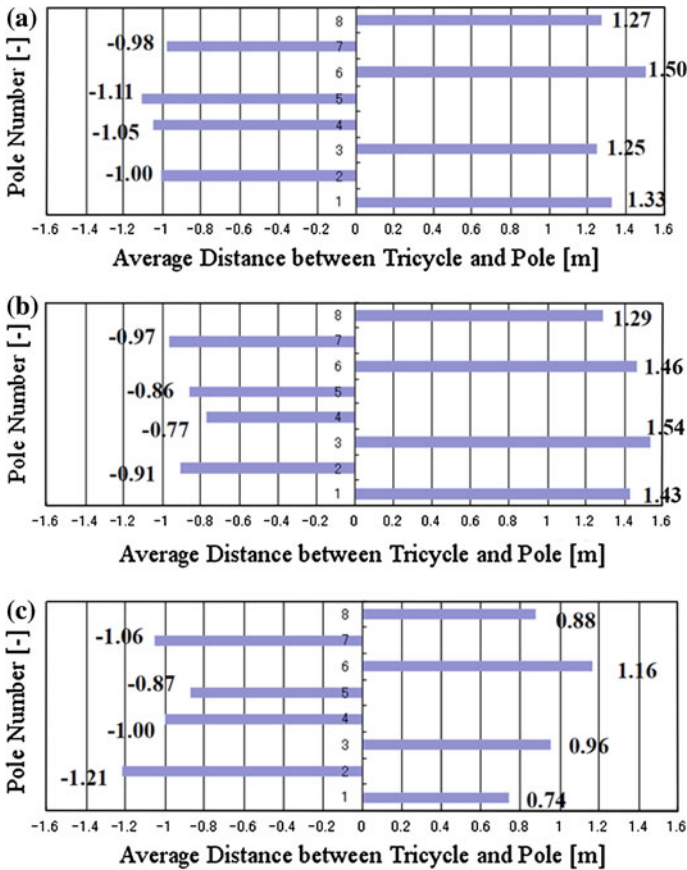


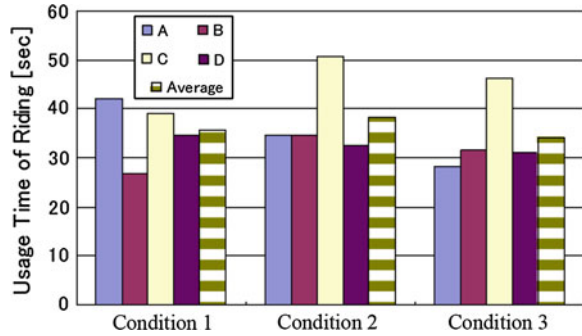
Fig. 9 Average distance between tricycle and pole. a Condition 1. b Condition 2. c Condition 3

right and left turning characteristics becomes smaller. In other words, condition 3 makes the characteristic difference between left and right turning is improved.

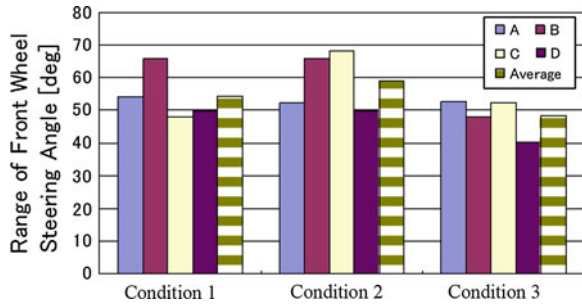
Figure 10 shows the running time in slalom course of 4 examines. From the figure, in condition 3, the examines trended to finish slalom course in the shortest period of time. Although the running time is vary widely due to individual differences, running time of condition 3 is the shortest compare to the two other condition. This is probably because the ease of steering results the running time to be shorter.

Figure 11 shows the amplitude of the front wheel steering angle (sum of maximum angle when turning left and right). We can say that the bigger values mean the examinees made bigger turning radius. In other words, the amplitude should become smaller if the examinees ran smoothly. Therefore, from Fig. 8 condition 3 is considered to be the smoothest running condition. In contrast, condition 2 has the biggest amplitude of steering angle. This is considered to be because of the unbalance of left–right steering characteristics.

**Fig. 10** Usage time of riding



**Fig. 11** Range of front wheel steering angle



**Fig. 12** Excessive number of steering times

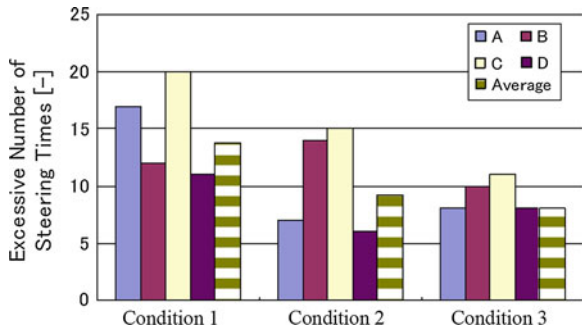


Figure 12 shows the number of excess steering times compare to the necessary times. While this number can be affected by the familiarity of the examinees, the number of excess steering time can be reduced by adjusting the left–right reaction force. Therefore, from Fig. 9, condition 3 which has the smallest number is the finest condition to control the vehicle, compare to the other two conditions.

As the conclusion, from the experiment result, it is able to reduce the different of the left–right unbalance turning characteristics by adjusting the ratio of left–right steering lever reaction force. This contributes significantly to the improvement of proposed new steering method.

## 6 Conclusions

In this paper, new steering method three-wheeled PMV was examined, and the conclusion is mentioned below.

1. The prototype of new steering method three wheeled PMV was made.
2. By using CVT to control the rotation speed of the left–right wheel, the PMV is possible to turn easily.
3. The relationship between the steering characteristics and operability is investigated.

In a future work, this new steering type PMV is developed in order to make the further improvement.

## References

1. Segway Inc.: <http://www.segway.com/>
2. Toyota wingle: [http://www2.toyota.co.jp/jp/tech/p\\_mobility/winglet/index.html](http://www2.toyota.co.jp/jp/tech/p_mobility/winglet/index.html)
3. Yamafuji K, Miyagawa Y, Kawamura T (1989) Synchronous steering control of a parallel bicycle. *Trans JSME Series C*, 55(513):1229–1234
4. Hirose N, Sukigara K, Kajima H, Yamaoka M (2010) Mode switching control for a personal mobility robot based on initial value compensation. *IECON 2010* 1914–1919
5. HONDA U3-X: <http://www.honda.co.jp/ASIMO/new-tech/u3x/index.html>
6. Sasaki M, Yanagihara N, Matsumoto O, Komoriya K (2005) Steering control of the personal riding-type wheeled mobile platform (PMP), *Proceedings of the 2005 IEEE/RSJ International Conference on Intelligent Robots and Systems (IROS 2005)*, pp 1697–1702

# Vehicle Performance Objective Management in Automotive R&D

Xuezhen Wu, Haiqiang Han, Liqiang Dai, Linghua Zou and Fuquan Zhao

**Abstract** The management process relating to automotive performance target is integrated into design and development in which each activity is executed as per phase. It mainly consists of target establishment, target decomposition, target inspection and target acceptance with regard to vehicle performance, thereby achieving effective and overall management of vehicle performance target.

**Keywords** Automobile · Performance target · Target management · Target decomposition

## 1 Introduction

Vehicle performance usually refers to the overall performance of the car which means the ability to adapt different conditions of use and then to maximize the work efficiency, including dynamics, economic, and brake, and security are shown in Fig. 1.

Car performance is the soul of cars. Vehicle performance should be considered at the beginning of automotive product design and development to ensure that models to be developed have great vehicle performance. Usually, the major automotive OEMs control the single performance and special performance

---

F2012-E01-018

---

X. Wu (✉) · H. Han · L. Dai · L. Zou · F. Zhao  
Zhejiang Geely Automobile Research Institute CO., LTD, Hangzhou, China  
e-mail: wxz@rd.geely.com



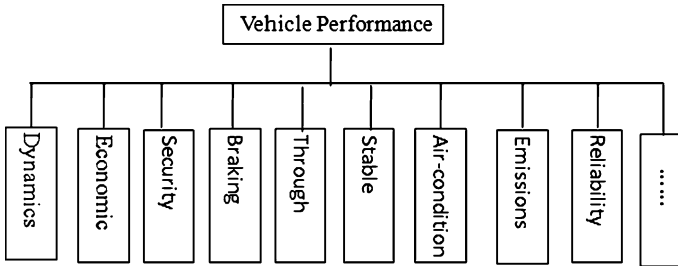


Fig. 1 Diagram of vehicle performance

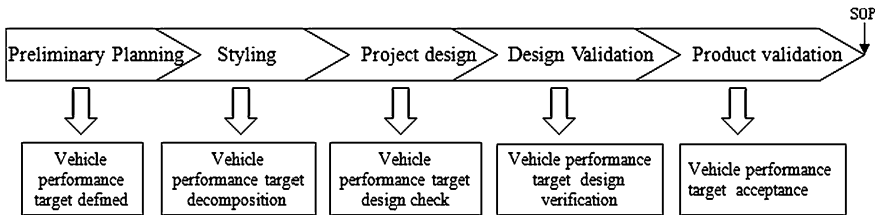


Fig. 2 Overall vehicle performance management by objectives

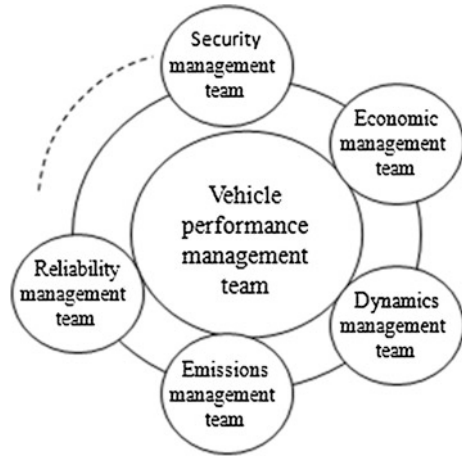
separately [1]. According to the features of modern automotive design, the coordinated performance management is put forward and the performance management relies on the design and development process to complete the grading work, including target establishment, target decomposition, target inspection and target acceptance with regard to vehicle performance. In the performance management process, performance standards and norms need to be set at the same time in order to guide the work for performance.

## 2 The Overall Vehicle Performance Management Process

### 2.1 Overall Vehicle Performance Management by Objectives

General idea for vehicle performance objectives management: vehicle performance objectives need to be defined in the preliminary planning stages of the project; during the project styling phase vehicle performance target should be decomposed; the vehicle performance target needs to be checked during the design phase; in the validate stage vehicle performance target needs design verification work; during product validation phase vehicle performance target needs to be accepted. It is shown in Fig. 2. At same time vehicle performance objectives management needs to be integrated into the research and design process. Vehicle

**Fig. 3** The vehicle performance management team



performance management processes needs to be established, and performance design standards and design specifications also need to be established.

The whole vehicle performance objectives management process also needs to set up a separate management team for performance objectives to manage and promote the development of the performance. This management team is different from the Project Management team, while at the same time serves project in performance objectives management process. This performance management team has a right to decide and the veto power. The mainly comprising schematic of performance management team is shown in Fig. 3.

### ***2.2 Vehicle Performance Target Defined***

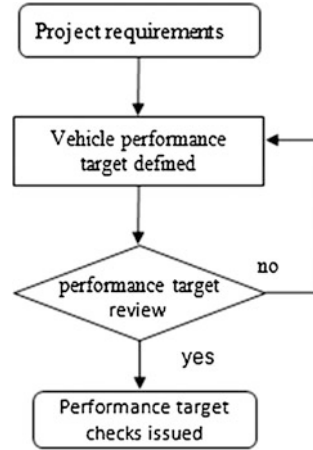
In preliminary planning phase of a project, you should define the vehicle performance target, before setting vehicle performance targets, first enter information that you want to collect, such as vehicle positioning, sales region, product life cycle, at the same time you need to collect performance information on competing vehicle.

Vehicle performance target needs to be convened by the performance management team after the review meeting; the vehicle performance target will be issued after reviews. It is shown in Fig. 4.

### ***2.3 Vehicle Performance Target Decomposition***

After the vehicle performance target is defined at the styling stage, each performance team is responsible for decomposition of performance objectives

**Fig. 4** Vehicle performance target defined



management. Performance target decomposition follows a top way, from vehicle performance target decomposition to system to parts. The decomposition diagram is shown in Fig. 5.

## ***2.4 Vehicle Performance Target Design Check***

In order to ensure that the whole car performance target, the vehicle performance target and parts performance target have been identified. During the design process, the designed detection check is needed to address performance problem. That is the car performance target for process management. Performance target check list is shown in Table 1.

## ***2.5 Vehicle Performance Target Design Verification***

In the verification phase of product design, design verification of vehicle performance, mainly for project prototypes or simulation performance validation, for rectification of problems found.

## ***2.6 Vehicle Performance Target Acceptance***

Product validation phase is primarily an acceptance on the performance target. Outstanding problems need solutions in the design phase up to the acceptance, by performance targets on acceptance of the performance objectives management team. It is shown in Fig. 6.

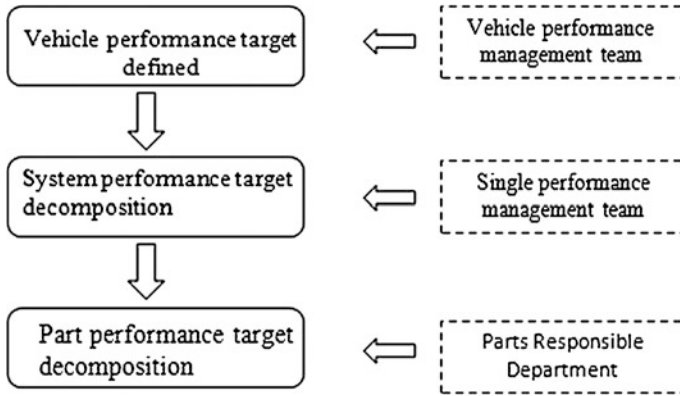
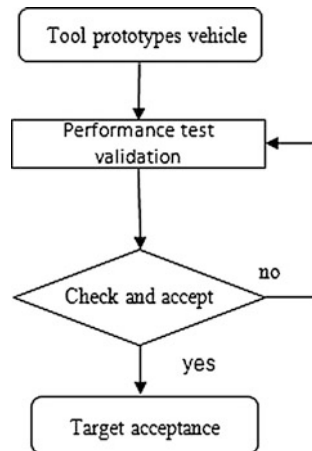


Fig. 5 Vehicle performance target decomposition

Table 1 Performance targetcheck list

No.	Name	Performance checking	Problems and solutions
1	Dynamics		
2	Economic		
3	.....		

Fig. 6 Vehicle performance target acceptance



### **3 Summary**

The implementation of performance target ensures the vehicle quality. The effective co-ordination of all performance management is another initiative in the automotive research and development design, and the blank in management of vehicle performance target is filled. At the same time, as the vehicle performance objectives management concerns much knowledge, you also need to accumulate experience to improve vehicle performance objective management in the actual work.

### **Reference**

1. Hu Liang, Kang F, Tong R, Rao Z (2011) Vehicle performance empolder summarize. Shanghai automobile

# Improving Energy Efficiency of Heavy-Duty Vehicles: A Systemic Perspective and Some Case Studies

Juhani Laurikko, Kimmo Erkkilä, Petri Laine and Nils-Olof Nylund

**Abstract** Today's advanced market economy relies in logistic operations that are both reliable and timely. Road transport is a major contributor to this daily logistics, but also a major consumer of fossil fuels, hence producing a lot of carbon emissions. Furthermore, most of the technologies recently introduced to cut down fuel use and emissions in passenger cars are not practical in heavy trucks running long-distances. This paper focuses on how to more systematically address the energy process and gives some case-examples of progress made in real-world HDVs. Several studies at VTT have been addressing energy use in HDVs. It has become evident that for real improvements in energy efficiency, the complete vehicle must be taken into consideration. We must have better understanding of the factors influencing the energy demand, and not just how to make engines more fuel efficient. For that purpose a break-down of energy use in a heavy truck-trailer combination has been made. The objective for this approach was to give proportions for the various contributors for the energy use, and be able to assess, what kind of progress in each field could be possible. Apart from the holistic and systemic approach, we need metrics to measure the energy consumption in such a way that the results reflect real-world situation as good as possible. Using a chassis dynamometer capable of taking a full-size vehicle and replicating its on-road driving operations has proven to be an excellent tool in terms of precision and repeatability of the results. Adding also road gradient (uphill/downhill) simulation further enhances the realism, and improves the accuracy how closely the duty-cycle is reflected in engine speed/load sequence compared to on-road driving. Eventually, this match is the measure for the success of the method. In case studies

---

F2012-E01-024

---

J. Laurikko (✉) · K. Erkkilä · P. Laine · N.-O. Nylund  
VTT Technical Research Centre Finland, P.O. Box 1000, FI-02044 VTT Otaniemi, Finland  
e-mail: juhani.laurikko@vtt.fi

several areas of energy use has been addressed, and the potentials for savings in real-use has been determined. These include e.g., choice of tyres for optimum rolling losses without compromising safety and most recently aerodynamic improvements for the complete truck-trailer combination for reduced drag. The paper will portray the achievable energy savings identified in these studies. Test results demonstrate that energy efficiency of heavy trucks can be improved, but for a long-standing and substantial impact the complete design of the vehicle should be viewed from the energy efficiency perspective.

**Keywords** Heavy transport vehicle · Energy use · Energy savings · Design · Test methodology

## 1 Introduction

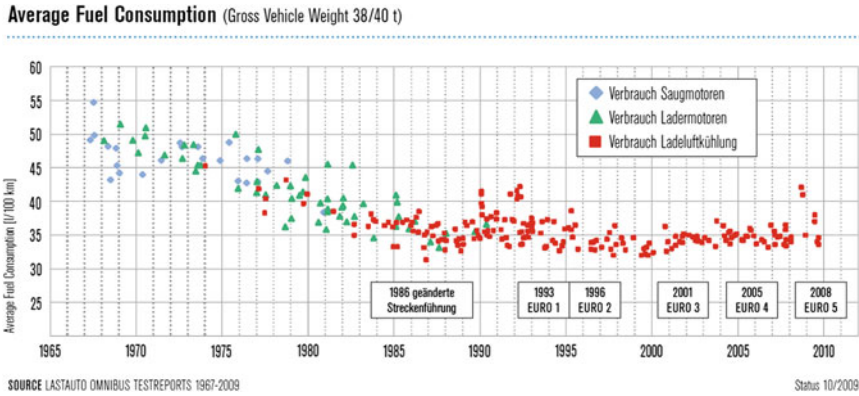
Road transport is a major prerequisite for today's advanced economy relying in logistic operations that are both reliable and timely. Because of its flexibility, road transport has taken an increasing share of the land transport of goods in most markets. Because of its wide use, road transport is also a major consumer of fuels derived from oil, and hence a major contributor of carbon emissions.

Furthermore, most of the technologies recently introduced to cut down fuel use and emissions in passenger cars are not practical in heavy trucks running long-distances. So far only advanced bio fuels seem to offer a viable solution, but their limited production capacity and high price call for more efficient use of energy. This paper focuses on how to address the process more systematically and gives some case-examples of progress made in real-world HDVs.

## 2 Target and Objectives

The European Road Transport Research Advisory Council's (ERTRAC) transportation sector has set a vision for 2020 calling for a 10 % reduction in CO<sub>2</sub> emissions for all new Heavy-Duty Vehicles (based on 2003 figures). ERTRAC has also set a more ambitious target that transportation should be 50 % more efficient by 2030 compared to today. However, studying how the efficiency of heavy trucks has developed in the recent decades, it is clear that the progress made from the 1970s to mid-1990s has stagnated. The main reason for this is the stringer emissions legislation, calling for increasingly cleaner exhausts emissions. Figure 1 illustrates this progress from late 1960s to late 2009. Since the effective emissions regulations (Euro III and later) were implemented, fuel economy has improved only marginally.

Against this background the improvements in engine efficiency itself seem to be very limited and target-setting should be shifted more on the vehicle as whole and addressing it as a system to be optimised.



**Fig. 1** Average fuel consumption of heavy goods vehicles in practical road tests from late 1960s to date. (source Lastauto-omnibus test reports, taken from “Commercial Vehicles and CO<sub>2</sub>”, published by European Automobile Manufacturers Association ACEA.)

### 3 Systemic Approach to Energy Use in a Heavy Truck

Traditionally the energy efficiency of a heavy vehicle has been first and foremost seen as the efficiency of the engine, leaving most of the other components aside, even if they could be equally relevant. Also the focus has been on producing power at best efficiency rather than how to lower the energy demand.

In order to get a more comprehensive and holistic view of the subject, we have taken a more systemic view of the whole energy process. To help us to understand the various interrelationships and their dynamics, we drafted a schematic of it, presented as Fig 2. As a key assumption we see that the total energy process in a HDV can be split into two main processes: energy demand and energy production. In addition, we have identified also a number of sub-processes linked to these main processes. These are energy transfer, energy recovery and re-use and energy storage. A fairly large number of variables affect to these processes. Some have either a fixed or static nature, but quite many are active or dynamic.

The static variables can be also seen as “constructive” (or permanent) items that affect energy efficiency. They come to play mainly up front while designing the vehicle and chassis construction, but also when making choices of e.g., tyres during the use of the vehicle. The active variables can be labelled as “instructive” (or non-permanent). Those are items that can—and need to—be monitored and controlled for an optimum result. The management of the static process variables can be grouped into Design Management that deals with the permanent design features that the engineers must get right already when designing the engine, driveline etc. These features are extremely important, as their impact are seen over the whole lifetime of the vehicle, and usually there is not much room for improvement once the vehicle has been completed. On the other hand the instructive items are processes that need to be monitored and continuously controlled for an optimum



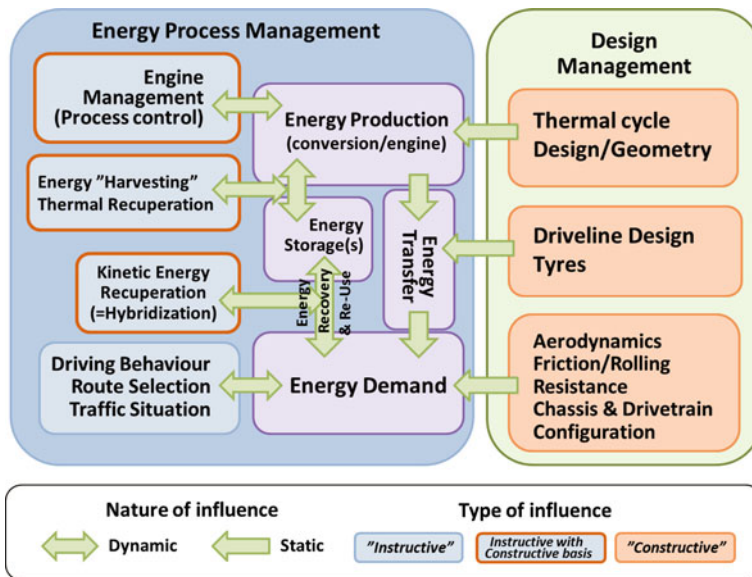


Fig. 2 Schematics of the energy process in a HDV

result. For these features, we need to set up and maintain a comprehensive Energy Process Management in order to achieve optimal results.

Some of these instructive items are present in all types of trucks, but an advanced design and construction may bring in more functionality and opportunities for energy management. Some examples of these features are energy recuperation and re-use processes that need specific hardware to support them. More common and applicable for all vehicles are issues like driver behaviour, route selection and traffic situation. However, these can also be enhanced with some specific hardware like GPS-navigation and active traffic management and control (TMC) systems enabling the driver to take the optimum route and avoid congestions.

## 4 Research Methodology

### 4.1 Chassis Dynamometer Testing

In order to assess and improve energy efficiency of a vehicle, it is compulsory to be able to measure both the fuel use (and other energies) as well as the work performed. At best this should be possible with a complete vehicle employing duty-cycles that are typical for the operation of the vehicle in real-world practise. Measurements in real use, however, are not precise enough, because in normal traffic there is always scatter due to the many variations that render the results

mostly useless for observing changes that usually lie in single-digit percentages. It may also be very difficult to have on-board instruments that are accurate enough. Therefore, more controlled and preferably stationary environment is called for.

A full-size chassis dynamometer that is able to simulate vehicle inertia, and is capable of fast transient load changes, is a preferred tool for making precise measurements. The basic technology has been used for passenger cars and other light duty vehicles for decades, but only a few installations has been built for large vehicles. High costs may have been at least one of the deterring factors. As certification for heavy-duty vehicle engines is also an engine dynamometer-based procedure, there have not been many inducements for chassis dynamometer installations.

In principle a chassis dynamometer (a.k.a “rolling road”) enables accurate simulations of real-world driving. With proper hardware and software, the rig is able to simulate all elements of the vehicle rolling resistance and air drag, resulting replication of the driving resistances, and hence also engine loading. If the driving schedule used is derived from actual in-use recording or data logging, the resulting emissions and energy use are a relatively accurate representation of the real-world driving, and the assessment gives very realistic picture of the real-world performance of the vehicle in question. Furthermore, the auxiliaries operation can be made to follow the patterns from actual driving situations.

## ***4.2 Test Facility at VTT***

VTT has since 2002 focused in developing methods for assessing these real-world emissions. For this purpose a special test facility was commissioned with equipment able to quantify energy use and emissions from heavy road vehicles, including both trucks and busses. The aim has been to produce realistic and comparable specific emissions factors to be used in comparing the environmental performance of these vehicles, as well as to calculate emissions output as input data for various emission and energy inventories and models.

The foundation for this work is the large chassis dynamometer with rollers of 2.5 m in diameter. The size of the rollers is large enough to bring the tyre-to-roller contact near to the conditions of normal level road surface, which is sufficient for lowering the parasitic losses due to tyre deformation and flexing near the level of normal tyre-to-road contact. In addition, using same type of tyres for all testing and keeping tyre temperatures constant will work further towards normalising tyre-to-roller contact.

The chassis dynamometer at VTT enables in-laboratory simulation of on-the-road driving, including not only the usual speed vs. time control and simulation of air drag and road resistance, but also modulation for grading uphill or coasting downhill. Thus, the duty-cycle that is recorder in real operating conditions and includes sufficient information of the road gradient can accurately and repeatedly be simulated to assess the performance of the vehicle. Adding the “third

**Fig. 3** Heavy-vehicle chassis dynamometer facility at VTT



coordinate”, i.e., uphill/downhill, is especially important when testing heavy trucks, as their engine operation is drastically dependent on the road gradient. Simulation of grade enhances the realism, and improves the accuracy how closely the duty-cycle is reflected in engine speed/load sequence compared to on-road driving. Eventually, this match is the measure for the success of the method.

The installation is mainly targeted towards simulation of dynamic duty cycles, and allows full inertia simulation up to 60 tonnes of total weight, which is currently the largest allowable GVW for road-going vehicles in Finland and Sweden. Maximum tractive force at the wheel (with 2.5 m diameter rollers) is 20,000 Nm. The continuous maximum power absorption of the rig is 300 kW at driving wheels, which can be translated to equal about 500 hp at engine crank, due to the losses in the complete power line. More details of the test methodology and its development can be found in [1]. Figure 3 shows a photo of the facility located in Espoo, Finland, western part of the Helsinki Metropolitan area.

## 5 Break-Down of the Energy Use

At this test facility VTT has investigated energy use of heavy road-going vehicles. Since 2002, more than 150 busses and over 100 heavy trucks has been tested. On this basis it has been possible to assess and set the dimensions for those items that together form the energy production and use processes in a truck. As an example this kind of break-down for heavy truck-trailer combination is depicted in Fig. 4.

According to the graph currently about 44 % of the total energy inserted in the system from fuel (100 %), is converted to mechanical work that propels the vehicle. Major losses at this stage are heat rejection losses and energy escaping with the hot exhaust gases, even if part of that loss is already recuperated with turbo charging. Of this mechanical work (100 %) the majority is used to overcome rolling resistances and aerodynamic air drag, both approximately 40 % in this particular example, whereas energy transfer, i.e., driveline and tyre losses together account for approximately 7 %. The auxiliaries (fan, alternator, compressor for

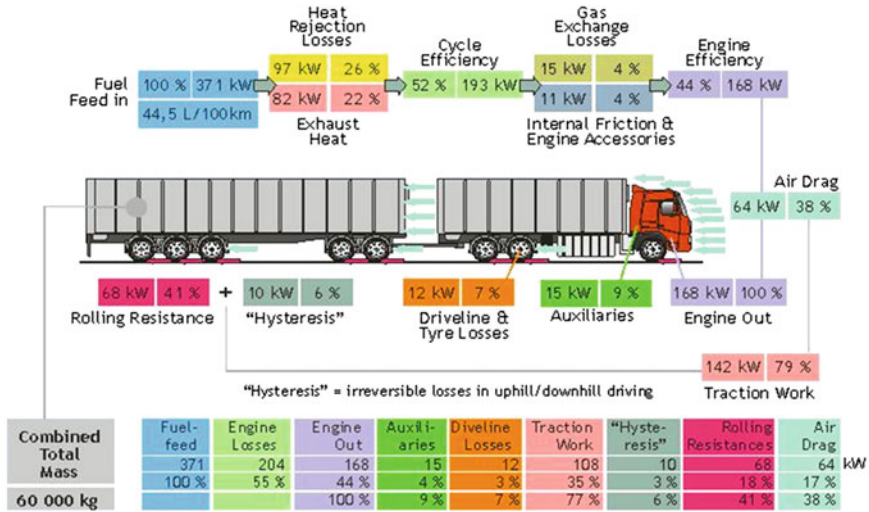


Fig. 4 Break-down of the energy use in a HDV (60 tonne GVW) at 80 km/h constant speed

pneumatic brakes) consume nearly 10 % of the output of the engine. A further loss of energy is also seen in vehicle dynamics in form of a kind of “hysteresis” phenomenon, when the driver needs to apply breaks in downhill driving, because otherwise the vehicle would over speed. This voids part of the recuperation of potential energy that the vehicle has gained when driven uphill. However, driver has some control over this, as when letting the vehicle slow down as it reaches the hilltop, it is less likely to over speed while going downhill again, albeit this may pose unwanted speed changes especially in road conditions, where lighter vehicles are unable to freely overtake the HDV that are crawling uphill.

These figures can also be used to assess the implications that further re-design and control of operations would have. For example if it would be possible to recuperate energy losses in exhaust with some 15 % recovery rate, it should equal nearly the amount of energy now used in auxiliaries. Furthermore, a mere 10 % reduction in air drag would produce a saving that is equal to a half of the losses in driveline and tyres.

## 6 Some Case Studies

### 6.1 Improving Fuel Efficiency by Choosing Right Tyres

In the systematic search for improvements in energy efficiency the influence of tyres on fuel consumption has been studied. Seven different tyres (size 275/70R22.5) all suitable to a heavy truck or a bus were compared. At first their rolling resistances were determined by fitting a pair of each tyre on a trailer dolly and

**Fig. 5** Determining rolling resistance by motoring the tyres fitted on an axle of a trailer dolly



motoring them on the chassis dyno roller, as depicted in Fig. 5. A few comparisons were also made with the full vehicle coast-down method, and the results seemed to agree quite well. Figure 6 depicts corrected resistive force results for all the seven tyres tested.

Based on these resistive forces rolling resistances were calculated, their effect on and fuel consumption were approximated by the increased work needed to run the vehicle over a driving cycle. In parallel fuel consumption of an urban bus was measured in Braunschweig city bus cycle using these different resistive forces for road load. The results for both calculations and measurements are depicted in Fig. 7.

As we can see from Fig. 7, calculated fuel consumption follows by nature the rolling resistance (CR) value. However, the measured consumption was not in full agreement with these figures, as up to 1.5 % higher consumption were measured compared to the “simulated” result, but with some tyres the difference was only marginal. An explanation for this phenomenon can probably be found, when we take a look at the thread configurations of the tyres. Figure 8 depicts some of them, along with the indicated difference between the two fuel consumption results. The more complex tread pattern the tyre had, the higher was the difference in these consumption figures. The more complex (and probably also more flexible) tread pattern with more transverse grooves seems to induce more power loss in a driving wheel compared to a straight rolling wheel that is the case in calculated consumption figures.

In conclusion it can state that as depicted in Fig. 7, the measured fuel consumption differed by a maximum of 4.5 % between the best (Michelin XZA) and the worst case (Noktop 21). However, it must be noted that the Noktop tyre with the most complex and flexible tread pattern is designed for winter/snow use whereas the Michelin is intended for regular summer use.

In this context it is also worth to mention the study of the influence of tyre pressure, imbalance and wheel misalignment that were also investigated as part of this research assignment. A clear increase in resistive forces was perceived, when the tyre was inflated from a normal  $8 \pm 0.5$  bar level down to as low as 3.5 bar.

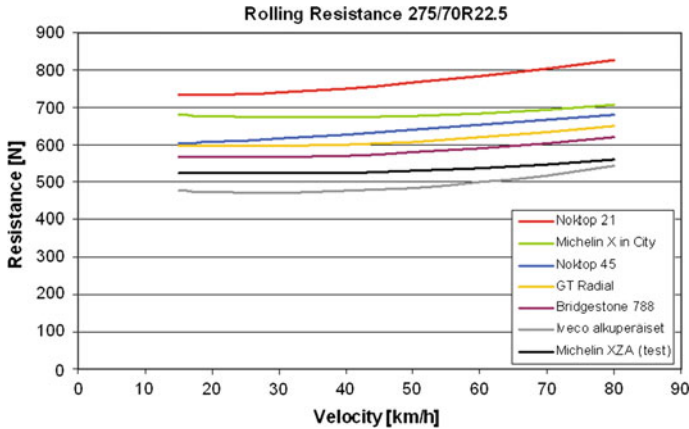


Fig. 6 Rolling resistance (force at wheel-to-roller contact) for tested tyres

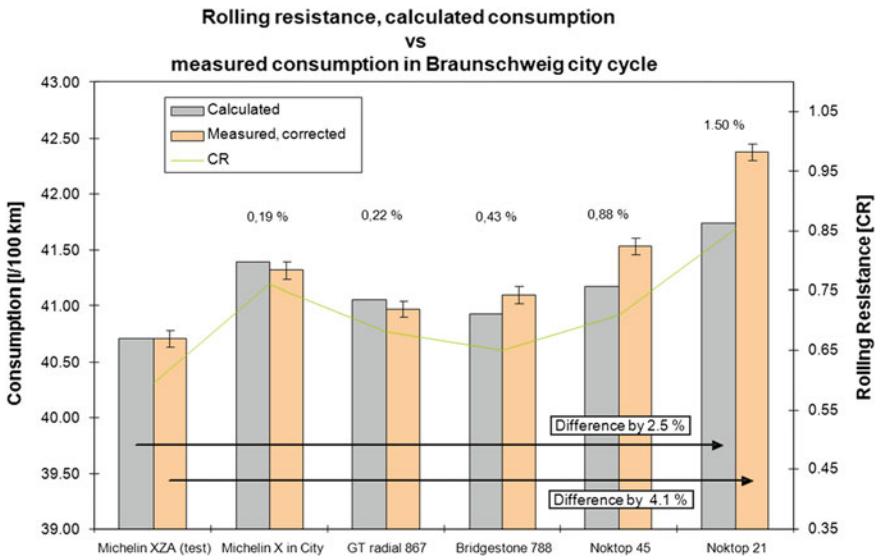
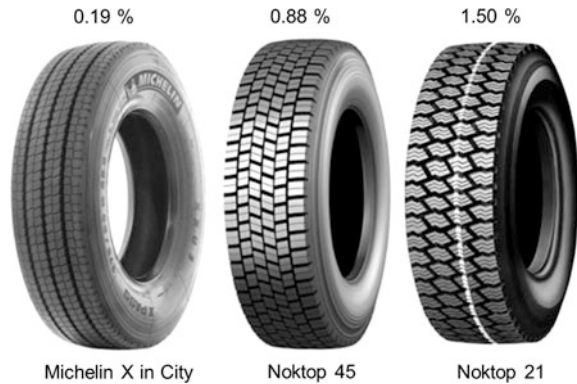


Fig. 7 Calculated and measured fuel consumption of an urban bus with tested tyres

This resulted into over 40 % higher rolling resistance, but already at 6 bar some 10 % increase was seen. Therefore regular check of tyre pressures is advisable.

Increased rolling resistance due to the misalignment of the wheels was also observed but the amount was only marginal at the typical misalignment rate measured from a batch of trucks and trailers. Furthermore, the effect of tyre deformation and imbalance were also found marginal in terms of increased resistance and higher fuel consumption. However, their effect in ride quality was significant.

**Fig. 8** A subset of tested tyres with the relative difference in calculated vs. measured fuel consumption of an urban bus



## 6.2 Improving Heavy Vehicle Aerodynamics

It was established that the choice of tyres has an implication on the rolling resistance forces, as well as partially in driveline losses. However, based on Fig. 4, air drag is of equal importance in energy use of a heavy truck. Therefore, VTT has also made an effort to improve aerodynamics of a truck-trailer combination, which traditionally has not very streamlined designs.

Modelling studies, as well as a few wind tunnel experiments with scaled-down models were made in order to design a set of panels, louvers, stabilisers, air deflectors and other add-on improvements that were to improve the aerodynamics of a truck and trailer combination. Figure 9 shows the CAD-model renderings and the resulting scaled-down solid model for wind tunnel work. One should note how also the under bodies of both the truck and the trailer have “bellypan” covers to keep the airflow smooth underneath the vehicle.

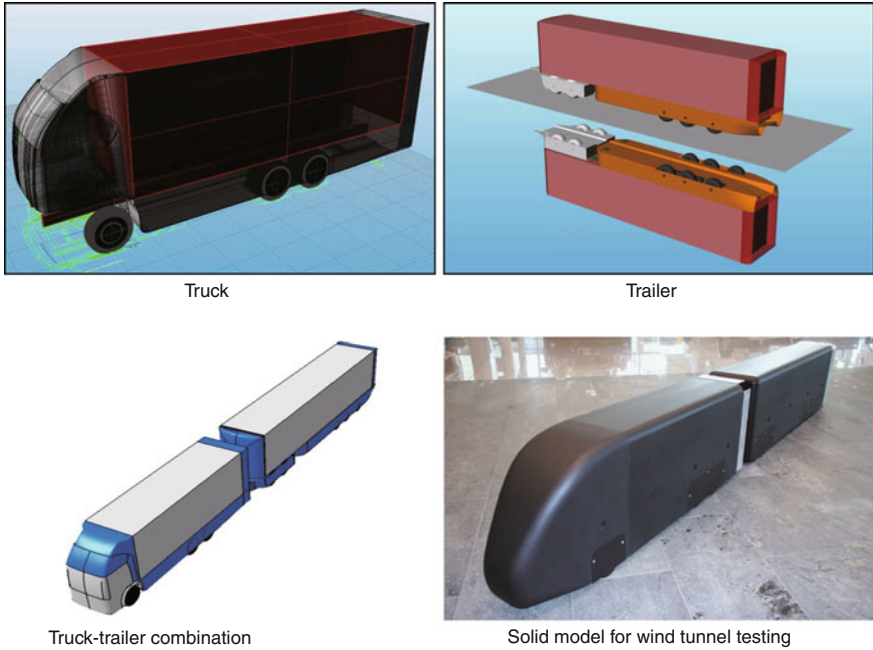
Figure 10 shows the comparison of the basic vehicle and the improved design with the aerodynamic upgrades. Note seamless integration of cab to the cargo space, side-skirts on wheels, as well as number of vortex stabilisers on the trailing edges. Figure 11 depicts the add-on kit installed on an actual test vehicle.

To demonstrate the effect of the add-on improvements, this full-size truck-trailer combination was tested on road. In the coast-down tests the aerodynamic performance at normal road-speed of 80 km/h was improved by some 30 %. When the share of the air drag at that speed is some 40 % of the total power use, this kind of improvement should result in some 10 % fuel consumption reduction. Dynamometer tests to prove this are still pending.

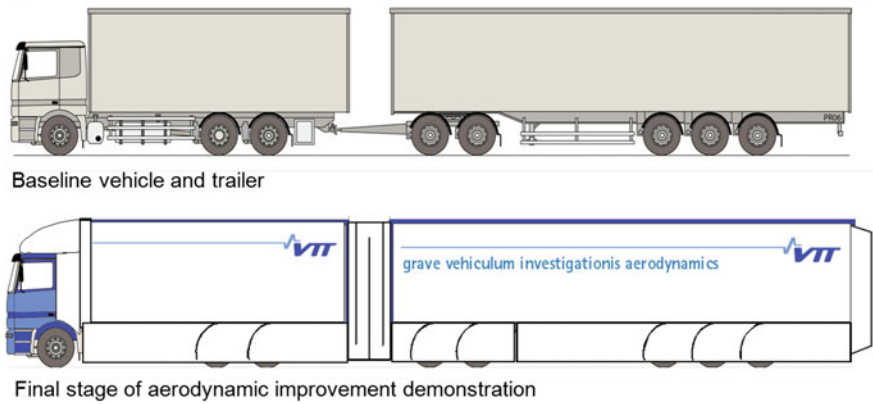
As the complete set may prove to be too complex and expensive to implement, we are also going to test the individual parts of the kit separately to see, which one’s have the best impact. More work should also be focused in making the add-on panels lighter, as this prototype set weighs around 3,500 kg.

Most of the add-on improvements implemented in our test vehicle are fully road-legal. However, as the contemporary design often tries to maximise the cargo





**Fig. 9** CAD-model renderings of the truck and trailer, combination vehicle, as well as a scaled-down solid model for wind-tunnel testing of advanced aerodynamics



**Fig. 10** Graphical representation of the baseline combination vehicle, and the aerodynamic upgrade kit for improved performance





**Fig. 11** Test vehicle with the aerodynamic upgrade kit

**Fig. 12** Aerodynamic upgrade of trailer trailing edge



space in terms of total vehicle length, using the trailing-edge improvements like those pictured in Fig. 12, may adversely increase the total length of the combination in some cases to exceed the maximum permitted length, which according to current regulations is 25.25 m.

A further area of work would then be to have legislation amended so that this kind of extensions are allowed, and do not compromise vehicle cargo carrying capacity.

**Acknowledgments** The authors acknowledge the valuable support of various organisations: the truck operator VR Transpoint in lending the truck used as full-scale demonstrator, as well as the trailer manufacturer Ekeri for the rental of the trailer. Furthermore, Finnish companies Ekin Muovi and Qviber deserve our gratitude for their high-class craftsmanship in manufacturing the various “bits-and-pieces” of the aerodynamic kit.

The studies mentioned in this paper were made within the national research integrate “TransEco” that focuses on energy efficiency and increased use of renewable energy in road transport. Main founding organisations for TransEco are the Finnish Funding Agency for Technology and Innovation (TEKES), as well as the Ministry of Transport and Communication and Finnish Transport Safety Agency (TraFi).

## Reference

1. Laurikko J, Erkkilä K, Nylund NO (2006) Generating realistic emission factors for heavy-duty vehicles—methods and first results. Paper F2006P238. In: Proceeding of FISITA 2008 conference, Yokohama, Japan

# Study on the Active Front Steering System with Steady Gain

Youkun Zhang and Baohui Liu

**Abstract** As a new technology in vehicle steering system, the active steering system (ASS) can change the ratio of steering system. The driving stability and maneuverability will be increased with it. The control strategy of active steering system is very important while vehicle is steering. There are many ways to solve the problem of the control strategy of ASS. The ratio of ASS will be controlled by the ruler of the steady gain of steering angular acceleration in this paper. The ratio of ASS can be controlled according to the speed of vehicle. So this method and its result are very useful in high speed steering condition. There are two ways to calculate the ideal ratio of steering system. One way is yaw velocity, the other is lateral acceleration. Compare the ideal ratio of steering system can be determined because the gain of yaw angular velocity and lateral acceleration are constant value.

**Keywords** Active steering system · Yaw angular velocity · Steady state

## 1 Introduction

Active front steering system is one of the vehicle chassis integrated control technology [1]. The main function is to improve the vehicle steering characteristics. The key is to input an additional angle to the steering wheel, so the driver's steering angle is corrected, and the vehicle is controlled by both the driver and the ASS, so

---

F2012-E01-025

---

Y. Zhang (✉) · B. Liu  
Jilin University, Jilin, China  
e-mail: zhangyk@jlu.edu.cn

that the steering performance in low speed and stability in high speed can be improved [2].

Mostly the ratio of vehicle steering system is a certain value or a variable value in very small range [3]. When vehicle is steering in low speed, the driver should turn the steering wheel substantially and with low portability and sensitiveness [4]. When vehicle is steering in high speed, a slight rotation of steering wheel will cause large lateral acceleration and it lead to the vehicle changes its path, increase the trend of vehicle steering instability, and reduce its security. So it is one of the key problem during vehicle design that the vehicle keep it's lexibility in low speed and stability in high speed [3, 5].

Steering work is defined as the product of steering angle and torque during designing a steering system. There are two ways to change the steering work: (1) to provide a steering torque, reduces the torque driver applied on steering wheel; (2) provide a superposition steering angle, change the steering angle that driver make [2]. Power steering system (such as the electric power steering system) can reduce steering work by provide an additional steering torque (method 1). In this paper, steering work is changed by adjusting the steer system ratio (method 2).

## 2 Vehicle Steering Dynamics Model

Usually the vehicle handling dynamics can be studied using the monorail model with two degrees of freedom known as the "bicycle" model. This two degrees model describes the vehicle yaw motion perpendicularly to the road. The variable quantities in vehicle model are the sideslip angle ( $\beta$ ) and yaw angular velocity ( $r$ ). The origin of vehicle coordinates is pointed at the vehicle centroid (Fig. 1).

By kinematics analysis, the motion differential equation of this system is:

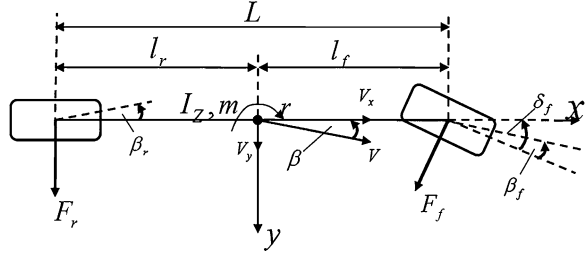
$$\begin{cases} (C_f + C_r)\beta + \frac{1}{V}(l_f C_f - l_r C_r)r - C_f \delta_f = mV(\dot{\beta} + r) \\ (l_f C_f - l_r C_r)\beta + \frac{1}{V}(l_f^2 C_f + l_r^2 C_r)r - l_f C_f \delta_f = I_z \dot{r} \end{cases} \quad (1)$$

Set  $\delta_f$  as the front wheel steering angle,  $C_f$  as the front tires cornering stiffness,  $C_r$  as the rear tires cornering stiffness, N/rad,  $l_f$  as the distance from the front wheel to the centroid of the vehicle,  $l_r$  as the distance from the rear wheel to the centroid of the vehicle,  $\beta$  as the side-slip angle,  $V$  as the vehicle speed,  $m$  as the vehicle mass,  $I_z$  as the inertia of car around the  $z$  axis,  $r$  as the vehicle yaw angular velocity.

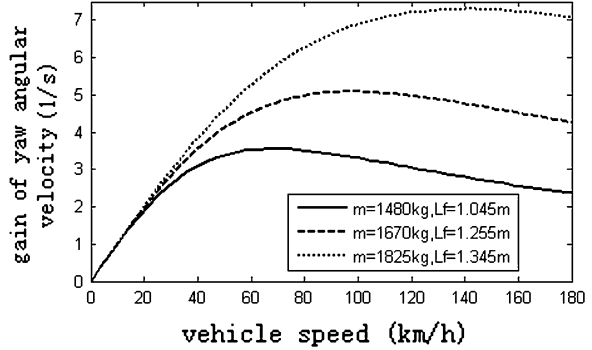
## 3 Vehicle Steering Steady State Gain

In general, with a constant speed and front wheel steer angle, the vehicle will move circling with a constant radius, it is called steady steering. Right now, the ratio of the

**Fig. 1** Vehicle linear dynamics model in two freedom



**Fig. 2** Gain of yaw angular velocity



yaw angular velocity of vehicle to the steering angle of front wheel, also the ratio of output to input, is called the gain of yaw angular velocity in steady steering state.

$$\frac{r}{\delta_f} = \frac{V/L}{1 + \frac{m}{L^2} \left( \frac{l_r}{C_r} - \frac{l_f}{C_f} \right) V^2} = \frac{V/L}{1 + KV^2} \tag{2}$$

$K$  as the stability factor, its unit is  $s^2/m^2$ , it is an important parameter that show the characterization of stationary response of vehicle.

To the FF car, the distance from the centroid to front axle will increase as adding of its mass (Fig. 2).

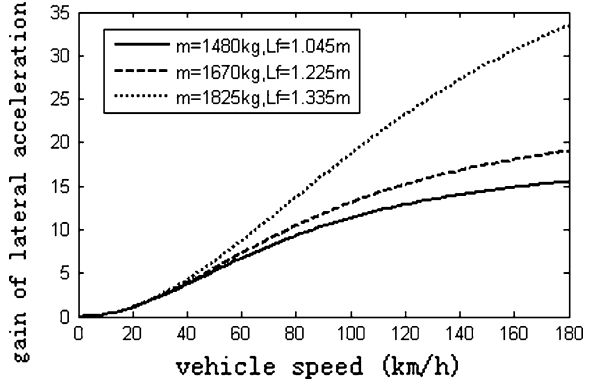
Increasing of mass, the position of car's centroid will change backward, the gain of yaw angular velocity will increase at the same speed, and the vehicle steering characteristics may be changed.

The gain of lateral acceleration at the centroid means the ratio of centroid lateral acceleration to the steering angle of front wheel in steady state.

$$\frac{a_y}{\delta_f} = \frac{V^2/L}{1 + \frac{m}{L^2} \left( \frac{l_r}{C_r} - \frac{l_f}{C_f} \right) V^2} = \frac{V^2/L}{1 + KV^2} \tag{3}$$

As increasing of car mass, the distance from centroid to the front wheel will increase too. Figure 3 is the simulation result of the gain of lateral acceleration.

**Fig. 3** Gain of lateral acceleration



## 4 Ideal Steering Ratio and Variable Steering Ratio

By analysis of steady gain, the ideal steering ratio can be determined through different way:

1. Keeping the gain of vehicle yaw angular velocity in a constant value. Ideal ratio of vehicle steering system is:

$$i_{cr} = \frac{V/L}{(1 + KV^2)G_{sw}} \quad (4)$$

The ideal steering ratio will change according to vehicle speed and  $G_{sw}$  (see Fig. 4).

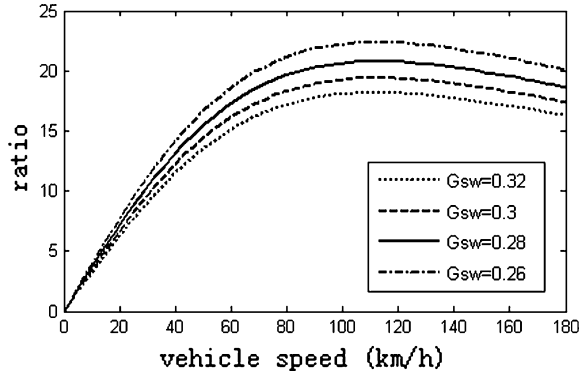
2. Keeping the gain of vehicle lateral acceleration as a constant value. The ideal ratio of vehicle steering system is:

$$i_{ca} = \frac{V^2/L}{(1 + KV^2)A_{sw}} \quad (5)$$

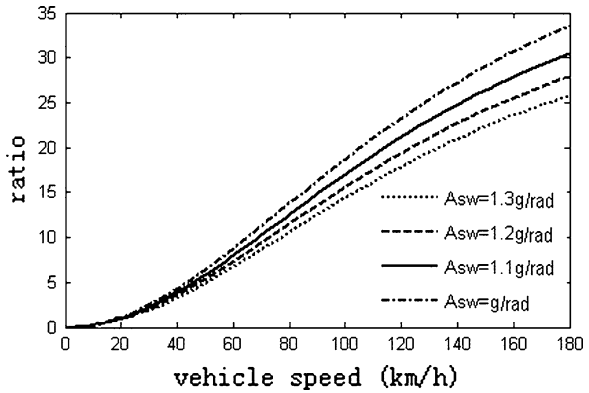
The ideal steering ratio will change according to vehicle speed and  $A_{sw}$  (see Fig. 5).

3. The ideal ratio of vehicle steering system can be determined by both the gain of vehicle yaw angular velocity and the gain of vehicle lateral acceleration. So the ideal steering ratio is:

**Fig. 4** The ideal ratio of steering system under different speed and  $G_{sw}$



**Fig. 5** The ideal ratio of steering system under different  $A_{sw}$



$$i_e = \alpha \frac{V/L}{(1 + KV^2)G_{sw}} + (1 - \alpha) \frac{V^2/L}{(1 + KV^2)A_{sw}} \tag{6}$$

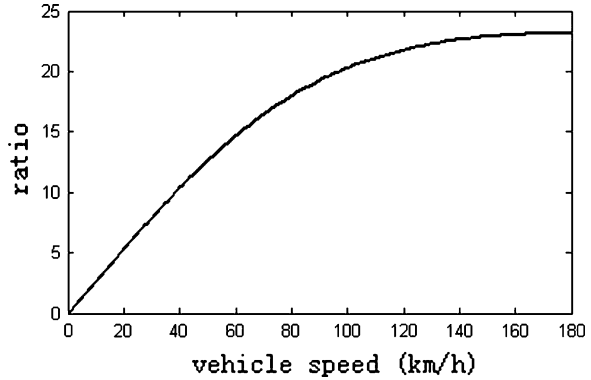
In this formula,  $\alpha$  is a weighted coefficient,  $0 < \alpha < 1$ .

If  $G_{sw} = 0.32$ ,  $A_{sw} = 1.3g/rad$ ,  $\alpha = 0.8$ , the ideal steering ratio curve is shown in Fig. 6.

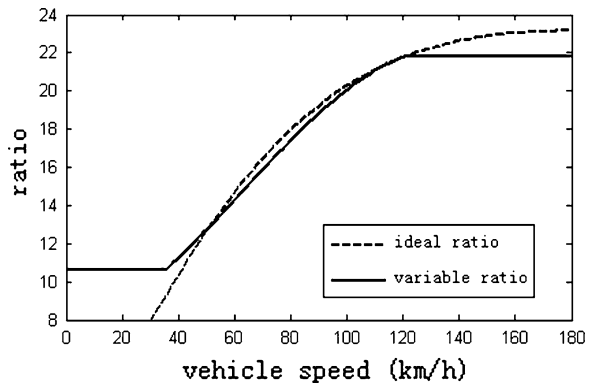
When a vehicle steering system is designed, the front wheel will turn very sensitively and the handle torque on steering wheel will be very big in low speed if the ratio is too small. Also the reaction of front wheel will be slowly to the steering wheel in high vehicle speed if the ratio is too big. The extreme values of the steering ratio are limited in high and low vehicle speed. Thus the driver can drive the vehicle easily.

How to limit the extreme value of steering ratio according to its driving condition? Usually vehicle can travel within the speed from 30 to 40 km/h in urban street, and more than 120 km/h on freeways. So the minimum steering ratio will be determined according to 35 km/h in urban streets and the maximum steering ratio

**Fig. 6** The ideal steering ratio when  $G_{SW}$  and  $A_{SW}$  was considered



**Fig. 7** The ratio of steering system adjusting with vehicle speed



according to 120 km/h on freeways. The steering ratio will not change when the vehicle speed is less than 35 km/h or more than 120 km/h. By simulation, the feasible ratio for a car is shown as Fig. 7.

## 5 Analysis About the Simulation Result of Active Steering System

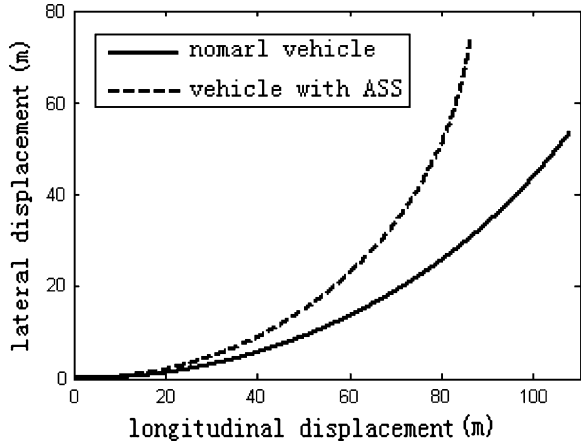
On the high attachment coefficient road, turn the steering wheel for  $20^\circ$  in 0.2 s respectively when the vehicle speed is 30 and 120 km/h.

In Fig. 8, the steering radius of ASS vehicle is decreased obviously than traditional vehicle. The vehicle takes more lateral displacement by the same longitudinal displacement. It is helpful for parking. In Fig. 9, the steering radius of ASS vehicle increases and lateral displacement decreased obviously. It's very important that the risk of lateral slip is reduced.

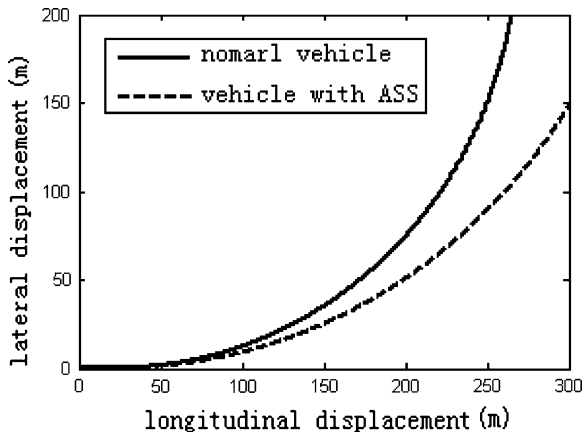
Because of the changing of steering ratio, the sensitivity to steady steering of ASS vehicle is decreased. See Fig. 10.



**Fig. 8** Comparison of trace at 30 km/h



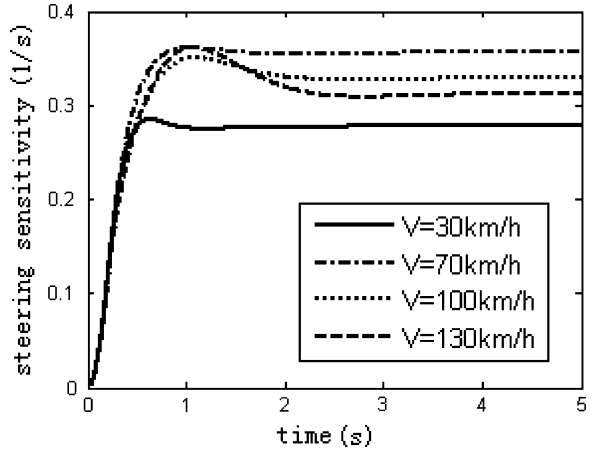
**Fig. 9** Comparison of trace at 120 km/h



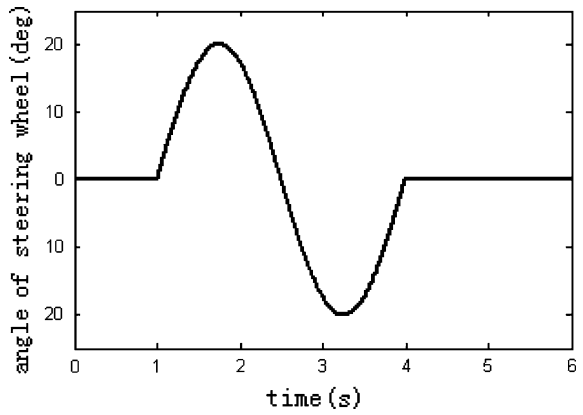
Other simulations on the vehicle routes are made when its steering wheel turns a 20° angle as a sine curve, cycle for 3 s, and its speed spread from 30 to 120 km/h. The surface of road has a high attachment coefficient certainly. The steering wheel turns as the curve in Fig. 11.

The ASS vehicle gets 0.5 m lateral displacement more than traditional vehicle. The higher motility is good at driving in urban street (See Fig. 12). The ASS vehicle saves about 3 m lateral displacement more than traditional vehicle in high speed on freeway. So the ASS vehicle can reduce the risk of traffic collision during overtaking on freeway. ASS can make the journey more safety. See Fig. 13.

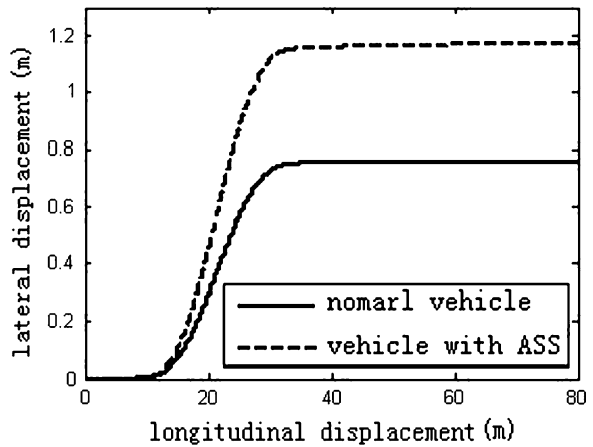
**Fig. 10** Sensitivity to steady steering of ASS vehicle



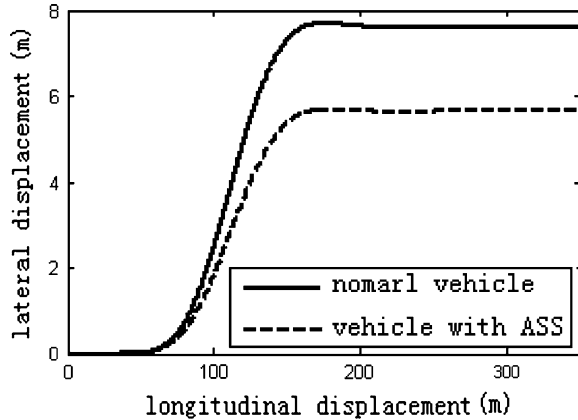
**Fig. 11** Sine angle input of steering wheel



**Fig. 12** Comparison of 30 km/h motion trace



**Fig. 13** Comparison of 120 km/h motion trace



## 6 Conclusion

ASS plays a major direction in the developing of vehicle steering system. It can change the steering ratio in a large range according to the speed.

The simulation results show that the lateral displacement of an ASS vehicle increases 51.7 % at the speed of 30 km/h when its steering wheel has been turned to 20° angle with sine style and 3 s cycle. The flexibility of low speed vehicle has been increased. The lateral displacement of an ASS vehicle decreases 27.3 % at the speed of 120 km/h when it's steering wheel has been turned to 20° angle with sine style and 3 s cycle. The driver has more time to correct the direction of vehicle. Then the risk of traffic collision due to a misoperation of driver has been reduced.

## References

1. Baohui L (2011) Study on active front steering system of vehicle. Jilin University, Jilin
2. Gao X, Yu Z, Zhang L (2006) The principle and application of mechanical active front steering system. Automot Eng 10
3. Mammari S, Koenig D (2002) Vehicle handling improvement by active steering. Veh Syst Dyn 38(3):211–242
4. Kojo T, Suzumura M, Tsuchiya Y (2005) Development of active front steering control system. SAE International, 2005-01-0404
5. Klier W, Reinelt W (2004) Active front steering (part1): mathematical modeling and parameter estimation. SAE International, 2004-01-1102

# Design Optimization of Full Vehicle Suspension Based on Ride and Handling Performance

Tey Jing Yuen, Ramli Rahizar, Zainul Abidin Mohd Azman,  
Alias Anuar and Dzakaria Afandi

**Abstract** In this paper, a new methodology is proposed to optimize a passive suspension system of a full vehicle system based on ride and handling. In passive suspension design, the conflicting design objectives are the ride comfort and handling performances. The ride comfort is defined as the level of comfort experienced by the passenger in a form of numerical values i.e. weighted root mean square (RMS) of acceleration (ISO 2631). The acceleration is measured when the car travels on a Class C random road profile adopted from ISO 8606:1995 standard. Meanwhile, handling performance is defined by quality of handling, which relate to subjective feeling of human driver and also objective measurement of the vehicle characteristics. Impulse steers maneuver (ISO7401) is employed to measure the required objectives defining handling performance, which included the RMS roll gain, phase angle of yaw rate at 0.2 and at 0.6 Hz, phase angle of lateral acceleration at 1 Hz and ratio of yaw rate gain at resonant frequency against the static yaw rate gain. These objectives will be minimized through multi-objective optimization methodology, which involves sampling technique, and regularity model based on multi-objective estimation of distribution

---

F2012-E01-026

---

T. J. Yuen (✉) · R. Rahizar  
Advanced Computational and Applied Mechanics (ACAM) Research Group, Department of Mechanical Engineering, Faculty of Engineering, Universiti Malaya, Kuala Lumpur, Malaysia  
e-mail: jingyuen\_tey85@yahoo.com

Z. A. Mohd Azman  
Faculty of Mechanical Engineering, Universiti Teknologi Malaysia, Kuala Lumpur, Malaysia

A. Anuar · D. Afandi  
Vehicle Engineering, Engineering Division, Proton Bhd, Shah Alam, Selangor, Malaysia

algorithm (RM-MEDA) to solve more than 100 dimensional spaces of design parameters. This methodology showed promising results in optimizing full vehicle suspension design compared to the conventional workflow of suspension tuning.

**Keywords** Multi-objectives optimization · Passive suspension · Suspension tuning · Suspension optimization

## 1 Introduction

In automotive industry, ride comfort and handling performance are important objectives required to define the vehicle dynamic characteristics. Ride comfort measures the comfort level experienced by the passengers while travel through rough road. In contrast, handling performance measures the response of maneuvers of the vehicle whilst maintaining its stability during cornering. However, in passive suspension design, both requirements are conflicting to each other. Softer suspension is required for a better ride comfort resulting in poor handling performance. On the other hand, stiffer suspension provides good handling and stability during cornering but at the expense of a bumpy ride. Conventionally, solving this problem often follows the suspension design cycle which require knowledge from experienced engineers or experimental benchmark to define the new performance target of the new suspension system. It follows by iterative tuning process and redesign until the target is met. This target orientated optimization process has a drawback in which the suspension system optimization is bounded by the predefined targets. In addition, most of the suspension tuning is performed using gradient-based approach which have a drawback in solving multi-objective functions and may trap in local optimum. These methods work well for a small number of design variables. As the design variables increase along with the conflicting design objectives, this method becomes inefficient. Therefore, in this paper, a new methodology is proposed specifically to address the problem of large design variables with conflicting design requirements. It consists of design of experiment (DOE) and a Regularity Model-Based Multi-Objective Estimation of Distribution Algorithm (RM-MEDA) to provide the Pareto Front to achieve the best compromised set of solutions between ride and handling performances.

## 2 Ride Comfort Criteria

Ride comfort often describes the subjective feeling of human experiences as the vehicle travels through the irregular road surface. However, subjective feeling may vary from one person to another thus requiring some measurement technique to quantify the comfort level. Thus random road profiles are employed to simulate the

**Table 1** Perception of human comfort according to ISO2631-1:1997

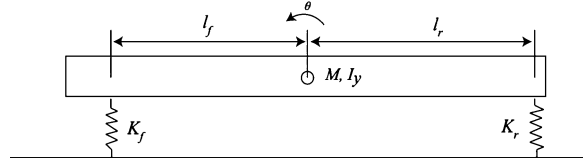
Acceleration (m/s <sup>2</sup> )	Comfort level
<0.315	Not uncomfortable
0.135–0.63	A little uncomfortable
0.5–1	Fairly uncomfortable
0.8–1.6	Uncomfortable
1.25–2.5	Very uncomfortable
>2	Extremely uncomfortable

rough road surfaces and ISO 2631: 1997 standard [1] is then used to measure the ride comfort of passenger in the vehicle.

International Standard Organization (ISO 2631) has developed detailed recommendations concerning acceptable vibration limits for both people and structures. Frequency analysis computes the weighted RMS acceleration to determine the human comfort level (Table 1). In the random road simulation, the vehicle is selected to travel at 80 km/h on a class C road profile adopted from the ISO 8606:1995 standard. Class C road profile emulates a rough road surface. Study showed that this objective measurement has a good correlation with the suspension design parameters in minimizing the objective function that improved the ride comfort [2–4]. In order to achieve the best comfort criteria, large suspension travel space is needed. However, the suspension working space is limited depending on the suspension packaging. Therefore, minimization of the RMS suspension travel for front and rear are crucial.

In addition to the ride comfort criteria by ISO 2631:1997 standard, there are other important ride comfort criteria based on the vehicle characteristics. Maurice Olley was one of the founders of modern vehicle dynamics established guidelines back in 1930s for designing vehicles with good rides. Those guidelines are considered as valid rule of thumb even for today's modern cars. In Olley criteria [5, 6], it stated that the front suspension should have a 30 % lower ride rate than the rear suspension, the pitch and bounce frequencies should be close together, and neither frequency should be greater than 1.3 Hz. Besides, there is a magic number in suspension design which also used to define the ride comfort vehicle characteristics. It is in the form of an empirical results based on experience from the engineer as proposed by Barak [6]. Both Olley and magic number criteria will be employed as constraints in the optimization problem formulation to optimize the vehicle suspension system. The pitch and bounce frequencies of the vehicle can be computed with the used of half vehicle mathematic model as follows:

$$f_1 = \frac{1}{2\pi} \sqrt{\frac{a+c}{2} + \sqrt{\frac{(a-c)^2}{4} + \frac{b^2}{K^2}}} \quad (2)$$

**Fig. 1** Half vehicle model

$$f_2 = \frac{1}{2\pi} \sqrt{\frac{a+c}{2} - \sqrt{\frac{(a-c)^2}{4} + \frac{b^2}{K^2}}} \quad (3)$$

where,  $a = (K_f + K_r)/m_s$ ,  $b = \text{coupling coefficient} = (K_r l_r - K_f l_f)/m_s$ ,  $c = (K_r l_r^2 + K_f l_f^2)/I_y$ ,  $DI = \text{Dynamic Index} = (K^2/l_f l_r)$ ,  $I_y = m_s K^2$ ,  $K_f = \text{Front spring stiffness}$ ,  $K_r = \text{Rear spring stiffness}$ ,  $l_f = \text{Distance from the front axle to the center of gravity (CoG)}$ ,  $l_r = \text{Distance from the rear axle to the CoG}$ ,  $K = \text{Radius of gyration}$ ,  $I_y = \text{Pitch moment of inertia}$ , and  $Z = \text{vertical displacement of body at CoG}$ .

The half vehicle model in Fig. 1 is an undamped two degrees of freedom model. It consists of two principal vibration modes, i.e. pitch and bounce motion. By summing the equilibrium force and moment of the system at CoG and the solution will lead to the two equations in Eqs. (2), (3) representing the two natural frequencies. Both equations have a common coupling coefficient. If the system is uncoupled (coupling coefficient = 0), the pitch motion and bounce motion will have an independent motion. However, the two vibration modes are generally coupled. Dynamic index is an indicator to identify when the pitch frequency and bounce frequency are equal. When the dynamic index close to one, it will eliminate the heterodyning effect on the vehicle. Heterodyning is a phenomenon when two closely spaced frequencies interact to produce a “beat” frequency which can induce motion sickness symptom.

### 3 Handling Performance Criteria

Handling performance involves subjective and objective evaluation of a vehicle. Subjective evaluation refers to driver feeling of the vehicle response when performing manoeuvring whereas objective evaluation refers to vehicle dynamic characteristics. It varies from one person to another and makes the evaluation difficult to be quantified. Many studies had been carried out using various methodologies to measure subjective feeling to ascertain the relationship between subjective and objective measurements [1, 4, 7–9]. Each methodology is suited for different cases of measurement and manoeuvring tests. At present, there is no general methodology to deal with relationship between subjective and objective evaluation of a vehicle handling performance [7]. However, there is common

outcome from various methodologies that can be adopted as the objective measurement function in the optimization process. Impulse steers maneuver (ISO7401—lateral transient response with open loop method [10]), is suitable to assess the quality of handling performance. Additionally, the measurement of frequency response function of steer input provides good interpretation between subjective and objective measurements [7, 11, 12]. Ash employed nonlinear correlation analysis to determine the relationship between the subjective evaluations through questionnaire and numerical measurement of vehicle motion [12]. The analysis suggested that the natural frequency of yaw rate within 1.7–2.1 Hz; damping ratio around 0.7; lateral acceleration phase delay at 1 Hz  $< -75$  deg; static yaw gain rate 0.1–0.2; will give good subjective rating. Additionally, in other works [7, 11] also suggested that the objective measurement of phase delay angle for yaw rate frequency response against steering at 0.2 Hz (which represents the yaw response at low speed steer) and 0.6 Hz (which represents the yaw response at high speed steer) should have a smaller phase delay to allow faster vehicle response. Ratio of yaw rate response gain against steering frequency resonant  $G(f_r)$  over static yaw rate gain  $G(f_0)$  should kept at minimum to minimize changes in yaw rate gain throughout the frequency range for better handling and improve stability during driving maneuver.

## 4 Vehicle Model Setup

The vehicle suspension is modelled using MSC.ADAMS/CAR as illustrated in Fig. 2. The suspension model is developed based on the existing CAD data. The front suspension of the vehicle is a McPherson strut, and rear suspension is a trailing arm design. All design variables that contribute to the ride and handling performance are identified. There are about 121 design variables comprises of design hard points of suspension in  $x$ ,  $y$ , and  $z$  directions, bushing stiffness, spring stiffness, damper profiles and antiroll bar stiffness. The design space of each design variable is defined based on the existing design which serves as a reference by considering the dimensional space of suspension packaging.

The nonlinear damper profiles used in original vehicle model are parameterized with the used of piecewise function (4) and the profile is shown in Fig. 3. This is to emulate the characteristics of nonlinear suspension damper whilst manipulation of damper profiles is possible with the optimization algorithms. Bushing profiles in  $x$ ,  $y$  translational directions as well as rotational  $x$ , and rotational  $y$  directions are modelled as linear function similarly for other components of suspension such as spring and antiroll bar stiffness. All the suspension components are connected using joints to define the degree of freedom for each component relative to others according to the actual physical suspension design. The complete full vehicle model consists of 61 degrees of freedom.





Fig. 2 Full vehicle assembly in MSC.ADAMS/Car

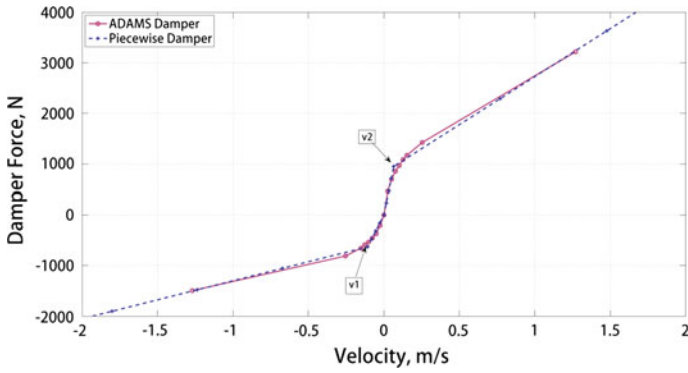


Fig. 3 Piecewise function of damper profile

$$F(v) = \begin{cases} C_1v + (C_2 - C_1)V_1, & v < V_1 \\ C_2v, & V_1 < v < 0 \\ C_3v, & 0 < v < V_2 \\ C_4v + (C_3 - C_4)V_2, & V_2 < v \end{cases} \quad (4)$$

where,  $F(v)$  is the damper force function,  $C_1 - C_4$  are the damper coefficients, and  $V_1 - V_2$  are the corresponding velocities.

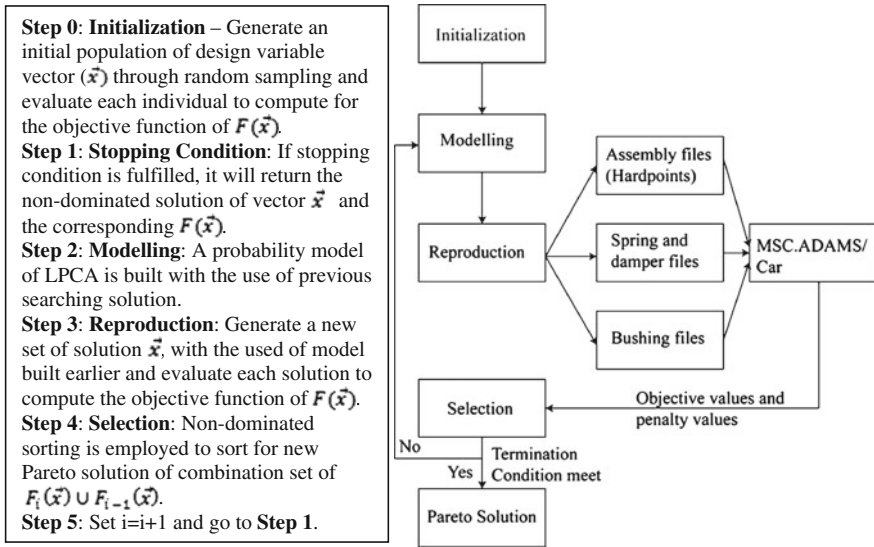


Fig. 4 Pseudo code of RM-MEDA and optimization workflow

## 5 Optimization

RM-MEDA is a statistical-based algorithm originates from the Estimation of Distribution Algorithm (EDA) [8]. RM-MEDA employed the regularity property of Karush–Kuhn–Tucker condition to solve continuous multi-objective optimization problems with variable linkages [13]. It uses local principal component analysis (LPCA) algorithm for building a model in a promising area of design variable space based on the previous search and estimated samples. Non-dominant sorting method is utilized for selecting the non-dominant solution from the evaluated samples for next generation. Statistical tests on RM-MEDA demonstrate that it is not sensitive to the algorithm’s parameters. It has good scalability in solving a large number of design variables and performs better in solving various kind of benchmark problems [13]. This makes the algorithm suitable to be employed to optimize full vehicle suspension system since it involves large design variables and robust in handling multi-objective problems.

In the optimization process, MSC.ADAMS/Car is integrated with RM-MEDA to perform software in the loop optimization as shown in Fig. 4. DOE is used to perform an initial searching on the large dimension design variables space. Sobol sequence sampling method [14] is employed to maximize the sparseness of each design variables combination across the design spaces. The optimization algorithm setup is initialized by population selected from the previous DOE results. This helps to speed up the searching into the Pareto Front and searching starts from the region of interest preselected from the DOE results. The preselected samples will be used to build LPCA meta-model and generate new solution (Reproduction

**Table 2** Objective functions and constrains functions employed in optimization

Objective functions	Rides
	(5) $Weighted\ r.m.s\ ACC = \sqrt{\sum_{i=1}^n (wacc_x^2 + wacc_y^2 + wacc_z^2)} / n$
	(6) $Mean\ r.m.s.Spring_{Front} = 0.5 \times \left( \sqrt{\sum_{i=1}^n (Spr_{f1}^2)} / n + \sqrt{\sum_{i=1}^n (Spr_{f2}^2)} / n \right)$
	(7) $Mean\ r.m.s.Spring_{Rear} = 0.5 \times \left( \sqrt{\sum_{i=1}^n (Spr_{r1}^2)} / n + \sqrt{\sum_{i=1}^n (Spr_{r2}^2)} / n \right)$
	(8) $RMS\ roll\ gain = \sqrt{\int_{f=0}^{2\pi}  H(f) ^2 df} / 2\pi$
	(9) Absolute yaw rate phase at 0.1 Hz
	(10) Absolute yaw rate phase at 0.6 Hz
	(11) Absolute lateral acceleration phase at 1 Hz
	(12) Yaw gain ratio of $G(f)/G(f_0)$
	(13) $V_{f1} =  Obj_{f1} - 1.3  / 1.3$
	(14) $V_{f2} =  Obj_{f2} - 1.3  / 1.3$
	(15) $V_{DI} =  Obj_{DI} - 1 $
	(16) $1.7 \leq \omega_{yaw} \leq 2.1\ V_{\omega_{yaw}} =  Obj_{\omega_{yaw}} - 1.9  / 1.9$
	(17) $0.6 \leq \xi_{yaw} \leq 0.8, V_{\xi_{yaw}} =  Obj_{\xi_{yaw}} - 0.7  / 0.7$
	(18) $0.1 \leq \text{yaw static gain} \leq 0.2,$
	(19) $V_{yaw\ static\ gain} =  Obj_{yaw\ static\ gain} - 0.15  / 0.15$
	$V = 0.5 \times (V_{\omega_{yaw}} + V_{\xi_{yaw}} + V_{yaw\ static\ gain}) / 3 + 0.5 \times (V_{f1} + V_{f2} + V_{DI}) / 3$
Constrain functions	
	Rides
	Handling
	Overall function

$wacc_x, wacc_y$  and  $wacc_z$  are weighted acceleration measured in x, y, and z. n is number of samples for discrete time step perform in simulation.  $Spr_{f1}$  and  $Spr_{f2}$  are the suspension travel for left and right wheel

$H(f)$  is transfer function of roll angle with respect to frequency response of steer input.  $f$  is frequency in rad/s

$\omega_{yaw}$  natural frequency of yaw rate,  $\xi_{yaw}$  is damping ratio of yaw rate, and the yaw static gain.  $V_{\omega_{yaw}}, V_{\xi_{yaw}}$  and  $V_{yaw\ static\ gain}$  are the penalty values for respective constraint function.  $Obj_{\omega_{yaw}}, Obj_{\xi_{yaw}},$  and  $Obj_{yaw\ static\ gain}$  are the objective measured values evaluated from new design parameters

step). Each solution consists of a vector of design variable. Each design variable in the solution is used to generate necessary model file required by MSC.ADAMS to perform different simulation to evaluate the objectives values (Fig. 4). Termination condition of the optimization algorithm is defined by 100 generations. Extending the search with increasing number of generation will help in improving the optimized results but at the expense of extensive solution time. In this study, 100 generations took one week of solving time.

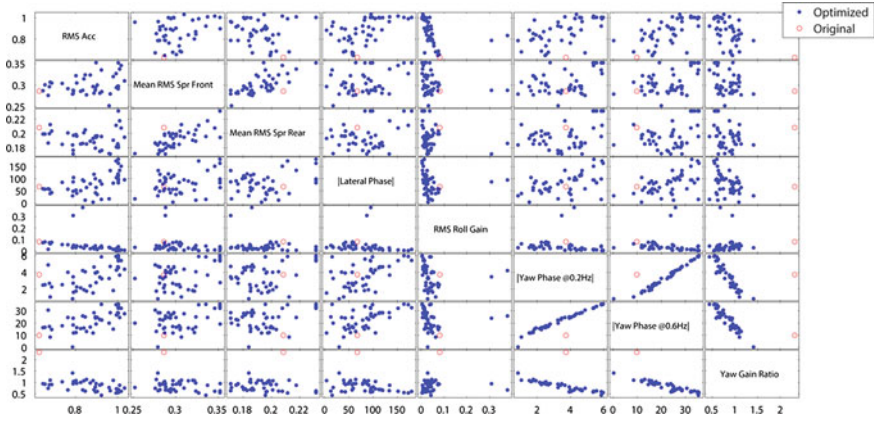
There are eight objectives used as minimization function defined by ride comfort and handling performance together with 6 constraint functions (Table 2). There are three objectives functions, which defined by ride comfort criteria i.e. weighted RMS acceleration (5), average RMS suspension travel for front and rear suspension (6–7).

Besides, it is also important to maintain the robustness of the vehicle in providing ride comfort in different road conditions. Therefore, the guidelines of magic ride numbers and Olley criteria are employed as the constraints (13–15). In handling performance, there are five objectives to be minimized (8–12). RMS roll gain against steer input is selected due to safety concerned in handling maneuver. A high roll gain with a given steer input is dangerous and may cause the vehicle to roll over. The penalty values for handling performance are defined in Eqs. (16–18). The constraint function in handling is included to enhance the subjective feel of handling performance.

In RM-MEDA constraint functions are handled by penalty values (soft constraint method). Non-dominant solution with minimal violation of constraint or minimal penalty values will be selected for the next generation to regenerate new offspring. All the constraint penalty values are defined in terms of a ratio which standardize the scale of the function and thus by employed the summation of all penalty will give the overall penalty value of equal weighting towards every constraint function of a given solution evaluated through simulation (19).

## 6 Results and Discussions

The Pareto solution in Fig. 5 represented the comparison between the optimized solutions and the original design values. It is noticeable that the original vehicle design is not fully optimized as compared to the Pareto solution. The original vehicle design has a good ride (RMS acceleration) as compared to the other Pareto design solution shown in Table 3. However, it showed a poor performance in terms of quality of handling i.e. high RMS roll gain, high yaw gain ratio, and poor yaw damping coefficient. Five Pareto solutions are selected out of 50 Pareto solutions for comparison and are shown in Table 3. Each of the design solutions represented the different characteristics of optimized vehicle dominating in different objectives. Comparison study is conducted on the selected Pareto design solution for further explore its different in the performance of vehicle's ride and handling characteristics. First and second vehicle designs were selected from



**Fig. 5** Pareto matrix plot of optimized objectives against original objectives values

**Table 3** Objectives values of selected five Pareto designs comparison with original objectives values

Objectives	Designs					
	1	2	3	4	5	6
RMS ACC	0.679	0.645	0.686	0.802	0.79	0.627
Mean RMS spring front	0.307	0.287	0.305	0.322	0.287	0.286
Mean RMS spring rear	0.212	0.199	0.203	0.198	0.197	0.208
Dynamic index	1	1.002	0.997	1.017	1.008	1.015
1st frequency	0.874	0.92	0.899	0.866	0.97	1.061
2nd frequency	0.85	0.905	0.879	0.858	0.859	0.866
Lateral phase at 1 Hz	-39.296	-58.871	-43.029	-53.1	-104.944	-67.545
RMS roll gain	0.063	0.073	0.075	0.03	0.05	0.082
Yaw phase at 0.2 Hz	-1.067	-2.482	-2.256	-1.764	-1.633	3.738
Yaw phase at 0.6 Hz	-8.548	-16.263	-14.637	-12.156	-11.898	9.931
Yaw gain ratio	1.101	0.947	0.906	1.084	1.043	2.322
Yaw natural frequency	1.717	1.736	1.831	1.761	1.686	1.136
Yaw damping coefficient	0.667	0.64	0.744	0.618	0.725	0.38
Yaw static gain	0.142	0.158	0.173	0.105	0.148	0.128

Design 6 is the original vehicle design values

Table 3. The first design showed equivalent ride comfort level as compared to original design which fell in the fairly uncomfortable (refer to Table 1). However, it gave a good performance rating in handling aspects. It has minimal of phase lag in lateral acceleration, yaw rate phase lag (either in high or low frequency steer) and yaw gain ratio. The second vehicle design has about the similar performance as compared to the first design. However, it has a slightly higher phase lag in lateral acceleration and yaw rate response. The selected designs were benchmarked against that of the original vehicle.

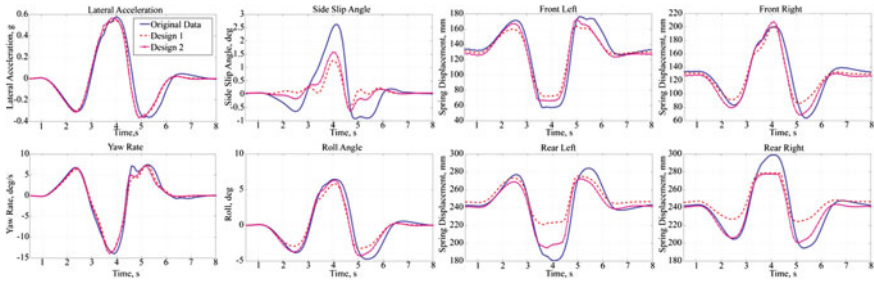


Fig. 6 Handling performance of double lane change test—100 km/h

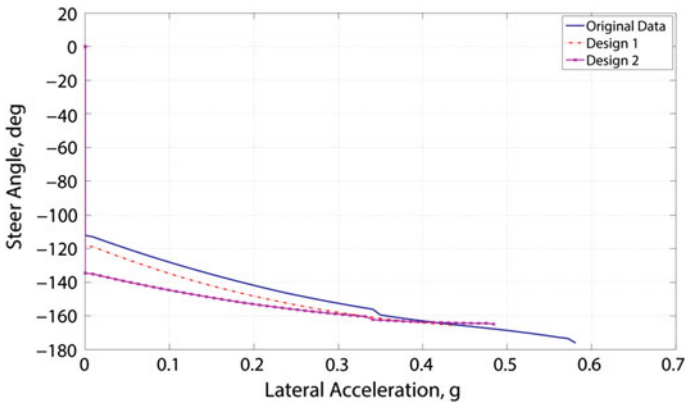


Fig. 7 Quasi-static constant cornering radius test—40 m radius

Transient maneuver test of double lane change and quasi-static constant cornering radius test were selected to study the vehicle dynamic handling characteristics. For double lane change, comparison between newly optimized designs plotted against the original design is shown in Fig. 6. Noticeable improvement of the optimized designs can be observed. The lateral phase lags in the optimized design are lesser as compared to the original design (Table 3) thus indicates faster lateral response time. The optimized designs also generate less roll gain (1st design < 2nd design < original design). Similar improvement can be observed in the transient response for roll angle and yaw rate response. The two optimized designs produce higher damping and reduce the yaw oscillation when performing the double lane change. Besides, the optimized designs also have less suspension working space as the spring deformation is smaller than that of the original design (Fig. 6). All these results suggest that the optimized suspension designs much better quality handling performance as compared to the original vehicle except for the RMS roll gain where the 2nd design gives a slightly higher roll gain. In constant cornering radius test as shown in Fig. 7, it is clearly noticeable that both designs give a different understeer characteristic. Design 1 has the similar understeer gradient as

compared to the original design at low lateral acceleration level. However, as the lateral acceleration increases the understeer gradient of design 1 decreases compared to original design. Whereas, for the design 2 the vehicle generally gives much lower understeer gradient compared to the others design.

Based on the case study, the optimized designs showed reasonable improvement as compared to the original design.

## 7 Conclusion

This methodology of optimizing full vehicle suspension based on ride and handling performances has been developed and examined. It was found suitable to optimize large suspension design variables with conflicting design requirements. The optimization technique can be employed as alternative technique in suspension tuning which can shorten the suspension design cycle thus reducing the vehicle development time during the design phase.

## References

1. ISO (1997) Mechanical vibration and shock—evaluation of human exposure to whole-body vibration—Part 1: General requirements, in ISO 2631-1:1997(E). Geneva: International Organization for Standardization
2. Tey JY et al (2010) Multi-objective optimization based on realistic quarter vehicle model, in international conference on sustainable mobility. SAE, Kuala Lumpur
3. Tey JY, Ramli R (2010) Comparison of computational efficiency of MOEA/D and NSGA-II for passive vehicle suspension optimization, in 24th European conference on modelling and simulation. ECMS, Kuala Lumpur
4. Ramli R et al (2011) Multi-objective optimization based for realistic quarter vehicle model. In: Proceedings computationally optimised fuel-efficient concept car (COFEC), University of Kebangsaan Malaysia, Bangi
5. Olley M (1961) Notes on Suspension
6. Barak P (1991) Magic numbers in design of suspensions for passenger cars. SAE International, 911921(SP-878):53–88
7. Abe M (2009) Vehicle handling dynamics: theory and application. Butterworth-Heinemann, Oxford
8. Larrañaga P, Lozano EJA (2001) Estimation of distribution algorithms: a new tool for evolutionary computation. Kluwer Academic, Norwell
9. Uys PE, Els PS, Thoresson MJ (2006) Criteria for handling measurement. J Terramech 43(1):43–67
10. ISO (2003) Road vehicles—lateral transient response test methods—open-loop test methods, in ISO 7401:2003 (E). Geneva: International organization for standardization
11. Dukkipati RV et al (2010) Road vehicle dynamics. SAE International, Warrendale
12. Ash HAS Correlation of subjective and objective handling of vehicle behaviour. Doctor of Philosophy, School of Mechanical Engineering, The University of Leeds
13. Zhang Q, Zhou A, Jin Y (2008) RM-MEDA: a regularity model-based multiobjective estimation of distribution algorithm. IEEE Trans Evol Comput 12(1):41–63
14. Sobol IM (1993) Sensitivity analysis of nonlinear mathematical models. Math Model Comput Exp 1(4):407–414

# Improve Fuel Economy of Commercial Vehicles Through the Correct Driving

Ping Guo, Zhenlei Li, Zhiwu Zhang, Jun Chi, Shuai Lu, Ye Lin, Zhengfa Shi and Jingcai Shi

**Abstract** High fuel consumption is a serious problem facing the Chinese government and commercial vehicle companies. While continuously optimizing vehicles' fuel performance and guiding customers to buy right vehicles, we are committed to teach the users to achieve the best fuel consumption through correct driving. In a 5 year project of the driving behavior of commercial vehicle drivers, we've found that different driving styles are able to cause a 30–50 % increase in fuel consumption. Through acquisition of a large amount of driving data, we've established identification methods for driving behaviour, namely, *APP Map* and *AET Map*. We have also summarized the operation key points of saving fuel and helped the transporters to improve their fuel consumption with the methods. At the same time, we've developed a device to help drivers to drive in a fuel-efficient way.

**Keywords** Commercial vehicle · Fuel consumption · Driving behavior · APP (AET) Map · Correct driving

## 1 Introduction

High fuel consumption is a serious problem facing the Chinese government. In December 2011, GB/T27840-2011 *Fuel consumption test methods for heavy-duty commercial vehicle* and QC/T924-2011 *Fuel consumption limits for heavy-duty*

---

F2012-E01-029

---

P. Guo (✉) · Z. Li · Z. Zhang · J. Chi · S. Lu · Y. Lin · Z. Shi · J. Shi  
Faw R&D Center, Changchun, China  
e-mail: guoping@rdc.faw.com.cn



*commercial vehicles (The first stage)* were released. The standards will speed up the development of advanced technologies used in commercial vehicles, but it's helpless in solving the fuel consumption problem at customer layer.

In order to achieve the best fuel consumption of commercial vehicles, there are three key points. First, the vehicle shall have a good performance, which could be provided by vehicle companies and enhanced by the new standards. Second, the customer shall buy the right vehicle, the power train of which matches the working condition, thus making it possible for the engine to work in a fuel-efficient manner. Third, the customer shall know how to use the vehicle correctly.

In the actual practice of transportation, the third key point is of the utmost importance. Even with the same vehicle and transportation mode, fuel consumption can be totally different. In a 5 year project of the driving behavior of commercial vehicle drivers', we've found that different driving styles are able to cause a 30–50 % increase in fuel consumption.

## 2 Identification Methods for Driving Behaviour

Since 2007, we have been solving the customers' problems regarding the fuel consumption of commercial vehicles. Some of our customers complained about the high fuel consumption problem of their commercial vehicles. In order to find out the reasons, we always went to their place, and travelled together with them to get the details of the transportation.

At first, we had to install many sensors on the vehicle to obtain the vehicle speed, engine speed, accelerator pedal position and the GPS signals, etc. However, from July of 2008, the acquisition became easier because we can gain much more data from CAN bus of the electronic controlled Euro III engine.

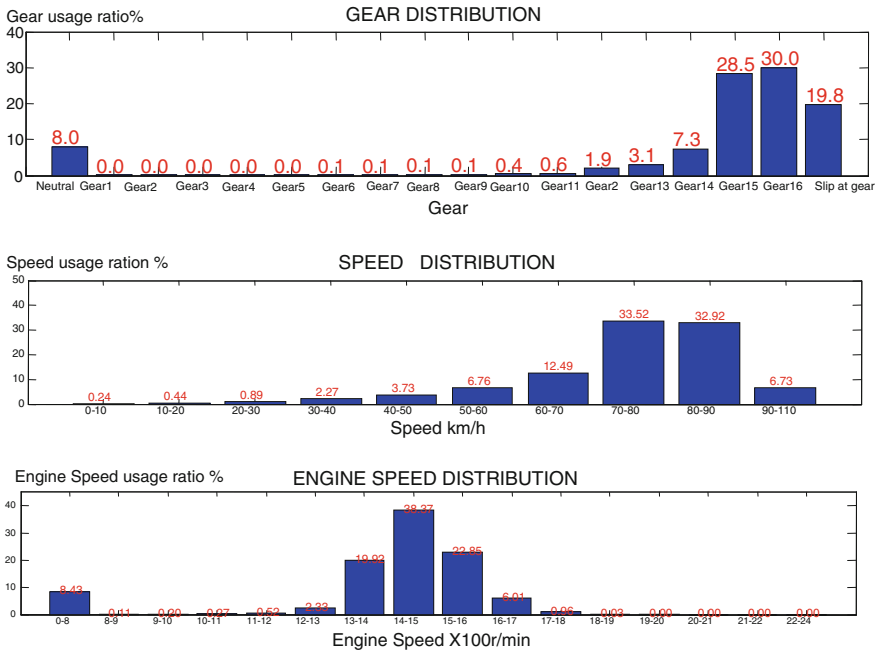
To analyse the problem of high fuel consumption, we manage the data in different ways, such as gear distribution, engine speed distribution, vehicle speed distribution and accelerator position distribution, etc., as is shown in Fig. 1.

Through these figures, we could know how the vehicle works. Together with the observation of the driver's driving behaviour during transportation, we can come to a conclusion of the customer's fuel consumption problems.

Nearly 80 % of these customers have driving problems. Yet without travelling with them, we can hardly describe the incorrect driving behaviours of these drivers with the illustrations above. And if we can't point out the concrete details, it's very difficult to persuade the drivers to change their driving habits that last for years.

### 2.1 Introduction of APP Map and AET Map

In order to find an easier and visual way to evaluate the driving behaviour of commercial vehicle drivers without travelling with them, we tried to put the



**Fig. 1** Gear distribution, vehicle speed distribution, and engine speed distribution

driver’s operation characteristics in one map, and after a great many attempts, we finally find out a perfect way.

Figure 2 is the driver’s accelerator pedal position (APP) Map. The horizontal axis indicates the engine speed, the vertical axis indicates the accelerator pedal position, and the colour is the third axis, which represents how much distance (or time) proportion in exactly the engine speed and APP region is. With the colour changing from dark blue to red, the proportion increases.

The APP Map is the driver’s action, and it represents the driver’s demand on the engine. From this map, we can identify the driver’s behaviour, speeding, high APP, swinging APP, idling, etc.

In some cases, we also use a similar map, the actual engine percent torque (AET) Map, shown in Fig. 3.

With the two-range governing engine, the APP Map and the AET Map are almost the same. But with a variable-speed governing engine, the APP Map and the AET Map could be much different. We also use these Maps to evaluate and optimize the governing characteristics of an engine. In cases when the engine has a multi switch to change its characteristics, the AET Map is also used.

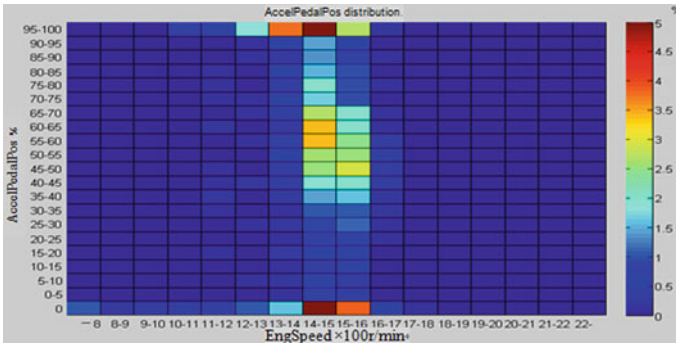


Fig. 2 Driver’s accelerator pedal position (APP) Map

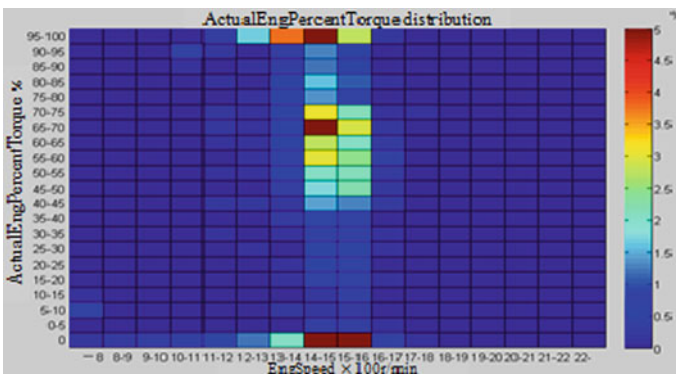


Fig. 3 Actual engine percent torque (AET) Map

### 3 Identification of Correct and Incorrect Driving Behaviour

With APP Map, the driver’s behaviour becomes visible, but how to distinguish between good and bad driving behaviour remains a question.

So we began to collect driving data of different commercial vehicles. After collecting driving data of hundreds of vehicles and identifying characteristics of different APP Map, we finally figure out the key points in APP Map for distinguishing between good and bad driving behaviour.

#### 3.1 Correct Driving Behaviour

When a driving APP Map looks like Fig. 4 the fuel consumption of the vehicle must be very excellent. And as to vehicles which have good fuel consumption, the APP Maps look alike.

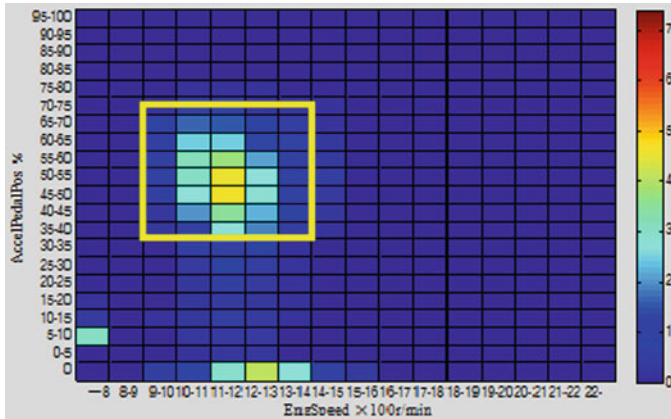


Fig. 4 Correct driving APP Map

The main points of correct driving can be summed up as follows:

1. The engine speed varies from about 1,000 to 1,500 r/min.
2. The actual engine percent torque varies from about 30 to 80 %.
3. The idling time takes up low proportion.

### 3.2 Incorrect Driving Behaviour

#### 3.2.1 Incorrect Driving Behaviour No 1: Throttle Wide Open

Some drivers, especially drivers from North China, like speeding. They do not accept any other vehicle moving ahead theirs, thus overtaking every vehicle is their habit. In APP Map of this kind of drivers, the 100 %APP ratio is very much, as is shown in the yellow circle of Figs. 5 and 6.

#### 3.2.2 Incorrect Driving Behaviour No 2: High Engine Speed

Working at high engine speed too much is another incorrect driving behaviour, shown in Figs. 5 and 6 the right part of the red line.

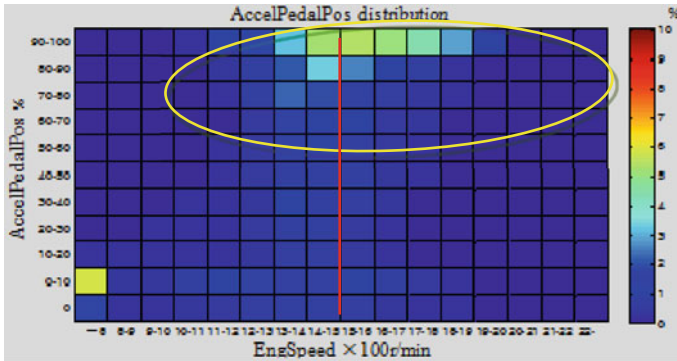


Fig. 5 Throttle wide open APP Map and high engine speed 1

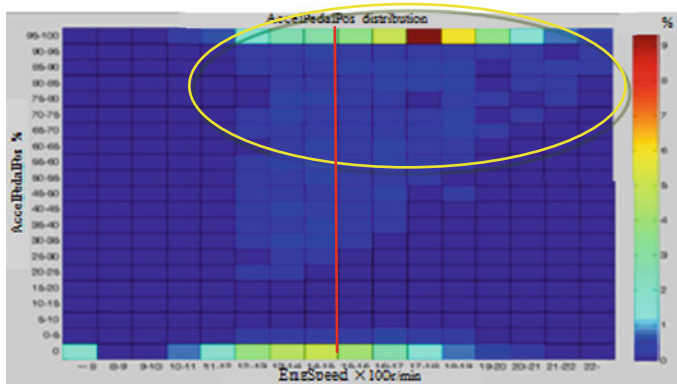


Fig. 6 Throttle wide open APP Map and high engine speed 2

### 3.2.3 Incorrect Driving Behaviour No 3: Swinging Accelerator Pedal Position

Some drivers like to accelerate the vehicle to a higher speed, then loosen the pedal and let the vehicle coast down. When the speed becomes lower, the above actions are repeated.

This kind of driving behaviour makes the engine working in an unsteady condition. Repeated acceleration makes the engine working under high load too much and meanwhile worsen the fuel consumption. In APP Map of this kind of drivers, the pedal position points have a wide distribution, shown in the yellow circle of Fig. 7.

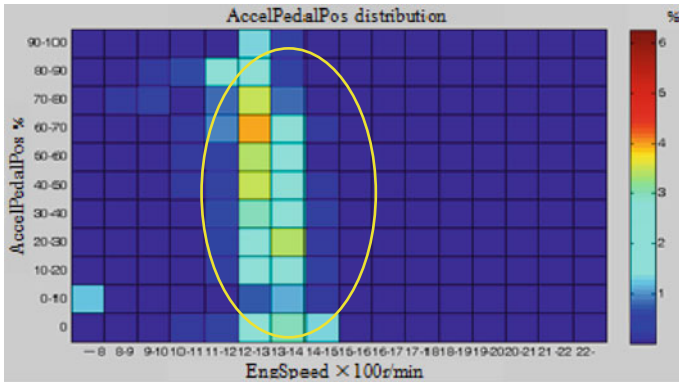


Fig. 7 Swinging accelerator pedal position

### 3.2.4 Incorrect Driving Behaviour No 4: idling for very long time

If the idling time is too long, the region will be lightened. The yellow rectangular in the lower left corner of Fig. 5 shows there is too much idling time during the transportation.

## 4 How to Drive Correctly

### 4.1 Hints of Correct Driving

From the APP (AEP) Map, we know how correct driving map is, and we summarize the correct driving points to help the customers to improve their driving behaviour.

#### 4.1.1 Enter Steady Speed Quickly

On clear road, accelerate fast to the demanded speed. When the vehicle reaches the proper gear and speed, keep the speed steady according to the tachometer. The best engine speed is around 1,000–1,200 r/min. The tachometer is a better reference than the speedometer.

On crowded road, reduce the demanded speed, select proper gear and keep the accelerator pedal at around 50 % and the speed around 1,200–1,300 r/min. After every acceleration and deceleration, return to steady status as soon as possible.

Keep the accelerator pedal position between 30 and 50 % during steady driving.

### **4.1.2 How to Drive Up a Mountain Slope**

Do not overtaking when drive up a mountain slope. Keep the accelerator pedal position between 50 and 80 % and the engine speed at about 1,500–1,600 r/min. Change gear timely when the slope varied. Don't let the engine speed reduce too much to lose the inertia of the vehicle.

### **4.1.3 Maintain the Accelerator Pedal Position Steady**

The electronic accelerator pedal is sensitive to driver's foot moving, therefore by keeping the pedal steady, the engine will work more smoothly and fuel consumption will be better. In some cases, unsteady pedal signals will make the fuel consumption raise about 15 %.

Some drivers like to swinging pedal while driving, accelerate to higher speed, then release the pedal and let the vehicle coast down. These actions are frequently repeated, making the engine work in transient state and increasing the fuel consumption.

### **4.1.4 Control Speed and Avoid Speeding**

Select proper speed that suits the needs of the transportation and avoid speeding. For a 500 km journey, travelling at speed 80 and 90 km/h results in a difference of only 40 min in the arrival time but the fuel consumption difference is about 4 L/100 km.

When travel together with other vehicles, avoid driving one after another. In this case, the fuel consumption of the rear vehicle is higher than that of the fore one and the fuel consumption of the final vehicle is the highest. The right way is to drive alone and meet at a preconcerted place.

### **4.1.5 Reduce Braking Frequency**

Change the driving style in advance and release the accelerator pedal earlier when it's crowded or the traffic light is changing to red in front. Avoid an urgent brake after a sharp acceleration to save energy.

## ***4.2 Examples***

Though the procedure of changing driving habit is hard and time-demanding, requiring patience and continued APP Map analysis, its result is very exciting.

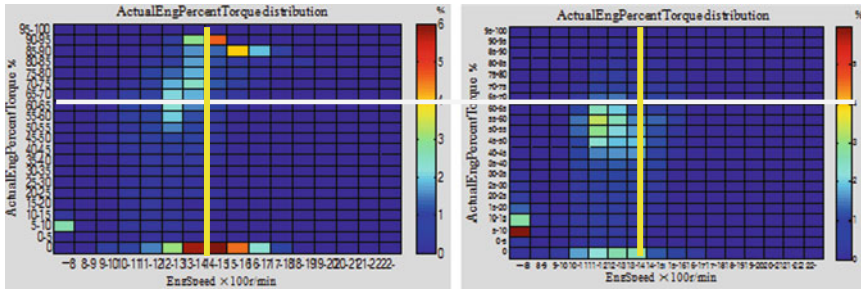


Fig. 8 The former and later APP Map (1)

After this procedure, the customer’s fuel consumption, which drops 10~20 % generally, becomes much better.

There’s an example. A customer has a semitrailer vehicle. The transport task is from Shanghai to Guangzhou. The round trip is about 3,000 km and the GCW is 55 tons. The original fuel consumption is 45.9 L/100 km, and after correcting the driving behaviour, the fuel consumption became 38.7 L/100 km, dropped by 16 %.

In the AET Maps of the former and later, shown in Fig. 8 the engine speed range becomes lower, the engine load drops down and the frequency of throttle swinging reduces. But the idling time is still very long. The fuel consumption is 38.4 L/100 km without including the fuel consumed by idling.

Another example is as follows. A truck belongs to a transport company, which complained about high fuel consumption. The transportation is from Shanghai to Hefei, the round trip is about 960 km and the GCW is about 25 tons. The original fuel consumption is 30.3 L/100 km, and after improving the driving behaviour, the fuel consumption became 22.7 L/100 km, dropped by about 25 %.

In the AET Maps of the former and later, shown in Fig. 9 the engine speed range reduces from 1,600–1,800 to 1,300–1,500 r/min, the accelerator pedal position drops from 100 % to under 70 % and the frequency of throttle swinging reduces. The idling time decreased from more than 5 % to around 3 %.

### 4.3 The Driving Guidance Device

After proving the driving identification method and identifying how to drive correctly, we are now designing a device to guide the driver to operate correctly in the process of driving.

The device reminds the driver of the right time to change gear, the best engine speed region, the good accelerator pedal position range and so on by different patterns of light, sound, voice, screen display, etc. And the device is only based on the data from the CAN bus.



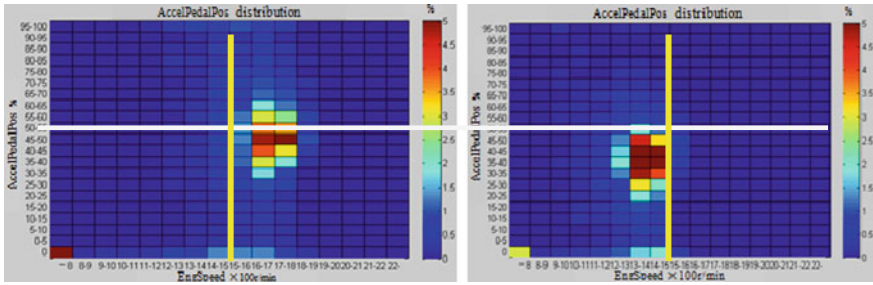


Fig. 9 The former and later APP Map (2)

Once the device is put into production, it will be more convenient to help the customers to correct their driving behaviour and improve their fuel consumption.

### 5 Conclusion

With the help of APP (AET) Map, we've established the method of identifying driving behaviour and provided correctly driving guidance. We've also helped many customers to improve the fuel consumption of their commercial vehicles. The semitrailer vehicle mentioned above will save about 21,000 L of diesel oil per year (the annual milage of the vehicle is about 300,000 km), and the above-mentioned truck will save about 8,000 L of diesel oil per year (the annual milage of the vehicle is about 110,000 km).

Though the commercial vehicle fuel consumption standard may speed up the development of advanced technologies used in commercial vehicles, it is still necessary to pay more attention to correct the driving behavior, which will be helpful to cut down fuel consumption and at the same time save our environment.

# Research on Test Method of Off-road Vehicle Trafficability

Wenhu Qin, Zhanjun Guo and Weigong Zhang

**Abstract** The off-road vehicle trafficability can guarantee the vehicles to pass the soft soil with certain speed, which is an important technology index for off-road vehicles. By now, the bearing capability of the soil and the vehicle traction are measured respectively to determine whether the vehicles can pass according to the experience. The vehicle trafficability depends on the features of the soil as well as the performance of the vehicles and however, traditional soil measurement method cannot analyze the relationship between the vehicles and the soil thoroughly. Therefore, a new test method should be proposed and studied to obtain the interaction force between the vehicles and the soil accurately in order to evaluate the vehicle trafficability quantitatively. This new method tests the longitudinal force, lateral force, vertical force and wheel torque of each wheel in real time when the vehicles are driving based on studying the force features of the soil and analyzing the influence factors of soft soil on vehicle running. Furthermore, the engine rotation speed and tire pressure are combined to test the interaction force and the torque between off-road vehicles and the soft soil under different working conditions. According to the tested interaction force and the torque between off-road vehicle and soft soil, the vehicle trafficability model is created based on wheel force, including the relationship between engine rotation speed of the vehicles and the wheel driving torque under the situation of the soft soil, the relationship between wheel vertical force and soil compactness and the relationship between

---

F2012-E01-031

---

W. Qin (✉) · W. Zhang

School of Instrument Science and Engineering, Southeast University, Nanjing, China  
e-mail: wenhuqin@gmail.com

Z. Guo

The Vehicle Proving Ground of General Armament Department of PLA, University of Aeronautics and Astronautics, Nanjing, China

wheel longitudinal force and the friction coefficient of the soil. The wheel force test technology is adopted to study the interaction force and the torque between off-road vehicles and the soft soil. As a result, it provides a new approach to evaluate the vehicle trafficability.

**Keywords** Trafficability · Wheel force transducer · Soft soil · Evaluation of vehicle trafficability

## 1 Introduction

The off-road vehicle trafficability can guarantee the vehicles to pass each kind of roads with certain speed, which is an important technology index for off-road vehicles. The off-road vehicle has good trafficability when driving on the ordinary road, however, the trafficability is greatly reduced when driving on soft ground. The soft ground is mainly composed of loose sand or the soil with a certain stickiness and plasticity. Compared with the rigid pavement, the soft ground has poor carrying capacity and low shear resistance. By now, the pressure- settlement (Bekk Method) and cone index are the main empirical methods to evaluate the vehicle trafficability at home and abroad [1, 2]. U. S. Army Engineer Waterways Experiment Station, WES have done a lot of pioneering work in the field of evaluating vehicle trafficability on the soft ground by applying the cone index. WES defines the cone index obtained through trafficability tests as Vehicle Cone Index (VCI), which is used as an index to evaluate the vehicle trafficability based on the deep analysis of the soil characteristics by use of the conical instrument. International Society for Terrain-Vehicle Systems (ISTVS) approves the research results of WES and gave the authoritative definition of the vehicle cone index. VCI refers to the minimum rating CI value when the certain vehicle passes the ground with specific condition. The frequently used items—VCI1 and VCI50 in engineering indicate the minimum rating value when the vehicle pass only once and 50 times. United Kingdoms Ministry of Defence (UK MOD) proposed to adopt Mean Maximum Pressure (MMP) as the evaluation index of vehicle trafficability and gave the definition of MMP. MMP refers to the average of the maximum positive pressure acted on the vehicle wheels that contact with the ground. It has been demonstrated that MMP is linearly related to VCI proposed by WES. In addition, MMP can be predicted based on very few parameters such as the mass and transmission device size and as a result, it is very convenient to use. Domestic research institutions have done much basic research in the field of vehicle trafficability. Xuewu Ji, from Tsinghua University, analyzes the tangential displacement of the soil under the wheels and creates the prediction model in which the elastic tires interact with the sand according to the sand pressure—settlement theory [3]. Jie Li and Jide Zhuang, from Jilin University, have analyzed the characteristics of the shear curve of the soft ground and propose a new method to determine the soil shear parameters [4]. The research group led by Jianqiao Li of Jilin University creates the interaction

relationship model between driving wheels and the lunar regolith based on the driving wheel traction performance test of the lunar rover and furthermore, they develop the simulation program of evaluating the vehicle trafficability in the environment of the lunar soil by use of discrete element method [5]. Hao Li from the Armored Force Engineering Institute conducts the research on the characteristics of the sandy beaches of southern China and the soil strength and meanwhile, he analyzes the vehicle trafficability by use of U.S. military mobility assessment approach [6].

By now, the approaches to evaluate the vehicle trafficability taken by domestic and foreign countries can provide or give in part the vehicle trafficability index under specific roads. However, these approaches mostly rely on the empirical formulas and experimental data, which are vulnerable to the influence of the test object and the external environments and furthermore, the above approaches are not adopted in the engineering field. Therefore, studying a fast evaluation method of the ground trafficability suitable for engineering applications has important engineering significance.

## 2 The Evaluation Method of the Vehicle Trafficability

When the vehicle is driving on the soft ground, the driving wheels are acting with the ground to make the ground shear and deform so that the vehicle can get the forward thrust on the one hand; and on the other hand, the vertical load of the vehicle generates the compaction resistance and traction resistance to the ground through the wheels. The condition that guarantees the vehicle driving on the ground is that the driving force is greater than the driving resistance. The vehicle trafficability can be considered from two aspects: the vehicle trafficability and the driving ability of the soil. The soil characteristic parameters, such as the soil cohesion, the soil internal friction angle, the soil compaction and the soil settlement index, need to be obtained to compute the driving ability of the soil, however, it needs a lot of discrete experiments and wastes a lot of time. In this paper, the trafficability is considered from the perspectives of the vehicle. Based on the Bekker soil pressure-bearing model, the vehicle trafficability is evaluated by the traction coefficient  $\Pi$ , which can be calculated by the following formula:

$$\Pi = \frac{H - \sum P_f}{W} \quad (1)$$

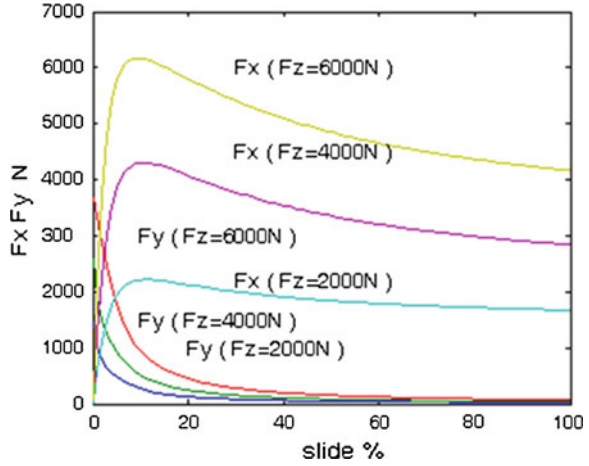
in which  $H$  is the driving force,  $P_f$  is the driving resistance and  $W$  is the mass of the vehicle.

As can be seen from the formula, the vehicle trafficability is related to the adhesion coefficient and the rolling resistance coefficient between the vehicle and the ground. The adhesion coefficient is related to the vertical load, the driving torque and the driving force of each wheel. The rolling resistance coefficient is proportional to the driving resistance. The driving resistance is the function of the

**Table 1** The rolling resistance coefficient and the adhesion coefficient of the ordinary road

Type of the ground	Rolling resistance coefficient	Slipping adhesion coefficient
Asphalt or concrete pavement	0.018–0.020	0.75
Dry soil road	0.025–0.035	0.65
Wet soil road	0.050–0.150	0.4–0.5
Icy road	0.015–0.030	0.07
Compressed snow road	0.030–0.050	0.15

**Fig. 1** The relationship between the longitudinal force, the lateral force and the slipping ratio



driving force and the slip ratio. The rolling resistance coefficient and the adhesion coefficient of the ordinary road are shown in Table 1.

The wheel slipping ratio is calculated as follows:

$$\lambda = \frac{V_t - V_\omega}{\max(V_t, V_\omega)} \tag{2}$$

$$V_\omega = \omega \bullet R \tag{3}$$

in which  $V_t$  is the actual speed of the vehicle,  $V_\omega$  is the wheel tangent speed,  $\omega$  is the wheel angular speed and  $R$  is the effective radius of the wheel.

The wheel adhesion coefficient  $\mu$  is the ratio of the road adhesion force and the vertical load acted on the wheel.

$$\mu_x = \frac{F_x}{F_z} \tag{4}$$

$$\mu_y = \frac{F_y}{F_z} \tag{5}$$

in which  $\mu_x$  is the longitudinal adhesion coefficient,  $\mu_y$  is the lateral adhesion coefficient,  $F_x$  is the longitudinal force,  $F_y$  is the lateral force and  $F_z$  is the vertical load.

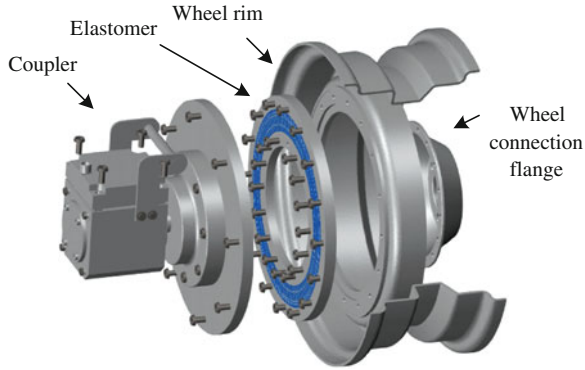


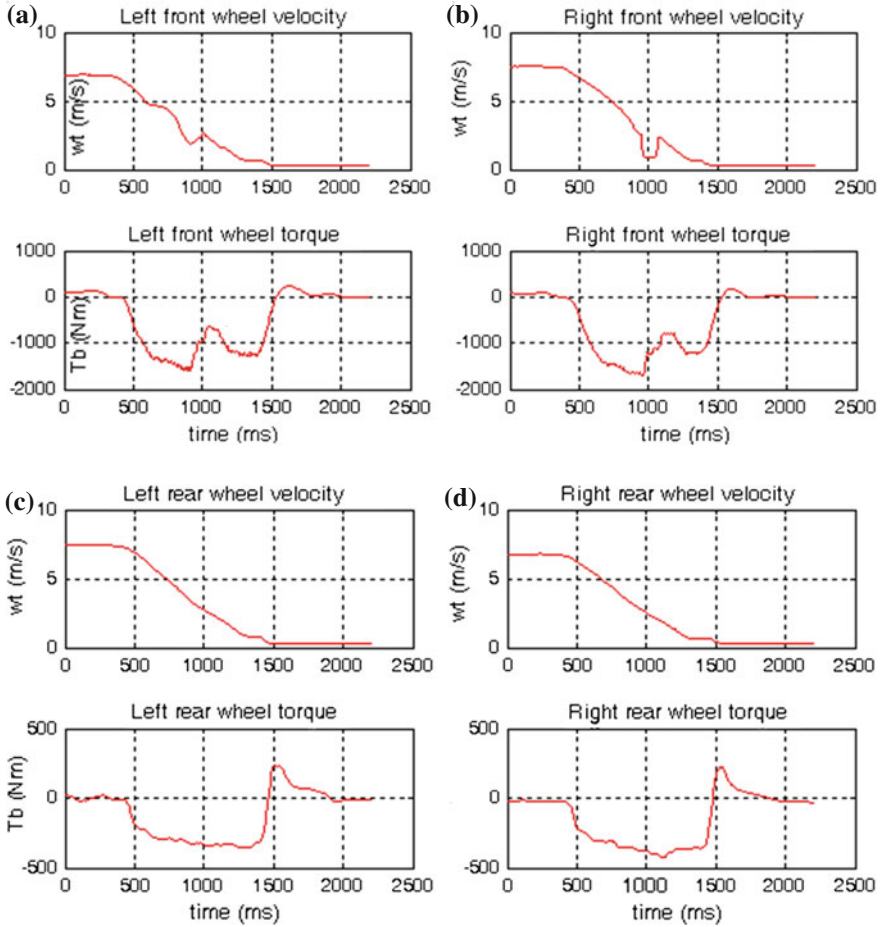
Fig. 2 The installation of wheel force sensor and the wheel hub



Fig. 3 The test vehicle equipped with the wheel force sensor

According to the tyre magic formula, the relationship between the longitudinal force, the lateral force and the slipping ratio under different loads is shown in Fig. 1.

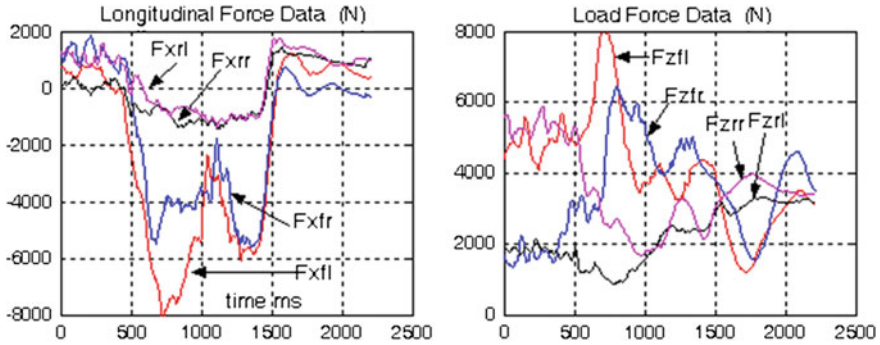
As can be seen in the figure, the longitudinal force will gradually decrease with the increase of the slipping ratio when the vertical load stays the same. It is consistent with the phenomenon that it is difficult for the vehicle to move forward when the wheels skid. Therefore, the road adhesion coefficient can be calculated by measuring the longitudinal force, the lateral force, the vertical load, the driving torque and the slipping ratio of the wheels, and furthermore, the trafficability index of the soft ground can be determined according to the formula 1.



**Fig. 4** The wheel speed and torque data when braking emergently at the speed of 30 km/h **a** The changes of speed and torque for *left front wheel* **b** The changes of speed and torque for *right front wheel* **c** The changes of speed and torque for *left rear wheel* **d** The changes of speed and torque for *right rear wheel*

### 3 The Measuring Technology of the Wheel Force

The wheels are subject to the longitudinal force, lateral force, vertical load and wheel torque when they contact with the road in the condition of at rest, acceleration, driving and braking. Through designing suitable elastomer structure and locating strain gauge on corresponding elastomer, the wheel force is measured according to the full bridge, multi-dimensional signal decoupling and non-contact signal transmission. The installation of wheel force sensor and the wheel hub is shown in Fig. 2.



**Fig. 5** The longitudinal force and the load force data when braking at the speed of 30 km/h ( $F_x$  longitudinal force;  $F_z$  load force;  $fl$  left front;  $fr$  right front;  $rl$  left rear;  $rr$  right rear)

As shown in Fig. 2, the wheel hub flange is connected to the inner ring of the elastomer. The wheel braking torque  $M_y$  is passed to the inner ring surface of the elastomer through the wheel hub flange to make the strain beam bend and deform. The longitudinal force  $F_x$  and lateral force  $F_y$  are passed to the outer ring surface of the elastomer through the wheel rim flange to make the strain beam stretching and bend and deform. The wheel vertical load  $F_z$  is passed through the bolt and the mating surface of the inner ring surface and the bolt and the mating surface of the outer ring surface.

The location of the strain gauge should take the deformation of the strain beam with the influence of the tension and compression, bending, lateral bending and torsion into account. The multidimensional wheel force sensor is in the state of high-speed rotation in actual use and each beam is subject to different forces, and therefore, the coupling between multi-dimensional forces is eliminated by selecting the locations of reasonable strain gauge.

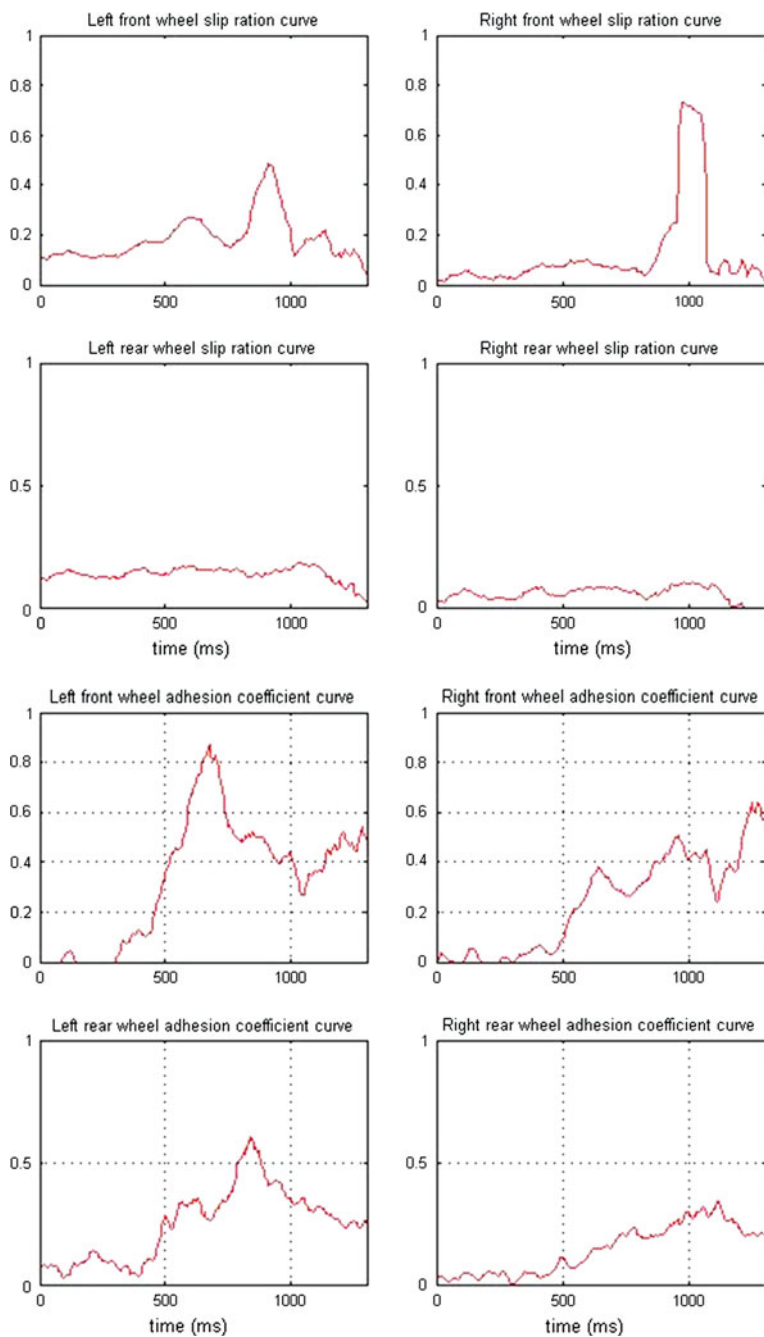
## 4 Experiments

The test vehicle is equipped with the wheel force sensor and corresponding data acquisition system for test on the performance road in dedicated testing yard, which is shown in Fig. 3.

Multi groups of starting, driving and braking tests for the test vehicle are conducted with the speed between 30 and 60 km/h on the performance road [7]. The data curves obtained through the tests are shown in Figs. 4 and 5. The calculated slipping ratio and adhesion coefficient of each wheel are shown in Fig. 6.

From the adhesion coefficient curve of each wheel, it can be seen that the calculated adhesion coefficient curve by measuring the wheel force is consistent with the characteristics of tyre model shown in Fig. 1. It demonstrates that the method of calculating the adhesion coefficient by measuring the wheel force is feasible.





**Fig. 6** The slipping ratio and adhesion coefficient when braking at the speed of 30 km/h

## 5 Conclusions

The research has shown that:

1. Through the wheel force measurement technology, the vertical load, longitudinal force and slipping ratio obtained by measurement when the wheels are interacting with the ground are consistent with the tyre magic model.
2. The adhesion coefficient between the tyre and the road can be calculated by measuring the wheel force, which provides the basis for quantitative judgment of the vehicle trafficability.
3. A lot of experiments and tests are needed to be done to improve the relationship between wheel force and vehicle trafficability.

In this paper, the interaction force and torque between the vehicles and the ground are studied using the wheel force measurement technology. It provides a new method to evaluate the vehicle trafficability quantitatively.

## References:

1. Chen BC (1981) Soil-vehicle system mechanics. China Agricultural Machinery Press, Beijing
2. Zhuang J (2002) Computational vehicle terrain mechanics. China Machine Press, Beijing
3. Xuewu J, Huiwen F, Yanchen Y (2000) Prediction model and experimental study on the interaction of tyre and sand. *Trans Chin Soc Agric Mach* 31(3):8–10, 14
4. Jie L, Jide Z, Nan Y (2000) A new method for determining the parameters of shear property of soft terrain. *Trans Chin Soc Agric Mach* 31(3):5–7
5. Meng Z, Jianqiao L, Jinhuan Z, Luquan R, Yinwu L (2009) Study on the traction performance for the driving wheel of lunar rover. *J Astronaut* 30(1):98–103
6. Hao L, Jun L, Zhanquan H (2010) Analysis of soil strength of south china sand beach based on the vehicle mobility. *Agric Equip Veh Eng* 8(26–28):47
7. Wenhui Q (2005) Research and development on evaluate system for vehicle ABS performance based on multi-dimension wheel force measurement. Southeast University, Nanjing

**Part II**  
**Vehicle Integration Platformized**  
**and Universal Design**

# A Design Method for Future Automobiles

Zhifeng Wang, Wu Yang, Zhiguo Le and Fuquan Zhao

**Abstract** The car manufacturers can achieve scale merit only by large-scale production to reduce the cost as much as possible. However, a large-scale production usually generates similar design, same manufacture and similar products. Moreover, the customers have increasing individuation demands since both the rich customers and ordinary customers desire to gain individuation products. The modularization can eliminate the conflict between customers and car manufacturers, thus satisfying not only large-scale production but also individuation customization. The automotive modularization design must follow the design principle. The division of sub-module and deepening of modular levels have significant impact on automotive modularization adaptability. To adopt the modularization method for automotive design, the OEMs needn't know design methods of all components except that they have to follow modularization design principle.

**Keywords** Individuation product · Design principle · Module level · Automobile design · Automotive modularization

---

F2012-E02-003

---

Z. Wang (✉) · W. Yang · Z. Le · F. Zhao  
Zhejiang Geely Automobile Research Institute CO., LTD, Hangzhou, China  
e-mail: wangzf@rd.geely.com

W. Yang  
e-mail: yangwork@hotmail.com



Fig. 1 Left is the assembly line of cars [1] and right the Ford model T [1]

Fig. 2 Rolls-Royce manual production line [2]



## 1 Introduction

The relationship between cars and people is reincarnation. In the beginning when automobile was manufactured, the car was a novel means of transportation only accessed by a few and the rich. Handmade and customization makes each vehicle a unique craft. Low efficiency of the handmade, difficult precision control and higher requirements of the craftsmen lead to its high cost, also progress was hardly achieved in the promotion and technological improvement.

Ford derived an inspiration from the slaughterhouse assembly line and applied it to automobile production. Ford began a large-scale production of the Model T. This enabled cars to enter a phase of rapid development (Fig. 1). Economic benefits from an economic point of view, validated through scale production, far outweighed the individual production.

On the other hand, in the Ford era, the society was not short of automobile consumers at all, typically a seller market. Therefore, Ford's success owed to the historical environment. At that time, consumers did not have to fully think about the automotive design. Produced is what consumers must accept what it was like.

**Fig. 3** BMW's highly automated production line [3]



Of course, always adhere to the manual operation of the auto companies (even initially can only be called workshops), such as Rolls-Royce has also retained (Fig. 2). However, history has proved that even the classic and legend could not withstand the economic laws. Rolls-Royce represents the highest level of the car manual work. It was acquired by BMW which also represents high-end automated machinery (Fig. 3). Like Rolls-Royce, a handcraft workshop can't stand alone which needs affiliation to a large-scale car manufacturer and become an individualized and luxury brand. However, this has profiled that Rolls-Royce consumers have special customized needs.

However, the need of individuality is not an exclusive for the aristocracy. Even ordinary automobile consumers tend to show individuality. Today, the big auto companies are enjoying the benefits of economies of scale, will not easily give up a large-scale manufacturing back to the hand-customized model. This raises the contradictions of the mode of production and individual needs. How to reconcile the contradiction between the large-scale manufacturing and consumer demand for personalized, automotive design and the manufacturer must now consider the problem. This is like a cycle referred at the beginning.

## **2 The Contradictions of the Automotive Design and Manufacturing**

At present, car manufacturers and engineers are in such series of contradictions as the following three main problems.

## ***2.1 The Choice of Automotive Design Method***

In China, the automobile, there are two main design methods. The first is the method of large state-owned auto companies. Relying on national policy and resource advantages, the localization rate of the hard targets, all auto parts are able to be developed [4]. This is the conventional thinking of automotive design. The result of this way of thinking is that the ability of the automotive design engineers will be enhanced. That is able to lay a solid foundation for long-term adherence. However, this approach often make automotive engineers “to redefine the wheel” [5], repeated low level of labor, which makes the car very long product development cycle from input to output, and longer vehicle replacement. Also, because of the complexity of social values, a lot of young engineers are difficult to be patient lonely, stick to the end, leading to the frequent movement of the automotive design talent. The traditional automotive design method has been a huge challenge.

There is also an automotive design from the emerging private car companies. Due to the limitations of economic strength, the lack of state policy, more attention to short-term development will see the benefits. They could not slow the traditional R&D, but to the vehicle development cycle as short as possible. Private car companies are good at using the method of integration of resources, extensive use of “reverse development”. And a lot of research and development work entrusted to the parts company, its “shelf products” is applied to the design and manufacture of vehicle, thereby reducing the cycle of automotive design. These are often undesirable consequences. Although the new car market, but due to the lack of a solid foundation for the automotive OEM, the ability to control the new car decreased. Many white boxes will turn gray and even black box parts. Automotive products need to meet the individual needs of the discerning consumer. Private car companies will be even more stretched.

## ***2.2 The Contradiction Between Vehicle Production and Consumer***

The pursuit of automobile manufacturers is profit. Profit is the product of sales with a single car profit. The profit of a single car is the price of a bicycle minus the cost of a single car.

Sales growth depends on whether the design of the car can seize consumer preferences; for the price of a single car, due to vehicle size, performance, configuration is not very different, the price has basically been bound by the rules of the market; a result, sales with a single car costs become the main way for automobile manufacturers to control profits. From a design perspective, to increase sales is to seize the hearts of consumers, and a car to meet the different needs of consumers more, the better the sales. The composition of the cost of a single car is

more complicated. Simple terms, a rough calculation of a single car costs following formula available: Cost of a single car = design fee + test cost + cost of mold + manufacturing cost + labor costs.

If one or several of expenses can be reduced, then the profits can be greatly improved. This is also the mainstream of the automotive industry to increase profits. Large-scale production enables design fees, testing costs, mold costs reduced due to sharing. So car manufacturers hope that the life cycle of their products can stay on the market longer and better sales, it is a good scale production. But manufacturers also hope that the demands of consumers as possible. This allows a vehicle to conquer the world. However, this is impossible.

With the development of society, the car is playing an increasingly important role in people's lives. Consumer demand is no longer just a means of transport. Sometimes on behalf of an identity, and sometimes represent a character, and even participate in different activities, but also require different models significantly appropriate [6]. Consumers want their favorite car has a very high price (which often means that the price is reasonable), but want to meet their own individual needs. Consumers want car manufacturers to give themselves more choices, favorite car at the show (and sometimes even just the concept car) at an early date listed.

In the game of car manufacturers and consumers, the pre-seller's market, car manufacturers have the initiative. Now, the right to choose has been transferred to the hands of consumers, it is already a buyer's market. This trend is difficult to reverse. Future consumers will be more and more the individual requirements of the automotive design.

### ***2.3 Simplistic Method of Complex Automotive Design***

For car-defined course of development can be summarized as: New transport → Convenient transport → Comfortable and convenient transport → Safe, comfortable and convenient transport → Safe, comfortable and convenient shortcuts personalized transport.

Car of the future may also need to add an adjective: Intelligence. From the perspective of the development process of the car, the car has been and will be more and more, the car itself has been, and will become increasingly complex. For complex products, the inspiration from a prominent or a few people together to design methods are no longer applicable. A new approach should be set to solve this complex problem of complex products.

At this point, the IT industry has for the automotive industry to make model. It is based on modular design method (Fig. 4). The display is a module, keyboard a module and case another module. Any selection can be done according to different needs. Even in the case, the CPU module, memory module, hard disk is a module, we can choose according to our needs and budget, even the appearance of the two computers is the same, but the personal needs of its internal configure and there will be a big difference [7]. This is the benefits of modular design,



**Fig. 4** Modular computer  
[7]



automotive industry experienced large-scale production, but also may follow the example of the idea of the computer assembly to carry out modular design and production.

### **3 The Basic Concept of the Module**

#### ***3.1 The Definition of the Module***

Modules and modular so far are not very accurately defined. Japanese scholar Aoki defined it as: the module is a subsystem of the self-discipline by the same subsystem according to certain rules, will be individually designed subsystems to unify, to form more complex systems. Modularity is a module of the process [8].

#### ***3.2 Division of the Module***

The module contains the design rules and hidden modules and structure of the module. The design rules are the rules to be observed by all sub-modules in the design process, is visible to the rules; hidden modules hidden inside information sub-module, internal design rules for the hidden design rules, module innovation and value creation source; structure module is the module contain visible information is formed on the basis of the common summing up the hidden module [9]. Modular design, the core parts of the division are the module and the formulation of design rules.

### ***3.3 Division of the Module Method***

Depending on the module design rules, we must first divide the module. Module division methods: the function method and the regional method.

Function method: the functionality of the module design rules, the modules within the sub-module to a function together. From space, spacing can be large, the assembly of more complex, but relatively simple design rules.

Regional method: structural area to divide the module may not be the sub-module of the module within the performance or configuration, only the link structure. The module can be completed part of the performance or configuration of multiple functions. Small spacing between the sub-module, and facilitate the assembly of the module, but the more complex design rules.

### ***3.4 The Module Level***

Mature modular design method should be a top-down. The bottom-up design methods can only be counted as a generalization of the parts. According to the complexity of the product, the module can be divided into first-level sub-modules, the second level sub-module. Platform development, the future of automotive design will be used mainly top-down approach. The module can be a car, a car product family. In this paper the motor module is an automobile product family and the traditional sense of the platform. And the first sub module is in platform vehicle.

### ***3.5 The Use of Modular Features***

The use of modular design of the following four characteristics: top-down design of the structure; modular design to develop a clear design rules; the complexity of the problem for modular division; standardization or series of sub-module is a modular common form.

## **4 Automobile and Modular**

The relationship between the automobile and the module has long been generated. In the automotive industry, the Nordic SCANIA, the first user of a general method to reduce the cost of automobile production, makes the modular concept of the initial use in the automotive industry.

Industry terminology in the car is divided into various systems. Actually, this is to apply the modular approach to deal with complex issues of a form. Only in the modular theory derives from, people do not know this method is the application of the modular principle. The new modular application in automobile is the introduction of a new module division method (the regional method), and automotive modules in the hierarchy were further subdivided.

#### ***4.1 The Early Automotive Modularization***

Early engineers put the vehicle into power, chassis, body, electrical appliances, interior and exterior, accessories, security system. These systems were addition to building design tree, and to make the car Engineer professional. So that they can be focused, professional processing of a system in the same problems. Of these systems from the beginning, the modularization theory began to grow in automotive designs. Later, a standardized and universal theory was applied to the car, marking the modularization large-scale development in the automotive industry and more advanced applications.

#### ***4.2 The Most Fashionable Car Modularization***

The major OEMs are working hard to advance in efforts to promote the automotive product platform. For example, Toyota NBC platform, Toyota COROLLA platform, GM DELTA platform, GM GAMMA platform [10].

Automotive product platform is fixed core components and core technologies, the formation of a basic model. And on the basis of this model can develop a series of models. From the characteristics of the module, the platform can be seen as a module. It meets all the characteristics of the module. Models can be regarded as sub-modules within the platform. The boundary conditions of the platform are the rules of the module. The style and shape changes of the different models in the platform are hidden module.

#### ***4.3 Modular Car-Future Trends***

After Volkswagen's integration of its product platform, modularization was achieved. When Pre-defining platform, engine compartment, front floor, before hoardings, powertrain, front suspension and front sub-frame are all defined as platforms. Meanwhile, in the platform boundary conditions on the vehicle's width, length, load restrictions. Volkswagen modularization theory to analyze the car module with the new module division has been divided. The new module uses a

broader scope of application of new rules, the Volkswagen and the following sub-modules to achieve a leap to use in the automotive module. Meanwhile, Volkswagen is also the module level of the car division of in-depth, in order to meet the needs of more consumers.

## 5 Modular Car

### 5.1 Automotive Modular Design Rules

In the automotive modularization design rules is the most important part. Design rules directly affect the life and the quality of automobile module. Toyota has not crossed the 10 million in annual sales mark, not Toyota design or quality control errors, but the platform can only accommodate to this capacity.

The modular design rules of the car should include: the range of vehicle parameters, hard spots, and hard-point range, performance, configuration, modeling, application of new technologies, human-computer comfort, style and brand.

Parameters of the entire vehicle are the automobile modular primary control. That is also the primary rule in the automotive modularization. Vehicle parameters should contain the vehicle length, width, height, wheelbase, track, weight, ground clearance and other parameters as well as their variable range.

Hard spots and hard-point range is the most important parameter in the chassis. Hard points in automotive modularization also need to be graded, and each level of the hard points corresponding to the same level of module. In the automotive module, the first level of the hard point corresponds to the second-level sub-module. Different levels of hard spots and design rules, low-level hard point can also be hidden design rules.

Range of performance will directly affect the scalability of the vehicle module space. Performance included in the power, economy, ride comfort, handling, and security. Power and economy can be defined numerically. The security can be star-defined. Ride comfort and handling stability is a subjective evaluation of the content. How to define value for them is still difficulty.

The configuration can be divided into two parts. Part of the design rules, the other part is hidden in hidden module design rules. Powertrain configurations belong to the design rules, the configuration of the outer rear-view mirror is a hidden design rules.

Most of the styling elements belong to the hidden design rules, but not all shapes are hidden design rules. For example, point C belonging to the automotive module design rules. Another example is the front bumper, to meet the internal structure of the pedestrian protection of design rules, and its shape is a hidden rule. The specific rules of attribution in the car shape according to the actual situation.

The application of new technologies is the lifeblood of the car development. In one sense, the new technology can be constrained to the useful life of the

automotive module. Most of the new technology is hidden design rules. If its level of jumping, you need to consider in the design rules.

Ergonomics is a very important part of the car modularization design rules. Product attributes of scalability, automotive modules and automotive modules have a direct impact. In a car module, ergonomics is the design rules, and as standardized parameters.

The style belongs to the hidden design rules. With a car module, you can transform from residential to commercial, a variety of styles from casual to sports. It is most active in the automotive module hidden design rules.

The brand is in fact a fixed design rules, the brand and style are closely connected and differences between them, the style may change as the market.

## ***5.2 The Division of Automotive Module***

In the early days, the car mainly divide the sub-module according to functions. The Automotive Systems division is the best example. Function method divided into modules, the objective function and simple design rules, each sub-module design changes is also relatively simple. This is a simple, modular design. But there are the following shortcomings: for example, occupy a larger space, and don't focus, and the more peripheral module interfaces, making the module difficult to play to the advantages of standardization and universal, the cost will also increase accordingly.

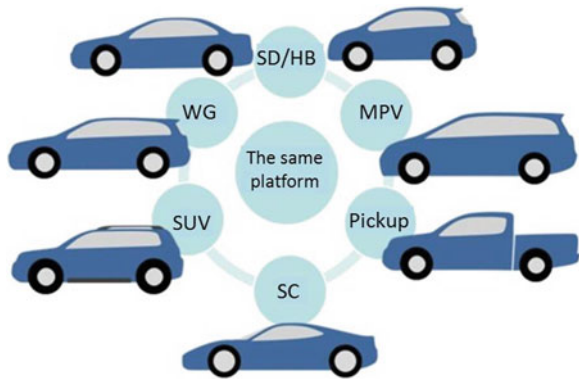
Regional method division of the module, the module interface is simple, easily standardized. And sub-module changes don't affect the interfaces between modules; greatly facilitate the standardization and serialization. Automotive modular design because of the unique rules of general arrangement, a regional method, can better follow the layout rules. Regional method has drawbacks: As more target functions within the modules and the rules are complicated.

Therefore, in the new modular design, it often using regional method and function by combining the partitioning method. Regional method division in the general arrangement rules demanding circumstances. Function is highlighted and the general arrangement is not strictly the case, the functional approach. Automotive modularization, the first-level sub-module suitable for use is regional division, and deep-seated sub-module suitable for use on the division of function method.

## ***5.3 Automotive Module Decomposition***

Basis for Modular Division, automotive modules can be divided into the first-level sub-module of the cars, sports cars, CROSS, SUV, MPC, MPV, etc. The first level of sub-modules can be divided into the second-level sub-module of front-end

**Fig. 5** Platform can be derived models [10]



modules, cockpit modules, the passenger compartment module, the back-end module, the second-level sub-modules, etc. The front-end module can be divided into modules of powertrain, chassis modules, body module, heat sink module, etc. Cockpit module can be divided into the dashboard modules, door modules, seat module, etc. The rest of the module division is not detailed examples.

### 5.4 The Level of the Vehicle Module

If only the module of the car divided into a first-level sub-module, this will form a platform. At the same level within a platform, the models from sedan to SUV, to sports car, to MPV change (Fig. 5). Volkswagen Group’s new modular process module is divided into the vehicle platform MQB, MLB, MSB. Platform module, divided into first-level sub-module is the Volkswagen models. For example, the new Golf and Jetta are part of the MQB module. The first level of sub-module is then divided down the engine module and suspension module. Such as Volkswagen for the MQB platform to introduce the concept of the engine module, including the gasoline engine module (MOB) and diesel engine module (MDB). The representative of the gasoline engine module is a new EA211 series diesel EA288 series. Such modular division is even able to cross the level limit. Wheelbase and tread can change, A0-class models may even belong to a module with Class B models.

The depth of the module level, hidden module contains more parts, the greater impact. Automobile manufacturers in pursuit of economies of scale will fail owing to the rest of the sub-module as a standard processing. In this way, the hidden module can’t play a role, making changes to reduce a car module. That can better meet consumer demand. In the depth of the division level, hidden module may play a role, can’t affect the mass production of automobile manufacturers. Hidden module role models can also be changed greatly, and can better meet the needs of the automobile manufacturers and consumers.

## 5.5 Modular Design Method

Because there are more of the shortcomings, the traditional design method is no longer suitable for the development trend of automobile design. The design of the integration of resources is imperative. Car modular design idea is “the integration of resources,” a manifestation of the way. It integrates all kinds of social resources (mainly the resources of the suppliers) together, to develop a project. Lack of knowledge to solve common integration of resources and efforts to control the project decline, the use of modular design method became effective strategy. The vehicle manufacturer before carrying out the automotive sub-module design, the first vehicle modules define the provisions of the automotive module design rules, the division of the module, the module level, so that the community’s resources in accordance with this definition of product development. Not only meet the requirements of the rules of the sub-module, but also has the flexibility and innovation.

## 6 Conclusions

In this paper, starting from car manufacturers and consumers, the direction of the development of automotive design and contradictions of automotive design and production contradictions, described the need for modularization thinking of automotive design. While automotive design theory and modularization theory, and briefly summarized the focus of the automotive modular design and difficulty. In the end, according to the modularization method of auto, preliminary the automobile module level are divided.

Automotive modularization design is a complex issue. Car modularization computer modularization (computers modularization has been popular and relatively complete) also need to improve the theory of continuous practice and theory go back to the actual operation. Automotive modularization consumers and automobile manufacturers is the perfect blend, a sustainable development approach for vehicles.

## References

1. Sina Auto Editorial Department (2011) Car in the history of today—the last a ford model T off the assembly line [E]. <http://auto.sina.com.cn/forum/2011-05-31/1009778671.shtml>. 31 May 2011
2. Nipic Editorial Department (2010) Rolls-Royce production line picture [E]. <http://www.nipic.com/show/1/20/1fd0980edefadcd6.html>. 24 Mar 2010

3. Jxiche Editorial Department (2011) Approached in Munich, Germany—quest BMW's new 3-series production line[E]. <http://jxiche.com/chezhangshow.asp?id=2702&page=2>. 2 Nov 2011
4. Gao J (2009) FAW—Volkswagen models localization project management methods [D]. Tianjin University, Tianjin
5. McGrath ME (2004) The power of pace. Shanghai Science and Technology Press, Shanghai, 2004.20–21
6. Sinotrust (2011) China's auto consumption trend reports. Peking, 2011. 07
7. Bear eyes Editorial Department (2004) Can't resist the charm—SAMBO LLUON series was released in [E]. <http://bak1.beareyes.com.cn/2/lib/200412/21/20041221246.htm>. 21 Dec 2004
8. Aoki M (2003) Modularization [M]. Far East Publishing House, Shanghai
9. Chuntian L (2007) Modern modularization theoretical basis 2. Enterp Standardization, Aug 2007
10. Cai H (2011) Vehicle platforms and general R&D model to explore. Automotive Eng, 15–18 Nov 2011



# Effect of Engineering Materials for Vehicle Collision Simulation

Yanling Huang, Gaoji Yin, Zhitao Wang, Juanli Ni, Li Li, Qiang Liu, Anzhi Yang and Fuquan Zhao

**Abstract** The research of collision security is mainly for the protection of personnel, but the invasion will induce to damage the crew cabin, so it is importance to select rational material for improving vehicle crash safety performance. This paper uses static and dynamic tensile curve to simulate vehicle collision, and combines with the real vehicle collision to research how material properties affect the simulation results. As a result, compared with static curve, the results are consistent with the research of the material properties under different rates and energy absorption of simulated parts under different loading speeds.

## 1 Introduction

In order to achieve energy-saving emission reduction targets, the world automobile manufacturers have lightweight as automobile development important task [1]. The rational use of different strength grade steel plate can not only realize the lightweight of automobile, but also improving the passive safety of automobile, so the plate material during a collision of changes in material properties and collision absorbing energy of vehicle collision behavior has great guiding significance.

Material strength and plasticity vary considerably under dynamic load and static load respectively [2]. This paper adopts static and dynamic tensile curve to

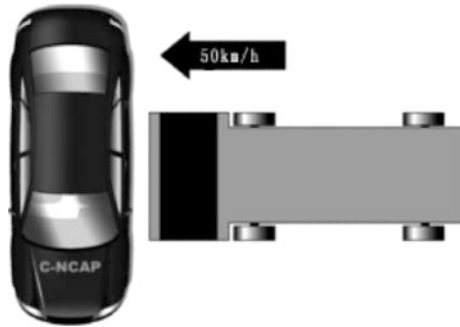
---

F2012-E02-005

---

Y. Huang (✉) · G. Yin · Z. Wang · J. Ni · L. Li · Q. Liu · A. Yang · F. Zhao  
Zhejiang Geely Automobile Research Institute Co., Ltd, Hangzhou, China  
e-mail: hyl330726@sohu.com

**Fig. 1** Deformable moving barrier side collision test



**Fig. 2** The way of energy transfer



simulate of vehicle collision, and combines with the real vehicle collision to research how material properties affect the simulation results.

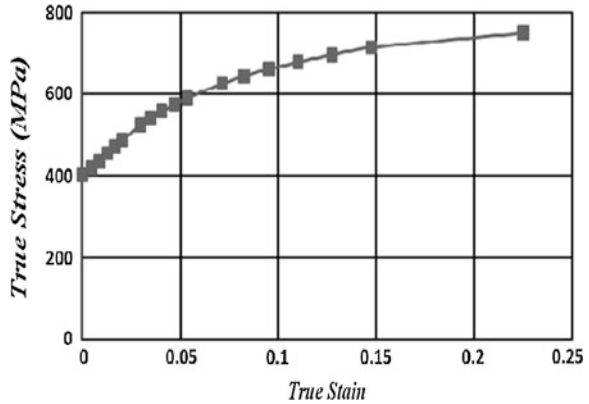
## 2 Examination

### 2.1 Side Collision Test

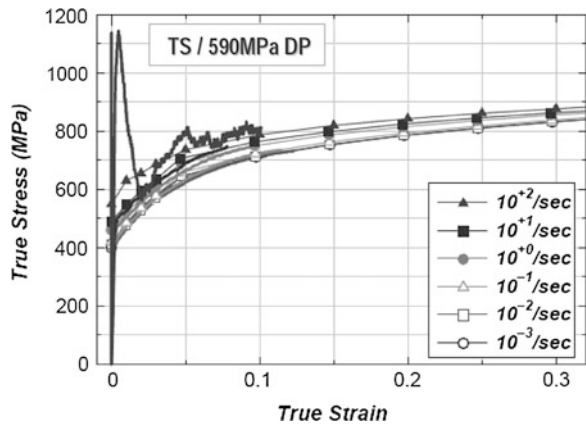
Side collision test simulation is illustrated in Fig. 1. The simulation is installed in front of the deformable aluminum honeycomb in the mobile trolley, moving barrier test vehicle vertically driving with vehicle, and collision speed of 50–51 km/h (the speed of testing shall not be less than 50 km/h).

As shown in Fig. 2, the column is the main transfer. The lower part of B pole is to be fully absorbed energy, the upper protecting head to prevent deformation, and excess energy transfer to other connected parts, reduced the side collision on head, chest and abdominal injury, therefore B pole plays an important role in the reduction of the compartment deformation. This paper will use different strain rate of material properties to simulate by CAE side collision and contrast to the real vehicle crash.

**Fig. 3** Static true stress-strain curve



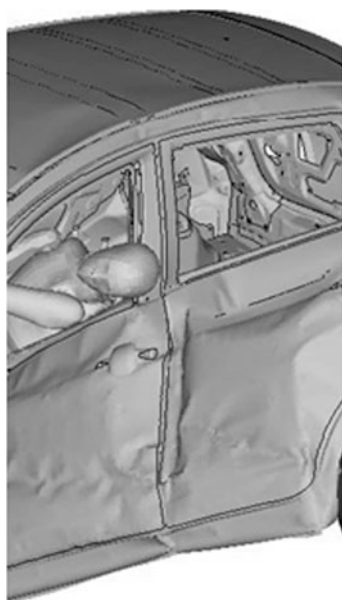
**Fig. 4** Dynamic true stress-strain curve



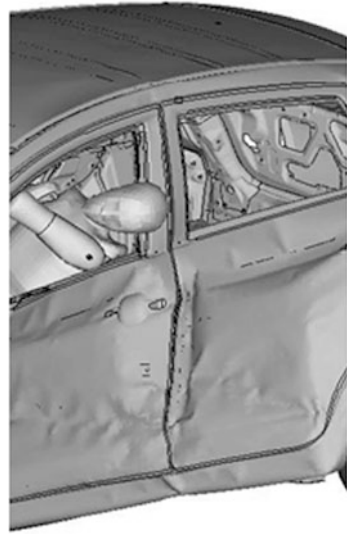
### 2.2 Collision Simulation and Test Analysis

White 3D model body as the basis, plus the powertrain, chassis and body closure model, the composition is used for crash simulation of vehicle model, using LS-DYNA software analysis under different material properties impacting with the collision simulation. Figure 3 shows the static tension after the true stress-strain curve, and Fig. 4 is dynamic true stress-strain curves, strain rate from  $10^{-3}$  to  $10^2 \text{ s}^{-1}$ , corresponding to the quasi static until to the high speed collision of strain rate.

Figure 5 shows the test analysis of B pole detection point, through inspecting 12 observation points to analysis different material properties on the safety impact collision. Figures 6 and 7 respectively, for static and dynamic simulation results, after measuring the displacement difference is shown in Table 1. Table 1 shows the deformation of dynamic curve and static curve analysis tend to uniform, but the static curves deformation is larger than the dynamic curve.

**Fig. 5** The point distribution**Fig. 6** Static simulation results

**Fig. 7** Dynamic simulation results



The vehicle collision test result is showed in Fig. 8, and 12 point of B pole is examined to contrast. Table 2 and Fig. 9 respectively, show three data, contained test data, dynamic and static simulation result of B pole collision. As showed in Fig. 9, the results deformation of the three state have the same tendency, but the dynamic simulation results more close to the real vehicle test. In contrast to the real vehicle test, static simulation intrusion error is larger 1–5 times than dynamic simulation intrusion error.

### 3 Analysis and Discussion

#### 3.1 Material Strength and Strain Rate

Vehicle collision simulation is accomplished by a subsection solution process; each step of the computation process is based on the previous step, rather than the collision initial state [3]. Therefore, the static strain  $\sigma = f(\epsilon)$  function relationships do not apply. With the collision occurred, mechanical properties of materials under dynamic loading is obviously changed.

In sheet metal forming, work hardening index ( $n$ ) is a very important process parameter. The  $n$  value is greater; the forming is better, because it can play a homogeneous deformation, expansion deformation zone, reduction of rough local thinning and increasing the limit parameters [4]. From Fig. 4, with the increase of strain rate, the same strain of 590 DP's stress is increasing.

According to the material characteristics:

**Table 1** Result of different materials simulation

Measuring point	1	2	3	4	5	6	7	8	9	10	11	12
Before collision	-569	-620	-663	-698	-726	-753	-763	-768	-771	-769	-770	-774
Static simulation	-543	-551	-558	-567	-575	-617	-607	-599	-584	-617	-625	-652
Dynamic simulation	-557	-574	-587	-599	-609	-655	-644	-635	-618	-655	-665	-690

**Fig. 8** The vehicle collision test result



$$\sigma = K \epsilon^n \quad K = \text{Const}$$

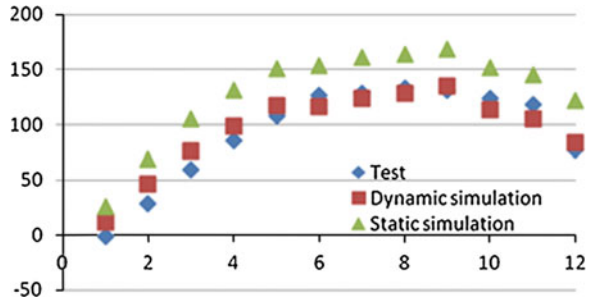
So with the material strain rate increasing, the n value is become greater, then the material is better to absorb the collision energy reducing deformation.

From the Fig. 10 shows the tensile strength and yield strength increases with the strain rate. Because of high strain rate, the material microstructure has changed. As result of many faults play at the same time, inhibit to a single crystal production and development during easy slip stage. In addition, high strain rate increase the number of dislocation density and slip systems, and twin emerging, the dislocation movement of free average length reducing, the concentration of point defects increasing. These points are made of metal materials difficult to fully deformation under high strain rate. Microscopic observation, plastic deformation is relatively uniform distribution in various grains during static load. However, plastic deformation is relatively concentrated in a local area reflecting the plastic deformation inhomogeneity under the impact load. This inhomogeneity limits plastic deformation development, leading to the yield strength and tensile strength increase. So in high speed tensile condition, the sensitivity of resistance material deformation is increasing.

**Table 2** B pole intrusion of different conditions

Measuring point	1	2	3	4	5	6	7	8	9	10	11	12
Test	-1	29	59	86	108	127	128	133	131	124	118	77
Static simulation	26	69	105	131	151	154	161	164	169	152	145	122
Dynamic simulation	12	46	76	99	117	116	124	128	135	114	105	84

**Fig. 9** The comparison of B pole intrusion



### 3.2 Simulation of Vehicle Parts Shape for Impact Test

High speed tensile test for determination of the strength of steel and plastic index and according to the stress-strain of the area under the curve calculation energy consumption indicators, although all can determine the material properties on the collision performance impact in a certain extent. But for more precise evaluation of material properties on body parts impact collision, this paper uses three point bending test to research. The dimension of test model as shown in Fig. 11, and trial design displacement is 100 mm, loading rate from 0.1 to 5.0 m/s.

Figure 12 shows that the various materials of average load increases with the loading velocity increasing, and material absorbs energy raising.

In a word, compared with static curves of simulation results, the use of dynamic curve simulation more close to the real vehicle test, corresponding with different rate reflects of the material properties and the research of absorption energy under different loading speeds.

## 4 Conclusions

In this paper, by contrast simulation and tests, material properties play a very important role during precise analysis of vehicle impact. With the strain rate increasing, the tensile strength and yield strength increase along with n value rising. Through the different loading speed of the three point bending test, material absorbs more energy with the loading speed increasing. Compared with static curves of simulation results, the dynamic curve simulation is more close to the real

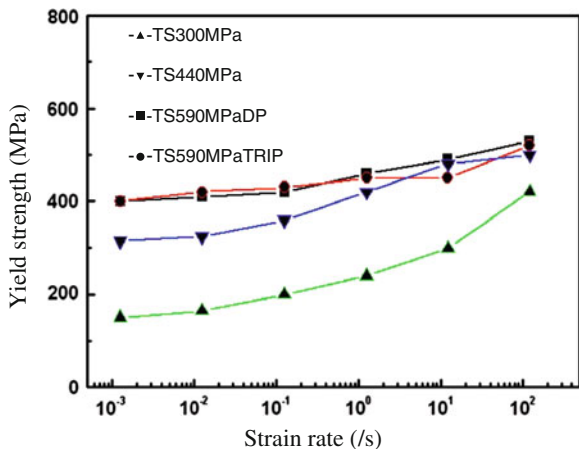


Fig. 10 The relationship between yield strength and strain rate

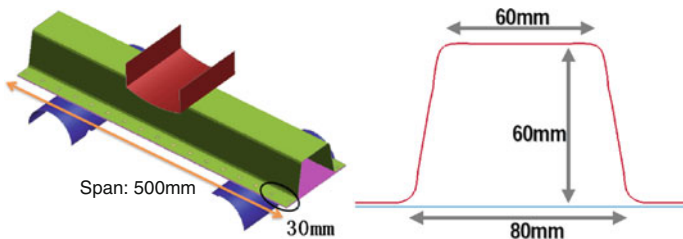
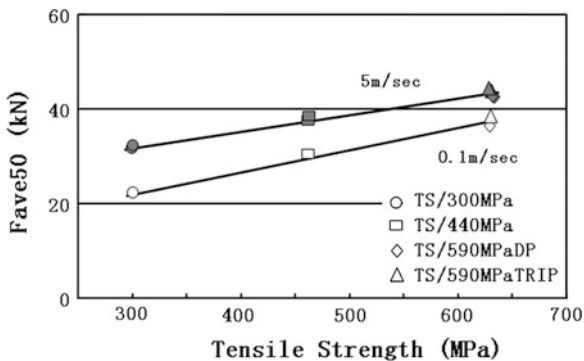


Fig. 11 The size of three point bending test model

Fig. 12 The relationship of material strength and average load under different loads



vehicle test, and the results are consistent with the research of the material properties under different rates and energy absorption of simulated parts under different loading speeds.



## References

1. Xu K, Wong C, Yan B et al A High Straining Rate Constitutive Model For High Strength Steels, SAE SP-1765. Model Mater Struct Crash Appl pp 19–25
2. Batra RC, Nechitailo NV (1997) Analysis of failure modes in Im-pulsively loaded pre-notched steel plates. Int J Plast 13(4)
3. Wu H et al (2009) True Stress-strain curves at different stain rates used in vehicle collision simulation. Mech Sci Technol Aerosp Eng 28(9)
4. Gui sheng Y (2006) Anticollision performance of body steel plate. Automobile Technol Mater 8

**Part III**  
**Development of CAD/CAE/CAM and CF**  
**Methods in Automotive Practice**

# Simulation of Leaf Spring Balanced Suspension Based on Virtual Test-Rig

Xinpeng Tang and Kun Liu

**Abstract** In ADAMS/Car, the simulation platform—six-post test-rig which can identify dual-tire model was developed specialty for testing leaf spring balanced suspension of heavy truck. Based on this, the virtual prototype model of the drive form of  $6 \times 4$  heavy truck was built, and simulation containing four excitation modes were conducted by assembling the virtual prototype model of heavy truck with leaf spring balance suspension to the special six-post test-rig. Design bugs of the leaf spring balance suspension were fund out and approach improving on these problems was proposed by analyzing computed results.

**Keywords** Balanced suspension · Leaf spring · Simulation · Virtual test-rig · Adams

## 1 Introduction

The leaf spring balanced suspension is commonly used in modern heavy-duty truck. It can improve the transportation efficiency and ensure the ride comfort and handling stability at the same time. As an indispensable part of the balanced suspension, the guide mechanism plays an important role in transmitting force and torque between the frame (or body) and the wheels. Therefore, scientific method and reasonable layout in guide mechanism design is essential to improving the performance of balanced suspension and even the vehicle [1–3].

---

F2012-E03-002

---

X. Tang (✉) · K. Liu  
Huazhong University of Science and Technology, Wuhan, China  
e-mail: tangxp@mail.hust.edu.cn

The integrated application of computer 3D modeling technology, virtual prototyping technology, CAD and CAE is the modern vehicle design and analysis direction. It is significant for improving vehicle design and analysis level [4–6].

In this paper, the multi-body system dynamic simulation software of ADAMS is used for detailed kinematics/dynamics simulation analysis to the leaf spring balanced suspension of the heavy truck. The goal is to find the deficiency of existing guide mechanism and propose improvement scheme. For this purpose, the simulation platform—six-post test-rig which can identify dual-tire model was developed in ADAMS/Car, especially for testing leaf spring balanced suspension of heavy truck. Simulation to virtual prototype is carried out with this test platform. The results show that both ends of the thrust rod bear the most serious force in warp condition, which has a great impact on rubber bush's life. On the other hand, there is interference between the leaf spring and lateral guide plate, which is a direct reason to lateral guide plate's serious attrition.

## 2 Development of Six-Post Test-Rig

Analysis to guide mechanism of tri-axial truck's leaf spring balanced suspension is carried out with virtual test-rig. The test-rig is simply defined by four parts representing the tire pads that support the vehicle. These tire pads are constrained to move in only the vertical direction and a displacement actuator (motion controller) controls their vertical motion. The only constraint between the pads and the vehicle's tires is the friction of the tire itself. Because the Delft tire model supports zero velocity tire friction, this is all that is required to constrain the vehicle during the dynamic portion of the simulation. So the guide mechanism's motion and force situation can be calculated [7].

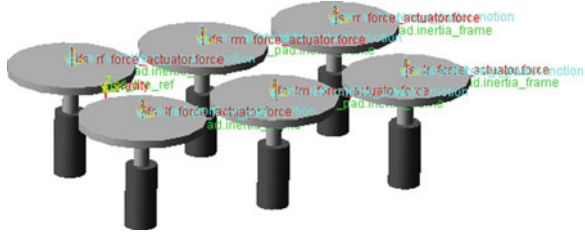
### 2.1 *Creating a Test-Rig Template in ADAMS/Car*

A test-rig in ADAMS/Car is almost completely comparable to a template in ADAMS/Car. Test-rigs differ from templates mainly because test-rigs contain actuator elements, such as motions and forces, to excite the assembly.

The procedure for creating a test-rig template in ADAMS/Car is just like the procedure of creating a normal template, with a few differences. The steps for creating a test-rig template are: Creating a test-rig template; saving the test-rig template; modifying the test-rig template.

ADAMS/Car works with test-rigs as templates. However, in order to incorporate a test-rig for use on an assembly, the test-rig must be converted to a test-rig model file (.cmd) and a private ADAMS/Car binary created. We can, of course, create a new test-rig template from the ADAMS/Car interface very easily, but it is often best to work with existing templates in order to better understand the capabilities of MSC.ADAMS.

**Fig. 1** Six-post test-rig templates



We start by modifying an existing test-rig model file (.cmd) in the template builder. Start by locating the file *acme\_4PostRig.cmd*. This is a test-rig model file (.cmd) that contains a test-rig currently equipped with four active posts. As simulation to three-axis vehicle needs six-posts, two more posts need to be added to the original four-post test-rig. For specific information about building six-post test-rig templates and communicators see [7, 8]. The six-post test-rig templates created is shown in Fig. 1. Communicators are shown in Table 1.

## 2.2 Creating a Private Binary

To use the six-post test-rig for vehicle simulation, We can now add both new test-rig model file *acme\_6PostRig.cmd* (This is a six-post test-rig model file) and the new macro files to build a custom private ADAMS/Car binary which can implement this new test-rig. These new macro commands include *acar\_build.cmd*, *mac\_ana\_ful\_six\_sub.cmd*, *macros\_ana.cmd* and *acme\_6PostRig.cmd*.

*acar\_build.cmd* is the file upon which MSC.ADAMS will call when building a private binary. In general, this file contains any commands to: modify the MSC.ADAMS car interface; import the test-rig model files; add libraries (which show up in the command navigator); add macros; as well as some standard commands which should be in any *acar\_build.cmd* file.

*acme\_6PostRig.cmd* file contains the test-rig model file (.cmd) that we just created. This test-rig model will be imported into our private binary and now be available to any future assemblies.

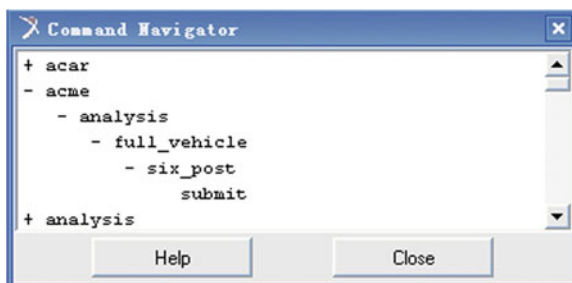
*macros\_ana.cmd* file serves as a pointer to *mac\_ana\_ful\_six\_sub.cmd*. It contains a hard-coded file location. It is good practice to use pointers like this rather than to import the simulation macros themselves. This allows for easy modification. Edit this file to make sure the commands are appropriate to our computer.

*mac\_ana\_ful\_six\_sub.cmd* is a macro that instructs ADAMS/Car on how to simulate the model. It contains parameters input window for simulation and four excitation modes (heave, roll, pitch and warp). This file is discussed in depth in Adding custom analysis procedures to ADAMS/Car, on [8].

Put the above macro command file into the *acar\_private* folder. Then enter command "*acar—cr\_privatebin*" in Adams command window and file *acar.bin* can be generated in the *acar\_private* folder. Restart the Adams command window

**Table 1** Communicators between test-rig and wheels

Name	Type	Match name	Object
Ci[lr]_front_wheel_center	Location	Wheel_center	Front tire
Ci[lr]_middle_in_wheel_center	Location	Middle_in_wheel_center	Middle inner tire
Ci[lr]_midele_out_wheel_center	Location	Midele_out_wheel_center	Middle outer tire
Ci[lr]_rear_in_wheel_center	Location	Rear_in_wheel_center	Rear inner tire
Ci[lr]_rear_out_wheel_center	Location	Rear_out_wheel_center	Rear outer tire
Co[lr]_front_pad_mount	Mount	Actuator_pad	Front tire
Co[lr]_middle_in_pad_mount	Mount	In_actuator_pad	Middle inner tire
Co[lr]_middle_out_pad_mount	Mount	Out_actuator_pad	Middle outer tire
Co[lr]_rear_in_pad_mount	Mount	In_actuator_pad	Rear inner tire
Co[lr]_rear_out_pad_mount	Mount	Out_actuator_pad	Rear outer tire

**Fig. 2** Simulation command navigators

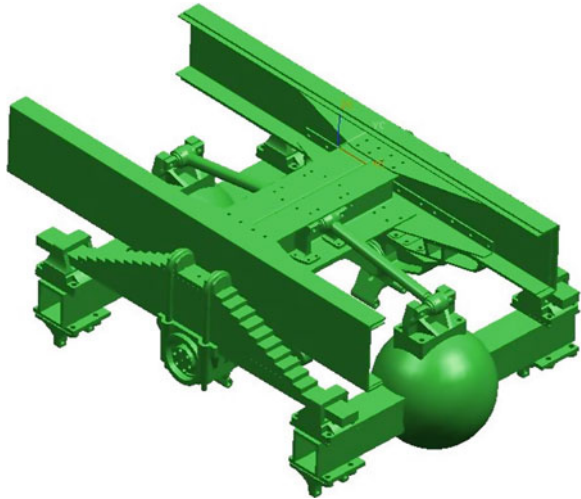
and input commands “*acar—ru\_private—i*”, the ADAMS/Car can be started. Now *\_acme.6PostRig* option can be seen in the drop-down menu of Vehicle Test-Rig. The option “*acme*” will also be added into the simulation command navigator, as is shown in Fig. 2.

### 3 Creation of Vehicle Virtual Prototype Model

All the models used in this paper are established in ADAMS/Car, and the following are some key points when building models.

1. The model is created by importing 3D balanced suspension (as is shown in Fig. 3) established in UG into the ADAMS/Car Template Builder interface. In this process, each assembly of the balanced suspension needs to be accordingly classified (middle and rear suspension, leaf spring and frame etc.). At the same time, the relative coordinates position relationship between different assemblies must be keep unchanged.
2. Each assembly’s geometric parameters, physical parameters and mechanical parameters need to be write into each template after each assembly template is imported and established.

**Fig. 3** 3D balanced suspension model



3. When changing the templates into subsystems, the Minor Role needs to be noticed as it concerns subsystems' effectiveness in assembling.
4. Reasonable match between various subsystems needs to be established when assembling. The assembly relationship between subsystems is transferred by communicators. So it is necessary to establish correct communicators in modeling.

It needs to be emphasized that establishing correct connection relationship and communicators in modeling is significant. These data cannot be changed in subsystem and assembly, although general parts' position and parameters can be changed in the following process. The balanced suspension model assembly model is shown in Fig. 4.

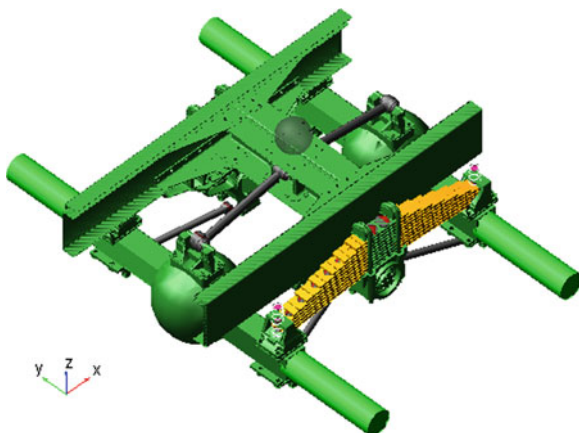
Each of the above assembly needs to be compiled into the corresponding subsystem (save as sub file) in the Standard Interface. Then the vehicle assembly can be created with the subsystems and the six-post test-rig (\_acme.6PostRig). The final vehicle model is shown in Fig. 5.

## 4 Analysis of Balanced Suspension's Guide Mechanism

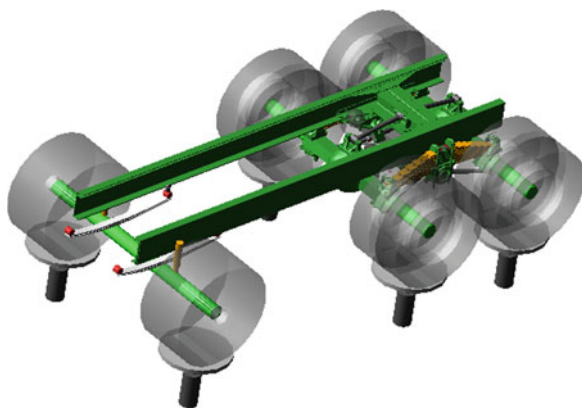
The six-post test-rig can be used for analyzing the balanced suspension's actual situation when the vehicle assembly is completed. There are four excitation modes, Heave: all tire pads move vertically in phase; Pitch: the front tire pads move  $180^\circ$  out of phase with the rear tire pads; Roll: the left tire pads move  $180^\circ$  out of phase with the right tire pads and Warp: the left-front and right-rear tire pads move  $180^\circ$  out of phase with the right-front and left-rear pads.

For heave motion simulation, the frequency is 0.5 Hz and the tire pads' maximum displacement is 120 mm, so as to analog the suspension's quasi-static

**Fig. 4** Balanced suspension model in ADAMS/Car



**Fig. 5** Vehicle assembly model



maximum vertical load situation. The simulation results are summarized in Table 2.

For the roll motion simulation (as is shown in Fig. 6), the frequency is 0.5 Hz and the pads' maximum displacement is 100 mm so as to analog the maximum roll angle situation. The simulation results are summarized in Table 2.

For the pitch motion simulation (as is shown in Fig. 7), the front and rear posts move up and down relatively. The tires tract the middle posts move. The frequency is 0.5 Hz and the maximum displacement is 100 mm so as to analog the situation that braking force and driving force works together. The simulation results are summarized in Table 2.

For the warp motion simulation (as is shown in Fig. 8), the frequency is 0.5 Hz and the maximum displacement is 90 mm so as to analog the suspension's force situation in rough road. The upper and lower thrust rod's maximum load (force and moment) in the above four situation simulation results are in Table 2.

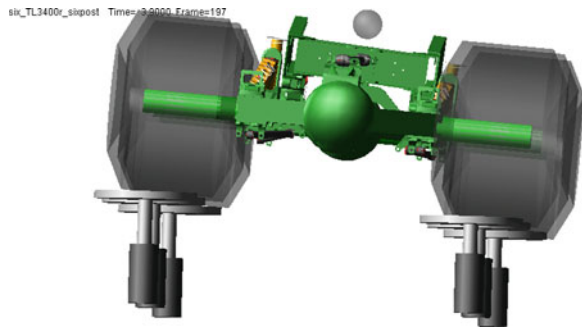
Data in Table 2 clearly shows the following rules.



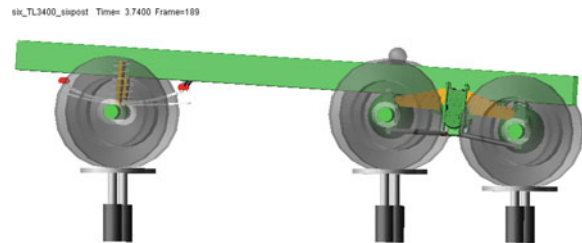
**Table 2** The upper and lower thrust rod's maximum load

Force Thrust rod	Force [N]				Moment [N mm]				
	F <sub>x</sub>	F <sub>y</sub>	F <sub>z</sub>	F <sub>m</sub>	T <sub>x</sub>	T <sub>y</sub>	T <sub>z</sub>	T <sub>m</sub>	
Heave	Upper	7474.4	0.24	733.7	7498.9	723.7	2064.1	63.9	2163.2
	Lower	5792.2	1626.7	355.5	6023.8	879.7	5511.99	10056.9	11468.2
Roll	Upper	4068.2	128.1	339.0	4073.7	16129.9	1587.7	36545.2	38004.3
	Lower	9580.0	2920.1	1296.9	10088.6	60721.5	7623.1	24223.6	65355.3
Warp	Upper	4520.9	258.9	339.8	4525.8	16733.8	2465.6	48280.6	<b>49456.9</b>
	Lower	18982.4	6255.5	2453.3	<b>20129.3</b>	64943.7	8107.1	56081.9	<b>85003.7</b>
Pitch	Upper	18526.6	397.4	1985.3	<b>18576.7</b>	1765.1	3711.3	16335.5	16802.6
	Lower	19137.3	6192.6	970.3	<b>20127.3</b>	4864.7	9876.7	34437.2	35518.3

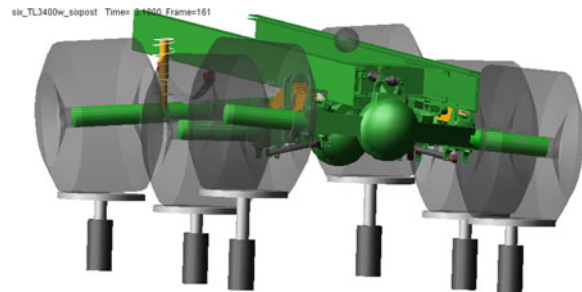
**Fig. 6** Roll motion simulation

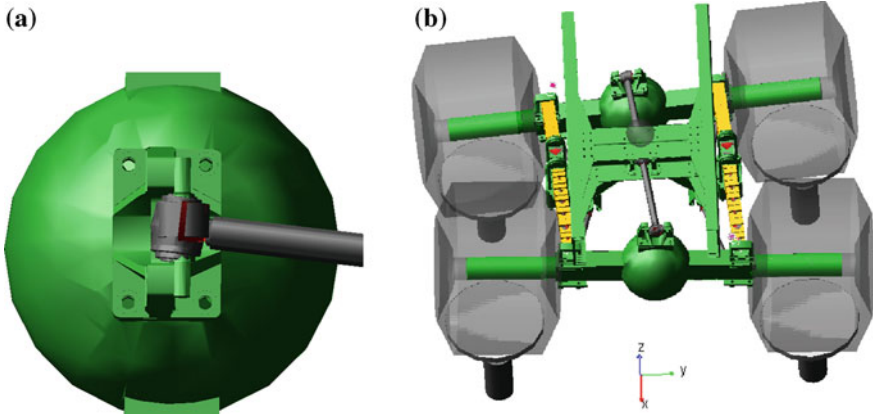


**Fig. 7** Pitch motion simulation



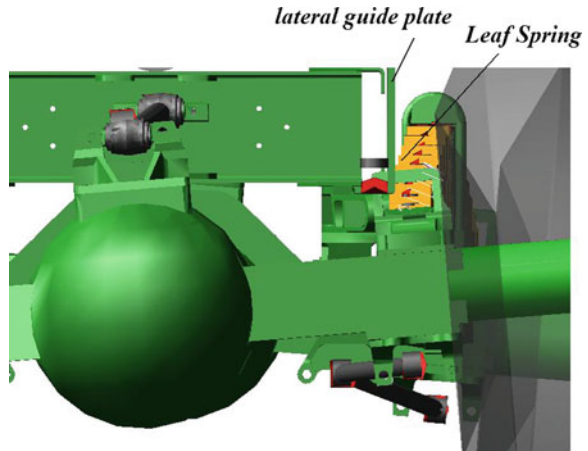
**Fig. 8** Warp motion simulations





**Fig. 9** The upper thrust rod's tensional deflection in warp condition

**Fig. 10** The interference of leaf spring and lateral guide plate



1. The vehicle gravity generates maximum axial force (resultant force) in the upper thrust rod in pitch and heave conditions. The maximum value is 18576.69 and 7498.85 N respectively.
2. Generally the axial force of the lower thrust rod is larger than upper thrust rod except the heave motion. The vehicle gravity generates maximum lateral force (Y axis) and axial force (resultant force) in warp and pitch conditions. The maximum values are 6255.48, 6192.63 and 20129.33, 20127.3 N respectively.
3. In warp condition, the upper and lower thrust rod gets the maximum moment. The upper thrust rod's maximum moment is  $R_z$  (48280.6 N mm) around Z axis, which is shown in Fig. 9. The lower thrust rod's maximum moment is  $R_x$  (64943.7 N mm) around X axis. These torques have little effect on thrust rod's strength but have a greater impact on rubber bushings' life.

Figure 10 show the interference of leaf spring and lateral guide plate in warp condition, which the main reason is leading to the leaf spring and lateral guide plate's abrasion.

## 5 Conclusions

1. A six-post test-rig which supports dual tires simulation is established by macro command development tools on basis of the existed four-post test-rig in ADAMS/Car. These extend the software function;
2. A vehicle simulation model is assembled by six-post test-rig. Simulation for a tri-axial vehicle with balanced suspension is carried out in four excitation modes. The results show that the upper and lower thrust rod gets the maximum moment in warp motion, which have a greater impact on rubber bushings' life. On the other hand, the interference of leaf spring and lateral guide plate in warp is the main reason leading to the leaf spring and lateral guide plate's abrasion.

The research method and conclusions of this paper have some reference value to the modeling of multi-axis heavy truck and the design of guide mechanism in balanced suspension.

## References

1. Li B (2007) Research on design method of double front axle truck balance suspension [D]. Jilin University, Changchun (In Chinese)
2. Wang S (2004) The suspension kinematics and elastic kinematics modeling, analysis and evaluation [D]. Jilin University, Changchun (In Chinese)
3. Wang Q, Fang X, Ma H (2001) Based on the virtual prototype technology in the design and analysis of automobile leaf spring [J]. Chin J Mech Eng (12):63–66 [In Chinese]
4. Zhao L, Wang Y, Xu D (2003) Multiple axle equilibrium suspension and Tts performance analysis of new structure form. Spec purp veh (5):10–12 [In Chinese]
5. Zhang Y, chen L (2005) The analysis of dynamics of mechanical systems and ADAMS applications [M]. Tsinghua University press, Beijing [In Chinese]
6. Makita M (1999) An application of suspension kinematics for intermediate level vehicle handling simulation. JSAE Rev 20(4):471–477
7. MSC Software (2003) ADAMS/Car training guide. Release 2003
8. MSC Software (2007) ADAMS 2007R2/help, ADAMS/Car

# A Simulation Analysis and Optimization of Mode and Stiffness of BIW

Qiuxia Zhang, Leyi Zhang and Mingtao Guo

**Abstract** Based on the compartmentalized grids, simulation analyses of the mode and stiffness of BIW were performed by using the FEM software; further validation had been conducted through a series of experiments. By comparing the results, it was proved that the BIW models as well as the simulation method were rational and reliable. The coherence of the stiffness from both sides of BIW was validated too. Finally, the BIW model was optimized in order to improve the local modes for a better body design and vehicle NVH. This article is suitable for body design and the future FEA research as reference.

**Keywords** Body in white · Simulation · Examination · Optimization

Following the developing of CAE, the FEM has been applied widely in BIW analysis. The mode features of the BIW, especially in low order case, reflect whole dynamic rigidity characteristic of the car body not only, but a key index in controlling the vibration features of the car. The total unitary construction of modern car body carry all the loads in running the car, mainly the bending and torsion loads, under these loads the rigidity feature of the car display a very important role. Irrational rigidity of the car body will affect directly the reliability, safety and NVH features, so the analysis of flexible rigid and torsion rigid of the BIW car body is the necessary work in developing process of the car.

To save time and reduce the computational work, this article uses the 20 mm mesh to establish finite element model for the BIW, and conducts mode and

---

F2012-E03-004

---

Q. Zhang (✉) · L. Zhang · M. Guo  
Brilliance Automobile Engineering Research Institute, Shenyang, China  
e-mail: qiuxia.zhang@brilliance-auto.com

rigidity analysis for BIW of a car model in aspects of simulation and examination, and improves the car body design by local optimizing to heighten some local modes. It may have certain reference value to the car body design and further simulation investigation.

## 1 Theoretical Basis for Mode and Rigidity Analysis

### 1.1 Theoretical Basis of Mode Analysis

The mode analysis includes the analytical analysis and examination analysis to the dynamic features of a structure, in which the dynamic features are expressed by modal parameters. Mathematically, the modal parameter is defined as the characteristic value and characteristic vector of the kinematics differential equation of a mechanical system, and its physical meaning is the apotheosis (natural frequency and damping) and vibration mode (modal vector) of the system measured through test.

For a linear stationary system with n-freedom, its basic vibration equation [1] may be in the form of:

$$M\ddot{X}(t) + C\dot{X}(t) + KX(t) = F(t) \quad (1)$$

In which, M is the mass matrix of the system, C the damping matrix, K the rigid matrix,  $\ddot{X}(t)$  the acceleration vector,  $\dot{X}(t)$  the speed vector,  $X(t)$  the displacement vector, and  $F(t)$  the dynamic exciting load vector.

In mode analyzing, as usually the damping of structure is small, it has only very tiny influence to the natural frequency and vibration mode, so it may be omitted. Therefore, for any damping-less linear elastic vibration system, the kinematics equation of free vibration may be expressed as:

$$M\ddot{X}(t) + KX(t) = 0 \quad (2)$$

In this case, the analysis of natural frequency and vibration mode to a structure will be changed into finding the characteristic value and characteristic vector of the equation.

In testing, take Laplace transformation [2] to Eq. (1) (with complex variable p), and set the initial displacement and initial velocity as 0, then we get:

$$(p^2M + pC + K)[X(P)] = F(p) \quad (3)$$

Change the above formulae to:

$$H(P) = \frac{X(p)}{F(p)} \quad (4)$$

Then the Eq. (4) is the transfer function. In testing, the frequency and the vibration mode of the system may be obtained by measuring the transfer function in three directions of the key point of the system.

## 1.2 Theoretical Basis for Rigid Analysis

In engineering applying, rigidity of a structure is very important, it is defined as the ratio of increment of force or torque worked on the elastic element to the increment of corresponding displacement or angular displacement, and is used to measure the ability of structure or structure member in resisting deformation.

Formula for calculating flexible rigid of BIW is:

$$K_f = \frac{force}{\Delta Z} \quad (5)$$

In which,  $K_f$  is the flexible rigid, with an unit of N/mm; *force* is the resultant force loaded on the front and rear row seats, N;  $\Delta Z$  is the average of the maximum Z direction displacement on lower part of left and right door threshold, mm.

Formula for calculating torsion rigid of BIW is:

$$K_t = \frac{Torque}{\alpha} \quad (6)$$

In which,  $K_t$  is the flexible rigid, with an unit of N-m/deg; *Torque* is the torque on mounting hole at front shock absorber, in N-m;  $\alpha$  is the twist angle of the front shock absorber seat to corresponding longitudinal beam, in deg.

In that, the twist angle is calculated by:

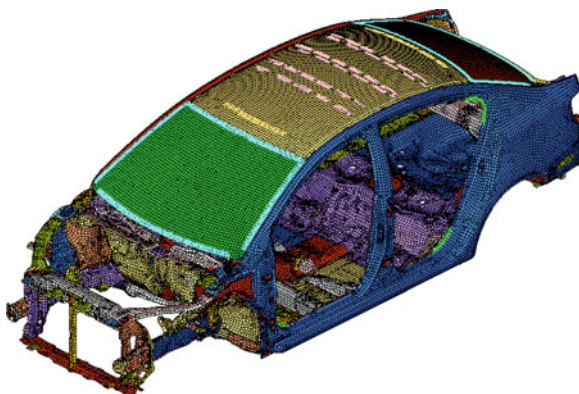
$$\alpha = \frac{180 \cdot \Delta Z}{\pi \cdot Y} \quad (7)$$

where,  $\alpha$  is the twist angle, deg;  $\Delta Z$  is the Z direction displacement of the measured point, mm; and  $Y$  the coordinate value in Y direction of the measured point, mm.

## 2 Modal Simulation and Examination Analysis to BIW

According to the interior standard of the company, we adopt Hypermesh to divide every part of the BIW. To save time and reduce calculating amount, the mesh is taken as 20 mm. The pressed parts adopt shell element for simulating, while for weld spot and the glue-smeared portion the joint element simulating is used [3]. The finite element model is shown as in Fig. 1.

**Fig. 1** Finite element model of BIW



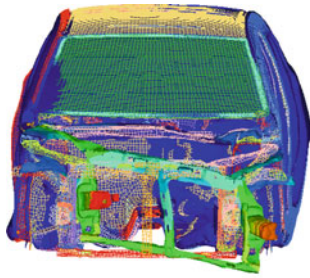
**Fig. 2** BIW testing arrangement



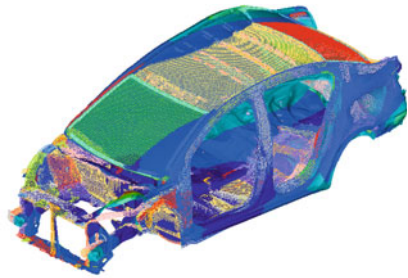
On test table, we use random signal to conduct single point exciting to the BIW, while multi-point sensing method to collect response signals. After the signals be treated, the natural frequency and corresponding vibration mode of the whole BIW and local modals are obtained. The testing arrangement is shown in Fig. 2.

Based on above finite element model and testing arrangement, free modal analysis is conducted, with the simulation analysis result as shown in Fig. 3, the examination analysis result in Fig. 4, and in Table 1 the comparison of simulation and examination results of the whole BIW and local modal are listed.

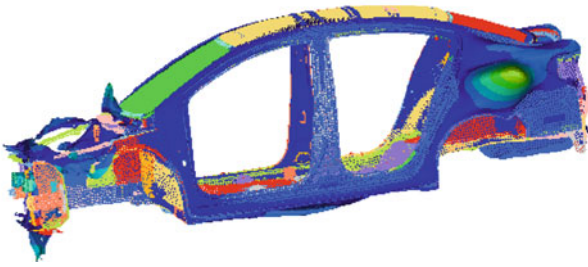
From Table 1, it can be seen that the error of the integer modal simulation result and the testing result falls in a range of 5%. This meets the requirement, and proves the rationality of the finite element BIW model, it also show that the local modal of front and rear canopy of BIW are all on the lower side, that should be further optimized.



Vibration model of cabin swing

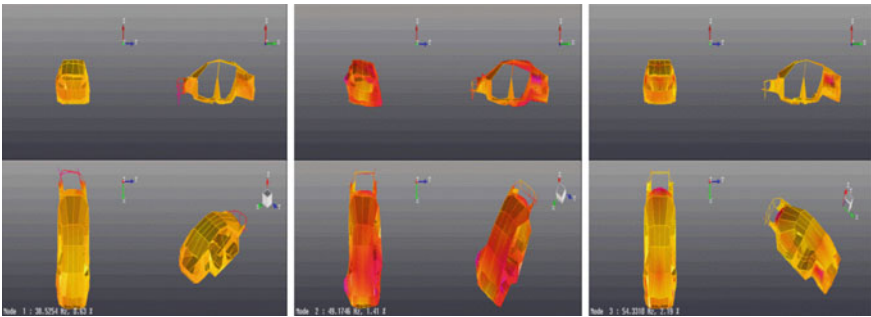


Vibration model of integer first order torsion modal



Vibration model of integer first order flexible modal

**Fig. 3** Simulation analysis result



Cabin swing modal (38.53 Hz)

Integer first order torsion modal (49.17 Hz)

Integer first order torsion modal (54.33 Hz)

**Fig. 4** Examination analysis result



**Table 1** Comparison of simulation and examination results

Vibration mode	Simulation value f/Hz	Testing value f/Hz	Error (%)
Cabin swing	40.40	38.53	4.8
Portion of front cover	49.14	49.17	0.061
Portion of rear cover	50.95	54.33	6.2
First order torsion	51.27	49.17	4.3
First order beading	55.57	54.33	2.3

**Fig. 5** Flexible rigid test arrangement

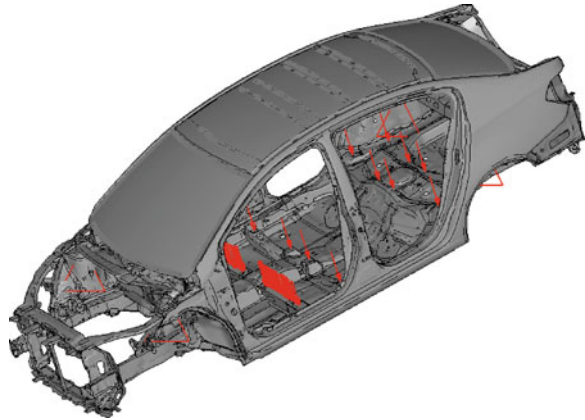
### 3 Rigidity Simulation and Examination Analysis to BIW

#### 3.1 Pre-treatment to the BIW Rigid Simulation and Examination Analysis

In testing of flexible rigid of BIW, the fixture works on both front and rear shock absorber seats through spherical hinge, so in the finite element model the boundary condition of bending is: at rear shock absorber seat, one side constrain X, Y, Z translational freedom; another constrain X and Z translation freedom; all constrains at front shock absorber seat are Z direction translation freedom. In testing, place wooden blocks onto the mounting points or mounting cross beam of the front and rear seats, then make loading to the wooden block with a load of 4000 N, as shown in Fig. 5; on the finite element model, place the same amount of load onto the mounting point or mounting cross beam in the form of concentrated force or uniform distributed force, as shown in Fig. 6.

In BIW torsion rigid testing, the rear fixture works on the rear shock absorber seat through spherical hinge, while front fixture works on the front shock absorber through spherical hinge as well, that ensure the load may work in vertical direction. In the finite element model, the boundary conditions for the bending case are:

**Fig. 6** Sketch for finite element model in bending case



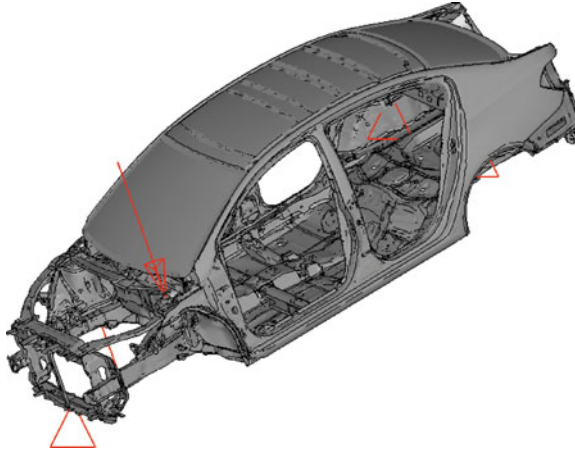
**Fig. 7** Arrangement for torsion rigid testing



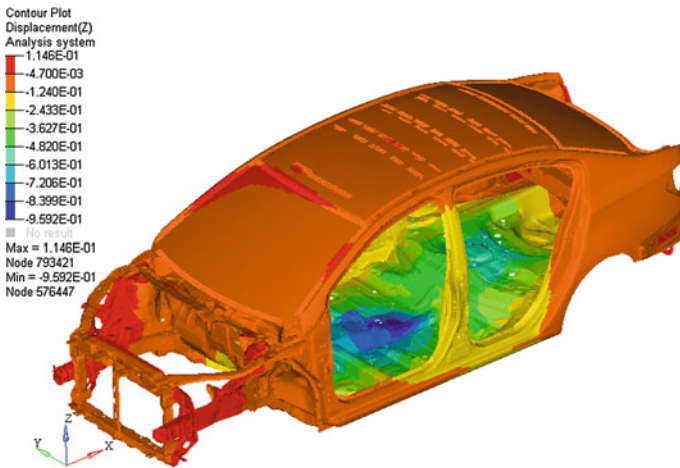
one side constrain at rear shock absorber seat X, Y, Z translation freedom, constrain on another side Z and Y translation freedom; at the same time, in the middle portion of the front cross beam ( $y = 0$ ) the constrain is Z direction translation freedom. According to the testing requirement, in torsion rigid analysis place 4,000 Nm torsion on the center point of front shock absorber seat, while in simulation analyzing apply a torque as the same for the testing. Testing arrangement and finite element models are shown correspondingly in Figs. 7 and 8.

### ***3.2 Data Processing for BIW Rigid Analysis***

By using MSC Nastran solver, a static rigid analysis to the BIW is conducted under above working condition and the cloud chart for Z direction displacement under bending and torsion cases are obtained, as shown in Figs. 9 and 10 respectively.



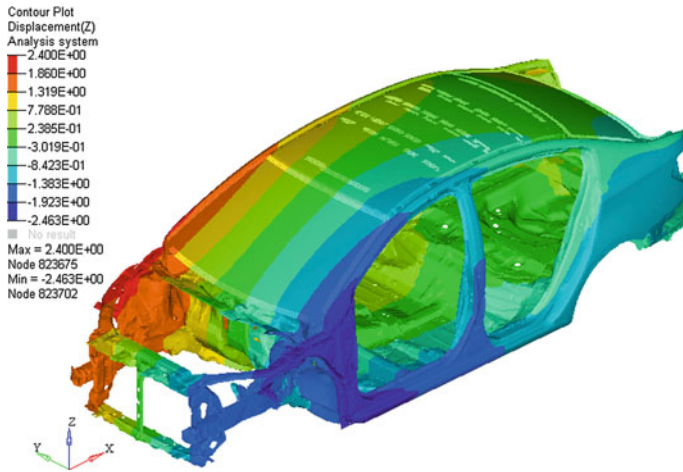
**Fig. 8** Sketch for finite element model in torsion case



**Fig. 9** In bending case

On Fig. 9 select the point of maximum Z direction displacement at the lower portion of the threshold beam of left and right doors to conduct flexible rigid calculation, by using formula (5); and on Fig. 10 select the Z direction of the center point of left and right shock absorber seats for torsion rigid calculation, by using formula (6) and (7), and then compare the examination results, as shown in Table 2.

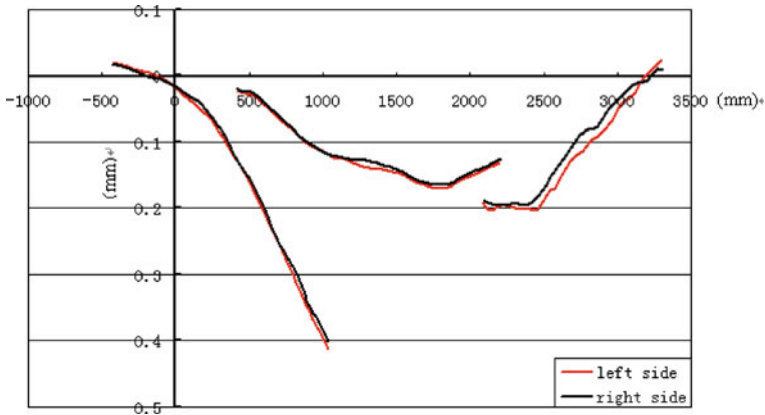
On Fig. 9 select the maximum Z direction displacement point at the lower portion on door threshold beam of left and right door for flexible rigid calculation, and in Hypermesh take a series of points in the lower portion on front and rear longitudinal beams and door threshold beam, with a spacing of 100 mm, then get the coordinate value and Z direction displacement of the series points; convert



**Fig. 10** In torsion case

**Table 2** Comparison of calculation and test result for BIW bending and torsion rigid

Working condition	Calculation value K	Test value K	Error (%)
Bending case	23845 N/mm	23088 N/mm	3.3
Torsion case	22198 Nm/deg	21706 Nm/deg	2.3



**Fig. 11** Flexible rigid curve of BIW

them to get Z direction displacement (bending) and twist angle (torsion), and then draw the flexible rigid curve and torsion rigid curve along the X direction. On the drawing the abscissa axis is the X coordinate of the measured points, mm; the vertical axis is the Z direction displacement or the twist angle, with the unit of mm or deg respectively. The results are plotted as in Figs. 11 and 12 correspondingly.

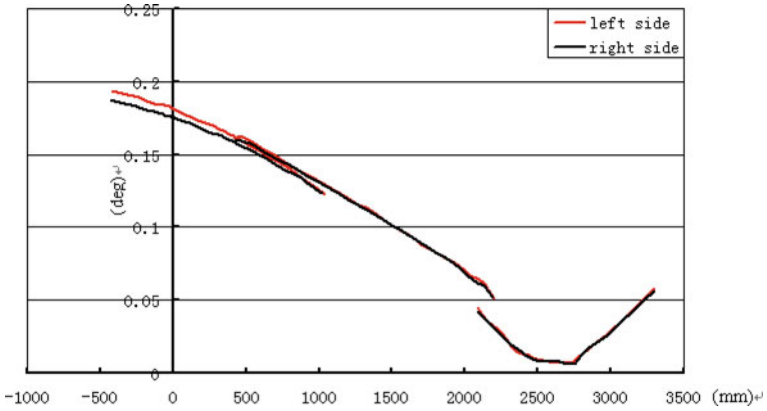


Fig. 12 Torsion rigid curve of BIW

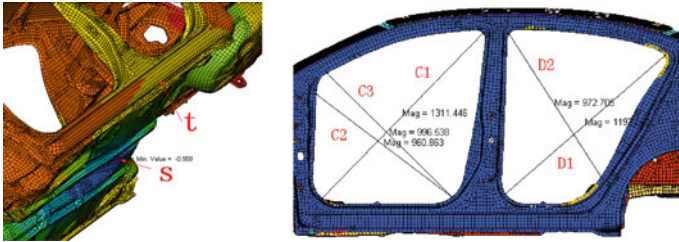
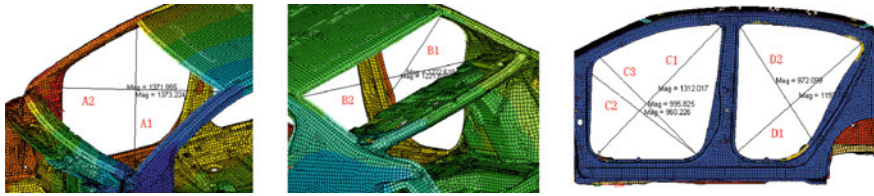


Fig. 13 Deformation in bending case

From the rigid analysis of BIW, it is known that compare to the testing results the error of both flexible and torsion rigid are in the permitted range of 5 %, and meet the requirement. This proves the rationality of this model. From Figs. 11 and 12, it can also be seen that both the flexible and torsion curves runs smoothly and with same tendency for left and right side, means that the rigid characteristics of left and right side of the BIW are uniform.

From above analysis, it is clear that the simulation result is close to the testing result, showing that rightness of BIW model is proved. Nevertheless, limited by the testing arrangement it is not possible to measure accurately the deformation amount of main position of the BIW in bending and torsion case, so in this paper we take simulation analysis to exam the deformation value of all main positions, and use target value for proving.

Based on the comparison of output points at front and rear windshield, front and rear doorframe, front seat floor and door threshold, analyze the front and rear coordinate values and calculate deformation values correspond to the bending and torsion case respectively, as shown in Figs. 13 and 14. The corresponding deformation values are listed in Tables 3 and 4.



**Fig. 14** Diagonal deformation in torsion case

**Table 3** Deformation of various positions in bending case

Position	Deformation (mm)	Target value (mm)
Transverse bending deformation at front seat floor cross beam	$s < 1.0$	1.0
Longitudinal bending deformation at door threshold	$t < 1.0$	1.0
Diagonal deformation at front doorframe	$C1, C2, C3 < 1.0$	2.0
Diagonal deformation at rear doorframe	$D1, D2 < 1.0$	1.5

**Table 4** Deformation values of various frames in torsion case

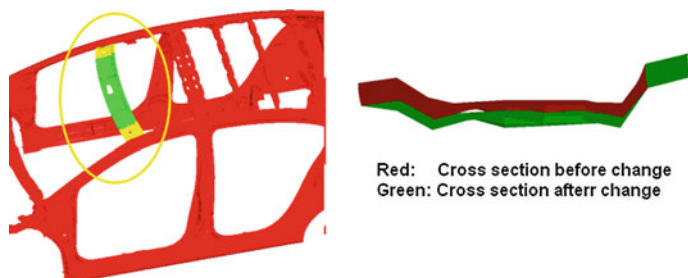
Frame position	Deformation (mm)	Target value (mm)
Diagonal of front windshield	$A1, A2 < 1.0$	5.0
Diagonal of rear windshield	$B1, B2 < 1.0$	5.0
Diagonal of front doorframe	$C1, C2, C3 < 1.0$	3.0
Diagonal of rear doorframe	$D1, D2 < 1.0$	3.0

From Tables 3 and 4 it can be seen that the deformation of all positions in bending and torsion cases are all less than 1 mm, and all meet the requirement for frame, floor and doorframe correspondingly [4].

## 4 Structure Optimization

From the analysis to the BIW, it can be seen that local modal of front and rear roof panel are all tend to low, they need to be further optimized. This article take following optimization, with the front roof panel as example: See Fig. 15, deepen the front cross beam of roof panel for 5 and 10 mm consequently and then conduct modal analysis. Results of optimization before and after are compared in Table 5.

From Table 5 it is clear that this optimization plan may improve the local modal of the roof panel, and meet the requirement.



**Fig. 15** Optimization plan for front cross beam of roof panel

**Table 5** Comparison of result before and after optimization

	Original plan	Deepen 5 mm	Deepen 10 mm
Frequency (Hz)	49.14	50.12	50.50
Frequency added (Hz)		0.98	1.36
Part quality (Kg)	1.151	1.17	1.207
Mass added (Kg)		0.019	0.056

## 5 Conclusion

From the view point of saving calculating time and reducing calculating works, and in consider of that the size of the mesh has no great influence to the modal, we take 20 mm mesh for mesh plotting, and establish the BIW finite element model. This paper explains thoroughly the process and steps of car BIW modal and rigid analysis, compares the results obtained from both analysis, and gets the conclusion that by 20 mm mesh the error of BIW modal and rigid are all in the allowing range of 5 %, that meets the design requirement, therefore it prove the rationality and reliability of the model; Limited by the testing arrangement, this paper proves that the deformation amount of all main positions in bending and torsion case meet the requirement of target value, take the advantages of simulation and examination techniques, conduct optimization to the local modal of roof panel, improve the local modal successfully, and shows certain reference value for further investigation.

## References

1. Helen W (2001) Modal analysis theory and practice. Beijing institute of technology press, Beijing, June 2001
2. Jian P, Gang Z, Hua H (2006) Automotive noise and vibration—theory and applications. Beijing institute of technology press, Beijing, June 2006
3. Li C, Zhang S (2008) Hyper works analytical applications and examples. Mechanical industry press, Beijing, July 2008
4. Liu X, Yin J, Zhang K (2001) Automotive engineering manual. Communications press, Beijing, May 2001

# Vehicle Wading Simulation with STRA-CCM+

Xin Zheng, Xin Qiao and Fanhua Kong

**Abstract** There might be a lot of water on road after a heavy rain. Car wading drive is very popular. Car wading capability is also an important indicator in measuring the car quality. This paper used STAR-CCM+ to carry out a model car wading analysis, watched the situation of firewall being washed by water flow, made modification thereof to avoid the direct washing of the firewall by water and solved the problem of firewall water seepage.

**Keywords** Car water seepage · STAR-CCM+ · Firewall · Washing · Water seepage

## 1 Introduction

Global climate now becomes warmer and rainfall increases in summer. There would be a lot of water on road after a heavy rain. Car wading drive is very popular and car wading capability therefore attracts attention of auto enterprises.

Serious car wading would result in situations below:

1. Car electronics increases now. Lines are particularly complex. Wadded car is easy to have its circuit interface and sockets wetted. Wadded car doesn't show

---

F2012-E03-005

---

X. Zheng (✉) · X. Qiao · F. Kong  
Brilliance Auto Engineer Research Institute Engineering Analysis Room,  
Shenyang 110141 Liaoneng, China  
e-mail: xin.zheng@brilliance-auto.com



any problem at that moment. The wet place, however, will be oxidized as time goes by and the problem will come along.

2. When a car drives on a road with water, a lot of water will impact the firewall inside the car, which will have a problem of water seepage due to fast flow and great pressure of water when the car wads too long.
3. Car wading will have a great impact on the engine, e.g. environmental water results in electric device short circuit, water entering air inlet pipe results in air cylinder water, entering engine body dilutes lubrication oil, having a cooling effect on the body.
4. Engine wading will have a great impact on the lubrication system. Sump locates at the bottom end of the engine. It contacts with water in the first place, in case of wading, and immerses partially or wholly under the water as long as the water increases in depth. High temperature lubrication oil sees an heat exchange with water through the wall of sump. Temperature of the oil drops and the viscosity reduces, resulting in poor lubrication, increase in friction loss and fuel consumption.

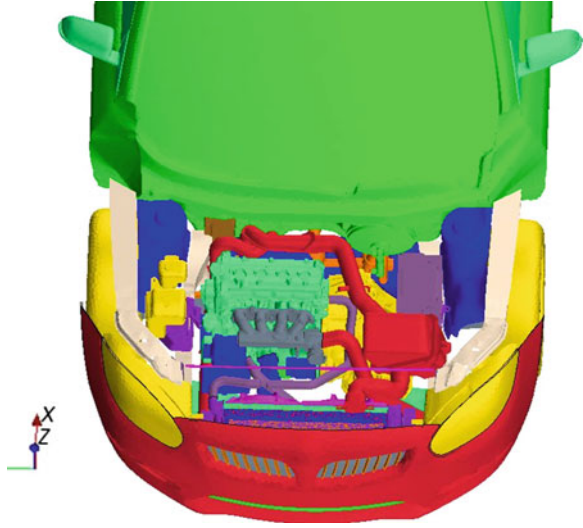
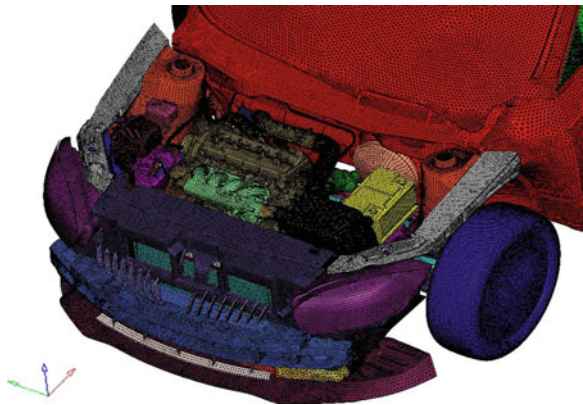
Based on information fed from actual road test, it was found that firewall experienced a water seepage during the car wading test. To find out the main point of water seepage, the CFD software STAR-CCM+ was employed to simulate the car wading.

## **2 Calculation Model Establishment and Program Determination**

### ***2.1 Establishment of Geometrical Model***

Based on three dimensional CAD solid model of a car, all parts and units inside the engine bay, front grille, wheels and car body's outer surface were chosen respectively to generate a simulation space. In consideration of the complexity of car product and in order to save time and reduce the number of grilles, car chassis was processed to a flat panel under the prerequisite that the simulation accuracy was not affected. However, key units under the simulation, such as front grille, fan and radiator in the engine bay were kept intact, as shown in Fig. 1.

Since CFD meshing had to be done in an enclosed space, and CAD model saw some gaps and vulnerabilities in between, a lot of time and efforts would be required if pre-treatment of the model was carried out directly by CAD software. We, therefore, did the triangular surface meshing in Hypermesh first, as shown in Fig. 2, thus making the connection and repair of the surface relatively easy and, then, the output format for Nastran.

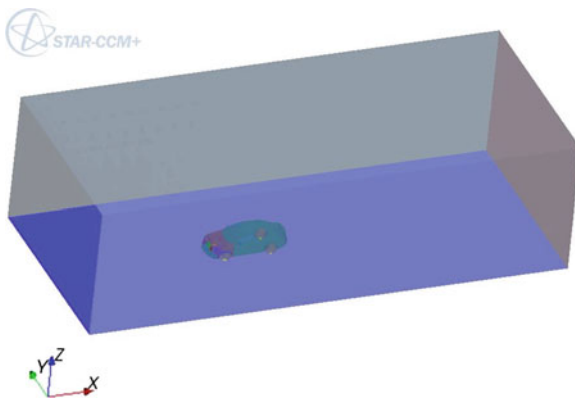
**Fig. 1** Geometrical model**Fig. 2** Hypermesh surface mesh

## 2.2 Mesh Generation

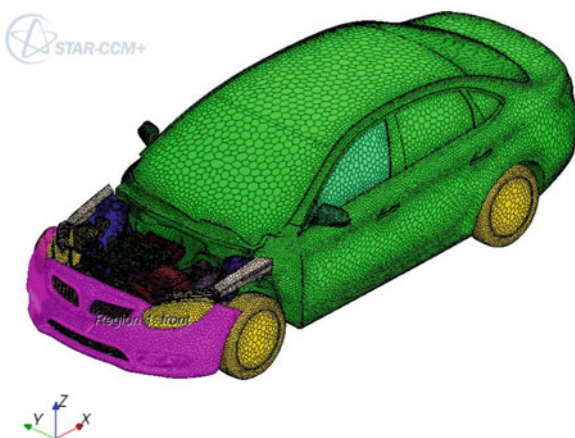
In this analysis, STAR-CCM+ advanced mesh generation tool was used to restructure the surface mesh and divide the volume mesh, where the calculation model of porous media was adopted for intermediate cooler, condenser and radiator.

Calculation area was taken as rectangular. Length, width and depth are respectively of  $32 \times 6 \times 7$  m. Upstream was 8 m from the front axle, as shown in Fig. 3. The entire model was divided by 12 icosahedral mesh [1]. Total number of volume mesh was of 3739120. Figure 4 shows the entire car volume mesh.

**Fig. 3** Calculation mesh



**Fig. 4** Entire car volume mesh



**Table 1** Initial conditions

Schemes	(I)	(II)	(III)	(IV)
Wading depth	100 mm	100 mm	200 mm	200 mm
Driving speed	30 kph	10 kph	30 kph	20 kph

### 2.3 Boundary Conditions Determination

Two fluid media of water and air were used in the analysis. Speed entrance boundary conditions were used for entrance. Entrance speed was set according to actual road condition speed, as shown in Table 1. Pressure exit boundary conditions were used for exit. Slip wall boundary conditions were used for side and top. Non-slip wall boundary conditions were used for bottom and body surface. High Reynolds number  $k-\epsilon$  turbulence model [2] was used for turbulence model. SIMPLE algorithm was used for calculation.

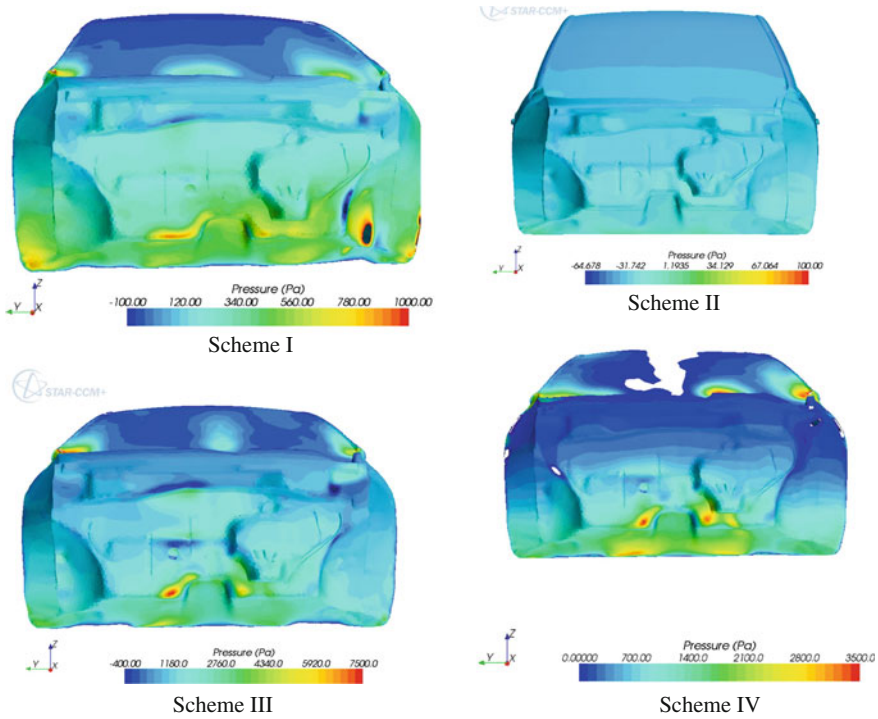


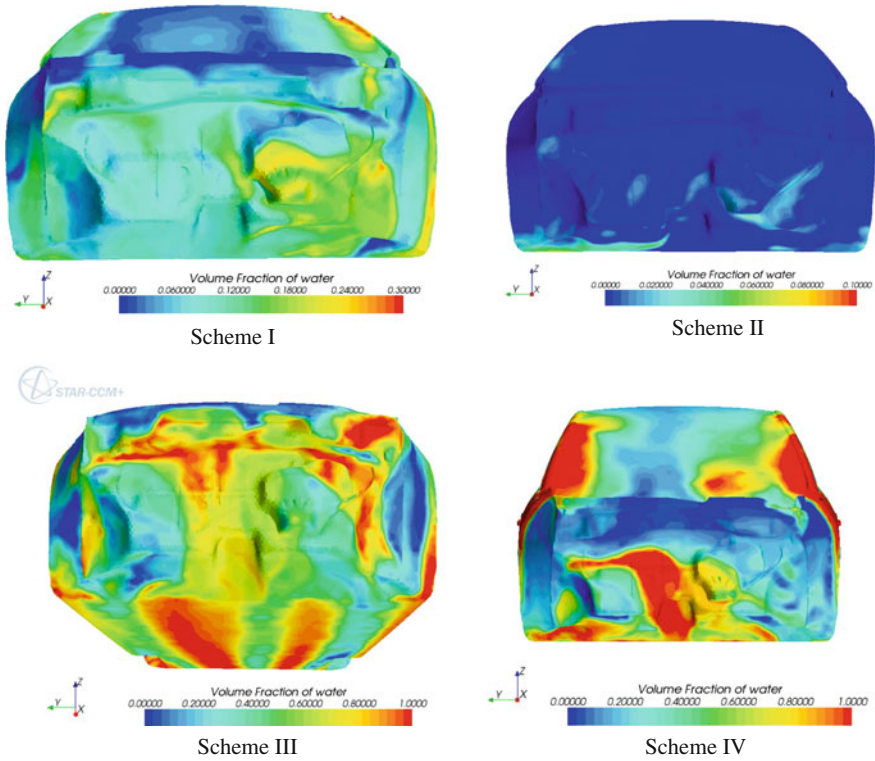
Fig. 5 Pressure of water on firewall at different wading depths and driving speeds

### 3 Results and Analysis

#### 3.1 Original Model Results

Pressure distributions on firewall at different wading depths and driving speeds are as shown in Fig. 5. We knew by calculation that the faster the driving speed and the deeper the water the greater the pressure impacted on firewall. At the same speed, pressure changed obviously along water depth increase. All schemes showed one point in common: the maximum values of pressure occurred at the center bottom of firewall, biased towards the co-driver side. The maximum value of pressure occurred a driving speed of 30 kph. With wading depth of 200 mm, the pressure value was of 7,500 Pa.

Water volume fraction represents water content. Volume fractions of water on firewall at different wading depths and driving speeds are as shown in Fig. 6. We knew from scheme I that much water splashed on firewall by the driver side. Scheme II saw less water splashed on firewall, as compared to Scheme I, due to reduction of driving speed, but the area with water was the same. Scheme III saw a large area of water splashed on firewall, almost throughout the entire firewall, due

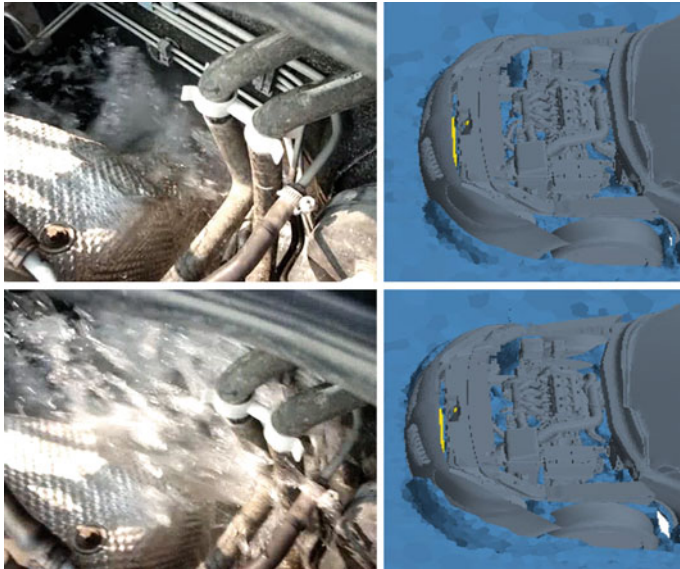


**Fig. 6** Display volume fraction of water on firewall at different wading depths and driving speeds

to great wading depth and driving speed. Scheme IV, as compared to Scheme III, saw a large water splash at the bottom of firewall towards co-driver side due to driving speed reduction. Water splashed from the car bottom was blocked by the bottom of firewall and could not but appressed to the firewall along its shape without splash [3].

It is known from comparison between screenshot of water influent process in road test and results of Scheme IV that car wading processes were quite similar, as shown in Fig. 7.

In summary, Scheme IV (wading depth 200 mm, driving speed 20 kph) is more common in practice and best reflects the performance of a real car in road test. Scheme IV simulation results are therefore of more reference value [4].



**Fig. 7** Road test compared to scheme IV

**Fig. 8** Engine bottom protective panel



### 3.2 Improvement

We knew from Scheme IV that there was a lot of water in the center of firewall, where water seepage could always be seen. For this concern, a protective panel was added to the engine bottom, as shown in Fig. 8, aiming at stopping water back firing from the bottom and impacting the firewall.

Based on Scheme IV, wading simulation of the modified scheme was carried out. Boundary condition parameter settings were the same as that of Scheme IV (wading depth was 200 mm, driving speed was 20 kph). Comparison between Scheme IV and the modified one in respect of wading simulation is as shown in Fig. 9. It could be seen from the simulation of Scheme IV, water entering the engine bay was divided into two. One went from grille, passing through intermediate cooler, condenser, radiator and fan, and impacted the engine body. The other washed the engine bottom, turned upward through the firewall and impacted the engine at the reverse side. It is observed from the modified scheme's



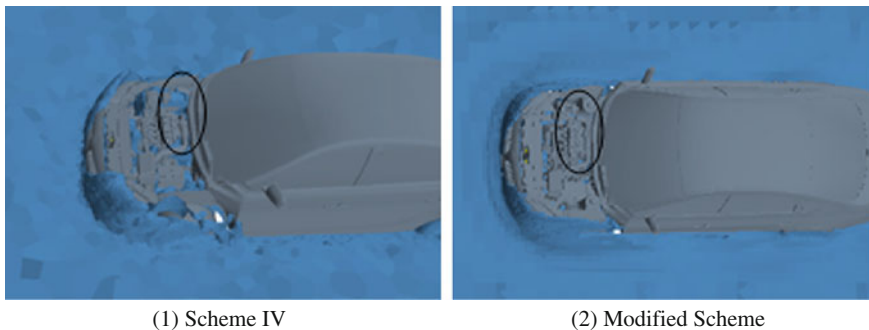


Fig. 9 Comparison between schemes of wading simulation

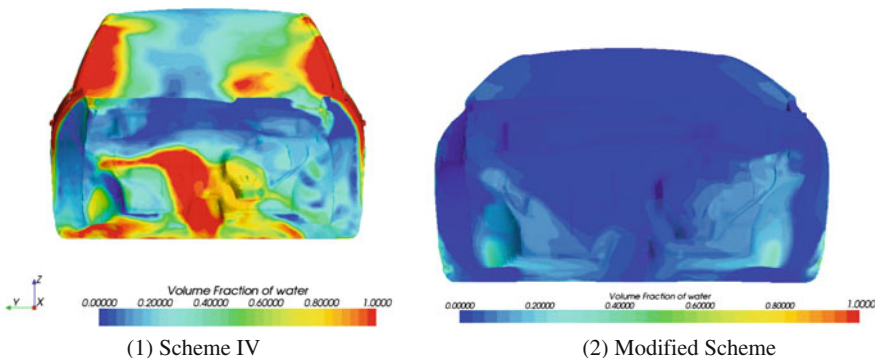


Fig. 10 Volume fraction of water on firewall

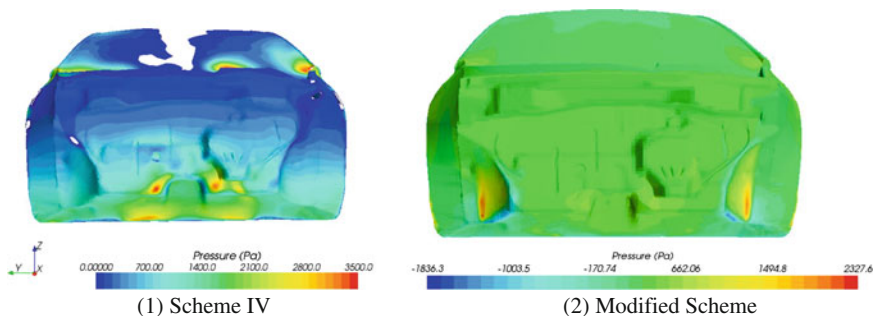


Fig. 11 Pressure distribution over firewall

simulation results that water washed the firewall from the engine bottom was stopped by the newly added engine bottom protective panel, which cut off the water flowing directly to and impacting the firewall [4].

It's seen from volume fraction of water on firewall that water on firewall was reduced remarkably by adding the engine bottom protective panel. It reflected more clearly the water resisting effect of the protective panel and, then, verified the feasibility of design changes, as shown in Fig. 10. Pressure area at the firewall bottom also saw an obvious change. Pressure on the entire firewall became more uniform. Pressure Max occurred inside the wheel cover, due to direct water washing of the cover (Fig. 11).

## 4 Conclusion

1. Wading analysis of a car done with the help of STAR-CCM+ software could provide more accurate pressure distribution and water on volume fraction of all parts and units during the whole process of car wading.
2. Calculated results of the modified scheme showed that water flow at the car bottom could be separated very well from directly washing the firewall by adding the engine bottom protective panel. Possibility of water seepage at firewall was reduced. The modified scheme is rational.
3. By use of CFD in product development, you may greatly shorten the development cycle and save the development cost. Analysis results are of important value for reference to the design and development staff in optimizing product design.

Deficiency of this article is that it lacks verification of overheat that might occur in the engine bay due to addition of the engine bottom protective panel. That will be covered later in our work.

## References

1. STAR-CCM+ help file
2. Yu Z (2006) Auto theory. Mechanical Industry Press, Beijing
3. Jimin N (1999) Principles of auto internal combustion engine. Tongji University Press, Shanghai
4. Rao H, Ni J, Li Y (2009) Study on performance of auto engine in wading. Auto Engine 180(1):63–66



# Developing Low-Noise Low Back Pressure Intake System by CAE Technology

Yue Chang Chen, Haotian Shi and Yang Guang

**Abstract** This paper describes the process of developing low-noise low-BP intake system by CAE technology. In the noise optimization, we can quickly find the solutions to noise problems by analyzing the characteristics of the noise transmission path. In the performance optimization, the performance of the engine can be met by CFD simulation. Finally, by the test, CAE technology has enough accuracy to meet the requirements of developing intake system.

**Keywords** Intake · Optimization · CAE

## 1 Introduction

The intake system of engine is one of the important sources of automobile noise. To reduce the noise of intake system has become an important measure for automobile noise reduction, and to develop low noise low back pressure intake system has also become one of the critical technologies. This paper raises a method for development of low noise low back pressure intake system, in which a model of complete intake noise transmission route is established, the transmission function of this transmission route is analyzed in an attempt to find out the weak point of intake noise on the transmission route and to propose effective noise

---

F2012-E03-006

---

Y. C. Chen (✉) · H. Shi · Y. Guang  
Brilliance Automobile Engineering Research Institute Engine General Technique Section,  
110141 Shenyang, People's Republic China

improvement measures against the weak point; meanwhile, comparative analysis on the schemes before and after the optimization is made by using CFD simulation technology so that the engine performance requirements are satisfied. Because this method does not need to collect the characteristics of engine intake noise source, the entire optimization process is especially fast by virtue of CAE technology.

## 2 Method for Analysis of Intake Noise Transmission Route Characteristics

In intake noise, impulsive noise covers the main composition, which is formed by the pressure fluctuation produced in the cyclic opening and closing of the intake valve [1]. It mainly affects the characteristics of low frequency noise of intake system, and it is closely related to the structural characteristics of intake system. Whether it is a borrowed engine or an independently developed engine, to improve impulsive noise from the noise sources shall have higher costs. Therefore, the main method for reduction of impulsive noise shall be realized by means of optimizing the structure of intake system, which requires analysis of intake noise transmission route characteristics.

### 2.1 Evaluation Indices of and Calculation Method for Intake Noise Transmission Route

The performance evaluation indices of acoustic transmission system are mainly composed of insertion loss, noise reduction amount and transmission loss. Transmission loss describes inherent characteristics of acoustic system, which has nothing to do with the sound source in the sound proofing system, therefore, it is usually used as the main basis for evaluation of acoustic system performance analysis calculation and structural design [2]. This paper also uses transmission loss as the evaluation index of intake system noise transmission route. Transmission loss is defined as the ratio of incoming sound power to transmitting sound power:

$$TL = 10 \log_{10}(W_i/W_t) \quad (1)$$

where:  $W_i$  is incoming sound power and  $W_t$  is transmitting sound power.

In one-directional dynamics simulation software GT-POWER, there is a standard module AcoustTransloss, which is specially used to calculate transmission loss. The module calculates transmission loss by processing 4 groups of pressure signals collected from 4 microphones. With this method, the pressure fluctuation signal on each measuring point is divided into forward incoming wave and backward reflected wave, according to the fluctuation equation of sound wave

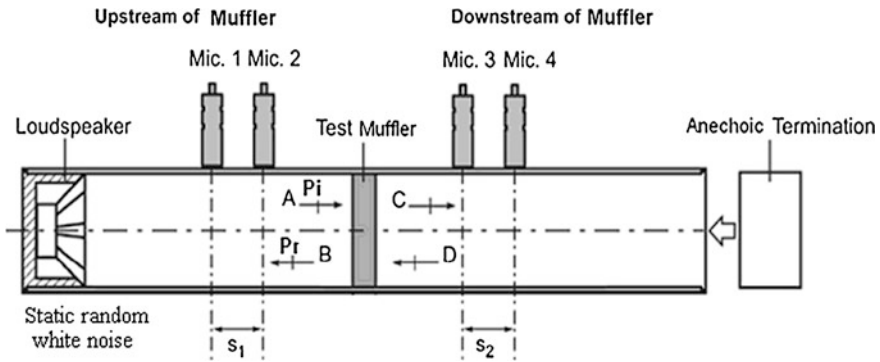


Fig. 1 Principle of transmission loss calculation

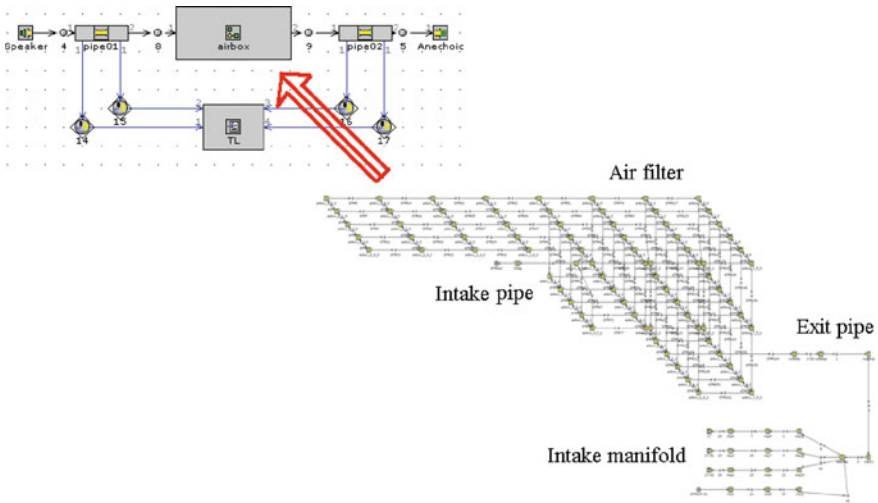
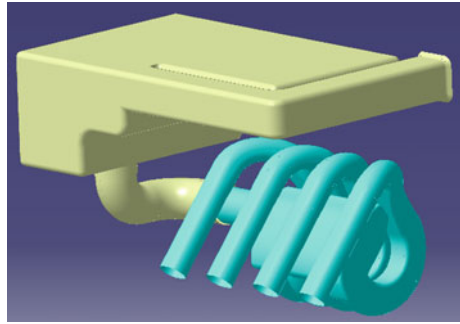
transmission, both the waves are decomposed on two positions of the system respectively: one is in the upstream of the muffler while the other is in the downstream of the muffler. Thus, the upstream incoming sound and the downstream transmitting sound are solved, then the sound power level difference is obtained according to the self-correlation and cross-correlation spectrums [3]. See Fig. 1 for principle of the calculation.

## 2.2 Calculation of Intake Noise Transmission Route Characteristics

Impulsive noise is formed by cyclic opening and closing of the intake valve, therefore, the transmission route of impulsive noise is the whole intake system including intake manifold. For analysis of impulsive noise transmission route characteristics, this chapter establishes the whole intake system (Fig. 2) including intake manifold. First of all, the geometric structure of the intake system is dispersed in GT-GME3D, and an acoustic calculation model (Fig. 3) of transmission loss is set up in GT-POWER. The calculation result of transmission loss of the whole intake system is shown in Fig. 4. It is obtained preliminarily from the calculation results that the muffling effect of frequency channel below 150 Hz is not idealistic, which may also be verified in the test results of real automobile.

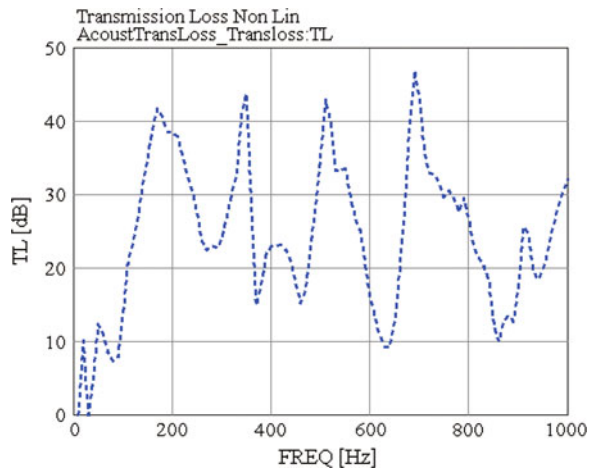
In order to verify the calculation accuracy of one-dimensional software GT-power, transmission loss of the whole intake system has been calculated by using a 3-D acoustic software. Shown in Fig. 5 is the finite element model of the original intake system. The comparison between the calculation results of this software and GT-power is shown in Fig. 6. It can be seen from the calculation results that the calculation accuracy of GT-power and the 3-D acoustic software are identical below 500 Hz, which can meet the requirements for intake noise optimization. However, the difference is greater in higher frequency channels,

**Fig. 2** Original intake system including manifold

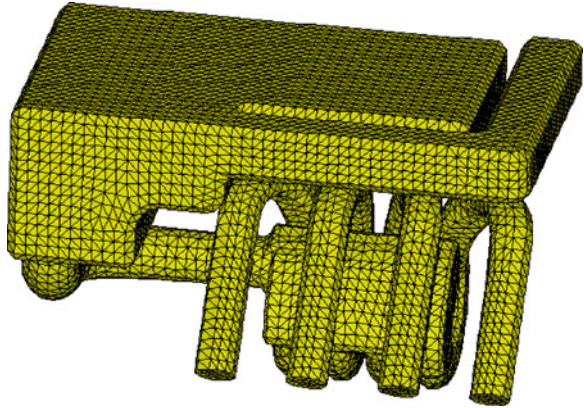


**Fig. 3** Calculation model of original intake system

**Fig. 4** Transmission loss of original intake system



**Fig. 5** Finite element model of original intake system



which is due to the higher harmonics in such frequency channels, therefore, the one-dimensional plane wave theory is no longer applicable.

Furthermore, this paper has made a comparative analysis of the transmission loss of the whole intake system by using intake port exits of different cylinders as noise exits (see Fig. 7). It may be seen from Fig. 7 that the transmission losses of the entire sound field are basically the same when intake port exits of different cylinders are used as noise exits. Therefore, the intake port exit of any cylinder may be used as the noise inlet for analysis of the property of the entire sound field.

### 3 Optimization of Intake System Noise

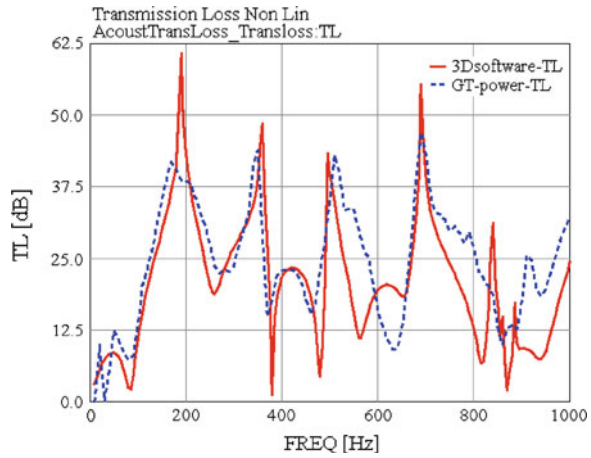
#### 3.1 Noise Problems Existing in Original Intake System

In order to analyze the noise problems existing in the original intake system accurately, Head testing equipment is used to test the noise at the intake port of the original scheme in full acceleration working condition. The test results are shown in Fig. 8. It can be seen from Fig. 8 that the gross noise pressure of intake noise is excessively high and the linearity is not high, moreover, multiple peak values exist in each stage of noise, causing serious resonance in the cab. See Table 1 for the rotating speed and frequency corresponding to each stage of peak value.

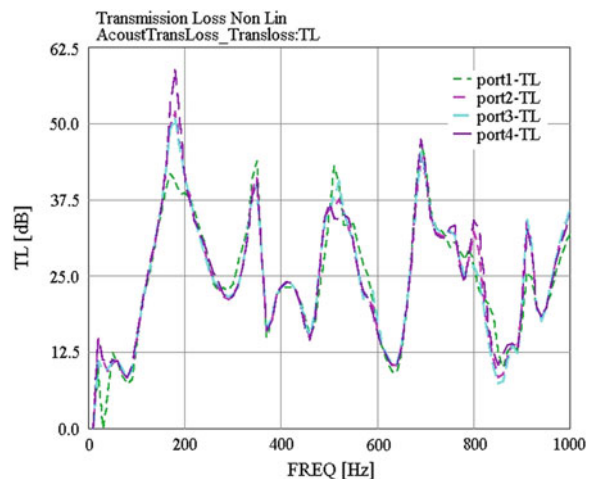
#### 3.2 Measures for Noise Improvement of Intake System

In Table 1, the peak value of Stage 4 noise at 2,150 rpm causes serious resonance in the cab, and it is within the common rpm range, therefore it is the problem to be optimized first. As for the noise peak value at 142 HZ, since the frequency is

**Fig. 6** Comparison between transmission loss calculation results by GT-power and 3D software



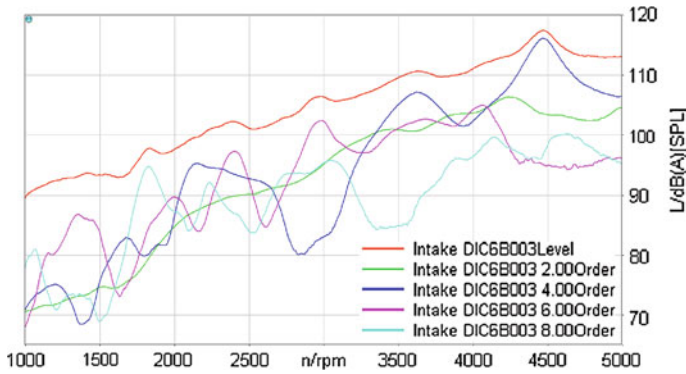
**Fig. 7** Comparison between sound field transmission losses at different noise inlets



relatively low, and the arrangement space to add resonance unit is limited, so it must be resolved by means of optimizing the air filter. Air filter is the most important muffling unit in the intake system.

In order to increase the muffling effect of the air filter, it must be started from two aspects: increasing the volume of the air filter and optimizing its internal structure. Similarly, due to the restriction of the arrangement space, it is impossible to increase the volume of the original intake system any more, therefore, the noise at this frequency can only be eliminated by optimizing the internal structure. Aiming at this problem, the internal structure is optimized in two aspects. One is to divide the original air filter into two cavities, and the other is to increase the length of the internal inserted pipe. See Fig. 9 for optimization plan of air filter.

The test result of intake port noise of the optimized structure is shown by the solid line in Fig. 10. It can be seen from the test results that the gross sound level

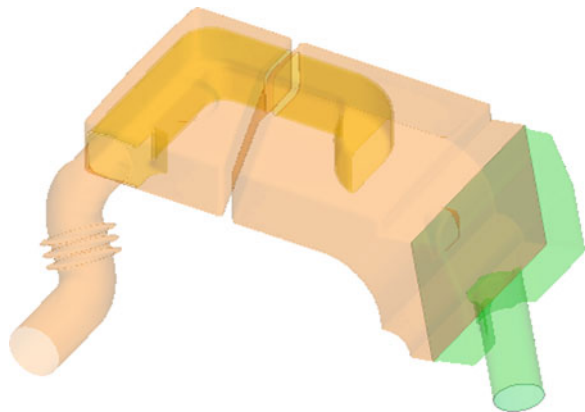


**Fig. 8** Testing curve of noise pressure level at full stage, Stages 2, 4, 6 and 8 of the original intake system

**Table 1** Peak value and frequency of noise at each stage of original intake system

	rpm/hz		rpm/hz		rpm/hz		rpm/hz	
OE 2	4,250	142						
OE 4	2,150	143	3,600	240	4,450	296		
OE 6			2,400	240	3,000	300	4,076	407
OE 8			1,800	240			4,050	407

**Fig. 9** Optimized structure of air filter



meet the target requirements; Stage 2 noise exceeds the target control line at 4,000 rpm and above, but it has no influence on the sound quality; Stage 4 noise has a peak value at 3,600 rpm; the sound pressure levels of Stages 6 and 8 are below the target control line.

In the next step, the peak value at 3,600 rpm of Stage 4 noise is optimized. For this purpose, a one-fourth wave length tube is designed and arranged on the exit pipe. It can be seen from the dotted line of the test results in Fig. 10 that the peak

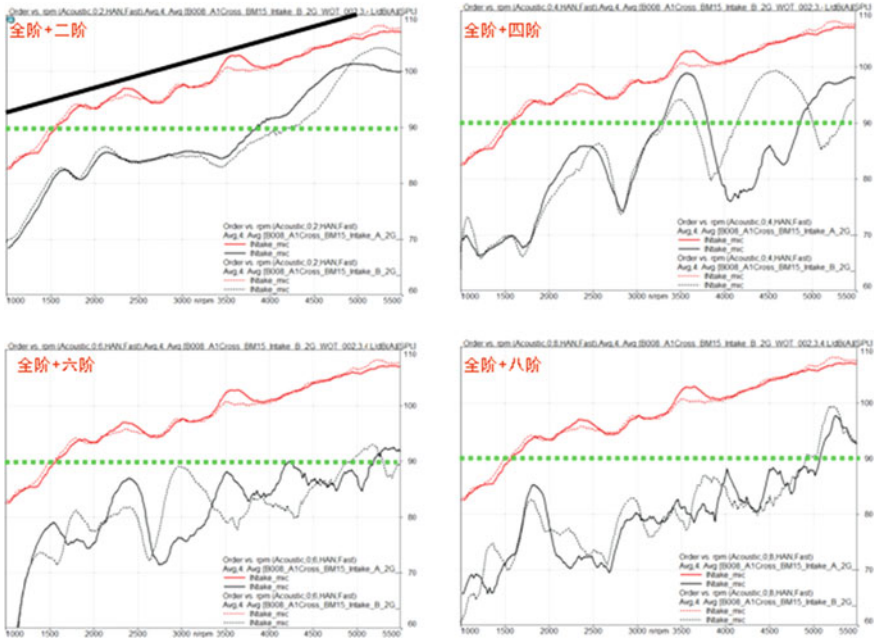
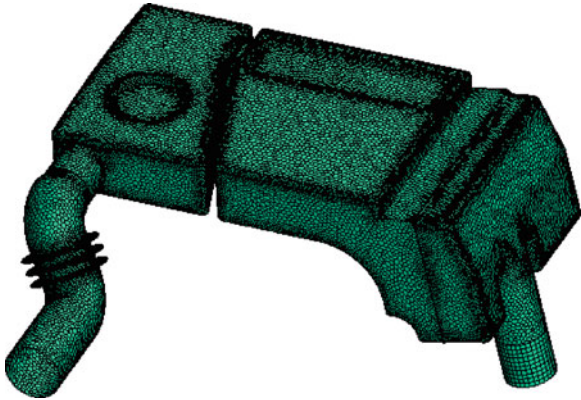


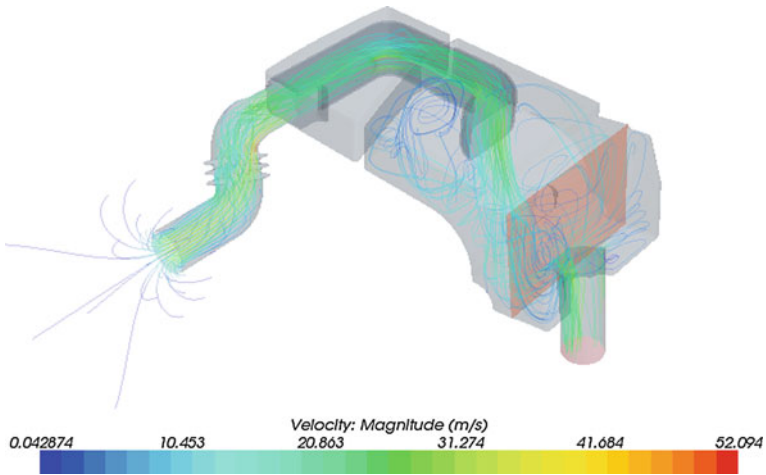
Fig. 10 Test results of noise at intake port of optimized structure

Fig. 11 Grid model of new air filter



value at 3,600 rpm of Stage 4 is reduced a bit, though it is not below the control target line, it has no influence on the interior noise when it is evaluated from a subjective angle, therefore, no further optimization is done for this problems. The optimization of the noise in the intake system has been completed.



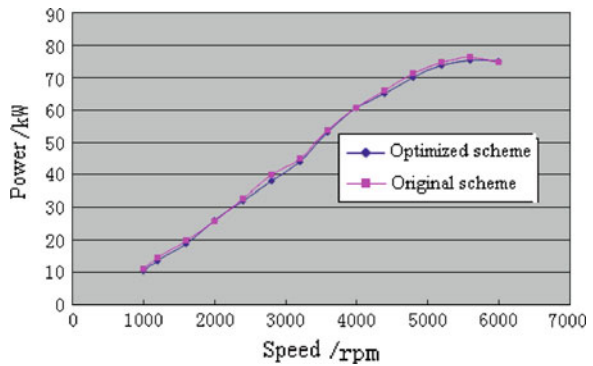


**Fig. 12** Velocity flow field trace inside the new air filter

**Table 2** Comparison between pressure losses of two air filter schemes

	Original scheme	Optimized scheme
Pressure loss(pa)	1,413	1,641

**Fig. 13** Comparison between engine powers in schemes with two types of air filters



### 4 Analysis and Verification of Intake System Performance

Since the internal structure of air filter has great changes when compared with the original scheme, in order not to affect the engine performance, a CFD comparative analysis has been made between the original scheme and the new one. CFD simulation analysis uses star-ccm+ software. Shown in Fig. 11 is the grid model used for CFD analysis. A  $k-\epsilon$  turbulence flow model is used as calculation model,

which is stable and compressible; Filter paper is processed as porous baffle, and the values of two resistance coefficients  $\alpha$  and  $\beta$  are determined on the basis of the test data; Intake port condition is set to atmospheric environment; Exit condition is set to gas flow rate; The wall surfaces beyond tension layers are processed as non-slip wall surface. Shown in Fig. 12 is the velocity flow field trace inside the new air filter. Through CFD analysis results, it may be concluded that the pressure losses of both the structures are not big (see Table 2). Based on the rack test data in Fig. 13 it is also verified that the optimization scheme has the influence on the engine power loss which is equivalent to the original scheme.

## 5 Conclusion

1. By analyzing the characteristics of entire transmission route of intake noise, the source of the problems may be found quickly and then effective improvement measures may be presented;
2. GT-POWER software has sufficient accuracy to meet the requirements for optimization of intake system noise, meanwhile, since it is a one-dimensional software, the grid processing is easy and the calculation is fast, so it may realize quick optimization of intake system noise;
3. With CFD simulation analysis, the design plan may be verified for the influence on engine performance so as to ensure that engine performance requirements are satisfied;
4. Through verification of final actual test results, it indicates that CAE technology has a higher precision to meet the design requirements for performance and noise of the intake system.

## References

1. Yuechang C (2010) Optimization of engine intake system noise. Auto Manuf Ind, Beijing 2010
2. Jian P, Gang Z, Hua H (2003) Automobile noise and vibration. Beijing Institute of Technology Press, Beijing
3. Gamma Technologies, Inc. (2006) GT-Power USERS MANUAL. Gamma Technologies

# Study on Vehicle Modeling and Steering Performance

Minglun Cao and Cai Yang

**Abstract** More attention is played on the variation of steering wheel torque while studying on steering performance, therefore, steering system has decisive influence to analysis accuracy, and it is necessary to establish precise model to present the characteristics-stiffness, friction and damping- of the steering system. Several factors have significant contribution on the steering torque, such as friction (viscous and dry friction), assistance effect and so on. This paper presents the method of modeling hydraulic powering steering system (HPS) and vehicle in AMESim<sup>®</sup> software, and a new method is used for calculating the crossed area of steering valve in order to get the actual assistance effect. A vehicle dynamic model including this complete steering model is developed for studying of steering performance, and several different experimental test results are confirmed for the validity of the vehicle model.

**Keywords** HPS · Steering wheel torque · Vehicle model · Simulation · Steering performance

## 1 Introduction

There were many researches on vehicle handling and stability [1–4], and different complexity (degree-of-freedom) of vehicle models with simplified steering system model were developed. All of these models were fairly good representation of the

---

F2012-E03-009

---

M. Cao (✉) · C. Yang  
Changan Auto Global R&D Center, 401120 Chongqing, China

vehicle roll and handling behavior in most cases, but little of these were concerned on the variation of steering wheel torque. Some researches manifested that friction, freeplay and hydraulic circuit have significant influence on the dynamics of HPS [4–6]. So it is important to model the complex and non-linear properties of steering system for steering performance.

In this paper, the vehicle model is established in AMESim<sup>®</sup> software, which includes more complex steering system as well as the kinematics and compliance of suspension and steering system. The friction and hydraulic circuit of hydraulic powering steering system are considered, and a new method is used for calculation of crossed area of the steering valve in order to get the actual assistance effect. Validation of the vehicle model with the experiments of dynamic steer maneuvers at different velocity are presented, the simulations indicate a close agreement in the results.

## 2 Steering System Model

### 2.1 Hydraulic Powering Steering System

Vehicle steering performance depends highly on steering system, which provides an accurate feedback about how the vehicle reacts to the road. So the precisely modeling of hydraulic powering steering (HPS) system is the key step to study vehicle steering performance. A schematic of a hydraulic powering steering system is shown in Fig. 1, the model may be separated into two parts: mechanical part and hydraulic circuit.

#### 2.1.1 Mechanical Part

Steering wheel has a moment of inertia when the torque input is exerted on, there are also viscosity and dry friction between steering column and housing. Generally, the stiffness of steering column is much greater than that of torsion bar, therefore it can be ignored, but is kept in this case. At the same time, the total inertia of intermediate shaft, input shaft and pinion of steering gear must be considered for connection rule, though which is relative small, and there is also the friction between input shaft, pinion and housing. The rack and pinion steering gear is treated as a linear converter between rotation and linear motion, and the relationship is listed in Eq. (1).

$$F_r = \frac{T_p}{R_p}, \theta_p = \frac{x_r}{R_p}, \dot{\theta}_p = \frac{\dot{x}_r}{R_p} \quad (1)$$

where,  $F_r$  is rack force,  $T_p$  is pinion torque,  $\theta_p$  is pinion angular displacement,  $x_r$  is rack displacement,  $R_p$  is equivalent radius, equal to the inverse of gear ratio.

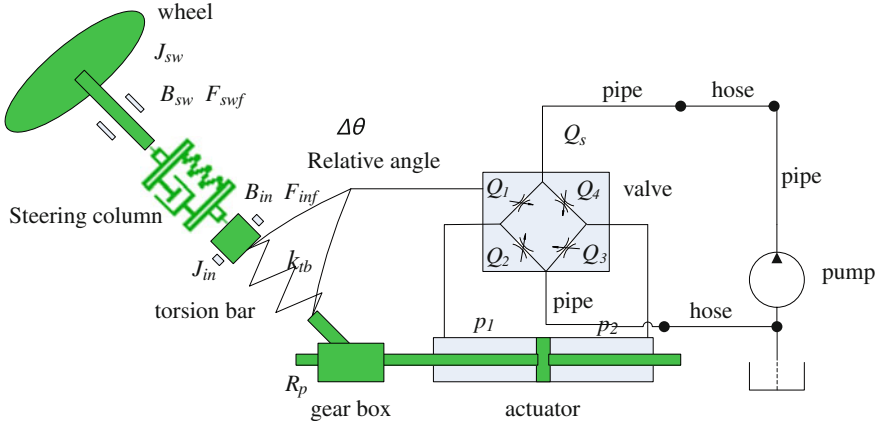


Fig. 1 HPS model

Within steering gear, stiffness of  $k$ , viscous of  $B$  and dry friction of  $F_f$  between piston/rack and housing of actuator are considered [7]. The motion of rack is modeled in other submodel (chassis submodel), the relationship between rack and steered wheel is represented by kinematics directly, therefore, the friction of kingpin and tie-rod are not considered individually, which must be added to rack motion equation. The model of friction is critical in that it strongly affects the accuracy and stability of the simulation model [8], in this paper coulomb and stiction friction are represented by reset integrator model, as shown in Eq. (2) [9].

$$\begin{cases} F_f = F_{slip} + (F_{stick} - F_{slip})e^{-3\frac{|v|}{astrib}} & x > dx \\ F_f = k_{stick}x + B_{stick}v & x \leq dx \end{cases} \quad (2)$$

where,  $F_{slip}$  is sliding friction (coulomb friction),  $F_{stick}$  is stiction friction,  $astrib$  is Stribeck constant,  $k_{stick}$  is stick stiffness,  $B_{stick}$  is damping coefficient, and  $dx$  is displacement threshold.

Then the parameters of  $F_{slip}$ ,  $F_{stick}$ ,  $k_{stick}$ ,  $B_{stick}$ ,  $k$  and  $B$  of steering gear must be identified by a specific test.

### 2.1.2 Hydraulic Circuit

Hydraulic circuit is used for providing appropriate assistance force according steering wheel torque, which is detected by relative twist of the torsion bar. Pump, pressure pipe and hose, return pipe and hose, steering valve and actuator are modeled. The flow rate of the pump is represented by table with the function of pressure and rotational speed, which comes from test results, but the fluctuation of flow rate is neglected. A lumped parameter model with fluid capacitance  $C$ , fluid resistance  $R$  and fluid inductance  $I$  is applied for Pipe and hose [6], and for the

elasticity of hose, the equivalent bulk modulus is used, but the process of expansion and contract is neglected.

As to steering valve, it is important to model its profile of control edge because it determined the shape of assistance curve, but for some tiny geometry, such as clearance, edge, it is difficult to accurately build the mathematic equation to represent the relationship between crossed area and relative twist angle of torsion bar, also which is not easy to be measured from test. Therefore, a new method is used for calculation of crossed area, which calculates it from tested data of assistance curve. At first, some assumptions are defined that the calculation will be based upon.

1. The test process of assistance curve is treated as static.
2. The steering valve is symmetrical, and the crossed area is increasing linearly with opening when it varies from central position to the max.
3. The pressure lose in pipe and hose is neglected.
4. The flow rate of relief valve is varying linearly with pressure.

So the equilibrium equations are get as listed in Eq. (3), and the relationship of crossed area versus relative twist angle from central position to the min will to be determined.

$$\begin{aligned}
 \Delta\theta &= \frac{T_w - T_f}{K_t} \\
 Q_1 - Q_2 &= 0 \\
 Q_4 - Q_3 &= 0 \\
 Q_s &= Q_1 + Q_4 = \begin{cases} Q_p & (p_s < p_{crack}) \\ k_{ps}(p_{Q=0} - p_s) & (p_s \geq p_{crack}) \end{cases} \\
 Q_i &= C_d A_i \sqrt{\frac{2}{\rho}} \Delta p \quad i = 1, 2, 3, 4
 \end{aligned} \tag{3}$$

where,  $\Delta\theta$  is relative twist angle of torsion bar,  $T_w$  is torque input,  $T_f$  is friction torque,  $K_t$  is stiffness of torsion bar,  $Q_i$  is flow rate of each orifice,  $Q_s$  is system flow rate which flow into steering valve,  $Q_p$  is flow rate of pump,  $p_{crack}$  is opening pressure of relief valve,  $p_s$  is inlet pressure of steering valve,  $k_{ps}$  is slop of flow versus pressure of relief valve,  $p_{Q=0}$  is the pressure when input flow rate is zero,  $\rho$  is the fluid density, and  $C_d$  is the flow coefficient.

Then the equilibrium equations in Eq. (3) are solved and the relationship between crossed area and relative twist angle of torsion bar is obtained as shown in Fig. 2.

### 3 Assistance Curve

The model with test conditions is developed to get the assistance curve as shown in Fig. 3. Then the comparison of simulation and test results is shown in Fig. 4, it can be seen from this figure that the model does a very good job of providing assistance characteristic (left half axis).

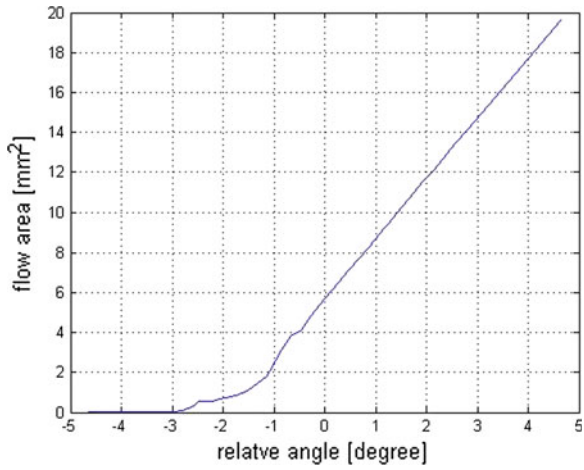


Fig. 2 Calculated crossed area of steering valve

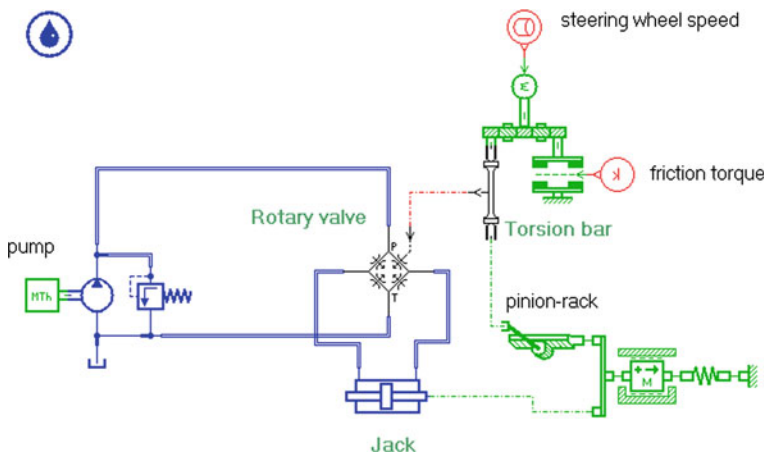


Fig. 3 AMESim model for assistance curve

## 4 AMESim Model

### 4.1 HPS Model

As shown in Fig. 5, the model of hydraulic steering system is developed in AMESim<sup>®</sup> software, as one of the submodels of vehicle dynamic model.

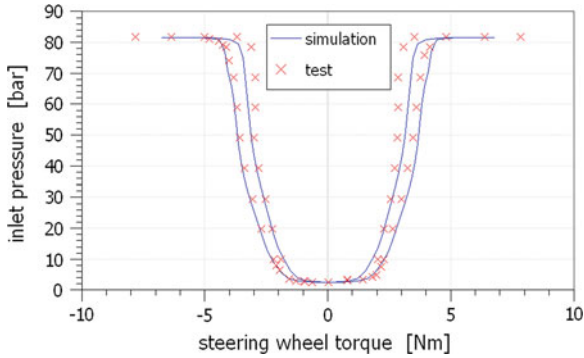


Fig. 4 Assistance curve

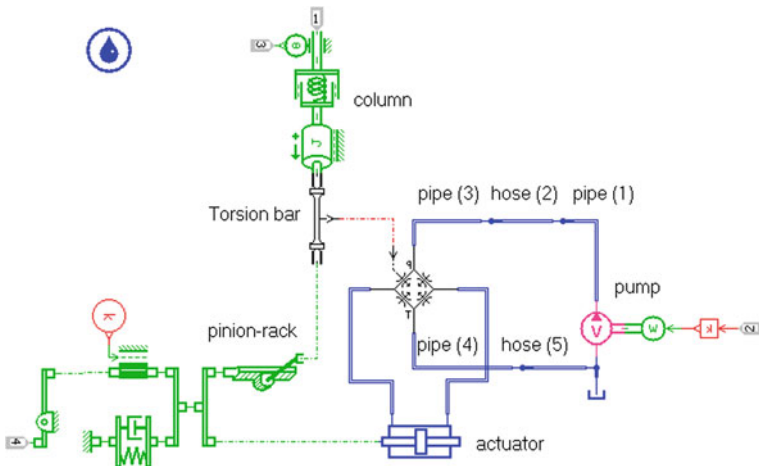


Fig. 5 AMESim model for steering system

### 4.2 Vehicle Dynamic Model

In order to develop vehicle dynamic model, the suspension, tire and chassis submodels must be added, thanks to AMESim<sup>®</sup> software, these models have been pre-defined, and which are suitable for this study, therefore, the only leave work are correctly choosing and connecting each submodels [8], as shown in Fig. 6.

Chassis submodel has 15 degree-of-freedom, which consists of three linear and three angular degree-of-freedom at the gravity center (CG) of sprung mass, four vertical suspension travel and four wheel spin degree-of-freedom at each wheel, and one degree-of-freedom of relative motion between steering rack and vehicle body. Suspension within linear damper, stiffness of limitation bar and anti-roll bar are modeled, the kinematics and compliances of the suspension and steering



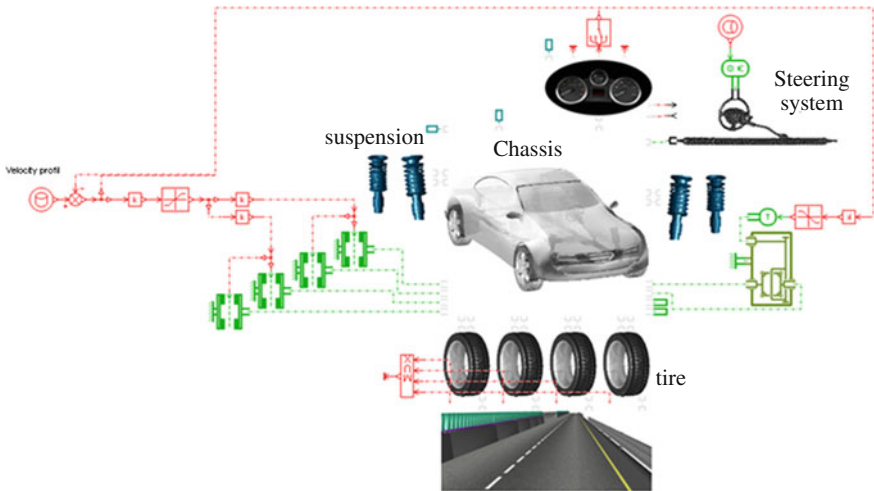


Fig. 6 Vehicle dynamic model

systems are also input. The magic formula tire model together with first order transient properties tire model are used. What's more, traction subsystem and brake subsystem are simplified to keep the anticipant velocity input, and aerodynamic forces and torques are neglected.

## 5 Simulation Results

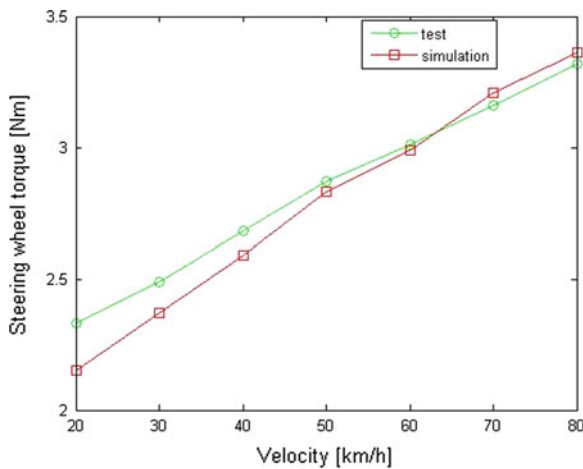
Once the vehicle model has been implemented, validation is conducted to show how well the model predict vehicle response in comparison to actual vehicle data. The overall parameters of a car used in this model are shown in [Appendix A](#), and others may be obtained from tests, such as K&C rig test. The actual vehicle tests include dynamic steer maneuvers at different velocity are used for validation of the vehicle model that simulates on a smooth road. The simulations use the actual measured steering wheel angle and vehicle speed from the test vehicle.

In dynamic steer maneuvers, the steering wheel angle is input as sinusoid-like with frequency is about 0.5 Hz and amplitude is about 35°. [Table 1](#) and [Fig. 7](#) show the steering wheel torque at left max steering wheel angle during dynamic steer at the velocity from 20 to 80 km/h. As these results show that the simulations are a little less than test data at low velocity, but however, this vehicle model do a good job of predicting the steering wheel torque.

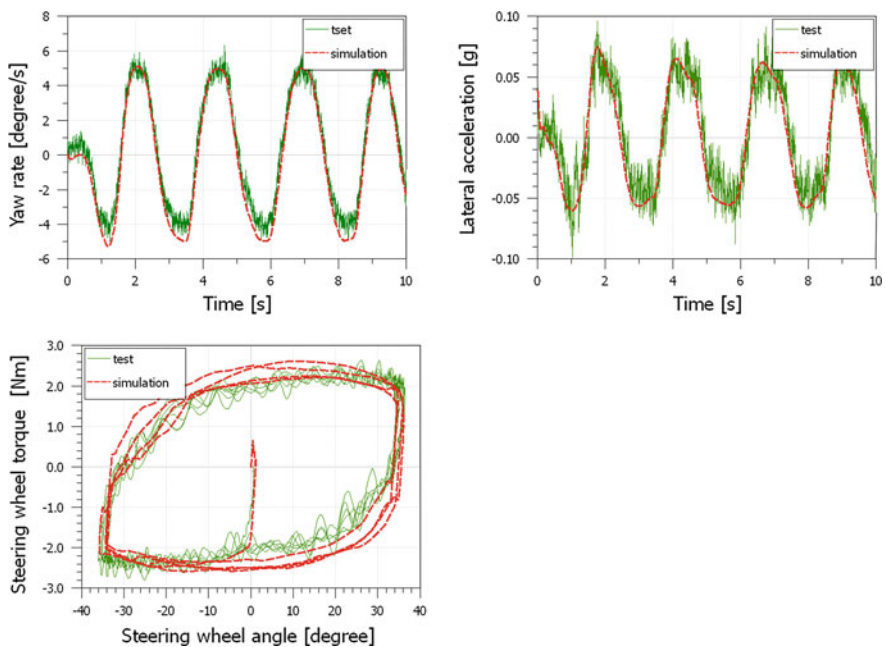
[Figures 8, 9 and 10](#) show the relationship of yaw rate, lateral acceleration, roll angle versus time and steering wheel torque versus steering wheel angel during dynamic steer at 20, 50 and 70 km/h. As can be seen from these figures, the simulation results are similar to the actual vehicle data. At each velocity, the

**Table 1** Steering torque at different speed

Speed (Km/h)		20	30	40	50	60	70	80
Steering wheel torque (Nm)	Test	2.33	2.49	2.68	2.87	3.01	3.16	3.32
	Simulation	2.15	2.37	2.59	2.83	3.01	3.21	3.36



**Fig. 7** Steering wheel torque at different velocity



**Fig. 8** Vehicle response at 20 km/h

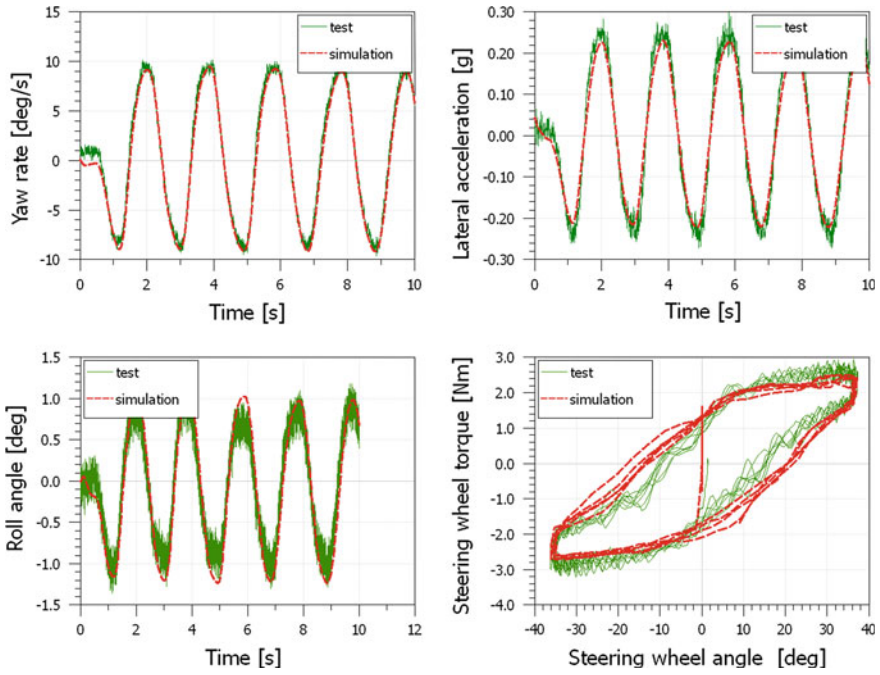


Fig. 9 Vehicle response at 50 km/h

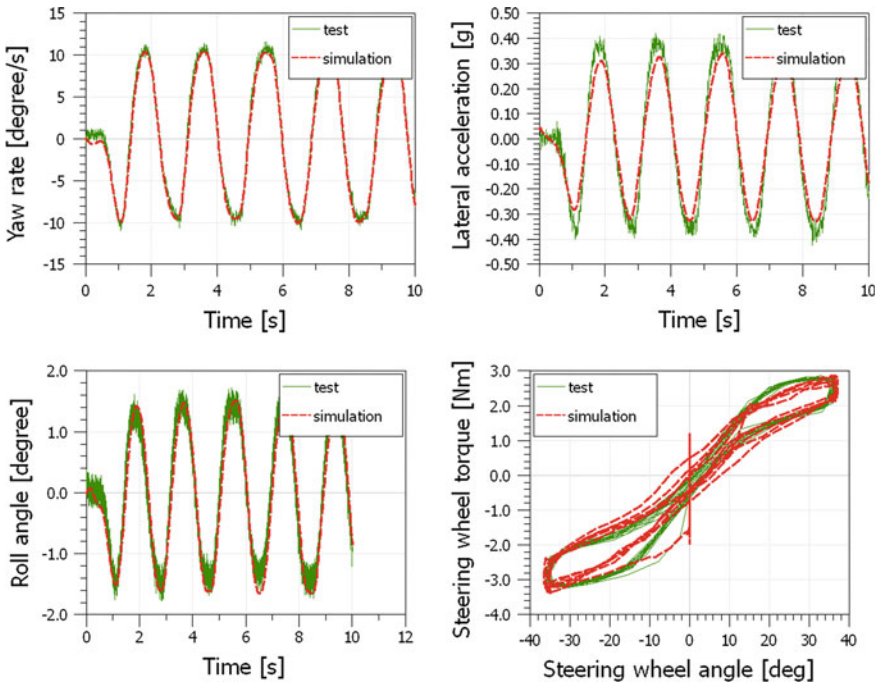


Fig. 10 Vehicle response at 70 km/h

simulation of the steering wheel torque versus steering wheel angel relationship is a little different from test data at some period of time, this is because some motions are also simplified in steering system, for example, the transfer characteristics of rack and pinion steering gear is neglected [10], in addition, the friction model and tire aligning torque may have not sufficient precision in dynamic response.

## 6 Conclusion

For more attention on variation of steering wheel torque in vehicle steering response, the more complete hydraulic powering steering system model has been established, and a new method has been applied for calculation of crossed area of steering valve. As can be seen from the validation, the vehicle model within this complete steering model, not only the yaw rate, lateral acceleration, but also the steering wheel torque, have excellent agreement with the actual test data. So the developed analytical method in this paper could assist the design and analysis of steering performance.

## Appendix A: Vehicle Parameters

Name	Value	Unit
Total vehicle mass	1,134	kg
Wheelbase	2,375	mm
Front track width	1,410	mm
Rear track width	1,417	mm
X distance between CG of sprung mass and front axis	993	mm
Height of CG of sprung mass	615	mm
Front suspension rate	25,500	N/m
Rear suspension rate	19,000	N/m
Tire vertical rate	2,04,000	N/m
Tire free radius	287	mm

## References

1. Wade Allen R, Myers TT, Rosemthal TJ, Klyde DH (2000) The effect of tire characteristics on vehicle handling and stability. SAE, 2000-01-0698
2. Demerly JD, Youcef-Toumi K (2000) Non-linear analysis of vehicle dynamics (NAVDyn): a reduced order model for vehicle handling analysis. SAE, 2000-01-1621

3. Ghike C, Shim T (2006) 14 Degree-of-freedom vehicle model for roll dynamics study. SAE, 2006-01-1277
4. Miao W, Nong Z, Misra A (2005) Sensitivity of key parameters to dynamics of hydraulic power steering system. SAE, 2005-01-2389
5. Zbigniew L, Dariusz Z (2002) Vehicle dynamics simulation with inclusion of freeplay and dry friction in steering system. SAE, 2002-01-0619
6. Wonho K, Chang-Seob S, Ji-Yeol K ( ) Modeing of a hydraulic power steering system and its application to steering damper development. SAE, 2005-01-1263
7. Diglio P, Falbo G, Bai J, Gu J (2009) A test-based procedure for the identification of rack and pinion steering system parameters for use in CAE ride-comfort simulations. SAE, 2009-01-2090
8. Pfeffer PE, Johnston DN, Sokola M, Harrer M (2005) Energy consumption of electro-hydraulic steering systems. SAE, 2005-01-1262
9. AMESim demo help (2010) version 10.1.0, LMS imagine SA
10. Kamble N, Saha SK (2005) Evaluation of torque characteristics of rack and pinion steering gear using ADAMS model. SAE, 2005-01-1064

# Surrogate Model for Aerodynamic and Handling Stability Optimization of a Tractor-Trailer in Crosswinds

Xu Gong, Zhengqi Gu, Jian Ye, Xu Yan and Zhiming Zhao

**Abstract** A surrogate model based aerodynamic shape optimization method applied to the wind deflector of a tractor-trailer in crosswind is presented in this paper. The aerodynamic drag coefficient and handling stability of the tractor-trailer subjected to crosswinds is analyzed. The numerical results show that the wind deflector can influence drag coefficient and the lateral displacement of the tractor-trailer in crosswinds in great degree. Four parameters are used to describe the wind deflector geometry: Width, Length, Height and Angle. A 30-level design of experiments (DOE) study using the optimal Latin hypercube method is conducted to analyze the sensitivity of the design variables and build a database to set up the surrogate model. The surrogate model is constructed based on the Kriging interpolation technique. The fitting precision of the surrogate model is examined using a computational fluid dynamics (CFD) and multi-body dynamics and certified using a surrogate model simulation. Finally, multi-island genetic algorithm is used to optimize the shape of the wind deflector based on the surrogate model. The maximum tolerance between the results of the CFD and multi-body dynamics simulation and the surrogate model is only 2.02 %. When using the optimal design variables, the aerodynamics drag coefficient decreases maximum by 6.23 % and the lateral displacement decreases maximum by 4.67 %.

---

F2012-E03-010

---

X. Gong (✉) · J. Ye · X. Yan · Z. Zhao  
Changan Auto Global R&D Center, Chongqing, China

X. Gong · Z. Gu  
State Key Laboratory of Advanced Design and Manufacture for Vehicle Body, Hunan University, Changsha, China

Z. Gu  
Hunan University of Technology, Zhuzhou, China

**Keywords** Multidisciplinary optimization · Vehicle aerodynamics · Multi-body dynamics · Crosswind

## 1 Introduction

Fuel economy, handling stability and driving safety would be significantly influenced when the vehicle is subjected to crosswind. In extreme case, crosswind would cause the vehicle deviate from the normal driving direction or even rollover, side slip, etc., triggering serious security problems. Reducing aerodynamic drag is crucial for improving fuel efficiency and changing aerodynamic forces and moments are crucial for improving handling stability and driving safety. For a tractor-trailer, additional equipment can help to decrease aerodynamic drag and improve aerodynamic characteristics. Improved aerodynamic characteristics can influence handling stability and driving safety. Tsutomu Fujimoto studied air deflector shape of truck and analyzed aerodynamic characteristics for different yaw angles to obtain excellent air deflector shape [1], [2]. In the Guide of Truck Aerodynamic Styling (Good Practice Guide 308), an advanced and widely applied good practice in energy efficiency of truck is provided, including cab side edge turning vanes, air dams, tractor/trailer side panels, low drag mirrors, trailer roof tapering, and so on [3]. Therefore, this paper studies shape optimization of wind deflector of tractor-trailer subjected to crosswind which can both improve fuel economy and handling stability both.

For shape optimization, several questions must be addressed. One of these primary questions deals with computational cost. Shape optimization requires a large number of solution evaluations, leading to amazingly large computational cost. For example, using a computer with eight CPUs, a conventional simulation of the automotive external flow field would take 8 h. Therefore, 80,000 h are needed to complete 10,000 optimization calculation iterations, which is impossible for practical applications.

Several techniques are available to reduce computational cost. The key idea is to replace the possible solution process with a simple and computationally inexpensive mathematical model, and to generate inputs for the optimization algorithm. Such a mathematical model is often referred to as the response surface of the system to be optimized, which is the basis for a surrogate model-based optimization methodology. This method has been extensively used in areas such as the aerodynamic shape optimization of the wing airfoil [4–8]. However, most of these optimizations were applied only to simple objects or two-dimensional shapes.

The aim of this paper is to use Kriging method to generate a reliable response surface for the shape optimization of a tractor-trailer wind deflector under crosswind. The use of Kriging method for surrogate model-based optimization with design variables generated by optimal Latin Hypercube method is considered, and the accuracy of the surrogate model is validated by simulations. Based on surrogate model and multi-island genetic algorithm, aerodynamic drag and lateral displacement of tractor-trailer under crosswind are both optimized.

This paper is organized as following. The CFD simulation and wind tunnel test of a tractor-trailer under crosswind are described in Sect. 2. The multi-body dynamics model is built in Sect. 3. The objectives and the process are presented in Sect. 4. The implementation of the optimal Latin Hypercube method, the Kriging method, the multi-island genetic algorithms are detailed in Sect. 5. The results are discussed in Sect. 6.

## 2 Case Setup

### 2.1 Computational Domain and Boundary Conditions

As the main form of road transportation, tractor-trailer vehicle can improve cargo security, thus reducing the unnecessary costs of processing and packaging. In turn, this reduces overall operational costs significantly. However, tractor-trailer vehicle is higher and the large frontal area leads to increased fuel consumption. A suitable wind deflector installed on tractor-trailer can significantly reduce aerodynamic drag. Therefore, the model studied in this paper is a full-scale tractor-trailer. The tractor-trailer is 16,903 mm in length (L), 2,438 mm in width (W), and 3,988 mm in height (H) (Fig. 1). Compares to the real vehicle, loudspeakers, doorknobs, wipers and some other small support parts, such as rearview mirrors, are ignored in the model. Moreover, the complicated structures of the tires, rear axles, and frame are replaced with simple forms.

When a tractor-trailer vehicle moving on road is subjected to crosswind, the yaw angle,  $\beta$ , changes with the vehicle velocity,  $V$ , and the crosswind velocity,  $V_w$  (Fig. 2). For example, with a constant vehicle velocity of 30 m/s and crosswind velocity of 10 m/s, the relative velocity,  $V_r$ , is approximately 31.6 m/s and the yaw angle is  $18.4^\circ$ . For a relative velocity of 30 m/s and  $6^\circ$  yaw angle, the vehicle and crosswind velocities are approximately 29.8 and 3.1 m/s, respectively.

Figure 3 presents the computational domain for the numerical simulation of the tractor-trailer subjected to crosswind. The size of the outer domain and the location of the vehicle are specifically chosen to minimize the boundary influence on the flow and maintain the CFD quality. The width and height of the outer domain are set to be 36,600 mm (15 W) and 20,000 mm (5 H), respectively, whereas the length is set to be 186,000 mm (11 L). The tractor-trailer is placed 50,700 mm (3 L) from the inlet and 12,200 mm (5 W) from the crosswind left side. At the inlet and the left side wall, a uniform flow with velocity  $V$  in the x-direction and  $V_w$  in the y-direction is imposed. The boundary conditions of the inlet and the left side wall are based on the Ref. [9]. The outlet and the right side wall are treated as pressure-out boundaries. Free-slip boundary is imposed on the ceiling, whereas the tractor-trailer body is treated as a no-slip boundary.



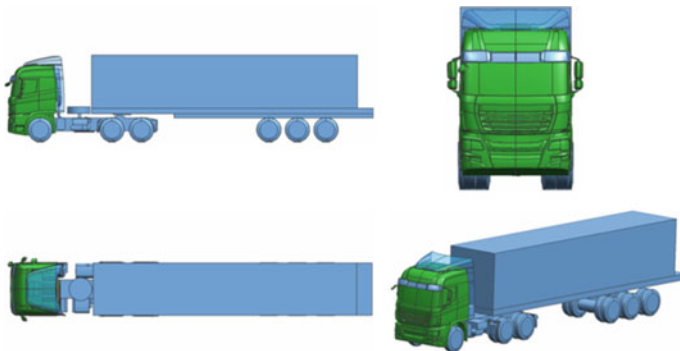


Fig. 1 Tractor-trailer vehicle model

Fig. 2 Velocity relationships

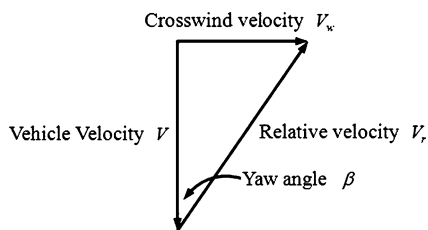
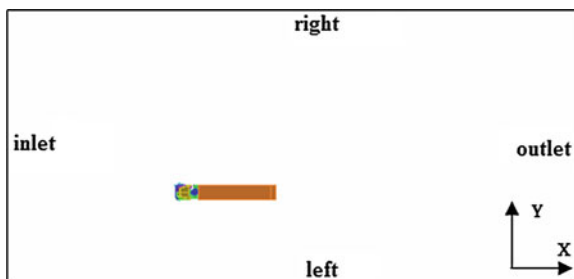


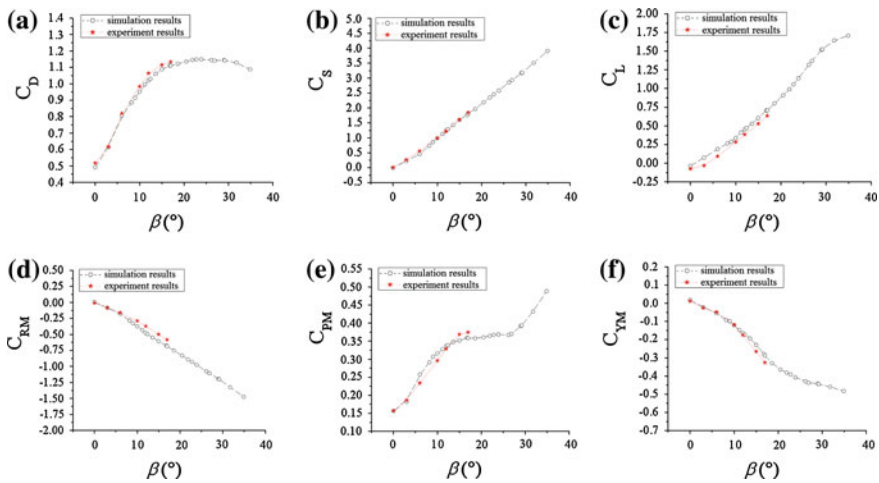
Fig. 3 Computational domain



## 2.2 Analysis

CFD simulations and wind tunnel experiments are used to analyze aerodynamic drag characteristics of the tractor-trailer vehicle under crosswind conditions. The experiments are performed on a 1/6-scale tractor-trailer test model at Hunan University vehicle model wind tunnel. The tractor-trailer model is fixed on a turn-plate, as shown in Fig. 4. Because of the difficulty of testing the tractor-trailer model when subjected to crosswind, the crosswind condition is achieved by rotating the turn-plate of the wind tunnel and changing the yaw angle, where the blockage ratio is 2.75 % when the yaw angle is 0°. Due to the restrictions of the wind tunnel experiment, the rotation range of the yaw angle is set from 0° to 17°.

**Fig. 4** Tractor-trailer experiment model

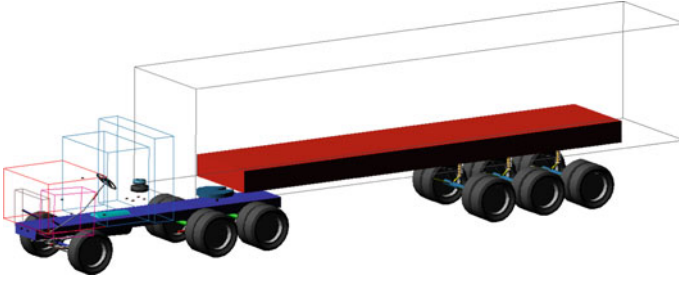


**Fig. 5** Aerodynamic force and moment coefficient contrast

Figure 5 illustrates the CFD simulation and wind tunnel experiment results of aerodynamic force and moment coefficient of the tractor-trailer vehicle at various yaw angles. It is clear that aerodynamic force and moment coefficient change drastically when the tractor-trailer vehicle is subjected to crosswind. As shown in Fig. 5, the CFD results of drag force coefficient  $C_D$ , side force coefficient  $C_S$ , lift coefficient  $C_L$ , roll moment coefficient  $C_{RM}$ , pitch moment coefficient  $C_{PM}$  and yaw moment coefficient  $C_{YM}$  fit well with experiment results. These results show that CFD method is feasible to simulate the tractor-trailer under crosswind.

### 3 Multi-Body Dynamic Analysis

Using ADAMS/CAR software, the multi-body dynamics model of tractor-trailer is built, as shown in Fig. 6. The multi-body dynamics model includes front and rear suspension system of tractor, suspension system of trailer, power-train, steering system, body of tractor and trailer, tires and so on.



**Fig. 6** Multi-body dynamics model of tractor-trailer

The handling stability analysis of tractor-trailer travels at straight road under crosswind is as following. The change of aerodynamic forces and moments includes tractor-trailer travel under no crosswind, tractor-trailer travels under crosswind and tractor-trailer travels under no crosswind again. The change of aerodynamic forces and moments can be simulated by a step function on the ADAMS/CAR software.

$$F_i = \text{step}(\text{time}, x_1, y_{i1}, x_2, y_{i2}) + \text{step}(\text{time}, x_3, y_{i3}, x_4, y_{i4}) + \text{step}(\text{time}, x_5, y_{i5}, x_6, y_{i6}) \quad (1)$$

$$M_j = \text{step}(\text{time}, x_1, y_{j1}, x_2, y_{j2}) + \text{step}(\text{time}, x_3, y_{j3}, x_4, y_{j4}) + \text{step}(\text{time}, x_5, y_{j5}, x_6, y_{j6}) \quad (2)$$

where,  $i = D, S, L$ ,  $F_i$  are the aerodynamic forces, drag force  $F_D$ , side force  $F_S$  and lift force  $F_L$ , respectively.  $j = R, P, Y$ ,  $M_j$  are the aerodynamic moments, roll moment  $M_R$ , pitch moment  $M_P$  and yaw moment  $M_Y$ , respectively. The *step* function is a function that changes with time.  $x_1, x_3$  and  $x_5$  are the time at start,  $y_{i1}, y_{i3}, y_{i5}, y_{j1}, y_{j3}$  and  $y_{j5}$  are the function values at start,  $x_2, x_4$  and  $x_6$  are the time at end,  $y_{i2}, y_{i4}, y_{i6}, y_{j2}, y_{j4}$  and  $y_{j6}$  are the function values at end.

The lateral displacements of tractor-trailer under different crosswind condition are shown on Fig. 7. The velocity of tractor-trailer is 80, 90, 100 and 110 km/h respectively. Based on the Beaufort scale, the crosswind is gentle breeze (three level), moderate breeze (four level), fresh breeze (five level), strong breeze (six level) and moderate gale (seven level), respectively. The velocity of crosswind is 4.4, 6.7, 9.9, 12.8 and 15.8 m/s, respectively.

The width of tractor-trailer is about 2,440 mm, and the width of vehicle lane is 3,500 mm. If the lateral displacement of the tractor-trailer is more than 500 mm, the tractor-trailer would travel to the other lane and cause crash or rear collision. It is dangerous to the driving safety. As shown in Fig. 7, when under moderate gale, the lateral displacement value would exceed safety range at a running speed of 80 km/h; when under strong breeze, the running speed must be less than 100 km/h.

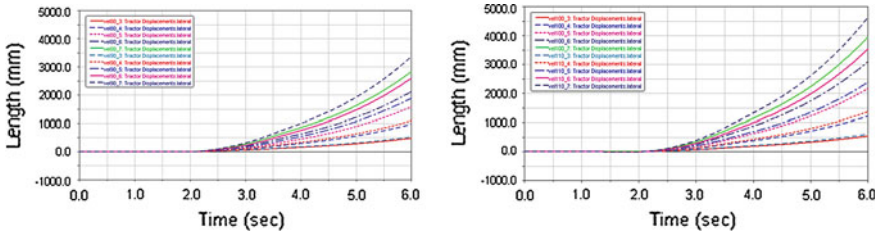


Fig. 7 Curve of the tractor’s lateral offset value versus time at the different speed

### 4 Objectives and Optimization Process

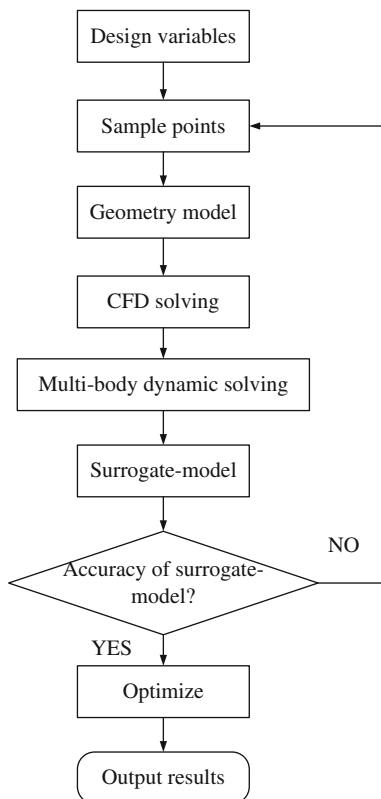
Aerodynamic characteristics is an important factor for fuel economy and driving safety. A suitable wind deflector installed on a tractor-trailer would greatly change the aerodynamic characteristics. Therefore, the main objective of this paper is to set up an optimization strategy for seeking suitable wind deflector shapes. The integrated process for aerodynamic optimization of wind deflector is illustrated in Fig. 8.

In the process, firstly, parameters’ initialization of Width, Length, Height, and Angle, which characterize the shape of the wind deflector (as shown in Fig. 9) is done. These four parameters are chosen as the design variables. The initial design values of the wind deflector are 380 mm in Width, 2,070 mm in Length, 35 mm in Height, and 0 in Angle. Secondly, an appropriate DOE method (i.e., the optimal Latin hypercube method) is chosen to build the database through simulations, and the influences of the design variables on the objectives are analyzed. Thirdly, a surrogate model is set up using Kriging model according to the above database. Another three design points, aside from the database, are selected and then calculated by the surrogate model and simulation to validate the accuracy and precision of the surrogate model. An optimization algorithm, the multi-island genetic algorithm in this case, is used to determine the optimum using the surrogate model. Finally, the optimization results are inputted to the simulation for the analysis.

For this process, the objective functions take the following form:

$$\begin{aligned}
 &\min f(p_1, p_2, p_3, p_4) \\
 &\quad g(p_1, p_2, p_3, p_4) \\
 &s.t. \quad p_1 \in X_1, p_2 \in X_2, p_3 \in X_3, p_4 \in X_4
 \end{aligned}
 \tag{3}$$

where  $f(p_1, p_2, p_3, p_4)$  and  $g(p_1, p_2, p_3, p_4)$  are the objectives of this paper, which are to minimize the aerodynamic drag and lateral displacement of the tractor-trailer under crosswind condition. The parameters  $p_1, p_2, p_3, p_4$  are the design variables which refer as Width, Length, Height, and Angle, respectively. The

**Fig. 8** Optimization process

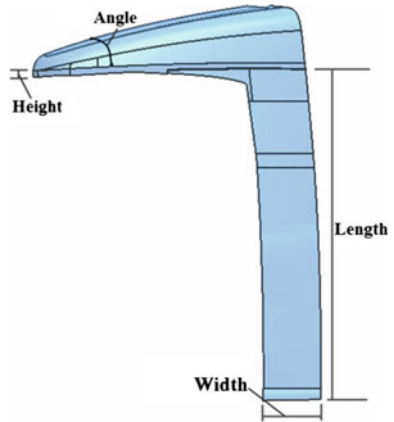
parameters  $X_1, X_2, X_3, X_4$  are the design space of the design variables, the ranges of  $X_1, X_2, X_3$ , and  $X_4$  are set as  $[0,600]$ ,  $[0,2320]$ ,  $[20,70]$ , and  $[0,30]$ , respectively.

## 5 Optimal Results

### 5.1 Design of Experiment Using the Optimal Latin Hypercube method

To explore the design space and identify the significance of design variables, a 30-level DOE study is conducted using the optimal Latin Hypercube method for the four wind deflector design variables. The 30 levels for each design variable are divided between the lower and upper bounds of the design space. With these 30 design points, the wind deflector model is updated, meshed, and the aerodynamic drag and lateral displacement are simulated automatically. DOE post-processing of the Pareto analysis is then performed.

**Fig. 9** Wind deflector model



Pareto plots for drag and lateral displacement are given in Fig. 10. They are order bar chart of the normalized drag and lateral displacement, which represent the % total effect on the response. The figure shows that the effect of the Angle is approximately 25 % for drag and 22 % for lateral displacement, and thus this parameter is the most influential factor of aerodynamic drag and the second most influential factor of lateral displacement. The Width is approximately 23 % for lateral displacement, and thus this parameter is the most influential factor of lateral displacement. The Pareto plots also show the interaction between the design variables. For drag force, the interaction between Angle and Width is the largest, approximately 15 % and the smallest interaction is between Width and Height, less than 0.5 %. For lateral displacement, the interaction between Width and Length is the largest, approximately 18 % and the smallest interaction is also between Width and Height, less than 0.5 %.

### ***5.2 Response Surface Construction Using the Kriging Model***

Based on the DOE results, a surrogate model is built. To verify the precision of the surrogate model, another three design points are chosen, in addition to the 30 DOE design points. These three points are used in the simulation and surrogate model simulation. The results are shown in Table 1. The relative error is the ratio of the absolute error to the simulation result. The absolute error is the absolute value of the difference between the surrogate model result and the simulation result.

### ***5.3 Optimization Method Using the Multi-Island GA***

The optimal design variables and objectives are calculated based on the surrogate model and the multi-island GA. The optimization results are shown in Table 2. Compares to the surrogate model results, the differences are only 0.64 % for drag

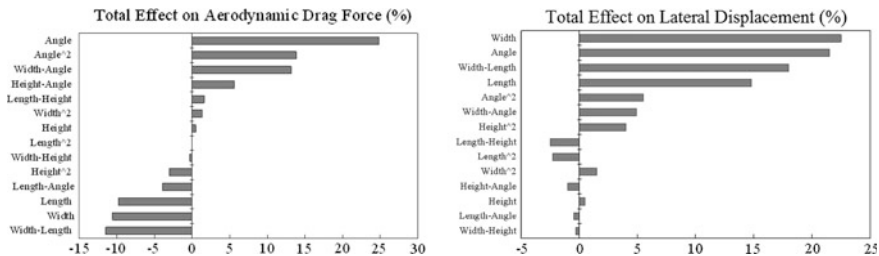


Fig. 10 Pareto plot for drag force and lateral displacement

Table 1 Comparison of results

Run counter	Design variables				Results					
	Weight (mm)	Length (mm)	Height (mm)	Angle (°)	Surrogate model (N)	CFD simulation (N)	Relative error (%)	Surrogate-model (mm)	ADAMS simulation (mm)	Relative error (%)
31	500	2,000	40	4	7149.7	7193.2	0.61	634	636	0.31
32	300	1,000	35	10	7660.5	7531.9	1.71	600	597	0.50
33	200	1,500	45	7	7531.1	7608.2	1.01	583	595	2.02

Table 2 The optimization results

Design Variables				Results					
Weight (mm)	Length (mm)	Height (mm)	Angle (°)	Surrogate model (N)	CFD simulation (N)	Relative error (%)	Surrogate-model (mm)	ADAMS simulation (mm)	Relative error (%)
536	850	51	3	7298.8	7345.9	0.64	593	591	0.34

force and 0.34 % for lateral displacement. The results validates the precision of the surrogate model.

The aerodynamic drag characteristics of tractor-trailer vehicle with the original and optimal wind deflector under crosswind conditions are as shown in Fig. 11. Compares to the original wind deflector, the drag coefficient of the tractor-trailer with optimal wind deflector decreases averagely by 3.44 and 6.23 % at most. This benefits for the fuel economy.

The lateral displacements of the tractor-trailer vehicle with the original and optimal wind deflector under strong breeze and moderate gale conditions are as shown in Fig. 12 respectively. The lateral displacements decrease under different vehicle speed and wind speed for the tractor-trailer with the optimal wind deflector. This benefits for the driving safety.

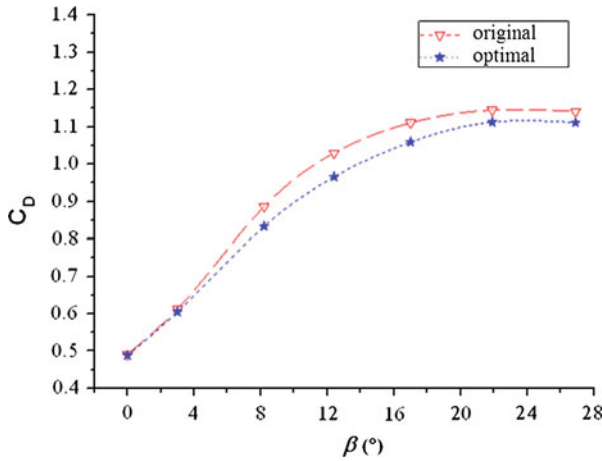


Fig. 11 Aerodynamic drag coefficient of the tractor-trailer

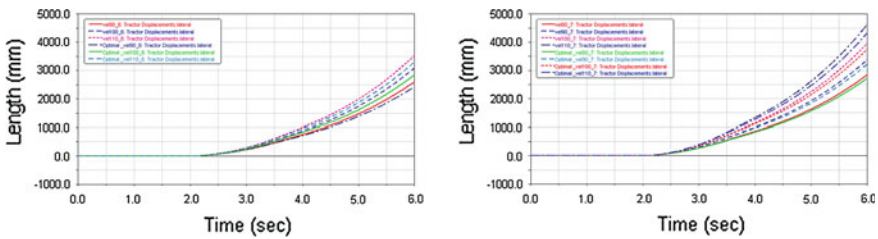


Fig. 12 Curve of the tractor’s lateral offset value versus time at strong breeze and moderate gale

## 6 Conclusions

A surrogate model-based aerodynamic shape optimization method applied to wind deflector of a tractor-trailer is presented in the paper. The aerodynamic characteristics and lateral displacement of the tractor-trailer vehicle with the wind deflector and subjected to crosswinds are simulated. The results show that the aerodynamic characteristics change drastically and the lateral displacement increases.

A 30-level DOE study using the optimal Latin hypercube method is implemented to analyze the sensitivity of the design variables and build a database to set up the surrogate model based on Kriging interpolation technique. The precision of the surrogate model is verified using the simulation and surrogate model simulation, and the relative error is verified to be within 3 %. Finally, the multi-island GA is used to optimize the shape of the wind deflector based on the surrogate model. The differences between the simulation results and the surrogate model results are less than 1 % when using the optimal design variables, and the



aerodynamic drag coefficient and lateral displacement decrease when optimal wind deflector is installed.

This paper presents an alternative method for reducing computational cost for real industrial optimization tasks. The time required to perform the design of a wind deflector is reduced to be less than a week, while it takes more than a month to design a wind deflector manually.

However, further studies are needed. The number of design variables should increase in order to have more freedom in the shape modification process. Multiple objectives, such as all kinds of aerodynamic characteristics and other targets of driving safety, should be considered during the optimization process.

## References

1. Fujimoto T (1993) Shape study for a low air resistance air deflector. SAE paper 930301
2. Fujimoto T, Niimura A, Sakai K (1995) Shape study for a low-air-resistance air deflector—the second report. SAE paper 950633
3. Truck aerodynamic styling. <[http://www.transport-research.info/Upload/Documents/200602/20060210\\_121817\\_04842\\_GPG308.pdf](http://www.transport-research.info/Upload/Documents/200602/20060210_121817_04842_GPG308.pdf) >
4. Kessler E, Vankan WJ (2006) Multidisciplinary design analysis and multi-objective optimization applied to aircraft wing. J WSEAS Trans Syst Control 1(2), ISSN 1991–8763
5. Jouhaud JC, Sagaut P, Montagnac M, Laurenceau J (2007) A surrogate-model based multidisciplinary shape optimization method with application to a 2D subsonic airfoil. Comput Fluids 36:520–529
6. Rai MM, Madavan NK (2000) Aerodynamic design using neural networks. AIAA J 38(1):173–182
7. Rai MM, Madavan NK, Huber FW (2000) Improving the unsteady aerodynamic performance of transonic turbines using neural networks. Proceedings of the 38th AIAA aerospace sciences meeting and exhibit. Reno, AIAA 2000–0169
8. Madavan NK, Rai MM, Huber FW (1999) Neural net-based redesign of transonic turbines for improved unsteady aerodynamic performance. AIAA/SAE/ASME/ASEE 35th joint propulsion conference, AIAA 99–0559
9. Bettle J, Holloway AGL, Venart JES (2003) A computational study of the aerodynamic forces acting on a tractor-trailer vehicle on a bridge in crosswind. J Wind Eng Ind Aerodyn 91(5):573–592

# Calculation of Drum Brake Temperatures in Ten-Cycle Braking

Kun Zhang and Cai Yang

**Abstract** Brake system which is the safety system has a high demand for heat fade. To predict the temperature of brake, especially in continuous braking conditions, is important for heat fade. In this paper a transient numerical heat transfer model is developed to estimate the time-dependent temperatures distribution in ten-cycle braking condition. When the highest temperature is determined, braking friction heat is directly applied to the friction surface in the form of heat flux; the braking heat dissipates to the ambient air via convection heat transfer and thermal radiation, which are boundary conditions. Temperature predicted by two-dimensional thermal analysis is acceptable compared with conventional three-dimensional thermal analysis and experimental dynamometer drum temperature measurements.

**Keywords** Drum brake · Finite element method · Transient temperature field · Heat fade · Ten-cycle braking

## 1 Introduction

Brake system which is one of the most important safety components can slow or stop a vehicle by converting kinetic energy into heat. Based on the design configurations, vehicle friction brakes can be grouped into drum and disc brakes.

---

F2012-E03-013

---

K. Zhang (✉) · C. Yang (✉)

Changan Auto Global R&D Center of Changan Automobile Co Ltd, Chongqing, China

The drum brakes use brake shoes that are pushed in a radial direction against a brake drum. The disc brakes use pads that are pressed axially against a rotor or disc.

Under extreme conditions, such as descending a steep hill with a heavy load, or repeated high-speed decelerations, drum brakes would often fade and lose effectiveness, this because the friction coefficient decreases with the rising temperature. For a typical phenolic novalak binder, the friction coefficient is stable (about 0.32) up to approximately 600 °F, then decrease steadily to 0.24 at 1,100 °F, and further degrades with increasing temperature [1]; on the other hand, excessive thermal loading may result in thermal cracking, premature wear, brake fluid vaporization, so to predict the temperature of brake, especially in the continuous braking conditions, is important for heat fade.

## 2 Brake Model

As the drum brake is an axi-symmetric structure, when ignoring the four screws of drum brake mounting holes, the heat transfer of the axial direction in the process of the braking, brake temperatures can be calculated only a two dimensional symmetrical radial section of the brake temperature distribution. In this paper conventional three-dimensional model is also developed in comparison with two-dimensional thermal analysis.

In order to simplify the analysis complexity, some small chamfers are ignored, and in the analysis the drum material is assumed isotropic, which thermo-physical parameters (density, conductivity, and specific heat) do not change with temperatures, while these parameters would change in actual braking process, showing a non-linear. At last, heat flux distribution coefficient was constant, but in fact it changes with the drum material parameters.

## 3 Calculation of Heat Flux

Each time, when we stop a vehicle, the brakes convert the majority of kinetic energy into heat due to friction between brake shoes and brake drums, and 95 % of the heat is absorbed by drums, and 5 % of the heat is absorbed by brake shoes. There are many ways to calculate the heat, but the common way to calculate the heat is through flux heat.

The first method to calculate the flux heat is given by [2]:

$$q'' = \mu p R \omega \quad (1)$$

where  $\mu$ : friction coefficient,  $p$ : contact pressure between drum (rotor) and brake shoes (pad) surfaces,  $R$ : distance between node and drum (rotor) center,  $\omega$ : angular velocity of the drum(rotor).

With Eq. (1), the heat flux can be calculated directly, but the distribution of pressure is uneven. Therefore it is difficult to calculate the contact pressure.

The second method to calculate the heat flux is based on conservation of energy, when a vehicle is braking from an initial speed to a given speed, the heat generation can be estimated by:

$$Q_1 = \frac{1}{2}mv_1^2 - \frac{1}{2}mv_2^2 + mg(\pm i - f)S \tag{2}$$

where  $v_1$ : the initial speed,  $v_2$ : the given speed,  $m$ : the mass of the vehicle,  $g$ : the gravity,  $i$ : Road grade (ascending grade is positive, otherwise is negative),  $f$ : coefficient of rolling resistance,  $S$ : braking distance.

Then derivative with respect to time (t), and get friction heat power:

$$q_1 = mav + mg(\pm i - f)v \tag{3}$$

where  $a$ : deceleration,  $v$ : instantaneous velocity.

When the wheel closes to lock braking state, the tires will have a certain amount of slip rate; some of the friction heat will be converted into friction heat between the tire and the ground.

Here  $Q_1, q_1$  is the total vehicle brake friction heat and friction heat power. In this chapter, only the single rear drum brake is analyzed, based on the braking force distribution coefficient, the friction heat and friction heat power of the rear drum can be calculated by:

$$Q_{1R} = \frac{1 - \beta}{2}(1 - s) \cdot Q_1 \quad q_{1R} = \frac{1 - \beta}{2}(1 - s) \cdot q_1 \tag{4}$$

where  $Q_{1R}$ : the single rear drum friction heat,  $q_{1R}$ : the signal rear drum friction heat power,  $\beta$ : the braking force distribution coefficient,  $s$ : tire slip.

The heat  $Q_{1R}$  which generates on the frictional contact interface will distribute between the drum and brake shoes, the heat flux into drum can be expressed as:

$$q = \frac{\eta}{1 + \eta} q_{1R}/A_b \tag{5}$$

where  $A_b$ : the surface area of the rubbing interface,  $\eta$ : the heat flux distribution coefficient, and

$$\eta = \left( \rho_d c_d \lambda_d / \rho_s c_s \lambda_s \right)^{0.5} \tag{6}$$

where  $\rho_d$ : drum density,  $c_d$ : drum specific heat,  $\lambda_d$ : drum thermal conductivity;  $\rho_s$ : brake shoe density,  $c_s$ : is brake shoe specific heat,  $\lambda_s$ : brake shoe thermal conductivity. In this paper, the second method is used.

## 4 Heat Dissipation

When the temperature rises above the ambient air, some of the friction heat goes out into air. There are three modes of heat dissipation from drum: heat conduction, heat radiation and heat convection.

### 4.1 Heat Conduction

Heat conduction exists between drum and brake shoes, as the rubbing interface generates heat, the thickness of brake shoes and drum is usually between 10 and 20 mm, moreover, the material of drum is conductive grey cast iron, the material of brake shoe's conductive is poor, so the difference of temperature between drum and brake shoes can be ignored, that is to say, ignoring heat conduction.

### 4.2 Heat Radiation

Heat radiation has relation with the temperatures of outside surface of drum, the higher temperature it has, the more heat dissipation through heat radiation. Generally speaking, the heat which dissipates through heat radiation is about 5 ~ 10 % of the total dissipation heat. The radiation heat dissipation is defined by:

$$Q_{radiation} = \sigma \varepsilon A_{Dradiation} (T_D^4 - T_\infty^4) \quad (7)$$

where  $Q_{radiation}$ : the heat dissipated by radiation,  $\sigma$ : the Stefan-Boltzmann constant  $5.67 \times 10^{-8} \text{w}/(\text{m}^2 \cdot \text{k}^4)$ ,  $\varepsilon$ : drum surface emissivity (For cast iron,  $\varepsilon = 0.55$ ),  $A_{Dradiation}$ : the surface area of the drum radiation heat,  $T_D$ : the average drum surface temperature,  $T_\infty$ : the ambient air temperature.

### 4.3 Heat Convection

In operations of braking systems, convection is the most important mode of heat transfer, dissipating the highest proportion of heat to surrounding air. In order to prevent the dust from going into drum inner surface, the surface is sealed, there is no airflow and heat convection, hence, when the transient temperature distribution in drum is calculated, the heat convection boundary is used on all surfaces except the inner surface and the hub portion of drum which connects to the axle.

However, it is very difficult to calculate it accurately, as the heat convection is affected by the shape of brake system, air flow, physical characteristics of air flow

**Table 1** Material properties of drum

Material	Young’s modulus <i>MPa</i>	Poisson’s ratio	Density Kg/m <sup>3</sup>	Conductivity W/(m)	Specific heat J/(Kg)
HT250	1,38,000	0.156	7,280	43	452

and so on; all of the formulas about the heat convection are approximated. So we use the experiential formulas. The convective heat transfer coefficient of the drum is quoted from the experimental formula given by [3]:

$$h = 0.92 + \beta v \times e^{-\frac{v}{328}} \tag{8}$$

where *v*: the velocity (*ft/s*),  $\beta$  empirical formula coefficient. The heat convection unit is *Btu s/h ° F ft<sup>2</sup>* (*1ft/s = 0.3048 m/s, 1Btu s/h ° F ft<sup>2</sup> = 5.67826 W/m<sup>2</sup> k*)

Among the three modes of heat dissipation (heat conduction, heat radiation and heat convection) heat conduction has the least effect on drum’s heat dissipation. The heat radiation only plays an important role at high temperatures and low speeds. The heat convection is considered the most important mode of heat dissipation.

## 5 Simulation and Experiment

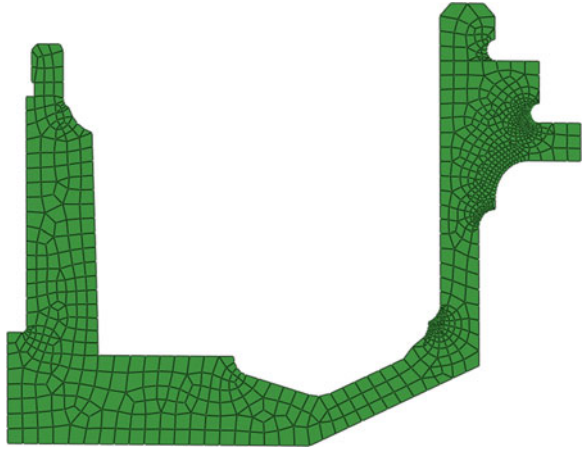
The simulation condition is: the vehicle weight is 1,475 kg, the initial velocity is 100 kph, constant deceleration is 0.45 g, braking intervals time is 45 s, the cycles are 10 times, the initial temperature of drum is 65 °C, and the ambient air temperature is 25 °C.

The bench test is carried out to determine the highest temperature in drum for verifying the analysis. The bench test condition is the same as the simulation condition, the drum-shoes system is applied brake 210 times in the experiment, the first 200 times are the burnish operation to make sure that drum and brake shoes touching completely, then we use the last 10 times to compare with analysis results. The temperature of drum is measured by thermocouple at depth of 0.5 mm below the contact surface.

When we calculate the heat flux based on vehicle parameters and the formula (5), the material properties of drum are described as the Table 1; the end velocity, road grade, coefficient of rolling resistance, tire slip is zero. The heat flux which is considered as a function of time can be directed into drum through the rubbing surface.

As a single drum is tested, the cooling wind is constant 11 m/s, so when the convection coefficient is calculated by using the formula (8), the value of  $\beta$  is 1, and the heat convection coefficient is 188 W/m<sup>2</sup>k. As for the radiation heat, surface emissivity is 0.55.

**Fig. 1** Mesh for the axisymmetric 2D model



**Fig. 2** Mesh for the 3D model

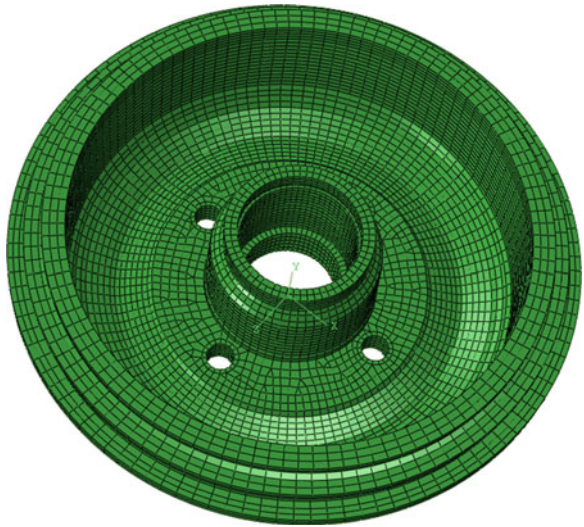


Figure 1 shows an axisymmetric two dimensional model of drum brake, the total number of nodes is 1,169, and total number of elements is 1,058. Figure 2 shows the three dimensional model of drum, the total number of nodes is 29,740, and total number of elements is 23,101.

## 6 Results

The Fig. 3 is the highest temperature distribution through ten-cycle braking by using two-dimensional finite element method. The Fig. 4 is the highest temperature distribution through ten-cycle braking by using three-dimensional finite

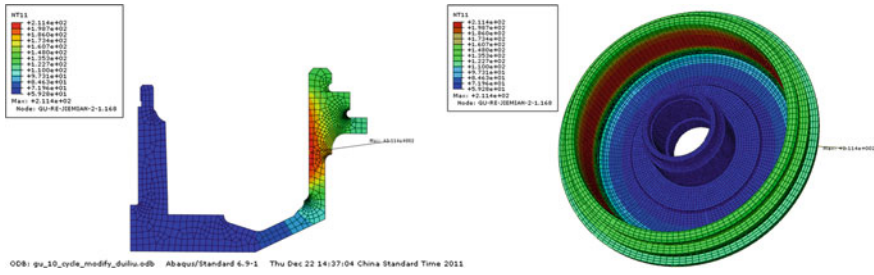


Fig. 3 The highest temperature distribution by using 2D finite element method

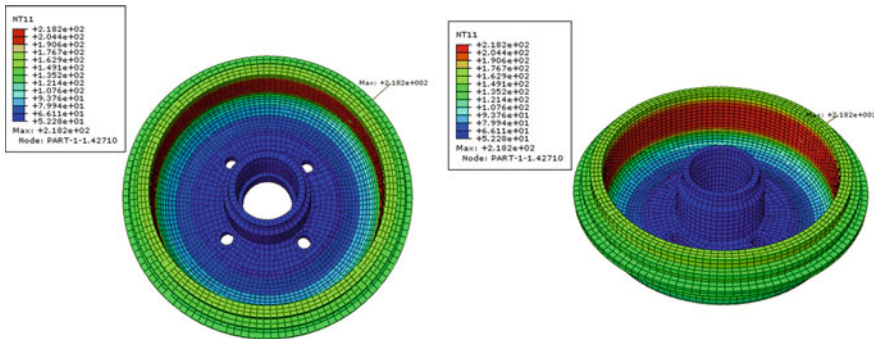


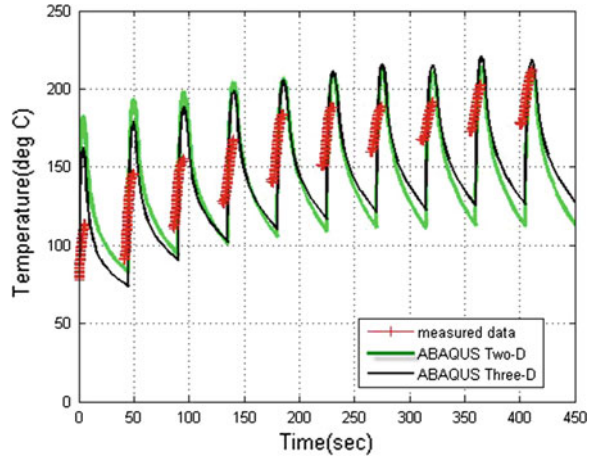
Fig. 4 The highest temperature distribution by using 3D finite element method

element method. The highest temperature on drum region is calculated to be 211.4 °C with two-dimensional analysis and 218.2 °C as a result of three-dimensional analysis. The figures show that the highest temperature at the surface can be calculated using the axi-symmetric analysis with only a 3.2 % difference from that of three-dimensional analysis. From the position of thermocouple and the analysis, we can conclusion that the highest temperature's location is in the middle of the rubbing surface. The farther from the rubbing surfaces, the lower temperature it has, this is because the heat derives from the rubbing surfaces and transfers to extremities.

The Fig. 5 is the comparison temperature among two-dimensional, three-dimensional analytic results and the bench tests. Note that the bench test temperature dates are only collected during brake apply portion of the heat cycles, and the bench test highest temperature is 215 °C. In each brake cycle, the highest temperature is not at the end of the braking, but at some time point during braking, then with the heat dissipates and the heat flux reduces, leading to the drum temperature falling. So in the whole ten cycles, the drum temperature raised in saw-toothed ways. Comparison two-dimensional, three-dimensional with bench test, the error respectively is 1.6, 1.4 %. As the conventional three-dimensional thermal analysis requires a huge amount of computational time and memory space to get



**Fig. 5** Comparison of analytic results and experimental results



the temperature rise for braking, It, therefore, the axi-symmetric temperature analysis can be adopted to predict the temperature distribution of drum.

## 7 Conclusions

From the comparison of analytic results of two-dimensional, three-dimensional model of drum brake, there is only small difference about the highest temperature. The drum brake can be analyzed simply by using two-dimensional finite element method. During the transient thermal analysis, the variable heat flux and heat convection coefficient can be directly applied to the model. Comparing with bench test results, the results of analysis are acceptable and credible, which can be useful to further study on the preventive measures for heat fade.

## References

1. Waston C (1995) The prediction of heavy duty brake performance, truck and commercial vehicle international, pp 135–138
2. Chi Z (2008) Thermal performance analysis and geometrical optimization of automotive brake rotors. University of Ontario Institute of Technology, Oshawa
3. Murphy R et al (1971) Bus Truck, tractor-trailer braking system performance. Final Report, Contract FH-11-7290, U.S. Department of Transportation

# Solution of the Glare Risk in Vehicle Inner Trim Designing

Mengdong Mi, Yongqing Liu, Congwen Yu, Sujuan Peng, Bin Feng, Jian Shi and Pin Wang

**Abstract** With the trend of vehicle inner trim design developing, quantities of highlight materials and auto amusement equipments are applied such as chrome-plate and DVD cruise system. The fashionable stuffs mentioned above, will provide customers with new feeling and extra driving joy compared with the former cars. At the same time a serious glare risk will come caused by the “highlights”, so that it may affect the driving safety. However, the traditional layout methods can only check out the potential “issues” by drawing some simple geometrical reflecting route of light, they can not evaluate the real ponderance when products come out. Therefore the main purpose of this term below concerns on finding a optimum solution not only by traditional ways but also by illuminating analysis to make a balance between the styling “highlights” risk and our Ergonomics., meanwhile it also can reduce the ratio of engineering modification and designing cost.

**Keywords** Inner trim · Package · Glare · Ergonomics · Illuminate

With developing of the times, more and more new styling elements and amusement equipments like the chrome parts, navigation system, and marching computer and so on are used in modern car design, as show in Fig. 1. But if those parts are located to the wrong place in the earlier product design, it will take diffuse reflection light and dazzling the driver and may affect the driving safety. So how to resolve the new problem is valuable for research by the professional.

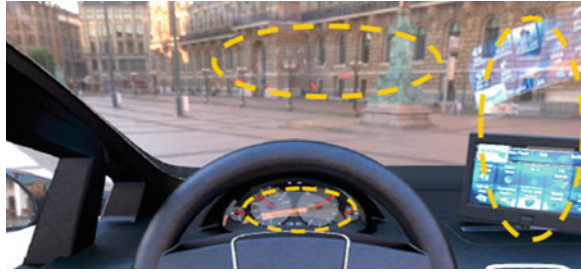
---

F2012-E03-014

---

M. Mi (✉) · Y. Liu · C. Yu · S. Peng · B. Feng · J. Shi · P. Wang  
Changan Auto Global R&D Centre of Changan Automobile Co LTD, Chongqing, China  
e-mail: sunqiemail@163.com

**Fig. 1** Actual situation of the glare risk



## 1 Introduction

The definition of the 95th percentile eyellipse used in this article is cited from ‘SAE J941-2002 Motor Vehicle Driver’s Eye Locations’ [1].

### 1.1 Glare Risk Analysis of Instrument Cover

In the plane through the point R and parallel to plane Y0, get the reflecting lines between instrument cover edge and windshield upper point, it can not intersect with the 95th percentile eyellipse, we can adopt similar way to check the sunroof, but projection angle through rear windshield is too small and unable to reach the instrument cover, so it is generally not considered (Fig. 2).

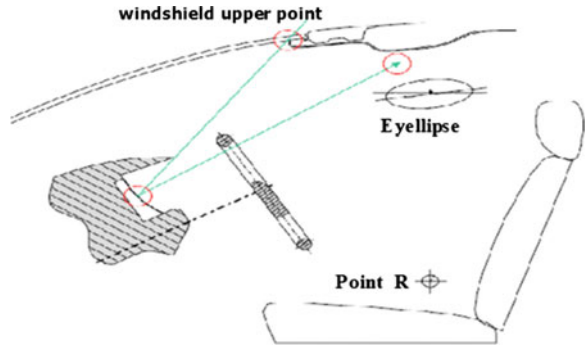
### 1.2 Glare Analysis of Instrument Lighting

In the plane though the point R and parallel plane Y0, get the reflecting lines between instrument cover edge and instrument panel downward point, it can not intersect with the 95th percentile eyellipse (Fig. 3).

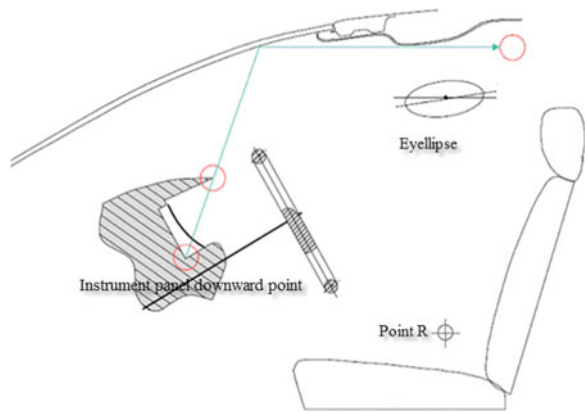
### 1.3 Instrument Lighting on the Exterior Mirror Glare Analysis

Such as dashboard lighting and the reflective component projection on the side windows, will obstruct the driver to observe exterior mirror. Through the exterior mirrors and each limit point on 95th percentile eyellipse surrounded the surface intersects with side window glass, and the intersection area known as the exterior mirrors on the side window of the projection plane, through the projection plane get the mirroring eye point. Then we can use the surface that is surrounded by the mirroring eye point and the exterior mirrors projection on the side windows to check if the instrument lighting be likely to cause glare (Fig. 4).

**Fig. 2** Glare analysis of instrument lighting



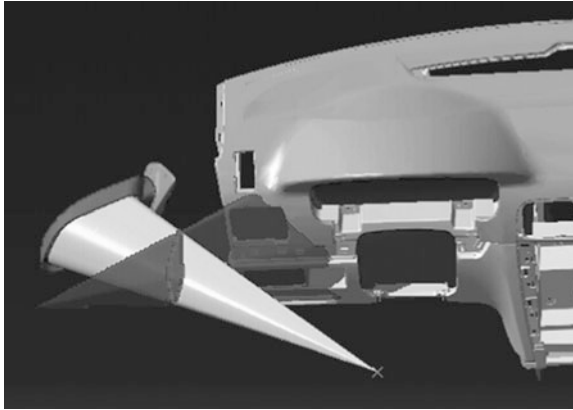
**Fig. 3** Glare risk analysis of instrument cover



### ***1.4 The Reflection and Glare Analysis of Dashboard and Other Inner Trim Parts on the Front Windshield***

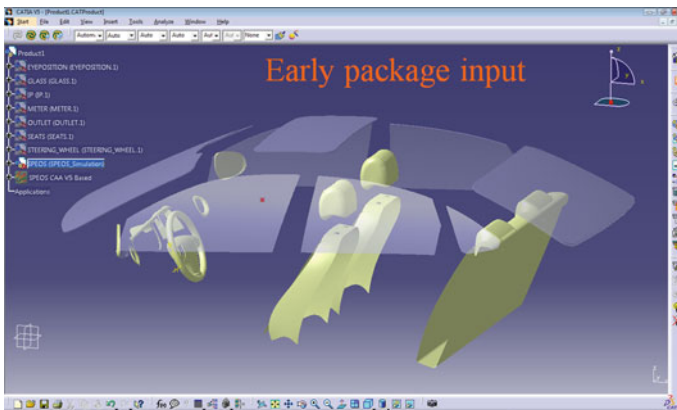
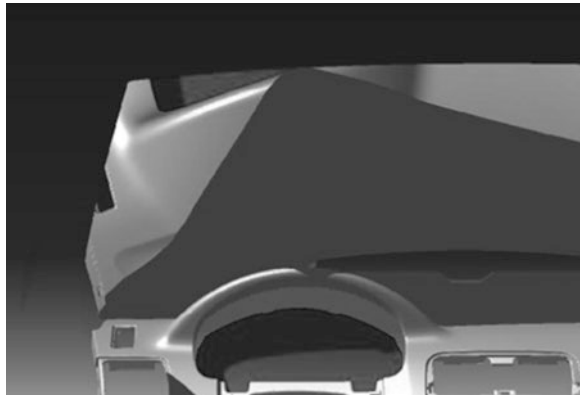
In the case of strong lighting, dashboard and other inner trim parts are easy to form a projection on the front windshield and will obstruct driver's view. So the layout of the dashboard should use dark and better materials for diffuse reflection. At the same time, the angle of the front windshield and dashboard plate can't too small (due to this value is directly related to the styling and the size of the drag coefficient, so the design must balance the relationship among the three), and most effective way is to check the model at the early stage (Fig. 5).

In the early design, we can use CATIA software to simulate the approximate range of reflection on the front windshield and prejudge the glare risk. So the component such as the high-gloss inner trim or seam areas appear in this area should be arranged outside of the main view area (The specific definitions of main view area is cited from 'GB 11555-1994 Car windshield defrosting system performance requirements and test methods for zone A') [2, 3].



**Fig. 4** Instrument lighting on the exterior mirror glare analysis

**Fig. 5** The reflection and glare analysis of dashboard and other inner trim parts on the front windshield



**Fig. 6** Early package input

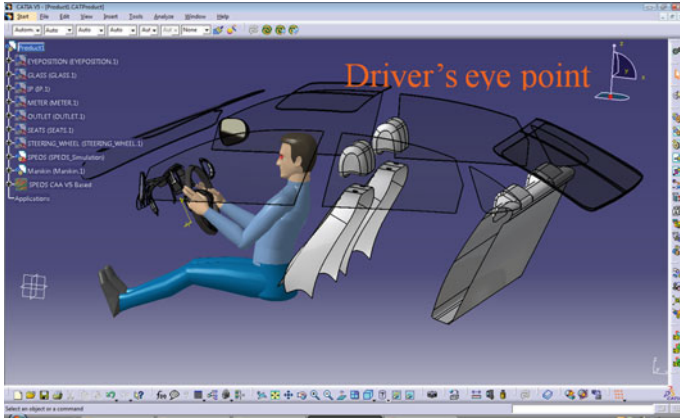


Fig. 7 Driver's eye point

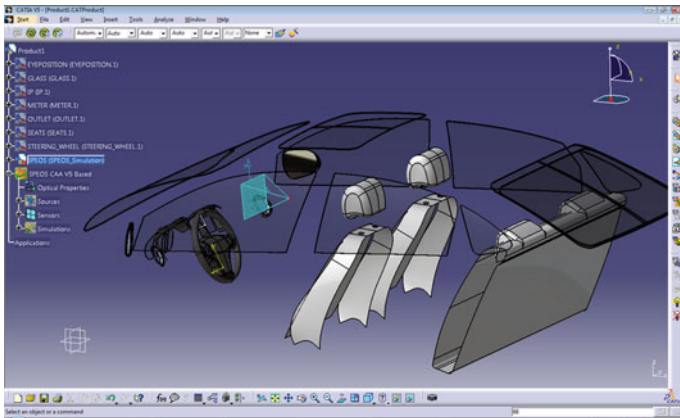


Fig. 8 Target area of view

## 2 The Optical Software Applications in Glare Analysis

In the period of the inner trim design of the vehicle, the traditional package can only use CAD software draw some simple geometrical reflecting lines to do the risk assessment. As mentioned earlier, with the styling developing, more and more modeling features elements bring problems to the package of inner trim designing that we can't evaluate the risk simply through CAD software, such as the optical property of inner trim, outside environmental light as well as the light of the DVD and other light-emitting parts. According to the above problem, we did the optical simulation analysis to design the inner trim of the XXX project in a 3D digital environment through professional optical analysis software combined with the traditional package methods, so we can accurately and directly evaluate the glare

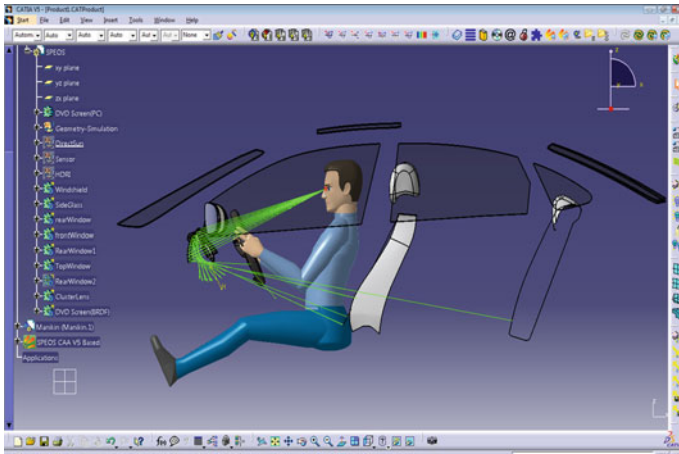


Fig. 9 The simulated optical path track of eye visual field

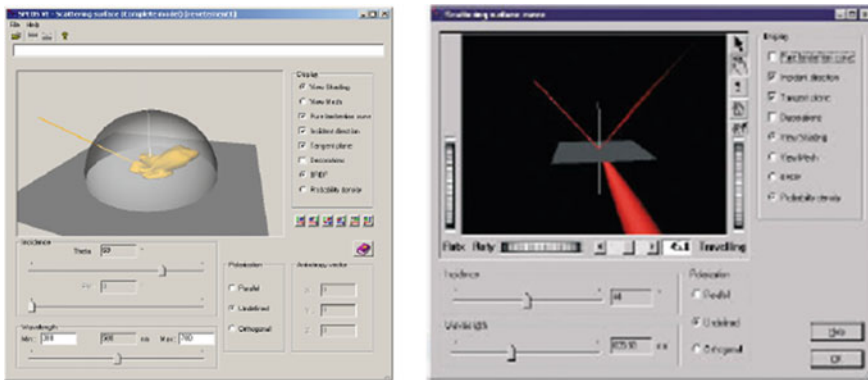


Fig. 10 The optical properties of the inner trim

risk of the occupant room in 3D environment, then to balance the conflict between the inner trim designing and the styling. Next we will take a glare analysis of a project of CHANGAN AUTO.

### 2.1 Early Package Input

In 3D environment, we need input this dates to the software, hard point, eyellipse, windshield, rear mirror surface, instrument surface, air conditioning outlet and other data planes related to this analysis (Figs. 6, 7).



Fig. 11 Windshield Glare risk analysis result on at night

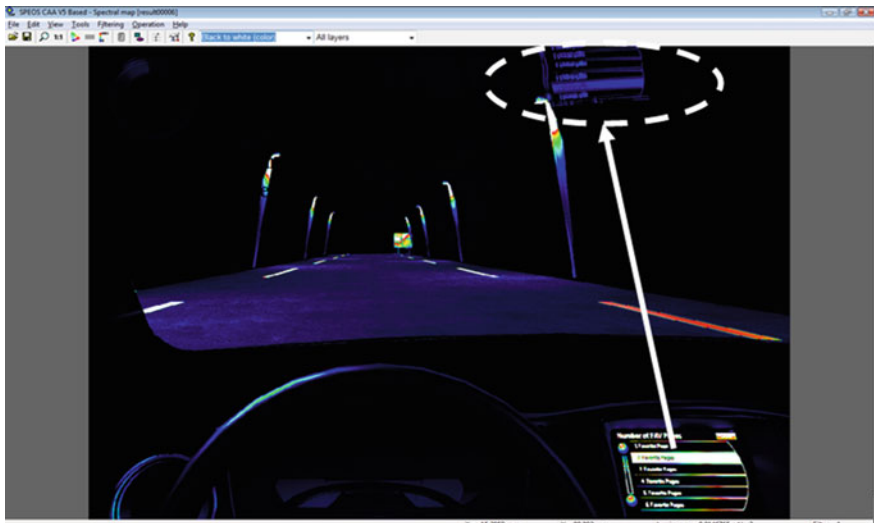


Fig. 12 The light intensity distribution on the windshield

We must acquire the optical properties of the various parts' CTF model of the inner trim by the laboratory equipment, then establish the material library in the optical software and assign to the corresponding inner 3D surface data.

Define the location of a certain percentile of the driver's eye point and the target area of view (Figs. 8, 9).



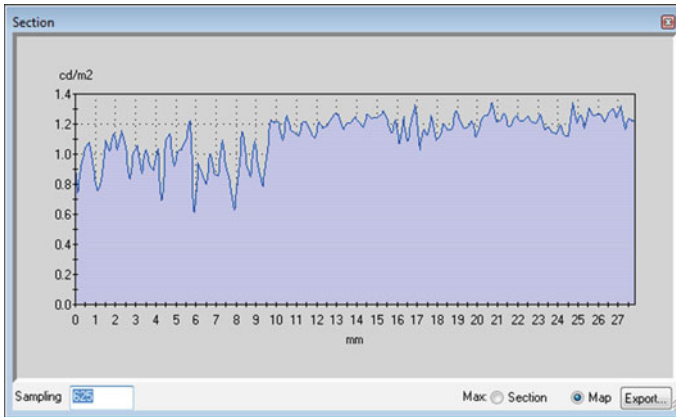


Fig. 13 The light intensity distribution graph of the DVD monitor reflection on the windshield

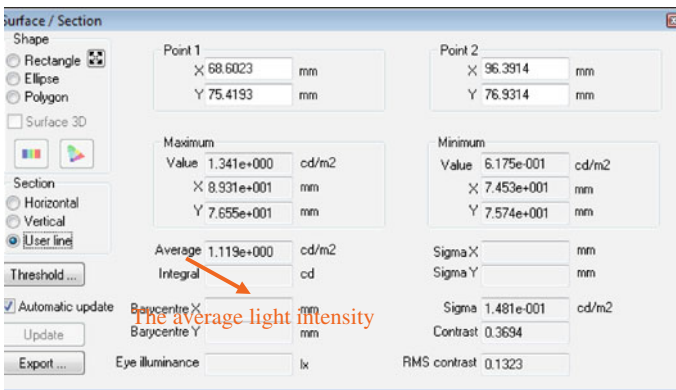


Fig. 14 Calculated result of the light intensity

## 2.2 Optical Path Analysis of the Human Vision Field Through Optical Software

Input above parameters to the human visual module of software then generate the simulated optical path track of eye visual field which is used to qualitatively judge the bad light reflection of the occupant room on these areas such as the windshield, rear mirror, instrument panel or other areas in the early designing period and we can easily get the propagation track of the light in CATIA in order to help designers to get the source of the bad reflection qualitatively. We must qualitatively analyze these situations if we want to know the bad reflection's extent, or how deeply can the harmful reflections affect the driver's vision.

### ***2.3 Optical Analysis Software on Inner Trim Glare of Virtual Simulation and Quantitative Assessment of Hazard***

Then we will depict a case about the windshield glare risk analysis at nighttime. In the SPEOS module of optical software, we will input the optical properties of the inner trim CTF model to the corresponding 3D surface data. In addition, loading the ambient light at night to the software that comes with the International Association of Lighting Standard, calculated using the finite element analysis rather than the commonly used real-time styling rendering software to analyze the glare risk under certain circumstances. It can be seen from the virtual results generated by the software to calculate the electronic model of car in the reflection on the windscreen of a nighttime environment (Figs. 10, 11).

The lightness of the external environment is relatively small at nighttime, so the reflection of inner trim on the front windshield than the daytime more apparent. We can use light intensity distribution to analyze the glare risk. For example, when the DVD monitor is turned on, the reflecting lightness in the windshield is about  $1.1 \text{ cd/m}^2$ , which is low enough and does not appear in the driver's main viewing area, so the glare risk is acceptable (Figs. 12, 13 and 14).

## **3 Postscript**

With the trend of vehicle inner trim design developing, large number of new materials and new entertainment devices are used to bring subjective experience to the consumers. At the same time, it also will bring glare risk which can't apply traditional package analysis methods to assess. According to the problem mentioned, I explore a combination of traditional analysis methods with finite element analysis methods to balance the contradiction between the inner trim and styling, and verifying the validity and accuracy of inner trim glare risk analysis methods by comparing early design with the actual glare situation of physical prototype vehicle.

## **References**

1. SAE J941-2002 Motor Vehicle Driver's Eye Locations
2. OPTIS solution applied in Automotive Vision System, OPTIS CO
3. OPTIS solution applied in Cluster design, OPTIS co

# Topology Optimization Design of a Heavy Truck Frame

Jingxin Wang, Tie Wang, Yanchao Yang, Zhaohui Peng, Zhi Li and Na Wang

**Abstract** The stress distribution and deformation of frame in bending and torsion condition with the load 30 tons are computed by FEA method. The result show that there is stress concentration. Using FEA and experimental method get the first two modal frequencies and modes of frame at free conditions. The results show that the frequency is low and the dynamic performance of the frame is not well. The frame structure was designed by the topological optimization method. To design the longitudinal beam for variable cross-section structure and redesign beams type. The results of finite element steady-state mechanics and modal analysis show that the stress of the improved frame structure reduced significantly and low order natural frequency improved. The design of the improved frame structure is reasonable.

**Keywords** Frame · Finite element analysis · Modal analysis · Modal test · Topology optimization

## 1 Introduction

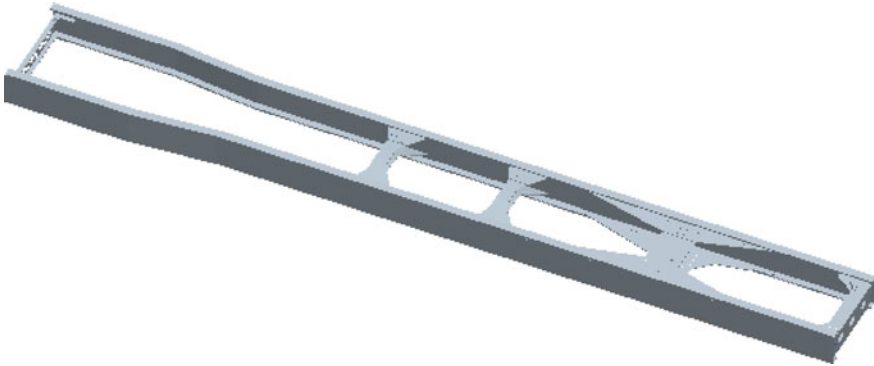
Heavy dump's frame needs good mechanical properties under complex condition. It should have light quality and even stress distribution as possible in case of sufficient strength, stiffness and stability conditions, but existing dump truck frame

---

F2012-E03-015

---

J. Wang (✉) · T. Wang · Y. Yang · Z. Peng · Z. Li · N. Wang  
Department of Vehicle Engineering, Taiyuan University of Technology, Taiyuan, China  
e-mail: vcv1986@163.com



**Fig. 1** 3D model of the frame structure

is designed by adding sub-frame on the general chassis. This method can lead to structurally local strength, uneven overall stiffness, Waste of material and large quality [1, 2]. The topology optimization of continuum structure is that we can access the best structure according to the known boundary conditions and load conditions under the condition of unknown structure topology [3]. The software HYPERMESH is used for the topology optimization of the frame in this chapter with the prototype of a heavy dump, to seek the optimal layout of the crossbar and to improve the whole stress level and the dynamic characteristics.

## **2 Analysis of the Original Frame Structure**

### ***2.1 Establishment of Finite Element Model of the Frame***

Figure 1 shows 3D mode of the heavy truck frame. All the components' material of unit assembly is 16 Mn. In order to preserve the mesh's quality, some geometric details (such as chamfering, pour round, process holes etc.) which has little effect on strength and stiffness of the frame are local modified and simplified. Longitudinal and transverse of the frame is composed by a series of thin walled parts whose shapes are complex. So the shell unit (PSHELL) was used to simulate model. This unit cans effectively descript the mechanical properties of the frame. In order to make the modeling simple and the calculation efficiently, the bolts and the rivets' deformation and there stress of corresponding place were ignored. The Rigid unit was used to simulate rivets connection in this chapter. Load quality of the frame includes cubs weighing 900 kg, power train weighing 1,100 kg, oil tank weighing 320 kg and storage battery weighing 100 kg, which load in corresponding place as the concentrated loading form and cargo weight weighing 30 tons which load as uniform loading form. The finite element model of the frame is shown in Fig. 2.

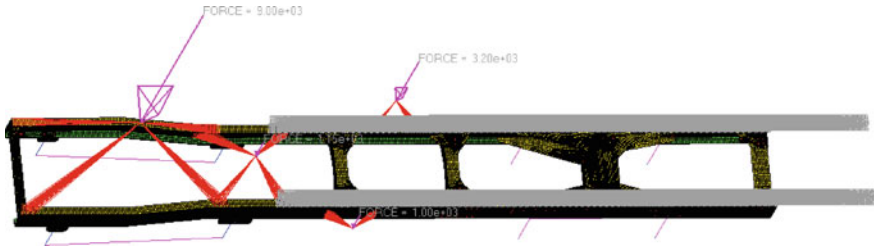


Fig. 2 Finite element model of frame structure

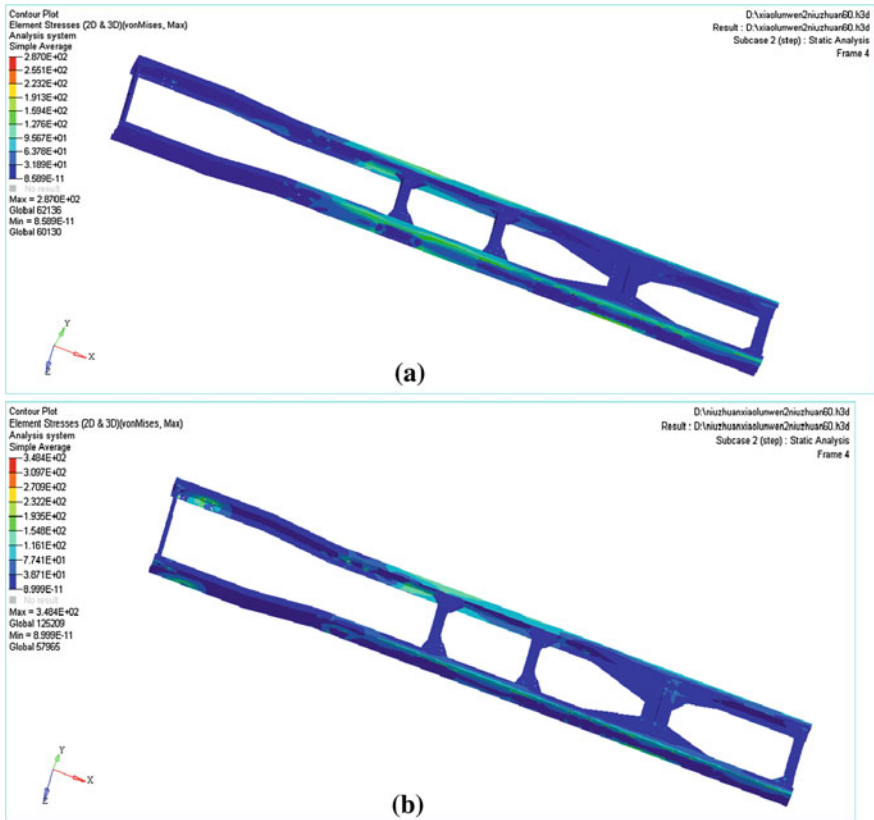
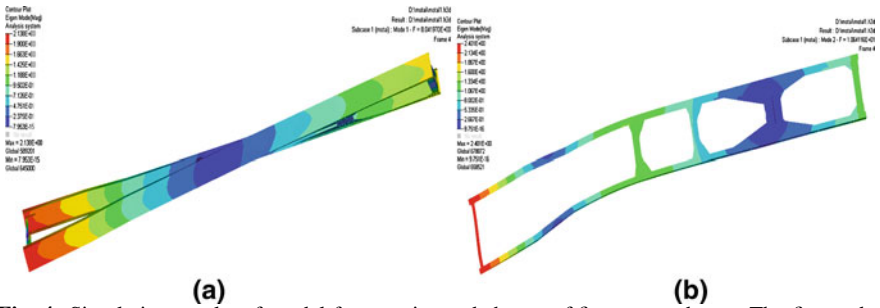


Fig. 3 Stress distributions of original frame. a Bending analysis, b Torsion analysis

### 2.2 Steady-State Mechanics Analysis of the Frame

According to the practical boundary condition and frame carrying case, calculating in the HYPERWORKS. The stress distributions of frame under the bending condition and torsion condition can be got in the HYPERVIEW as Fig. 3.



**Fig. 4** Simulation results of modal frequencies and shapes of first two orders. **a** The first order torsion (8.04 HZ) **b** The first order bending (10.64 HZ)

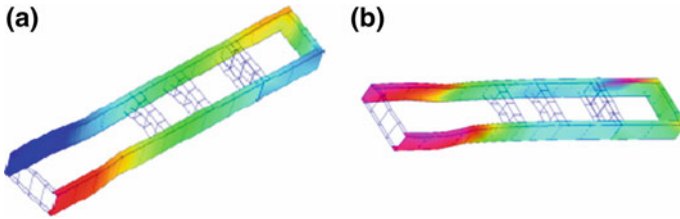
In the bending condition, connectors of suspension and frame appear larger stress, so does the connector of the second beam and girder. These stresses conform to the load of frame. The maximum stress appears in the connect hole of the forth beam and girder which is 322.5 MPa. This with the rigid connection REB2 unit simulation rivets connection that causes rivets holes in the stress concentration relevant. In the reverse condition, the second frame beam and right longitudinal joint and former leaf-spring bearing with longitudinal joint stress is bigger. The maximum stress appears in the longitudinal leaf-spring bearing hole in the right connections which is 348.4 MPa, the stress values greater than the allowable stress 345 MPa. The result is due to appear the bolt connections simulated by REB2 units and there is a constraint, hindering reverse deformation along the right longitudinal transferring, causing the larger stress concentration phenomenon. The frame of dump truck which driving in this condition is often destroyed, so improvement of the frame is necessary.

### 2.3 Modal Analysis and Experimental Verification of Original Frame

Any constraints in the calculation were not imposed on the frame. Modal frequencies and modal shapes of first two orders of frame on free condition is show in Fig. 4.

In this paper, modal testing was also conducted by INV3060A (16 channel) dynamic testing system and DSP analysis software. Figure 5 shows the first two order natural frequencies and shapes of frame which was measured in the modal testing.

The results of finite element modal analysis and experiment modal can be a good correspondence,so the creditability and rationality of the simulation method are verified. The results indicate that low order frequency of frame is small. Frame structure should be improved to enhance frame stiffness and increase low order frequency of frame appropriately.



**Fig. 5** Testing results of modal frequencies and shapes of first two orders. **a** The first order torsion (9.33 HZ), **b** The first order bending (11.88 HZ)

### 3 Topology Optimization of Frame Structure

#### 3.1 Topology Optimization of Unknown Structure

The main idea of structure topology optimization is converting the problem of looking for excellent structure topology to searching for excellent material distribution in specified design region [4, 5]. By variable density method, this paper realized topology optimization of car frame in bending and twisting conditions by using OPTISTRUC of HYPERWORKS [6]. During the optimizing process, we taken the mesh density as the design variables and the minimum deformation energy in any conditions as the target function as well the volume ratio as the objective constraint function. The optimization results of bending and torsion conditions are shown in Fig. 6.

#### 3.2 Redesign of Frame Structure

According to the result of topology optimization and the functional requirements of the frame structure, we redesign the dump truck frame. Figure 7 is the new frame structure. The longitudinal beam of the frame was changed into straight beam which is variable cross section structure, the middle section is wide and the ends of the frame are narrow. Beam arrangement has changed greatly, the second and third arched beams have been changed into back-to-back type which position changed corresponding. According to the actual measurement, the new frame meets the installation requirements Assemblies and components. There is no interference between the new frame and the drive shaft. The original frame and the new frame quality contrast as shown in Table 1. Although the weight of new frame increase 87 kg, material distribution more ideal and strength of frame increase.

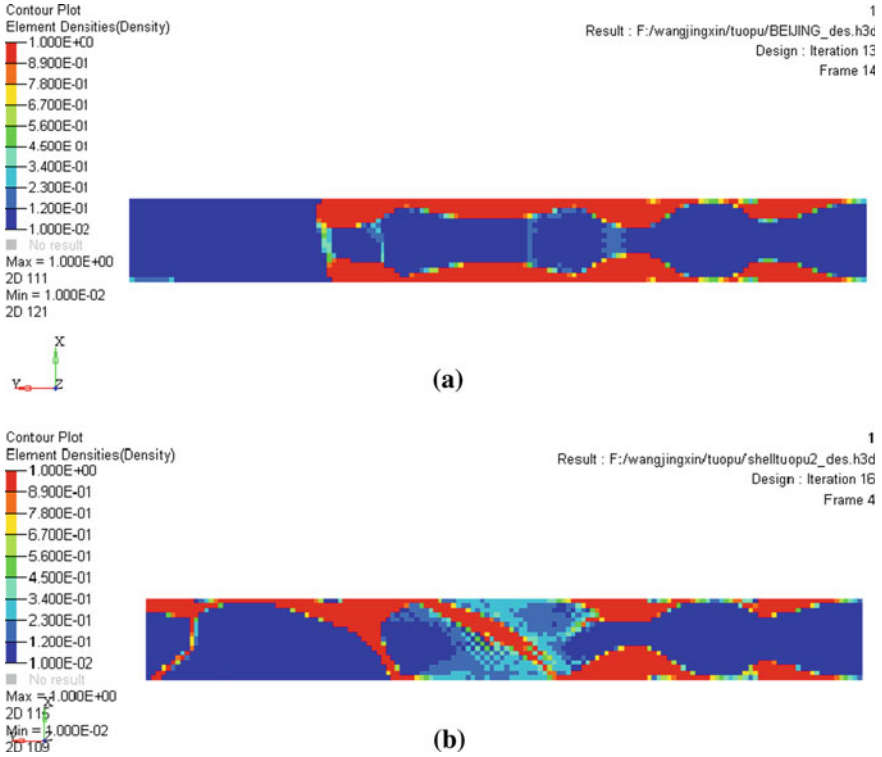


Fig. 6 Results of topology optimization. a Bending analysis, b Torsion analysis

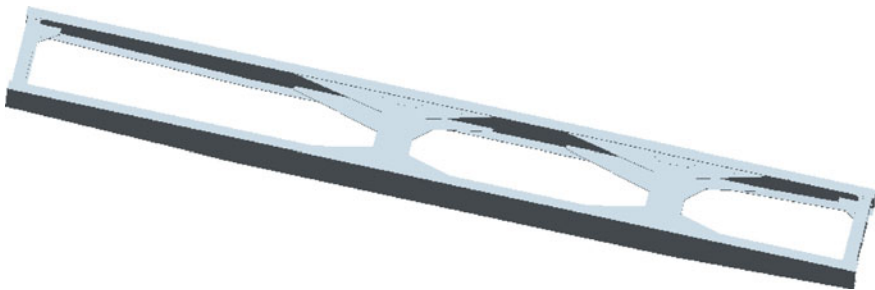


Fig. 7 3D model of the new frame structure

Table 1 Comparison of the frame mass between original frame and new frame

	Original frame	New frame
Mass (Ton)	1.093	1.18



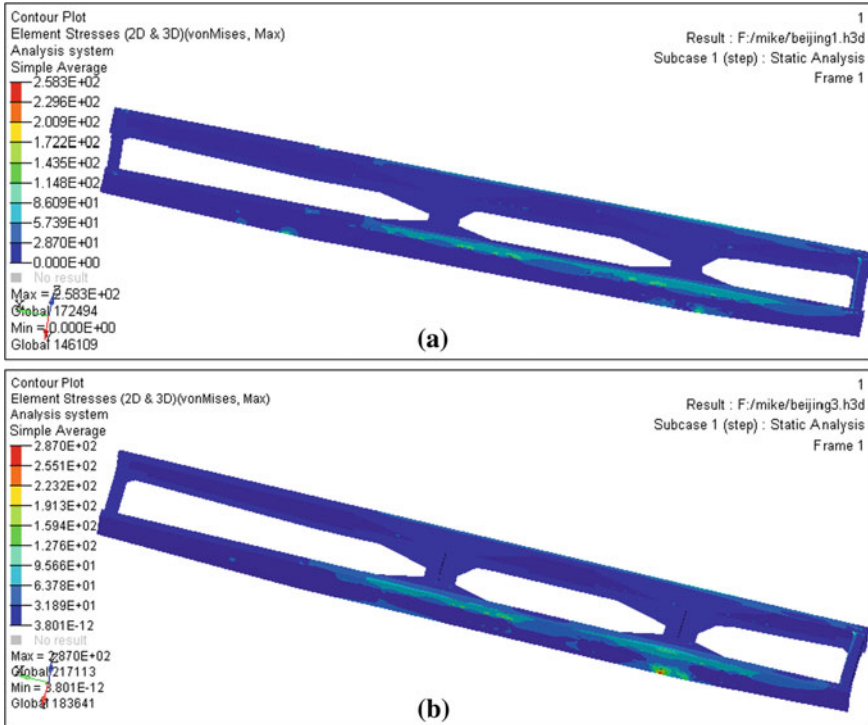


Fig. 8 Stress distributions of new frame. a Bending analysis, b Torsion analysis

## 4 New Frame Structure Analysis

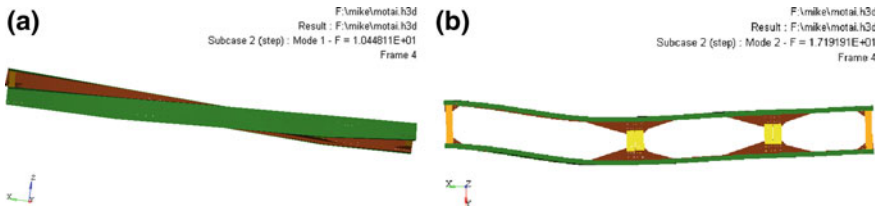
### 4.1 Steady-State Mechanics Analysis

To analysis the frame structure in HYPERMESH software, the stress distributions of frame under the bending condition and torsion condition can be got in the HYPERVIEW as Fig. 8.

Two kinds of condition show that the stress of the junction between balance suspension and the frame is large. The maximum stress occurs at the connecting hole of balance suspension and the frame. It shows the maximum value on the bending condition is 258.3 MPa, on the torsion condition is 287 MPa. This is caused by the frame load. Compared with the original frame, the stress is obviously reduced. The maximum stress contrasting results between original frame and new frame are given in Table 2.

**Table 2** The maximum contrasting results between original frame and new frame

Stress	Original frame	New frame
Bending (MPa)	322	258.3
Torsion (MPa)	348.4	287

**Fig. 9** Modal frequencies and modal shapes of first two orders after optimized. **a** The first order torsion (10.45 HZ) **b** The first order bending (17.19 HZ)**Table 3** Comparison of the modal frequencies of first two orders

Frequencies	Original frame	New frame
The first order bending (HZ)	8.04	10.45
The first order torsion (HZ)	10.64	17.19

## 4.2 Modal Analysis of New Frame

Modal natural frequencies and modal shapes of first two orders as shown in Fig. 9. A contrasting result of the first two natural frequencies between original frame and new frame is shown in Table 3. The result shows that the first two order frequencies of new frame are improved, which imply a good dynamic characteristics.

## 5 Conclusions

In this paper, the frame structure performance are obtained by static and dynamic analysis, and the frame model of topology optimization is established based on variable density method to carry out the local topology optimization. The stress in front of the heavy dump truck frame is low, longitudinal beam adopts the variable cross-section structure can be appropriate to increase the material utilization rate. To strengthen frame part, such as lift cylinder installation, stress was significantly reduced by beam strengthening design. The frame optimization structure is analyzed and verified by finite element method, analysis results show that the frame overall stress level and dynamic properties are significantly improved.

## References

1. Liu D (2009) Finite element analysis and optimization of heavy duty truck frame. Master thesis, Hefei University of Technology, pp 1–27
2. Zhu L-P (2011) Finite element analysis and improved design of heavy tipper frame [J]. *Mech Des* 28(2):74–76
3. Lu LP (2009) Topology optimization design and finite element analysis of truck frame. Master thesis, Hefei University of Technology, pp 17–24
4. Fukushima J (1992) Shape and topology optimization of a car body with multiple loading conditions. SAE technical paper series 920777, pp 1–3
5. Zhang S-L, Kang Y-C, Wang W (2011) Topology optimization for a mini-bus frame structure [C]. International technical conference of Altair 2011 HYPERWORKS
6. Zhao Z, Wang T, Chen Z (2012) Optimization design of tipper frame based on sensitivity analysis. *Mech Sci Technol*

# Bridging the Gap Between CAD and CAE in Composite Structures Development Process for the Automotive Industry

Samouil Saltiel, Michalis Giannakidis and Nikos Toulas

**Abstract** Composite materials demonstrate significant advantages such as weight saving potential, increased strength and larger design flexibility, but these are combined with significant design restrictions and considerations. In order to exploit the most composite materials potential, cost and time effective design, analysis and manufacturing processes are required. Composite materials, specially the fiber reinforced laminated composites, are increasingly becoming attractive to the Automotive Industry due to their properties. The existing practices for the design, analysis and manufacturing, previously used in other industrial sectors, are proved insufficient for complex composite structures, intended for massive production, in affordable cost for the consumer. In order to reach the required performance characteristics, the Automotive Industry, needs to establish new design processes and deploy software tools that facilitate them. This applies not only to CAD, but also to CAE analysis and simulation that already plays an important role to the upfront design. Consequently, innovative methods and tools are also required for the CAE pre-processing, analysis and post-processing, of complex, large scale product models of composite materials. Moreover, bridging the gap between CAD and CAE, with specialized data handling solutions emerges as a challenge. The aim of this work is to highlight the Automotive Industry's requirements for the improvement of the design and analysis methodologies for the development of composite material parts and complex structures and to showcase offered solutions. New software tools for the modelling, simulation and analysis of the behaviour of fiber reinforced laminated composites, which have been developed and integrated into the complete pre- and post-processing environments

---

F2012-E03-016

---

S. Saltiel (✉) · M. Giannakidis · N. Toulas  
BETA CAE Systems S.A, Thessaloniki, Greece  
e-mail: sam@beta-cae.gr

of ANSA and  $\mu$ ETA software, are presented. The deployment of these software tools within the industry's processes is demonstrated. The bridging of the gap between CAD and CAE is examined with cases of interfacing between software tools oriented to the design of composite materials parts with the CAE pre- and post-processors. The emerging conclusion is that significant time and cost reduction can be achieved by the introduction of efficient and smart CAE software tools and methods, which effectively stream and process the composite materials parts design data towards the products behaviour simulation and further more downstream to the comprehensive results study for preemptive decision making.

**Keywords** Composite materials · Fibber reinforced laminated composites · CAE pre-processing · CAE post-processing

## 1 Introduction

Among of the performance targets for the contemporary and future car development are the body weight reduction and the strength optimization. These are driven, among others by the requirements for the reduction of carbon emissions, economy, recycling etc. One of the factors on which the industry focuses in order to reach the target of the evolution for lightweight vehicles is the use of lightweight materials, with fiber-reinforced composite materials being increasingly important [1, 2].

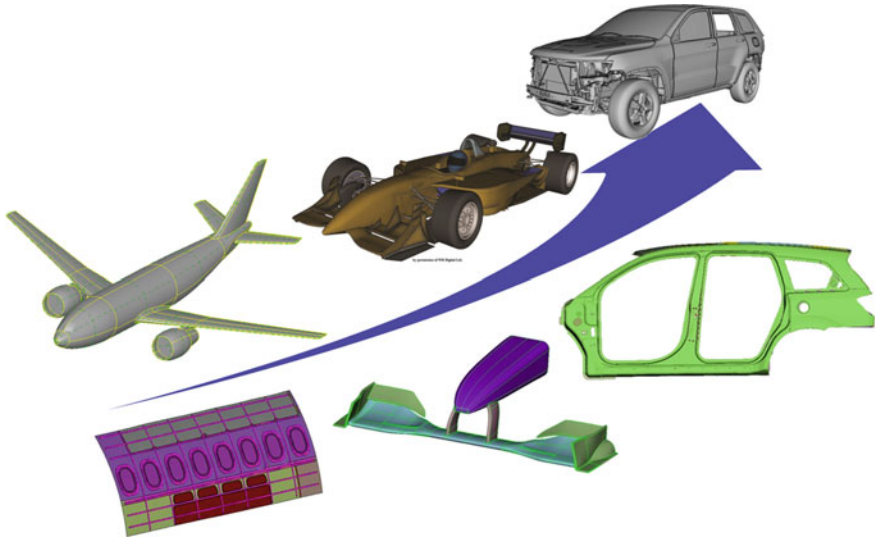
The use of new materials is becoming increasingly complex and introduces new challenges because, among others, new CAD data and simulation methods have to be introduced for the cost and time efficient design and the upfront prediction of the car's behavior with computational methods [3].

## 2 Challenges in the Automotive Industry

Composite materials and fiber-reinforced materials particularly are not new to the Industry. They are widely used in the aerospace industry and the motorsport for long time. They are not unknown to the automotive industry either, as they are used for server decades, but for applications with low production volumes.

The above mentioned industries differ to each other to the following key points that influence the introduction of the fiber-reinforced materials to the product design (Fig. 1).

In the aerospace industry, we meet: long product development cycles, few product variants, simple and repetitive geometries. In the motorsport, we meet: short product development cycles, few product variants, complex geometries, but non massive production. At the same time, in the automotive industry, we meet: short product development cycles, large number of product variants, complex



**Fig. 1** Complexity of parts geometry is increased in production car industry

geometries, large number of parts per product, and the most important, massive production, addressed to a competitive market that expects affordable products.

The necessity for the use of composite materials in the automotive industry today, is not limited to niche market applications, or secondary parts, as in the past. Those materials are being used for important load carrying structural components, whose performance should be studied thoroughly.

An impeding factor for the fast grow on the use of composites in the automotive industry is also the geometric complexity of the automotive vehicles structures, which introduces additional design concerns, along with significant difficulties in the upfront simulation of the product’s behavior. Even though the use of fiber reinforced materials, thanks to their properties allow the simplification and consolidation of some parts, up to a point, the automotive parts geometry remains quite complex due to several reasons such as: the styling requirements, the need for combining composite to metallic components, the necessity to maintain openings for wiring, instrumentation, venting etc.

Another factor that contributes to the maintenance of the complexity of the parts is that designers, traditionally, were designing parts from isotropic metallic materials, which require different considerations for granting to those parts the required behavior. So, designers several times still implement traditional design methods, until training gives them special design skills and experience leads them to new approaches.

Moreover, the design of new products for mass production in the automotive industry is usually extensively based on existing products designs. This imposes startup restrictions and decreases the margin for drastic part design modifications and innovations.

This complexity in part and product level propagates from design to analysis. Analysts who pursue the validation of the complete vehicles behavior have to deal with a large number of parts with complex geometry connected by a large number of different connections.

A typical part is made of tens of individual plies of various materials, each having a unique shape, orientation, and location. This complexity is compounded by the fact that in most cases the final design of a part cannot be analyzed in its to-be-manufactured state. This greatly increases both the perceived and real risk of using composite materials [4].

In the automotive industry, there is always a need for low cost and short time product development, using high performance software and procedures. As the spreading of composite materials brings new conditions to car development, the software must be able to meet the new challenges.

### 3 Meeting the Challenges

Several software solutions are being offered for streamlining a design and analysis process for composite parts [3]. CAD-integrated software products for composites are being used in order to determine the initial and final shape and lay-up of the part to meet the product's specifications. At the same time, during the product behavior simulation, dramatic changes in fiber orientation can occur, inducing large thickness changes, loss of laminate stack-up symmetry and balance. All of these issues can have a considerable effect on the detailed design of the final part and correlation to test results. It becomes apparent that the tight integration of composites design software with an advanced CAE pre-processor is required, which allows analysts to access the same CAD master model of a composite part in its to-be-manufactured state, at any time during the design process, and verify that the part meets the design requirements. Moreover, several analyses of the overall structure performance are required in order to assure that the weight, stiffness, strength and crashworthiness of the vehicle meet the required performance specifications.

A two-way interaction between designers and analysts, allows the multiple iteration of design changes to CAE and updates to detailed design and properties back to the CAD model [5]. Eventually, this integration accelerates the conclusion to a final product design, with assured performance characteristics, with reduced cost.

The CAE pre-processing software to be introduced in the laminates design and analysis cycle should be able to meet the special challenges emerging in the automotive sector, as described above, in a highly productive and efficient manner. Also, it needs to remove from CAE modeling all the solver induced concept restrictions and terminology, and handle modeling in an abstract manner.

The majority of the software in the field, offered as a solution for complete process, or the solutions combining different software, is able to address issues related to single part design. The presented solution is able to handle full-model

built-up, of models comprised of a large number of parts, of a variety of materials and properties, joined with numerous and of different type connections. This solution, apart from having the proved legacy of efficiently completing FEA modeling procedures, is enhanced with a Laminates Tool, properly designed for the level of tasks to be performed by an analyst.

The implementation of laminates modeling functionality into a high-performance CAE pre-processor for the full model buildup is also supported by the fact that such software is also able to handle efficiently the model updates, to build and handle model variants and to perform multidisciplinary modeling for numerous FEA solvers. It allows the analyst to master composite parts properties and detailed composite lay-up descriptions, with the required level of abstraction, and with capability to adapt the model to the requirements of the analysis type.

In addition to the above, analysts demand to evaluate analysis results of complex models in a high-performance manner, with direct references to the initial materials of the design process. Therefore, special consideration is given to the provision of automated tools for the post-processing of results deriving from the analysis of products from laminated composites. The findings and conclusions of this stage have to be meaningfully redirected to the designers for the design improvement.

On that ground, the Laminates Tool, and other special features were developed and integrated within ANSA pre-processor of BETA CAE Systems S.A. [6, 7], which already meets the aforementioned requirements. Also, the Composite Post Toolbar is offered within  $\mu$ ETA post-processor of BETA CAE Systems S.A. [8], integrated with the rest of the high performance functionality of the software, is developed to meet these challenges.

Interfacing this tool to the software intended for the detailed design of the parts from composite materials is imperative and allows the iterative, non-linear product development. These tools are able to interface with dedicated software for the design of laminated parts, which are already deployed in the automotive industry, in order to allow analysts to operate on the same detailed ply layup and true fiber orientations defined on a master design model and the designers to exploit the analysis results and update their data towards the products improvement. In such an environment, designers and analysts still focus on their domain of expertise, using their own software tools.

## 4 The Process and the Tools

As depicted in Fig. 2, the design/analysis integration process involves the CAD-based laminates design software, ANSA, the advanced CAE pre-processor with laminates modeling capability, the solver, and  $\mu$ ETA post-processor.

The design cycle may start in the CAD-based laminates design software (\* in Fig. 2), with the detailed definition of an initial layup, or within ANSA (\*\* in Fig. 2), with the meshing of the geometric part.



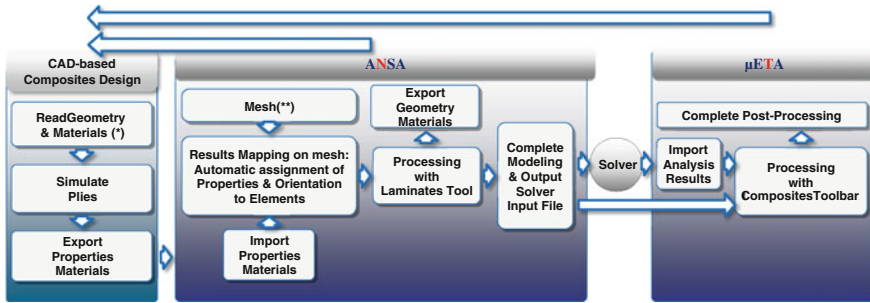


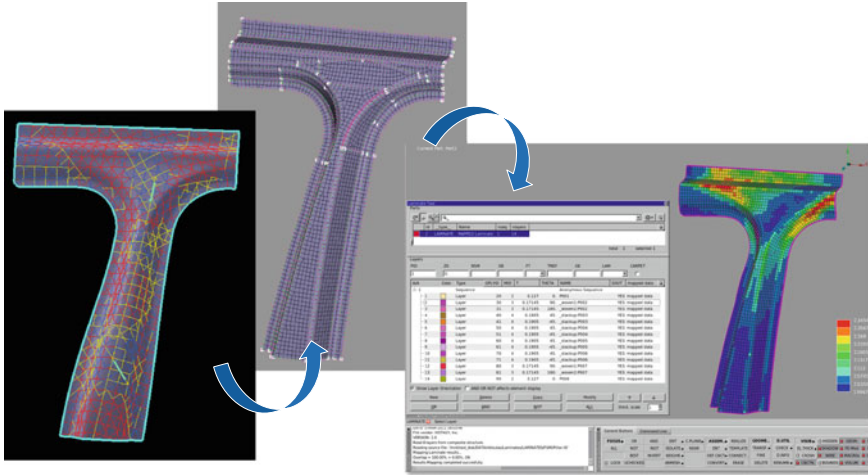
Fig. 2 Design/analysis integration process for laminates design

The CAD-based software, defines an initial composite layup, which includes definition of materials, boundaries, orientations etc. of the laminates layers, taking under consideration numerous manufacturability factors and effects. ANSA is able to import and properly parse the data exported by the CAD software, in order to adapt them into meaningful input to the analyst.

The ANSA Results Mapping tool is used to map the laminates information, derived from CAD-based software, to the discipline specific finite element mesh model within ANSA. In principle, the various FEA meshes, defined and handled by ANSA in order to accommodate the requirements for analysis for different disciplines, are not identical to the one initially used by the design software. Different levels of model idealization, simplification or details capturing may be used. Therefore, the ANSA Results Mapping tool plays a strategic role for the adaptation of the laminates definitions to CAE. The mapping procedure using the ANSA Results Mapping tool, leads to the lossless assignment of: material orientation, material definition, element thickness per layer and element orientation per layer, attributes to the CAE meshed parts (Fig. 3).

The ANSA Laminates Tool then allows the analyst to visualize, check and modify the FEA model laminates properties. The local orientation of the laminates influences significantly the strength or failure of the components. A change in fiber orientation by only  $15^\circ$  from the desired orientation can reduce the part's strength by 75 % [9]. More over the stacking sequence affects the part's performance. Therefore, as analysts need to investigate the contribution of composites to the model's performance, comprehensive tools that allow them to control the laminates properties definition are being offered.

A special Laminate Property generated in ANSA is used for the management of composite parts. Through this, the user can build a composite model, defining or modifying all the Layers and Sequences (Groups of Layers) without any concern for the solver induced constraints. During FE-model output, ANSA writes out the appropriate keywords, with properly filled-in fields, for the accurate representation of the model for each solver. Composite material and property for NASTRAN, LS-DYNA, Abaqus, RADIOSS, ANSYS and Pam-Crash is supported.



**Fig. 3** Streamlining and mapping of laminates design attributes on CAE-meshed model

Through the Laminates Tool, in combination with a collection of software features, the analyst can master the laminates model to be submitted to the solver. ANSA enables the analyst to perform through a graphics user interface and with the assistance of comprehensive interaction, several distinct tasks, such as to:

- Visualize, check and modify the material orientation.
- Check the material definition.
- Synchronize the material definition with available material database.
- Visualize the element thickness.
- Visualize element information.
- Review the orientation and thickness values, per layer, through a comprehensive report.
- Manage the properties list.
- Check the laminates property, by acquiring report on nominal thickness and orientation of fabrics.
- Generate summaries and reports of the laminates model.
- Generate and output to CAD updated layer boundaries and layer attributes.
- Create automatically 3d-curves per ply for the ply boundaries and obtain them as geometric description into a file, which can be propagated back to the design.
- Preview how the laminate property will be outputted to each solver.

The final laminates definitions, based on the FEA model as is prepared to be submitted to the solver, can be outputted and returned to the CAD-based composites design software (Figs. 4, 5).

The solver results are being fed into  $\mu$ ETA post-processor for evaluation, report generation and decision making towards the design improvement. In order to accommodate the requirements of the analysis of laminates,  $\mu$ ETA offers an

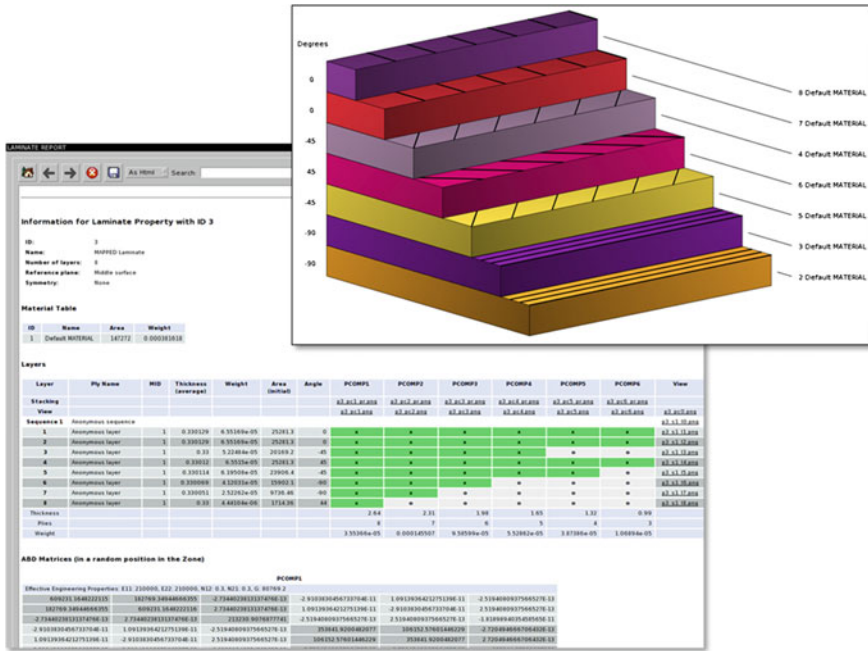
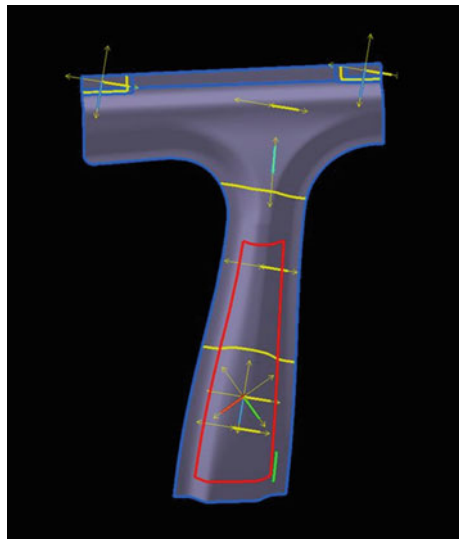
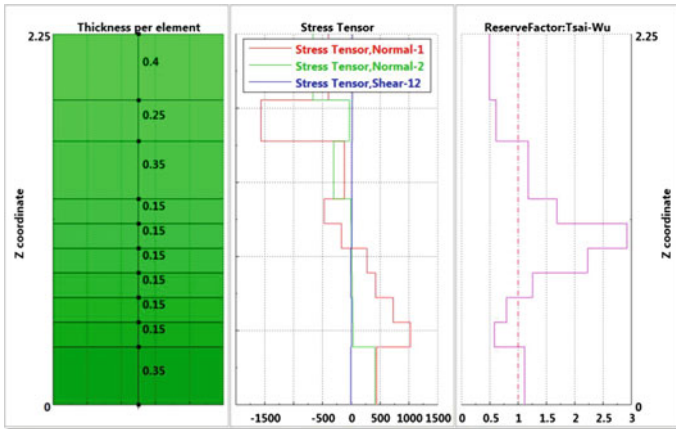


Fig. 4 Visualize the element thickness and information

Fig. 5 Updated layer boundaries and attributes fed back to the CAD-based design tool





**Fig. 6** Plot of stress tensor results across each element thickness, generated by  $\mu$ ETA post-processor

integrated toolbar, a set of specialized functionality, collected into a single user interface. This collection of functions offers:

- Calculation of Failure criteria, Reserve Factor and Effort (Tsai-Wu, Puck, etc.)
- Identification of the layer with the max failure
- Identification of critical directions
- Identification and isolation of failed elements
- Plot of stress tensor results across each element thickness
- Re-evaluation of failure criteria after modifying material properties
- Identification of layers as they were defined in pre-processing.

This set of functions is integrated to the complete post-processing environment of  $\mu$ ETA, therefore, the analyst can end up to an automatically generated report to be used as a decision making tool towards the improvement of the product design (Fig. 6).

Notably, within this procedure,  $\mu$ ETA is able to parse from the solver input file generated by ANSA, additional information related to the layers identification, e.g. their names, which otherwise would not be propagated through the solver.  $\mu$ ETA exploits this information in order to indicate to the analyst the exact positions and layers where issues appear according to the analysis results. Eventually, this critical or failed areas identification can be fed back to the CAD-based design software for further design improvement.

## 5 Full CAE Model Buildup and Results Handling

Analyses based on full-vehicle CAE models are being performed today for the complete product performance evaluation. This imposes a wide range of requirements for the functionality of the CAE pre- and post-processors, which are called to handle a large number of complex data and metadata, and streamline analysis cases to different solvers, with various modeling specifications.

The pre-processor, in brief, is called to:

- import and mesh a large number of parts, in different levels of abstraction and with different specifications,
- compose the full vehicle model by using the proper part representation for each analysis type,
- assemble all the component parts, by using a variety of standard or customized representations of the parts connections,
- and complete the analysis scenario definitions for submitting a ready-to-run model to numerous solvers, for various analysis types, scenarios and disciplines.

The post-processor, in brief, is called to:

- handle results files of huge size, deriving from diverse solvers, accommodating different disciplines and analysis types,
- allow the generation and synchronization of 2D and 3D visuals that interpret those results,
- correlate simulation results to physical test measurements and visuals,
- generate comprehensive reports about the product's performance results.

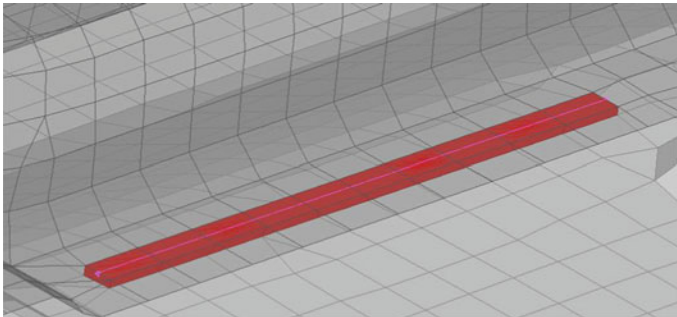
All those, in the environment of the automotive industry, should be performed in an automated way, with minimum user interaction and with high performance.

ANSA pre-processor and  $\mu$ ETA post-processor have a proven record for complete CAE model buildup and analysis results handling [10]. They meet the above requirements and exceed legacy procedures expectations, thanks to the level of automation and customization they offer (Fig. 7).

Among the notable software features is the ability of ANSA to connect the models of the vehicle's parts with a variety of FEA representations, according to the joining type (spotwelds, seamwelds, adhesives, bolts, rivets etc.). As new parts materials are being introduced and new joining methods and materials are being examined or finally used, their FEA representations may exceed the legacy types. ANSA is able to cope with new FEA representations of connections, by having a high level of customization for their generation, the assignment of special properties to them and adjusting the parts mesh at those areas (Fig. 8).



**Fig. 7** Full vehicle body CAE model courtesy of delta motorsport Ltd



**Fig. 8** Adhesive connection FEA representation generated by ANSA connections manager

## 6 Conclusion

The described process and the available pre- and post-processing software features are deployed, in full or partially, today in the automotive industry [11]. The continuous evolution of the deployed method and tools is rapid and their benefits are being increased by the time. Automotive industry, by having available a versatile set of combined high-performance software features, is now able to investigate further the use of new composite materials in more extent, by deploying efficiently a CAD/CAE cycle.

## References

1. Kaiser OS, Eickenbusch H, Grimm V, Zweck A (2008) The future of the car. Zukünftige Technologien Consulting of VDI Technologiezentrum GmbH, Düsseldorf
2. Ghassemieh E (2011) Materials in automotive application, state of the art and prospects. In: Marcello Chiaberge (ed.) Chapter 20 of New trends and developments in automotive

- industry. InTech [<http://www.intechopen.com>] [<http://www.intechopen.com/books/new-trends-and-developments-in-automotive-industry>]
3. Waterman PJ (2011) Options for composites analysis and simulation, desktop engineering, May 2011
  4. FiberSIM (2011) Analysis Interface for ANSA. VISTAGY Inc., Waltham
  5. Guillermin O (2000) Advanced composite engineering using MSC.Patran and FiberSIM, 2nd worldwide automotive conference papers, MSC
  6. ANSA v13.2.x (2011) Users guide, BETA CAE systems SA
  7. ANSA v13.2.x (2011) A guide for setting Up laminate models in ANSA, BETA CAE systems SA
  8.  $\mu$ ETA v6.8.0 (2011) Composite post toolbar, BETA CAE systems SA
  9. Bernardon ED (2012) Automotive composites go high volume—composites for complex curvatures. Polymers and e-mobility in the automotive industry, vol 10. No 1–2
  10. ANSA and  $\mu$ ETA for multidisciplinary CAE pre- and post-processing—solutions booklet, BETA CAE Systems S.A., 2012
  11. Nossek M, Hanigk M, BMW Group (2011) Drapier- und mappingprozess mittels CATIA/CLX/ANSA für CFK komponenten, VDI-Tagung simulation im automobilen leichtbau, Nov 22

# Ensuring Reliability of Automotive Electronics by Using Thermal Analysis

Boris Marovic and Alexandra Francois-Saint-Cyr

**Abstract** With motor control units being located close to the hot motor and navigation systems being located in the air-conditioned passenger cabin, the thermal challenges vary with the product and application. This paper will address how heat can be dissipated most efficiently in various environments and under various conditions, to ensure reliability and product quality. Using thermal and fluid flow analysis for electronics cooling applications, critical component junction temperatures that can be improved can be identified through the visualization of the patented bottleneck and shortcut numbers. The high current and voltage drops running through the PCB traces were simulated with HyperLynx PI and the Expedition PCB interface was used to get detailed PCB traces and both then used for the thermal simulation. By applying these methods, an efficient cooling system can be found for various automotive electronic systems from navigation system and dashboard instruments to engine control units and inverters for EVs and HEVs. Increased shielding from EMI is increasing the complexity of efficiently and easily cooled electronic systems. With the bottleneck and shortcut number, new unseen ways to improve the heat flow path can be detected and used to achieve an efficient cooling system even in complex assemblies. This paper gives an overview of interoperability between ECAD and CFD software with help of interfaces to transfer the PCB layout and power density on the PCB traces to use in detailed Joule heating effects in CFD. It not only considers electronic components as heat sources but also the heating effects in high power traces on the PCB. In

---

F2012-E03-019

---

B. Marovic (✉)  
Mentor Graphics (Deutschland) GmbH, Aachen, Germany  
e-mail: amy\_knutson@mentor.com

A. Francois-Saint-Cyr  
Mentor Graphics, Wilsonville, USA



addition, new post processing methods will be shown to visualize heat flow path shortcuts and bottlenecks to improve the thermal design in ways never visible to engineers before. By using ECAD interfaces and unique post-processing technologies, it is possible to analyse the systems in high detail and evaluate the results by showing directly locations that, when improved, can improve the thermal management. With this type of assistance it is possible to enhance the thermal design to safely cool power electronics and reduce the energy consumption which is especially important to EVs and HEVs where reduced energy consumption increases the traveling range. Weight and size reduction also can be optimized to increase the range of the vehicle.

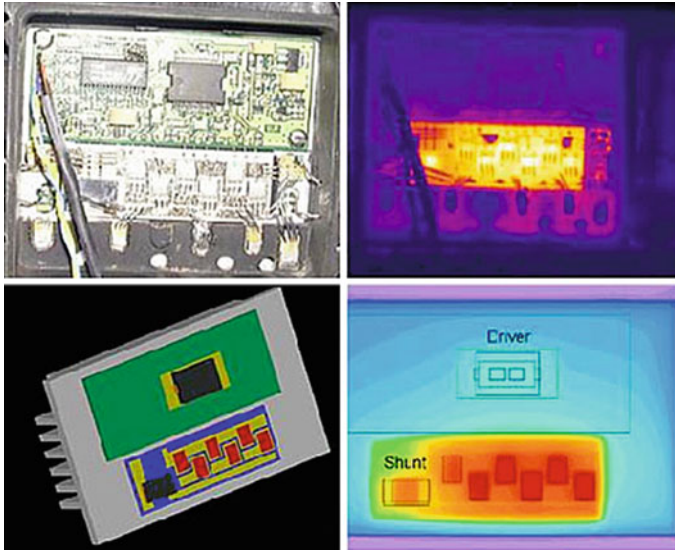
**Keywords** Electronics cooling · Thermal analysis · CFD · PCB · Thermal management

## 1 PCB Thermal Analysis

Thermal analysis of electronic devices in the automotive industry cannot be neglected anymore. With applications such as engine control units (Fig. 1) that are installed somewhere in the engine compartment and are therefore subjected to a harsh environment such as temperatures up to 120 °C, dust, dirt and water exposure, these devices need to fulfil certain criteria. An open enclosure with built-in fans as we know it from notebooks and computers is not possible due to the water and dirt exposure. Different materials and design decisions have to be considered to be able to provide an enclosed housing with great thermal management performance. Natural convection and radiative heat transfer are the only methods to dissipate heat to the environment but within a hot engine compartment, these methods are also limited and have to be applied the best way possible.

Additionally devices such as dashboard electronics (Fig. 2) or Infotainment systems have thermal challenges even though they are not located in a hot environment but in a very crowded environment. The increasing demands for these systems such as lane assist, rear view camera, night vision, heads-up-display (HUD), MP3 player and DVD video capability demand a lot of performance in a tight space but still thermally manageable. Often it is hard to find the right positioning of the single components such as microprocessors on their PCBs as the hot components influence each other depending on their position etc.

With electric vehicles (EVs) and hybrid electric vehicles (HEVs) even more systems come into the car. Systems that control the battery charging, the electric motors, inverters and converters have to take even higher electrical loads than an infotainment system. In these applications the traces on the PCB play an important role as their routing with width changes and bends also create changes in the power density in the trace which is causing Joule heating effects on the PCB and not just heat losses from the components. Thus considering a more detailed



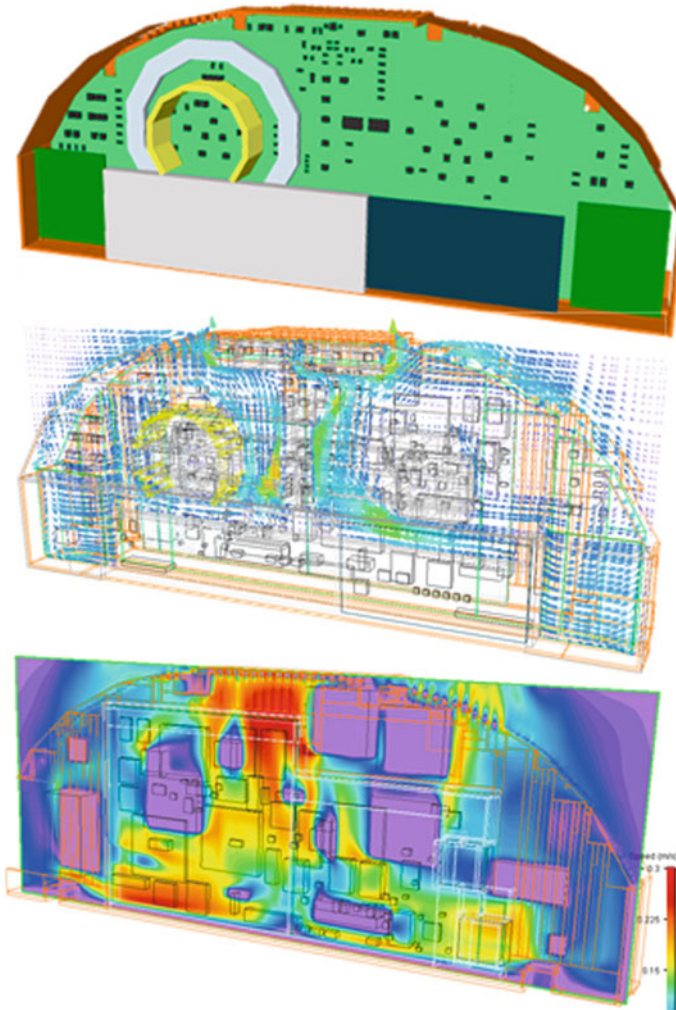
**Fig. 1** Engine control unit system (Courtesy of Valeo France)

modelling of the losses in the PCB traces and power losses in the components, result in better thermal model to avoid trace delamination or melting conditions on the PCB. In addition to that, a detailed copper distribution of the PCB trace layers result in a more accurate heat transfer model of the PCB. Often the PCB is used as a heat sink and therefore a detailed copper content representation is crucial for accurate simulation results.

### ***1.1 Detailed PCB Data Import***

The variety of Electronic Computer Aided Design (ECAD) tools for PCB design is as large as there are Computational Fluid Dynamic (CFD) and Mechanical Computer Aided Design (MCAD) tools. Each of these tools has their own file format to store the information and therefore detailed models with all the information about component size, position and power consumption are stored differently by each software. One way is to use standardized exchange formats such as Gerber files and Intermediate Data Format (IDF) files.

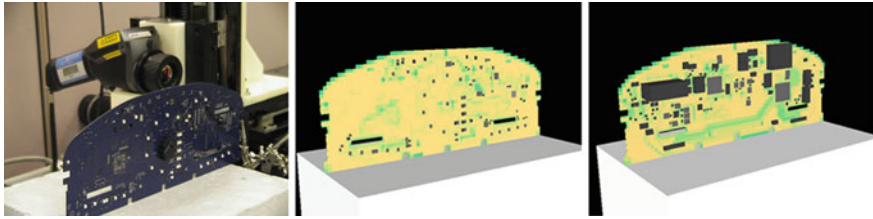
From these files the CFD software can get the information on PCB size and shape, the position and size of the components and also information on the copper traces in each layer. This is the basis for a good representation of the model itself. The 3D model representation is important and since an IDF format does not contain too much detail it is widely spread in its usage as it builds a barrier between the internal knowhow of the supplier of the PCB and the customer. If a Gerber file is not available a simple black and white image of the copper traces is



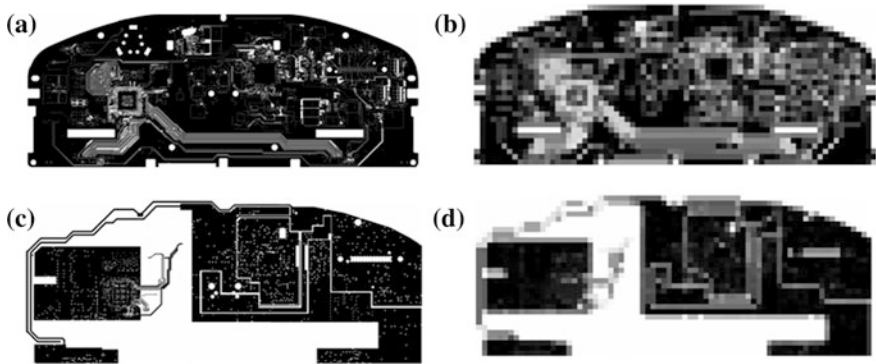
**Fig. 2** Dashboard model in a natural convection case with simulation results

sufficient for a good thermal simulation and also contains no critical and sensitive information.

With the capability to read native ECAD files the CFD software can get better and more detailed information on all the data that is stored in the file, and maybe necessary for a thermal simulation. It is also a convenient way of importing the information into the thermal simulation software. Ideally information on Vias, component power dissipation and thermal resistance models (2R model) can be shared between the two tools. With such detailed information the simulation project setup is almost complete just from importing the geometry information. This can be a huge time-saver when considering large PCBs with lots of



**Fig. 3** Dashboard PCB example: original (*left*), FloTHERM model *top side* (*middle*) and FloTHERM model *bottom side* (*right*) (Courtesy of JCI Automotive Group, MI)

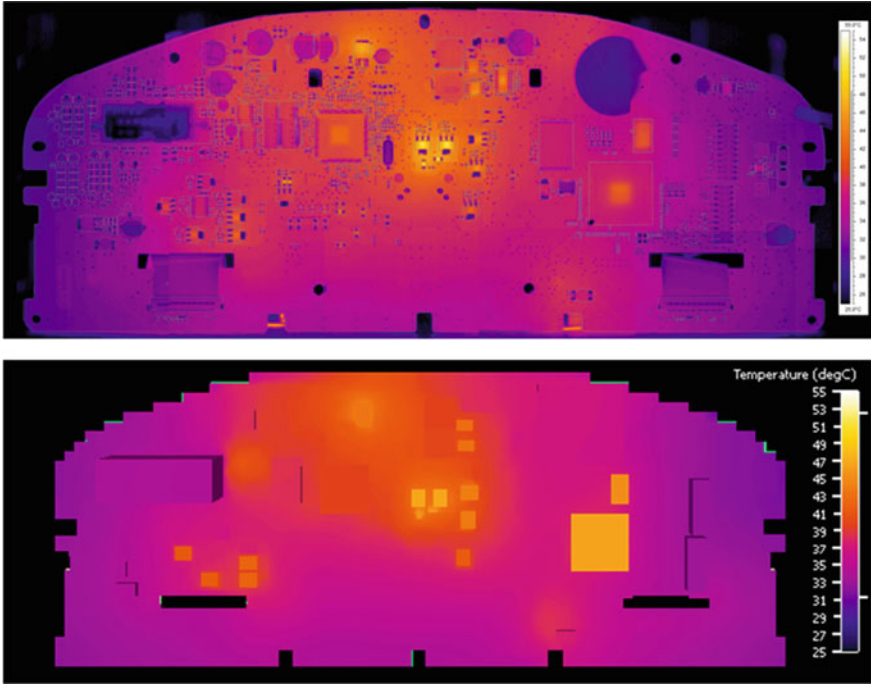


**Fig. 4** PCB trace discretization for CFD simulation: **a** *bottom* trace before discretization, **b** *bottom* trace after discretization, **c** trace 4 before discretization, **d** trace 4 after discretization (Courtesy of JCI Automotive Group, MI)

components whose power dissipation would have to be entered manually. Such interfaces do exist for PCB design tools from Cadence, Mentor and Zuken and with that to the major design tools in the Electronic Design Automation (EDA) Market. An example of a dashboard PCB is shown in Fig. 3.

The representation of the geometry is highly detailed with the shape of the PCB and the single components from small LEDs to larger chips. A detailed representation of the copper distribution in each layer of the PCB is done by an image import. The layers will be pixelated (discretized) and can be very fine or very coarse to adjust it to the necessary accuracy and the optimal calculation time (Fig. 4). Each pixel is assigned a value for  $k_x$ ,  $k_y$  and  $k_z$  as determined by the image processing and becomes a layer patch. A similar approach is used for the Via representation.

The Dashboard was tested in a 26 °C still air environment and had a total dissipation of 9 W. The comparison between Infra-Red (IR) images from the measurements and the FloTHERM simulation show very high correlation (Fig. 5) for the bottom side of the PCB, the top side showed also very high correlation but is not displayed in this paper.



**Fig. 5** Result comparison of the *bottom* side of the PCB: IR image of the tested PCB (*top*), FloTHERM result of the simulated PCB (*bottom*) (Courtesy of JCI Automotive Group, MI)

## 1.2 PCB Trace Power Density Import

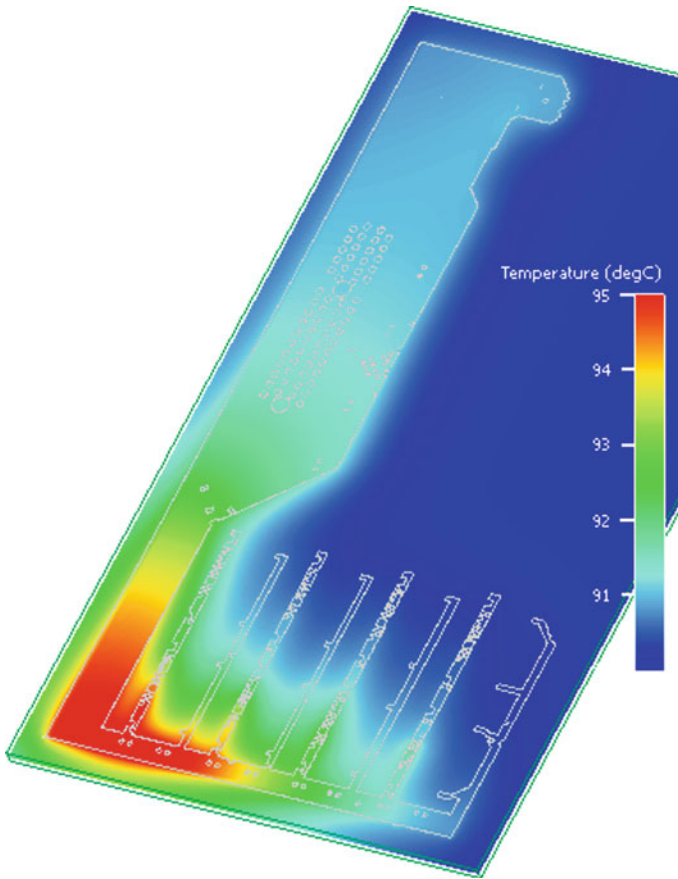
For high power applications the PCBs usually carry thick wide copper traces to reduce the generated heat due to the Joule heating effect of the current flowing through thin traces and therefore reducing the effect of damaging the PCB and the traces due to too hot temperatures. In EV/HEV applications, such traces can carry some hundreds of Volts and Ampere which can create a lot of heat in the PCB itself already, not to mention any power electronic components on the PCB in addition to that.

The power density data can often be calculated also with EDA software such as HyperLynx Power Integrity (PI). Here the software calculates the high current and voltage drops in the PCB nets that can create such additional heating issues known as Joule heating (Fig. 6). Such information imported into a CFD simulation would then consider net self-heating, background heating from active components and the effect of the PCB environment all together and would enable the designer to identify for example trace delamination and FR4 melt conditions.

From HyperLynx PI the data is then represented in an array of power values on each metallic layer that contains a section of the analysed net (Fig. 7). The resolution is chosen to ensure the smallest copper feature is captured and Vias are







**Fig. 8** Thermal simulation result of the power dissipation from the copper trace itself

defined more explicitly with location, diameter, plating thickness and power dissipation.

Finally a thermal simulation of the imported data shown in Fig. 6 for the whole thermal spread inside the PCB is shown in Fig. 8. In this case no active components, which would pose additional heat sources, were included in the simulation.

## 2 Interpretation of Thermal Analysis Results

Since computational fluid dynamics has become a standard in the automotive industry, not just for external aerodynamics for drag prediction but also for thermal simulation of the engine, cabin comfort and electronics, the tools basically have all the same visualization capabilities. Parameters such as velocity, pressure,

temperature and others can be displayed in sectioning or cut plots, surface plots, flow trajectories and other ways but also in numerical form like a variety of parameters with minimum and maximum values of the surface or volume in a spread sheet or single values in pointers directly to the location they are located at.

Often these parameters just give the engineers the idea of the magnitude and some understanding of the flow or thermal behaviour of the analysed model but leave it to him to find a possible solution and the location to apply this solution to solve a thermal or flow problem.

With the, by Mentor Graphics patented, Bottleneck and Shortcut number this guess work is reduced drastically. The engineer receives two parameter at hand which help him find critical areas to improve the heat flow path (Bottlenecks) and areas he can leverage for a better or additional cooling source (Shortcut). By leveraging these parameters the engineer is able to optimize the geometry to a point where the heat flow path is optimized and the cooling sources are leveraged the best way possible. Hence, it is a guide for best thermal design possible for the chose design.

The Bottleneck (Bn) and Shortcut number (Sc) are only thermal parameters, flow optimization such as locating narrow passages for the flow that cause a high pressure loss is not possible.

## ***2.1 Bottleneck Number***

A thermal bottleneck is a path where a lot of heat flows “and” where the resistance is high. With this definition, a variety of such cases can appear in a design, for example when looking at a chip where the large bottom surface of the chip package has direct contact with the PCB but the PCB is covered with an insulation thin paint at this location. The big surface would be a good way to conduct heat out of the chip into the board, away from the chip as the source. Now the heat flow path is big here but the insulating paint is a high thermal resistance.

The dimensionless Bottleneck number is defined as the dot product of the heat flux and temperature gradient vectors. The dot product of two vectors are the largest when the two vectors are aligned and the angle between them therefore zero as the scalar notation shows [1]:  $Bn = |Heat\ Flux \times Temperature\ Gradient \times \cos(\Theta)|$ .

## ***2.2 Shortcut Number***

A thermal shortcut opportunity is where an additional heat flow path might be added to bypass the heat to cooler areas. Also here there are some cases in a design that can occur where an optimized heat flow path can result in a reduced



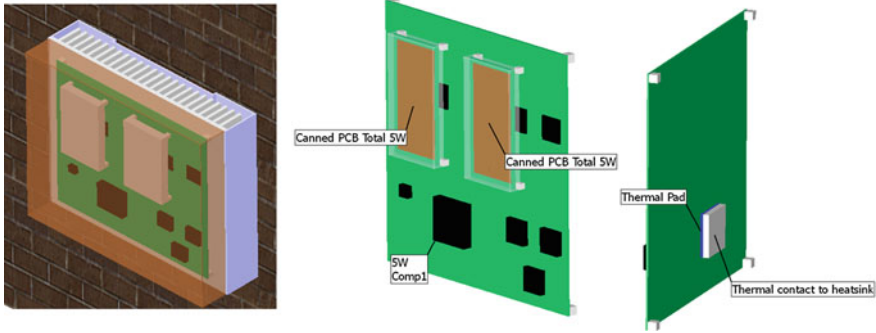


Fig. 9 Wall mounted electronics box demonstration model for Sc and Bn number

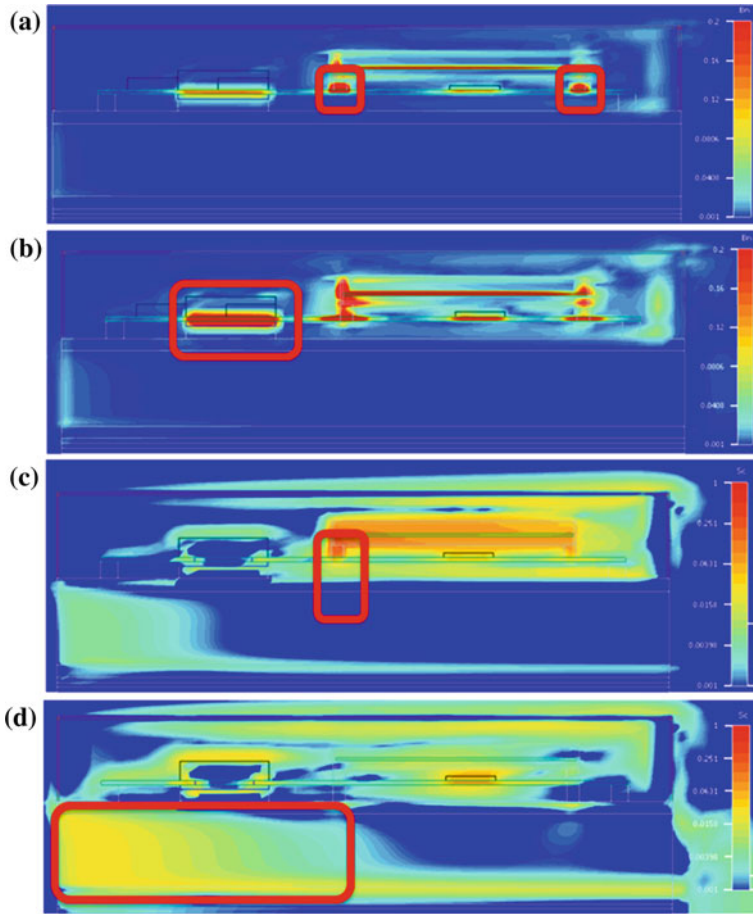
component temperature. For example if there is colder part of the housing directly behind the PCB on which a hot chip is located, maybe a thermal pad or Via can transport the heat either between the PCB and the housing (bridging the air gap) or better contacting the heat flow path through the PCB respectively.

The dimensionless Shortcut number is also calculated from the heat flux and temperature gradient vectors but in this case as the magnitude of the cross product of the two vectors. The amount of the cross product of the two vectors is the largest when the two vectors are at an angle of  $90^\circ$  as the scalar notation shows [2]:  $Sc = |\text{Heat Flux} \times \text{Temperature Gradient} \times \sin(\Theta)|$ .

### 2.3 Application of Bottleneck and Shortcut Number

This example of an application of the two parameters shows how they can be applied to find areas of improvements in the design. The model (Fig. 9) shows a wall mounted electronics box with an active chip and two canned PCBs, both have a heat loss of 5 W and behind the chip is a thermal contact to the heat sink on the back of the electronics box.

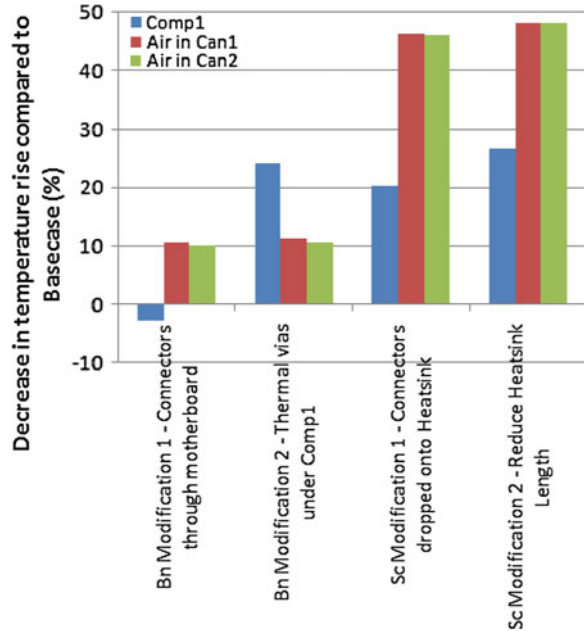
In Fig. 10 one can see the iterative approach to improve the model. Image (a) was the first iteration of the Bn number where a high bottleneck was identified at the legs where the canned PCB is sitting on the larger PCB, and therefore, only a heat flow introduction into the top surface of the PCB and it was improved by putting the legs through the PCB and therefore introducing the heat over the whole depth of the larger PCB. Image (b) then was the second iteration of the Bn number and it was found that the chips conductivity through the PCB to the thermal pad, and connection to the heat sink was the weak spot so some Vias were applied below the chip, which led to an improved conductivity into the heat sink. The third image (c) is the first iteration of the Sc number was again showing a potential improvement at the area of the legs which was leveraged by further extending the



**Fig. 10** Results of the step wise improvements via the Sc and Bn number

legs up to the heat sink and therefore creating a direct contact to a cooling source. And finally the fourth image shows the second iteration with the Sc number where we can see a good cooling capability at the lower end of the heat sink but not so much at the top end which can be explained by a bigger pressure loss due to the long heat sink passage. In this case the heat sink was reduced to only the lower half of the model and the reduction of the temperatures in percentage for each improvement made (Fig. 11) and shows how much the geometry has been optimized due to directly highlighting the bottlenecks and shortcuts for the heat flow.

**Fig. 11** Temperature improvements for each design optimization step



### 3 Conclusion

With a more detailed model setup, by considering detailed model geometry even with copper trace distribution and power dissipation in the copper traces, the results are getting more accurate and closer to the reality. Often this information is not used as there is no interface or capability to use it in CFD tools but it is in some cases strongly necessary to find potential causes of failures over the life time and to avoid them in an early design stage. Also with new visualization techniques such as specialized parameters it is possible to make the life and decision finding for engineers easier and can increase the reliability of a product and save money when considering the heat sink reduction in the example above.

### References

1. Bornoff R, Blackmore B, Parry J (2011) Heat sink design optimization using the thermal bottleneck concept. Proceedings of 27th IEEE SEMI-THERM symposium, San Jose, USA, pp 76–80
2. Blackmore B, Parry J, Bornoff R (2012) Heat sink design optimization using the thermal shortcut concept. Proceedings of 28th IEEE SEMI-THERM symposium, San Jose, USA, pp 195–204

# Effects of Frequency Response Spacing on Vibration Fatigue Analysis

Jasuk Koo

**Abstract** Vibration fatigue analysis, which is established by Dirlik at 1985 for the random load PSD, is widely used to develop automotive components or parts. For the vibration fatigue analysis, normal mode analysis and frequency response analysis precede in order to obtain the system transfer function. The estimated fatigue life by vibration fatigue analysis is highly affected by the frequency request method in the frequency response analysis. In this study, we proposed the most effective frequency request method, which is requiring small number of frequency response points, producing less output file size and giving reasonable results. For this study, we made a primitive analysis model and compared 18 frequency request methods to find out the best method. 18 methods can be categorized by four classes—equally spaced, natural frequency included, half power bandwidth included, and transmissibility frequency included. For each methods, frequency response analysis and vibration fatigue analysis is performed and fatigue life and output file size of each models are compared. As a result, natural frequency peaks play an essential part in fatigue life estimation, so the peaks should not be omitted. Half power bandwidth highly related with damping ratio can provide criteria for the frequency response spacing and transmissibility frequency can set the limit of influence area. The proposed method, which needs only 11 points per natural frequency, reduces output file size by 1/20 and gives 0.69 times of fatigue life compare to 1 Hz equally spaced frequency request method. Current study provides the guide post to frequency response spacing, but the number of request points and the positions may not be the optimal values. We are finding out the optimal values by using optimization process. Most of the vibration fatigue analysis studies

---

F2012-E03-020

---

J. Koo (✉)  
Hyundai Mobis, Seoul, Korea  
e-mail: momo@mobis.co.kr

overlook the frequency request methods, because their models are not so large. For their works, only using equally spaced frequency request method could be sufficient. But nowadays there is a growing need to deal with large size models, so we consider the new method that can deal with large size models. With the proposed method to determine frequency response spacing for the vibration fatigue analysis, criteria of spacing and limit of influence area are set by half power bandwidth and transmissibility. This method could be utilized for the large sized models like as head lamp, front end module or automotive battery system, etc.

**Keywords** Vibration fatigue · Frequency response spacing · Frequency domain · Stress response

## 1 Introduction

Vibration fatigue analysis, which is established by Dirlik [1] at 1985 for the narrow and wide band random load power spectral density (PSD), is widely used to develop automotive components or parts, especially engine part, chassis part, bracket for ABS, hosing of various electronic units [2–11]. In particular, the electronic components of a automobile are subjected to the vibration condition, and the frequency range is so wide that consideration of resonance is necessary.

For the vibration fatigue analysis, normal mode analysis and frequency response analysis precede in order to obtain the system transfer function. The estimated fatigue life by vibration fatigue analysis is highly affected by the frequency request method in the frequency response analysis. With wider spacing, the peak response could be omitted, which result to predict longer fatigue life. With narrower spacing, although we may predict the fatigue result more accurately, data storage and solving time for the analysis increase exponentially.

We proposed the most effective frequency request method, which is requiring small number of frequency response points, producing less output file size and giving reasonable results. For this study, we made a primitive analysis model and compared 18 frequency request methods to find out the best method. 18 methods can be categorized by 4 classes. For each methods, frequency response analysis and vibration fatigue analysis is performed and compared.

## 2 Vibration Fatigue Analysis

In 1964 Bendat [12] proposed the method of determining fatigue life from PSDs. He showed that the probability density function (pdf) of peaks for a narrow band signal tends towards a Rayleigh distribution. And he assumed that all positive peaks in the time history would be followed by corresponding troughs of similar

magnitude regardless of whether they actually formed stress cycles. Using this assumption the pdf of stress range would also tend to a Rayleigh distribution. Bendat’s narrow band solution for the range mean histogram is expressed in Eq. (1).

$$N(S) = E[p]T \left\{ \frac{S}{4m_0} e^{-\frac{S^2}{8m_0}} \right\} \tag{1}$$

$$E[p] = \sqrt{\frac{m_4}{m_2}},$$

where N is the number of cycles of stress range S occurring in T seconds.  $m_0$ ,  $m_2$  and  $m_4$  are 0th, 2nd and 4th moments of area under the PSD, respectively and  $E[p]$  is the expected number of peaks. The nth moment of area is obtained as

$$m_n = \int f^n G(f) df \tag{2}$$

and G(f) is the value of the single sided PSD at frequency f Hz. The term in brackets in Eq. (1) is the Rayleigh distribution. The problem of Bendat’s narrow band solution is that it is extremely conservative when wider band histories are used. The reason for this lies in the assumption that peaks are matched with corresponding troughs of similar magnitude. A wide band time history is characterized by smaller waves riding on a low frequency carrier.

In 1985 Dirlik [1] proposed an empirical closed form solution to the problem following extensive computer simulations using the Monte Carlo technique. Although apparently more complicated than some alternative methods it is only a function of four moments of area of the PSD;  $m_0$ ,  $m_1$ ,  $m_2$  and  $m_4$ . This method has been found to be widely applicable. The Dirlik’s solution is given by Eq. (3) and  $\gamma$  is the irregularity factor.

$$N(S) = E[p]T p(S) \tag{3}$$

where

$$p(S) = \frac{\frac{D_1}{Q} e^{-\frac{z}{Q}} + \frac{D_2 Z}{R^2} e^{-\frac{z^2}{2R^2}} + D_3 Z e^{-\frac{z^2}{2}}}{2\sqrt{m_0}}, \quad \gamma = \frac{m_2}{\sqrt{m_0 m_4}}, \quad D_1 = \frac{2(x_m - \gamma^2)}{1 + \gamma^2},$$

$$D_2 = \frac{1 - \gamma - D_1 - D_1^2}{1 - R},$$

$$D_3 = 1 - D_1 - D_2, \quad Z = \frac{S}{2\sqrt{m_4}}, \quad Q = \frac{1.25(\gamma - D_3 - D_2 R)}{D_1},$$

$$R = \frac{\gamma - x_m - D_1^2}{1 - \gamma - D_1 + D_1^2}, \quad x_m = \frac{m_1}{m_0} \sqrt{\frac{m_2}{m_4}}.$$

Bishop [13] achieved the theoretical verification when a theoretical solution for predicting rainflow ranges from the moments of area of the PSD was produced. The theoretical approach devised by Bishop is computationally intensive and

shows little improvement on accuracy over Dirlik's empirical approach. For this reason, Bishop's method gives credence to the Dirlik's method but is seldom used for analysis purposes. In addition, Bishop [14] carried out a notable comparative study. He computed fatigue lives in the frequency domain and compared these with the life obtained from the time domain approach. In the study, the Dirlik's approach is remarkably robust. After that, there are many applications of Dirlik's method due to its easy usage but good results [15, 16]. Rice [17] developed a theoretical expression to determine the probability density function of peaks for a signal of arbitrary bandwidth. Lalanne [18] used this expression and showed that it could also be used as a basis for determining the probability density function of cycle stress range. Lalanne's formula is given in Eq. (4).

$$N(S) = \frac{1}{\text{rms}} \frac{\sqrt{1-\gamma^2}}{\sqrt{2\pi}} e^{\frac{-S^2}{2\text{rms}^2}} + \frac{S\gamma}{2\text{rms}} \left[ 1 + \text{erf} \left( \frac{S\gamma}{\text{rms}\sqrt{1-\gamma^2}} \right) \right] \quad (4)$$

$$\text{erf}(x) = \frac{2}{\sqrt{\pi}} \int_0^x e^{-t^2} dt$$

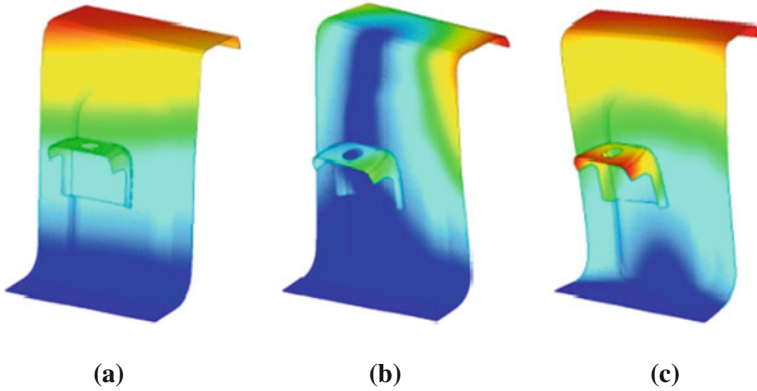
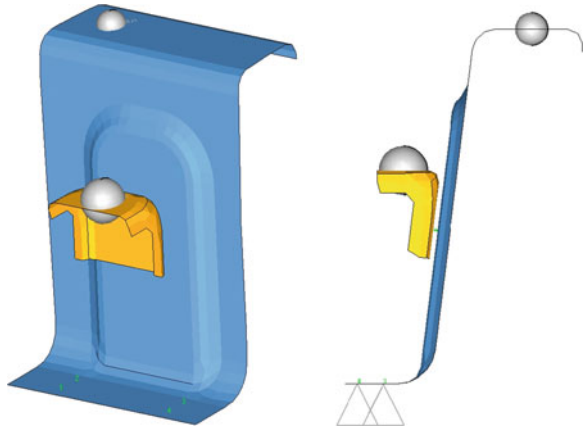
The Lalanne/Rice approach is as robust as Dirlik's approach. It gives similar results and offers the advantage of being less empirical.

### 3 Analysis Model

We are introducing a primitive analysis model shown in Fig. 1. The model is composed with a 2 mm thickness shell plate and two lumped masses—100 and 75 g, respectively. The model size is width: 64 mm, depth: 27 mm and height: 86 mm. It is fixed at 4 points at bottom with 3 translational and 3 rotational constraints. Normal mode analysis is usually used to determine the natural frequencies and mode shapes of a component. It can also be used as the starting point for the frequency response analysis. The model has 3 modes below 200 Hz and 7 modes below 600 Hz. The 1st mode is bending mode at 46.4 Hz and 2nd mode is torsional mode at 173.4 Hz as shown in Fig. 2.

Figure 3 is the frequency response analysis results. That is, when the model is excited with 1 g acceleration in global x, y, and z direction, the each directional acceleration responses at the top of the sheet are recorded in the range between 10 and 200 Hz. The 1st mode which is the global bending mode is related with the x excitation and the 3rd mode is related with y excitation around the frequency of 180 Hz. The 2nd mode is not represented in each directional excitation because the 2nd mode is torsional one. Figure 4a is the stress contour of the model at the 1st modal frequency (46.4 Hz). We can expect that the critical points would be the bolted mounting points in the bottom area and the lower rounded area.

**Fig. 1** Primitive model for FE analysis



**Fig. 2** Mode shapes and frequencies **a** 46.4 Hz **b** 173.4 Hz **c** 186.6 Hz

### 4 Frequency Request Methods

Nowadays there is a growing need to deal with large size models. If we can control the frequency response spacing efficiently, we would deal with large size models easily. To study the effect of the frequency request method in modal frequency response analysis, 18 models are introduced. 18 methods can be categorized by 4 classes. Table 1 is summarized the model descriptions and the number of frequency response points when there are 3 frequency peaks in range of 0–200 Hz.



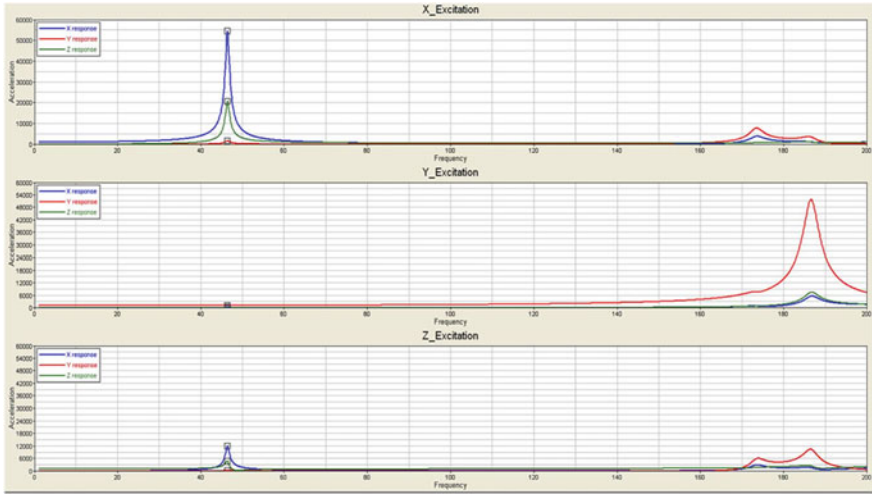
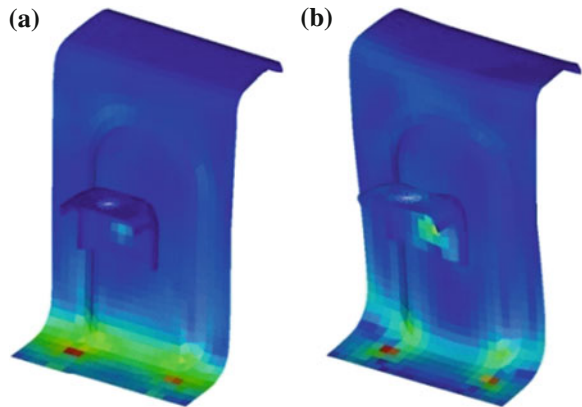


Fig. 3 Frequency response curve

Fig. 4 Stress contour at  
a x excitation and  
b y excitation



### 4.1 Class I: Equally Spaced

This method is most user-friendly method, so many studies are using this method. Model B01, B02, X01 has equally spaced frequency of 1.0, 0.1 and 10.0 Hz, respectively. In case of frequency range between 20 and 200 Hz, each model has 181, 1801 and 19 frequency response points, respectively. Though using more frequency request points gives more accurate results, necessarily more data storage and solving time are required.

**Table 1** Analysis model definition and number of data points

Class	Model	Description	No of Points
Class I	B01	1.0 Hz equally spaced	181
	B02	0.1 Hz equally spaced	1801
	X01	10.0 Hz equally spaced	19
Class II	X02	Natural frequency peaks ( $F_{Ni}$ ) only	3
	X03	$F_{Ni}$ , 5 linear interpolated pts, cluster = 1.0	17
	X04	$F_{Ni}$ , 5 linear interpolated pts, cluster = 2.0	17
	X05	$F_{Ni}$ , 5 log interpolated pts, cluster = 1.0	17
	X06	$F_{Ni}$ , 5 log interpolated pts, cluster = 2.0	17
	Class III	X07	$F_{Ni} \pm n\zeta$ , $n = 0, 1$
X08		$F_{Ni} \pm n\zeta$ , $n = 0, 1/2, 1$	15
X09		$F_{Ni} \pm n\zeta$ , $n = 0, 1, 2$	15
X10		$F_{Ni} \pm n\zeta$ , $n = 0, 1/2, 1, 3/2, 2$	27
X11		$F_{Ni} \pm n\zeta$ , $n = 0, 1, 2, 3$	20
X12		$F_{Ni} \pm n\zeta$ , $n = 0, 1, 2, 3, 4$	25
X13		$F_{Ni} \pm n\zeta$ , $n = 0, 1, 2, 3, 4, 5, 6, 7, 8$	47
X14		$F_{Ni} \pm n\zeta$ , $n = 0, 2, 4, 6, 8$	25
Class IV		X15	$F_{Ni} \pm n\zeta$ , $n = 0, 2, 4, 6, 8, F_{Ni} \pm 1.41F_{Ni}$
	X16	$F_{Ni} \pm n\zeta$ , $n = 0, 1, 2, 4, 8, F_{Ni} \pm 1.41F_{Ni}$	30

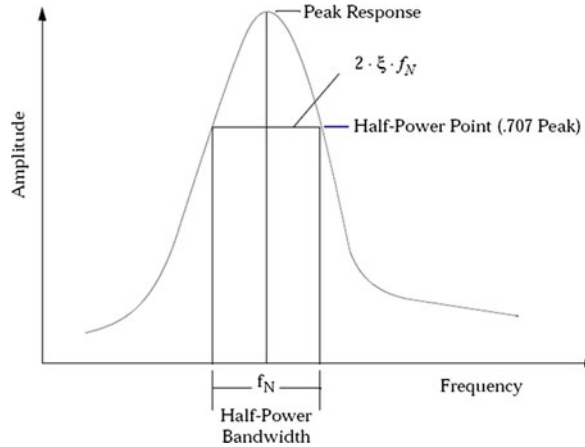
### 4.2 Class II: Natural Frequency Peaks Included

If we always include the natural frequency peaks, we can reduce the frequency response points. MSC.Nastran provides the input card `FREQ3` which enables us to request modal frequency peaks and the set of frequencies between modal frequency peaks. Specifying linear or logarithmic interpolation between frequencies is possible. Clustering is used to obtain better resolution near the modal frequencies where the response varies the most [19].

### 4.3 Class III: Half Power Bandwidth Included

Specifying the amount of “spread” around each natural frequency and the number of equally spaced excitation frequencies within the spread is very important to minimize the analysis result difference between analyzers. The frequency spread can be used also to define the half-power bandwidth. The half power point of an electronic amplifier stage is that frequency at which the output power has dropped to half of its mid-band level. This occurs when the output voltage has dropped by  $1/\sqrt{2}$  or 0.707 (approximately 1.5 dB) and the power has dropped by half (approximately 3 dB). The bandwidth of an amplifier is usually defined as the difference between the lower and upper half power points. This is therefore also known as the  $-3$  dB bandwidth [20]. Half-power bandwidth is given by  $2 \cdot \zeta \cdot F_N$ ,

**Fig. 5** Half power bandwidth [20]



where  $\xi$  is the damping ratio, and  $F_N$  is peak response frequency, as shown in Fig. 5. In this study, damping ratio is used as 0.2. We can use the MSC.Nastran input card `FREQ4` or `FREQ5` for this purpose (Fig. 6).

#### **4.4 Class IV: Transmissibility Frequency Included**

Now we have a question how far we have to spread around each natural frequency. The solution of this question can be found in the definition of the vibration transmissibility. Transmissibility is the ratio of output to input. You will note that for forcing to natural frequency ratios greater than 1, the transmissibility falls rapidly back to the 1.0 value when the  $F_r/F_N$  ratio reaches  $1.414(\sqrt{2})$ , and becomes less than 1 for all values greater than this [22]. So we can define the limit frequency of the each natural frequency as transmissibility frequency ( $1.414 F_N$ ). The best reason of using transmissibility is that transmissibility frequency ( $1.414 F_N$ ) is not affected by the damping value.

### **5 Vibration Fatigue Analysis**

Fatigue analysis is performed by S–N approach using MSC.Fatigue [23]. Fatigue properties of the steel shell plate are estimated using uniform material law by Bäumel and Seeger [24], assuming their ultimate stress 500 MPa. Mechanical properties of steel shell plate for vibration analysis are summarized in Table 2. We used hypothetic PSD profile shown in Fig. 7. It is come from vibration test specifications for the electronic component. But its values are changed properly for our study. The analysis conditions are as follows—analysis method: Dirlik, mean

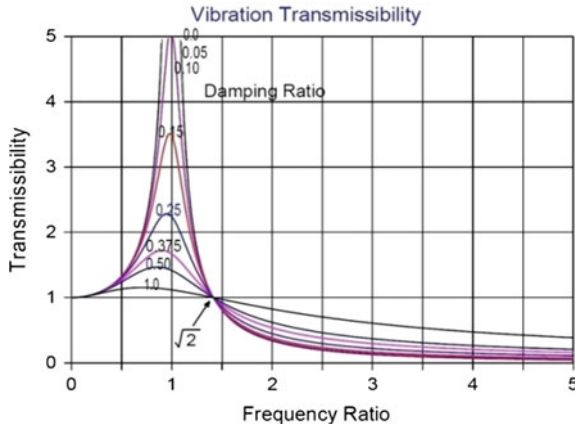


Fig. 6 Vibration transmissibility curve [21]

Table 2 Mechanical properties of sheet steel for fatigue analysis

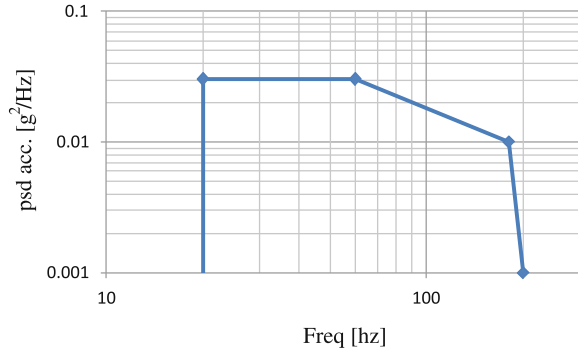
Property	Value	Property	Value
Ultimate tensile strength [MPa]	500.0	Stress range intercept, SRI [MPa]	2269.0
Elastic modulus [GPa]	210.0	Slope, b [-]	-0.1339
Poisson’s ratio [-]	0.3		

stress correction: none, combination method: maximum absolute principal, rain-flow matrix size: 128, and interpolation method: log–log. Most of the selections in the parameter are default values in MSC.Fatigue.

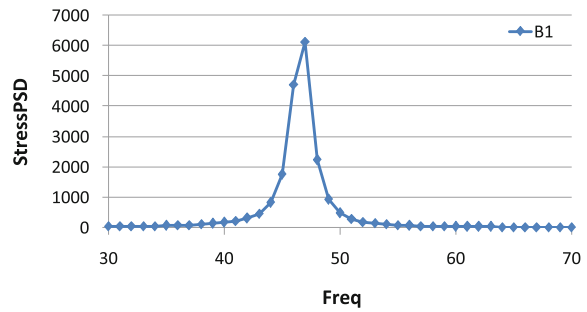
Stress PSD output in model B01 is shown in Fig. 8. The stress PSD is only reported in the frequency response points in the frequency response analysis. When the calculation out of the response point is needed, linear interpolated stress value is used in fatigue analysis. Therefore, it is important to determine the frequency response points around the natural frequency peaks consistently and accurately. For such a reason, if we miss the natural frequency peaks, we would underestimate the stress at the natural frequency peaks. If we are lack of data between the natural frequencies, we would overestimate the stress in the range. Figure 9 is the example of the rainflow cycle counting profile at critical point in model X16. Because Dirlik’s approach do not consider the mean stress effect, the range-mean distributions looks like a curved plate.

The full set of the results at critical location (node A, B) is given in Table 3 and Fig. 10 with various frequency request methods. The point A is located in near the bolting and the point B is located in near bending area. Result file sizes of model X15 and X16 are reduced to 4.5 and 0.45 %, compared with model B01 and B02, respectively. That is, output file size of X16, which needs only 11 points per natural frequency, is only 1/20 compared with 1 Hz equally spaced frequency request method (model B01). But the fatigue life of X16 is 0.69 times at point A,

**Fig. 7** Hypothetic PSD profile for analysis



**Fig. 8** Stress PSD output in model B01



0.57 times at point B compared with model B01. This means that the fatigue life of X16 lies in the range of a factor of 2.

## 6 Discussion

If the frequencies are extracted by equally spaced, the narrower space is better. The frequency space 0.1 and 1.0 Hz does not show significant difference in fatigue life. But the result of the frequency space 10.0 Hz gives 100 times more fatigue life. It can be conclude that each model may have proper frequency response spacing. Natural frequency peaks play an essential part in fatigue life estimation, so the peaks should not be omitted. When we are using the natural frequency peaks, the more interval points, log spacing rather than linear spacing and denser points at around the peaks give better results. Half power bandwidth ( $2 \cdot \xi \cdot F_N$ ) highly related with damping ratio can provide criteria for the frequency response spacing and transmissibility frequency ( $1.414 F_N$ ) can set the limit of area influenced by natural frequency. Current study provides the guide post to frequency response spacing, but the number of request points and the positions may not be

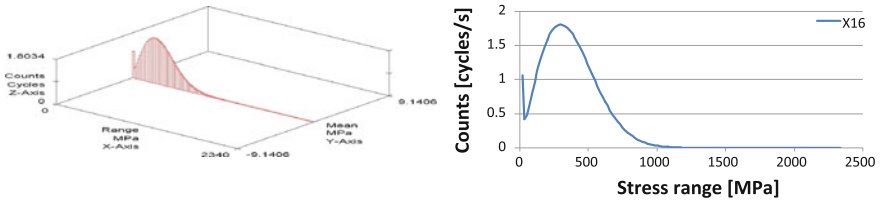


Fig. 9 Rainflow cycle counting results in model X16

Table 3 Vibration fatigue life results for each model

Class	Model	Fatigue life		Life ratio		Output file size	
		Point A	Point B	Point A	Point B		
Class I	B01	8.951	5544.0	1.02006	1.02876	34895	10.2 %
	B02	8.775	5389.0	1.00000	1.00000	341014	100.0 %
	X01	27900	914000	3176.1	169.6		
Class II	X02	0.014	0.021	0.00164	0.00000		
	X03	0.044	0.130	0.00505	0.00002		
	X04	0.085	0.490	0.00970	0.00009		
	X05	0.071	0.325	0.00813	0.00006		
	X06	0.175	0.219	0.01998	0.00004		
Class III	X07	0.020	0.040	0.00231	0.00001		
	X08	0.020	0.040	0.00231	0.00001		
	X09	0.046	0.217	0.00521	0.00004		
	X10	0.046	0.216	0.00521	0.00004		
	X11	0.128	1.916	0.01463	0.00036		
	X12	0.348	15.46	0.03969	0.00287		
	X13	3.373	1302.0	0.38439	0.24160		
	X14	2.366	653.6	0.26963	0.12128		
Class IV	X15	4.752	2048.0	0.54154	0.38003	1537	0.45 %
	X16	6.166	3170.0	0.70268	0.58824	1537	0.45 %

the optimal values. We are finding out the optimal values by using optimization process.

So far, most of the vibration fatigue analysis studies overlook the frequency request methods, because they do not deal with large models. For their works, only using equally spaced frequency request method was sufficient. But nowadays there is a growing need to deal with large size models, so we proposed the new method that can deal with large size models. This method could be utilized for the large sized models like as head lamp, front end module or automotive battery system, etc.

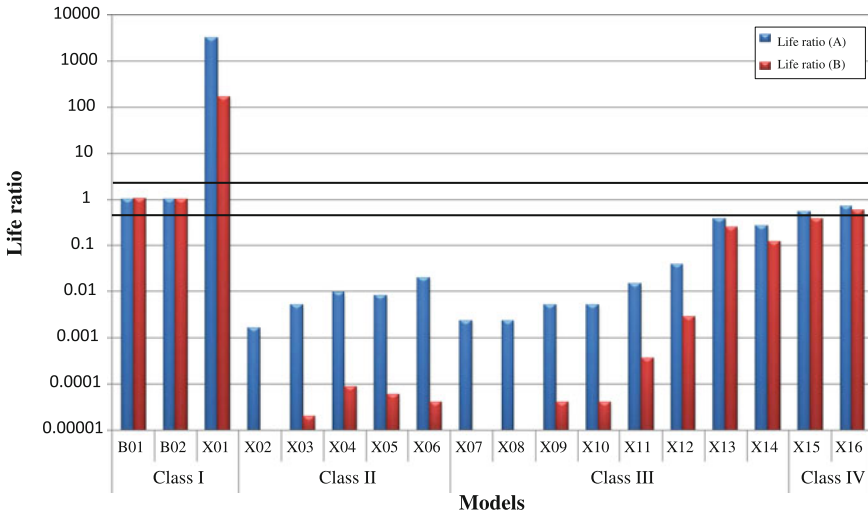


Fig. 10 Comparison of fatigue life ratio among frequency request methods

## 7 Conclusion

We proposed the most effective frequency request method for the vibration fatigue analysis, which is requiring small number of frequency response points, producing less output file size and giving reasonable results. In this study 18 methods are used and they can be categorized by 4 classes—equally spaced, natural frequency included, half power bandwidth included, and transmissibility frequency included. For each methods, frequency response analysis and vibration fatigue analysis is performed and fatigue life and output file size of each models are compared. The model X16 which needs only 11 points per natural frequency produces less output file size and gives reasonable results. That is, output file size and the fatigue life are only 1/20 and 0.69 times compared with 1 Hz equally spaced frequency request method. This method is includes natural frequencies and set criteria of spacing by half power bandwidth, and have a limit of influence area defined by vibration transmissibility. This method is expected to be utilized for the large sized models like as head lamp, front end module or automotive battery system, etc.

## References

1. Dirlik T (1985) Application of computers in fatigue analysis. University of Warwick thesis
2. Koo J, Choi J, Jeon T (2005) Vibration fatigue analysis of automotive bracket. JSAE
3. Koo J, Choi J, Jeon T (2005) Vibration fatigue analysis of automotive bracket subjected to dynamic loading. MSC VPD conference

4. Koo J, Choi J, Jeon T (2005) Vibration fatigue analysis of TPMS housing. KSAE spring conference, vol 3. pp 1421–2106
5. Kim H, Koo J, Baek K (2009) Correlation and validation of analytical models for vibration fatigue prediction of ABS assembly brackets. MSC conference
6. Lee H, Yoo Y (2011) Vibration fatigue analysis of chassis parts considering vehicle durability test. MSC VPD conference
7. Moon S, Cho I, Yoon D (2009) Fatigue life evaluation of mechanical components using vibration fatigue analysis technique. *J Mech Sci Technol* 25(3):631–637
8. Moon S, Jeon J, Yoon D(2009) Determination of component test mode for unit brackets using vibration fatigue analysis technique. KSAE autumn conference, pp 2302–2308
9. Kang K, Chang I, Kim J (2010) Vibration fatigue analysis for multi-point spot-welded SPCC structure considering changes of dynamic response. KSME spring conference, pp 105–111
10. Su H (2008) CAE virtual durability tests of automotive products in the frequency domain. SAE international
11. Rahman MM, Ariffin AK, Jamaludin N, Haron CHC (2009) Finite element based vibration fatigue analysis for a new free piston engine component. *Arabian J Sci Eng* 34(1B):231–246
12. Bendat JS (1964) Probability function for random responses. NASA report on contract NAS-5-4590
13. Bishop NWM (1988) The use of frequency domain parameters to predict structural fatigue. Ph.D. Thesis, University of Warwick, UK
14. Bishop NWM, Hu Z, Wang R, Quarton D (1993) Methods for rapid evaluation of fatigue damage on the Howden HWP330 wind turbine. British wind energy conference, York
15. Andrew Halfpenny What is the frequency domain and how do we use a PSD
16. Andrew Halfpenny (1999) A frequency domain approach for fatigue life estimation from finite element analysis. International conference on damage assessment of structures (DAMAS 99) Dublin
17. Rice SO (1954) Mathematical analysis of random noise. Selected papers on noise and stochastic processes, Dover, New York
18. Lalanne C (2002) Mechanical vibration and shock. vol 3, 4 and 5. Hermes Penton Science, London
19. MSC/Nastran V2007r1 quick reference guide (2007) MSC Corporation, Los Angeles, CA
20. [http://en.wikipedia.org/wiki/Half\\_power\\_point](http://en.wikipedia.org/wiki/Half_power_point)
21. Yang BS Lecture note—introduction to vibration. Pukyung National University
22. [http://en.wikipedia.org/wiki/Transmissibility\\_\(vibration\)](http://en.wikipedia.org/wiki/Transmissibility_(vibration))
23. MSC/FATIGUE V2004 User Manual (2004) MSC Corporation, Los Angeles, CA
24. Bäümel A Jr, Seeger T (1990) Materials data for cyclic loading. Elsevier Science Publishers, Amsterdam Supplement I



# CAE Supported ESC Development/ Release Process

Yiqin Mao, Johannes Wiessalla, Jan Meier, Wolfgang Risse,  
Guy Mathot and Manfred Blum

**Abstract** The take rate of Electronic Stability Control (ESC) systems is constantly growing worldwide. From 2012 onwards ESC systems are mandatory for all new vehicles in the North American and European markets. Due to the continuously growing amount of models and variants, and due to the shortened time for bringing a vehicle to the market, the ESC development and tuning work is increasing rapidly. In addition, the Ford product development process requests ESC performance for the initial prototype release without a physical prototype being available. All these challenges increase the demands on development and sign-off for both the ESC suppliers and for Ford as the vehicle manufacturer. Computer Aided Engineering (CAE) is an enabler to help resolve these issues. A “CAE supported ESC development and release process” (hereafter “CAE process”) has been set up to support these requirements. Within the project, the team developed the CAE process from virtual vehicle testing for the initial ESC design to the ESC performance check in the Software-In-the-Loop (SIL) environment. The corresponding tool chain was developed and verified. The whole CAE environment including post processing and reporting is shared with the ESC supplier. To have confidence in the CAE process, a correlation study with defined test and validation procedures was executed together with the ESC suppliers to verify the entire tool chain. Both Ford and supplier testing catalogues were performed. The simulation results were compared with the real-world tests. Correlation workshops with different vehicle programmes showed positive results, so that both Ford and the suppliers were convinced to jointly run the CAE process. The CAE process is so far well accepted, implemented and applied by the ESC suppliers, so that the initial ESC release can be done without

---

F2012-E03-021

---

Y. Mao (✉) · J. Wiessalla · J. Meier · W. Risse · G. Mathot · M. Blum  
Ford Motor Company, Niehl, Germany  
e-mail: ymao1@ford.com

physical vehicle prototypes. This CAE process may also be extended for other chassis and driver assistance functions/features. The latest regulation of the Economic Commission for Europe (ECE) R13-H allows a CAE based homologation. Following the same validation principle and model fidelity requirement, the same simulation environment can be utilised for ESC certification. This provides further advantage of time saving and completes the CAE usage from ESC development to homologation.

**Keywords** CAE · SIL · ESC development · ESC homologation · Correlation

## 1 Background

Electronic Stability Control (ESC) systems are becoming increasingly standard worldwide. According to regulations FMVSS126 and ECE R13H, ESC is mandatory for all new passenger cars in the USA from September 2011 and in the European Union countries from November 2011 onwards, respectively [1, 2]. Meanwhile, the amount of models and variants keeps growing continuously and the time for bringing a vehicle to the market is getting shorter. These facts result in a dramatic increase of the ESC development and tuning work.

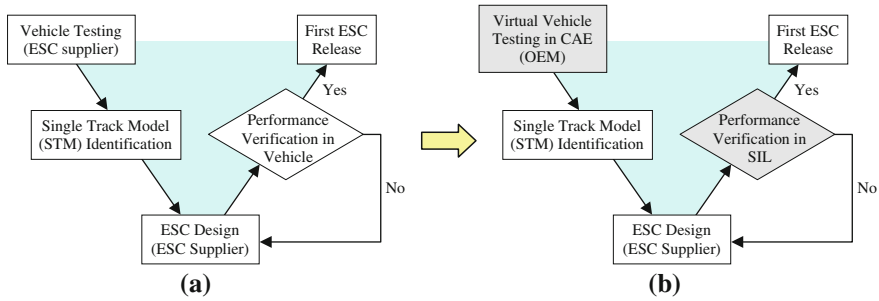
The conventional way for the ESC development and release is based on physical vehicle prototypes. This, however, is connected with considerable costs and time. Furthermore the Ford product development process requests a more flexible, faster and efficient ESC development with a reduced number of vehicle prototypes. The main ESC performance is required for the initial release before a physical prototype of a vehicle is available. In addition, it is useful to show evidence of a functional ESC system for those vehicle variants, which will never be built as physical prototypes. This increases the development and sign-off requirements both for the ESC suppliers and the vehicle manufacturer. Extensive usage of CAE during development and verification is seen as an enabler to cope with these challenges.

## 2 Development of the CAE Process

### *2.1 Transition from a Real-World Vehicle Based Process to the CAE Process*

The above mentioned challenges require a change to the ESC development process. Figure 1a shows a high level V-model of a conventional ESC development.

The left (decreasing) line of the V-model describes the ESC development. The right (increasing) line represents the ESC performance verification. Conventionally,



**Fig. 1** Transition from the real-world vehicle based process to the CAE supported process. **a** Real world based ESC development. **b** CAE supported ESC development

the ESC is developed and verified in a physical prototype vehicle. Since the main ESC functionalities have to be shown for initial release before the physical prototypes are available, the V-model has to be adapted to Fig. 1b. Here the vehicle tests for the identification of the bicycle model (Single Track Model, STM) and the ESC performance check are carried out in CAE instead of in a physical vehicle.

### 2.2 Overview of the CAE Process

Figure 2 shows the comprehensive CAE process.

The process can be divided in following parts (separated with the dashed lines): the Single Track Model (STM) parameter identification, the ESC control development and the final verification and release.

The process steps done by Ford and by the ESC supplier are marked with different colours as indicated at the bottom left in Fig. 2. A mix of colours indicates joint work of both partners.

### 2.3 STM Parameter Identification

In this phase, the ESC supplier defines the manoeuvres, signals and the data format for the STM parameter identification. Without a physical vehicle prototype existing, Ford is responsible for delivering the simulation results for these manoeuvres in CAE. Vehicle properties—like vehicle mass, wheel base and steering ratio—are provided by Ford as well. The responsibility of the STM parameter identification itself should stay at the ESC supplier.

The virtual vehicle testing for the STM identification is carried out in ADAMS, a multi-body-system simulation program. The ADAMS model is considered as a good representation of the target vehicle.

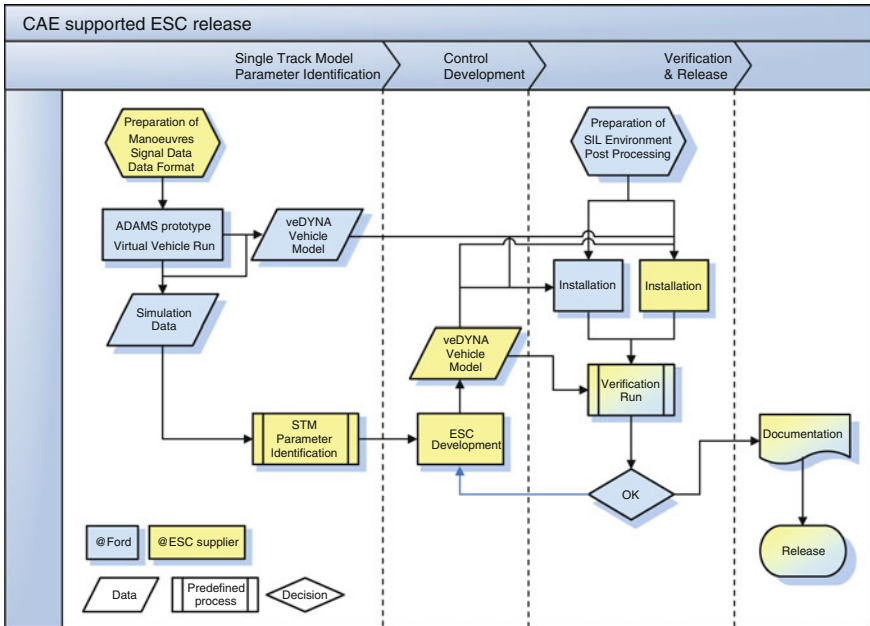


Fig. 2 Overview of the CAE process

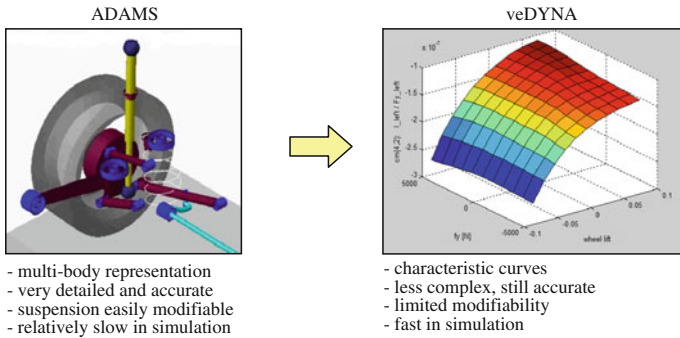
### 2.4 ESC Control Development

In the second part, the ESC supplier develops the ESC, which is based on its own procedures, but done with the virtual vehicle results instead of the real vehicle output.

### 2.5 Performance Check in SIL for Verification and Release

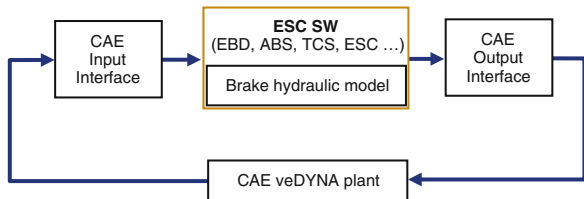
For the third part, the SIL environment is developed by Ford. To have the real-time capability, the SIL environment is based on veDYNA/Matlab/Simulink. Ford is responsible for the veDYNA vehicle model and the post processing tools. The ESC supplier is responsible for delivering the ESC algorithm and pertinent subsystems (i.e. hydraulic brake system). The ESC algorithm is provided in compiled form (e.g. Simulink S-function) to preserve the intellectual property.

The veDYNA model is simpler and faster than the ADAMS representation but still delivering the required accuracy. To keep the vehicle characteristic as consistent as possible, Ford established a virtual tool chain to structure-wise generate and parameterise veDYNA models from the ADAMS vehicle dynamics models. Many components like the tyres are not simplified, while the multi-body



**Fig. 3** Conversion of ADAMS to veDYNA

**Fig. 4** Implementation of the ESC software-in the SIL environment

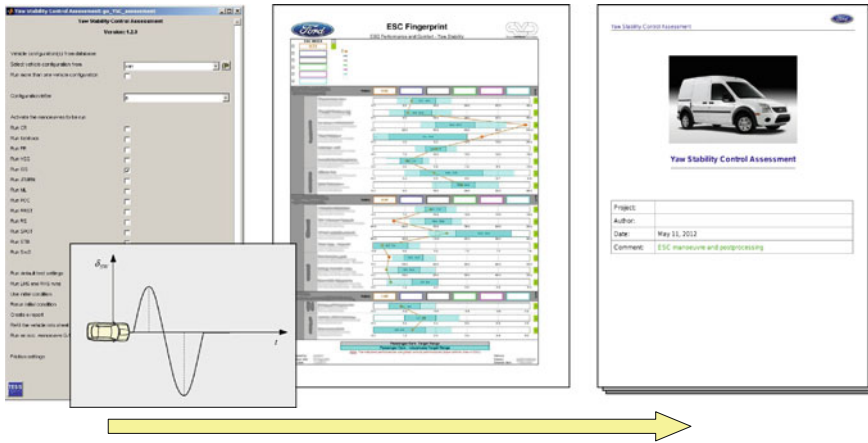


representations of the suspensions are converted to kinematics and compliance look-up tables (Fig. 3). To ensure the quality of the conversion, a quality check with defined test procedures is carried out against the ADAMS model with checks from system level (e.g. the suspension) to full vehicle level (full vehicle simulations).

Using defined interfaces, the delivered ESC software is integrated into the veDYNA vehicle model. Figure 4 shows the architecture of the SIL environment. In the virtual world, the vehicle is equipped now with the ESC system and ready to be driven for a performance check.

When developing ESC systems using real vehicles, an extensive list of manoeuvres is driven on the proving ground to confirm the performance of the system. From these tests, metrics are derived that characterise the dynamic behaviour of the vehicle. These metrics define the ESC characteristic. Both legal and Ford internal requirements are used for the assessment. The requirements and metrics are evaluated in fingerprints, showing whether the targets for the ESC system are met or not.

Ford developed the CAE post processing tools that do the same procedure as described for the real vehicle in a SIL environment. Thereby a large set of virtual driving manoeuvres are simulated and evaluated. After getting the results from the simulation, the same tools as used for the measurements are applied to get the manoeuvre metrics. In addition, a report is generated to show the details of vehicle configuration and the corresponding test results (Fig. 5).



**Fig. 5** Generating fingerprints from the SIL environment

### 3 Correlation Study

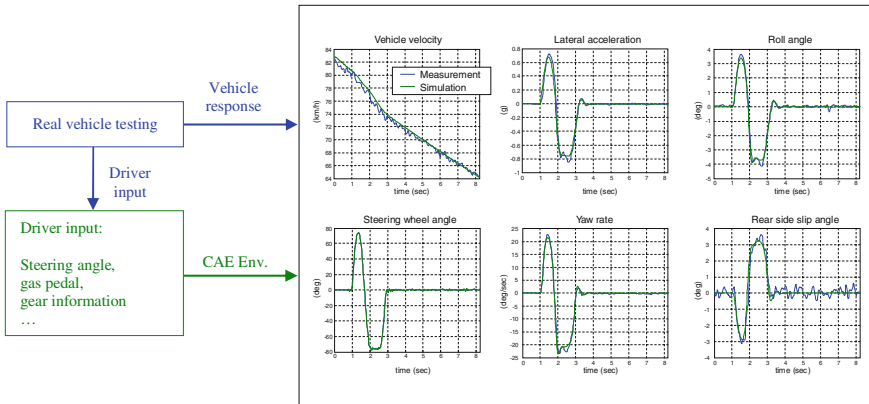
To prove the validity of the CAE process a full correlation study was executed. The test and validation procedure was defined together with ESC suppliers for verification of the whole tool chain. Both Ford and supplier testing catalogues were performed. The simulation results in terms of vehicle response and ESC intervention were compared with the real-world test.

To eliminate the driver influence systematically, the input parameters of the correlation were specified as the driver inputs like gas pedal (resp. vehicle velocity) and steering wheel angle. They were directly taken from real-world measurements. Figure 6 shows the principle of the correlation study, and as an example, the vehicle response like yaw rate or lateral acceleration obtained from the simulation (in green) was compared with the measurement (in blue).

The correlation study consisted of two parts: passive vehicle with ESC off and active vehicle with ESC on. Both supplier and Ford test methods are utilised. Finally, the correlation study should demonstrate the quality of the SIL environment for the virtual ESC performance check by required tests.

#### 3.1 *Passive Vehicle with ESC Off*

To get the characteristic of the passive vehicle, the ESC was switched off. Manoeuvres like constant radius and high g sweep steer were used to maximise the passive vehicle model quality. At this stage, the ADAMS model was validated. The veDYNA vehicle model quality was ensured by the previously mentioned conversion process.



**Fig. 6** Correlation between real-world vehicle and simulation

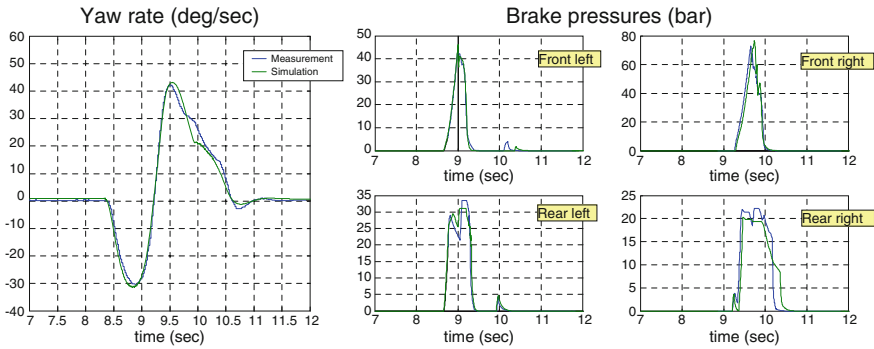
### 3.2 Active Vehicle with ESC On

Next the vehicle was driven with activated ESC to check the vehicle response under ESC intervention. The used manoeuvres are mainly open loop, which excludes the influence of the driver.

The correlation for the controlled model was checked with both Ford and supplier defined test methods and manoeuvre catalogues. The correlation study began with simple manoeuvres like straight line braking to validate the hydraulics model and check the ABS functionality. Finally the high dynamic manoeuvres, combining lateral and longitudinal dynamics with active brake interventions at different wheels were performed. The Sine-with-Dwell (SwD) manoeuvre as defined by legislation will be taken as an example in this paper.

Figure 7 shows a SwD manoeuvre with a steering wheel angle of about 200°, driven in a right-left turn direction. The vehicle responses like yaw rate and the brake intervention from simulation are compared with the real-world measurement. The good correlation between simulation and measurement indicates that the quality of the simulated SwD manoeuvre is comparable with the real vehicle testing. This gives additional confirmation for the potential for CAE to be used to support homologation, which will be discussed in the Sect. 4 (Application).

The correlation workshops were carried out with different vehicle programmes and suppliers. All of them show positive results, so that both Ford and suppliers were convinced to jointly run the CAE process. This enabled, for the first time in Ford, the initial release of an ESC system to be based on CAE.



**Fig. 7** Vehicle response and ESC intervention in a SwD manoeuvre

## 4 Application

### 4.1 CAE Supported ESC Development

The successful correlation study demonstrated the validity of the CAE process and motivated its application on different vehicle programmes. Meanwhile this process is well accepted, implemented and applied by the ESC suppliers, so that the initial ESC release can be done without physical vehicle prototypes. Since this process has been established, it is becoming increasingly utilised for the ESC development within Ford. Compliance to the procedure will be guaranteed with inclusion into the statement-of-work between OEM and supplier.

The application began with passenger cars and was later transferred to commercial vehicles. The commercial vehicle programmes with high complexity benefit even more from this process, since they have a huge amount of variants, many of which may not be built as prototype vehicles. Detailed performance results for the whole variant range would not be possible without the CAE application.

### 4.2 CAE Supported ESC Homologation

In November 2009, a new supplement was published to the Economic Commission for Europe (ECE) Regulation 13-H [2]. For the first time, the regulation specifically allows the use of computer simulations to prove the performance of the ESC, if a vehicle of the same type has been physically tested and the simulation has been validated through comparison with this real vehicle testing. According to the regulation, the performance of the vehicle stability function has to be demonstrated by SwD manoeuvres.

With this regulation the CAE application can potentially be extended to support the homologation process. The CAE process described before was originally



targeted at the development of an initial ESC release however; the correlation study executed for the validity proof of the CAE process follows the same principle as defined by the legal requirement. The modelling complexity level meets the legal requirement and the SIL environment used within Ford is able to comply with the EU regulation as well. As shown in the correlation study, the simulation environment can simulate the SwD manoeuvre with comparable quality of a real vehicle testing. This provides further confirmation for the potential CAE based homologation in addition to the investigations done in [3, 4].

Utilising the CAE application for homologation would potentially significantly reduce the amount of real testing with prototypes necessary. This would lead to considerable time savings especially for the vehicles with a large number of variants.

### ***4.3 Transfer to Further Active Control Systems***

The CAE process was developed for ESC, but can potentially be extended to other active control systems, for instance other chassis and driver assistance functions/features, whereby these systems are integrated and the traffic model is included in the CAE environment.

## **5 Conclusion**

Based on extensive correlation studies the validity of the “CAE supported ESC Development/Release Process” has been demonstrated. The process is well accepted, implemented and applied by the ESC suppliers, so that the initial ESC release can be done without physical vehicle prototypes. The application allows a significant reduction in development time for Ford and its suppliers.

The new ECE R13 regulation allows simulation-based homologation. Following the same principle of validity proof, the same CAE environment can be utilised to support the certification of ESC systems. This provides a further advantage of time saving and completes the CAE application from ESC development to certification.

## **References**

1. Federal motor vehicle safety standard: FMVSS 126, Docket No. NHTSA–2007–27662
2. Economic commission for Europe regulation: ECE R13-H, 11 Nov 2011
3. Wurster U, Ortlechner M, Schick B, Drenth E, Crawley J (2010) First ECE 13/11 homologation of electronic stability control (ESC) by vehicle dynamics simulation—challenges, innovations and benefits, chassis. Techplus, Munich Germany, pp 8–9
4. Hahn K, Holzmann H, Weyer F, Roemer M, Webb J, Boltshauser S (2012) Simulation-based certification of ESC systems for passenger vehicles in Europe SAE Int. 2012-01-0235

# Application of Optimization Algorithm to HVAC Configuration Design

Tatsuro Kyuto, Motohiro Kitada and Hideo Asano

**Abstract** It is required to attain performance goals at the development early stage for short period development of air conditioner. To attain basic A/C performance goals (high cooling performance, good temperature control property, good flow distributions to outlets, low noise), it is important to balance competing goals for heat exchanger transit flow distribution uniformity and pressure drop lowering within configuration limitation. In this study, we tried an optimization calculation of a HVAC configuration upstream the evaporator which governs evaporator transit flow distribution uniformity and the HVAC total pressure drop for short period development.

**Keywords** Heat fluid · Air conditioner · CFD · Optimization · HVAC

## 1 Introduction

Due to the recent automotive development period shortening, the demand for efficient A/C system design method is increasing. It is required to attain performance goals at the development early stage. To attain basic A/C performance goals (high cooling performance, good temperature control property, good flow distributions to outlets, low noise), it is important to balance competing goals for heat exchanger transit flow distribution uniformity and pressure drop lowering within configuration limitation [1].

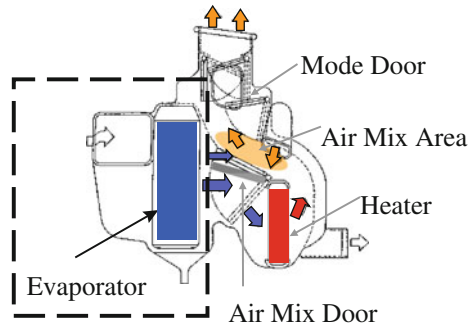
---

F2012-E03-023

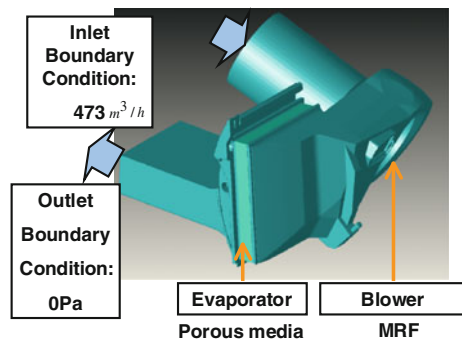
---

T. Kyuto (✉) · M. Kitada · H. Asano  
DENSO Corporation, Kariya, Japan  
e-mail: tatsuro\_kyuto@denso.co.jp

**Fig. 1** The part to optimize in the HVAC



**Fig. 2** CFD model



## 2 Analysis

### 2.1 Decide the Part to Optimize

A HVAC has a cooling heat exchanger evaporator and a warming heat exchanger heater. Controlling the flow by moving an air mix door, wanted temperature air which is carried to the cabin can be obtained. The HVAC is modeled to the area from the blower to the evaporator as shown in Fig. 1 dotted area to reduce the calculation cost. The heater case which includes the heater is omitted.

### 2.2 Make CFD Model

CFD model is shown in Fig. 2. Flow rate  $473 \text{ m}^3/\text{h}$  is put to the inlet, and pressure 0 Pa is put to the outlet. The calculation mesh is about 3.2 million. Evaporator pressure loss is modeled as porous media based on the experimental result. The blower is modeled as MRF, and body force corresponding to 2,077 rpm rotative force was applied. Steady state calculation is conducted. SC/Tetra [2] is used for this calculation as CFD solver. Standard  $k-\varepsilon$  turbulence model is applied.

Fig. 3 Objective functions

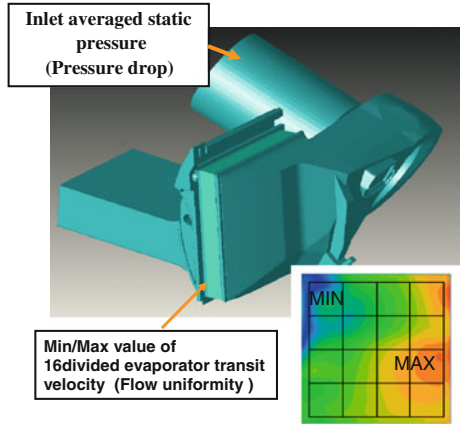
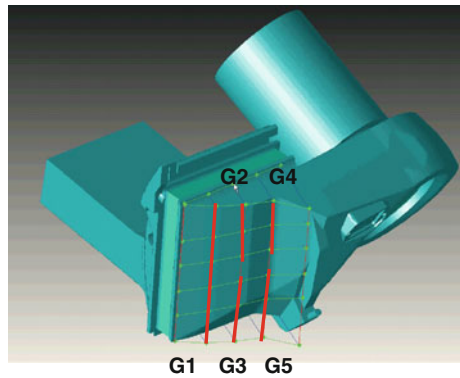


Fig. 4 The mesh morphing model



### 2.3 Decide Objective Functions

Objective functions are Min/Max value of 16 divided evaporator transit velocity and inlet averaged static pressure shown in Fig. 3. High Min/Max value means good flow uniformity, and low inlet static pressure means low system pressure drop.

### 2.4 Decide Design Variables

A plane configuration is adopted for the optimization base configuration. And design variables are decided as lines which are set in the mesh morphing model of the base plane configuration shown in Fig. 4. The lines are moved vertically to the base plane shape, and surrounding areas are followed as curves in the mesh morphing technology.

**Table 1** Range of design variables

Design variable	Range (unit mm)
G1	0 ~ 15
G2	0 ~ 26
G3	0 ~ 26
G4	0 ~ 35
G5	0 ~ 35

The mesh morphing is a new technology which can make the CFD mesh ready to calculate by moving the existing mesh. We used SCULPTOR [3] as a mesh morphing software. Range of design variables is shown in Table 1.

The idea to adjust evaporator transit flow velocity is to change the cross section area upstream evaporator. For example if we push the plane, the cross section decreases, and velocity increases, and static pressure decreases, then evaporator transit flow increases. The confirmed result is shown in Fig. 5. In reverse if we pull the plane, the cross section increases, and velocity decreases, and static pressure increases, then evaporator transit flow decreases.

## 2.5 Make the Response Surface Model

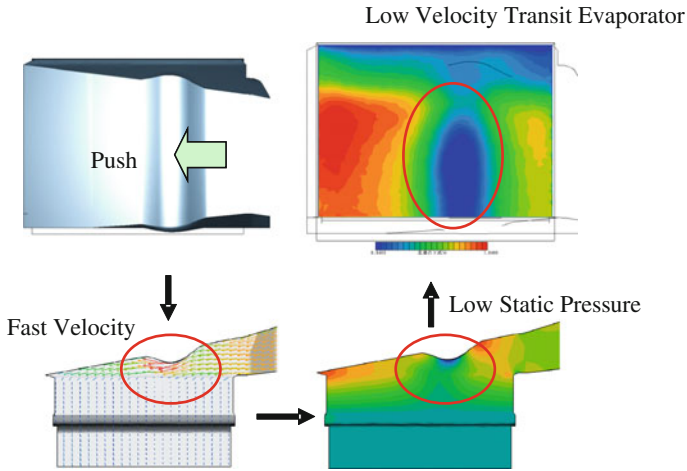
If all CFD calculations are conducted in the multi objective optimization, it cost too much calculation time. So a response surface model is utilized to reduce calculation cost.

### 2.5.1 Decide Sampling Points

We decided sampling points based on the DOE (reduced factorial sampling and SOBOL). Reduced factorial sampling is a method that can gather information from the edges of design space, and SOBOL is a sampling method that can gather information from the midst of design space. 16 sampling points are decided on reduced factorial sampling, and 24 sampling points are decided on SOBOL as shown in Table 2.

### 2.5.2 CFD Calculations

Response on sampling points can be obtained by conducting CFD calculations. Automatic batch CFD sampling calculations are realized using optimization software (modeFRONTIER).



**Fig. 5** The result of the confirmation about the idea to adjust evaporator transit flow velocity

**Table 2** Examples of sampling points

Sampling points	Design variables				
	G1	G2	G3	G4	G5
1	15	26	26	35	35
λ	λ				
16	0	0	0	0	35
17	0.76	1.31	1.31	1.77	1.77
λ	λ				
40	2.27	13.9	22.1	9.9	31.8

} reduced factorial sampling  
 } SOBOLSampling

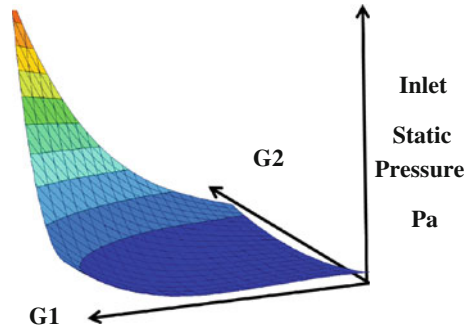
**2.5.3 Make Response Surfaces**

Response surfaces are made using the Neural Network model which can predict the nonlinear design space accurately. Response surfaces are good in accuracy, all response surface’s multiple correlation coefficients are more than 0.98. The example of a response surface about inlet static pressure is shown in Fig. 6. In this graph design variables G3, G4, and G5 are fixed, and only design variables G1 and G2 are changed.

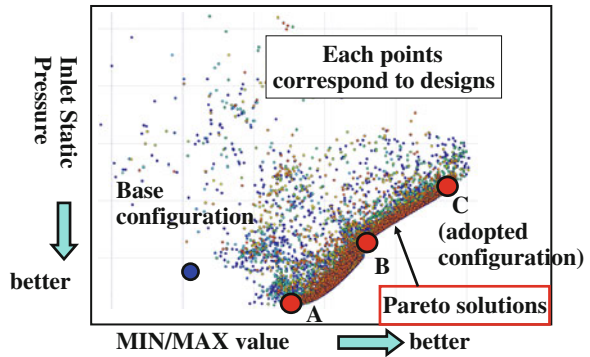
**2.6 Conduct Optimization Calculations**

Because there is a need to optimize two objective functions, MIN/MAX value of 16 divided evaporator transit velocity and inlet averaged static pressure, multi objective optimization algorithm is required. In this study multi objective GA

**Fig. 6** The example of a response surface



**Fig. 7** Optimization result



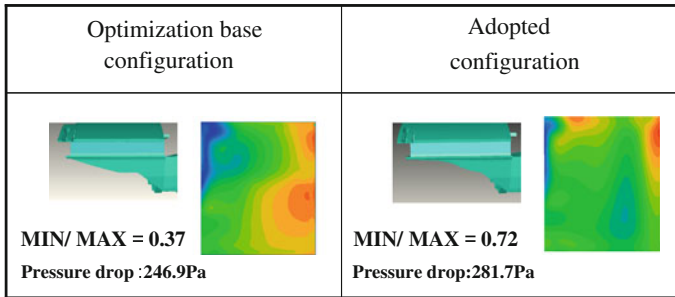
(MOGA) is applied as optimization algorithm, and Pareto solutions which is an assembly of optimized solutions can be obtained by searching response surfaces at the condition of initial individuals 32, and evolution generations 500.

### 2.7 Select A Design to Adopt

The optimization result is shown in Fig. 7. The Horizontal axis means MIN/MAX value of 16 divided evaporator transit velocity. The vertical axis means inlet static pressure. A dot point in the graph corresponds to a design's result. An engineer can adopt a design from the Pareto solutions based on his value judgment. For example if pressure drop is of importance, the configuration A is adopted. If balanced performance is of importance, the configuration B is adopted. If flow uniformity is of importance, the configuration C is adopted. In this study the configuration C is adopted as an optimized design.

**Table 3** Results of confirmation calculation

MIN/MAX value of 16 divided evaporator transit velocity		Inlet static pressure Pa	
Response surface	CFD	Response surface	CFD
0.74	0.72	-115	-110



**Fig. 8** Comparisons between the optimization base configuration and the adopted configuration

### 2.8 Confirm the Adopted Design by CFD Calculations

Optimization is carried out on the response surface, so it is required to confirm the accuracy. CFD calculations are conducted to confirm the accuracy. The result is shown in Table 3. The predicted optimization result on response surfaces is almost the same as CFD calculation.

The CFD results of velocity contour are shown in Fig. 8. Velocity distribution of the adopted configuration has been improved compared with the optimization base configuration.

### 2.9 Confirm the Adopted Design by the Experiment

The experiment was conducted to validate the adopted configuration. CFD result agrees well with experiment in qualitative velocity distribution and quantitative MIN/MAX value, pressure drop as shown in Fig. 9.

## 3 Discussions

Why the optimized configuration is good in flow uniformity is discussed here. The base configuration has much flow on the opposite side of the blower in the wide direction of the evaporator, and also much flow on the lower side in the height direction of the evaporator as shown in Fig. 8. So the optimized configuration



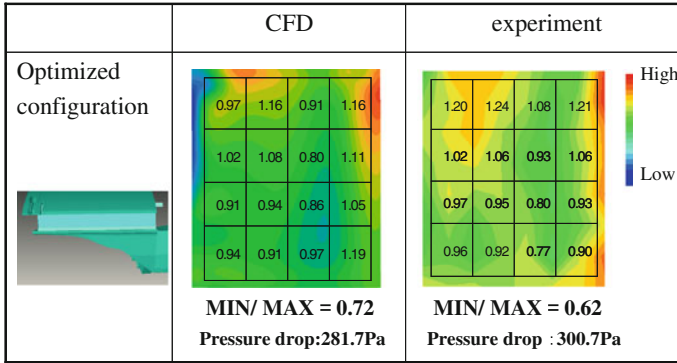


Fig. 9 Comparisons of optimized configuration between CFD and experiment

moves the G5 variable much to correct the wide direction flow bias, and moves the G1 variable much to correct the height direction flow bias. The design variable settings are show in Fig. 4.

The number of design variables set in this study is five. If more variables are set, there is more possibility to improve a result. To achieve a good result in a limited time, it is required for engineers to reduce the number of design variables by setting a good base configuration and good design variables which can control the performance.

### 4 Summary/Conclusions

The parameter optimization in flow analysis which usually cost much time can be conducted in a short period of time using the response surface and the mesh morphing technology. The configuration upstream the evaporator which has good performance can be designed rapidly by conducting a sequence of optimization procedures.

### References

1. Kitada M et al (2001) Study concerning estimation for temperature control characteristics of automotive air conditioning unit. JSAE Annu Cong (Spring)
2. Software Cradle Co., Ltd.:SCRYU/Tetra. <http://www.cradle.co.jp/products/scryutetra/index.html>
3. VINAS Co., Ltd.: SCULPTOR. <http://www.vinas.com/jp/seihin/sculptor/>

# Research of Flow Field Simulation for Lubrication System and Effect Evaluation on a 7-Speed Dual Clutch Transmission

Yinhui Lin, Zhihua Hu, Chaoqiang Xiong, Mengyan Zang, Yuan Jia, Yong Chen, Daguo Luo and Fuquan Zhao

**Abstract** The evaluation of lubricating effect of the transmission lubrication system is an important part in the transmission design. The Ansys-Fluent software is used in this paper. Firstly, the flow field of the single oil orbit of 7DCT transmission is simulated and the mass flow rate of each nozzle is taken as the input condition of the lubricating simulation and analysis in the whole transmission model. Then the whole transmission model is established to facilitate evaluating the lubricating effect of the oil catcher by setting the monitor surfaces at the positions of the oil catcher. The complex oil and gas phase flow field of transmission is simulated and analyzed so that the lubrication effects of three lubricating method are evaluated to achieve the purpose of evaluating the performances of the transmission lubrication system, including the forcing ejective oil lubrication, splash lubrication and oil passage lubrication.

**Keywords** 7DCT · Transmission · Lubrication · CFD · Effect evaluation

---

F2012-E03-033

---

Y. Lin (✉) · C. Xiong · M. Zang  
South China University of Technology, Guangzhou, China  
e-mail: tx416757210@163.com

Z. Hu · Y. Jia · Y. Chen · D. Luo · F. Zhao  
Zhejiang Geely Automobile Research Institute Co Ltd, Hangzhou, China

## 1 Introduction

Effective transmission lubrication cannot only reduce the abrasion of contact surface of moving parts (shaft gears, gears, bearings, synchronizers, etc.), but also take away the impurities and heat of friction contact surface and act on cleaning and cooling, and also serve as the seal, antirust, damping and buffer. Thus it can ensure the normal operation of transmission and increase the service life of transmission.

In the transmission lubrication system, the key problem is the lubrication of the gear. Due to the limitations of computing resources and other factors, the gear-driven flow field simulation presently focuses on the internal flow field of two-dimensional gear pump, such as Kris Riemslogh and etc., have calculated the flow characteristics of internal fluid of the rotary displacement pumps (cam pump and gear pump) by Lagrangian–Eulerian finite volume method [1]; John Vande Voorde etc., have calculated the internal flow field of rotary volumetric pump by the Fluent software [2]; Jiang Fan etc., have done the dynamic simulation of the internal flow field of the gear pump for diesel engine lubrication by the moving mesh method [3]. Considering aspects of transmission lubrication, Lemfeld etc., have done the related analysis of the two-phase flow model for the non-toothed gear under the conditions of different tilt angles and oil temperature [4]; Dong Chunfeng etc., have used the technique of dynamic mesh to carry on the flow field simulation for a pair of straight gears in gearbox [5]. Since the model of transmission lubrication system is a complex two-phase flow model of multi-pair driving bevel gears, its complexity is high and no analysis of such case has been presented in public at present.

7 Dual Clutch Transmission (7DCT) is a dual clutch automatic transmission including seven forward gears, dual input shafts and dual output shafts. Because of special layout structure for 7DCT transmission, the designers have used three lubrication methods including the oil bath lubrication, splash lubrication and pressure lubrication to achieve the purpose of lubrication for all moving contact parts of the transmission, and it can be expressed particularly as three ways including the forcing ejective oil lubrication, splash lubrication and oil passage lubrication, which have a direct impact on the performance of the transmission. Therefore the evaluation of the lubricating effect is an important part in the transmission design.

The traditional evaluation method of lubrication is that the housings of major observation parts are wiped off and re-sealed using transparent materials and the experimental prototype is made to observe the lubricating effect of the key parts by running the bed experiment. Although the evaluation method of experimental prototype is intuitive and of high reliability, only the several local observation parts can be observed and the global understanding of the operating conditions of the lubrication system cannot be known, and this method can only be used in the late period of the transmission development. Thus it has an important engineering significance that one simulation analysis method is used to evaluate the lubricating

effect of the transmission lubrication system at the time of the transmission design stage.

The Ansys-Fluent software is used in this paper. Firstly, the flow field of the single oil orbit of 7DCT is simulated and the simulated result of the mass flow rate of each nozzle is taken as the input condition of the lubricating simulation and analysis in the whole transmission model, which is based on simulation confirmation and experimental results are basically the same. Then the whole transmission model is established to facilitate evaluating the lubricating effects of the concerned points by setting the monitor surfaces at the observing positions. Finally, the working condition of the first speed is simulated with the whole transmission model as the research object and the lubricant effects of three lubricating methods of 7DCT transmission have been studied particularly, including forcing lubrication, splash lubrication and oil passage lubrication.

## 2 CFD Theory Basis of a Transmission Lubrication System

Compared with other automatic transmission oil, dual clutch automatic transmission oil (following lubricant oil for short) has better lubricating properties, which is used by 7DCT [6]. In the lubrication analysis, lubricating fluid is deemed usually as incompressible fluid, and the thermal expansion coefficient is ignored. Oil property standard is the property at 20 °C. Without considering heat conduction, convection and thermal radiation of the transmission lubrication system, the paper focuses on the problem of flow field calculation of the transmission lubrication system. In other words, energy conversion is ignored in this paper. Considering the disturbance of the transmission lubrication system,  $k-\varepsilon$  turbulence model is used for lubrication analysis [3]. The region of flow field for lubrication system of the transmission will change over with time because of the rotating movement of gears. Therefore the technology of moving mesh is adopted in the simulation analysis.

### 2.1 Control Equations

The continuity equation (mass conservation equation) and the equations of motion (momentum equation) are met firstly, when the liquidity problem of the transmission lubrication system is performed. Secondly, the rotating movement of the gears leads to the inner cyclone movement of the transmission, which makes the strain rate of the fluid higher and the degree of bending of flow lines bigger. The problems can be solved using the RNG  $k-\varepsilon$  turbulence model [7].

The RNG  $k-\varepsilon$  turbulence model is used for describing the fully developed turbulence model that has the high Re number. But the wall function method is used for dealing with the flow near wall region and low Re number flow [5].

## ***2.2 The Technology of Moving Grid***

The moving mesh can be used for simulating the flow field which changes shape with time because of boundary movement. The rotational movement of the gear can be achieved by compiling code. The grids change with the rotatable movement when gear is rotating, which leads to worse quality of grids and the more difficult computing convergence of the next step. Therefore the local re-mesh method is adopted by agglomerating the grids of poor quality and updating the moving grids of the mesh agglomerates, thus ensuring the quality of the grids and the success of computing process [5]. When the technology of moving mesh is used, the initial grids of good quality need to be defined and then grids can be automatically updated according to the boundary changes in each iteration step in the calculation process by setting the relevant parameters in order to achieve the purpose of the smooth calculation.

## **3 CFD Analysis of the Transmission Lubrication System**

### ***3.1 Simplification of Whole Model of Transmission***

Closed flow region should be established for the CFD analysis of the whole transmission model. Figure 1 shows that there are numerous parts in a transmission. It is difficult to form a closed chamber calculation because of complex geometry. So the geometry of transmission should be simplified and then surfaces of parts should be extracted. Finally, the closed flow region can be sutured successfully.

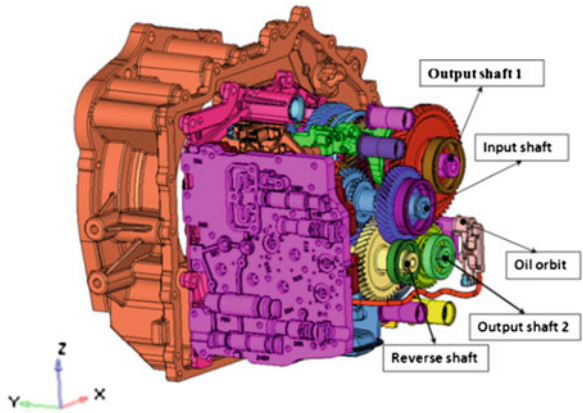
#### **3.1.1 The Oil Orbit Model**

Figure 2 shows the solid model of oil orbit formed by extracting and suturing the inner surface. The oil orbit model consists of an inlet and seven nozzles. The shape of inlet and nozzle is all circular.

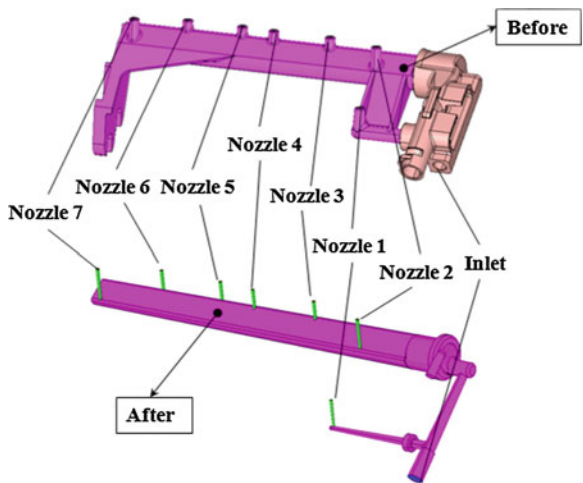
#### **3.1.2 Dealing with the Joggled Gears**

The power transmission depends on the joggled contact of pairs of gears when the transmission is working. The oil film attaching to surface of gear is used for lubrication and cooling. The flow field of a pair of straight tooth gear can be simulated by increasing distance between two gears and adjusting tooth profile. Due to the limitations of computing resources, it is very difficult to simulate the process of bevel gear pairs in the transmission as shown in Fig. 1. Therefore, models of gear pairs are simplified by cutting tooth. As shown in Fig. 3, the tooth

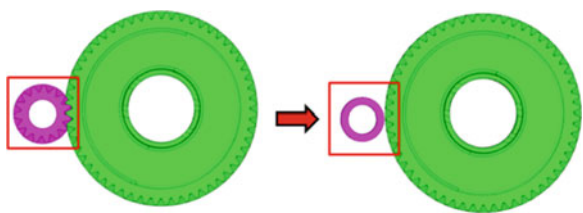
**Fig. 1** Structure of transmission



**Fig. 2** Solid model of oil orbit

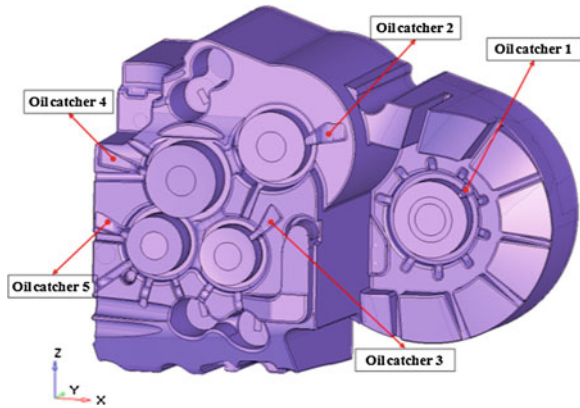


**Fig. 3** Simplification of jogged gear

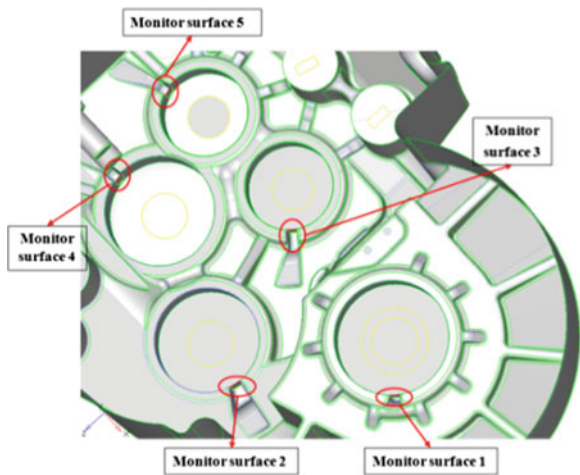


of one gear in any pair is removed. In the whole transmission model, the drive gears on the input shaft should be jogged with several pairs of driven gears on the output shaft 1 and output shaft 2. The method of cutting teeth of drive gears above transmission oil surface and retaining teeth of driven gears is used to reduce the

**Fig. 4** Simplification of transmission housing



**Fig. 5** Setting monitor surface

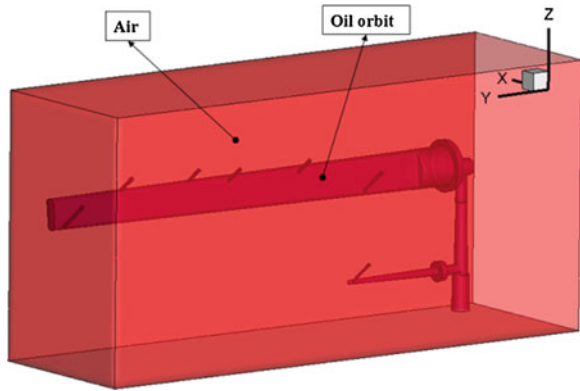


influence of splash lubricant effect of the oil liquid, which is caused by cutting teeth.

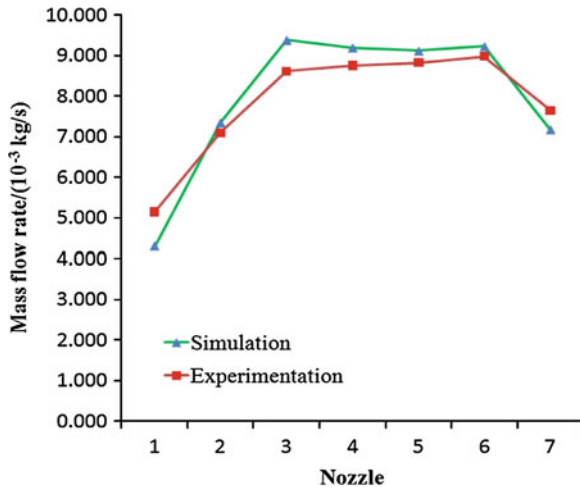
### 3.1.3 Simplification of Transmission Housing

A closed chamber is formed by extracting and suturing the housing of inner surface after plenty of geometry cleanup of the transmission, as shown in Fig. 4. There are five oil catchers in the housing. Monitor surfaces are set at the position of the oil catchers for directly observing whether the oil enters these oil catchers and are obtaining the mass flow rate of the oil, as shown in Fig. 5. The number of monitor surfaces is the same as that of oil catchers shown in Fig. 4. In the CFD computing, the monitor surface is set to interior boundary condition, thus flow fluid can pass the monitor surface freely so that the effect of collecting oil will not be affected.

**Fig. 6** Model of oil orbit at two-phase flow



**Fig. 7** Simulation and experimentation result of mass flow rate of each nozzle



### 3.2 The CFD Analysis of Transmission Lubrication System

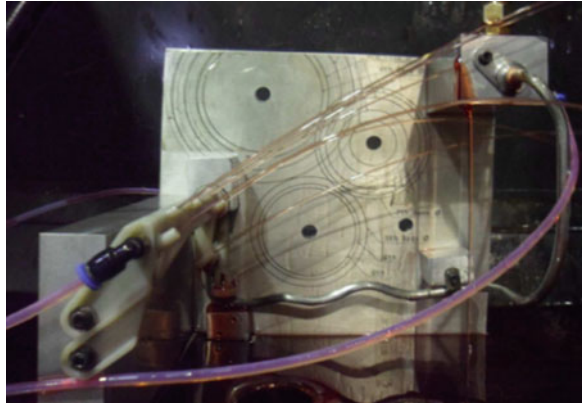
#### 3.2.1 The CFD Analysis of Single Oil Orbit

The CFD analysis of the ejective oil condition of single oil orbit has been firstly carried on and compared with the related experiment result to validate the feasibility of the simulation method. The simulation result of mass flow rate of each nozzle of the oil orbit is taken as the input condition of the whole transmission model.

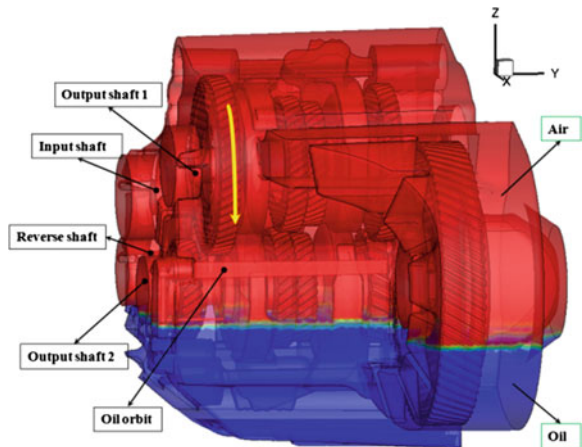
Since the working condition of oil orbit is the complex two-phase flow of oil and gas in transmission, a rectangular chamber is built in the lateral of nozzles of oil orbit as shown in Fig. 6. Oil is inside and air is outside the oil orbit in the initial condition.



**Fig. 8** Experiment of oil orbit



**Fig. 9** The whole model of 7DCT transmission



Unstructured tetrahedral grids of oil orbit shown in Fig. 6 is meshed using Gambit software. Transient simulation of oil orbit is computed with the VOF model of the Fluent software. The density and the dynamic viscosity of the oil are  $840 \text{ kg/m}^3$  and  $0.0324 \text{ Pa s}$  at  $20 \text{ }^\circ\text{C}$  respectively; the corresponding parameters of air are  $1.225 \text{ kg/m}^3$  and  $1.789 \times 10^{-5} \text{ Pa s}$ . The design value of the volume flow of the oil orbit inlet is  $4\text{L}/\text{min}$ . The simulation result of the mass flow rate of each nozzle, as shown in Fig. 7, is similar to the experimentation result shown in Fig. 8, which indicates the validity of analysis result of the mass flow rate of each nozzle.

### 3.2.2 CFD Analysis of the Whole Model of Transmission

The closed chamber of the transmission inner, shown in Fig. 9, is meshed with unstructured tetrahedral grids, and the initial number of grid is 2.6 million. Simulation conditions are as follows: working temperature  $20 \text{ }^\circ\text{C}$ , the direction of

gravity negative z-axis, the rotational speed of input shaft 1,000 r/min and the working condition first speed. The mass flow rate of each nozzle obtained by the single oil orbit simulation is set as the mass inlet condition and the rotation direction of output shaft 1 is set as Fig. 9, which is corresponding to other working parts. The model of VOF, RNG k- $\epsilon$  and the technology of moving mesh are used for simulating and computing [7]. Although the model has been simplified farthest by the method of cutting tooth, the present number of computing grids has been almost 6 million because of the complex of the structure of the research object and the flow field, and the use of the technology of moving mesh, which is a big challenge to the computing resources.

## 4 The Effect Evaluation of Transmission Lubrication System

### 4.1 The Forcing Ejective Oil Lubrication

An oil orbit spout assembly is used in the forcing ejective oil lubrication, in which the lubricant oil orbit supplies the oil to the inlet through the filter and cooler under a certain pressure and then sprays on the gears, shift synchronizer set and other parts of the output shaft 1 by the nozzle to realize the lubrication and cooling through the oil orbit nozzle. The objective of the forcing lubrication is to confirm whether the oil ejected from the oil orbit can reach the lubricant point and is affected by the splash oil.

Figure 10 shows the transmission oil liquid volume distribution observed from the front side of the model when the physical time is 0.0234 s and the ejected oil of each nozzle can be clearly observed. From the figure, the oil thrown by the gears of the output shaft 2 and final drive gear cannot interrupt the oil ejected from the oil orbit nozzle. Figure 11 shows the condition at the same physical time that the oil ejected from the nozzle 2 and nozzle 4 rotates with the gears. It indicates that the ejecting oil which reaches the gears can overcome the centrifugal force generated by the gears rotation and rotates to the jogged position together with the gears.

The above result shows that oil ejected by the oil orbit can successfully reach the corresponding gears and rotate with the gears to the jogged place, which can lubricate the jogged gears and is not affected by the splash oil. It proves the rationality of the forcing lubrication system including the oil orbit.

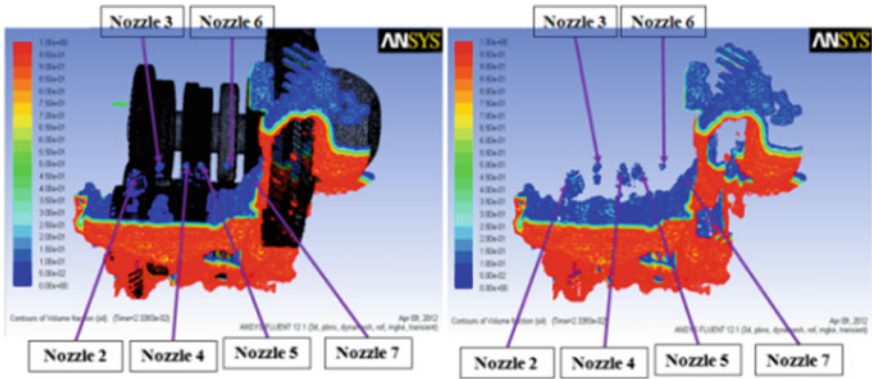


Fig. 10 Volume distribution contour plot of transmission oil at the front side

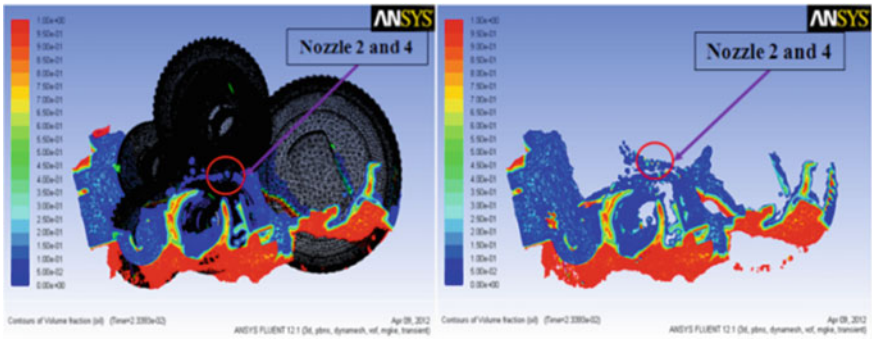
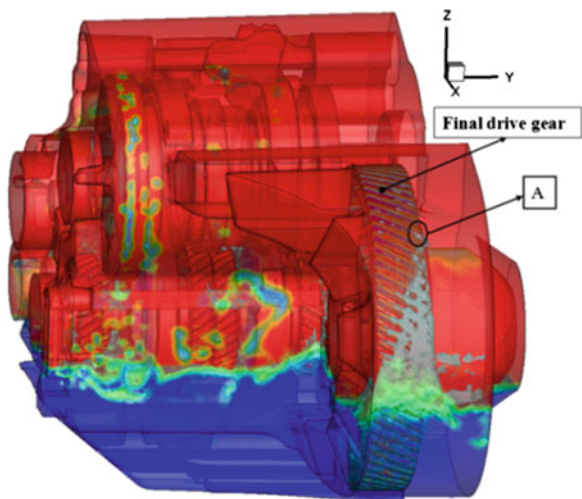
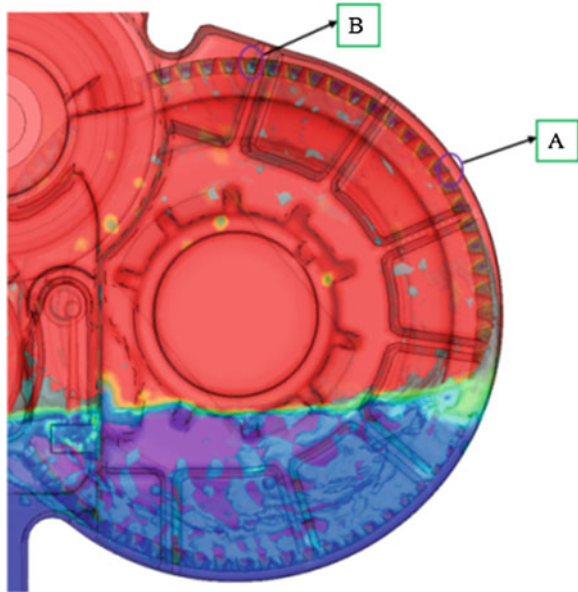


Fig. 11 Volume distribution contour plot of transmission oil on the left side

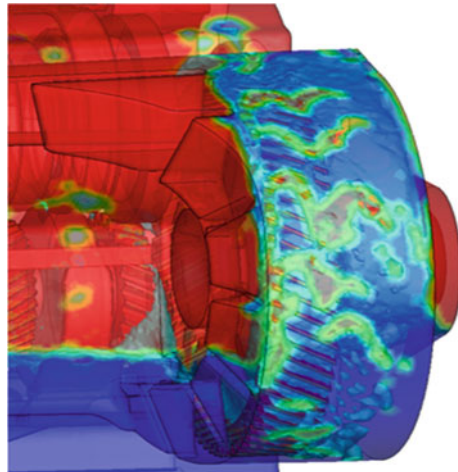
Fig. 12 Splash oil liquid distribution at first speed



**Fig. 13** Oil liquid distribution around the final drive gear at first speed



**Fig. 14** Splash condition of the final drive gear at seventh speed



## 4.2 *The Splash Lubrication*

The splash lubrication, as an automatic lubrication that is formed from which the rotation gears immersed in the oil sump of a sealed case, can bring the lubricant oil from the oil sump into the friction pair.

**Fig. 15** Left view of the lubricant oil splash condition

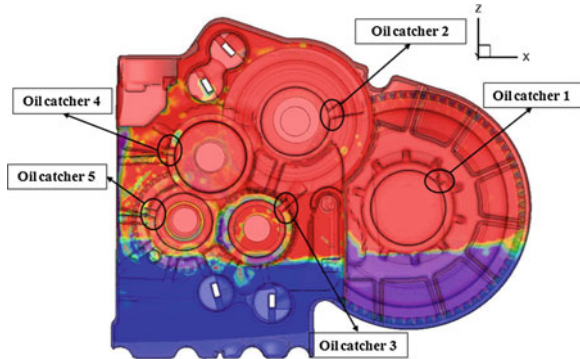


Figure 12 shows the condition of the splash lubrication of the transmission lubricant system at the first speed at the physical time of 0.6 s. The oil liquid splashed by the driven gear of the output shaft 2 and immersed in the oil sump has already reached the top of the output shaft 1. But because of the low rotation speed, the oil liquid splashed by the final drive gear leans to the right due to the influence of the bevel gear and gravity, and thus it makes against the supply of oil to the left oil catcher 1. According to Fig. 13, the gear lateral has already broken away from the oil liquid which only leaves a little of oil in the gear root after the gear rotates to the point A and there is not any oil liquid thrown from the highest point B of the gear. So the splash lubrication effect of the transmission under the first speed condition is poor because only little oil liquid can be splashed by the final drive gear.

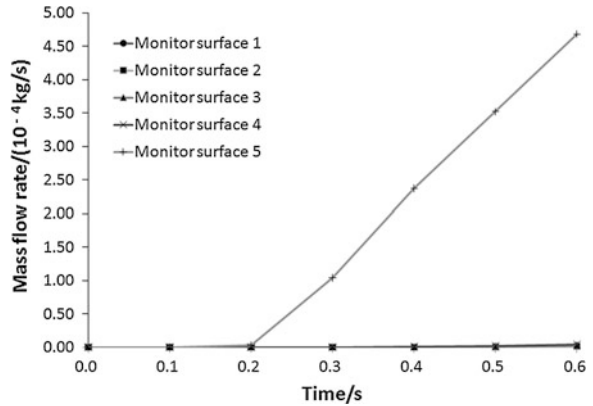
In order to further verify the splash lubricant effect of the final drive gear, the seventh speed condition has been simulated and the result is shown in Fig. 14 that the final drive gear is enwrapped completely by the oil liquid and can realize the oil supply of the oil catcher 1.

### ***4.3 The Oil Passage Lubrication***

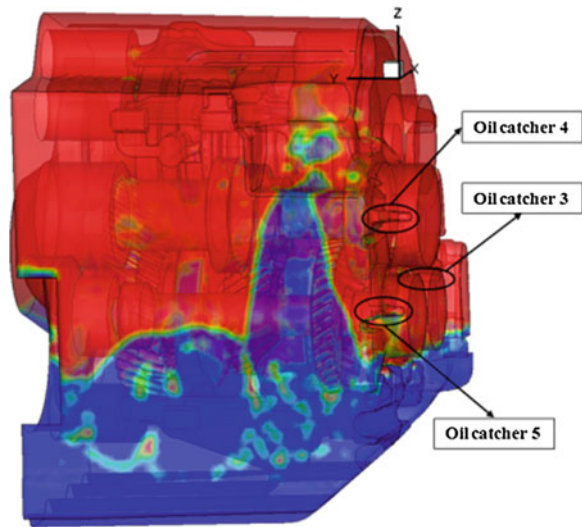
The oil retainer and oil catcher are designed under the transmission housing. The oil retainer can bring the oil liquid splashed by gears into the oil catcher, which will flow into the hollow drive shaft and realize the lubrication of needle bearing between each gear and shaft. This paper sets the monitor surface at the oil passage inlet of the oil catcher to confirm the mass flow rate of the lubricant oil of each oil passage.

Figure 15 shows the left view of the lubricant oil splash condition at the time of 0.6 s. Although there is no lubricant oil splash into the oil catcher 1 and oil catcher 2, the oil liquid seems to enter the oil catcher 3, oil catcher 4 and oil catcher 5. But this does not happen in truth. Figure 16 shows the relationship between the lubricant oil flux entering each monitor surface of the oil catcher and the physical time, which indicates that the oil only has entered the oil catcher 5 and the mass

**Fig. 16** Time course of the mass flow rate of entering each monitor surface



**Fig. 17** Front view of the oil passage lubrication



flow rate of the inlet oil increases with the time, but the oil has not entered other oil catchers. The result illuminates that the transmission lubricant system has not reached the dynamic stability far away and needs the further calculation. The condition that the oil catcher 3 and oil catcher 4 have not captured oil also can be affirmed by the front view of the lubricant oil splash condition as shown in Fig. 17. There are truly several oil liquid assembled around the oil catcher 5, but there are still some distances between the splash oil and the wall of the oil catcher although the splash oil has reached the height of the oil catcher 3 and oil catcher 4. Therefore there is basically no oil entering the monitor surface of the oil catcher 3 and oil catcher 4.

Obviously, what can be avoided includes not only making the wrong estimation result because of the different observation angle, but also quantitatively evaluating the oil collecting condition of each oil catcher set to the monitor surface

near each oil catcher. Due to the limitation of the computing model size and the computing resource, the physical time of the simulation computing is only 0.6 s which cannot surely judge whether the oil can enter each oil catcher and the mass flow rate of the inlet oil, so the effect of the oil passage lubrication cannot be evaluated. But what can be sure is that the transmission splash oil will enter the dynamic stability state with the physical time increase and the mass flow rate of the lubricant oil which enters each oil catcher through each monitor surface, which will also become more stable. The evaluation standard of the stable state is that the mass flow rate entering each oil catcher is no longer changing.

## 5 Conclusion

With the software Ansys-Fluent, the paper firstly simulates the flow field of the single oil orbit of 7DCT transmission and takes the simulation result of the mass flow rate of each nozzle as the input conditions which are based on confirming simulation and experimental results are basically the same. Then the lubricant simulation model of the transmission has been established and the monitor surfaces have been set up at the positions of the oil catcher for the evaluation of the oil passage. Finally the working condition of the first speed is simulated with the whole transmission model as the research object and the lubricant effects of three lubricating methods of 7DCT transmission have been studied particularly, including the forcing lubrication, splash lubrication and oil orbit lubrication. Although the dynamic stability state of the splash lubricant oil has not been obtained because of the restriction of computing resources, the simulation method presented in the paper will undoubtedly have important significance for simulation evaluation of the lubricant properties of the transmission.

## References

1. Riemslag K, Vierendeels J, Dick E (2000) An arbitrary Lagrangian-Eulerian finite-volume method for the simulation of rotary displacement pump flow. *Appl Numer Math* 32:419–433
2. Vande VJ, Vierendeels J, Dick E (2004) Flow simulations in rotary volumetric pumps and compressors with the fictitious domain method. *J Comput Appl Math* 168:491–499
3. Fan Jiang, Weiping Chen, Yuanyuan Li (2007) Dynamic simulation of flow field inside of lubricate gear pump. *Mod Manufact Eng* 6:116–118
4. Lemfeld F, Fran K, Unger J (2007) Numerical simulations of unsteady oil flows in the gearboxes. *J Appl Sci Thermodyn Fluid Mech* 1:1–5
5. Chunfeng D, Tengjiao L, Zeyin H (2011) Numerical simulation of flow field in the gearbox based on moving mesh. *Mech Res Appl* 22(2):17–19
6. Gengbo Tang, Yong Chen, Daguo Luo (2011) Study on dual clutch transmission fluid. *Lubr Eng* 36(6):107–110
7. Armfield SW (1989) Comparison of  $k-\epsilon$  and algebraic Reynolds stress models for swirling diffuser flow. *Int J Numer Meth Fluids* 9(8):987–1009



# Application of Stiffness Estimation and Structure Optimization in Rubber Component Development

Min Sun, Yuan Qu, Youfeng Qiu and Shenrong Wu

**Abstract** Rubber bushing is a very important connection component in vehicle suspension. It plays an important role in vehicle performance. To resolve a crack issue of the bushing occurred in load test, the optimal design is requested. The material parameters of rubber are identified by minimizing the errors between the simulated and tested stiffness curves of bushings. The structure optimization is studied to obtain a new design, which reduces the stress in the crack area and keeps nearly the same stiffness of the original design. The investigation with several load cases shows that the stresses of the optimized bushing decreases significantly from the original design.

**Keywords** Rubber · Material · Identification · Stiffness · Optimization

## 1 Introduction

Rubber's ability to withstand very large strains without permanent deformation or fracture makes it ideal for many applications, such as tires, elastomer bushings, seals. The elastomer bushings are critical components in vehicle suspension systems. Due to complex service loads, the elastomer is exposed to various strain status. In certain cases the bushing may be damaged, but the measurement of stress

---

F2012-E03-036

---

M. Sun (✉) · Y. Qu · Y. Qiu · S. Wu  
Automobile Engineering Research Institute, Chery Automobile Co., LTD, Wuhu, China  
e-mail: sunmin@mychery.com



and strain is considerably difficult. Therefore the finite element method is used for analysis.

Before the analysis, Material parameters must be determined. Simple material tests, such as uniaxial test and biaxial test, can be used to obtain some parameters of the constitutive models. But, not all bushing suppliers can provide these data appropriately. Without knowledge of material parameters it is hard to predict the stiffness characteristics and load capacity when the design is changed.

For material parameter identification of vulcanized rubber bushings, Ref. [1] reported a new method to find the parameters of constitutive equations by correlating the test data for translational stiffness curves. In this paper, neo-hookean model with compressibility is utilized to simulate a bushing. The software ABAQUS is used for modelling and analysis; and OPTIMUS is employed to find the optimal material parameters. Then MeshWorks is applied to modify the mesh of the model for design changes, and OPTIMUS is utilized to search the optimal structure of the bushing. The constitutive equations of rubber and basic theory are explained in Sect. 2; a case study is presented in Sect. 3; finally, conclusions and suggestions are in Sect. 4.

## 2 Basic Theory

Rubber is considered a Hyperelastic material. Among various rubber material models, neo-hookean model is expressed below with strain energy [2]

$$U = C_{10}(\bar{I}_1 - 3) + \frac{1}{D_1}(J_{el} - 1)^2 \quad (1)$$

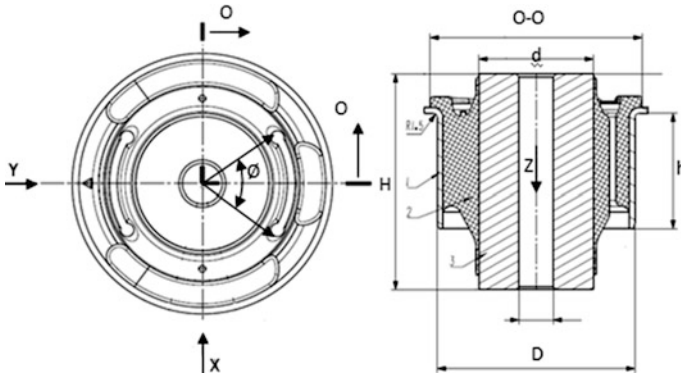
This is a relatively simple model with good approximation at small strains [3]. Where  $\bar{I}_1$  is for deviatoric strain.  $J_{el}$  is for volumetric strain.

As studied in [4],  $C_{10}$  and  $D_1$  can be determined by using a gray-box model, in which some physical insight is available, but several parameters remain to be determined from test data. The finite element model of the rubber bushing with Eq. (1) can be viewed as an available physical insight. Stiffness curves are obtained from tests, while parameters  $C_{10}$  and  $D_1$  need to be determined.

When the finite element model is built, the force–displacement curves for certain load conditions obtained by simulation are compared to the corresponding stiffness curves from tests. Let  $Z_{ij}$  be the  $j$ th displacement point of the  $i$ th curve. The objective is to minimize the sum of errors defined below [1]

$$\Psi(X) = \text{Min} \sum_{i=1}^n \sum_{j=1}^{m_i} |err(Z_{ij})| \quad (2)$$

Here,  $X$  represents the parameters in Eq. (1),  $n$  is the number of input curves from tests,  $m_i$  is the number of experimental points of the  $i$ th test curve,  $err(Z_{ij})$  represents the error at the displacement point  $Z_{ij}$ . Generally, stiffness of bushing is



**Fig. 1** Bushing configuration

nonlinear. Therefore, it is necessary to minimize errors at all points of the whole curves.

### 3 Case Study

#### 3.1 Problem Description

A crack is found in a bushing near the structure holes during the road test. The bushing needs to be redesigned with the same material, to reduce the maximal stress and to keep the stiffness of bushing nearly the same. But material parameters of rubber for this bushing are not available.

#### 3.2 Configuration and Experiments

The configuration of the bushing is shown in Fig. 1.  $H = 70$  mm,  $h = 40$  mm,  $d = 40$  mm, and the thickness of the bushing equals  $t = (D - d) / 2 = 12.5$  mm. There are two arc shaped holes in the Y direction with an angle  $\phi$ .

The bushing is mold-bonded and composed of a hollow elastomer cylinder contained between the inner and outer cylindrical steel sleeves. The sleeves connect to components of suspension systems. During vehicle movement, the bushing sleeves undergo translations and rotations. Therefore the deformation of the bushing in this study includes axial, torsional, and combined load cases. The axial mode is defined as a translation of one sleeve relative to the other sleeve parallel to the centerline. The torsional mode is defined as a rotation of one sleeve relative to the other sleeve about the centerline.

Fig. 2 Translational stiffness curves

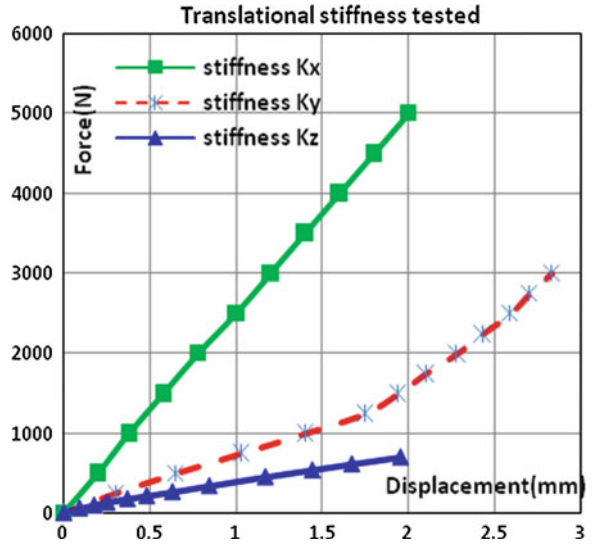
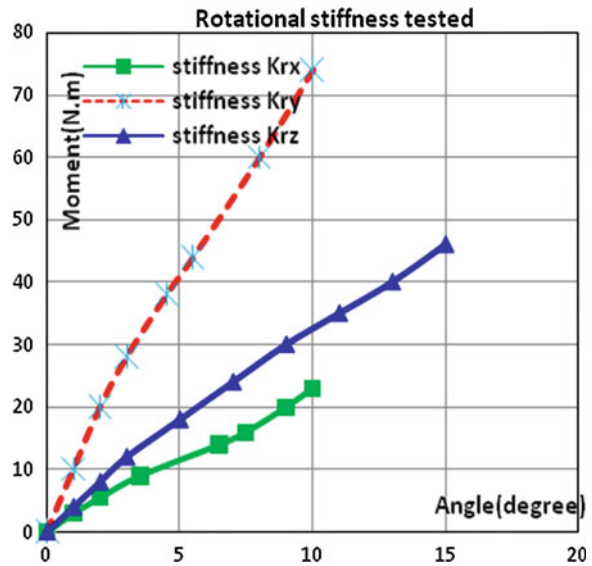


Fig. 3 Rotational stiffness curves



For this bushing, the axial stiffness  $K_z$  is along  $z$  direction. Because of the holes in the rubber bushing, there are two radial stiffnesses,  $K_x$  along  $x$  direction and  $K_y$  along  $y$  direction. In addition, there are three rotational stiffnesses accordingly. The stiffness curves from tests are shown in Figs. 2 and 3.

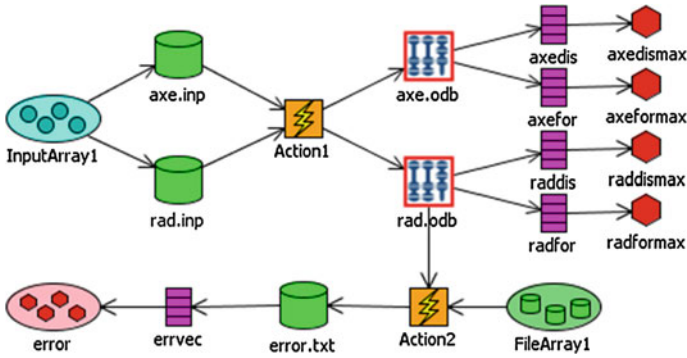


Fig. 4 Process of material parameter optimization

Table 1 Parameters identified of rubber

Parameter	$C_{10}$	$D_1$
Value	0.55	0.01824

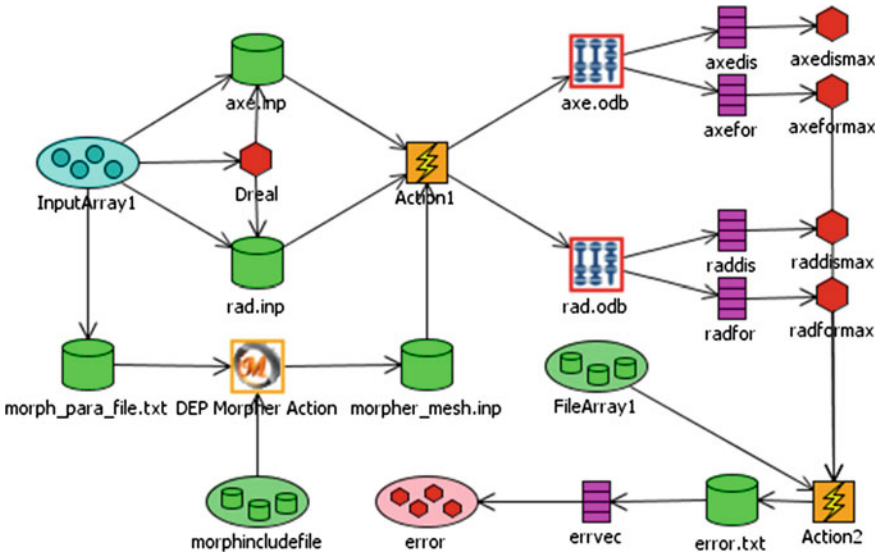
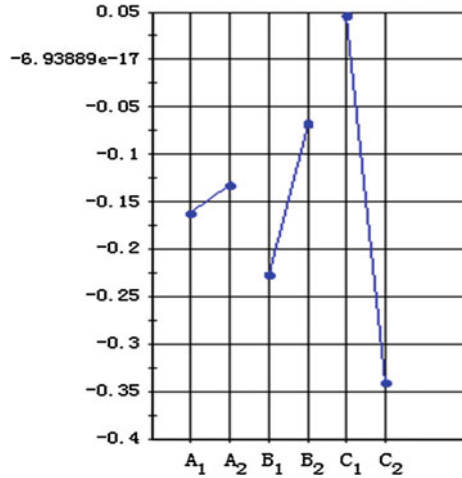


Fig. 5 Flow chart of structure optimization

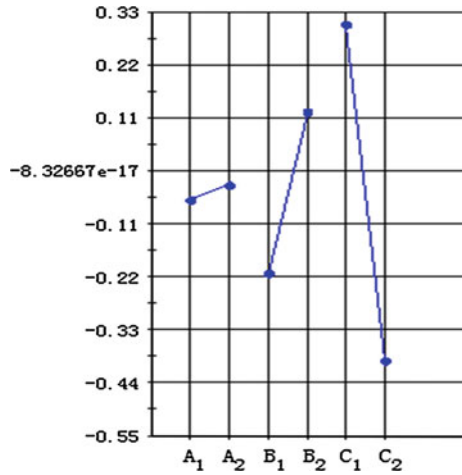
### 3.3 Parameter Identification

To obtain the parameters of the constitutive equation, ABAQUS is used to simulate the rubber deformation in Action 1, and MATLAB is used to calculate the

**Fig. 6** y-error sensitivity analysis



**Fig. 7** x-error sensitivity analysis



error between test data and computational results in Action 2. And the self adaptive evolution method with OPTIMUS is used to optimize the material parameters. The population size, the maximum number of iterations and initial step width are chosen to be 10, 30 and 1 respectively. The step mutation factor is assigned to be 1.3 [5]. The analysis process is shown in Fig. 4. The material parameters in Eq. (1) are obtained and shown in Table 1. The error in stiffness is acceptable [1].

Fig. 8 Translational stiffness Kz

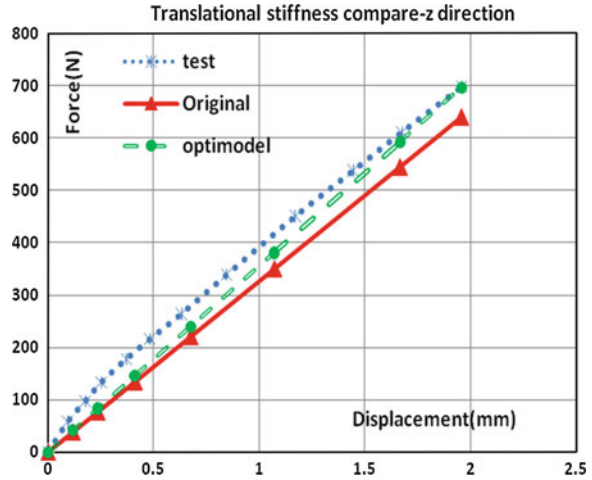
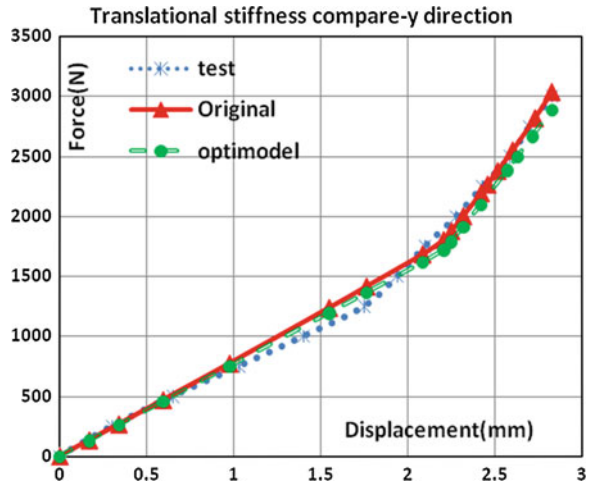


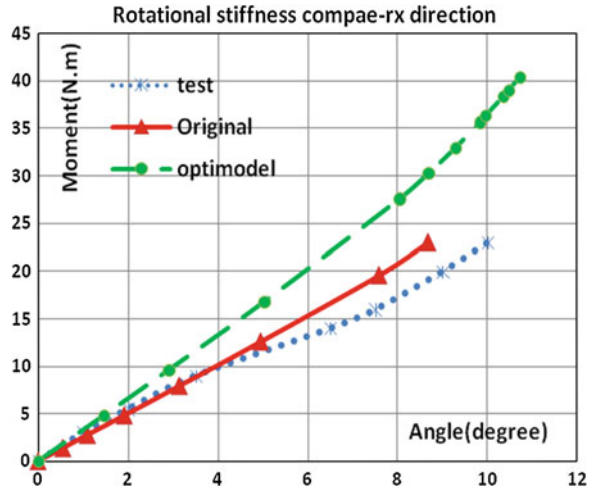
Fig. 9 Translational stiffness Ky



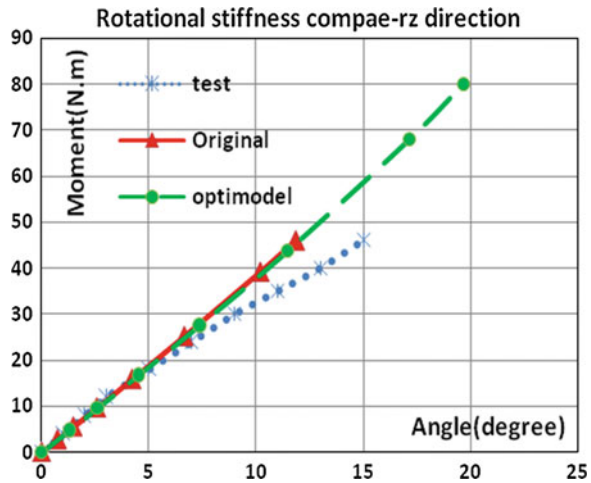
### 3.4 Structure Optimization

To resolve the crack issue, the structure optimization is performed to find a better design. Here three design variables are defined: angle of the holes  $\phi$ , height  $h$ , and the thickness  $t$ . The finite element bushing model correlated in the last step is used. The target is set to reduce stress at the crack area and keep the bushing stiffness nearly the same. Therefore, during the structure optimization, the difference between the new calculated stiffness curves and the initial test curves should be minimized.

**Fig. 10** Rotational stiffness  $K_{rx}$



**Fig. 11** Rotational stiffness  $K_{rz}$



The flow chart of structure optimization is shown in Fig. 5. ABAQUS and MATLAB are used in the Action 1 and Action 2. They play the same roles as those in parameter identification. The mesh modification software MeshWorks is used in the DEP Morpher Action to change the finite element model of the bushing with the three parameters. The self adaptive evolution method is chosen, and the maximum number of iterations and initial step width are chosen to be 15, 25 and 1 respectively. The step mutation factor is assigned to be 1.1.

In Fig. 5, 'errvec' consists of error between the computational results and the tested data in the x-, y-, and z-directions.

**Table 2** Translational stiffness and error of simulation

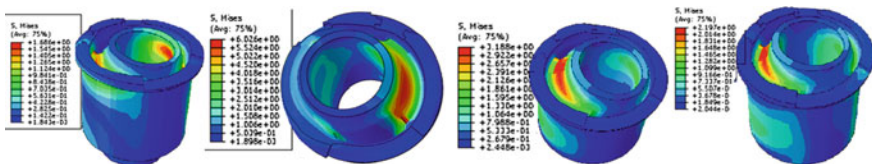
	Kx		Kz		Ky			
	Value (N/mm)	Error (%)	Value (N/mm)	Error (%)	First part		Second part	
					Value (N/mm)	Error (%)	Value (N/mm)	Error (%)
Test data	2,500		300		750		1,700	
Original design	2,540	1.6	310	3.3	770	2.7	1,750	2.9
Optimized design	2,560	2.4	305	1.7	760	1.3	1,750	2.9

**Table 3** Rotational stiffness and error of simulation

	Krx		Krz		Kry	
	Value (Nm/deg)	Error (%)	Value (Nm/deg)	Error (%)	Value (Nm/deg)	Error (%)
Test data	2.08		3.2		6.75	
Original design	2.67	28	4	25	6.76	1
Optimized design	2.75	32	4	25	6.76	1

**Table 4** Maximal calculated stress of the bushing (Mpa)

	Case1	Case2	Case3	Case4
Original design	2.28	6.54	3.74	2.267
Optimized design	1.686	6.02	3.188	2.197
Change (%)	26	7.95	14.7	3.2



**Fig. 12** Stress contour of cases 1–4

Taguchi design method is used to study the parameters sensitivity. The results are shown in Figs. 6 and 7, where A is angle of the holes  $\phi$ , B and C is the height h and the thickness t respectively.

It is observed that the height and the thickness are the main factors, and therefore chosen as the optimization structure parameters. The process leads to a new design with  $h = 50$  mm and  $t = (D-d)/2 = 15$  mm ( $d = 35$  mm).

The stiffness of the newly designed bushing is calculated. As examples, the calculated translational stiffness Kz, Ky, and torsional stiffness Krx, Krz are shown in Figs. 8, 9, 10, 11, with the test data and original design data.



For comparison, the displacement from 1 to 2 mm is used to express axial stiffness  $K_z$  and radial stiffness  $K_x$ . Because of strong geometrical non-linearity in the radial stiffness  $K_y$ , as shown in Fig. 9, displacements from 1 to 1.7 mm and from 1.7 to 3 mm are used for a bilinear averaging. Torsion angles from  $5^\circ$  to  $10^\circ$  are used for rotational stiffness  $K_{rz}$ ,  $2^\circ$ – $8^\circ$  for  $K_{rx}$ , and  $2^\circ$ – $6^\circ$  for  $K_{ry}$ .

The test data and the computed results of the translational stiffness of bushings are shown in Table 2. The error of the computed stiffness is small. The difference in stiffness between the new design and the original design is small.

The results of the rotational stiffness for this bushing are shown in Table 3. The error for  $K_{ry}$  is small, and the errors for  $K_{rx}$  and  $K_{rz}$  are large, reaching 25–32 %, only acceptable for torsional angle less than  $5^\circ$ – $8^\circ$  respectively.

With material parameters in Table 1, the stresses of the newly designed bushing with 4 different load cases are calculated. The maximum Mises stresses are listed in Table 4 and the stress contours are presented in Fig. 12. Case 2 has the highest stress, which is reduced by 8 % for the new design. The maximal reduction in stress reaches 26 % in case 1.

## 4 Conclusions

The rubber material parameters of the bushing were obtained by using parameter identification method. A new design was found by conducting a structure optimization, which reduced stress at the crack area and kept the stiffness of the bushing nearly the same as the originally designed.

The following topics deserve efforts for future studies:

1. To consider the effect of the compressibility of rubber;
2. To improve the accuracy in determining the parameters of the constitutive equations;
3. To simulate the fatigue behavior of rubber.

## References

1. Qu Y, Sun M, Qiu Y et al (2012) Selection of constitutive models in rubber bushing simulation. SAE technical paper 2012-01-0761, doi:[10.4271/2012-01-0761](https://doi.org/10.4271/2012-01-0761)
2. Dassault Systemes SIMULIA, ABAQUS 6.8 HTML Documentation: ABAQUS theory manual, 2008
3. Zhuang Z, Zhang F et al (2005) ABAQUS nonlinear finite element analysis and examples. Science Publishing House, Beijing
4. Finca V, Zglimbea R, Greaban E, Marin C (2009) Methods for parameters identification of a HAVC installation, WSEAS Trans Syst Control 4(9):455-464
5. Noesis Solutions NV (2010) Theoretical background for OPTIMUS

# Brake Cooling Simulation: A Combined Procedure of CFD, Thermal and 1D Software

Enric Aramburu and Roger Calvo

**Abstract** The prediction of brake temperatures by means of numerical simulation is always a challenging objective. The main difficulties in brake cooling simulation are the correct definition of the brake heat generation and an accurate thermal simulation of the brake system, which includes the main heat exchange mechanisms, such as convection, conduction and radiation. This paper describes a simulation process that combines 1D simulation with 3D thermal simulation of brake systems. 1D simulation was used to compute the heat generation during driving cycles, CFD was used to compute the air speed around the brake, and thermal software was used to compute the temperature distribution in the brake. An innovative procedure using numerical simulation and its validation is presented in this paper, in order to help prevent temperature-related brake problems.

**Keywords** Brake cooling · CFD · Thermal simulation · 1D simulation · Fade

## 1 Introduction

To stop the wheel in a braking action, friction material in the form of brake pads is forced mechanically, hydraulically, pneumatically, or electromagnetically against both sides of the disc, causing the wheel to slow down or stop. When the brake pedal is pressed, the brakes on the vehicle heat up, slowing it down. But if the

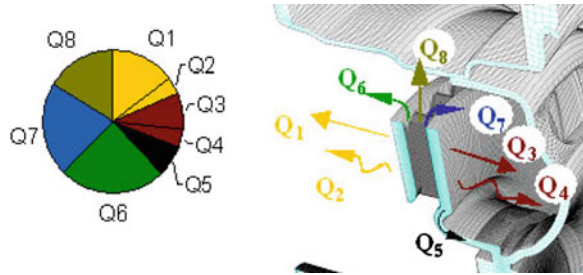
---

F2012- E03-037

---

E. Aramburu (✉) · R. Calvo  
IDIADA Automotive Technology, Santa Oliva (Tarragona), Spain  
e-mail: earamburu@idiada.com

**Fig. 1** Heat transfer balance in brake [1]



brakes are used rapidly, the discs and brake pads will stay hot and will not be able to cool off. The brake cannot absorb much more heat because the brake components are already hot, so the braking efficiency is reduced. This malfunction of the brake system is called brake fade.

In every brake pad there is the friction material which is held together with some sort of resin. Once the brake pad starts getting too hot, the resin holding the pad material together starts to vaporize (forming gas). That gas can't stay between the pad and the disc, so it forms a thin layer between the brake pad and rotor trying to escape. The pads lose contact with the disc, thus reducing the amount of friction and consequently the braking torque.

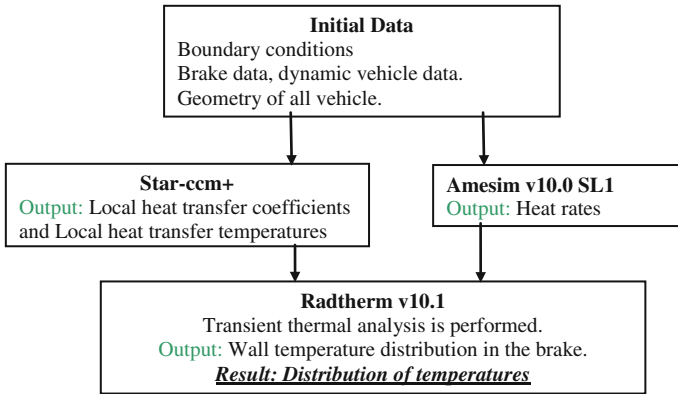
The heat is carried away from the brake disk in various ways. As it was explained in [1], the heat flux can be divided in several parts:

- The heat carried off by forced convection through the face of disk into the wheel arch.
- The heat carried off by radiation through the face of the brake disk into the wheel arch.
- The heat carried off by forced convection through the face of the brake disk out of the vehicle.
- The heat carried off by radiation through the face of brake disk out of the vehicle.
- The heat carried off by conduction into the wheel hub and the wheel nave.
- The heat carried off by forced convection through the rear face of the channel.
- The heat carried off by forced convection through the front face of the channel.
- The heat carried off by forced convection through the channel. (Fig. 1).

## 2 Case of Study

The evaluated vehicle corresponds to a car of segment C. Due to confidentiality reasons it is not possible to specify the vehicle model.

The test that has been correlated is the test Type I, included in the reglamentation GB 21,670, this test consists in the evaluation of brake loss efficiency. It



**Fig. 2** Workflow of the methodology

consists in the performance of 15 brakings (120–60 km/h) in intervals of 45 s, with a constant deceleration of 3 m/s<sup>2</sup>. The test was performed in the IDIADA testing facilities.

### 3 Fe-Approach

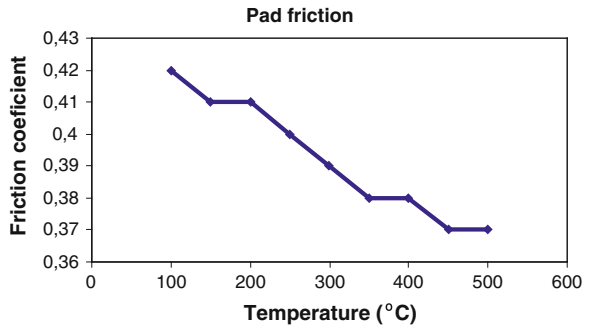
The simulation process combines 1D simulation, with 3D thermal simulation of brake systems. The 1D simulation was used to compute the heat generation during driving cycles, CFD was used to compute the air speed around the brake and thermal software was used to compute the temperature distribution in the brake (Fig. 2).

#### 3.1 Usage of 1D Model

LMS Imagine.Lab AMESim is a simulation software for the modeling and analysis of one-dimensional (1D) systems. The software package offers a 1D simulation suite to model and analyze multi-domain, intelligent systems and to predict their multi-disciplinary performance. Model components represent the system’s actual hydraulic, pneumatic, electric or mechanical behavior.

In the brake performance it is especially useful due to Amesim’s ability to obtain a complete car model, taking into account the dynamics, kinematics, aerodynamics, engine, etc. It is possible to calculate the heat dissipation in brake disk, with Amesim using the heat dissipation blocks of the thermal libraries coupled in the all car schematics. Sometimes a high level of accuracy is necessary in this heat dissipation.

**Fig. 3** Friction coefficient vs Temperature



There are many heat dissipation strategies such as the design of internal ribs, the area of the holes in the brake disk, etc. Moreover there is an air flux that is incoming to the brake due to the aerodynamics of the front part of the car (bumpers and wheelhouse parts) that has to be taken into consideration.

Amesim can not consider all these geometric variables, which could change the values of HTC in the brake disk, so it is necessary to perform a CFD simulation that is coupled with the results of 1-D system, to obtain an accurate result. Furthermore, with the use of Amesim we can reduce the dependence of input data from the testing department, to perform the brake fade simulation, because Amesim allows us to obtain the heat rate curves generated in the braking cycle.

### 3.1.1 Data Requirements from Testing in 1-D Model

(a) Test: Friction coefficient versus temperature.

The target of the test is to study the variations of friction as a function of temperature (Fig. 3).

(b) Kinematics and Elastokinematics modelization

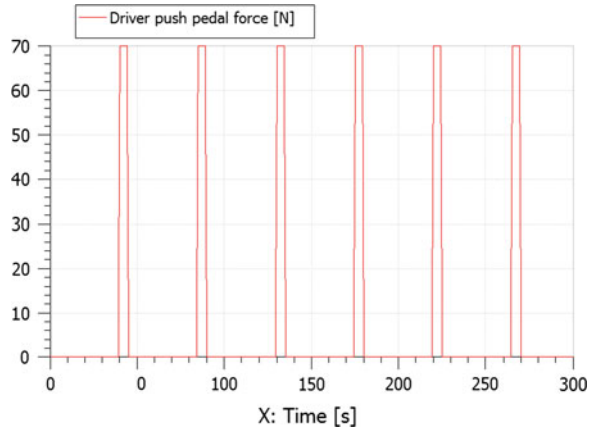
In order to model the car with Amesim, it is necessary to introduce the dynamic data of the car. Kinematics refers to five major displacements in the steering. To model it, it is required to introduce a 3-D kinematics plots such as; Halfwheel Base, Half track, Toe Angle, Camber Angle and Self rotating angle.

The elastokinematics model is globally seen as a flexibility component, providing a displacement from an effort. In order to model it in Amesim, a flexibility matrix is needed.

(c) Test: Dynamic adherence of wheels, and Pacejckca characterization

The modelization of the Tires is performed throughout the iCar component of Amesim. The required data from testing are the tires stiffness and Pacejckca coefficients.

**Fig. 4** Input pedal force



### 3.1.2 Description of 1-D Model

In Fig. 5 the model of the complete car implemented in Amesim is shown. It is composed by an iCar [2], that allows the user to model the car structure in the 1-D simulation. The model is focused in a detailed modeling of the brake system controlled by the Electronic Brake Distribution (EBD). One of the components of the braking system is the hydraulics system, which receives an input pedal force from the driver. This input was modeled with the data shown on Fig. 4, obtained empirically.

The rotor brake disk has been modeled with a block that allows the user to define the specific curve of friction coefficient as a function of temperature and obtain the heat dissipated in the rotor disk (Fig. 5).

### 3.1.3 Obtained 1-D Results

The results obtained in the Front right brake of the vehicle with Amesim, are the friction torque and the heat generated on the brake (Fig. 6).

## 3.2 CFD Simulation

Due to the complexity of the interaction between the external aerodynamics flux and the outlet flux from the rotational movement of the brake [3], some considerations must be taken into account when performing the set-up with Star-ccm+, such as:

- Definition of the angular velocity of the wheel.
- Definition of the Moving Rotation Fan (MRF), involving all brake parts. The parts that are not rotating and are intersecting with the control volume of the

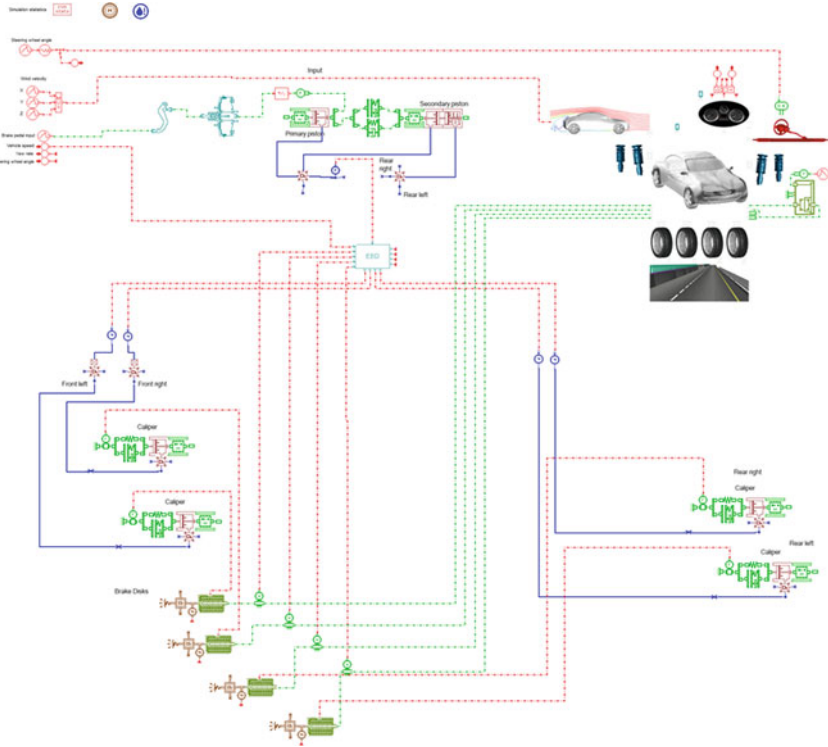


Fig. 5 Complete car implemented to study the braking fade in the 1-D stage

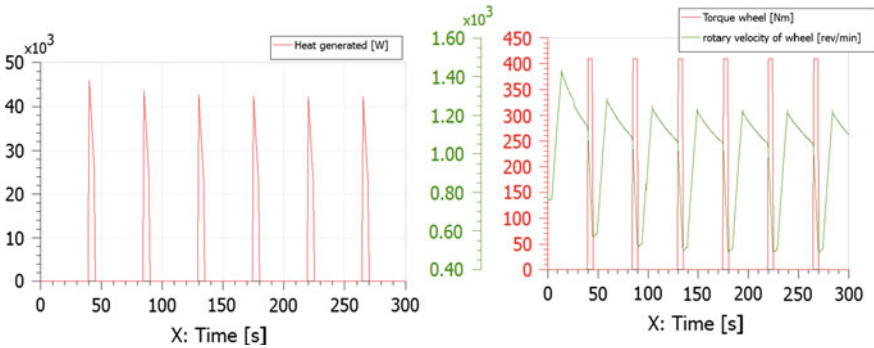
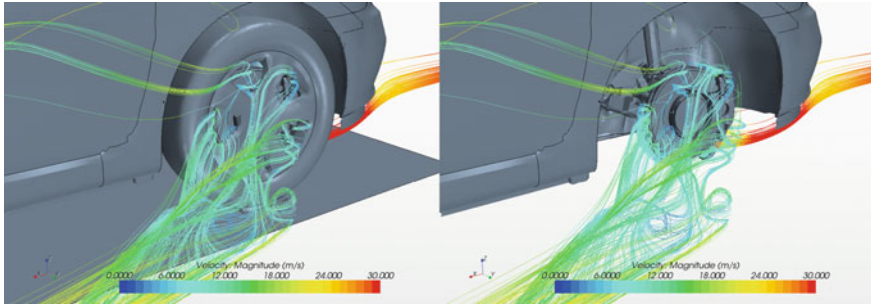


Fig. 6 Heat rate obtained (left). Torque and rotary velocity (right), both in front right wheel

MRF, have to be defined with an opposite angular velocity in order to simulate the fixed position of the part.

- Definition of the property interfaces between the MRF and the volume mesh.



**Fig. 7** Fluid streams through the car wheel at 120 km/h

Figure 7 shows the fluid streams through the car wheel [4], as a representation of velocity magnitude, due to the underhood air flux and the rotary velocity of the wheel.

Figure 8 shows the fluid streams as a representation of velocity magnitude, in this picture the air flux through the internal vents due to the rotary movement of the disk is represented.

Figure 9 shows the two CFD states calculated at maximum and minimum vehicle test conditions.

The mappings have been performed at different Radtherm time steps, depending on the braking cycle of the test. In our correlated case, the gap time between braking actions was 45 s. The Local Heat transfer coefficients and the Local Heat Transfer Reference Temperatures are mapped to Radtherm from Star-ccm+ (Fig. 10).

### 3.3 Thermal Simulation

The CFD results of the maximum and minimum speed scenarios, were imported into the thermal model and mapped on the thermal mesh, to compute the temperature distribution in the brake components. To perform a Radtherm set-up, an appropriate Radtherm model, with the definition of all of materials as well as all the connections between lumped capacitance and geometries of the model has to be created in the models based with a Lumped Capacitance. In the case of a simulation with Solids, is necessary to create a volumetric mesh that represents the Solid in Radtherm. After this first set-up the following steps must be followed:

- Import the CFD results in the time steps according to the times where the braking action is performed and taking into account to map the corresponding Star-ccm+ faces.
- Import to Radtherm the dissipation heat curve of each brake and assign it to the Rotor contact face. In case to employ a co-simulation technique, due to requirements of the simulation, it will be necessary instead of import the curve, just link the part face with the co-simulation option.



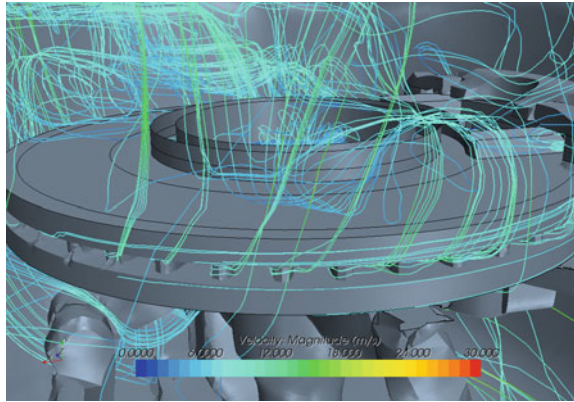


Fig. 8 Air flux through the internal vents at 120 km/h

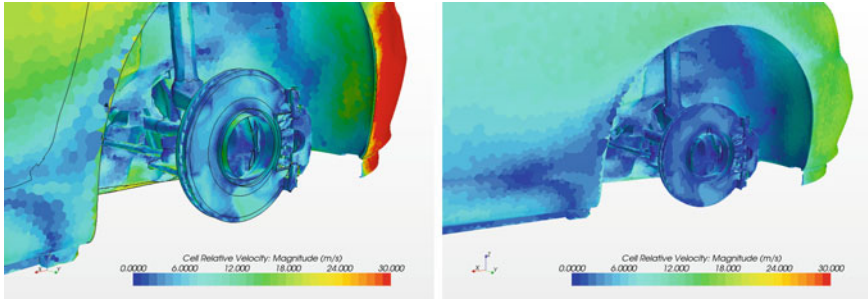


Fig. 9 Velocities in brake surroundings 120 km/h (left), 60 km/h (right)

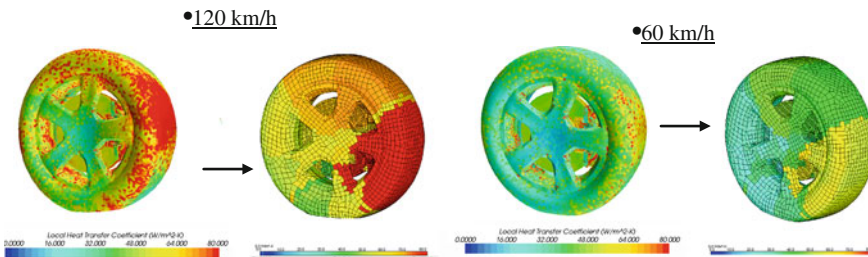


Fig. 10 Mapping results from Star-cm+ to Radtherm

## 4 Results and Correlation

As said before, the target of the paper is to develop a methodology to simulate the braking fade. The simulation was supported by the test data in order to correlate the simulation. The test consists in fifteen brakings of which the first five brakings of the front right side of the vehicle have been correlated.

Once the methodology was explained, it was applied to a real case. The car evaluated corresponds to a car of segment C. The CFD, Amesim and Radtherm results have been showed in the previous chapters. Two different set-ups were studied with Radtherm, the scope was to develop a great definition of the brake rotor, because it is the heat source of the problem, moreover the other parts have been also developed with detail.

The first variation corresponds to a Lumped Capacitance model, this model consists in the definition of shells model connected through one equivalent thermal node [5]. The scope of this modelization was to obtain a simplest model with a high level of accuracy.

The second one corresponds to a Solids model, which consists in a volumetric definition on the volume enclosed inside the disc. The scope of this modelization was to obtain a more accurate definition of the rotor (Fig. 11).

The obtained Radtherm results with the Solids model, are shown in Fig. 12.

With this visualization, it is possible to analyse the distribution of temperatures in the rotor disc solid, and the temperatures around the brake (Fig. 13).

The Lumped Capacitance model, shows a high level of discrepancy, the peaks are so high in each braking. Furthermore the simulated transient evolution of the temperature after the peak of heat rate due to the braking presents a bigger slope than the test.

On the other hand, the results of Solids Radtherm model show a high correlation level with the test data, the solids definition of the rotor disk captures with high accuracy all the transient temperature evolution. Therefore, the model that correlates with the test, is the solids model.

Taking into account that the friction coefficient is constant in the range of temperatures of study, it could be considered constant for this time range in the Amesim model. Therefore it is not necessary to employ a co-simulation model in this correlation. However, it will be studied as a key factor in scenarios where it is not constant.

## 5 Improvement of Methodology: Co-Simulation

To improve the accuracy of our methodology, the co-simulation by 1D and 3D thermal software has been studied. The aim of this procedure is to fix a two way coupling methodology using the heat rate generated in the Amesim model and transferring it to the Radtherm model in a transient analysis. The brake-disk

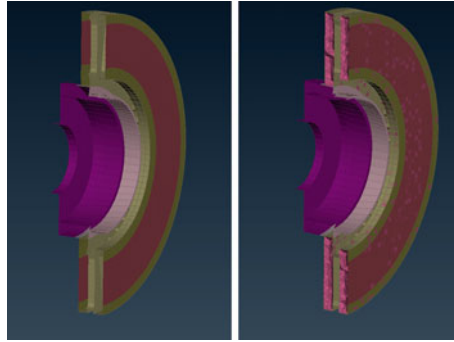


Fig. 11 Lumped capacitance model (left). Solids model (right)

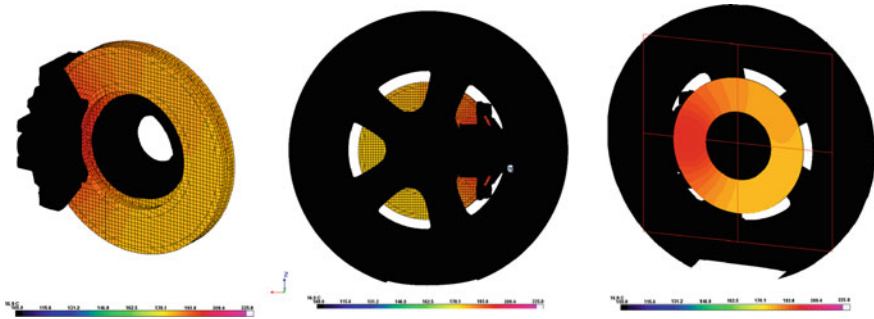


Fig. 12 Thermal results obtained with Radtherm

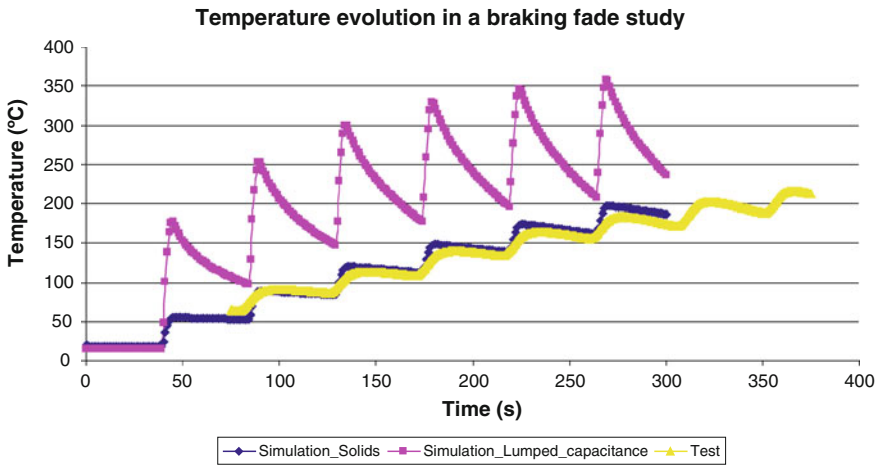
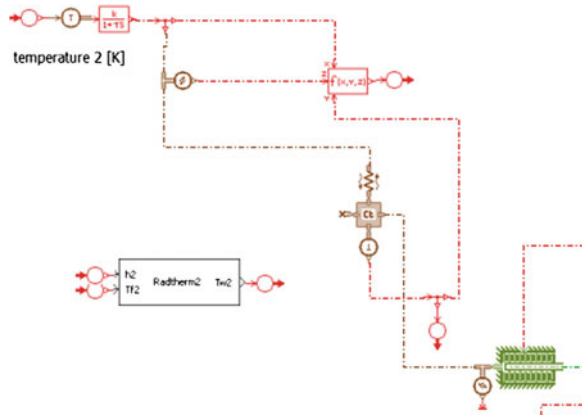


Fig. 13 Thermal results obtained with Radtherm

**Fig. 14** Thermal results obtained with Radtherm



temperature calculated in the thermal simulation with Radtherm will be an input of the 1D simulation to re-compute the braking cycle, thus taking into account the brake fading effect.

With this technique, one can study braking pads with a strong dependence between temperature and friction coefficient in a transient simulation. To implement it in the co-simulation in our workflow, it was necessary to change the connection between Amesim and Radtherm, establishing a co-simulation link between rotor parts of each model. The workflow is the same as it has been presented in the methodology workflow in the first part of the paper.

### 5.1 Co-Simulation Schematics

The co-simulation blocks will transfer the heat flux obtained during the braking action (Fig. 14).

Due to the high level of accuracy obtained in the results with a solid model of the brake disk, a co-simulation was not needed. If the variation of the friction coefficient of the pad has a strong dependence on temperature, i.e., in racing cars, a co-simulation scheme of Amesim coupled with Radtherm with a two-way-coupling will be necessary. With this model, the variations in a brake torque due to the increment/decrement of friction coefficient because of the amount of heat in the rotor brake, will be captured.

At this point, the design of brake vents and adjacent parts of the brake could be improved in order to increase the air flux throw the brake, increasing therefore the cooling effect and avoiding braking fade problems.

## 6 Conclusions

In the present work an additional step has been done in the area of thermal brake performance. Some improvements have been introduced in the methodology and also in the brake fade correlation in order to obtain better results. One of the main conclusions is that a more realistic representation of the 1D scheme of car with a 1D software helps to improve the accuracy of the brake fade simulation.

The usage of the co-simulation technique allows to take into account the curve of friction as a function of temperature. The cooling effects on disks that are given by the CFD simulations are also introduced in the performance of the thermal simulation. This information, combined with the 1D simulation allows to obtain an accurate prediction of brake torque in our 1D simulation.

The simulation procedure for braking fade detection presented here was able to prevent temperature-related fade problems. Moreover it is possible to perform a robust design of the brakes rotor cooling.

## References

1. Polansky J, Bingen PK (2003) Simulation of the cooling of a brake disk. Germany
2. Amesim v10.0 SL1 user's guide
3. Jerhamre A, Hunter CB Numerical study of brake disc cooling accounting for both aerodynamic drag force and cooling efficiency, SAE technical paper. 2001-01-0948
4. Star-ccm v.7.02.008 user's guide
5. Radtherm 10.0 user's guide

# BIW Optimization by Means of an Automated CAE Process for the Reduction of Welding Points

Pérez Mario, Calvo Roger and Hirschbeck Bernhard

**Abstract** The reduction of vehicle manufacturing costs is one of the most important targets in the development phase. One way to reduce this cost is by means of the reduction of welding points. Another challenge lies in reducing the development time. Both for reduction of costs as well as development time, simulation is increasingly important. This paper explains how both objectives can be achieved by means of spot weld optimization applying the finite-element method. The BIW has to satisfy certain requirements. The most important requirements concern fatigue, stiffness and crashworthiness. Some requirements may cause conflicting solutions, for example, a good solution for stiffness (such as a high eigenvalue), could be an unacceptable solution for crashworthiness. For this reason, joints or other parts are sometimes oversized. In order to reduce the cost of the project and simplify the manufacturing process, an optimization study is performed. In this project, all spot welds used in the manufacturing process of the BIW will be analysed with optimization software (PAM-OPT) for all load cases mentioned earlier (crashworthiness, stiffness and fatigue). The objective is to minimize the number of welds and improve the defined targets. After this spot weld reduction, the BIW must still meet all structural targets defined in the project. This means that the target in BIW stiffness (first eigenvalue), crash targets (pulse, deformation pattern, intrusions) and fatigue targets must be respected. In order to perform the optimization, it is necessary to define the target (e.g. spot weld reduction), the constraints for each load case (structural targets), the best optimization algorithm to be used and design parameters, as well as considering issues such as optimizing CPU usage. This study is limited by the amount of available

---

F2012- E03-038

---

P. Mario (✉) · C. Roger · H. Bernhard  
Applus+ IDIADA, Tarragona, Spain  
e-mail: mperez@idiada.com

CPU's. Analysing different load cases for a complete BIW, implies a significant calculation capacity, especially for load cases calculated with the explicit method (offset crash, side crash, etc.). The limited availability of CPUs could mean that only a partial study of the vehicle is feasible.

**Keywords** Optimization · Spot weld · Body in white (BIW) · Costs

## 1 Introduction

The BIW is subject to many requirements, mainly concerning fatigue, stiffness and crashworthiness. The distribution of spot welds plays an important role in achieving these requirements. On the other hand, minimizing the total number of spot welds, leads to a significant cost reduction. The objective of this investigation is to reduce the costs of the BIW by minimizing the total number of spot welds (maintaining or improving its performance), through an automated CAE process.

The benefit of automatic optimization is the reduction of the time spent by engineers on the issue (and therefore a reduction of the project lead time). The way of working is shown in Fig. 1.

Further benefits of the optimization are:

- More accurate solution at the end of the development process
- New physical solutions at the beginning of a development process

For this project, the optimization software applied is PAM-OPT. This software offers various optimization algorithms [1] (Adaptive RSM, Gradients, Branch and Bound, Iterative Random, Genetic). During this project, the following two algorithms are investigated:

- **Algorithm Genetic:** The genetic algorithms use a set of points called population. A point is also called an individual. The genetic algorithm performs an evolution of the population in order to reach a better population. A better population is a population that contains a higher number of points that meet the criteria of the optimization problem (objective and constraint functions). This method is appropriate for solving problems with many local minima and without linear behaviour. In return, this algorithm needs many solver calls.
- **Algorithm Adaptive RSM:** This method uses approximated functions, which have similar characteristics to the B-Splines in CAD applications. This algorithm combines robustness with fewer solver calls.

For all algorithms it is necessary to define the following parameters:

- Design parameters
- Objective function
- Constraint functions
- Parameters limit

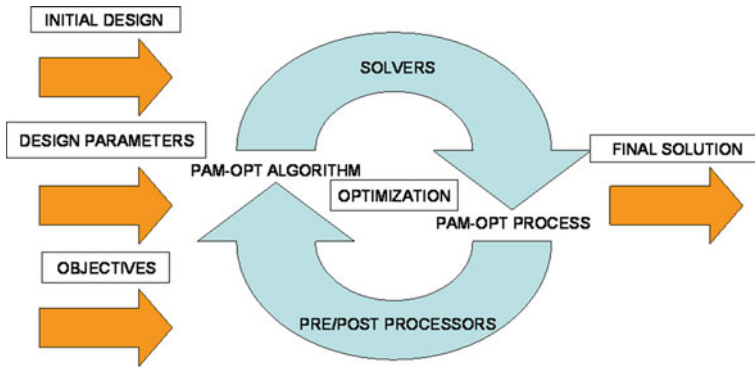


Fig. 1 Sequence of the optimization

## 2 Spot Weld Optimization with Algorithm Genetic

This methodology is recommended if spot weld reduction is needed in an advanced stage of the project (in which most spot welds have been defined already). In this case, the objective is to reduce the number of spot welds or to optimize a certain requirement of the vehicle, by modifying the spot weld distribution.

Three simple examples are performed with different objectives, in order to show the potential of the PAM-OPT tool.

*The first example* consists of a simple long member with 24 spot welds and a separate deformation box mounted onto it. This assembly is subjected to an impact with an undeformable wall of 200 kg. The goal is to minimize the deformations in the long member, and concentrating it into the deformation box (as in AZT test). Therefore, the objective is to minimize the internal energy curve of the long member.

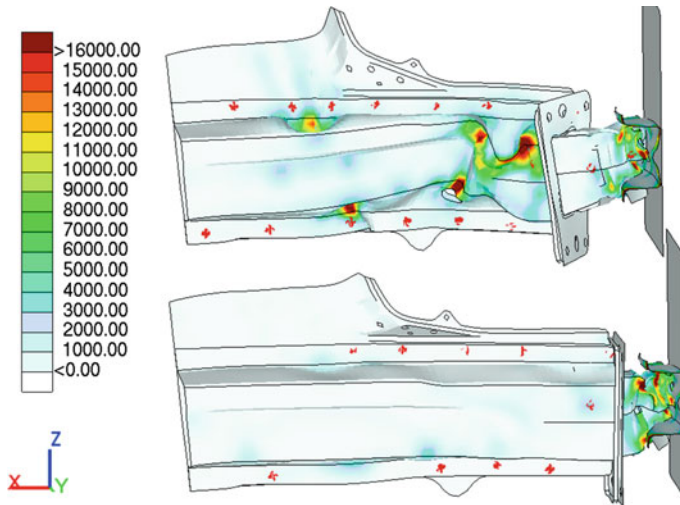
The programs used for this optimization are PAM-CRASH for the explicit simulation, Visual-Environment to obtain the energy curve and PAM-OPT to manage [2] the optimization.

For all the optimizations a Linux Platform is applied, but it is possible to use UNIX and Windows platforms as well.

To minimize the energy the PAM-OPT uses the existing spot weld and it chooses between applying rupture or not applying rupture in the material of the spot weld. Two different spot weld materials are defined for this simulation: one without rupture and another with rupture (with a low rupture value, which is equivalent to removing the spot weld at the start of the simulation).

After the optimization, the long member spot welds are decreased to half of the initial amount and the long member internal energy is reduced to 15 % of the original value (Fig. 2).





**Fig. 2** Comparison between the original long member and the optimized version

*The second example* is the same long member assembly but in this case a combination of two load cases is defined. One explicit (exactly the same load case as the first example) and one implicit (a modal simulation). The objective defined is a combination of both load cases, since only one objective function can be defined. For a better understanding, a pre-simulation is performed.

For this optimization, the software applied is PAM-CRASH for the explicit and implicit simulation, Visual-Environment to obtain the energy curve and PAM-OPT to manage the optimization.

In this case, the objective is to minimize the following function:

$$(174 - (\&Eigenvalues * 1000)) + (\&Max\_int\_energ * 0.01)$$

This equation proposes to minimize the internal energy absorbed and maximize the second eigenvalue. The main objective is to find equilibrium between both cases: the best combination between a good energy absorption and high stiffness.

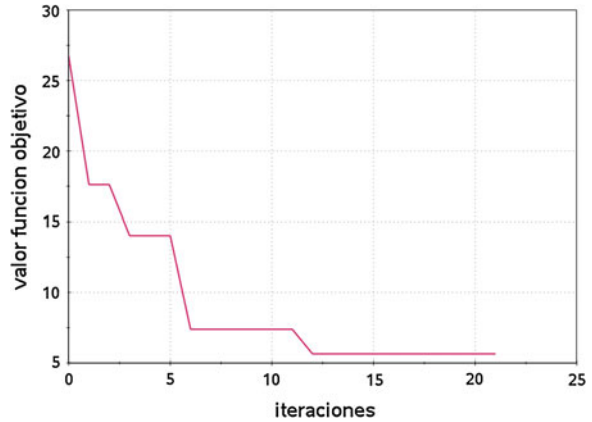
It is highly important to have a good objective definition. If this function is not defined correctly, undesired solutions can be obtained or it might not be possible to find a solution (Fig. 3).

The optimization process discussed here leads to a removal of three spot welds. With this solution, the modal eigenvalue has a small increment. The internal energy significantly improves: the original value reduces to 35 %.

*The third and last example* involves the complete BIW. In this case the objective is to minimize the number of spot welds in a modal simulation. The target concerns the final value of the first eigenvalues.

In order to limit the number of iterations, the investigation is reduced to the spot welds in the upper structure. In this optimization the objective is to minimize the

**Fig. 3** Evolution of the value of the objective function



number of spot welds, respecting a maximum decrease of 2.5 Hz of the first eigenvalue.

The software applied in this optimization is PAM-CRASH for the implicit simulation and PAM-OPT to manage the optimization.

In this case the population size is 200 and the number of iterations is 40. This leads to a maximum of 7,400 simulations. Estimating each simulation with 40 CPU's to last around 150 s, the total duration of the optimization is around 15 days (Fig. 4).

This optimization results in the number of spot welds being reduced by 40 %, while the modal values reduce by 2.5 Hz.

### 3 Spot Weld Optimization with Algorithm Adaptive RSM

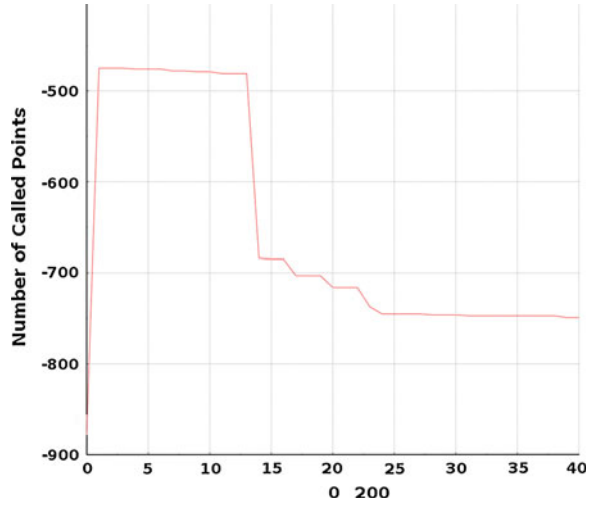
This methodology is recommended when the global spot weld distribution has not been defined yet. This algorithm can provide an accurate spot weld distribution at the beginning of the project.

In this optimization the objective is the same as in the first Genetic example: the internal energy of the long member is minimized, while adding spot weld positions to the process (Fig. 5).

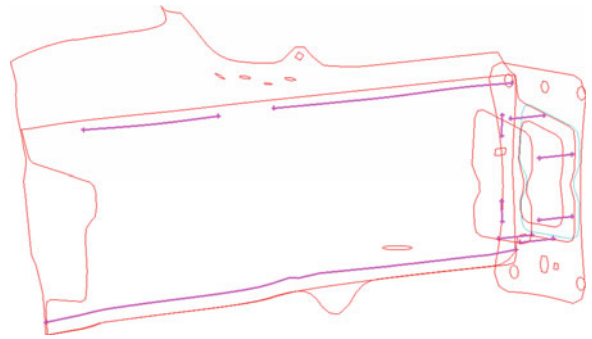
In this case, geometrical lines (curves) are defined, on which spot welds are placed. The variable is the density of points on these lines. In ANSA the spot weld points can be distributed in a non-linear manner and thus the spot weld density can be increased where needed [3].

The software used for this optimization process is ANSA for the pre-processing, PAM-CRASH for the explicit simulation, Visual-Environment to obtain the energy curve and PAM-OPT to manage the optimization.

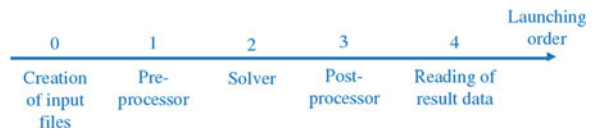
**Fig. 4** Number of spot weld evolution



**Fig. 5** Spot weld lines



**Fig. 6** Optimization sequence



The advantages of the Adaptive RSM algorithm compared to the Genetic algorithm are that it is more robust and faster. The optimization sequence of this method is explained in Fig. 6.

After the optimization, the result values were very similar to the example with the generic algorithm; but in this case, the spot welds are more evenly distributed.

## 4 Summary

This paper presents two ways of working with two different algorithms. The RSM adaptive is recommended in the earliest stages of the project, since it can define an accurate spot weld position only with the definition of the spot weld lines. The

Genetic algorithm is recommended to minimize spot weld or maximize certain targets in the later stages of the project.

Both methods have some limitations in CPU cost, especially in the simulation of a full car crash, due the high CPU requirements of explicit calculation methods. If an investigation involves many load cases and a high number of variables, the CPU cost could be unacceptable.

## References

1. ESI group (2009) PAM-OPT. Solver reference manual
2. ESI group (2005) PAM-OPT. Editor
3. BETA CAE systems (2012) Task manager

# Establishing a Carbon Fiber Material Database for Crashworthiness Structural Development

Pablo Cruz and Raúl Ureña

**Abstract** Current climate change conditions together with new environmental regulations are boosting research and use of new materials in order to reduce both the use of petroleum products and CO<sub>2</sub> emissions. Composite material becomes an excellent candidate in order to achieve the abovementioned challenges. The stiffness-weight ratio of composite materials provides an optimal intrinsic material characteristic when compared with the traditional metal approach. This is the reason why aeronautical and automotive industries are increasingly trying to incorporate these materials into structural parts design. The aeronautical sector is leading this challenge and has already designed planes whose structure has 35 % of the parts made of composite materials. Crashworthiness performance is important in both the automotive and the aeronautical sectors. Nevertheless, some of the automotive impact load cases, such as the Side Pole and Frontal Impact, imply structural behaviour scenarios that reach and probably surpass the state-of-art of the current virtual development tools regarding carbon fiber material laws and finite element modelling techniques. This chapter describes the necessary steps to follow in order to be able to introduce carbon fiber parts in vehicle structural development. The process should consider: (1) Criteria definition for the selection of parts to be made of carbon fiber. (2) Carbon fiber material selection for each part. (3) Carbon fiber material properties characterization including the required tests and samples. (4) Finite element modelling guidelines to carry out the body structural development. The integration of CFRPs materials in vehicle structural parts is achievable through a multidisciplinary team combining deep knowledge and expertise in vehicle functionalities, material science and

---

F2012-E03-039

---

P. Cruz (✉) · R. Ureña  
Applus+ IDIADA, Tarragona, Spain  
e-mail: pcruz@idiada.com

manufacturing together with excellence in managing the development tools: CAD, CAE and Testing. IDIADA's approach to the integration of CFRPs provides a comprehensive environment offering the required cornerstones to act as a seamless development partner for OEMs.

**Keywords** Composite · Carbon fiber · Crash · Simulation · Material characterization

## 1 Introduction

Carbon fiber structures have been successfully introduced in the aeronautical industry in order to improve the structure's strength behaviour. Carbon fiber allows obtaining high performance structures under static and dynamic, crash and fatigue load cases, and saves weight.

Carbon fiber manufacturing processes contribute to reducing CO<sub>2</sub> emissions and allow conforming complex geometries simplifying manufacturing process. In the automotive industry, continuous evolution of the safety requirements and asymptotic weight reduction for the current material data base have pushed the need for innovation.

## 2 Vehicle Development: Fundamentals and Cornerstones

In a vehicle development process different stages can be identified: Styling, Vehicle Functionalities, Packaging, Concept, Design, Metal Database, CAE Modelling Guidelines & Best Practices, Structural Analysis, Manufacturing, Tooling & Joining, Prototyping, Testing, Validation, Integration, Cost and Sustainability.

The impact of the introduction of carbon fiber must to be analysed individually at each stage (Fig. 1) and for the development process as a whole.

## 3 CFRP: Styling Design Influence

Carbon fiber manufacturing processes allow creating complex structural shapes as single parts.

Automotive industries have started to introduce carbon fiber parts in designs (Fig. 2). These parts have been introduced in small series manufacturing processes [1, 2].

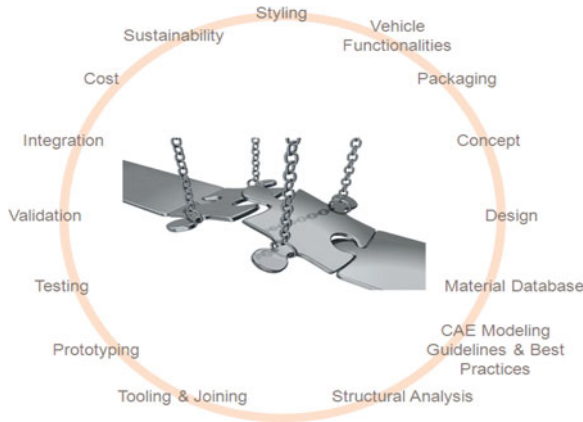


Fig. 1 Vehicle development



Fig. 2 Examples of vehicles that have been introduced carbon fiber parts in small series manufacturing processes

Manufacturing productions of 100.000 units/year are the manufacturing target in order to make them compatible with the current automotive industry production level.

Analysing from the manufacturing point of view, there are some structural items that could be manufactured in carbon fiber. Currently, some automotive structural parts could be designed using carbon fiber material and introduced in the manufacturing productive cycle. The automotive parts that could be studied in order of feasibility:

- Front/rear absorbers
- Stiffeners (pillars, frames, doors)
- Exterior surfaces (bonnet)
- BiW (beams, pillars, frames)
- BiW full

## 4 CFRP: Concept and Design Influence

Manufacturing methodologies and non-isotropic characteristics of composites require a significant change of current design methodologies. Carbon fiber parts must be designed according to the structural function they must carry out in order to obtain the best structural performance. Layouts of composite plies can be designed in order to obtain excellent mechanical properties in a specific direction. Thus, it is important to understand the load cases involved at this stage.

Designers must consider from the initial definition of the part the manufacturing process to be carried out because the mechanical properties of the carbon fiber part will depend on it.

## 5 CFRP: Establishing the Material Database

As is well known, material characterization is one of the main cores of reliable virtual development. The intrinsic complexity of CFRP requires close support from material science experts to characterize the CFRPs material properties.

IDIADA is collaborating with the reputed AMADE Research Group from Girona University to close the material innovation gap around CFRPs. Thanks to this collaboration IDIADA obtains state-of-art CFRPs material characterization.

Material law definitions of the composite materials for the required development fields (e.g. stiffness and crash) are provided. The material laws are generated and validated for the different development CAE codes (e.g.: Pam-Crash, Abaqus, LS-Dyna, Nastran, etc.).

When the standard material laws included or the development CAE codes are not accurate enough, additional User Defined Material Laws can be provided.

A complete testing program is performed in order to obtain composite elastic, damage initiation and damage evolution properties.

### 5.1 Carbon Fiber Material Properties Characterization

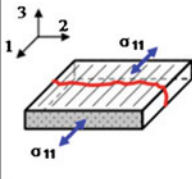
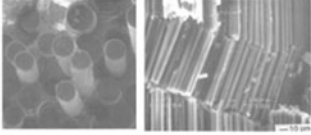
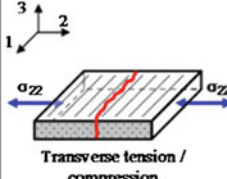
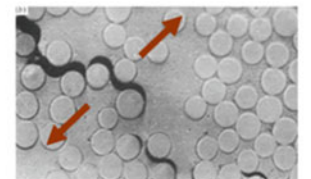
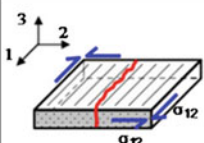
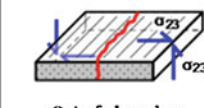
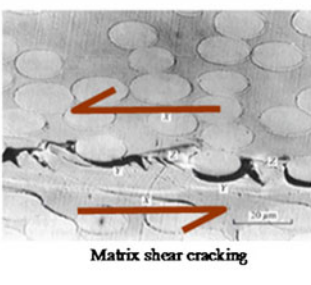
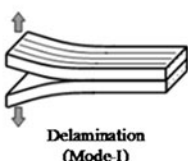
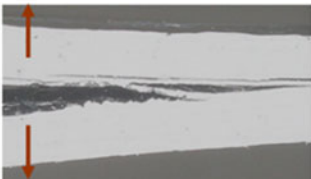
Due to the non-homogeneous properties of the material, composites damage could be classified [3]:

- Fiber failure: Tensile fiber fracture, local instability, fiber kinking
- Matrix failure: Matrix cracking, aging, thermal stresses
- Fiber debonding at fiber-matrix interface: shear loads
- Delamination: separation between plies at the interface

All previous damage modes could be classified as interlaminar or intralaminar damage as it is shown in the Table 1.



**Table 1** Composite damage

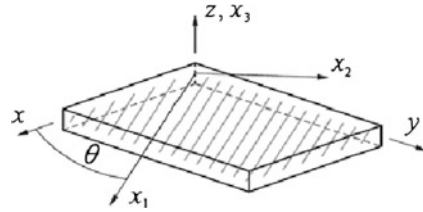
	Mechanical Loading	Fractographs of the Failure Zone
Intra-lamellar Failure	<p><b>Fibre Failure</b></p> 	 <p>Fibre tensile rupture      Fibre compression kink band</p>
	<p><b>Matrix Failure</b></p> <p><b>Transverse tension / compression</b></p> 	 <p>Matrix transverse tensile cracking</p>
	<p><b>Matrix Failure</b></p> <p><b>In-plane shear</b></p>  <p><b>Out-of-plane shear</b></p> 	 <p>Matrix shear cracking</p>
<p><b>Inter-lamellar Failure</b></p>  <p>Delamination (Mode-I)</p>	 <p>Ply separation</p>	

In order to define previous material behaviour, composites elastic, strength and damage properties some tests must be performed [4].

- Elastic and strength characterization tests: following properties must be obtained (according to Fig. 3):

- $E_{t11}$  Tensile elastic modulus in the fibre direction
- $E_{c11}$  Compression elastic modulus in the fibre direction
- $E_{t22}$  Tensile elastic modulus in the transverse direction
- $E_{c22}$  Compression elastic modulus in the transverse direction

**Fig. 3** Composite axis system



$\nu_{12}$	Poisson's ratio in plane 1–2
$G_{12}$	Shear Modulus in plane 1–2
$X_t$	Tensile strength in the fibre direction
$X_c$	Compression strength in the fibre direction
$Y_t$	Tensile strength in the transverse direction
$Y_c$	Compression strength in the transverse direction
$S_L$	In-plane shear stress

- Interlaminar Fracture toughness tests (Mode I and Mode II)
- Interlaminar Fracture toughness tests (Mixed-Mode)
- Compact Tension (CT) and Compact Compression (CC) Tests

In the following figure some Cohesive Law are shown for an interlaminar damage test (Fig. 4).

## 6 CFRP: Structural Analysis and Fe-Modeling Guidelines

Definition of appropriate finite element (FE) modelling guidelines is extremely important to capture the real structural behaviour. Modelling guidelines must include best practices to follow the virtual assessment of the structural performance in all required development fields (e.g. crash, static & dynamic stiffness, fatigue, etc.).

The correct use and combination of the available development tools (i.e. CAE, CAD and Testing) is essential at material sample, component, sub-system and vehicle level.

In the specific case of CFRP structures, where several kinds of failures may arise, the modelling guidelines are even more critical than the known behaviour of the metal structures.

Modelling guidelines strongly depend on manufacturing, assembling and joining conditions and technology and should be defined and checked during the initial phases of the development. The definition should be based on physical samples and/or prototypes manufactured and assembled in conditions as similar as possible to the final manufacturing and assembling conditions (Figs. 5, 6).

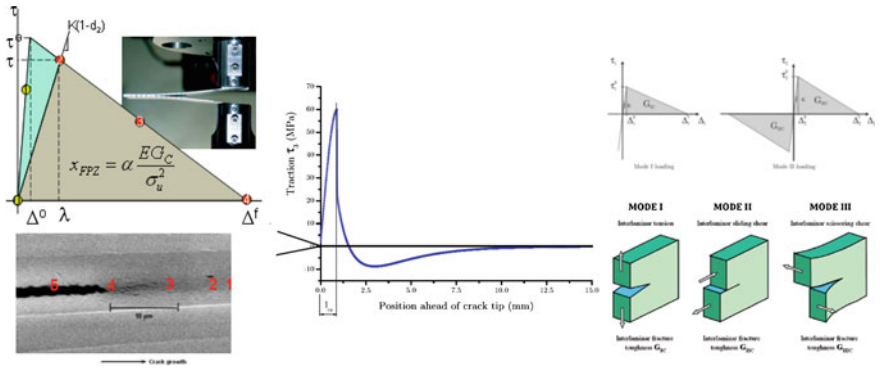


Fig. 4 Interlaminar damage test. Cohesive law

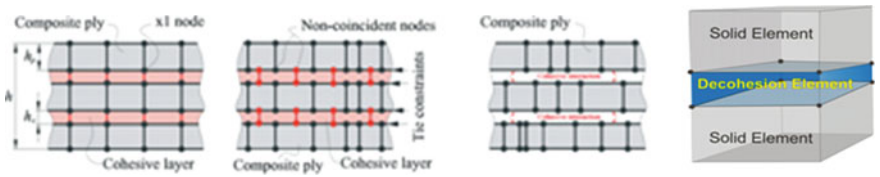


Fig. 5 Example of composite FE modelling

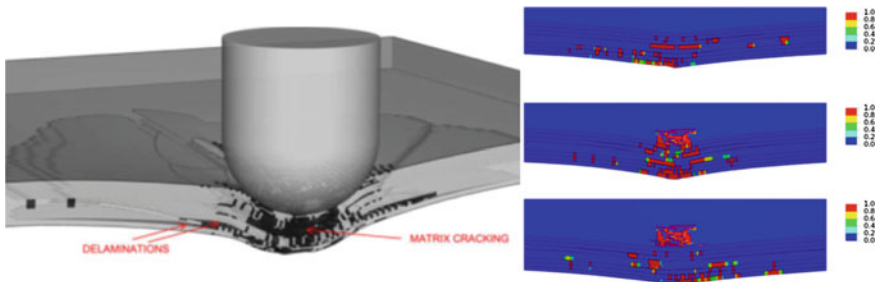


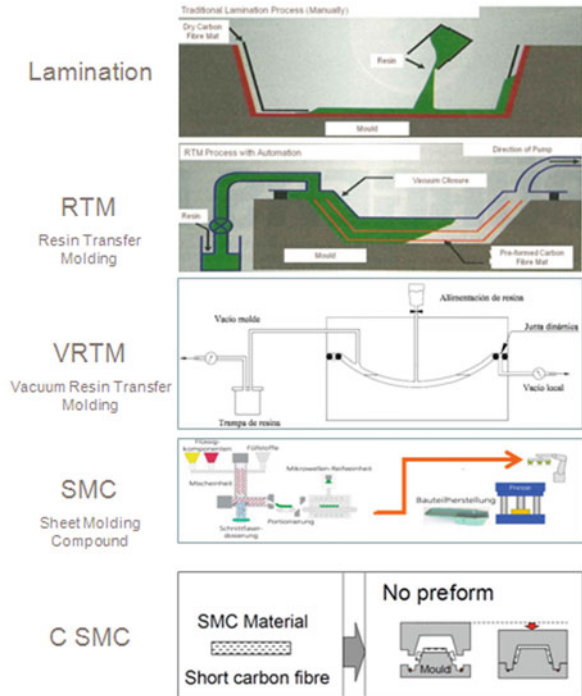
Fig. 6 Example of composites simulation (source AMADE)

## 7 CFRP: Manufacturing, Tooling and Joining

Choosing the appropriate manufacturing technology is a milestone during the development of CRFP structures.

IDIADA collaborates with best-in-class CFRP component suppliers in order to add their extensive manufacturing, tooling and joining experience, expertise and advice to the development team (Fig. 7).

**Fig. 7** Example of current manufacturing processes



## 8 Conclusions

The integration of CFRPs materials in vehicle structural parts is achievable through a multidisciplinary team combining deep knowledge and expertise in vehicle functionalities, material science and manufacturing together with excellence in managing the development tools: CAD, CAE and Testing.

IDIADA’s approach to the integration of CFRPs provides a comprehensive environment offering the required cornerstones to act as a seamless development partner for OEMs.

## References

1. 12th international CarBody benchmarking conference
2. Euro CarBody exhibitors 2010/2011
3. Pickett A (2011) Impact and crash simulation of composite materials. ESI Group
4. González E (2010) Simulation of interlaminar and intralaminar damage in polymer-based composites for aeronautical applications under impact loading

# Full Vehicle Durability Analysis by Means of the IDIADA Virtual Proving Ground

Jordi Arbiol, José Antonio Muñoz, Xavierl Armengo and Enric Aramburu

**Abstract** It is usual that the applied loads on structural elements are in fluctuating situations. Sometimes the component can break under its ultimate or its yield strength. This break situation is due to the fluctuating loads that have been applied for long periods. For this purpose this breaking type is called “fatigue breaking”. Fatigue breaking is a consequence of a crack growth. When no prototypes are available, it is necessary to calculate the life prediction as soon as possible. Simulation through the VPG is being increasingly used for life prediction. The present work shows a methodology that uses a Finite Element Model (FEM) that runs on a proving ground. In this case, no MBS (multi-body software) model is used to obtain the loads on the structure. Because the whole simulation of the finite element model needs a lot of time, a co-simulation is carried out. An implicit FE solver is used for problems in which the response is moderately nonlinear. This implicit method is computationally expensive. On the other hand, an explicit FE solver is ideal for modelling highly nonlinear problems such as changes in contact surfaces. This explicit method is relatively inexpensive. The ideal situation is to use the correct solver where it will be needed. Components with moderate non-linear behaviour (Body, Suspension) will be solved using the implicit method. Explicit method will be used to model the impacts of the tire against the Virtual Proving Ground. Fundamental parts of this methodology are the digitalization of IDIADA’s proving ground, its implementation as a rigid body and co-simulation.

**Keywords** VPG (Virtual Proving Ground) · Fatigue · Durability · Road · Vibration

---

F2012-E03-040

---

J. Arbiol (✉) · J. A. Muñoz · X. Armengo · E. Aramburu  
Applus + IDIADA, Tarragona, Spain  
e-mail: jarbiol@idiada.com

## 1 Introduction

The Virtual Proving Ground becomes the most accurate methodology to estimate suspension component durability and is, also, useful to know the component loads on the finite element model.

Several processes are used for fatigue life prediction. Some of them come from tests and others come from virtual inputs. Some of these methods are:

- Equivalent quasi-static from RLDA (Road Load Data Acquisition)
- Unitary responses from RLDA
- VPG using MBS software
- VPG using FEM

## 2 Fatigue Analysis from RLDA

### 2.1 *Equivalent Quasi-Static*

This methodology is a simple one, but it is effective in the early stages of the vehicle's development phase. It permits several loops with less CPU time consuming. The base of this process consists of obtaining quasi-static inputs that produce the same damage on the vehicle as the real test.

These inputs are very easy ones. They consist of pairs of amplitudes and mean stresses representative of average real working situations of the vehicle. They are obtained from the RLDA from the point of view of damage structure.

Some of them can be: turn left/turn right, braking/accelerating, vertical oscillations (Fig. 1).

### 2.2 *Unitary responses*

The RLDA of a vehicle over a fatigue track is used as inputs on a finite element model. These inputs are forces and moments.

To know stress levels on the component, it is necessary to know the stresses for a unitary load. Multiplying these values by the force of the test at each time step, a stress state can be obtained. A linear superposition of the unitary responses is performed: (Fig. 2)

The forces come from a dynamic test, but the simulation is a static one. The dynamic effect is not supported in this method. To avoid this situation, a modal analysis has to be done to assure that the frequency of the components will not be excited by the inputs.

Figure 3 shows the fatigue analysis procedure using RLDA inputs.

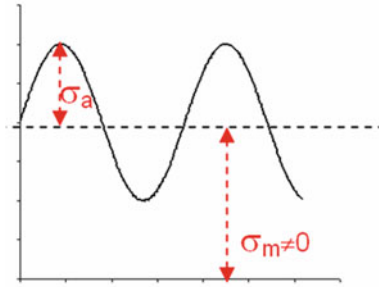


Fig. 1 Each amplitude-mean pair is representative of one cycle

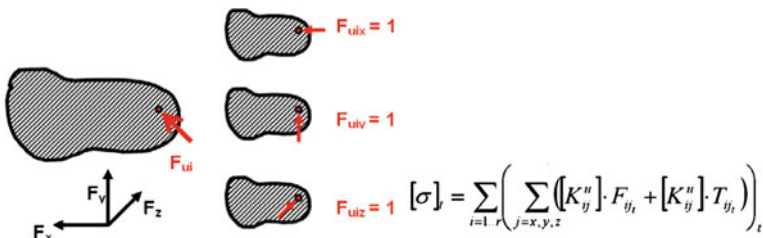
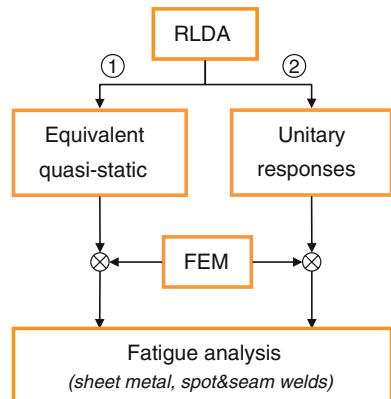


Fig. 2 Unitary loads on a connection point. On right side is showed the superposition at each time step

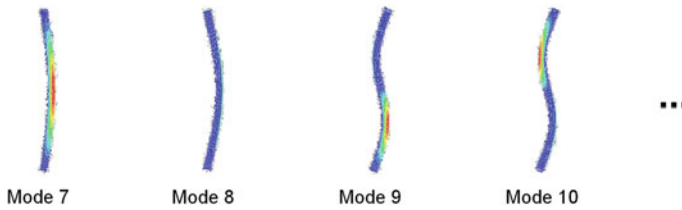
Fig. 3 Fatigue analysis from RLDA



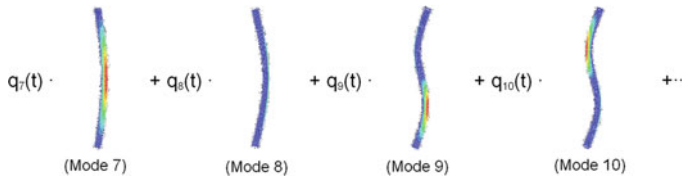
### 3 Fatigue Analysis from VPG

#### 3.1 VPG using MBS Software

Multi-body software is used to introduce the VPG as input. There are two different outputs that will be used for fatigue simulation:



**Fig. 4** Unitary responses of mode shapes



**Fig. 5** Linear superposition

- **Modal contributions:** In this case, flexible bodies are included in the model. During MBS simulation, a contribution factor is reached for each mode at each time step.
- **Forces:** It is not necessary to include flexible bodies. The results of the MBS simulation are the forces on each connection point at each time step.

Using the *modal contribution* procedure, a modal superposition method is performed which takes into account the dynamic effects of the structure, possible excitation of some modes and correct boundaries on each component. The unitary responses are obtained from a modal analysis. Figure 4 shows some modes of a simple finite-element model.

A linear superposition of the modes is performed: (Fig. 5)

Using the *force* procedure, the linear superposition explained in the *Unitary responses* headland have to be done.

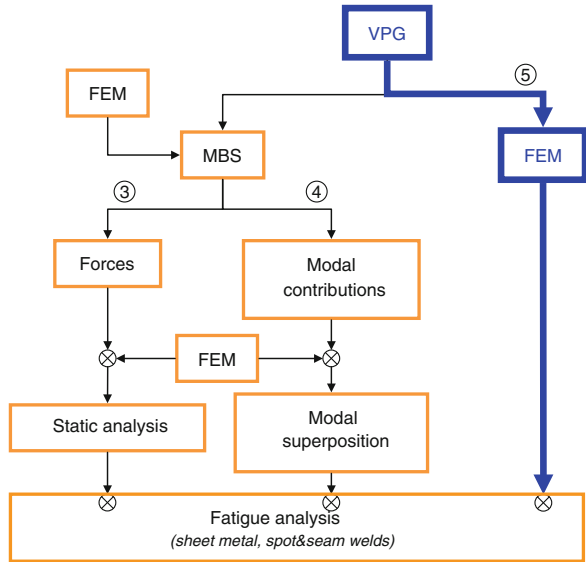
### 3.2 VPG using FEM

Finite element model is used to perform the fatigue analysis. All of the phases, from the road input to the fatigue analysis, are performed on the same model. It is not necessary to build an additional MBS model. The main topics of this option are the following:

- The body and the component suspension are built as superelement.
- All of the connections (bushings, shock absorbers, springs, and joints) have been modelled by connector elements.
- A tire with an easy correlation phase is built.



**Fig. 6** Fatigue analysis from VPG. The presented procedure of this work is remarket as number 5



- Contacts between tires and ground have been defined.
- Co-simulation: The combination of implicit and explicit methods makes this option effective.

Figure 6 shows the fatigue analysis procedure using VPG inputs. The following Tables 1, 2 show the highlights of each method.

## 4 Vehicle Model

The components are modelled as superelements. ABAQUS permits decomposing big finite element models to small substructures called superelements. This procedure becomes efficient due to the small CPU time consuming.

Lumped masses are added to the model to account for all non-structural masses, as well as powertrain components, fuel tank, spare tire, tools, etc. Each component is defined as superelement: wishbones, antiroll bar, and knuckles. Bushings, joints, shock absorbers, bump stops, springs and links are modelled by connector elements (Fig. 7).

### 4.1 Spot Welds

Stress intensity of spot welds is determined from the local force components because direct computation of load spot-weld stresses is not practical for large-scale structural finite element analysis.

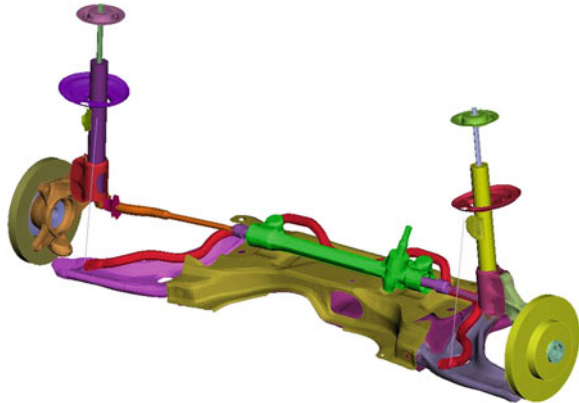
**Table 1** Advantages of each method. Numbers in brackets match with Figs. 3 and 6

Input	Method	Advantages		
		Design's loops	Accuracy	Others
RLDA	Equivalent quasi-static [1]	Fast	–	–
	Unitary responses [2]			
VPG	MBS Forces [3]	–	Good	–
	Modal contributions [4]			
	FEM [5]			In-house tire model

**Table 2** Disadvantages of each method. Numbers in brackets match with Figs. 3 and 6

Input	Method	Disadvantages		
		Design's loops	Accuracy	Others
RLDA	Equivalent quasi-static [1]	–	Moderate	Additional modal analysis
	Unitary responses [2]			
VPG	MBS Forces [3]	Moderate	–	Additional MBS model
	Modal contributions [4]			Tire model from supplier
	FEM [5]			–

**Fig. 7** Front suspension components

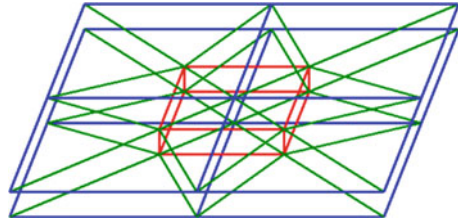


All structural components are modelled and connected by means of beam elements (for a refined analysis) or solid elements (for a not-refined analysis).

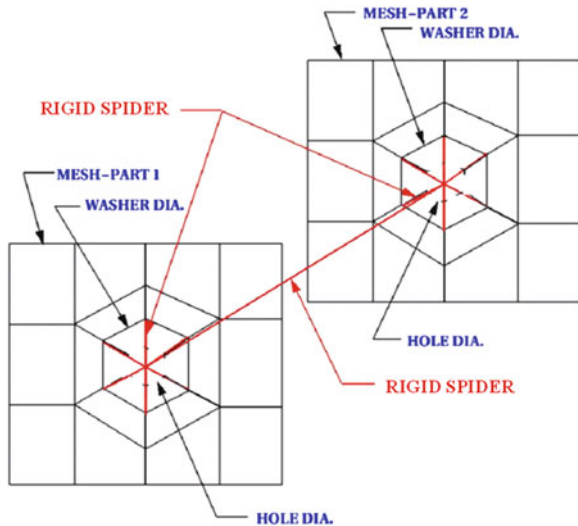
**4.1.1 Not-Refined Analysis**

In the industrial process of design and analysis, the parts of a structure are meshed individually. If these parts have to be connected by spot welds the meshes are not compatible and a manual connection is very time consuming.

**Fig. 8** Non-refined spot weld. Shell elements (*blue*), hexahedral element (*red*), interpolation constraints (*green*)



**Fig. 9** Refined spot weld. The nugget is a rigid cylinder and it is connected to shell elements by rigid spiders



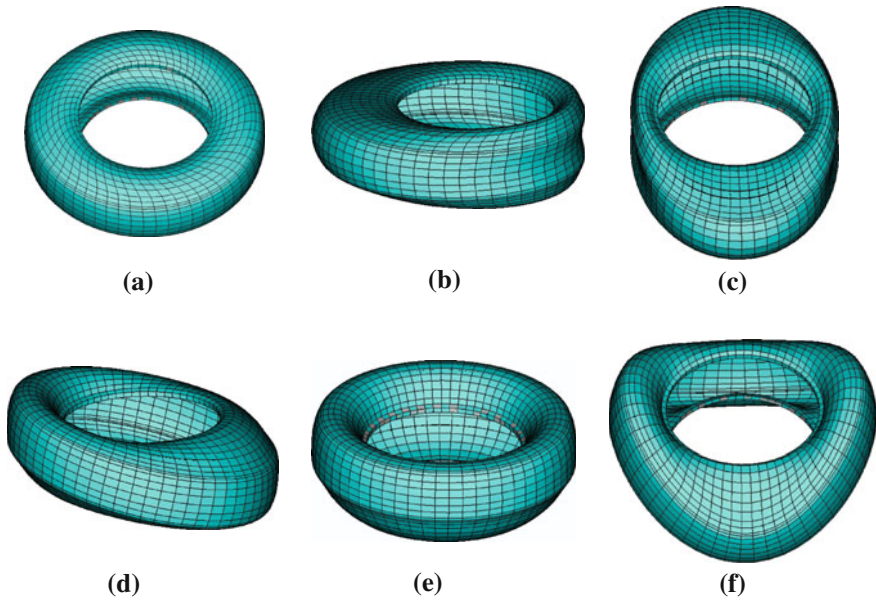
It is a way to replace a spot weld by a hexahedral element connected to the sheet by interpolation constraints (Fig. 8). These interpolation constraints are built in a way to reflect the shape functions of the shell elements under consideration.

### 4.1.2 Refined Analysis

The nugget is modelled as a rigid cylinder, i.e. two or more rigid spider disks that are connected and the discs are connected to a ring or at least 6 (typically more) quad-shell elements.

Two kinds of solutions to stress intensity factors at spot welds are considered, without using solid elements: (Fig. 9)

- The structural-stress-based solution, in which the stress intensity factors are determined by stresses in the shell elements around the spot weld,
- The force-based solution, in which the stress intensity factors are estimated by the interface forces and moments in the beam element that simulate the spot weld.



**Fig. 10** Torsion and radial tire modes are the most relevant ones (**a**, **b** & **c**). Flexural modes are not so important. **a** Torsion mode, **b** Radial mode 1, **c** Radial mode 2, **d** Flexural mode 1, **e** Flexural mode 2, **f** Flexural mode 3

## 4.2 Tire Model

The tire is the primary load transfer mechanism between road surface and vehicle. For Virtual Proving Ground simulations it is a very important component. Accurate tire models must be performed in order to transmit the road perturbations with the correct amplitude and frequency content to predict the spindle forces contributing to vehicle noise and vibration.

Several impacts are applied to the tires, and all of them have a significant impact on ride quality and durability of the vehicle. Accurate tire frequency behaviour is essential for fatigue life prediction. For this purpose, good dynamic behaviour is fundamental.

A Mooney-Rivlin hyperelastic definition is used to model the strain energy potential of the rubber material. The plies and belts are modelled using embedded rebar layers into the rubber matrix.

A simple modal test is defined in order to correlate the tire model. It is possible to define the dynamic behaviour in the frequency range 0–100 Hz. The most important influencing modes during the durability simulation on a Virtual Proving Ground are torsion and radial; flexural modes are not so relevant. All of these modes have been correlated (Fig. 10).

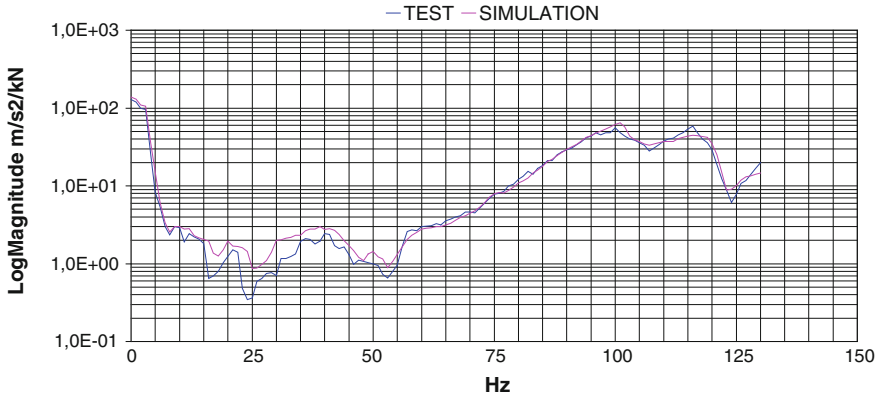


Fig. 11 Comparison between tire test and tire simulation



Fig. 12 a IDIADA’s pavé track b Virtual track

Figure 11 shows the correlation between tire test and simulation from 0 to 125 Hz.

### 4.3 VPG Digitalization

The accurate numerical description of the proving ground is of major importance in durability simulation. For this work, IDIADA’s pavé track has been digitalized and modelled with a  $5 \times 5$  mm resolution in horizontal spacing. Figure 12 shows the pavé track of the Virtual Proving Ground.

A tool has been developed to automatically include different VPG tracks to the simulation.

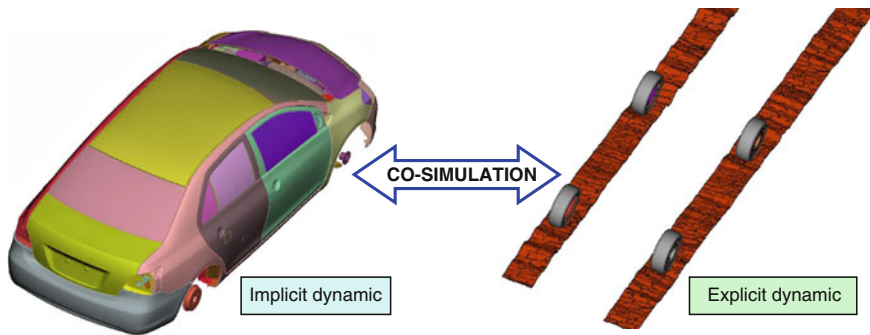


Fig. 13 Co-simulation model (implicit/explicit)

## 5 Simulation

### 5.1 Co-Simulation

Because explicit and implicit methods have advantages and disadvantages, a co-simulation process between them has been used in this work.

The implicit and explicit dynamic schemes have a uniform time step for all of the mesh. The element size of a whole vehicle model can vary greatly and during recent years they have been refined.

The use of only one explicit or implicit scheme with a unique uniform time step is very inefficient. The use of small element size is discouraged to speed the analysis for an explicit method due to the great number of increments needed for the simulation. On the other hand, using an implicit method, a large time step would not be able to accurately capture the response of the mesh with big variations with the time. Moreover, the implicit scheme is very inefficient when there are several contact areas that change from open to closed or vice versa.

The vehicle body and suspension are solved using the implicit dynamic method. Tire models and road contact are simulated using the explicit scheme. Wheel centres are the co-simulation interface nodes (Fig. 13).

A previous implicit inflation and footprint tire simulation is performed before co-simulation.

## 6 Conclusions

A Virtual Proving Ground methodology has been implemented for fatigue life prediction. During this methodology the following have been performed:

- Digitalization of IDIADA's pavé test track has been carried out.
- Automatic implementation to the ABAQUS code model of the VPG.

- Tire model correlated with simple test.
- Substructure elements of suspension components connected by ABAQUS connector elements.
- Implicit/Explicit co-simulation in ABAQUS code.

The Virtual Proving Ground methodology is a good tool not only for durability analysis but also for predicting the forces generated by the excitations of the track.

## References

1. Stephens R, Fatemi A, Stephens R, Fuchs H (2001) Metal fatigue in engineering. Wiley, NY
2. Lee Y, Pan J (2005) Richard Hathaway, and Mark Barkeys. Fatigue testing and analysis. Elsevier, Amsterdam
3. Dixon JC (1991) Tires, suspensions and handling. Cambridge University Press, England
4. Virtual.Lab Manual, LMS, 2012
5. Abaqus Analysis User's Manual, Simulia, 2012

# The Parametrical Design and Optimization of Body Frame Based on Crashworthiness and Lightweight

Yongxin Men, Guojun Zheng, Huicai Zelong Lu and Zelong Wang

**Abstract** *Research and/or Engineering Questions/Objective:* The crashworthiness and lightweight of a vehicle were directly affected by the front structure of body frame, including the front-end impact beam, side rails, crash boxes and A-pillars. The key to lightweight is how to design a body frame that could reduce weight and meet safety requirements. The design optimization method based on finite element simulation could save cost and improve efficiency. In this research, this method is applied to the safety and lightweight design of the body frame, and a parametrical design optimization method is explored in consideration of safety and lightweight, offering technical support for automotive lightweight design. *Methodology:* Firstly, a parametrical modelling process was implemented on the substructure of a certain car according to the parametrical simulation. Secondly, a design optimization model was established with the parameters of body frame as the design variables, lightweight as the objective, and the front crashworthiness as the constraint. Thirdly, the design optimization model was solved and the optimal design parameters were obtained. Finally, the real vehicle was built up with optimal design parameters and experimental validation was carried out for safety and lightweight. *Results:* The fast modelling method about parametrical finite element model of body frame was constructed in the study, taking a real car of a Chinese domestic brand as the example. The optimization of finite element design method based on crashworthiness and lightweight of body frame was achieved and this method takes the safety and lightweight into account at the same time. It serves as an effective way to

---

F2012-E03-042

---

Y. Men (✉) · G. Zheng · H. Z. Lu · Z. Wang  
Zhejiang Geely Automobile Research Institute Co., Ltd, Hangzhou, China  
e-mail: menyongxin@rd.geely.com

G. Zheng  
School of Automotive Engineering, Dalian University of Technology, Dalian, China



improve the efficiency of vehicle lightweight. *Limitations of this study:* Due to the complexity of vehicle structure, the parametrical design was merely implemented on some key sizes and parts which can affect structure strength obviously, however, the crash safety and lightweight requirement could be fulfilled from the final parametrical design. *What does the paper offer that is new in the field including in comparison to other work by the authors?* Through this parameterization process, which was based on the substructure, the rapid modifications of actual structures and automatic finite element model development became reality. Therefore, this technique was different to the parametrical designs and simulations of the traditional CAD/CAE method. *Conclusions:* The fast modelling method of finite element parametrical model and its optimization in respect of safety and lightweight is feasible. It can offer technical support for automotive lightweight.

**Keywords** Body frame · Parametrical design · Crashworthiness · Lightweight · Design optimization

## 1 Introduction

Based on China's serious mixed traffic, road infrastructure lags behind economic development and other special national conditions, China's car on road safety issues frequently, which cannot be ignored. Road safety, especially car collisions, has become the outburst of our country harm in all kinds of public safety; vehicle safety has aroused more and more attention. According to statistics, the chance probability of the front impact is about 58 % in all the car accidents, in which 39 % people involved can be injured seriously. It is of great importance to improve the car frontal impact safety as well as to improve vehicle crashworthiness.

However, with the leap-forward development of China's automobile industry in recent years, car ownership has increased rapidly every year. Thus energy and environment has become an important factor affecting the automotive development. Data shows that for the car weight 1,000 kg, reducing its weight by 10 % can save fuel consumption by 8 % and reduce emissions of about 4 %. Therefore, the lightweight technology for vehicle fuel economy, environmental friendliness is of great benefit. Lightweight technology to reduce energy consumption, noise, and emissions has become a key factor for the various car manufacturers to enhance their competitiveness.

The promotion of new materials such as aluminium, magnesium alloy, high strength steel, plastic and composite materials, large-scale application of the laser welding technology, internal high pressure forming technology and ultra high strength steel hot forming technology and other new new technology, have greatly promoted the automobile lightweight technology. New materials, new processes combined with conventional structural optimization, topology optimization techniques become new trend for the automotive lightweight technology.

This paper analyzes the advantages and disadvantages of the two parametric design, and point out that the crashworthiness and lightweight-based research need the combination of CAD and CAE parameterization to achieve automatic optimization loop, and take one self-owned brand vehicles' front crash for example, parametric modelling through its part of the body skeleton structure, whichever impact collision properties of the key structural parameters for the design variables in order to meet the full front/offset front crash constraints to the body the lightweight design goals, combined with ultra high strength steel hot forming technology, in-depth research on the vehicle front crash safety. Under the final optimized design, vehicle crash testing, and its excellent results show that: the crashworthiness parameters is an important means to optimize vehicle structure, and it can greatly improve the efficiency of R&D and shorten the development cycle.

## 2 An Analysis Based on the Parameter of the Crash Simulation

With the increasingly sophisticated application of the finite element method in the automotive crash simulation, CAE technology in reducing development costs and shortening the development cycle has made great progress, at the same time, it makes up for the deficiencies of the vehicle crash test, and gradually a design and analysis of parallel R&D process has been formed.

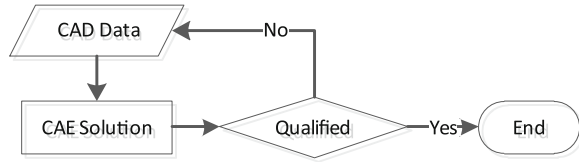
However, the CAE overall technical level in China is not as mature as foreign countries. At present, crash simulation analysis of the body structure is confined to the performance verification, lack of performance design. The main reason is that performance verification is carried out after the completion of the detailed design stage, the input condition is the CAD data as shown in Fig. 1. Typically, the product prototype has been completed; the improvements will be subject to significant limitations and constraints, lack of support and guidance from the beginning of product design.

Figure 1 shows the process can also be seen in this way, the CAE data is subject to the pre-CAD design data and cannot be modified freely. Therefore, the CAE analysis results often need to manually feedback to the CAD environment, and through the CAD data to finish modifications. Because the whole process of cross-platform (CAE → CAD) operation, it is difficult to optimize the design of the automatic cycle.

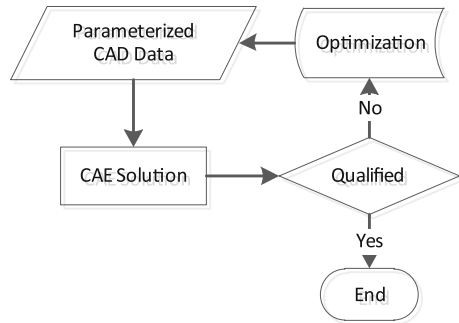
With the improvement of domestic R&D capabilities, how to effectively achieve the simulation analysis of drive and guidance on the design has gradually become a topic of concern.

Parametric design is the basis to automatically optimize the design cycle. Through a certain part of the adjustment of the product or parts of the size parameters or geometric parameters, the changes in other parts of the graphics can update automatically, thus realizes parametric design-driven.

**Fig. 1** CAE analysis process



**Fig. 2** CAD parametric-based CAE analysis process



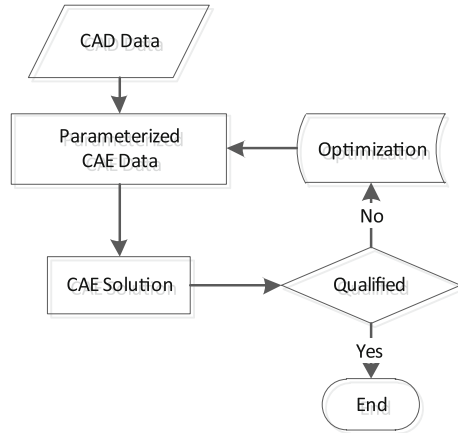
Typically, parametric design in car collisions can be divided into CAD parameterization and CAE parametric. CAD parametric, in accordance to the parameter description equation, can be divided into “explicit” parameter and the “implicit” parameters. The “explicit” parameter is the geometry formed by a series of abstract parameters, the relationship between the geometry is clearly described by linear equations; and “implicit” parameter refers to the geometry formed by the control point position, curvature and cross-section, the relationship between the geometry are generated by the topological relations between the above parameters and the model automatically, without the need for a clear description of linear equations.

Based on CAD parameterization, the automation of the CAD data modifications and adjustments can be achieved, combined with optimization designer, the designer can drive the CAD model update automatically, thus to achieve optimization of the design cycle, as shown in Fig. 2.

With CAD “implicit” parameter, you can easily create and modify the relationship between topology and geometry of the CAD model, without the need of turning complex mapping rules into mathematical description. At the same time, with the automatic finite element mesh generation technology, as well as a predefined range of external parameters, a rapid performance evaluation and optimization of the design model can be realized, which is very conducive to rapid implementation and performance evaluation of the design in the concept design phase.

However, due to the limitations of the automatic finite mesh generation technology, the degree of precision of the parametric model in the concept design phase is not particularly high, but the collision simulation analysis desires a high quality of mesh. As CAD parameterization based on crash simulation analysis is mainly used in the conceptual design phase so it is difficult to guarantee good

**Fig. 3** The process of CAE analysis based on CAE parameterization



results for the local details of the adjustment and optimization in the detailed design stage.

CAE parameterization based on Morphing Technology is one of the local details of the adjustment and automatic optimization tool.

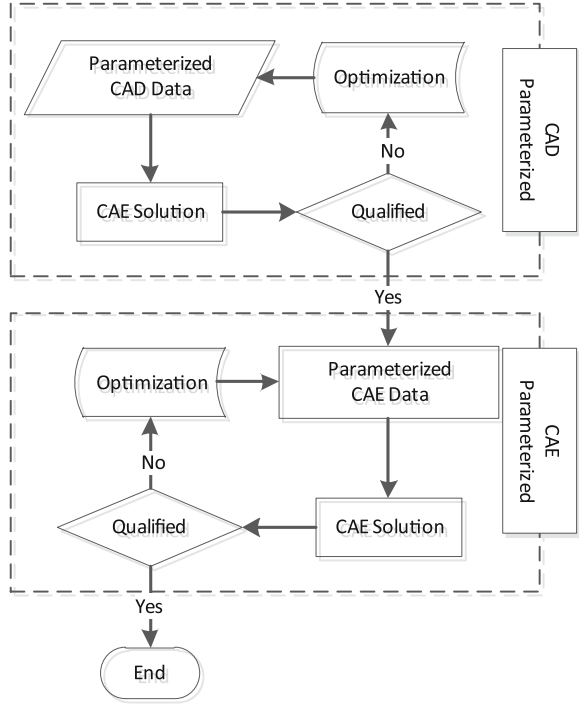
Figure 3 shows the analysis process, to build a series of parameters in CAE data based on Morphing Technology, CAE mesh data can be changed by the Morphing parameters, thus to realize the finite element nodal coordinate adjustment, and ultimately drive the shape change of the CAE model. In the optimization of the design cycle, the optimizer can drive Morphing parameters directly; model update operations can be done in pure CAE environment, without the cross-platform CAD to CAE.

Morphing technology limitations: When the geometric parameters changes greatly, the topological relations may be difficult to maintain stability, resulting in the deterioration of mesh quality, which makes the simulation results become inaccurate because there are a large number of low-quality grids, or even cause the calculation to terminate. Therefore, the technology is generally used in relatively simple model for local optimization, but it is hardly used in system-level model for topology modification.

According to the development process of actual models, the combination of CAD and CAE parameterization can be used to make use of their respective advantages, and achieve optimization based on the crashworthiness and weight design (Fig. 4).

In the optimization design of Crashworthiness and lightweight-process, by building a CAD parametric model first to realize optimal design for topology and cross section of the main crash structure; based on the optimization results, a more sophisticated CAE parametric model can be built, and optimal match the contents of local detail and material, sheet thickness. Since the whole process using the parametric design, the automatic computer optimization can be realized, greatly improving the work efficiency.

**Fig. 4** The combination of CAD and CAE parameters



### 3 The Structure Optimization Analysis Based on the Crashworthiness

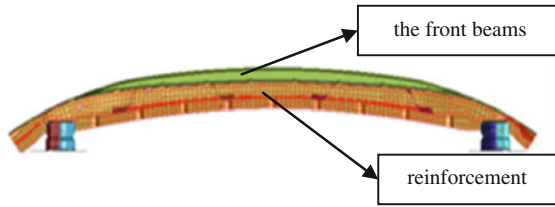
Take a model’s positive development of one self-brand car for example, with the combination of CAD and CAE parameterization; optimize its front impact crashworthiness and lightweight.

#### 3.1 An Overview of the Models

In the early design stage of the model, its crash safety rating as C-NCAP five-star. In the front area, it takes the form of outer plate of the front beams and reinforcement in order to strengthen the local structure as shown in Fig. 5.

Material information is shown in Table 1:

As can be seen from Table 1, the outer plate and the reinforcement is the low strength material, with yield strength about 347 MPa, Therefore, in order to improve the overall stiffness of front in crash, and to prevent the front beams become devious when the offset crash occurs, resulting in local instability, thus need to strengthen the front part.



**Fig. 5** The structure of the front beam with a reinforcement

**Table 1** The material information of the front carling

	Yield strength (MPa)	Sheet thickness (mm)	Quality (kg)
Outer plate of the front beam	347	1.6	3.021
Reinforcement	347	1.6	2.513

Hot forming technology is a new technology in recent years for forming high strength steel stampings. Compared with common forming steel plate, hot forming steel plate has obvious merits in high strength and hardness, light weight, and no rebound due to its high yield point (up to 1,100 MPa), thus the quality of the plate will not be affected by reducing its thickness, therefore the goal of lightweight can be achieved. High-strength steel also has higher impact resistance and fatigue strength, and its collision energy absorbing properties is far beyond the common forming steel, and improves vehicle safety effectively.

Therefore, based on considerations of lightweight, tentatively put forward the proposal: merge the front beams and the stiffener to a hot forming ultra high strength steel part.

### 3.2 CAD Parametric Model and its Optimization

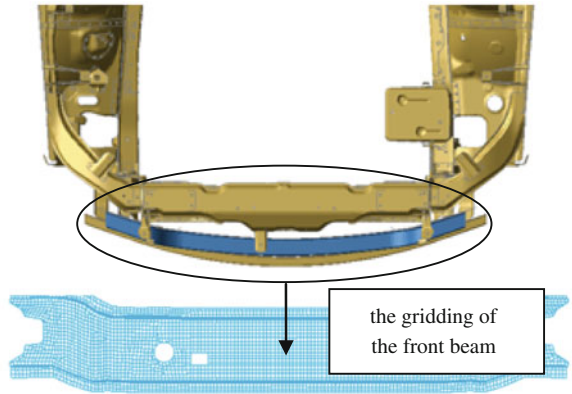
The initial improvement of the models is to put the two parts into one, thus need to re-design the new part’s geometric modelling, shape, topology and section shape within a certain range. As described in the first section we need to parameterize the new front beam in CAD, in order to optimize the best cross-section shape and topology.

The SFE CONCEPT software applies analysis-driven design concept, by building the “implicit” fully parametric model [1] (including the reinforcing ribs, marking, punching, etc.), can make the CAE analysis free from the traditional CAD geometry. Moreover, the SFE CONCEPT integrates powerful tool for automatic mesh division, when the geometric model parameters change, the finite element generation module will run automatically in the background, and the model will re-meshing. At the same time, the original connection in the model will be updated to better guarantee the quality of the analysis.

**Fig. 6** The front beam parametric model in CAD



**Fig. 7** The finite element model connected with other parts



Set the front beam's cross-section parameters and the cross-section's adjustment coefficient can create the beam parameters in the SFE CONCEPT. Figure 6 shows the model surfaces with different parameters.

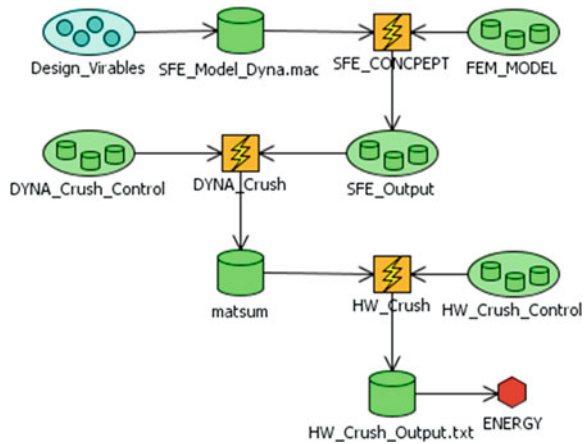
Combined with automatic mesh division tool, divide the front beam into a finite element mesh which is easy for crash simulation analysis. The rest part of the vehicle collision model can be imported from external model, and can quickly form a new vehicle collision model. Figure 7 shows the vehicle collision model contains a new front beam. In order to show the front beam clearly, only the part which connected with the front-end skeleton is displayed. Coupled with an external finite element model in CAD parametric modelling, not only can optimize the key part's parameter analysis, but also reduce the scale of parametric modelling.

To find the optimal cross-section parameters, set the front cross-section parameter as the optimization variables, and take the amount of suction in the collision which concludes the front beam, stringer and energy absorbing box as the standard, to optimize the structure.

**Table 2** Cross-section parameters

Parameter code	Lower limit	Upper limit	The optimal value
P1	0	1	0.537
P2	0	1	0.801
P3	-1	1	-0.005
P4	0	1	0.238
P5	-1	0	-0.757

**Fig. 8** Optimus workflow



Vehicle collision has significant geometric nonlinearity (large displacement, large deformation), the boundary and material nonlinearity characteristics; it is difficult to gain the parametric relationship between the body energy absorption and the front beam directly. Therefore, to directly gain the optimal shape of the model in the permission of the front beam is very difficult.

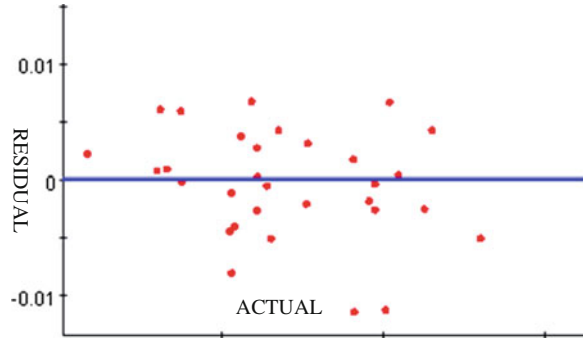
By constructing an approximate mathematical model to find the functional relationship between the design variables (cross-section parameters) and response variables (collision energy absorption) [2], is one of the solution to simplify the above optimization model. As radial basis function has high accuracy in the collision energy absorption and peak acceleration, so the paper chooses the radial basis function as the regression mathematical model.

To improve the accuracy of the approximate model and reduce the impact of nonlinearity on the results as much as possible, each parameter needs to take much number of levels. Take the reality that the calculation time for single-vehicle crash simulation is too long into account; in addition overall number of tests should be reduced. In Table 2 is the front beam parameters' vary range, the upper and lower range are normalized, and therefore belong to the range [-1, 1].

Shown in Table 2, there are a total of five cross-section parameters, if each parameter were taken four level, according to factorial experimental design it



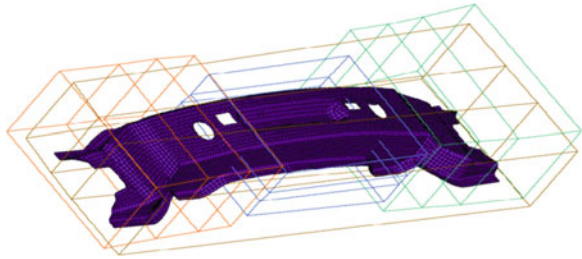
**Fig. 9** An approximate model error analysis



**Fig. 10** Preliminary optimization results



**Fig. 11** CAE parameterized input meshes



requires  $4^5 = 1,024$  trials, and the number of orthogonal experimental design is  $n \in (16, 32, 64, 128, 256, \dots)$ , its samples number are hard to control; But using the uniform super-Latin method can gain the most level for each sample and more evenly distributed sample points. Sample forms in this article is created by the uniform super-Latin method with a total number of 32 samples.

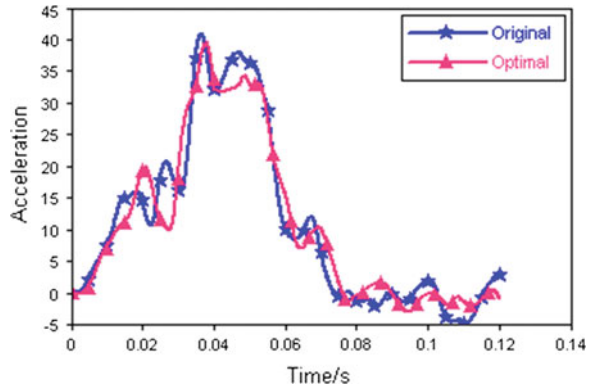
To build the workflow in OPTIMUS software as shown in Fig. 8, and in turn drive the SFE CONCEPT, LS-DYNA HYPERVIEW/HYPERGRAPH software, serial/parallel complete the pilot programs in the sample table.

Based on test results, an approximate mathematical model to generate radial basis function is created. Figure 9 shows the error analysis results of the approximate mathematical model and it shows that the mathematical model has a high credibility. In the end, to optimize the numerical mathematical model, the optimal value can be obtained as shown in Table 2 and Fig. 10 shows the results of preliminary optimization of the CAD model.

**Table 3** The final optimization results

	Front beam (kg)	Stiffener (kg)	Total weight (kg)
The original scheme	3.021	2.513	5.534
Optimization scheme	3.697	0	3.697

**Fig. 12** Acceleration curve comparison before and after lightweight



### 3.3 CAE Parametric Model and Optimization

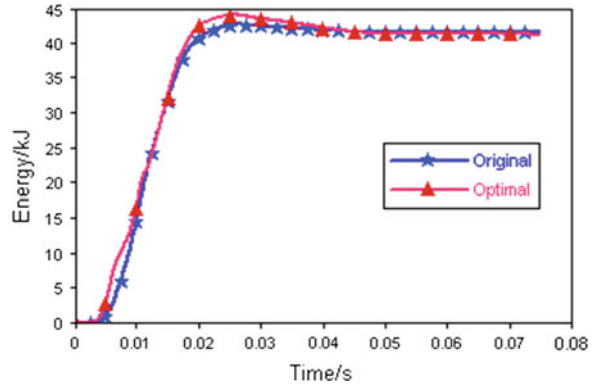
Take the preliminary optimization results shown in Fig. 9 as the input conditions, to optimize the local details and sheet thickness of the front beam, thus achieve the lightweight under the requirements of the crashworthiness (Fig. 11).

Take the radian and board thickness of the front beam respectively as the design variables, the whole vehicle’s peak acceleration as the constraint goal, and lightweight as the final goal, in turn drive MORPHING, LSDYNA, HYPERGRAPH software to complete uniform super-Latin sample with the total number of 23, Similarly, to optimize the value of the approximate mathematical model generated in accordance with the sample results, can get an optimized theoretical results. Table 3 shows the quality comparison before and after optimization.

## 4 Results and Analysis

Put the numerical optimization results into the finite element model and the simulation, the optimal results can be obtained. Such as the vehicle acceleration and the front beam energy absorption curve comparison chart before and after the lightweight design. From the figure, we can draw the conclusion that vehicle performance remains the same as before the lightweight, and the vehicle is able to meet the crashworthiness requirements. The optimization program can lose weight 1.837 kg (Figs. 12, 13).

**Fig. 13** Energy absorption contrast of front part before and after the lightweight



## 5 Conclusions

By using the combination of CAD and CAE parameterization, set the parameters in the optimization designer, can achieve the automatic optimization cycle of the body structure and the sheet thickness, and complete the drive direction in the early structural design of the simulation.

The paper based on the crash worthiness lightweight design of own-brand vehicles, crashworthiness parameterization is an important tool for optimization design, which can improve the efficiency of R&D greatly and shorten the development cycle.

## References

1. Li N, Gao W, Dai Y (2008) Optimization design of car body structure based on implicit parametric model. *Automot Eng* 30(10):857–860
2. Craig KJ, Stander N, Dooge DA (2005) Automotive crashworthiness design using response surface-based variable screening and optimization. *Eng Computations* 22(1–2):38–61

# Development of Concept Analysis and Multi-Objective Optimization Platform for Body-In-White Structure

Yiwen Li, Hongjian Li, Zuofeng Pan and Tao Xu

**Abstract** To achieve the integrated control of body-in-white (BIW) performance at the concept design stage, several parametrical optimization technologies are proposed in this paper in seeking lightweight, stiffness and crashworthiness targets. A professional platform—Concept Analysis and Multi-objective Optimization (CAMO) is developed, which has the capability of the rapid reduction, parametrical simulation and optimization. The optimization algorithms database is developed based on. NET framework to ensure the global convergence and robustness of the optimal results. The theories discussed in the paper are great help of the concept design process improvement, body database development and knowledge utilization.

**Keywords** Body-in-white · Concept design · Rapid analysis · Multi-objective optimization · Platform development

---

F2012-E03-046

---

Y. Li (✉) · H. Li · Z. Pan  
R&D Center, FAW, Changchun, China  
e-mail: liyiwen1@rdc.faw.com.cn

H. Li  
e-mail: lihongjian@rdc.faw.com.cn

Y. Li · H. Li · Z. Pan · T. Xu  
State Key Laboratory of Comprehensive Technology on Automobile Vibration and Noise and Safety Control, China FAW Co.Ltd R&D Center, Changchun, China

T. Xu  
College of Mechanical Science and Engineering, Jilin University, Jilin, China

## 1 Introduction

The vehicle development process demands quick design and evaluation at the concept stage. Typically, a large number of alternatives of BIW have to be considered. The conventional BIW product developments are heavily relied on complex CAD and CAE models. These modeling or analysis process are not efficient for the concept evaluation and useless for the design data accumulation.

The goal of the conceptual phase is to generate alternative concepts that can be simulated and compared. The First Order Analysis (FOA) is put forward by Toyota Central R&D Labs to evaluate the simplified BIW performance in the first stage of development [1, 2]. This program is based on Microsoft/Excel so that the expansibility becomes poor. SFE Concept uses the implicit parametrical technology to construct the concept body structure and realizes the CAE upfront [3, 4]. Although the model is full parameterized, the flexibility of joints is dependent on the geometric shape beam elements, and that causes more modeling time. An intelligent tool named IVCD based on NX is developed by Hu et al., which can integrate body design, analysis and optimization on one platform through parametrical variable database [5, 6]. But it is only available for the static and mode characteristics.

To satisfy the global performance target including lightweight, stiffness and crashworthiness, also to speed up the concept design process, an independently platform—Concept Analysis and Multi-objective Optimization (CAMO) platform is successfully developed. It provides the comprehensive functions as simplified and parametrical detailed body modeling, static and mode analysis, design of experiment (DOE) and fast optimization. In the following sections, the details of the platform development are discussed.

## 2 Platform Function and Technology

The CAMO platform for BIW is a professional tool oriented to product design of automotive. It has not only the basic functions of general CAE and optimization software, but also the professional characteristics of concept design. The modeling cycle can be obviously reduced by the rapid reduction and parametrical detailed modeling modules. The optimal element mechanical properties and beam-section geometries can be obtained rapidly, which benefits from the algorithm database of the optimization module. GDI+ and DirectX ensure the 3D graphics and optimal results display. The integrated control of lightweight, stiffness and crashworthiness is realized by this platform. Especially, the platform is suitable for the transformation and expansion of passenger car platform.

## ***2.1 Rapid Reduction Module***

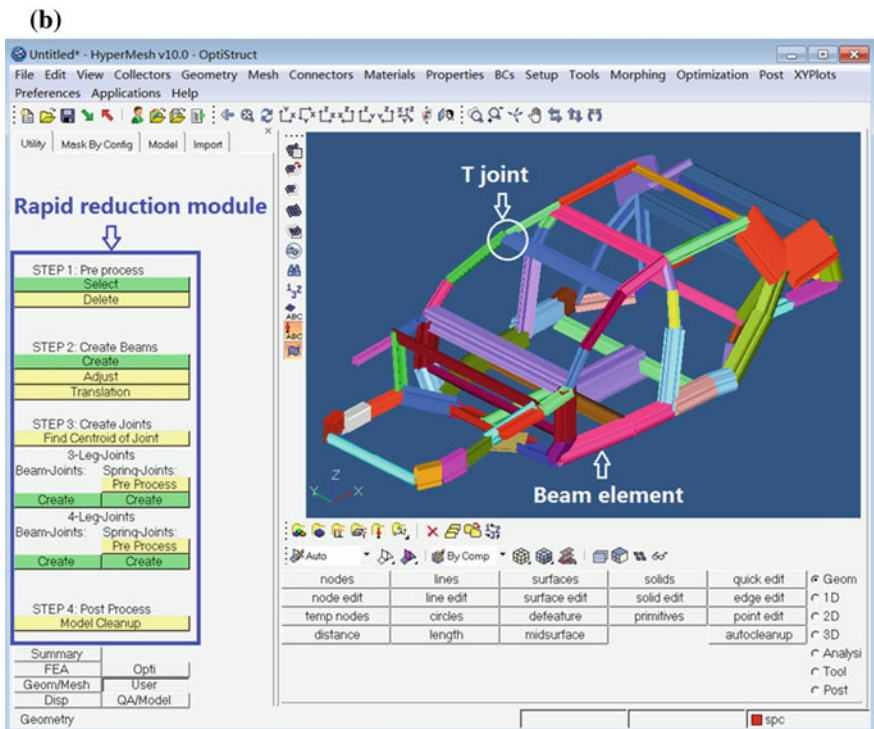
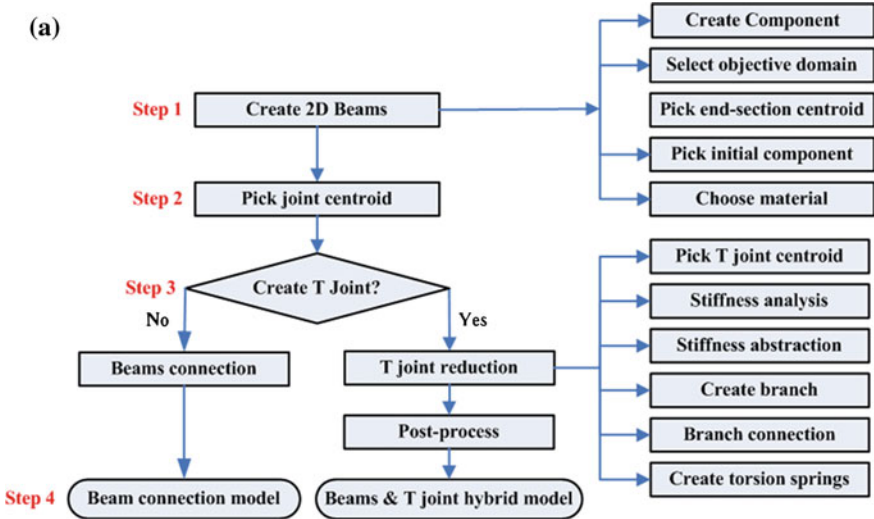
The rapid reduction definition comes from the template concept which references Object Oriented technology to define geometrical features and mechanical characteristics of the objective body frame. This module is developed based on Altair HyperWorks software. The beam cross-section properties can be obtained by running HyperBeam module in the software. By calling and recompiling its macro and TCL/TK command, the reduction process can be integrated and realized automation. After several steps, as shown in Fig. 1a, b, an objective body frame constructed by 2D beams and simplified T joints can be obtained. In the T joint model, the torsion springs and the direction vectors are used to simulate the flexibility and the coupling of angular rotation, respectively [7]. This simplified frame can be used to rapidly evaluate the basic mechanical characteristics such as static and mode performance [8]. The morphing function of the module also ensures the transformation of vehicle type. The output FE model can be read and optimized by the optimization module, which will be discussed later in the paper.

## ***2.2 Parametrical Detailed Modeling Module***

The simplified frame body has its advantages such as fast model modification and low calculation cost, but it is not accurate enough on crash analysis. Therefore, parametrical detailed modeling module based on Altair HyperWorks is also developed to achieve fast modeling for crash analysis. Unlike the rapid reduction module, Process Studio is utilized to define the process flow and automation. As shown in Fig. 2a, b, the geometrical dimensions of main frontal crash energy absorbed assembly—bumper, crash-box and frontal rail are fully parameterized. Also, several types of triggers are embedded into the crash-box and frontal rail construction process. Main crash conditions such as FRB, ODB, MDB and Sled test can be modularized and integrated in the module, so a complete analysis model (K file) can be output. This module allows the user to rapidly evaluate the current model and obtain the desired body.

## ***2.3 Multi-Objective Optimization Module***

To optimize the obtained body frame above, multi-objective optimization module is developed based on .NET framework to achieve the close-loop design. The .NET framework provides a managed execution environment, simplified development and deployment, and integration with a wide variety of programming languages. We utilize the key feature of .NET as follows: cross-language interoperability for GUI in VB.NET and the kernel code in VC#.NET; managed



**Fig. 1** Rapid reduction module based on Altair HyperWorks. **a** Reduction auto-process, **b** main interface of the module

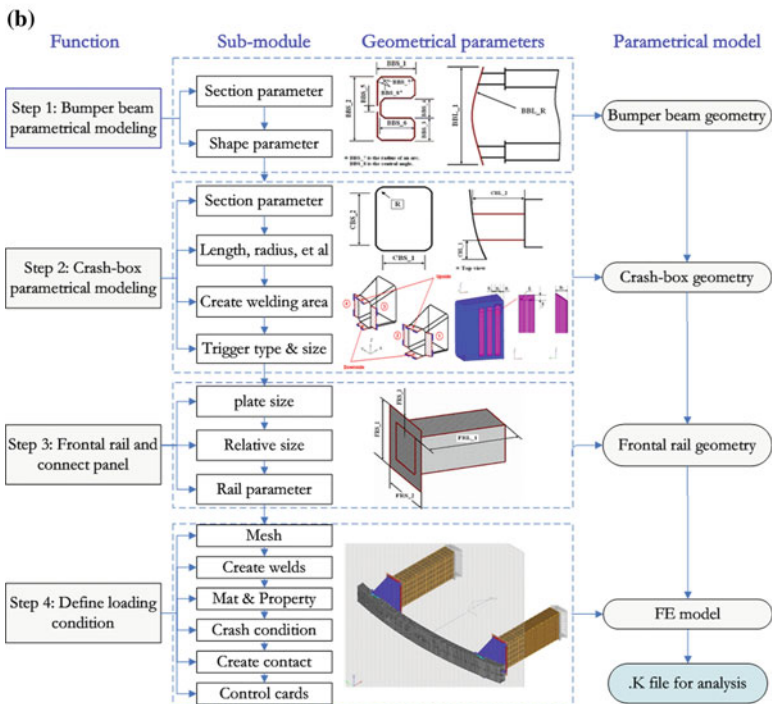
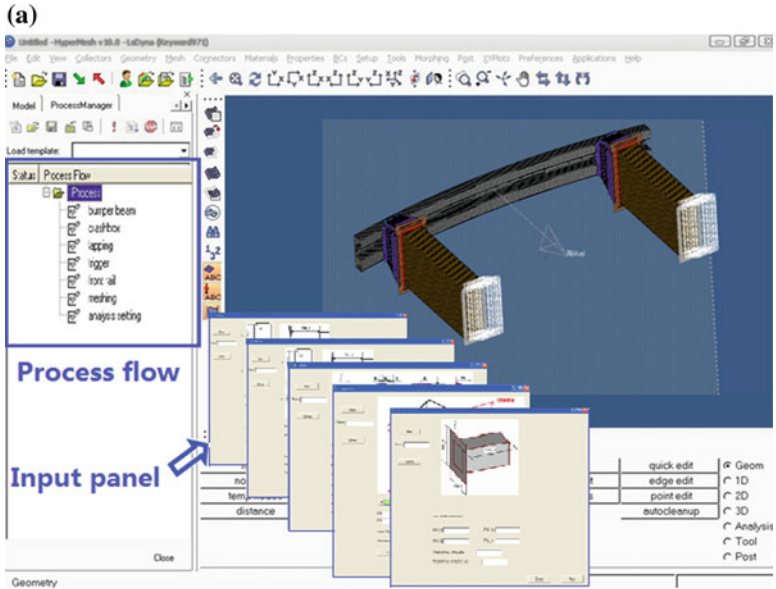
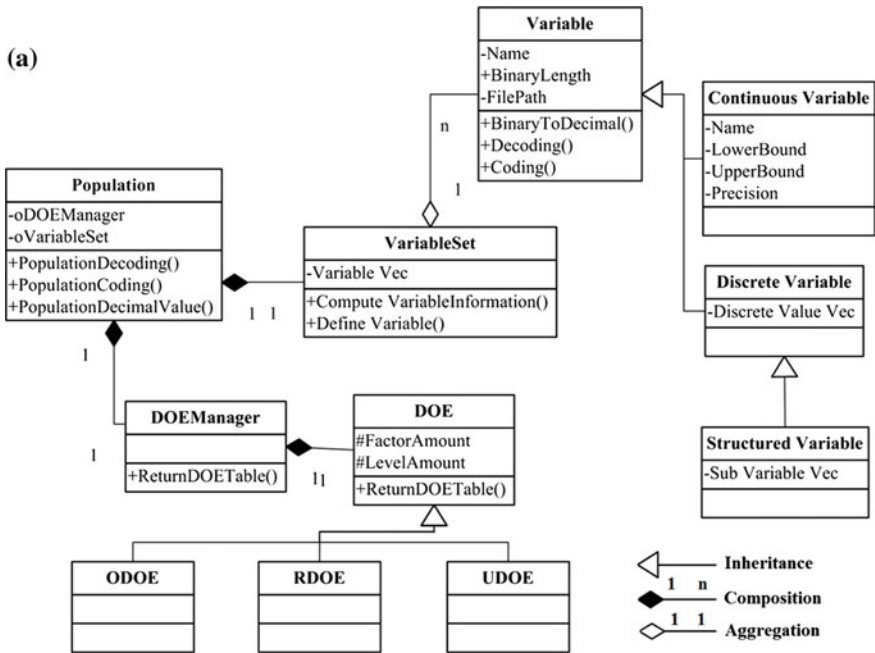


Fig. 2 Rapid reduction module based on Altair HyperWorks. a Main interface of the module, b process flow

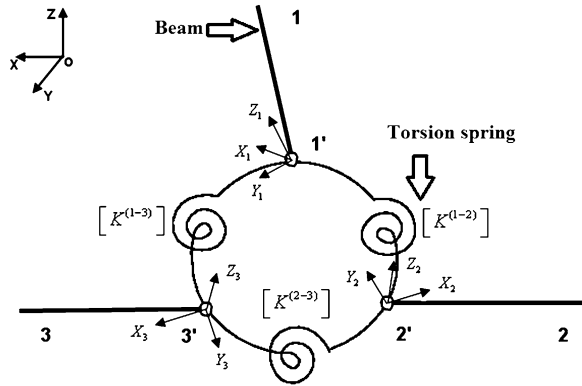




**Fig. 3** Multi-objective optimization module based on .NET frameworks. **a** Class diagrams of the variables and population, **b** main interface of the module

DirectX 9.0 for 3D graphic display of BIW structure; ADO.NET for the development of cross-sectional database and BIW assembly database; OOP for FE

**Fig. 4** Simplified T joint based on flexibility method



analysis; multi-threaded application for parallel computing; crystal report designer and MSCChart control for the data report [9]. The evolutionary algorithm combined with orthogonal design of experiment (ODOE), uniform design of experiment (UDOE) and random design experiment (RDOE) which makes full use of .NET feature is shown in Fig. 3a. And Fig. 3b displays the main interface of the optimization module.

### 3 Key Theory and Method in the Platform

The simplified body frame belongs to multi-elements (beam, plate, T joint) hybrid structure, and multi-variables (for example, inertia moments and section area of beam element, thickness of plate and torsion stiffness of T joint spring) model, that cause great difficulty in modeling or optimization process. Therefore, how to accurately simulate the practical mechanics and execute fast optimization are the key problems to be solved.

#### 3.1 Simplified T Joint Theory in Modeling Process

##### 3.1.1 Flexibility Method

The flexibility of T joint can not be ignored because of its influence on total stiffness (nearly 50–70 %) of BIW [10]. In the rapid reduction module, the flexibility properties of T joints are explained based on super-element theory. The terms “characteristics direction” and “characteristics system” are defined and used to deal with the coupling phenomenon between different rotational degrees. A new simplified T joint model composed of beams (represent joint legs) and torsion springs (represent joint flexibility) is put forward, as shown in Fig. 4. This flexibility method is easy to be programmed and applied in the Altair HyperWorks, moreover, it has been testified that can obviously improve the simulation precision of total mechanics [7].

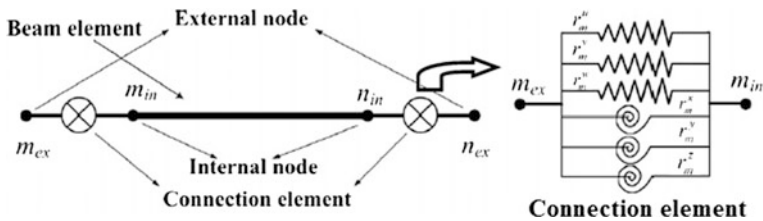


Fig. 5 Semi-rigid beam element and its components

### 3.1.2 Semi-Rigid Beam Element Method

The thin-walled beam of BIW is short and thick in the length and height, so classic Timoshenko beam theory should be introduced to consider the transverse shear, whose element stiffness matrix is denoted by  $K^e$  ( $12 \times 12$  dimension). The 3D semi-rigid beam with a joint at both ends is modeled by a beam element with a connection element at each end, as shown in Fig. 5. This hybrid element contains four nodes: two internal nodes  $m_{in}$  and  $n_{in}$ ; two external nodes  $m_{ex}$  and  $n_{ex}$ . The connection element consists of three tensional springs and three rotational springs, which are all zero-length and massless [9].

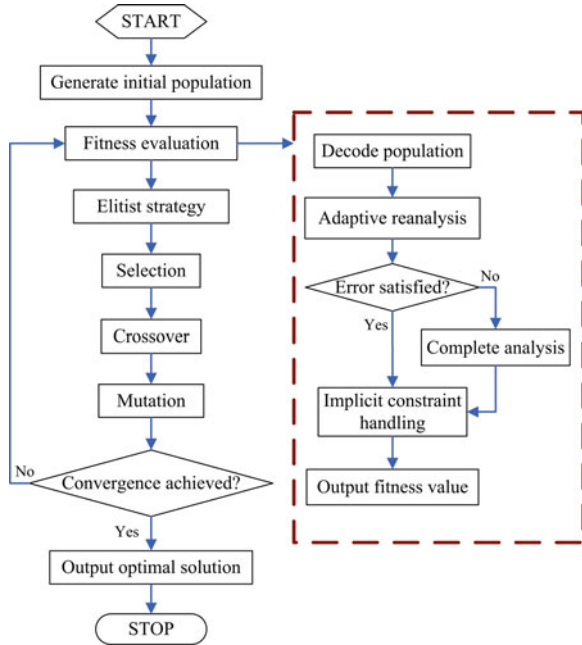
Usually, the simplified body frame has hundreds spring elements are necessary to model the joints. Consequently, the modeling of FE pre-process is tremendous. To solve this problem, Guyan reduction method [11] is employed to express internal DOFs with external DOFs. All the loads are applied at the external nodes, internal loads are always zero. The stiffness terms related to the internal nodes can be eliminated and the condensed stiffness matrix relating the loads and displacements about the external nodes can be obtained. Therefore, it need not create spring elements to simulate joints but input the stiffness of springs during the modeling process. The DOF's reduction speeds up the pre-process significantly.

## 3.2 Intelligent Optimization Algorithm

### 3.2.1 Multi-Objective Optimization Model

To facilitation solution, the mechanical property parameters of beam element are transformed to cross-section geometric variables. A multi-objectives optimization model is established with the cross-sectional geometric parameters of beam, plate element and T joint element as design variables and the minimum mass and maximum stiffness as objectives, the optimal mathematical model [12] is shown as follows

**Fig. 6** Flowchart of the reanalysis based on GA optimization



$$\min \begin{cases} W = \sum_{i=1}^l L_i \rho_i A_i + \sum_{i=1}^m T_i \rho_i A'_i \\ E = \frac{1}{2} \sum_{i=1}^s u_i p_i \end{cases}, \quad s.t. \begin{cases} A_{\min} < A < A_{\max} \\ I_{y \min} < I_y < I_{y \max} \\ I_{z \min} < I_z < I_{z \max} \\ I_{t \min} < I_t < I_{t \max} \\ T_{\min} < T < T_{\max} \\ K_{r \min} < K_r < K_{r \max} \end{cases} \quad (1)$$

In which  $W$  and  $E$  represent total mass and strain energy of BIW, respectively. The strain energy can be seen as inverse measurement of total stiffness [13].  $s$  is the number of total DOFs;  $L_i$ ,  $A_i$  and  $\rho_i$  are the length, sectional area and density of  $i$ th beam element;  $T_i$  and  $A'_i$  represent thickness and sectional area;  $u_i$  and  $p_i$  are the displacement and load of  $i$ th node;  $l$  and  $m$  represent the number of beam and plate element, respectively;  $A = (A_1, A_2, \dots, A_l)$  is cross-section area vector;  $I_y = (I_{y1}, I_{y2}, \dots, I_{yl})$ ,  $I_z = (I_{z1}, I_{z2}, \dots, I_{zl})$  and  $I_t = (I_{t1}, I_{t2}, \dots, I_{tl})$  are bending inertia moment and torsion inertia moment vector, respectively;  $T = (T_1, T_2, \dots, T_m)$  is the thickness vector of plate element;  $K_r = (K_{r1}, K_{r2}, \dots, K_{r3})$  is the stiffness vector of connection element.

It has also been testified that mechanical property variables of beam section can be transformed to geometrical variables. Therefore, the geometrical properties of beam and plate element are treated as objective. That is called “mechanical properties-based” method, as Eq. (2). The method can provide both the optimal geometrical size and optimal element mechanical property for the designer. And it is a great help of lightweight and high performance optimization.

$$\text{Min}(A, I_y, I_z, I_t, T, K_r), \text{ s.t. } W \leq W_{allowable} \quad (2)$$

### 3.2.2 Adaptive Reanalysis Method for Genetic Algorithm

Although the genetic algorithm (GA) is very robust, it is very computationally intensive and hence slower than optimality criteria and mathematical programming methods, especially for the multi-variables BIW structure. To speed up the optimization process, we present an adaptive reanalysis method for GA and its applications in the optimal design of body frame. This reanalysis technique is primarily derived from Kirsch's combined approximations (CA) method [14]. An iteration scheme is adopted to adaptively determine the number of basis vectors at every generation. The flowchart of the reanalysis based GA optimization process is shown in Fig. 6. The presented numerical results demonstrate that the adaptive reanalysis technique does accelerate the design process and affects the accuracy very slightly, especially for large-scale structures such as BIW structure [15, 16].

## 4 Conclusion

The paper systematically illustrated the functions and theoretical innovations of CAMO. This platform has advantages during concept process such as rapid simplified modeling based on comparative BIW, parametrical detailed modeling and crashworthiness evaluation of key components, multi-objective optimization based on multi-parameters of mechanical characteristics and geometrical dimensions.

The optimization models and theories of platform have the theoretical innovation; correspondingly, the module functions have the originality. The platform is a great help to the improvement of concept design, body database development and knowledge utilization. Moreover, it has significance of national independent development of professional platform.

## References

1. Nishigaki H, Nishiwaki S, Amago T et al (2001) First order analysis—new CAE tools for automotive body designers. SAE World Congress, Detroit
2. Kunishi D, Kikuchi N (2004) Analysis of FEM results based upon FOA. SAE Technical Paper Series, 2004-01-1729
3. Zimmer H, Umlauf U, Thompson J (2000) Use of SFE CONCEPT in developing FEA models without CAD. SAE Technical Paper Series, 2000-01-2706
4. Volz K, Frodl B, Dirschmid F et al (2007) Optimizing topology and shape for crashworthiness in vehicle product development. International Automotive Body Congress (IABC), Berlin

5. Hou WB, Hu P, Liu DY et al (2006) Knowledge embedded tool for vehicle body conceptual design (IVCD). *J Jilin Univ (Eng Technol Ed)* 36(5):814–818
6. Hou WB, Zhang HZ, Chi RF et al (2009) Development of an intelligent CAE system for auto-body concept design. *Int J Automot Technol* 10(2):175–180
7. Xu T, Zuo WJ, Ju W et al (2010) Simplified joint model established by rigid beam and spring elements in car body structure. *J Wuhan Univ Technol* 32(6):98–102
8. Li YW, Xu T, Zuo WJ (2010) Topology optimization design of T-joints in concept autobody. *J Jilin Univ (Eng Technol Ed)* 40(2):351–356
9. Zuo WJ, Li WW, Xu T et al (2011) A complete development process of finite element software for body-in-white structure with semi-rigid beams in.NET framework. *Adv Eng Softw*. doi:[10.1016/j.advengsoft.2011.10.005](https://doi.org/10.1016/j.advengsoft.2011.10.005)
10. Huang JL, Lou YQ, Gong LZ (2000) Joint modeling method in the concept model of car body structure. *Chinese J Mech Eng* 36(3):78–81
11. Panayirci HM, Pradlwarter HJ, Schueller GI (2011) Efficient stochastic structural analysis using Guyan reduction. *Adv Eng Softw* 42(4):187–196
12. Xu T, Zuo WJ, Xu TS et al (2010) Parameter optimization of cross section with multiple variables for the frame structure of conceptual car body. *Automot Eng* 32(5):394–398
13. Li YW, Xu T, Zuo WJ et al (2009) Modification method of autobody structure model based on relative sensitivity. *J Jilin Univ (Eng Technol Ed)* 39(6):1435–1440
14. Kirsch U, Papalambros PY (2001) Exact and accurate reanalysis of structures for geometrical changes. *Eng Comput* 17(4):363–372
15. Xu T, Zuo WJ, Xu TS et al (2010) An adaptive reanalysis method for genetic algorithm with application to fast truss optimization. *Acta Mech Sin* 26(2):225–234
16. Zuo WJ, Xu T, Zhang H et al (2011) Fast structural optimization with frequency constraints by genetic algorithm using adaptive eigenvalue reanalysis methods. *Struct Multi Optim* 43(6):799–810

# Fatigue Life Prediction of Spot-Weld for Auto Body Based on Multiple Load Cases

Liling Zhang, Qing Jiang, Xuefeng Chen and Xu Wang

**Abstract** *Objectives:* A typical modern car body (BIW) has about 4,000–6,000 spot welds. It is important for the automotive design engineers to understand the mechanical behavior of different joints and furthermore, to incorporate static, impact, and fatigue strength of these joints using CAE methods. The main failure mode of spot welds for most of applications in a car body is fatigue failure. So, the way to layout the spot welds and predict the fatigue strength distribution in the early design stage of car body development has been one of the most interesting and significant topics in recent years. The main objective of this paper is to suggest multiple load cases considering customers usage for fatigue life prediction of spot-weld for the passenger car in order to improve simulation accuracy and CAE capability in vehicle performance development process. *Methodology and Results:* Loading, geometry and material fatigue properties (SN or EN curve) are three key elements for structural fatigue simulation. During the fatigue life simulation of spot welds in car body, the selection of load cases, the accuracy of welding fatigue SN curves, as well as weld nugget diameter of the selected spot weld and finite element modeling accuracy substantially affect spot weld fatigue damage and life prediction. This paper presents a method for fatigue analysis of spot-weld joints and the evaluation of the group of spot-welds having insufficient fatigue life. The authors focus on finding out more realistic load input condition and spot-welded joint modeling methods in order to conduct structural optimization design by using FEA. A multiple load case analysis process for spot weld fatigue life prediction is developed. Under the multiple load case combining torsion, bump, cornering, braking & accelerating, and by using nCode software, the spot weld fatigue

---

F2012-E03-049

---

L. Zhang (✉) · Q. Jiang · X. Chen · X. Wang  
Beijing Automotive Technology Center, Beijing, China  
e-mail: zhangll@beijing-atc.com.cn

analysis is done. As a result, the prediction of weak joints by simulation matches experimental results quite well, applications for several car body design programs conduct good results. *Conclusion and Future Potential Researches*: The advantages and the limitations of the multiple load case analysis method for spot weld fatigue life prediction in auto body design process are discussed. In the literature very few papers are focused on the loading condition improvement. The applications also indicate that current simulation technology is suitable for spot weld fatigue strength distribution prediction, weak spots identification, and A to B comparison in the early design process. However, the correlation analysis between fatigue test results and simulation results should be done. The accuracy of spot weld joint fatigue property (S–N curve) needs to be improved in the future because of the S–N curve significantly affecting the fatigue life and damage calculation.

**Keywords** Fatigue analysis · Spot weld · Multiple load cases · Auto body

## 1 Introduction

In modern automobile industry field, the spot weld is applied widely in the manufacture of car body component. The quantities of spot weld in typical car body are between 4,000 and 6,000. The arrangement and number of spot weld directly influence the stiffness, durability and crashworthiness of car body. Because in the practical application the main failure mode of spot weld is fatigue damage, it is significant to further understand the fatigue behavior of spot weld, predict the fatigue life of spot weld in car body in early designing stage and optimize the weak parts of structure, weld quantity and position for shortening research circle and reducing cost of car body.

In recent years, with the rapid development of CAE technology and FEM mathematical theory together with their application, the spot-weld fatigue life could be predicted based on the test data and FEM mathematical simulation. The fatigue damage of spot weld under actual loads conditions could be calculated through the local stresses which are obtained from FEM method according to fatigue life prediction method on spot-weld. This method could support the research and development of automobile engineering. However, in the simulation process of weld spot fatigue life, the simulation results of fatigue damage and life for spot weld are influenced by the accuracy of loads that car body undertake, the accuracy of S–N curve of spot welded joint material, the choice of weld nugget diameter and the accuracy of FEM model.

The objective of this paper is giving a fatigue analysis method for spot-weld under multiple load cases considering the loading conditions of car body in driving process. It is proved to be reasonable in the durability test.



## 2 Fatigue Life Simulation on Spot-Weld

### 2.1 Introduction on Fatigue Life Simulation of Spot-Weld

The loads, stress in structure and material property (S–N or E–N curve) are three critical factors for simulation analysis of structure fatigue. Based on the different objective for spot weld research, there are two main methods to assess spot-weld fatigue life at present. Radaj and Sheppard think that under different structure and loads the weld fatigue life could be assessed by mathematical analysis on local stress around spot weld. That is the weld joint assessment method based on local stress. Rupp et al. give another assessment method based on the spot weld force. The fatigue life of spot weld is simulated by calculating spot weld force and making use of the maximum and minimum stress and loading spectrum.

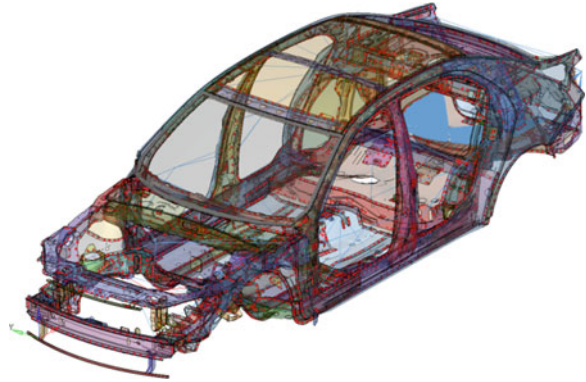
The simulation method in the software adopted in this paper is similar to the research achievement of Rupp et al. The main process is simulating the spot weld with beam element to connect the shell element on top and bottom sheet. The structural stresses of weld nugget and sheet around are calculated with element forces transferred by beam elements. Then the structural stress of weld nugget and junction plate, in conjunction with the fatigue properties of weld nugget and base material are used in fatigue analysis. The spot weld damage and life distribution could be calculated according to rain flow counting method and Miner damage rule by quasi-static analysis on every calculation point. In recent years, this method is extended and developed. The non-beam elements are allowed to simulate spot weld, which is the “regional contact” connection.

### 2.2 FEM Model

Figure 1 is the FEM model of some car body which has 4,500 spot welds. The size of element is 10 mm, and the main elements are shell elements. In order to improve the calculation accuracy, the triangle elements should be controlled within 5 % of the total elements.

### 2.3 Modeling Method for Spot Welds

The modeling methods for spot welds have some distinction according to different fatigue analysis method on spot welds. When the fatigue analysis method on the basis of stress is adopted, good shell elements around spot weld are required. Two different kinds of modeling method for spot welds are shown in Fig. 2. The diameter of washer or weld nugget size is the actual spot-weld size (Fig. 3).

**Fig. 1** Body FE model

When using the fatigue analysis method on the basis of weld force, the spot welds could be simulated through rigid beam element, cweld element or acm element. Because this method is to calculate the structural stresses of weld nugget and sheet around through the element forces transfer by beam elements, the accurate transfer of element forces is one of the important conditions which are related to the reasonable result of fatigue analysis. In order to get more accurate analysis result and improve the analysis efficiency, it is necessary to discuss the modeling methods for spot welds.

### 2.3.1 Beam Element

When the beam element is used to simulate spot weld, the beam elements are required to be vertical to shell elements which are connected by the beam elements. The beam element diameter is the actual weld nugget diameter and beam element should have enough stiffness. Besides, the mesh refinement is not needed for the shell elements around beam element. The experiences indicate that the requirement could be satisfied when the shell elements around spot weld are two times of weld nugget diameter or have the size of about 10 mm. There are two obvious disadvantages for this method in which beam elements are used to present spot weld. On one side, the beam element would cause the stiffness reducing of entire structure, leading to the wrong result in vibration analysis. On the other side, the beam elements are required to be vertical the connected shell elements. So the establishment of model would be a great work when creating the entire car body model, which does not satisfy the requirement of time cost.

### 2.3.2 ACM Method

ACM method describes spot weld through CHEXA and RBE3 element, as shown in Fig. 4. The nodal force of hexahedral element or MPC force are transformed

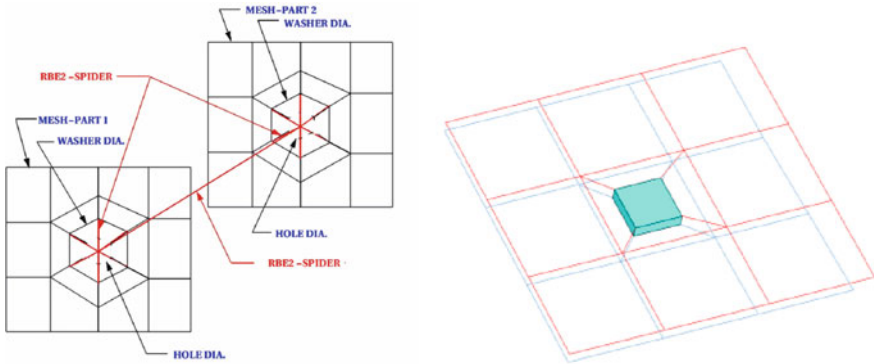


Fig. 2 Two kinds of modeling methods for spot welds

Fig. 3 Spot weld modeled by bar directly connected to nodes of shell element

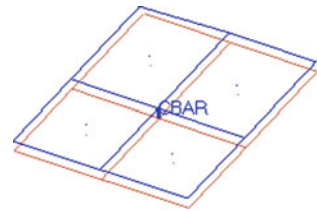
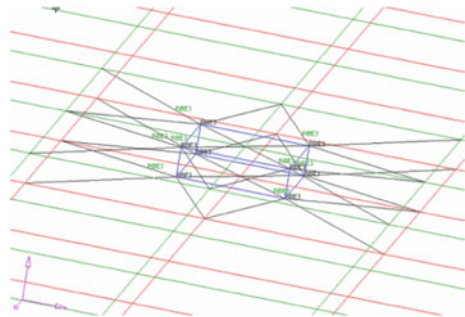


Fig. 4 ACM method of spot weld



into equivalent force and moment of beam element, as shown is Figs. 4 and 5. Then the fatigue analysis is processed by calculating structural stress (Fig. 6).

The advantage of this simulation method is that it is relatively easy to create model and the same elements on top and bottom shell are not needed. The entire structural stiffness is much closer to actual situation. But the uncertainty of regional stiffness for different spot weld might reduce the accordance fatigue life calculation. For example, if some RBE3 elements of two spot weld use the same node, unreasonable calculation result would be caused. If RBE3 element of weld is connected to the edge of shell, the analysis result might be far away from actual result. The connection position where the spot weld connects shell element affects the equivalent force and moment of spot weld obviously and then influences the

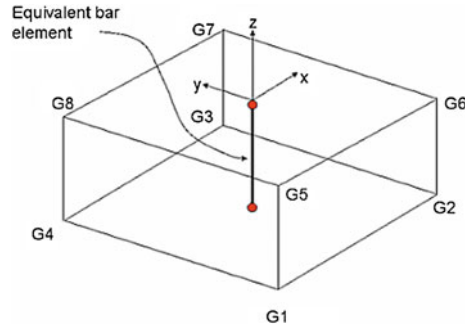


Fig. 5 Hexahedral element and equivalent bar element

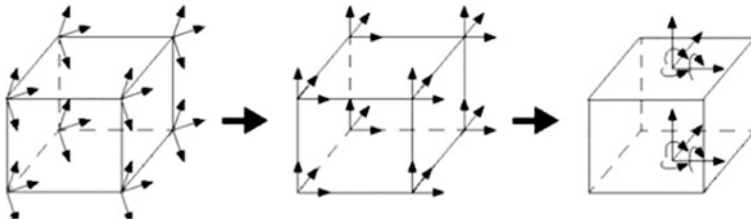


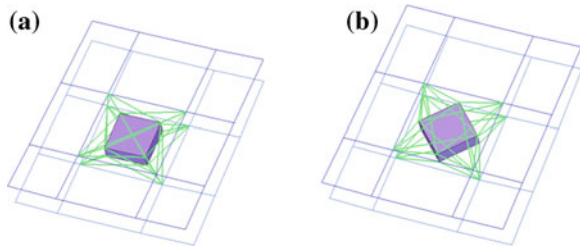
Fig. 6 Forces are transformed from global to local coordinates and then transferred to the centroids of the opposing element faces

result of fatigue life. It is shown according to experiences that the edge of shell element where spot weld exists should keep at least three rows of elements. The RBE3 elements connect to the four corner nodes of the same shell element, as shown in Fig. 7. Based on the characteristic of creating model, relative material properties (S–N curve) are given respectively and then relatively reasonable result could be got. Research shows that more accurate result could be achieved when hexahedron of weld nugget has an angle of  $45^\circ$  with shell element, as shown in Fig. 7b. In this paper, the spot weld is simulated by ACM method.

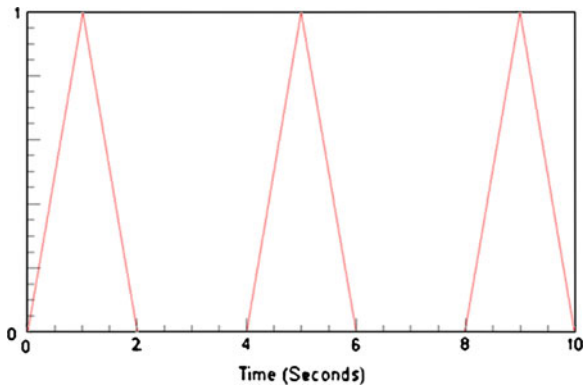
## 2.4 The Introduction of Fatigue Analysis on Spot Weld Under Multiple Load Subcases

The vehicle might meet different complicated conditions in driving process which could be separated into some standard subcases including torsion, bump, cornering, braking, accelerating and the combination of these subcases. According to Miner linear damage rule, fatigue is a linear accumulation process of damage and independent with the loading sequence. So the spot-weld fatigue life is calculated under these typical cases of simple constant amplitude cycle equivalent with the

**Fig. 7** ACM connection lying within a single element



**Fig. 8** Simple load data



damage in actual driving conditions in order to predict dangerous fatigued region and point on car.

In calculation, four groups of subcases, which are symmetrical torsion cycle, vertical bump cycle under different amplitude, cornering cycle, accelerating and braking cycle, are building considering the actual loading conditions on car body. Fatigue load spectrum (Fig. 8) in the form of series of half triangular wave or impulse wave is produced by using nCode software. The static analysis result, S–N curve and fatigue load spectrum are used as the input of fatigue analysis. The fatigue life distribution for car body weld under multiple load combination cases could be achieved on the basis of Miner damage rule. The required loads in static analysis are usually got from multi-body dynamic simulation. It should be noticed that the weld nugget and base material have different mechanical properties, and their corresponding S–N curves are also different. The S–N curve of weld nugget is given in Fig. 9.

### ***2.5 Analysis on Fatigue Life of Spot Weld and Test Result***

The fatigue life of spot weld is calculated through Design life module in nCode software based on the subcases, materials and S–N curve which are described before. The calculation result indicates that several spot welds where the hat rack

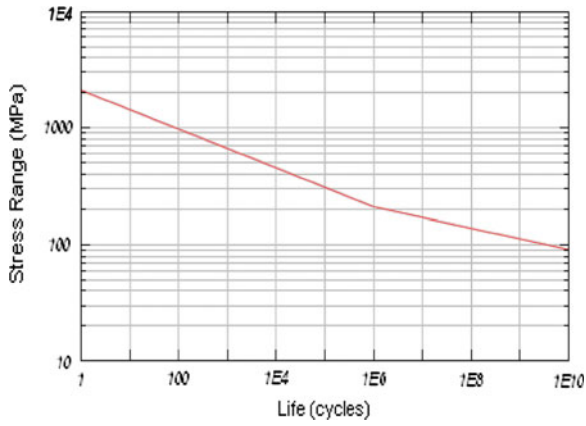
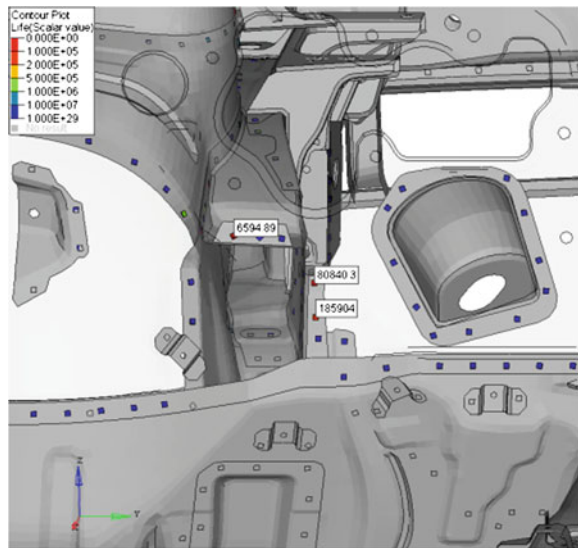


Fig. 9 S–N curve of nugget

Table 1 Spot weld fatigue calculation results with S–N

Spot weld ID	Torsion loadcase		Bump loadcase	
	Life	Damage	Life	Damage
1	6594	1.52e-4	5.9e4	1.69e-5
2	8.08e4	1.24e-5	2.85e5	3.51e-6
3	1.86e5	5.38e-6	1.86e5	5.36e-6
4			2.5e5	4.0e-6

Fig. 10 Spot weld with low fatigue life under vertical bump cycle



**Fig. 11** Spot weld with low fatigue life under symmetrical torsion cycle

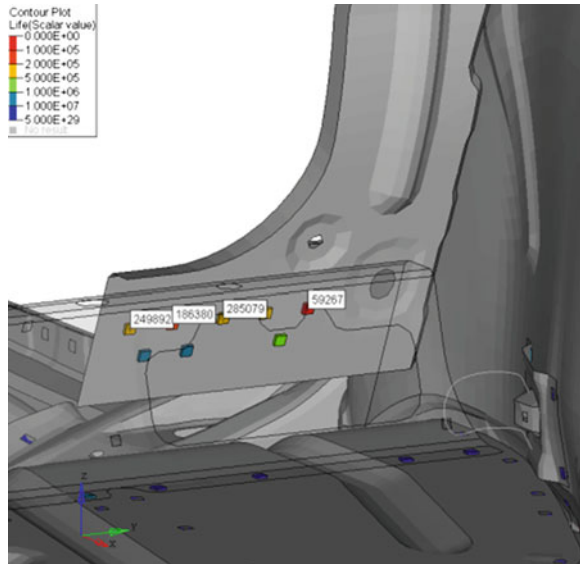


plate connects with floor upper beam have relatively low fatigue life under symmetrical torsion cycle. The fatigue life of some spot welds on front wall and front longeron do not satisfy the assessment standard under vertical bump cycle condition. The calculation results are shown in Table 1. In post-processing software The fatigue life and damage distribution of spot welds could be easily identified by different colors, as shown in Figs. 10 and 11. According to the analysis result, modification methods could be taken to the spot weld regions which have high fatigue damage in cooperation with structural designing engineers at the early designing stage in order to eliminate investment risk in advance, reduce the research cost and guarantee the durability requirement.

Figures 12 and 13 give some test photos which are taken in processing of durability test for prototype vehicles on comprehensive road. In the durability test, it was found that different degrees of crack appeared in the spot weld regions which just have low fatigue life in simulation result. It further indicates the prediction way for spot weld fatigue life is reasonable in early designing stage of car body by multiple load cases method.

### 3 Conclusions

In this paper, the multi-load standard fatigue subcases are used to predict fatigue life of spot weld on car body through FEM analysis in conjunction with actual supporting loads of car body in driving process. The simulation results are well tested and verified in real durability test for prototype vehicles. So the FEM

**Fig. 12** Crack on spot weld of front wall



**Fig. 13** Crack on spot weld of hat rack



method described before could be widely applied in the research and development of automobile.

Based on the fatigue life simulation method under multi-load fatigue cases, the dangerous fatigue regions on car body could be predicted relatively accurate before producing prototype vehicles. The investment risk could decrease through structure and spot weld optimization at early designing stage which is very important for shortening the research cycle and reducing research cost.

The current fatigue simulation technology of spot weld is appropriate for prediction of spot weld fatigue strength distribution, weak spot identification, and comparison between program A and B in early designing stage of car body. The accuracy of spot weld S-N curve greatly affects the calculation of fatigue life and damage. So it is necessary to further improve the test accuracy of fatigue property (S-N curve) for spot weld.



# Acoustic Isolation Analysis of Weatherstrip Considering Door Opening Condition

Tae Hyung Kim, Hak Jin Kim, Heon Young Kim, Joon Chul Park,  
Byung-Kwon Min and Chang-Kuk Yim

**Abstract** Automotive weatherstrips have the function of isolation of water, dust and noise from outside. Weatherstrips are mainly made of EPDM rubber. In general, however, rubber components tend to change physical properties and shapes after using for long time. In addition, vehicle doors tend to be opened by the effect of external pressure drop at high speed. Therefore wind noise may occur at high vehicle speed. With an effort to minimize the problem, this paper introduces an analytical prediction process to evaluate acoustic isolation according to variety door opening conditions by the Fluid Structure Interaction (FSI) analysis. By using the process of FSI analysis, the shape of the weatherstrip can be predicted. And by considering the aging effect, such as permanent deformation and compression load, it is possible to predict the durability. Also, the acoustic isolation is evaluated by using the Statistical Energy Analysis (SEA).

**Keywords** Door weatherstrip · Acoustic isolation · FSI analysis · Permanent deformation · SEA

---

F2012-E03-050

---

T. H. Kim · H. J. Kim · H. Y. Kim (✉)

Department of Mechanical and Biomedical Engineering, Kangwon National University,  
Chuncheon, Korea

e-mail: kth0416@kangwon.ac.kr

J. C. Park · B.-K. Min · C.-K. Yim

Polymeric Materials Research Team, Advanced Technology Center R&D Division  
for Hyundai Kia Motors, Seoul, Korea

## 1 Introduction

Car door weatherstrips have important functions like blocking noise transmission and foreign matter intrusion, as well as preventing vibration transmission. Recently, as the emotional perspective in vehicle performance evaluation has been emphasized, efforts to enhance sound insulation performance of door weatherstrip have increased [1, 2]. The double sealing method is currently used to improve sound insulation in vehicles that are semi-medium size or larger. The door seal, which is installed on the door frame, has sufficient pressure distribution with a deflection of approximately over 6 mm, so the impact it receives from door opening is small. However, the body seal, which is installed on the body frame, has a deflection of approximately 3 mm, so if the amount of door opening occurs more than that, the seal opens, reducing sound insulation performance.

Door opening refers to the phenomenon in which the door frame widens from inside out when pressure drops due to the vehicle's external flow at high speed, and is greatly influenced by the angle of the A filler. That is, the larger the A filler's angle, the bigger the change in external flow, which causes the door frame to widen.

This paper introduces an analytical prediction method for the sound insulation performance of the door weatherstrip by considering door opening effects. Fluid–Structure Interaction (FSI) analysis was used to predict the deformation of a door weatherstrip, which occurs due to the pressure difference between the inside and outside of a vehicle at high speed. Statistical Energy Analysis (SEA) was applied to evaluate the sound insulation performance when the weatherstrip is opened. Also, FSI analysis was conducted by considering the aging and permanent deformation of EPDM rubber, which is the main material of the weatherstrip, and the influence that these characteristics have on sound insulation performance were evaluated.

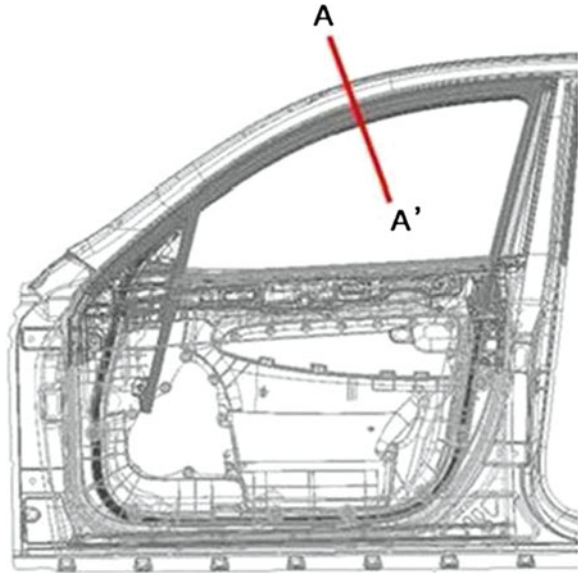
## 2 Weatherstrip Deformation Prediction Using FSI Analysis

FSI analysis [3] was applied to predict the weatherstrip deformation which occurs when driving at high speed. The analysis was conducted using ADINA<sup>®</sup>, a commercial program. The cross section of a door, including the weatherstrip, was selected as the analysis model, see Fig. 1. As the part where the A filler and loop area meets, the cross section A–A' is where door opening most frequently occurs.

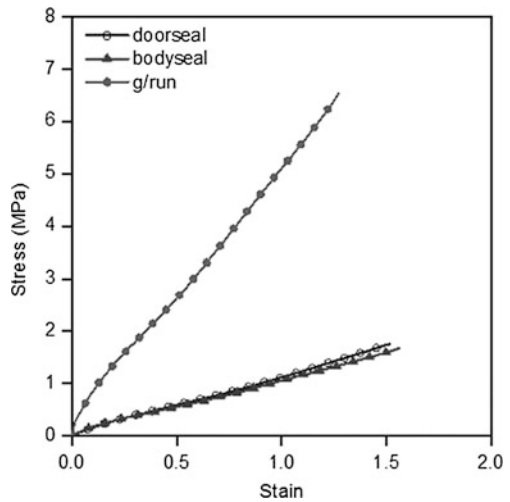
### 2.1 Finite Element Modeling

After conducting window installation and closing analysis, a two-dimensional cross section was modeled to predict the air flow when weatherstrip deformation occurs by dividing the vehicle into the car frame and seal and the fluid area. Car components like the body frame and seal used 1 mm 3-node elements and 4-node elements,

**Fig. 1** Illustration of the door and target point

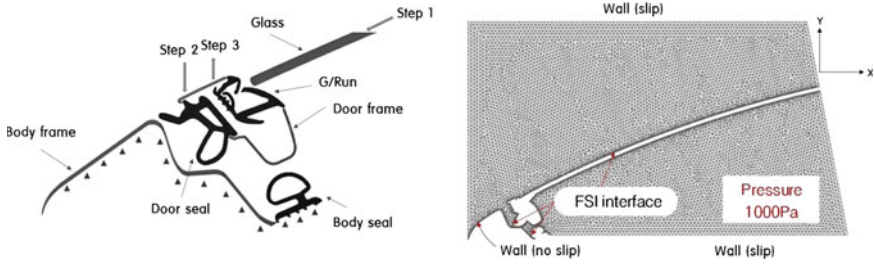


**Fig. 2** Stress-strain curve of seals

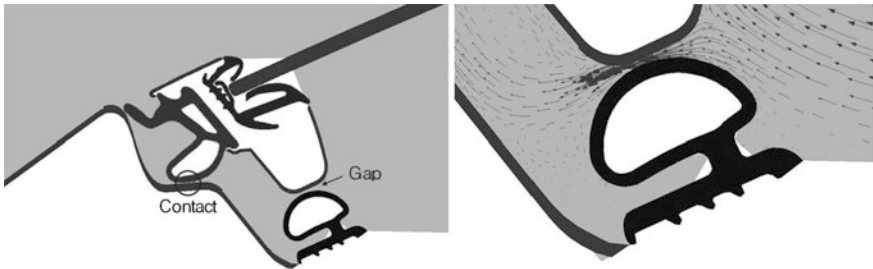


whereas the fluid (air) area was modeled using 1 mm 3-node elements. The materials model of the seal applied the stress–strain curve obtained from the uniaxial tension test, and its behaviour was expressed by considering the hyper elasticity model. Ogden model [3–5] was used as the energy equation, and the stress–strain curve is as shown in Fig. 2. Being air, a density of  $1.983e-08 \text{ kg/mm}^3$ , and viscosity of  $1.205e-12 \text{ Ns/mm}^2$  was applied to the fluid area.

To considering door opening, the analysis was divided into the window installing procedure and door closing procedure, as shown in Fig. 3. Fixating the body frame and body seal, the installation analysis of the window was conducted



**Fig. 3** Boundary condition of the structure and fluid model



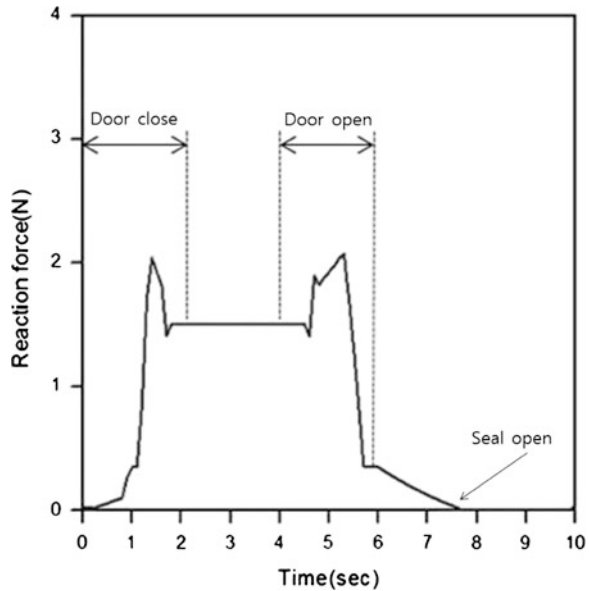
**Fig. 4** Analysis result of door open condition. (3 mm-open)

in step 1, while door closing was simulated by moving window, glass run, and door seal in step 2. Finally, in step 3, to consider door opening, an analysis was conducted by moving models, which were moved when closing the door, on the Y axis from 0.5 to 3 mm at a 0.5 mm interval. Because the axis of flow direction and the axis of the analysis model cross section were different, the pressure value, instead of the fluid speed, was applied to analyze external flow following high speed driving. Using the data in the references, pressure was applied to the inside of the car as much as the amount reduced from the outside, and the amount of pressure change that occurs at the door loop area when driving at a high vehicle speed (180 km/h) is approximately—1000 Pa, as shown in Fig. 3 [6].

## 2.2 Analysis Result

When moving the door outwards at a 0.5 mm interval, the door seal and body seal both maintained contact up to 2.5 mm, but at the door opening condition 3 mm, the body seal was separated from the frame due to fluid flow, as shown in Fig. 4. Also, the fluid inside escaped through the open space between the body frame and body seal. Figure 5 shows the result of measuring the reaction force of the body frame on the body seal during the analysis time. At the door opening condition 3 mm, contact was maintained, but when pressure was applied in the interior space, the reaction force was eliminated.

**Fig. 5** Reaction force of normal body seal



### 3 Weatherstrip with Aging or Permanent Deformation

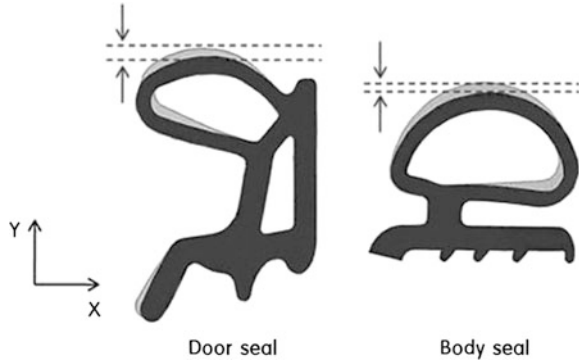
To predict the permanent deformation, a weatherstrip was aged for long time in high temperature chamber. Compared to the stiffness obtained from the material tests of an initial product sample, the aged sample had approximately 40 % lower stiffness [5]. Also, to obtain the deformed door seal shape, the viscoelasticity analysis was conducted in time domain (Fig. 6).

In case of the aged and permanently deformed model, the body seal was opened at door opening condition 2 mm. The reaction force was decreased by 50 % compared to the initial state as shown in Fig. 7. Considering that the amount of permanent deformation on the body seal, it was confirmed that change in form, rather than the change in material stiffness, is a major factor of body seal opening.

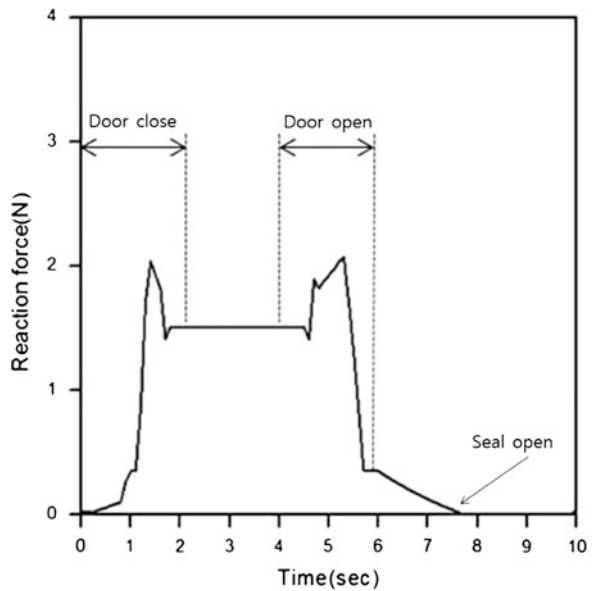
### 4 Evaluation of Sound Insulation Using SEA

Generally, it is impossible to evaluate the response characteristics on the entire system using FEM and BEM because many modes exist in the high frequency range. Also, the accuracy of the results, which is based on element size and analysis time, decreases the analysis efficiency when using FEM and BEM due to using many elements [1, 7]. On the other hand, SEA is appropriate for noise analysis at high frequency range, which has large number of vibration modes. Also, it is a very practical method for analyzing the noise of the entire system,

**Fig. 6** Measurement of permanent deformation



**Fig. 7** Reaction force of aging body seal



rather than individual parts which form the system. The basic principle of SEA is that it divides the analysis system into subsystems, and computes the energy transmission and loss between each system, as shown in Fig. 8 [1, 7]. Many vibration modes exist in the case of door seal sound insulation evaluation analysis, and because the goal is a sound insulation performance evaluation at the high frequency range of over 1000 Hz, SEA was used [8].

As shown in Fig. 9, the models for evaluation of sound insulation were obtained from the final shapes of the FSI analysis for the initial state and permanently deformed body seals under the given opening condition. The sound insulation performances in these two cases were then compared to each other. The modeling of cross sections with various thicknesses was done by using several components. After generating a three dimensional model by extruding a two

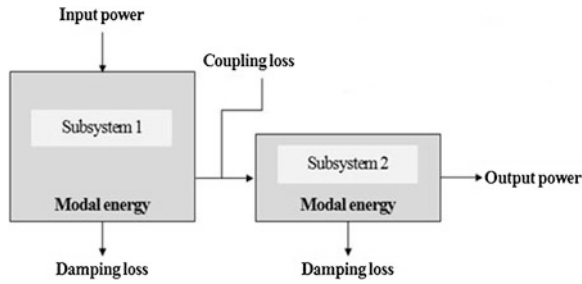


Fig. 8 Boundary condition of the structure model

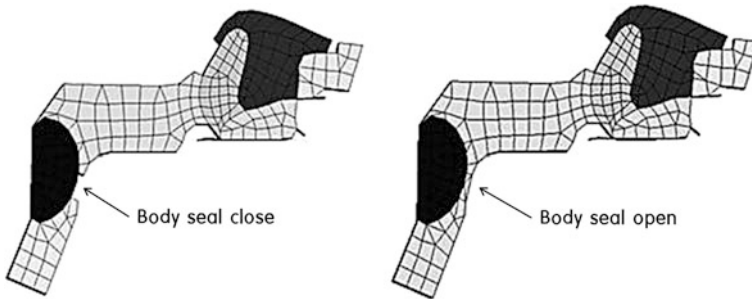
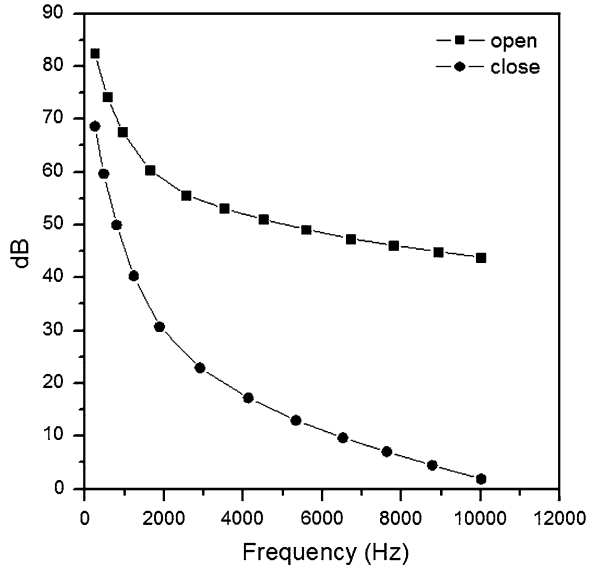


Fig. 9 SEA model

dimensional shape to a certain length in the machine direction, the spaces between the frame and door weatherstrip were defined as subsystems in the SEA model [7]. Also, a junction was defined for each subsystem [8]. External sound pressure was decided by using the sound pressure measured in the door loop area inside the car during the wind tunnel test. Because the measured interior sound pressure was 73.3 dB, the measured result and analyzed result of the sound pressure transmitted inside were identical when the external sound pressure was 112.7 dB. Therefore, when the body seal was separated from the frame, sound pressure transmitted to the interior was evaluated by setting the external sound pressure condition at 112.7 dB.

The SEA result is shown in Fig. 10. In the case of the shape after aging, where the body seal is apart from the frame, the sound pressure transmitted to the interior was 85.1 dB. As shown in Table 1, the noise transmissibility increased approximately 10 % compared to the initial state, in which the body seal was in contact with the frame. Therefore, it was confirmed that the most important factor in sound insulation performance evaluation was whether or not the body seal and frame were in contact [9].

**Fig. 10** Comparison of sound pressure for two scenarios



**Table 1** Comparison of sound pressure for two scenarios

	Seal close (initial state)	Seal open (aged state)
Average sound pressure (dB)	73.3	85.1
Noise transmissibility (%)	65.0	75.5

## 5 Conclusion

This paper proposes an analytical method for evaluating sound insulation performance of a door weatherstrip by considering door opening. Door weatherstrip deformation caused by external pressure drop at high speed was identified through FSI analysis, and characteristics were compared to understand the effect of aging and permanent deformation of the material. Also, by using SEA to comparatively evaluate sound insulation performance when there is/isn't body seal contact, it was found that whether or not there is contact with the frame following permanent deformation of the door weatherstrip is an important factor for sound insulation performance.

**Acknowledgments** This research was conducted with the support of NGV's industrial-academic research project and the General Researcher Program (2012-0006918) funded by the Korean government (Ministry of Education, Science, and Technology).



## References

1. Lim JY, Lee CS, Kim DH, Joo HS, Kim HY(2009) Acoustic performance analysis of automotive weather strips using SEA, Spring Conference of KSAE, pp 1175–1180
2. Jeoung SK, Yoo SE, Lee JY, Koh JS, Kim DH, Lee KY, Lee SC (2009) A study on elevating durability performance and an anti-environment property of a weather strip for the window of a vibration-noise reduction type automobile, Spring Conference of KSAE, pp 1361–1366
3. ADINA R&D (2010) Theory and modeling guide -ADINA CFD & FSI, Vol. 3
4. Simulia DS (2009) ABAQUS theory manual
5. Park JC, Min BK, Oh JS, Moon HI, Kim HY (2010) Numerical prediction of permanent deformation of automotive weatherstrip, Transactions of KSAE, No. 18, Vol. 4, pp 121–126
6. Seo KD, Kim DH, Oh SH (2007) Analysis of major design factors for door frame stiffness at a high speed wind tunnel, Spring Conferece of KSEA, pp 1289–1294
7. ESI group (2010) VA-ONE theory manual
8. Moon HI, Kim HJ, Kim HY, Park JC, Min BK (2011) Acoustic isolation analysis of door weatherstrip considering permanent deformation effects, Spring Conference of KSAE, pp. 1934–1939
9. Munson BR, Young DF, Okiishi TH (2006) Fundamentals of fluid mechanics, pp 319–369, Wiley

# Assessment of Modeling Individual Physiological Differences when Predicting Thermal Comfort

Curran Allen and Hepokoski Mark

**Abstract** Segmental human thermoregulation models are increasingly being used to predict thermal comfort in vehicle passenger compartments. These computational models simulate the process by which the human body maintains a nearly constant core temperature. The primary output of thermoregulation models is the predicted time history of the body's core and skin temperature, which is subsequently used as input to a model that predicts corresponding thermal sensation and comfort perceptions. The advantage of this method of predicting thermal comfort is its applicability to non-uniform and transient environments, such as the passenger compartment of an automobile. In this paper we assess the importance of modelling individual physiological differences when predicting thermal comfort using a segmental thermal model.

**Keywords** Thermal comfort · Thermoregulation · Modelling

## 1 Introduction

Although it is known that variations in physiological characteristics among humans affect their thermal response to the environment [1], many segmental human models implement a single representative “standard” (i.e., 50th percentile in height and weight) male physiology. To examine this practice in the context of thermal comfort

---

F2012-E03-053

---

C. Allen (✉) · H. Mark  
ThermoAnalytics, Inc, calumet, USA  
e-mail: arc@thermoanalytics.com

prediction, we have developed software for building a physiological description for non-50th percentile humans [2]. Only the target body size (expressed as a (separate) percentile of height and weight of the population), the percent body fat (optional) and the baseline 50th percentile physiological description are required as inputs. The outputs from the software are body segment lengths and the per-segment thicknesses of the constituent tissue types (e.g., bone, muscle, fat and skin).

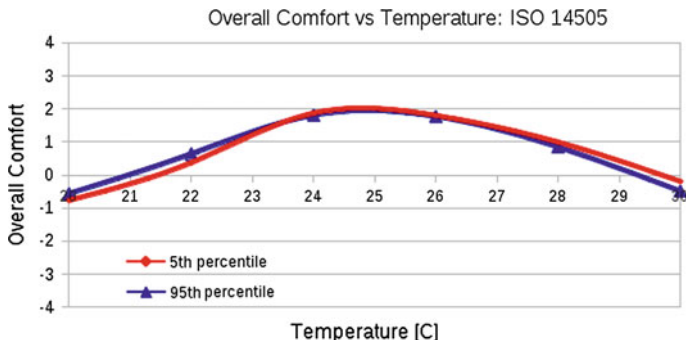
## 2 Methodology

A shell-element based segmental thermoregulation model [3] coupled with the Berkeley Comfort Model [4–6] was used to conduct this study. The Berkeley Comfort Model predicts comfort on a scale that ranges from  $-4$  to  $+4$ , which represents perceptions of “very uncomfortable” to “very comfortable,” respectively. Human thermal models of this type require “reference states,” the deviations from which are used to simulate human thermoregulation and to predict thermal sensation and comfort. For thermoregulation, the reference state is defined by the (nude) model’s steady-state tissue temperatures when subjected to a thermoneutral environment (nominally  $30\text{ }^{\circ}\text{C}$  air and radiant temperature and  $40\%$  relative humidity). For thermal comfort, the reference state is ideally set to the clothed model’s tissue temperatures obtained by simulating a comfortable environment as defined by human-subject experiments.

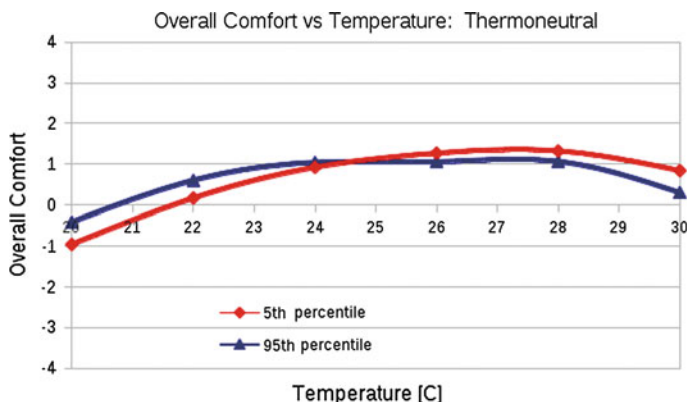
## 3 Results

The advantage of utilizing a separate, human-subject determined reference state for comfort is that cultural and physiological preferences of a specific population can be readily accommodated. Typical thermal comfort results, using a comfort reference state obtained from ISO 14505-2, Appendix D [7] (summer conditions), are shown for a steady, homogeneous environment (Fig. 1). The maximum comfort value reported by the Berkeley Comfort Model for *steady* environments is approximately  $2.0$ , which occurs at about  $24.5\text{ }^{\circ}\text{C}$  for this case. (Higher values of comfort can only be achieved when using the Berkeley Comfort Model to model transient environments that change from uncomfortable to comfortable). Note that comfort decreases and the passengers eventually become uncomfortable as the temperature of the environment is either increased or decreased from  $24.5\text{ }^{\circ}\text{C}$ .

The thermoregulatory reference state is generally not appropriate for use as the thermal comfort reference state. To illustrate this, the simulation described above was repeated using a comfort reference state that was set to be identical to the thermoregulatory reference state (Fig. 2). Note that thermal comfort predicted in this manner is asymmetric and relatively insensitive to the temperature of the environment.



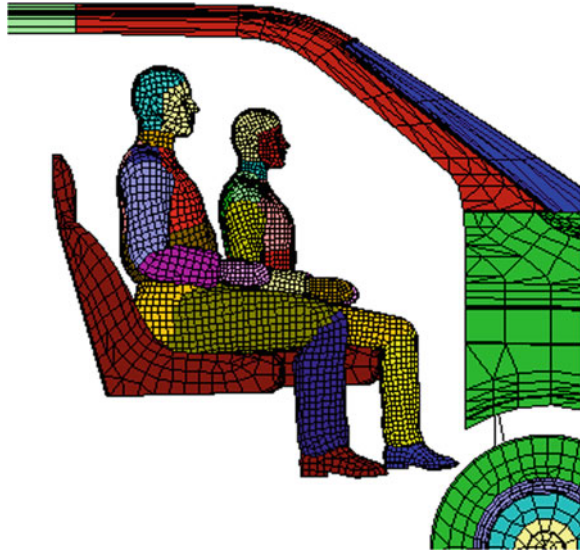
**Fig. 1** Whole-body comfort is plotted as a function of the temperature of a homogenous environment for two different percentile passengers. The comfort reference state was obtained from ISO 14505-2, Appendix D, for summer conditions



**Fig. 2** Whole-body comfort is plotted as a function of temperature of a homogenous environment for two different percentile passengers. The relatively poor comfort prediction is due to the use of the (nude) thermoneutral reference state as a comfort reference state

The relative importance of modelling individual physiological differences when predicting thermal comfort was examined by simulating the thermoregulation and comfort of western males who were between 5th and 95th percentile in height and weight. In a steady, homogenous environment (refer again to Fig. 1) the use of a unique physiological description (body mass, fat, etc.) made little difference. We believe that a single comfort reference state, which is defined by average comfort “votes” from human-subject tests but is unique for each physiology modelled, tends to reduce the impact of which physiological description is used. We expect that this will less likely to be the case for transient, asymmetric environments where differences in body segment fat and thermal capacitance will have a larger impact; this will be the subject of future research.

**Fig. 3** Simulation geometry for a 5th percentile passenger (sitting closer to an air vent) and a 95th percentile passenger

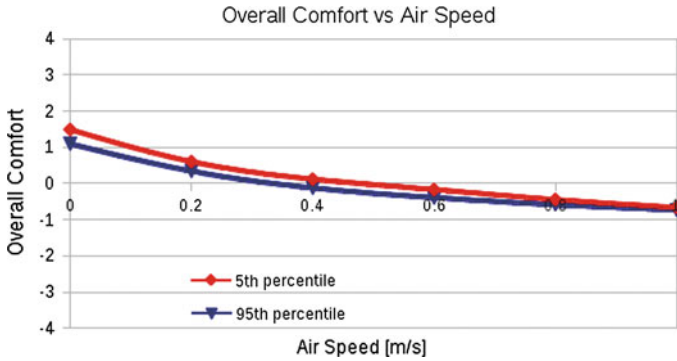


We then examined the relative importance of modelling unique physiologies by simulating 5th and 95th percentile passengers that, due to their physical size, would sit closer or further from an air vent (Fig. 3). This scenario was modelled by adjusting the air velocity experienced by the passengers from 0.0 to 1.0 m/s to provide a representative range of conditions that the individuals might experience. (In this scenario, the 5th percentile passenger would be more likely to experience higher air velocities than the 95th percentile passenger). Air temperature was set to 20 °C with a radiant temperature of 30 °C. The simulations show that comfort predictions are much more sensitive to changes in environmental boundary conditions due to physical size than to modelled physiological differences (Fig. 4).

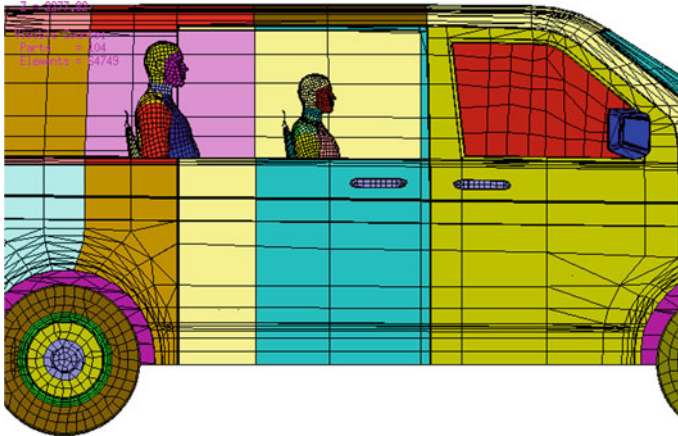
Finally, we modelled two passengers that experienced different solar loading due to their seating position relative to the windows of a vehicle (Fig. 5). The vehicle heading, latitude, longitude, time of year and time of day were set such that the head and torso of the 5th percentile passenger was completely subjected to the solar load coming through the side window of the vehicle, while the 95th percentile passenger's head was shaded by the vehicle's roof. The *transient, local* comfort experienced by head of each passenger after entering the vehicle is shown in Fig. 6.

## 4 Conclusions

This paper presents an assessment of the thermal comfort results obtained by simulating different sized individuals in a vehicle passenger compartment. Good results were obtained with a segmental human thermoregulation model that used a

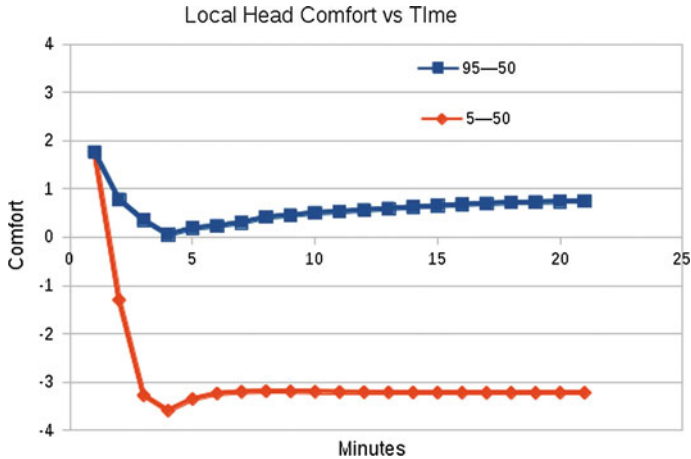


**Fig. 4** Whole-body comfort is plotted as a function of air speed experienced by passengers in an automotive cabin with a radiative temperature of 30 °C and an air temperature of 20 °C. In this scenario, the 5th percentile passenger would be more likely to experience higher air velocities than the 95th percentile passenger



**Fig. 5** Simulation geometry for a 5th percentile passenger and a 95th percentile passenger seated in a vehicle subjected to solar loading. The vehicle is positioned such that the head and torso of the 5th percentile passenger is completely subjected to solar load through the side window while the 95th percentile passenger's head is shaded by the vehicle's roof

comfort reference state obtained from ISO 14505-2, Appendix D (summer conditions) for steady, homogeneous environments. It was shown that the thermoregulatory reference state is generally not appropriate for use as the thermal comfort reference state. Regardless, using human-subject determined reference states for comfort is preferable since cultural and physiological preferences of a specific population can be readily accommodated. Physical size was also shown to be an important factor for predicting thermal comfort, since passenger location within a vehicle will often influence environmental heat exchange, such as when a passenger sits further or closer to an air vent or receives less or more solar loading.



**Fig. 6** Local (head) comfort is plotted as a function of time for 5th and 95th percentile passengers. The difference in comfort is due to the amount of solar load experienced

## References

1. Zhang H, Huizenga C, Arens E, Yu T (2001) Considering individual physiological differences in a human thermal model. *J Thermal Biol* 26:401–408
2. Mark H, Allen C, Mark K, Rob S, Vamshi K (2012) Analysis of soldier effectiveness in a mine resistant ambush protected ground vehicle. In: NDIA ground vehicle systems engineering and technology symposium, Dearborn, MI, USA
3. Curran AR, Hepokoski MA, Curlee JS, Nelson DA, Biswas A (2006) Adapting segmental models of human thermoregulation and thermal sensation for use in a thermal simulation of a vehicle passenger compartment, F2006D129T, FISITA transactions 2006. International Federation of Automotive Engineering Societies, London
4. Zhang H, Arens E, Huizenga C, Han T (2009) Thermal sensation and comfort models for non-uniform and transient environments: part I: local sensation of individual body parts. *Building and Environment*
5. Zhang H, Arens E, Huizenga C, Han T (2009) Thermal sensation and comfort models for non-uniform and transient environments: part II: local comfort of individual body parts. *Building and Environment*
6. Zhang H, Arens E, Huizenga C, Han T (2009) Thermal sensation and comfort models for non-uniform and transient environments: part III: whole-body sensation and comfort. *Building and Environment*
7. ISO 14505-2:2006(E) (2006) Ergonomics of the thermal environment—evaluation of thermal environments in vehicles—part 2: determination of equivalent temperature. International Organization for Standardization, Geneva

# The Multi-Physics Coupling Analysis Based on Electro-Magnetic, Structural and Acoustic Characters for a Drive Motor in EV

Jinling Zeng, Yingzi Piao, Bingwu Lu, Fuxiang Huo and Qun Zhang

**Abstract** According to generating mechanism of electromagnetic noise from the permanent magnet synchronous motor on EV, this paper proposed how to use a multi-physics coupling analysis based on the electromagnetic, structural and acoustic fields of the motor to estimate the noise and vibration characteristics. Firstly, the two-dimensional transient electromagnetic field of the motor was calculated by using the step finite element method, and the electromagnetic excitation force on the surfaces of the stator in both frequency and time domain are obtained; Then, based on three-dimensional structure of the motor assembly, the simulation of the entire system natural frequencies and mode shapes was executed, and coupling the electromagnetic field analysis results of the motor, the vibration velocity level of the motor surface was achieved through the frequency response analysis. Finally, the coupled three-dimensional acoustic boundary element model was employed to calculate the motor acoustic radiation. The experimental results demonstrated that this multi-physics coupling numerical analysis method can effectively predict the electromagnetic noise in the motor design phase and help low-noise motor design and development.

**Keywords** Electric vehicle · Permanent magnet synchronous motor · Electromagnetic exciting force · Vibration response analysis · Electromagnetic vibration and noise

---

F2012-E03-057

---

J. Zeng (✉) · Y. Piao · B. Lu · F. Huo  
The FAW Co., LTD R&D Center, Changchun, China  
e-mail: zengjinling@rdc.faw.com.cn

Q. Zhang  
INTESIM (Dalian) CO., LTD, Dalian, China



## 1 Introduction

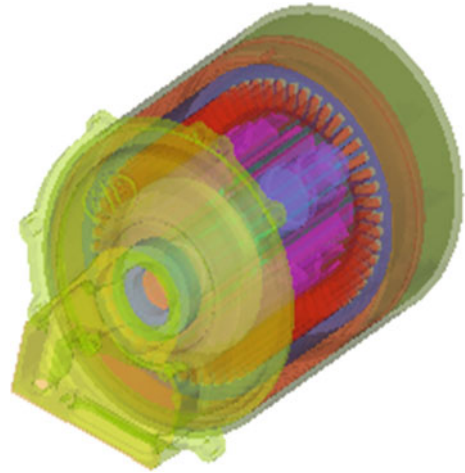
With the deepening of the global energy crisis, as well as air pollution, and the intensifying of global warming, the energy saving of electric vehicle technology has become the hotspot of the major car companies in China and abroad [1]. The drive motor is a key component of electric vehicle drive system, and also has higher performance requirements than common industrial drive motor: (1) extreme changes in the load conditions, wide speed range; (2) in order to reduce vehicle weight, and to extend the driving range, the motor needs to have higher power density and better efficiency characteristics; and (3) the installation space is small, under poor working conditions, that require higher reliability and cooling capacity [2]. The particularity of these performance requirements and working environment of the motor exacerbate its noise and vibration issues, and that have become important indicators to measure the motor quality, as well as the difficulty of the motor design.

In recent years, there have been a number of articles and books on the drive motor noise and vibration, since this is a very important and complex subject, advanced numerical analysis methods, test equipment and tools keep on updating and developing. For this reason, this paper regarding the new knowledge and experience on how to predict the motor noise and vibration is very worthwhile. In the project, when the motor noise and vibration occur, the first thing is to identify the sources of the noise and vibration, in other words, high frequency vibration generated by the excitation force, or because of the structural stiffness is not enough to avoid a system resonance; and then to solve the problem. It is difficult to identify noise sources and to reduce the noise after the completion of the motor manufacture, as a result accurate noise sources identification and low-noise design in the design phase is critical for the motor design [3–9]. In order to quickly and effectively predict and resolve the noise and vibration problems in the product design stage, electromagnetic-structure-acoustic coupling numerical analysis method are studied in this research.

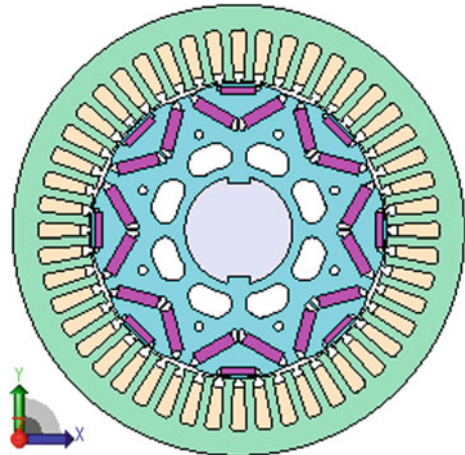
## 2 Magnetic Field Analysis of the Motor

To analyze the vibration and noise characteristics of the permanent magnet synchronous motor, you should first analyze the variation of the electromagnetic excitation force in the stator teeth. For a permanent magnet synchronous drive motor of an electric vehicle that is used in this research, the basic parameters are as follows: the nominal bus voltage is 288 V, the continuing power 20 KW, continuous torque 120 Nm, the peak power 40 KW, peak torque 260 Nm, the speed range 0–7,600 rpm, the number of stator winding 3, number of stator slot 48, and the stator winding is a single-layer winding, the stator winding connection is star connection, the length of the core 140 mm, the stator outer diameter

**Fig. 1** Geometric model of motor assembly



**Fig. 2** Electromagnetic field analysis model of motor



200 mm, the stator inner diameter 132 mm, rotor internal diameter 47.5 mm, the pole number 4, and the air gap is non-uniform air gap.

The three-dimensional assembly model of a permanent magnet synchronous drive motor is shown in Fig. 1; it can be approximated as a two-dimensional model of the cross section if the end effects can be ignored. In this paper a two-dimensional transient field-circuit coupling method is used to simulate electromagnetic field, the finite element analysis model is shown in Fig. 2. To improve the analysis accuracy of the flux density in the air gap, along the thickness direction of the air gap, the air is evenly divided into seven equally spaced meshes, in the circumferential direction one element is adopted for each degree of circumferential angle, the mesh discretization of the air gap is demonstrated in Fig. 3. The accuracy of the numerical results of the electromagnetic finite element analysis model can be

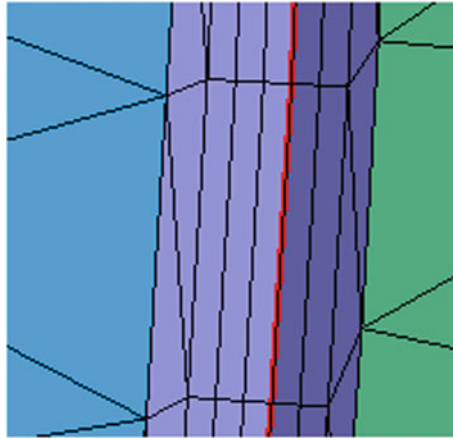


Fig. 3 Mesh subdivision model of air-gap

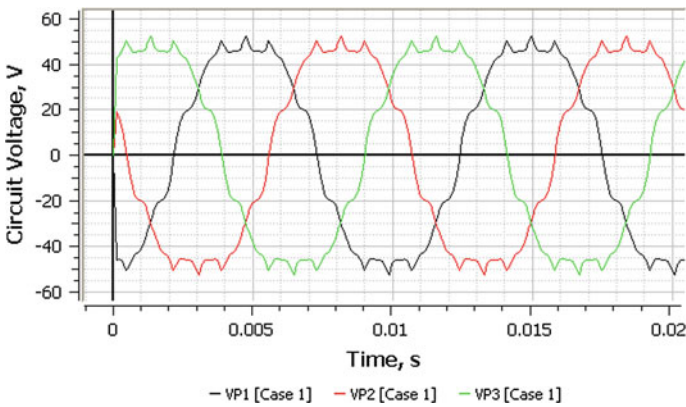


Fig. 4 EMF curve of opening circuit

verified by comparison with the experimental data. The inverse electric potential constants measured at no-load condition is 25.39 mV/rpm, and the FEA results of inverse electric potential at speed of 1,469 rpm obtained in this research is 37.38 V (RMS), Fig. 4 shows the comparison. The difference between the numerical simulation and the experiment is only about 0.22 %, which is mainly due to ignorance of the end magnetic flux leakage in the 2D numerical model; this satisfies the accuracy requirements in engineering.

The interaction between the harmonic magnetic field in the rotor, stator and air-gap causes the excitation force on the stator tooth, that results in the vibration and noise on the motor surface. The two-dimensional transient magnetic field can be simulated by the field-circuit coupling finite element method for the permanent

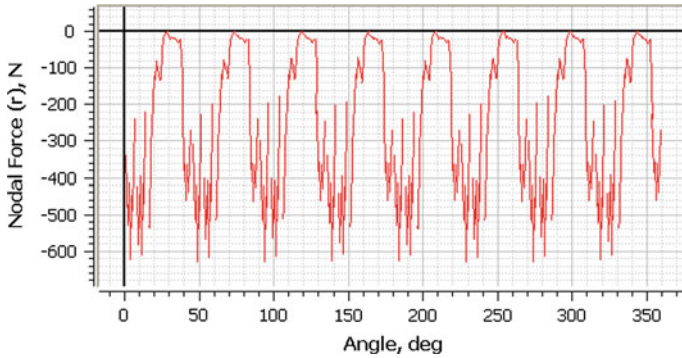


Fig. 5 Spatial radial force distribution curve of stator tooth surface

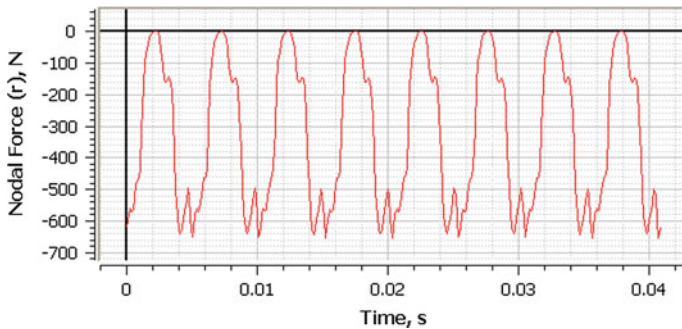
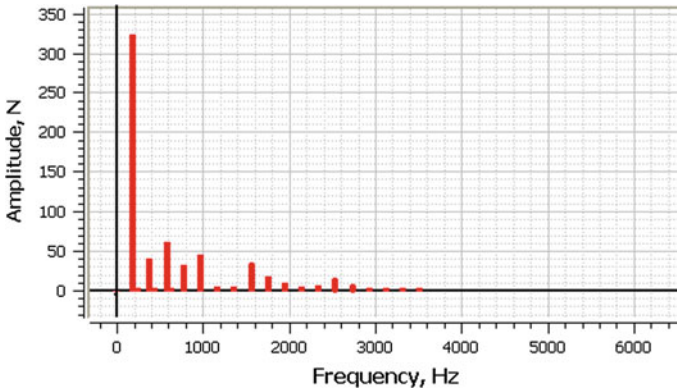


Fig. 6 Time radial force distribution curve of stator tooth surface

magnet synchronous motor; the electromagnetic excitation force on the stator tooth can be calculated according to Maxwell’s law. The time history and spatial distribution of the electromagnetic force in the radial direction on the surface of the stator teeth are shown in Figs. 5 and 6, respectively. These curves consist of a large number of harmonic responses at different frequencies, which will be detrimental to the motor vibration and noise. Using spectrum analysis, the frequency and amplitude of the main component of electromagnetic excitation force can be obtained (Fig. 7 and Table 1); the base excitation force frequency is 195.9 Hz. There is a corresponding relationship between the frequency of the vibration and noise of the motor and the frequency of the electromagnetic excitation forces.

### 3 Structure Analysis of the Motor

The electromagnetic noise of the motor is caused by the vibration of the stator assembly that consist of the stator winding, water, housing, end caps, etc., in this research the vibration characteristics of the stator assembly will be studied in two



**Fig. 7** Radial force spectrogram of stator tooth surface

**Table 1** The main frequency and amplitude of radial force in stator tooth surface

Frequency (Hz)	Amplitude (N)
195.9	321.4
391.7	38.2
587.6	59.1
783.5	30.6
979.3	43.3
1566.9	36.7
1762.8	16.0
2546.3	18.5
2742.1	8.4

ways: the modal and natural frequency analysis for the stator assembly, and the vibration response analysis of the stator under electromagnetic excitation force.

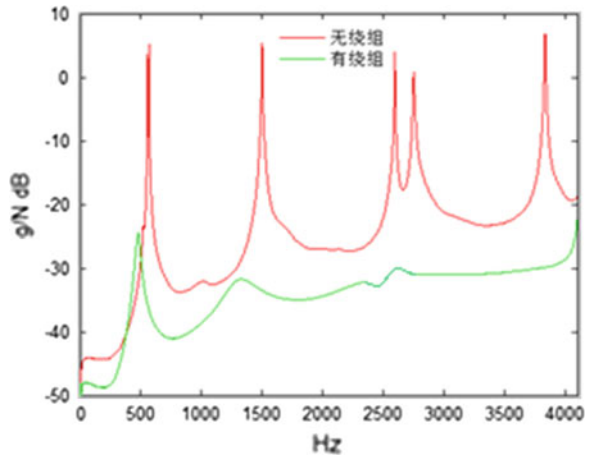
The core structure of the motor stator consists of 380 thin silicon steel laminations, the elasticity modulus in the axial direction is much smaller than those in the laminated plane, and the orthotropic elastic material will be adopted for the core structure in the finite element model. In order to obtain the mechanical parameters of the stator core in the axial direction, modal testing and parameter identification of the stator core need to be carried out. Figure 8 shows a modal test model of the stator core in the winding and without winding state, it also demonstrate the distribution of excitation points. Figure 9 gives the average FRF curve of a measuring point for the winding and without winding state under freely handling state. The comparison of the natural frequency of the stator core in freely handling state is obtained by the modal analysis and the tests are listed in Table 2, the corresponding vibration modes are shown in Fig. 10.

Linear elasticity in an orthotropic material can also be defined by giving the nine independent elastic stiffness parameters, as functions of temperature and other predefined fields, if necessary. In this case the stress–strain relations are of the following form:



Fig. 8 Free suspension diagram of the stator with and without winding modal test

Fig. 9 Average FRF curve of No. 6 node in the free suspension state

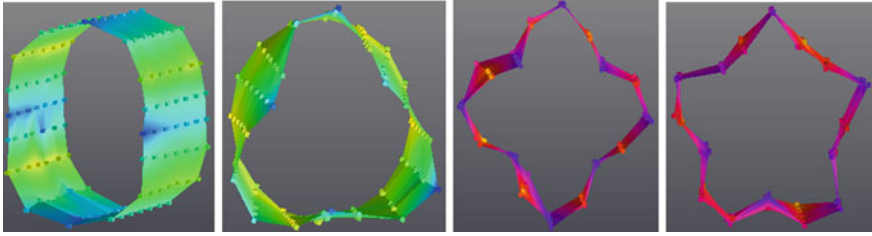


$$\begin{Bmatrix} \sigma_{11} \\ \sigma_{22} \\ \sigma_{33} \\ \sigma_{12} \\ \sigma_{13} \\ \sigma_{23} \end{Bmatrix} = \begin{bmatrix} D_{1111} & D_{1122} & D_{1133} & 0 & 0 & 0 \\ 0 & D_{2222} & D_{2233} & 0 & 0 & 0 \\ 0 & 0 & D_{3333} & 0 & 0 & 0 \\ 0 & 0 & 0 & D_{1212} & 0 & 0 \\ 0 & 0 & 0 & 0 & D_{1313} & 0 \\ 0 & 0 & 0 & 0 & 0 & D_{2323} \end{bmatrix} \begin{Bmatrix} \varepsilon_{11} \\ \varepsilon_{22} \\ \varepsilon_{33} \\ \gamma_{12} \\ \gamma_{13} \\ \gamma_{23} \end{Bmatrix} \quad (1)$$

The above equation,  $p, t$  (refers to the subscript number 1,2,3) representing the material properties of the stator plane and pressed the direction of, representing the material properties of the stator plane and the laminated direction,  $E_1 = E_2 = E_p$ ,  $\nu_{31} = \nu_{32} = \nu_{tp}$ ,  $\nu_{13} = \nu_{23} = \nu_{pt}$ ,  $G_{13} = G_{23} = G_t$ ,  $G_p = E_p/2(1 + \nu_p)$ ,  $\nu_{tp}/E_t = \nu_{pt}/E_p$ . In the stiffness matrix of the Eq. (1),

**Table 2** Main modal parameters of the stator in the freely suspended state

Vibration characteristics		2nd-order	3rd-order	4th-order		5th-order
Stator model		bending	bending	bending		bending
With winding	Test frequency (Hz)	567	1,500	2,592	2,751	3,832
	Analysis frequency (Hz)	559	1,492	2,654	2,744	3,814
	Error (%)	-1.4	-0.5	2.4	-0.3	-0.4
Without winding	Test frequency (Hz)	472	1,350	2,325	2,523	-
	Analysis frequency (Hz)	471	1,296	2,307	2,493	3,654
	Error (%)	-0.2	-0.7	-0.8	-1.2	

**Fig. 10** Main modal shapes of the stator in freely suspended state

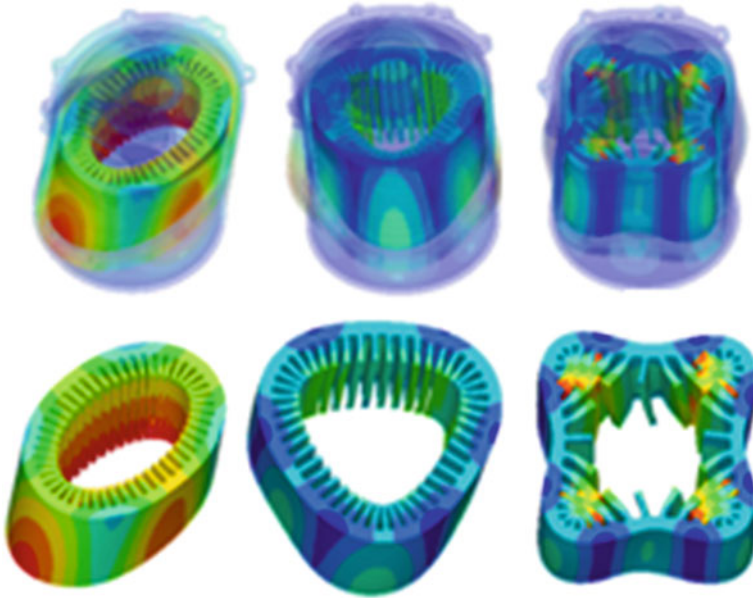
$$\begin{aligned}
 D_{1111} &= E_1(1 - \nu_{23}\nu_{32})\Gamma, \\
 D_{2222} &= E_2(1 - \nu_{13}\nu_{31})\Gamma, \\
 D_{3333} &= E_3(1 - \nu_{12}\nu_{21})\Gamma, \\
 D_{1122} &= E_1(\nu_{21} + \nu_{31}\nu_{23})\Gamma, \\
 D_{1133} &= E_1(\nu_{31} + \nu_{21}\nu_{32})\Gamma, \\
 D_{2233} &= E_2(\nu_{32} + \nu_{12}\nu_{31})\Gamma, \\
 D_{1212} &= G_{12}, \\
 D_{1313} &= G_{13}, \\
 D_{2323} &= G_{23},
 \end{aligned} \tag{2}$$

In Eq. (2),  $\Gamma = \frac{1}{1 - \nu_{12}\nu_{21} - \nu_{23}\nu_{32} - \nu_{31}\nu_{13} - 2\nu_{21}\nu_{32}\nu_{13}}$ , when the material stiffness parameters are given, the structure can not produce tensile stress in the laminated direction, so use  $\sigma_{33} = 0$  as a mandatory constraint. According to the above formula, combining with the experimental data, using the finite element method, the elastic modulus of the stator core in the axial direction is 1/30 of those in the cross-section plane, the modal analysis results for different modes are listed in Table 2. From Table 2 we know that in both cases of with or without the windings, the mechanical parameters of the stator core obtained in the axial direction satisfy the accuracy requirements for engineering purpose. Applying these mechanical properties into the modal analysis for the stator assembly, Table 3 gives the natural frequency and Fig. 11 shows the corresponding vibration modes. From Table 3 one can see that the interference fit stiffening effect of water jacket on the stator core assembly is much larger than the added mass effect which leads to higher frequency in the modal analysis than those of the core structure with winding.



**Table 3** Main modal parameters of the stator assembly in the assembly constraints state

Vibration characteristics	2nd-order bending	3rd-order bending	4th-order bending	
Test frequency (Hz)	498	1,435	2,401	2,649
Analysis frequency (Hz)	503	1,428	2,427	2,703
Error (%)	1.0	-0.5	1.1	2.0



**Fig. 11** Main mode shapes of the stator

In order to get the vibration response of the stator assembly under the electromagnetic excitation force, an electromagnetic-structure-acoustic coupling numerical analysis module (Fig. 12) is used in this paper. The electromagnetic force from the two-dimensional electromagnetic field analysis is mapped to the three-dimensional structure FEA model, combining with previously calculated modal results of the stator assembly, using the modal frequency response analysis method, to carry out the structural response analysis under the excitation force, to get the vibration response of the motor in the range of 20–5,000 Hz. Figure 13 is a comparison chart of the measured vibration spectrum of the velocity level of the stator shell with the calculated values. This figure tells us that the trend of the calculated and measured values of vibration velocity level is basically the same, although there are certain deviations in the range of 2,000–3,000 Hz, this is possibly due to the dynamic effects of the rotor assembly and bearing vibration being neglected in this calculation mode.



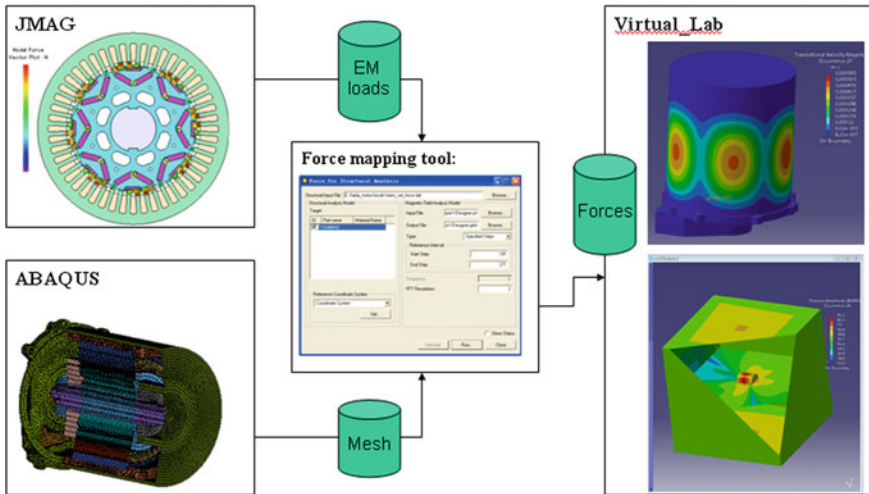
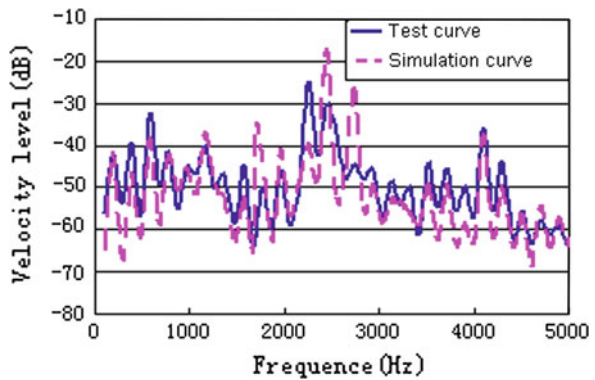


Fig. 12 Coupling electromagnetic, structure and acoustic fields numerical analysis module of the motor

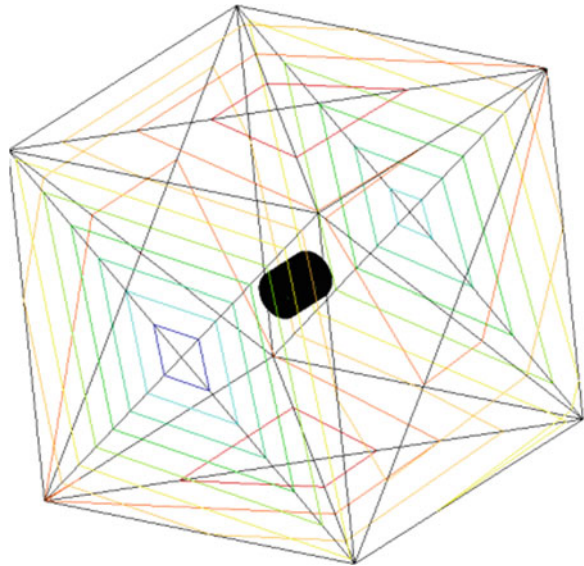
Fig. 13 Comparison of vibration velocity level spectrum



### 4 Acoustic Analysis of the Motor

The sound wave is the transmission of the vibration of the medium particle; in general sound pressure is used to describe its acoustic characteristics. For a linear acoustic problem, you can establish a linear relationship between the input (the vibration on the surface of the mechanical structure) and output (sound pressure at a point in the sound field). In this research the acoustic transfer vector method that belongs to the acoustic boundary element method is used to establish the following relationship between the sound pressure and the vibration velocity at a point in the sound field:

**Fig. 14** Measurement point of the motor's SPL



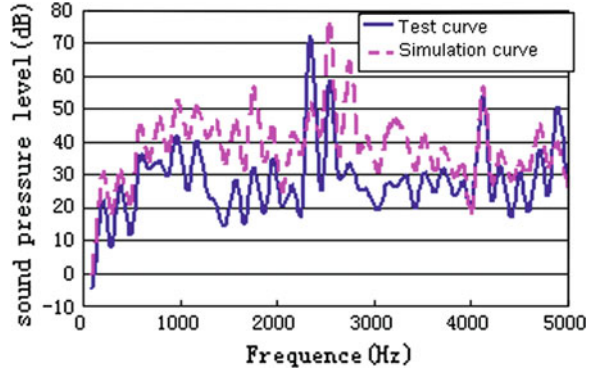
$$P(\omega) = \{ATV(\omega)\}^T \bullet \{v_{ns}(\omega)\} \tag{3}$$

- $P(\omega)$  Sound pressure of radiation field point with relationship of the frequency;
- $\{ATV(\omega)\}$  acoustic transfer vector with relationship of the frequency;
- $\{v_{ns}(\omega)\}$  the vibration velocity of structure with relationship of the frequency.

The vibration velocity on the surface nodes from the structural finite element analysis is then applied to the acoustic boundary element model, which calculates the acoustic radiation at each frequency of the motor.

The sound pressure level at specific locations is the directional noise indicators for evaluation of motor radiated noise. According to the ISO 3744-1994 international standards, the six sound pressure test points as shown in Fig. 14 are in the left and right, up and down, front and back, 1 meter away from the motor housing. Figure 15 is the comparison chart of the sound pressure level spectrum between the tests and the simulations at a measuring point of the motor. Figure 15 demonstrates that the radiated noise is only apparent peak at  $f = 2,448$  and  $f = 2,742$  Hz (the peak of the radiated noise from the test are at  $f = 2,252$  and  $f = 2,448$  Hz), there is no obvious peak for the low frequency region, this is due to the fourth frequency in the circumference direction of the stator assembly being close to the frequency of the electromagnetic excitation force, that leads to the resonance of the stator assembly. Figure 15 also tells us the consistency of the calculation and measurement values of the electromagnetic noise, it reveals the effectiveness of the proposed coupling method in predicting the main frequency components and amplitude of motor noise, and lays the foundation for prediction and suppression of noise and vibration in the design of permanent magnet motor.

**Fig. 15** Comparison of the motor's SPL spectrum



## 5 Conclusion

In this paper the electromagnetic-structure-acoustic coupling method is proposed and used to simulate the radiated noise for the electric vehicle drive motor. The followings are the main conclusions from this research:

- (1) The electromagnetic forces in space and time of this motor have many harmonic components, which will be not conducive to the vibration and noise performances, in order to achieve low-noise motor design, the motor's electromagnetic program needs to be optimized to minimize the harmonic components and amplitude of the exciting force.
- (2) The elastic orthotropic materials constitutive relation can be used to approximate material properties of the laminated structure of the stator core, compared with the experiment, the calculation accuracy has reached the engineering requirements.
- (3) From the comparison of vibration velocity level on the motor housing surface, we learned that there are certain effects of the rotor and the bearing on the vibration characteristics of the motor assembly, so we should establish a complete model of the motor in the noise and vibration analysis.
- (4) The peak of the radiated noise of the motor is concentrated in 2,500 Hz, which is due the fourth frequency in the circumference direction of the stator assembly being close to the frequency of the excitation force, this leads to the resonance of the stator assembly. Therefore, we can improve the assembly process of the stator core, such as increasing the sacking factor of the laminated stator core, increasing the sticking level between the winding and stator core, adding damping, making the natural frequency of the main structure to deviate from the frequency of the excitation force, especially the resonant frequency of the structure away from the higher order electromagnetic excitation force frequency, so as to achieve the goal of low-noise motor design.

## References

1. Yang X, Liu X (2007) The development trend and foreground of the electric vehicle. *World Inverters* (7):36–40
2. Hwang S-M, Lee H-J (2006) The influence of electromagnetic force upon the noise of an IPM motor used in a compressor. *IEEE Trans Magn* 42(10):3494–3496
3. Finley WR, Hodowanec MM, Holter WG (1999) An analytical approach to solving motor vibration problems. *IEEE Pet Chem Ind Conf* 217–232
4. Pillay P (1999) An investigation into vibration in switched reluctance motors. *IEEE Trans Ind Appl* 35(3):589–596
5. Jover Rodríguez PV, Arkkio A (2008) Air-gap force distribution and vibration pattern of induction motors under dynamic eccentricity. *Electr Eng* 90:209–218
6. Xun W, Arui Qiu (2011) Simulation analysis of electromagnetic noise from squirrel-cage asynchronous motors. *Micromotors* 44(7):15–19
7. Zhu ZQ, Howe D (2000) Influence of design parameters on cogging torque in permanent magnet machines. *IEEE Trans Energy Convers* 15(4):407–412
8. Ishibashi F, Matsushita M (2010) Change of mechanical natural frequencies of induction motor. *IEEE Trans Ind Appl* 46(3):922–927
9. Le Besnerais J, Lanfranchi V (2010) Prediction of audible magnetic noise radiated by adjustable speed drive induction machines. *IEEE Trans Ind Appl* 46(4):1367–1373

# Modular Car Body Design and Optimization by an Implicit Parameterization Technique via SFE CONCEPT

Fabian Duddeck and Hans Zimmer

**Abstract** This paper presents recent developments on implicit parameterization techniques (based on the software SFE CONCEPT) for shape optimization of vehicles in the context of modern modular car body design. Because of the implicit definition of the parameters complemented by the mapping and re-meshing techniques inherent to the software, a flexible and powerful optimization approach can be realized, where the connectivity is maintained, the accuracy of finite element computations assured and the efficiency improved via appropriate definition of design variables and optimization algorithms. This is first demonstrated on component and module level and finally confirmed by a full vehicle problem.

**Keywords** Platform design • Modularity • Implicit parameterization • Shape optimization • SFE CONCEPT

## 1 Introduction

About 10–15 years ago, platform strategies were introduced into the automotive product development processes (PDP), e.g. [1], to enable a wider variability and flexibility of vehicles at a reasonable cost level. To increase further flexibility to

---

F2012-E03-058

---

F. Duddeck (✉)  
Technische Universität München, Munich, Germany  
e-mail: duddeck@bv.tum.de

H. Zimmer  
SFE GmbH, Krumbach, Germany

reduce development time or costs and to meet changing customer demands for higher quality and individuality, the traditional strategy based on a fixed platform with exchangeable “hats” is not appropriate any more. Hence, the concept of “modularity” is now more and more introduced into the PDPs, e.g. [2]. To benefit from the true value of this modularity, a multi-generational perspective considering the real design options for the full vehicle life cycles is required. In 2011, Volkswagen for example started to move the bulk of its volume cars to the MQB architecture (*Modularer Querbaukasten* = Modular Transverse Toolkit). MQB started in 2011 and it is expected that the MQB platform will include all of VW’s volume offerings in the B, C and D classes. In this type of modular concept, components can be exchanged in a flexible manner between the product families to realize scaling effects and reduce drastically development costs.

Special development tools are required to support the development of these modular concepts, for example the Modular Function Deployment (MFD) or the Generic Process for Toolkit Development (GPTD) discussed in [3] for the management of variants and complexity at the BMW Group and its suppliers to reduce the inherent risks of modular product development. In addition, today’s vehicle development process is driven by Computer Aided Engineering (CAE), where the functionalities are assessed by virtual simulations for safety, comfort, etc. The corresponding model development, which is normally based on finite element methods (FEM), is still cumbersome and can take several weeks for a single model. A transfer from package geometry to CAD-based representations (Computer Aided Design) and to the CAE fields is required and often still realized more or less manually. Here advanced virtual methods offer a huge potential for reduction of costs and development time. In particular, so-called parameterized techniques are beneficial because they allow the automated adaptation of the models via the modification of the design parameters to the different variants of vehicles. Combined with a specialized library of pre-designed modules, the PDP can be rendered much more efficient than by traditional approaches. They enable the usage of automated optimization methods to derive the best compromises between all functional requirements.

To realize such a parametric modular development and optimization, there are two main approaches. The first—for example available via the CAD software CATIA V5/6—is based on explicit parameterizations, which allow automated variations only when the dependencies of the different components are defined explicitly by the users. This is in general rather cumbersome due to the complexity of modern car architectures. Hence the technique presented here based on the software SFE CONCEPT with its implicit parameterization approach is much better adapted to the requirements of the new modular vehicle PDP. The dependencies between the parts and modules are defined implicitly and do not require that the users implement them directly. Modifications can be realized easily and automatically. Examples of the new developments for this implicit parameterization approach are presented here focusing on the potential for early concept design. In particular, the recent developments in realizing efficient module development via automated shape optimization are presented.

## 2 Shape Optimization

Recently, the research in optimization shifted from simple size optimization considering the panel thicknesses as design variables, e.g. [4], to more powerful design tasks how to identify the best topology and shape of a car body structure, e.g. [5]. These methods address structural aspects in earlier design stages where the structural concept is not as frozen as at the end of the product development process. To realize a shape optimization, several techniques have been discussed in the literature. A classical approach to modify the shape of a structure is based on so-called morphing techniques, e.g. [6]. For most of these approaches, morphing boxes have to be defined, which can be a rather cumbersome process and demands for expert knowledge to assure a successful optimization. Special morphing parameters or “handles” are used, which are then linked to the changes of the structural shape. This requires a careful selection of the parameters and it is, to the authors’ knowledge, not always possible to obtain the intended alterations of one structural component without unwelcomed “side-effects”. Modifying a box and the related parameters does not give the required freedom in design variables to really obtain optimal shapes. It seems to be more appropriate to use parameters directly linked to the structure like cross-sectional corner points, angles and radii or in three-dimensional parameterizations curvature, joint positions or other connection types of several components. A mesh-based morphing approach is promising here, but there remain two problems, first the assurance of mesh quality for larger geometrical changes and second the maintenance of the connectivity between the parts of the vehicle. The connections (tied, spotwelds, glue etc.) should follow automatically the variations.

## 3 Parameterization Techniques for Shape Optimization

In the literature, there is a high number of different approaches to parameterize geometry for optimization. Often a CAD software is used to define the parameters, e.g. [7]. As an alternative, some CAE tools (Computer Aided Engineering) offer the possibility to use a parametric description for optimization, e.g. ANSYS Parametric Design Language APDL, e.g. [8]. The CAD-CAE integration is today an important aspect to assure smooth transitions and a good simulation data management (SDM) between the different departments involved in car development. Ideally we have a parametric description of the geometry which can be used in both areas.

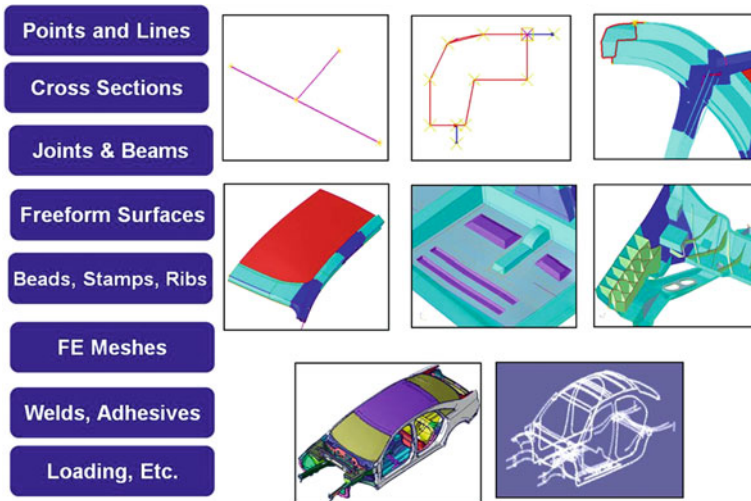
Regarding the publications related to crashworthiness and shape optimization, first works on CAD parameterization were published by Chiandussi et al. [9–12]. Changes in geometry were first realized in a CAD program and then transferred via a boundary surface displacement field to the CAE model. Important in this approach was to maintain the degree of continuity between modified and unmodified

structural areas and to reduce mesh distortion by propagating the geometrical change also to interior nodes of the finite element (FE) mesh. By this approach, they optimized a single component. The changes in geometry were small and the complexity of the parameterization was moderate (e.g. length and smaller diameter of the tapered zone). Both, range of geometrical change and definition of parameters, did not lead to problems with respect to connectivity between parts normally seen in more complex cases. Farkas et al. [13, 14] used explicit parameterization offered by CATIA to establish a CAD-integrated optimization procedure for the bumper. The CAD model was pre-processed (e.g. defeaturing of small geometrical details to avoid small elements and small time steps) and an automated meshing was used. The parameterization was carefully chosen such that the connectivity was not touched, i.e. the issue of adapting adjacent components and joints did not become relevant. This restriction can be overcome by implicit parameterization where the structure or package parameters are defined implicitly, which is discussed in the next section.

## 4 Implicit Parameterization via SFE CONCEPT

SFE CONCEPT (see [www.sfe-berlin.de](http://www.sfe-berlin.de)) uses implicitly parametric geometry models to realize easily shape or topology changes, e.g. [15–19]. From this the FE meshes and models are generated, hence a re-meshing procedure can be included into the optimization process to enable large geometrical changes. This model can then be computed with all important commercial FE solvers for the different functionalities. As shown in Fig. 1, the parametric model consists of Influence Points (IP) defined for Base-Lines (BL) and the corresponding Base-Sections (BS). Together, the beams/members of the structure are hereby declared. The BSs can be derived from the cross-sections of existing vehicle FE models or are defined from scratch. Their shape can be modified via these influence points, changing size, proportions, connection locations, angles etc. More complex shape variations can be realized by using special mapping techniques. The mapping of IPs to other geometrical objects is essential to the implicit parameterization because it defines that certain geometrical features follow the changes of other objects. Hereby it is not necessary that the objects correspond to real parts of the structure. Thus a high flexibility in defining geometrical variation and structural dependencies is obtained. To create more complex structures, joints are automatically generated at the connection points of beams based on the cross-sections of the adjacent members. Additional variability (e.g. tangents at the interfaces) can be introduced. By appropriate definition of IPs and mappings, the connected components follow the changes of each involved part controlled by the optimizer. Free Surfaces (FS) can be included to represent large panels of automotive structures or more complex geometries. Because all connectivities are defined implicitly, the adjacent parts follow the changes during an optimization for one component. This is essential for the success of automated optimization procedures of more complex





**Fig. 1** SFE CONCEPT objects, Zimmer et al. [5]

structures. For all components, joints and (multi-)flanges also follow the geometrical changes. The optimization is finally prepared by defining interactively so-called Parametric Records based on the upper and lower bounds of the shape parameters.

Because the optimization model is defined as a SFE CONCEPT model, it can be used to generate different FE models for various functional assessments (all crash load cases, stiffness, durability, structural dynamics, acoustics, etc.). Large geometrical changes are possible because the FE-mesh is only generated after the shape modification (this can be regarded as re-meshing during the optimization). Hence in contrast to morphing approaches, no critical mesh distortions occur. The re-meshing is challenging for the optimization algorithm because it introduces discontinuities in the objective functions and constraints in cases the results are mesh dependent. For crash optimization this is not really relevant because it is well known that crash simulations are not exactly repeatable (in particular when computed in parallel). Numerical noise due to stability or contact bifurcations and numerical rounding errors also occur in optimizations without re-meshing procedures, see [20].

## 5 Shape Optimization of Components and Modules

### 5.1 Cross-Section Optimizations

Most of the publications on shape optimization for crashworthiness focus on the derivation of optimal cross-sections for single beams. This might be due to the relative simplicity of the parameterization (two-dimensional design problem),

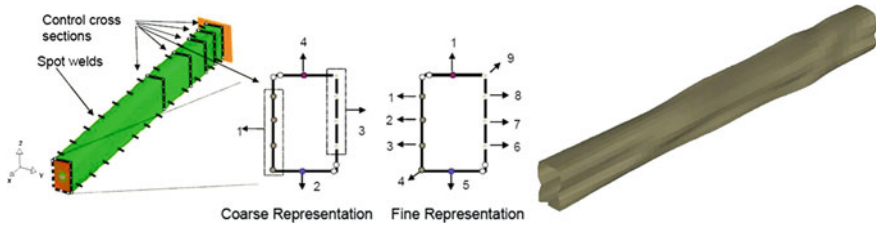


Fig. 2 Example of a cross-section optimization, [26]

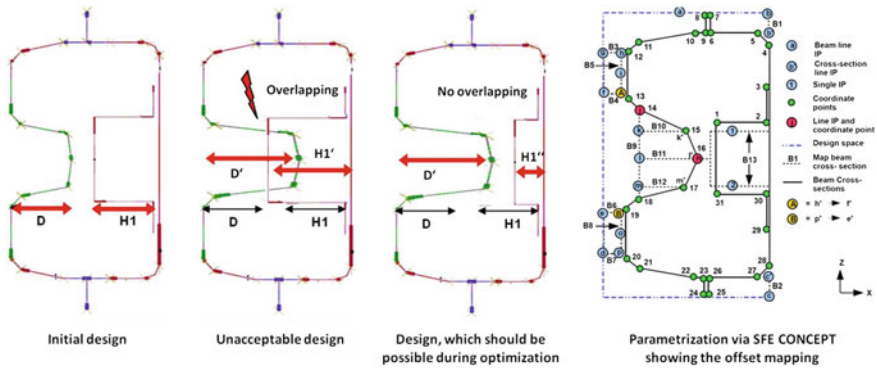
the availability of analytical reference solutions (e.g. [21]) and the possibility of reduced model simulations. Studies have been realized on quasi-static crush or in some cases dynamic crush for a wide range of materials including foam, single/multi-cell and honeycomb structures, e.g. [22–24]. Nevertheless, most of these studies do not address complex shape variables.

Looking more for true shape variations, Zhang et al. [25] present the optimization of an interior reinforcement of a hollow cross-section described by a spline curve and modified via the corresponding control points. Eby et al. [26] define the geometry variation via specific points on the cross-section. Then they use a hierarchic and agent-based optimization scheme where on a coarse level a group of points is changed and on a finer level single points can be moved, see Fig. 2. To avoid conflicts in geometry, the design parameters were all chosen such that the points are moved outward only. Overlapping/crossing during the optimization process of parts of the cross-section is avoided but the design space is restricted.

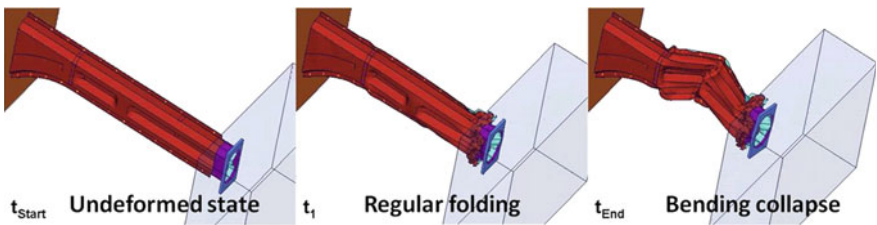
This restriction in design space is often not desirable. To demonstrate this, a bumper optimization was realized, [27, 28], where the geometrical changes were defined with SFE CONCEPT. As shown in Fig. 3, a cross-section for the bumper is chosen with an exterior bead at the front and an interior reinforcement at the back. Here the depth of the exterior bead (variable  $D$ ) should have a large variability, which might clash with the variation of the interior reinforcement characterized by the shape variable  $H1$ . It is relatively difficult to define the upper and lower limits for the design variables when morphing or other mesh-based methods are used. Based on implicit parameterization (SFE CONCEPT), an offset mapping technique is used to avoid implicitly geometrical clashes.

## 5.2 Non-Cross-Section Optimizations

Additionally or alternatively, design variables can be defined in axial direction of the member. Again most of the publications use rather simple design variables; Wu et al. [29] consider beside height and width of an s-rail the angle in the s-bend. Crush initiators were studied for example in [30] and beads were optimized in [31, 32]. Often these studies are realized on component level and not in the context of complete vehicle simulations to reduce computational effort. This approach



**Fig. 3** Demonstration example (bumper) showing geometrical conflicts due to parameter variations (SFE CONCEPT) and offset mapping definition  $B_i, i = 1 \dots 13$ , [27]



**Fig. 4** Optimal front rail behavior with initial local folding followed by planned buckling collapse obtained by shape optimization with SFE CONCEPT, [35]

should be discussed more, because the optimality of the optimized component in the context of the full vehicle is in general not assured. A more accurate approach would use sub-structuring techniques, e.g. [33, 34], where the influence of the part of the car which is not modeled explicitly for optimization is represented by special interface conditions at the cut-lines of the component. To realize optimization in the context of a complete vehicle, Volz [35] addressed shape and thickness optimization of a front rail using design variables for lateral beads and tapering based on the implicit parameterization technique of SFE CONCEPT. In contrast to a large number of publications, e.g. [29], he did not consider a component only where folding at the front can develop freely without constraints from other components (e.g. at the mounting points of the engine), see Fig. 4.

In [35] a shape optimization of the complete frontal part of the vehicle is realized to improve the performance in a high speed crash test. The initial design was obtained by a topology optimization, which is not discussed here, see [35, 36]. In addition to the parameters discussed in the section above further design parameters were defined via SFE CONCEPT as shown in Fig. 5. Using a standard evolutionary algorithm, the mass was reduced by ca. 4 % and the intrusion in total was lowered.

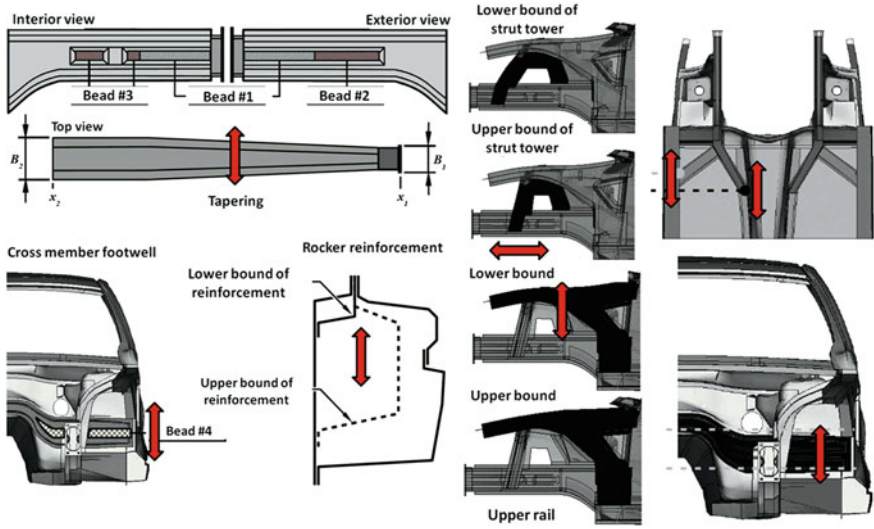


Fig. 5 Design variables for the full car (front) optimization, [35]

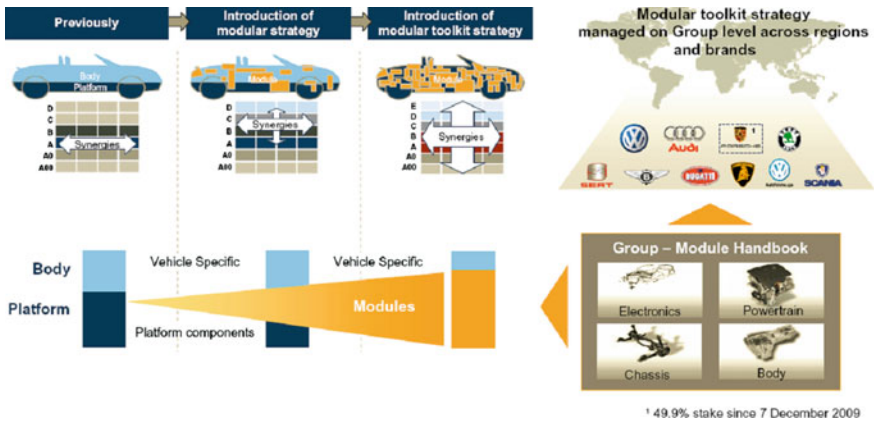


Fig. 6 Volkswagen group's modular toolkit strategy, [37]

## 6 Modular Approach

The technology discussed above based on the implicit parametric modelling by SFE CONCEPT is ideal for realizing modular vehicle concepts which are for example used when a platform concept is chosen. This is one of the dominating current trends in vehicle design as demonstrated for example by Volkswagen in their MQB designs (Fig. 6).

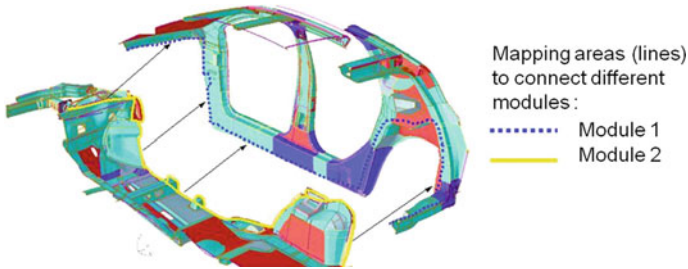


Fig. 7 Example for automatic assembly of different modules by the mapping technology offered by the implicit parametric software SFE CONCEPT, [39]

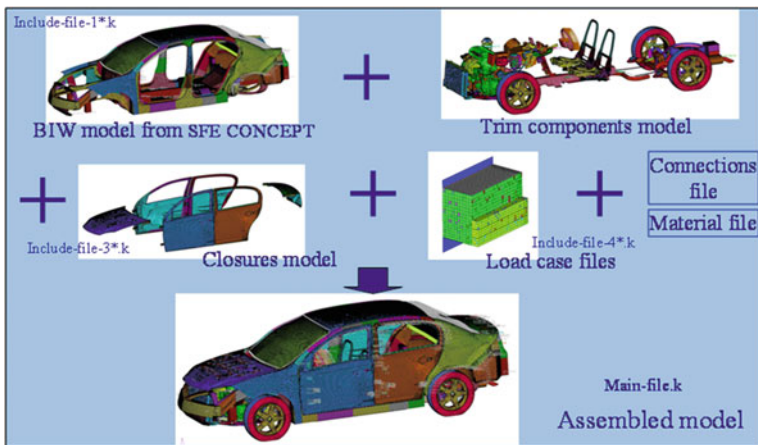


Fig. 8 SFE CONCEPT approach to realize a flexible full vehicle model assembly, [40]

Here, the original modular strategy is extended to a more flexible modular toolkit strategy where synergies among different families can be realized to reduce costs. In [38] a methodology is proposed for uncertainty analysis and optimization of such flexible platform component designs. To facilitate these approaches, the parameterization and automatic geometry generation via SFE CONCEPT offers a special library where modules can be stored and reused easily because they adapt automatically to the changes in geometry.

Due to the maintenance of the connections the different components and/or modules can be varied automatically and all functionalities (crash, NVH etc.) can be assessed either on component basis or on full vehicle simulations because SFE CONCEPT allows that the modules are fitted into the other parts of the virtual models, see Fig. 7. This can be used for car body design but also for full vehicle concepts, as shown in Fig. 8.

## 7 Conclusions

As shown by the examples above on component and full car level, the optimization approach based on implicit parameterization (SFE CONCEPT) is able to derive optimal shapes and topologies for single components, modules or other assemblies. The high flexibility offered by this approach enables the appropriate and efficient definition of design variables (or noise variables in case of robustness analysis). Via mapping techniques the connectivity can be maintained during optimization and via a re-meshing technique with mesh quality control the computational results remain accurate although larger geometrical changes are realized. This methodology is currently not only used in several academic research projects but also exploited in several industrial development projects, e.g. [39, 41, 42]. Especially the new developments for CAD-CAE integration, package optimization, new optimization algorithms (shape and topology) and sub-structuring techniques will enhance future product development. Thus it may help to improve the applicability of shape optimization in industrial context and especially for modular design methodologies.

## References

1. Muffatto M (1999) Introducing a platform strategy in product development. *Int J Prod Econ* 60–61:145–153
2. Ishii F, Yang TG (2003) Modularity: international industry benchmarking and research roadmap. In: Proceedings of DETC/ASME design engineering technical conference and computers and information in engineering conference, Chicago, 2–6 Sept 2003, DFM-48132
3. Renner I (2007) Supporting methods for function oriented modular toolkit development with focus on the automotive industry (in German), PhD thesis, Technische Universität München, Munich
4. Duddeck F (2008) Multidisciplinary optimization of car bodies. *Struct Multidisc Optim* 35(4):375–389
5. Zimmer H, Prabhuaingankar M, Duddeck F (2009) Topology- and geometry-based structure optimization using implicit parametric models and LS-OPT. In: Proceedings 7th European LS-DYNA conference, Salzburg
6. Georgios K, Dimitrios S (2009) Multi-disciplinary design optimization exploiting the efficiency of ANSA-LSOPT-META coupling. In: Proceedings 7th European LS-DYNA conference, Salzburg
7. Dietrich T (2013) PhD thesis, Fachgebiet computational mechanics, Technische Universität München, Munich, to be submitted, 2013
8. Hou S, Li Q, Long S, Yang X, Li W (2007) Design optimization of regular hexagonal thin-walled columns with crashworthiness criteria. *Finite Elem Anal Des* 43:555–565
9. Avalle M, Chiandussi G, Belingardi G (2002) Design optimization by response surface methodology: application to crashworthiness design of vehicle structures. *Struct Multidisc Optim* 24:325–332
10. Chiandussi G, Fontana R, Urbinati F (1998) Design sensitivity analysis method for multidisciplinary shape optimization problems with linear and non-linear response. *Eng Comput* 15:391–417
11. Chiandussi G, Bugada G, Onate E (2000) Shape variable definition with C0, C1 and C2 continuity functions. *Comput Meth Appl Mech Eng* 188(4):727–742

12. Chiandussi G, Avalle M (2002) Maximisation of the crushing performance of a tubular device by shape optimisation. *Comput Struct* 80:2425–2432
13. Farkas L, Canadas C, Donders S, van Langenhove T, Tzannetakis N (2009) Optimization study of a parametric vehicle bumper subsystem under multiple load cases using LMS Virtual. Lab and OPTIMUS. In: *Proceedings 7th European LS-DYNA conference*, Salzburg
14. Farkas L, Donders S, Schildermans D, Moens D, Vandepitte D (2010) Optimisation study of a vehicle bumper subsystem with fuzzy parameters. In: *Proceedings ISMA: international conference on noise and vibration engineering*, Leuven
15. Heiserer D, Zimmer H (2004) Shape optimization in the early phase of car body development (in German). In: *Proceedings VDI Conf on numerical analysis and simulation for vehicle engineering*, Würzburg
16. Hilmann J, Paas M, Hänschke A, Vietor T (2007) Automatic concept model generation for optimisation and robust design of passenger cars. *Adv Eng Softw* 38:795–801
17. Hilmann J (2009) On the development of a process chain for structural optimization in vehicle passive safety. PhD thesis, Technische Universität Berlin, Berlin
18. Hilmann J, Scalera S, Arlt A (2011) Correlation of simulation models using concept modeling. In: *Proceedings European hyperworks technical conference*
19. Meyer O, Krumenaker T, Bernhard R, Dreses C, Schelkle E, Hänschke A, Pohl T, Hillebrand A, Zimmer H (2010) Parametrischer Bauraum-synchronisierter Fahrzeugentwurf. In: *Proceedings SIMVEC*, Baden Baden
20. Duddeck F (2007) Survey on robust design and optimisation for crashworthiness. In: Duddeck F, Bletzinger K-U, Bucher C, Matthies H, Meyer M (eds) *Proceedings EUROMECH colloquium 482 efficient methods for robust design and optimisation*, Queen Mary University of London, London
21. Lu G, Yu T (2003) *Energy absorption of structures and materials*. Woodhead Publ Ltd, Cambridge
22. Kim H-S, Chen W, Wierzbicki T (2002) Weight and crash optimization of foam-filled three-dimensional S-frame. *Comput Mech* 28:417–424
23. Yin H, Wena G, Hou S, Chen K (2011) Crushing analysis and multiobjective crashworthiness optimization of honeycomb-filled single and bitubular polygonal tubes. *Mater Des* 32: 4449–4460
24. Zarei H, Kröger M (2008) Optimum honeycomb filled crash absorber design. *Mater Des* 29:193–204
25. Zhang Z, Liu S, Tang Z (2009) Design optimization of cross-sectional configuration of rib-reinforced thin-walled beam. *Thin-Walled Struct* 47:868–878
26. Eby DJ, Averill RC, Goodman ED, Sidhua RS (2002) Shape optimization of crashworthy structures. *Proceedings 7th international LS-DYNA users conference*
27. Rayamajhi M, Duddeck F, Hunkeler S (2010) Shape optimisation of vehicle frontal structure using evolutionary algorithm. In: Duddeck F, Querin OM, Siens J, Toropov VV, Shaheed MH (eds) *Proceedings 8th ASMO UK/ISSMO conference on engineering design optimization, product and process improvement*, Queen Mary University of London, London, July 2010
28. Rayamajhi M (2013) PhD thesis, Queen Mary University of London, UK, to be submitted 2013
29. Wu H, Xin Y (2009) Optimal design of the S-Rail for crashworthiness analysis IEEE. In: *Proceedings international joint conference on computational sciences and optimization*
30. Wang H, Müllerschön H, Mehrens T (2005) Shape optimization of a crashbox using hyperMorph and LS-OPT. In: *Proceedings 4th German LS-DYNA forum*, Bamberg
31. Cho Y-B, Bae C-H, Suh M-W, Sin H-C (2006) A vehicle front frame crash design optimization using hole-type and dent-type crush initiator. *Thin-walled Struct* 44:415–428
32. Redhe M, Nilsson L, Bergman F, Stander N (2005) Shape optimization of a vehicle Crash-box using LS-OPT. In: *Proceedings 5th European LS-DYNA users conference*, 5a-27
33. Averill RC (2004) Efficient shape optimization of crashworthy structures using a new substructuring method. *3rd LS-DYNA users forum*, Bamberg

34. Chase N, Sidhu R, Averill RC (2012) A new method for efficient global optimization of large systems using sub-models: HEEDS COMPOSE demonstrated on a crash optimization problem. LS-DYNA user forum
35. Volz K (2011) Physikalisch begründete Ersatzmodelle für die Craschoptimierung von Karosseriestrukturen in frühen Projektphasen. PhD thesis, FG computational mechanics, Technische Universität München, Munich
36. Duddeck F, Volz K (2012) A new topology optimization approach for crashworthiness of passenger vehicles based on physically defined equivalent static loads. In: Proceedings ICRASH conference, Milano
37. Volkswagen (2010) Annual media conference
38. Suh ES, de Weck O, Yong Kim I, Chang D (2007) Flexible platform component design under uncertainty. *J Intell Manuf* 18:115–126
39. Hänschke A, Zhou S, Lee M, Hilmann J, Kaba E, Prabhuwaingankar M (2007) Parametric model knowledgebase for vehicle design to improve the early vehicle attribute assessments. In: Proceedings international automotive body congress (IABC), Berlin
40. Xu S (2007) Use of topology design exploration and parametric shape optimization process to development highly efficient and lightweight vehicle body structure. In: Proceedings international automotive body congress (IABC), Berlin
41. Volz K, Dirschmid F, Duddeck F (2006) Body-in-white crash optimization in the early phase of product development. In: Proceedings VDI conference on numerical analysis and simulation in vehicle engineering, Würzburg
42. Volz K, Frodl B, Zimmer H (2007) Optimizing topology and shape for crashworthiness in vehicle product development. In: Proceedings international automotive body congress (IABC), Berlin



# A New Approach for Vibro-Acoustic Optimization Using Discrete and Continuous Shape Variables Applied to a Car Body

Hans Zimmer, Arnold Gross-Thebing, Manohar Prabhu  
and Fabian Duddeck

**Abstract** The vehicle development process demands quick evaluation of new designs. CAE and CAD tools are essential in order to perform these assessments in a very narrow time frame. New design variants with desired criteria should be quickly created and analyzed. Geometry based topology and shape optimization can accelerate such a process when changes in body structure are automatically updated. FE mesh generation during topology and shape optimization runs should not require any kind of user intervention. The above mentioned requirements are fulfilled by *SFE CONCEPT<sup>TM</sup>*. This paper describes the feasibility of a vehicle development process where geometry modifications lead to a reduction for the interior noise of a full-trimmed car body model. In order to demonstrate this, a vibro-acoustic optimization is carried out for types of bead patterns in the BIW.

**Keywords** Acoustics · Optimization · Parametric design · Bead pattern · Discrete design variables

---

F2012-E03-059

---

H. Zimmer (✉) · A. Gross-Thebing · M. Prabhu  
SFE GmbH, Voltastrasse 5, Berlin, Germany  
e-mail: h.zimmer@sfe-berlin.de

F. Duddeck  
Technische Universität München, Arcisstrasse 21, Munich, Germany

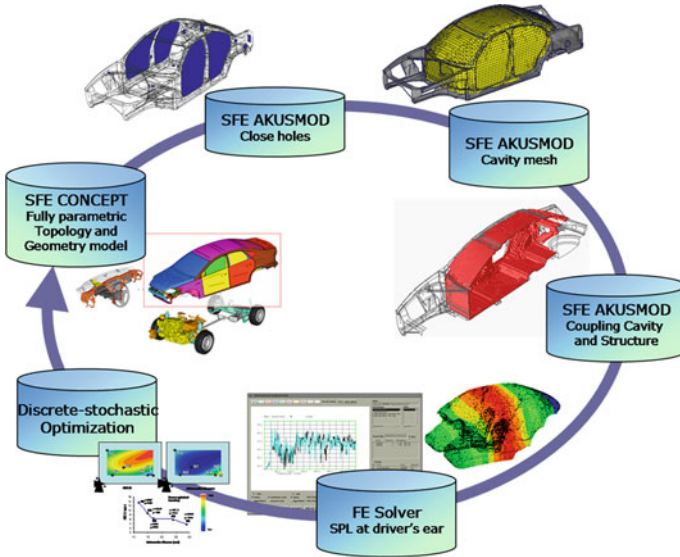


Fig. 1 Vibro-acoustic optimization

## 1 Introduction

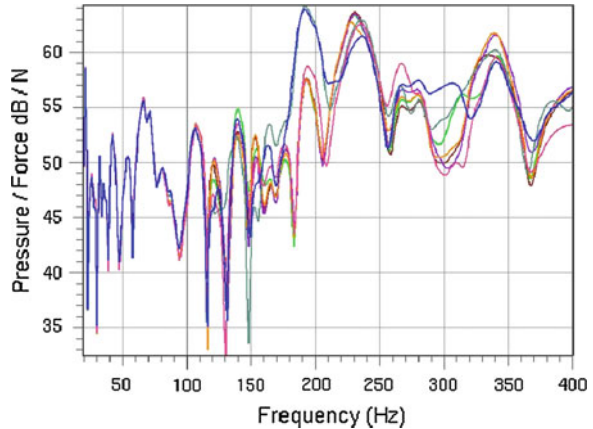
In the car body structure development process *SFE CONCEPT<sup>TM</sup>* [1–7] has become an efficient tool to accelerate the workflow. Figure 1 presents a process for a vibro-acoustic optimization of a full-trimmed car body, including an implicitly parameterized geometry generation using *SFE CONCEPT<sup>TM</sup>* [8], an acoustic analysis using *SFE AKUSMOD* [9, 10] and a new discrete-stochastic implemented optimization algorithm. [7].

Based on the design variable definition on implicitly parameterized geometry model the optimization algorithm modifies the topology and shape using standard ASCII interfaces in *SFE CONCEPT<sup>TM</sup>*. These interfaces include two different kinds of design variables. The first group of design variables are discrete ones like topology changes. The second group are continuous design variables used in well known shape optimization. The parametrical structure allows an automatic consideration of both types in an optimization loop.

After modifying the geometry, the FE-representation of the car body structure is generated. The FE mesh includes all connector elements such as spot welds, laser seams and adhesives. During the optimization loop FE meshes with connections like welds and adhesives and fulfilling the solver quality criteria are generated by a built-in finite element mesh generator in *SFE CONCEPT<sup>TM</sup>*.

*SFE AKUSMOD* provides the data files for an execution of the vibro-acoustic analysis. The steps are closing the holes, generation of the cavity mesh and coupling the cavity mesh and the structure.

**Fig. 2** Two high peaks in frequency responses at driver's ear



The FE-solver calculates the Sound Pressure Level (SPL) at driver's ear for the objective function for the optimization method and a new value set of design variables is generated. Iterations involving automated geometry update, FE (structure) mesh generation, cavity mesh generation, coupling and analysis are done in a batch loop until the optimization criteria for objective and constraints are fulfilled.

## 2 Problem Identification

For a new car development a vibro-acoustic analysis is done in order to reduce the SPL at driver's ear. Particularly a reduction is required for two high peaks excited by one critical load case (Fig. 2).

The part of the structure responsible for the peaks was identified at the lower dash region (Figs. 3 and 4). The narrow distance between excitation point and the lower dash leads to a vibration dynamics characterized by enforced motion. The dynamic load is directly transferred to the lower dash via the relatively inflexible longitudinal rail. Changing the connection of the lower dash to the longitudinal rail or the dynamic stiffness of the dash has a relevant impact on the resonances of frequency response.

In former investigations parameters of the structure were changed manually. The results showed that a reduction is achieved either for the resonance at first peak frequency or for the second peak frequency. It was very difficult to get an improvement good for both resonances. A manual trial and error approach was too time consuming and didn't lead to a good design solution for the frequency range of interest. This required a smart optimization procedure to try out wide range of design parameters and find the rare combination of these parameters in an automated process which leads to the desired reduction in both resonances.

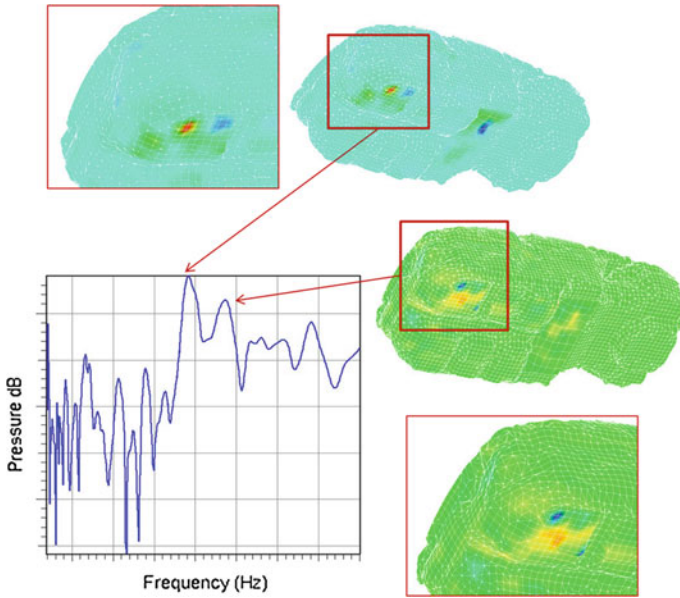


Fig. 3 Section of interest

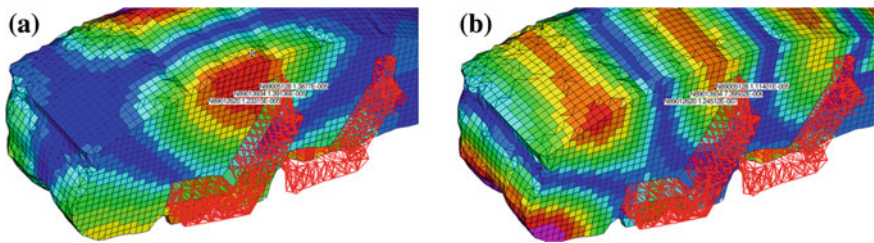


Fig. 4 Dominant fluid modes for the resonances at first peak (a) and second peak (b)

Preferred modifications were the type and location of bead patterns in the lower dash region. Considering the phase of vehicle development and cost involved these were the only allowable changes. A very new and unique approach described below was taken to solve the issue.

Due to higher computation time for the vibro-acoustic analysis the use of full trimmed car body model in the optimization loop is not desirable. The reduced model considers the excitation mechanism. While an influence of the other structure parts cannot be excluded the full trimmed model is used to validate promising results of the optimization.

### 3 Automated Generation of Structure Models

The original bead patterns are removed from the regions of interest and are replaced by the new bead patterns automatically. The model for the vibro-acoustic analysis is divided in a substructure (implicitly parameterized *SFE CONCEPT<sup>TM</sup>* model) providing the geometrical modifications and a substructure (carryover FE-mesh) unchanged during the optimization procedure. The geometry model is controlled by implicit geometrical parameters and is a FE-mesh with all bead patterns for the vibro-acoustic analysis is automatically generated. All this is done while maintaining and redefining connections (wherever necessary) between the FE-meshes of dash model and the carryover substructure. This is a fully automated procedure in *SFE CONCEPT<sup>TM</sup>*.

### 4 Vibro-Acoustic Analysis

*SFE CONCEPT<sup>TM</sup>* deals with parametric modifications of the structure part in the vibro-acoustic analysis. Besides the structure FE-mesh for the analysis in addition a cavity mesh is also required. An automated generation of such a cavity mesh is done by *SFE AKUSMOD*. While generating the cavity mesh cut outs are automatically closed and a fixed microphone position is considered.

In this investigation the volume mesh for the cavity including volume absorber for the seats is unchanged during optimization procedure. The participation features of *SFE AKUSMOD* identify important structure and fluid modes as well as dominating structure parts (panel or grid based). Figure 4 shows the fluid modes dominating the transfer function from excitation to SPL at driver's ear. These modes are characterized by high amplitudes simultaneous at driver's ear and in the lower dash region.

The cavity mesh needs to be coupled to the structure mesh. During optimization the cavity structure coupling needs to be done automatically for each geometric change in structure. For the calculation of the SPL at driver's ear the coupling is transferred via binary data file to the NASTRAN solver. *SFE AKUSMOD* provides the cavity and coupling data file in batch mode.

### 5 Optimization Procedure

Figure 5 shows the flowchart for the vibro-acoustic optimization. The procedure is driven by a integrated-function and combines the automated generation of structure model and the vibro-acoustic analysis. The FE-mesh of the lower dash for a given set of design variables is created by *SFE CONCEPT*. The auto-generated

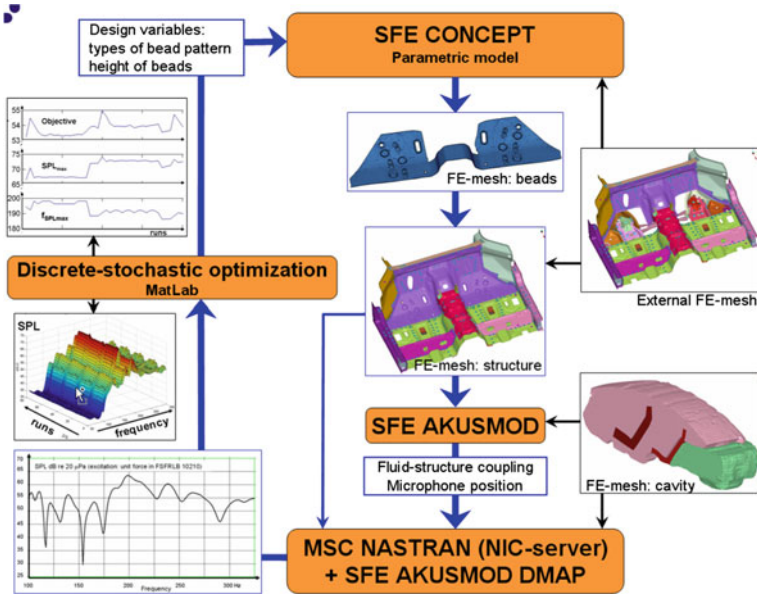


Fig. 5 Vibro-acoustic optimization loop

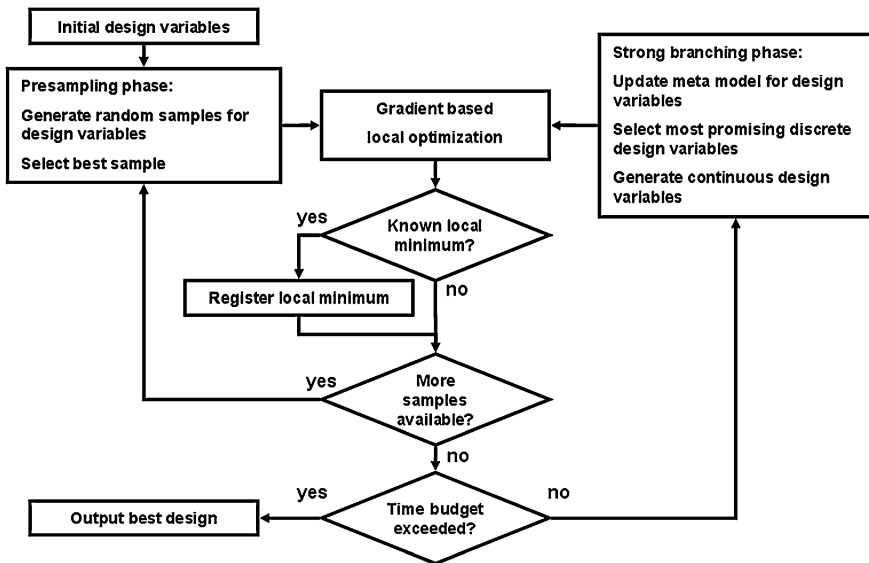


Fig. 6 Flow chart of discrete-stochastic optimization [7]

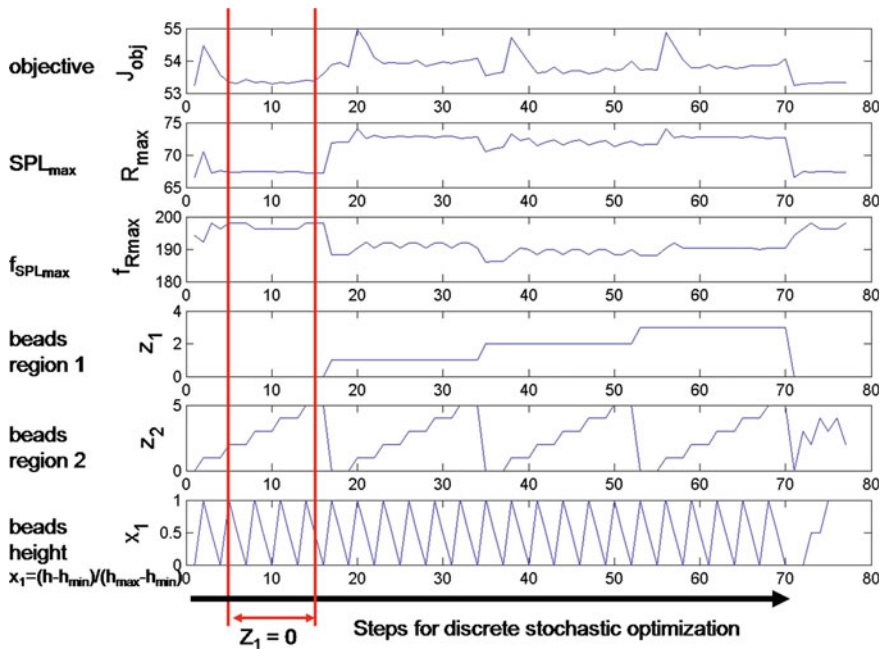


Fig. 7 History: objective, types of bead pattern in region 1 and 2 and bead height

FE-mesh and the constant part of the structure are combined to the structure model. Considering the external volume mesh for the cavity SFE AKUSMOD provides the fluid–structure definition for the FE-analysis. The FE-analysis calculates the frequency responses of the SPL at driver’s ear and provides these responses to the objective function of the optimization algorithm. In order to assess the optimization results in the user-defined frequency range frequency responses are stored for all optimization steps.

An overview of the optimization algorithm [7] is given in Fig. 6. The algorithm consists of a presampling and a strong branching phase. The presampling phase maintains a user-defined number of samples for the design variables. The algorithm evaluates the samples and starts from the best one a local, gradient-based optimization using a sequential nonlinear programming method with trust region globalization. After the provided samples are exhausted, new ones are created essentially randomly.

For the strong branching phase a meta model of the discrete designs is constructed. Based on the model, the discrete design with largest expected improvement is selected for starting the next local optimization, whereby the values for the continuous design are generated randomly.



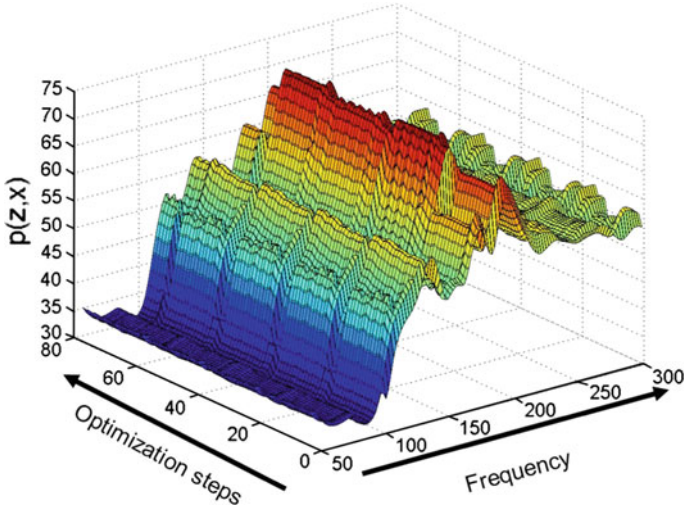


Fig. 8 History: frequency responses of sound pressure at driver’s ear

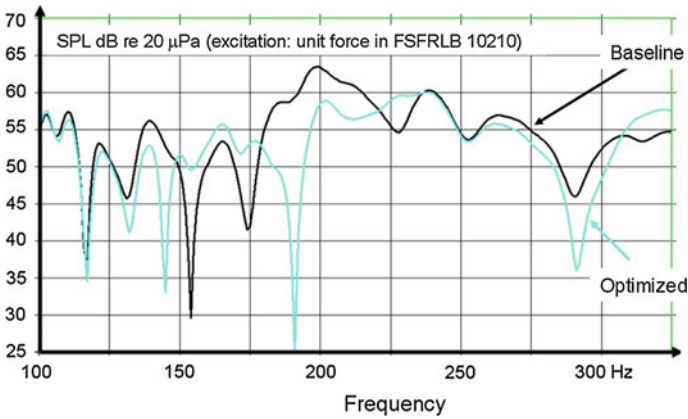


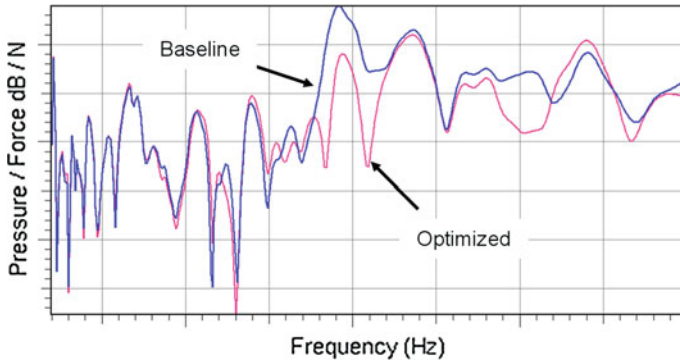
Fig. 9 SPL for bead patterns from base line model and from optimization results validation using the full-trimmed body model

## 6 Design Model and Optimization Results

The design model consists of discrete and continuous design variables. The design variables are provided by *SFE CONCEPT<sup>TM</sup>* and described in Sect. 4.

Figure 7 shows the history of the objective, the maximum of SPL, the frequency for the maximum, and the discrete and continuous design variables. As a first step the optimization starts a DOE regarding a full-factorial design with many variants. The marked section in the history shows the section without beads in





**Fig. 10** Numerical validation results using the full-trimmed model

region 1. Obviously a noise reduction can be stated in this area. The minimum for this optimization is the reference state without beads.

In order to control the vibro-acoustic analysis for every optimization step the frequency response is shown in Fig. 8. The main influence on the frequency responses is given by changing the discrete design variables. Figure 9 compares the frequency response of SPL at driver's ear for the reference model with a model without beads in region 1. The optimization results can be summarized in the following statements:

- SPL is influenced by type and location of bead patterns,
- smaller independent beads tend to yield better results,
- in this particular case and in the frequency range of interest no beads in region 1 results in a lower SPL.

The numerical validation was done using the full trim body model and sub-structures shown in Fig. 10.

## 7 Conclusions

In this paper a new optimization procedure has been presented that enables the improvement of the vibro-acoustic behavior of body structures efficiently. With the use of *SFE CONCEPT<sup>TM</sup>* it is possible to generate a realistic representation of a structure using implicitly parameterized geometry for the vibro-acoustic simulation. The essential structural elements such as beads and spot welds could be considered without user action in the optimization loop.

The new discrete-stochastic optimization algorithm promises to reduce the expense of a vibro-acoustic optimization significantly because discrete design variables are directly integrated in the design model.

In this particular case the achievement was not only to lower the two critical peaks at desired frequencies but also to maintain the SPL below a certain level over the entire frequency range of interest.

A combination of powerful toolset *SFE CONCEPT<sup>TM</sup>*, *SFE AKUSMOD* and a discrete continuous optimization technique was used to solve vibro-acoustic problems on localized areas and results are scalable on a global scale.

## References

1. Zimmer H, Prabhuwaingankar M (2005) Implicitly parametric crash-und NVH-analysis models in the vehicle concept design phase; LSDYNA. User conference, Bamberg, Germany
2. Volz K, Duddeck F (2005) Crash optimization of bodies in the concept stage of vehicle development. In: Proceedings of the third M.I.T. Conference on computational fluid and solid mechanics, Cambridge, MA
3. Duddeck F, Volz K (2005) Evaluation of optimization algorithms for crash and NVH. In: Proceedings of the third M.I.T. Conference on computational fluid and solid mechanics, Cambridge, MA
4. Zhou S, Lee M, Cai H, Shahidi B (2006) Upfront body structure development process using parametric concept modeling. In: Proceeding of international auto body congress (IABC), Novi, 19–21 Sept 2006
5. Stuhec U, Zhou S, Shahidi B, Zimmer H, Prabhuwaingankar M (2005) CAE concept design: a key enabler in virtual product development, human-computer interaction international 2005, Las Vegas, 22–27 July 2005
6. Zhou S, Senn G, Nguyen C, Stuhec U (2004) A new technology of SFE concept model to drive upfront body structure design for better NVH performance, 2004 ford global noise and vibration conference, Dearborn, 17–19 May 2004
7. Weiser M (2010) Discrete-stochastic optimization, technical report, SFE GmbH Berlin
8. SFE GmbH (2010) SFE concept reference manual
9. SFE GmbH (2004) SFE AKUSMOD reference manual
10. Zimmer H, Hövelmann A (1993) Practical applications of acoustical calculations with SFE AKUSMOD and MSC/NASTRAN. In: Proceedings of the 20th MSC European users conference Vienna

**Part IV**  
**Advanced Chassis, Body Structure**  
**and Design**

# Integrated Architectures for Third Generation Electric Vehicles: Technical Challenges Meeting Customer Requirements

Micha Lesemann, Leif Ickert, Lutz Eckstein, Sven Faßbender,  
Michael Funcke and Jac Wismans

**Abstract** In order to fully exploit new freedom in design and to achieve a significant increase of energy efficiency, the third generation of electric vehicles requires dedicated architectures. The consortium of the joint research project ELVA—Advanced Electric Vehicle Architectures is developing until mid-2013 three detailed vehicle concepts which are intended to not only meet all technical requirements, but especially take customer preferences directly into account. ELVA can be regarded as one of the first European joint projects dealing with the investigation of vehicle architectures for fully electric vehicles. Aiming at series adoption in 2020, a comprehensive forecast of technology options and market requirements has stood at the beginning. This includes particularly the in-depth analysis of customer requirements. They are investigated based on studies and OEM-internal information, but also on a large-scale public customer survey. In the second phase, these requirements need to be brought in line with technology options by innovative architectures focussing on urban electric vehicles. To complement the expertise within the consortium a public design contest is drawn, allowing designers to present their ideas for future urban mobility. Based on an assessment of all ideas and options, three dedicated vehicle concepts are developed in detail, enabling optimisation and assessment of all relevant vehicle features. Technology options (e.g. batteries and electric motors) and customer expectations are still difficult to predict. On the

---

F2012-E04-001

---

M. Lesemann (✉) · L. Ickert · L. Eckstein  
Forschungsgesellschaft Kraftfahrwesen mbH Aachen (fka), Aachen, Germany  
e-mail: lesemann@fka.de

L. Eckstein · S. Faßbender · M. Funcke  
Institute for Automotive Engineering (ika), RWTH Aachen University, Aachen, Germany

J. Wismans  
SAFER/Chalmers University of Technology, Gothenburg, Sweden

technology side, substantial improvements especially regarding battery capacity, size and weight are expected. Customer requirements however are very much linked to the use-cases current conventional cars are offering, especially when it comes to the desired range. This has a clear impact on future electric vehicles, but cannot be fully predicted yet. ELVA is the first European project which is dedicated to specific vehicle architectures for urban electric vehicles. Especially the incorporation of customer requirements based on a pan-European survey and the public design competition must be emphasized in this context. The ELVA project brings together technical excellence and customer requirements in order to develop the most promising architectures for urban electric vehicles.

**Keywords** Electric vehicle · Architecture · Design · Lightweight · Urban commuting

Only dedicated architectures allow the full exploitation of new design freedoms and the achievement of a significant increase of energy efficiency. This must be the objective for the third generation of electric vehicles (EVs). The consortium of the joint European research project ELVA is currently developing three detailed vehicle concepts which are intended to not only meet all technical requirements, but especially take customer preferences directly into account.

A comprehensive forecast of technology options and market requirements was carried out in the first phase of the project. This included particularly the in-depth analysis of customer requirements which are investigated based on studies and OEM-internal information, but also on a large-scale public customer survey. In the second phase, these requirements are brought in line with technology options by innovative architectures focussing on urban EVs.

To complement the expertise within the consortium a public design contest was organised, allowing designers to present their ideas for future urban mobility. Based on an assessment of all ideas and options, three dedicated vehicle concepts are now being developed in detail, enabling optimisation and assessment of all relevant vehicle features (Fig. 1).

However, technology options (e.g. batteries and electric motors) and customer expectations remain difficult to forecast. On the technology side, substantial improvements especially regarding battery capacity, size and weight are expected. Customer requirements are very much linked to the use-cases current conventional cars are offering, especially when it comes to the desired range. This has a clear impact on future electric vehicles, but cannot be fully predicted yet.

## 1 Customer Requirements

The market success of electric vehicles is largely influenced by the acceptance of customers. However, the behaviour of customers in 2020 and beyond, i.e. the potential SOP of vehicles based on ELVA ideas is difficult to predict. This concerns all stakeholders and is of particular importance for the OEMs.

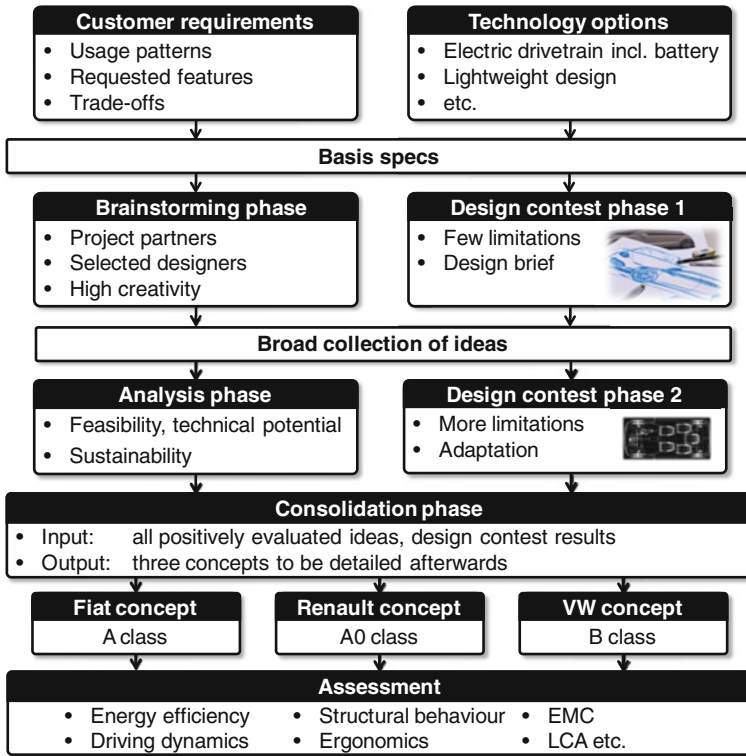


Fig. 1 ELVA approach

In order to define a future vehicle, it is hence essential to project the future vehicle market. Possible changes in customer behaviour and customer requirements need to be taken into account as well as environmental and societal changes. Accordingly, numerous studies have been performed with the intention to generate a market forecast for electric vehicles. Besides the analysis of these studies within ELVA a dedicated customer survey is performed.

### 1.1 Review of Studies

As a first step towards an appropriate conclusion for the targeted market about 20 selected publications regarding the future of mobility are analysed. The publications consider automotive mobility in particular as well as mobility in general. Current and future developments in environment, society and resources are the foundation for most of the predictions. Respondents to customer surveys are also taken into consideration.

The research identifies four major topics: current mega trends, mobility specific requirements, vehicle specific requirements and vehicle buying criteria. Mega

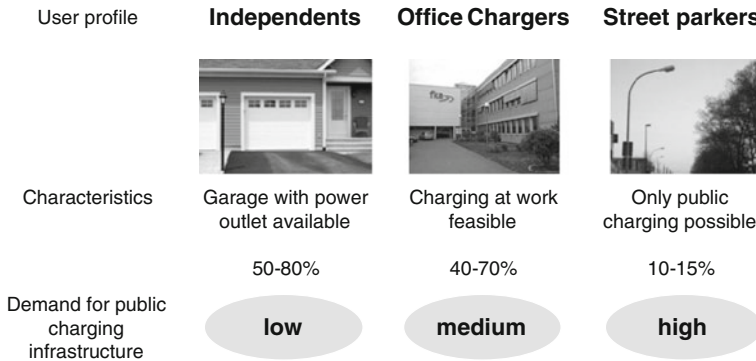


Fig. 2 Public charging infrastructure demand [12]

trends in transport are presented in several publications [1–3]. Mobility and vehicle specific requirements are derived from these mega trends.

The mega trends are not EV specific, but rather are valid for the entire future of (personal) transport. The same applies for customer patterns such as changes in mobility models [4] or the decreasing commitment of customers for a specific model or brand [3]. The influences of rising energy cost and the ageing society are discussed for several years already and have a likewise influence on all future vehicles [5].

More vehicle specific are maintaining expectations for high safety standards and reliability. An increase in connectivity seems to be obvious, what might include communication between cars or cars to infrastructure [6].

Several studies have investigated user expectations for EVs. In general, customers show an interest in purchasing EVs. However, the accepted extra that buyers are willing to pay is as low as 10 % for the majority [7].

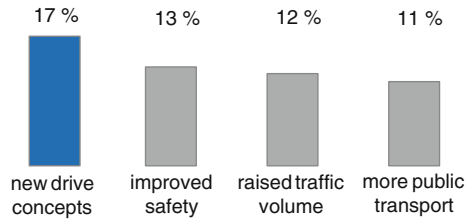
Another major aspect is the significantly different process for recharging the batteries compared to conventional refuelling. Here, studies show a large difference depending on the type of user. Figure 2 sums up three different user types and their demand for public charging infrastructure.

The most widely discussed aspect of fully EVs is their autonomous driving range. Especially the difference between actual daily ranges (5–70 km) [8] and the expected offered range of the vehicle (>300 km) [9] differ widely. This has a large influence on the vehicle concept definition and the battery as the most expensive component.

## 1.2 Customer Survey

In parallel to the above described analysis of studies, a public customer survey is performed from April to June 2011. The goal is to receive direct input for the concept definition. Therefore, general questions about mobility are posed, but also very specific ones regarding acceptance of and requirements for electric vehicles.

**Fig. 3** Expected change



The majority of answers are received via the project’s website on which three different language versions of the questionnaire are available. Paper questionnaires are furthermore used in some European cities.

In total, about 1,100 persons answered the questionnaire. However the results cannot be regarded as representative as for instance about 88 % of the respondents are male, and 78 % hold a university degree. Nevertheless the replies of this selection of the population show that there is only little willingness for compromises e.g. in the autonomous range, the number of seats in the car or cost extra. This particular holds for the first car of the person/family.

Uncompromised as well is the importance of a car for life with an average value of 4.7 on a scale from 1—not important to 6—important. Personal mobility remains a major demand and offers potential for EVs e.g. in densely populated areas such as mega cities.

When asking about expected changes with regard to mobility and transport, a slight majority expects new drive concepts to be introduced (Fig. 3). It is however unclear if this expectation is a neutral customer expectation or already influenced by the promotion of such new concepts (like hybrid and fully electric vehicles) over the past years.

The same holds true when asking about advantages and disadvantages of EVs. These questions are posed open, i.e. without suggesting specific replies. The replies are nevertheless very similar and represent the topics which are widely discussed also in the general public. Figure 4 shows the clouds of given answers to these questions.

For the participants of the survey the average car size is a mid-size car, and is thus in line with the number of 4–5 seats that are expected. As stated in the previous chapter, this is a major deviation from actual car occupancy rates. Also the expected range of the main car of the person/family is with 400 km or more way above what current battery technology reasonably offers today and potentially in 2020 and beyond. This is closely related to the question of recharging. Here, two different scenarios can be interpreted from the replies. About one third of the user group expects a charging time of not more than 30 min. Half of the users would also be accepting charging times of 2–5 h. Currently presented concepts with quick charges (e.g. up to 80 % state of charge) and over-night charges seem to be addressing these expectations fairly well.

With the current limitations given by battery, but also the electric drive train technology, it is of special interest what compromises the customer would accept.



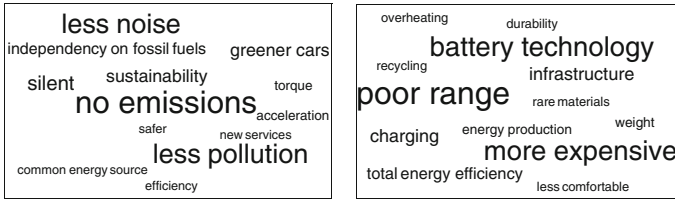


Fig. 4 Expected advantages (left) and disadvantages (right) of electric vehicles

Fig. 5 Trade-offs

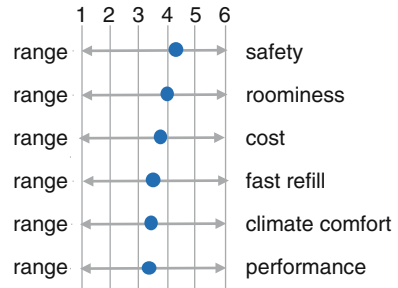


Figure 5 gives an example of trade-offs between range and some key features of the vehicle. There is limited willingness to compromise the autonomous range with safety, interior space or cost. For climate comfort and performance, certain compromises seem to be possible.

For cost, the replies to the ELVA customer survey support the outcome of the study research that was described in the previous chapter. More than 50 % of customers would be accepting no to maximum 10 % additional cost. The average value of accepted additional cost is 163 €.

## 2 Conclusions

In general, customers expect electric vehicles to provide the same values as conventional cars these days. This concerns the transport function as such including the autonomous range, number of seats and space for luggage. In addition it is expected that electric cars are more efficient, more quiet and easier to handle. Requirements such as safety and comfort cannot be compromised at all or only to a little extent. Study results, OEM-internal information and the ELVA customer survey all confirm these trends.

It is still very difficult to predict in how far aspects such as use cases, business case or intermodality in transport will be changing over time. Within the horizon of the ELVA project, these changes may be rather small, but are at the same time depending very much on external factors such as political decisions. One of the

often cited examples is limitations for entering urban environments with vehicles that produce local emissions (e.g. congestion charge in London). This is in line with studies about EV customer expectations that were published after the conclusion of the ELVA market forecast [10, 11].

The autonomous range of the vehicle is the most influencing factor in terms of concept definition. It affects the size of the battery being the most expensive single component that needs to be integrated in the vehicle. The range which is expected by the customer and the actual daily range which is driven in reality differ widely. As a consequence, different concepts may be developed in the later stage of the project offering significantly different autonomous ranges.

As for all vehicles it can be stated that only when the requirements and expectations of the customer are met in most, if not all cases, the model can be a success. The sales price of the electric vehicle may be slightly higher compared to a conventional car. The EV must then however offer a clear benefit for the customer by reduced usage cost or other advantages such as inner city access. The most important buying criteria can be summed up to fuel-efficiency, eco-friendliness, safety, cost effectiveness and driving experience.

### 3 Concept Development

Taking into account the customer requirements, but also other boundary conditions such as the availability of components and feasibility of technical solutions, the ELVA partners have agreed on the following basic specifications that need to be fulfilled by all concepts:

- Use case: urban/commute
- Seats: 2+2
- Max. range: 200 km (125 miles)
- $v_{\max}$ : 110 km/h (70 mph)
- Weight: 800...1,000 kg (1,800...2,200 lbs)
- SOP: 2020

While the architecture is a core activity driven by the concept leaders Fiat (CRF), Renault and Volkswagen, the exterior design was drawn as a contest for design students, free lancers and other interested persons. They were given only some basic requirements in the beginning (four wheels, room for 4–5 passengers, urban/commute usage and a defined battery volume). This resulted in almost 40 mostly high quality design proposals being submitted to the jury consisting of design and engineering experts.

Out of the proposals, the jury selected six designs for proceeding to stage two. Therefore, the designers had to incorporate a given basic package and adapt their design accordingly. After another jury vote, the winner and two runner-up designs were awarded (Fig. 6):



Fig. 6 Design contest winners

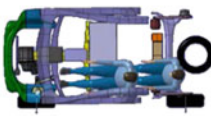

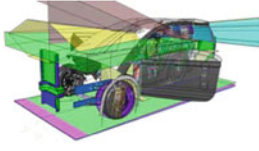
Fiat concept	Renault concept	VW concept
 <ul style="list-style-type: none"> <li>• A-segment car</li> <li>• Modular electric powertrain for shorter and longer range</li> <li>• Two identical batteries</li> <li>• Four-wheel drive</li> <li>• Central motors w/ gearbox</li> <li>• Short turning circle</li> <li>• High metal application</li> </ul>	 <ul style="list-style-type: none"> <li>• Affordable lightweight car</li> <li>• Target weight: 800 kg</li> <li>• No expensive materials</li> <li>• Easy to manoeuvre</li> <li>• 3+1 seats</li> <li>• Rear-wheel drive</li> <li>• Batteries under floor</li> </ul>	 <ul style="list-style-type: none"> <li>• Two propulsion options (2WD/4WD)</li> <li>• Potential platform for SUV and roadster</li> <li>• Mono volume</li> <li>• "Polo plus"</li> <li>• Steer by wire</li> <li>• Progressive material mix</li> </ul>

Fig. 7 Concept characteristics

Started in parallel to the design contest, the architectures of the three concepts are developed. This process is driven by the three concept leaders, who are responsible for the overall development. They are supported by the other partners that are responsible for dimensioning and development of the electric drive train, the chassis, the body structure and material application. Each concept leader interprets the basic specifications in accordance with its brand philosophy and own understanding of customer expectations. Consequently, somewhat different vehicle concepts are defined, e.g. by means of dimensions. The Renault concept is an A0 class vehicle, while the Fiat concept is slightly larger, thus being an A class car. The Volkswagen is even larger and can be considered as a B segment vehicle. The concepts have the following characteristics (Fig. 7):

Currently, the full virtual development of the three concepts is under way. This will lead to simulation models that allow the assessment against key criteria such as energy efficiency, driving dynamics, structural behaviour including crash safety, ergonomics and electromagnetic compatibility. In addition, a life cycle assessment will allow the comparison with conventional vehicles as well as among the three concepts.

## 4 Summary

After a deep investigation of customer requirements and technology options for purpose designed electrical vehicles, the ELVA project has developed innovative ideas for fully exploiting the design options provided by the new drive train architecture. Three virtual concepts are currently developed under the leadership of Fiat, Renault and Volkswagen.

The completion of the concept development, which is done using two optimisation loops, and the related assessment is scheduled for May 2013. Due to the production deadline, latest results cannot be part of this paper, but will become available on the project website which can be reached under [www.elva-project.eu](http://www.elva-project.eu).

The deeper understanding of customer requirements, the overview of technical options/components and the accelerated design process will be covered with a compilation of design practices/rules/freedoms and limitations for urban EVs. This design process can become a role model for future EV development. The final ELVA concepts will showcase most promising solutions for urban/commute focused EVs.

**Acknowledgments** The ELVA project is coordinated by the Forschungsgesellschaft Kraftfahrwesen mbH Aachen (fka) for RWTH Aachen University. Furthermore, four of the largest European automobile manufacturers and suppliers, namely Fiat, Renault and Volkswagen as well as Continental participate in the project. The consortium is supplemented by RWTH's Institute for Automotive Engineering (ika), the Swedish Vehicle and Traffic Safety Centre SAFER and IDIADA Automotive Technology.

The research leading to these results receives funding from the European Community's Seventh Framework Programme (FP7/2007-2013) under grant agreement no. 265898.

This publication solely reflects the authors' views. The European Community is not liable for any use that may be made of the information contained herein.

## References

1. Dannenberg J, Burgard J (2007) Car innovation 2015—innovation management in the automotive industry. Oliver Wyman Automotive, Munich
2. Hoelzl M, Collins M, Roehm H (2009) A new era—accelerating toward 2020—an automotive industry transformed. Deloitte Touche Tohmatsu, Stuttgart
3. Weiss T et al. (2011) Our car of tomorrow—study on the German's wishes for the car of tomorrow, AutoScout 24-Magazin, Munich

4. Winterhoff M et al (2009) Future of mobility 2020—the automotive industry in up-heaval? Arthur D Little, Wiesbaden
5. N.N. (2009) Passenger car scenarios up to 2030—facts, trends and options for sustain-able auto-mobility, Shell Deutschland Oil GmbH, Hamburg
6. Matthies G, Stricker K, Traenckner J (2010) The e-mobility era: winning the race for electric cars—flipping the switch to electric cars: seven factors transforming the future of the automotive industry. Bain & Company Inc, Munich
7. Becker D et al (2011) KPMG's global automotive executive survey 2011—creating a future roadmap for the automotive industry. KPMG International, Stuttgart
8. Wagner U (2011) Transportational integration of e-mobility. VDI car congress, TU Munich
9. Rishi S et al (2008) Automotive 2020—clarity beyond the chaos. IBM, Somers
10. Giffi C, Vitale J Jr, Drew M, Kuboshima Y, Sase M (2011) Unplugged: electric vehicle realities versus consumer expectations. Deloitte Global Services Ltd., New York
11. Sommer K (2011) Continental mobility study 2011. Continental, Hanover
12. Badstuebner J (2011) The frenzy of the kilowatt hour, automobil industrie. Vogel Business Media, Wurzburg

# The Ring-Shaped Route Body Structure Design and Evaluation Method

Feng Xiao and XinHua Gao

**Abstract** The performance matching between material and structure is the most fundamental matching relationship during car body engineering development. In this paper, the “3S-Targets” conception of car body structure design is summarized by studying theme reports of automotive original equipment manufacturers (OEM) published in previous Euro-Car-Body conferences. Meanwhile, the “Ring” structure feature is concluded which has been proposed by OEMs from different points of view and can meet different performance requirements simultaneously. Finally, ring-shaped route body is proposed by regarding the car body skeleton as being made up of 16 Rings. From ring-structured materials and performance evaluation matrix, on one hand, this method can reasonably explain the relevance between crash safety star rating and torsion stiffness; on the other hand, the “3R-BODY” evaluation method for design itself is proposed which is independent and ahead of simulation and test. It provides an important theoretical significance and value in engineering for car body lightweight design.

**Keywords** Performance matching · 3S-Targets · Ring-shaped route body · 3R-BODY evaluation method

---

F2012-E04-002

---

F. Xiao (✉)

Wuhan ShangShan Simulation Technology Co., Ltd, Mainland, China  
e-mail: feixin5214@qq.com

X. Gao

HeFei University of Technology, Hefei, China

## 1 Introduction

Car body is a community of the performance for crash safety, structure NVH and strength and durability. The substance of car body structure forward development engineering is the performance development under lightweight design which needs to face at least five basic questions: reference structure, performance matching, assessment criteria, evaluation method and development procedure. The ring-shaped route body structure design and evaluation method makes an attempt to give its own answer.

## 2 Car Body Performance Matching

Under the global background of lightweight design, car body is the key point to achieve lightweight design. Car body forward development involves three keywords: material, structure and performance. How to understand the relationship among these keywords is quite crucial to the success or failure of car body engineering development. Both ECB2010 Audi New A8 and ECB2009 Jaguar XJ adopted aluminium alloy car body, the former adopted the ASF structure, which resulted in a decrease of car body weight and an obvious increase of various kinds of performance, and its torsion stiffness reached to 37.6 kN m/Deg. The body of the New A8 earned Audi the Euro Car Body Award in 2010. The latter still used traditional car body structure form, whose torsion stiffness was 20.5 kN m/Deg. It was awarded a four-star rating according to the Euro NCAP crash test.

From the relationship among material, structure and performance that above two car models involved, it can be concluded that the starting point of car body lightweight design is material, the terminal point is performance, and structure is a carrier that exerts material characteristics and determines performance. There is a best performance matching relationship between car body structure and material, that is, for a given car body material, there is an ideal form of body structure to achieve the union of body lightweight and performance goal. This relationship is the most fundamental matching relationship during car body engineering development. The research purpose of this paper is to find out the best body structure form for metallic material from the viewpoint of the performance matching between material and structure.

## 3 Lightweight and Assessment Criteria

The technology roadmap of car body lightweight is mainly lightweight of material and structure. For car body of traditional material, the increasing proportion of the high strength steel applications is a commonly used method in lightweight design, while the change in the structure is relatively small. Car body of new material is more suitable in the structural design of the body framework, which will help

improve the overall stiffness of the structure. Therefore, the application of new materials in the body of the vehicle is not simply changing steel into a light-weight material, but also changing the traditional form of body structure. Audi's light-weight design is not so much the result of aluminium alloy application but it is success of the ASF structure design. Once OEMs make the choice of the body material, the determinant factor of car body lightweight will be the structure. Crash safety performance is firstly a problem of structure, followed by the quality of the material. The torsion stiffness performance is totally a structural problem, thus, structural lightweight is the fundamentality while material lightweight is the auxiliary.

How to effectively evaluate the result of the car body lightweight? The light-weight coefficient is commonly used [1], which is the key indicator for the evaluation of the lightweight body design. Its physical significance is to maximize the torsion stiffness of a given car body mass or to minimize the car body mass under the established conditions of torsion stiffness. However, the lightweight body design needs to consider performances including structure NVH performance, crash safety performance, and durability performance. The lightweight coefficient has been widely used for the overall effect assessment of the lightweight body.

According to the input–output ratio analysis, quality represents cost; torsion stiffness represents the overall profit. Car body lightweight is good for fuel economical efficiency and environmental protection. It is suitable to use quality as the representation of the cost. Therefore, the efficacy of the lightweight coefficient assessment method depends on whether torsion stiffness can represent the whole body benefits or not, which inevitably require it as a comprehensive performance indicator that not only represent structures NVH performance but also be on behalf of the body collision safety performance and durability performance.

## 4 Body Performance Structural Dependence

The challenge of the car body structure design is the lightweight design. On the one hand, lightweight is directly in conflict with performance goal; on the other hand, there is a conflict between various kinds of performance, for example, a balanced design method and idea is needed for crash safety and stiffness performance, but meanwhile, there is structural correlation between all kinds of properties.

### 4.1 3S-Targets

In the ECB2003, Ford raised “The target to develop a stiff and safe body structure for the Focus C-Max” in the report of its car model New Focus C-Max; in the ECB2004, PSA proposed “Increased performances” in the report of its car model New Peugeot 407, which includes three aspects: “5 stars Euro-NCAP high speed



crash performances”, “Road stability: high structure stiffness”, “Weight reduction: increase high strength steel grades”; in the ECB2008, Honda made three points of Body In White (BIW) performance requirements in the report of its car model New JAZZ: “Handling and Comfort”, “Safety”, “Achievement of Weight Reduction”; in the ECB2010, Audi proposed “technical development targets” in the report of its car model New A8, which contained the following three points: “weight reduction as basis for efficiency and sustainability”, “rigid construction for driving dynamics at the highest level”, “achieving the safety standards in the luxury segment”. OEM’s body development goals involve three common aspects: “Stiffness, Safety, Saving”, which can be summed up as “3S-Targets”, among which the “Saving” refers to “Save mass, Save money, Save time”.

## ***4.2 Crash Safety Performance***

Car body crash safety performance development is one of the core content of the vehicle research and development. OEMs develop it as a priority from design, simulation, testing to production. A brief summary of car body crash safety design conception is “crushing energy absorption and dispersing loads”. It was firstly proposed by the safety design leader Volvo. Its specific design requirements are “full crushing energy absorption of the cockpit and remained intact of the crew cabin”, which has become the starting point of car body crashworthiness development for global OEMs.

### **4.2.1 Collision Safety Body Structure**

According to previous ECB materials over the years, Audi, Honda, Nissan and Volvo clearly proposed car body crash safety structure, while Toyota proposed the security conception. In the ECB2003, Audi showed “Audi Space Frame (ASF)” body structure in the report of its models A8, which is actually a space frame structure formed by the body skeleton. The salient features of ASF structure are: A-pillar is extended to C-joint, side sill structure stretches across the front and rear doors; in the ECB2005, Honda put forward the “ACE body structure” in the report of its model New CIVIC; In the ECB2006, Nissan proposed the “Advanced Zone Body Concept” in the report of its car model NOTE, which takes the front of the cabin as the “Crushable zone” so as to fully absorb the collision energy and takes the crew cabin as the “Safety zone” so as to ensure the integrity of the crew compartment; in the ECB2007, Volvo proposed “strong the safety cage to secure occupant space” in the report of its model NewV70; in the ECB2010, Volvo extended “the safety cage” to the entire body frame structure in the report of its model New S60; in the ECB2008, Toyota gave a comprehensive report of the GOA conception in the report of its model New AVENSIS, which aims to reduce the impact suffered by crew and to protect the integrity of the crew compartment.

### 4.2.2 Crashworthiness Ring Structure Features

According to the ECB materials over the years, the effect of “Ring” structure to enhance body crash safety performance was not brought to the forefront; “Ring” structure that is proposed from the angle of collision safety structure is very rare. All security-related ring structures proposed in previous ECB materials can be listed: in the ECB2002, Ford proposed “continuous ring around front door opening” in the report of its model Fiesta from viewpoint of front crash; in the ECB2003, Renault proposed “ring side body reinforcement” in the report of its model SCENIC2 from front the viewpoint of collision and side collision; in the ECB2005, Saab proposed the “C-Ring” in the report of its model 9-3 Sport Combi from point view of roof compression; in the ECB2005, Honda proposed “consolidated front floor frame” in the report of its car model New CIVIC from the viewpoint of front collision; in the ECB2010, Honda marked the “B-Ring” in the report of its model CR-Z from the perspective of the side collision.

### 4.3 Torsion Rigidity and Durability

Vehicle NVH performance depends primarily on the overall car body stiffness index, where torsion stiffness plays a decisive role. In previous ECB materials, how to improve body torsion stiffness is the key of reports from all OEMs. Constructing a horizontal ring structure can obviously improve the torsion stiffness effect. Therefore, the ring structure improvement scheme is most commonly used in ECB. However, it is mainly confined to local structure or local area characteristics, and is sporadically distributed in various parts of the car body.

As one of the most important inspection points of car body structure design, the essence of durability is the same as torsion stiffness. The root cause of the body structure durability problem is because the torsion stiffness is not high enough. A large number of engineering experience shows that most car body durability problems can be effectively solved by enhancing torsion stiffness. Thus, it can be inferred that there are common structural features between the body torsion stiffness and durability, which can meet the two key performance requirements simultaneously.

In the ECB2007, Renault proposed “stiffness of C frame” in the report of its model Laguna III and explained its role, that is, “30 % increase stiffness of the rear frame and high durability”; in the ECB2008, Renault proposed “D-Frame” in the report of its model Laguna III Coupe, and explained its role, that is, “25 % increase stiffness of rear frame stiffness from hatchback to high durability”, which indicates that the rigidity performance and durability have the same structural characteristics, especially that the evaluation of length changes of car body doorframe diagonal can directly reflect the correlation between body durability and torsion stiffness.

#### ***4.4 Torsion Stiffness and Crash Safety Star Rating***

Key parameters statistics of the involved ECB2010 car models are shown in Table 1. By using lightweight materials, the mass of the body is more than 50 % lighter than body of traditional materials and also generally has a higher torsion stiffness, the average stiffness reaches 24.55 kN m/Deg. Because of the light weight and the high torsion stiffness, the Lightweight Index of lightweight material body is much lower than the body of traditional materials; the overall safety performance is very high according to statistical test results from the Euro-NCAP and IIHS official website.

Preliminary inferences can be drawn from the torsion stiffness and safety star rating data: there is correlation between the torsion stiffness and crash safety star rating, car body structure with higher torsion stiffness are more likely to obtain high crash safety star rating result, which inevitably requires a common structure feature between the torsion stiffness and crash safety to meet requirements of these two performances. In previous ECB materials over the years, the “Ring” conception was only proposed twice from the perspective of two properties at the same time: in the ECB2005, Saab proposed “C-Ring” in the report of its model 9-3 Sport Combi from the viewpoint of “Reinforcement for general stiffness and roll-over protection”; in the ECB2010, Honda marked “B-Ring” in the report of its model CR-Z from viewpoints of the side crash and car body stiffness.

### **5 Ring-Shaped Car Body**

The research object of ring-shaped car body is body skeleton structure. Reference [2] broken it down into 16 basic ring-shaped structure characteristics, and each ring structure was described in detail, covering three aspects involves the ring structure characteristic (Ring), the substantive requirements (Route) and performance goals (Resist), “Ring” and “Route” are based on the concept of a body frame structure, “Resist” is the effect that ring-shaped car body can reach, the ring shaped car body is also known as the “3R-BODY”.

#### ***5.1 “Ring” Structure Feature***

The definition of “Ring” chooses random joint of car body skeleton structure as the starting point, along with a shorter path back to the starting point for the formation of a “Ring-Shaped” structure. The ring can be a plane or space, can be round or square, the key is to form a closed loop. If the ring meets in form, but the closed loop can not be formed because the body frame removed the structural parts that can not form a closed cross section or whose thickness is less than or equal to

**Table 1** Key parameters and crash safety evaluation statistics of car body in ECB2010

2010 ECB	Material and structure				Joining				Safety performance				
	Mass (kg)	Torsion (kN m/)	Area (m <sup>2</sup> )	Index	Parts	WSE/SP	Euro-NCAP			IIHS rollover			
							ODB	SIDE	Star	Rating	Weight (kg)	Force (kN)	Ratio
Audi A8	231.0	37.6	4.92	1.25	243	8,115/202	-	-	-	-	-	-	-
Lexus LFA	193.0	39.3	4.12	1.19	555	3,573/178	-	-	-	-	-	-	-
BMW 5Series	347.0	33.0	4.79	2.20	405	8,873/5,800	15.5	15.4	5	G	1,729\1,790	70	4.04
VW Sharan	389.0	22.4	4.65	3.73	-	8,275/5,600	15.4	15.5	5	-	1,774	-	-
AlfaRomeo Giuetta	280.0	18.6	4.07	3.70	354	4,724/3,676	-	-	5	-	-	-	-
Opel Meriva	325.0	21.0	3.96	3.91	606	5,059/4,533	14.2	14.5	5	-	1,359	-	-
AstonMartin Rapide	325.0	28.4	4.68	2.45	362	6,029/0	-	-	-	-	-	-	-
Volvo S60	321.5	23.3	4.41	3.13	366	5,276/3,966	-	-	-	G	1,616	80	4.95
Honda CR-Z	270.4	17.6	3.69	4.16	450	4,724/4,254	14.6	15.9	5	A	1,208\1,225	47	3.88
Ferrari 458 Italia	226.4	22.5	4.45	2.26	-	4,777/0	-	-	-	-	-	-	-
Citroen C4	290.6	19.8	3.98	3.69	349	5,624/3,938	15.2	14.3	5	-	1,205	-	-
Ford Grand C-Max	346.0	14.4	4.31	5.58	398	5,418/5,011	15.5	15.4	5	-	1,504	-	-
Saab 9-5	395.4	20.3	4.50	4.33	735	5,068/4,250	15.1	15.6	5	G	1,738\1,689	102	5.85
Renault Latitude	323.9	25.5	4.32	2.94	-	6,825/5,208	-	-	-	-	-	-	-

1 mm, then it will not constitute the structure of the “Ring” characteristics. If a ring is divided into a plurality of annular regions or a ring edge evolves into two parallel edges to form three-dimensional frame structure. If these two kinds of forms are equivalent from the effect with the original “Ring”, it can also be regarded as a ring structure.

From the point of view of structural design, the space frame structure has a very good overall stiffness and compatibility ability of deformation to achieve the purpose of “local stress, global share”. The “Ring” is the ideal structural characteristics that constitute a space frame structure to achieve the rapid triage of loads.

## **5.2 “Route” Substantive Requirements**

“Route” means that any location of each closed “Ring” structure constituted by sheet metal welding has a closed or semi-closed cross-section to avoid the abrupt changes in the cross-sectional area or weakness of stiffness in local position. Especially the “Ring” of the edge and the edge junction is needed to be considered in the design, in order to ensure cross docking along the load transfer direction as much as possible.

“Route” is the substantive requirement when “Ring” meets the closed-loop condition-cross-section closed or semi-closed, which is to ensure the continuity of the stiffness rigidity. The “Ring” can not be constituted if it does not meet the substantive requirements. According to the substantive requirements of the “Route”, collision related “Ring” section should be closed in principle, and closed cross-section should be as large as possible, while the stiffness associated “Ring” section can be semi-closed.

## **5.3 “Resist” Performance Objective**

If the car body frame has as many ring structure features as possible, and each ring meets route substantive requirements, which is to ensure the white body has the ideal space frame structure. Using appropriate materials design based on performance goals, BIW structure will have the ideal body torsion, bending, compression, resistance to deformation, that is, “Resist” performance objectives.

## **6 Ring Structure Evaluation Matrixes**

According to the material, the collision performance and stiffness performance requirements, Table 2 conducted a comprehensive assessment for 16 “Ring” to establish a matrix of relationship between the different ring structures with

**Table 2** Ring-shaped structure material and performance evaluation matrix

Structure and material		Structure performance assessment										Sum	
Ring	Direction	No.	Name	Saving		Safety				Stiffness			Lateral
				Material	Material	Frontal crash	Side impact	Rear crash	Rollover	Torsion	Bending		
X-Surface	1	Front-ring	-	0	+	-	-	-	-	+	-	+	3
	2	A-ring	+++	3	++	+	-	-	-	++	-	-	5
	3	B-ring	++++	4	+	+++	-	-	+++	++	-	-	9
	4	C-ring	+	1	-	+	-	+	+	++	-	-	5
Y-Surface	5	Damper-ring	-	0	-	-	-	-	-	++	-	-	2
	6	D-ring	+	1	-	-	+	+	+	++	-	-	4
	7	Front door opening-ring	++++	4	+++	++	++	-	++	+	-	-	8
	8	Rear door opening-ring	++	2	-	++	+	+	++	+	-	-	6
Z-Surface	9	Front absorber energy-ring	++	2	+++	-	-	-	-	+	+	-	5
	10	Front floor-ring	++	2	+++	++	++	+	+	+	++	-	9
	11	Fuel tank-ring	+	1	-	+	+	++	-	+	+	-	5
	12	Rear absorber energy-ring	++	2	-	-	+++	+	+	+	-	-	5
Assessment criteria	13	Hood opening-ring	+	1	+	-	-	-	-	++	-	+	4
	14	Shotgun-ring	+	1	+	-	-	-	-	+	-	+	3
	15	FR windshield opening-ring	+	1	-	-	-	-	+	+	-	-	2
	16	RR windshield opening-ring	-	0	-	-	-	-	-	-	-	-	0
Total score				25	15	12	9	9	10	21	5	3	75
Assessment criteria		Material	Structure	++++ UHSS	+++ EHSS	++ VHSS	+ HSS	- MS(Reference Volvo criteria)					
Assessment criteria				+++ Essential important	++ Very important	+ Less important	- Not important						

different properties. According to a large number of engineering analysis, and combined with the ECB reports, each Ring was assessed. Using the number of “+” to indicate the material ideal strength grade or importance degree of performance, namely score, “-” means zero points, and also calculate the summation score under the different ring-shaped structure and different performance.

It can be inferred from Table 2 that “Ring” material and structure performance evaluation is divided into three parts: for “Ring” and material ideal strength grade assessment, more plus sign indicates that higher level of material strength is needed to be used, its maximum score is “25”; for “Ring” and crash safety performance assessment, the key “Ring” related with each type of collision can be identified according to local or regional characteristics of collision effect on the body, three plus sign means the ring is crucial to the forms of collision, its maximum score is “46”; for “Ring” and stiffness performance assessment, the “Ring” that is needed to be considered can be identified according to the overall characteristics of the stiffness to the body structure design performance. The correlation between torsion stiffness and the overall structure is the maximum. All “Rings” are related, and the correlation is close, its maximum score is “21”. The total evaluation score of three parts is “100”.

According to Table 2, if the torsion stiffness of car body is higher, the number of the “Ring” to meet structural features and substantive requirements will be more, which will avoid most of the design flaws in the collision safety performance; if the collision safety star rating is higher or the safety tests are up to the evaluation of the “GOOD”, the 16 “Ring” can meet the basic structural features and substantive requirements, then the body must have a high torsion stiffness.

## 7 3R-BODY Assessment Method

In the 3R-BODY structure, each “Ring” has its unique function and design requirements, the lack of a “Ring” means weaken or vanish of some properties, therefore, 3R-BODY architecture design and evaluation method was proposed based on the ring structure material and performance evaluation matrix according to Table 2, which includes three aspects: “Ring structure and substantive requirements assessment”, “Ring material actual strength grade assessment” and “Ring comprehensive evaluation score calculation”. In the ECB2007, Volvo compared “front and rear door openings design” and “Predecessor” of its car model NewV70 from ring structures and materials, which is the first time to evaluate the car body design with the ring-shaped structure; in the ECB2008, Ford compared “B-Ring design” and “Old Fiesta” on New Fiesta from the ring shaped structures and materials, which is the second time to evaluate the car body design with the ring-shaped structure.

### ***7.1 The Structural Characteristics and Assessment of Substantive Requirements***

In accordance with the “Ring” structure features and substantive requirements, the number of Ring structure of car body frame can be objectively assessed. Generally speaking, more “Ring” structure means a better the performance of car body structure. Because the contribution to the performance of each ring’s rigidity is needed to be considered, therefore, the ring number can not completely represent the level of performance between different models.

Traditional material car body structure involved in the ECB2010 conference reports were assessed according to the 3R-BODY structure design evaluation method. Table 3 shows the assessment of the structural characteristics of the “Ring” with the substantive requirements of various OEMs based on the ECB2010 meeting reports. “1” indicates that the ring structure’s existence can be directly judged from the theme reports or indirectly from its traditional design gene and meets the structural characteristics and the substantive requirements; “0” means that the ring does not exist or is unable to judge or not to meet the structural characteristics and the substantive requirements.

### ***7.2 Material Actual Strength Rating Evaluation***

According to the Ring material ideal strength rating evaluation criteria in Table 2, the “Ring” material actual strength rating of body structure of OEMs in the ECB2010 meeting reports were assessed, the assessment score is given in Table 4.

### ***7.3 Comprehensive Assessment Scores***

A comprehensive evaluation of car body can be obtained from two aspects of material and structure according to the Ring structure feature and substantive assessment and Ring material strength grade evaluation. Structural performance evaluation scores of OEMs can be obtained from structural performance evaluation scores in Table 2 and structural characteristics and assessment of substantive requirements results of OEMs in Table 3. Material actual strength rating results of OEMs can be obtained from material actual strength rating scores of OEMs in Table 4 and structural characteristics and assessment of substantive requirements results of OEMs in Table 3. The overall Ring assessment of the structure can be obtained by summing up Structural performance evaluation scores and material actual strength rating scores, which is shown in Table 5.



**Table 3** Car body ring structure feature and substantial requirements of OEMs in ECB2010

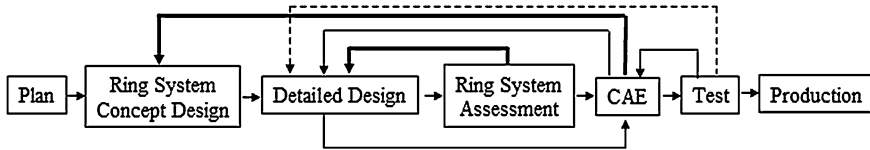
Ring		ECB2010 conventional material vehicle										
No.	Name	Alfa Romeo Giuetta	Opel Meriva	Volvo S60	New BMW 5Series	Ford Grand C- Max	Honda CR- Z	Citroen C4	VW Sharan	Saab 9-5		
1	Front-ring	0	1	0	0	0	1	0	0	0		
2	A-ring	1	1	1	1	1	1	1	1	1		
3	B-ring	1	1	1	1	1	1	1	0	1		
4	C-ring	0	1	1	0	0	0	0	0	1		
5	Damper-ring	0	0	0	1	0	1	0	0	0		
6	D-ring	0	1	1	0	1	1	1	1	1		
7	Front door opening-ring	1	1	1	1	1	1	1	1	1		
8	Rear door opening-ring	0	0	0	0	0	0	0	1	0		
9	Front absorber energy- ring	0	0	1	1	1	0	0	0	0		
10	Front floor-ring	1	1	1	1	1	1	1	1	1		
11	Fuel tank-ring	1	1	1	1	1	1	1	1	1		
12	Rear absorber energy- ring	1	1	1	1	1	1	1	1	1		
13	Hood opening-ring	0	0	0	1	0	1	0	0	0		
14	Shotgun-ring	0	1	1	1	0	1	0	0	1		
15	FR windshield opening ring	1	1	1	1	1	1	1	1	1		
16	RR windshield opening ring	1	1	1	1	1	1	1	1	1		
Total		8	12	12	12	10	13	9	9	11		

**Table 4** Ring material actual strength rating of body structure of OEMs  
ECB2010 conventional material vehicle

No.	Name	Alfa Romeo Giuetta	Opel Meriva	Volvo S60	New BMW 5Series	Ford Grand C-Max	Honda CR-Z	Citroen C4	VW Sharan	Saab 9-5
1	Front-ring	0	0	0	0	0	0	0	0	0
2	A-ring	1	1	2	3	2	2	0	2	2
3	B-ring	3	4	3	3	3	2	4	2	3
4	C-ring	1	1	1	1	1	1	0	1	1
5	Damper-ring	0	0	0	0	0	0	0	0	0
6	D-ring	1	1	1	0	1	1	0	1	1
7	Front door opening-ring	4	1	4	4	4	3	3	4	4
8	Rear door opening-ring	1	0	2	1	0	0	0	2	2
9	Front absorber energy-ring	2	1	2	2	2	2	0	2	2
10	Front floor-ring	2	2	2	2	2	2	2	2	2
11	Fuel tank-ring	1	0	1	1	1	1	1	1	1
12	Rear absorber energy-ring	2	1	2	2	2	2	1	2	2
13	Hood opening-ring	1	0	0	1	1	1	1	1	1
14	Shotgun-ring	1	1	1	1	1	1	1	1	1
15	FR windshield opening ring	0	0	1	0	0	0	0	0	0
16	RR windshield opening ring	0	0	0	0	0	0	0	0	0
Total		20	13	22	21	20	18	13	21	22

**Table 5** Car body structure ring comprehensive assessment result

	Alfa Romeo Giuetta	Opel Meriva	Volvo S60	New BMW 5Series	Ford Grand C-Max	Honda CR-Z	Citroen C4	VW Sharan	Saab 9-5
Material	13	12	20	19	17	15	11	14	17
Structure	43	58	60	57	52	59	47	44	55
Total	56	70	80	76	69	74	58	58	72



**Fig. 1** 3R-BODY evaluation method and car body development procedure

## 8 Evaluation Method and Development Procedure

Design is the root of most of the problems during the Car Body engineering development process. The simulation (CAE) and Test are both external methods to aid design to identify and solve problems; the simulation is a mean of matter control, which aims at discovering design defects, while the test is a mean of feed back control to verify a design flaw. Any small design flaw will increase the complexity and difficulty to solve the problem, resulting in significant increase of the cost. Therefore, prevention is better than control, which in turn is better than remedy after the event.

The 3R-BODY structural design and assessment methods is a mean of control in advance, which is independent with and way ahead of simulation and test. It is an assessment method focuses on design itself, which is aimed at avoiding design flaws. Using the 3R-BODY structural design assessment method can ensure that the model submitted to the simulation and experiment as much as possible the optimal structural design of the best performance, which can also reduce unnecessary repeated design and verification and makes the whole process constitute a complete body structure design assessment and control system before, during and after the event, as is shown in Fig. 1, in order to more effectively improve the design level.

## 9 Conclusions

After fully abstracted, absorbed and digested good genes of the OEMs in the design of the lightweight car body, the 3R-BODY structural design assessment method, which is independent and ahead of simulation and test, is established by

unifying crash safety performance, torsion stiffness performance and durability into the ring structure feature and by setting up ring system for the car body frame. This method is based on the ring structural material and performance evaluation matrix. It has an important theoretical significance and value in engineering for car body lightweight design.

**Acknowledgments** The development of the 3R-BODY structural design and evaluation method has gone through three stages. Firstly: work experience at simulation department in Chery Automobile Company accumulated the author with design experience of different car body performances, and a clear understanding of the critical problems faced in car body structure lightweight design; Secondly, the author accumulated a lot of successful design experience and rich data by repeatedly study reports of OEMs in previous ECB conferences, and thus has a more comprehensive understanding of the body performance development; thirdly, the author confirmed that ring structure is key structural features to improve torsion rigidity and crash safety performance through in-depth analysis of Honda car body structure. Finally, the 3R-BODY structural design and evaluation method was proposed.

The 3R-BODY structural design and assessment method is an appropriate method proposed at the appropriate time to appropriately summarize and conclude car body engineering design. It is inseparable with accumulated practical experience in engineering as well as successful experience published by OEMs in reference materials. Thus, the author would like to express sincere gratitude to all authors and organizations, whose technical information deeply inspired the author to imagine and think.

## References

1. The 4–12th International Car Body Benchmarking Platform. ECB2002–2010
2. Feng X The evaluation method for the ring-shaped route body structure design. China Patent Application No. 201110223295.5

# The Study of Wheeled Semi-trailer Design and Development Based on Scale Model

Xiong Xin, Xuexun Guo and Libo Wang

**Abstract** The wheeled semi-trailer is usually used to transport heavy-duty equipment, engineering machinery and other heavy-load cargo. With the wheel semi-trailer, it is convenient to transport the heavy-duty equipment to the destination area and will play a great role in heavy-duty transportation for long distance. Nowadays, the relative enterprises all over the world focus on the modern design methods which could enhance the manoeuvrability, the ride and flexibility of the semi-trailer. The scale model we used in the research is a 50:1 semi-trailer simulation model. The reverse engineering technology is adapted to primarily design the relative parts and components of the wheeled semi-trailer. Then, the digital mock-up technology is used to design the details of the whole vehicle model. Finally, the optimization is completed for solving the relative problems in the multi-axis turning. For the limitation, the testing data for manoeuvrability could not be gotten, so the simulation precise can not be checked for further improving design. The semi-trailer simulation model is firstly used rather than the actual vehicle for the development of vehicle designing. Diversified methods and technologies is adapted successively and the optimization 3-D model is achieved. The simulation results show fine multi-axis turning condition. The development cost is cut and the development cycle is shortened. All above will provide the valuable references for the research of the wheeled semi-trailer.

---

F2012-E04-003

---

X. Xin (✉) · X. Guo  
Hubei Key Laboratory of Advanced Technology of Automotive Parts,  
Wuhan University of Technology, Kunming, China  
e-mail: aime\_bx@163.com

L. Wang  
Hubei Sanjiang Space Wanshan Special Vehicle CO., LTD, Xiaogan, China

**Keywords** Wheeled semi-trailer · Reverse engineering · Digital mock-up · Steering mechanism · Optimization design

Vehicles include two main kinds, the wheeled vehicle and the tracked vehicle. The wheeled vehicle has become one of the most commonly used equipment in armies of countries all over the world for the properties of good flexibility, extensive use of geographical, environmental adapt ability, good reliability, economy and versatility [1]. The wheeled semi-trailer is necessary for long-distance transport and usually used to transport heavy equipment, construction machinery and other heavy good. Therefore, using modern design methods which could improve the mobility of wheeled semi-trailer and improve its smoothness and ease of operation has been the issue that attaches great importance of related enterprises in major nations.

## **1 Preliminary Design of Semi-trailer's Parts Based on Reverse Engineering**

### ***1.1 Introduction to Reverse Engineering***

Reverse engineering which is also known as reverse seeking engineering [2] is establishing CAD models, then using these models and characterization in the procedure of product analysis, manufacturing and production. Now the reverse engineering is aiming to an existing artifact (sample or model), and using 3-D digital measuring instruments to measure profile coordinates accurately and quickly, and after the constructing, the surfaces should be edited and revised, and then sent to the general CAD/CAM system, and finally the surface is sent to CNC to process mold that mechanism needed through NC processing path of knives generated by CAM, or to rapid prototyping to produce sample model. This process is called reverse engineering (Fig. 1).

With the development and progress of modern computer technology, the reverse engineering has been widely used in aerospace, shipbuilding, automobile manufacturing, etc., especially in the field of wheeled vehicle design, which has gradually embarked on the development track of digital and high-tech. The reverse engineering has become an advanced wheeled vehicle design method which can create digital model products quickly and accurately, and greatly shorten development cycles of new product as well as improve productivity.

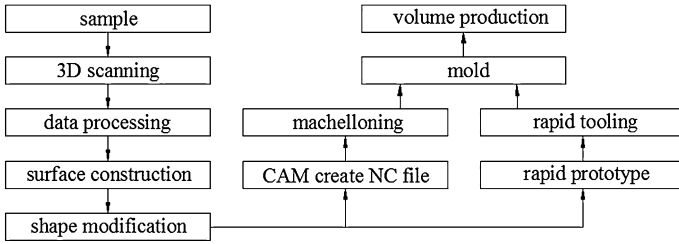


Fig. 1 Reverse engineering

## 1.2 Preliminary Design of Semi-trailer Parts

### 1.2.1 Point Cloud Data Collection

A scale model of one wheeled semi-trailer (1:50) is very fine. The suspension, the gooseneck, ramps, auxiliary power units, lighting system and other equipment are readily available, contains all the details of the real car.

The scale model is small, so the outer surface is not allowed to be sprayed so as to satisfy the high precision measurement. On the base of analyzing advantages and disadvantages of the contact and the non-contact measurement, use Konica Minolta non-contact 3-D scanner RANGE7 to complete the surface point cloud data collection of a scale model. This scanner can measure the cloud data without spraying reagent or in a dark room, which would eliminate measurement errors caused by the thickness of the reagent, avoid spraying before measurement and cleaning after measurement, reduce the potential environmental pollution caused by cleaning reagent and be measured in the general office environment. Specific parameters are in Table 1.

### 1.2.2 Data Processing of the Point Cloud

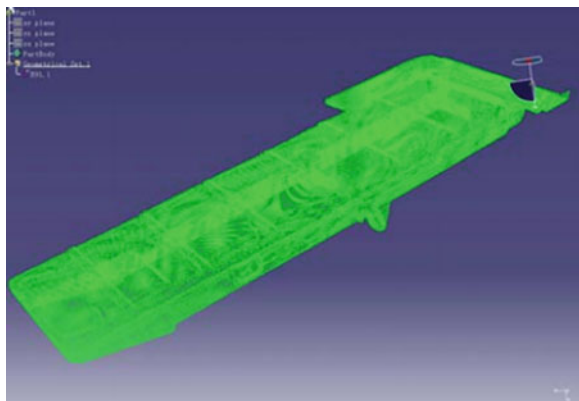
The result of structured light scanner measuring surface is a discrete set of spatial coordinates of points. This collection can be called “point cloud”. The data processing of the point cloud that gets from the model surface is the most important part of reverse engineering. The quality of treatment is directly related to the follow-up reconstruction of the model.

The measured point cloud of semi-trailer parts scale model is imported into CATIA V5 digitized shape editing module and the zoom ratio is set to 50 times, then make the scale model point cloud data into the physical model of point cloud data (Fig. 2). The DSE module can be converted into import point cloud files in multiple formats, such as Ascii free, Atos, Cgo and other ten species, and provides

**Table 1** Specifications table of Konica Minolta RANGE7

Measurement methods	Triangulation principle			
Light source	Semiconductor laser: wavelength: 660 nm			
Laser level	Class2(IDC60825-1 amendment 2)			
Effective pixels	1.31 million pixels (1280 × 1024)			
Measuring distance	450–800 mm			
Receiving lens	TELE; WIDE			
	TELE450 mm	TELE800 mm	WIDE450 mm	WIDE800 mm
	79 × 99	141 × 176	150 × 188	267 × 334
Measurement range (unit: mm)	54	97	109	194
XY direction measurement interval (unit: mm)	0.08	0.14	0.16	0.28
Accuracy	±40 μm			
Error (Z, σ) <sup>2</sup>	4 μm			
AF	Yes			
AE	Yes			
Scan time	About 2 s (1 scan)			
Preview	Yes (about 0.4 s/scan)			
Ambient light conditions	Less than 500 lx			
File format	Input/output: Konica Minolta proprietary formats: RGV, RVM; Output: STL, ASC			
Output interface	USB 2.0			
Power supply	With AC adapter Input voltage: AC 100–200 V (50/60 Hz) current: 1.4 A (at AC 100 V input)			
Size	295 (W) × 200 (D) mm (excluding lens)			
Weight	About 6.7 kg			
Operating temperature and humidity range	10–40 °C; relative humidity below 65 %, no condensation			
Storage temperature and humidity range	–10 to 40 °C; relative humidity 85 % (35 °C when) the following, non-condensing			

**Fig. 2** Point cloud data of road model





digital data import, sorting, portfolio, bad removed, cross-section generation, feature line extraction, real time shape quality analysis to process point cloud.

The final step in point cloud processing is to generate grids of the point cloud. The quality of the grid point cloud directly affects the next step point cloud data block and has certain impact on the surface generation. Establishing the correct topological relations between points, forming triangular plane are the key of point cloud grid. Besides, reasonably reduce the number of triangular plane in the relatively flat surface, reasonably increase the density of triangular plane in the relatively larger surface curvature.

### 1.2.3 Reconstruction of the Characteristic Surface

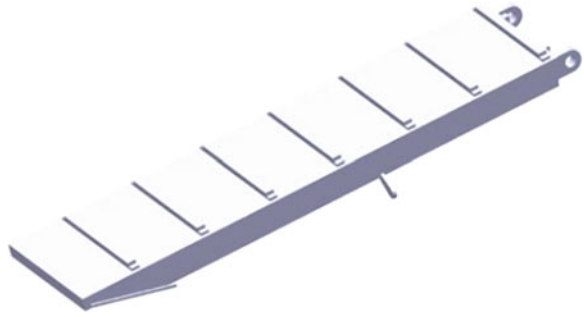
In reverse engineering, 3-D reconstruction of physical model is the most critical and complex part of the whole process. The reconstruction of characteristic surface is the key in this session. Currently, in the process of physical reverse engineering, there are three general methods for the characteristic surface reconstruction. The first one is the surface construction based on triangular Bezier; the second is the surface construction based on B-Spline or NURBS; the third is to describe curved objects ion polyhedron way.

After processing semi-trailer parts point cloud data, QSR could be directly accessed: CATIA Quick Surface Reconstruction module. QSR module can reconstruct surface quickly and easily based on digital data and bad points in the digital data should be removed and meshed through DSE. Depending on the type of shape, QSR provides a number of surface reconstruction methods: free-form surface fitting; mechanical shape recognition (plane, cylinder, sphere, and cone) and extension of original surface.

For relatively complex surfaces, we can use the corresponding tools in CATIA V5 Generative Shape Design module to model surface. GSD can do advanced surface design with full design specifications based on the combination of stand, variety of surfaces and advanced features. GSD also provides a widely set of tools to create and modify complex shape design or mechanical parts form in mixed parts modeling.

### 1.2.4 CAD Model Reconstruction

After reconstruction of characteristic surface, the resulting model is surface model, but the model that following manufacturing or simulation analysis need must be the physical model which should have thickness and quality, so it's general to convert surface model to solid model. In CATIA V5 Part Design module, it's easy to achieve this conversion and get solid models of semi-trailer parts (Fig. 3).

**Fig. 3** Solid model

## 2 Detailed Design of Semi-trailer Based on Digital Mock-Up

### 2.1 Introduction of Digital Mock-Up

Digital Mock-Up (DMU) is understood by many people that assembling parts together through 3-D model. In fact, achieving 3-D prototype is the most basic step to achieve Digital Mock-Up. According to the definition from Europe senior information technology: “Digital Mock-Up is the true computer simulation of products, meeting a variety of functions, providing simulation environment that used to engineering design, manufacturing and disassembly or maintenance of products. Besides, it is also a public platform where product and process can be supported, information can be delivered and decisions can be made. Digital Mock-Up covers the products’ whole life circle from conceptual design to maintenance services.” [3].

From those we can see, Digital Mock-Up technology mainly refers to the establishment of a complete digital prototype of the product which is achieved by using 3-D CAD/CAE/CAM software on the computer platform. Every component in Digital Mock-Up should not only make a precise definition of 3-D geometry, but also contains the information such as: assembly relationship between each other, technology association, process, tolerance, human resources, material, manufacturing resources, cost and so on. Digital Mock-Up should have all the functions which are needed for the product design, manufacturing to maintenance. Then a platform for information exchange and decision-making can be provided where we can achieve product and process development as well as the product life circle from conceptual design to maintenance [4].

Digital Mock-Up technology is not just a simple 3-D assembly. It also has the following characteristics:

Fully integrated with CAX system and operation with a “contextual design” way.

- (1) Offers powerful visual tools: not only the virtual display and a variety of browsing but also advanced means such as roaming and sectional perspective.
- (2) With various functional testing tools like installation/removal, mechanism motion, interference and cross-section scanning.
- (3) It has the capabilities of configured product structure and information communication.

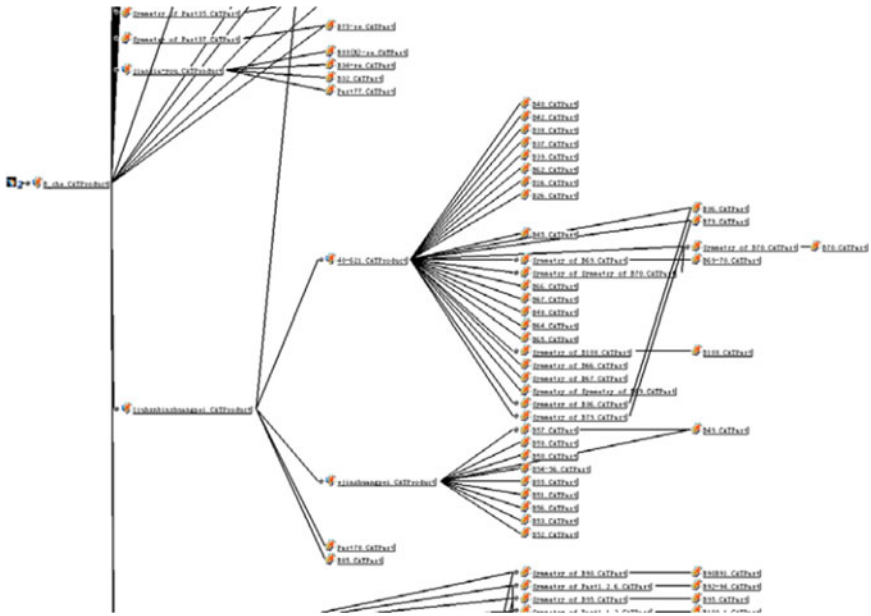


Fig. 4 Assembly structure tree

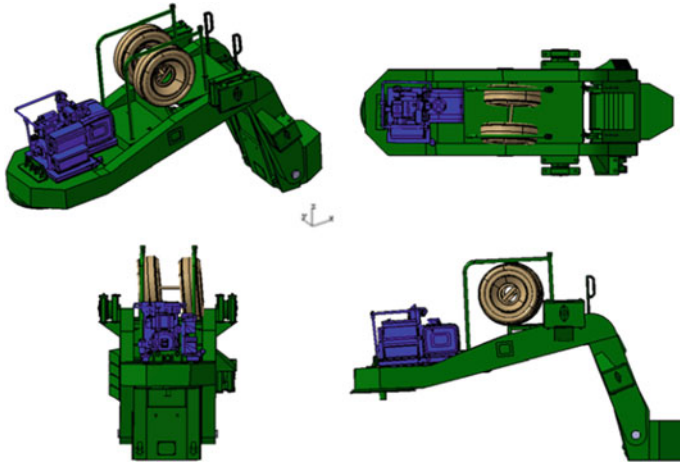
## 2.2 Detailed Design of Semi-trailer Vehicle

### 2.2.1 Virtual Assembly Design of Semi-trailer Vehicle

Virtual Assembly is an extremely important part in the virtual manufacturing process and is widely used in the research of virtual reality technology and the process simulation technology. It is a process of repositioning the part model according to the constraint relations. Besides, it is also an effective way to analysis the rationality of the product design.

We can import the part models of semi-trailer obtained by Reverse Engineering into CATIA Assembly Design and assemble them by adding constraints (such as parallel, coaxial or coplanar, etc.). Through constraint management, the assembly specific relationship or constraints of the models can be preserved in the repeated process of semi-trailer's design or improvement, remodeling design. It has nothing to do with the modification of the models.

One type of wheeled semi-trailer is a complex system which consists of many models who has the hierarchical relationship. This is reflected in the virtual assembly: an assembly can be divided into several parts and subassemblies. A subassembly can be decomposed into several parts and subassemblies in the next layer. This process is actually an up-down design process. In the structural design of hydraulic torque converter, we use the hierarchical multi-fork tree to describe the relations. That is to say, according to the logic of dependency, we can



**Fig. 5** Gooseneck sub-assembly model

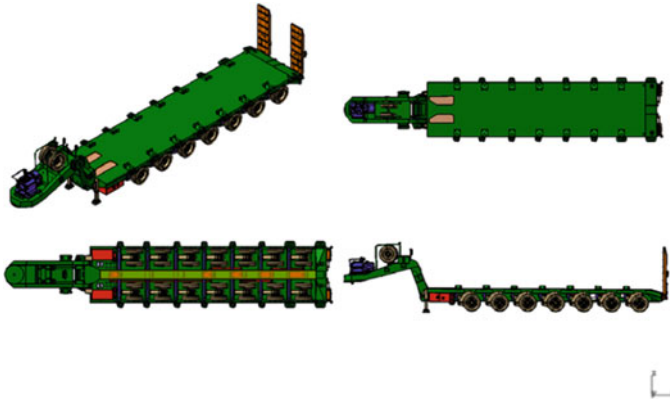
determine the set membership between the various models. Thus, assembly design level can be realized (Fig. 4).

### 2.2.2 Detailed Semi-trailer Part Design for Assembly

There are some errors in the measurement of point clouds for the wheeled semi-trailer scale model. This is because the point cloud data is magnified by 50 times in the data processing stage. As a result, these errors also been magnified by 50 times. Coupled with the reconstruction of characteristics surface and CAD model, more errors are generated. Then a relatively large deviation occurs between the preliminary design of parts and physical model. This led directly to lots of unreasonable or interferential regions in the vehicle assembly model. Design for Assembly is the best way to solve this problem.

Design for Assembly (DFA) means that in the early stage of product design, we can consider and solve problems that may exist during assembly process. Then, the parts can be assembled faster, more efficient and with lower cost. DFA, whose aim is the links for assembly, is a design idea and method that takes all factors into consideration. This is, in the product design process, it uses a variety of techniques like analyses, evaluation, planning and simulation to take assembly and the associated factors into fully consideration. DFA improves the product assemble structure on the condition that the performance and functions are satisfied and ensures the design of the product is assembled. What's more, DFA will minimize assembly cost and total cost of the product. DFA is a method of optimizing the structure of product, but also a design philosophy.

In CATIA V5, we can switch directly from ASD module to their respective module and define the structural information by adding the corresponding parameter constraints. When you change a parameter of one part, then other parts of the



**Fig. 6** Digital mock-up of a semi-trailer vehicle

parameters will change with the time immediately. We can make detailed designs for the structures that have assembly relationship. And then finish the detailed part design for one type of the wheeled three-trailer. The assembly model is shown in Fig. 5.

**2.2.3 Semi-trailer Vehicle Digital Mock-Up**

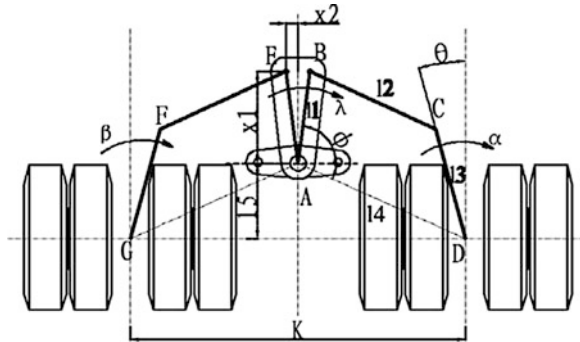
Now you can build a complete Digital Mock-Up of the wheeled three-trailer by the method described above and Fig. 6. In addition, a complete Digital Mock-Up of a wheeled three-trailer needs several coordination analyses like static and dynamic interference analysis, disassembly simulation analysis, spatial occupied analysis, structural strength analysis and vibration modal analysis. However, integrity of the model must be checked before the analyses. The check include: correct name, update status, correct assembly classification and the unified version.

**3 Optimal Design of Multi-axles Turning Mechanism for Semi-trailer**

**3.1 The Original Steering Mechanism**

When the vehicle steers, the sliding of wheels and the wears of tires are the problems of the semi-trailer vehicle. As it is shown in Fig. 7, the steering is a double-locked organization with two parallel, symmetric linkages. Double-locked mechanism ABCD and AEFG turn left and right. This is driven by the shared

**Fig. 7** Semi-trailer steering mechanism diagram



steering board rotating around point A. Then the steering wheels will be driven and the steering function of the vehicle can be achieved.

When the steering board turns to one side, then this side will be called outside of the vehicle. This is to say, the other side is inside when the vehicle is steering. If the steering board makes a clockwise rotating around point A, then the right steering angle  $\alpha$ , which results from the rotating of steering board, is formed and this angle is known as steering angle of outer wheel.

Accordingly, the steering angle  $\beta$  related to left wheel is called inside angle. Here we have known the coordinates of A, abscissa of D, the length of 13 and the angle with the vertical line. Then we will make an optimal selection for the coordinates of point B and the longitudinal coordinate of point D.

### 3.2 Optimal Design of Semi-trailer Steering Mechanism

#### 3.2.1 Principle of Optimality

According to the structural of semi-trailer, we calculate the idea steering angle of each wheel on condition of that all steering wheels can achieve pure rolling. Then compare the ideal angle with the actual steering angle determined by steering trapezoidal mechanism and work out an appropriate objective function. Find out the minimum of the function and the corresponding structural of trapezoid. The actual angle, which is decided by the steering trapezoidal mechanism, is the closest one to the ideal angle. The principle to calculate the ideal angle is shown in Fig. 8.

We can get a point of intersection, which is called the turning center, through the steering ray of the inside wheel on the first axle and the steering centerline. Ideally, all the other centers of steering wheels should be on this point. Then all wheels operate with pure rolling and ideal angle can be calculated according to this principle.

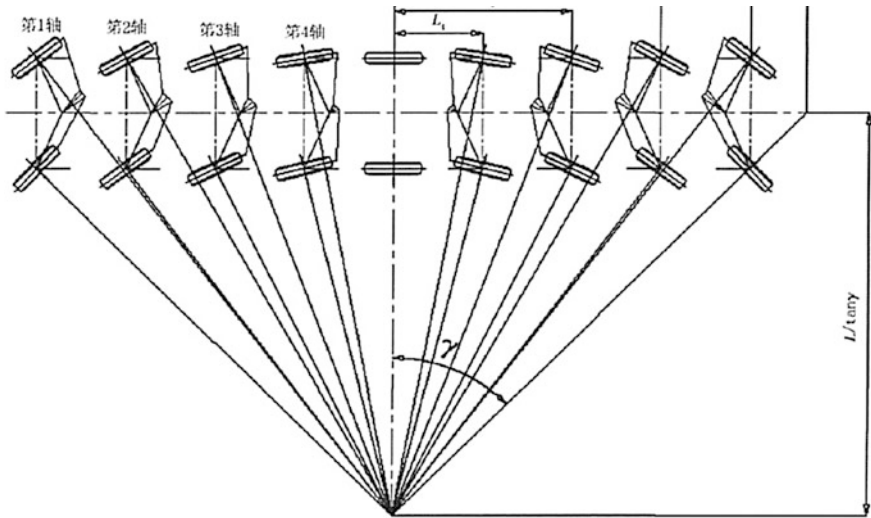
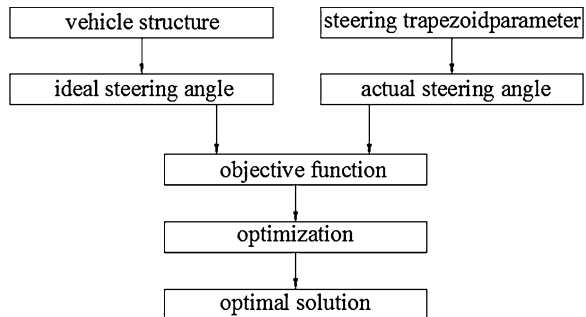


Fig. 8 Calculation principle of the ideal steering angle

Fig. 9 Steering optimization program flow



### 3.2.2 Objective Function

Least square objective functions are commonly used in related articles. The one used in this article is as follows:

$$objfun = \sum_{\lambda=1}^{45} ((\beta_t - \beta_r)^2 + (\alpha_t - \alpha_r)^2) \times weight(\lambda) \tag{1}$$

Where  $\beta_t, \beta_r$  represent the inside ideal angle and the inside actual angle.  $\alpha_t, \alpha_r$  represent the outer ideal angle and outer actual angle.  $\lambda$  stands for the steering board corner,  $weight(\lambda)$  means the weights and is related to  $\lambda$ .

In the objective function, we can calculate 45 groups of ideal angles according to the steering board rotating (1–45°). In order to make it easier to optimize, we provide the same angle for the steering board of each axis and always have the

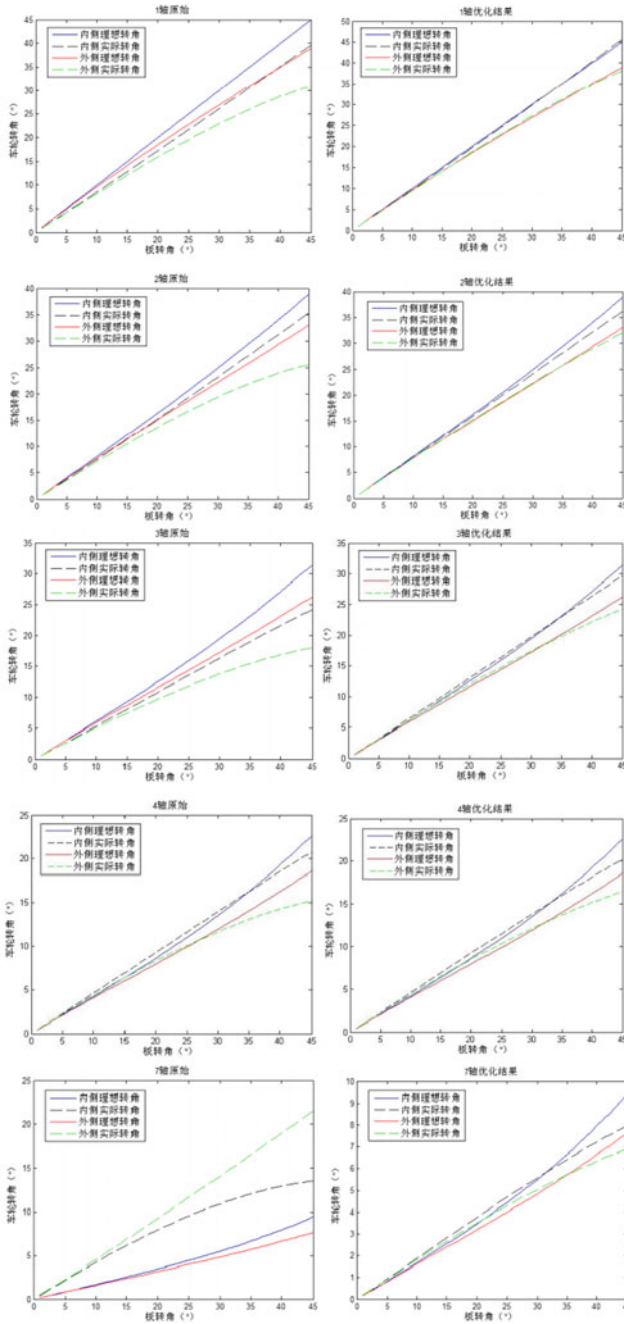


Fig. 10 Ideal angle and the actual angle of all steering shaft rotation, optimized data and the original data



same value with the inside wheel on the first shaft. We can get the objective function by calculating the difference between the ideal angle and the corresponding actual one, giving their appropriate role by making a sum of squares.

Weight is determined by the frequency of  $\lambda$ . In this paper, when  $\lambda \in [1\ 20]$ ,  $\text{weight}(\lambda) = 1.5$ . When  $\lambda \in [21\ 35]$ ,  $\text{weight}(\lambda) = 1$ . When  $\lambda \in [36\ 45]$ ,  $\text{weight}(\lambda) = 1.5$ .

### 3.2.3 Constraints

Taking the actual situation of semi-trailer into consideration, we divide the constraints of optimization into two parts.

Part 1: According to the real size of the semi-trailer, here we set some constraints to the steering trapezoid. The values of its structural parameters are just allowed in a certain range. Then there will no interference between steering trapezoids and axes or frames.

Part 2: Restrain the transmission angle of steering trapezoid. The minimum transmission angle is not less than  $20^\circ$  and ensures good stress state.

### 3.2.4 Optimize Programs

With the help of MATLAB optimized tools [5], the steering mechanism is optimized. The flow chart of steering optimal program is shown in Fig. 9. It is easy to solve the ideal steering angle. Just set a deflection angle, and then we can calculate the ideal deflection angle of each wheel using the basic knowledge of plane geometry. The steering trapezoid should be used to find out the actual angle. Three parameters are needed to keep the ladder stable. Then actual angle can be obtained through the help of sine theorem and Cosine theorem. And then import into the objective function respectively, after this we can get the optimal solution by optimized the function.

### 3.2.5 Optimization Results

Counting from the tail, from one to four, it is in the same side of the wheelbase centerline and shift toward the same direction. The fifth and sixth axes are fixed and not steering. The seventh axis is on the other side of the wheelbase centerline, turning toward the contrary direction. The original values of each axis in objection function are: 931.75, 388.4, 743.2, 46.6, 3081. After optimization, the objective function values are: 5.61, 4.0, 21.87, 33.5. Optimization results are shown in Fig. 10.

Horizontal represents the steering angle of the board. Longitudinal coordinate stands for the ideal angle and the optimized real angle. We can see that the optimized angles are much closer to the ideal angle. The first and second shafts

have the best results. The actual angle and the ideal angle are very consistent. The result of the seventh axis is relatively poor. This is because the steering axes are closer to the center line and the ideal corner slants small. This trend is consistent with the optimal results in other related articles.

## 4 Conclusion

The wheeled semi-trailer is mainly used for mobility with caterpillar heavy equipment. It is convenient and flexible to transport caterpillar heavy equipment to the reserve area just rely on the road. With the continuous development of mobile operation, wheeled semi-trailer attracts the growing attention in the force where equipped mobile supports are needed. This article is based on a scale model of a wheeled semi-trailer. A preliminary model through the reverse engineering is built. And then the detailed design is given on the bases of Digital Mock-Up. Finally, the design of semi-trailer steering mechanism is optimized and the multi-axis steering problems are tentatively solved, which would provide a useful reference for the future development of the wheeled semi-trailer.

## References

1. Chen X (2009) Reflection on the development of military wheeled vehicles. *J Acad Military Transp* 1:1–5
2. Tao J, Tong S (2003) Reverse engineering. China Machine Press, Beijing
3. Huang ZW (2002) The research of digital mock-up technology and engineering applications based on CATIA. University of Aeronautics and Astronautics, Nanjing, p 6
4. Li Y, Bao WJ, Zhang GF, Qiang Z (2006) Research on the development of digital mock-up based on CATIA. *Machinery* 5:30–31
5. Huang H-H, Chen C (2002) Optimized design of integral steering trapezium with MATLAB programming. *Guangxi Machinery*, 4:17–19/42

# The Concept and Methodology of Creating the Universal Life-Saver with Rotary-Screw Mover

Maxim Krasheninnikov, Anatoly Kulashov, Viktor Shapkin  
and Alla Koshurina

**Abstract** At the present time there is active development of oil and gas fields located offshore in the northern seas. Mineral resources are mined in severe natural and climatic conditions. This paper shows the analysis of accidents that occurred on the platforms, reviews existing means of evacuation, indicates solutions to some actual safety problems. This paper offers a universal life-saver with rotary-screw mover, which can effectively overcome various environments. Features of rotary-screw mover allow to use technological and transport means in such areas where the usage of other movers is impossible or irrational. However, the creation of such devices is possible only with relevant research; such studies are conducted by Nizhny Novgorod State Technical University named after R.Y. Alekseev. The article gives the general form of conceptual design of the machine for rescuing personnel from ice-resistant oil and gas platforms. Requirements to the design of life-saver devices are strictly regulated by normative documents. The article provides a methodology for determining the optimal size and constructive forms of rotary- screw movers depending on the weight of the machine and its destination, as well as areas of the machine's usage. A calculative program was created on the basis of this methodology. The program consists of three major "blocks". The first block is responsible for modeling a rotary-screw mover. This block takes into account all possible combinations of constructive forms of movers, and contains the algorithm of size variation for each structural element. Thus, all possible type-dimensional variants of rotary- screw movers are considered in the process of modeling. The second block allows simulating a variety of terrains, as well as their

---

F2012-E04-004

---

M. Krasheninnikov (✉) · A. Kulashov · V. Shapkin · A. Koshurina  
Automobile Institute, Nizhny Novgorod State Technical University named after R.Y.  
Alekseev, Russia  
e-mail: maks21118@mail.ru

combinations. It also considers the forces and occurring processes, arising in the contact zone of a mover and terrain. The third block was responsible for the behavior of rotary-screw machine. Thus, the program allowed to define two important things: the best parameters of a mover according to the given conditions, and identifying the character of each option's influence on the traction-speed parameters of the machine. To verify the size of mover have been made strength calculations. At the same time the least reliable design solution was chosen. As a result, recommendations on constructions of a rotary-screw mover in various conditions were obtained. The optimal ratio of the size of mover for driving on snow cover is given as an example of recommendations. These research's results are not limited by creating life-saver devices, but may also be applied to the creation of other special vehicles. However, determination of optimal parameters of a mover is based on the uncontrolled linear movement of a rotary-screw machine simulation, which is obviously a drawback of the created model. That is why we plan to improve the model in future. The main aim of this article is to show the methodology for determining the optimal parameters of rotary-screw mover, and to show the first results of its implementation.

**Keywords** Methodology · Simulation · Optimization · Rescue vehicles · Rotary-screw mover

## 1 Introduction

Currently about 35 % petroleum and 32 % of gas produced in the world are taken from the offshore fields [1]. Since oil and gas reserves on the continental fields have been steadily decreasing, the question of oil and gas production from offshore fields is becoming more urgent. Work on these platforms is more dangerous than on ground complexes. It is connected with severer conditions in which minerals are extracted.

The most important role in ensuring the safety of these facilities is played by technical and technological innovations, as well as modern norms and rules controlling the procedure for conducting the operations and activities on the platforms. A good example of the implementation of modern safety standards was a system of self-regulation of oil and gas companies operating offshore. This system is used in Norway, Holland, Britain and some other countries. In addition to the efficiency feature of the reforms there is a tendency to focus on the reduction of accidents with serious and significant consequences alongside with a focus on the total exclusion of accidents. Transition of big oil companies to self-regulation has allowed to reduce the number of accidents with significant impact down to 1/3 of the previous number in the last 5 years [2].

But the remaining probability of major accidents calls for a reliable evacuation of personnel platforms. A review of the major accidents on oil and gas platforms

**Table 1** Some major accidents on the oil and gas platforms located on offshore area

The platform	The owner	Date of the accident	Location of the accident	Distance to shore (km)	Personnel of the platform	The number of lost people
Bohai-2	China petroleum department	25.11.1979	Bohai gulf between China and Korea	150	74	72
Alexander L. Kieland	Stavanger drilling	27.03.1980	The field Ekofisk in the North sea	320	212	123
Ocean ranger	Mobil	15.02.1982	The North Atlantic	267	84	84
Piper alpha	Occidental petroleum	06.07.1988	120 miles northeast of Aberdeen, England	310	224	167
Mumbai high North	Oil and natural gas corporation	27.07.2005	Mumbai coast, near the town of Maharashtra, India	150	384	362 people were damaged and 22 perished
Deepwater horizon	Transocean (Switzerland)	20.04.2010	Mexican gulf	84	126	17 people were damaged and 11 perished
Kolskaya	Arktikmor neftegaz razvedka	18.12.2011	Region of the Sakhalin island	200	67	53

will determine the prevailing risk factors that need special attention when designing life-saving equipment (Table 1).

In the period from 1965 to 2012, i.e. over the past 47 years, over 60 incidents have occurred on oil and gas platforms in which at least 670 people perished and 93 people were seriously injured.

## 2 Consequences of Accidents and Causes of Crashes

Review and consideration of the character of most major accidents on oil and gas platforms, points out the following risk factors (hazards): 1. Weak control over the state technological systems and the state of the process, as well as the situation in the rooms and compartments of the platform; 2. Weak monitoring of the dynamic parameters of the system “platform—anchoring devices—borehole machinery”; 3. Lack of emergency management systems that could impact the condition of technological systems and platforms as a whole in the event of loss of control over the standard control system; 4. Dangerous and uncontrolled maneuvering boats in the vicinity of the platform; 5. The impact of wave and wind not taken into account in designing, leading to tensions exceeding the permissible values; 6. Loss of use of regular rescue facilities in emergency situations; 7. The lack of ships and rescue squads in the area of a 15 min distance to the platform. According to the statistics of emergencies, this is the time interval needed for emergency crew to get the platform.

Among the major threat occurrence catastrophic consequences after accidents are:

1. Oil and gas emissions;
2. The sudden destruction of equipment and pipelines, as well as the supporting structures of drilling rigs and platforms;
3. Leakage of hydrocarbons from the serviceable equipment in combination with the wrong personnel actions;
4. Clash of the equipment, pipelines, and supporting structures of platforms with foreign objects such as ships or helicopters.

These analysis' results suggest that, along with the improvement of management systems and organization of work, special attention must be paid to ensuring the safety of platforms by technical means. We are talking about actual problem of timely, fast and effective evacuation of the personnel platform in case of emergency.

## 3 Arctic Shelf and Modern Means of Escape

It is known that the most perspective water areas on the possibility of creating oil and gas production facilities, are the Arctic Sea, which accounts for more than 85 % of potential oil and gas resources [3]. The main areas of concentration of hydrocarbon resources in the Barents are (3.8 billion tons), Kara (4.7 billion tons), the East Siberian (2.1 billion tons) and the Sea of Okhotsk (2.1 billion tons) Sea [3].

Characteristic arrangement of conditions for Russian oil and gas platforms may be considered on the example of the Shtokman field in the Barents Sea (Fig. 1).

**Fig. 1** Arrangement of the Shtokman field



**Fig. 2** Oil and gas platform in the ice cover



Compilation of submissions of various organizations allows us to formulate the following main characteristics operating conditions extractive equipment in the Shtokman field. Distance to the continent 680 km; water depth 320–350 m; duration of the polar day, 102 days; low visibility due to fog, precipitation, blowing snow and low clouds; maximum wind speed 49 m/s; fluctuations in water level from +90 to –125 cm; maximum flow rate: 0.9 m/s—on the surface and 0.3 m/s—at the bottom; the maximum wave height 24 m; the maximum ice thickness 1.2 m. At operation of drilling equipment icebergs posing a danger must to blow or take away to the side to avoid collision with the rigs.

Requirements to platforms are determined by external conditions of their operation (Fig. 2). Meeting these requirements is instrumental to the optimality of designing, technical and environmental safety, and general decline the cost of field development.

As seen from the Shtokman field conditions characteristic feature of Russian Arctic shelf is the presence of ice cover. Therefore, widely used in the world saving means not satisfy the conditions of Russia.

**Fig. 3** Aerial evacuation mean



**Fig. 4** An example of an inflatable life raft for evacuation



The use of aerial evacuation (Fig. 3) on oil and gas platforms in the offshore zone of the Arctic will be limited because of the strong and gusty wind, and the emergence of powerful air currents rising up from the burning oil stains that may arise in the event of an accident. The helicopters could not accommodate the entire staff of the platform. For the evacuation of personnel required at least 6–7 units of equipment while on the platform has only one heliport.

The use of life rafts (Fig. 4), used together with a special system of descent (Fig. 5), will also be ineffective, because these rafts could not move in the Arctic seas and ensure the necessary level of safety.

The use of lifeboats (Fig. 6) will be limited because of their functional limitation of motion in the water, as well as a high probability of freezing in case the boat stops. They need to bypass the ice fields, which is not always possible. The boats are not designed for movement on an ice surface. The use of the lifeboats would not be rational in case of frostbite platform.

Consequently, there is a need to develop life-saving equipment, adapted to the northern seas.



**Fig. 5** Means of transporting people from the platform onto life rafts



**Fig. 6** Lifeboat



#### **4 Universal Life-Saver with Rotary-Screw Mover**

Demands for life-saver equipments based on the review of conditions of the location of Russian oil and gas platforms are formulated. In general, life saving equipment for the Arctic must: 1. Operate under low temperatures, ice, strong wind, storms and poor visibility; 2. Owning a high passability in different environments and amphibious qualities; 3. Have a large reserve buoyancy and stability curve; 4. Be able to overcome the stains of burning oil; 5. To support the regime of autonomous work for several days.

**Fig. 7** Demonstration of output to the ice machine with rotary-screw mover GPI-72



In this situation it is necessary to consider the use of vehicles, movers of which possess distinctive character of interaction with a supporting surface. Among the floating machines the ones with rotary-screw mover (RSM) occupy a special place. The features of this mover allow to use technological and transport means under different operating conditions, where the use of other types of movers is impossible or inefficient. The rotary-screw mover would allow movement in freezing waters throughout the year and conduct evacuation of people in case of accidents in the Arctic regions (Fig. 7).

A distinctive feature of the rotary-screw mover that combines the quality of hydraulic movers and onshore movers is the fact that it can work effectively in the highly water-logged soil, snow, ice, water and surface, which is a combination of these environments. The rotary-screw mover is used on the machines for different purposes—road construction, agricultural, military, etc. For example, in Russia, rotary-screw mover is used in heavy and powerful machines for cutting the ice and on light cross-country vehicle. In the U.S.—on military armored personnel carriers to move through the swamps and flooded fields. In Poland, the rotary-screw mover is used on a special towing vehicle for movement on a thick layer of silt on fish farms. In Japan, rescue and recreational vehicles with the rotary-screw mover are made.

In particular, the Japanese company Mitsui built a few rotary-screw vehicles (RSV), one of which is specially designed for the movement in Arctic ice off Alaska. Testing has shown that the machine on ice thickness of 30–50 cm reached the highest maximum traction ratio (the ratio of thrust to weight ratio) that equaled 45 % with an inclination of the helical blade 30 degrees and with a ratio of height of the helical blade to the diameter of base cylinder as 0.15. The machine had a mass of 10.8 tons and a length of 7 m. The engineers of Mitsui gave the following results: the machine can tow loads of 200 tons on water at a speed of 3 knots, on the ice—a speed of 25–40 knots, the machine can move in ice covered with water over 50 cm, where any other machine and ship cannot move, the machine breaks the ice thickness up to 43 cm.

Compared with other types of ground rotary-screw mover propulsion has many advantages [4]: 1. Ensures a particularly high cross vehicle; 2. Creates a very low

ground pressure; 3. Provides huge traction; 4. Provides output to ice and unequipped shore; 5. Provides amphibious qualities.

Experience of using a rotary-screw mover on the amphibious transport technological machines and ice-breaking machines shows the perspective of development of autonomous universal machines and the rescue funds should help the distressed vessel crews and staff of ice-resistant stationary platforms.

## 5 The Concept of the Universal Life-Saver

In Figs. 8 and 9 shown the developed in NNSTU project of universal life-saver with rotary-screw mover and conditions of use.

After determining the operating conditions and constructional features the existing rescue facilities for evacuation from oil and gas platforms on the continental shelf of the Arctic seas formulated the basic concept of a universal funds rescue.

Designed life-saver device is a rotary-screw floating machine with the following parameters: Dimensions: Length 12 m; Width 6 m; Height 4.5 m. Draught at full load 1.0 m. Gross weight 10 tons. Capacity 42 person (two person crew). The rate of ice—up to 35 km/h; snow—up to 40 km/h; water—up to 7 km/h. The diameter of the cylinder rotary-screw mover 1.2 m. The length of rotary-screw mover 9.0 m. The height of the helical blade 0.2 m. Road clearance 0.5 m.

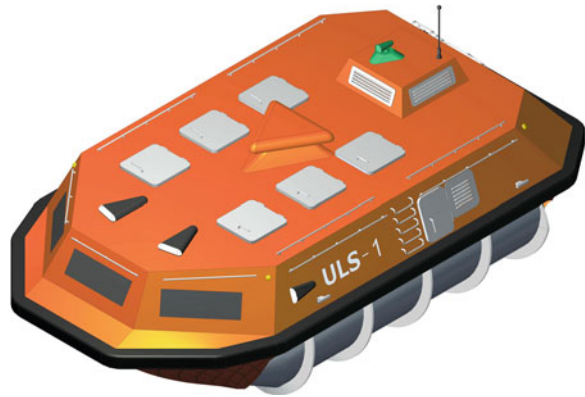
The machine can move from the area of burning oil due to isolation corps heat-resistant tiles. Such tiles are used on the hulls of space shuttles. Determination of the environment is provided by the usage of systems of technical vision. Autonomous operation for several days is achieved through the use of life support systems. A distinctive feature is the use of machine vision systems and systems of the autopilot. These funds will help to evacuate in an automatic mode and reduce the workload on the crew.

## 6 First Steps of Creation: Simulation

Of course the creation of such vehicles which could move in difficult conditions (non-cohesive grounds, snow, ice, water and a combination of these media) is impossible without research in relevant fields. Such studies will include the mathematical modeling of various processes. It helps on the one hand to develop and verify in practice the theory of motion rotary-screw machines and the other to get due to this theory, the recommendations for the design of modern transport and technological machines for special purpose.

Obtained in the course of the project mathematical model the motion RSV will be a system of “terrain-vehicle” [5], which in general is the union of the following models:

**Fig. 8** Model of the universal life-saver with rotary-screw mover



**Fig. 9** Illustration of the operating conditions of the universal life-saver with rotary-screw mover

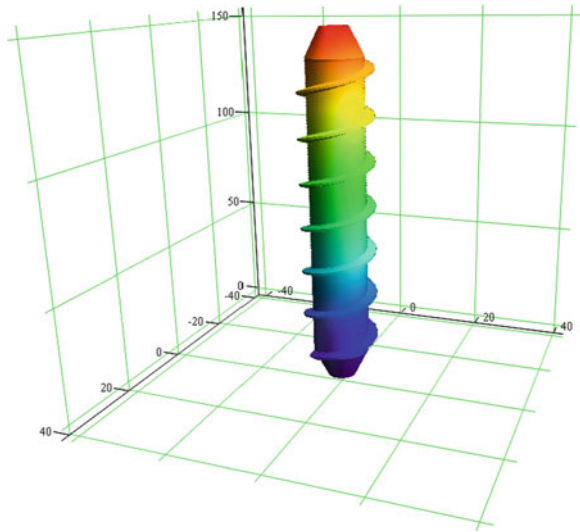


1. Model of the rotary-screw mover;
2. Model of different movements environments, taking into account their possible combinations;
3. A model that describes the characteristics and behavior of the machine.

Model of the rotor will be the set of equations of its surfaces. It is advisable to divide it by the following entities: the surface of the base of the cylinder, the surface of the rotary-screw blade, the surface of the tip of the rotor (with rotary-screw blade and without) the surface of the ends of the rotor, middle surface to describe the two-cylinder rotor (Fig. 7). This decomposition allows to obtain a very accurate description of the rotor surface.

In addition to the separation of one-and two-cylinder rotaries, this mover can have different ends (conical, spherical, parabolic shape, as well as combinations thereof), the different helical blade (triangular, trapezoidal and sheet) and may be a multistart (till 3–4 helical blades). In general, the model of the rotary-screw mover, such as single-cylinder (Fig. 10), or rather its surface, is a generalization of the helicoid. The surface is determined by a system of parametric equations (for a Cartesian coordinate system) of the form:

**Fig. 10** The result of the construction of the surface single-cylinder screws on the basis of the parametric equations



$$\begin{cases} X = f(r) \cdot \cos[f(P)], \\ Y = f(r) \cdot \sin[f(P)], \\ Z = f(h) \cdot \frac{f(P)}{2 \cdot \pi}. \end{cases} \tag{1}$$

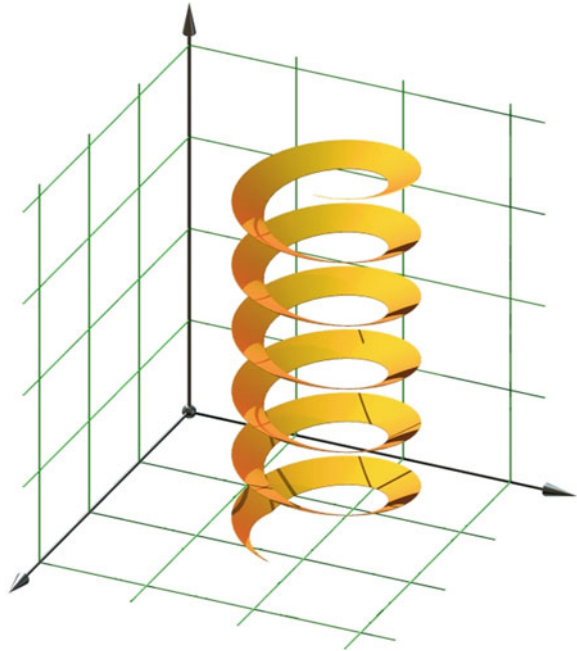
$f(r)$ —function of changing the distance from the axis of symmetry;  $r$ —the specified range of the radius;  $f(h)$ —function changes the height of the being constructed figure;  $h$ —range of changes of height;  $f(P)$ —function that determines the shape of the figure in the plane perpendicular to the axis of symmetry;  $i, j$ —the parameters of the equation, which are not shown in the formula of general form.

In particular, the system of parametric equations which describes the surface of one side of the helical blade (Fig. 11) looks like:

$$\begin{cases} X = (r + h \cdot i) \cdot \cos\left(\frac{L_B}{P} \cdot 2\pi \cdot j - \frac{t_O - t_B}{P} \cdot \pi \cdot i\right), \\ Y = (r + h \cdot i) \cdot \sin\left(\frac{L_B}{P} \cdot 2\pi \cdot j - \frac{t_O - t_B}{P} \cdot \pi \cdot i\right), \\ Z = L_H + L_B \cdot j. \end{cases} \tag{2}$$

$r$ —radius of basic cylinder;  $h$ —height of helical blade;  $L_B$ —length of basic cylinder;  $P$ —pitch of helical blade;  $t_O$ —thickness of helical blade at the base;  $t_B$ —thickness of helical blade at the vertex;  $L_H$ —length of part of the rotary-screw head.

**Fig. 11** The surface of one side of the helical blade



### ***6.1 The Technique of Modelling***

These systems of mathematical equations will take into account the effect of each structural element rotary-screw mover (its shape and size) to the traction-speed parameters of the vehicle. The idea is to determine the direction of normals and tangents to the surface of RSM. Forces and reactions which act on the rotor will operate on the directions of these normals and tangents. Thus, the presence and influence of RSM on the motion of vehicles is taken into account in the mathematical model by simulation of the processes that occur in the area of contact with the mover and supporting surface. The model allows setting the various forms of structural elements and their sizes, such as length and diameter of the base of the cylinder, the shape and size profile of the helix, and the angle of winding, and many others. The RSM model is the first block of simulation model of the rotary-screw vehicle.

The second block of the mathematical model is responsible for the simulation of physical–mechanical properties of the supporting surface. Type of supporting surface determines the character of dependences “load-sludge”, “load-shift” and determines the value of frictional force with mover. Simulation of viscous and fluid supporting surfaces, such as a swamp or the water is in a stage elaboration. Of particular interest is the simulation of snow cover. This is due to the fact that the snow is one of the major work environments for the rotary-screw vehicles. Also, the character of dependence “load-sludge” and “load-shift” for the snow is strongly dependent on the density, temperature, humidity and thickness of snow cover [6].

In particular, for describing the deformation of the snow from the vertical load used the equation of Malygin [7]. This Eq. (3) was obtained after processing a large number of experimental data and has been repeatedly confirmed in practice and is widely used by researchers of Nizhny Novgorod scientific school.

$$h = \frac{q}{\left[ \frac{(b+0.0287H^{1.5})}{H \left[ 0.0287H^{1.5} + \frac{ab}{\rho_0+a} \right]} \right] q + 0.735K_g} \tag{3}$$

$h$ —immersion into snow (m);  $q$ —pressure on the snow (1 MPa = 106 N/m<sup>2</sup>);  $b$ —width of the stamp (m);  $a$ —constant equal to 0.3 g/cm<sup>3</sup>;  $K_g$ —stiffness coefficient of snow (N/m<sup>3</sup>);  $\rho_0$ —snow density before deformation (g/cm<sup>3</sup>); 0.735—coefficient of proportionality; 0.735 •  $K_g$ —coefficient of the initial stiffness of snow.

The third block of the model is responsible for the behavior of the rotary-screw vehicle and it combines other blocks. In this block the center of gravity and moments of inertia of the rotary-screw vehicle are set. Also in this block the positions of movers and the principal scheme of a vehicle are determined. After determining the various parameters of a mover, parameters of a vehicle and parameters of the supporting surface the calculations and comparison of results are made. It allows choosing the best design solution and choosing the best concept for a specific type of supporting surface. Thus, the mathematical model allows us to optimize the design and get recommendations.

It is noteworthy that the results of the first calculations showed the efficiency of using the rotary-screw mover with sheet-form helical blade. This is due to the fact that this form of mover will have less surface contact with the ground and therefore have a lower energy cost to overcome the frictional force. Moreover, this form allows us to develop large traction efforts. However, this solution has an undeniable disadvantage of structural strength. Mover with this form there would be a breakdown in the fastening of the screw blade and the base of the cylinder.

Further refinement of the model allowed us to obtain more realistic results. The calculations showed that the triangular shape of the helical blade is the optimum from the standpoint of strength and traction effort. Credibility of the triangular shape is confirmed in practice with rotary-screw vehicles. This form of blade is the most rigid and allows to withstand heavy loads.

## 6.2 The First Results

As an example of recommendations received after calculations the optimal ratio of the size of the rotary-screw mover for driving on snow can be addressed. The most optimal form of the rotor ends is the parabolic shape. This form allows to reduce energy costs for the formation of a track. A range of rational combinations of

lengths and diameters of the rotors for speeding up are the following: with the rotor's length from 3.5 to 6 m, diameter in the extreme values of length should be—1/7...1/6 of rotor's length; with an exception for the length from 4.5 to 5.5 m where the diameter of rotor should be from 1/8 till 1/5 of rotor's length. The boundaries of this region are determined by the maximum slipping. To perform the rotation it would be rational to use ratio of the rotors length to vehicle's track width in the vicinity of 2...3. At 25–30 % (most common) slippage on the snow the angle of inclination of the helical blade rotors should not exceed 25°. On transport vehicles it is necessary to carry out turning with the maximum speed. At the design stage of technological machines it is necessary to prevent the displacement of the centre of gravity of more than 0.3 m of the machine. For all types of snow cover the preferred scheme to reduce the withdrawal from the trajectory is to use a single-cylinder mover with a direction of rotation of the rotors called "under themselves". Withdrawal from the trajectory of those machines will be less at any snow density and at any difference between rotating moments on the movers. For transport vehicles it is recommended to use the rotary-screw mover with single basic cylinder. RSVs with single-cylinder movers have more linear dependence of the rotation angle on the difference of moments (more controllable), and rotates at a greater angle on packed snow (density of 0.5 t/m<sup>3</sup>) at low speed rotation. With increasing speed this advantage decreases and RSV with single-cylinder movers can make smaller angle turns than the RSV with two-cylinder movers. On a machine with a single-cylinder mover it is recommended to perform the rotation at lower speeds than on a machine with two-cylinder movers.

These research's results are not limited by creating life-saver devices, but may also be applied to the creation of other special vehicles. However, determination of optimal parameters of a mover is based on the uncontrolled linear movement of a rotary-screw machine simulation, which is obviously a drawback of the created model. That is why we plan to improve the model in the future and add a control action.

## References

1. Osadchy A (2006) Oil and gas of the russian shelf: estimates and projections. *J Sci Life* 7
2. Mokrousov S (2006) Security issues in the development of oil and gas resources on the continental shelf and on land of the Russian Federation. *J-directory Transp Secur Technol* 1
3. Bohatryyova E (2004) Methods of ensuring the safety of oil and gas platforms of the Arctic shelf. Dissertation of candidate of technical sciences, Moscow
4. Kulashov AP, Shapkin VA, Donato IO and other « Screw machine (2000) Fundamentals of the theory of motion »>. Nizhny Novgorod: NNSTU, 451
5. Bekker MG (1973) Introduction to terrain-vehicle systems: Trans. from English/Ed. VV Guskov. Mashinostroenie, Moscow, 520
6. Shapkin V (2001) Fundamentals of the theory of motion machines with rotary-screw mover on snow-covered terrain. Dissertation of doctor of technical sciences N.Novgorod, 219
7. Malygin V (1970) The study of the deformation process of snow under influence of track and the rationale for selecting the size of the track reference surface of the snowmobile machines. Dissertation of candidate of technical sciences. Gorky, 250



# Research on the Development Procedure of Light-Weight New Body Architecture

Xiangyang Fu, Guohong Shi, Xin Jiang, Yunhui Duan  
and Zhengchao Song

**Abstract** This research focuses on how to develop a new, light-weight body architecture efficiently. And the full-procedure light-weight design method for new body architecture was studied and the technical approaches for light-weight research were further exerted. The process of body architecture design development can be divided into two phases: conceptual design phase and detailed design phase. Conceptual design phase can also be divided into concept selection phase and concept optimization phase. In the phase of scheme selection of conceptual design, the key load paths of the total vehicle and body architecture are developed by ways such as topology optimization, section load analysis and so on. In the phase of conceptual design optimization, shape and dimension are optimized by Multidisciplinary Optimization (MDO) based on the methods of Design of Experiment (DOE) and Approximation Model, and also the region-dividing optimization, so that the multi-objective of total body architecture is optimized. In the phase of body architecture detailed design, the body architecture and its subsystems are totally optimized by using all kinds of methods comprehensively and the best combination of materials, section shape, dimension, position and thickness are generated. Through the flow of the three phases, a light-weight and efficient body architecture comes out in the paper which is 9 % lighter than its previous generation.

**Keywords** Body architecture · Conceptual design · Detailed design · Light-weight · Optimization

---

F2012-E04-005

---

X. Fu (✉) · G. Shi · X. Jiang · Y. Duan · Z. Song  
Pan Asia Technical Automotive Center Co., Ltd, Shanghai, China  
e-mail: xiangyang\_fu@patac.com.cn

## 1 Introduction

Safety, environment protection and energy consumption are major challenges which modern automobile industry confronts. It's important task to improve fuel economy, reduce emission, reinforce architecture and improve crashworthiness by reducing vehicle weight. It's said according to statistics that fuel consumption can be reduced by 6–8 % while reducing 10 % of total vehicle weight [1]. For ride performance, if the vehicle gets lighter, acceleration time gets shorter, the vehicle gets more stable and NVH performance also gets better. For safety performance, the braking distance also gets shorter and inertia gets smaller during crash. For this reason, vehicle light-weight and new energy are considered the two major energy-saving themes of automobile development.

Body architecture weight accounts for 30 % of the whole vehicle weight. So, body architecture light-weight is the key point of vehicle light-weight. There are many achievements on light-weight research and application such as topology optimization [2] and [3], shape and dimension optimization [4–10]. The complex body architecture optimization should satisfy multi-disciplinary constraints such as NVH, safety, architecture stiffness, durability and vehicle dynamics requirements [11]. In order to realize body architecture light-weight, the knowledge of mechanics of materials, structural mechanics, algorithm technology, manufacture technology is required.

The current foreign and domestic researches on vehicle light-weight considered rarely on the multidisciplinary effects, and the multi-effects resulted from multi-aspects comprehensively such as optimizing the gauge and strength of a part without considering the shape of this part. For this reason, the light-weight design is not the optimum of the whole architecture and the potential of light-weight design is not yet developed.

In order to improve the light-weight depth of body architecture, the ideology of light-weight must be applied to all the phases of body architecture design and the light-weight technology must be used flexibly and comprehensively. In this paper, the concept of full-procedure body architecture light-weight is proposed as follows. At the beginning of conceptual design and scheme selection phase, use the method of topology optimization and load analysis to produce efficient body architecture. During the phase of concept optimization, realize the multi-objective optimization of the whole body architecture through MDO and region-dividing optimization process which are based on DOE and Approximation Model. During the phase of detailed design, optimize the body architecture and all of the sub-systems or even parts to make weight optimal within reasonable cost scope.

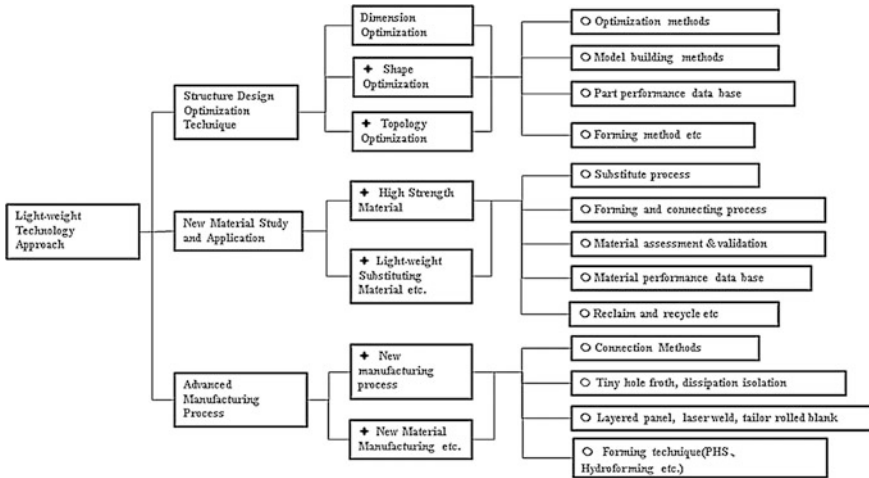


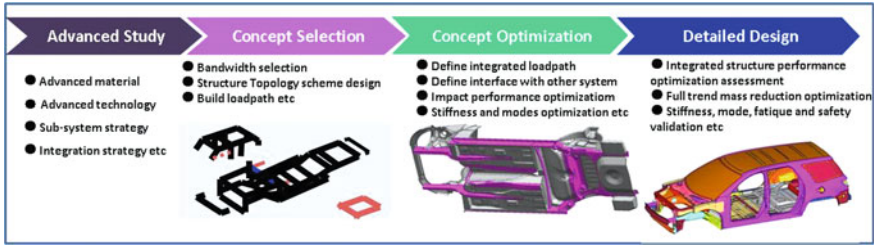
Fig. 1 Approaches of light-weight research

## 2 Procedure of New Body Architecture Light-Weight Development

### 2.1 Approaches of Light-Weight Research

The approach to vehicle light-weight consists of three major aspects: architecture design optimization, new material application and advanced manufacture process. The approaches of light-weight and the fundamental studies leading to them are summed up in Fig. 1. Architecture optimization design is using CAE simulation and optimization technology to research on the architecture (body architecture, chassis, etc.) light-weight without sacrificing the performance of the whole vehicle. It includes the researches on the matching of different light-weight materials, optimal shape and dimension of parts and so on. New material application is to reduce weight through material replacement or new material usage. As to material replacement, the materials with low density and high strength such as Al-Mag alloy, plastic polymer, ceramic materials and high strength steel materials with same density, same modulus of elasticity but small gauge and good manufacturing performance are prior alternatives. As to advanced manufacture process, light-weight materials manufactured by new technologies such as tailor rolled blank (TRB), tailor welded blank (TWB) and metal matrix composite can also lead to vehicle light-weight.

Among all kinds of body architecture optimization methods, topology optimization is considered a whole-architecture-oriented and effective method to explore optimal material distribution in given design space [11]. Dimension and shape optimization is for the optimization of an existing architecture through innovative improvement or modification methods. Dimension optimization mainly focuses on



**Fig. 2** Major process of body architecture design

weight reduction by decreasing part gauges. It's simple but very effective because it deals with many thin-gauged sheet metals. Architecture optimization design can exert its ability to the maximum degree once new material application and advanced manufacture process are considered together.

## 2.2 Process of New Body Architecture Design Development

Generally speaking, the process of body architecture design development can be divided into two phases: conceptual design phase and detailed design phase. Conceptual design phase can also be divided into concept selection phase and concept optimization phase as shown in Fig. 2.

In advanced research, the studies on advanced light-weight architecture, material and manufacture process are very important because they are the foundation and very decisive to the light-weight degree of the whole architecture. During the phase of conceptual design, it focuses on the design of architectural parts. The non-architectural parts like outer cover panels and floor panels can carryover the design of the other similar vehicles for design analysis. The light-weight design of these non-architectural parts is performed later in the detailed design phase.

## 2.3 Procedure of New Body Architecture Light-Weight Design

The process of body architecture light-weight design is shown in Fig. 3. The methods of topology and load analysis are used to explore the main architecture and key load paths of body architecture.

During concept optimization phase, the key load paths and architectures are designed and optimized in detailed. At the level of the whole body architecture and subsystems, the part shape, position, section size, gauges and material strength of the key load paths and architectures are optimized and the optimum of mass reduction is generated. The application of light material such as high strength steel,

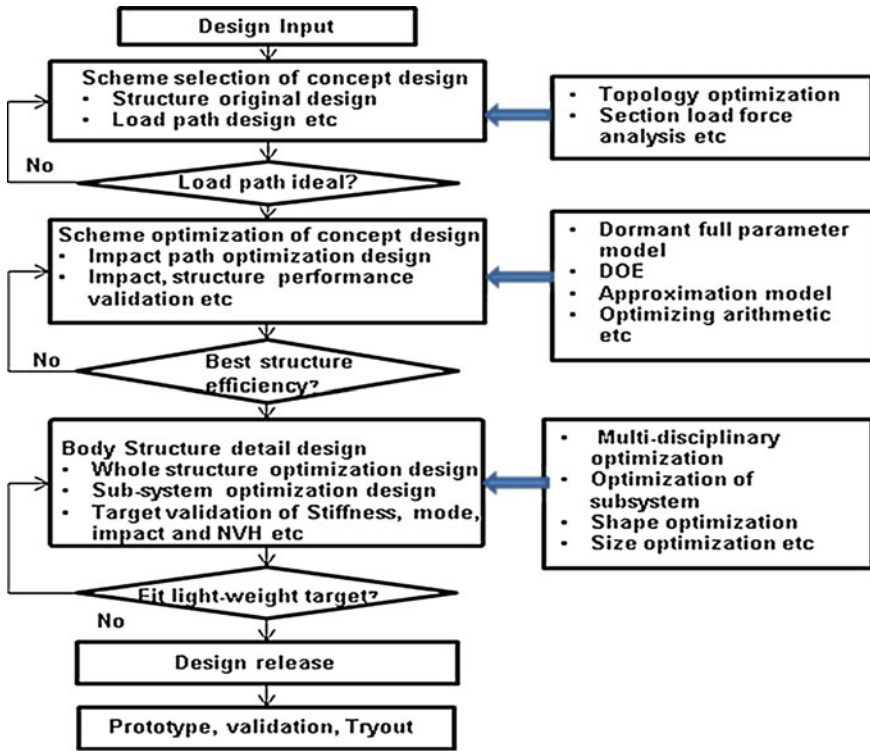


Fig. 3 Process of body architecture light-weight design

Al-Mag alloy and the application of light-weight manufacture process are also very important in this phase. During the phase of detailed design, body architecture is comprehensively and thoroughly optimized to get optimal mass within reasonable cost scope.

### 3 Scheme Selection of Conceptual Design

#### 3.1 Topology Optimization Design of Body Architecture

The phase of conceptual design is very important for the structural performance of body architecture because deficiencies in this phase are very difficult to be eliminated in the future. The main work of this phase is to design load paths to distribute impact load properly, satisfy global vehicle performance requirements and meet the weight target.

The load paths are mainly for front impact, side impact, roof crash, bending, torsional and so on. As people pay more and more attention on safety, the

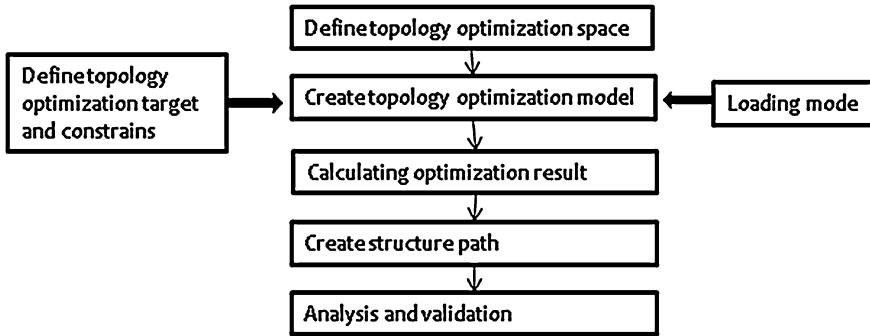
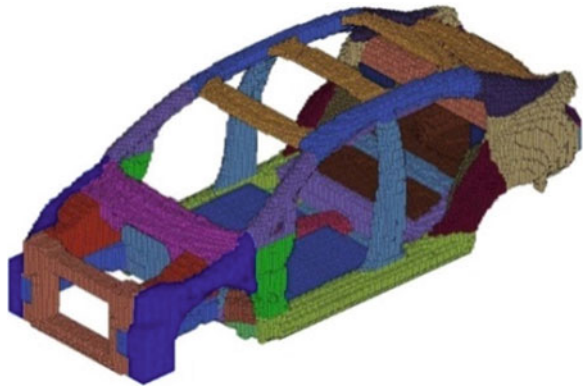


Fig. 4 Topology optimization process

Fig. 5 Generated topology space model



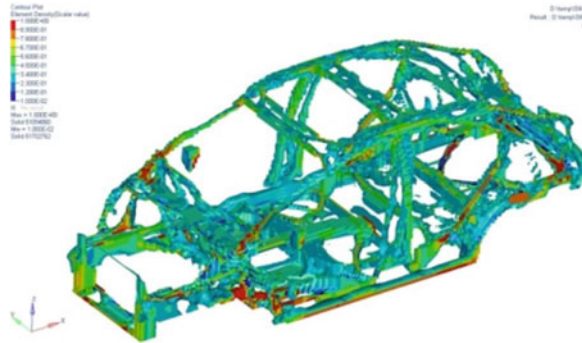
enhancing crashworthiness makes more requirements on load paths for impact. When the safety requirement is satisfied, it's relatively easy to satisfy structural performance requirement. So it's the key point of body architecture development to develop the crash load paths.

The topology optimization process of whole body architecture design is shown in Fig. 4. The topology space is generated from two kinds of constraints. One constraint is from the engine room and passenger room packaging requirements, the other constraint is from styling requirement. Figure 5 is the generated topology space of a passenger car and Fig. 6 is the topology optimization result.

### 3.2 Load Design of Paths

After finding out the proper load paths by topology analysis, it's going to study the proper loads of the paths and then develop the architecture of the paths. The front impact load can be generated as follows:

**Fig. 6** Topology optimization result



Expected Effective Acceleration:

$$EEA = V^2 / (2 * CS) \tag{1}$$

CS stands for Energy Absorbing Apce, V stands for Velocity.

Total crash load:

$$TCL = m * EEA \tag{2}$$

m is the weight of vehicle.

Loads of the paths are allotted by the value of EEA and experience as the start of structural design. The allotted loads of paths which are developed by topology optimization and the analysis of section force are shown in Fig. 7.

## 4 Optimization of Conceptual Design

### 4.1 MDO Based on DOE and Approximation Model

During the concept selection phase, loads and paths were decided. After building preliminary CAD model of body architecture, more optimization work will be done in concept optimization phase. It's impossible for the method of topology optimization to deal with a task with multi-disciplinary constraints because it takes too much time on non-linear FE analysis. So, in the concept optimization phase, shape and dimension optimizations combined with advanced material and manufacture process are the main methods to validate structural design and realize efficient architecture.

Body architecture light-weight design is a multi-parameter and multi-constraint engineering task [5, 12]. It takes much time to analyse only one impact simulation task, so the direct crashworthiness optimization will be very time-consuming. In every round of analysis, different precise CAE model is needed but the process of generating these models is not automatized. At the same time, engineer needs to

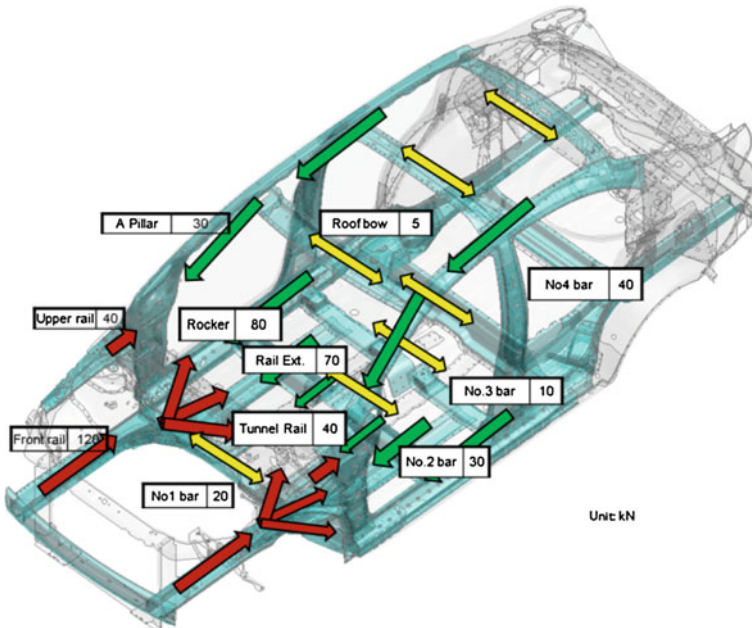


Fig. 7 Allotted front impact loads of paths

find out the inherent relationship between parameters in design space and performances. In order to realize the optimization, approximation model is built by DOE and the indirect optimization based on it is performed. The direct optimization is replaced with the indirection optimization through approximation model. In this paper, the MDO based on DOE and approximation model was used and the process is shown in Fig. 8.

In this indirect way, design variables, optimization space, optimization objectives, constraints, DOE method should be defined firstly. Then DOE array will be generated and FE models of body architecture are built according to the DOE array. Based on the analysis result of these FE models by high performance computers, approximation model is built. By analysis of variance (ANOVA) of the approximation model, we can know how the variables affect performance respectively. In the end, perform iterative optimization according to the load cases decided by light-weight requirements. The optimal body architecture design can be produced through comparisons of different optimization results.

When performing MDO, if we use conventional method to build FE models of DOE samples, it becomes very time-consuming because the body architecture to be parametric is assembled by several hundreds of parts. But through the implicit parametric method, engineers can get parametric models by defining the topology relationship among different geometries. By defining the relationship between models and DOE array, the architecture in the database can be modified



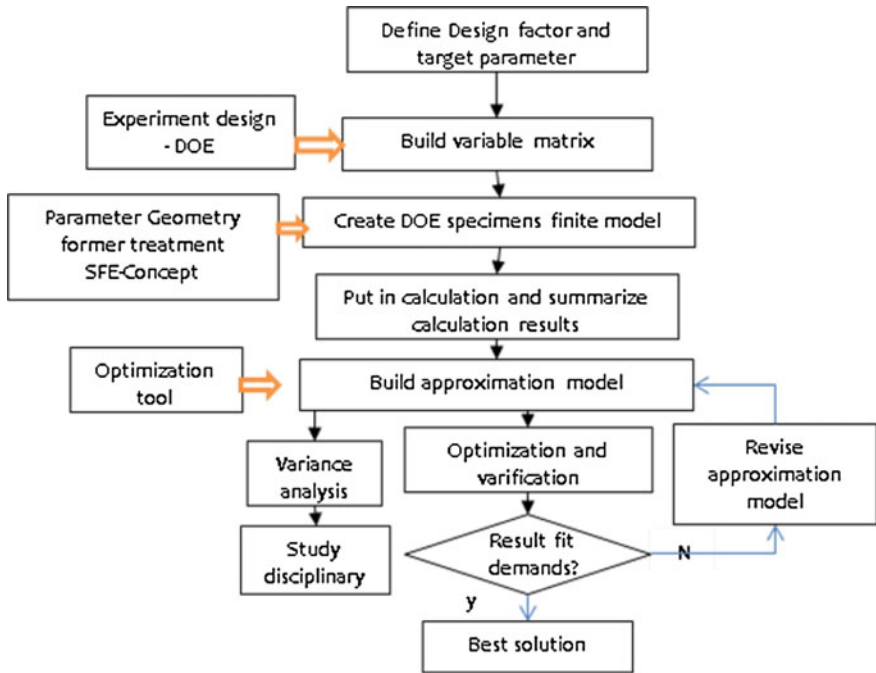


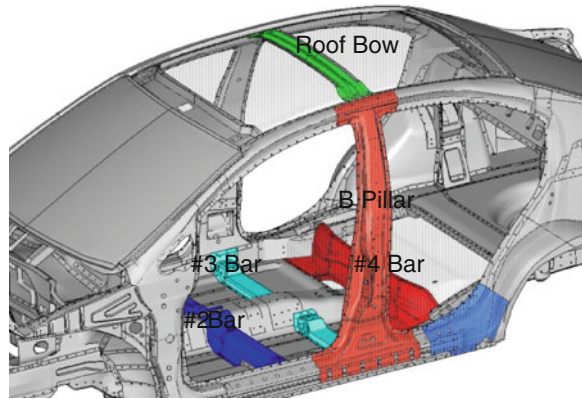
Fig. 8 Process of MDO

self-adaptively according to new geometry environment and the FE models are generated automatically. In this paper, SFE implicit parametric modelling method was used to build full parametric model of the whole body architecture and the FE models of DOE samples were generated rapidly.

### 4.2 Process of Region-Dividing Optimization

After built the full parametric model of body architecture, MDO is performed. In order to make the optimization more precise, more samples are required. This means the engineer will deal with enormous design variables and outputs and the time it cost will be out of control with limited computers. In this paper, the key point of optimization was focused on using the method of region-dividing optimization. Through this way, the amount of design variables and samples is properly arranged in order to save calculation and optimization time. Design variables in conjunct regions should be considered comprehensively. According to structural performance requirements and engineer’s experience, the body architecture was divided into three regions which affect front crashworthiness, side crashworthiness and rear crashworthiness respectively. Meanwhile, the stiffness

**Fig. 9** Side impact region in full parametric model of body architecture



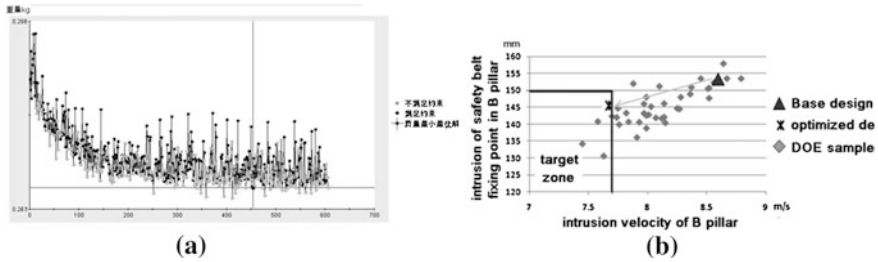
and NVH performance requirements of the three regions are considered. Then MDO will be performed.

Take the B pillar region's optimization which affects the side crashworthiness for example. The model of this region is shown in Fig. 9. The optimization objective is minimum weight of body architecture while satisfying all defined performance requirements. The variables in this example include the shape and gauge of rocker panel, shape and gauge of B pillar, position, material grade and gauge of reinforcement parts, shape, position, gauge of #2, #3 and #4 bars and so on. The load cases are 50 km/h Side Moving Deformable Barrier (MDB) impact, global bending stiffness, 1st global torsion mode and 1st global bending mode. Orthogonal Array, Kriging approximation model and Adaptive Simulated Annealing algorithm are used in this example. As the optimization result, the weight of the parts in this region reduces 2.2 kg (shown in Fig. 10a) while satisfying side crashworthiness (shown in Fig. 10b).

## 5 Detailed Design of Body Architecture

Through the body architecture conceptual design, a preliminary efficient body architecture design which can satisfy multi-disciplinary requirements such as BIW stiffness, mode and crashworthiness is developed. Then in the phase of detailed design, different optimization proposals are selected to develop refined, efficient and light-weight architecture.

In this phase, not only the whole body architecture but also the subsystems are comprehensively optimized. Not only are the subsystem optimization proposals considered, but also the evaluation and validation methods at the whole body architecture level are considered. At the same time, the optimization of subsystems contributes greatly to vehicle light-weight because proper material grade and gauge are deeply considered and strain energy distributes properly with weight



**Fig. 10** **a** Weight result of side crash region optimization. **b** Side crashworthiness optimization result

reduced [13]. The optimization objective of this phase is minimum weight within reasonable cost scope.

In this paper, several optimization proposals are used during detailed design phase:

- Closure and its subsystem optimizations through topology and size optimization;
- Optimization of certain regions by material gauge optimization which is universally used for light-weight optimization;
- Decrease the amount of output variables to save region-dividing optimization time. For example, optimize the parts in rear region only according to the load cases of rear impact and structural stiffness because these parts are not critical to front crashworthiness;
- Topography optimization of certain parts such as wheel house panel;
- Decrease optimization scope to get optimum within shorter time through direct optimization.

One example is detailed design of a car’s front architecture by material grade and gauge optimization which is shown in Fig. 11. Figure 11a shows the design variables which are the gauges of 23 parts. Optimization objectives: weight optimum; Constraints: intrusion and EA satisfy requirement; DOE: Orthogonal array  $L_{128}(4^{12} \times 8^{11})$ ; Approximation model: Kriging model; Optimization algorithm: Genetic algorithm. Figure 11b shows the optimization result of front architecture part gauges. It shows weight reduces 6.7 kg.

Figure 12 shows the topography optimization of rear wheel house panel. Improper design of this panel will cause NVH problems while good design of this region can reduce the gauge of this panel with satisfying NVH requirements.

Design variable: wheel house inner (shown in Fig. 12a);

Optimization objective: maximum the 1st mode of wheel house inner;

Constraint: height, width, draft angle and direction of beads in the panel;

In this example, use OptiStruct to calculate and the optimization result is shown in Fig. 12b.

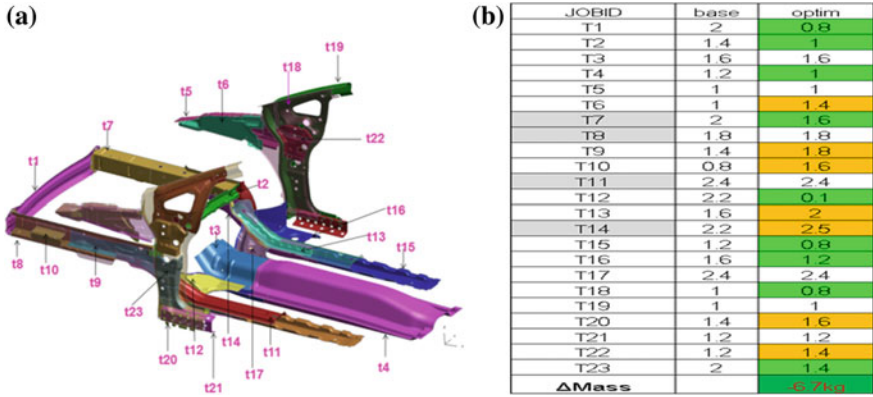


Fig. 11 a Optimization variations of front architecture. b Optimization result of gauge optimization

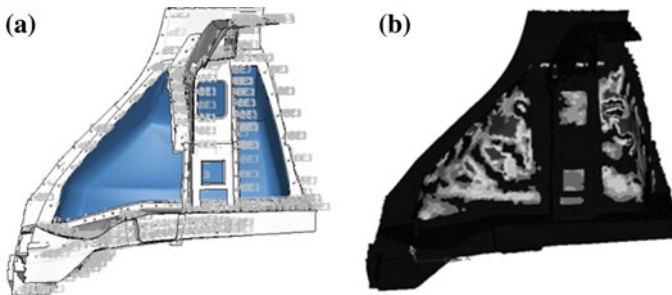


Fig. 12 a Design variables. b Topography result

## 6 Conclusions

- (1) The procedure of new body architecture light-weight design was developed in this paper. Advanced light-weight technologies are used in every design phase to make sure the efficiency of the body architecture design and make sure the result optimum;
- (2) During the phase of conceptual design and scheme selection, make sure the whole architecture's efficiency by topology optimization and the analysis of section load;
- (3) The shape, dimension, position, gauge and so on can be made into optimization variables used in full implicit parametric model. The potential of light-weight can be developed to the extreme through multi-disciplinary design process;

- (4) The fundamental light-weight researches shown in Fig. 1 are very important to light-weight degree. So the fundamental researches should be thoroughly studied. Meanwhile, the engineers should accumulate their experience so that the design variables can be properly selected and the whole structural property can be under control.

## References

1. Benedyk J (2000) Light metals in automotive applications. *Light Met Age* 58(10):34–35
2. Go Y, Zhou X, Yu H (2010) Topology optimization design of bus body architecture. *Technol Highw Transp* 27(9):154–157
3. Zhigang X, Zhongqing L, Laimin W, Hao W (2007) The body architecture light-weight by level set topology optimization. *J Shanghai Jiaotong Univ.* 41(9)
4. Jung B, Yang C, Xu S (2007) Early architecture concept exploration using topology optimization. General motors corporation. GM Global CAE conference
5. Xu S (2007) Use of topology design exploration and parametric shape optimization process to development highly efficient and light-weight vehicle body architecture. General motors corporation. GM Global CAE conference
6. Pan F, Zhu P (2010) Application of a weighted average surrogate to light-weight design of automotive front side rail. SAE technical paper 2010-01-0395. doi:[10.4271/2010-01-0395](https://doi.org/10.4271/2010-01-0395)
7. Shi G, Chen Y, Yang Y (2012) Research on application of multidisciplinary design optimization for biw light-weight design. *J Mech Eng* 48(8):110–114
8. Zimmer H, Prabhuwaingankar M (2009) Topology & geometry based architecture optimization using implicit parametric models and LSOPT. 7th European LS-DYNA Conference, May 14th-15th 2009. Salzburg
9. Jiang X, Chen Y, Shi G, Jiang F (2010) Body-in-white architecture optimization in early phase of development. *Automot Eng* 32(8):682–685
10. Lan F, Zhuang L (2010) Study and practice of car body architecture light-weight design. *Automot Eng* 32(9):763–768
11. Deb A, Chigullapalli A, Chou C, Dutta U (2011) A practical approach for cross-functional vehicle body weight optimization. SAE technical paper 2011-01-1092. doi:[10.4271/2011-01-1092](https://doi.org/10.4271/2011-01-1092)
12. Kodiyalam S, Yang RJ, Gu L et al (2004) Multidisciplinary design optimization of a vehicle system in a scalable, high performance computing environment. *Struct Multidisciplinary Optim* 26(3/4):256–263
13. Shaw J, Kuriyama Y, Lambriks M (2011) Achieving a light-weight and steel-intensive body architecture for alternative powertrains. SAE technical paper 2011-01-0425. doi:[10.4271/2011-01-0425](https://doi.org/10.4271/2011-01-0425)

# Control and Simulation of Regenerative Suspension Using Permanent Magnetic Synchronous Motor

Weihua Wang and Songshan Liu

**Abstract** Regenerative damper is used to recycle the suspension vibration energy with motor. Compared with other kinds of motors, PMSM has advantages to be used in regenerative damper. The detailed regenerative suspension model is established in Matlab/Simulink. Simulation results on C level road show that the motor controller can make the regenerative motor output torque accurately follow the reference motor torque change. The battery current and regenerated power is negative which indicates the motor recover energy from suspension vibration. And the inertia force has little influence on regenerative damper output force attributed to small PMSM motor inertia.

**Keywords** Regenerative · Suspension · PMSM · Control · Simulation

## 1 Regenerative Suspension Structure

Regenerative suspension is a novel kind of suspension. Just as conventional hydraulic suspension does, it can attenuate vibration. Meanwhile it can convert suspension vibration energy into reusable energy by certain equipment other than dissipated as heat.

In the past decades, researchers consistently focused on motor generating electricity driven by suspension up and down, but detailed structures were

---

F2012-E04-007

---

W. Wang (✉) · S. Liu

State Key Laboratory of Automotive Simulation and Control, Jilin University, Jilin, China

e-mail: ww\_h\_jlu@126.com

different. The major variance was the movement conversion mechanism. For rotary motor, suspension's linear movement needs to be converted into rotary motion first. Conversion mechanisms include hydraulic type [1], which use fluid push a hydraulic motor and then drive the generator, ball screw and nut [2], rack and pinion [3], and suspension swing arm [4], whose function are the same as convert the linear movement to rotary movement. For linear motor, it can be directly driven by suspension up and down [5]. In this paper, the ball screw and nut mechanism was chosen to fulfil the task of movement and force conversion for its high efficiency both for drive and back-drive.

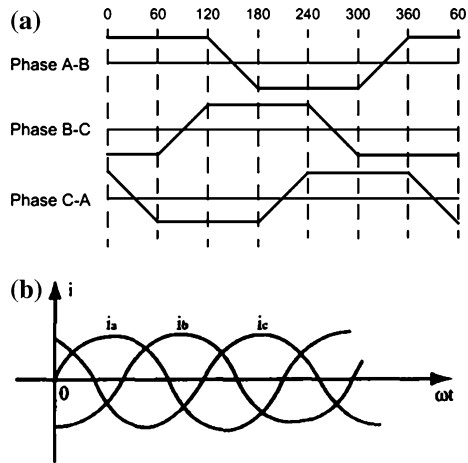
Another important component of regenerative suspension is regenerative (RG) motor, which is the core of energy conversion and damping force control. By controlling RG motor, the passive, semi-active and active damper characteristics can achieved. Theoretically, direct current motor, induction motor and synchronous motor all can be used as regenerative motor, however, complicated control and no performance advantages makes seldom researches on induction motor as application on regenerative suspension. Compared to excited motor, permanent magnetic (PM) motor is more efficient and simpler. It includes PM direct current (DC) motor, brushless DC (BLDC) motor and PM synchronous (PMSM) motor. In previous literatures, for convenience sake, PM DC motor model was adapted [6–7]. But BLDC has gradually superseded the DC motor, as power electronics developing. Literatures [8] use BLDC as RG motor. Meanwhile, PMSM begin to emerge in literature [9] for its high accurate torque control and fast dynamic response. Different structures between DC, BLDC and PMSM lead to different control strategies and performance which will be analyzed in the next part. By directly adding battery or capacitor on output of RG motor without control, when the motor back EMF is lower than battery voltage, RG motor will have no damping force output that is called dead zone. Lower the battery voltage can decrease the dead zone, but when the motor in high speed, the high back EMF will lead to tremendous current which in turn will cause damage to motor. If energy storage device is capacitor, the dead zone will change as the change of capacitor voltage during charging process. Conclusively, RG motor needs to be controlled to fulfil tasks of energy harvest and proper damping force.

## 2 Regenerative Motor

### 2.1 PM DC motor

PM DC motor include DC motor and brushless motor. The torque of both motors can be controlled by adjusting the armature current, because no matter where the rotor is, the magnetic motive force of armature current is orthogonal with permanent magnetic field, which is achieved by brush and commutator in DC motor

**Fig. 1 a** BLDC armature current wave. **b** PMSM armature current wave



and by electronic commutator in brushless motor. The back EMF and torque equations can be expressed as following:

$$\begin{aligned}
 E &= C_e \Phi n \\
 T &= K_T \Phi_f I_a
 \end{aligned}
 \tag{1}$$

It can be shown that in PM DC motor back EMF is proportional to motor rotary speed and torque is proportional to armature current. Adjusting the current can fulfill torque control, so control strategy is simple and performance is good. Therefore, previous literatures mostly used PM DC motor model in research on regenerative suspension. Compared to DC motor, BLDC achieved electronic commutator through rotor angle provided by resolver mounted in motor end. It removed the brush and commutator, so improved speed range, reliability and operation life. Meanwhile it retained merits of DC motor. But the current of BLDC is triangle (Fig. 1a), there exist torque fluctuation during current reverse which result in inaccurately torque control.

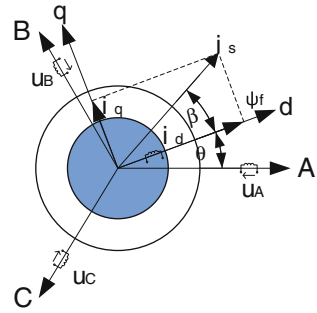
## 2.2 PMSM motor

PMSM also belongs to PM brushless motor, but its armature current is sine wave (Fig. 1b), which can avoid torque fluctuations during commutating. So PMSM has been widely used in modern high performance servo systems, and it is more suitable in regenerative suspension damping force control.

The basic difference between BLDC and PMSM is that PMSM armature reaction magnetic field is not orthogonal with permanent magnetic field [10]. PMSM torque depends on the armature current space vector which is mixed by three phase current  $i_a$ ,  $i_b$ ,  $i_c$ . Commonly, dq coordinate system is used to analyze



**Fig. 2** Exterior mounted PMSM model



the PMSM. According to Eq. (2), after Clarke and Park transformation, it can be divided into direct axis current  $i_d$  and quadrature axis current  $i_q$ , as illustrated in Fig. 2.

$$\begin{bmatrix} i_d \\ i_q \end{bmatrix} = \sqrt{\frac{2}{3}}[A] \begin{bmatrix} i_a \\ i_b \\ i_c \end{bmatrix} \tag{2}$$

where,

$$[A] = \begin{bmatrix} \cos \theta & \cos(\theta - 2\pi/3) & \cos(\theta - 2\pi/3) \\ -\sin \theta & -\sin(\theta - 2\pi/3) & -\sin(\theta + 2\pi/3) \end{bmatrix}$$

As to surface mounted PMSM, torque equation is:

$$T = p * \psi_f * i_s * \sin \beta = p * \psi_f * i_q \tag{3}$$

where,  $p$  is motor pole;  $\psi_f$  is permanent magnetic flux linkage;  $i_s$  is represents the armature current;  $\beta$  is the angle between  $i_s$  and  $d$ -axis as illustrated in Fig. 2.

It can be shown that different from DC motor, PMSM torque is proportional to  $i_q$ , not armature current  $i_s$ . But if we control  $\beta = \pi/2$  ( $i_d = 0$ ) through motor control strategy, all armature current will be converted to torque current  $i_q$ , that means the PMSM torque is proportional to armature current just like DC motor.

### 3 Regenerative Suspension Simulation Model

The researched regenerative damper is composed of ball screw and nut, PMSM and battery. The ball screw and nut convert the nut linear movement to screw rotary movement. The regenerative motor is driven by screw and generate electricity which is then stored in battery. The damping force can be controlled by motor generated torque. The 1/4 vehicle model including regenerative damper is shown in Fig. 3.

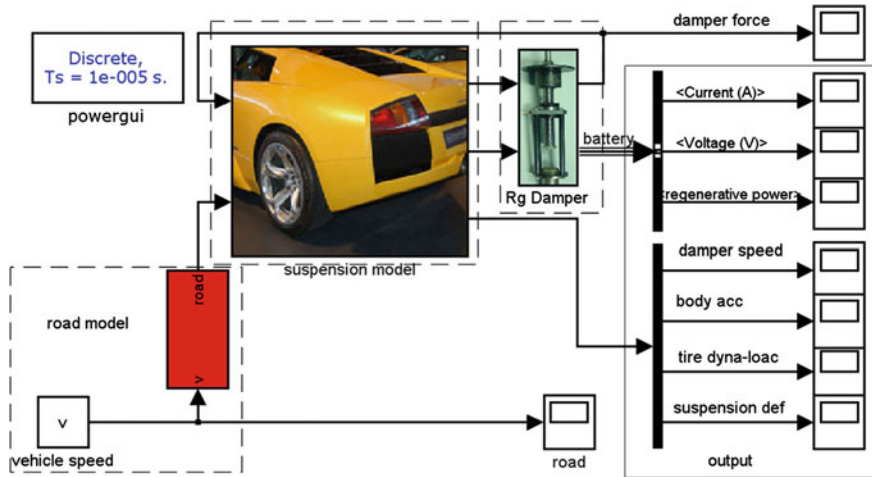


Fig. 3 1/4 vehicle Simulink model with regenerative damper

Table 1 Vehicle parameters of simulation

Symbol	Name	Value
$m_b$	Mass of body	267 kg
$m_w$	Mass of wheel	43 kg
$k_s$	Suspension stiffness	21,184 N/m
$k_t$	Tire stiffness	180,000 N/m

### 3.1 1/4 Vehicle Model

Establish the vehicle motion equation, as following:

$$\begin{aligned}
 m_b \ddot{x}_b &= k_s(x_w - x_b) + F_{rgforce} \\
 m_w \ddot{x}_w &= k_t(x_g - x_w) - k_s(x_w - x_b) - F_{rgforce}
 \end{aligned}
 \tag{4}$$

where,  $x_g$ ,  $x_w$ ,  $x_b$  indicate road input, wheel and body displacement respectively.  $F_{rgforce}$  represents the RG damper output force which we will analyzed in the next part, other parameters is shown in Table 1.

### 3.2 RG Damper Model

The RG damper model mainly is composed of PMSM, motor vector controller module (VECT) [11], battery model and regenerative damper controller. The inputs of whole model are suspension speed (spe), acceleration (acc) and the RG

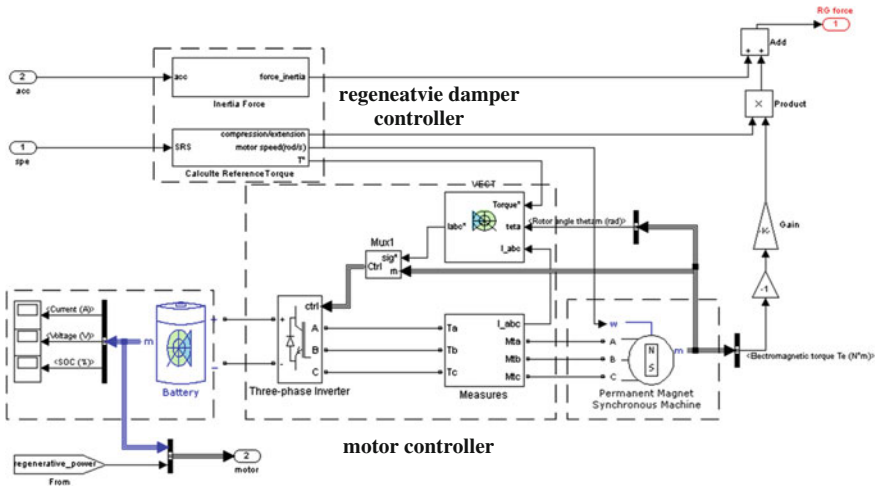


Fig. 4 Detailed regenerative damper model

damper output force consist of two parts: regenerative damping force ( $F_m$ ) and inertia force ( $F_i$ ), as shown in Fig. 4. The RG damper control systems calculate the corresponding angular speed  $\omega$ , reference torque  $T^*$  and inertia force  $F_i$  according to  $spe$  and  $acc$ .  $\omega$  is the input of PMSM, and  $T^*$  is the input of regenerative damper controller. The vector control make the PMSM output torque follow the reference torque. The motor output torque and inertia torque are converted to regenerative damping force  $F_m$  and inertia force  $F_i$  by screw. The motor and battery module are the MATLAB/Simulink PMSM and Lithium- Ion module.

### 3.3 Regenerative Damping Force

This paper is aimed at matching a small SUV hydraulic damper characteristic by control of PMSM. Figure 5 is the comparison of regenerative motor damping region and hydraulic damper curve. Firstly, according to suspension relative speed, the required damping force and RG motor max damping force is calculated by look-up table. Then the reference damping force is obtained by comparing required damping force with motor max damping force. At last, the reference damping force is converted to motor reference torque  $T^*$  send to motor controller, as illustrated in Fig. 6.

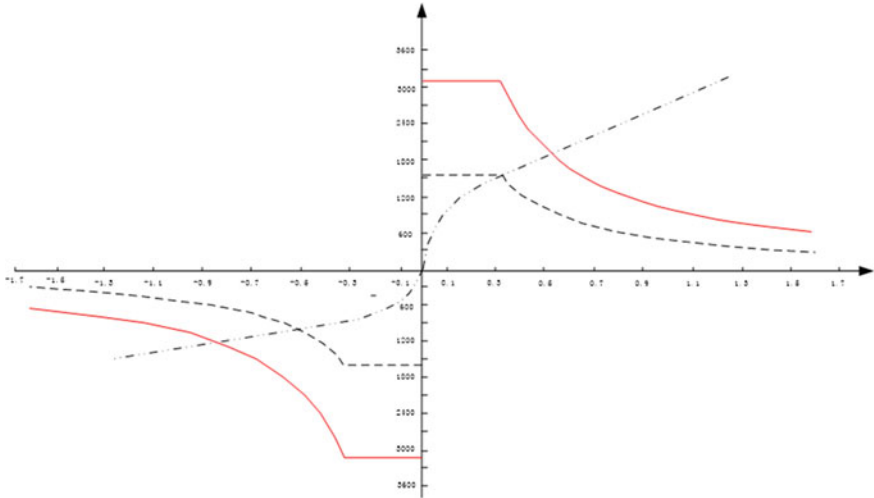


Fig. 5 Comparison between motor damping region and conventional damper curve

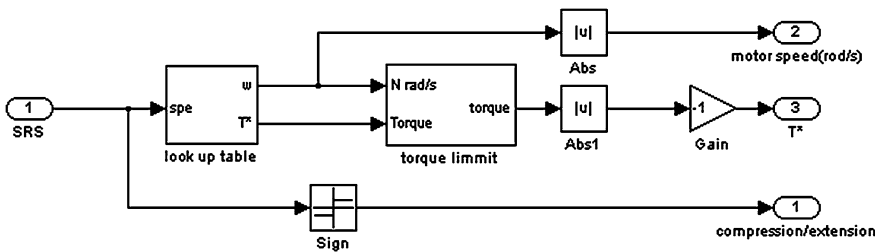


Fig. 6 Regenerative damper controller

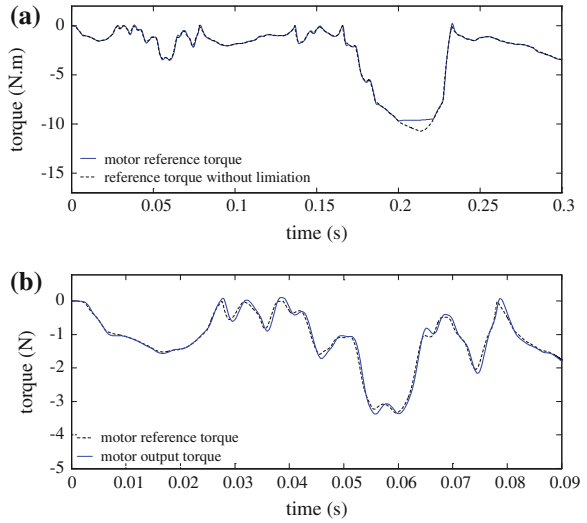
### 3.4 Inertia Force

Replaced the hydraulic damper with RG damper will introduce rotary parts including motor rotor and screw. These rotary parts will generate inertia force during the suspension reciprocating movement and inertia force is proportional to suspension relative acceleration. The inertia force can be expressed as following [9]:

$$F_i = \left(\frac{2\pi}{l}\right)^2 * (J_m + J_s) * (\ddot{x}_w - \ddot{x}_b) \tag{5}$$

where,  $l = 25 \text{ mm}$ , is the screw lead;  $J_m$  and  $J_s$  respectively represent the RG motor and screw moment of inertia. Assumed  $J_m = 0.769 \text{ e}^{-4} \text{ kg m}^2$   $J_s = 1.24 \text{ e}^{-6} \text{ kg m}^2$ ;  $\ddot{x}_w$  and  $\ddot{x}_b$  are the wheel and body acceleration.

**Fig. 7** Damper controller and motor controller characteristics. **a** Force limit of regenerative damper controller. **b** Motor torque



## 4 Simulation Analysis

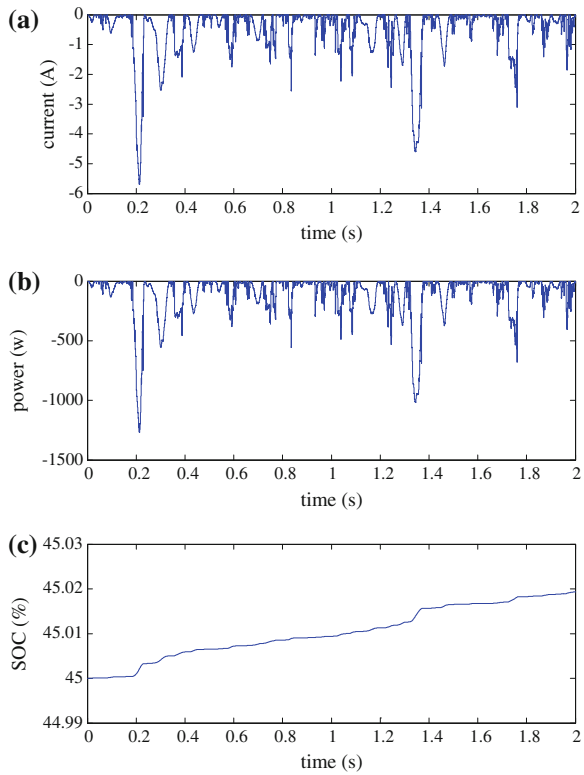
To test and verify the RG suspension characteristic, the established regenerative suspension model in part III is simulated. The white noise road is the road input; the vehicle speed is 15 m/s. Take C level road simulation results as an example, the regenerative motor control characteristic and energy recovery characteristic and damping characteristic were analyzed.

RG motor control characteristic is shown in Fig. 7. When the relative speed is high, the required torque will exceed the max torque of motor. The regenerative damper controller will restrict reference torque in the range of motor torque region and send it to motor controller, as shown in Fig. 7a. This will lead to lack of damping force phenomenon of regenerative damper in high speed. However, we can match the speed ratio, overloading ratio and power of RG motor to eliminate this phenomenon. In the other hand, the RG motor output torque can accurately follow the reference torque as illustrated in Fig. 7b.

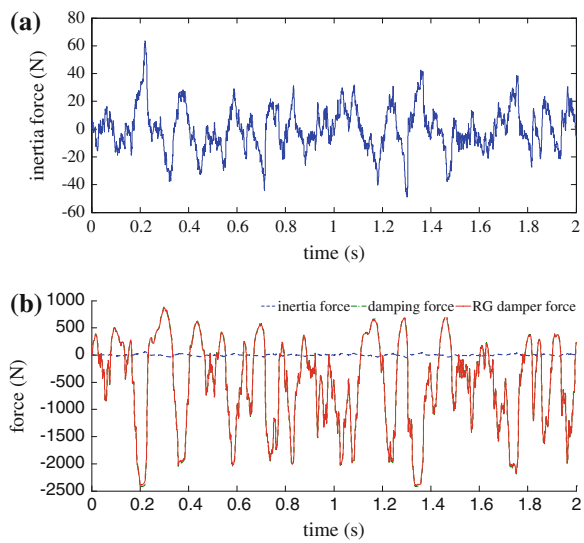
The RG damper's energy recovery characteristic is shown in Fig. 8. The battery charging current is negative, which indicates the motor is in the regenerating state. The amplitude of charging current depends on the motor output torque, which lies on the suspension relative speed and RG damper damping region. During two seconds simulation time, the average charging current is  $-0.49$  A, max current is 5.43 A which did not exceed the motor max current (7.2 A). The average regenerated power is 107 W, and total regenerated power is 1,270 W. The power recovered is 214 J, and battery SOC increase to 45.02 from 45 % as shown in Fig. 8c.

The RG damper damping force, inertia force and output force is compared in Fig. 9. It is shown that the inertia force is relatively smaller than damping force, so

**Fig. 8** **a** Battery charging current. **b** Regenerated power. **c** Battery SOC



**Fig. 9** Force comparison of regenerative damper. **a** Inertia force. **b** Force of regenerative damper



its influence to total output force is insignificant. This attributes to the small moment of inertia. Compared to motor moment of inertia, the screw moment of inertia is relatively small. The RG damper moment of inertia depends on the motor inertia which is related to motor type and power. PM motor replaced the excited part with permanent magnetic, so its inertia is small.

## 5 Conclusion

Although PMSM control strategy is relatively more complex than DC and BLDC motor, the torque accuracy and dynamic characteristic are improved, so it is more suitable for RG suspension. Simulation results show that PMSM RG motor output torque can accurately follow the demand of reference torque derived by suspension relative speed. Meanwhile, suspension vibration energy is recycled and stored in battery. Owing to small inertia of RG damper, the inertia force has little influence to RG damper output force.

## References

1. Lin X, Bo Y, Xuexun G et al (2010) Simulation and performance evaluation of hydraulic transmission electromagnetic energy-regenerative active suspension. In: Second WRI Global Congress Intelligent System, pp 58–61
2. Kawamoto Y, Suda Y (2007) Modeling of electromagnetic damper for automobile suspension. *J Syst Des Dyn* 1(3):524–535
3. Weeks DA, Bresie DA, Beno JH, Guenin AM (1999) The design of an electromagnetic linear actuator for an active suspension. 1999-01-0730
4. Jonasson M, Roos F (2008) Design and evaluation of an active electromechanical wheel suspensions system. *Mechantronic* 4(18):218–230
5. Gysen BLJ, van der Sande TPJ, Paulides JJH (2011) Efficiency of a regenerative direct-drive electromagnetic active suspension. *IEEE Trans Veh Technol* 60(4)
6. Hsu P (1996) Power recovery property of electrical active suspension systems. In: Proceedings of the intersociety energy conversion engineering conference. IEEE, Washington, pp 1899–1904
7. Nakano K, Suda Y, Nakadai S (2003) Self-powered active vibration control using a single electric actuator. *J Sound Vib* 260(2):213–235
8. Cao M, Liu W, Yu F (2008) Development on electromotor actuator for active suspension of vehicle. *Chin J Mech Eng* 44(11):224–228
9. Liu S, Wei H, Wang W (2011) Investigation on some key issues of regenerative damper with rotary motor for automobile suspension. *EMEIT* (2):1435–1439
10. Wang C, Xia J, Song Y (2010) Motor control technique of electric machines. China Machine Press, Beijing
11. Krishnan R (2010) Permanent magnet synchronous and brushless DC motor drives. Taylor and Francis Group, LLC, UK

# The Application of Tolerance Analysis During Engineering Process

Wei Wang and ZhiHan Zhou

**Abstract** During the engineering process of the BIW development, in order to fulfill the requirements of design and the demands of customers, it is extraordinarily necessary to conduct tolerance analysis of each pivotal and vital feature of Body In White opportunely based on the body structure, the process route and the level of manufacturing. The application of tolerance analysis in the engineering process can help achieve the purpose of optimizing the body structure as well as the process route, and promoting the accuracy control of the body.

**Keywords** Tolerance analysis · Body structure optimization · Process route optimization

## 1 The Importance of Tolerance Analysis

After the model is determined, the automobile development will follow two main threads, namely the product performance development and the manufacturing accuracy control.

With regard to the automobile development based on the development of product performance, to guarantee the body structure's rationality and accuracy, R&H, NVH, collision simulation, stiffness and other CAE analytical methods are introduced to analyze from different technical perspectives every aspect of a car including its maneuverability, vibration noise and white body performance

---

F2012-E04-009

---

W. Wang (✉) · Z. Zhou

Chang'an Automotive Engineering Institute, 401120 Chongqing, China  
e-mail: sunqiemail@163.com



feasibility. The purpose is that with the use of virtual computer techniques, based on existing BIW data, the real state of the manufactured car will be simulated as closely as possible so that consumer demands, laws and regulations, design objectives and so on can be met. By means of virtual techniques, vital performance and elements of a car which can only be tested after a real car is produced can now be verified at the design stage, potential risks can be detected and design plans can be timely adjusted and optimized based on the design requirements. As a result, the risks and costs of the automobile development will be reduced and the development will also speed up. The automobile development based on the development of product performance is a general trend domestic car manufacturers follow. After years of efforts, it can generally fulfill the need of those car manufacturers with the aid of relevant design companies home and abroad [1].

The automobile development based on the manufacturing accuracy control is what domestic car manufacturers find increasingly important. Pioneering car manufacturers like Chang'an Inc. have created special dimensional engineering departments to conduct development and technology research. Accuracy control, just like performance control, must be involved in the project development at the early stage. Through virtual analytical techniques, factors concerned with accuracy control will be optimized, including product structure, process route as well as datum references and design errors will be decreased. Of simulative analyses in accuracy control, an important one is tolerance analysis.

## **2 Methods of Tolerance Analysis**

### ***2.1 The Analysis of the Error Sources of the BIW [2]***

Tolerance analysis is a simulative means, by which the BIW's error accumulation can be quantitatively evaluated. To make the analysis perfectly accurate, it is necessary to study the causes of the BIW's errors during the design and manufacturing process. Only by taking every cause into full account can engineers make the calculations completely accurate, thus guiding engineers to work out better designs.

Error accumulation is inevitable but can be decreased. Factors affecting measurement systems might include: people, equipment, samples, process, environment, management. The sources of the BIW's dimensional accuracy deviation mainly include: the interference of parts, the jigs' instability, the deviation of the parts, and the influence of manual operation and deformation of welding. To sum up, errors can be caused at four stages, namely design, manufacturing, assembly and measurement. (See Fig. 1).

How to avoid errors made at the design stage is not only the key problem to deal with during the engineering stage but also one of the most important tasks dimensional engineers have to tackle. During this period, based on the requirements of the car's appearance, assembly, performance and process control, the

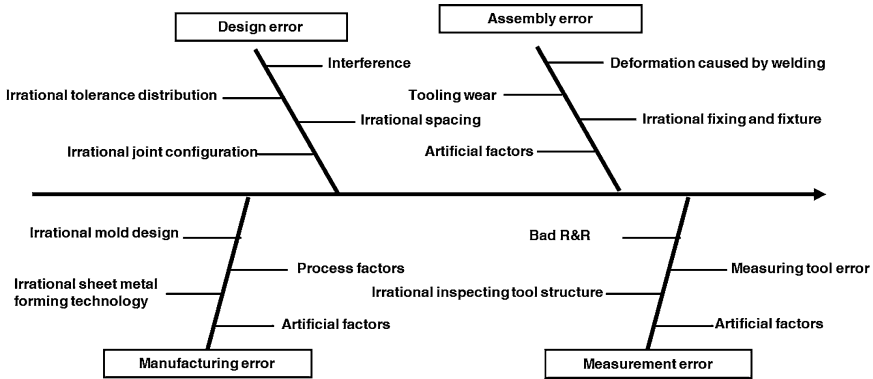


Fig. 1 BIW error source fishbone diagram

detailed vital control points of the BIW and corresponding tolerance control targets are to be formulated. Then, quantitative tolerance accumulation analyses of each and every control point are conducted, thus giving feasibility assessments and putting forward optimized plans where there are risks.

Interference of parts can be avoided through routine data check.

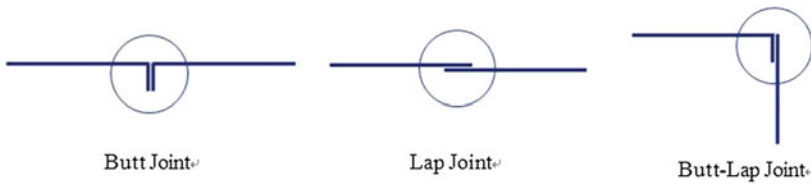
Irrationality of tolerance allocation can be avoided by means of tolerance analysis, which can help generate dimensional chain based on existing BIW structure, process route as well as way of location, co-ordinate manufacturing costs of parts' accuracy control, and allocate proper tolerances to different parts.

To minimize the effect of spacing irrationality, tolerance analysis is still essential to determine acceptable spacing between parts. In this case, tolerance calculation can be made by means of the limit method. Deviation tolerances are calculated and as long as the parts' performance requirements are met, they can be used as a general criterion for product design, which needs no further calculation or verification.

Irrational joint configurations can be optimized depending on specific structure. Joint configurations can be simplified in three types: butt joint, lap joint and butt-lap joint. See Fig. 2. The butt joint will cause full accumulation of all errors, and therefore should avoid being used in accuracy control. The lap joint is recommended because it can absorb error accumulation. The butt-lap joint is a combination of the two. Through optimized joint configurations, unnecessary error accumulation can be eliminated so that the BIW's accuracy control level can be promoted. Meanwhile, error accumulation will occur in unimportant and unnoticed places to ensure the controllability of important areas' accuracy control.

## 2.2 Generation of a Dimensional Chain

Manufactured parts, affected by many factors, can't be a perfect reproduction of the model, thus causing dimensional tolerance and geometric tolerance. When different parts are welded or assembled together, tolerances of the features of the



**Fig. 2** Joint configuration

parts involved in the welding or assembly will accumulate and affect the final control targets. The interrelated features connect each other to create a geometrically closed circuit, which is referred to as a dimensional chain. Each feature's tolerance is called a link.

As long as the joint configuration and process route of the parts involved in welding or assembly is accurately described, engineers can draw a dimensional chain with ease. A dimensional chain can be seen as the numerical expression of the production process of parts. The generation of a BIW's dimensional chain needs to take into account factors including tolerances of parts, datum references of parts, joint configurations of parts, plans of jigs, co-ordination of holes and pins, process route, etc.

### 2.3 One-Dimensional Analysis

After knowing exactly the component links of a dimensional chain, engineers can analyze specific error accumulation based on our needs.

At present, in performing the analysis of dimensional chains, two one-dimensional calculation methods are commonly adopted in practice: limit and probability.

#### 2.3.1 Limit

To calculate tolerance accumulation, limit tolerance studies the worst case of error accumulation, where each plus link has the maximum (or minimum) value of limit dimensioning while each minus link the minimum (maximum). This method is simple yet reliable, but the major drawback is that it requires very tight individual component tolerances, thus making processing parts more difficult and increasing fabrication costs.

The calculation formula is  $T_{\Delta\Sigma} = \sum_{i=1}^{n-1} T(A_i)$ .  $N$  refers to the total link number.

See Fig. 3.

Fig. 3 Limit

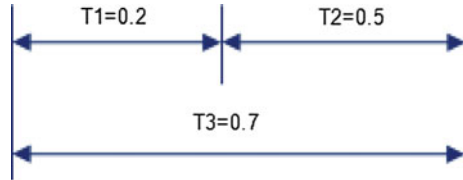


Fig. 4 The probabilistic method

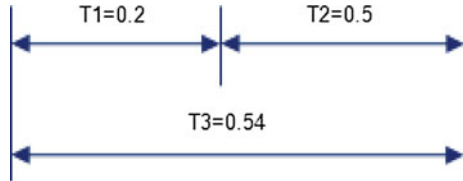
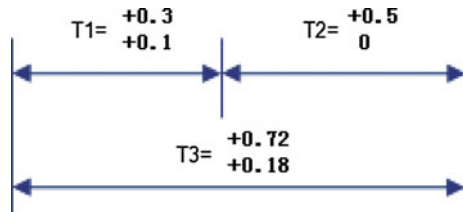


Fig. 5 Nonequivalent upper and lower deviation



### 2.3.2 The Probabilistic Method

By using the theory of probability, engineers study statistical distribution to calculate dimensional chains. If the tolerance of the BIW's sheet metal shows normal distribution, then the tolerance zone will have the value  $6\sigma$ , which can fulfill the requirements of 99.7 % of the products and is a better choice in cases where there are many links and a high degree of accuracy is required.

If the dimensional errors of all dimensional chain links have normal distribution, then the closed circuit also shows normal distribution.

The calculation formula is  $T_{A\Sigma} = \sqrt{\sum_{i=1}^{n-1} T(A_i)^2}$ . N refers to the total link number. See Fig. 4.

When each component link has the same upper and lower deviation, the upper and lower deviation of the closed circuit will be the average of the total tolerance.

When each component link does not have the same upper and lower deviation, the upper and lower deviation of the closed circuit will be calculated respectively as follows:

Upper deviation: the sum of the average deviation of the component links  $+\frac{T_{A\Sigma}}{2}$ ;

Lower deviation: the sum of the average deviation of the component links  $-\frac{T_{A\Sigma}}{2}$ .

See Fig. 5.

$$T3 \text{ upper deviation} = (0.1 + 0.3)/2 + (0 + 0.5)/2 + 0.54/2 = 0.72;$$

$$T_3 \text{ lower deviation} = (0.1 + 0.3)/2 + (0 + 0.5)/2 - 0.54/2 = 0.18.$$

If the dimensional errors of all dimensional chain links do not have normal distribution, then  $K$ , the coefficient of relative distribution, will be introduced. The

calculation formula will be:  $T_{A\Sigma} = \sqrt{\sum_{i=1}^{n-1} [KT(A_i)]^2}$ . If the links have normal distribution, then  $K$  equals 1.73.

### 2.3.3 The Calculation Methods of the BIW's Dimensional Chain

In calculating the BIW's dimensional chain, engineers need to fully consider the size, integrity, distribution, and available calculations methods of each chain link. In order to achieve economies of all manufacturing processes, engineers adopt probabilistic methods to c the BIW's tolerance accumulation based on the following hypotheses:

- (a) All manufactured parts can meet the determinate tolerance requirements.
- (b) All jogs' accuracy can meet the determinate tolerance requirements.
- (c) All the tolerances' probability distribution is general distribution. That is to say, the parts' tolerance has normal distribution, the jig's tolerance has even distribution, and the spacing between holes and pins is a constant.
- (d) Effects of artificial adjustments, deformation of welding, wear or deformation of fixture are not taken into consideration.
- (e) All manufacturing capability can fulfill  $C_{pk} \geq 1$ .

Based on the above hypotheses, considering different calculation methods available to different chain links, the calculation formula for the BIW's one-dimensional dimensional chain can be simplified as follows:

$$T_{\Sigma} = \sqrt{\sum_{i=1}^n (A_i)^2 + 3 \times \sum_{i=1}^n (B_i)^2 + \sum_{i=1}^n C_i}$$

Note:

- A refers to dimensional chain links which comply with normal distribution, such as: the profile tolerance of line and surface, the positional tolerance of holes, straightness, parallelism, the diametrical dimensional tolerance of holes and pins, and dimensional tolerance of other types;
- B refers to dimensional chain links which comply with even distribution, such as: the profile tolerance of the fixture locating surface and the positional tolerance of locating pins;
- C refers to dimensional chain links which comply with the extreme value distribution (constant), such as: the spacing between holes and pins (the nominal value), compensation for deformation of welding and so on.

## 2.4 Three-Dimensional Analysis

One-dimensional analysis is simple and quick and does not depend much on the degree of perfection of the products' data. It can also quickly verify the design plans made by BIW structure engineers from qualitative perspectives. However, one-dimensional analysis also has its limitations. Since one-dimensional analysis is based on the hypothesis that tolerances accumulation in one direction, it is hard to evaluate the effects of tolerances from other directions. Meanwhile, the calculation will become really complicated if there is an angle between two tolerances. When the BIW has a three-dimensional stereoscopic structure, three-dimensional tolerance analysis has to be introduced to achieve more accurate assessment of the BIW's tolerance accumulation.

At present, two pieces of three-dimensional tolerance analytical software are commonly used and commercially successful: Vis-VSA and 3DCS. Take 3DCS as an example.

3DCS is a tolerance analytical tool built in CATIA software and can directly carry out tolerance accumulation simulations and analytical assessments based on the product engineers' data. 3DCS can serve as a platform of products' dimension quality management, where product engineers, process engineers, measurement engineers, manufacturing engineers and so on can work together to analyze and optimize the dimension quality and tolerance accumulation of products. Through the software, engineers can know in advance which are key dimensions and which follow-up needs close control and regulations. Meanwhile, engineers can detect cases where tolerance requirements are not met and make adjustments to products at an early stage.

Below is 3DCS's core mechanism. After the parts' basic tolerance, the assembly and welding sequence of the process planning, the parts' datum references are input, 3DCS will give tolerances of fixture jigs based on processing capability, give information like tolerances of deformation of welding based on actual capability, build tolerance analytical data, drive based on locating system and tolerance, calculate each feature's tolerance based to the parts' virtual spatial position, and simulate the tolerances' transmission and conversion in three-dimensional space based on the parts' geometric shape as well as tolerances, and the fixture alignment tolerance.

The principle of 3DCS's three-dimensional tolerance stack is like this. All the feature points' tolerances have normal distribution (or other distributions like even distribution). According to the Monte Carlo rule, all feature points (the tolerances of parts' holes and planes, the tolerances of jigs, the tolerances of deformation caused of welding, etc.) are given randomly virtual tolerances which show normal distribution. Then, based on parts' assembly relations, superposition calculation of all geometric shaped is made in three-dimensional space and thus vital features' dimensional tolerances will be calculated. To put in a simple way, in a three-dimensional environment, each part is considered a real part. According to the Monte Carlo rule, a group of tolerances are given, which represent the true

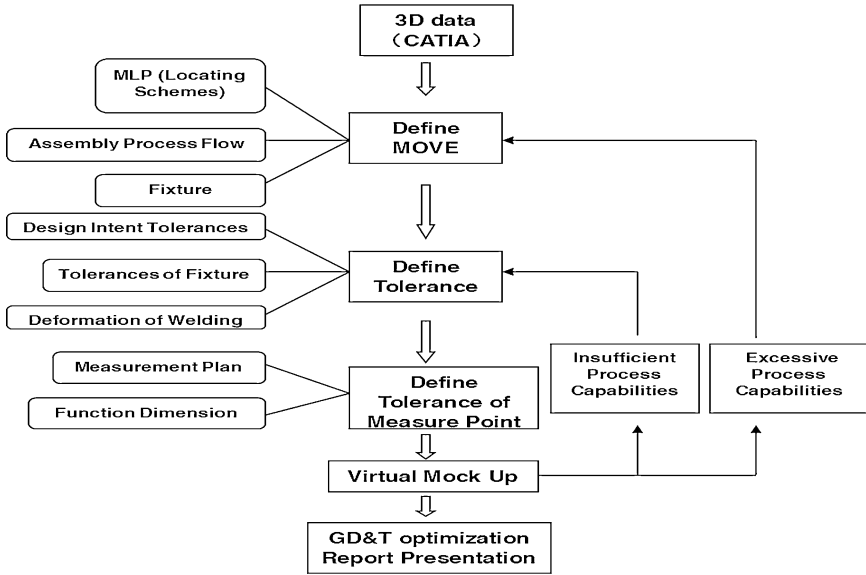


Fig. 6 3DCS analysis flow diagram

tolerances of parts caused in the manufacturing process. Then all the parts are assembled and welded in accordance to the process flow in practice, with tolerances caused by jigs’ positioning and welding deformation carefully considered. The built BIW’s tolerance analysis data represent the manufactured BIW. We can easily test and assess every measuring point and every group of functional dimensions of the BIW to check whether they meet the designing requirements.

Meanwhile, virtual welding or assembly can be done many times (even hundreds or thousands of times) so that enough results can be collected. Engineers can then conduct statistical process control (SPC) analysis and error source impact factor analysis to collect a series of assessment indexes and parameters such as  $6\sigma$ , CPK, tolerance contribution degree, based on which we can assess the BIW dimension and make adjustments.

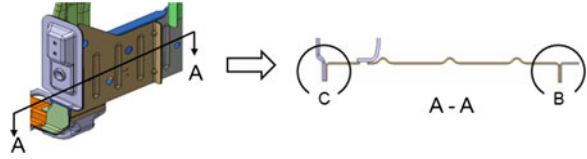
The 3DCS’S BIW tolerance analysis flow is illustrated in Fig. 6.

3DCS can help visually optimize the parts’ positioning system, tolerances as well as product structure and accurately calculate tolerance accumulation and the proportionality factor of each part’s influence on the final tolerance.

### 3 Methods of Optimizing Dimensional Chains

The purpose of conducting tolerance analysis at the engineering stage is to predict tolerance accumulation at the design stage and devise proper tolerance and rational structure. To optimize structure is an important part at this stage.

**Fig. 7** U-shaped structure



**Fig. 8** Structure optimization plan



There are mainly two ways to promote the BIW accuracy at the design stage. One is to raise the parts' accuracy requirements and the other is to reduce dimensional chain links. The former will increase costs and instability of process control, which is not a best choice. The latter, however, does not affect costs much by optimizing structure and process flow and can promote the stability of accuracy control, which is the best choice of engineering optimization at this stage.

### 3.1 Optimization of the BIW

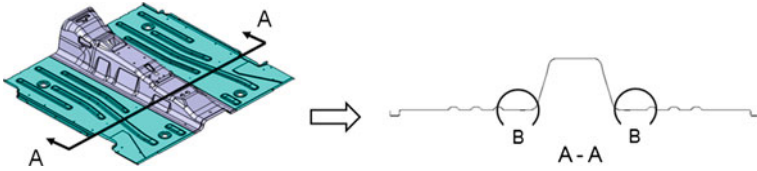
From the causes of errors mentioned above, we can see that the BIW structure optimization process is main the process of converting the butt joint into the lap joint.

#### 3.1.1 Optimization of U-Shaped Structure

U-shaped structure in the BIW will make it difficult to weld or assemble, so it should be avoided or optimized based on practical situations. Optimization plans are as follows:

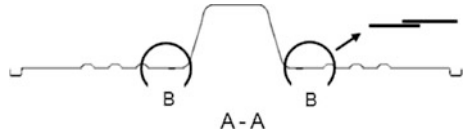
- (a) Convert the butt joint into the lap joint on one side. See Figs. 7 and 8. In this way, the interference or complete tolerance transmission of the parts in the middle and the parts on two sides in the U-shaped structure.
- (b) The floor structure can be optimized to control accuracy over the width of the floor. Optimization plans are illustrated in Figs. 9 and 10.
- (c) When U-shaped structure can't be optimized, engineers can define deviation tolerance to avoid interference caused during the parts' assembly process. See Figs. 11 and 12.



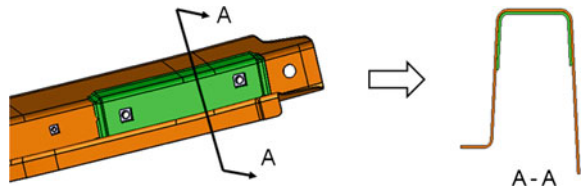


**Fig. 9** The floor structure

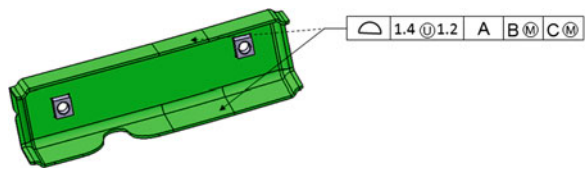
**Fig. 10** Structure optimization plan



**Fig. 11** U-shaped structure



**Fig. 12** Define deviation tolerance



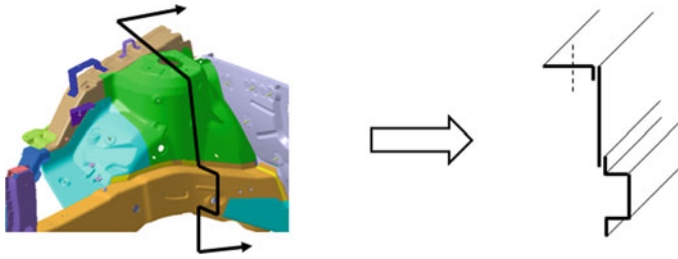
### 3.1.2 Structure Optimization Based on Target Demands

Based on target demands, some control points has to be controllable in a certain direction. In this case, engineers need to analyze product structure and consider how to optimize product structure from the perspective of reducing the control points' dimensional chain links. For example, the camber angle control of a certain car needs to be optimized. Its structure is illustrated in Fig. 13.

In this structure, the dimensional chain of the front strut's mounting holes is illustrated in Fig. 14.

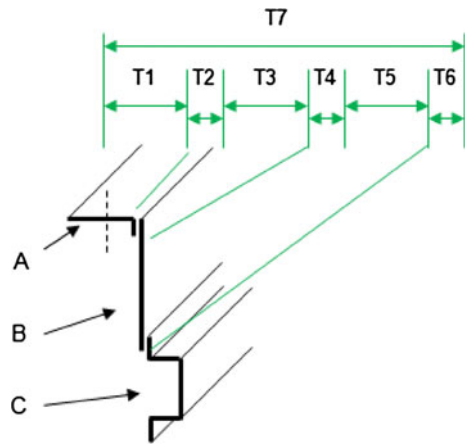
Below is what the dimensional chain links refer to.

- T1 refers to the profile tolerance of the abutted surface of part A;
- T2 refers to the combined deviation of fixture as well as co-ordination of holes and pins of part A;
- T3 refers to the profile tolerance of the abutted surface of part B;
- T4 refers to the combined deviation of fixture as well as co-ordination of holes and pins of part B;
- T5 refers to the profile tolerance of the abutted surface of part C;



**Fig. 13** Simplified structure diagram

**Fig. 14** Dimensional chain



- T6 refers to the combined deviation of fixture as well as co-ordination of holes and pins of part C;
- T7 refers to the tolerance accumulation of the front strut’s mounting holes along the y-axis.

From the dimensional chain we can see that for the front strut’s mounting holes, many influencing factors lie along the y-axis and are difficult to control, thus needing to be optimized. The optimization plan is illustrated in Fig. 15.

Both plan A and B are aimed at modifying the joint configurations of parts A, B and C along the y-axis. The butt-joint is converted into the lap joint and thus the corresponding dimensional chain also changes. See Fig. 16.

For plan A:

- T1 refers to the combined deviation of parts A and B’s integrated fixture and co-ordination of holes and pins;
- T2 refers to the combined deviation of fixture as well as co-ordination of holes and pins of part C;

Fig. 15 Optimization plan

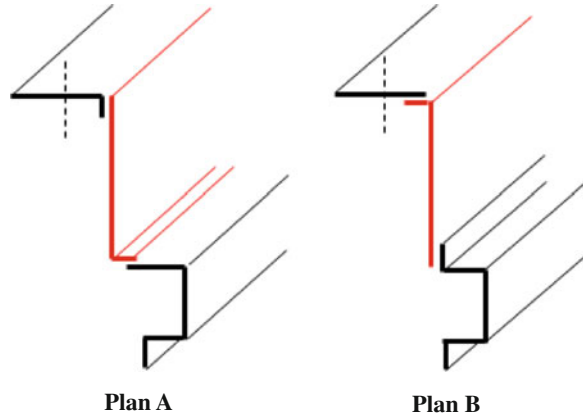
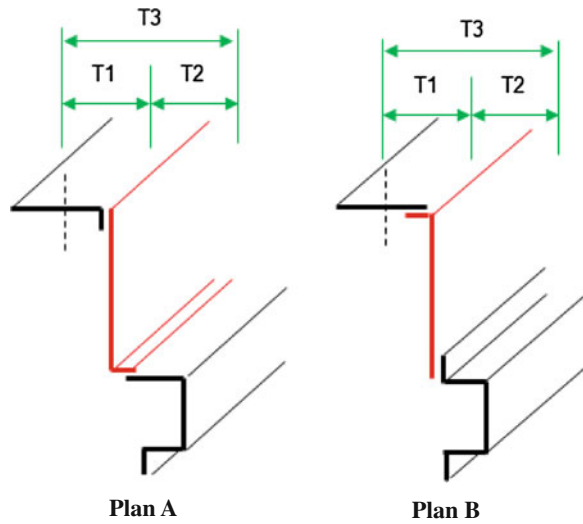


Fig. 16 Dimensional chain

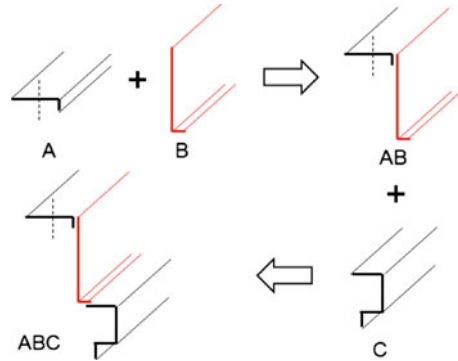


T3 refers to the tolerance accumulation of the front strut's mounting holes along the y-axis.

For plan B:

- T1 refers to the combined deviation of fixture as well as co-ordination of holes and pins of part A;
- T2 refers to the combined deviation of parts B and C's integrated fixture and co-ordination of holes and pins;
- T3 refers to the tolerance accumulation of the front strut's mounting holes along the y-axis.

Fig. 17 Welding Route 1



From the dimensional chain we can see that the number of the dimensional chain links of the front strut’s mounting holes along the y-axis is obviously reduced. That is, fewer influencing factors are left and the remaining factors are concerned with jigs’ accuracy, which can be better controlled.

Therefore, with definite targets engineers can conduct specific tolerance analysis and reduce the number of dimensional chain links through structure optimization to promote accuracy control.

### 3.2 Optimization of the Process Route

The optimization of the process route and the optimization of the product structure are conducted simultaneously. With the same structure, different product routes give rise to different dimensional chains. The process route affects the BIW’s dimensional chain and the parts’ positioning system, both of which are an important part of BIW accuracy control. So to guarantee BIW accuracy, the process route has to be verified and optimized while tolerance analysis is conducted.

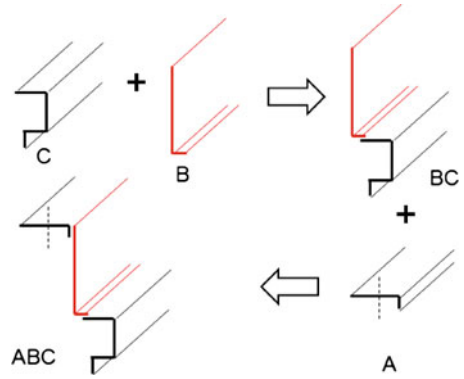
From the perspective of the BIW accuracy control, the sequence of optimizing the welding process route is like this. First, weld the butt joint. Next, weld the lap joint and eliminate the tolerance accumulation during the process. Take plan A illustrated in Fig. 15 for example. If the welding sequence of parts A, B and C is  $A+B \rightarrow AB$ ;  $AB+C \rightarrow ABC$ , as illustrated in Fig. 17, then the dimensional chain of the front strut’s mounting holes along the y-axis will be the one illustrated in Fig. 16A.

If the welding sequence of parts A, B and C is  $B+C \rightarrow BC$ ;  $A+BC \rightarrow ABC$ , as illustrated in Fig. 18, then the dimensional chain of the front strut’s mounting holes along the y-axis will be the one illustrated in Fig. 19.

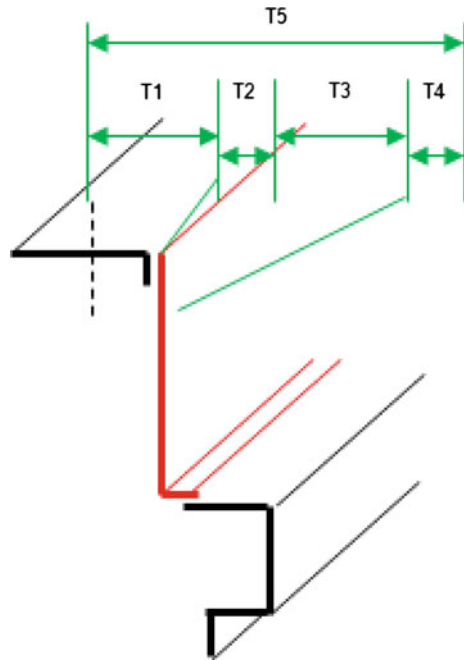
Below is what the dimensional chain links refer to.

- T1 refers to the profile tolerance of the abutted surface of part A;
- T2 refers to the combined deviation of fixture as well as co-ordination of holes and pins of part A;

**Fig. 18** Welding Route 2



**Fig. 19** Dimensional chain



- T3 refers to the profile tolerance of the integrated surface of parts B and C;
- T4 refers to the combined deviation of the integrated fixture and co-ordination of holes and pins of parts B and C;
- T5 refers to the tolerance accumulation of the front strut's mounting holes along the y-axis.

We can see that following different welding sequence making a different to the dimensional chain of the same target. Therefore, necessary optimization should be conducted based on demands to reduce or avoid accuracy control risks.

## 4 Conclusion

The development of a car is time-consuming and involves many departments. The faults of body structure or process route, if detected during the trial production period instead of being detected and optimized at an early stage, will be irreversible. In most cases, enormous modification expenses are involved and the project development has to be unduly prolonged, which will force car manufacturers sacrifice BIW accuracy or part of the performance parameters. To wholly assess the rationality of the BIW structure by means of BIW accuracy control at the early stage of the project development, it is necessary to introduce tolerance analysis during the project's engineering process and timely assess the target accuracy degree of every pivotal and vital feature of the BIW based on the body structure, process route and manufacturing level.

## References

1. Zhou, Z (2008) Tolerance analysis in automobile dimensional engineering. Proceedings of the 2008 congress of society of automotive engineers of China, Tianjin, China, pp 7–9
2. ASME Y14.5-2009 Dimensioning and tolerancing 2009

# Synchronized Design Optimization Method of Body Joints and Major Cross Sectional Members

Jie Xiang, Yong Chen and Youmin Guo

**Abstract** Stiffness designs of joints and major cross sectional members are a crucial step in a body structural design process. Traditionally, joints and cross sectional members are designed and optimized separately that potentially may result in some parts mismatching in geometry. The research objective is to develop a synchronized design optimization method of body joints and major cross sectional members to avoid this frequently encountered problem. The effectiveness of this optimization method is demonstrated with real world body design examples. The research method consists of four stages: (1) analyze a baseline joint for its stiffness performance, weight and cost; (2) optimize the joint design by maximizing its stiffness/weight ratio; (3) conduct synchronized design optimization of the joint together with its adjacent cross sectional members for maximizing stiffness/weight ratio of the combined structure; and (4) compare stiffness performance, weight and cost between the optimized joints in stages 2 and 3 with the baseline joint. The synchronized design optimization method was successfully applied to new vehicle programs at Changan and resulted in significantly improved cost- and weight-efficient body structural designs with good stiffness performance. This optimization method has been implemented as part of a formal vehicle design and development process and will be applied to all major new vehicle programs at Changan. The synchronized optimization method provides a systematic method for achieving optimized conceptual designs of a body joint and its adjacent major cross sectional member with respect to stiffness, weight and cost efficiency. But the actual feasible engineering design of the connection between the two parts sometimes still presents a challenge. Further research is needed to explore feasible

---

F2012-E04-010

---

J. Xiang (✉) · Y. Chen · Y. Guo  
Automobile Engineering Institute of Changan Automobile Ltd. Co, Chongqing,  
People's Republic of China  
e-mail: sunqiemail@163.com

design alternatives for the connection designs. Regardless of the limitation of the research work, it still represents an innovative idea from the viewpoint of a practicing body design engineer. The application of the synchronized design optimization method does help design engineers achieve more effective body designs than those achieved with traditional optimization method.

**Keywords** Joint stiffness • Section stiffness • Synchronized design optimization

## 1 Introduction

Stiffness designs of joints and major cross sectional members are a crucial step in a body structural design process. A good way to improve the body performance is optimizing the stiffness of joints and major cross sectional members. Traditionally, joints and cross sectional members are designed and optimized separately, and this results in frequently encountered problem. A synchronized design optimization method of body joints and major cross sectional members can avoid this problem [1].

Joints locate at body cross area (Fig. 1 and Table 1 shows) and are main parts that influence the body dynamic and static stiffness, and also the key structural that influence the NVH and durability of the body. These cross areas translate the main force of the body. Using the joint stiffness design to optimize the body performance comprehends following steps:

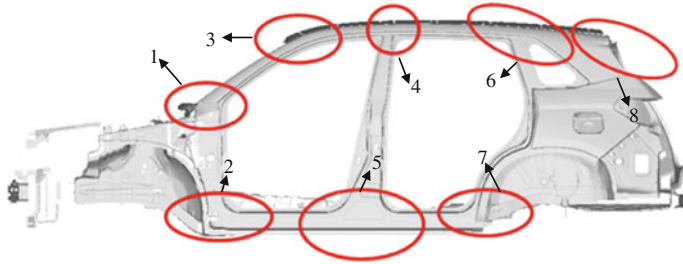
- (1) The performance requirements of the car body and joint stiffness;
- (2) Take the joint models from the 3D math data with standard specification;
- (3) Create the finite element joint models;
- (4) Calculate the response of joints under standard load;
- (5) Check the results and optimize the joint to achieve the target.

Major cross sectional members lay on the areas that translate most of the body load (layout as Fig. 2 shows). A better body performance is obtained through optimizing the section shape or size. The way using major cross sectional members comprehends following steps:

- (1) Build the target of the sectional characteristic;
- (2) Create standard sections follow the section specification;
- (3) Calculate the characteristic of sections with finite element software;
- (4) Change the section size to get better sectional Characteristic and investigate the changing of body performance.

Joints stiffness and major cross sectional members design both optimize the main force translate routeway to get a better body performance. Two methods synchronized used is more effectively than the traditional method, an example is offered to approval this view. To better describe the efficiency of optimization with different methods, a value  $k$  is imported. The formula lists below:





**Fig. 1** Main joints of the car body

**Table 1** Main joints of the car body

Serial	Name
1	A pillar to hinge
2	Hinge pillar to rocker
3	A pillar to roof
4	B pillar to roof
5	B pillar to rocker
6	C pillar to roof
7	Rear quarter to rocker
8	D pillar to roof

$$k = t/m$$

t the stiffness of joint

m the weight of joint

## 2 Example

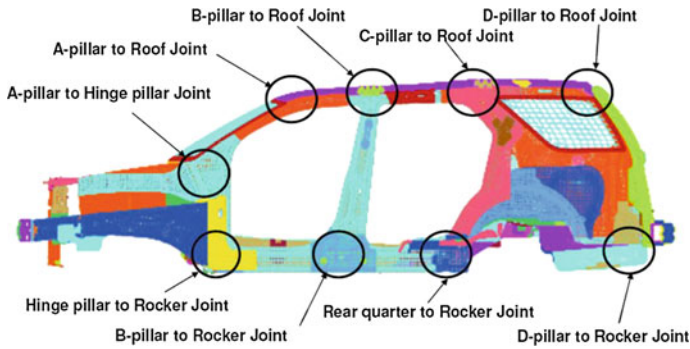
In this paper, the joint 6 (c pillar to roof, Fig. 3) and the section at here are offered to investigate joint stiffness and body performance with different optimizing methods. The baseline of the section, joint and body characteristic without any optimization are exhibited (Tables 2 and 3).

Here two items don't meet the requirement of the target. These items need optimize to achieve the target. Three solutions are used to optimize the joint stiffness. Solution 1 is the joint separately optimized, solution 2 and 3 are the section design and joint design synchronized optimized.

### Solution 1

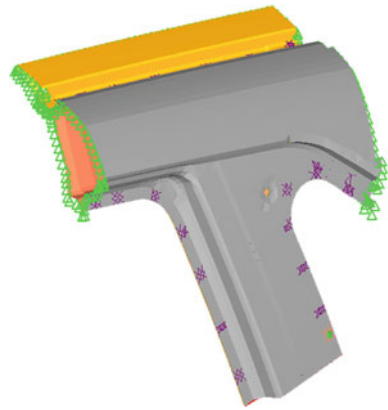
The groove of the outer surface of the joint is moved (Fig. 4), and the section hasn't any change, then recalculate the joint characteristic (Table 4).

The joint stiffness has improved, but one item does not meet the requirement, and the weight of the joint does not change.



**Fig. 2** The layout of the major cross sectional members

**Fig. 3** C pillar to roof



**Table 2** The characteristic of section

Area (mm <sup>2</sup> )	Torsional constant	Centroidal		
		I <sub>x</sub>	I <sub>y</sub>	I <sub>z</sub>
378.859	110,897	321,563	240,141	209,205

**Solution 2**

The section wide is added from 47 to 55 mm (Fig. 5), and the joint will also follow the section optimization. The stiffness of the section, the joint and the body is recalculated (Tables 5 and 6).

Results change much and meet the requirement, the body performance is also improved, but the I<sub>z</sub> of the section is debased.

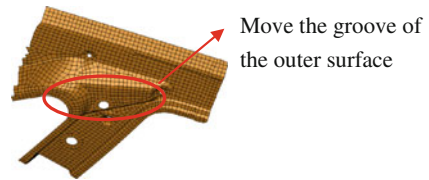
**Solution 3**

The section wide is added from 47 to 62 mm (Fig. 6), and the joint follow the section changing, then recalculated the stiffness of the section, the joint and the body (Tables 7 and 8).

**Table 3** The characteristic of the joint and body

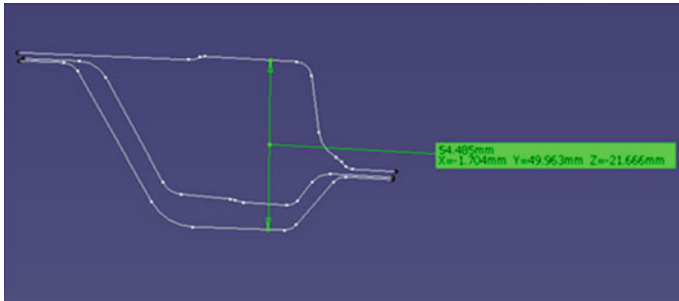
	Joint				Body			
	FRT-RR	In-out	Torsion	Weight	Bend stiffness	Torsion stiffness	Bend model	Torsion model
Target	96-1,088	7-185	1-215					
Result	21	3.6	7.6	2.23	8,449	818.4	46.3	30.6

**Fig. 4** The joint modify



**Table 4** The characteristic of the joint and body

	Joint				Body			
	FRT-RR	In-out	Torsion	Weight	Bend stiffness	Torsion stiffness	Bend model	Torsion model
Target	96-1,088	7-185	1-215	-	-	-	-	-
Baseline	21	3.6	7.6	2.23	8,449	818.4	46.3	30.6
Solution 1	52.6	12.1	19.4	2.23				



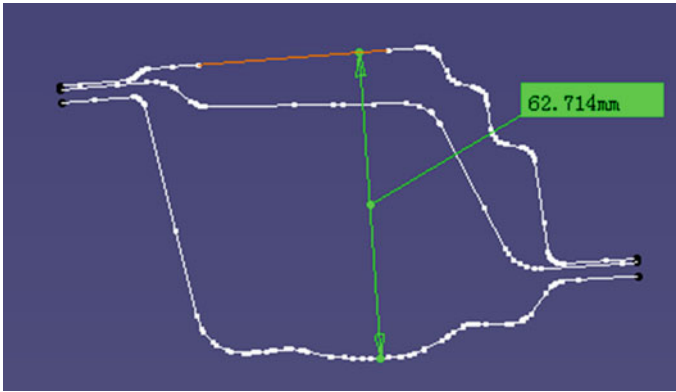
**Fig. 5** The section modify

**Table 5** The characteristic of section

Area (mm <sup>2</sup> )	Torsional constant	Centroidal		
		I <sub>x</sub>	I <sub>y</sub>	I <sub>z</sub>
390.095	137,061	351,669	248,669	202,140

**Table 6** The characteristic of the joint and body

	Joint				Body			
	FRT-RR	In-out	Torsion	Weight	Bend stiffness	Torsion stiffness	Bend model	Torsion model
Target	96-1,088	7-185	1-215	-	-	-	-	-
Baseline	21	3.6	7.6	2.23	8,449	818.4	46.3	30.6
Solution 2	98.1	16.3	30.4	2.46	8,516	826.6	46.3	30.65



**Fig. 6** The section modify

**Table 7** The characteristic of section

Area (mm <sup>2</sup> )	Torsional Constant	Centroidal		
		Ix	Iy	Iz
538.379	322,963	599,054	305,838	220,523

**Table 8** The characteristic of the joint and body

	Joint				Body			
	FRT-RR	In-out	Torsion	Weight	Bend stiffness	Torsion stiffness	Bend model	Torsion model
Target	96-1,088	7-185	1-215	-	-	-	-	-
Baseline	21	3.6	7.6	2.23	8,449	818.4	46.3	30.6
Solution 3	130.5	50.3	60.7	2.61	8,601	832.4	46.4	30.8

**Table 9** Section results compare

Item	Target	Baseline	Solution 1		Solution 2		Solution 3			
			value	$\Delta V$	$\Delta V$ (%)	value	$\Delta V$	$\Delta V$ (%)	value	$\Delta V$
Area	-	378.9	378.9	0	0	390.1	11.2	538.4	159.5	42.1
Torsional	-	110,897	110,897	0	0	137,061	26,164	322,963	212,066	191
Ix	-	321,563	321,563	0	0	351,669	30,106	599,054	277,491	86.3
Iy	-	240,141	240,141	0	0	248,669	8,528	305,838	65,697	27.4
Iz	-	209,205	209,205	0	0	202,140	-7,065	220,523	11,318	5.4

**Table 10** Joint results compare

Item	Target	Baseline		Solution 1		Solution 2		Solution 3	
		Value	k	Value	k	Value	k	Value	k
FRT-RR	96–1,088	21	9.4	52.6	23.6	98.1	39.9	130.5	50
IN–OUT	7–185	3.6	1.6	12.1	5.4	16.3	7.3	50.3	19.3
TORSION	1–215	7.6	3.4	19.4	8.7	30.4	13.6	60.7	23.3
WEIGHT	–	2.23	–	2.23	–	2.46	–	2.61	–

Results are much better and exceed the target more, and the body performance also improved more.

Results analysis

All values are collected and compared the change (Tables 9 and 10).

The main values of the section and the joint are improved most with solution 3, and the solution 1 changes some values, but one of the key values does not meet the target.

### 3 Summary

The conclusion exhibit as follows:

1. The stiffness of joint can be optimized without major cross sectional members, but this maybe have a frequently encountered problem;
2. It's more efficiently with major cross sectional members and stiffness of joints synchronized designed.

### Reference

KUO EY, Mehta PR Body joint modeling method and creation of joint stiffness knowledge base in support of CMTS software development

# Design and Development of Contractive Suspension in Hill-Climb Races

Antonini Pierluigi and Cibrario Valerio

**Abstract** The study of racing car suspension is always a key issue when looking for improvements in car performance [1–4]. The experience, knowledge and data obtained in operational conditions is analysed through simulation, allowing adjustments in the car set-up. An advanced design solution is the implementation of a double opposing spring system, commonly used in Formula 1, in LMP1 or LMP2 but not in minor racing [5], named “contractive suspension”. Such designs integrate an additional spring in the damper system to push the tire down into the ground and increase the understeer effect, thus correcting the setup of the antiroll bar. A study was carried out on a Hill-Climb Race Car, starting from the full vehicle multi-body model of the car with the complete front and rear suspensions. The vehicle was simulated running on an uphill track with the primary manoeuvre bring low-speed cornering with high lateral and longitudinal accelerations. To find the best stiffness ratio between front and rear, a contractive mathematical model has been implemented. Simultaneously, the mechanical design process started with the objective of designing a compact system with elastic elements that could be easily replaced and inserted in place of the traditional spring-damper solution. The results, primarily performed in multibody simulation environment and then verified by the measurement data acquired from on the track, showed an improvement in terms of load transfer at contact patch wheel area with respect to the traditional set-up solution. The evident reduction of the vibration level of the wheel with

---

F2012-E04-014

---

A. Pierluigi (✉)  
ETA S.r.l, Como, Italy  
e-mail: pierluigi.antonini@etaautomotive.com

C. Valerio  
LMS Italiana, Novara, Italy  
e-mail: valerio.cibrario@lmsintl.com

corresponding increase of traction is confirmed by the pilot, who had a better feeling of the car in comparison to the existing solution. Finally, improvement of the mechanical system helped set-up operations during the racing and to achieve weight reduction and space optimization for aerodynamic scope. In conclusion, the adoption of the multibody simulation has been the key aspect to design, verify and optimize all possible variant set-ups before the test phase. Although it is always needed a series of tests for the final tuning, simulation has enormously decreased the time and cost requirements for the experimental development activity, allowing identifying a selected number of optimized set-up solutions.

**Keywords** Chassis · Suspension design · Contractive suspension · Multibody simulation · Hill-climb race

The following topics will be treated in this paper:

- Car Analysis: the problem of the Transfer Load to Front Axle;
- Dynamic Analysis: the Load Wheels Reaction;
- Solution Analysis: the Contractive Suspension;
- Implementation of the solution;
- Simulation of the system;
- Design and Testing of the racing car;
- Conclusions and Outlook.

## 1 Introduction

Hill-Climb racing is a form of motor sport where drivers compete in a timed race on a section of closed public road, properly secured. The competition is usually aimed at non-professional drivers but quite often, champions from tracks participate. Despite the amateur nature of the discipline, skill levels can reach very high levels due to advanced technical solutions adopted from professional track racing. ETA has collaborated with Picchio in the development of the car P4E2, which has reported numerous successes in recent years thanks to the innovative characteristics of the car which includes a dedicated turbo engine.

The need for technical solutions in response to the control requirements for such racing cars has prompted the implementation of a contractive scheme for the front suspension.

This paper aims to show the design criteria and the virtual solution adopted during the development of the prototype.



## 2 Load Transfer Issue

The load transfer in a racing vehicle has important effects on car behaviour while entering and exiting corners, with a direct influence on the car speed [6–8].

Load transfer is the variation of the vertical force on the wheels due to the effects of longitudinal and lateral acceleration of the vehicle.

The case of study is on a rear-wheel drive vehicle which includes important aerodynamic load, the vehicle runs on bumpy roads with several dips, gaps and other joints of asphalt.

In particular the study here performed addresses the acceleration in the final stretch of the curve when the pilot continues delivering engine torque in order to gain additional speed. The aim of suspension set-up adjustment in this phase has the scope:

- to guarantee the rear axle can ensure sufficient adherence to achieve the right traction torque while minimizing the loss of lateral grip due to the “adherence circle” of the tires;
- to guarantee the front axle can ensure sufficient adherence despite the load transfer effect;
- to avoid an excessive increase of the pitch of the car (in front suspension).

Normally, these effects are obtained by adjusting the front shock absorbers with a preload equal to the static weight of the vehicle, so that reductions of the vertical forces less than this value does not result in increasing the vertical travel of the wheel (i.e. avoiding unwanted bump/rebound travel) [9–10].

Unfortunately, the negative effects of this set-up influence the behaviour of the tire which, subjected to load changes, tends to oscillate due to the reduced damping.

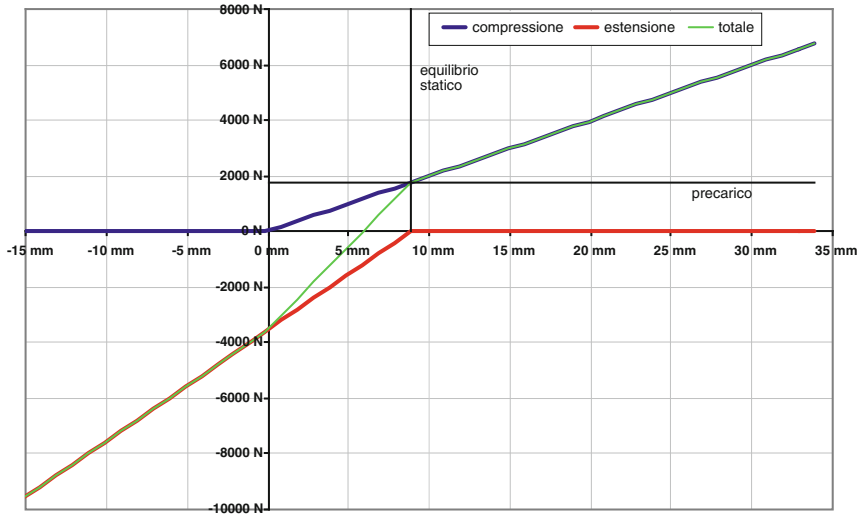
## 3 Dynamic Analysis

The behaviour of the wheel during acceleration has been simulated into two steps:

- physical model of the front suspension on the vertical direction only to better understand the mechanism;
- detailed multibody model of the vehicle during a cornering manoeuvre, while running on a portion of the road obtained by the telemetry.

## 4 Contractive Suspension

The suspension is named “contractive” from the idea to realize a variable optimized equivalent vertical suspension stiffness at the wheel centre, starting from a particular point of work named “Tilting Point” [11–14], around which the stiffness



**Fig. 1** Stiffness of “opposition spring” configuration

characteristic in extension has a slope greater than that found in compression, shown in Fig. 1.

Many people say this solution has been successfully used on the BMW McLaren F1 GTR in international competitions, and on Mercedes CLK GTR. It is still debated today whether this type of suspension system was present on the McLaren F1 1998, MP4/13 model, while it is confirmed that this technology was present on all F1 cars in the following year onwards [15–18]. A recent application on passenger car concerns the rear suspension of Alfa Romeo Mito. Since 2002, some vehicles of the endurance Le Mans Prototype—LMP—category include “contractive” suspensions.

The configuration here developed is defined as an “opposite springs” configuration.

## 5 Implementation of the Scheme

The scheme has been developed for the front suspension. The device was designed to achieve the following targets [19–22]:

- adjustability of the preload of the main spring;
- adjustability of the preload of the extension spring;
- adjustability of the point of work of the main spring;
- replacement of the springs;
- bulk space;
- lightness.

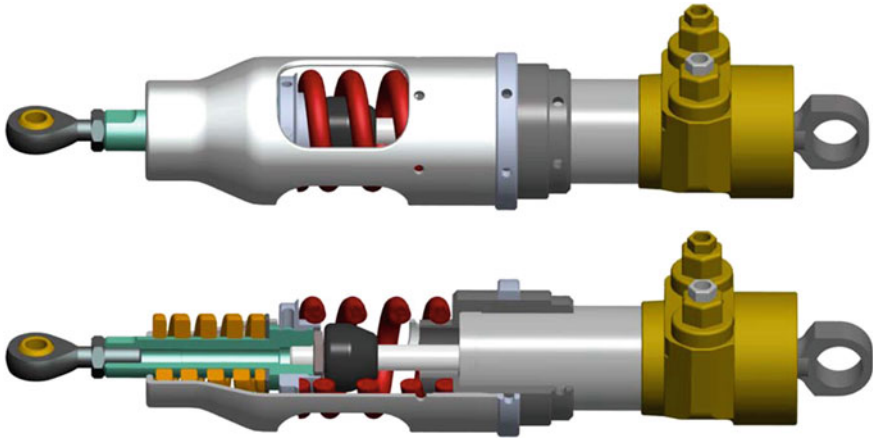


Fig. 2 Contractive damper device

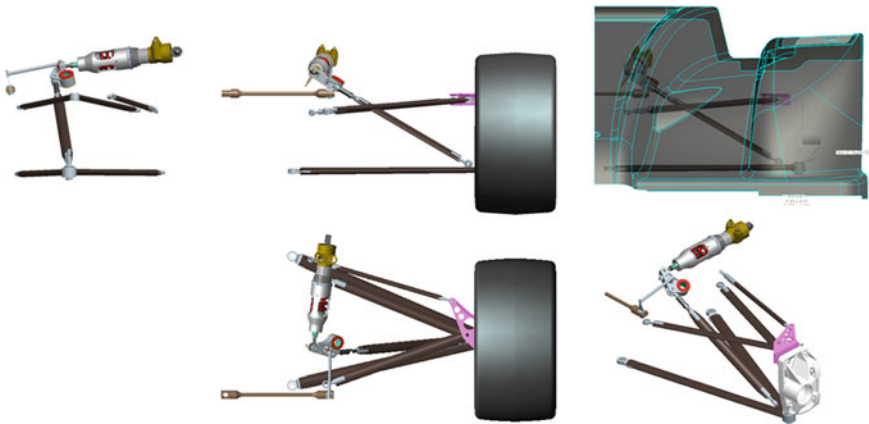
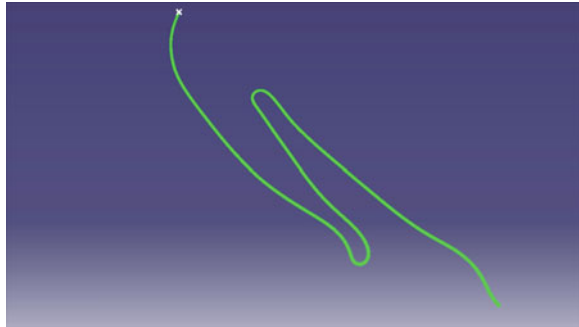


Fig. 3 Views of the suspension scheme with device

The design of the damper, optimized using finite element analysis [23–25], based on the dynamic loads detected in previous sessions of racing and testing, has led to the development of the device in Fig. 2.

The kinematics of the front suspension were then revisited in order to limit the wheel envelope [26, 27], avoiding changes in the external front aerodynamics. The final design can be viewed in Fig. 3.

**Fig. 4** Simulation path

## 6 Simulations

The simulation work has been focusing on developing:

- the kinematic geometry;
- the dynamic parameters.

Multibody simulations were carried out on a complete vehicle model with tires models based on the cornering stiffness (obtained from the input data supplied by the tire manufacturer) and on the vertical stiffness. The variation of the adherence with respect to the vertical force is decreasing as the vertical force increases.

The track path, seen in Fig. 4, has been extracted through telemetry measurement with usage of a GPS system of a car in a previous configuration.

The first set of simulations was performed aiming the development of the suspension kinematics. The first approach was based on a unifilar diagram scheme, shown in Fig. 5, where the points of attachment of the various elements were moved from their original locations and optimized.

Different vertical variations in stiffness at the wheel centre have been analysed, by setting a correct slope progression, Fig. 6, which increases the compression stiffness during vertical upper travel, i.e. when the upper body moves in the vertical lower travel.

After the kinematic definition analysis, the next step was the implementation of full multibody model of an open path, with a speed profile not completely equal to the real one, but defined by means of the maximum speed on entering the corner, the average deceleration in the first portion of the corner, the traveling speed and the acceleration out of the corner.

In particular for the case here analysed particular attention is paid to the last phase of the corner manoeuvre, shown in Fig. 7, establishing the point where the acceleration takes place.

Consequently, it is possible to define an optimized speed profile, see Fig. 8. A series of selected manoeuvres were analysed to view the evolution of the forces acting on the suspension.

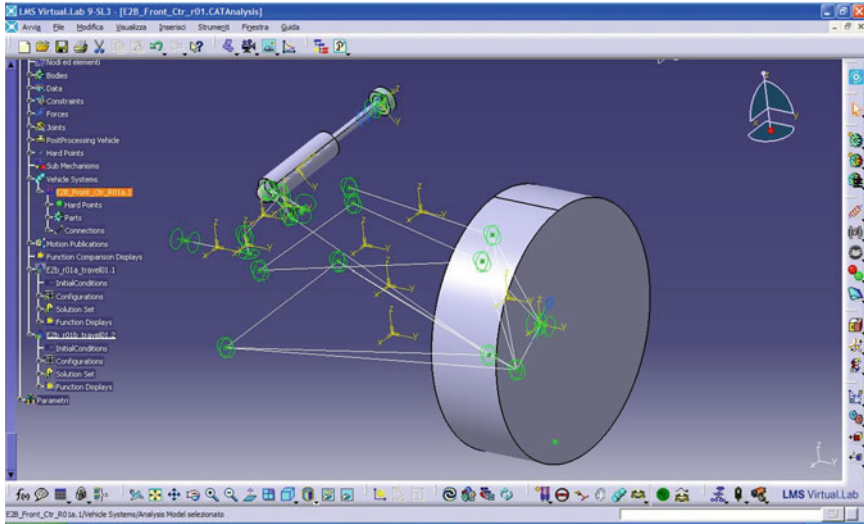


Fig. 5 Unifilar model for kinematic analysis

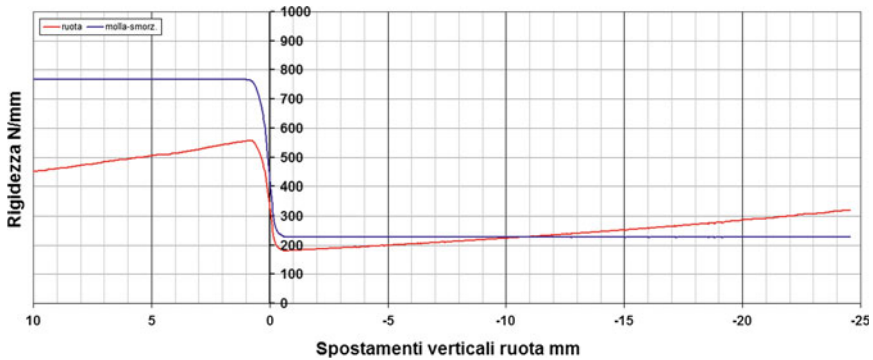


Fig. 6 The equivalent stiffness related at wheel centre

Once the optimization of the stiffness values are carried out and completed, a series of simulations were performed with the aim of evaluating the effect of the device on suspension performance.

In particular the suspension is analysed in two extreme cases and in the optimal solution [28–31], i.e.:

- shock-absorber with extension spring infinitely rigid (end of extension stroke), called “NoContr”;
- shock-absorber with compression spring only (preload less than the car weight), called “Normal”;
- shock-absorber with extension spring with higher stiffness, called “Contr”.

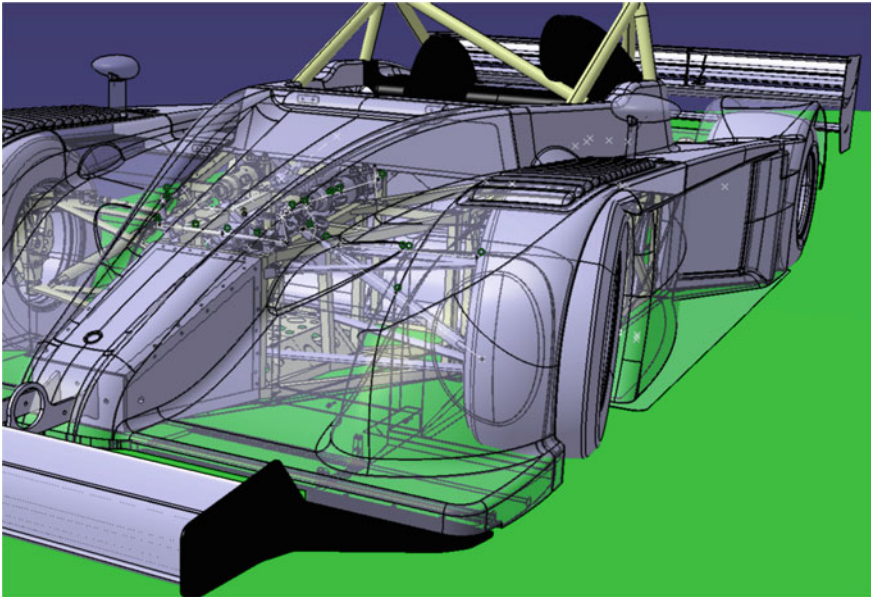


Fig. 7 The vehicle viewed during the cornering maneuver

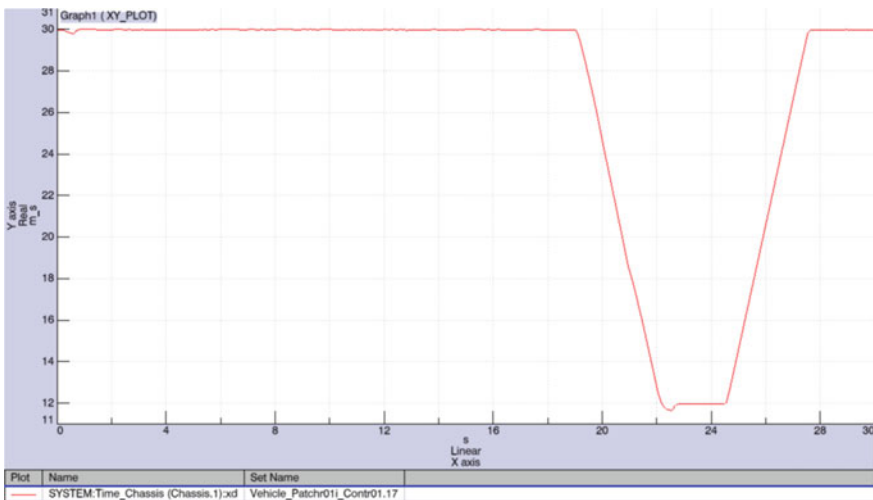


Fig. 8 Speed profile of the car

It is then possible to observe the behaviour of this suspension set-up, specifically the limitation of the pitch of the car during acceleration.

In Fig. 9 it is possible to observe that, as expected, the pitch decreases in absolute terms during the acceleration phase (b) and remains equal between the

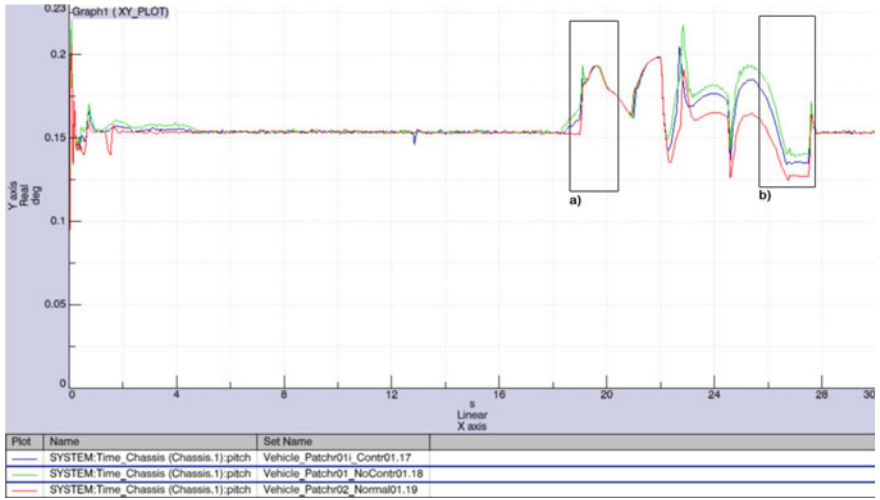


Fig. 9 Pitch response

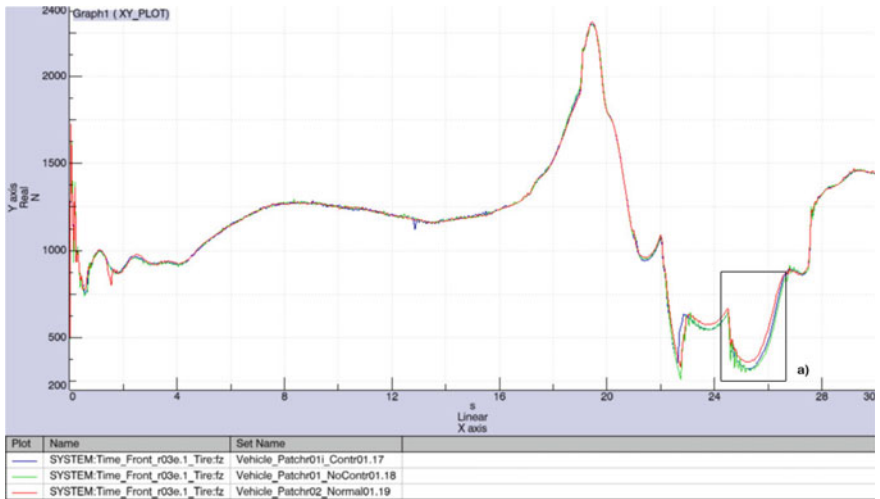


Fig. 10 Vertical force on inner wheel

various configurations in the deceleration phase (a). Between the two phases the pitch angle is influenced by the vehicle during the cornering manoeuvre due to the interaction of the lateral inclination, the suspension geometry and the road surface. The first 4 s of simulation should not be considered because it was used for the tool set-up of the initial conditions, including the cancellation of the initial conditions.

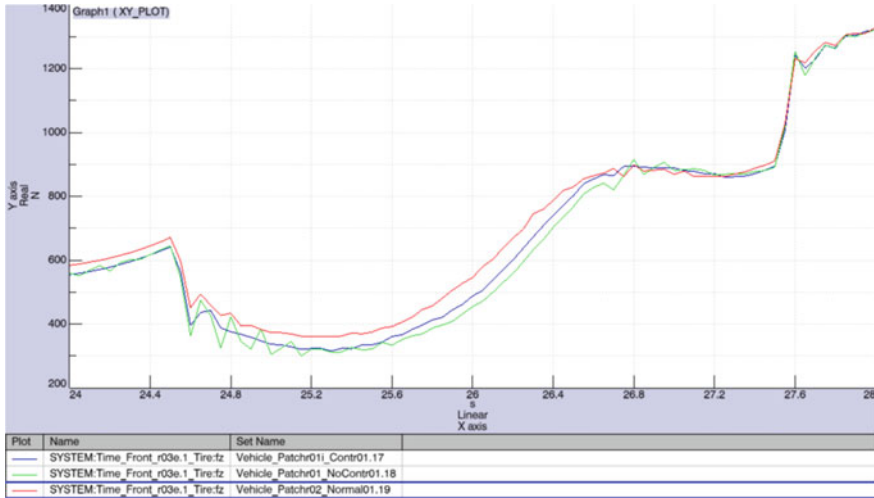


Fig. 11 Detail of vertical force on inner wheel during load transfer phase

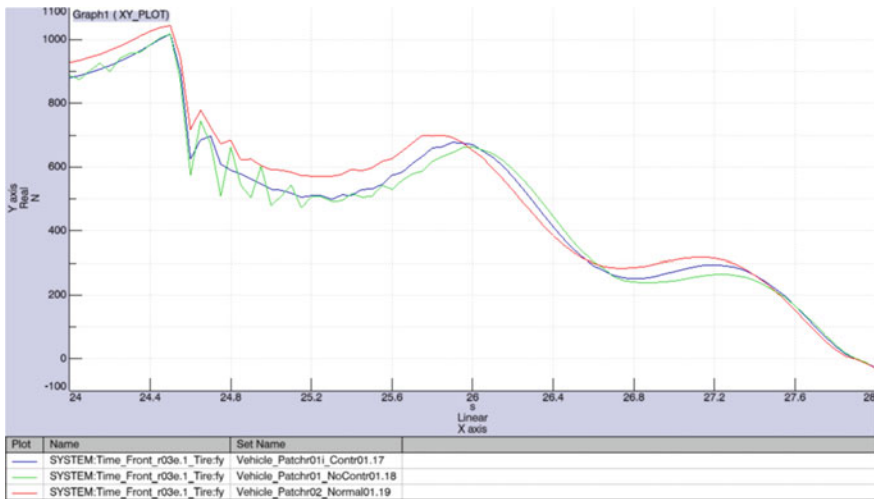


Fig. 12 Lateral force on inner wheel during the same interval of Fig. 11

Obviously the lowest pitch angle is obtained with the suspension in total extension.

It is important to evaluate the behaviour of the vertical load of the wheel during the acceleration phase.

As highlighted in phase (b) and reported in Figs. 10 and 11, wheel vibration effects occur due to load transfer, which are not damped. The tire, which in the “NoContr” case is the only elastic element within the suspension system, has very



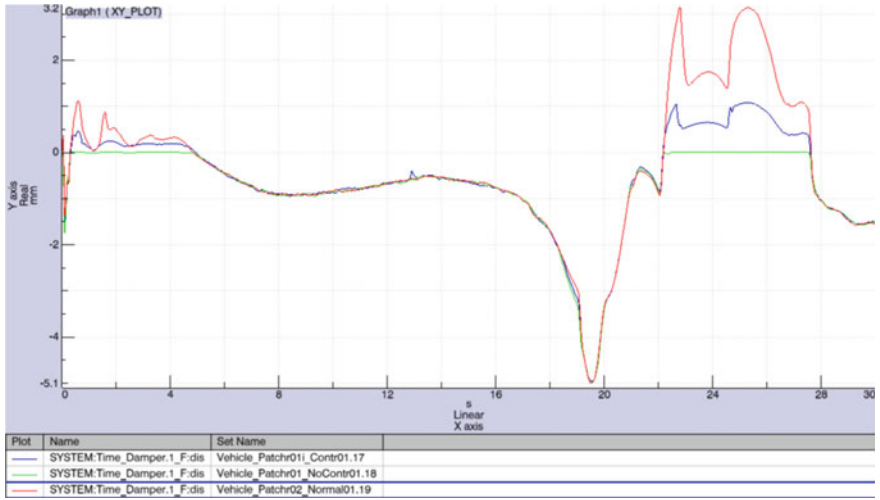


Fig. 13 Damper displacement

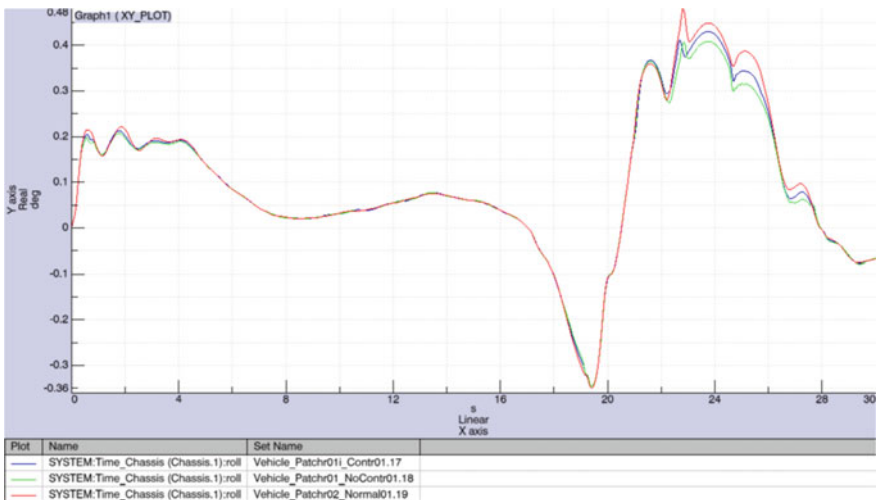


Fig. 14 Roll angle

limited damping and consequently generates pronounced oscillation which affects the lateral force.

The lateral force is in fact represented in Fig. 12.

The suspension damping is important, as it reduces the vertical travel variations to a minimum, as typically desired during the suspension set-up.

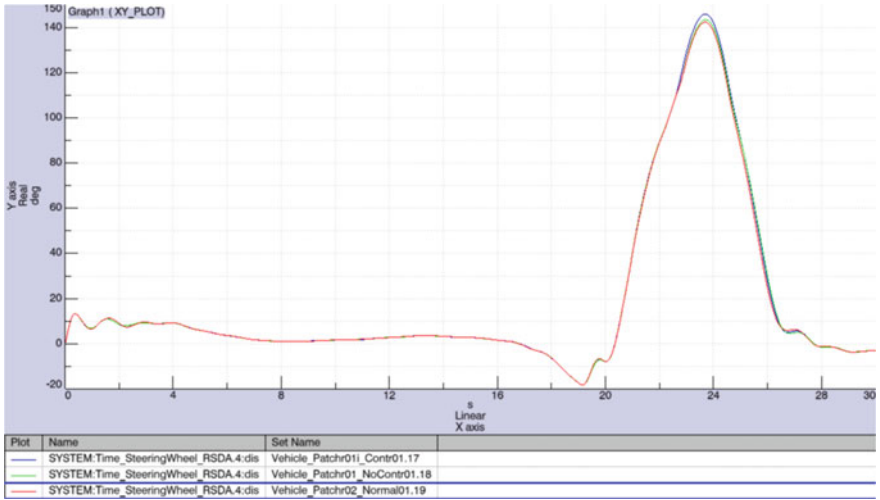


Fig. 15 Steer wheel angle

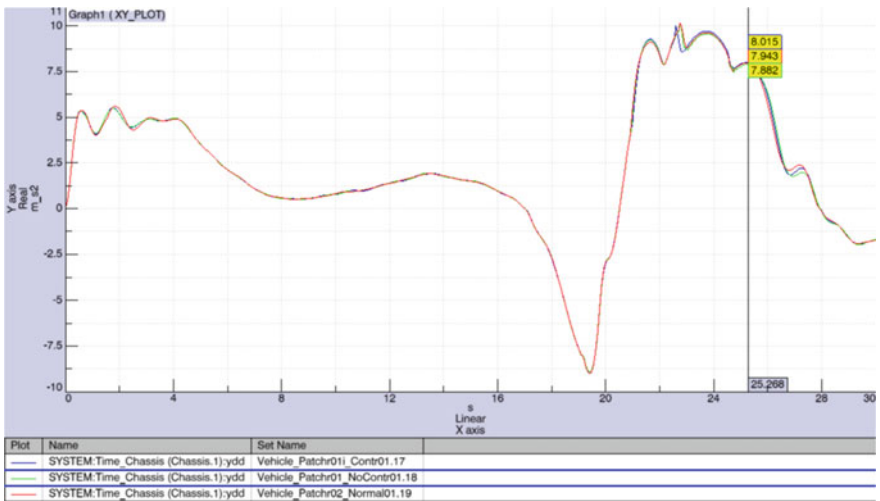


Fig. 16 Lateral acceleration

Figure 13 shows the travel of the shock-absorber during the entire manoeuvre in the three cases analysed; it is possible to observe that the maximum extension is reached with different stiffness settings before the end of the analysed interval. When the car accelerates and generates the load transfer, this is the main cause of the induced vibrations in the wheel.

Simulation also shows:

- decreased roll angle, as expected, see Fig. 14;
- unexpected increase of the steering wheel angle in the center of the cornering in case of the contractive suspension, even more than observed in the “NoContr” case; see Fig. 15
- increase of the lateral acceleration in case of contractive suspension, see Fig. 16.

## 7 Conclusions

The work emphasizes that a design process, when driven by simulation, allows evaluation of the effects of technical suspension set-up variants in different and complex configurations.

The design process involves not only parametric variations (between contractive and normal suspension) but also model variations (for instance the non-contractive solution implemented a stroke-end device with very high stiffness value), allowing the designer to evaluate and select the most promising solutions, minimizing the experimental activity.

The tests carried out on the track together with competition testing and the achieved results confirmed concretely that performance improvements with respect to the car in the previous set-up configuration were achieved as a result of the study.

## References

1. Gillespie TD *Fundamental of vehicle dynamics*. SAE International, ISBN 978-15-609-1199-9
2. Genta G (2000) *Meccanica dell'autoveicolo*, Levrotto and Bella, ISBN 978-88-821-8042-3
3. Milliken WF, Milliken DL (1995) *Race car vehicle dynamics*. Soc Automot Eng. 367–372 ISBN 1560915269
4. Guiggiani M (2007) *Dinamica del veicolo*. De Agostini Scuola Spa, ISBN 978-88-251-7300-0
5. Staniforth A (2006) *Competition car suspension: a practical handbook*. Haynes Publishing, ISBN 1844253287
6. Smith C (2004) *Racing chassis and suspension design*. Soc Automot Eng ISBN 0768011205
7. Smith C (1978) *Tune to win*. Aero Publishers, ISBN 0879380713
8. Jazar RN (2008) *Vehicle dynamics: theory and applications*. Springer, Berlin, ISBN 0387742433
9. Dixon JC (2009) *Suspension geometry and computation*. Wiley, New York, ISBN 978-0-470-51021-6
10. Dixon JC (2007) *The shock absorber handbook*. Wiley, New York, ISBN 978-0-470-51020-9
11. Bianchi M (1993) *Suspension process and apparatus of the type having different stiffnesses with provision to smooth the change from one stiffness to another*. US5183285
12. Bianchi M (1993) *Vehicle wheel suspension method*. US5244190

13. Bianchi M (1993) Suspension of vehicle using two stiffnesses, adapted respectively for obtaining a good level of comfort and a good level of behaviour. US5263695
14. Bianchi M (2001) Vehicle wheel suspension using spring combined with flexible armouring for modifying the stiffness curve. US6237901
15. Tesi di F Raimondi Studio e realizzazione di una sospensione contrattiva. Università degli Studi dell'Aquila, Anno accademico 2007–2008, Relatore Prof. Ing. De Paulis A, Tutor aziendale Ing. Carfagna G
16. Fuke WA (1968) Variable rate suspension. US3417986
17. Joseph L (1972) Spacer and stabilizer for insertion between adjacent convolutions of an automobile coil spring. US3674250
18. Moehle KA, Taschner RG (1977) Dual spring support. US4033542
19. Milliken WF, Milliken DL (2002) Chassis design: principles and analysis. Professional Engineering Publishing, ISBN 978-1-860-58389-6
20. Genta G, Morello L (2009) The automotive chassis. Components design, vol 1. Springer, Berlin, ISBN 978-1-4020-8674-8
21. Genta G, Morello L (2009) The automotive chassis. System design, vol 2. Springer, Berlin, ISBN 978-1-4020-8673-1
22. Gilles T (2004) The automotive chassis: brakes, suspension and steering. Cengage Learning, ISBN 1401856306
23. Juvinall R, Marshek K (2002) Fondamenti della progettazione dei componenti delle macchine. edizioni ETS, ISBN 978-88-774-1730-5
24. et altri Andreini P (2005) Manuale dell'ingegnere meccanico. Hoepli, ISBN 978-88-203-3380-5
25. Zagatti E, Zennaro R, Pasqualetto P (1994) L'assetto dell'autoveicolo, sospensioni, pneumatici, sterzata, comportamento dinamico. Levrotto and Bella, ISBN 978-88-821-8022-5
26. Reimell J, Stoll H, Betzler JW (2001) The automotive chassis. Butterworth Heinemann, ISBN 0750650540
27. Adams H (1993) Chassis engineering. Penguin, ISBN 1557880557
28. Wood JK (1943) Variable support hanger. US2335834
29. Wood JK (1948) Support. US2437631
30. Fenton AJ (1961) Lowering device applicable to automobile springs. US3014713
31. Hines JE (1967) Combination shock absorber and spring. US3297312

# Modularized Design of the Engine Compartment Design Based on the Theory of CBR

Honghua Li, Wei Li and Fuquan Zhao

**Abstract** With the increase of automobile number, more and more consumers are concerning the safety and styling of automobile. While for car manufacturers, it means to spend much more time and money to develop new components. The objective of this study is by use of mature modules, to reduce the costs and the cycle of development on the basis of satisfying the demands of consumers.

**Keywords** Modularization · Engine compartment · CBR

## 1 Introduction

Nowadays, the competition of automotive products is more and more intense all over the world. With the development of automobile inventory, the competition about the market and trademark of vehicle is increasing. China's automobile production enterprises need to strengthen their competitiveness in order to gain a firm foothold in this fierce competition and to keep up with the pace of the auto companies. The key to enhance the competitiveness is to accelerate the development of new models, which is largely reflected in replacement of power. In order to match different engines, numerous similar but not universal parts are generated in the engine compartment. Therefore, fast and stable design of engine compartment is required. However, traditional design methods and process cannot meet the

---

F2012-E04-016

---

H. Li (✉) · W. Li · F. Zhao  
Zhejiang Geely Automobile Research Institute Co. Ltd, Hangzhou, China  
e-mail: lihonghua@rd.geely.com

requirements of rapid development of the engine compartment, and a new design idea is urgently demanded.

In the traditional design process, the direct designers are taken as the center to conduct construction and optimization of engine compartment according to the experience of the designers. A design engineer tends to adopt a way of similar design, which is to recall the former designs similar to the current instance first, and to use the past design ideas and methods for reference to avoid the problems occurred earlier instead of from scratch when starting design of a new engine compartment. The core ideology of similar design is to modify the original design to meet the requirements of new design.

## **2 Case-Based Design**

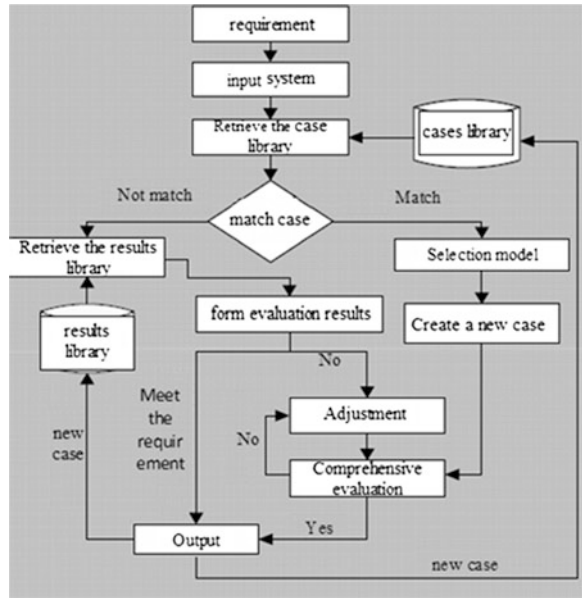
Case-Based Design is an application of Case-Based Reasoning (abbreviation CBR) in the design field. The basic idea of CBR is to store the prerequisite, the solution and the result of the past problem in the form of a case. When solving, first inquire the case which is the most similar to the current issue, in order to meet new needs by adjusting the case in the library. Knowledge is used in CBR cases rather than artificially developed rules, which makes CBR very applied to the field with large amount of historical data. Case-based reasoning is in line with people's mental cognitive process, and reflects process of people's reasoning for solving based on past experience, and the characteristics of learning from failures and successes. And Case-Based Design is a practical application of the CBR design idea.

The design process of the case knowledge is generally a process to find similar design from case database, which can replace the process that the designer recalls the former designs. When receiving a new design task, firstly the designer will access to the case database, input query, select similar cases from the search result, and then conduct design and add the new design to the database as a new case after the design is completed, thus the case database can be updated.

## **3 Establishment of CBR Model**

The Case-based design process is divided into four steps: conditions analysis, case database retrieve, case modification and database update. The specific process is shown in Fig. 1.

Fig. 1 Design flow chart



### 3.1 Conditions Analysis

Conditions analysis means to list indicators of the plan for this design through analysis of current layout conditions. For engine room, the type of the assembly hole of various parts is set as the Condition  $v_1$ , the size of hole is set as Condition  $v_2$ , 3D coordinate of the hole center as Condition  $v_3$ , analysis needs to conduct as Condition  $v_4$ , and problems and solutions as Condition  $v_5$ . Each of them can be analogized from the former one, and a set is applied for condition feature set.

### 3.2 Case Database Retrieve

In this part, we need to calculate the similarity degree between indicators value of the retrieved case and required value of designed indicators by grey correlation similarity degree calculating method [1] and find out the most similar case from the database in order to retrieve the matched case in the database.

Select case number from case database.

Where type number = "Engine room"

And  $f(v_1) \geq$  "The specified value"

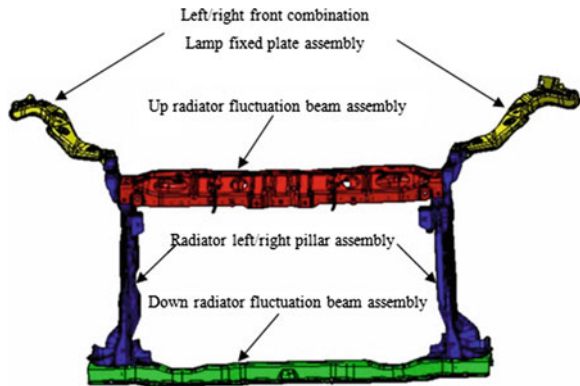
And  $f(v_2) \geq$  "The specified value"

.....

And  $f(v_n) \geq$  "The specified value"

And  $v_1, \dots, v_n$  indicate characteristics of each indicator

**Fig. 2** Design data of engine compartment



### 3.3 Case Modification

In the last step, if similar cases to match with the design requirement can be found, we will need to retrieve the case valuation in results database. If the evaluation results do not meet the requirements, we need to adjust some of the parameters of similar program until it meets the requirements. If we cannot find a case similar to the design, we need to build a new model, complete the comprehensive evaluation and then output.

### 3.4 Database Update

The evaluation results of the modified cases and new cases are re-stored in the case database and results database to facilitate retrieve and the next call.

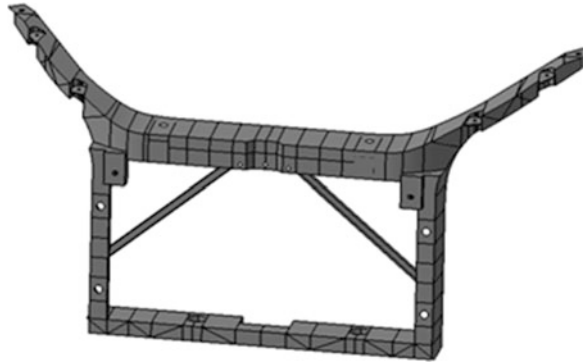
## 4 Modular Design Process of Engine Compartment

Take the front-end design of compartment for example, Fig. 2 shows the compartment front-end data of a certain vehicle. The front-end of compartment was made of stamping parts by welding, including left/right front combination lamp top clamping plate assembly, radiator left/right pillar assembly, and radiator top/bottom beam assembly [2].

In order to ensure the installation position strength of left/right front combination lamp, left/right front light, water tank, radiator, engine hood latch, horn,



**Fig. 3** Front module of engine compartment



front grille, front bumper, wind guide plates, decorative laminates of engine compartment, engine bottom guard board, various reinforcing structures are laid out.

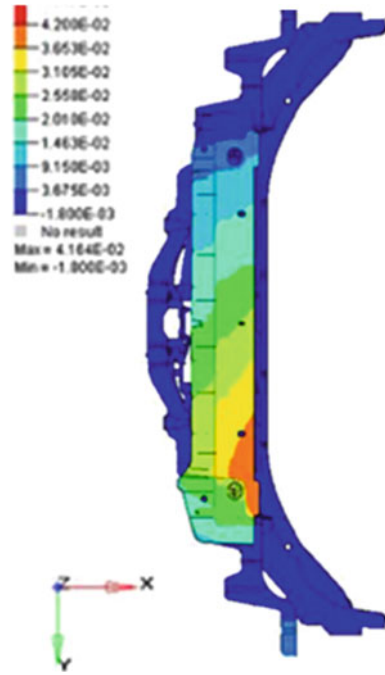
The design of engine compartment, based on the case knowledge, the mechanism to be designed should be considered as a whole, and the function and performance of each part as the whole's features. These features are stored in the case database, and mapped to the data in the database. In order to facilitate understanding, each feature can be virtualized into data, i.e. virtual module data. The virtual module data reflects each installation point, installation area and its structure rigidity of compartment assembly. Take the design of engine compartment front for example, its front module data of an engine compartment in a certain vehicle is shown in Fig. 3.

When the similar compartment parameters are retrieved from the case database, data can be extracted from the related database. After matching the data with surrounding components, some modifications are needed to satisfy the current requirement on layout. The modified data should be evaluated comprehensively via simulation assembly, CAE analysis or other method. Figure 4 shows the ready data of the compartment front part completed only according to installation points. Because the working condition in the current design of the surrounding components, such as radiator, was different from the original design, stiffness of some location was inadequate according to CAE analysis.

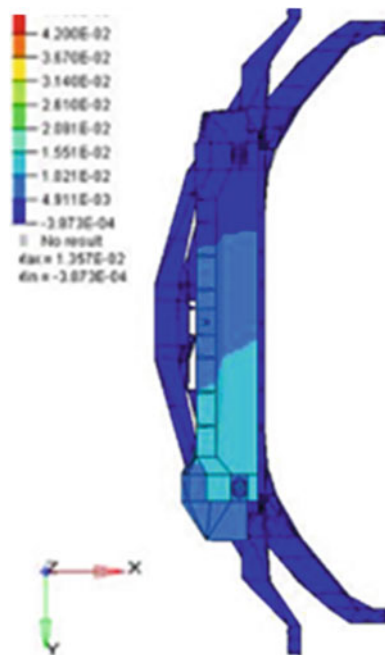
Referring to the CAE analysis results, partial optimization is made to the data of the compartment front, and then analysis is conducted again. Figure 5 shows the final analysis result.

Up to now, the design of a new engine compartment is completed. However, the case knowledge-based design is not finished, the result of the above design should be stored in the case database after characteristic conditions are set up, which will provide references for the follow design.

**Fig. 4** Data of engine compartment front



**Fig. 5** Data of engine compartment front after modification



## 5 Conclusions

When we used the traditional design methods to conduct similar designs, we have to do a lot of duplicated work for lack of sharing and inheritance of the data, resulting in extending product design cycle.

According to statistics, the engineers often need to spend 60–75 % of the time of the entire design process to work over all related reference materials and data. This will result in a substantial increase in design costs. So, during the development of the new motor, how we could be more effective and quickly in using the existing resources will become the key to reduce design costs. The product design based on cases may make use of the theory of similar design to quickly check the effective case so that assists in completing the development of new products. And, if you apply the product design based on case to CAD system, it will improve the design quality and reduce the design cycle. In addition, it will enable enterprises to quickly meet the changing needs of the users in the increasingly fierce market competition.

## References

1. Liu S, Dang Y, Fang Z (2004) Gray system theory and application. Science Press, Beijing
2. Benli J (2006) Database theory and application: SQL server 2000. China Railway Publishing House, Beijing

# Development of First Order Analysis for Torsion Beam Suspension (FOA/TB) Corresponding to Modular Design

Kazuaki Chiku, Hideki Sugiura, Takaaki Uno and Toshiji Hirotani

**Abstract** The First Order Analysis for Torsion Beam Suspension (FOA/TB)/design tool has been developed as a CAE tool for suspension designers. Reflecting the needs of suspension designers, this tool tends to become more detailed and complex. In addition, FOA/TB is also used by torsion beam component designers since it is capable of creating detailed models of the torsion beam itself. However, in the design phase, torsion beam designers cannot obtain all the parameters included in the current FOA/TB model and have to provisionally set unknown parameters. To overcome this problem, this paper introduces a method for abstraction and masking of design parameters based on the concept of modular designing. It also shows how usability was improved using the new concept FOA/TB.

**Keywords** First order analysis · Torsion beam suspension · Modular design · Structural analysis · Interdependence analysis

## 1 Introduction

The torsion beam suspension is widely used for the rear suspension of front-engine front-wheel drive (FF) cars by many automobile manufacturers. The elastic deformation behavior of the beam significantly affects various performance

---

F2012-E04-017

---

K. Chiku (✉) · H. Sugiura  
Toyota Central R&D Labs., Inc, Nagoya, Japan  
e-mail: kchiku@ket.tytlabs.co.jp

T. Uno · T. Hirotani  
Futaba Industrial Co., Ltd, Tokyo, Japan

aspects such as vehicle handling & stability and fatigue strength. Therefore, CAE analysis that considers elastic deformation of the beam is required at the planning stage. However at this stage, detailed drawings and specifications are not determined. As a result, designers need to predict reasonably accurate suspension characteristics from a small amount of information. Even if there is a detailed drawing, most of the designers can't create a detailed CAE model which needs special skills. Therefore, when planning the vehicle in automobile manufacturers, First Order Analysis (FOA) concept that can be operated even without special skills or know-how about numerical analysis and CAE is proposed and FOA for Torsion Beam suspension (FOA/TB) is also developed for early design phase [1].

The FOA/TB design tool can greatly reduce the amount of work in the early design phase and is widely used by many designers [2, 3]. However, for this reason, demands to improve its accuracy have increased the detail and complexity of the FOA model. This has adversely affected usability to the extent that FOA/TB no longer fulfils its original purpose of an easy-to-use design tool. Shape optimization was applied to address this problem, but the essential issue has yet to be resolved.

At the same time, in recent years, the modularization of vehicle components has made great progress with the aims of improving productivity and reducing costs. Although there are various definitions of modularization, it generally means to achieve a target performance while verifying the relationship between parts that have a high interdependence, and to standardize the interaction between the parts. A torsion beam suspension is one of the modules of an automobile and the interactions between the parts also have a significant impact on the total performance. Furthermore, the design and development of suspension components are often shared among automobile manufacturers and component suppliers from the initial stage of suspension development. In this case, designers of component suppliers have little information about design variables because some of them have not yet been determined at this stage. This lack of information makes it difficult for component designers to accurately predict total suspension performance.

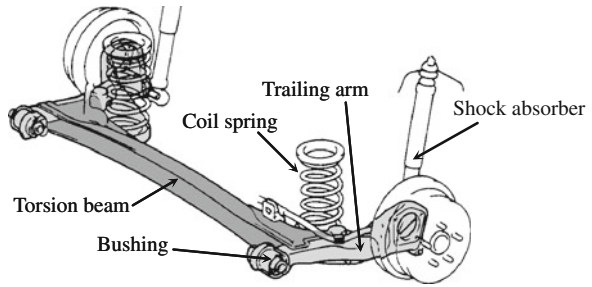
This paper describes a method for simultaneously solving the two problems mentioned above by applying the concept of modularity proposed by Baldwin [4] to the initial designing tool, FOA/TB. More specifically, this method replaces design variables, which cannot be obtained, with standardized values and masks them. It then extracts the minimum functions from current FOA/TB while taking advantage of the characteristics. Selection and standardization of the functions of the tool and design variables are based on the results obtained from the interdependence analysis using FOA/TB.

## **2 Development of FOA/TB for Suppliers**

### ***2.1 Beam Suspension and Suspension Characteristics***

A beam suspension has a simple structure. As shown in Fig. 1, the main parts consist of two trailing arms attached to the body via a rubber bushing, and a torsion

**Fig. 1** Torsion beam suspension



beam that connects these two arms. The wheel hub is mounted via a bearing at the tip of the trailing arms, and input force from the road surface is transferred to the beam suspension through these parts. In addition, a major feature of a torsion beam suspension is that the torsion beam twists to absorb displacement when the right tire bounds and the left tire rebounds and vice versa (Fig. 2).

The performance of a beam suspension can be evaluated by various indicators, and so-called suspension characteristics are used as measurements of handling, stability and ride comfort. The main characteristics are longitudinal compliance, compliance steer due to lateral force, roll stiffness, and the roll steer coefficient. Longitudinal compliance is the amount of elastic deformation of a loading point when a force is applied backward at the center of the right and left wheel. Roll stiffness is the rigidity in the roll direction when the right tire bounds and left tire rebounds and vice versa. This is mainly caused by torsion of the beam. The roll steer coefficient expresses the toe angle change rate with respect to the roll angle.

## 2.2 Functions of FOA/TB

Figure 3 shows the flow of the design process and the configuration of the current FOA/TB using Microsoft Excel spreadsheets. Calculation of suspension characteristics are performed by entering data for the suspension layout in the main sheet. Designers draw a cross-sectional shape of the torsion beam using a simple CAD tool and the FOA/TB automatically creates a 3D finite element model. Other components like bushings and so on can be modeled using a different sheet. Figure 4 shows the data flow of FOA/TB. Since the suspension characteristics are strongly influenced by the mutual dependence of the torsion beam, trailing arms, and bushings, it is necessary to input the characteristics of these components in detail. However, a torsion beam component designer cannot obtain detailed characteristics of other components in the early design phase. Therefore, a key issue is the development of a method that supplements the other missing component characteristics and that accurately calculates the suspension characteristics.

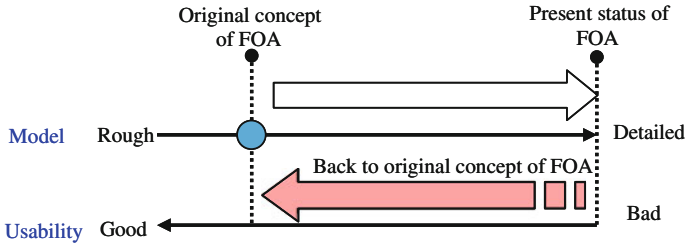


Fig. 2 Detailed FOA model vs. usability

### 2.3 Abstraction and Standardization Using Interdependence Analysis

When calculating each suspension characteristic, the location and direction of force application are different. Components that affect particular suspension characteristics differ according to the relative stiffness difference of the components. In order to clarify these complexities, Tables 1 and 2 show the analysis results for interdependence between components and suspension characteristics using FOA/TB. In order to create Table 1, the stiffness of each component is mainly increased about 20 % against original configuration. From these tables, designers can quantify the interdependence of components and suspension characteristics. For torsion beam component designers, the roll steer coefficient and roll stiffness are the most important suspension characteristics because the design of the torsion beam greatly affects these two characteristics. Shaded areas of Tables 1 and 2 show that, trailing arms can be regarded as relatively rigid compared to the torsion beam, which has an open cross-section. Therefore, the design variables for the shape of the torsion beam are left (extracted), but the design variables for the trailing arms are automatically set as standard values and are masked (hidden). This interdependence analysis is one of the key concepts of modular design and this method enables the standardization of other component design variables.

### 2.4 Application of Interface for Component Design

The results from interdependence analysis are applied to solve the problems mentioned in Sect. 2.2. More specifically, application is done by creating a new interface that hides the interdependence of non-targeted characteristics.

As an example, Fig. 5 shows the configuration of the FOA/TB developed for torsion beam component designers. The shaded area in the figure is the newly developed Excel interface sheet. The suspension characteristics that greatly affect the torsion beam design can be calculated by simply entering the necessary design variables for modeling the torsion beam and its attached location. In order to

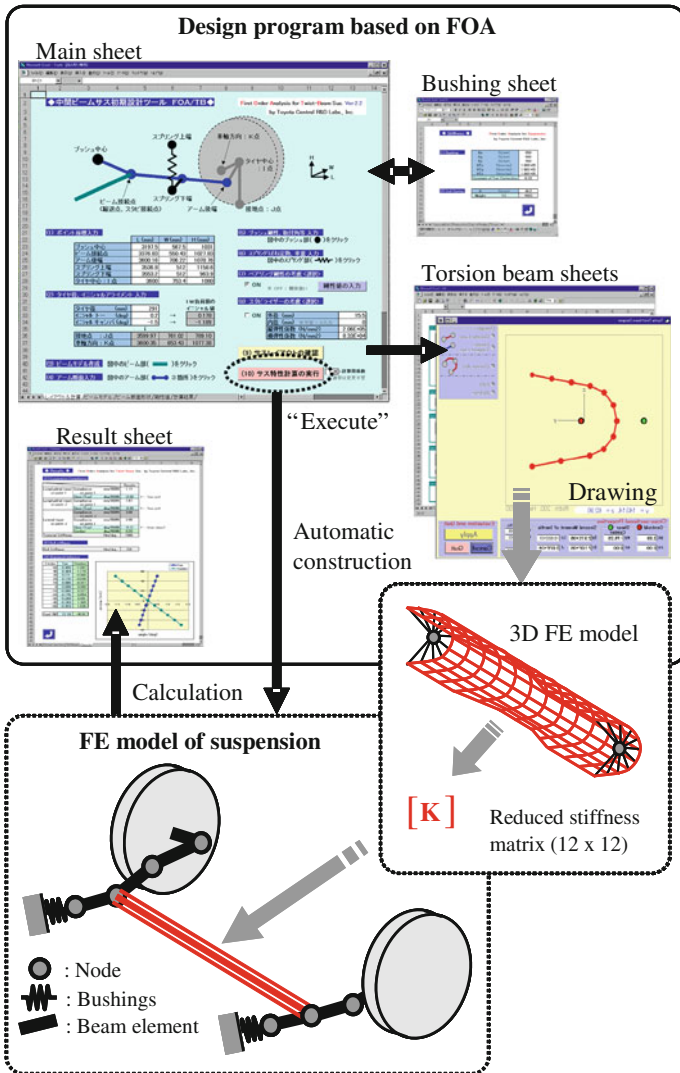


Fig. 3 Structure of FOA/TB and flow of calculation

prevent data typing mistakes, the sheet is configured to sequentially input the necessary data in accordance with the procedures of the design process. The characteristics of components other than the torsion beam are automatically replaced by standardized values. In addition, this sheet is simply added-on to the current FOA/TB, so the designer can also use the functions of the current FOA/TB. This interface sheet is arranged to fit on one A3-size page, including both input data and output results, and the printed paper can be used as a report immediately.



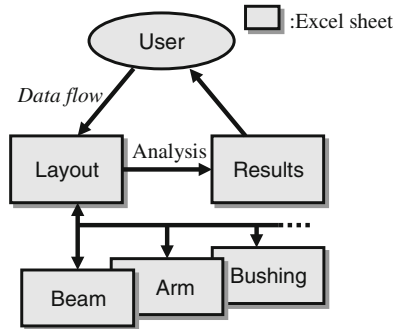


Fig. 4 FOA/TB for suspension designer

Table 1 Effect of components to suspension characteristics (Change rate %)

	Torsion beam	Trailing arm	Bushing	Bearing	Spring
Longitudinal compliance	-1.5	-0.9	-13.9	-0.1	0.0
Longitudinal steer	-7.0	-7.6	-9.4	-9.0	-9.0
Lateral compliance	-1.6	-3.3	-23.8	-16.2	-13.0
Compliance steer due to lateral force	-3.4	-7.0	-17.0	-10.9	-10.9
Compliance camber due to lateral force	-3.4	-9.4	-49.0	-59.8	-48.3
Roll stiffness	17.5	0.1	2.4	0.1	4.9
Roll steer coefficient	43.4	-0.5	-0.6	-1.7	-1.8
Roll camber coefficient	8.8	-0.4	-1.7	-1.2	-1.1

Table 2 Effect of components to suspension characteristics (Symbolic)

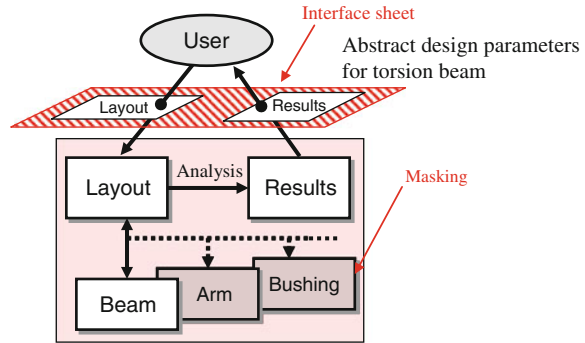
	Torsion beam	Trailing arm	Bushing	Bearing	Spring
Longitudinal compliance	×	×	⊙	×	×
Longitudinal steer	⊙	○	○	○	○
Lateral compliance	×	Δ	⊙	⊙	⊙
Compliance steer due to lateral force	Δ	○	⊙	○	⊙
Compliance camber due to lateral force	Δ	○	⊙	⊙	⊙
Roll stiffness	⊙	×	Δ	×	Δ
Roll steer coefficient	⊙	×	×	×	×
Roll camber coefficient	○	×	×	×	×

### 3 Validation Results

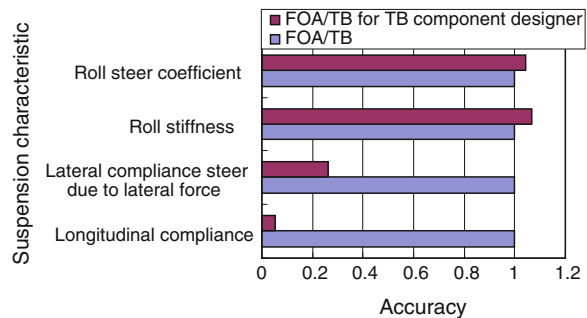
#### 3.1 Extracted Parameters

In order to validate the accuracy of the developed interface sheet, suspension characteristics were calculated using only the design variables extracted using

**Fig. 5** FOA/TB for torsion beam component designer



**Fig. 6** Accuracy of FOA/TB for TB component designer

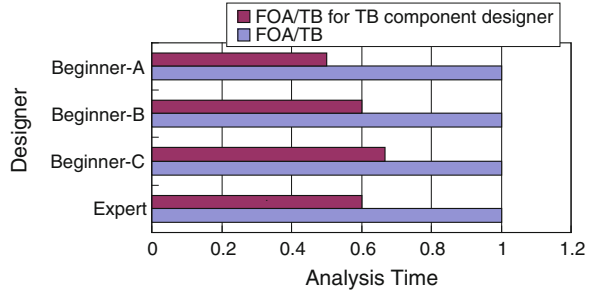


results of interdependence analysis. Figure 6 compares the results of the calculated suspension characteristics using the current FOA/TB and the developed interface sheet. Roll stiffness and the roll steer coefficient, which are key characteristics for torsion beam designers, have almost the same values as the current FOA/TB. This indicates that the extracted design variables are correct in order to keep the accuracy. In contrast, the longitudinal compliance and lateral force steer differ greatly from the results of the current FOA/TB. This is because the design variables for the bushing and trailing arm are replaced by standardized values and masked by the interface sheet. However, this will not be a major problem because these characteristics are not important for torsion beam component designers.

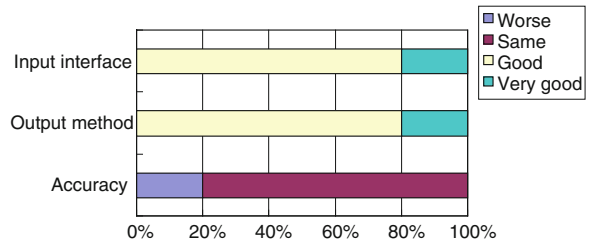
### 3.2 Verification of Usability

Figure 7 compares the time required by the current FOA/TB and FOA/TB for torsion beam component designers to obtain results from the beginning of creating the analysis model. It was confirmed that the analysis time of both experts and beginners was reduced by an average of approximately 40%. This is probably

**Fig. 7** Reduction of analysis time



**Fig. 8** Improvement of usability



because the new tool enables modeling using one Excel sheet and because the design variables of other components are set automatically.

Figure 8 compares the results of a subjective study of torsion beam component designers about the usability of the newly developed FOA/TB for torsion beam designers and current FOA/TB. The effects of the easy-to-read output results and easy creation of models can be confirmed. In addition, this usability study also found the possibility that this tool can be used as an educational tool for understanding the relationship between the torsion beam shape and suspension characteristics.

## 4 Summary

- (1) A new FOA/TB tool for torsion beam component designers was developed by extracting important design variables and masking (hiding) design variables that are not important using the interdependence analysis results.
- (2) The results of suspension characteristics that are important for torsion beam component designers, such as roll stiffness and the roll steer coefficient, have equivalent accuracy to the original FOA/TB. At the same time, analysis time was reduced by approximately 40 % while improving usability.

## References

1. Nishigaki H, Nishiwaki S, Amago T, Kikuchi N (2000) First order analysis for automotive body structure design. ASME DETC2000, DAC-14533
2. Sugiura H, Mizutani Y, Nishigaki H (2001) First order analysis for automotive suspension design. R&D Review of Toyota CRDL, Publication, vol 37. no 1
3. Sugiura H, Kojima Y, Nishigaki H, Arima M (2000) Trailing twist axle suspension design using ADAMS. FISITA, F2000 G306
4. Barldwin Carlis Y, Clark Kim B (2000) Design rules, vol1; the power of modularity. The MIT Press, Massachusetts

# A Pillar Structure Optimization Design of Driving Safety

Guolin Li, Jun Sui, Xiang Zheng, Honghua Li and Fuquan Zhao

**Abstract** Taking the widely used A pillar structure as the research object, this paper discusses the impact of A pillar structure on driving safety through analysis of obstacle angle and structural strength of A pillar. In addition, combining with CAE analysis, sectional area of A pillar is properly reduced, the internal structure and joint-structure of A pillar is optimized, and obstacle angle is reduced in the premise of meeting the requirements of the strength. Therefore, the driving safety is improved and the fuel economy is also promoted to a certain extent.

**Keywords** A pillar · Obstacle angle · Strength · Driving safety · Optimization design

## 1 Introduction

Nowadays, China's automobile production has been the mainstay industry of economy after the 30 years' reform and opening up. Related data has shown that China had been the biggest production and consuming country in 2009. With the expansion of car market, the traffic accident is becoming more frequent. In this case, consumers pay more attention to and even take the driving safety as the chief

---

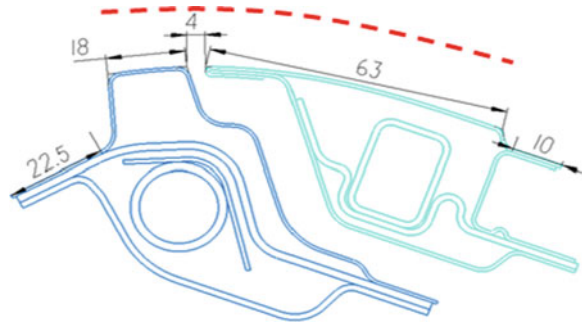
F2012-E04-018

---

G. Li (✉) · J. Sui · X. Zheng · H. Li · F. Zhao  
Zhejiang Geely Automobile Research Institute Co. Ltd, Hangzhou, China  
e-mail: liguolin@rd.geely.com

X. Zheng  
e-mail: zhengxiang@rd.geely.com

**Fig. 1** A pillar section structure of a model



factor when they purchase cars [1, 2]. As A pillar has obvious effect to protect the driver and improve the driving safety, this paper takes the widely used A pillar structure as the research object, by analysis of the A pillar obstacle angle and structural strength to optimize the design of A pillar and improve driving safety.

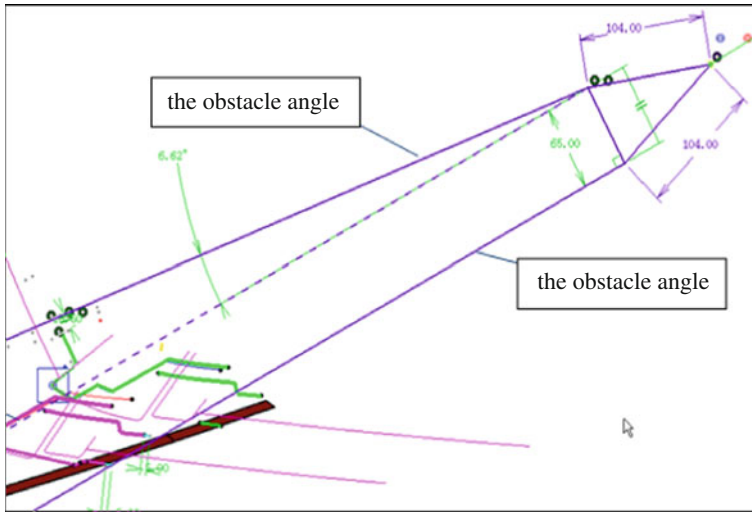
## 2 Description of the Problem

The A pillar has significant meaning for the safety of pedestrians and occupants. On the one hand, the higher strength of A pillar structure can protect occupants better, so in the case of fixed material, the large A pillar section area has a better safety performance. On the other hand, the size of the section area of A pillar has a direct impact on obstacle angle. And in order to have better understanding of the road conditions, the obstacle angle should be smaller. Certainly, the smaller obstacle angle can significantly improve the driving comfort ability. In summary, the structure of the A pillar design is a difficult research topic, which shall ensure collision strength and meet the requirements of obstacle angle both.

## 3 The Optimization of Internal Structure of Obstacle Angle and A Pillar

### 3.1 A Pillar Structural Design of a Specific Model

The A pillar section structure of a model is shown in Fig. 1. The size of obstacle angle can be calculated by analyzing the A pillar section structure. The width of each part on entire cross-section can be measured respectively, as shown in the red zone. Width of the cross-section is about 120 mm and the width of the external sectional area is about 85 mm. And then the obstacle angle can be calculated according to structure of the cross section, as shown in Fig. 2. Firstly, the spatial location of the driver's eye is determined, and then the impacted driver's view



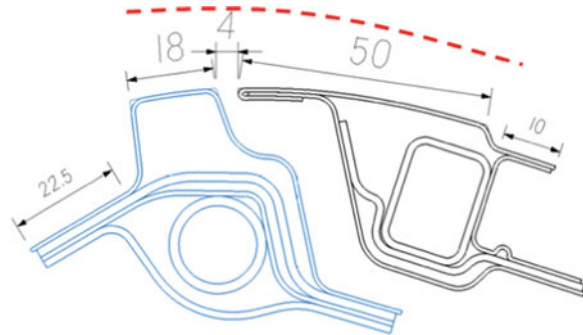
**Fig. 2** Size of A pillar angle of a model

range is obtained through sectional structure, so the boundary of the two A-pillar obstacle angles can be determined. Finally, the structural obstacle is calculated as  $6.6^\circ$  according to the above data with combination of the eye position. The current related laws and regulations require that the obstacle angle should be within  $6^\circ$ . Therefore, optimization design should be conducted to satisfy the provisions in laws and regulations.

### ***3.2 The Optimization of A Pillar Internal Structure***

In order to reduce the size of obstacle angle effectively, the direct measure is to reduce the size of A pillar cross-sectional area which affects the view of the driver. However, that will lead to the weakening of structural strength. Therefore, optimization design should be conducted according to the practical structure to reduce the obstacle angle as much as possible while ensuring sufficient strength, and the optimized section of A pillar is shown in Fig. 3. In order to reduce the size of obstacle angle effectively, the external cross section area decreases from original 85 to 72 mm and then the obstacle angle analysis is conducted with the same measuring method. Through verification, two boundaries of obstacle angle of A pillar are determined, and the impacted angle is calculated as  $5.4^\circ$ . Therefore, the optimized size of obstacle angle satisfies the related provisions in laws and regulations. However, the decrease of external cross section area leads to the structural strength of A pillar. Thus, the internal structure of A pillar should be optimized to meet requirement on strength and improve safety performance.

**Fig. 3** Optimized A pillar structure



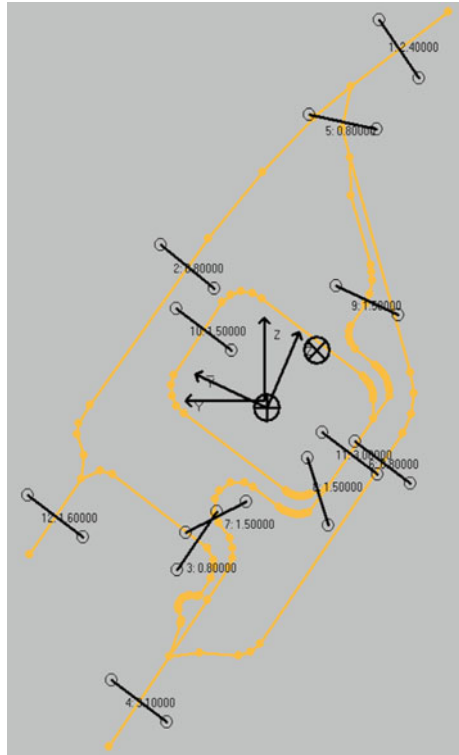
In order to optimize the internal structure, the first measure is to increase the overlapping area of each part in the structure to improve the overall structural strength, e.g. applying two overlapping surfaces in rectangular steel tube structure instead of the former one has generated obvious improvement in A pillar strength. In addition, the internal welding mode can also be optimized. In this structure, the shielded welding can be used for welding the rectangular steel tube and surrounding parts. Shielded welding will not only improve welding quality but also make welding efficient, which is an effective method to improve welding strength of the internal structure. However, in welding process the welding technology requirement should be strictly controlled. Therefore, through the above two methods, structural strength of A pillar can be effectively improved.

## 4 CAE Analysis

We have discussed to reduce the size of obstacle angle by decreasing cross-sectional area of A pillar, which directly causes the A pillar structure strength weakening. Although the internal structure optimization is conducted to improve strength, CAE analysis is still needed for comparison the structural strength before and after optimization. Figure 4 shows the A pillar section model before optimization, and Fig. 5 shows the optimized A pillar section model. Through CAE analysis, the cross-sectional area, polar moment inertia and torque coefficient of A pillars before and after the optimization are obtained, as shown in Table 1. From comparison and analysis of A pillar section attribute parameters before and after optimization, A pillar section area is smaller than that before optimization scheme, the overall mass of A pillar has reduced, and polar moment of inertia has been smaller. In addition, the torsion coefficient has reduced, so twisting resistance of A pillar is reduced. Through the comprehensive analysis, in order to meet the obstacle angle regulatory requirements, each indicator value of the optimized cross-section is lower than that before optimization. Compared with indicators of some current models, requirement on structural strength is still satisfied although each indicator value is lower.



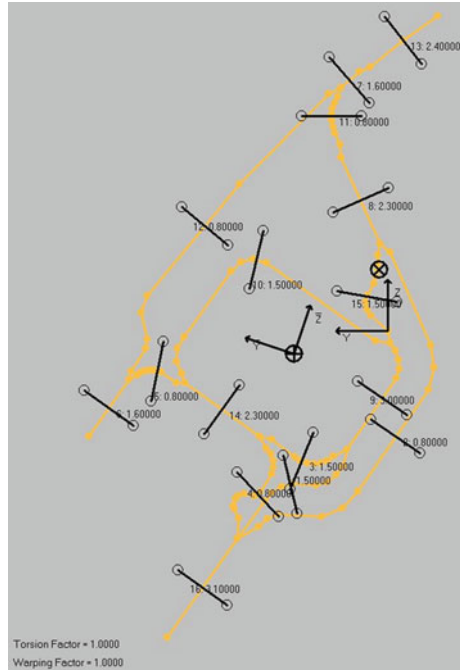
**Fig. 4** Section model before optimization



## 5 Optimization of A Pillar Overlapping Joint

Based on the above analysis, in order to meet the obstacle angle regulatory requirements, optimization is conducted while each indicator value of the optimized cross-section is lower than that before optimization. Although the internal structure is optimized and requirement on structural strength is still satisfied, the overall strength has reduced compared with that before optimization. Therefore, with the premise to satisfy the obstacle angle, optimization design can be conducted to overlapping joints around A pillar to improve structure strength and driving safety of vehicle. Figure 6 shows the joint chart between reinforcing plate in A pillar internal plate and roof side rail internal plate. From the figure, it can refer to another joint mode, as shown in Fig. 7. It joins the reinforced plate of A pillar inner panel and upside beam and improves the structure strength evidently. The joined structure can be designed according to the A pillar inner panel reinforced plate and upside beam of different vehicles. As the joined structure in the figure, it welds A pillar inner reinforced plate, upside beam and side outer panel. It is worth noticing that there are many reinforced plates in A pillar inner structure, such as some vehicle structure. It need to avoid four layer panels to weld A pillar inner panel reinforced plate and upside beam and it can reduce welded layers by

**Fig. 5** Section model after optimization



increasing flute in welded position. In addition, it also optimize joined structure to meet two ranks or many ranks welded points lay requirement by extending the joined width between A pillar inner reinforced plate and upside beam inner plate. According to upper optimized project, it can evidently improve strength in welded point forming direction. A pillar structure strength of whole vehicle is improved greatly. This makes up the problem that smaller section area of A pillar decreases structure strength in some extent and reduces the intruded measure when crashing to improve safety performance.

## 6 Conclusion

As we have expatiated above, in order to reduce the incidence of A pillar structure when driving, the smaller A pillar obstacle angle the better. Under this background, in response to a vehicle A pillar obstacle angle too big case on A column structure to optimize the design, to ensure sufficient structural strength condition, appropriate to reduce A pillar section area, optimizing the internal structure of A pillar, A pillar to reduce barriers to angular size, to ensure A pillar structural strength requirements. In addition, based on the A pillar at the peripheral joint

**Table 1** Comparison of parameters of section attribute before and after optimization

	Before	After	Variation rate (%)
A	470	408	-13
I	42118	37663	-10
J	41053	36483	-11

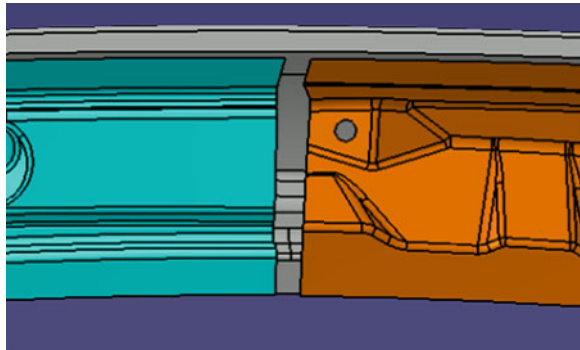
Note 1. Meaning of the parameters in the section analysis:

A is cross-sectional area, the unit is mm<sup>2</sup>

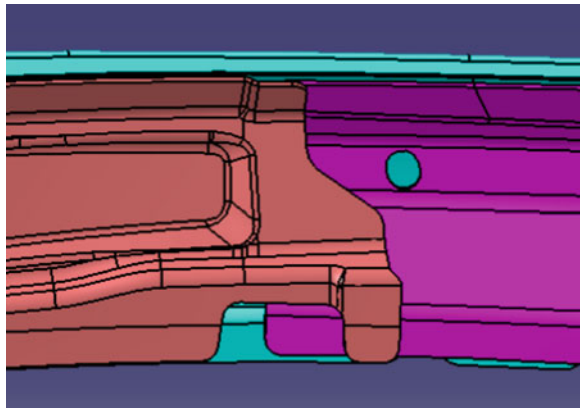
I is the polar moment inertia, which affects flexural properties, the unit is mm<sup>4</sup>

J is coefficient of reversing section, which affects the torsional capacity

**Fig. 6** Joint structure of A pillar inner panel with reinforced plate of a vehicle



**Fig. 7** Other joined structure of A pillar inner panel reinforced plate



structure design optimization, which can further improve the vehicle structure strength, greatly improve the safety performance of. Notably, the optimized A pillar structure of a cross-sectional area decreases, the overall quality loss, to improve vehicle air power, lower fuel consumption rate has a significant role.

## References

1. Men F, Wang J (2011) The trend forecast of China's auto industry development. *Auto Ind Res* (2):2
2. Liu L, Du A (2012) Application and development trend of automotive safety technology. *Automobile Parts* (3):26

# A New Body Concept for Electric Vehicle: PBC-EV

Jaehyun Kim, Hongwoo Lee, Kyunghwan Chung, Hyounyoung Lee, Yeonsik Kang and Jaebok Nam

**Abstract** POSCO developed a new body concept for electric vehicle, POSCO Body Concept—Electric Vehicle (PBC-EV) with the aim to provide steel solutions to the challenges facing automakers around the world to increase the fuel efficiency of automobiles and reduce greenhouse gas emissions, while improving safety, performance and maintaining affordability. The objectives are achieved by advanced steel grades, engineering design optimization and advanced steel technologies with the best attributes of steel—its design flexibility, strength, formability, low manufacturing emissions and comparative low cost. PBC-EV features steel body structure designs that reduce weight to 218 kg by 26 % over a benchmarking body of 296 kg. The weight reduction has been realized through the use of advanced high strength steel grades by 64 % of total body weight combined with the aforementioned steel technologies. Even though there is a cost premium associated with the use of higher grade steels, the consequently achieved weight savings minimize the increase of overall costs of manufacturing and assembly. A total life cycle emission of PBC-EV is reduced by nearly 50 % comparing to benchmarking internal combustion engine vehicle. These are accomplished while meeting a broad list of global safety requirements such as US FMVSS, IIHS and EuroNCAP. No damage of battery cell in the crash simulations is observed. In the last stage hardware demonstration was done by building Body-in-White (BIWs) excluding opening parts and fenders. With this study advanced steel solutions which are not only lighter and safer but greener can be provided to automakers. And it is very important for automakers to avoid unintended consequences by using eco-friendly steel technologies for advanced powertrain vehicle.

---

F2012-E04-020

---

J. Kim (✉) · H. Lee · K. Chung · H. Lee · Y. Kang · J. Nam  
POSCO, Pohang, Republic of Korea  
e-mail: barney.j.kim@gmail.com

**Keywords** Electric vehicle · Body concept · AHSS/U-AHSS · LCA · Lightweight

## 1 Introduction

As the mass production of high speed battery electric vehicles (BEVs) such as Nissan Leaf and Mitsubishi I-MiEV was started automotive industries accelerate preparation for the new era of BEVs. However, up to now the battery cost is too expensive as much as a half of car price. High battery cost can induce “mass-cost paradigm shift” for light weighting in electric vehicle. It means that the high cost of batteries increases the value of mass reduction. The WorldAutoSteel’s Future Steel Vehicle study indicated that for the 2015–2020 timeframe vehicle manufacturers could employ light weight solutions that are more costly, up to US\$ 9.39 per kg saved in this case [1]. This value is based on an anticipated battery cost of \$ 450/kWh. As the costs of batteries are reduced the value of mass savings will be reduced. Even if battery cost get reduced due to battery technology advance it will be still a significant portion of vehicle total cost. Light materials such as aluminium or composites can be good a substitution of steel for vehicle body structure because of high light weighting effect if their greenhouse gas emission of primary production are not considered.

Figure 1 shows that aluminium and multi-material BIWs are lighter than steel BIWs. But the lightweighting of BIWs and vehicle should be considered in total life cycle assessment. The greenhouse gas (GHG) from material primary production of Fig. 2 indicate that aluminium and CFRP can cause unintended consequences. In other words, even though vehicle manufacturers use them for light weighting it can cause unintended effect to environment due to their high GHG emission of primary production.

In order to support automotive manufacturer regarding avoidance of unintended consequences POSCO developed a new body concept for electric vehicle with advanced steel technology and made an effort to reduce its weight to achieve the same level as aluminium body. This paper addresses the final outcomes of PBC-EV development, detailing steel body structure concepts for the aforementioned vehicles that achieved the target of mass reduction while meeting global crash performance objectives as well as total life cycle greenhouse gas emissions targets, and stiffness.

## 2 Objectives

The main objective of this study is to develop the lightweight steel body concept optimized for BEV. To develop vehicle body for BEV it is necessary to have many objectives and targets. First of all, target year for this body concept is 2015.

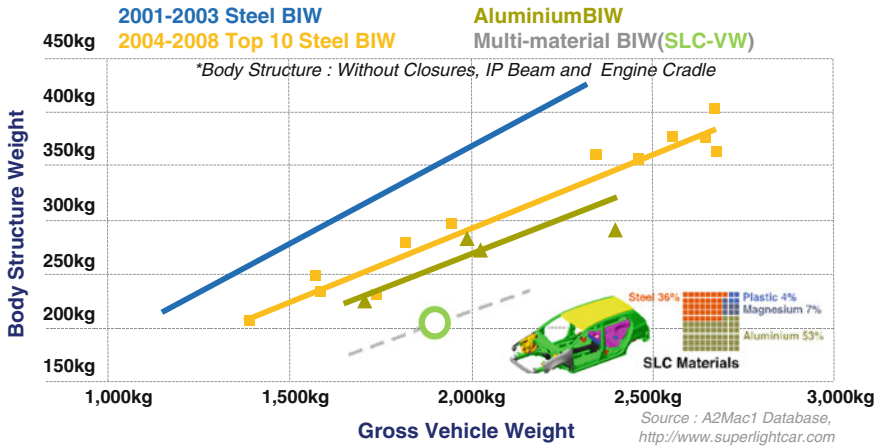
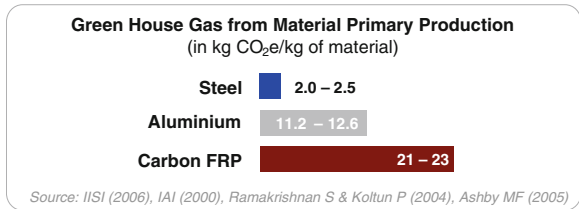


Fig. 1 Body structure weight comparison

Fig. 2 Greenhouse gas from material primary production



Though there is a large difference between optimistic and conservative scenario of battery electric vehicle sales a steep increase is expected in 2015. POSCO has been developing advanced steel grades and also researching most advanced manufacturing technologies to utilize these materials. It will be possible to provide these new technologies to the customer in 2015. The mass target for the body concept is 222 kg, which represents a 25 % reduction over a baseline body of 296 kg. The baseline vehicle is Internal Combustion Engine (ICE) vehicle and its size is similar with PBC-EV's. Baseline body weight is determined based on WorldAutoSteel's Future Steel Vehicle Phase 1 study [2]. Basic vehicle specifications such as powertrain performance and overall size are required as Table 1 including safety targets for crashworthiness. PBC-EV has 100 kW Permanent magnetic AC Motor with 30 kWh Lithium ion Polymer Battery in order to ensure 160 km electric range and 150 km/h maximum speed. This target was decided from our preliminary studies on electric vehicle market trend. For crashworthiness worldwide safety requirements of the target year are considered. Figure 3 shows vehicle dimension of PBC-EV. The motor room of BEV is smaller than that of ICE vehicle due to compact powertrain. This means electric vehicle might have larger passenger zone compared to same sized ICE vehicle. PBC-EV has very similar in overall length to European C-segment but larger wheel base with shorter front overhang.

**Table 1** Vehicle powertrain performance and safety targets

Powertrain/performance	Crashworthiness/safety	
Permanent magnetic AC motor: 100 kW	Roof crush (FMVSS 216 and IIHS)	Offset frontal impact (EURONCAP and IIHS)
LiPB battery: 30 kWh	Side impact (FMVSS 214D and IIHS)	Rear crash (FMVSS 301)
All electric range: 160 km	Side pole impact (FMVSS 214P)	Low speed crash (RCAR and IIHS)
Maximum speed: 150 km/h	Full frontal impact (USNCAP)	Pedestrian protection (EU PED-PRO phase2)

When the era of BEV comes it is expected that small automotive company can manufacture BEV models in small production volume. The body type of PBC-EV is monocoque but it features the combination of space frame and monocoque considering easy conversion to space frame fit for small production.

### 3 Methodology

PBC-EV development process is not only analogous to a normal vehicle development process but focusing on optimized lightweight body. To meet the aggressive mass target, the body structure design methodology combines an advanced steel materials portfolio, advanced steel manufacturing technologies, topology optimization and CAE analysis. Aforementioned advanced steel grades are shown in Fig. 4. Not only conventional Advanced High Strength Steel (AHSS) such as DP, TRIP, CP and HPF, but also Ultra-AHSS (U-AHSS) and eXtra-AHSS (X-AHSS), TWIP and DUPLEX respectively, are the candidates of PBC-EV material grades. Exceptionally, Mg sheet is also a possible choice for PBC-EV regarding its lightweight ability and NVH performance. New forming technologies such as Multi-strength Hot Press Forming (MS-HPF) and Multi-directional Roll Forming (MD-RF) are enablers of adopting new steel grades. Warm forming method is chosen for Mg sheet. Conventional manufacturing methods like stamping, hydroforming, and laser welded blank are also included undoubtedly.

As shown in Fig. 5, studies of powertrain packaging, suspension type, battery packaging, interior occupant space, ingress/egress requirements, vision/obscuration, luggage volume requirements, and ergonomics established the component and passenger package space requirements. An exterior styling inspired by a deep sea creature was applied to the packaging, followed by several computational fluid dynamic (CFD) simulations, resulting in a drag coefficient of  $C_d = 0.286$ . High roof package is applied to maximize passenger and battery space and it leads to have difficulties to get lower drag coefficient. Figure 6 shows final exterior styling and CFD result.

The objective of the topology optimization is to provide an initial structure based on the available structure package space. This optimization has 5 load cases



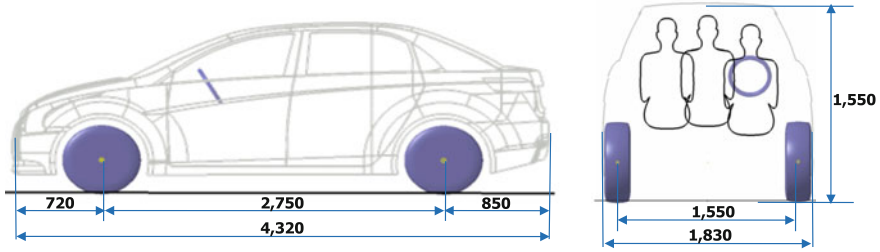
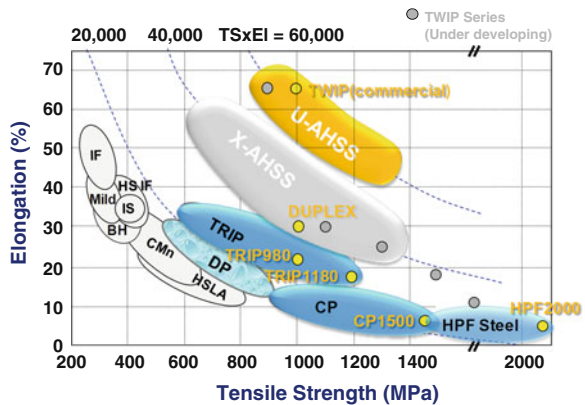


Fig. 3 Vehicle dimension for PBC-EV

Fig. 4 Material portfolios for PBC-EV

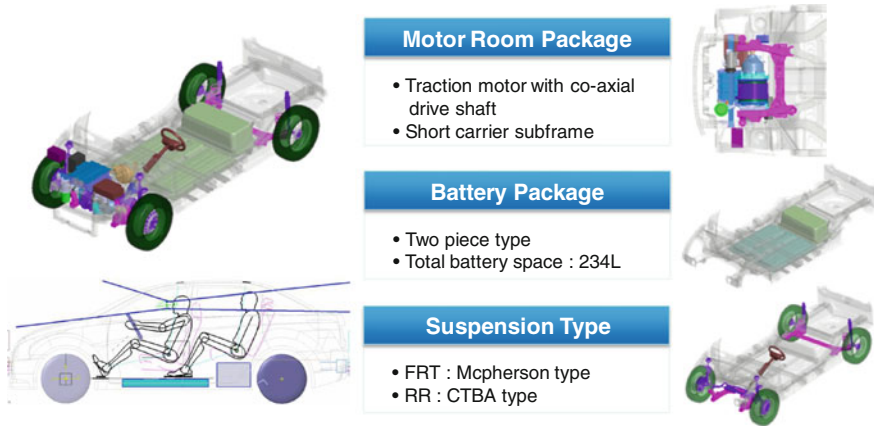


\* Specification of developing steels might be changed according to POS market and R&D policies

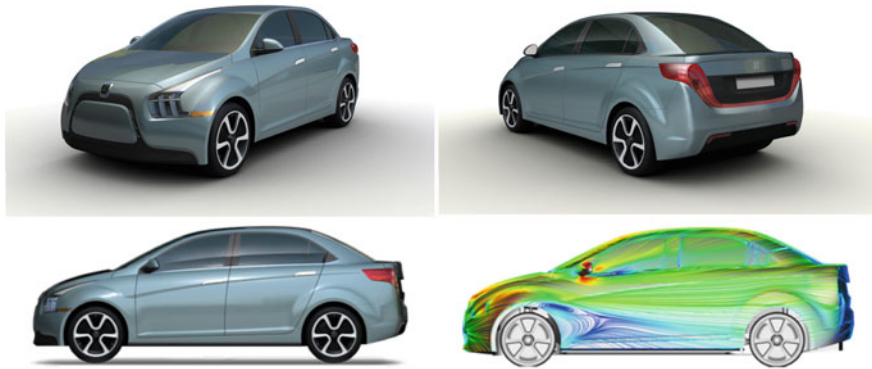
which are frontal, side, rear, bending, and torsional. The topology optimization eliminates elements from a finite element mesh that represents the available structural design space, i.e. the volume within which structure can exist. The elimination of elements is based on strain energy, thereby revealing the optimal load paths. With topology optimization result empirical frame concept can be extracted by engineering judgement as shown in Fig. 7. Lee et al. [3] explained the topology optimization of PBC-EV in detail [3].

Application strategy of advanced steel grade to under body is shown in Fig. 8. For crushable zone in the box with blue line, high elongation AHSS such as DP780, TRIP980, TWIP980 and etc. is applied for absorbing crash energy in efficient way. On the other hand, for passenger and battery zone in the yellow box, Ultra High Strength Steel (UHSS) such as DP980, HPF 2000, Duplex980 and etc. is applied for minimizing the intrusion into this zone.

For crash load management multi-load paths are considered as shown in Fig. 9. 7-way load paths for frontal crash in the longitudinal direction and 3-way load paths in the lateral direction basically can help to deal with not only crash energy absorption but also crash load resistance efficiently. Side crash management is



**Fig. 5** Package layout



**Fig. 6** Final exterior styling and CFD simulation result

very critical factor in electric vehicle, because the battery package should be protected. Basic concept for battery protection is dual ring structure, which means combination of the longitudinal and cross members forms two separate ring structure. But even dual ring structure it is difficult to completely prevent the battery damage especially for side pole impact. To resolve this problem a seat cross member directly connected between both side sill sections is suggested. This concept is called as “Dual+1 Ring Structure” which enables to perfectly protect battery from side pole impact. To assess crashworthiness and stiffness of body structure CAE analysis is carried out with LS-Dyna and Nastran. The manufacturing feasibilities are demonstrated by several ways. The formability of advanced steel grades were evaluated with incremental forming simulations of the major parts using LS-Dyna and Pamstamp. To perform a life cycle assessment (LCA) and cost estimation the University of California at Santa Barbara (UCSB)

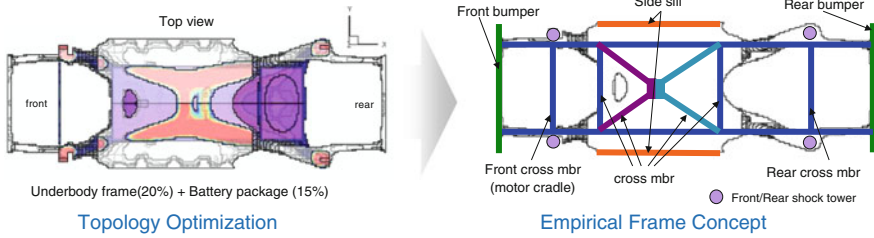


Fig. 7 Topology optimization and empirical frame concept

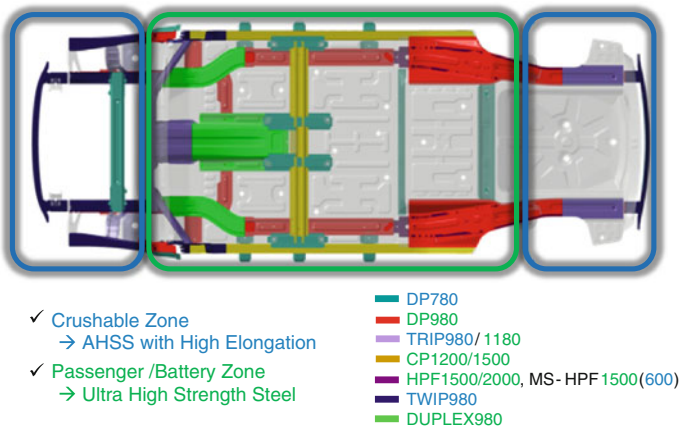


Fig. 8 Application strategy of advanced steel grade

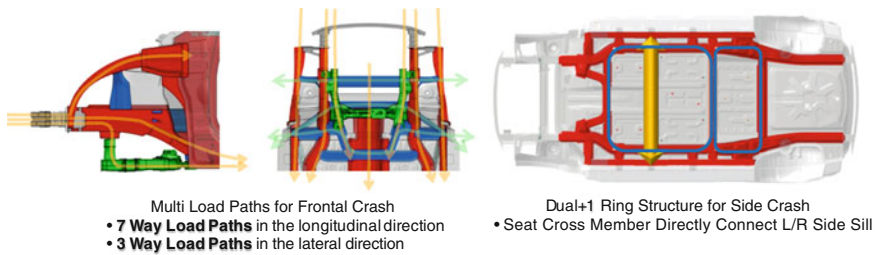


Fig. 9 Crash load management for frontal and side impact

Greenhouse Gas Materials Comparison Model and WorldAutoSteel’s Future Steel Vehicle Cost Model [1] is used respectively. Crash, stiffness, forming, joining, cost and LCA are covered in the next section.

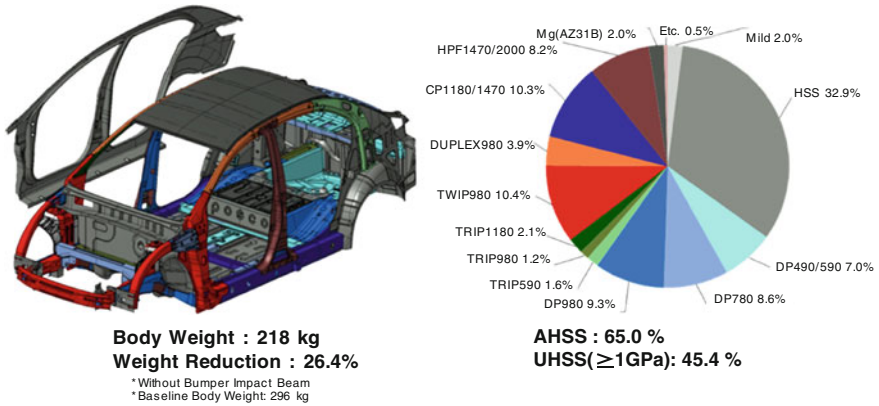


Fig. 10 Steel grades and distribution (as % of body weight)

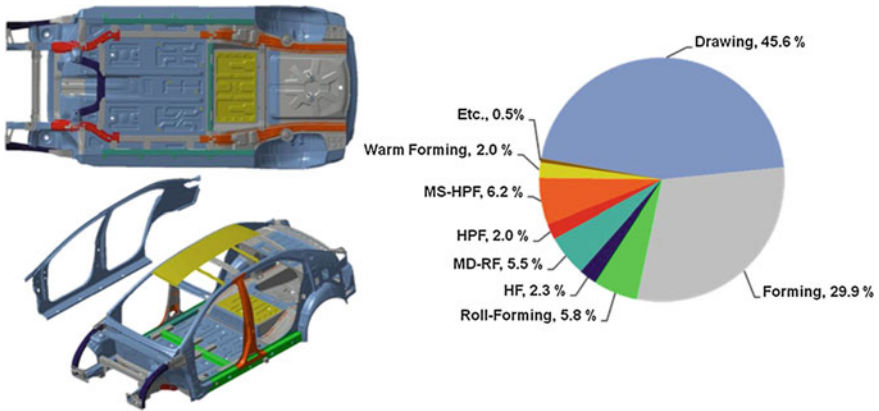


Fig. 11 Manufacturing process and distribution (as % of body weight)

## 4 Results

PBC-EV achieved weight savings of 78 kg (−26.4 %) compared to the baseline body structure weight as shown in Fig. 10. Final body weight is 218 kg and weight reduction has been realized through the 65 % use of AHSS and 45.4 % use of UHSS combined with manufacturing technologies such as MS-HPF and MD-RF. The BIW structure, the different grades of steel and the steel grade distribution are also shown in Fig. 10.

Manufacturing process adopted in PBC-EV and its distribution are shown in Fig. 11. Parts which adopt advanced manufacturing process such as MS-HPF and MD-RF are illustrated in Fig. 12. Basically, conventional stampings such as Drawing and Forming is major manufacturing method in PBC-EV. And cost efficient process like Forming, Roll-Forming and MD-RF is applied 41.2 % of total processes considering cost increase.

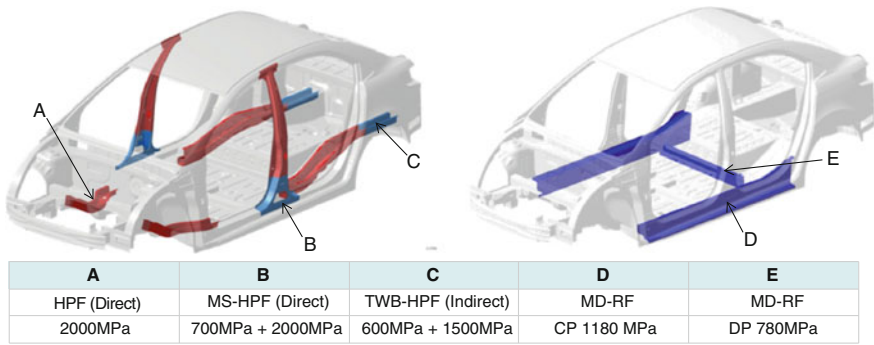


Fig. 12 HPF, MS-HPF, TWB-HPF and MD-RF parts

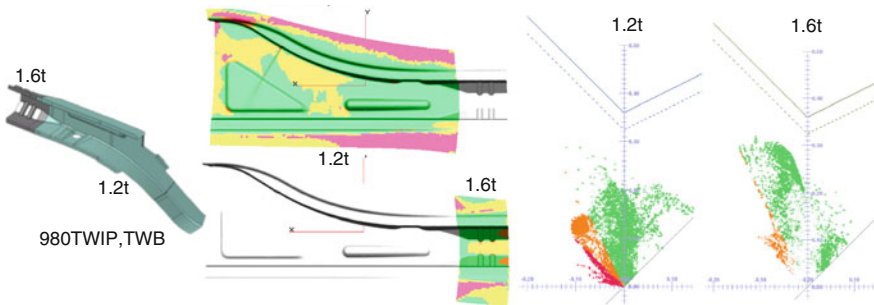


Fig. 13 Incremental forming analysis of front side member

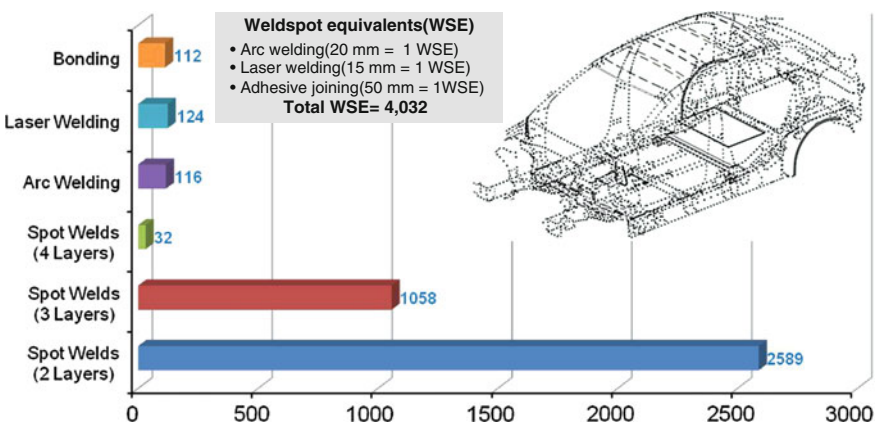
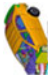







Fig. 14 Joining techniques and quantity

**Table 2** CAE analysis results—crashworthiness and stiffness

Load cases		Target	Result	
 Front	IIHS (EuroNCAP) ODB 40 % offset	A-pillar displacement (mm)	14.1	
		IP Beam Intrusion (mm)	29.1	
 Side		Toe panel intrusion (mm)	79.2	
	USNCAP Full Frontal	Peak pulse (g)	44.1	
	IIHS Side MDB 50KPH	Residual space (mm)	154	
	FMVSS214 Side Pole	Battery damage	No Damage	
 Rear	FMVSS301 MDB70 % offset	Battery damage	No damage	
			No damage	
 Roof	IIHS roof strength	Peak Strength to weight ratio	4.06	
 Low speed	RCAR 15kph	Maximum Effective Plastic Strain	0.024(+5.3 kg)	
	 Stiffness	Static	Bending (N/mm)	15,857
Dynamic(modal analysis)			Torsion (Nm/deg)	16,644
			Bending (Hz)	51.2(2 node)
			Torsion (Hz)	47.4(1 node)

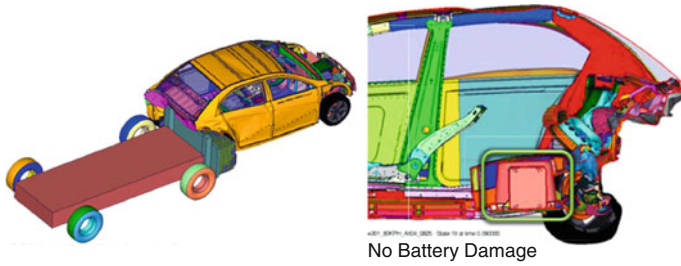


Fig. 15 FMVSS301 70 % MDB rear impact CAE result

Table 3 BIW manufacturing costs breakdown

Manufacturing method	Weight (kg)	Cost (USD)	Joining method	Connects or length	Cost (USD)
Stamping	164.7	522.7	Spot	3,679 EA	224
Hot stamping	17.9	79.9	Laser	1,860 mm	10.5
Roll forming	12.7	26	Arc	2,328 mm	17.7
MD-RF	12.1	27	Adhesive	5,619 mm	12.5
Hydroforming	5.1	26.9	Hemming	1,600 mm	2.5
Warm Forming	4.5	60.2	Mastic sealer	4,260 mm	8.4
Total	217	742.7	Total		275.6

BIW manufacturing cost: \$1,018

Some parts which have complicated shapes like front side members, body side outer and rear side members require the incremental forming analysis for predicting the manufacturing results more accurately. In Fig. 13 the results of the incremental analysis of the front side member made with TWIP980 1.6 and 1.2 mm. Although some minor changes are needed, it proves that the stamped component design is safe. Some of the most common assembly joining techniques are considered.

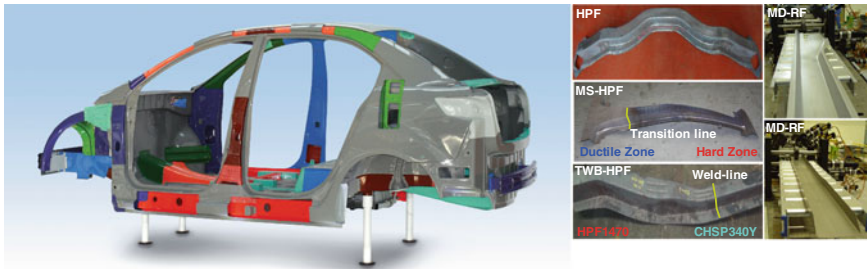
The joining processes selected for PBC-EV BIW assembly are resistance spot welding, laser welding, arc welding, and adhesive bonding. Figure 14 detail the quantity for each joining technique used. Weldability of advanced steel grades and its combinations was tested to set suitable conditions. The detailed design of PBC-EV was supported by CAE analysis, to verify the structural performance. The CAE analysis results were compared to the targets to quantify the performance of the body structure in terms of static stiffness, crashworthiness. As illustrated in Table 2, it can be seen that PBC-EV body structure meets or surpasses the performance targets. As an example, FMVSS301 rear impact test result is shown in Fig. 15. No battery damage is observed during the simulation.

Cost analysis is used to assess the manufacturing costs of the BIW and its components. No supplier cost estimates were used. The manufacturing costs were estimated for all the body structure components, using the different manufacturing processes. As the result of cost analysis, BIW manufacturing cost is estimated to be \$1,018. Basic assumptions for the cost analysis are an annual volume of



**Table 4** LCA result using UCSB greenhouse gas comparison model Ver 3.0

Vehicle (powertrain)	Body material	Material production	Use phase	Recycling	Total life cycle	Unit: kg CO <sub>2</sub> e
Baseline (ICE-G)	Mild steel	3,180	34,007	-1,380	35,808	Base
Baseline (BEV)	Mild steel	8,361	13,287	-1,545	20,102	Base
PBC-EV (BEV)	AHSS	7,218	12,328	-1,252	18,293	-
	48.9 %	-9 %				
AL (BEV)	Aluminium	9,429	12,127	-3,116	18,441	



**Fig. 16** PBC-EV BIW demonstrator, MS-HPF and MD-RF parts

150,000 and a 5 year production life. Even though there is a cost premium associated with the use of higher grade steels, the consequently achieved weight savings balances the overall costs of manufacturing and assembly and minimizes the cost increase. The cost breakdown for the fabrication of the steel components/systems is shown in Table 3.

LCA results shown in Table 4 vividly demonstrate that the coupling of a light weight AHSS body structure combined with a battery electric powertrain results in a 48.9 % reduction in life cycle emissions compared to baseline ICE vehicle. If baseline vehicle is BEV, life cycle emissions can be reduced by 9 % due to light weighting. PBC-EV has also advantage over BEV of aluminium body in life cycle emissions due to emission of material production.

After all the design and CAE analysis were completed, in order to verify the feasibility of part manufacturing and assembly, hardware demonstration was done by fabricating all body components and building BIW excluding opening parts and fenders. Total 10 BIW demonstrators were built and one of them is shown in Fig. 16.

## 5 Conclusion

Durability performance check, crash simulation considering forming result, and development of closure parts of PBC-EV can be next step of this study. It is also very challenging to optimize gage, grade and geometry of PBC-EV combining



various crash constraints in one iteration, a.k.a. Multi-Disciplinary Optimization (MDO) for further mass reduction. Incremental forming simulation can be integrated with crash simulation to evaluate both manufacturing feasibility and crashworthiness simultaneously. Over 10 years have passed since POSCO started early vendor involvement (EVI) in automotive application product. Regarding customer value creation POSCO had provided independent and partially integrated technologies in various automotive applications such as forming, joining, painting, corrosion, cost analysis, and etc. Now with PBC-EV fully integrated solutions which are not only lighter and safer but greener can be provided to automotive customers who prepare for the new era of advanced powertrain vehicle. Those solutions include life cycle assessment can be turned out to be environmentally friendly. And it is very important for automakers to avoid unintended consequences by using eco-friendly steel technologies for advanced powertrain vehicle.

## References

1. WorldAutoSteel (2011) Future steel vehicle phase2 engineering report <http://www.worldautosteel.org/projects/future-steel-vehicle/phase-2-results/>
2. WorldAutoSteel (2011) Future steel vehicle phase1 engineering report <http://www.worldautosteel.org/projects/future-steel-vehicle/phase-2-results/>
3. Lee HW, Kang YS, Kim J (2011) The application of topology optimization to lay-out design of auto body, KSAE, 2011, KSAE annual conference, pp 2405–2409

# The Study on Development of High Security and High Comfort Commercial Vehicle Cab

Yuhai Chang and Xiaojun Yang

**Abstract** *Research and/or Engineering Questions/Objective:* Development of commercial vehicle cab are moving in the car of the trend, customers for cab safety and comfort requirements are getting higher and higher. How to meet customer needs through technology? What are the technical difficulties in the process to meet customer needs? This study is to answer these questions, and indicate the direction of a solution. *Methodology:* Tracking the international commercial vehicle show, studying the development trend about Scania series Volvo series DAF series Iveco series Mercedes-Benz Actros series and so on, Summarize commercial vehicle cab in the trend of future development. Combined with the current technology development level and speed, According to the cab of each subsystem of classification is described to meet the future requirements of the measures of cab. *Results:* Commercial vehicle cab development will surround the safety and comfort of the direction to undertake a series of reform and innovation, and considering energy saving and environmental protection requirements. The people-oriented design concept will become the core concept of product development. For high security, high comfort cab must consider the body, door, air conditioning, internal and external decoration, car accessories, cab suspension system, and find improvement measures from each subsystem one by one. *Limitations of this study:* This paper is based on the development of modern science and technology and the level of people's needs change, it is studied on the basis of the future a cab of a commercial vehicle development. It represents a trend of research, not necessarily meet the

---

F2012-E04-021

---

Y. Chang (✉) · X. Yang  
China Faw Group Corporation R&D Center, Changchun, China  
e-mail: yangxiaojun@rdc.faw.com

X. Yang  
e-mail: yangxiaojun@rdc.faw.com.cn

present needs and the situation of a country. What does the paper offer that is new in the field in comparison to other works of the author: This paper is to describe how to achieve high safety and high comfort cab of a commercial vehicle development from the cab of each sub system. *Conclusion:* With advanced technology as the support, the use of advanced structure, to meet the functional requirements and performance requirements for the purpose, to develop the high security and high comfort cab of a commercial vehicle.

**Keywords** Security · Comfort · Commercial vehicle · Cab

## 1 Introduction

With the constantly improvement of people's life, the demand on function of car change greatly. The car is constantly moving forward around feel of person. Design concept of "people-oriented" take up critical position gradually. For commercial vehicle cab, two important aspects reflecting the "people-oriented" are the safety and comfort. Safety includes security of outdoor of the cab (viz. passengers) and safety of indoors of the cab. From the perspective of technology, safety can be divided into active and passive safety. The comfort is that physiological or psychological feeling of drivers on Indoor environment and parts assembly, while they driving or taking the car, working or entertaining in the car. In fact, the safety and comfort involve many aspects of the entire automotive and [1–4] its components assembly. This article focuses on the cab's safety, and the comfort related to the cab.

## 2 Trend of Development on Commercial Vehicle Cab

Germany Hannover auto show has been vane of technology and development of the commercial vehicle. Through analysis of the Scania R series, Volvo series, FH DAF LF and XF series, Iveco Stralis, Mercedes-Benz Actros II, Actros III, Actros successive, high-end truck in the previous show and European annual truck, we can find that commercial vehicle cab is becoming more and more car and humanity obviously. The cab will became the multiple function system of work, live, entertainment. Its Characteristics of residential, recreation and living space will be more and more outstanding. The design concept of "People-oriented, customers first" develop in a cab of a commercial vehicle. The primary factor of people-oriented Concept is to ensure the safety the drivers and indoor property. Safety is one of the most basic performances. The second, the design should reflect the comfort of driving, meet the physical and psychological function of the driver.

Considering the attention on the energy use and environmental problem increasing, they are all incorporated into considerations of design of commercial vehicle cab, that to save energy by lightweight, to protect environmental by using replacing non-renewable materials by renewable materials. In conclusion, development of the commercial vehicle cab will undertake a series of reform and innovation around the direction of the safety and comfort, give full consideration to energy saving and environmental protection. The people-oriented design concept will become the core concept of product development.

### **3 Research Strategy on Commercial Vehicle Cab of High Safety**

Safety is most basic and important performance of commercial vehicle cab, and it is always the recognized base line of user. High safety cab is the embodied the concept of People-oriented. It will be primary factor in the competition of commercial vehicle cab in the future. The whole cab contains car body, door, air conditioning, internal and external decoration, car accessories cab suspension system and so on. So the high security should be reflected in each subsystem.

#### **3.1 High Safety Body**

The body portion is main body structure of the cab, should be considered as the main subsystem in the safety design. The ECER29 law of The European Economic Commission is the threshold of cab safety in Europe. It focuses on three aspects of frontal impact, roof collision and rear impact. The maximum collision energy of frontal collision should be 30,000 Nm for 7,000 kg vehicles. It should be 45,000 Nm for more than 7,000 kg vehicles. Dummy of 5,000 bits has enough living space after the collision, and suspension of cab still remain connected with the vehicle frame. It requires that the coping endure maximum permissible load (max. 10 tons) in roof collision, and the dummy of 5,000 sub-bit has enough living space. In rear impact, it requires that the rear of the cab endure static force according to calculation of 2,000 N/t according to the permissible load. Usually the cab design consider the ECE R29 safety regulations, and advance the body strength from the structure. Sweden collision test regulation is much more rigorous than ECE. Especially, frontal impact and roof collision (147 KN load) on the A column is demanded highly. In the future, safety regulations will be more stringent, to further ensure and improve the safety coefficient of indoor drivers.

In addition, in the design of high safety, the lightening design of car body should also be taken into consideration, which is a difficulty in high safety. We can take measures from the following several aspects: (1) Structure optimization is one

of the most common means. Optimize body structure form efficiently and improve body strength by means of CAE analysis. (2) Material optimization. The current basic materials should be replaced of high strength material that can be produced batched and cost controllable. In order to improve car body strength, composite materials should be developed. (3) The adoption of new technology can make up for strength loss problem brought in the actual production process.

For example, composite structure of the stamping and welding with the moulded frame is worth to study that.

### ***3.2 High Safety Door***

The high safety of door is mainly reflected in the white door structure with high safety, high safe door hinge and door lock with high safety. The design of high safe door structure can be analogous to the three aspects of body design. In addition, special attention should be paid to meet the requirements of side collision. The strengthening beam structure, to ensure side impact protection of drivers, should be distributed reasonably and used the high strength of materials. From the trend, composite frame structure will become the development direction of door structure.

Door hinge should select the holistic structure but not a plate welding structure. Door hinge safety also depends on the hinge arrangement, In the case of structure allowed, to ensure that upper and lower hinge bearing minimum and equalized torque as far as possible. Thus the door safety should be analyzed and calculate from the force. The CAE analysis and experimental verification is used to improve safety.

Car door lock and the lock ring is very important to strengthen structure. In the event of a collision, the lock of high safety door can be opened, the lock ring can't be broken. In the side collision of the cab, the door usually deformed, and the lock mostly damages. High security design is to guarantee that the deformation is small, function of the door lock is normal and opened, ensure the occupants to escape.

### ***3.3 Air Conditioner of High Safety***

For safety of air conditioner, it mainly to ensure the motor reliable and durable. There should be motor automatic protection function, to avoid the fire caused by burned out circuit. Self-test device and protective device should be introduced in technical aspects. It will protect air conditioner Intelligently in fault. At the same time, the refrigerant must be environmental and non-toxic, make sure safe to the environment.

### ***3.4 Internal and External Decoration of High Safety***

Internal and external decoration of Commercial vehicle cab is more and more like cars. Streamline of cab exterior appearance, large fillet shape, arc side window and special-shaped diamond integrated headlamps, they have become pop elements of cab exterior styling. Interior design and layout is also moving towards car features gradually, such as wrap-around dashboard, the softening interior and knitted fabric, which make the cab interior high-graded. Therefore it also tends to cars in the security, mainly reflected in two aspects: firstly, internal and external decoration material must be retardant flame, improve internal and external decorations retardant flame by the modification or compound of material, make sure that it wouldn't combust spontaneously in case that there is fire source in the car. Secondly, consideration of collision buffer design of personnel. Softening structure is used in the site of frequent collision, increase the energy absorbing effect, eliminating corners or increase its round to reduce damage in collision.

In addition, the seat system plays an important role in the safety as a large assembly of the interior. The connection strength between seat and body, strength of seat frame, they should be strengthened through material upgrading and structure optimization. The effect of shock absorbing should not be ignored. The seat should be designed according to the human spine location, make sure that damage to spine is as small as possible in emergent stop or collision.

### ***3.5 Attachment of High Security***

The most important is the rear view mirror system for attachment of the body, Rear view mirror system is related to the driver's field of vision, and impact driving safety greatly. So the intelligent control and image device can make up or replace the existing rear view mirror system, in order to ensure the safety of driving vision.

### ***3.6 High Safe Suspension System***

Suspension system of Commercial vehicle cab is a transition device connected the cab with the body. The connection strength is directly related to the cab safety. Suspension system security relates to the mounting bracket, we should ensure the strength and the cab safety through structure optimization and materials improvement. And it also relates to reliability of the turnover mechanism, to ensure repair personnel safe. The design of turnover mechanism should not only take into consideration of safe strength, but also consider several design elements, such as barycenter should be through hinge point, and can not be too large, it should have locking and limiting mechanism after turnover.

## **4 Research Strategy of High Comfort Commercial Vehicle Cab**

Commercial vehicle cab is “carlized”, the design is of human nature gradually. The cab is not only to provide a driving work space, but also as a multiple function system of working, living, entertainment, life. Therefore comfort will be one of important index in competition of commercial vehicle cab. Man-machine engineering technology is one of the best strategies for comfort. In the process of cab development, Ergonomic engineering is mainly reflected in comfort in the driving and operation, comfort in rest, comfort in entertainment.

### ***4.1 Comfort of Driving and Operation***

Driving comfort embodies in the driving posture firstly, make sure that the key positions of drivers keep in a comfortable range. Therefore we need to study fully comfort zone of human physiological joint, and evaluate the driver’s posture, to exterminate comfort level of the driving posture. For the comfort of operation, we should research the driving operation habit and the operating frequency of specific parts, then arrange the parts in the driver’s peripheral according to the priority. To judge the mode of operation through the perception is an important content in the cab layout of ergonomic. At present, there are several advanced methods to judge the comfort of driving and operation in stage of model. Firstly, we can perceive comfort directly by virtual reality simulation system. Secondly, we can analyze by 3D human model, such as EAI’s JACK software create a precise 3D human model. It can carry out the posture prediction, comfort evaluation, analysis of adaptability of hand reached space, and biomechanical analysis based on the novel data of human anatomy and physiology. RAMSIS not only provide the detailed human body size, but also focus on setting up the special application environment. It can measure and analyse body posture and movement, it can take interactive operation as view simulation, motion simulation. Thirdly, the application of DMU technology. We can analyse through the platform of electronic vehicle.

### ***4.2 Comfort in Driving and Rest***

Firstly, it emphasizes comfort of the whole cab. We can improve the comfort of the whole cab by active control suspension system to control and reduce the vibration of a cab.

Secondly, seat system should adopt more comfortable shock-absorbing form (airborne), heating and ventilation, the automatic control function. The application of the intelligent seat system can improve comfort.

At last, sleeper system requires abundant space, adjustable hardness, adjustable position and sense of home, and automatic control system can also be used a to operate the sleeper action.

### ***4.3 Entertainment and Comfort***

Entertainment and comfort are mainly embodied in contenting with the functional configuration and application of intelligent control, such as application of the future network, video conversation, conference function should be taken into consideration. Intelligent control means, such as automatic control, voice control, also will be used. All the advanced technology and method will be applied to the cab in order to improving recreational comfort.

## **5 The End**

For the future development of commercial vehicle cab, human-oriented design concept will become the core concept of product development. With the advanced technology, the use of advanced structure, to meet the functional requirements and performance requirements as a purpose, the development of high security and high comfort cab will become a focus of research.

## **References**

1. Badler N (1997) Virtual humans for animation, ergonomics, and simulation, non-rigid and articulated motion workshop. Proc IEEE, pp 28–36
2. Gill SA, Ruddle RA (1998) Using virtual humans to solve real ergonomic design problems. In: International conference on simulation '98, pp 223–229, Andreas Seidl. Ramsis—a new cad-tool for ergonomic analysis of vehicles developed
3. Wang Cheng W, Ga W, Wang Xing R (2002) VR (virtual reality) technology theory [5] ning wave. Digital prototyping application in aircraft design. The aeronautical manufacturing technology, vol 10. pp 20–21, 34
4. Zeng Jian C, Virtual reality technology and application. Beijing: Tsinghua University press



# The Design and Simulation Analysis of Electromagnetic Energy Regenerative Suspension System

Hongbin Ren, Sizhong Chen and Zhanzong Feng

**Abstract** The paper estimates the power dissipation of the traditional passive suspension under the different work condition, and the practicability of regenerative shock absorber is proved. Based on the fact, a novel scheme of electromagnetic regenerative shock absorber is proposed. The damper and electronic characteristics of the regenerative shock absorber are studied, and to improve vehicle comfort, a control algorithm is suggested, the controller uses the information from accelerometers and other sensors to change the external resistance of the circuit, which stiffens or softens the suspension. The modeling of the regenerative suspension system is studied and simulated in Matlab/Simulink. The results indicate that the regenerative suspension works best when used on the off-road. And compared with the traditional passive suspension or other semi-active suspension, the regenerative suspension could reduce the vibration of vehicle body and improve the passengers' comfort.

**Keywords** Electromagnetic suspension · Energy regenerative · Structural design · Damping characteristics · Skyhook control

---

F2012-E04-023

---

H. Ren (✉) · S. Chen · Z. Feng  
Beijing Institute of Technology, Beijing, China  
e-mail: renhongbin2106@126.com

## 1 Introduction

The regenerative suspension is a novel suspension system [1] that converts the vehicle body vibration energy into the electrical energy, and the damping force could be adjusted easily and in real time. As automobile industry development, energy crisis and environment pollution problem are increasing, energy-saving in automobile industry attracts more attention and is the most practical measure to solve these problems. The study of regenerative suspension is a hot research topic in recent years [2, 3].

The significant characteristic of the suspension is that vibration energy from the road excitation can be regenerated and transformed into electric energy while satisfying performance could be maintained. The energy-regenerative suspension mainly incorporates of the springs, motor and guiding mechanism. The springs bear the static load of vehicle body, so that the energy consumption could be reduced considerably if the suspension is working in the active mode. The most obvious features of the energy-regenerative suspension system is that it could works in three operational modes through the control algorithm: when the motor works in electromagnetic brake mode, it is the passive mode; when the resistance in the circuit is adjusted according to the logical control algorithm, so that the damping force could be changed and suitable to different working condition, it is the semi-active mode; when the power sources in the vehicle supply to the motor, the motor will be as actuator, and it is the active suspension mode [4]. The core technologies of the energy-regenerative suspension are the design of the mechanical structure and the control algorithm, the control algorithm decides when and how many Newtons of the actuator's force, as well as the energy management.

Several scholars and companies have studied the energy-regenerative suspension systems. Okada researched the electromagnetic regenerative suspension used the linear DC motor to achieve a good damping performance and recovery the vibration energy [5]. Suda suggested the self-power active control using the coupled electromagnetic device [6]. Yu Fan suggested an electromagnetic active suspension combination of a ball screw and permanent-magnetic DC brushless motor [7]. Yu utilized the dual-overrunning clutched electro-mechanical regenerative damper, and it could achieve high-low semi-active damping in a passive mode [8].

In the paper, the 1/4 car model is established, and the energy dissipation of traditional passive suspension is estimated under the different road condition. A novel scheme of electromagnetic shock absorber is proposed, it uses the rack and pinion mechanism to convert the unwanted upward and downward linear motion of the piston to the rotary motion to drive an electronic generator, and the electronic energy is fed into the car's battery. And the mathematic model of the permanent-magnetic DC brushless motor is established. The damping characteristic of the energy-regenerative shock absorber and the damping performance of the vehicle are studied.

## 2 The Energy Consumption of the Passive Suspension

To estimate the dissipation of tradition passive suspension, the 2DOF of 1/4 car model is established, as in Fig. 1. When the mass distribution coefficient  $\xi = \rho_y^2 / ab$  is closing to 1, the vibration of front and rear suspension system is almost independent. So the full car vibration could be simplified 2DOF vibration model, and it simulates the vertical and lifting movement of the vehicle.

According to the Second Newtonian Law, the vehicle dynamic equation can be describing as following:

$$\begin{aligned} m_s \ddot{z}_s + c_p (\dot{z}_s - \dot{z}_u) + k_s (z_s - z_u) &= 0 \\ m_u \ddot{z}_u + c_p (\dot{z}_u - \dot{z}_s) + k_s (z_u - z_s) + k_t (z_u - q) &= 0 \end{aligned} \tag{1}$$

where,  $m_s$  is the spring mass;  $z_s$  is the displacement of the spring mass;  $k_s$  is the equal stiffness of suspension;  $c_p$  is the damping coefficient;  $z_u$  is the displacement of the unspring mass;  $k_t$  is the equal stiffness of wheel;  $q$  is the road random excitation.

Based on the established 1/4 car model, the dissipation energy of the traditional passive suspension under different speeds and variable roads. Supposing that the damper converts the vibration of the system into heat, and the dissipation energy could be estimated by the following equation:

$$\begin{aligned} P &= \frac{1}{T} \int_0^T F_c(t) d[Z_s(t) - Z_u(t)] \\ &= \frac{1}{T} \int_0^T c_p (\dot{Z}_s(t) - \dot{Z}_u(t))^2 dt \end{aligned} \tag{2}$$

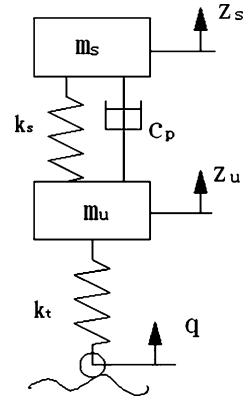
where,  $F_c$  is the damping force;  $P$  is the power dissipation of the passive suspension.

Based on an example of a heavy vehicle, the dissipation of the passive suspension is analyzed. The parameters are as following: the spring mass  $m_s = 1,400$  kg, unspring mass  $m_u = 140$  kg, the equal stiffness of suspension  $k_s = 60,000$  N m<sup>-1</sup>, the stiffness of wheel  $k_t = 60,0000$  N m<sup>-1</sup>, the damping coefficient  $c_p = 4,200$  N s m<sup>-1</sup>.

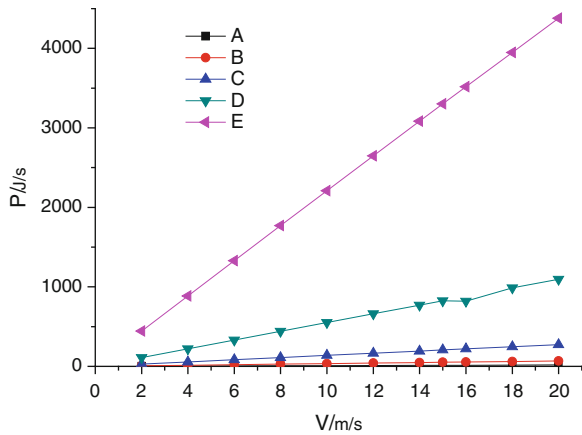
The energy dissipation of traditional passive suspension is estimated under A, B, C, D, E road condition. And the results are shown in Fig. 2.

The simulation results show that: the higher the velocity of the vehicle, and the rougher of the random road excitation, the greater energy consumption of the suspension. And it also means that the energy recovery potential is greater.

**Fig. 1** 1/4 car schematic



**Fig. 2** The energy dissipation of passive suspension



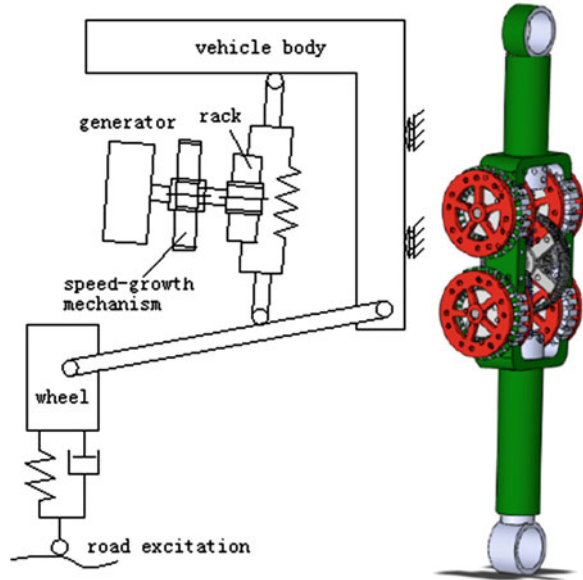
### 3 The Design of the Structure and Control Algorithm

The traditional passive suspension mainly consists of the spring elements and damper. The energy regenerative suspension is that the energy recovery device replaces the traditional damper. There are many devices of the energy recovery, such as the hydraulic energy storage, linear motor, rack and pinion mechanism, etc. Because of the rack and pinion mechanism is simple in design and other advantages, so it is used in the paper.

#### 3.1 The Working Principle and Characteristic of the Energy Regenerative Shock Absorber

The electromagnetic energy regenerative suspension consists of the DC brushless motor, rack and pinion mechanism and rectifier circuit. As the Fig. 3 shows, when

**Fig. 3** The structure scheme of the shock absorber



the wheel is excited from the random uneven road input, the rack and pinion mechanism converts the unwanted upward and downward linear motion between the spring mass and unspring mass to the rotary motion, and through the speed-growth mechanism to improve the rotator speed of the generator. The rotary coil cut the magnetic lines, the change of the flux that crosses the coil made inductive electromotive force and inductive current. The electricity and the magnetic field interact and produce the electromagnetic force. And the electromagnetic force could constrain the vehicle body's vibration, and at the same time, the vibration energy is converted into the electricity energy.

The rotating magnetic field of the brushless permanent magnetic motor is approximately sin distribution. And the magnetic flux  $\Phi$  could be expressed by the following formula:

$$\Phi = \Phi_m \sin wt \tag{3}$$

where,  $\Phi_m$  is the maximum flux of each phase, Wb.

$$\Phi_m = BS \tag{4}$$

where,  $B$  is the induction intensity of the magnetic poles, T;  $S$  is the cross-sectional areas of the magnetic poles,  $m^2$ ;  $w$  is the speed of the motor rotor,  $rad/s$ .

The inductive electromotive force of the motor stator is:

$$e = -N \frac{d\Phi}{dt} \tag{5}$$

The effective of the electromotive force is:

$$E = \frac{1}{\sqrt{2}} N \frac{d\Phi}{dt} = \frac{1}{\sqrt{2}} NBSw \quad (6)$$

Suppose that the relative velocity of the shock absorber is  $v$ , i.e. the velocity of the rack is  $v$ ; the radius of the gear that meshed with the rack is  $r$ ; the transmission ratio of the speed-growth mechanism is  $i$ . And the speed of rotor is:

$$w = \frac{v}{r} i \quad (7)$$

$$E = \frac{1}{\sqrt{2}} NBS \frac{v}{r} i \quad (8)$$

$$E = k_e v \quad (9)$$

where,  $k_e = \frac{1}{\sqrt{2}} NBS \cdot \frac{1}{r} \cdot i$ ,  $k_e$  is the physical quantity that reflects the structure parameter of motor.

From the Eq. (9), we may conclude that, the inductive electromotive is proportional to the relative velocity, the amplitude is greater, and  $E$  is greater.

From the viewpoint of energy conversation, the damping force could be deduced:

$$Fv\eta = EI \quad (10)$$

$$F = k_e i \frac{1}{\eta} \quad (11)$$

where,  $\eta$  is the mechanical efficiency;  $I$  is the current Value in the closed circuit.

By the above analysis, we could acquire the following conclusion: the damping force of the energy regenerative shock absorber is inversely proportional to the resistance in the circuit; and proportional to the current in the circuit.

### 3.2 Skyhook Control Algorithm

The skyhook control algorithm was proposed by Karnopp, and it is based on the optimism control theory [9]. The skyhook controller could constrain the vibration of the vehicle body. Though the controller is impossible of achievement, it provides a good idea. The shock absorber fitted between the spring mass and unspring mass tracks the skyhook force, and it is proved that the control algorithm could reach or approach the ideal controller and achieve a good performance. The control algorithm could be expressed by the following equation:

$$F_d = c_d(\dot{z}_s - \dot{z}_u) \rightarrow c_{sky}\dot{z}_s \quad (12)$$

where,  $c_d$  is the equivalent damping coefficient;  $c_{sky}$  is the skyhook damping coefficient. And the ideal control force is:

$$u_s = \begin{cases} c_{sky}\dot{z}_s & \dot{z}_s(\dot{z}_s - \dot{z}_u) > 0 \\ 0 & \dot{z}_s(\dot{z}_s - \dot{z}_u) \leq 0 \end{cases} \quad (13)$$

## 4 The Generating Mechanism of the Energy Regenerative Suspension

### 4.1 The Mathematics Model of the Generator Motor

The stator winding is run by the square current so as to reduce the torque ripple. To simplify the analysis, we supposed that: when analysis on the magnetic circuit, we ignore the magnetic saturation, magnetic hysteresis and eddy current; and the three-phase winding is symmetry.

The mathematics model of the permanent magnetic motor is following:

$$\begin{cases} u_d = -R_s i_d - L_d \frac{di_d}{dt} + wL_q i_q \\ u_q = -R_s i_q - L_q \frac{di_q}{dt} + wL_d i_d + w\psi_f \end{cases} \quad (14)$$

where,  $u_d$  is the voltage of the  $d$  axis, and  $u_q$  is the voltage of  $q$  axis;  $i_d$  is the current of the  $d$  axis, and  $i_q$  is the current of  $q$  axis;  $L_d$  is the inductor of the  $d$  axis, and  $L_q$  is the inductor of  $q$  axis;  $\psi_f$  is the flux of permanent magnetic;  $w$  is the rotator velocity of the magnetic field;  $R$  is the stator resistance.

### 4.2 Modeling and Simulation of the Motor

The simulation model of the motor is establish in Matlab/Simulink, and considering the 1/4 car model, as the Fig. 4. The input physical values are the relative velocity of the suspension and the acceleration of the vehicle body. And the driving module of the permanent magnetic motor mainly includes:

1. The main circuit module includes the motor module and the frequency converter module.
2. The switch logical module, its function is to have a logical decision to the input signal and output the control signal.
3. The motor logical control module, it decides the switch of the main circuit open or close, so as to soft or harden the damping force.

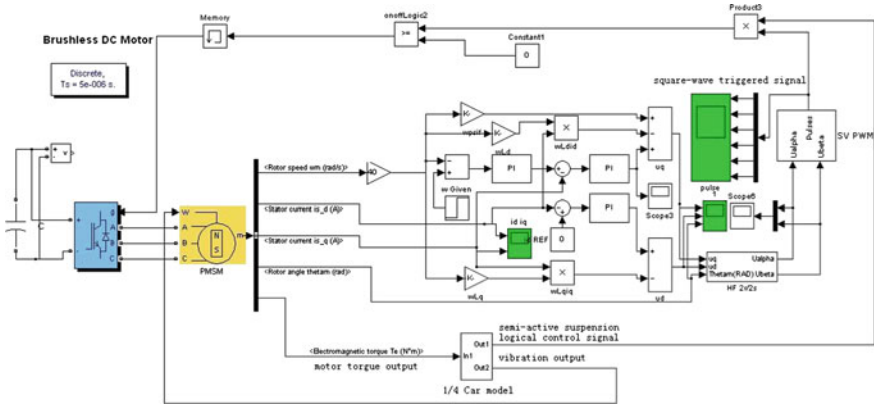
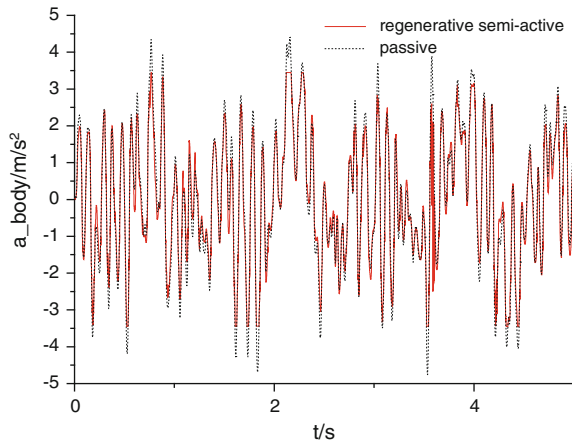


Fig. 4 Matlab/Simulink scheme of the controller model

Fig. 5 The vertical acceleration of the spring mass



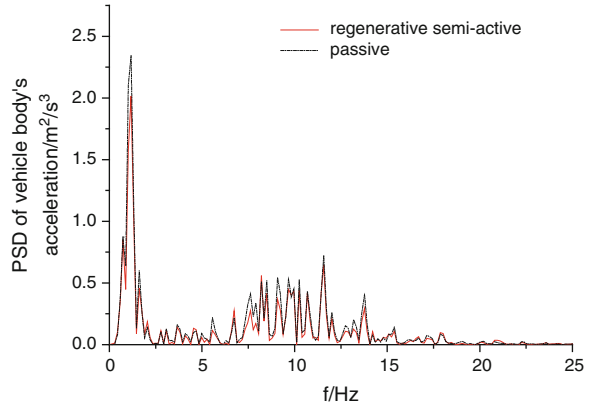
### 5 The Simulation of the Energy Regenerative Suspension

To analysis the performance of the energy regenerative suspension for the vehicle comfort and its potential of energy recovery, the simulation model is establish based on the sky hook control algorithm in Matlab. And compared with the traditional passive suspension, the results are shown in Figs 5, 6, 7, 8.

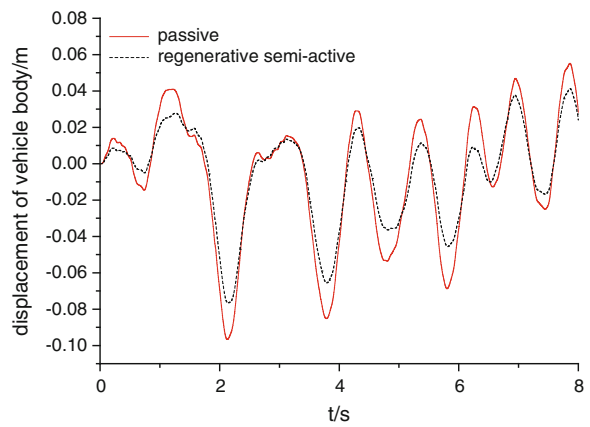
From Figs. 5, 6, 7, it can be conclude that, compared with the traditional passive suspension, the energy regenerative suspension could constrain the vibration of the vehicle body and the root mean square value of the vehicle body acceleration declines by 13.5 %, so it could improve the vehicle comfort remarkably.



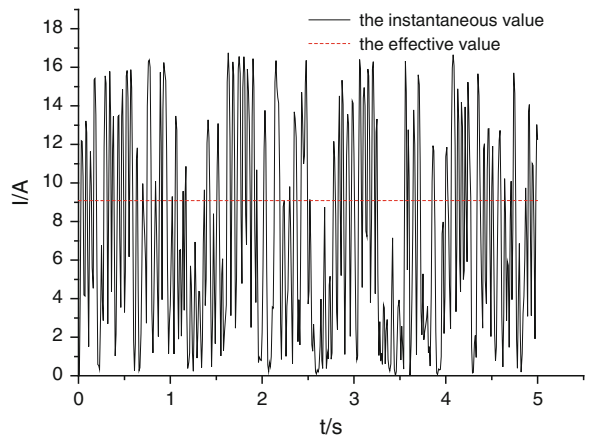
**Fig. 6** The PSD of the vertical acceleration of spring mass



**Fig. 7** The vertical displacement of vehicle body



**Fig. 8** The instantaneous and effective current value of the generator



The results of the Fig. 8 indicate that, the energy regenerative suspension could recovery some vibration energy, and the instantaneous current can be rectified and store the energy into the battery.

## 6 Conclusion

The study was conducted to determine the possibility and limitation for the energy regenerative suspension, and then suggested a design scheme of the energy regenerative damper.

A novel scheme of electromagnetic regenerative shock absorber is proposed, it uses the rack and pinion mechanism to convert the unwanted upward and downward linear motion of the piston to the rotary motion to drive an electronic generator, all the electronic energy is then fed into the car's battery, and it could lower the fuel consumption depending on the vehicle and driving condition. Especially when such a system is adapted to a hybrid vehicle or electronic vehicle, it is possible to recharge the vehicle's battery with this energy and hence extend its mileage.

Compared with the traditional passive suspension or other semi-active suspension, the regenerative suspension could reduce the vibration of vehicle body and improve the comfort and handling stability.

**Acknowledgments** This work was supported by Ministerial Level Foundation of China (2220051229). The authors express gratitude to MLFC for the financial support. The authors would also like to thank the reviewers for the valuable observations and suggestions.

## References

1. Okada Y, Harada H (1996) Regenerative control suspension systems active vibration damper and sue [C]. Proceeding of the 35th conference on design and control, Japan, 1996
2. Cao D, Song X (2011) Advanced suspension systems and dynamics for future road vehicles [J]. Veh Syst Dyn 49:1
3. Energy Recovery in Recuperative Damping Systems (Regenerative Suspension Systems) [E]. In: 4th International conference advanced suspension systems, 2011
4. Xuechun Z (2007) Theoretical and experimental study of automobile electrical energy-regenerative active suspension [D], Shanghai Jiao Tong University, 2007
5. Okada Y, Harada H, Suzuiki K (1995) Active and regenerative control of linear DC motor type damper [C]. Proceedings of the third international conference on motion and vibration control, vol 3. Chiba, pp 321–326
6. Nakano K, Suda Y, Nakadai S (2003) Self-powered active vibration control using a single electric actuator[J]. J Sound Vib 260(2):213–235
7. Zhao Y, Yu F, Huang K (2009) Permanent-magnet DC motor actuators application in automotive energy-regenerative active suspension [C]. SAE 2009
8. Yu C, Wang W (2012) Experiment and analysis of the dual-overrunning clutches electro-mechanical regenerative damper property [J]. Journal of Jilin University 42:3
9. Karnopp D, Crosby MJ, Harwood RA (1974) Vibration control using semi-active force generators [J]. Journal of Engineering Industry, 1974

# Optimization of the Magnetic Property of a Magnetorheological Squeeze Mount

Xinjie Zhang, Fangwu Ma, Fuquan Zhao, Konghui Guo  
and Mehdi Ahmadian

**Abstract** Magneto-rheological fluid squeeze mode investigations have shown that MR fluids show large force capabilities in squeeze mode and it can be used for isolating vibration. An MR squeeze mount's magnet system will be designed and optimized in this research. An FEM model of the magnetic supply system of a Magnetorheological squeeze mount is developed and the parameters are studied firstly. And then, the magnetic property is optimized by the co-simulation of the Matlab and FEMM, which will be used to improve the range of the damping of a Magnetorheological squeeze mount. At last, a mathematical model for this magnetic system is proposed for solving the applied current in the real time control.

**Keywords** Magnetic property · FEMM · Sensitivity analysis · Optimization · Mathematical model

## 1 Introduction

The essential characteristic of magneto-rheological (MR) fluid, consisting of a suspension of micron-sized ferromagnetic particles in a non-magnetic carrier fluid

---

F2012-E04-024

---

X. Zhang (✉) · F. Zhao · K. Guo  
State Key Laboratory of Automotive Simulation and Control, Jilin University, Jilin, China  
e-mail: xjzhang5885@gmail.com

X. Zhang · F. Ma · F. Zhao  
Zhejiang Geely Automobile Research Institute Co., Ltd, Zhejiang, China

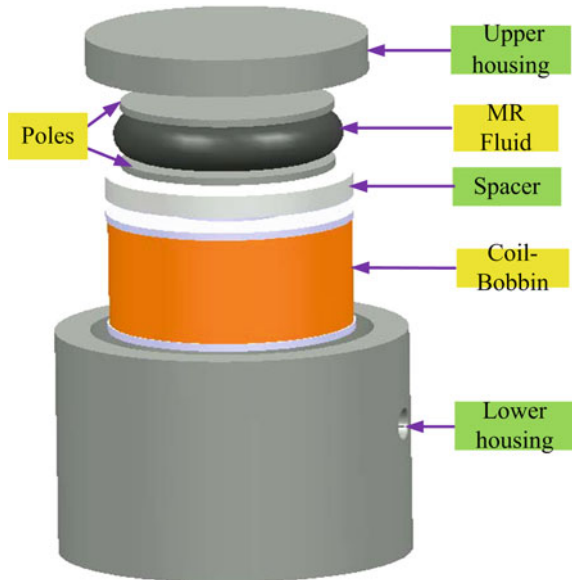
M. Ahmadian  
Center for Vehicle Systems and Safety, Virginia Tech, Blacksburg VA 24060, USA

(e.g. mineral oil, synthetic oil, water, or glycol), is the rapid and reversible transition from the state of a Newtonian-like fluid to the behaviour of a stiff semi-solid by applying a magnetic field of 0.1–0.4 T. Due to this rheological behaviour, MR fluids are currently being used in a wide variety of applications such as: controllable dampers, rotary brakes [1, 2], seismic vibration mitigation devices [3], and prosthetic devices [4]. MR fluid offers three modes of operation, namely the direct shear mode, the valve mode, and the squeeze mode. The latter is of particular interest due to its wider range of controllable force compared to shear and valve modes, which is still not fully understood and therefore expected to give rise to new industrial applications.

The compressive behavior of magneto-rheological (MR) fluids has been studied for industrial applications such as in dampers and as a mechanism for strengthening the materials by increasing their yield stress [5–9]. The behavior of MR fluids in squeeze mode under oscillatory conditions below 8 Hz was investigated by Vieira et al. [7]. It was found that the damping performance of an MR damper can be obtained by increasing the magnetic field strength or the displacement amplitude. Changing the frequency of the system also contributed to various behaviours of MR fluids and the peak compressive force was found to increase with the increase in the number of cycles. The ER and MR squeeze mode properties was study by McIntyre [8] and the tensile and compressive strain of MR squeeze mode was tested by Mazlan [9] in which the current applied to the coil, the initial gap size and the compressive or tensile speed are considered. The overall thrust in these studies was either towards higher yield stresses or the utilization of a commercial MR fluid that already had a high yield stress [10]. Forte et al. [11] optimized the design of a MR damper for rotor applications and showed that the damping characteristics of rotor vibrations can be controlled by varying the current in the magnetic coils. Later on, they improved both the design and the model through a more practical design process [12]. Moreover, Wang et al. [13] investigated and subsequently analyzed the mechanical properties of squeeze film and the unbalanced response characteristics of a MR fluid squeeze film damper. The squeeze mode of a MR damper has significant advantages such as simple structure, clear effectiveness and quick response [14]. The stress produced by the squeeze mode is the highest stress amongst other modes and can be used in damping vibrations with low amplitudes and high dynamic forces [15]. Examples for vibration control are isolation turbomachinery [16] and squeeze film damper [17]. An ER squeeze mode was applied in a prototype automotive engine mount [18]. The experimental (1–20 Hz) and theoretical development of a multiple fluid mode magneto-rheological isolator is studied [19], in which a nonlinear hysteretic model was used to improve the model ability to analytically predict the damper characteristics.

Some MR squeeze mounts were designed and built at CVeSS [14], which are self-sealed and modular unit and can deliver a very large range of force. The magnetic system of an MR squeeze mount is designed and studied by the co-simulation of the Matlab and the Finite Element Method Magnetics (FEMM). An FEM model of the magnetic supply system is developed and the parameters are studied firstly. And then, the magnetic property is optimized by the co-simulation

**Fig. 1** 3-D decomposition diagram of the magnetic system



of the Matlab and FEMM, which will be used to improve the range of the damping of a Magnetorheological damper. At last, a mathematical model for this magnetic system is proposed for solving the applied current in the real time control.

## 2 Magnetic System Design

It is easy to control the magnetic density by controlling the applied current. However, the magnetic density is very sensitive with the gap of the MR squeeze mount, especially, when the gap is very small. The design parameters for the mount and magnetic system were constrained due to availability of tooling, materials, and testing equipment. Fortunately, we can just update some parts of the one designed by Brian [20] since the height of the Mount is different, which is shown as Fig. 1.

An upper housing is used to create an efficient return path in the magnetic circuit and also constrain the upper-pole plate of the of the MR squeeze mount. The case is then able to sit inside the upper housing which extends the upper-pole plate toward the lower housing. It creates a flux return path to the lower housing of the magnetic system. The thickness of the upper housing provides sufficient thread length for fastening a test fixture at the perimeter of the housing. And the main focus for the lower housing is a centered magnetic core that mates to the magnetic-pole plate of the MR squeeze mount. A coil bobbin that would not interfere with the diameter of the magnetic core was selected and 24 AWG magnet wire at 800 turns was selected to fit the coil bobbin and to provide a large  $Ni$  value with a

minimal current supply. Using a low current supply is necessary to avoid overheating the coil when testing over continuous cycles. Therefore, the lower housing model design takes into account the electro coil and MR squeeze mount elements. An aluminous spacer is used to provide a solid base for the mount which also locks the coil in the lower housing and constrained the lower plate of the MR squeeze mount by two side screws. The lower housing then provides a return path for the upper housing. At last the testing equipment defined the use of a 1.6 mm. Air gap, between the upper housing and the lower housing to allow for improper axial alignment within the testing equipment. This space prevents any mode of binding, either axial or torsion, from occurring and possibly adding friction which might misconstrue the test results. This air gap could be reduced or removed if placed in a permanent application, but a blow-off route for the air in the bulge volume would need to be created. The bulge space around the circumference of the MR squeeze mount is to allow room for expansion of the elastic membrane during compression.

### 3 Parameter Study of the Magnetic System

The main objective of the magnetic circuit was to produce the correct magnetic flux density across the MR fluid. From the electromagnetic point of view, the test equipment could be treated as a circuit concentrating the magnetic field generated by a coil and guiding it from the core to and across the fluid. Here, the effect of electric current and mount gap size on the magnetic field density in the mount are studied by the co-simulation of a finite element modeling software, FEMM, and Matlab.

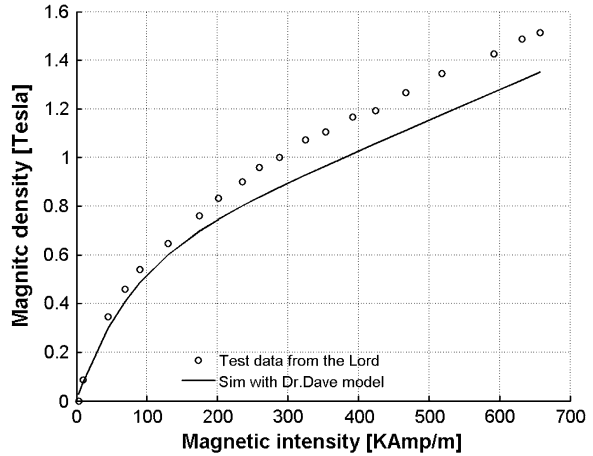
#### 3.1 FEMM Model of the Magnetic System

With the aforementioned MR squeeze mount case, the magnetic model is prototyped in finite element methods magnetics (FEMM) analysis software. FEMM analyzes the axis-symmetric vertical cross-section of a magnetic circuit. From this software, contours of the magnetic flux density  $|B|$  as well as the magnetic field intensity  $|H|$  in the model can be extracted. The necessary inputs to create an accurate model are the dimensions, material properties, coil windings and wire gauge of the system, and the circuit current. An empirical model for the  $B-H$  curves of MR fluid was proposed by Dr Dave [2] shown as (1)

$$B = 1.91\Phi^{1.133}[1 - \exp(-10.97\mu_0H)] + \mu_0H \quad (1)$$

where  $B$  is the magnetic flux density,  $H$  is the magnetic field intensity,  $\Phi$  is the percentage of ferrous iron in the fluid, and  $\mu_0$  equals  $4\pi 10^{-7}$ . Therefore,  $\Phi$  is set to 0.32 based on the ferrous iron percentage making up the MR fluid. Next, the

**Fig. 2** B–H property of the MRF-132 MR fluid



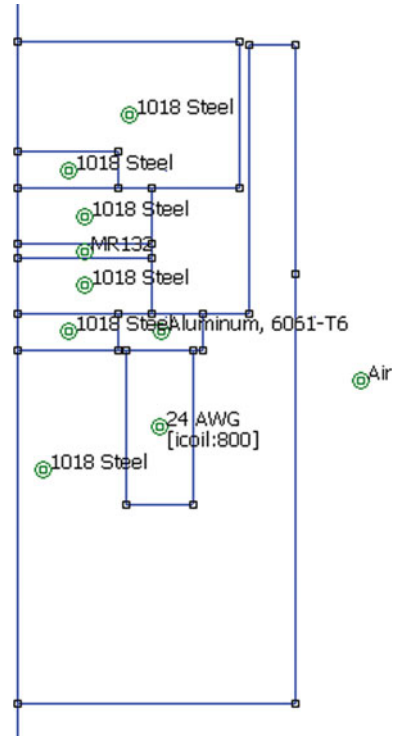
magnetic field intensity is increased from 0 to 600 kAmp/m to generate the magnetic flux in Eq. (1). Additionally, this simulation accurately represents the empirical B–H curve for MRF-132DG published by Lord Corp shown as Fig. 2. It shows the Dr Dave’s empirical model can match the test data very well under the low magnetic intensity but it will be smaller than the test data as the increasing of the magnetic intensity. In this research, a cubic spline interpolation based the Lord Corp.’s test result, covering a wide range, without extrapolation, was used for estimating the B–H property of the MRF-132DG MR fluid, which is fast and precise.

Figure 3 shows the FEMM model of the MR squeeze mount and case. The Fig. 4 is the distribution of the magnetic density. A couple of other additional features for the test setup, which are not included in the FEMM model from Fig. 3, are the non-magnetic test fixtures. These fixtures are required mounting for the Roehrig shock dyno, but would not be necessary if the mount and magnetic system were placed in a permanent application. Moreover, the mount could be rigidly attached to the core of the magnet, but for testing purposes the upper housing is the only alignment constraint placed on the mount.

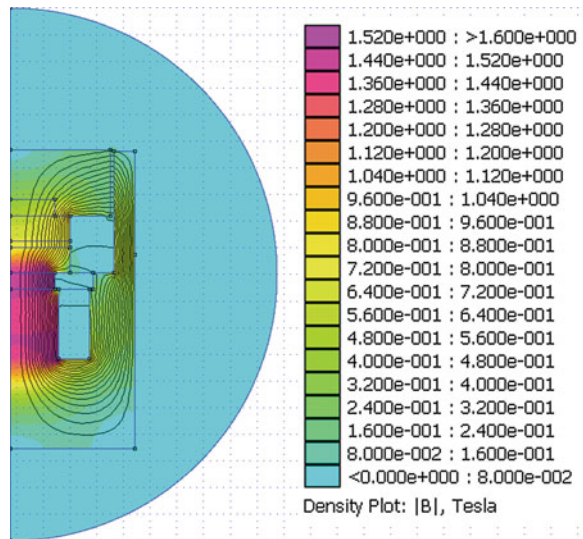
### 3.2 Effect of the Upper Housing and Lower Housing’s Height

There are some invariable parameters in the MR squeeze mount and the case, especially, the structural parameters which are not easy to change once the prototype has been made. Only the height of the upper housing and lower housing are considered since the other parts of the case is same as Brain’s. It’s easy to add some spacer to extend the height of the upper housing and another extruded lower housing can be assembled to extend the height of lower housing to provide a return path for the upper housing. The effect of the height of the upper housing is shown

**Fig. 3** Cross-sectional view of the FEMM model of the MR squeeze mount and magnetic system

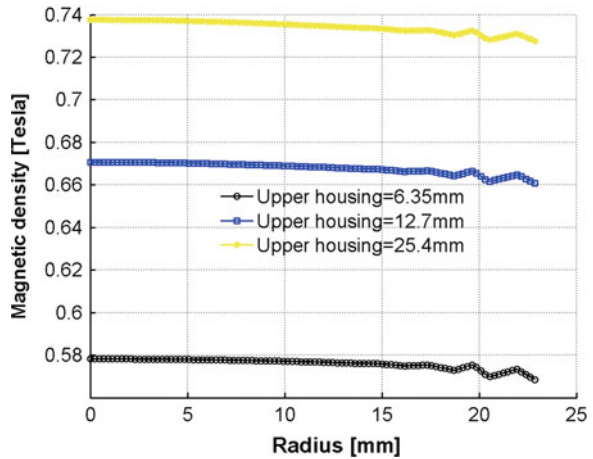


**Fig. 4** Distribution of the magnetic density

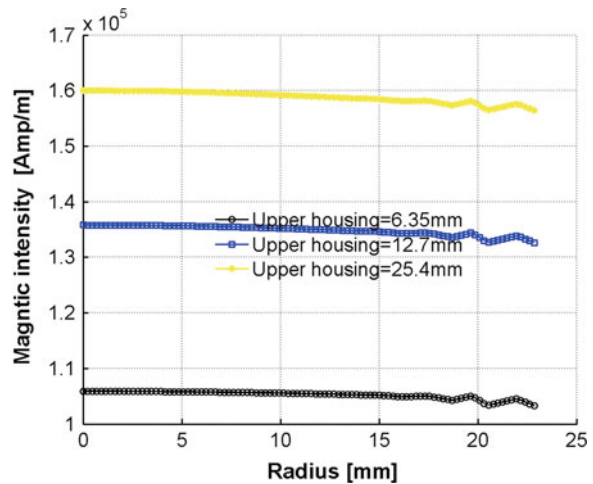




**Fig. 5** Magnetic density distribution with different upper housing  
(Current = 1 Amp,  
Gap = 2.54 mm, Lower housing = 46.0 mm)

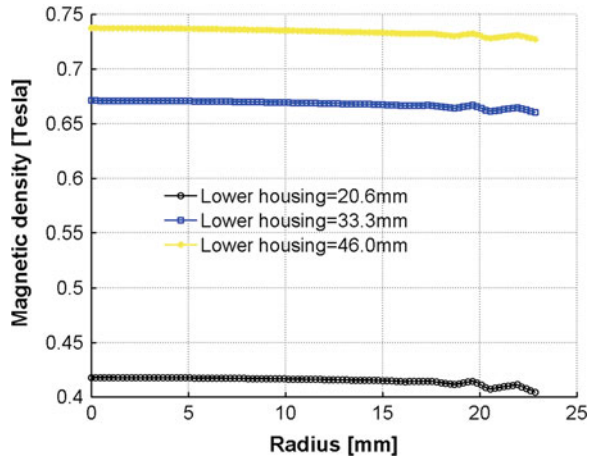


**Fig. 6** Magnetic intensity distribution with the different upper housing  
(Current = 1 Amp,  
Gap = 2.54 mm Lower housing = 46.0 mm)

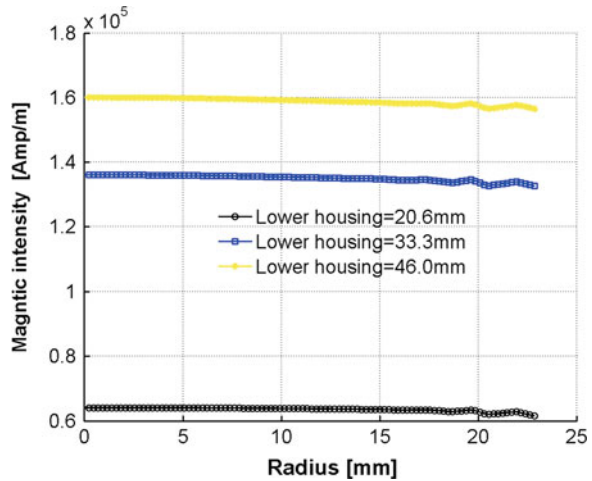


as Figs. 5 and 6, the height of the upper housing was set to 6.35, 12.7 and 25.4 mm, the initial gap between two poles is 2.54 mm, and the height of the lower housing was 46 mm. Figure 5 shows that the magnetic density increased from 0.58 to 0.74 Tesla while the magnetic intensity increased from 106 to 160 kAmp/m shown as Fig. 6 as the height of the upper housing increased from 6.35 to 25.4 mm. In other words, magnetic density will increase 28 % and the magnetic intensity will increase 52 % when the height of the upper housing increased from 6.35 to 25.4 mm. The influence from the height of the lower housing is shown as Figs. 7 and 8, the height of the lower housing was set to 20.6, 33.3 and 46.0 mm, the initial gap between two poles is 2.54 mm, and the lower of the lower housing was 25.4 mm. Figure 7 shows that the magnetic density increased from 0.42 to 0.74 Tesla while the magnetic intensity increased from 65

**Fig. 7** Magnetic density distribution with the different lower housing (Current = 1 Amp, Gap = 2.54 mm, Upper housing = 25.4 mm)

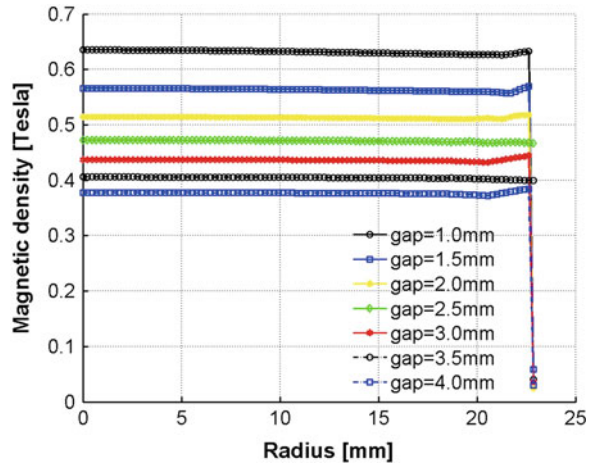


**Fig. 8** Magnetic intensity distribution with the different lower housing (Current = 1 Amp, Gap = 2.54 mm, Lower housing = 25.4 mm)

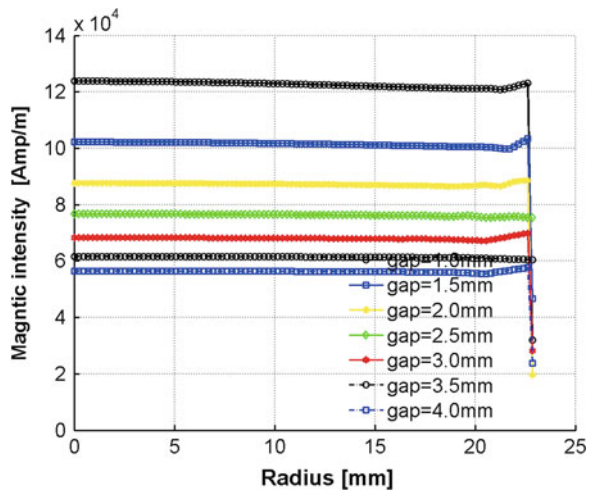


to 160 kAmp/m shown as Fig. 8 as the height of the upper housing increased from 20.6 to 46.0 mm. In a word, increasing the height of the housing will increase the magnetic density and magnetic intensity since there will be a better return path in the magnetic circuit and less energy will dissipate. In other hand, the housing can't be too large since a larger mass will need bigger space and more cost. Here the upper housing set to 25.4 mm and lower housing is 46.0 mm.

**Fig. 9** Magnetic density distribution with the different gap (Current = 1Amp)



**Fig. 10** Magnetic intensity distribution with the different gap (Current = 1Amp)

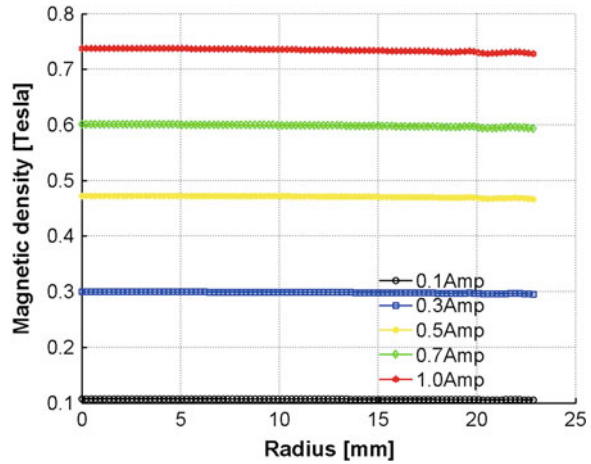


### 3.3 Effect of the Applied Current and Initial Gap

The applied current is a key parameter of the magnetic field which is easy to control and adjust and the magnetic also very sensitive with the gap of the MR squeeze mount, especially, when the gap is very small. Here the influence from the applied current and gap are studied by the co-simulation of FEMM and Matlab.

Figure 9 shows that the magnetic flux density distribution with the different gap from 1 to 4 mm with the step is 0.5 mm at the middle line between the upper and lower plate of the MR squeeze mount (applied current is 1 Amp) and Fig. 11 shows that the magnetic flux density distribution with the different current from 0.1 to 1 Amp (initial gap is 2.54 mm). Figure 10 (applied current is 1 Amp) and

**Fig. 11** Magnetic density distribution with the different current (gap = 2.54 mm)



**Fig. 12** Magnetic intensity distribution with the different current (Gap = 2.54 mm)

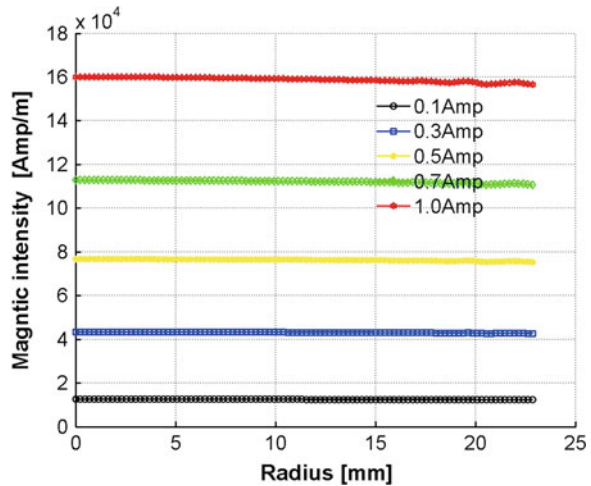
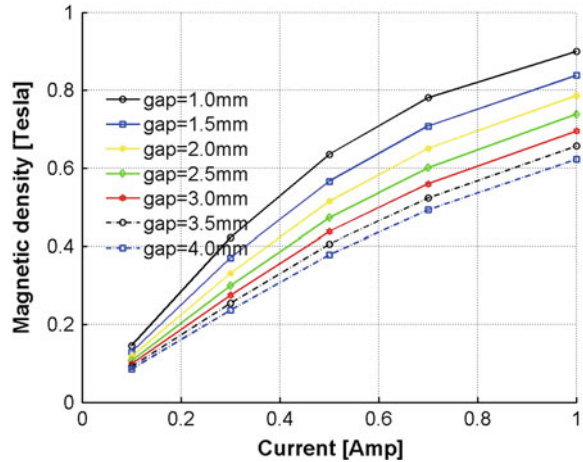


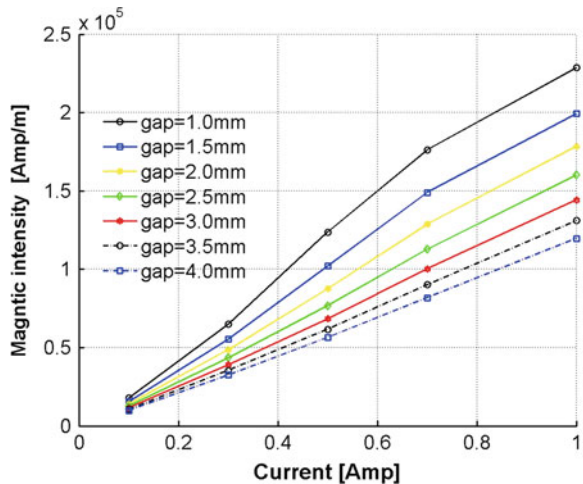
Fig. 12 (initial gap is 2.54 mm) are the magnetic intensity distribution under different gap and current. It is easy to get that increasing the current or decreasing the gap will increase the magnetic density and magnetic intensity.

Figures 5–12 shows the radial distribution of the magnetic field is nearly uniform. The radial distribution of the magnetic field can be instead by the center point’s magnetic field of MR Squeeze mount. The simulated effects of initial gap size on magnetic flux density and magnetic intensity when increasing the applied currents are shown in Figs. 13 and 14. As the applied current increased, the values of magnetic flux density increased. The simulated effects of the applied current on magnetic flux density when increasing the initial gap sizes shown in Figs. 15 and 16. As the initial gap size increased, the values of magnetic flux density decreased.

**Fig. 13** Magnetic density of the center point versus current for different initial gaps



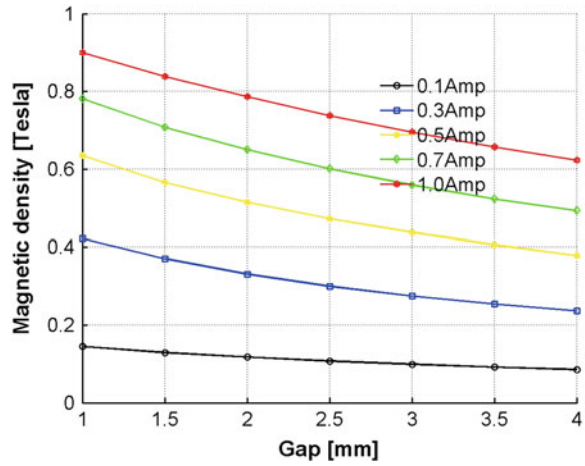
**Fig. 14** Magnetic intensity of the center point versus current for different initial gaps



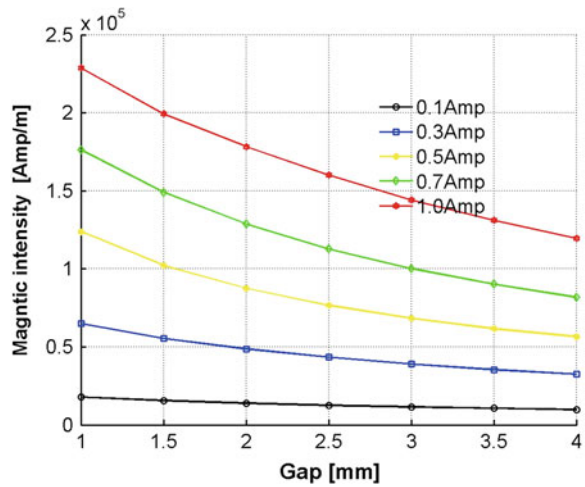
### 4 Mathematical Modeling

As mention before, the  $B-H$  curve of MRF-132DG is non-linear shown as Fig. 2. It is much easier to get the semi-empirical model for the magnetic field intensity  $H$  since it is independent with the permeability  $\mu_0$ . Figure 14 shows the magnetic intensity is proportional with the current, which is same with the Ampère’s circuital law, and nearly inverse with the initial gap shown as Fig. 16. The initial conditions and the boundary conditions of the first derivative is as Eq. (2) and a semi-empirical mathematic model for magnetic field intensity shows as Eq. (3)

**Fig. 15** Magnetic density of the center point versus initial gap for different currents



**Fig. 16** Magnetic intensity of the center point versus initial gap for different currents

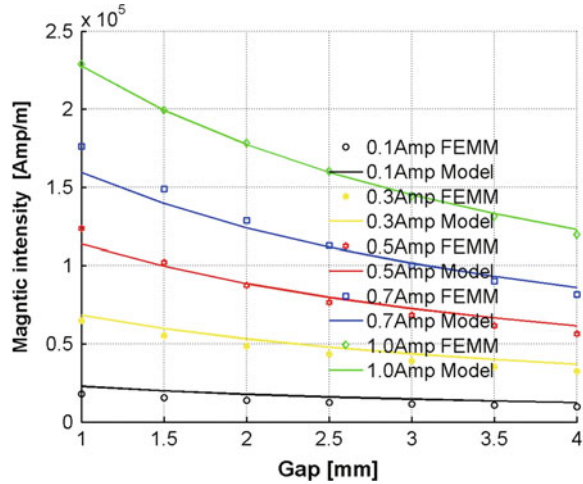


$$\begin{cases} H(0, h) = 0 \\ H(I, \infty) = 0 \\ \frac{\partial I}{\partial h} \Big|_{h=\infty} = 0 \end{cases} \quad (2)$$

$$H = \frac{NI}{(ah + b)} \quad (3)$$

where  $N$  is the number of the coil and here is set to 800,  $I$  is the current,  $h$  is the gap between two plates of the MR squeeze mount. Parameter  $a$  and  $b$  will get from simulation data from the FEMM since the center plane of the MR squeeze mount

**Fig. 17** A compare of magnetic intensity between FEMM model and semi-empirical model



is not at the end plane of coil. Nonlinear least squares estimation is used for identifying the parameter via Matlab. The magnetic field intensity is identified as Eq. (4)

$$H = \frac{NI}{(h + 0.0025)} \tag{4}$$

A compare of the magnetic field intensity between the FEMM and semi-empirical model is shown as Fig. 17. The semi-empirical model matches the FEMM model very well, which will be used to reverse the control current from the expected magnetic field intensity.

## 5 Conclusion

A MR squeeze mount’s magnet system is designed and optimized in this research. Parts of the key parameters of magnet system are studied and optimization by Co-simulation of the FEMM and Matlab. It shows that increasing the height of the housing will increase the magnetic density and magnetic intensity. In other words, an efficient return path will reduce the power dissipate since there will be a much stronger magnetic field with a better return path. Increasing the current or decreasing the gap will also increase the magnetic density and magnetic intensity. In this magnet system, the magnetic density will be up to 0.75 Tesla with 2.54 mm gap, 1 Amp current and 800 turns 24 AWG magnet wire. At last, A semi-empirical model is developed depending on the FEMM simulate results. The semi-empirical model matches the FEMM model very well, which will be used to reverse the control current from the expected magnetic field intensity.



**Acknowledgments** Special thanks are due to Young Teachers Innovation Fund Program of Jilin University (450060481170) for supporting authors' researches.

## References

1. Li W, Du H (2003) Design and experimental evaluation of a magnetorheological brake. *Int J Adv Manuf Technol* 21:508–515
2. Carlson JD (2005) MR fluids and devices in the real world. *Int J Mod Phys B* 19:1463–1470
3. Cho SW, Jung HJ, Lee IW (2005) Smart passive system based on magnetorheological damper. *Smart Mater Struct* 14(4):707–714
4. Chen JZ, Liao WH (2010) Design, testing and control of a magnetorheological actuator for assistive knee braces. *Smart Mater Struct* 19(3):035029
5. Tang X, Tao R, Zhang X (2001) Enhance the yield shear stress of magnetorheological fluids. *Int J Mod Phys B* 15(6–7):549–556
6. Tang X, Zhang X, Tao R, Rong YM (2000) Structure enhanced yield stress of magnetorheological fluids. *J Appl Phys* 87(5):2634–2638
7. Vieira SL, Ciocanel C, Kulkarni P, Agrawal A, Naganathan N (2003) Behavior of MR fluids in squeeze mode. *Int J Veh Des* 33(1–3):36–49
8. McIntyre EC (2008) Compression of smart materials squeeze flow of electrorheological and magnetorheological fluids. Ph.D Dissertation, University of Michigan
9. Mazlan SA (2008) The behaviour of magnetorheological fluids in squeeze mode. Ph.D Dissertation, Dublin City University
10. Kittipoomwong D, Klingenberg DJ, Ulicny JC (2005) Dynamic yield stress enhancement in bidisperse magnetorheological fluids. *J Rheol* 49(6):1521–1538
11. Forte P, Patern OM, Rustighi E (2004) A magnetorheological fluid damper for rotor applications. *Int J Rotating Mach* 10(3):175–182
12. Carmignani C, Forte P, Rustighi E (2006) Design of a novel magneto-rheological squeeze-film damper. *Smart Mater Struct* 15(1):164–170
13. Wang J, Meng G, Feng N, Hahn EJ (2005) Dynamic performance and control of squeeze mode MR fluid damper-rotor system. *Smart Mater Struct* 14(4):529–539
14. Craft MJ, Ahmadian M, Farjoud A, Burke WCT, Nagode C (2010) Force characteristics of a modular squeeze mode magneto-rheological element. *Active and passive smart structures and integrated systems 2010*, Proceedings of the SPIE, 2010, 7643: 764313-764313-11. doi:[10.1117/12.848856](https://doi.org/10.1117/12.848856)
15. Wang J, Feng N, Meng G, Hahn EJ (2006) Vibration control of rotor by squeeze film damper with magnetorheological fluid. *J Intell Mater Syst Struct* 17:353–357
16. Burrows CR, Kucuk NC, Sahinkaya MN, Stanway R (1990) Linearized squeeze-film dynamics: a model structure and the interpretation of experimentally derived parameters. *Proc Inst Mech Eng, Part C, J Mech Eng Sci* 204(4):263–272
17. Kim KJ, Lee CW, Koo JH (2008) Design and modeling of semi-active squeeze film damper using magnetorheological fluid. *Smart Mater Struct* 17:1–12. doi:[10.1088/0964-1726/17/3/035006](https://doi.org/10.1088/0964-1726/17/3/035006)
18. William EW, Rigby SG, Sproston JL (1993) Electrorheological fluids applied to an automotive engine mount. *J Nonnewton Fluid Mech* 47:221–238
19. Brigley M, Choi YT, Wereley NM (2008) Experimental and theoretical development of multiple fluid mode magnetorheological isolators. *J Guidance Control Dyn* 31(3):449–459
20. Southern BM (2009) Design and characterization of tunable magneto-rheological fluid-Elastic mounts. M.S. Thesis, Virginia Polytechnic Institute and State University



# Semi-Active Suspension Adaptive Control Strategy Based on Hybrid Control

Xinjie Zhang, Wuhui Yu, Fangwu Ma, Fuquan Zhao  
and Konghui Guo

**Abstract** An adaptive Control strategy for hybrid control logic of a quarter-car is proposed in this paper, which makes better compliance between the handling and ride comfort. An algorithm for identifying road unevenness is abstracted via RMS of the suspension travel under variable road input and vehicle speed firstly, and then all optimal control parameters under different driving conditions are optimized off line by the  $H_2$  optimization. At last, the optimal control parameters are applied on an online control system, which demonstrates that the Adaptive Hybrid Control Strategy can improve the ride comfort in “soft” driving mode and handling stability in “sport” driving mode effectively.

**Keywords** Semi-active suspension · Hybrid control · Road identification · Adaptive control strategy ·  $H_2$  optimization

## 1 Introduction

A typical vehicle suspension contains a spring and a damper. A soft suspension provides good isolation of the sprung mass at the cost of large tire displacements, while a hard suspension provides poor isolation of the sprung mass but reduced tire

---

F2012-E04-025

---

X. Zhang (✉) · W. Yu · F. Zhao · K. Guo  
State Key Laboratory of Automotive Simulation and Control, Jilin University, Changchun,  
Jilin, China  
e-mail: xjzhang5885@gmail.com

X. Zhang · F. Ma · F. Zhao  
Zhejiang Geely Automobile Research Institute Co., Ltd, Linhai, Zhejiang, China

displacements. An active suspension can trade off between the ride comfort and handling easily. However, it is hard to be commercialized since its complexity and large power requirements. Semi-active suspension has been a hot topic these years since it is less complex, more reliable, and much cheaper than an active suspension.

Lots of control strategies have been proposed to improve the properties of a semi-active suspension. A sky-hook control is used widely since it is easy to be carried out in a real vehicle system, which gives better ride comfort, with higher tire deflection compared with a passive one [1–3]. A ground-hook control gives better road holding, with worse ride comfort. An alternative semi-active control policy known as hybrid control takes advantage of both the skyhook and ground-hook control [4]. The control parameters were obtained via  $H_2$  optimization under the velocity white noise signal based on an ideal hybrid control model [5].

Most hybrid control sets control parameter  $\alpha$  as a constant, which can be effective in some driving condition. But a smart suspension should have an ability to adapt to various driving conditions, such as variable vehicle speeds and road unevenness. In this paper, an adaptive control strategy based on hybrid control is proposed, which will make a better compliance between the handling, ride comfort and safety. A quarter-car model with hybrid control is represented via Simulink, then all optimal control parameters under different driving conditions are optimized off line via  $H_2$  optimization. At last, the optimal control parameters will be applied on an online control system.

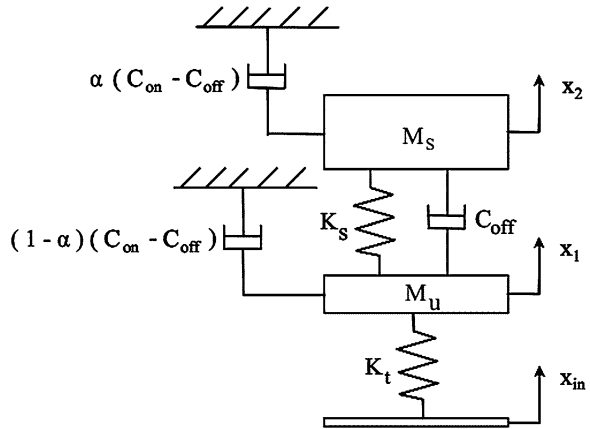
## 2 Quarter-Car with Hybrid Control

As shown in Fig. 1, the model uses the actual passive representation of the semi-active suspension with hybrid configuration. The model consists of a single sprung mass ( $M_s$ ) free to move in the vertical direction, connected to an unsprung mass ( $M_u$ ) free to bounce vertically with respect to the sprung mass. The tire is modelled as a spring of stiffness  $K_u$ . The tire damping is small enough to be neglected. The suspension between the sprung mass  $M_s$  and the unsprung mass  $M_u$  is modelled as a linear spring of stiffness  $K_s$ , and a linear damper with a damping coefficient of  $C_{off}$ . A linear damper with a damping rate of  $\alpha(C_{on}-C_{off})$  connects the sprung mass to some inertial reference in the sky and a linear damper with a damping rate of  $(1-\alpha)(C_{on}-C_{off})$ , connects the unsprung mass to some inertial reference in the sky. When  $\alpha$  is 1, the control policy reduces to a pure skyhook, and the control is a purely ground-hook when  $\alpha$  is 0.

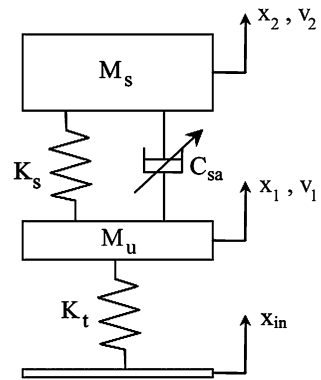
The motion equation is as Eq. (1)

$$\begin{cases} M_s \ddot{x}_2 + \alpha(C_{on} - C_{off})\dot{x}_2 + C_{off}(\dot{x}_2 - \dot{x}_1) + K_s(x_2 - x_1) = 0 \\ M_u \ddot{x}_1 + (1 - \alpha)(C_{on} - C_{off})\dot{x}_1 + C_{off}(\dot{x}_1 - \dot{x}_2) + K_s(x_1 - x_2) + K_u(x_1 - x_{in}) = 0 \end{cases} \quad (1)$$

**Fig. 1** Ideal hybrid control configuration



**Fig. 2** Semiactive equivalent model



where  $x_{in}$ ,  $x_1$ ,  $x_2$  represent to the road input, displacement of unsprung mass and sprung mass. The model introduced in Fig. 1 is an ideal model and can't be applied on an actual car due to no inertial reference in an actual car system. A semi-active equivalent model is adopted in Fig. 2.

Motion equation is as Eq. (2)

$$\begin{cases} M_s \ddot{x}_2 + C_{sa}(\dot{x}_2 - \dot{x}_1) + K_s(x_2 - x_1) = 0 \\ M_u \ddot{x}_1 + C_{sa}(\dot{x}_1 - \dot{x}_2) + K_s(x_1 - x_2) + K_t(x_1 - x_{in}) = 0 \end{cases} \quad (2)$$

where  $C_{sa}$  is given by:

$$C_{sa} = \begin{cases} C_{max}, C_d > C_{max} \\ C_d, C_d \leq C_{max} \end{cases} \quad (3)$$

where  $C_{max}$  is the maximum damping coefficient of the suspension.  $C_d$  is given as Eq. (4)

$$C_d = \frac{(C_{on} - C_{off})[\alpha\sigma_{sky} + (1 - \alpha)\sigma_{sky}]}{v_{12}} \quad (4)$$

$$\text{where } \sigma_{sky} = \begin{cases} v_2, v_2 v_{21} \geq 0 \\ 0, v_2 v_{21} < 0 \end{cases}, \sigma_{gnd} = \begin{cases} v_1, -v_1 v_{21} \geq 0 \\ 0, -v_1 v_{21} < 0 \end{cases}$$

### 3 H<sub>2</sub> Optimization

The value of  $C_{on}$ ,  $C_{off}$  and  $\alpha$  has a great influence on the performance of this suspension. H<sub>2</sub> optimization is used to get the control parameters in different driving conditions.

#### 3.1 Objective Function

Both ride comfort and the handling should be considered in the objective function as Eq. (5)

$$F_{obj} = w_1 p_1 \sqrt{\sum \ddot{x}_2^2/n} + w_2 p_2 \sqrt{\sum K_u(x_1 - x_{in})^2/n} + w_3 p_3 \sqrt{\sum (x_2 - x_1)^2/n} \quad (5)$$

where  $p_1$ ,  $p_2$  and  $p_3$  are the weight coefficients which can be adjusted according to the vehicle requirements. General speaking, luxury cars pay more attention on ride comfort and get a relatively higher value of  $p_1$ , in this paper, there are assigned according to different driving conditions showed as Table 1.  $w_1$ ,  $w_2$  and  $w_3$  are set as 10, 0.01, 1,000, which make the magnitude of the three parts of the objective function in the same level. The first and third parts of the Eq. (5) are used as comfort index and the second part is represented as a handling index.

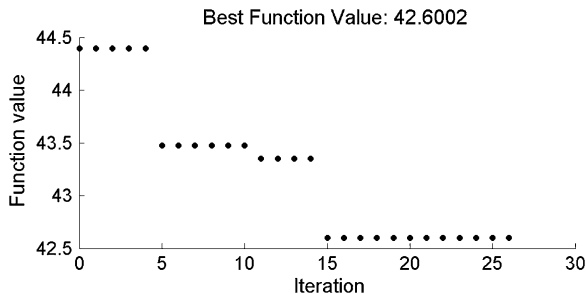
#### 3.2 Constraints

Considering the actual damping system,  $C_{off}$  should be greater than 200 Ns/m,  $C_{on}$  should be less than 6,000 Ns/m, and value of  $\alpha$  should be between 0 and 1.

**Table 1** Value of  $p_1, p_2, p_3$  under different driving condition

Driving condition	$P_1$	$P_2$	$P_3$
Good road && $V < 120$ km/h	0.7	0.2	0.1
Good road && $V \geq 120$ km/h	0.3	0.6	0.1
Average road && $V < 80$ km/h	0.7	0.2	0.1
Average road && $V \geq 80$ km/h	0.3	0.6	0.1
Poor road	0.3	0.1	0.6

**Fig. 3** Best fitness function trend



### 3.3 Optimization

When the vehicle is driven on ISO C class road with speed  $v = 80$  km/h, With the Psearch tool of Matlab, the optimization result is showed in Fig. 3.

The best control parameters is obtained as  $[C_{on} C_{off} \alpha] = [200 \ 6000 \ 0.68]$ . With the same method for different driving conditions, the results are given as Table 2.

From the optimization results, it is easy to find that no matter what driving condition is, the greater value of  $C_{on}$  and the smaller value of  $C_{off}$  yield the better performance. It also can be concluded that when the objective function pay more attention on the ride comfort,  $\alpha$  is set to 0.7, and it will be 0.25 when the objective function pay more attention on the handling, and for the safety,  $\alpha$  equals 0.63.

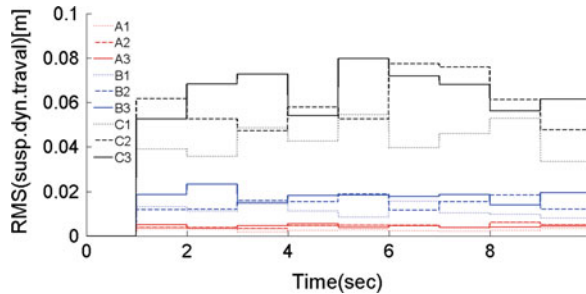
## 4 Adaptive Control Strategy

From the optimization results above, we known that the road class and vehicle speed have a great influence on the vehicle performance. Generally, vehicle speed can be obtained easily. Hence, identification of road unevenness level is necessary.

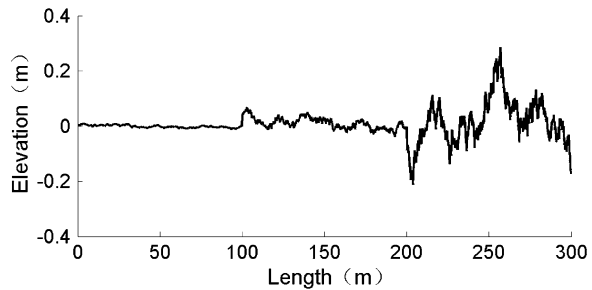
**Table 2** The optimate value of  $C_{on}$ ,  $C_{off}$  and  $\alpha$  under different driving conditions

Driving condition	$C_{off}$ (Ns/m)	$C_{on}$ (Ns/m)	$\alpha$
Good road && $V < 120$ km/h	200	6,000	0.70
Good road && $V \geq 120$ km/h	201.3	5999.4	0.24
Average road && $V < 80$ km/h	200	5999.6	0.69
Average road && $V \geq 80$ km/h	200.4	6,000	0.26
Poor road	200	6,000	0.63

**Fig. 4** RMS (Susp.dyn.travel) under different roads and speeds: A, B, C refers to good road, average road and poor road, 1, 2, 3 refers to high speed, average speed and low speed



**Fig. 5** Road input



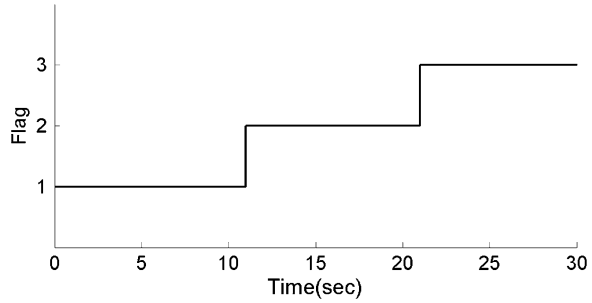
### 4.1 Road Identification

In this paper, the road is classified into three class: good road (corresponding to ISO A~B class), average road (corresponding to ISO C~D class) and poor road (others). Through quantity simulation analysis, the suspension travel performance due to different road inputs and vehicle velocities is showed as Fig. 4.

Figure 4 shows that the three class road, proposed in this paper, can easily identified through the RMS of Suspension dynamic travel. It is a good road when RMS (Susp.dyn.travel) is smaller than 0.01 m, it will be an average road when the RMS (Susp.dyn.travel) is between 0.01 and 0.03 m, and it is a poor road while RMS (Susp.dyn.travel) is greater than 0.03 m.

Figure 5 shows a 300 m long road profile, contains the ISO A, C, E road, is reconstruct via Simulink. The length of each class road 100 m. The vehicle speed on each class E road is 36 km/h. So the vehicle can pass all the three parts in 10 s.

**Fig. 6** Result of road identification



**Table3** Parameters of a quarter car

Parameter	Value
Sprung mass	337
Unsprung mass	55
Tire stiffness	235,000
Suspension stiffness	22,750

Figure 6 shows that method can identify the road class effectively. Where the Flag = 1, 2 and 3 refers to good, average and poor respectively.

### 4.2 Simulation Analysis

The performance of a passive suspension system, a hybrid control system and the proposed adaptive hybrid control system are compared in this section. Their system parameters are shown in Table 3.

The sprung mass acceleration and tire dynamic force are adopted to represent ride comfort and handling respectively. The result of the three suspension system above is given in Table 4 and Table 5. Comparing with a passive suspension and a hybrid suspension, the adaptive hybrid suspension has following benefits: (1) it can improve ride comfort effectively while the vehicle speed is low and has a good performance in road holding, (2) it can improve handling effectively when the vehicle speed is high, (3) When the road surface is poor, it can guarantee safety and improve the ride comfort.

**Table 4** Comparison of RMS (tire dynamic force) under different conditions

Driving condition	Adaptive hybrid	Hybrid	Passive
ISO A class road $v = 80$ km/h	626.9	596.8	539.0
ISO A class road $v = 140$ km/h	763.8	911.8	824.6
ISO C class road $v = 60$ km/h	3010.0	2858.9	2562.1
ISO C class road $v = 90$ km/h	2968.3	3532.7	3253.8
ISO E class road $v = 40$ km/h	6497.2	5777.8	5562.4

**Table 5** Comparison of RMS (Sprung mass vertical acc.) under different driving conditions

Driving condition	Adaptive hybrid	Hybrid	Passive
ISO A class road $v = 80$ km/h	0.467	0.503	0.578
ISO A class road $v = 140$ km/h	0.850	0.727	0.826
ISO C class road $v = 60$ km/h	2.214	2.370	2.705
ISO C class road $v = 90$ km/h	3.457	2.927	3.288
ISO E class road $v = 40$ km/h	5.074	5.368	6.294

## 5 Conclusion

An adaptive Control strategy with hybrid control logic of a quarter-car is proposed in this paper, which makes better compliance between the handling and ride comfort. An algorithm for identifying road unevenness is abstracted via RMS of the suspension travel under variable road input and vehicle speed. The control parameters under different driving conditions are optimized off line via  $H_2$  optimization, and then they are applied on an online control system, which demonstrates that the Adaptive hybrid Control Strategy can improve the ride comfort in “soft” driving mode and handling stability in “sport” driving mode effectively.

**Acknowledgments** Special thanks are due to Young Teachers Innovation Fund Program of Jilin University (450060481170) for supporting authors’ researches.

## References

1. Savaresi SM, Spelta C (2009) A single-sensor control strategy for semi-active suspensions. *IEEE Trans Control Syst Technol* 17(1):143–152
2. Di Milano P, Da Vinci PL (2005) Acceleration-driven- damper (add): an optimal control algorithm for comfort- oriented semi-active suspensions. *ASME* 127:218–229
3. Motta DS, Zampieri DE, Pereira AKA (2000) Optimization of a vehicle suspension using a semi-active damper. *SAE paper* 2000-01-3304
4. Ahmadian M (1997) A hybrid semi-active control for secondary suspension applications. *Proceedings of the sixth ASME symposium on advanced automotive technologies, 1997 ASME international congress and exposition*
5. Blanchard ED (2003) On the control aspects of semi-active suspensions for automobile applications. *Virginia Polytechnic Institute and State University*



# Optibody Project: Optimizing Vehicle Structures for Electric Light Trucks and Vans

Eduardo del Pozo de Dios, Arturo Dávila, Juan José Alba  
and Massimiliano Avalor

**Abstract** The OPTIBODY project is focused on developing new modular structure architectures for electric light trucks and vans (ELTVs) which will improve the passive safety of the vehicle to help reduce the number of fatalities and severe injuries. The new concept will develop a structure composed of a chassis, a cabin that includes improved levels of comfort, protection and ergonomics of the user, a number of add-ons that provide protection in case of impact or rollover and also covering the topic of crash compatibility, including a good amount of the interaction with vulnerable road users. To achieve the objectives, an initial analysis of the ELTVs that are found on today's markets is being made. Selected markets include Europe, U.S.A., Japan and Australia Together with an in-depth review on accidentology of these vehicles and a state-of-the-art research, a basis of requirements will be established. This is the starting point of the project, from which the first results have delimited the study to only L7e category vehicles (light urban delivery vehicles). These requirements will include legal aspects to be covered in the terms of passive safety, homologation, reparability and the integration of structural add-ons for added safety. Special attention is paid also to energy storage solutions, frontal and lateral compatibility, new design guidelines adequate to feasible solutions and new materials and processes. All the work is focused on improving all aspects considering the incoming electric vehicle

---

F2012-E04-026

---

E. del Pozo de Dios (✉) · A. Dávila  
Applus IDIADA, Tarragona, Spain  
e-mail: adavila@idiada.com

J. J. Alba  
Universidad de Zaragoza, Zaragoza, Spain

M. Avalor  
Politecnico di Torino, Turin, Italy

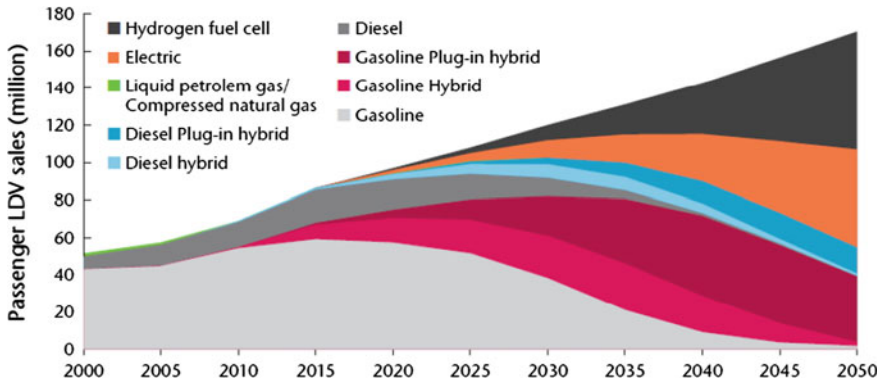
technologies, which can be adequately applied in a very near future. All the work done will be exemplified at the end of the project by the demonstration of the designed add-ons and systems with a pilot demonstrator vehicle. This vehicle will show the developed chassis and cabin concept, complemented by different add-ons that could be utilized throughout different markets. Complimentary, the entire process is to be documented and a specialized publication with the best practices will be made available to the interested public, especially designers and vehicle manufacturers. With this attempt, the OPTIBODY project will provide new and improved safety systems for a segment of vehicles which do not take into account the same requirements as “regular” N1 category vehicles and which have shown to have a large percentage of fatalities on the road, including pedestrian incidents. This study has been limited to a selected type and category of vehicle, the L7e category (in Europe). The characteristics of these vehicles make them quite unique, since their low weight and low power make them apt only for urban driving and are widely used by goods delivery companies, urban services, etc. the requirements for their homologation are lower in terms of structure and safety, including pedestrian protection, hence the objective of this project to improve protection for occupants and vulnerable users. High accident rates with fatalities and severe injuries have been found for these vehicles. The OPTIBODY project is a pioneer enterprise in terms of improving safety in selected vehicle categories which have been traditionally less developed than regular cars or heavy goods vehicles. This approach will lead to an improvement in safety for all road users while interacting with these urban vehicles, which have less strict requirements than the rest. It is important to adequately design a chassis and body for the new upcoming electric technologies which now pose different risks in various aspects, such as energy storage, dynamics and accident behaviour. In general, the approach taken during this project will generate new and innovative ideas on the way that vehicles are designed and built with the use of electrical energy for their power. The risks of electrical mobility are being tackled as we speak, and the technological solutions that will be developed will improve the safety on our roads.

**Keywords** Optimization • Electric light trucks • Components • Structure • Add-ons

## 1 The Optibody Project

The evolution of Electric Vehicles in the last years has been so important that almost every car manufacturer has presented its own prototype and some of them even have fully functional vehicles on the roads.

Last trends in electric vehicles design show the increasing importance of dedicated vehicles instead of the classic general purpose concept that has massively used in the past. Manufacturers are developing specific vehicles for urban



**Fig. 1** Prediction of annual light duty vehicle sales, according to its technology (International Energy Agency)

logistics, urban mobility, etc. As the current status of the technology used in the electric vehicles impose very light vehicles to optimize energy consumption, most of the electric vehicles that we are and will be on the roads in the near future will still run in urban areas in consequence at low-to-medium speed in short range displacements.

For all these reasons, the OPTIBODY project is focused in electric light trucks and vans (ELTV) that are worldwide homologated as N<sub>1</sub> and N<sub>2</sub> vehicles and, in Europe, also include the L7e category (Directive 2002/24CE) (Fig. 1).

Most of the existing ELTVs adopt the powertrain lay-out used in classic thermal engine vehicles, but some companies are starting to introduce new solutions in the design of this type of vehicles. This new designs provides a considerable amount of space in the former location of the engine where is no longer necessary to accommodate some awkwardly-shaped mechanical components. These changes allow the engineers to concentrate on performance and safety when the new frontal part of the vehicle is designed. Some examples of these changes include:

- eliminating the entire engine block,
- reducing the weight,
- totally flat floor design,
- chassis design focused on passengers' safety and frontal design focused in vulnerable road users' safety.

OPTIBODY has been defined as a new structural concept of ELTVs composed of a chassis, a cabin and a number of specific add-ons. The chassis will act as a key structural supporting element for any other components in the vehicle. The cabin will improve current levels of EVs' comfort, occupant protection and ergonomics. Finally, a number of add-ons will bring specific self-protection in case of front, rear and side impacts, as well as in case of rollover. Additionally, these add-ons

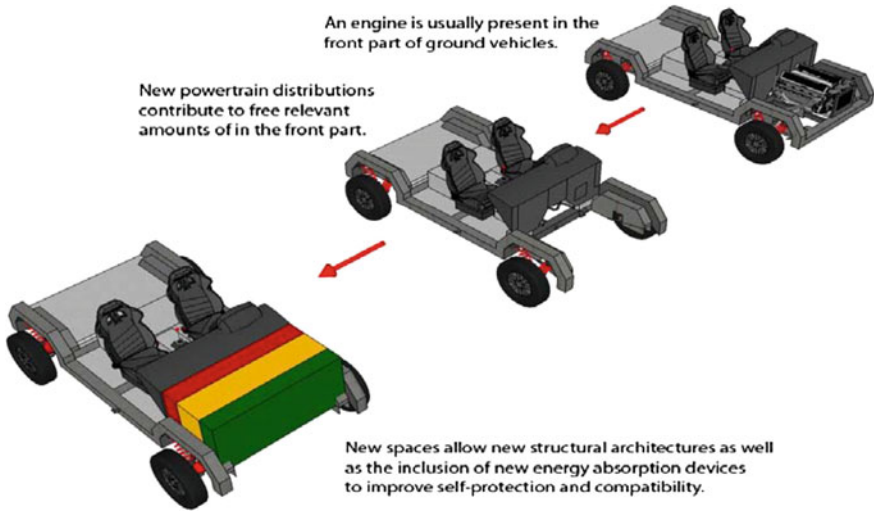
will also provide partner protection in case of interaction with other vehicles (crash compatibility) or vulnerable users (pedestrian, cyclists and motorcyclists).

The OPTIBODY concept has two kinds of objectives. On one hand the improvement of passive safety for vehicles under the category L7e and, on the other hand, theoretical concepts must be shaped as a pilot demonstrator. The OPTIBODY concept will be achieved if the following objectives are reached:

1. **Enhance crash compatibility for ELTVs (L7e).** The free room available after removing the thermal engine provides the opportunity to introduce new load paths and energy absorbing add-ons. This type of vehicles has very high fatality ratios when crashing with other vehicle categories due to their typically light design and less restrictive regulations than the existing for passenger cars.
2. **Enhance passive safety.** Following the analysis of previous projects (FP6-PLT-506503 APROSYS), the introduction of specific add-ons will ensure the enhancement of pedestrians, cyclists and infrastructure protection. OPTIBODY will implement these add-ons in a much less restrictive concept of modular vehicle than the classic vehicle concept provided with thermal engines.
3. **Optimized reparability in small crashes.** Reparability will be introduced as a key factor in the design of the different add-ons in order to optimize the damaged parts reparation or substitution cost.
4. **Optimized ergonomics and space distribution for passengers and main components accessibility.** The whole architecture will be redesigned and will give more flexibility distributing the different components. It will allow introducing ergonomics and accessibility as key factors in the design of the vehicle.
5. **Better maintainability.** Due to the optimized reparability and component accessibility.
6. **Establishments of the requirements for impact-safe ELTV's.** Technical requirements for an "OPTIBODY" quality marking will be determined.
7. **Applicability of the results to other categories.** OPTIBODY could be exported to other vehicles categories such as N<sub>1</sub>, N<sub>2</sub>, M<sub>1</sub>, M<sub>2</sub>, etc.

Finally, OPTIBODY will aim to improve and provide innovative solutions for three main areas:

1. **Pedestrian protection.** In order to improve this area, the extra space available will be used to incorporate new optimized front parts.
2. **Crashworthiness and compatibility.** In the automotive industry, for conventional vehicles as well as for electric vehicles, "crashworthiness" is a measure of the vehicle's structural ability to plastically deform and still maintain a sufficient survival space for its occupants in crashes involving reasonable deceleration load. "Compatibility" is a term that refers to the "quality" of structural interaction in collisions, and this "quality" depends on several factors that are common to all kind of vehicles and means the good performance of traffic participants among each other in the event of an accident. Self-protection



**Fig. 2** Evolution of vehicle fronts (from classic cars to EVs) and the resulting possibility to use the front for the installation of new safety components METHODS

and partner protection can be improved by developing optimized crash energy absorbing add-ons.

3. **Reparability.** The main idea is to provide new basis for fully modular concepts like OPTIBODY. As a modular concept, OPTIBODY will take an extra advantage of reduction of architectural constraints and will make reparability and maintenance procedures easier and more cost efficient (Fig. 2).

The OPTIBODY project is structure as is shown in Fig. 3.

## 2 State of the Project

In this moment the OPTIBODY project is still on-going. The WP1 has already finished and the accident analysis research, the review of the legislation applicable to L7e vehicles and the reparability and damageability study has been performed. More information about the rest of the topics can be found in the projects deliverables that will be available to the public in the project website: <http://optibody.unizar.es/>

The first phase of the project consisted in a review of the state of the art of ELTVs in different markets. The main parts of the review were:

- Regulations in different geographical areas (Europe, U. S., Canada, Japan and Australia).
- Accident analysis using different databases (worldwide, European and national databases).

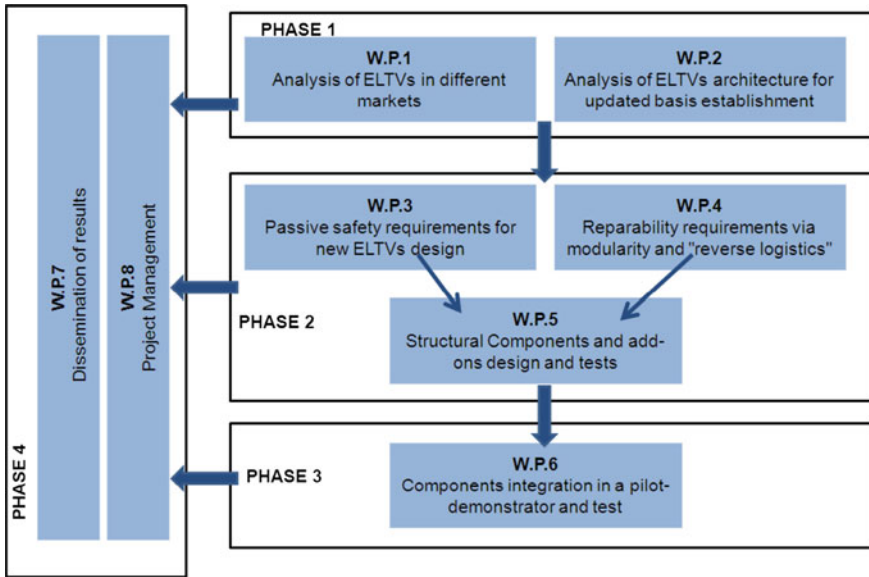


Fig. 3 Project flow

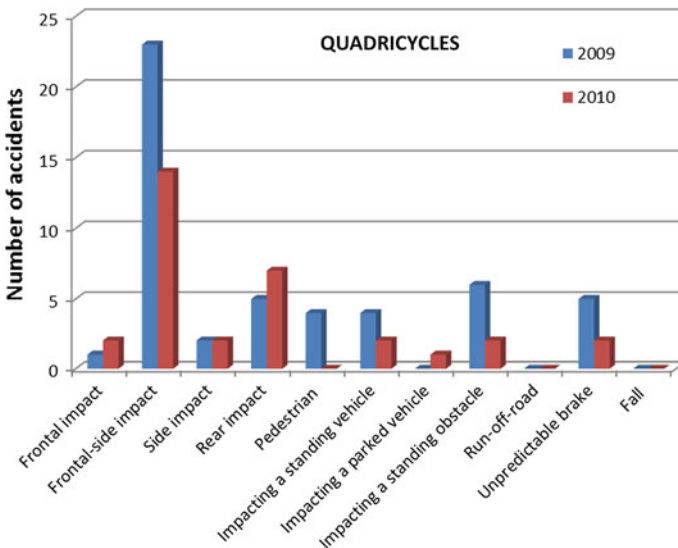


Fig.. 4 Total number quadricycles accidents per type of crash in the Piemonte region

The main objective of the regulations review was to establish the technical requirements to be fulfilled by an L7e vehicle (European category) in order to be used as the baseline for the design of the OPTIBODY. The main objective of the accident analysis was to determine the main issues related to the injuries occurring

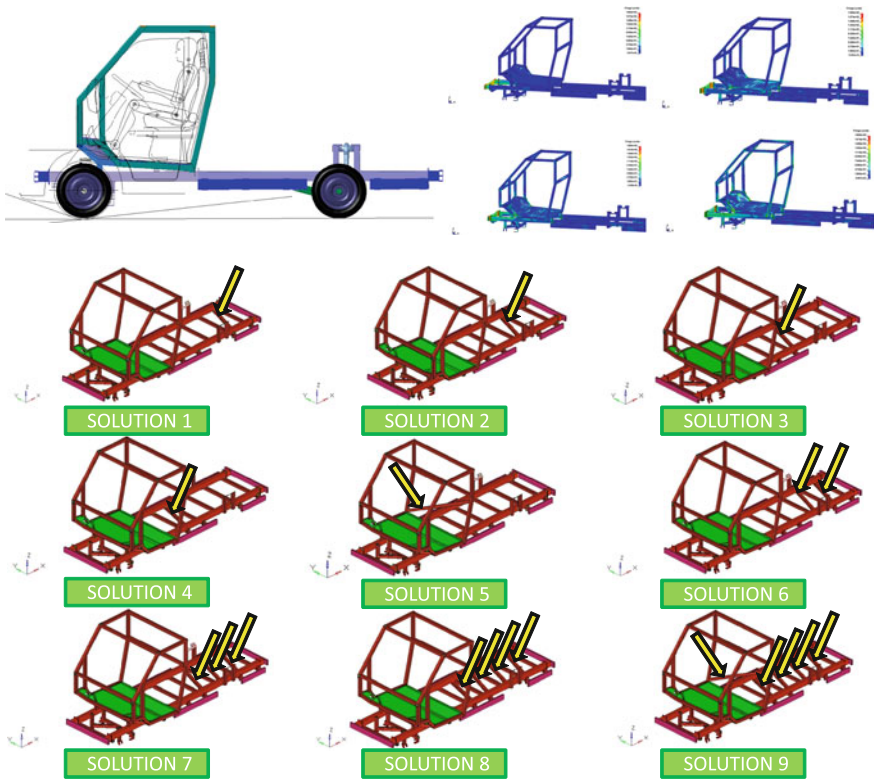


Fig. 5 Different structure solutions virtually tested

in accidents involving L7e vehicles to prioritize the safety design of the vehicle in those areas [1–4] (Fig. 4).

The second phase of the project is the design of the vehicle. At this moment, the OPTIBODY project is focused in the design of the structure of the vehicle, the add-ons, the energy storage (which battery pack should be used and where it should be located) and the powertrain. Different battery configurations and locations are been considered to optimize weight distribution and safety.

The design of the structure includes selecting the materials and also establishing the crash targets that the structure must fulfil based on the regulatory and accident analysis. Different structural architectures are being considered as well as different materials (High strength steel, aluminium, composites, etc.). For the materials selection, aspects like the Greenhouse Gas (GHG) Emissions for production are also considered in addition to the classic selection criteria as weight, strength, etc. Nowadays, the different structures considered are being tested virtually to optimize their dynamic and crash behaviour, introducing in the design the reparability and maintainability concepts. The same approach in terms of materials and structural behaviour is being considered for the add-ons (Fig. 5).

### 3 Conclusions

Most of the EV use the classic powertrain lay-out used in thermal engine vehicles. The OPTIBODY project has been defined as a new structural concept of ELTVs composed of a chassis (the key structural supporting element), a cabin and a number of specific add-ons, which will bring specific self and partner protection in case of front, rear, side impacts and rollover.

In this stage of the project, the requirements and regulations that apply to L7e vehicles in the four major economic areas (United States of America and Canada, Europe, Japan, and Australia) were studied. This work was done to establish the baseline that will be used in the OPTIBODY design. In general, the construction requirements for L7e vehicles in Europe and Low Speed Vehicles in the US and Canada are very low and no structural tests are needed.

The accident analysis highlighted that especial effort need to be done to reduce the number of pedestrian accidents in both quadricycle and truck cases. For this reason, especial attention is being paid to the front-end design and especial add-ons are being design for pedestrian protection.

**Acknowledgments** The authors would like to acknowledge the European Commission that co-funded this project through the FP7 program. The authors wish to acknowledge the Partners of the OPTIBODY consortium for their contributions. The consortium comprises: University of Zaragoza, Politecnico di Torino, PIMOT, IDIADA Automotive Technology, Centro Zaragoza, AMZ, Italdesign - Giugiaro, BELLA, SSAB and Mondragón Automoción.

### References

1. Gabler HC, Hollowell WT (1998) The aggressivity of light trucks and vans in traffic crashes. SAE International, paper 980908
2. Gabler HC, Fitzharris M, Scully J, Fildes BN, Digges K, Sparke L (2005) Far side impact injury risk for belted occupants in australia and the United States. In: Proceedings of the nineteenth international conference on enhanced safety of vehicles, paper no. 05-0420, Washington, DC
3. Scarboro M, Rudd R, Sochor M (2007) Near-side occupants in low delta-V side-impact crashes: analysis of injury and vehicle damage patterns. Enhanced safety vehicles 07-0225. National Highway Traffic Safety Administration, Lyon, France
4. NHTSA Traffic Safety Facts (2007) A compilation of motor vehicle crash data from the fatality analysis reporting system and the general estimates system



# Linear Quadratic Gaussian Optimal Control Strategy for Four-Wheel Steering Vehicle

Yan Chen, Wenqiang Chen, Xingmin Wei and Fuquan Zhao

**Abstract** To utilize the advantages of four-wheel steering (4WS) technology in improving the vehicle handling, an adaptive gain schedule (linear Quadratic Gaussian, LQG) control strategy based on vehicle speed estimation is proposed. In this control strategy, the vehicle speed is selected as the gain schedule variable. The controller parameter can adaptively vary with operation points of vehicle speed so that the optimal control can be achieved at each operation point. The wheels steering response is simulated when the vehicle speed changes. The simulation results show that the proposed control strategy can achieve the estimation of the vehicle speed accurately. Compared with the conventional control strategy, the transient response overshoot of the proposed steering controller is smaller and the stability time is shorter, thereby improving the handing of vehicle steering.

**Keywords** Four-wheel steering · Vehicle speed estimation · Extended Kalman filter · Linear quadratic Gaussian optimal control · Adaptive gain schedule

## 1 Introduction

With the development of science and technology, the automotive performance will be required more highly. The handling and stability of vehicle become an important aspect of research contemporary. The steering system will have a direct

---

F2012-E04-028

---

Y. Chen (✉) · W. Chen · X. Wei · F. Zhao  
Zhejiang Geely Automobile Research Institute Co., Ltd, Linhai, China  
e-mail: chenyan1@rd.geely.com

impact on vehicle portability, handling and stability, even the driver's work strength and work efficiency. Compared with the front wheel steering (FWS), the 4WS has better tracking capability as well as handling and stability.

In recent years, there are some researches on the control of rear wheel for 4WS vehicle by using 4WS technology [1–3]. However, the obvious disadvantage of those ways is that, when attached to the rear wheel angle, the yaw velocity gain changes greatly at high vehicle speed. Therefore, the drivers lost their steering feels, which increases the difficulties of steering and results in fatigue for drivers.

In this paper, by taking the handling characteristics of the two-degree-of-freedom vehicle as the control objectives, constructing a reasonable model, selecting an appropriate objective function, the gain-schedule adaptive LQG control strategy based on vehicle speed estimation is proposed. According to the vehicle speeds estimated by Extended Kalman Filter (EKF), the control strategy determines series of steady-state operating points. Then imply the LQG optimal control near the steady-state operating points, and make the simulation when the vehicle speed changes.

## 2 System Dynamic Model

The vehicle can move along three directions: longitudinal, lateral and vertical, and also can rotate around the three directions, which are called roll, pitch and yaw. The motion of vehicle is shown in Fig. 1.

When establishing the vehicle dynamics equations according to Newtonian mechanics, most researchers usually consider only two-degree-of-freedom model to analyse the basic characteristics of vehicle handling and stability. Therefore 4WS vehicle can be reduced to two-wheeled vehicle, which only has two motions: cornering and yaw. In the situation of normal speed range and small steering angle, this model simplified can accurately represent the actual physical process of vehicle turning.

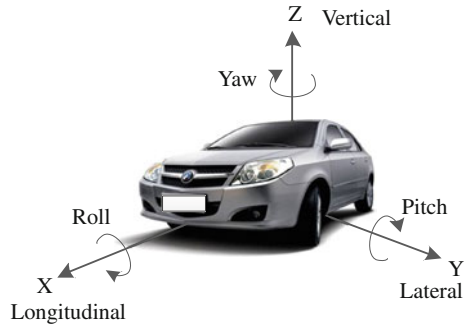
Under some assumptions, the two-degree-of-freedom 4WS vehicle model is shown in Fig. 2 [4]:

In Fig. 2:  $\beta$  is the centroid sideslip angle;  $\beta_f$  and  $\beta_r$  are respectively the front and rear wheel sideslip angle;  $r$  is the vehicle yaw angle velocity;  $u_y$  is the centroid side speed;  $u_x$  is the centroid forward speed;  $u_f$  and  $u_r$  are respectively the front and rear axis midpoint speed;  $\xi_f$  is the angle between  $u_f$  and X-axis, and  $\xi_r$  is the angle between  $u_r$  and X-axis;  $a$  and  $b$  are respectively the distances from vehicle centroid to the front and rear axle;  $\delta_f$  and  $\delta_r$  are respectively the front and rear wheel steering angle;  $F_f$  and  $F_r$  are respectively the lateral force on the front and rear wheel.

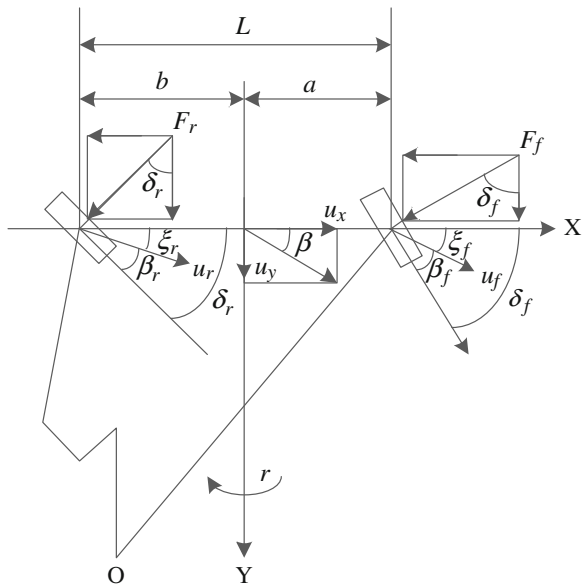
In the case of the small steering angle, the sideslip angle  $\beta \approx u_y/u_x$ . Figure 2 shows:

$$\xi_f = \frac{v_y + ar}{u_x} = \beta + \frac{ar}{u_x} \quad (1)$$

**Fig. 1** Motion of vehicle



**Fig. 2** Two-degree-of-freedom 4WS vehicle model



Front wheel sideslip angle  $\beta_f$  is:

$$\beta_f = -(\delta_f - \xi_f) = \xi_f - \delta_f = \beta + \frac{ar}{u_x} - \delta_f \tag{2}$$

Similarly, for the rear wheels there is:

$$\xi_r = \frac{u_y - br}{u_x} = \beta - \frac{br}{u_x} \tag{3}$$

Rear wheel sideslip angle  $\beta_r$  is:

$$\beta_r = -(\delta_r - \xi_r) = \xi_r - \delta_r = \beta - \frac{br}{u_x} - \delta_r \tag{4}$$

Under normal circumstances, the  $\delta_f$  and  $\delta_r$  is very small, so  $\cos \delta_f = 1$  and  $\cos \delta_r = 1$ . The force on the Y-axis is as follows:  $F_f \cos \delta_f = F_f$  and  $F_r \cos \delta_r = F_r$  [5].

Therefore the total the force and torque is such that:

$$\begin{cases} \sum F = F_f \cos \delta_f + F_r \cos \delta_r = F_f + F_r = k_f \beta_f + k_r \beta_r \\ \sum M = aF_f - bF_r = ak_f \beta_f - bk_r \beta_r \end{cases} \tag{5}$$

where,  $k_f$  and  $k_r$  are respectively the front and rear wheel equivalent sideslip stiffness.

Substitution of Eqs. (2) and (4) into (5), then what can be obtained is as follow:

$$\begin{cases} \sum F = (k_f + k_r)\beta + \frac{1}{u_x}(ak_f - bk_r)r - k_f \delta_f - k_r \delta_r \\ \sum M = (ak_f - bk_r)\beta + \frac{1}{u_x}(a^2k_f - b^2k_r)r - ak_f \delta_f + bk_r \delta_r \end{cases} \tag{6}$$

Because  $\beta \approx u_y/u_x$ , when the vehicle turns as a constant speed there is:

$$\dot{\beta} = \frac{\dot{u}_y}{u_x} \tag{7}$$

Substitution of Eq. (7) into Eq. (6), then dynamic differential equations can be drawn from the 4WS vehicle with two-degree-of-freedom as follows:

$$\begin{cases} m u_x (\dot{\beta} + r) = (k_f + k_r)\beta + \frac{1}{u_x}(ak_f - bk_r)r - k_f \delta_f - k_r \delta_r \\ I_z \dot{r} = (ak_f - bk_r)\beta + \frac{1}{u_x}(a^2k_f - b^2k_r)r - ak_f \delta_f + bk_r \delta_r \end{cases} \tag{8}$$

where  $m$  is the vehicle mass,  $I_z$  is the inertia moment around the vehicle centroid.

In a real world environment, as there will inevitably be measurement noise in the process of measurement and transmission, the system model transformed from Eq. (8) with the system noise and measurement noise can be written as:

$$\begin{cases} \dot{x}(t) = Ax(t) + Bu(t) + G\zeta(t) \\ y(t) = Cx(t) + \varepsilon(t) \end{cases} \tag{9}$$

where:  $x = [\beta \ r]^T$  is state variable;  $u = [\delta_f \ \delta_r]^T$  is control variable;  $y = x =$

$$[\beta \ r]^T \text{ is output variable; } A = \begin{bmatrix} \frac{k_f+k_r}{mu_x} & \frac{ak_f-bk_r}{mu_x^2} - 1 \\ \frac{ak_f-bk_r}{I_z} & \frac{a^2k_f+b^2k_r}{u_x I_z} \end{bmatrix}; \quad B = \begin{bmatrix} -\frac{k_f}{mu_x} & -\frac{k_r}{mu_x} \\ -\frac{ak_f}{I_z} & \frac{bk_r}{I_z} \end{bmatrix};$$

$C = \begin{bmatrix} 1 & 0 \\ 0 & 1 \end{bmatrix}$ ;  $G = \begin{bmatrix} 1 & 0 \\ 0 & 1 \end{bmatrix}$ ;  $\zeta(t)$  is the system random noise, and  $\varepsilon(t)$  is the measurement noise. Both of  $\zeta(t)$  and  $\varepsilon(t)$  are zero-mean white noise, and they are unrelated, that is [6]:

$$\begin{cases} E\{\zeta(t)\} = 0, t \geq t_0 \\ E\{\varepsilon(t)\} = 0, t \geq t_0 \\ E\{\zeta(t)\zeta^T(t)\} = Q_0\delta(t - \tau), \tau \geq t_0 \\ E\{\zeta(t)\varepsilon^T(t)\} = 0, \tau \geq t_0 \\ E\{\varepsilon(t)\varepsilon^T(t)\} = R_0\delta(t - \tau), \tau \geq t_0 \end{cases} \quad (10)$$

where:  $Q_0$  is the system noise variance;  $R_0$  is the measurement noise variance.

What should be noted is that: the vehicle speed is not always constant when actual driving, so the steady-state operating point of the 4WS system will change when the speed  $u_x$  changes. The concrete embodiment is the change of the system matrix  $A$  and the control matrix  $B$  in Eq. (9). So the system of (9) is a system of variable parameters. To solve this problem, the real parameters estimated by EKF are used to design the optimal controller whose parameters change adaptively when the vehicle speed changes.

### 3 Optimal Controller Design

#### 3.1 Control Principle

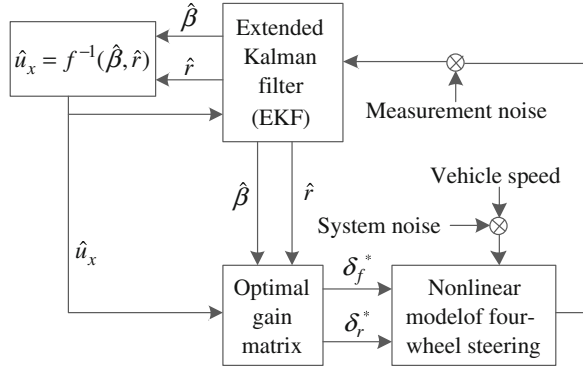
Learning from the modern state feedback control theory, we linearize the 4WS system near the steady-state operating point. Considering the system noise and measurement noise, we apply LQG optimal control to achieve the purposes of coordinating and optimizing the multi-variable.

When the vehicle speed changes, the steady-state operating point of the 4WS system will change. At this time if we continue to use the model linearized with the original operating point, this will inevitably result in inaccurate model and affect the control effect. To solve this problem, the method of speed estimation based on EKF is proposed. Using the speed estimated as the gain-schedule variable of controller, we can make the parameters of controller change adaptively following the change of the 4WS system operating point. The control principle is shown in Fig. 3.

#### 3.2 Extended Kalman Filter (EKF) Design

Kalman filter which is applied for linear system state estimation is an optimal autoregressive filter. Its advantage is that it can accurately estimate the state of linear system which includes system noise and measurement noise, and its general form can be expressed as [7]:

**Fig. 3** Schematic diagram of dynamic optimal control



$$\begin{cases} \dot{x} = Ax + Bu + L(y - \hat{y}) \\ \dot{y} = Cx \end{cases} \tag{11}$$

The filter gain  $L$  can be obtained through:

$$L = P_0 C^T R_0^{-1} \tag{12}$$

where  $P_0$  is exported from the following Riccati equation:

$$AP_0 + P_0 A^T + GQ_0 G^T - P_0 C^T R_0^{-1} C P_0 = 0 \tag{13}$$

The gain matrix  $L$  of the filter has relationship with system matrix  $A$ , the perturbation matrix  $G$ , the output matrix  $C$ , and the covariance matrices  $Q_0$  and  $R_0$  of system noise  $\zeta(t)$  and measurement noise  $\varepsilon(t)$ . For the 4WS system, with the operating point changes, the matrix  $A$  and  $B$  will change. If we adopt the constant gain matrix  $L$ , it will definitely affect the estimated results.

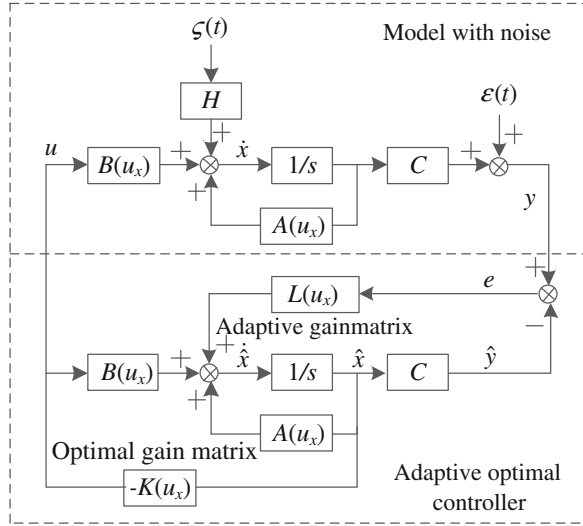
EKF applied for nonlinear system is the extended application of Kalman filtering algorithm. The EKF gain can be adjusted automatically when the model changes, so the EKF is an adaptive system. The EKF structure diagram is shown in Fig. 4.

In Fig. 4, the adaptive gain  $L$  will change when the system matrix  $A$  and control matrix  $B$  change. Therefore, the model can accurately estimate the system status on different operating points.

### 3.3 Speed Estimation

We can get the estimated values of centroid sideslip angle and yaw angle velocity through EKF. Then combined with Eq. (9), the vehicle speed can be solved [8]. The vehicle speed determines the steady-state operating point of the 4WS system. The EKF can achieve linearization of local model near the steady-state operating point, which can be designed for optimal controller.

**Fig. 4** System block diagram of EKF



### 3.4 Optimal Control Gain Matrix Design

As shown in Fig. 4, we design the optimal controller based on the speed estimation. Choose the extended quadratic optimal controller with cross-product terms in the objective function, so the system performance indicator is [9]:

$$F = \frac{1}{2} \int_0^{\infty} (x^T Q x + u^T R u + x^T N u + u^T N^T x) dt \quad (14)$$

where: the terminal time is infinite,  $Q$  is a  $2 \times 2$  semi-positive definite real symmetric constant matrix,  $R$  is a  $2 \times 2$  positive definite symmetric constant matrix. Therefore, the optimal gain matrix is:

$$K = R^{-1}(B^T P + N) \quad (15)$$

The unique optimal control law is:

$$u^*(t) = -Kx(t) \quad (16)$$

where:  $P$  is a positive definite constant matrix, which is the unique solution of Riccati algebraic equation:

$$A^T P + P A - (P B + N) R^{-1} (P B + N)^T + Q = 0 \quad (17)$$

It should be noted that the system matrix  $A$ , control matrix  $B$  and optimal gain matrix  $K$  in Eq. (16) will change when the schedule variable  $u_x$  changes, so as to adapt the change of steady-state operating point for the 4WS system.

## 4 Simulation and Analyse

To compare and analyze the control effect, we do the simulation of the FWS vehicle and the traditional fixed-proportion 4WS vehicle as well as the optimal control 4WS vehicle which have the same structural parameters. The ratio of the fixed-proportion 4WS is defined as  $K_b$  [10]:

$$K_b = \frac{\delta_r}{\delta_f} = \frac{-b - mau_x^2/[k_r(a+b)]}{a - mbu_x^2/[k_f(a+b)]} \quad (18)$$

The parameters of simulation model are as follows [11]:  $m = 1707$  kg,  $a = 1.014$  m,  $b = 1.676$  m,  $I_z = 2,741.9$  kg m<sup>2</sup>,  $k_f = 68,909$  N/rad,  $k_r = 5,140$  N/rad, Assuming the system noise variance as  $Q_0 = 0.2$ , measurement noise variance  $R_0 = 0.005$ ,  $Q = \begin{bmatrix} 1 & 0 \\ 0 & 0.1 \end{bmatrix}$ ,  $R = \begin{bmatrix} 0.1 & 0 \\ 0 & 0.01 \end{bmatrix}$ ,  $N = \begin{bmatrix} 0.4 & 0 \\ 0 & 0 \end{bmatrix}$ .

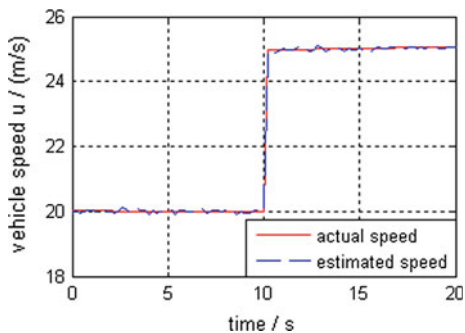
Assume that the actual vehicle speed changes from 20 to 25 m/s at 10th second, which is represented by the solid line in Fig. 5. The estimated vehicle speed follows the dotted line shown in Fig. 5 by using the EKF in MATLAB environment. As shown in Fig. 5, the actual vehicle speed and the estimated vehicle speed overlap almost. Therefore, the estimated vehicle speed can represent the actual vehicle speed, which can be an effective control reference value. Figure 6 shows the vehicle speed estimation error calculated by using the datum in Fig. 5, which is less 0.5 % than the actual speed. As shown in Fig. 6 the estimated vehicle speed is very close to the actual speed, which achieves a good soft measurement for vehicle speed.

Figure 7 shows the centroid sideslip angle for the FWS vehicle and the traditional fixed-proportion 4WS vehicle (proportion) and the dynamic optimal control based on LQG vehicle (optimized) under the vehicle speed shown in Fig. 5. As shown in Fig. 7, compared with the FWS and proportion 4WS, the centroid sideslip angle of optimized 4WS is almost zero whether it is under 20 or 25 m/s. And the adjustment time near 10th second is very short, which reduces the sideslip and improve the safety and handing stability when the driver changes lane, overtakes or steers when speed changes.

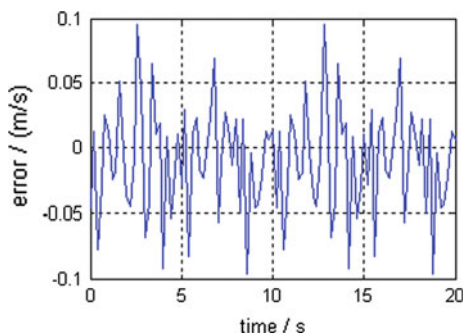
Figure 8 shows the yaw angle velocity for the FWS vehicle and the traditional fixed-proportion 4WS vehicle (proportion) and the dynamic optimal control based on LQG vehicle (optimized) under the vehicle speed shown in Fig. 5. As shown in Fig. 8, the yaw angle velocity for the proportion 4WS vehicle is very low whether it is under 20 or 25 m/s, of which results are that the driver has to steer more when turning the same corner. That means the driver could not keep the original steering feel, adding to the burden for the driver. The yaw angle velocity for the optimized 4WS vehicle and the FWS are basically the same all the time, of which results are that driver can well keep the original steering feel. That means the optimized 4WS can reduce the driver's fatigue and the difficulty of manipulation the same as FWS.



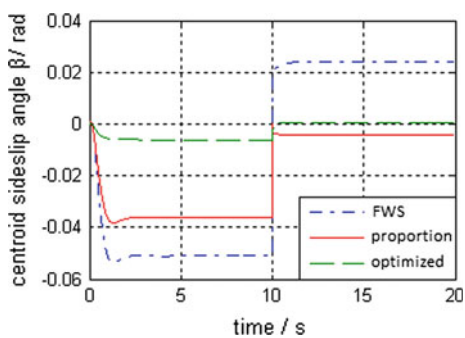
**Fig. 5** Estimated value of vehicle speed



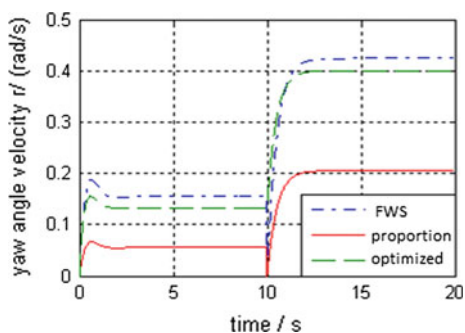
**Fig. 6** Estimation error



**Fig. 7** Centroid sideslip angle



**Fig. 8** Yaw angle velocity



But the optimized 4WS overshoot near 10th second is significantly less than the FWS vehicle and the proportion 4WS vehicle.

## 5 Conclusions

The LQG control strategy based on vehicle speed estimation is proposed for 4WS vehicle using optimal control theory. The LQG control strategy can achieve the optimal control when the vehicle speed changes, and reduce the overshoot and adjustment time compared with the FWS vehicle and the traditional fixed-proportion 4WS vehicle.

Simulation results show that, the LQG control strategy can nearly turn the centroid sideslip angle to zero, and also ensure the yaw angle velocity following the FWS. Therefore, the LQG control strategy reduces the sideslip and improves driving safety and vehicle handling, while it ensures the driver to keep the original steering feel, and reduces the driver's fatigue and the difficulty of manipulation.

## References

1. Kim D, Kim K, Lee W et al (2003) Development of mando ESP (electronic stability program). SAE paper 2003-01-0101
2. Ding H, Guo K, Chen H (2010) LQR method for vehicle yaw moment decision in vehicle stability control. *J Jilin Univ (Eng Technol Ed)* 40(3):597–601
3. Hui W, Fan Y (2006) Simulation study on handling and stability performance of four-wheel steering vehicle in matlab software environment. *J Syst Simul* 18(9):2620–2622
4. Zhisheng Y (2009) Vehicle theory. Mechanical Industry Press, Beijing (in Chinese)
5. Feng D, Lang W, Jianyou Z (2008) Optimization control of four-wheel steering vehicle based on state feedback. *J Chang Univ (Nat Sci Ed)* 28(4):91–94
6. Fan X, Bai Y, LÜ Y, Xu D (2010) Linear quadratic gaussian optimal control strategy for large wind turbine. *Proc CSEE* 30(20):100–105
7. Chengyuan W, Jiakuan X, Junyou Y et al (2006) Motor modern control technology. China Machine Press, Beijing (in Chinese)
8. Muhando EB, Senjyu T, Kinjo H et al (2008) Augmented LQG controller for enhancement of online dynamic performance for WTG system. *Renew Energy* 33:1942–1952
9. Bai Y, Fan X, LÜ Y, Xu D, Yang X (2010) A study on dynamic optimal control strategy for large-scale wind power generation system. *Automation Electr Sys* 34(12):90–94
10. Pengmin LÜ, Limei HE, Jinmin Y (2007) Optimization of vehicle suspension parameters based on comfort and tyre dynamic load. *China J Highw Transp* 20(1):112–117
11. Hiraoka T, Nishihara O, Kumamoto H (2009) Automatic path-tracking controller of a four-wheel steering vehicle. *Veh Sys Dyn* 47(10):1205–1227

# Design and Validation of a Race Car with Respect to Aerodynamics and Body Styling

Abdul Vaseem Akram, M. Ajay Kumar, K.C. Vora and  
Mohammad Rafiq

**Abstract** An open wheeled open cockpit race car with 800 CC MPFI engine was developed, validated and run at 105 kmph. The key focus was to build a car with superior aerodynamic characteristics especially in terms of drag. This work discusses in detail about the design and simulation of car using CFD package followed by Wind Tunnel testing. The design of race car starts with design of seat according to the ergonomics of the driver followed by the space frame. Based on the space frame designed the body panels are sketched and CAD model developed. The CAD model is imported in CFD package for virtual testing and validated through wind tunnel results. For this 1:3 scale model was manufactured using Rapid Prototyping.

## 1 Introduction

Aerodynamics is one of the most important aspects while dealing with the design of race car. Maximum downforce or negative lift plays an important role in maintaining traction at high speeds. Drag has its effect at low speeds which is important especially in the case of FSAE type of events where the car can run at

---

F2012-E04-029

---

A. V. Akram (✉)  
Mahindra Two Wheelers, Pune, India  
e-mail: vaseem6.shine@gmail.com

M. Ajay Kumar  
Varroc Polymers Pvt. Ltd, Aurangabad, India

K.C.Vora · M. Rafiq  
ARAI Academy, the Automotive Research Association of India, Pune, India

maximum speed of 105 kmph and an average speed of 60 kmph. This paper discusses about the drag force and its effect on fuel economy for FSAE type race car. The car is designed aerodynamically best in terms of drag experienced, using CFD package FLUENT and validated through wind tunnel testing carried out with a 1:3 scale model.

## **2 Competitive Benchmarking**

The design process started with competitive benchmarking. Their design specifications were analysed and it helped in determining some of the critical and key parameters such as frontal area, wheel base, wheel track and ergonomics of driver.

## **3 Identifying Constraints**

The outcomes of the previous step led to identifying constraints such as space availability in the cockpit, manufacturing limitations and tolerances thereby setting starting points for the design.

## **4 Design Methodology**

### ***4.1 Seat Design***

Anthropometry data of the three different drivers were obtained with the help of lab facility available at ARAI, Pune. The three positions checked were arm reach, seated position and standard position (Figs. 1 and 2).

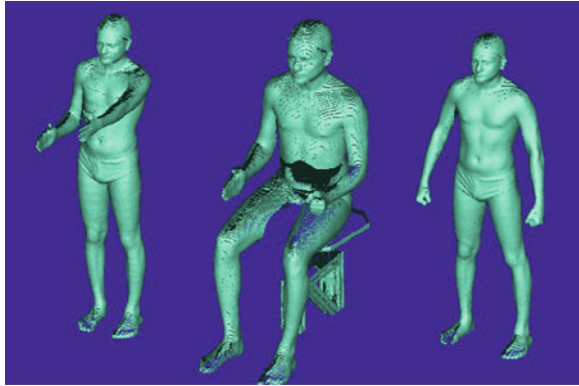
Based on the values obtained of the three driver's proportions the seat was designed and then checked with the 95th percentile dimensions. One of the main considerations in seat design was back rest angle of the seat that was dependent on driver's comfort with respect to the line joining the top surfaces of both the Roll hoops to clear the top most surface of the driver's helmet by 2 inches (Fig. 3).

Hence based on the comfortable posture of the driver the seat was designed.

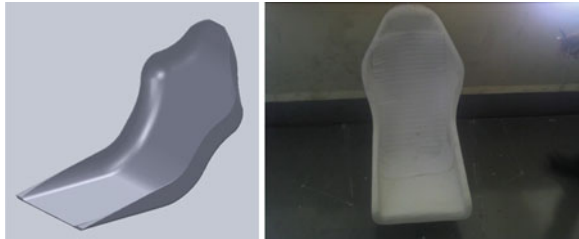
### ***4.2 Roll Cage Design***

Roll cage design was started by making the driver seated in driving position and imagining cockpit room around him. The main aim was to ensure compactness for reducing the frontal area (Fig. 4).

**Fig. 1** Arm reach, seated and standard position (*From Left*)



**Fig. 2** CAD model (*Left*) and actual manufactured seat (*Right*)



The side pods were integrated inside the Roll cage structure to stiffen the structure during torsion loading conditions. Triangulations are made wherever necessary to improve the analysis results during various loading conditions that include torsion, longitudinal/lateral accelerations and static bending etc. (Fig. 5).

### **4.3 Body Design**

Once the Roll cage was ready all the subsystems were modeled and assembled to the Roll cage. This included the Impact attenuator, engine, wheels and tyres, seat and driver. The body panels were sketched and incorporated in the model. Hence the model was designed aesthetically looking good (Fig. 6).

### **4.4 Rapid Prototyping**

The scale model for wind tunnel testing was manufactured using Fused Deposition Modeling by STRATASYS. This technique of rapid prototyping helped the project completion on time as it was less time consuming than the conventional clay modeling or any CNC operated product. This also helped in learning the concepts of Rapid Prototyping (Fig. 7).

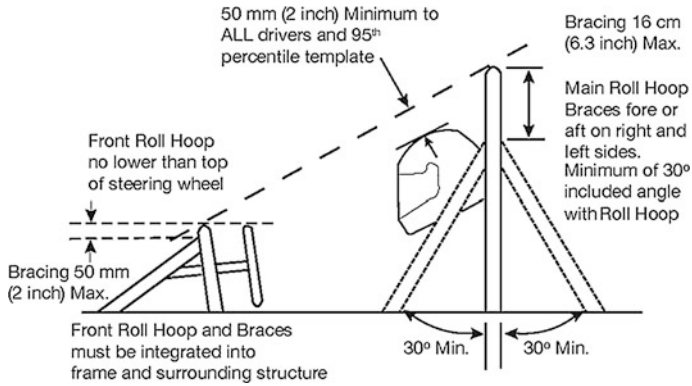
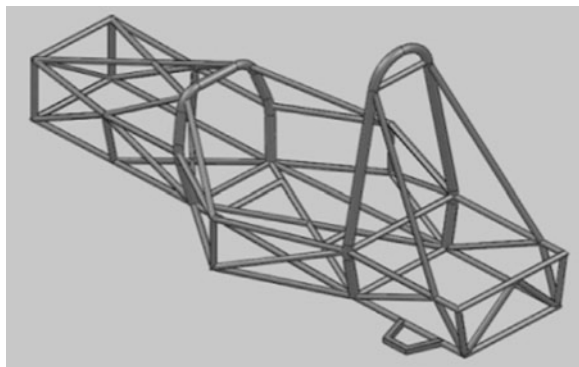


Fig. 3 Roll hoop requirements

Fig. 4 Cockpit design



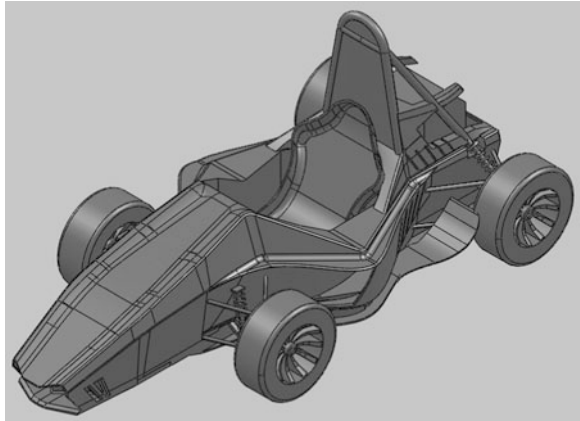
Fig. 5 Rollcage developed



### 4.4.1 Fused Deposition Modeling

FDM works on an “additive” principle by laying down material in layers. A plastic filament or metal wire is unwound from a coil and supplies material to an extrusion nozzle which can turn the flow on and off. The nozzle is heated to melt the material and can be moved in both horizontal and vertical directions by a numerically controlled mechanism, directly controlled by a computer-aided

**Fig. 6** Final CAD model of car



**Fig. 7** 1:3 scale rapid prototype of car



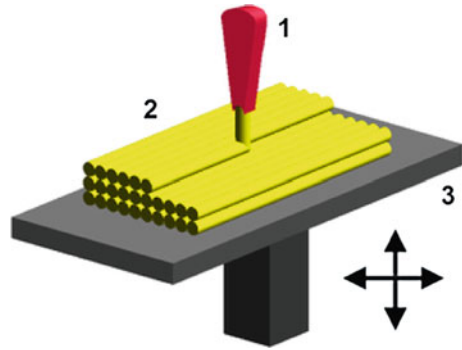
manufacturing (CAM) software package. The model or part is produced by extruding small beads of thermoplastic material to form layers as the material hardens immediately after extrusion from the nozzle. Stepper motors or servo motors are typically employed to move the extrusion head (Fig. 8).

#### **4.5 CFD Analysis**

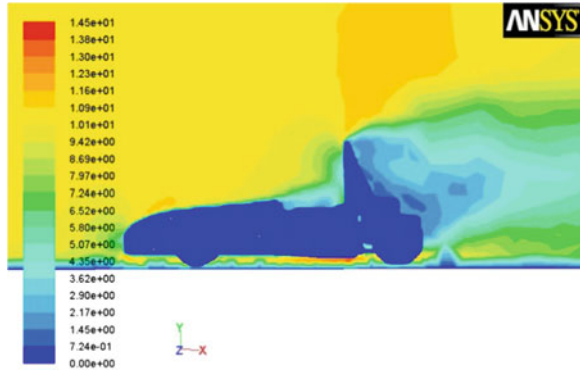
The analysis results of baseline car are shown in Figs. 9 and 10 to understand the pressure and velocity distributions at 11 and 30 m/s respectively. From the figures below, large wake region can be observed at 30 m/s.

The drag force is obtained in the Fluent software with frontal area known and hence the using the formula below the coefficient of drag is calculated.

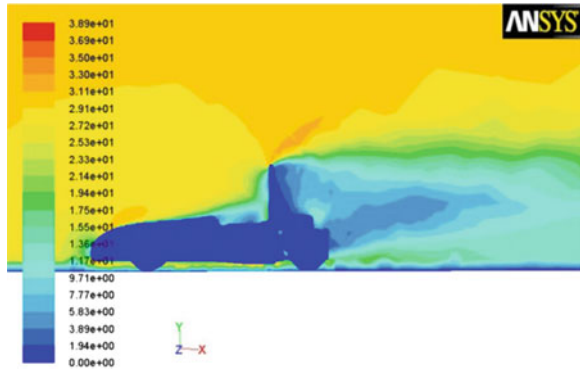
**Fig. 8** RP manufacturing process



**Fig. 9** Velocity contour of baseline car at 11 m/s



**Fig. 10** Velocity contour of baseline car at 30 m/s



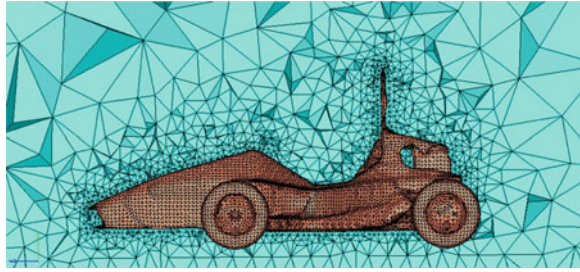
$$\text{Drag force, } D = C_D(0.5 * \rho v^2 * A) \text{ N/m}$$

$$C_D = \frac{D}{0.5 * \rho v^2 * A}$$

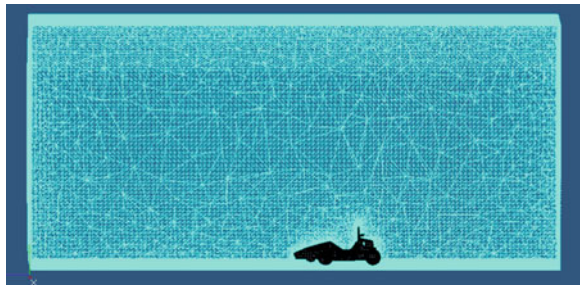
The calculated value of  $C_D$  is 1.3 for baseline car.



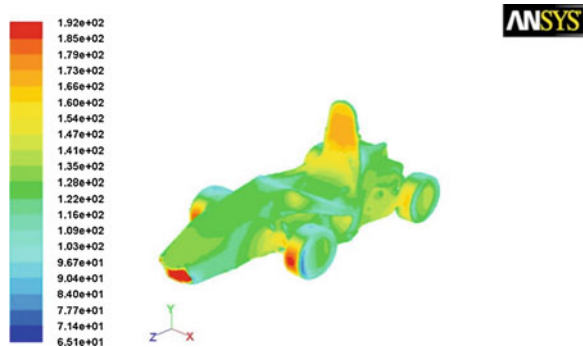
**Fig. 11** Meshing of car model



**Fig. 12** Meshing of control volume



**Fig. 13** Pressure contour of modified car at 11 m/s

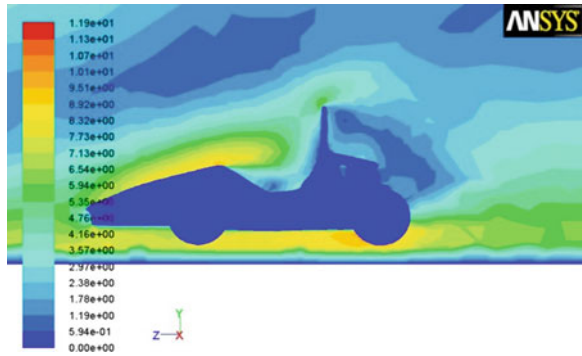


Similarly, the analysis of modified car was carried out. The control volume for the analysis was taken similar to wind tunnel test section so as to obtain close proximity with the wind tunnel testing. Hence the wind tunnel was modeled using CAD package like SolidWorks and then imported into Hypermesh for meshing (Figs. 11 and 12).

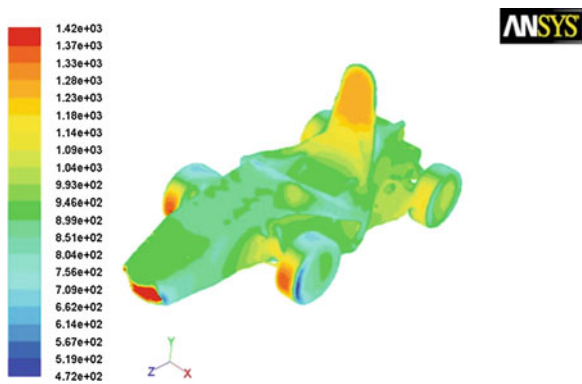
The meshed model was then imported into Fluent and the boundary conditions were applied with inlet velocities set for 11 and 30 m/s for average and maximum speeds respectively. The  $k-\epsilon$  turbulence model was selected (Figs. 13 and 14).

By using the formula mentioned above the calculated Drag coefficient is 1.18 (Figs. 15 and 16).

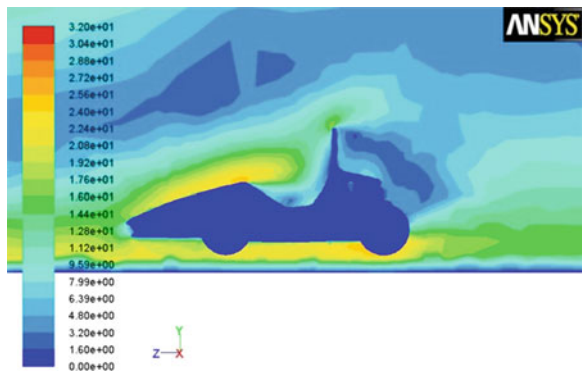
**Fig. 14** Velocity contour of modified car at 11 m/s



**Fig. 15** Pressure contour of modified car at 30 m/s



**Fig. 16** Velocity contour of modified car at 30 m/s



Reduction in Drag coefficient:

$$\frac{1.3 - 1.18}{1.3} \times 100 = 9.23$$

Hence there is a reduction of around 9 % drag with the new car model.

## 4.6 Wind Tunnel Testing

### 4.6.1 Open Circuit Wind Tunnel

In an open circuit wind tunnel, fresh air is drawn into the machine, passes through the test section and discharged through the machine. It is relatively much cheaper to build except that the ambient conditions are subjected to change based on the atmospheric changes (Fig. 17).

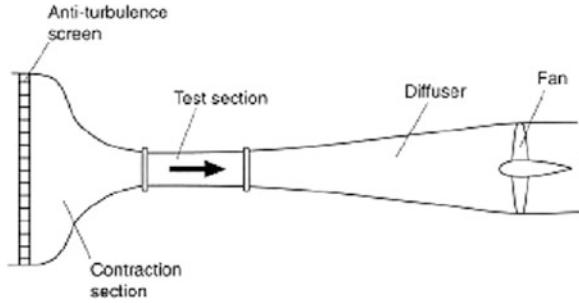
The car was mounted on the platform balance by means of four bolts tightened. A test run was initiated at 10 m/s to check the readings obtained by varying the yaw angle. Once the results of the test run were satisfactory, the actual run was started with speeds at 11 and 30 m/s (Figs. 18, 19 and 20).

## 5 Results

The variations of Coefficient of Drag and Coefficient of Lift with velocity are shown below.

S. No	Velocity (m/s)	Cd
1	10.52	0.87
2	14.26	0.86
3	18.82	0.83
4	20.80	0.82
5	21.61	0.80
6	22.70	0.79
7	24.02	0.77
8	25.10	0.75
9	26.45	0.74
10	27.90	0.75
S. No	Velocity (m/s)	Cl
11	10.59	0.18
12	14.26	0.21
13	16.79	0.18
14	18.82	0.18
15	20.80	0.17
16	22.70	0.16
17	24.02	0.14
18	26.45	0.14
19	30.75	0.16
20	39.84	0.15

**Fig. 17** Open circuit wind tunnel



**Fig. 18** Car mounted on platform balance



**Fig. 19** Testing in process



It can be incurred that with the increase in the velocity of air the Coefficient of Drag is decreasing. This shows the effect of drag at low speeds. The average Coefficient of Drag obtained is 0.9 while Coefficient of Lift obtained being 0.17 from the wind tunnel experiment.

**Fig. 20** Instrumentation setup



**Fig. 21** ARAI Academy 2011 supra car



## 6 Conclusions

Hence the car is designed for low drag and roll cage is developed with the intension of reducing the overall weight considering the ergonomics and safety of the driver. The other areas of reducing weight were with the manufacturing of Seat in composit and the body panels in plastic.

	Baseline car		Target	Modified car	
	CFD	WT		CFD	WT
$C_D$	1.3	-	<1.0	1.18	0.9
$C_L$	-0.29	-	<0.5	-0.34	0.17

The surprising value of  $C_L$  is due to the fact that the CAD model of the baseline car was not exactly the same as the original one. As engine and its sub components in the car were simply closed by a smooth surface which is not the case in the baseline car but is going to be the case with modified car (Fig. 21).

**Acknowledgments** The author expresses immense gratitude towards Mr. Aswin Deshpande, STRATASYS for sponsoring Rapid Prototype for Wind Tunnel testing and Mr. Shrikant Marathe, Director, ARAI for supporting in CFD assistance at ARAI CAE Department.

## References

1. SAEINDIA Publication (2011) "SUPRA SAEINDIA 2012, Rulebook" Release 3 on 1st October
2. Jawad BA, Longnecker MM, Nagy K, Timmer JS (2001) 2001-01-2554, SAE technical paper series, Lawrence Technological University, Lawrence
3. Wordley S, Saunders J (2006) Aerodynamics for Formula SAE: a numerical, wind tunnel and on-track study, 2006-01-0806, SAE technical paper series, Monash wind tunnel, Mechanical Engineering Monash University, Melbourne
4. Daisuke Ueno from DOME Co., Ltd., Gusheng Hu from Upwind Technology Inc., Ichiro Komada, Kazutomo Otaki and Qinyin Fan from Software CRADLE Co. Ltd, CFD Analysis in Research and Development of Racing Car, 2006-01-3646, SAE technical paper series
5. Fidan I (2004) Rapid prototyping for DFM, 2004-01-1246, SAE technical paper series, Technological University, Tennessee
6. Way ML, Berndt N, Jawad B (2003) The study of a cockpit with a fixed steering wheel position: methods and model, 2003-01-2180, SAE technical paper series, Lawrence Technological University, Michigan
7. Mariotti E, Jawad B (2000) Formula SAE race car cockpit design an ergonomics study for the cockpit, 2000-01-3091, SAE technical paper series, Lawrence Technological University, Michigan
8. Katz J, Garcia D, Sluder R (2004) Aerodynamics of race car liftoff, 2004-01-3506, SAE technical paper series, SDSU
9. Morelli A (2000) A new aerodynamic approach to advanced automobile basic shapes, 2000-01-0491, SAE technical paper series, Torino Technical University, Italy
10. Khalghi B, Zhang S, Koromilas C, Balkanyi SR, Bernal LP, Laccarino G, Moin P (2001) Experimental and computational study of unsteady wake flow behind a bluff body with a drag reduction device, 2001-01-1042, SAE technical paper series, General motors R & D center, University of Michigan, Cascade Technologies, Michigan

**Part V**  
**Automotive Ergonomic, Interior**  
**and Exterior Trim Design**

# Driver Accommodation Assessment Using Physics-Based Posture Prediction Model

Ozsoy Burak and Jingzhou (James) Yang

**Abstract** Driver accommodation plays an important role in driver and vehicle safety. Many vehicles on the market do not have proper driver seat adjustment range due to the lack of efficient methods to assess an optimal adjustment range for all drivers. Traditional methods are mainly from experiments. They are time-consuming and expensive. This study aims to develop a simulation-based method by using physics-based posture prediction to assess driver accommodation easily and efficiently. Three different types of vehicles—a sedan (Car 1), a SUV (Car 2) and a truck (Car 3) were used to demonstrate the procedure of the proposed method. A global optimization technique—pattern search was adapted for solving the physics-based posture prediction. Population sampling method was used to generate the digital human models between 5th and 95th % females and males (in stature and weight) separately. Also, for a special population—pregnant woman, digital human models were created and used in simulations. The maximum break force 100 N was implemented in the prediction model. As a result, driver seat adjustment ranges in horizontal direction were found to be  $218 \pm 14$ ,  $222 \pm 17$  and  $207 \pm 12$  mm for Car 1, Car 2 and Car 3, respectively. Likewise, adjustment ranges in vertical direction were found to be  $54 \pm 3$ ,  $57 \pm 2$  and  $59 \pm 3$  mm. The proposed method can be used in early stages of design as a computer aided engineering tool in order to reduce time and cost.

**Keywords** Physics-based posture prediction · Driver accommodation · Digital human model

---

F2012-E05-001

---

O. Burak (✉) · Jingzhou (James) Yang  
Human-Centric Design Research Laboratory, Department of Mechanical Engineering,  
Texas Tech University, Lubbock, TX 79409, USA  
e-mail: james.yang@ttu.edu



## 1 Introduction

Comfort plays an important role in vehicle safety because a comfortable design can reduce drivers' fatigue especially in long term drives. Variability in user body dimensions, anthropometry makes this problem challenging. In order to reduce the total number of driver complaints, an optimum driver seat adjustment range is a must. An optimum driver adjustment range is a key factor in whether the driver can accommodate in the vehicle and safely drive it.

Mostly, experimental methods have been used to determine the driver seat adjustment range. Kolich [1] used experiments to develop a model to predict driver-selected seat positions. 12 subjects, 6 male and 6 female, were asked to sit in each of the three compact cars in a comfortable seat position. After gathering the selected track position data, a model that would be used to predict the seat position as a function of stature was obtained. McFadden et al. [2] studied the reason for differences in seat position of male and female drivers to determine why women typically sit closer to the steering wheel. Differences were attributed mostly to the stature. Park et al. [3] studied the comfortable seated postures of Koreans using a driving posture monitoring system. Also, postural angles and anthropometric characteristics were measured. Relationships between the translational range of the driver seat, postural angles and anthropometric characteristics were discussed. Reed et al. [4] examined the effects of the height of the top of the instrument panel on driving posture using an interactive simulator. Increasing the height of the panel by 150 mm caused a horizontal hip movement of 7 mm towards the steering wheel. The result indicated that the effect of vision restriction imposed by the instrument panel has not significantly changed the driver seat adjustment. Parkinson and Reed [5] showed a case study including three types of populations of simulated drivers, the vehicle cab interior layout-passenger cars and light trucks, focusing on placement and adjustment range of the seat and steering wheel. The first type of population of simulated driver was 28 boundary manikins with no associated random variance. In order to see the effect of random postural variance, the second population was defined with 280 boundary manikins-28 manikins 10 times, each randomly sampled with postural variance values. The third population-1,000 drivers defined as randomly sampled from anthropometric distributions of each gender and including random variance. 4 different scenarios were used for the simulations including: with an adjustable steering wheel configuration, with permitting a small amount of disaccommodation, with a non-telescoping steering wheel and with up vision and down vision requirements for the sight clearance. For the first three scenarios, in optimization formulation, objective function was defined as minimizing the multiplication of adjustment ranges in horizontal and vertical directions. However, for the last scenario, the optimization procedure was split into two parts: first, an optimization procedure to find the steering wheel pivot location which maximizes average down vision, then the second optimization procedure was used to determine the smallest seat track

that will achieve 95 % accommodation on seat position for randomly sampled population, and obtaining the maximum average down vision angle maintained earlier. Driver seat adjustment ranges and seat locations were shown in results. It was concluded that the boundary manikin approach does not generally provide accurate assessments of accommodation. Also, it was shown that the inclusion of a steering wheel with a 50 mm telescope range allowed 43 and 2 mm decrease in horizontal and vertical track travels respectively. Finally, the last scenario, where sight clearance was included, yielded a very large adjustment range, and it was stated that a multi-objective approach might reduce the required adjustments. Parkinson et al. [6] included driver variability in the optimization problem in terms of body anthropometry, posture, and eye location as the only source of uncertainty. The design problem was defined as optimizing truck cab layout for driver accommodation. Motozawa et al. [7] studied the difference in longitudinal displacement of the driver seat for 40 women, 20 pregnant women and 20 age-matched non-pregnant women. Gragg et al. [8] proposed a hybrid method for predicting the optimum driver seat adjustment range based on a optimization-based kinematic posture prediction method. Hybrid method included a boundary manikin approach, a population sampling approach and a special population of pregnant women. The results of these three approaches were combined to determine an optimum driver seat adjustment range in horizontal direction only.

In literature, both experimental and simulation approaches have been investigated. Experimental methods are expensive and time consuming. Also, for the simulation-based methods, most of them only considered kinematic aspects of the driver and environment and predicted horizontal adjustment range only. None of them considered joint torque and human environment interaction forces. The objective of this paper is to develop a method to predict an optimum adjustment range in vertical and horizontal directions considering not only varying anthropometry of drivers but also driver-vehicle interactions. A global optimization algorithm was used for the solving the physics-based posture prediction.

## 2 Problem Definition

In this study, in order to predict an optimum driver seat adjustment range, vehicle cab interior are modeled including a fixed steering wheel, a brake pedal with a maximum pedal force of 100 N, a seat pan and a seat backrest. The layout is shown in Fig. 1. Three types of vehicles, a compact car (Car 1), a SUV (Car 2) and a truck (Car3) were modeled in this study.

Global origin is attached at the contact point of the right heel with the ground. A brake pedal with an angle of  $\beta$  about  $x_0$  axis is defined. Center of steering wheel which has a radius of  $C$  is attached at M,B,A in  $x_0$ ,  $y_0$  and  $z_0$  coordinates with an

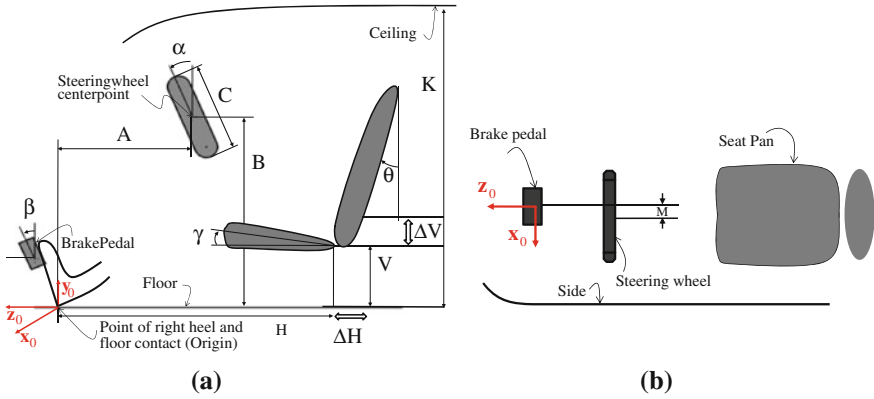


Fig. 1 Vehicle cab interior layout. a Side view. b Top view

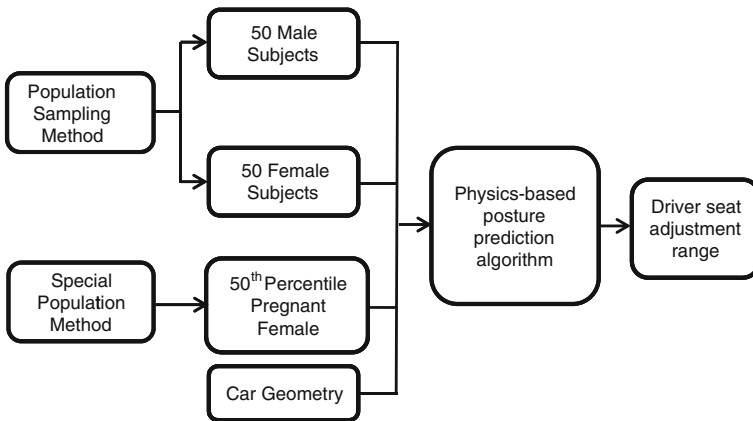
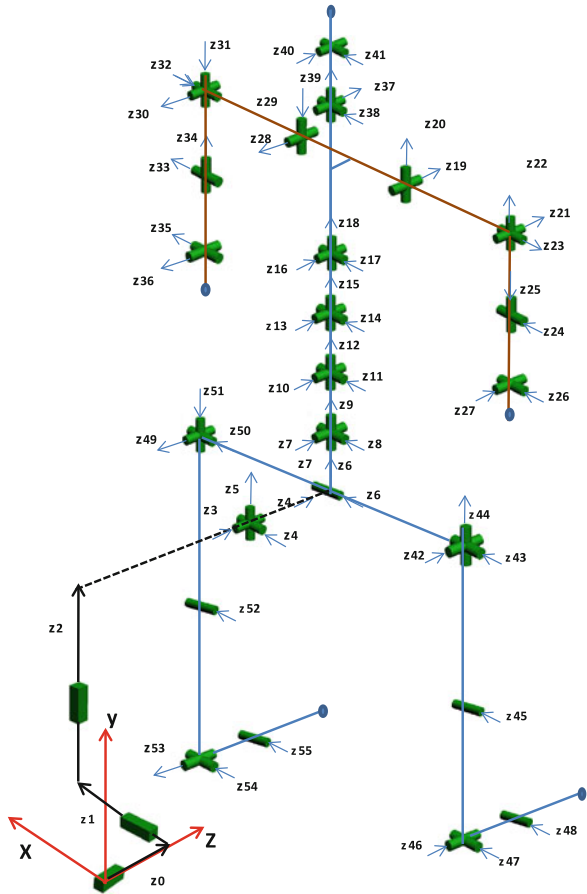


Fig. 2 Flowchart of the proposed method

angle of  $\alpha$  about  $x_0$  axis. Parameter  $H$  and  $V$  are the location of driver’s hip point location in horizontal and vertical where they are adjustable. Seat pan and seat backrest are inclined with an angle of  $\gamma$  and  $\theta$  about  $x_0$  axis respectively. Parameter  $K$  is the height of the vehicle ceiling from floor.

The problem is defined as follows: given the geometry of vehicle cab interior, predict the position of the hip in vertical and horizontal directions by physics-based seated posture prediction algorithm. This procedure is repeated with different anthropometric data in order to have an optimal adjustment range,  $\Delta H$  and  $\Delta V$  for the majority population including pregnant women with different belly sizes for different months of pregnancy. A flowchart for the procedure is shown in Fig. 2.

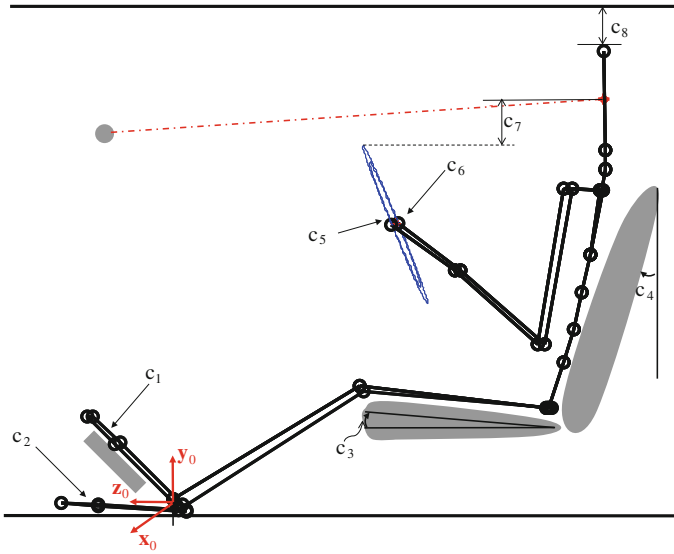
Fig. 3 Digital human model



### 3 Digital Human Model

In order to predict an optimum driver seat adjustment range, a digital human model with appropriate degrees of freedom (DOF) is necessary. In this study, 56 DOF digital human model as shown in Fig. 3 is used.

The human body can be modeled as a kinematic chain consisting of revolute joints representing the musculoskeletal joints and are connected by links that represent the bones. A local Cartesian coordinate system was fixed to each link and predicted posture is created by rotating each of the joints about this local z-axis. The model is represented by generalized coordinates  $(q_i, i = 1, \dots, n)$ , where  $n$  is



**Fig. 4** Schematic of the simulation constraints

total number of degree of freedom. Since the generalized coordinates are measured about the local axis, transformation matrices are needed for each joint. The kinematics of the body model is represented by Denavit–Hartenberg [9] method and the global position of any joint can be calculated in the kinematic chain with multiplication of transformation matrices.

#### 4 Physics-Based Posture Prediction Formulation

The simulation is constructed as a nonlinear constrained optimization problem that is solved with a commercial solver, MATLAB<sup>®</sup>. The optimization problem is considered as a multi-objective optimization (MOO) problem with two individual terms and each term is normalized by a corresponding maximum value. The weights in MOO are considered to be 1. A pictorial representation of constraints is shown in Fig. 4.

The optimization problem is defined as follows:

- Find :  $\mathbf{q} = [q_0 q_1 \dots q_{56}]^T$
- Minimize :  $f(\mathbf{q}) = \left\{ \left[ w_1 \frac{\text{Torque}_{\text{joint}}}{\text{Max}_{\text{joint}}} \right]^2 + \left[ w_2 \frac{\text{Backrest Reaction Force}}{\text{MAX}_{\text{Backrest Reaction Force}}} \right]^2 \right\}$
- Subject to :
  - $c_1 = (\mathbf{X}_{\text{right foot}} - \mathbf{X}_{\text{pedal}})$
  - $c_2 = (\mathbf{X}_{\text{left foot}} - \mathbf{X}_{\text{target point}_1})$
  - $c_3 = \text{seat pan angle}$
  - $c_4 = \text{backrest angle}$
  - $c_5 = (\mathbf{X}_{\text{left hand}} - \mathbf{X}_{\text{target point}_2})$
  - $c_6 = (\mathbf{X}_{\text{right hand}} - \mathbf{X}_{\text{target point}_3})$
  - $c_7 = \text{sight clearance}$
  - $c_8 = \text{clearance of head with ceiling}$
  - $h_{1_i} = \text{Self - collision avoidance}$
  - $h_{2_i} = \text{Torque Limits}$
  - $q_i^L \leq q_i \leq q_i^U$
  - $-\infty \leq c_1, c_2, c_5, c_6 \leq 0.001$
  - $c_7 \geq y_{\text{wheel}} + \delta_1$
  - $c_8 \leq y_{\text{ceiling}} - \delta_2$

$c_1$  is a contact constraint for the right foot. As mentioned in problem definition, global frame is attached at the right heel. Therefore, a constraint is used to satisfy the position of the right heel coinciding global origin in three dimensions. Although the connection of the virtual joints to the body is at the pelvis, it does not mean that the position of pelvis is at zero in  $x_0, y_0, z_0$  coordinates, but the position of the right heel still can be at zero in  $x_0, y_0, z_0$  coordinates by adjusting global translations and rotations.  $c_2$  constraint depends on the car type/geometry. For the sedan car used in this study, a left foot support exists, however for the truck and the SUV it does not. Therefore, for the sedan car left foot position is constrained to have a contact with the support, but for the other types of the vehicles left foot is constrained to have contact with the floor only.  $c_3$  constraint is used for the inclination of seat pan. According to the geometry of the car seat, this constraint is used to define a vertical position difference between the knee and hip for each leg. In order to see the effect of seat pan inclination on human-seat interaction forces, in this study it is constrained to be 5–10°.  $c_4$  constraint is used for backrest angle. In this study it is determined to constraint the backrest angle at 10, 15 and 20° in order to see the effect of back-rest angle to the seat shear and normal forces.

$c_5$  and  $c_6$  constraints are used for end-effector positions of the hands. Since grabbing the steering wheel is not included in this study, two constraints to

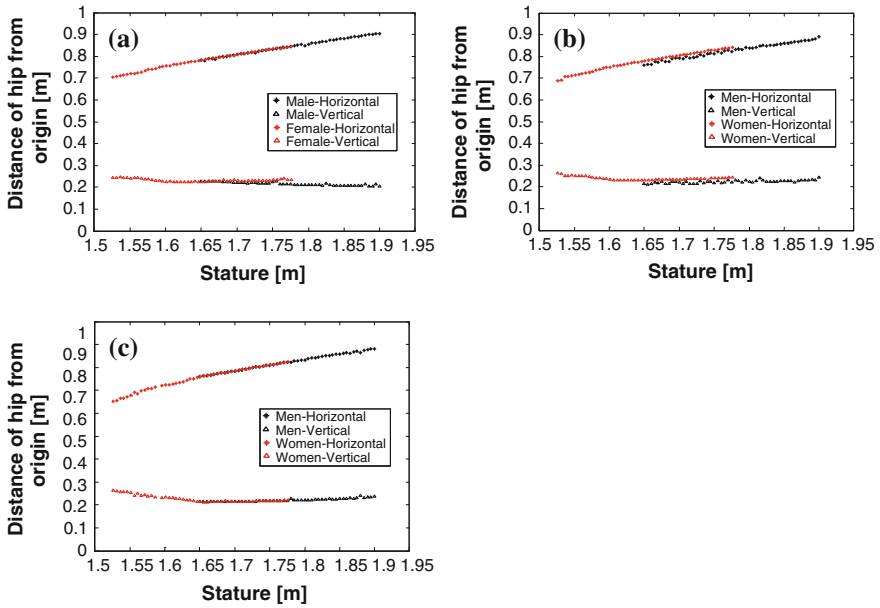
establish a contact of middle fingertips at each hand to the steering wheel at nine and three position are used.  $c_7$  constraint is used to ensure that the sight vector of the digital human model is above the top position of the steering wheel.  $c_8$  constraint is used to have a clearance of head with the ceiling of the car. Additional to these kinematic constraints, two other constraints were used to avoid self-collision and joint torque limits. Certain posture may be found where segments are colliding with each other which make the predicted posture unrealistic. This constraint ensures that the segments are not colliding with other segments. Spheres are placed at each segment's center of mass position in local coordinate except feet and head. Each sphere is constrained so that the distance between two spheres must be greater than or equal to corresponding two radius. Also, the joint torques are constrained in order to predict posture in a physical range.

## 5 Results and Discussion

In this study, a population of 50 men and 50 women was obtained through linear interpolations between 5th and 95th percentile males and females. After defining the constraints and objective functions, each body model is used in a single optimization formulation for physics-based posture prediction. In Fig. 5, obtained distances of hip from right heel (global origin) in both vertical and horizontal directions for Car 1 with backrest angle  $10^\circ$  and seat pan angle  $5^\circ$ , backrest angle  $15^\circ$  and seat pan angle  $5^\circ$ , backrest angle  $15^\circ$  and seat pan angle  $10^\circ$  are shown. In this figure it is seen that female digital models sit closer to the steering wheel and need a higher accommodation in vertical direction because of the vision constraint. Driver seat adjustment range for each vehicle is determined from the difference between the maximum and minimum values of hip positions with pre-defined combination of seat pan and backrest angle. Also, in Table 1, tabulated results for all combinations of the backrest and seat pan angles are shown.

For the special population type, pregnant woman case, seat angle and backrest angle are constrained to be both  $10^\circ$ . This configuration is chosen due to in this case the driver seats closest to the steering wheel. Additional sphere is attached to the belly for the existence of pregnancy. 5 and 20 cm belly sphere radius and corresponding weights are chosen for different gestational ages of fetus. In Table 2 pregnant driver accommodation is shown and compared to the non-pregnant case.

The results of the proposed method in this study for adjustment ranges which is shown in Table 3 are in good agreement with the result of the studies given above. In this study predicted hip position for seated posture 95th percentile male is at  $898.97 \pm 15.28$  and  $214.51 \pm 20.86$  mm in horizontal and vertical directions respectively. Likewise, for 5th percentile female the position of hip is predicted at  $688.75 \pm 22.54$  and  $253.91 \pm 22.54$  mm. Driver seat adjustment ranges are found to be in good agreement to the results in literature with a value of  $215.78 \pm 15.14$  and  $56.61 \pm 3.37$  mm in horizontal and vertical tracks.



**Fig. 5** Driver accommodation in Car 1 **a** backrest angle 10° and seat pan angle 5° **b** backrest angle 15° and seat pan angle 5° **c** backrest angle 15° and seat pan angle 10°

**Table 1** Tabulated results for varying seat pan and backrest angles

Seat pan angle [degree]	Back rest angle [degree]	Car 1 adjustment range [mm]		Car 2 adjustment range [mm]		Car 3 adjustment range [mm]	
		Vertical	Horizontal	Vertical	Horizontal	Vertical	Horizontal
5	10	51	203	55	222	62	197
10	10	55	232	60	248	60	221
5	15	51	201	57	208	60	206
10	15	50	228	55	231	53	216
5	20	58	214	59	199	61	191
10	20	56	229	58	225	58	213

**Table 2** Pregnant and non-pregnant 50th percentile female driver seat accommodation in Car 2

	Pregnant		Non-pregnant
Sphere radius [cm]	5	20	0
Vertical adjustment [mm]	224	222	218
Horizontal adjustment [mm]	776	777	773





## 6 Conclusion

This paper presented a method to determine driver seat adjustment range in vertical and horizontal directions considering not only the varying anthropometry of drivers but also driver and vehicle interaction such as pedal forces, driver-seat, and driver-floor interaction. Three vehicles- a sedan, a SUV and a truck were modeled including seat, backrest, brake pedal, steering wheel. Driver seat adjustment ranges in horizontal direction were found to be  $218 \pm 14$ ,  $222 \pm 17$  and  $207 \pm 12$  mm for Car 1, Car 2 and Car 3 respectively. Likewise, adjustment ranges in vertical direction were found to be  $54 \pm 3$ ,  $57 \pm 2$  and  $59 \pm 3$  mm. Validation of the proposed was given through experimental and simulation studies that were found in literature. The proposed method was shown to be useful and can be used in early stages of design process as a computer-aided engineering tool in order to reduce time and cost. Also, the proposed method can be used for custom-made design for other seated applications for injured or disable people.

## References

1. Kolich M (2000) Driver selected seat position: practical applications. SAE Technical Paper 2000-01-0644
2. McFadden M, Powers J, Brown W, Walker M (2000) Vehicle and driver attributes affecting distance from the steering wheel in motor vehicles. *Hum Factors* 42(4):676–682
3. Park SJ, Kim C-B, Kim CJ, Lee JW (2000) Comfortable driving postures for Koreans. *Int J Ind Ergon* 26(4):489–497
4. Reed MP, Manary MA, Schneider LW (2000) The effects of forward vision restriction on automobile driver posture. *Transp Hum Factors* 2(2):173–189
5. Parkinson MB, Reed M (2006) Optimizing vehicle occupant packaging. SAE Trans J Pass Cars–Mech Sys, vol 115, Technical Paper No. 2006-01-0961
6. Parkinson MB, Reed M, Kokkolaras M, Papalambros PY (2007) Optimizing truck cab layout for driver accommodation. *ASME J Mech Des* 129(11):1110–1117
7. Motozawa Y, Hitosugi M, Tokudome S (2008) Analysis of seating position and anthropometric parameters of pregnant Japanese drivers. *Traffic Injury Prev* 9(1):77–82
8. Gragg J, Yang J, Howard B (2012) Hybrid method for driver accommodation using optimization-based digital human models. *Comput Aided Des* 44(1):29–39
9. Denavit J, Hartenberg RS (1955) A kinematic notation for lower-pair mechanisms based on matrices. *J Appl Mech* 22:215–221

# Design of the Adjustable Vehicle Seating Buck for Ergonomics Verification

Hongfang Ling, Li Wu and Gang Li

**Abstract** In ordering to avoid the risk of big change cause by unreasonable ergonomics parameter and save development time, vehicle research institute usually build a seating buck. The Seating buck is a physical cabin model of passenger car for ergonomics verification. It is widely used to assess the amenity, ingress and egress, visual field, habitability, etc. This paper aims to introduce the design of an adjustable seating buck, which can be significantly reduce the development risk, time and cost. The interior dimensions can be adjusted as needed. It is able to emulate cabins from class-A to class-C. By the help of the highly adjustable seating buck, most of the ergonomic verification can be performed on this Seating Buck quick and easily.

**Keywords** Adjustable · Ergonomics · Seating buck · Subjective evaluation

## 1 Introduction

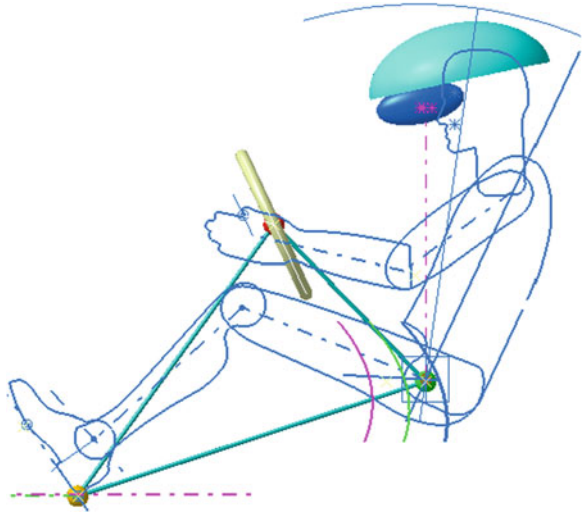
With the rapid development of China car market, customers are attaching greater importance to the ease of man-machine interaction. However, the trends of sporty vehicle styling results in the down size of interior roominess [1], and people are still growing tall in these days. These make the design of ergonomics become more challenging in now day [2].

---

F2012-E05-002

---

H. Ling (✉) · L. Wu · G. Li  
Guangzhou Automobile Group CO., LTD, Automobile Engineering Institute,  
Guangzhou 510640, China  
e-mail: linghf@gaei.cn

**Fig. 1** Driver-manikin

The ergonomic software is a very powerful tool for virtual verification. It is good at evaluate the occupancies' fatigues in certain posture, however, if the evaluation involve some complex movements (e.g. the movements of ingress and regress), the analysis result may vary from the reality.

Hence the physic ergonomics verification method is in demand. The traditional seating buck is built for the particular project i.e. the cabin size is fixed and it can be only used on one project. This practice result in low efficiency and high development cost.

This paper aims to introduce the design of an adjustable seating buck, which can be used for physical ergonomic verification.

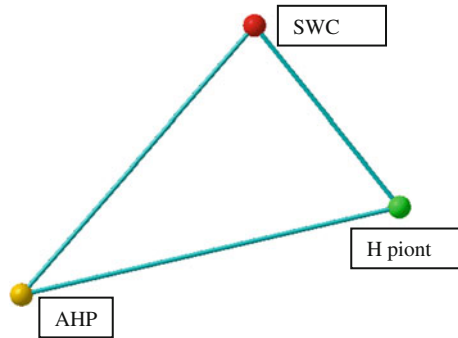
The key ergonomics parameters can be fast adjusted in order to have a quick verification of design concept. This model can be used for verify the ergonomics boundary in concept design stage, and subjective assessment in engineering design stage. Moreover, this model can simulate the vehicle interior from class-A to class-C. it is a standardize ergonomics platform to server more and one project [3].

## 2 Methodology

### 2.1 Define Driver's posture

Accelerator heel point (AHP), H point and the steering wheel center point are three design hard points to constraint driver's posture. The coordinates of these three points are defined in the package drawing (Fig. 1) and the relative coordinates should be built in the physical model [1].

Fig. 2 Hand point triangle



Although there has not precise formula to describe the relation of these three points, the empirical formula can be still applied to define the steering wheel center by known the location of the other two (Fig. 2).

Formula is given below:

$$W_x = 640.1 - 0.10325 * (H30) - 0.0005 * (H30)^2$$

$$W_z = 405.17 + 0.8715 * (H30)$$

W<sub>x</sub>: longitudinal steering wheel center to BOF

W<sub>z</sub>: Vertical steering wheel center to AHP

H30: Vertical height of driver's H point.

## 2.2 Mechanism for Hard Points Co-ordination

In order to has the coordination of hard points between physical model and design. The AHP is considered as the origin point. It is marked on the floor, and the location is fixed respect to the model.

Two mechanisms are designed to realize the coordination: the adjustment of steering wheel center can allowed the steering column move along three directions, the simplify disc with the center marked in red would be fixed on the column to represent the steering wheel center; the adjustment of driver's seat has designed to a level platform with the SgRP point has projected on it. The distance between AHP, SgRP and steering wheel center can be easily measured.

The coordinates of these three points are different from car to car. Hence 36 sedans have been benchmarked, from class A to class C. the benchmarking result are used to set the stroke of the benchmarking, to ensure the model can be used on the future projects [4].

The H point can be located by the parameters L53, W20, and H30<sup>13</sup>. According to the benchmarking data, the stroke of mechanism was set: X = ±110 mm, Y = ±80 mm, Z = ±90 mm (Tables 1, 2).

The steering wheel center can be located by the parameters L11 W7 and H17<sup>13</sup>. The stroke of the mechanism was set : X = ±110 mm, Y = ±64 mm, Z = ±35 mm.

**Table 1** Key dimension

	A class	B class	C class
L53	676–840	810–890	840–920
W20	330–350	350–380	360–400
H30	260–310	250–285	230–275

**Table 2** Steering wheel location

	A class	B class	C class
L11	360–450	350–470	335–490
W7	263–333	315–370	377–390
H17	620–674	609–679	600–670

**Fig. 3** Seating buck

### ***2.3 Design of the Framework***

To design the adjustable framework, the coverage of the seating buck should be fully considered at beginning. The framework size and stroke are depends on the parameters of coverage vehicles.

This model is designed emulate the sedans with wheelbase from 2,500 to 3,000 mm. Hence the framework (Fig. 3) has designed to be adjusted in length and height. The longitudinal stroke is 300 mm, and the vertical stroke is 120 mm. To simplify the structure, the width of the framework is fixed. The parameters in width are adjusted by door panels and pillars [5].

### ***2.4 Validation Parts for Concept Design Phase***

In concept design phase, the parts are used to validate the ergonomics layout before the design of styling. Hence the components are built with simple shape and highly adjustable.

For example, the roof is made of eight pieces ( $2 \times 4$ ) of individual sheet and two rails. These sheets have simple arch shape without any styling feature in

detail. Each sheet can be slide and rotate along the rail. It is very convenient to have analysis the driver and passengers' headroom space individually.

The following parts should be designed to have adjustment mechanism: A pillar, B pillar, C pillar, roof, instrument panel, centre console panel, inner door panels, seat, steering column, acceleration pedal, braking pedal, clutch pedal, foot rest pedal, handbrake, shift lever, cluster, etc.

The parts are design to adjusted along Adjustable rang contain straight line (X direction, Y direction, z direction) and angle. Each adjustment mechanism has the calibration labeled on the mechanism, to make the adjustable more precision.

## ***2.5 Verification Parts for Detail Design***

In detail design phase, the interior should be evaluated in more detail. The styling of the trims becomes more important.

Another type of components would be applied to evaluate the influence of the particular styling features. These components are the rapid prototypes of the latest styling CAS surface.

For example, to evaluate the A-pillar obstacle angle, the parts of A-pillar can be made in different shapes, so that it can be easily exchange and compare during the evaluation. The parts are used to assess the actual interior environment.

The following parts should be built: the steering wheel, pedals, handbrake, gear shift knob, instrument panel, floor consol, inner door panel, A/B/C pillar, roof, mirror, door sill, hood and trunk surface, they could be the rapid prototypes parts or parts from the car with similar appearance.

Two parts are also added in addition, in order to evaluate the visual ergonomics. Such as cluster and navigation screen, they can be rotated within certain angle, in order to evaluate the reflection of the screen. The navigation system can be also functional by connecting a external battery.

## **3 Subjective Evaluation**

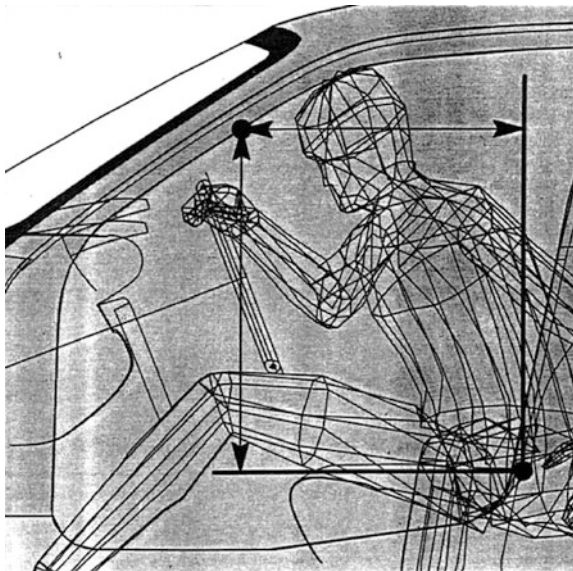
### ***3.1 Verification Subjects***

Several subjects can be verified on this model. Including the ingress and egress, visual field, habitability, driving convenience and comfort, display screen reflection and glare and storage. And each subject have a evaluation list. For instance Table 3 is the ingress and egress [6] evaluation list and Fig. 4 ingress and egress sketch map.

In the following Sect. 4.1 you will see how to verify door flange.

**Table 3** Ingress and egress evaluation list

1	Distance between inner door panel and seat
2	Distance between knee and instrument & cover
3	Doorsill height and width front carpet
4	Distance between heel point and lower A pillar
5	Door open angle (A125)
6	Distance between steering wheel and seat (H74)
7	Distance between steering wheel and thigh (H13)
8	Distance between steering wheel and trunk (L7)
9	Distance between H point and B/C pillar
10	Distance between head and roof
11	Doorsill height (H115)
12	Door flange height
13	Door flange width
14	Distance between door and ground (H50)
15	Seating height to ground (H5)
16	Distance between side panel and door sill in Y direction

**Fig. 4** Ingress and egress sketch map

### 3.2 Subjective Evaluation Method

The most importance factor for using this physic seating buck is the ergonomics subjective evaluation team. This kind of team contains almost all representative anthropometry samples. Until now, we already build a subjective evaluation team,



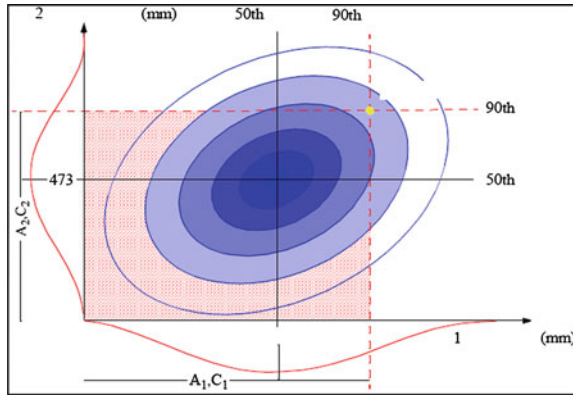


Fig. 5 Anthropometry percentile planar map

including 76 person. The characteristic of the team is that contain 1–99.9 % and the age contain 23–50. The percentile base on China forecast proportion data [7]. The forecast year is base on the car laundry to the market. The Fig. 5 is anthropometry percentile planar map.

According to the report of voice of customer, we select the certain team percentile area. For example, the SUV car we will select relatively big percentile. The certain teams are assigned to participant of the ergonomics subjective evaluation and detective potential ergonomic failures which are difficult to find out in CAD. The team will mark project by the separateness [8].

All the mark sheet will be putted into the calculation system and use the spider map to output the result. And compare the result with the target to decide if needing to optimize it or not. If need, we do it on the Seating Buck easy and quick by adjust machine or rapid prototypes replace.

And then feed back to the CAD. The Fig. 6 is subjective evaluation result of one passenger vehicle.

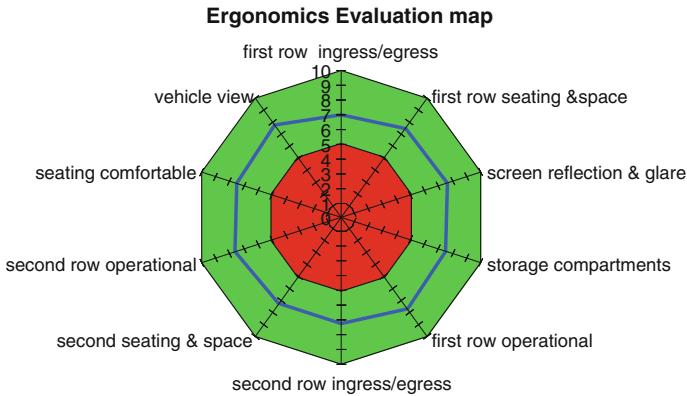
By the way, team’s feedback are also valuable to review and revise the current ergonomics standard.

The Fig. 7 maybe show cleary how to use the seating bu ck to design, verify and improve the vehicle ergonomics.

## 4 Applications

### 4.1 Ingress and Egress

The convenience of Ingress and egress are mainly influenced by the shape of the door flange. The following is a case of how to apply the evaluation of seating buck



**Fig. 6** Subjective evaluation result

to refine the door flange. The Fig. 8 shows below are the main dimensions of the door flange.

The shape of door flange effect couples of issues, including ergonomics, styling, side crash, insulation, and so on. These issues are conflicting to each others.

For example, the H11, H11-200× and H11-300× are three critical dimensions to represent the opening the door flange in height. On the other hand, they represent the shape of the A pillar. Therefore, they're important to both ergonomic and exterior styling. If the car has a sporty styling, the A pillar would be more backwards and have a big incline angle that will lead H11-200× and H11-300× is relatively small. In this case, even H11 is big enough, the Ingress and Egress is still bad.

In additional, If CZ1 is too big, side crash would become weak. If CZ1 is too small, the distance between heel point and the door sill will be increase and the Ingress and Egress would be bad.

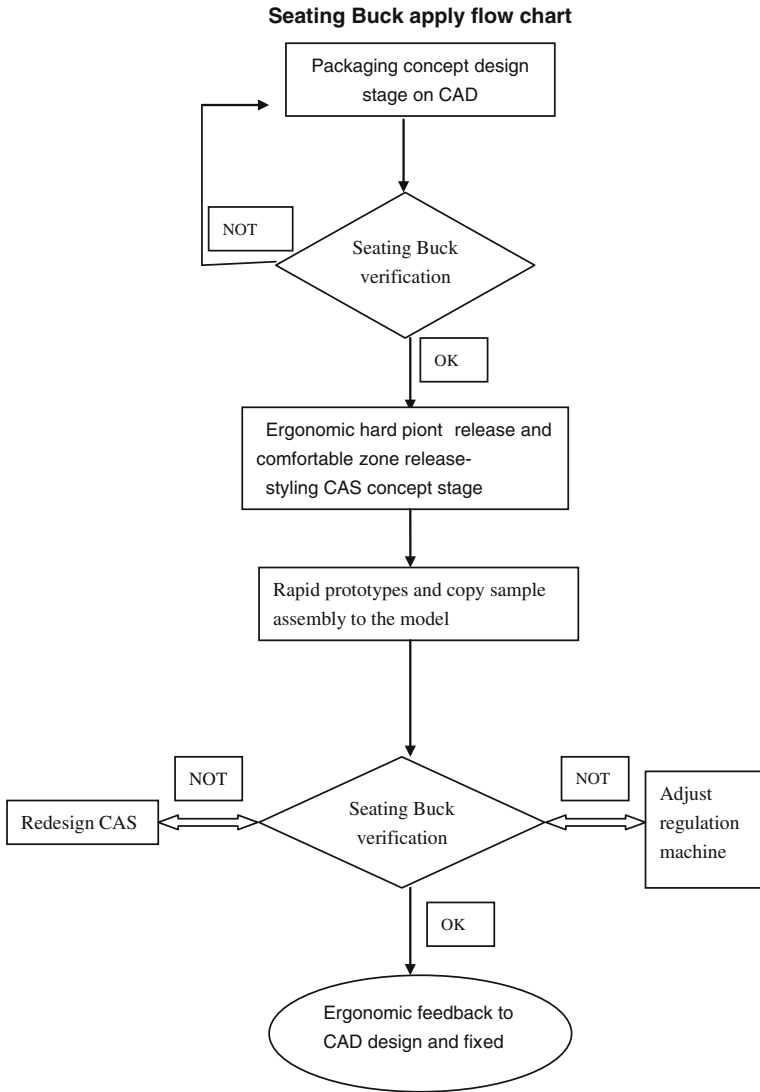
All the dimensions mentioned can be adjusted on the seating buck, CZ1 can be adjusted by the door sill adjustment, the H11-1 H11, H11-200× and H11-300× can be adjusted by replacing different rapid prototypes like Fig. 9.

In order to balance all these issues to find out the best solution, usually several proposals should be made. The subjective evaluations have performed, to rate the convenience of ingress and egress.

Finally, one of the proposal has been selected, base on the result of subjective evaluation and all the other concerns.

## ***4.2 Cluster Visual Field Verification***

Cluster issue for example reflection, image, glare, obstacle is difficult to avoid base on virtual check. After some project experience we reckon that cluster issue must be verification according the Seating buck. Regulate machine and rapid prototypes



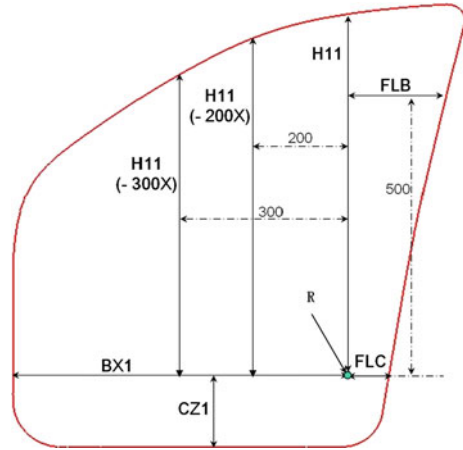
**Fig. 7** Seating Buck apply flow chart

both need to use. The angle has designed, front and rear regulate machine for the display plane. About the lens cover, needing rapid prototypes, because the curvature of it can not be simulate [7]

The Fig. 10 is some car virtual check result, showing no problem.

Actually, subjective result got a low mark. Base on the evaluation, we adjust the angle of the display until got a best mark. And then feedback the angle to the CAD design.

**Fig. 8** Main dimensions of the door flange








**Fig. 9** Rapid prototypes



**Fig. 10** Virtual check result



**Table 4** Lens cover

Cluster lens benchmarck			
Lens type	lens direction	benchmarck	picture
Integration	toward up	Lavida, Bora, Golf-7	
	toward down	Accord Spotage, Trumpchi	
separate	toward up	Golf-6	
	toward inner	ix 35	
	toward down	Lacross, Regal	

The Table 4 Show different kind of lens cover, including the advantage and disadvantage. If any problem was found in the evaluation have problem, we will according the issue, styling and packaging space to select one kind of the lens cover.

### 4.3 Handbrake Reach and Comfortable

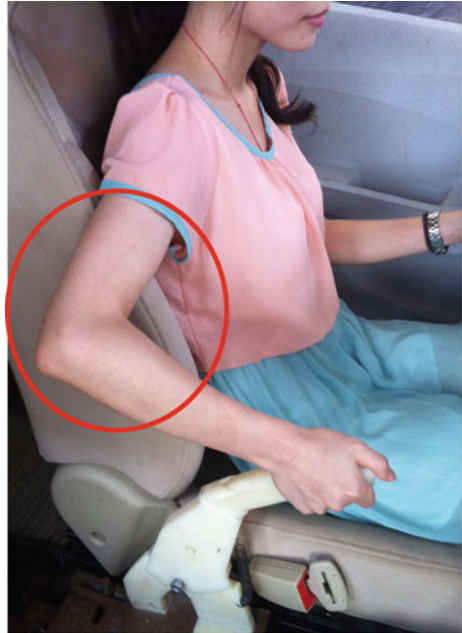
In the evaluation of a compact sedan seating buck, the low rating of level of comfort was found on 50–5 % females. They complained the handbrake was too rearward to operate, like Fig. 11. However, the CAD analysis indicated that this operation is comfort for all the percentile body [9].

A probable reason was found after some observation of participants’ maneuvers: during the travel, the 5th percentile driver’s elbow will collided with side support cushion of the seat. While in CAD model, the manikin’s upper arm was not well constrained, which made his elbow more outward from the body, like Fig. 12.

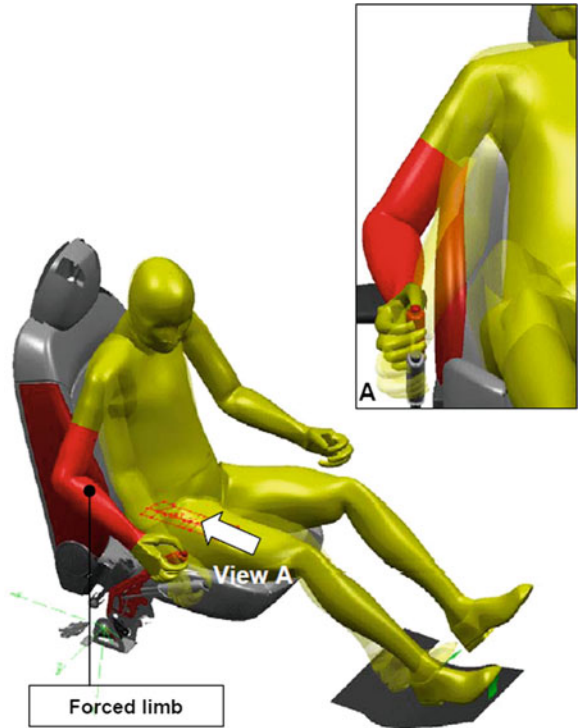
A quick re-assessment has done after the problem identified, by the helps of the adjustable handbrake mechanism, the handbrake location can be changed easily. The optimized locations have been evaluated by the team, and the preference location of handbrake was decided in the end.

The correction on the CAD model was applied and the good correlation has found between reality and CAD (Fig. 12).

**Fig. 11** 5 percentile females situation



**Fig. 12** CAD check



## 5 Conclusion

The adjustment seating buck is a standardized ergonomic platform which is able to emulate different size of cabin in order to serve different projects. This seating buck can be applied to verify the ergonomic performance such as ingress and egress, visual field, habitability, driving convenience and riding comfortable. An operable and efficiency subjective evaluation method and procedure are summarized based on this model.

With this seating buck, the physical ergonomics verification become more efficiency and low cost. It can significantly reduce the project development time, discover and avoid the potential ergonomics problems in concept design period, minimize the risks. Moreover, this is a low cost solution, the normal seating buck needs 2–3 months to build up. But with this model, it takes one month to finish the entire vehicle ergonomics verification.

## References

1. Yang C (2009) Analysis on sedan entry convenience influencing factors. *Auto Engineer* (7):44–46
2. Driver Hand Control Reach. (1988) SAE J827
3. Reed MP (2000) A new approach to modeling driver reach
4. Parking MB (2003) Assessing the validity of kinematically generated reach envelopes
5. GB 10000-88 China human dimension
6. Wu H (2004) Preliminary Discussion on Application of Ergonomics in Car General Layout Design. *Auto Technol* (2):6–10
7. Tang Y (2007) The method of controlling reflection and glare caused by the displays in vehicles. SAE China
8. Chaffin DB (2001) Digital human modeling for vehicle and workspace design
9. Porter JM (1993) Computer-aided ergonomics design of automobiles

# Study on Preventing Dazzle of Meter

Luo Pan, Xiaolin Liao, Guozheng Luo, Jing Wang, Dejian Cheng and Li Yu

**Abstract** This article analyzed in detail the key technologies of the dazzle and the dazzle direction of optimization. It is base on full consideration of cockpit ergonomics. So as to effectively avoid dazzle during CAS phase and then ensure the driving safety.

**Keywords** Motorcar · Meter · Dazzle · Check · Optimize

## 1 Introduction

People become increasingly depend on the automobiles, because the automobiles became the most common means of transportation in the modern society. More and more attention is paid to safe use of the car. Drivers get 80 % information through vision during driving, so good vision is a prerequisite of safe driving. Meter Dazzling makes drivers cannot concentrate on driving, resulting in the driver's mistaken judgment or misuse, and leading to traffic safety incidents, how to avoid the glare is one of the most important subjects worthy of study. This article analyzed how effectively avoids the dazzle problems in the vehicle development stage.

---

F2012-E05-006

---

L. Pan (✉) · X. Liao · G. Luo · J. Wang · D. Cheng · L. Yu  
Changan Auto Global R&D Center of Changan Automobile Co LTD, Chongqing, China



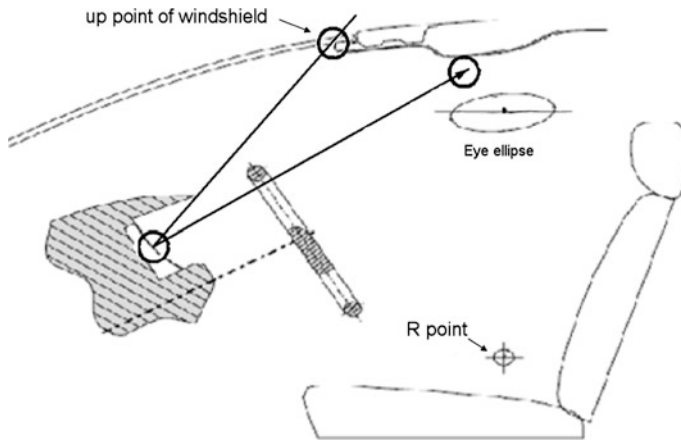


Fig. 1

## 2 Meters Dazzle Checking and it's Optimization Direction

Meter dazzle mainly has following several kinds: Meter curved glass lead to dazzling, Meter curved glass existence projection, Windshield reflection meter lighting cause dazzling, side window reflects meter lighting cause dazzling, the following, we simply introduce their way of checking above several dazzling, analyzed it's Optimization direction.

### 2.1 Meter Curved Glass Lead to Dazzling

Daytime, the light though front windshield is reflected through meter glass, it enters into driver's eye, causing the driver's ill or affecting the clarity of the front view. We are able to check on the 3D data in this situation, such as in the YR parallel plane (Refers to a series of parallel-planes whose surface is gap 20 mm, each plane is examined one time according to the same way, the following same.) why do like this, even if it isn't dazzled through checking on the YR cross section, other parallel section may still not meet the requirements for reason of meter hat shape; generally speaking, the light from the front windshield was reflected though the meters glass which do not intersect with the eye ellipse [1] and be lower than it (Sees Fig. 1), strictly speaking, the light of reflect should be apart from eye ellipse at least 10 mm, otherwise causing dazzle phenomenon, If the new design was examined dazzling in CAS phase, the optimized direction has the following several kinds approximately; (1) increase the meter cover height (Fig. 2) or increase the black border of the front windshield to the light cannot directly irradiate the meter glass. (2) Meter glass or meter sink along the plane of normal, the light of reflect though meter glass are blocked (Fig. 2); (3) Change the meter

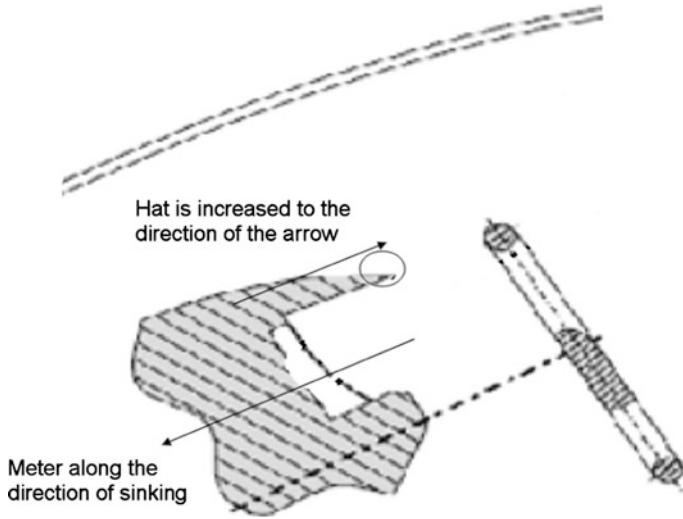
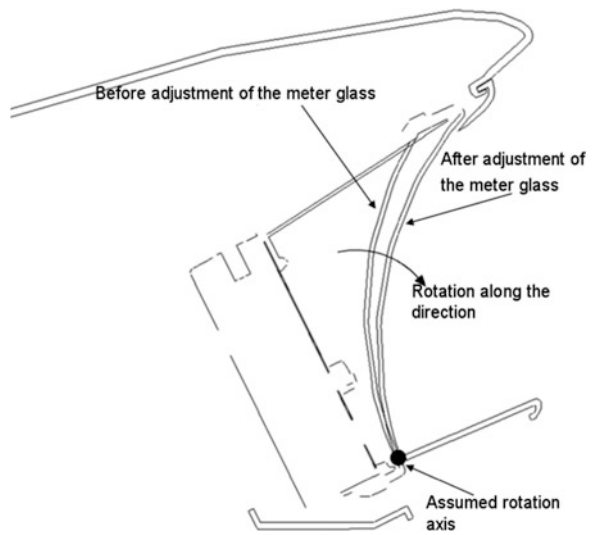


Fig. 2

Fig. 3



glass dip angle, the effect is obvious while the meter cover is deep enough (Fig. 3). (4) we may change curvature of meter glass (note that the radius must be above 250 mm, otherwise the meter image will be distortion), reflected light does not intersect with the eye ellipse. (5) Meter glass was changed to anti-gradient (Fig. 3) to avoid to dazzling, the effect is most obvious; the similar way can also check the sunroof; Due to the angle of incidence of light from behind windshield is small and

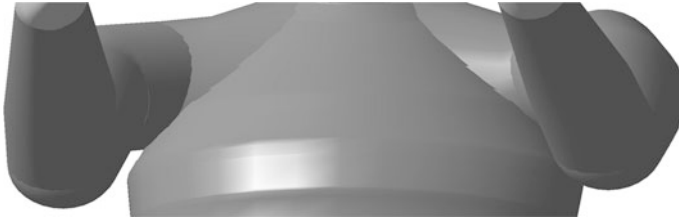


Fig. 4

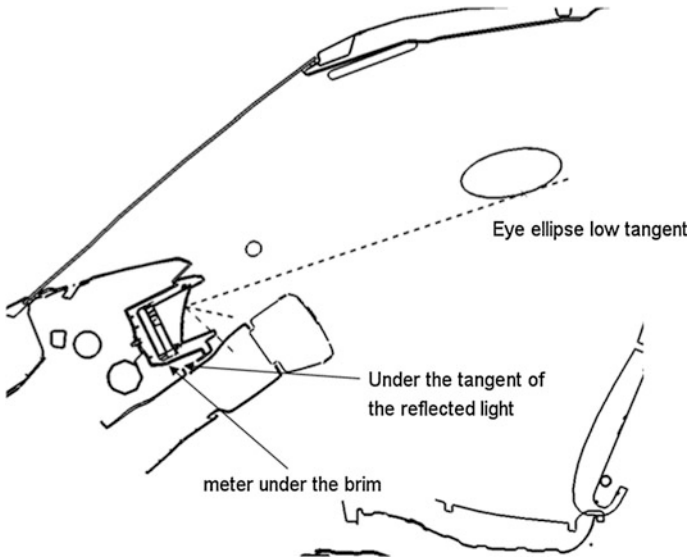


Fig. 5

most was blocked which cannot arrive meter hood, So generally it does not consider.

### 2.2 Meter Curved Glass Existence of Reflection

The steering lock shell, clothing, etc. though meter glass reflect image (Fig. 4), which makes driver to get dark meter information, affect driver judgment. The phenomenon can check on 3D data, such as on the YR parallel to the plane, the reflected light from the eye ellipse limit point to the meter glass blocked completely by meter hat. (check way shown in Fig. 5), if the new model meets the conditions difficult, at least, meter critical data (such as the speedometer,

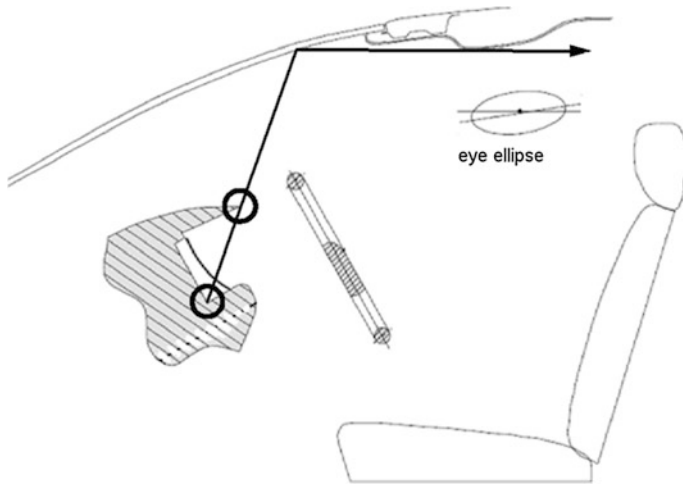


Fig. 6

tachometer, turn signal, etc.) should be require to layout beyond the reflection, finally, the above situation needs to tests and verify.

### 2.3 Windshield Reflection Meter Lighting Cause Dazzling

At night, the front windshield like a mirror which will reflect the meter light into the driver's eyes, thus it affects the driver to view the road conditions ahead, above situation as a larger traffic safety hazards. General check of the way in the plane parallel to the YR: reflection which is the meter light projects windshield must not intersect and below the eye ellipse (see Fig. 6), strictly speaking, the reflected light should be far from the eye ellipse at least 10 mm, so as to eliminate glare phenomenon. The optimize direction of the above dazzling phenomenon are: (1) increasing meter hat make meter light be blocked which is not enter into front windshield, (2) meter glass surface or meter to sink along the normal plane, It make the meter lighting blocked by hat; (3) In the allowed circumstance, we change the front inclination, adjust the location of the R point also could resolve Problem, but it Changes too much so it is generally not used.



Fig. 7

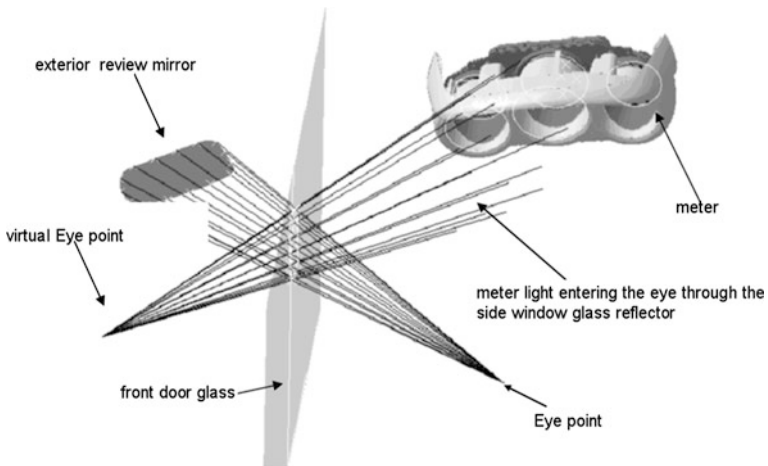


Fig. 8

### ***2.4 Side Window Glass Reflects Meter Lighting Cause Dazzling-Outer Mirror Dazzle***

Meter light project on the front door side window glass, which reflect into the driver's eye, it results in hybrid meter light and other parts of the image when driver watch the outside mirrors (Fig. 7), consequently, driver cannot effectively see the rear car location and status and affect traffic safety. Checking method on the 3D data as follows: For a cluster of rays from the driver's eye ellipse center to the exterior mirrors edge, if we demanding more, front and rear limit point of the eye ellipse can be used separately check and then get the combination, Finally, it conduct Boolean on the side windows; Surrounded surface by the above-mentioned ray and front side window glass intersect, intersection is exterior rear-view mirror projection area on

Fig. 9

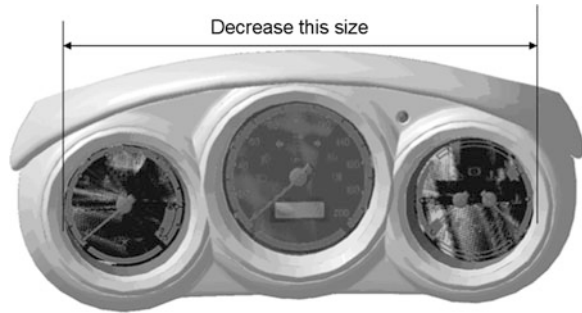
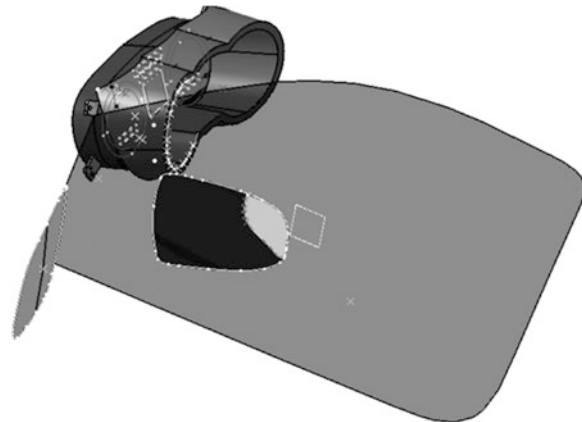


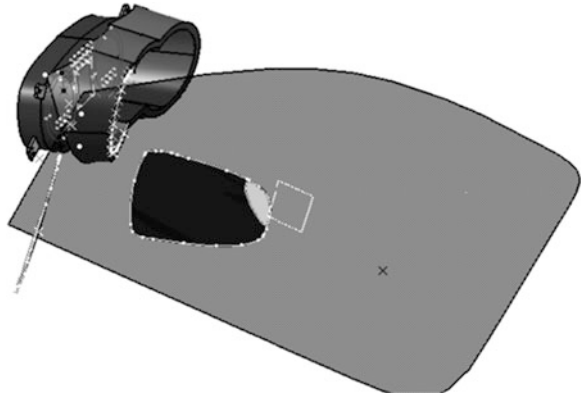
Fig. 10



the front side windows; Then, we obtained the driver's virtual eye point based on the approximate plane of the projection area as a plane of symmetry. For a cluster of rays from virtual eye point to the projection area edge of the entire exterior mirror, though checking the above-rays to determine whether it Include the meter lighting or not (see Fig. 8).

If the cockpit exists the condition of meter dazzle by checking, optimized directions as follows: (1) optimize the meter styling, such as add isolation wall between the engine speed indicator and speedometer, or making it barrel styling directly, etc. Which have a positive effect on avoid-avoid the meter dazzle because of front windshield reflect. (2) The three positions of Eye ellipse, meter and exterior mirrors are optimized, which have a obvious effect to avoid the side window dazzle. Ordinarily, the location of exterior mirrors adjust the space is larger (The driver side of the rear view mirror must be installed in the rear-view mirror center to the driver of the two eyespots center which the angle between vertical surface and longitudinal datum plane is not more than 55 range.) So, the rear view mirror moved forward or behind to avoid the blinding area of the side windows which is caused by the meter. (3) To change the side window angle can effectively improve and to avoid the side window glare, Inclination of the side window glass increased, the reflected light meter on the side window will not be

Fig. 11



able to enter the eye ellipse, effectively avoid the side window glare. But the measure should be taken when design the hard point of side window, later the feasibility of adjust the side window slope angle is very small; (4) appropriate reduce the size of meter or exterior mirror, on the blinding has contributed greatly to the ways to avoiding dazzle (Fig. 9); (5) the above-mentioned four measures avoid dazzle only from geometric dimensions, dazzle and meter light have great relationship, so it reduce the meter brightness which may be appropriate to avoid dazzle when other data have been frozen, this is an effective measure.

### 3 Optimize Application Examples

This article combines with a new car's the side window glare and the optimization case, which elaborate how to ensure that the meter does not produce side window dazzle phenomenon in the shape of the early. (1) A new kind of models by checking, we discover the side windows dazzle is serious in the CAS phase (see below), Because the meter light caused dazzle area of the side window accounts for the area ratio of the rear view mirror 15.6 %. (2) while guarantee that the meter hat has sufficient safety clearance (85 mm above) with steering wheel and the exterior mirrors satisfy regulations, if we put the meter hat raise 10 mm and put the exterior mirrors move backward 10 mm, the dazzling proportion would be reduced significantly (3 %) (Figs. 10, 11).

### 4 Conclusion

This paper detailed introduces meter curved glass lead to dazzling, meter curved glass existence of reflection, windshield reflection meter lighting cause dazzling, external rear-view mirror reflection meter lighting cause dazzling were mainly

introduced in this paper. Focused on the optimization methods of dazzling with the contents of the front especially and focus on the optimization methods, such as. Those optimization measures such as increasing the hat height, changing the angle of meter glass and the surface radius, changing the location of the exterior mirrors etc. and eventually through a case verify the correctness of the method.

In hard point design, the meter dazzle should be taken into account so that the dazzled problem will be eliminated in the modeling and designing stage, which will avoid a large amount of the change of the design and mould modification to appear. So, it saves the time and costs.

## Reference

1. Saej941v002-2002 (R) Motor vehicle drivers' eye locations



# A Study and Application of Optimization on Console Development

Ruiyan Zhang, Ni Cao and Miao Luo

**Abstract** *Objectives* The purpose of this paper is to study optimization methods and apply them to automobile plastic parts development. With the floor console development as an example, some optimization methods have been applied to the design with different stage. As the console design with optimization developed successfully, a new guideline came out to the plastic console development. It's with great meaning to the other plastic subsystem development on the vehicle. *Methodology* As optimization has been used very well on metal parts of vehicle, we apply these methods to the plastic parts for the first time, and design the floor console successfully. In this process, topology optimization, shape optimization and size optimization have been used properly with the design came to different stage. At first, topology optimization was used to find the load path and body\_join position; then, shape optimization or topology optimization was applied to find detailed structure design; and then, lightweight was done with gauge optimization. Every optimization has been run many times to find the best structure for the mathdata, until the design met the targets in the standard. *Result* With structure optimization applied on floor console development, the mass of floor console was reduced about 12 %. And a procedure which could guide floor console development successfully was come out. This procedure is not only used in console development, but also can apply to other plastic parts on vehicle, such as IP trim, door trim and pillar trim. *Limitation* In this paper, the floor console has reduced 1.3 kg in optimization, but only 1.0 kg mass has come true on the hard tooling model. This is because in optimization, not every parameter of injection molding

---

F2012-E05-009

---

R. Zhang (✉) · N. Cao · M. Luo  
Pan Asia Technical Automotive Center Co. Ltd, No 3999 LongDong Avenue,  
201201 Shanghai, China  
e-mail: ruiyan8407@163.com

can be set in software, and the ideal thickness CAE analyzed won't be realized in the injection molding. At the same time, many other parameters of the floor console design should be considered. So the mass reduction in hard tooling parts is not equal to that in optimization software. *Innovation and Conclusions* All the analysis shows that the optimization is effective and feasible on plastic system design. It is the first time to apply optimizations all through the console development successfully. The optimization flow can be a console design guideline. Also this process can not only guide the console development, but also other plastic subsystems. It's with great meaning to the development of automobile development and lightweight.

**Keywords** Optimization · Design guideline · Plastic · Development · Console

## 1 Introduction

Optimizations have been in application of automobile for a long time, such as topology optimization, size optimization and shape optimization [1], but most are in metal parts, except plastic parts. In this paper, the optimization was applied to the plastic systems of automobile; topology optimization was used to find the load path and connection to the body; gauge optimization was used to mass saving. Optimization is all through the plastic system development. It is the first time to apply optimization all through the plastic system development successfully, and it can be the guideline for that.

In this paper, optimization was applied to console system development. Console structure design is a very lengthy process within Automobile's development, so optimizations are accompanied throughout the whole process. When console design comes to different stages, optimization theories and process are different with the target changed. At concept design stage, topology optimization was helpful to find the load path of the system and the connection to the body structure. As the process came to the first generation of mathdata, the important performance requirements were analyzed to evaluate the elements of the design and the mathdata. If some performances did not meet the target, the second topology or shape optimization was done on the local structures. Based on the optimization result, the mathdata was updated for next stage. Then gauge optimization with mode, stiffness and fatigue load cases as constraints and minimum mass as objective were done to mass saving. After a few rounds, when the performance and mass came to a new balance, the optimization was over and the result was used to the final mathdata.

## 2 Optimization Theory

There are three main optimizations in Optistruct, topology optimization, shape optimization and size optimization. Each has different theory and usage [2].

Topology Optimization is a mathematical technique that produces an optimized shape and material distribution for a structure within a given package space. By discretizing the domain into a finite element mesh, Optistruct calculates material properties for each element. The Optistruct algorithm alters the material distribution to optimize the user-defined objective under given constraints [1].

Optistruct solves topological optimization problems using the density method. Under topology optimization, the material density of each element should take a value of either 0 or 1, defining the element as being either void or solid, respectively. So the material density of each element is directly used as the design variable, and varies continuously between 0 and 1; Intermediate values of density represent fictitious material. The stiffness of the material is assumed to be linearly dependent on the density. This material formulation is consistent with our understanding of common materials [1].

Topology optimization aims to seek the layout of the component and connection to other structures within an identified contiguous area to meet the constraints, such as stress and displacement constraints [3].

In Optistruct, gauge optimization is one of size optimization [4]. In size optimization, the properties of structural elements such as shell thickness, beam cross-sectional properties, spring stiffness, and mass are modified to solve the optimization problem [1].

In gauge optimization, the thickness of property is the design variable. For a gauge optimization of a shell structure, the design variable  $DV_i$  to property relationship is

$$T = DV_i$$

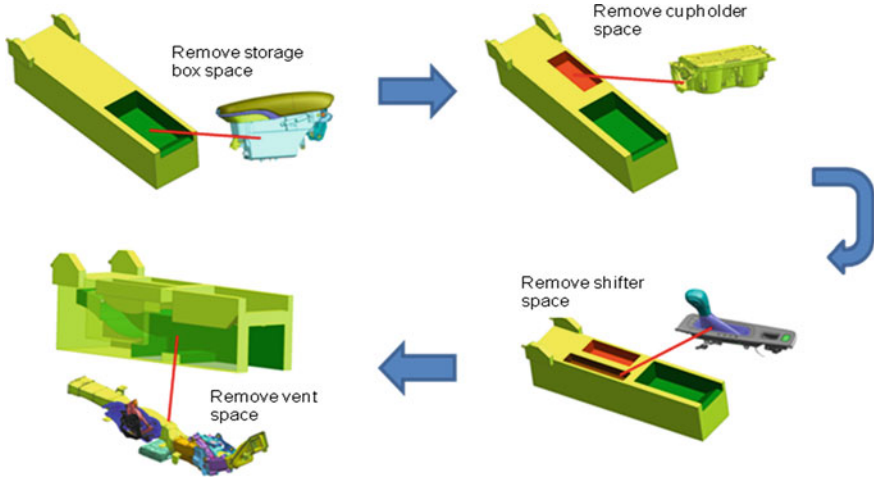
where the gauge thickness  $T$  is identical to the design variable [1].

## 3 Topology Optimization

### 3.1 Model Setup

#### 3.1.1 Design Optimization Space

For the console system in the concept design stage, only the console space and its subsystems' spaces are defined. In this console, the subsystems fixed to the console assembly included armrest and storage box, cup holder, shifter, blower and air conduction vent. So the optimization space could be confirmed and was created in



**Fig. 1** Optimization space design

the Hypermesh with full of solid elements. Follow shows the optimization space console model at this stage (Fig. 1).

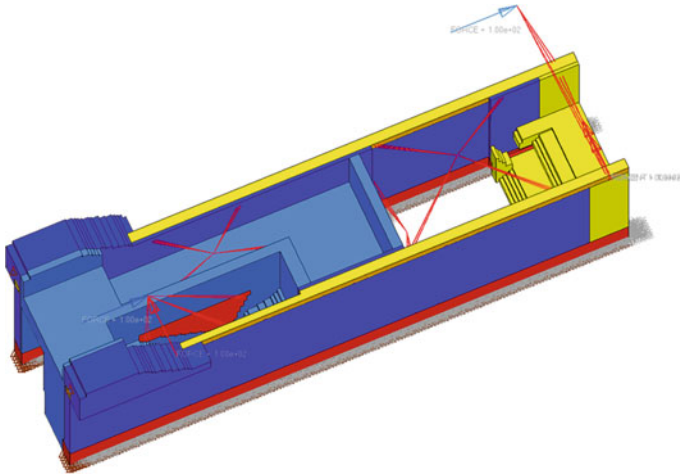
### 3.1.2 Design Constraints and Response

The constraints for topology optimization based on the core performances of the system. At this stage, the design constraints were defined as below:

- Disp. of armrest hinge and moment;
- Volume fraction;
- Shifter stiffness;
- Mode (1).

But before optimization, all analysis above of base model should be run first to acquire the base constraints for topology. According to the base values, ‘dconstraints’ of optimization should be defined properly. The last constraint is the volume fraction of optimization space. The volume fraction has to be determined for each of the topology design space [4]. The PSOLID card determines each topology space. In this optimization, each fraction of subsystem is 0.3 respectively.

All of the constraints are set in constraints subpanel, at the same time 10 % lower and upper boundaries were defined than the base model cases. So the variations could not be changed too much to affect other performances.



**Fig. 2** Topology optimization

### 3.1.3 Design Objective

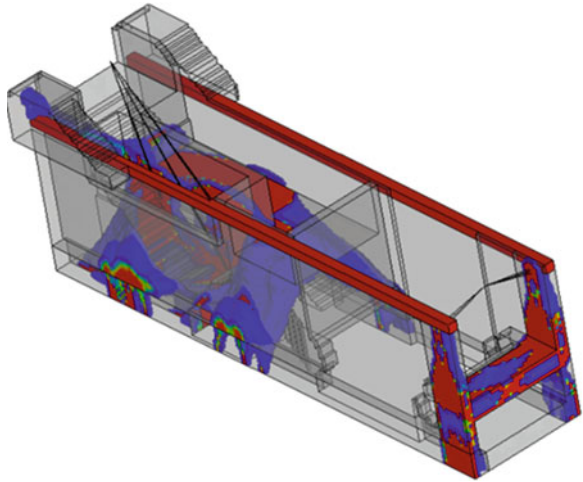
The objective for topology optimization is min.—mass. The mass includes all the parts in optimization space. So the mass of parts is more obvious and clear in each iteration of analysis. (Fig. 2).

### 3.1.4 Design Control Cards

As the design was modified throughout the development process, the order of the mode shapes could be changed. So mode tracking was necessary to this problem, and MODTRK = YES under the relevant parameters of control card. The other control cards, such as DENSITY card, usually the FORMAT and OPTION are chosen to be defined to output the density of topology result. DENSRES card is also defined to accompany with the DENSITY card.

	FORMAT	TYPE	OPTION
D E N S I T Y	H3D		YES

In GLOBAL\_OUTPUT\_REQUEST card, all the load-step’s results can be output. Such as DISPLACEMENT, STRAIN, STRESS and so on. Which parameter is needed to be output depends on the loadsteps which have defined in the loadcases.

**Fig. 3** Topology result

### 3.2 Post-Processing Results

Results can be viewed in Hyperview. On completion of topology optimization, all the topology elements will be divided equally into 10 layers, and the 1st layer is a volume fraction between 0.0 and 0.10. Typically the topology elements in the 9th and 10th layers are selected.

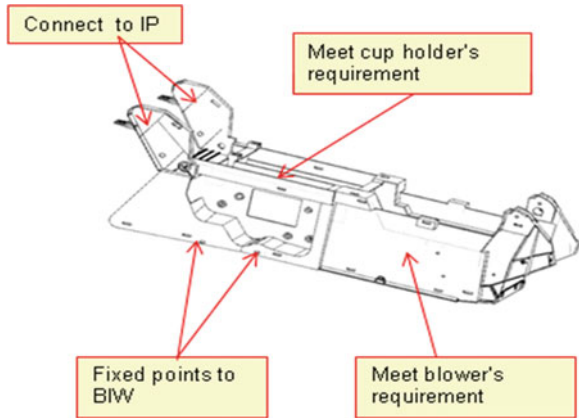
The picture shows the density of topology. Three colors were used to identify the material distribution, gray, red and blue. Obviously the main load path was located at the red path all through the structure. More important, more colors in deep. As in mathdata, this area was recommended to be defined as connections to other parts. Blue means sub load path was passed through. In mathdata, material distributed more and the thickness was higher than other areas (Fig. 3).

## 4 Mathdata

Based on the result, the first mathdata was developed. Described in the red area, steel frame was designed to the BIW except the wrapped trim. The blue area was developed to be thicker structures of plastic material than other area to support the subsystem. The gray area was developed based on the other subsystems that fixed to the console substrate. So the first mathdata was setup as (Fig. 4).

As the first mathdata was generated and completed. The design came to the next stage. In this stage, all the performances were analyzed to review the structure design. If all performances met the target, the structure was perfect; if not, then the local structure topology was done to advance optimize the console structure and the mathdata was updated as well.

**Fig. 4** Updated mathdata from topology result



## 5 Gauge Optimization

### 5.1 Model Setup

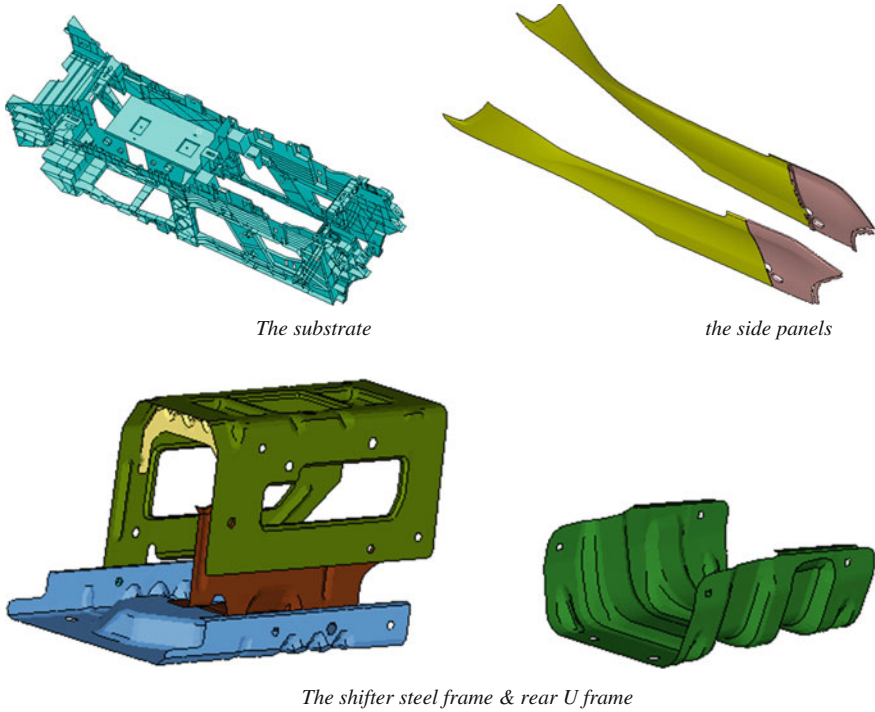
#### 5.1.1 Design Optimization Space

The purpose of this gauge optimization was mass saving and balancing the mass and performance, so the optimization space was not only the substrate, but also the console subsystem, and the objective was obviously the minimum mass of the console system.

In this stage, the optimization space was the whole console system, the side extension panels (both R.H. and L.H.), shifter steel sub frame, rear U-frame and the substrate. In these four parts, the materials of side panels and substrate were plastics and the shifter subframe and rear U frame were steel. The structure is shown (Fig. 5).

#### 5.1.2 Design Constraints and Response

In the Optistruct model, the substrate is partly organized to many components based on its thickness. In gauge optimization, the substrate was parted to be more components, which were from 24 to 93 components. As side panels, shifter steel frame and rear U frame, their thicknesses were clear, so the definitions were simple. As to the lower and upper boundary thicknesses of the properties of each component, it's different definitions with different constraints. Ribs on the substrate was defined from 0.5 to 2.5 mm, 0.1 mm increase of thickness per iteration for each increment; while the base substrate was defined from 2.5 to 3.5 mm, 0.1 mm increases as well.



**Fig. 5** Optimization space

So in the defined subpanel, the DDVAL should be defined for this request. Based on the model, the thickness of steel frame was from 1.0 to 3.0 mm, 0.1 mm increases per integration.

As a console system, there are almost 100 loadcases to test its performances. But not all can be used to define the optimization, so the most important cases are chosen to constraint the optimization. Here, load 900 N on the armrest, armrest stiffness in open, shifter stiffness and mode were defined as constraints to the optimization. As described above, 10 % lower and upper boundaries were defined for this optimization “dconstraints”.

### 5.1.3 Design Objective

As the optimization purpose, the objective was minimum mass of the parts which were defined in the optimization space.



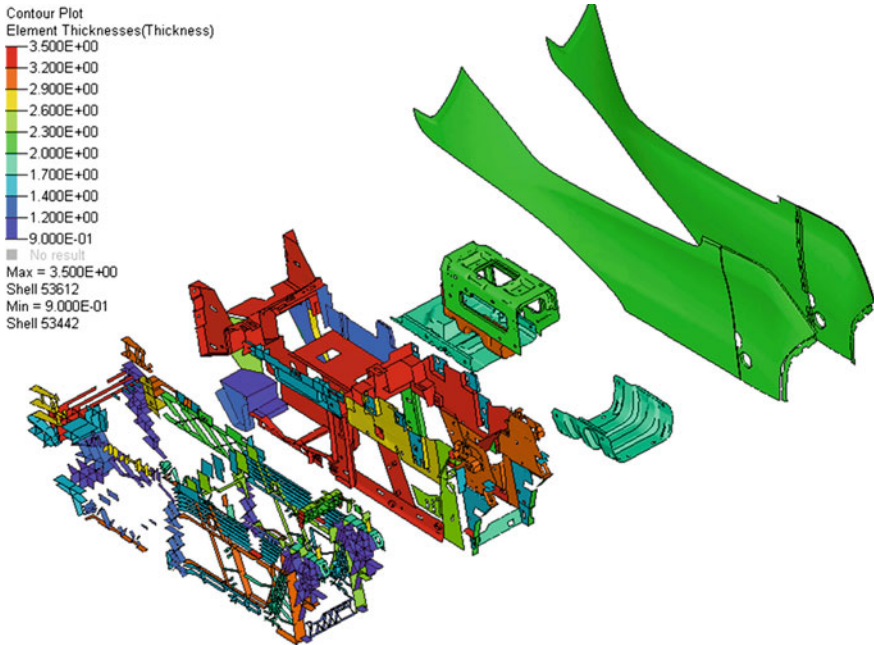


Fig. 6 Thickness after optimization

### 5.1.4 Design Control Cards

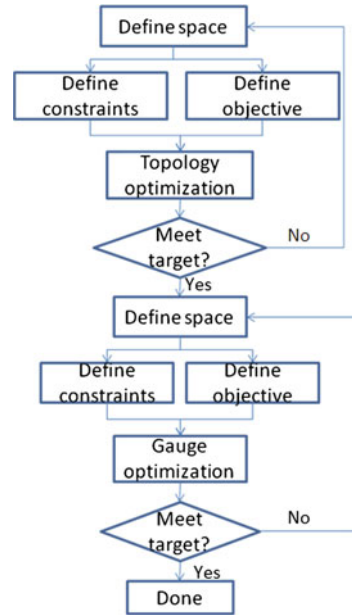
Most control cards defined for optimization were explained above; therefore only special cards for gauge optimization were described below.

The first card was SENSITIVITY [5]. The purpose was to request the output of the responses and sensitivities for design variables to a Microsoft Excel spreadsheet. There are six options to control the output, NONE, NO, YES, ALL, NOSTRESS and STRESS. Which is defined depend on the engineer's requirement [1].

## 5.2 Post-Processing Results

As gauge optimization is an exact analysis, the parts thickness can be detailed to 0.1 mm. Therefore in the result, the different thicknesses were shown by different colors. More thicken, more red darken colors. The thin parts were show as dark blue; while the most thicken parts were shown as bright red. More detailed thickness for each part, Query subpanel could be used in Hyperview. Also you could get the detail about per iteration from the out file (Fig. 6).

Fig. 7 Optimization flow



## 6 Mathdata Update

In this round of optimization, the optimization mass reduced from 8.1 to 6.7 kg, 1.3 kg is saving. Eventually, the mass and the performances came to a new balance. Based on the detailed gauge optimization, the mathdata could be revised. Considering the molding conditions and appearance requirements, small adjust should be done to the last mathdata. And this mathdata was used for the DV test to evaluate the performances of this console.

Actually, when this optimization is put into action, not all the results of thickness can be verified. This is because there are many other limitations, such as materials, temperature, molding conditions affect the products. So there is only about 1.0 kg reduced from the old model.

## 7 Conclusion

From the process of optimization on console development, the guideline can be abstracted as below (Fig. 7).

The first topology optimization is aimed to find the loadpath and connections to the body. So the optimization is rough and the result is abstract. But the load path is clearly enough to define the connections to the body. As the mathdata is done and most performances are meet the target, gauge optimization is helpful to mass

saving. Then the optimization comes to the next stage to lightweight. Elements with less contribution rate can be identified to remove, and the mass can be less than before.

It is the first time to apply optimization all through the console development successfully. So this process can not only guide the console development, but also other plastic subsystem. The optimization flow can be system design guideline.

All the analysis shows that the optimization is effective and feasible on plastic system design, and there's no precedent for optimization to plastic parts, so it's with great meaning to the development of automobile development and lightweight.

## References

1. Hypermesh help—RADIOSS, MotionSolve and Optistruct
2. Eschenauer, Olhoff (2001) Topology optimization of continuum structures. American Society of Mechanical Engineers
3. <http://forum.simwe.com/forum-150-4.html>
4. <http://forum.simwe.com/forum.php?mod=viewthread&tid=920875&highlight=gauge>
5. Bendsoe MP, Sigmund O Topology optimization theory, methods and Applications. Engineering Online Library

# Enhancing Vehicle Ingress/Egress Ergonomics with Digital Human Models

Nanxin Wang, Ksenia Kozak, Jian Wan,  
Gianna Gomez-Levi and Gary Strumolo

**Abstract** The ease of getting in and out of a vehicle (or ingress/egress) is one of the most important ergonomic issues for automotive manufacturers. It represents the first physical contact of a customer with a vehicle. A pleasant sensation while interfacing with the vehicle plays a vital role in vehicle purchasing decisions. Understanding and being able to assess vehicle ingress/egress performance early in a design process is therefore critical to a successful vehicle design. Conventional method relies on clinic research with physical bucks, which is a time consuming and pure subjective process. A new hardware-in-the-loop motion analysis system has been developed, which uses the latest motion capture, biomechanical and digital human modelling technologies to capture and analyse human motions as the driver or passenger interacts with a vehicle. The design assessment is provided in both subjective ratings and, for the first time, the physical data (e.g., swept volumes in CAD). The use of the system avoids costly seating buck builds and reduces engineering time and cost associated with both buck build and conducting the tests. Most importantly, it enables engineers to assess a vehicle's ingress/egress performances early in its design process, which will lead to better vehicle packages and better customer satisfaction.

**Keywords** Vehicle ergonomics · Ingress/egress · Motion capture · Biomechanics · Digital human modelling

---

F2012-E05-010

---

N. Wang (✉) · K. Kozak · J. Wan · G. Gomez-Levi · G. Strumolo  
Research and Advanced Engineering, Ford Motor Company, Dearborn, USA  
e-mail: nwang1@ford.com

## 1 Background

Vehicle package design is generally divided into the mechanical package design and the occupant package design. The occupant package design determines the occupant's spatial environment, including the location of the occupant with respect to the physical locations of components in the vehicle, as defined in SAE Motor Vehicle Dimensions J1100 [1] to achieve the most efficient and cost effective allocation of space that meet or exceed customer expectations.

Understanding how drivers/passengers move and interact with respect to a vehicle is critical to vehicle packaging design. A typical such motion/interaction includes, but is not limited to, opening/closing a door, getting in and out of a vehicle, buckling a seat belt, and reaching for a control dial on the instrument panel. It reveals how vehicle design affects the occupant accommodation and the usage of vehicle control and storage. Currently, evaluating whether or not sufficient space has been allocated for packaging is conducted using either the Programmable Vehicle Model (PVM) [2] or expensive static seating bucks. Once the PVM is setup or a seating buck is built, subjects need to be brought into perform assessments. It is a very subjective process since the decision on what constitutes a good or bad vehicle package design solely resides in a few experienced engineers. There are no satisfactory measureable standards or requirements. Deviations or late design changes are very common for vehicle package design.

### 1.1 *Static Seating Buck*

A static seating buck is a full size property of a vehicle interior seating area designed and built per design targets and assumptions for a vehicle. It is a physical prototype or buck that represents the design intent of a vehicle interior occupant package. In the early stage of a vehicle design process, rough shaped, less expensive surrogate seating bucks with carry over or baseline vehicle information are built for target setting and analysis (Fig. 1). As the design progresses, more detailed seating bucks are built for various packaging and ergonomics analysis and design sign-off. Toward the later stage in a vehicle design process, a more realistic seating buck is built for market research. They can provide more accurate feedback to the design teams and are more expensive to build.

### 1.2 *Programmable Vehicle Model*

“Programmable Vehicle Model” (PVM) [2] is an alternative to the static seating bucks that are typically used in the early stages of a vehicle design. A PVM is an articulated buck of a vehicle, which moves from one vehicle configuration to another via sliding panels and movable components that are actuated by software-multiplexed electric motors. It was first introduced in late 1980s by Prefix Corp. for market research studies in clinic settings. It has also been used for various

**Fig. 1** A sample seating buck



**Fig. 2** A Ford PVM



vehicle interior package studies [3]. Major shortfalls of these early generation PVMs include their lack of dimensional accuracy and lack of the ranges and flexibility to meet today’s automotive package design/appraisal needs.

In the mid-2000s, Ford developed a new generation of PVM [4], which is armature based with bidirectional connection to the vehicle package design in CAD (Fig. 2). This new generation of PVM provides the flexibility and accuracy that vehicle package design needs, while maintaining the fast setup timing of the original PVMs.

### ***1.3 Motion Capture Technology***

Motion capture technologies have been used in academia for biomechanical research, in the movie industry for animated films, and in the manufacturing

industry for simulating and planning operators' paths in the work environment. Commonly used commercial software includes Vicon [5] and Motion Analysis [6]. Motion capture technologies have also been used in vehicle design for various applications, such as vehicle seat belt usage [7], in vehicle reach [8, 9], and ingress/egress [10, 11]. For most of these applications, motions are captured in open space with little to no camera view obstructions. However, human motions with respect to the use of a vehicle are constrained by various vehicle components, for example, seat, steering wheel, instrument panel, door, etc., especially for the ingress/egress motions. It makes the motion capture for automotive applications very challenging. No existing methods or systems provide a systematic approach to incorporate motion capture tests and analysis in an integrated environment. Issues exist that prevent the effective use of this technology in vehicle packaging design:

- (1) It is very difficult to capture quality motion data using conventional seating bucks or production vehicles due to the fact that vehicle components obstruct camera views.
- (2) There is no link between the testing hardware, the cameras, the motions that can drive a digital human model, and the vehicle design in CAD.

### ***1.4 Digital Human Models***

There are several commercially available digital human models, for example, Ramsis [12], Jack [13] and Human Builder [14], which have been used for analyzing ergonomic tasks such as seated postures and sequence of assembly line operations. These digital human models all have surface representation of a human body and their own underneath kinematic representations for setting the joint angles of human body segments. Controlling the motions of a human body is traditionally conducted by setting the joint angles at several key postures and then interpolating the joint angles between them. The resultant motions are not realistic human motions, thus are not suitable for ingress/egress analysis. To overcome the shortfall, Jack offers an API for live connection with the motions captured in a motion capture system for example, Vicon. The motions can then be recorded in Jack for later use. Recently, Human Solutions announced a new tool that can take motion capture data and convert them into Ramsis motions.

## **2 Method**

The presented method uses the motion capture, biomechanical and digital human modeling technologies to capture and analyze human motions as the driver or passenger getting in and out of a vehicle. Key components of the method include:

- (1) A state-of-the-art motion capture lab with equipment that can be quickly changed to present various vehicle packages and can overcome the difficulty of capturing quality motion data due to camera view obstruction by vehicle components.
- (2) A software link between the testing hardware, the cameras, the motions that can drive a digital human model, and the design in CAD.
- (3) A method to analyze/visualize motions in CAD system using commercial digital manikins.

## ***2.1 Human Occupant Package Simulator***

The new Ford PVM [4], though it provides much needed accuracy and flexibility for vehicle packaging study, still presents too much blockage for cameras and thus is not suitable for motion capture. In order to capture quality real ingress/egress motions, a new system was designed and built based on the same design concept of the Ford PVM with unique features that are important for motion capture, for example, minimum structure that can still represent realistic vehicle packages, easy camera attachment, fixed floor as global referencing for both camera and mechanical systems, etc.

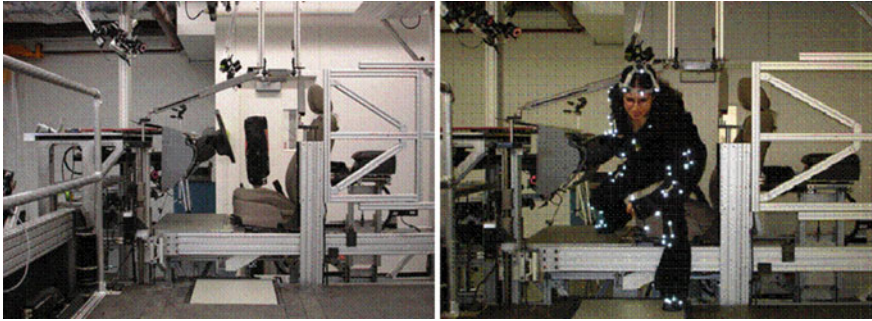
The new system, named Human Occupant Package Simulator (HOPS, Fig. 3), is a quarter PVM that can be quickly configured to represent driver or second and third row passenger compartments. Similar to the Ford PVM, HOPS is an armature system. It has a set of generic panels and components, and is capable of simulating vehicle packages with a wide range of dimensions and any combination of those dimensions. HOPS can also be mocked up with vehicle specific panels and components to represent a targeted vehicle package. Integrated in HOPS are 14 Vicon cameras, 3 force platforms, and a force sensor built into the steering column, which can capture an occupant's motion and record the forces exerted on the occupant's body during the motion.

The physical HOPS is a hardware-in-the-loop system. It is connected to its virtual representation in CATIA (VHOPS) for quick and accurate package setup. As illustrated in Fig. 4, VHOPS accepts input directly from vehicle packages, computes the necessary dimensions for HOPS setup and then sends them to the computer that controls the movement of the physical HOPS.

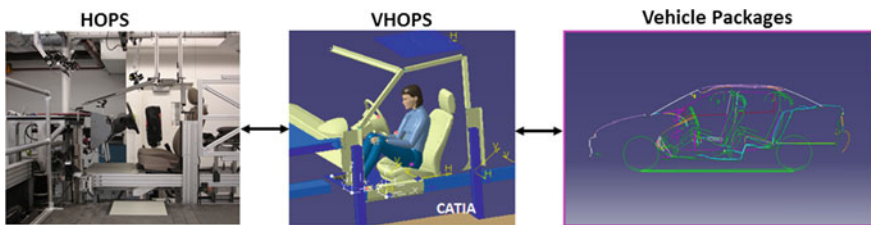
## ***2.2 Motion Capture and Digital Human Model***

Vicon Nexus system is used for motion capture and CATIA Human Builder is chosen as the digital human model. Whenever possible, multiple markers are placed on a body segment for increased possibility of marker presence on the body segment during a motion. For each test subject, 19 anthropometric measurements





**Fig. 3** HOPS (*left*) and a subject suited with markers (*right*)



**Fig. 4** Connections between HOPS and package design in CATIA

are taken, including weight, height etc. These measurements are used to scale the corresponding Human Builder manikins (Fig. 5). Since it is impractical to measure all 103 anthropometric dimensions Human Builder uses, the default values supplied by CATIA are used for the missing measurements.

Subjective questionnaires regarding the ease of getting in and out of a vehicle in the scale of 1–10 are also asked. The responses to the questionnaires together with the motion data captured are stored in a comprehensive motion database which is indexed by key vehicle dimensions and subjects' anthropometric measurements.

### 3 Application

A motion analysis and visualization tool is developed on top of CATIA, which enables engineers to:

- (1) specify a vehicle package of interest and the demographic target the vehicle intends to serve
- (2) retrieve the motion(s) from the database
- (3) generate motion animations using Human Builder in CATIA
- (4) visualize a single motion or motions of a demographic group in CATIA

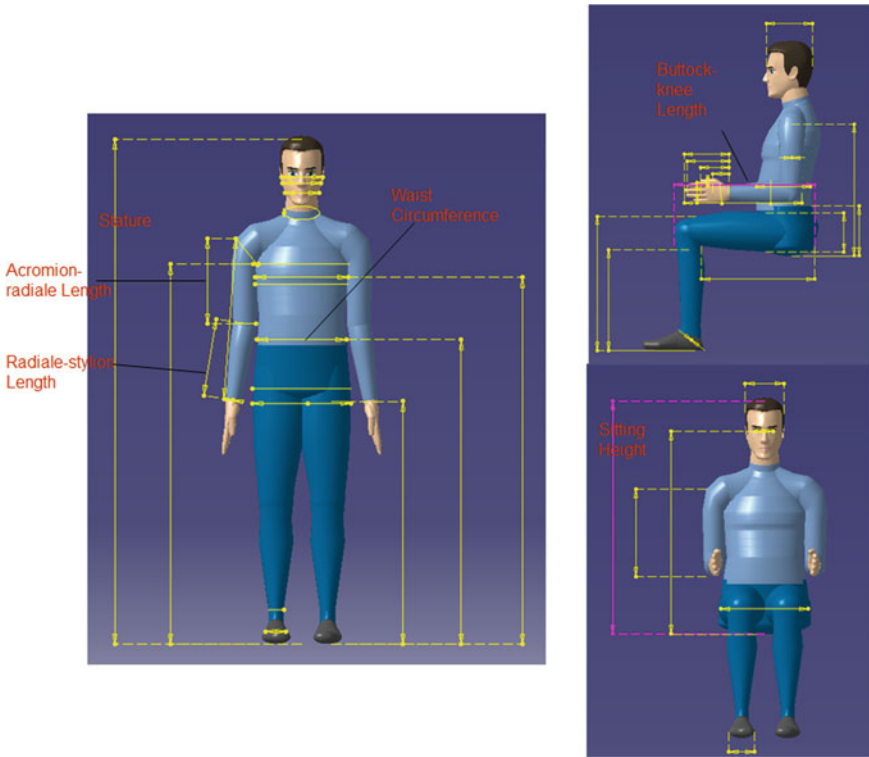


Fig. 5 Anthropometric measurements

- (5) calculate clearance and check interferences between Digital Human body segments (e.g. toe) and vehicle components (e.g. rocker sill of door opening)
- (6) generate swept volumes for selected body segments of a single motion or motions of a demographic group
- (7) identify the critical components that affect the motion
- (8) assess the impact of design changes.

Figure 6 depicts a typical application scenario. Once a vehicle package data is received, HOPS will be mocked up to represent the package, and then subjects will be recruited for the test. Motion data collected will be stored in a motion database for easy access. A user can choose to view the motions in the design environment or check specific postures of interest. Swept volumes can be generated for targeted body segments and interferences, if any, will be revealed.

The new system has been used in various vehicle applications, from analyzing foot swing to calculating head or knee clearances. The design assessment was provided in both subjective ratings and, for the first time, the physical data (e.g. swept volumes in CAD). It completely changed the decision making process from pure subjective driven to data driven.

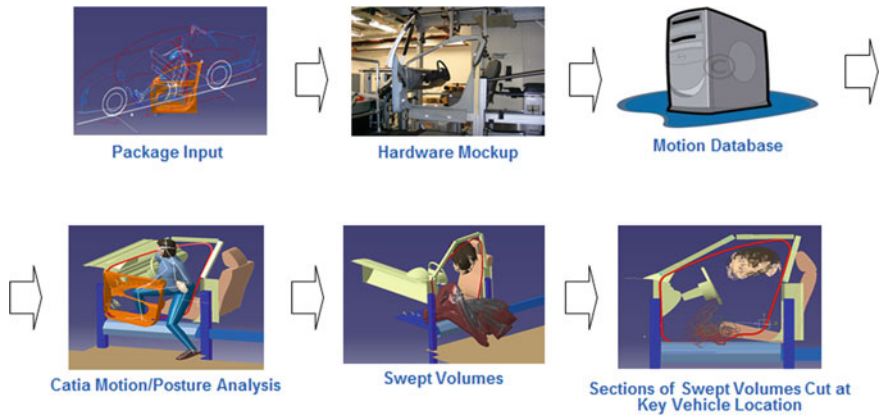


Fig. 6 An application scenario

## 4 Conclusion

A new integrated system has been developed for studying how drivers/passengers move and interact with respect to a vehicle, which is critical for vehicle packaging design. This system can be used, but is not limited to, opening/closing a door, getting in and out of a vehicle, buckling a seat belt, and reaching for a control dial on the instrument panel. It seamlessly integrates technologies of PVM, motion capture, digital human models, and package design in CAD. The system includes a state-of-the-art hardware-in-the-loop physical buck (HOPS) that can be quickly set to a target vehicle package, a motion capturing system that integrated in the HOPS with minimal camera blockage, and a software system that visualizes and analyses the captured motions using Human Builder in the native vehicle design environment in CATIA. It has been used to study ingress/egress performances for the design of multiple vehicles. The use of the system avoided costly seating buck builds and reduced engineering time and cost associated with both buck build and conducting the tests. Most importantly, it enables engineers to assess a vehicle's ingress/egress performance early in its design process. The captured motions and the swept volumes generated provide more objective data that better guide engineers with their designs, which leads to better vehicle packages and better customer satisfaction.

## References

1. SAE J1100 (2002) Surface vehicle recommended practice—motor vehicle dimensions
2. Programmable Vehicle Model, Prefix, <http://www.prefix.com/services.htm>
3. Richards A, Bhise V (2004) Evaluation of the PVM methodology to evaluate vehicle interior packages. SAE Technical Paper 2004-01-0370

4. Wang N, Kiridena V, Wan J, Gomez-Levi G (2006) Design and verification of a new computer controlled seating buck. DETC2006-99393 ASME International design engineering technical conferences and computers and information in engineering conference. Philadelphia, 10–13 Sept 2006
5. Vicon, <http://www.vicon.com/>
6. Motion analysis, <http://www.motionanalysis.com/>
7. Monnier G, Wang X, Verriest JP, Goujon S (2003) Simulation of complex and specific task orientated movements—application to the automotive seat belt reaching. SAE international conference and exposition of digital human modelling for design and engineering, Monreal, SAE Technical Paper 2003-01-2225, 17–19 June 2003
8. Reed M, Parkinson M, Chaffin D (2003) A new approach to modeling driver reach. SAE World Congress, Detroit, SAE Technical Paper 2003-01-0587, 3–6 Mar 2003
9. Wang X, Chevalot N, Trasbot J (2008) Prediction of in-vehicle reach surfaces and discomfort by digital human models. SAE Technical Paper 2008-01-1869
10. Dufour F, Wang X (2005) Discomfort assessment of car ingress/egress motions using the concept of neutral movement. SAE Technical Paper 2005-01-2706
11. Monnier G, Renard F, Chameroy A, Wang X, Trasbot J (2006) A motion simulation approach integrated into a design engineering process. SAE Technical Paper 2006-01-2359
12. Ramsis, Human Solutions, [http://www.human-solutions.com/mobility/front\\_content.php](http://www.human-solutions.com/mobility/front_content.php)
13. Jack, Siemens, <http://www.siemens.com/entry/cc/en/>
14. Human Builder, Dassault Systems, <http://www.3ds.com/>

# Preliminary Research on Muscle Activity in Driver's Steering Maneuver for Driver's Assistance System Evaluation

Ryouhei Hayama, Yahui Liu, Xuewu Ji, Takahiro Mizuno, Tomoyasu Kada and Liming Lou

**Abstract** The quantification of the driver's workload to complement the subjective evaluation is required in order to evaluate the driver assistant system. Preliminary investigation results of muscle behavior during steering maneuver have been described. The role and the feature of muscle activities in simulated steering conditions have been clarified. Driver tends to maneuver with "push steering" in both clockwise direction and counter-clockwise direction. Muscle alternation and co-contraction between the two muscles corresponding to the opposite one could be seen at the change of the torque directions. According to the result, the driver's steering workload might be estimated by evaluating the simultaneous activities of pectoralis clavicular and anterior deltoid of the both arms. The result of this research can be considered to be useful for the evolution of driver assistant system. Furthermore, it would contribute to spread the system and improve its performance. It might contribute to reduce traffic accidents as well.

**Keywords** Steering · Maneuver · Muscle activity · EMG · Driver assistance

---

F2012-E05-011

---

R. Hayama (✉) · T. Mizuno · T. Kada · L. Lou  
R&D Department, R&D Center, JTEKT Corporation, Aichi, Japan  
e-mail: ryouhei\_hayama@jtekt.co.jp

Y. Liu · X. Ji  
State Key Laboratory of Automotive Safety and Energy, Tsinghua University  
Beijing, China

## 1 Introduction

Various driver assistance systems [1–3] such as a lane departure warning system have been put onto the market. Especially, a function of driver's steering workload reduction has been required for the system. Subjective and sensory evaluation by the test driver is usually carried out for the workload evaluation. However it has a difficulty of reproducibility and reliability because the results are affected by test driver's sensibility. Therefore establishment of quantitative evaluation method for the workload is expected in order to improve their performances and to put these systems to practical use.

In this study, muscle behavior investigation during steering maneuver has been carried out in order to establish an estimation method of driver's steering workload. In the Sect. 2, a selection of muscles and measuring methods were described. Experimental results of the muscle activity in active steering maneuver were described in the Sect. 3 and the results in passive steering maneuver were described in the Sect. 4. And in the Sect. 5, some conclusions were described.

## 2 Muscle Activity Experiment

### 2.1 Steering Maneuver and Muscle Activity

In order to measure a muscle electromyography (EMG) signal [4] that could reflect the muscle behavior during steering maneuver, it is necessary to determine the key muscles which are involved in steering maneuver to generate steering torque. A published literature [5] has indicated some key muscles, including anterior deltoid, pectoralis clavicular, pectoralis sternal, posterior deltoid, middle deltoid, and triceps long head. And it has also been indicated that the muscles of the shoulder is likely to be important for generating steering torque. These results were used here. Furthermore, not only extension and flexion of the upper arm which are around the shoulder joint but also abduction, adduction, supination and pronation have been included based on kinesiology. Figure 1 indicates these muscle movements. Thus, biceps, teres major, and infraspinatus have been measured in addition to the muscles described above in this experiment.

### 2.2 Experimental Scheme

Table 1 indicates the steering maneuver considered in the experiment. Active steering means the steering maneuver for entering corner and returning from corner to straight driving, and passive steering means the steering maneuver which restrains the steering angle movement against to the external disturbance torque.



**Fig. 1** Upper limb motions round shoulder joint in steering

**Table 1** Steering maneuver considered in this experiment

Active steering maneuver	The steering maneuver for entering corner and returning from corner to straight driving
Passive steering maneuver	The steering maneuver which restrains the steering angle movement against to the external disturbance torque

The clockwise direction steering (hereinafter, CW direction steering) means the maneuver which adds the torque in the clockwise direction, and the counter clockwise direction steering which adds the torque in the counter clockwise direction (hereinafter, CCW direction steering). In this paper, the steering activities in active steering and passive steering by the right arm only and the both arms have been investigated. Table 2 shows scheme of their experiment.

### 2.3 Experimental Condition

The test subjects have been required to sit on a driver’s seat of a driving simulator, which includes a driver’s cab of passenger vehicle with steering system. The experimental scene is shown in Fig. 2. Reaction torque actuator equipped in the simulator can generate steering torque based on the calculation results of vehicle model in its controller. It is useful for evaluating the performance of driver assistance system included in advanced steering system such as a steer-by-wire system with vehicle dynamics control. In this experiment, only a function of steering torque control has been used.

The basic posture of test subject is shown in Fig. 3. The seat and steering wheel have been adjusted so that the upper limb was slightly bent at the elbow (approximately 110° between the forearm and upper arm). And the line along steering axis was approximately parallel to the line through the shoulder and wrist joints during holding at the 3 o’clock position by the right arm and at the 9 o’clock position by the left arm. The basic posture of the test subject was approximately the same as their driving environment and was easy to maneuver in the experiment. The electrode placements of EMG measurement are shown in Fig. 4.

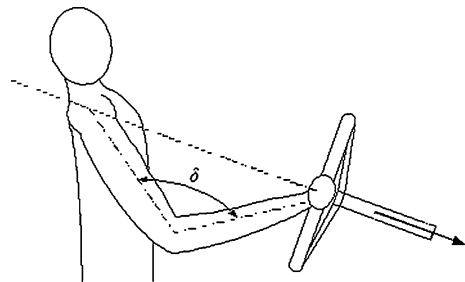
**Table 2** Experiment scheme

	By the right arm	By the both arms
Active steering maneuver	I	II
Passive steering maneuver	III	IV

**Fig. 2** View of the driving simulator experiment



**Fig. 3** Basic posture



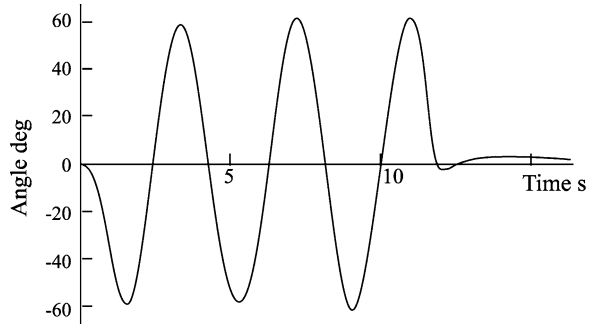
**Fig. 4** Electrode placements of EMG measurement



- |                          |                       |
|--------------------------|-----------------------|
| 1. Pectoralis clavicular | 6. Pectoralis sternal |
| 2. Anterior deltoid      | 7. Teres major        |
| 3. Middle deltoid        | 8. Triceps long head  |
| 4. Triceps lateral head  | 9. Posterior deltoid  |
| 5. Biceps                | 10. Infraspinatus     |



**Fig. 5** Input steering wheel angle in active steering maneuver experiment



**2.3.1 Experimental Conditions in Active Steering Maneuver (I, II)**

The test subjects were required to operate sine wave steering input with approximately 120° of steering wheel angle and 0.25 Hz of frequency as shown in Fig. 5. In an active steering experiment by the right arm (I) means a maneuver by the right arm only (the left hand was released from steering wheel).

**2.3.2 Experimental Conditions in Passive Steering Maneuver (III, IV)**

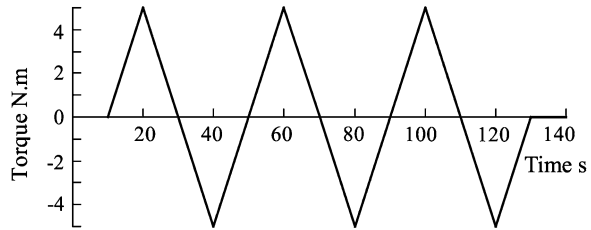
The test subjects were required to keep the steering wheel at the neutral position when the external disturbance torque was given by the driving simulator. The external disturbance torque was given by triangle wave with 10 Nm of amplitude and 0.025 Hz of frequency indicated in Fig. 6. The amplitude value has been settled with reference to the steering torque value in a normal driving of the vehicle equipped with a power steering system. The frequency value has been settled in a semi-static level in order to research preliminary activities of muscle. Experiment under dynamic condition of passive steering is the next issues. In a passive steering experiment by the right arm (III) means a maneuver by the right arm only (the left hand was released from steering wheel).

**2.4 Test Subject Selection**

Test subject has been selected according to the following guideline taking account of a possibility of the influence on the difference of the subject’s driving skill.

Group A:	Professional test drivers who have an experience of driving and evaluation skill training	7 persons
Group B:	Normal drivers	7 persons
Group C:	Inexperience drivers without enough skill.	6 persons

**Fig. 6** External disturbance torque from the driving simulator



### 3 Experimental Results of Active Steering Maneuver

#### 3.1 Active Steering Maneuver by the Right Arm (I)

An example of the experimental results is shown in Fig. 7. The horizontal axis shows the time and the vertical axis shows steering torque and EMG signal of pectoralis clavicular, anterior deltoid, middle deltoid, posterior deltoid, triceps long head, triceps lateral head, infraspinatus, biceps, pectoralis sternal, and teres major from the top. The positive value of steering torque means the CW direction torque and the negative value means the CCW direction torque. Each EMG signal has been filtered by a band pass filter between 15 and 500 Hz, and calculated by root-mean-square value of 100 samples. The measured muscles have been categorized in the next three kinds by their role. Anterior deltoid, pectoralis clavicular and infraspinatus are the main agonist when CCW direction steering torque is generated. Triceps long head is the main agonist when CW direction steering torque generated. Teres major is the neutralization muscle. The result is shown in Table 3. Additionally, it has been confirmed that these result was no influence by the test subject's driving skill according to the statistics analysis of the experimental result of 20 subjects.

#### 3.2 Active Steering Maneuver by the Both Arms (II)

The 10 muscles of each arm (right arm and left arm) of 1, 2, 7, 8 and 9 in Fig. 4 which were relatively active in the active steering maneuver by right arm (I) have been measured. An example of EMG signal (subject group A) for the steering torque in the experiment is shown in Fig. 8. The left graph means the left arm's value in steering by both arms and the central graph means the right arm's value in steering by both arms. Pectoralis clavicular (a), anterior deltoid (b), posterior deltoid (c), triceps long head (d) and teres major (e) of the muscle activity are shown from the top to the bottom. The results of the right arm in active steering maneuver by the right arm only (I) are shown in the right graph for the reference.

Focusing in positive value of the steering torque (CW direction steering), triceps long head (d) and teres major (e) were very active in steering by the right arm

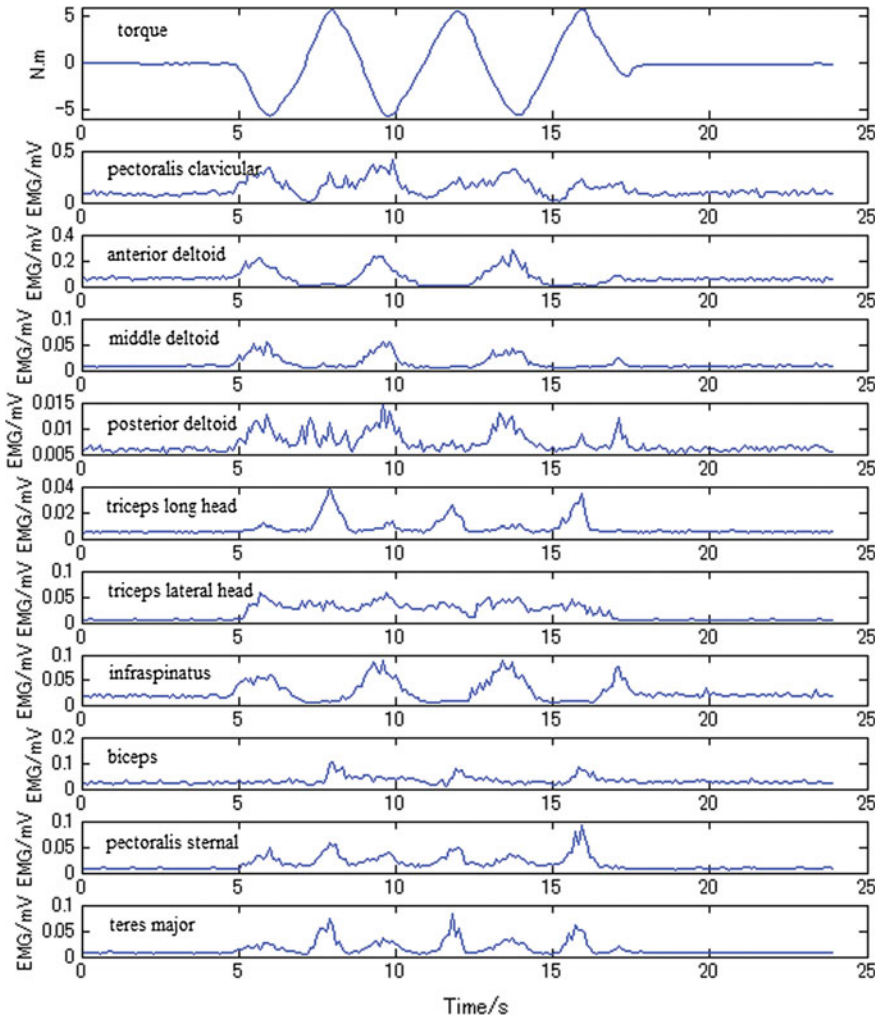


Fig. 7 Skilled driver's EMG signals of active steering maneuver by right arm only

only (right graph of Fig. 8). On the contrary, steering by the both arms which was added the left arm muscle activity, the muscle activities of (d), (e) of the right arm (the central graph of Fig. 8) were small, and those of pectoralis clavicular (a) and anterior deltoid (b) of the left arm (left graph of Fig. 8) were large. Therefore, the agonist in CW direction steering by the both arms would be (a) and (b) of the left arm.

As in negative value of the steering torque (CCW direction steering), (a) and (b) were very active in steering by the right arm only (right graph of Fig. 8). And in steering by the both arms, (a) and (b) of the right arm (the central graph of Fig. 8)

**Table 3** Classification results of muscles' roles in steering maneuver by right arm only

Role	Muscle
CW agonist	Triceps long head
CCW agonist	Pectoralis clavicular
	Anterior deltoid
	Middle deltoid
	Posterior deltoid
	Infraspinatus
Neutralization muscle	Pectoralis sternal
	Triceps lateral head
	Biceps
	Teres major

were active similarly. Therefore, the agonist in CCW direction steering by the both arms would be (a) and (b) of the right arm.

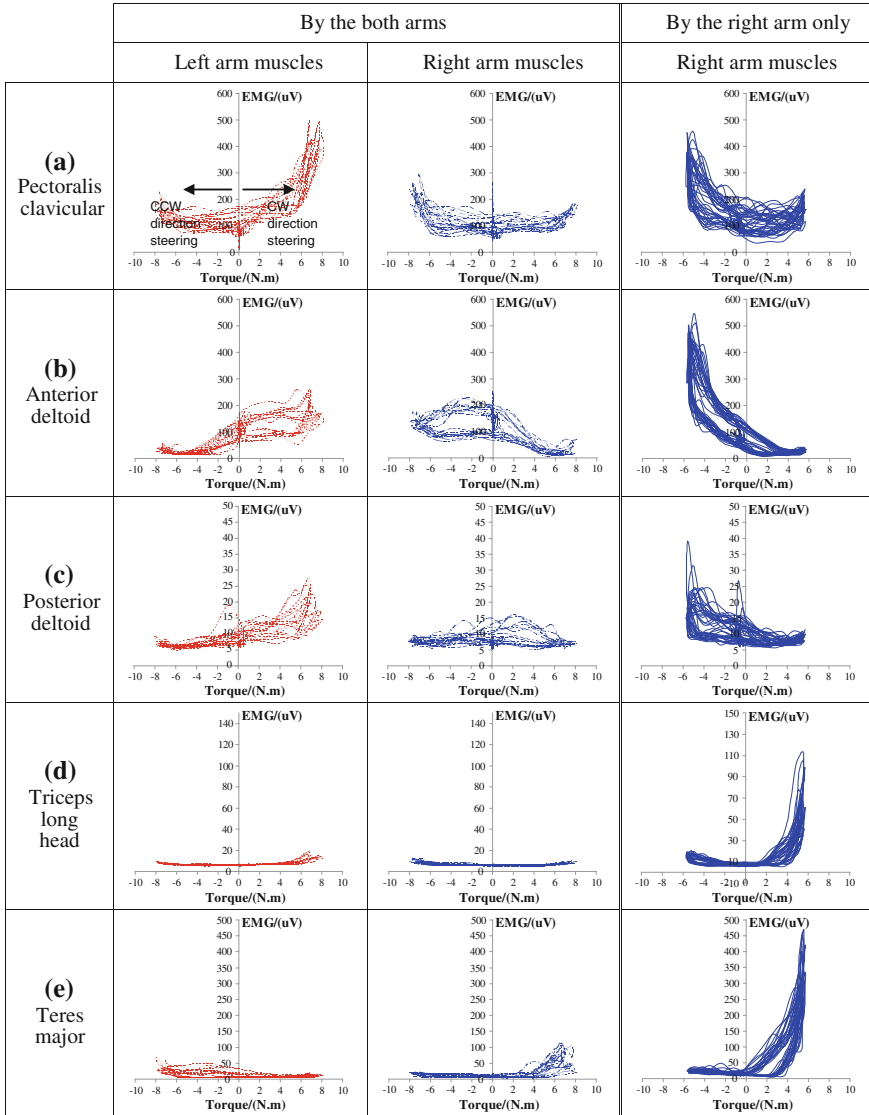
Based on the experimental results, in case of defining of CW direction steering by the left arm and CCW direction steering by the right arm as the “push steering” and CCW direction steering by the left arm and CW direction steering by the right arm as the “pull steering”, “push steering” seems to be essential in case of active steering operated by the both arms in CW direction steering and in CCW direction steering.

## 4 Experimental Results and Considerations of Passive Steering

### 4.1 Passive Steering Maneuver by the Right Arm (III)

An example of the experimental results is shown in Fig. 9. The horizontal axis shows the time and the vertical axis shows steering torque and EMG signal of biceps, anterior deltoid, middle deltoid, pectoralis clavicular, infraspinatus, triceps lateral head, triceps long head, posterior deltoid, pectoralis sternal, and teres major from the top. In the maneuver of CW direction (from 15 to 25 s, from 45 to 60 s, from 85 to 105 s in Fig. 9), triceps long head, triceps lateral head, posterior deltoid and teres major have been largely activated. On the other hand, in case of CCW direction (from 25 to 45 s, from 65 to 85 s, from 105 to 125 s in Fig. 9), anterior deltoid, middle deltoid, clavicular portion of pectoralis major, infraspinatus and teres major have been largely activated.

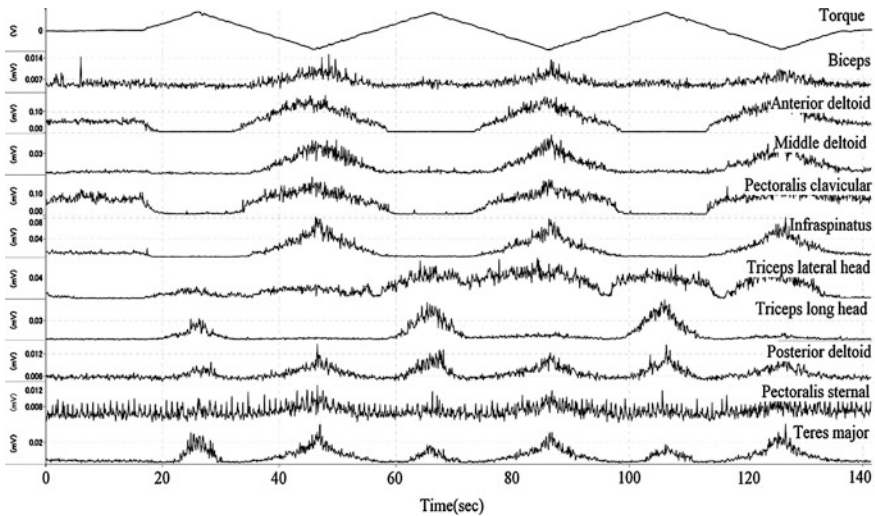
Additionally, it has been confirmed that these result was no influence by the test subject's driving skill according to the statistics analysis of the experimental result of 20 subjects.



**Fig. 8** Comparison of muscle activities in active steering

### 4.2 Passive Steering Experiment by the Both Arms (IV)

The 10 muscles of each arm of 1, 2, 7, 8 and 9 in Fig. 4 which were relatively active in the passive steering experiment by the right arm have been measured. An example of EMG signal (test subject group A) corresponding to the steering torque in the experiment is shown in Fig. 10. The left graph means the left arm's value in



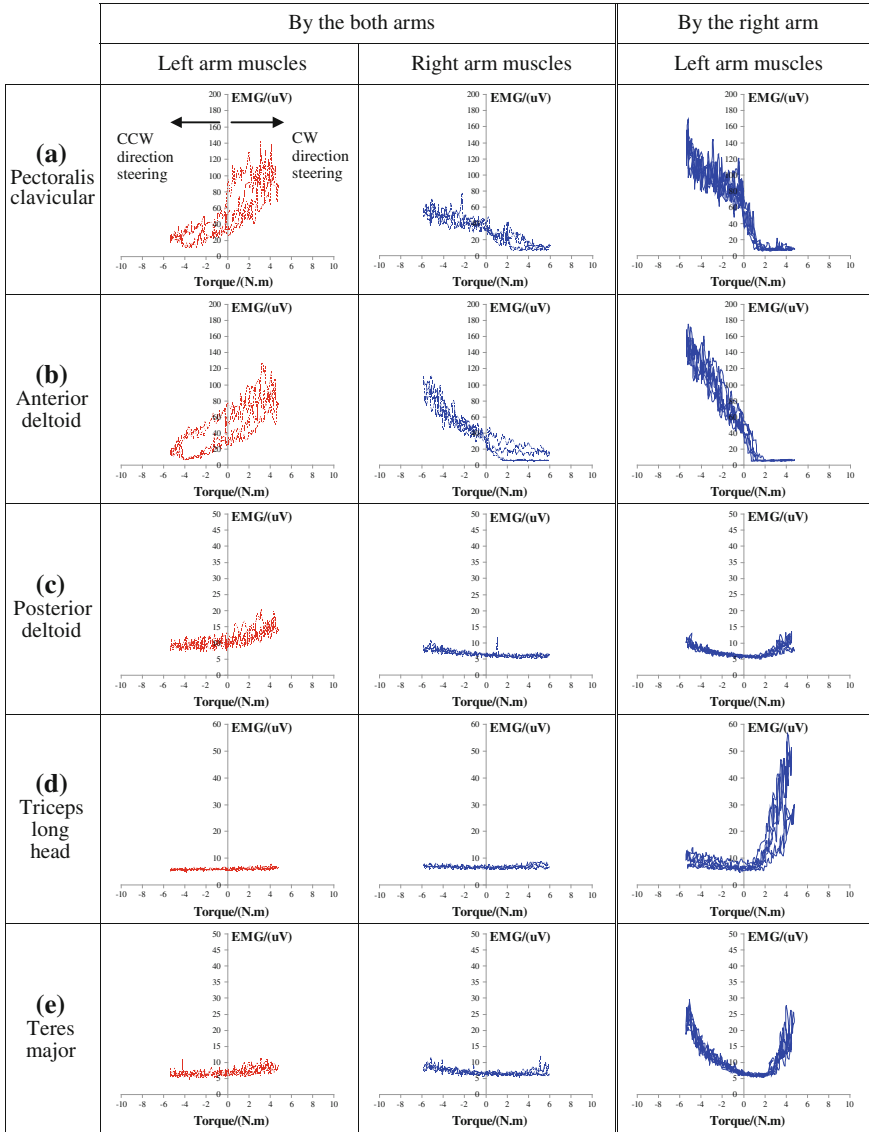
**Fig. 9** Example of EMG signals in passive steering maneuver by right arm only

steering by the both arms and the central graph means the right arm's value in steering by the both arms. Pectoralis clavicular (a), anterior deltoid (b), posterior deltoid (c), triceps long head (d) and teres major (e) of the muscle activity are shown from the top to the bottom. The results of the right arm in steering by the right arm only (III) are shown in the right graph for the reference.

In positive value of the steering torque (CW direction steering), triceps long head (d) and teres major (e) were very active in steering by the right arm only (right graph of Fig. 10). On the contrary, in case of steering by the both arms, the muscle activities of (d), (e) of the right arm (the central graph of Fig. 10) were small, and those of pectoralis clavicular (a) and anterior deltoid (b) of the left arm (left graph of Fig. 10) were large. Therefore, the agonist in CW direction steering by the both arms would be (a) and (b) of the left arm. This result is similar to the case of active steering by both arms (II).

Contrary in negative value of the steering torque (CCW direction steering), (a) and (b) were very active in steering by the right arm only (right graph in Fig. 10). And in steering by the both arms, (a) and (b) of the right arm (the central graph of Fig. 10) were very active similarly. Therefore, the agonist in CCW direction steering by the both arms would be (a) and (b) of the right arm similar to in active steering by both arms (II).

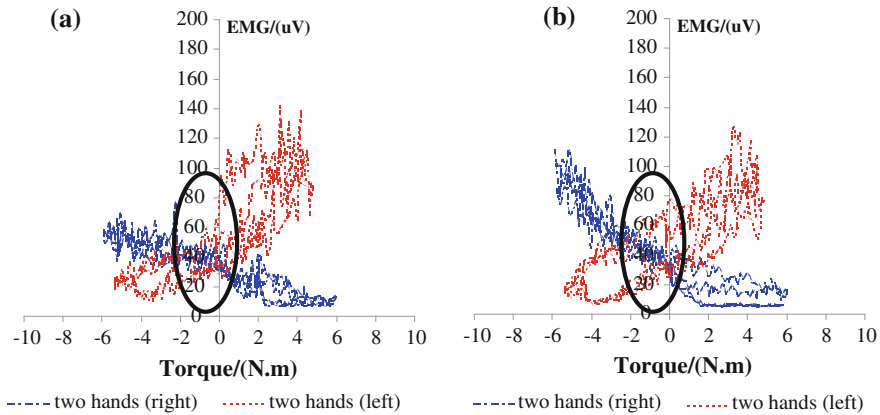
Based on the experimental results, “push steering” seems to be essential in both CW and CCW direction steering. This result is similar to the case in active steering by the both arms (II). Thus, the agonist might be alternated at the change of steering direction. Figure 11 shows the result (a) overlaid on (b) of Fig. 10 in order to confirm the above assumption. The gradually interchange of the CCW agonist and CW agonist and simultaneous activities of counter-muscles can be seen in the



**Fig. 10** Comparison of muscle activities in passive steering

period where steering wheel torque is nearby 0 Nm. Thus, the following activities might be happen.

- Pectoralis clavicular (a) and anterior deltoid (b) of the both arms generate counterbalanced torque.



**Fig. 11** Overlap of left and right arms muscles. **a** Pectoralis clavicular. **b** Anterior deltoid

- Driver generates axial force on steering wheel along with the steering column shaft direction. (Based on the force direction of the muscle in view of kinesiology)
- These muscles are strained.

Even in any case, these muscle activities have a possibility to be a cause of the decrease of steering efficiency, because they are negative effect to steering wheel rotation. According to the result, the evaluation of the simultaneous activities of pectoralis clavicular (a) and anterior deltoid (b) during steering maneuver by the both arms can be considered to be useful for estimating of driver's steering workload.

## 5 Conclusions

The role and the feature of muscle activities during active and passive steering maneuver have been investigated using a driving simulator in order to establish a driver's workload estimation method which will be required to evaluate a driver assistant system for steering function. According to the result, "push" and "pull" steering have been operated corresponding to the steering direction in case of steering maneuver by right arm only. And in case of steering maneuver by both arms, the main operating muscle to give a "push steering" has been switched positively from left to right according to the steering direction.

- In case of active steering and passive steering by the right arm only, anterior deltoid, pectoralis clavicular, infraspinatus of the right arm is the agonist for generating the CCW direction steering torque and triceps long head of that is the agonist for generating the CW direction steering torque.



- In case of active steering and passive steering by the both arms, pectoralis clavicular, anterior deltoid, posterior deltoid of the left arm is the agonist for generating the CW direction steering torque and pectoralis clavicular, anterior deltoid, posterior deltoid of the right arm is the agonist for generating the CCW direction steering torque. Moreover, the activity of triceps long head and teres major of right and left arm are small at this time. The “push steering” is main maneuver in steering by the both arms.
- In steering by the both arms, the agonist interchanges in CW direction steering and CCW direction steering, and simultaneous activities occur in the period of interchanging. The driver’s steering workload is considered to be presumed by evaluating the simultaneous activities of pectoralis clavicular and anterior deltoid.

The results of this research can be useful for the establishment of the evaluation technology of driver workload, and are considered to contribute to the evolution of driver assistant system in the future.

## References

1. Shimizu Y, Kawai T, Yuzuriha J (1999) Improvement in driver-vehicle system performance by varying steering gain with vehicle speed and steering angle. SAE Paper, No. 1999-01-0395
2. Hankovszki Z, Kovacs R, Palkovics L (2010) Active steering enhanced ESP for commercial vehicles. AVEC2010, p 1
3. Rieth PE, Schwarz R (2004) ESCII—ESC with active steering intervention. SAE Paper, No.2004-01-0260
4. Cole DJ (2008) Steering feedback mathematical simulation of effects on driver and vehicle. ATZ Autotechnol 8:2–6
5. Pick AJ, Cole DJ (2006) Measurement of driver steering torque using electromyography. Trans ASME 128:960–968

# Color TFT Instrument Clusters in the Chinese Market

Huibin Li, Gerhard Mueller, Karl Reich and Leo Glasenhardt

**Abstract** In recent years a strong, worldwide trend towards high resolution displays with photorealistic graphics has been observed in instrument clusters. This trend is also observed in China, although it lags some years behind Europe. Additionally, there is another trend in China, namely, color TFT displays with fewer or even without animations, since the cost pressure in China is very high and the OEMs are not yet ready for complicated animations. To master this challenge Continental has developed a hardware/software platform which is scalable to support color TFT displays with different sizes and different animation levels. Furthermore Continental as a global player has an international engineering footprint and thus offers local engineering support in combination with optimized development cost.

**Keywords** Color TFT · IC (instrument cluster) · FPC (free programmable instrument cluster) · Cost sensitive HMI solution · Animations · Photo realistic graphics

## 1 Situation and Challenge

Two major technical trends have been observed in the last years which have a dramatic impact on the development of information systems for vehicle cockpits.

---

F2012-E05-012

---

H. Li (✉)  
Continental Automotive (Wuhu) Ltd., Wuhu, China  
e-mail: Huibin.Li@Continental-Corporation.com

G. Mueller (✉) · K. Reich · L. Glasenhardt  
Continental Automotive GmbH, Regensburg, Germany

First, new technologies foster the development of Advanced Driver Assistance Systems generating a rapidly increasing amount of information which needs to be presented to the driver. New information sources arise starting from in vehicle ECUs like navigation systems and ranging up to information even from the internet. Second, with the rise of the iPhone users of smart-phones and other consumer electronics products get used to photorealistic graphics in a quality formerly only available on PCs.

Driven by those trends, displays in the vehicle cockpit like instrument clusters become larger, with higher resolution, and grow from segment and monochrome dot matrix displays to color TFTs. In Europe and in the USA we even see full size display clusters (Free Programmable Instrument Clusters (FPCs) with display sizes up to 12.3 in) without mechanical pointers and physical telltales.

A closer look at the Chinese OEMs shows that we expect that the introduction of color TFT displays in the higher value classes, such as the C, D and E segment, will start in 2014 (possibly end of 2013). The portion of Instrument Clusters with TFTs will then increase rapidly. The A and B segment will follow in 2016. In addition we expect that full display Free Programmable Clusters will enter the D and E segment of the Chinese OEMs.

This situation presents two challenges to the automotive industry.

- The flow of information has to be managed effectively in order to present only the information to the driver which is needed in the current driving situation.
- For the automotive market in general, but even more for the emerging markets, cost effective technical solutions have to be developed.

## 2 Information Management

The layout of the overall HMI system of the cockpit is of crucial importance in order to present information to the driver in an ergonomic way and to support him in his task to safely guide the vehicle through the traffic. In modern cars the traditional mechanical input systems are supported by new technologies like sensitive multi-touch surfaces, character recognition, active tactile feedback and camera based gesture recognition. Among the various feedback possibilities of a multimodal HMI system the visual channel yields the best way to inform the driver in an intuitive way. Possible visual output media in the vehicle cockpit are the instrument cluster, head-up display and secondary display of the head-unit (Fig. 1).

The head-up display is in the primary view of the driver. It generates a virtual image via an optical system in a short distance in front of the windshield—as an overlay to the street—and visible to the driver only. It also allows a short accommodation time of the eye. Therefore the head-up display is the ideal place to show information which either requests an immediate action by the driver (e.g. warning messages), which needs permanent monitoring by the driver (e.g. the velocity) or which is related to the road (e.g. turn by turn navigation information).



**Fig. 1** Multimodal HMI solutions

The cluster instrument as well being in the primary view of the driver is used to display information which is needed frequently by the driver. Examples are board computer and speedometer. With the introduction of large area and high resolution color TFT displays it is possible to support the driver with a more intuitive understanding of assistance systems. New features are photorealistic graphics, pseudo-3D information and large scale animations.

For a look on the head-unit the driver is distracted from his primary view to the road. Therefore secondary displays are mainly used for comfort functions, infotainment and complex HMI operations.

The main tasks in the design of a visual HMI system include information distribution and information management. Information is assigned to the various displays according to their priority with respect to the current driving situation [1]. For a night vision with pedestrian recognition for example the information management methodology advises to show an abstract warning in the head-up display while the instrument cluster shows the high resolution night vision video with the detected pedestrian.

## **3 The Continental Approach**

### ***3.1 Platform Development***

Continental has defined a controller platform which covers the instrument cluster range from the basic to the premium segment. Through volume grouping an economical and competitive system solution can be achieved. The Continental hardware platform is accompanied by a software platform which guarantees by its inherent software reuse the reduction of development cost and an increase in software quality. Both hardware and software platforms are highly scalable.

### 3.2 *Graphical Features and Technical Solutions*

For the graphics solution the feature-driven clusters at the high end of the spectrum and the cost-driven clusters at the lower and middle range have to be distinguished.

For the feature-driven upper end of the spectrum, the challenge is to cover the customer requirements with a still affordable single-chip graphics solution. Customers are expecting performance similar to the most current consumer electronics solutions. The development cycles and the lifetime expectations in the consumer area are however quite different from those in the automotive area. Nevertheless, the hardware solutions in this range are becoming more and more similar to those in current tablet computers. There is still quite a difference to a desktop PC. Whereas in a PC there are dozens of memory (RAM) chips especially on the graphics cards, only two or four will be available for a high-end cluster ASIC. This is the most severe limitation, because the high-resolution displays require a lot of memory bandwidth which can only be obtained by the parallel usage of many chips.

Some of the features customers expect in the FPC range are a photo-realistic appearance showing:

- Real 3D models of the car to display e.g. driver assistance scenarios
- Large scale transparency with many layers to give the impression of depth
- Mimicking real material like metal, glass or even water and steam on the display
- Video overlays showing content from a head unit or driver assistance system (e.g. night vision)
- Unique to the FPC clusters are the very demanding display of animated graphical pointers, which need always to be shown at the full display refresh rate (60 Hz or even faster)
- Reconfigurable views for different driving situations or driver preferences

On the lower end, customers still want to see high quality content, but are willing to accept compromises for better cost. It can even be acceptable to limit the number of colors to just a palette of 256 values. In this case real transparency is not possible—it requires much more processing power and also more memory. With a clever approach such a limitation will fortunately not be visible to the end customer. Also, advances in semiconductor technology will soon allow also provide low-cost ASICs specifically for instrument clusters with high-color rendering up to display sizes of WVGA (Fig. 2).

Features expected in this range are:

- High-quality anti-aliased text
- Color icons
- Simple Animations created by e.g. sequences of pictures, moving text or icons etc.
- Limited transparency showing only a few layers



Fig. 2 Different views of a free programmable cluster prototype

Even though the two ends of the spectrum require very different solutions, the goal of an optimal performance is common to both. It requires a very deep understanding of the graphics hardware architecture in order to get the best usage by software. Continental Automotive as the world-wide market leader in instrument clusters is even driving the requirements for the development of new generations of ASICs for instrument clusters for the Continental hardware and software platforms.

The graphics rendering software employed in the software platforms is highly scalable: It extends from a CPU renderer for a low-cost display solution to multi-GPU real-time graphics for the high-end Free Programmable Cluster instruments. A strong emphasis is on optimal storage of the graphical resources like bitmaps, texts and fonts in special compressed formats. The generation of these graphical resources is tightly integrated in the HMI tool chain.

### 3.3 HMI Development Process

With the extension of graphical features and the growing complexity of visual- and dynamic HMI behavior, model driven HMI technologies have been introduced into the software development for instrument clusters at Continental.

Besides technical challenges the development of HMI centered projects also demands a new look at the classical software development process. Requirements are often not supplied in text format but modeled by using a tool environment. The developments at the OEM and at the supplier are strongly interleaved. The development cycles get shorter. To cope with these changes the methods, processes and tools have to be adopted: a change from quarterly deliveries to weekly builds supported by a continuous integration, automated system testing and the introduction of agile development methods is necessary (Fig. 3).

The development of user interfaces for embedded automotive devices is a sequential and incremental process, which incorporates the collaboration of a couple of HMI experts and HMI specific tools. In a very early stage of the HMI product development cycle, screen designers, interaction designers and ergonomists will generate the HMI core concepts for the product. In this phase, the

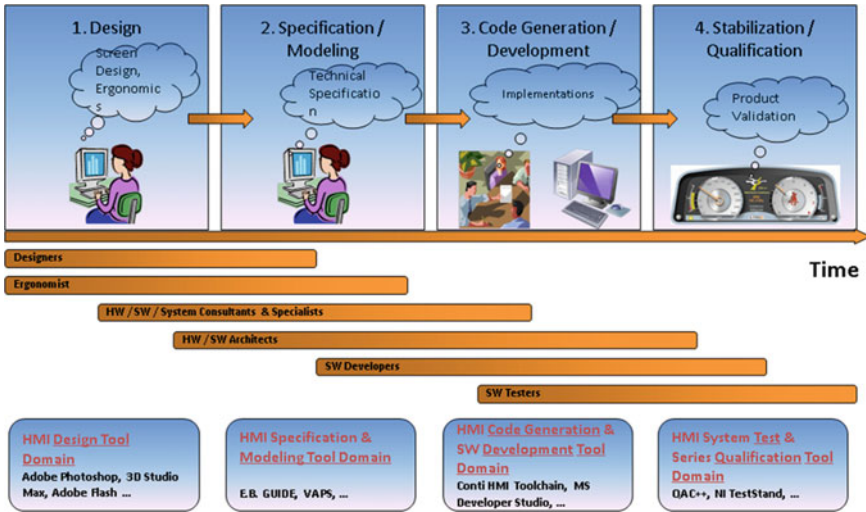


Fig. 3 HMI development process

consultation of system experts and system architects is of major importance. They permanently will have to analyze the requirements and align them with the system costs. As an example, the way of usage and also the complexity of animations can impact the hardware costs by multiples. Once the core HMI concept has been agreed, the detailed product development phase starts, which includes the specification, the implementation and the product validation. Within these phases, hardware-, software developers and testers are involved.

Within each development domain, specialized tools are available, which in general can be inter-connected by exchanging the work results via tool specific export- and import functions. In practice, the work results of the design domain are typically reduced to Adobe Photoshop/Adobe Flash artifacts and the work results from the specification phase are reduced to PDF formatted MS Word documents, which illustrate and verbally describe the screens and the HMI behavior. At this point, the degree of automation can be strongly increased by replacing the PDF documents with HMI model databases. The HMI specification directly can be implemented with an HMI modeling tool, which generates the model database. Typically modeling tools are also capable to import artifacts from design tools, to export the HMI model into a code generator and to simulate it in the PC environment.

Continental offers to their customers all required experts for each development phase: from the HMI design phase until the final product validation phase. With the ARTEMMIS HMI tool chain solution (see below), Continental additionally can offer technical services, which help to increase the degree of automation of the HMI development process and to decrease product development costs.

### 3.4 HMI Technical Solutions

The absence of HMI development standards and a wide spectrum of off-the-shelf HMI embedded target solutions make it difficult to find a cost effective hardware/software solution, which fulfils the customer demands.

To cope with these requirements, Continental has developed a scalable HMI platform, called ARTEMMIS. It supports projects ranging from low-cost display solutions up to high-end Free Programmable Cluster instruments. The ARTEMMIS HMI software architecture is designed to drive cluster instruments, head-up displays and secondary displays as integral part of the interior of a vehicle. It has capabilities for corporate OEM designs and a unique presentation among the different devices. In order to build cost-optimized solutions, ARTEMMIS offers a high bandwidth of feature- and hardware scaling capabilities, which ranges from low-end to premium class devices.

The ARTEMMIS architecture is divided into three major functional blocks. All three entities together build the ARTEMMIS HMI tool chain with an HMI model as its input and the executable for the target device as the output of the chain [2].

- (1) Model Cross-Compiler
- (2) ARTEMMIS HMI Language and HMI Language Compiler
- (3) ARTEMMIS HMI Framework

By means of the Model Cross-Compilers approach, the ARTEMMIS tool chain is adaptable to a wide spectrum of off-the-shelf HMI modeling tools and OEM proprietary databases interfaces (Fig. 4).

Within the next development phase of the ARTEMMIS tool chain, a new HMI modeling tool platform will be established as a plug-in based solution on an existing off-the-shelf tool solution. This modeling platform will offer OEM's which have not yet decided on a HMI modeling tool and internal software developers at Continental rapid prototyping and series development features for visual models (2D, 3D Models, animations) and system/driver interaction models. For each cluster class, a specialized modeling profile will be available, which reflects the given hardware capabilities and—features within the modeling environment.

An automotive HMI model typically describes three core entities

- (1) The resource model, containing all graphical resources
- (2) The visual model, like widgets and animations
- (3) The behavior model, consisting of descriptions for system- and user interactions

The ARTEMMIS tool chain generates such HMI models into target devices by using a two step conversion process. The Model Cross-Compiler converts a tool- or OEM specific HMI model into a meta-language, which is called ARTEMMIS HMI Language. In the second conversion step, the meta-model is translated by the HMI Language Compiler into C++ code. The code will be compiled, linked and



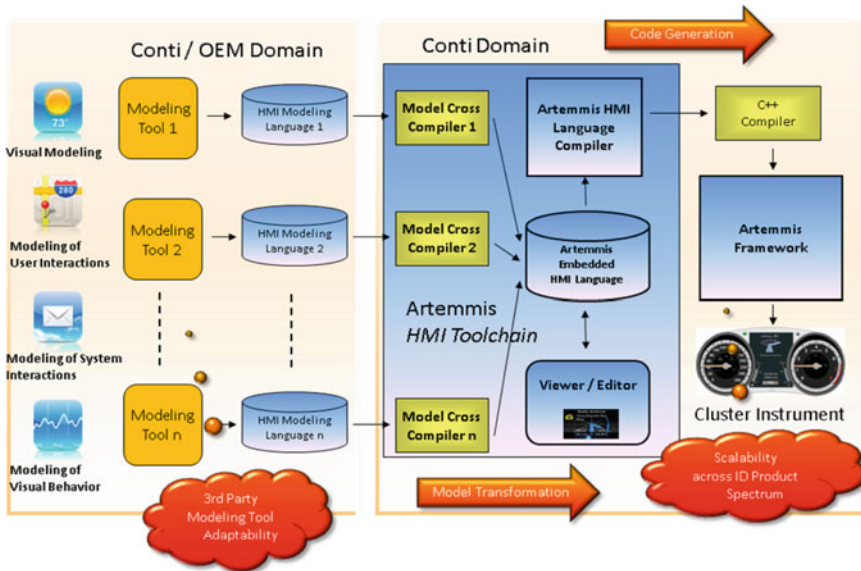


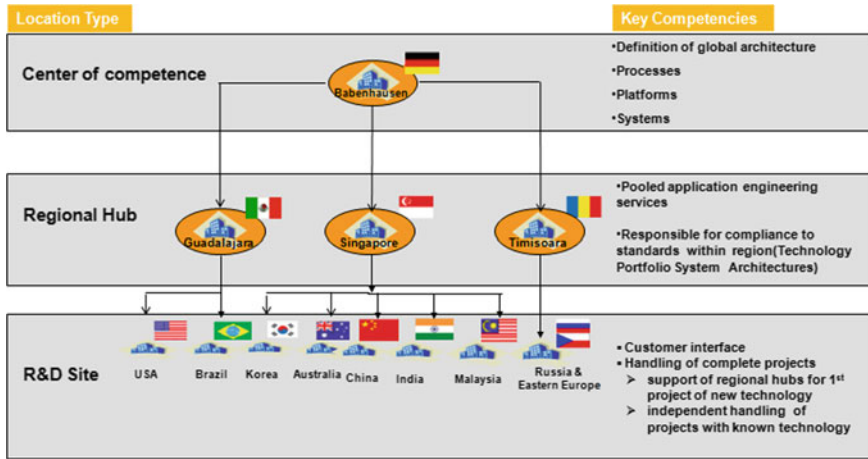
Fig. 4 ARTEMIS architecture overview

Fig. 5 Automotive HMI model sample



executed by the ARTEMIS run-time framework. When executed, the HMI model will be presented on the device screen(s) including all visual aspects and its dynamic behavior (Fig. 5).

The functional core elements of the ARTEMIS Framework are widgets, standard- and real-time animations and a 3D pointer engine, which emulates one or multiple mechanical pointers including their associated dials on the screen. Each animation can be executed in an own time domain with e.g. 10, 30, 70 Hz, ... time bases. ARTEMIS supports the simultaneous execution of multiple time domains and also offers mechanisms to prioritize the physical execution of animations, which enables real-time rendering behavior. Real-time rendering is required to avoid artifacts, e.g. for a smooth movement of the pointer on the screen.



**Fig. 6** Continental business unit ID (instrumentation and driver HMI) international engineering footprint

All components of the ARTEMMIS Framework and all HMI model data as generated by the ARTEMMIS Language Compiler are highly memory- and computation time optimized, which is essential for cost optimized solutions. For cost-driven clusters, the complexity and footprint can be reduced by further simplifications of the animation engine and by omitting the 3D capabilities. In such a case, only one time domain will be applied.

### 4 Adaption to the Chinese Market

As first step, considering the Chinese market’s expectation on extremely short development time and on affordable cost, Continental adapts the solution from Europe as following:

- (a) Scalable platforms: The Continental hardware and software platform can be scaled from basic to premium instrument clusters. Therefore the HMI and graphics system of this platform can be scaled to fulfill the demands of the color TFT clusters for the cost sensitive emerging markets. With the reduced software complexity Continental can realize a color TFT cluster on single MCU which handles both the automotive and the graphic features.
- (b) Reduce complexity: Especially a reduction in complexity of animations will help to reduce both development time and development cost. The Continental tool approach is also highly scalable and defines profiles and corresponding toolboxes which can be mapped to the different cluster variants.

- (c) Dedicated screen design: Today neither local Chinese OEMs nor local suppliers of cluster instruments have the knowledge needed to do screen designs for an automotive HMI. In order to close this gap Continental offers support for screen design by its own screen designers or by involving experienced 3rd party design studios who are specialized in automotive interior design.

In addition to the strategy to introduce the color TFT IC development in the Chinese market step by step, we fully use our international engineering footprint (Fig. 6) to ensure a smooth technology transfer from head quarter to the local engineering organization in China.

Like for any other new technology we take the following approach:

- (a) Enabling of the regional development center by our head quarter, in this case our Asian development center in Singapore.
- (b) Implementation of a first project jointly by the Asian development center and the local Chinese engineering team.

As a next step, we are going to introduce color TFT cluster instruments with high level animations to the Chinese market. In order to shorten the development time and to reduce development cost, we adopt the following approach:

- (a) Define a generic HMI which could be accepted without any change or with small changes by the majority of the OEMs,
- (b) Organize a pre-development of the product based on the generic HMI,
- (c) Use the pre-developed product as base to further develop customized color TFT instrument clusters with high level animations for specific customers.

In this way, we can re-use one solution for all customers, but still achieve different HMI appearance for different customer. This approach makes the high level animation in color TFT ICs affordable for Chinese OEMs which usually have a lower volume of vehicles.

## References

1. Abel H-B, Leuchtenberg B (2007) HMI und Technologien zukuenftiger Informationssysteme im Kraftfahrzeug und deren Beitrag zur Fahrerassistenz. GZVB Braunschweig, AAET 2007
2. Mueller G (2011) Advanced and premium clusters, talk given at the International Frankfurt Motor Show 2011

# Color and Texture Design of Chinese Automobile Brand

Yanhong Hao and Fuquan Zhao

**Abstract** *Research and/or Engineering Questions/Objective* To purchase automobiles, consumers will not only consider functional demands, but also take into account the aesthetic function and symbolic value. In addition, beautiful and harmonious colour and texture can not only raise a vehicle level, but also allow enterprises to create greater profits with low cost, as well as promote brand image and competitive edge. More importantly, with aesthetic demands satisfied, consumers shall feel humane automobile and cheerfulness in body and mind. Thus, objective of this research is to create glamorous colour and texture design of Chinese automobile. *Methodology* Based on automobile brands of each country on the market, especially Japanese, German and America vehicles, research method of summary and comparison is applied to analyze similarity and diversity between automobile color and texture design of China and other countries from the view of overall color matching, texture matching and color psychology. *Results* Through analysis of the current shortcomings in colour and texture design of Chinese automobiles, with the method of learning and absorption, it is summarized that colour and texture design of Chinese automobile shall mix elements of Chinese traditional culture and design principles of colour and texture design of Chinese automobile. Therefore, the research not only lays foundation for specific achievement of Chinese automobile design in colour and texture, but also serves as a reference for foreign automobiles to enter Chinese market. *Limitations of this study* Limitations of the present research is that no experience is gained of localized conditions and folk cultures in these foreign countries where the brands belong to, so no research is conducted on how the glamorous colour and texture design of

---

F2012-E05-014

---

Y. Hao (✉) · F. Zhao  
Zhejiang Geely Automobile Research Institute Co., Ltd., Hangzhou, China  
e-mail: haoyanhong@rd.geely.com

these brands is realized with integration of objective and subjective factors. What does the paper offer that is new in the field in comparison to other works of the author: The design principle of automobile colour and texture is initially presented in this paper, and the analysis of development direction for colour and texture design of Chinese automobile is innovative. *Conclusion* The design principle of automobile color and texture summarized serves as an important guideline to vehicle styling design. And 'people' is the center of automobile color and texture design all along, because harmonious and beautiful color and texture design is significant to consumers, automobile styling, and automobile enterprises, which serves as a symbol of automobile brand images, national culture and times.

**Keywords** Chinese automobile brand · Color and texture · Design · Design principle · Traditional culture

## 1 Introduction

With the rapid economic development of globalization and the development of the automobile industry, the automobile has become the important means of transport in people's lives. It is hoped that the automobile is not just with the use of functions, and also has a beautiful functional and symbolic value. In automobile design, colour and texture are the most direct manifestation of the visual language. Harmonious and beautiful of colour and texture design, not only allows the automobile itself to improve quality, and allows companies to create high profits at low cost, and improve brand image and competitiveness. Experimental studies have shown: the human visual organ in the first 20 s of the observed objects, the sense of colour accounted for 80 %, shape feeling accounting for 20 %; 2 min later, the sense of colour accounted for 60 %, body feeling 40 %; after 5 min, colour feelings and shape feelings half and half, and this state will continue [1]. Therefore, research on the colour and texture of automobile design is of a great significance. The colour and texture of design of automobile is not a simple automobile which is processed into products with colour and texture, its ultimate shape is linked each other and the automobile itself as well as human culture. The color and texture design of Chinese automobile brand development is relatively slow, and designers are very less in this industry. Colour and texture design of Chinese automobile brand as a whole lags behind other countries, with matches and new materials, new technologies, the use of out of date. Organized by the China Colour Consortium colour with colour matching designer training, promote the development of the domestic colour industry. Major colleges and universities have not the colour and texture of design of automobile professional. Therefore, study colour and texture design of Chinese automobile brand is a vacancy. Through this study, colour and texture design of Chinese automobile brand has great significance.

## **2 The Definition and Impact of Elements of the Color and Texture Design of Automobile**

### ***2.1 Definition of the Color and Texture Design of Automobile***

The colour and texture design of automobile is to give the automobile's interior and exterior trim colour and texture to the colour and texture with a reasonable automobile styling more culture and competitiveness. Automobile interior colour texture design as the interior design can create an ideal and comfortable space.

The color changes the world of all things colorful, great charisma and influence to human vision. The colour's three attributes is hue, lightness and purity. In automobile color design, color is divided into the exterior color and interior color. A good grasp of the reasonable match of the three properties will be able to create the right color in color design. The color can not only provide the beauty enjoying to the people visually, but also affect people psychologically. The color has the following main psychological feeling: cold and warm color, the colors of the soft and hard, the color of the light and heavy, the color of expansion and contraction, the color of the forward and backward as well as the color of calm and excitement. The color also has cultural characteristics; individual countries have different color preferences and contraindications. In the automobile color design, the designer purpose design is based on country, specific models, the use of location and consumer groups, in order to meet consumer demands.

Texture generally refers to the surface texture and lines. It allows any object becomes more alive and full of level changes. In the automobile interior and exterior design, the texture is divided into the injection texture, decorative texture, leather texture, and fabric texture. Injection texture is with chemical materials processing corrosion of a texture on the surface of the mould. It is generally divided into fine matte texture, regular geometric texture and coarse texture. Fine matte texture is generally used in automobile exterior plastic parts, the buttons in the interior, air conditioning leaves and blocking cover a small appearance. Regular geometric texture and coarse texture generally are used for the IP, door panels, sub-dashboard and column and so on. Decorative texture refers to the carbon fibre texture, the texture of mahogany, piano paint effects, matte painting effects, electroplating effects play a decorative role in the automobile interior and exterior. The processing method is more diversified, including water transfer printing, thermal transfer, the IMD, painting and plating. The leather texture is generally used for the seat cover, built-in door panels and door armrests. Due to feel well, so it looks quality. In automobile interiors, in order to reduce production costs, the use of PVC, PU and Microfiber leather modelled on the texture and feel of the leather. Leather texture effects are many; the designer can design according to the model interior style. The fabric texture is used for the seats, roof, skylights, carpet, and luggage compartment partition and so on.

## ***2.2 The Factors of the Color and Texture Design of Automobile***

### **2.2.1 The Color and Texture Design of Automobile with its Form**

The color is invisible, the texture is touch, color and texture are served for form, they can let the automobile form more humane, artistic and attractive value. Color and texture design can reduce the shortcomings of the automobile on the form, but can also strengthen the performance of the local morphology, by induction, contrast and rich manner and form of integration to meet the aesthetic needs of people. As long as the rational color and texture design, you can make automobile form more attractive.

### **2.2.2 The Color and Texture Design of Automobile and Processing Techniques and Materials**

In the automobile color and texture design, the designer should pay attention to the embodiment of materials color and texture. In Audi interior directly uses aluminium trim. The same color and texture design, the use of different materials will produce different visual effects and aesthetic taste. The level of the process impacts automobile interior and exterior.

### **2.2.3 The Color and Texture Design of Automobile with Personality Factors and Socio-Cultural Factors**

The color is gender-specific. Females are more like youth, sweet, high-purity color. Smart uses the pieces of red decorative in automobile interior and exterior trim obtained many female consumers favourite at the 2012 Beijing Auto Show, as shown in Fig. 1. Men prefer low purity and stable class color. In texture design, the young people like some lively exaggeration, innovative textures, while the elderly prefer low-key conservative quality texture. Ethnic customs, different regions, so there will be some different preferences in color, but texture are more lenient.

### **2.2.4 The Color and Texture Design of Automobile with Fashion Color**

The fashion color represents the times and trend, the clothing is very broad, relatively weak performance in the automobile. Automobile exterior color can carry out the design according to fashion color, automobile interior color use fashion color to part embellishment, so that consumers feel the automobile is advancing with the times.

**Fig. 1** Feminine style interior color



### 3 Analysis the Color and Texture Design of Automobile Brands in Different Countries

Analysis one the color and texture design of automobile brand must not be divorced from its background, the automobile has a different design culture and design style. Showing the trend of globalization of the automobile industry worldwide, mainly divided into three styles: Japanese automobiles, German automobiles and America automobiles. The color and texture design of three national automobile brands interpretation of the different design styles.

Japan is a combination of traditional culture and modern culture. Japan's traditional culture respects the people and the environment to the harmonious coexistence of Zen Buddhism. The lives of the Japanese emphasis on etiquette, living foods in the attention to fine, so Japanese products have demonstrated the exquisite detail. The design of the national implements the two-track. The traditional design with Japan's traditional national aesthetics, religion, and daily life is closely related to. And the modern design is bold and innovative, but still cannot be separated from the Japanese aesthetic ideas. Due to natural environmental factors in Japan, held in high esteem the wood culture, the construction of Japan attaches great importance to the material texture and color of America. The form of the Japanese automobile brand is not like automotive brands in the European countries to pursuit family characteristics instead of the trend of the times, it can be said that Japanese automobiles are fashion. But there is no formation of the color and texture of the brand design DNA. In automobile styling, the Japanese automobile gives a feeling of comfort and moderate interior relative to other automobile brands, fresh, comfortable and sophisticated. Japanese automobile brands mainly have Toyota, Nissan and Honda. These three brands selling vehicles in the domestic is Toyota; it represents the trend of Japanese automobile culture and development.



Germany is located in Western Europe, with a century of automobile culture. Germany in life and work are punctual, compliance, serious and rigorous, the German automobile will be Germany's geographical environment, social customs and lifestyle. Germany's industrial design respected the rational functionalism, so the product is a good simple, rigorous and concerned about product quality. Germany's automobiles culture is an important component of the German culture sector, and affects all countries in the global automobile design. German automobile has a rigorous, reliable and good quality. German automobile brands main has Mercedes-Benz, BMW and Audi, the design of these three brands are very classic, leading the development of the global automobile industry.

America is a developed country; it does not have a long cultural history like European country. The American design has close contact with market, and highlights the competitiveness. The America automobile is generally pretty luxurious domineering, performance is very stable and flamboyant heroic America automobile greatest feature is the emphasis on comfort and space. American automobile brands mainly have Ford, Chevrolet and Buick. These three big brands of vehicles represent America's automobile culture.

### ***3.1 Japanese Automobiles, German Automobiles and America Automobiles Brands of Exterior Color and Texture Design***

Through Japanese automobiles, German automobiles and America automobiles find: Exterior color have white, silver, black, red, green, yellow, blue, purple, and gray, these color add some more texture of the pearl pink visual sense. The exterior color of almost every hue has just lightness and saturation is slightly different. The exterior paint is mainly divided into: the monochromatic paint, metallic paint, pearl paint, chameleon and matte paint. The automobile's exterior is like the flow of sculpture in the city, bring vitality and color to the entire city. From the exterior color, reflecting the local culture is not very obvious, almost each country automobile brands have black, white, silver and red as a mainstream color, and then positioning the design according to different models of other colors, but in each different color on sales. When the exterior color design is performed in various countries; they are more concerned about the positioning of the models and the color preferences of consumers. Overall exterior color matching with almost all exterior paint color, just the appearance of small plastic parts is black. Generally the use of chrome-plated, bright bars and fine matte texture, mainly used in the grille, lower bumper decoration and fog around. In a number of concept automobiles, the rims with carbon fibre elements have extraordinarily dynamic fashion.

**Fig. 2** Fresh style interior color



### ***3.2 Japanese Automobiles, German Automobiles and America Automobiles Brands of Interior Color and Texture Design***

With the development of the globalization of automobile technology level and technical level, the automobile's interior design is the most likely to attract the eye. From the development trend in recent years, the overall interior design of the international fashion trend is a growing tendency in science and technology, elegance and digital form tend to be three-dimensional. However, the color and texture design puts more emphasis on applications and with a variety of materials matching.

#### **3.2.1 Japanese Automobile Interior Color and Texture Design**

The overall color matching design, interior color basically features a fresh and comfortable warm. It does not stimulate the dazzling color, mainly the pursuit of inner peace, and living habits and preferences of the Japanese. Color matching has two ways: monochrome interior and two-color interior. The main color of monochrome interior is a mainly all black interior and grey interior. The main color of the two-color interior has two, mainly black with beige, black with grey, grey with beige, and grey with white. Warm interior color can make it easier for people close to the point of view of color psychology. Japanese automobiles do not use too large high color purity, the peaceful use of low purity of color let people's mentality. Nissan brand automobile interior color performance is very warm and comfortable, as shown in Fig. 2.

The view of overall texture matching design, the interior texture of the Japanese automobile brand design is very delicate, and reflected in every detail. Unlike the Korean automobile interior extensive use of chrome trim, but instead of using paint treatment in the ecological point of view to consider more environmentally friendly. In texture design of injection moulded parts, Japanese automobiles pay

more attention to the geometric texture, focus on the rhythm. In SUV models, strong three-dimensional coarse sense is used to reflect the performance of the movement. The main and auxiliary injection texture is divided into geometric texture with coarse texture and coarse texture matching with a fine matte texture. Decorative texture design, mostly mahogany texture paint treatment, the geometric texture of water transfer, the overall interior feel stylish. Cortex sense of genuine leather and a variety of leather with the texture of the leather are adopted. In the class texture design on fabric, generally the small automobile like that can reduce the cost of textile fabrics; pattern selection can make the automobile livelier.

### 3.2.2 German Automobiles Interior Color Texture Design

In the overall color matching design, the German automobile's interior color is vividly reflected in the four brands of Audi, BMW, Mercedes and Volkswagen. These three features of the same brand are generous, rigorous and elegant. The difference is that different models positioning focus is different, Audi interior color reflect the science and technology and elegant, such as Fig. 3, BMW interior color expression of color emotion a little more strongly, Mercedes-Benz automobile interior color to reveal a more elegant atmosphere, Volkswagen is more diversified and more fashionable. Several brands of sports automobile design, a large number of dazzling red and orange to stimulate the driver's desires, and passions, and demonstrated the characteristics of personality open publicity, as shown in Fig. 4. Mercedes automobiles are good at with fresh white and light beige, but it creates the atmosphere and the same color of the automobile interior there is a difference. Due to German automobile interior styling is rational and rigorous, so it looks relaxed slightly with a more rigorous and noble, unlike Japanese automobiles like the feeling of the populace, as shown Fig. 5. Through the study can find German automobile interior color is close to Germany life and culture. German automobile interior color has monochrome interior and two-color interior. Monochrome interior with black interior and brown interior, Two-color interior has the collocation of black and beige, black and red collocation, black and orange collocation as well as light gray and white collocation. In the entire automobile interiors, and attaches great importance to the unity of hue. With the area, the IP at the upper and lower two colors, seats, roof, carpet and dashboard body colors. When IP is one color in a monochrome interior, seat and dashboard with the same color; in the two-tone interior trim, seats has another color.

In the overall texture matching design, injection texture used by the German automobile are basically coarse texture, different depths of different coarse texture with each other, to convey to consumers the quality of the feelings. Research from the classic German automobile brands, various brands of injection moulding texture is inheritance and family. The same kind of texture in the different models of automobiles, it will not only reduce costs, and formed their own brand of DNA. Some automobile brands in the injection texture is always changing, the advantage of follow fashion, the disadvantage lies in the difficulty to form the DNA of the

**Fig. 3** Technology elegant style interior color



**Fig. 4** Passion style interior color



**Fig. 5** Noble style interior color



**Fig. 6** Fashion style interior color



brand. German automobiles are many types of decorative textures and leading automobile fashion, the German automobile interior with a large area of peach wood, high-gloss matte, can convey the high-end feel. Bold use of carbon fibre texture, the various patterns of geometric textures, piano painting, and metal materials and so on, so that the German automobile classic fashion. In Audi interior, use a variety of materials, mix and match a variety of textures intertwined, so that the patchwork rhythm is felt in the whole interior trim. German automobile seat texture choose to focus on the sense of the details of the cortex sense and sutures in the texture of the leather. Some models are a match of suede and leather, leather and fabric mix and match. German automobile seats rarely choose the texture of the fabric class, generally the sports models of Volkswagen select lively patterns to express the interior style.

### 3.2.3 America Automobile Interior Color Texture Design

In the overall color matching design, the interior color of the America automobile partial uninhibited and movement. Overall automobile interior color is mostly dark, and then coupled with chrome trim and sporty. America automobile interior color, depending on the brand positioning in the interior color are also different, Chevrolet positioning consumer groups for young people, use the actively color, the SPARK interior color is very fashionable, as shown Fig. 6. Buick's positioning is a high-end automobile, passed by the interior color beige and black with a large area of the atmosphere, stable and noble taste, as shown in Fig. 7. America automobile interior color has monochrome interior and two-color interior. Monochrome interior is all black interior color, in the America automobile interiors, not the color of the whole light-coloured interior, which thrilled and domineering of the America character. The two-tone interior has the collocation of black and beige, brown and beige collocation black and orange mix. No matter what kind of color matching the interior color is uniform.



**Fig. 7** Luxury style interior color

In the overall texture matching, the America automobile in small automobile with injection texture is the texture of the rules of geometry; most automobiles are still use coarse texture in sports automobile, the coarse texture express crazy to serve as a foil to style. Decorative texture uses a lot of peach wood, geometric texture, metal wire drawing and painting. Lacrosse choose peach wood around the entire interior, it feels especially grand. Chevrolet's low-end automobiles use the texture of fabric class, texture characteristics prefer smooth and lively pattern to the performance of small automobiles. The leather texture chooses looks like and high quality touches a good texture, and focus on different leather textures matching.

## **4 Analysis the Color and Texture Design of Chinese Automobile Brand and Chinese Traditional Culture Impact on the Design of the Automobile Color and Texture**

### ***4.1 Color and Texture Design of Chinese Automobile Brand***

The late development of the color industry in China than in other developed countries in the world, so the automobile's color and texture design is develop slowly, Chinese brands of major companies in the color and texture design are not mature enough. Due to the exterior of the structure is less, the main emphasis on the integration of a sense of movement in exterior color texture design. The exterior color and texture design can keep up with the other countries, but the color of the corrosion resistance, volatility is relatively poor, mainly due to the product and the quality of the paint coating process water. Chinese localization automobile is lack of innovation; some automobile brands imitate the color and texture design of other countries. In a short period of time, corporate savings in research and development costs of the color texture design, but to make the trade a look at plagiarism is not conducive to the growth of Chinese brands on a global scale.

Some color and texture design well embodied in a number of well-known brands, but used in the domestic automobile styling will be different, because the form of the color and texture design and automobile design, production processes are inextricably linked. Chinese automobile brands in the color texture design has not yet formed their own DNA, designers can learn from Japanese automobiles, German automobiles and America automobiles color and texture design, its essence to be applied to the Chinese automobile brands.

The color and texture design of Chinese automobile brand is similar to other countries on the ways matching, you can learn from German, Japan and the America monochrome interior and two-tone interior matching, but how to match color and texture has great differences. Different countries have different social customs, so Chinese traditional culture also affects the aesthetic culture of the Chinese people.

#### ***4.2 Chinese Traditional Culture Impact on the Design of the Automobile Color and Texture***

Chinese traditional culture of China handed down in the course of historical development along the national culture, the aesthetic character and individuality. China has a long history and culture, these deep-rooted traditional cultures is always influenced by the Chinese people's aesthetic taste and lifestyle. Traditional Chinese culture, including a very wide range, philosophy, religion, literature, history and art, a different representation of these elements affect the Chinese people, thus affecting the design of the automobile color and texture.

System concept in philosophy, Confucianism and Taoism, the Chinese culture to determine the core of a wonderful, which is advocated by the Chinese culture, the greatest virtue, that is, "and" (moderation) [2]. In daily life, people buy an automobile do not buy color is too bright texture exaggerated automobile will pay attention to the moderation, and will consider other people's vision and value-added. As the world's cultural blending and of course the personality of the minority will enjoy the challenges prominent personality to buy an automobile with a special color texture. Religion on the people of China have a huge impact, especially Buddhism and Taoism, they are living in a subtle influence on people's minds, but also benefits to the people. Chinese art has left a valuable asset like Dunhuang and Longmen Grottoes, these murals, the use of color and pattern mix can be applied to the automobile's color texture design. The ancient Chinese literature pay attention to "beauty", The beauty of the so-called "beauty", is the intrinsic quality of an impartial, outside is now one is neither excessive and non-shortage of contradictory, harmony and unity [3]. This "beauty" advocating of harmony and unity is the automobile color design needs, emphasizing the whole of the United States. The ancient Chinese poetry like to reflect the mood to reach the realm of recalling the tragic art, the color texture of the automobile is the easiest styling elements of the manufacturing atmosphere, to allow motorists to

reach the starting point and automobile integration can be used as design. Chinese art in painting, calligraphy, sculpture, furniture, architecture, ceramics, drama and dance, and art are mutually penetrate and influence each other. Chinese automobile color and texture should be designed to tap the use of these arts to express the mood and color patterns, Such as the morphology of the ceramics can be designed into a texture using the texture in the automobile interior can reflect the characteristics of Chinese automobile. Color and texture designer should consider the localization of the art in the design of the automobile color and texture and the formation of the color texture of the Chinese automobile brand design DNA.

## **5 The Design Principles of Chinese Automobile Color and Texture**

The color and texture design of Chinese automobile brand is continuous development, but the development needs directivity. Based on the above research, the automobile color and texture design principles are summarized as follows:

Firstly, overall matching design of color and texture, first overall and then local with contrast and harmony and unity. During the matching color, the main color is first determined and then the secondary color and embellishment of color are used to create atmosphere. The final design of color and texture is required to achieve China's traditional philosophy, which means the perfect combination of nature and human.

Secondly, Chinese traditional cultural elements are applied in the Chinese automobile brands design. During the preliminary design of the color and texture, vehicle positioning which is consistent with Chinese traditional cultural elements is collected. The color and texture design with Chinese characteristics is performed through refinement and innovation.

Thirdly, automobile user-friendly design principles. The "people" are always regarded as centre in any design; color and texture are designed not only to meet functional requirements but also harmonious and beautiful requirements. For the safety of driving area, the reflection degree of texture surface should be considered when the design is performed. Meanwhile, designers should consider psychological impact of interior color on vehicle users as well.

Fourthly, the natural color is integrated into automobile color. The people like nature color; therefore the adding of natural color in the automobile can make people feel warm and natural, while allowing automobile, people and natural environment to achieve harmony and unity.

Fifthly, the color and texture design of Chinese automobile brand should have the DNA of domestic brands. The design is performed based on brand culture so as to form the DNA with family characteristics, focusing on heritage and continuity in color texture design.



## 6 Conclusion

The automobile is the product of spiritual culture and material culture of human society. The different societies and cultures have different color and texture designs. China has a profound culture; the designers should exploit the essence of Chinese traditional culture in automotive color and texture design, and reflect the Chinese design characteristics. The Chinese brands should focus on what kind of color and texture design can fully interpret cultural connotation of brand heritage and market positioning. With the rapid development of global automobile industry and more academic attention, automotive color and texture design will be getting better and color and texture design with domestic brand DNA will be gradually formed.

## References

1. Chinese and Western Color (Beijing) (2007) Management Consulting Co.Ltd. Color Matching Designer Training Course. Third level. China Textile Press, Beijing, 8, 2
2. Hongyue G (2008a) Chinese traditional culture introduction. Ji'nan University, Guangzhou, 3, 97
3. Hongyue G (2008b) Chinese traditional culture introduction. Ji'nan University, Guangzhou, 3, 148

# Development of Shock-Absorbing Grip-Handle Structures on the Headliner

Hee Sang Park, Yongsu Chang and Jun Ho Jung

**Abstract** Occupant protection during interior head impact is should be consider while designing the headliner. There is a Federal Motor Vehicle Safety Standard, FMVSS201 to ensure the occupant's safety during an interior head impact. Energy absorbing components are used to protect the occupant in the event of impact with components of upper passenger compartment. Automobile manufacturers have been developing suitable designs without Energy absorbing components because of cost issues. The objective of this study is to develop the design method without Energy absorbing components on the grip-handle areas. Grip-handles are located on upper roof in the vehicle where is impact zone that must meet the occupant safety requirement during interior head impact such as FMVSS201U. The head acceleration must be reduced to lower the Head Injury Criterion (HIC) to 1,000. To reduce the head acceleration without energy absorbing components, Grip-handles and related components should absorb the impact by themselves. Grip-handles are connected to brackets. The bracket is used to assemble the headliner with grip-handles. Grip-handles and the brackets should endure the downward force. On the other hand, when FMH impact Roof trim, the bracket is deflecting upward and it will absorb the impact energy The bracket needs to meet two demands. In order to meet these demands, Experiment of design will be carried out with the help of CAE and DOE.

**Keywords** FMVSS201 · Energy absorbing bracket · Grip-handle · Upper roof · HIC(d)

---

F2012-E05-015

---

H. S. Park (✉) · Y. Chang  
Hyundai Motor, Seoul, Korea  
e-mail: heesang@hyundai.com

J. H. Jung  
VP-KOREA, Seoul, Korea

## 1 Introduction

The federal Motor Vehicle Safety Standard 201 test stipulates that HIC(d) obtained from the resultant acceleration of the free motion headform (FMH) model to be below 1,000 [1]. Thus interior trim of a vehicle is designed not only to provide aesthetic look but to reduce risk to the occupant during a crash. To reduce impact of head injuries 30 mm of space between trim and body roof panel is recommended, Energy absorbing space is related with Styling and head room. Especially upper roof (UR) zone is related with head room among FMH target points. To get more head room we have to reduce more absorbing space. Otherwise to lower down the HIC(d) value thermoplastic energy absorbers are recommended to manufacture interior components. UR target zone and plastic energy absorbing component are shown in Fig. 1. It uses ribs to improve part stiffness in bending and thus avoiding the use of thick section to look slim. Although ribs structure absorber is used, there is limit to reduce the space [2]. Figure 2 show energy absorber after FMH impact test. When ribs and energy absorbing height are below 15 mm. The result of test repeatability is decreasing. Left picture show energy absorber didn't break and energy dissipation is not occurred. When breaking strength is close to criteria or there is noise factors such as sinking, warping, energy absorber may not break and HIC(d) exceed the target value. The best way to eliminate this unexpected problem, we'd better not use plastic energy absorber. Steel energy absorber show uniform energy absorbing property. Without additional energy absorber, we can utilize grip-handle bracket.

Grip-handle and bracket are located on roof trim shown in Fig. 3. If we use grip-handle and bracket as energy absorber we can eliminate plastic energy absorber instead. This paper presents a numerical study of an energy absorbing component for UR location in order to achieve the FMVSS201 requirement for existing vehicle design.

## 2 Factors Influencing HIC(d) Value

Primary function of grip-handle is assisting passenger. There is extension bracket connecting grip-handle to Car body Panel. This extension bracket shown in Fig. 3 should endure the downward force and minimize the deflection of the bracket. On the other hand, to use the bracket as energy absorber, we have to consider opposite direction force. If free motion headform (FMH) impact Roof trim, the bracket will deflect upward. To absorb impact force, the bracket have to be deflected within controlled space. The bracket needs to meet two demands. In order to meet these demands, we have to find design factors for the bracket. The bracket behaviour like cantilever beams. Vertical/horizontal dimension and clamping boundary condition should be considered. The design factors were selected for the experiment shown in Table 1. There are 4 factors we can control. Level 1 is base line and level 2/3 is

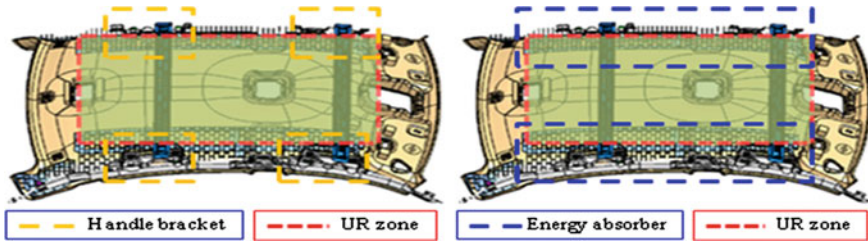
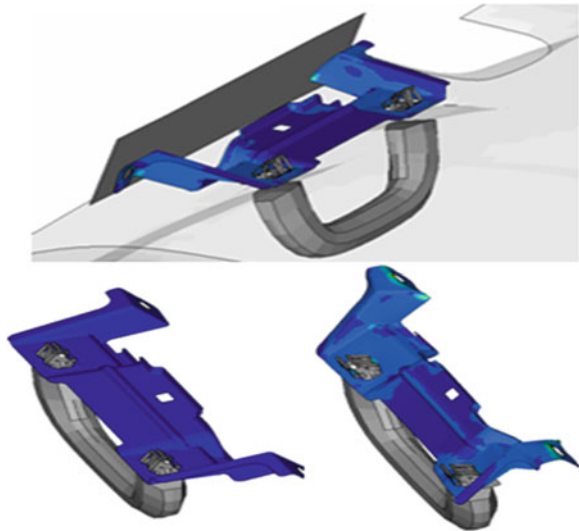


Fig. 1 Energy absorber and handle bracket in UR target zone



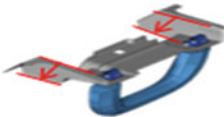



Fig. 2 Test result after FMH impact test

Fig. 3 Grip-handle bracket deflection



modified model. There are two target point we have to consider to minimize HIC(d), one is UR zone and second is side rail (SR) point. When FMH impact on SR target point directly, most kinematic energy is delivered to the bracket but When FMH impact UR target point, first, forehead impact UR target and mouth of FMH impact handle grip next (Fig. 4).

**Table 1** Design factor of grip-handle bracket

Design parameter (mm)	Picture	Level 1 (Base line)	Level 2	Level 3
A. Vertical dimension		0	+5	+10
B. Bolting hole location		0	+3	+5
C. Horizontal dimension		0	-4	+4
D. Bolting area thickness		0	+1t	+2

### 3 Experimental Layout for the Design Factors and Conduct of the Experimental Runs

To optimize the grip-handle bracket for multipurpose, DOE method is required. L9 orthogonal array is made shown Table 2 to optimize grip-handle bracket. HIC(d) value and deflection of the bracket is obtained by CAE. The deflection of the bracket is obtained when grip-handle is under load of 90 kgf. The bracket is a lower-the-better type of quality characteristic. The result of deflection show we can take any design factor for reducing HIC(d) value because every results are better than base line for deflection.

Proper selection of design factors would lower the HIC (d) values. Two target points are considered in relation with grip handle bracket area. One is SR and the other is UR. The HIC (d) value at SR and UR targets must be below 1000 simultaneously. Separate analysis is required to know the influence of plastic energy absorber for UR zone. Impact condition is selected with worst approach angle and location [3]. The results of the experimental runs are shown in Table 3. According to HIC (d) value in UR area, even though some values are higher than the base line values, it is found that better values resulted without energy absorber. This is because of FMH rotation and availability of sufficient impact space after eliminating the energy absorbers [4].

### 4 Data Analysis to Identify High Contributing Factors of the Bracket

The aim of the current study is to select the best levels for the control factors that give minimum HIC(d) values. Three separate analysis is carried out to identify control factors that have influence on average of HIC(d) values. A3, B2, C3, D3 levels are selected for minimum HIC(d) at SR(2A). A3, B3, C1, D3 levels are

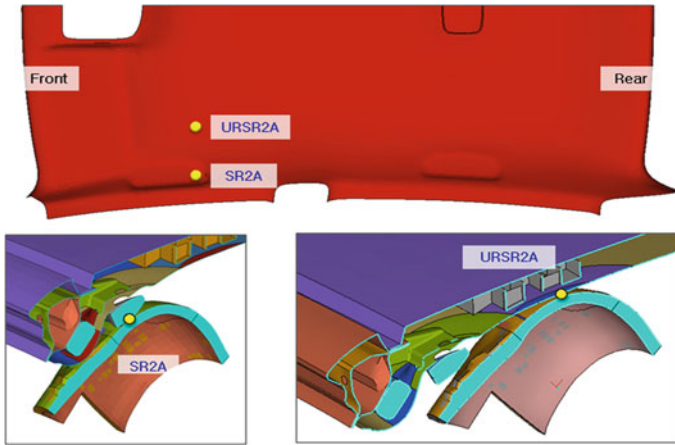
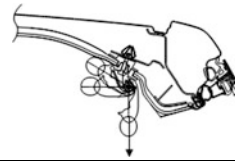


Fig. 4 SR and UR target point

Table 2 Result of CAE

No.	A	B	C	D	Bracket vertical deflection (mm)
1	0	0	0	0	34.3
2	0	3	-4	1	23.3
3	0	5	-8	2	22.8
4	5	0	-4	2	21.3
5	5	3	+4	0	27.3
6	5	5	0	1	21.3
7	10	0	+4	1	28.1
8	10	3	0	2	20.9
9	10	5	-4	0	20.9



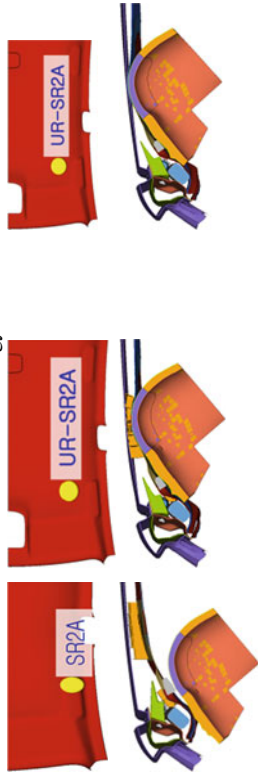
selected at UR-SR2A with Energy absorber. A2, B3, C1, D3 levels are selected at UR-SR2A without Energy absorber. Design factor levels are selected differently except factor D (bolting area thickness) (Tables 4 and 5).

### 5 The Comparison of Improved Design Verse Baseline Design of the Bracket

We reduced L9 array to three cases. Table 6 show that we can improve HIC(d) value without plastic energy absorber. HIC(d) value is improved both SR and UR target point at case A. HIC(d) is reduced by about 11 % without plastic absorbers at UR. Vertical deflection of grip-handle bracket is improved by about 34 %. The

**Table 3** Result of design factors array

No.	FMH impact test HIC(d)			D	FMH impact test HIC(d)			Base line: 747.7	Base line: 730.3	Base line: 645.0
	A	B	C		@ SR2A	@ UR-SR2A with energy absorber	@ UR-SR2A without energy absorber			
1	0	0	0	0	0	0	747.7	730.3	645.0	
2	0	3	-4	1	1	1	737.3	737.9	638.3	
3	0	5	-8	2	2	2	733.9	725.0	656.9	
4	5	0	-4	2	2	2	739.2	757.9	628.2	
5	5	3	+4	0	0	0	722.8	757.2	639.4	
6	5	5	0	1	1	1	743.0	737.0	635.4	
7	10	0	+4	1	1	1	715.0	739.3	643.1	
8	10	3	0	2	2	2	714.1	674.1	648.0	
9	10	5	-4	0	0	0	736.3	671.4	635.6	







**Table 4** Significant design factors

A @ SR(2A)	B @ UR-SR2A with energy absorber	C @ UR-SR2A without energy absorber

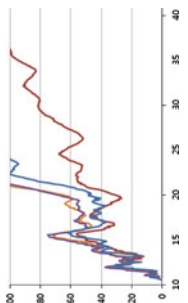
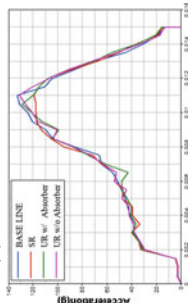
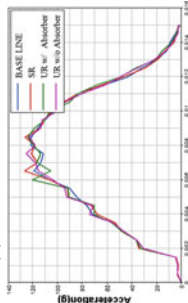
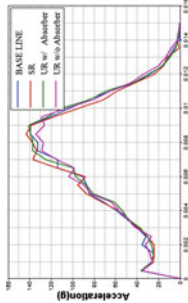


**Table 5** Optimized grip-handle bracket at each target point



Optimized model case	A	B	C	D	Grip-handle design FIG
Base line	0	0	0	0	
A @ SR 2A	10	+3	+4	+2	
B @ UR SR2A with absorber	10	+5	-4	+2	
C @ URSR2A W/o absorber	5	+	-4	+2	

**Table 6** Improved design verse base line design

Optimized model case	SR2A FMH HIC(d)	URSR2A w/absorber FMH HIC(d)	URSR2A w/o absorber FMH HIC(d)	Vertical deflection (mm)
Base line	747.7	730.3	645.0	34.3
A @ SR 2A	721.6 (3.4 % ↓)	742.2 (1.6 % ↑)	647.4 (0.3 % ↑/11.3 % ↓)	20.5
B @ UR SR2A with absorber	748.9 (0.1 % ↑)	738.2 (1 % ↑)	666.7 (3 % ↑/8.7 % ↓)	20.4
C @ URSR2A with absorber	762.4 (1.9 % ↑)	753.4 (3.1 % ↑)	636.3 (1.3 % ↓/12.8 % ↓)	21.5
W/o absorber				



**Table 7** Final design factors

Final model	A	B	C	D	Grip-handle bracket final design	Non-energy absorber headlining roof trim
A @ SR 2A	10	3	+4	2		

final design factor is selected after comparing case A/B/C. HIC(d) value is not improved at SR target comparing case. B/C to case A.

Final design is shown Table 7.

## 6 Conclusions

A robust design approach to improve occupant safety is described for headlining roof trim of a vehicle. Simulation-driven tools are used to minimize HIC(d) values. A new energy absorbing method has been presented in this paper for eliminating plastic energy absorber with optimized grip-handle bracket. This method is useful when absorbing space is not sufficient at UR zone. The grip-handle bracket met two demands simultaneously.

- (1) HIC(d) is reduced by about 11 % without plastic absorbers at UR zone.
- (2) Vertical deflection of grip-handle bracket is improved by about 34 %.

## References

1. FMVSS: Head impact protection, national highway traffic safety administration (NHTSA), DOT; <http://stnw.nhtsa.gov/cars/rules/rulings/headprot/pubnprm.html>
2. Kim JH (2010) The study on design method of FMH absorption using subcomponent collapse simulation, KSME
3. Park G (2005) Numerical implementation for effect of forehead impact zone in FMH impact, KSAE
4. Deb A (2004) A lumped parameter-based approach for simulation of automotive headform impact with countermeasures. Int J Impact Eng

# SEMG Based Recognition for Lumbar Muscle Fatigue During Prolonged Driving

Xin Tao, Bo Cheng, Bo Wang, Feiruo Zhang, Guofa Li  
and Chaoyang Chen

**Abstract** This study presents a method for supervised classification of multi-channel surface electromyography (SEMG) signals with the aim of recognizing drivers' lumbar muscle fatigue during prolonged driving. An experiment was carried out to investigate the SEMG manifestations of 8 drivers' lumbar muscle fatigue with recording of SEMG from 4 locations over lumbar erector spinae. Based on the wavelet packet transform (WPT) and continuous wavelet transform (CWT) of each SEMG segment, a representation space composed of 176-dimension features was extracted to classify three muscle fatigue statuses. The 176D features were calculated from Shannon entropy and relative energy of wavelet packets, along with instantaneous median frequency (IMDF), mean frequency (IMNF), and energy (IE) from CWT of wavelet packet (4, 15). The classification was performed by a C typed support vector machine (SVM) with a radial basis function (RBF) kernel, which was compared with a linear kernel. Parameters of SVM were optimized with the grid search method. Results: Correct classification rate (CCR) of the testing set was around 82.69 % (1.46 %)—an average (STD) value from 10 successive tests using a RBF-SVC, while the accuracy dropped to 78.94 % (1.63 %) with a linear kernel. Optimum parameters (c, gamma) for the RBF kernel were identified to be (110, 0.082), which affected the classification capacity in a serious way. The AUC (normalized area under the curve) values (0–1) of receiver operating characteristic (ROC) curves for the 10 successive tests were all above 0.9,

---

F2012-E05-017

---

X. Tao (✉) · B. Cheng · B. Wang · F. Zhang · G. Li  
State Key Laboratory of Automotive Safety and Energy, Tsinghua University  
Beijing, China  
e-mail: taox09@126.com

C. Chen  
Department of Biomedical Engineering, Wayne State University, Detroit, USA

which proved our method to be reliable and promising in a detection system of drivers' lumbar muscle fatigue.

**Keywords** Prolonged driving · SEMG · Wavelet · Fatigue · SVM

## 1 Introduction and Theoretical Background

With the progress of modern automobile society, low back pains have become extremely common afflictions for people who drive a lot, especially professional drivers. As the lowest level of low back pains evolution, lumbar muscle fatigue during long-term driving may play an important role in the chronic injury accumulation and recessively do harm to drivers' health. Besides, the muscular stiffness and pains coming with the lumbar muscle fatigue may further divert drivers' attention from the transport and cause potential safety risks. It's necessary to recognize the lumbar muscle fatigue progress for early warning and possible intervention in order to protect drivers from possible health risks.

Among all objective tools used in the vehicle ergonomics, the surface electromyography (SEMG) has huge advantages in the study of drivers' neuromuscular activity, such as non-invasiveness, applicability in situ, real-time fatigue monitoring during the performance of defined work, ability to monitor fatigue of a particular muscle and correlation with biochemical and physiological changes in muscles during fatiguing [1]. The SEMG signal has been widely used to determine local muscle fatigue progression since the power spectrum of SEMG signals became compressed with fatigue [2], which was commonly manifested by the corresponding reduction of the instantaneous mean and median frequency of the signals' spectrum [1–4], and also corresponding increase of the signals' amplitude [5].

Despite wealth of information could be extracted from SEMG signals, there were several problems concerning signal analysis and interpretation considering the continuous monitoring of local muscle fatigue during prolonged driving. Firstly, based on the results of preliminary tests, the magnitude of lumbar muscle SEMG signals in driving could be as low as 10 % of that in maximal voluntary contraction (MVC), which meant SEMG signals could be easily disturbed by occasional trunk movement interruptions and other noises. Secondly, large amounts of data collected from long-duration driving need to be processed to extract the representation space. Therefore, a powerful algorithm for noise reduction and feature extraction is essential for the recognition of the lumbar muscle fatigue.

As a commonly used tool in signal de-noising and multi-scale decomposition [6, 7], wavelet packet decomposition (WPD) is a wavelet transform where the signal is passed through more filters than the discrete wavelet transform (DWT). Wavelet packet transform (WPT) decomposes both approximation and detail coefficients into further levels to create full binary tree, while just the approximation coefficients were decomposed in DWT. That means WPT could offer richer contents of SEMG signals, in which significant frequency contents are achieved in high scales [7].

Previous studies demonstrated that features extracted from wavelet packet coefficients (WPC) such as entropy [8] and relative energy [9] could work well in the classification of electrophysiological signals. In addition, continuous wavelet transform (CWT) also plays an important part in spectral feature extraction [10–13]. Unlike DWT, CWT could decompose signals at any scale and make the mother wavelet perform continuous time-shifting to calculate the continuous wavelet coefficients (CWC) with rich time-scale information. As for SEMG signals with low signal to noise ratio, CWT could work better than DWT because DWT down-sampling of the signals can cause the loss of significant information [7].

Like any pattern recognition system, the SEMG-based fatigue detection needs an excellent classifier. From all the classification algorithms, support vector machines (SVM) have been proved efficient, powerful and capable of dealing with high-dimensional features and also theoretical bounds on the generalization error and sparseness of the solution provided by statistical learning theory [14]. It has been proved that the support vector classifier could work well in the classification of SEMG signals [7, 15].

This study proposes a method for supervised classification of multi-channel SEMG signals with the aim of recognizing drivers' lumbar muscle fatigue during prolonged driving. Based on the WPT and CWT analysis of SEMG signals, a novel high-dimension representation space composed of Shannon entropy, relative energy and statistic features of instantaneous median frequency (IMDF), instantaneous mean frequency (IMNF), instantaneous energy (IE), and root mean square (RMS) was proposed to train an optimized support vector classifier (SVC) for the recognition of drivers' lumbar muscle fatigue.

## 2 Materials and Methods

### 2.1 Subjects

Eight healthy subjects (seven male and one female) participated in the experiment and gave their written informed consents about the study. Their mean (STD) age, weight and height were 24.5 (2.6) years, 73.9 (13.0) kg and 171.9 (5.2) cm respectively. Before the tests, all subjects were informed to keep healthy daily routine without strenuous exercises. None of the subjects reported any musculoskeletal or neurological conditions that precluded their participation.

### 2.2 Experimental Design and Protocol

Each subject performed two tasks over the whole procedure: (1) prolonged driving tests for studying the evolution characteristics of drivers' lumbar muscle fatigue, (2) MVC (maximum voluntary contraction) tests before driving tests for scaling muscle activity.



**Fig. 1** The driving simulator and freeway scene used in the prolonged driving tests

### 2.2.1 Prolonged Driving Tests

With surface electrodes for SEMG signal acquisition, each subject participated in a simulated driving test. The test was conducted on a 6 DOF (degree of freedom) simulator with excellent driving experience. A specific scene of freeway with low-density traffic was used as the road environment (Fig. 1).

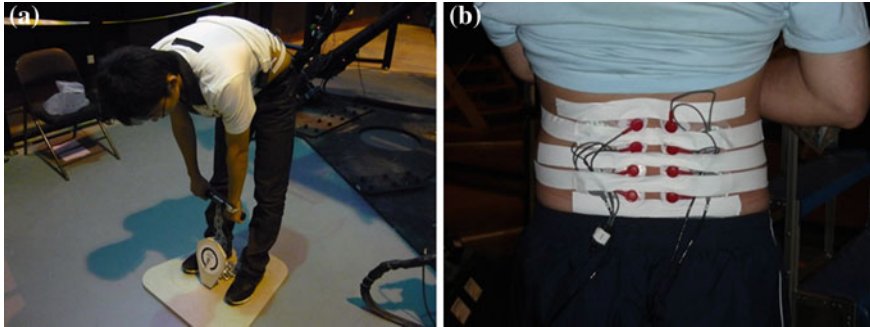
In the beginning subjects needed to adjust their seats to a comfortable position with the safety belt buckled. After 5 min training, subjects were free to drive using a standard driving posture with two-hand operation. In compliance with traffic regulations in China, the speed was limited at 90–120 km/h.

The driving test lasted 180 min. This duration was chosen with reference to the result of preliminary tests, in which most subjects reported significant discomfort after 2 h. An addition hour was added to reinforce the progression of drivers' muscle fatigue. Driving for every 15 min, subjects were required to pull off the road and hold still with the driving posture. During the parking periods, SEMG signals were collected for 5 min along with a subjective comfort survey from the beginning of the tests. By the end of the driving test, there had been 10 segments of 5 min SEMG signals and 10 corresponding records of the subjective comfort for each subject (11 for a strong male).

### 2.2.2 Maximum Voluntary Contraction Tests

Carrying the surface electrodes, each subject was required to perform an isometric Maximum Voluntary Contraction (MVC) test before the driving test in order to measure the maximal electromyography activity. The subject stood comfortable on a specialized dynamometer that was designed to measure the maximal amount of force generated in the trunk extension with original hip angle at 90° (Fig. 2a). SEMG signals were recorded during three successive isometric MVC tests with a rest interval of 2 min. Each contraction lasted about 5 s. The possible muscle fatigue caused by MVC tests was minimized by a 15 min rest before driving tests.





**Fig. 2** **a** An isometric MVC test with the original hip angle at  $90^\circ$ . **b** Surface electrodes were placed cm apart overlying two bilateral positions, corresponding to the muscle bellies of erector spinae 3 cm from midline at the level of L1 and L3 respectively

### **2.3 Surface Electromyography Acquisition**

SEMG signals were collected bilaterally from lumbar erector spinae (Fig. 2b) using 4 data acquisition channels of a SEMG recording device (ME6000-T8, Mega Electronics Ltd., Finland) with sample rate 1,000 Hz. After appropriate skin cleaning with alcohol cotton in order to reduce skin impedances, bipolar Ag–AgCl surface electrodes were placed 2 cm apart overlying two bilateral positions, corresponding to the muscle bellies of erector spinae 3 cm from midline at the level of L1 and L3 respectively (Channel 1, L1 left; Channel 2, L1 right; Channel 3, L3 left; Channel 4, L3 right). The ground electrodes were placed next to the iliac crest. After baseline tests, all electrodes were fixed tightly using medical tapes.

### **2.4 Subjective Comfort Survey**

A subjective comfort survey of lumbar muscle was conducted during each parking period. A specific questionnaire was used in the survey. Subjects rated levels of comfort and discomfort from 1 to 7 corresponding to 7 feelings of lumbar muscle: 1 quite comfortable, 2 barely comfortable, 3 barely uncomfortable, 4 noticeably uncomfortable, 5 stiff and numb, 6 painful, and 7 unbearably painful. To reduce subjective errors and enhance the training effects of classifiers, raw subjective ratings were divided into three classes: 1–3, 4–5, and 6–7 with a new label of 0 comfortable, 1 fatigue, and 2 painful respectively.

### **2.5 Data Processing and Feature Extraction**

All data processing was conducted off-line using the Matlab software. Minus constant offset voltages, multi-channel SEMG signals were divided into segments of 30 s. The choice of this time interval was based on two points: (a) subjective

ratings were found relatively stationary in 30 s by preliminary tests; (b) The feature vector calculated from these segments showed better divisibility using this time interval. Each segment was processed by a 4-level WPT with a bio-orthogonal asymmetrical wavelet db5 (Fig. 3). The Shannon entropy and relative energy values were calculated from wavelet packets in the fourth level. The Shannon entropy of the wavelet packet was defined as [16]:

$$E(x) = - \sum_i x_i^2 \log(x_i^2) \quad (1)$$

with the convention  $0 \log(0) = 0$ , where  $x$  was the signal and  $x_i$  the coefficient of  $x$  in an orthonormal basis. Relative energy of the wavelet packet could be expressed as:

$$RE_{(j,k)} = \frac{\sum |WPC_{(j,k)}|^2}{\sum_0^{2^j-1} \sum |WPC_{(j,k)}|^2} \quad (2)$$

where  $(j, k)$  represented the sequence number of the wavelet packet nodes.

Since decomposing the signals into higher scales led to a greater focus on the frequency domain and the 4th level of decomposition was considered reasonable by trial-and-error [7], wavelet packet coefficients of node (4, 15) were analysed with a CWT. As one of the most suitable mother wavelets for EMG data analysis, db5 was used in this study with scales from 10 to 130 with a resolution of 10 [13]. Classic spectral features commonly used in EMG analysis like instantaneous median frequencies (IMDF), instantaneous mean frequency (IMNF), and instantaneous energy (IE) were obtained from the scalogram of the continuous wavelet coefficients (CWC). The scalogram (general power density along time and scale) was calculated with:

$$S(s, \tau) = |CWC_x(s, \tau)|^2 \quad (3)$$

The IMDF, IMNF, IE was defined as

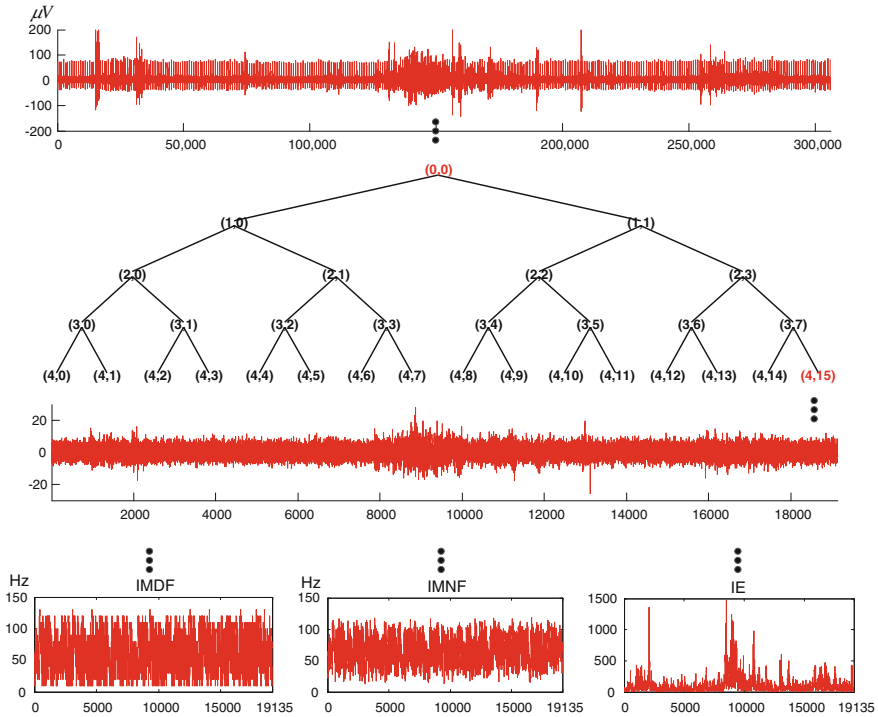
$$\int_0^{IMDF} S(s, \tau) ds = \int_{IMDF}^{\infty} S(s, \tau) ds \quad (4)$$

$$IMNF(\tau) = \frac{\int_{ls}^{hs} s \cdot S(s, \tau) ds}{\int_{ls}^{hs} S(s, \tau) ds} \quad (5)$$

$$IE = \int_0^T \int_{ls}^{hs} S(s, \tau) ds d\tau \quad (6)$$

where  $ls$  represented the lowest scale,  $hs$  was the highest scale of interest, and  $T$  was the time length of the segments.

As the temporal feature, RMS values of SEMG signals in driving tests were calculated from every 256 points (256 ms) without overlaps and normalized by the



**Fig. 3** Wavelet packet decomposition and the IMDF, IMNF, IE got extracted from CWT of the packet (4, 15). As the high-pass detail coefficients of the raw signal (0, 0), wavelet packet (4, 15) suppressed the noises from occasional trunk movement interruptions, and was better for the analysis of SEMG scalogram during muscle fatiguing

maximal RMS value of SEMG signals from MVC tests to minimize the individual difference between different subjects. Then 3 statistic features such as the average value, the slope of the linear regression, and area under the curve (AUC) were extracted from the normalized RMS (NRMS), IMDF, IMNF, and IE respectively to reduce the dimensions of the data.

Finally the statistic instantaneous spectral features, statistic temporal feature, and wavelet packet features together formed a 176-dimension feature space from 4 SEMG channels to classify 3 physiological statuses of the lumbar muscles. After data standardization and normalization for each subject, 810 samples were extracted from the SEMG signals of 4 lumbar muscles. The number of samples in 3 classes is 330, 330 and 150 respectively.

### 2.6 Classification

A C typed support vector classifier (C-SVC) was used in the study to conduct a classification of the 3-class status of drivers' lumbar muscle fatigue during

**Table 1** Distributed number and rate of three classes in the testing set with CCR 83.95 %

Prediction label		0	1	2	0	1	2
True label	0	142	20	7	84 %	12 %	4 %
	1	9	136	10	6 %	88 %	6 %
	2	6	13	62	7 %	16 %	77 %

long-term driving. Half of 810 samples were randomly picked out as the training set in each classification, and the others formed the testing set. Training set was used to train the SVC and the testing set was used to validate the prediction. An optimization of SVC parameters ( $c$ ,  $\gamma$ ) was conducted by grid search method for the best 5-fold cross validation accuracy. Grid search regions for two parameters were both defined as geometric progression  $2^a$ ,  $a \in [-8, 8]$  where scaling factor was defined as  $qa = 0.2$ . Based on the optimal parameters, the average correct classification rates (CCR) for the whole testing set and each class were obtained from 10 successive tests to test the classification capacity. Furthermore, receiver operating characteristic (ROC) curves were drawn to demonstrate the classification reliability.

### 3 Results

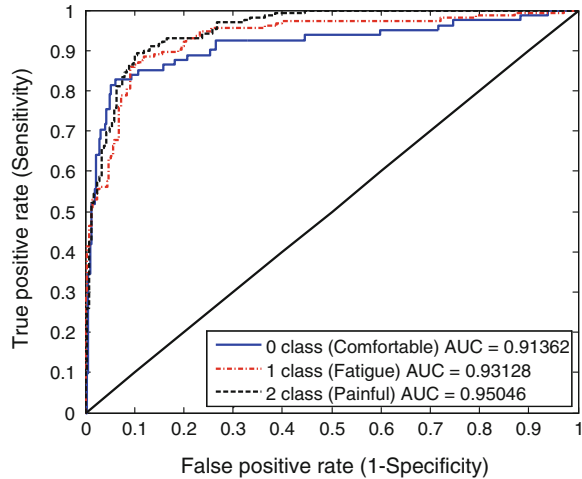
Half of 810 samples were randomly picked out as the testing set in each classification test. With RBF-SVC parameters ( $c$ ,  $\gamma$ ) optimized to (110, 0.082), the average (STD) testing CCR in 10 successive repeated tests was identified as 82.69 % (1.46 %).

To evaluate the classification quality, the result of one in 10 repeated tests was analysed and explained in Table 1, including the CCR of each class along with distributed number and rate. The whole CCR of the testing set was 83.95 % (340/405). Data underlined demonstrated the correct classification number and CCR for each class. Furthermore, three receiver operating characteristic (ROC, representing the relationships between false positive rates and true positive rates) curves were drawn to intuitively manifest the classification reliability in Fig. 4. The area under curves (AUC) was calculated as a metric of the classification quality. All AUC values in 10 successive tests were above 0.9, which meant the 176D feature vector and optimized SVC had a quite reliable classification capacity.

### 4 Discussion

The aim of the study was to determine the classification feasibility of multi-channel SEMG signals varying with lumbar muscle fatiguing due to prolonged driving. An experiment was conducted to investigate the progression of drivers'

**Fig. 4** ROC curves and AUC values of three classes in testing set with CCR 83.95 %

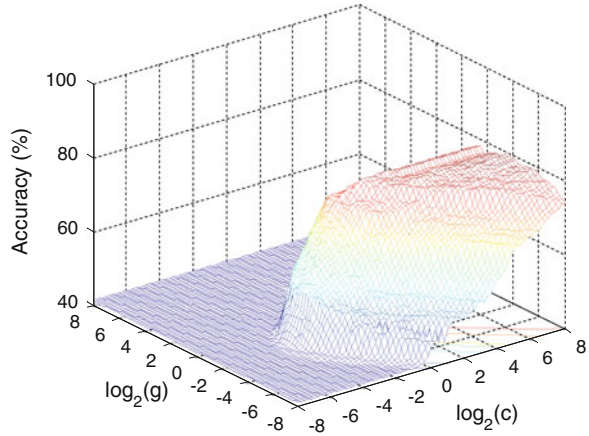


muscle fatigue. It can be expected that signs of fatigue were present in the muscles caused by 3 h driving. The reported muscle discomfort, stiffness and even pains in the driving tests are just an indication for the fact. The repeatability of the experiments was guaranteed by repeatable road environment and data acquisition procedures.

The discrimination of the SEMG signals with different status depends on the representation of the signals. A 44-dimension feature vector was extracted from SEMG signals of each erector spinae muscle. As a measure of the uncertainty associated with a random variable, Shannon entropy is commonly used to quantify the expected value of the information contained in a signal [8]. The 16 values of Shannon entropy from the 4th-level wavelet packet decomposition represented the information-related properties for a nonlinear describe of 16 selected frequency bands. Relative wavelet packet energy could describe the change of energy distribution between different frequency bands, as the frequency component of the power spectrum of SEMG signals became compressed with fatigue [2]. Besides, a conventional feature extraction method, in which the corresponding reduction of the instantaneous mean and median frequency of the signal and the corresponding increase of the EMG amplitude could be used to identify the onset and progression of muscular fatigue [5, 7, 11], was combined with the entropy and relative energy to form a compound feature vector for comprehensive representation of the SEMG signals. Considering the short time spent in training and predicting (0.375 s), methods of dimension reduction were not used in the study to avoid the information loss of SEMG signals.

Classification of multi-channel SEMG signals was performed with a high-dimension compound feature vector and optimized SVC. The results obtained from 10 successive tests have shown that the optimization of the classifier led to substantial improvement of performance with respect to a priori selection of kernel and parameters. The choice of the kernel depends on the representation space of

**Fig. 5** The result of parametric optimization based on grid search method for the best 5-fold cross validation accuracy: optimum  $c = 110$ ,  $\gamma = 0.082$



samples. The prediction accuracy of SVM could be strongly affected by the adaptability between kernel function and data structure [14]. Linear kernel and radial basis function kernel were commonly used in SVM classification [14, 15], and both were tested to compare the classification capacity. With the same training set and testing set and best  $c = 100$ , the testing CCR of linear-SVC dropped 3.75 % ( $78.94 \pm 1.63$  %) compared the results of RBF kernel. This result demonstrated the better adaptability of RBF kernel in the classification of SEMG signals. The parameter of the classifier is also a key factor that affects the accuracy of the recognition system in a serious way (Fig. 5). Parametric optimization based on grid search method could find an optimum combination of the binary parameters.

This study mainly focuses on the freeway environment without high density traffic, and therefore the established recognition model seemed weak in wide universality. Furthermore, the number of participants is not sufficient to conclude the general evolution of drivers' lumbar muscle fatigue.

## 5 Conclusion

A novel method was presented in the study for supervised classification of multi-channel SEMG signals with the aim of recognizing 3 levels of drivers' lumbar muscle fatigue during prolonged driving. Based on the WPT and CWT analysis of SEMG signals, a compound high-dimension representation space composed of Shannon entropy, relative energy and statistic features of instantaneous median frequency (IMDF), instantaneous mean frequency (IMNF), instantaneous energy (IE), and root mean square (RMS) was proposed. The average CCR of 10 successive tests using a RBF-SVC was around 82.69 % with AUC all above 0.9.

**Acknowledgments** This work was supported by the Opening Fund KF11011 of State Key Laboratory of Automotive Safety and Energy, Tsinghua University.

## References

1. Cifrek M, Medved V, Tonkovic S et al (2009) Surface EMG based muscle fatigue evaluation in biomechanics. *Clin Biomech* 24(4):327–340
2. De Luca CJ (1984) Myoelectrical manifestations of localized muscular fatigue in humans. *Crc Crit Rev Biomed Eng* 11(4):251–279
3. El Falou W, Duchene J, Grabisch M et al (2003) Evaluation of driver discomfort during long-duration car driving. *Appl Ergon* 34(3):249–255
4. Merletti R, Loconte LR, Orizio C (1991) Indices of muscle fatigue. *J Electromyogr Kinesiol* 1(1):20–33
5. Luttmann A, Jager M, Laurig W (2000) Electromyographical indication of muscular fatigue in occupational field studies. *Int J Ind Ergonomics* 25(6):645–660
6. Wang G, Yan ZG, Hu X et al (2006) Classification of surface EMG signals using harmonic wavelet packet transform. *Physiol Meas* 27(12):1255–1267
7. Rafiee J, Rafiee MA, Yavari F et al (2011) Feature extraction of forearm EMG signals for prosthetics. *Expert Syst App* 38(4):4058–4067
8. Wang D, Miao DQ, Xie C (2011) Best basis-based wavelet packet entropy feature extraction and hierarchical EEG classification for epileptic detection. *Expert Syst App* 38(11):14314–14320
9. Hu X, Wang Z, Ren X (2005) Classification of surface EMG signal using relative wavelet packet energy. *Comput Methods Programs Biomed* 79(3):189–195
10. Hostens I, Ramon H (2005) Assessment of muscle fatigue in low level monotonous task performance during car driving. *J Electromyogr Kinesiol* 15(3):266–274
11. Coorevits P, Danneels L, Cambier D et al (2008) Correlations between short-time Fourier- and continuous wavelet transforms in the analysis of localized back and hip muscle fatigue during isometric contractions. *J Electromyogr Kinesiol* 18(4):637–644
12. Beck TW, Housh TJ, Johnson GO et al (2005) Comparison of Fourier and wavelet transform procedures for examining the mechanomyographic and electromyographic frequency domain responses during fatiguing isokinetic muscle actions of the biceps brachii. *J Electromyogr Kinesiol* 15(2):190–199
13. Hostens I, Seghers J, Spaepen A et al (2004) Validation of the wavelet spectral estimation technique in biceps brachii and brachioradialis fatigue assessment during prolonged low-level static and dynamic contractions. *J Electromyogr Kinesiol* 14(2):205–215
14. Davy M, Gretton A, Doucet A et al (2002) Optimized support vector machines for nonstationary signal classification. *IEEE Signal Process Lett* 9(12):442–445
15. Lucas MF, Gaufriau A, Pascual S et al (2008) Multi-channel surface EMG classification using support vector machines and signal-based wavelet optimization. *Biomed Signal Process Control* 3(2):169–174
16. Coifman RR, Wickerhauser MV (1992) Entropy-based algorithms for best basis selection. *IEEE Trans Inf Theor* 38(2):713–718

**Part VI**  
**Vehicle Style and Aerodynamic Design**



# Aerodynamic Investigations in Conceptual Vehicle Development Supported by Integrated Design and Simulation Methods

Mario Hirz, Severin Stadler, Martin Prenner and Johannes Mayr

**Abstract** In automotive development, the main characteristics of a new car model are determined in the initial phases of product generation. Since the conceptual definition has to consider various, partially conflicting boundary conditions and requirements, the resulting vehicle concept always represents an outcome of intensive optimization processes. This multidisciplinary optimization requires a high flexibility from the tools, methods and processes applied. In the present approach, an integration of computer-aided design (CAD) and computer-aided engineering (CAE) disciplines form an easy-to-handle tool to support and maintain the entire conceptual full-vehicle process. This starts with initial ideas, sketches and specifications, continues with 3D-CAD representation of boundary conditions, forming preliminary and eventually final vehicle concept geometries, and finally provides functional layout procedures for weight estimation, propulsion layout, driving dynamics behaviour and aerodynamic characteristics.

**Keywords** Concept phase · Integrated design · Knowledge-based engineering · Aerodynamics · CFD simulation

---

F2012-E06-004

---

M. Hirz (✉) · S. Stadler · M. Prenner  
Graz University of Technology, Graz, Austria  
e-mail: mario.hirz@tugraz.at

J. Mayr  
MAGNA Steyr Fahrzeugtechnik, Graz, Austria

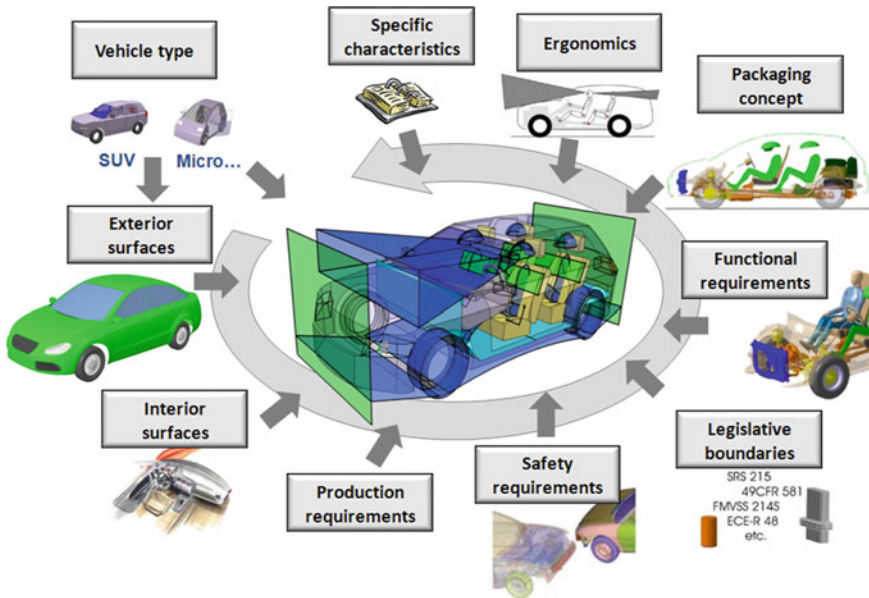
# 1 Introduction

In automotive development, the main characteristics of a new car model are determined in the initial phases of product generation. Since the conceptual definition has to consider various, partially conflicting boundary conditions and requirements, the resulting vehicle concept always represents an outcome of intensive optimization processes. This multidisciplinary optimization requires a high flexibility from the tools, methods and processes applied. In the present approach, an integration of computer-aided design (CAD) and computer-aided engineering (CAE) disciplines form an easy-to-handle tool to support and maintain the entire conceptual full-vehicle process. This starts with initial ideas, sketches and specifications, continues with 3D-CAD representation of boundary conditions, forming preliminary and eventually final vehicle concept geometries, and finally provides functional layout procedures for weight estimation, propulsion layout, driving dynamics behaviour and aerodynamic characteristics.

## *1.1 The Automotive Concept Phase*

During the initial design and layout phase of a new car, an optimal interaction between the styling process, technical engineering operations, cost accounting and customer-related inputs represent an important factor for an efficient concept generation. The concept phase of automotive development has to consider numerous factors that influence the definition of a full-vehicle concept model. In virtual development, this vehicle model is displayed in different ways to account for the product structure list, the conceptual vehicle cost structure, weight- and mass lists, finite element meshes, styling models and of course a 3D-CAD model structure. All of these representations of a concept vehicle serve for specific fields of development and are generated and maintained in different departments. In most development processes, these subareas are treated more or less separately, and the data transfer between the disciplines is focused on the tasks in each section. This procedure leads to an opaque full-vehicle development process, which has to be monitored carefully and with a significant organizational effort.

Figure 1 shows a selection of most important influencing factors in the early development phase. In the present approach, an integrated vehicle model stands in the middle of different working areas, linking the disciplines and serving as a data collector and representation model for the entire development progress. At the beginning, initial styling studies are implemented into the geometry model to enable an adjustment of the targeted geometry data (vehicle dimensions, wheel base, gauge, etc.) with the styling proposals. This initial styling information can be integrated in the form of simple 2D sketches, drawings or first surface data derived from clay models. In later phases, computer-aided exterior and interior styling surfaces are imported into the 3D-CAD model to facilitate detailed studies of the



**Fig. 1** Influencing factors in the early development phase of new car models

vehicle styling in view of legislation-based boundaries (crash and pedestrian safety regulations), ergonomic tasks and dimensional viewpoints. Initial styling surfaces provide a basis for several technology-oriented development steps, e.g. the vehicle packaging, initial body design, ergonomic studies and others. In this way, the type of the car and the shape of its exterior represent an important characteristic in conceptual development. Early exterior styling proposals also provide an important basis for initial aerodynamic assessment and investigations.

## 2 Integrated Approach to Virtual Concept Development

The present approach includes the implementation of an integrated vehicle model for the improvement of conceptual automotive development. All of the processes in the concept and pre-development phases are linked to the comprising car model in order to connect the different fields of development (geometry, legislation, functional aspects, etc.). This integrated full-vehicle model concerns geometry data, functional data and different interfaces for data transfer to connected processes. A powerful database contains a list of all information relevant for the control of geometry models and for other simulation and calculation procedures. The product visualization is performed by an integrated, parameterized 3D-CAD full-vehicle model, which is controlled by the main database. The 3D-CAD geometry model serves as a basis for far-reaching geometrical-related investigations and also as a

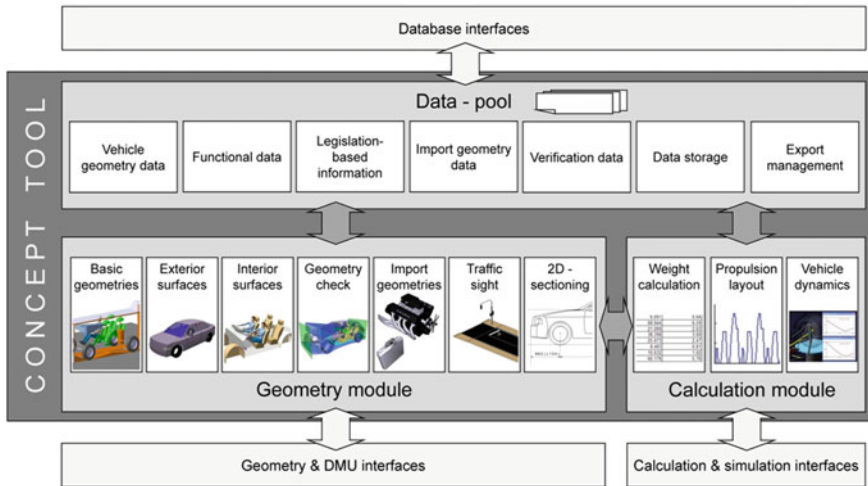
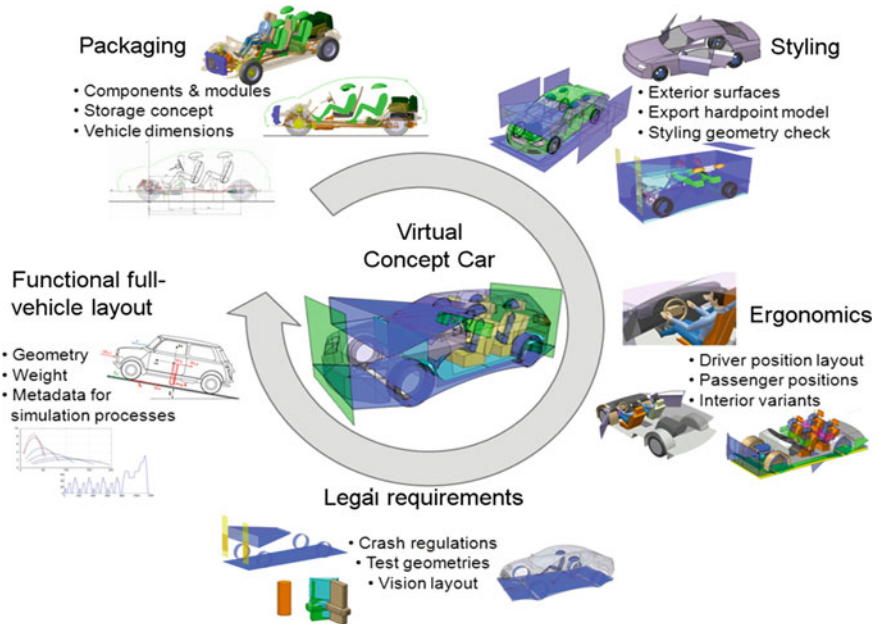


Fig. 2 Principle architecture of the concept tool [9]

demonstration unit of the entire concept model. A bi-directional connection to the database enables a parametric geometry control, as well as a tracking procedure and data archiving. This virtual concept model is connected to several supplementary tools and procedures via data interfaces. Thus, the geometry model can be understood as display of the overall vehicle concept model [1, 2].

The influencing parameters of the early development phase predefine the structure of an integrated concept car, which forms the core of a supporting tool for all concept phases of automotive development projects [3]. This concept tool consists of a database that includes a logical order of data-modules and a linked 3D-CAD model comprising seven main sections (Fig. 2). An externally controlled 3D-CAD-based development strategy simplifies the conceptual design and packaging process by using an external data pool, which controls the parameterized model. The external data collector includes a key collection of relevant dimensions, positions and/or ergonomic viewpoints. The data sheets also permit modifications and variant studies of the virtual car by project partners who are not primarily specialized in the applied 3D-CAD design software, thereby providing direct access to the relevant information on vehicle geometry.

Figure 3 gives an overview of the applications based on the workflow of typical project engineering procedures. Starting from first vehicle data, an initial conceptual 3D-CAD model is defined. Depending on the requirements of each individual development step or verification process, different modules of the virtual concept car are used. Figure 3 shows an interdisciplinary consideration in which all tasks from the conceptual development cycle are performed within the virtual vehicle model. Data transfers to external applications are triggered and monitored by the virtual model, too, so that the general data flow is managed by one centralized system. The results of all working procedures are saved and maintained in



**Fig. 3** Interdisciplinary consideration of the workflow in an automotive concept phase using the integrated approach [9]

an integrated database structure. The centralized data management concept avoids inconsistent information flow and supports the execution of variant studies and optimizing cycles significantly.

The package development and verification includes the definition of packaging-relevant vehicle data, which correspond with the requirements in the specification table. This process includes the representation of vehicle main dimensions through appropriate parametric boundary surfaces and geometrical elements in the 3D-CAD model. An additional implementation of predefined components and human models enables the definition of an initial full-vehicle packaging concept. The virtual ergonomic investigations treat the definition of ergonomic solutions for driver and passengers. The virtual interior model comprises of seats, dashboard, control elements and cabin-limiting surfaces and is directly connected to the positions of human models as driver and passengers. Derived from the seating positions and the space requirements, a variable configuration of the 3D-CAD interior model supports the initial definition and optimization cycles under the consideration of specific ergonomic necessities.

The legal requirements for full-vehicle development include instructions for passive safety, geometrical prescriptions for lighting equipment and relevant standards for driver vision and passenger safety. A representation of each regulation as a geometric check surface enables a direct implementation into the data structure of the integrated virtual vehicle model and thus a consideration

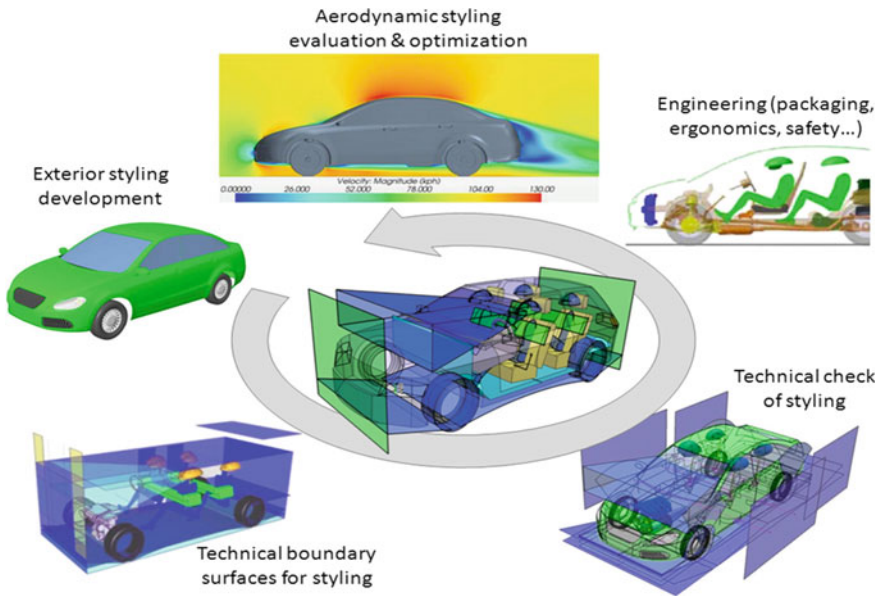
throughout the entire development cycle. Besides different geometry-based applications, the functional layout and evaluation represents a main area in conceptual full-vehicle development. This includes the estimation of vehicle weight and the position of the vehicle balance point, an estimation of driving performance and fuel (i.e. energy) consumption, and a pre-computation of lateral driving and vehicle handling characteristics. Due to the focus of the present publication, the integration of the styling process in automotive concept development, with a focus on aerodynamic investigations, is treated more detailed in the following sections.

## ***2.1 Integration of the Styling Process***

During the initial phase of development, the limited availability of information about the vehicle styling makes it difficult to consider the future outline shape. To avoid problems in later steps, two-dimensional styling sketches can be implemented directly into the 3D-CAD vehicle model. This procedure allows for an early assessment of the technology-styling convergences and makes it possible to carry out modification or optimization cycles from the beginning. The implementation of the styling process itself into the conceptual full-vehicle development is performed by a derivation of relevant geometries from the virtual concept car.

These surfaces are summarized in technical boundary surfaces for styling, which represent the specification geometries of vehicle main dimensions and the space requirements for passenger, luggage or components, as well as legal instructions. An import into the applied styling software is accomplished via neutral geometry data interfaces. The specifications for the styling process are saved in the database based on the current project progress. In the inverse process, 3D-styling surfaces are also delivered via a neutral data format and can be implemented directly into the virtual vehicle model as geometry elements. A separate check process enables the inspection of styling data with respect to the fulfilment of packaging-relevant and legislative predictions (Fig. 4).

Today, vehicle styling is mainly created in computational styling software (CAS), which supplies subsequent engineering processes with geometrical information of different visible interior- and exterior surfaces of a car. This geometrical information is transferred from CAS into computer-aided design (CAD) software to be revised to fulfil different in view of surface quality, tolerances and data formats under consideration of technical related boundary conditions, e.g. from packaging and simulation. Implemented in a vehicle product structure of a comprehensive CAD model, the styling surface data influence the boundary conditions of several engineering procedures. In case of the exterior surfaces of a new car model, the styling surfaces are considered in the vehicle packaging, the development of vehicle and pedestrian safety, in ergonomics investigations and of course in the aerodynamic optimization.



**Fig. 4** Integration of styling, engineering-oriented influences and aerodynamic investigations in early vehicle development

### 3 Aerodynamic Investigations in Automotive Development

The aerodynamic behaviour of vehicles directly influences the air resistance and thus the overall driving resistance. In case of automobiles, the drag is one of the important influencing factors of the fuel consumption [4]. In addition, the aerodynamic lift has an important influence on vehicle driving behaviour and thus on vehicle safety characteristics, especially at higher vehicle speed. These are the reasons, why the optimization of aerodynamics plays an important role in the development of new models. Besides several technology-based influencing factors, e.g. the type of vehicle, its size, the flow characteristics of the cooling system and others, the exterior styling plays a major role in aerodynamic investigations. In this way, the prediction of aerodynamic characteristics of different early styling proposals is carried out in parallel to the development of the vehicle outline. Due to the fact, that in these initial phases styling surfaces mainly exist as virtual models within CAS-software, the assessment and evaluation is performed based on computer-aided aerodynamic simulation processes.

In the early conceptual phase, the general shape of the car is developed and optimized; detailed modifications are performed in later steps. As an example, the angles of the front- and rear window, the shape of the engine hood, the car roof-contour and the rear end are defined by stylists and evaluated regarding their aerodynamic behaviour in more or less parallel simulation sequences. This simultaneous development requires a close co-operation of styling and simulation



departments and in addition an efficient data management process. Another challenge of this early development phase represents the uncompleted data status of the vehicle model. Due to the fact, that important components and modules of a new car model are developed in later steps, there is a big lack of information for a timely evaluation. With the target to bring the simulation close to early exterior styling development, the present approach provides a start-up model for aerodynamic investigations, which includes several simplified components for the creation of a conceptual vehicle model including all required components and modules for aerodynamic investigations.

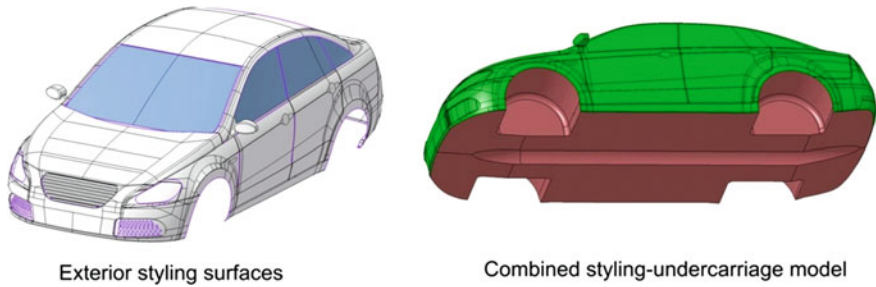
In a workflow of aerodynamic investigations in automotive development, the computational-fluid-dynamics-(CFD) based evaluation and optimization starts very early in the concept phase, supporting the styling process of a new car model. Once having available scaled hardware models of the car (e.g. clay or foam models), the wind tunnel development starts and delivers both, measured values of aerodynamic behaviour for the support of simulation processes and the possibility of aerodynamic fine-tuning by application of detailed modifications directly at the hardware model. In later development phases, e.g. in the series development, the wind tunnel development becomes more and more important because of the availability of detailed hardware models including all mechanical components. During initial phases, simulation procedures are able to deliver information for the evaluation of different aerodynamic measures on the vehicle outer shape. In this way, variant studies and optimization cycles are often performed in combined processes, which include wind tunnel development and CFD simulation.

The main potential for aerodynamic improvements can be achieved in the early phase during the definition of the general vehicle shape characteristics. Throughout later development phases, the car's main outline is determined; aerodynamically relevant modifications are performed by application of detailed modifications only. In an exemplary development process, 70 % of the drag coefficient reduction was achieved in the concept phase by optimization of the exterior surfaces [5]. This fact points to the significance of CFD-based optimization in initial vehicle development.

### ***3.1 Geometry Model***

Similar to the comprehensive concept model, the geometry model for aerodynamic investigations is developed within CAD-environment [6] and includes all geometrical information of the vehicle. In the course of conceptual design processes, the styling surfaces are delivered from CAS and integrated into the CAD model. Due to the fact, that the vehicle styling is accomplished under different boundary conditions and by use of different software packages, there often occur problems in the data transfer from CAS to CAD [7]. In any case, the delivered surface data



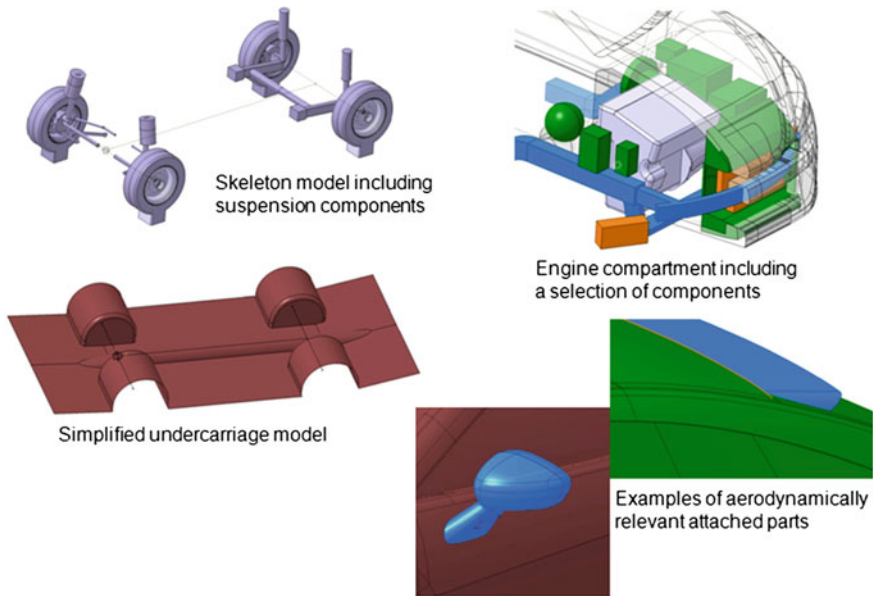


**Fig. 5** Example of exterior styling surfaces and a conceptual combined styling-undercarriage model

have to be modified according the technology-based requirements of modern parametric-associative design. This includes the repairing of gaps, overlapping, discontinuous surfaces and other erroneous elements as well as the consideration of the higher demands on geometrical tolerances. In addition to the lack of surface quality, styling models do not include mechanical components or modules of undercarriage, wheels, suspension, brakes and others, which are basically required for an aerodynamic evaluation of a vehicle concept.

In the present approach, these missing technically detailed surfaces are added within the design process by use of a predefined catalogue of CAD models of specific modules and components. These models are combined in a CAD-based product structure and have a variable, parametric-associative structure which can be adapted to the corresponding exterior styling surface.

Figure 5 shows an example of exterior styling surfaces and a conceptual combined styling-undercarriage model. The parametric CAD model for aerodynamic simulation consists of a skeleton, which controls the main dimensions, an undercarriage module, suspension components including wheels, an engine compartment composed of dummy geometries of the corresponding components, several attaching parts and the geometry of the simulation environment. All modules are managed in a CAD-based assembly, whereby the geometrical dimensions are controlled by a generic parameter structure. Depending on the dimensions of the treated vehicle concept, the geometries are adjusted and positioned by defining the corresponding parameter values. In the following step, the components are joined with the imported and revised styling surfaces and form a vehicle geometry model, which fulfils the requirements of the subsequently performed CFD processes. Finally, the simulation area is defined in CAD too and the prepared geometry is transferred from the CAD environment into the pre-processor of the CFD software for further operations. Figure 6 shows a selection of components of the parametric CAD-model for early aerodynamic investigations.

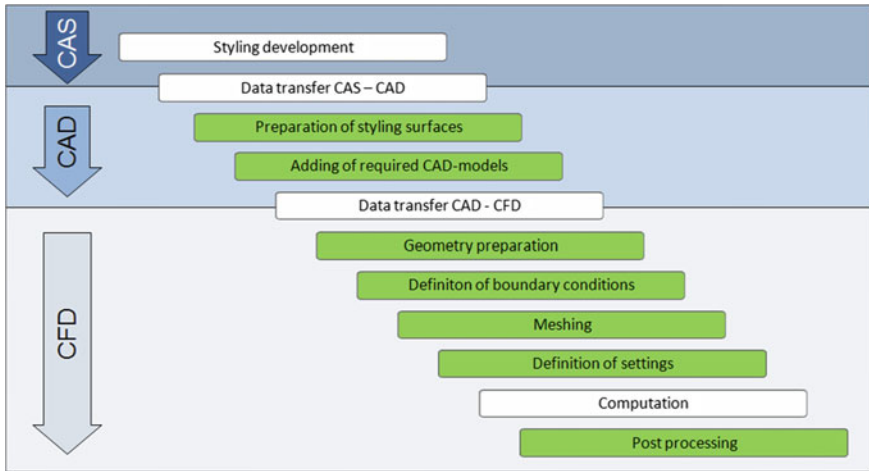


**Fig. 6** Components of the parametric CAD-model for early aerodynamic investigations

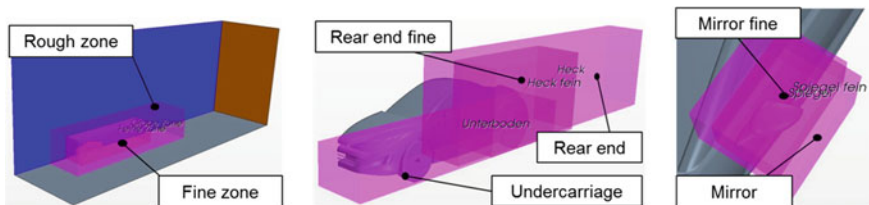
### 3.2 CFD Simulation

The aerodynamic simulation is performed in commercial CFD software, e.g. [8], whereby the conventional simulation process has been optimized under consideration of the specific requirements of conceptual development. Figure 7 includes the sequences of an optimized aerodynamic simulation process. The process is divided into the three main areas styling (CAS), design (CAD) and simulation (CFD), which are carried out sequentially theoretically. Within an actual application, variation- or optimization cycles can lead to the implementation of different recapitulation cycles in the workflow. The green shaded bars indicate working packages, which are performed supported by automated routines, the implementation of knowledge-based templates or the application of specific methods and tools. The implementation of these measures enables a significantly improvement of the overall aerodynamic simulation process.

After provision of styling data, the process starts with the transfer of geometry followed by CAD-based data processing, including the preparation of styling surfaces and the implementation of required CAD-models. The data transfer from the CAD environment into the CFD-software is carried out by use of neutral data formats. The pre-processing sequence within CFD environment includes a final preparation of geometry, the definition of boundary conditions, model meshing and the input of fluid mechanics related settings and physical adjustments. After having performed the computation procedure, the simulation results are worked out in the post-processing sequence.



**Fig. 7** Sequences of an optimized aerodynamic simulation process

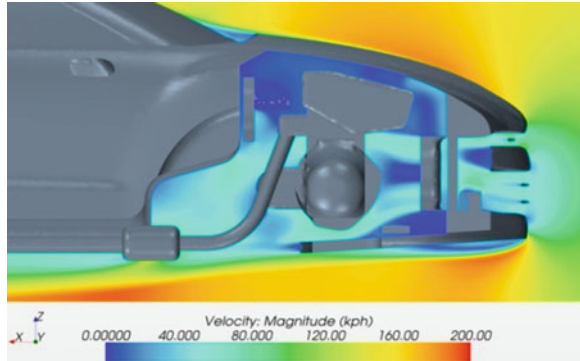


**Fig. 8** Examples of local mesh refinement areas of the start-up file for CFD [10]

The optimization includes several modifications of a conventional process. CAD-based start-up models contain variable template models of components for the early creation of comprehensive full vehicle models for aerodynamic simulations. A standardization of data import and export between CAD and CFD simplifies the geometry data exchange by use of predefined settings and adjustments. The CFD-simulation process itself is optimized by implementation of a start-up file including different information and predefined adjustments. In addition, the CFD workflow is partially automated by use of specific programmed routines (macros). The start-up file for CFD includes three different meshing regions (surrounding areas, radiators and fan) with a number of local mesh refinement areas (Fig. 8).

These specified local areas cause a reduced total number of cells and so a reduced computing time but also enable accurate simulation results at the same time. The systems of coordinates in this file correspond with those of the CAD-geometry model. Physical boundary conditions and pre settings as well as reports and plots for the subsequent post-processing are integrated in this file. To reach the targets of automation and reduction of time consuming pre- and post-processing, a

**Fig. 9** Exemplary engine compartment flow [10]



macro-based workflow has been developed. It starts with the import of neutral geometry data, followed by the preparation of the simulation area, the radiators or the fan and finally supporting the post-processing. In this way, the manual data processing is reduced significantly.

The post-processing section enables a user-defined visualization of flow- and pressure characteristics in different areas like the vehicle environment, the engine compartment or the cooling system. In addition, turbulences, flow velocities and pressure distributions can be illustrated. As a main result of the CFD-simulation, specific values of drag- and lift coefficients are calculated, which serve as a basis for the assessment and evaluation of early vehicle exterior styling surfaces. As an example of post-processing results, Fig. 9 shows a representation of flow characteristics through an engine compartment.

## 4 Conclusion

Increasing competitive pressure and constantly shortened development time in the automotive industry requires the introduction of efficient virtual development methods and tools. The presented collaborative development methods possess the potential to significantly reduce design and time effort during the layout and concept phase of a car by increasing the product data quality at the same time. The integrated representation of vehicle concepts and variants enables a quick and binding evaluation of customer orders and additionally the study of technical possibilities is less time-consuming. The centralized character of the virtual product model supports an efficient collaboration of several involved development departments and suppliers.

Focusing on aerodynamic investigations by application of computational fluid dynamics, the integration of knowledge-based engineering methods supports an efficient development and optimization of vehicle exterior styling even during conceptual development. The introduced optimized process covers the entire data

flow, starting up with styling processes, the general vehicle layout and packaging studies within computational design software and considering several technical aspects, like crash- and pedestrian safety as well as legislation based boundary conditions. The generation of parametric start-up models and the programming of automated workflow-routines within the applied software packages are able to increase the efficiency during the entire workflow significantly.

Combining the requirements of styling, design and simulation, the presented methods and strategies support an optimization of conceptual aerodynamic development by enhancement of data quality and reduction of computation effort at the same time.

## References

1. Göber T, Hirz M, Krammer S, Pollheimer D (2007) Conceptual automotive design and digital mock-up methods supported by external parameter control. SAE World Congress, Detroit
2. Hirz M, Hirschberg W, Dietrich W (2008) Integrated 3D-CAD design methods in early automotive development processes. International Federation of Automotive Engineering (FISITA) World Congress, Munich
3. Rossbacher P, Hirz M, Dietrich W (2010) 3D-CAD parametric design strategies with interlinked CAE reference object creation for the overall vehicle layout optimization in the early automotive concept phase. International Federation of Automotive Engineering (FISITA) World Congress, Budapest
4. Hirschberg W, Hirz M, Eichberger A (2011) Automotive engineering 1. Lecture script at Graz University of Technology
5. Liebl J, Kerschbaum H, Pfannkuchen E (2008) Die Aerodynamik des neuen BMW X5. Automobiltechnische Zeitschrift (ATZ). ISSN: 0001-2785
6. Dassault Systèmes, homepage of CATIA V5: <http://www.3ds.com/>. Accessed 09 Nov 2011
7. Bonitz P (2009) Freiformflächen in der rechnerunterstützten Karosseriekonstruktion und im Industriedesign, 1st edn. Springer, Berlin. ISBN: 978-3-540-79439-4
8. CD—adapco, Star-CCM+, homepage: <http://www.cd-adapco.com/>. Accessed 07 Nov 2011
9. Hirz M (2011) An approach of multi-disciplinary collaboration in conceptual automotive development. Int J Collab Enterp—IJCent. ISSN: 1740-2085
10. Prenner M (2012) Abschätzung des aerodynamischen Verhaltens in der konzeptionellen Fahrzeugentwicklung. Diploma Thesis, Graz University of Technology

# Research on Drag Reduction of Commercial Vehicle Based on Aerodynamics

Shijie Fan, Qiang Fu, Jialin Zhang, Jinying Ma, Jing Zhao and Kelong Lu

**Abstract** One of the effective ways to reduce the fuel consumption for vehicles is the aerodynamic drag (Cd) reduction. In this paper, both the numerical simulation method and wind tunnel test were taken to research the factors influence on the aerodynamics drag reduction of commercial vehicles. The add-on parts including deflector, side fenders, visor, engine compartment flow etc. The validity of their abilities to reduce the value of Cd was investigated. The results show that, for a tractor with a container, using add-on parts can obviously reduce the aerodynamic drag (Cd) and save the vehicle energy. It was proved that some of the aerodynamic drag reduction methods in this paper were useful and powerful when they added on the typical commercial vehicle.

**Keywords** Commercial vehicle · Aerodynamic drag reduction · Energy saving · CFD analysis · Wind tunnel test

## 1 Introduction

Nowadays, the research on the vehicle energy saving and emission reducing enters the advanced stage, as a result, more and more attentions are paid to the aerodynamic drag. The aerodynamic drag is an important part of the vehicle driving resistance. When the vehicle velocity becomes higher and higher, the percentage

---

F2012-E06-007

---

S. Fan (✉) · Q. Fu · J. Zhang · J. Ma · J. Zhao · K. Lu  
China FAW Co., Ltd. R&D Center, Changchun, China  
e-mail: fanshijie@rdc.faw.com.cn

of aerodynamic drag in the total drag will rise rapidly and the aerodynamic drag soon become the main element which consumes the vehicle energy. In general, the aerodynamic drag reduction is important to the vehicle energy saving.

In the context of the booming highway development, the heavy commercial vehicle with the unique container becomes the main transportation of the logistics industry. The aerodynamic drag reduction is becoming more and more important to energy saving. In this paper, a typical commercial vehicle was taken as the research object, the aerodynamic principle was chosen as the research foundation. The numerical simulation method and wind tunnel test were both used to study the various factors influenced on the aerodynamic drag reduction and different methods of the aerodynamic drag reduction. The practical application and mechanism analysis were also both considered in the study. The finite volume method which was based on the CFD software was used for numerical simulation. The full scale wind tunnel test was taken in the largest wind tunnel of China. Through a comprehensive study, the influences of various factors on aerodynamics drag reduction were found. The result was applied in the real vehicle and a good feedback was got.

## 2 CFD Analysis of Basic Model

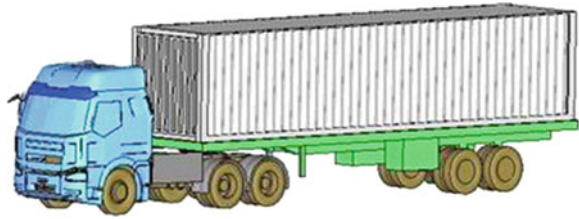
Compared with passenger car, commercial vehicle has bad streamline and entirety shape, which contains cab, cargo body and so on, so the entirety of the whole flow is destroyed and many parts of the vehicle make the pressure drag and separation, leading the drag coefficient to increase. Drag reduction of the commercial vehicle should start with analyzing the basic model firstly, find the position where drag happens and take effective measure to reduce the drag coefficient.

### 2.1 Basic CFD Simulation Model and Analyzing Tools

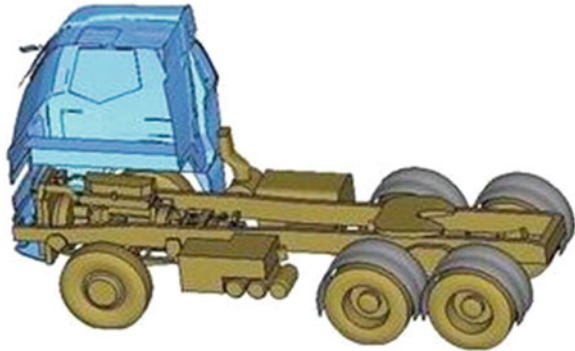
Selecting the commercial vehicle that contains tractor and container as basic model, with the trailer contains 40 ft cargo body. The tractor is the typical commercial vehicle of FAW. The CFD model was built based on the product of FAW including actual tractor, container, chassis, engine compartment, sun visor, cargo body with surface character, rear-view mirror etc. Figures 1 and 2 show the CFD model. All the other models modified below were built based on the basic model (Fig. 3).

Star CMM+ (64 bit, 6.0 version) was chosen as the CFD analyzing soft, with  $k-\varepsilon$  turbulence model, 0 yaw angle, velocity as 80 km/h, about 20 millions volume mesh, mesh type was trimmer with prism layer.

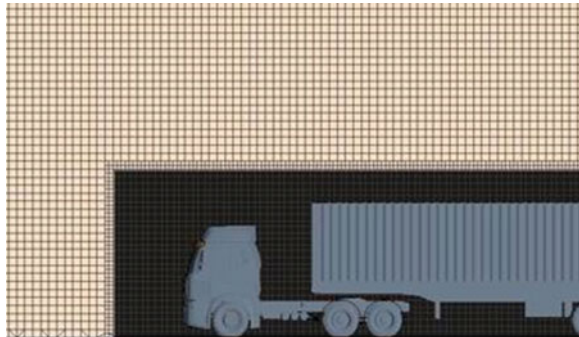
**Fig. 1** Basic CFD model



**Fig. 2** Tractor and actual chassis model



**Fig. 3** Trimmer mesh (a part of all)



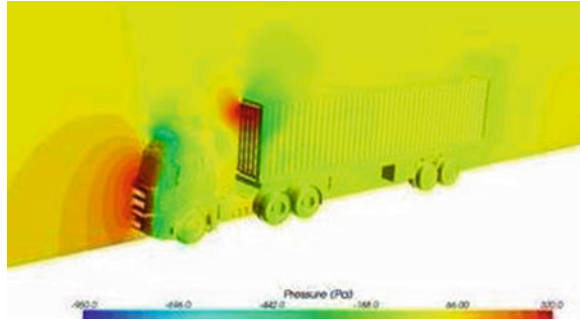
## ***2.2 Result of Basic Model Analysis and Improved Scheme***

Figures 4 and 5 show the simulation results of basic model, its drag coefficient, marked as “a”, is the benchmark of the follow-up CFD analysis.

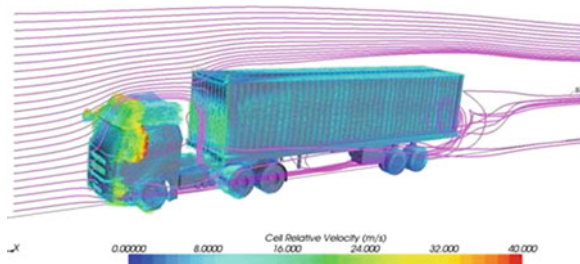
By analyzing the pictures, there are two large positive pressure areas at the front of the vehicle. One positive pressure is happened at the front of the container and another appears on the front of the tractor while a negative pressure area appears at the back of the vehicle. The pressure drag is the main source of the aerodynamic drag. It is found that there are some flow separate areas: the corners of tractor and container, rear-view mirror, chassis, wheel-arches etc. They are also the sources of the aerodynamic drag.



**Fig. 4** Simulation pressure distribution



**Fig. 5** Simulation surface velocity distribution and velocity streamlines



To reduce the aerodynamic drag of the basic model, the CFD analysis of following schemes were carried out:

- (1) Adding deflector;
- (2) Adding deflector and side fenders;
- (3) Adding deflector and closing the grille;
- (4) Adding deflector and removing sun visor;
- (5) Extending the deflector.

### 3 CFD Analyses of Improved Cases

The five CFD improvement cases were analyzed by the same method mentioned above. Some of the CFD models were shown in Figs. 6, 7, 8, and 9. Table 1 shows analysis results.

The results are analyzed as below:

Case 1: The CFD result of the basic vehicle indicated that the pressure drag between front and rear parts of the vehicle bring on main aerodynamic drag. In this case, the positive pressure area, which distributed in front of the container was eliminated by the installation of a deflector (see Figs. 10 and 4). As a result, the vehicle drag coefficient decreased obviously by 23.3 % in contrast to the basic vehicle.

**Fig. 6** Basic vehicle with deflector (Case 1)



**Fig. 7** Basic vehicle with deflector and side fenders (Case 2)

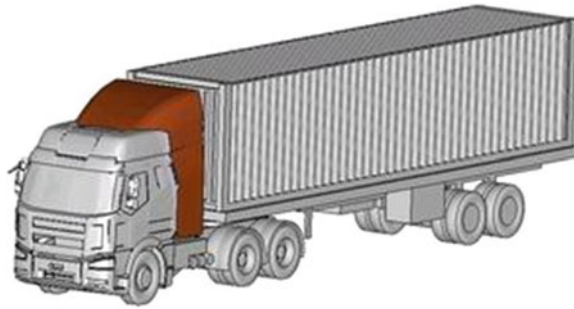


**Fig. 8** Basic vehicle with deflector and without visor (Case 4)



Case 2: The side fenders were installed on the basis of case 1 to prevent the drag caused by lateral air swirling under the vehicle. The effect was obvious, for the drag coefficient decreased by 7.9 % on the basis of case 1 and decreased by 29.3 % in contrast to the basic vehicle.

Case 3: The grille was closed on the basis of program 1, leading to the drag coefficient increased by 4 % in contrast to program 1. Because of this heavy truck had a forward control cab, the cab front face perpendicular to the ground. The closing grille will form a large surface being perpendicular to the airflow and form a larger positive pressure area, resulting in increasing drag.

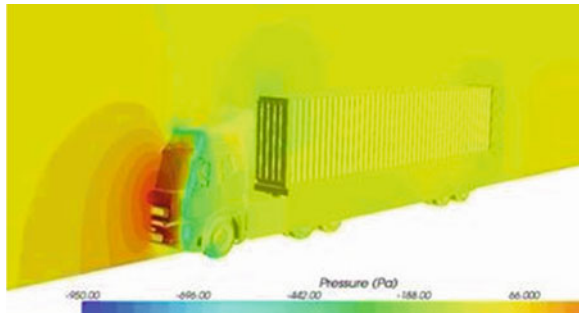


**Fig. 9** Basic vehicle with a longer deflector (Case 5)

**Table 1** CFD results of all cases

Case	Case	Drag coefficient a	Relative variation Base (%)
Basic vehicle	—		
Case 1	Installing deflector	0.767a	-23.3
Case 2	Installing deflector and side fenders	0.707a	-29.3
Case 3	Installing deflector and closing the grille	0.798a	-20.2
Case 4	Installing deflector and removing visor	0.772a	-22.8
Case 5	Installing a longer deflector	0.725a	-27.5

**Fig. 10** Case 1 simulation pressure distribution



Case 4: Removed the visor over the front windshield, the drag coefficient increased by 0.7 % in contrast to case 1. The result shows that the visor has a slightly effect on the drag reduction, which is influenced by the pressure distribution of the visor.

Case 5: Extended the deflector on the basis of program 1, the drag coefficient decreased by 5.5 % in contrast to case 1 and decreased by 27.5 % in contrast to the basic vehicle. But the deflector extension may influence the steering system, which means that the project is still necessary to discuss.

According to these CFD analysis results, installing deflector is the most effective measure to reduce aerodynamic drag, which can greatly reduce the

**Fig. 11** The test vehicle and the test environment



pressure drag. The side fenders and visor have a certain effect on the drag reduction.

Based on the CFD analysis results in this section, the actual deflector was designed for this truck and practical result was tested through the full-scale wind tunnel.

## 4 Wind Tunnel Testing

Based on the CFD analysis results above and concerned about the rules of auto-body construction, deflectors (including upper and side) were designed fit the industry requirements. The wind tunnel test was taken in a full scale  $8 \times 6$  m low velocity wind tunnel to verify the aerodynamic drag reduction effect. Figure 11 shows the test vehicle and the test environment. Figure 12 shows the smoke visualization test. Table 2 gives the test results.

According to the practical vehicle wind tunnel testing, the effect of the deflector aerodynamic drag reduction was verified. Compared with the CFD analysis, their conclusions were basically the same. In the situation the yaw angle was  $0^\circ$ , for the commercial vehicle with a container, the aerodynamics drag could be reduced by 19 % when all the deflectors were added. As the contribution of the side deflector was weak in this yaw angle, in order to further research the effect of the side deflector, another test was taken in the situation of yaw angle  $10^\circ$ . The result shows that, the aerodynamic drag would rise by 3.7 % in contrast to not use the side deflector.

From the Fig. 13 [1], if the aerodynamic drag reduced by 19 %, the fuel consumption would reduce by 6.52 %. As a result, if the fuel consumption of a truck is 50 L/100 km, the fuel consumption reduction would be 3.26 L/100 km.

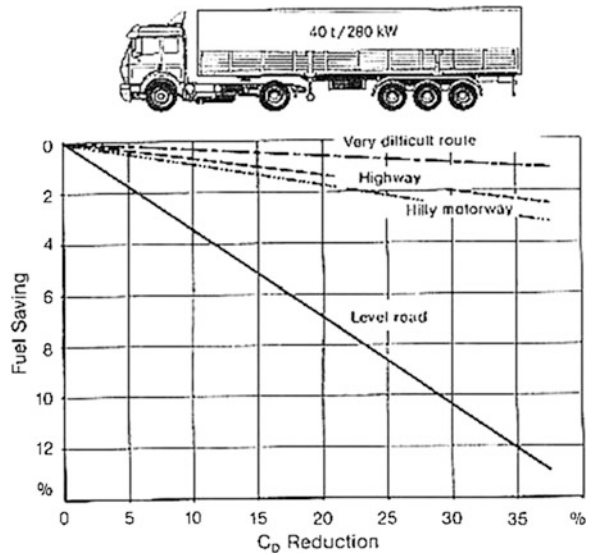


**Fig. 12** Smoke visualization test

**Table 2** The results of real vehicle wind tunnel test

	The situation of the test vehicle	Yaw angle (°)	Cd	Relative variation
1	Tractor with container, no deflector	0	a	Base
2	Tractor with container, all deflectors	0	0.81a	-19 %
3	Tractor with container, all deflectors	10	b	Base
4	Tractor + container, only upper deflector	10	1.037b	+3.7 %

**Fig. 13** The relationship between aerodynamic drag reduction and fuel consumption



The result above was supported by the users of this commercial vehicle which was shown as Fig. 1. One driver driven 2800 km at the average speed of 90 km/h, the fuel consumption reduced 97 L which equal to a reduction of 3.46 L/100 km because of adding the deflectors.

## 5 Conclusion

Taking a tractor semitrailer with a container of 40 in as the study object, both the CFD analysis and full scale wind tunnel testing were carried out to research the effect of add-on parts including deflector, side fenders, visor, engine compartment flow etc. It was found that the aerodynamic drag could get 20 % reduction by adding a suitable deflector, the fuel consumption could reduce by more than 3 % using this method. As the same time, the result shows that some factors such as the length of the deflector, whether using side fenders and visor can also influence on the aerodynamics drag of the vehicle. As a result, to achieve the best engine saving effect, during a vehicle design, the aerodynamic drag reduction methods mentioned above should be considered depending on the specific vehicle situation.

## Reference

1. Hucho WH (1998) Aerodynamics of road vehicles. Society of Automotive Engineers, Inc., Warrendale, p 418

# The State of Equilibrium in Car Body Design: The Application of Asymmetry for Enhanced Harmony

Liming Fu, Mingyang Sun and Alvin Chan

**Abstract** This paper is based on the results of a series of car design research literature to briefly explore “the state of equilibrium” in car body design by applying the principles of asymmetrical-balanced design. The paper includes several case studies to showcase the application of the asymmetrical-balanced design principles in car body design of the past two decades.

**Keywords** The state of equilibrium · Car body design · Aesthetics · Asymmetry · Chinese philosophy

## 1 Introduction

In recent years, there is a phenomenon surrounding car body design in auto industry. More and more car designers prefer to adopt the aesthetics of asymmetry in car body design to achieve a state of equilibrium.

The “state of equilibrium and harmony” is derived from *Zhongyong* “*The Doctrine of the Mean*” in ancient Chinese Thought by Confucian classic [1].

---

F2012-E06-009

---

L. Fu (✉) · M. Sun  
College of Automotive Engineering, Jilin University, Changchun, China  
e-mail: gavsun@hotmail.com

A. Chan  
Raffles University System, Beach Road, Singapore

*There are no stirrings of pleasure, anger, sorrow, or joy, the mind may be said to be in the state of Equilibrium. When those feelings have been stirred, and they act in their due degree, there ensues what may be called the ‘State of Harmony’.*

Asymmetry means uneven or absence of symmetry. It implies that there is no symmetry in a composition. The term, however, is usually used to describe a kind of balance that does not rely on symmetry: asymmetrical balance. There is no simple formula for achieving balance in asymmetrical balance or informal balance. Thus, for a designer, he/she must sense whether or not the composition is balanced.

An asymmetrical design warrants attention thanks to their lack of balance and feeling of wholeness. Furthermore, an asymmetrical design offers much more variety than symmetrical designs. They project an unusual look and special feel to a design, and offer a sense of vitality.

Asymmetrical design is typically off-centred or created with an odd or mismatched number of disparate elements. However, a car body designer can generate interesting designs without the need for perfect symmetry.

## **2 The Application of the Aesthetics of Asymmetry for Harmony**

The research shows that asymmetry for harmony in car body is a new trend in auto industry. Many people are captivated with this new and progressive asymmetrical looks. This method pertains to the traditional Chinese culture of Zhonghe’s school of thoughts (Table 1).

### ***2.1 The Application of Asymmetry in Car Exterior Design***

The aesthetics of asymmetry is an experimental or explored application in car exterior design.

While employing asymmetrical principles, a designer tries to achieve a state of equilibrium by ensuring that the wholes and parts are placed in symbiotic relationship with each other. Thus, the overall design should not be perceived to be random but more so, holistically thought through.

#### **2.1.1 The Whole Car Body**

Uneven elements present customers with more possibilities for arranging space and creating interesting designs than perfectly symmetrical objects. The asymmetrical layouts are generally more dynamic and by intentionally ignoring



**Table 1** A Survey of the psychological and aesthetic properties of symmetry and asymmetry according to artists, designers and philosophers’ perspectives [5]

Symmetry	Asymmetry
Steady (rest)	Motion
Binding	Loosening
Order	Disorder
Law	Accident
Formal rigidity	Life, play
Constraint	Freedom
Boredom	Interest
Stillness	Dynamic (chaos)
Monotony	Surprise
Fixity	Detachment
Stasis	Flux
Banality	Unique
Simplicity	Complexity

balance, the designer can create a sense of tension, express movement, or convey a mood such as anger, excitement, joy, or casual amusement (Fig. 1).

The entire design of 2008 Fiat Phylla and 2009 Kia No3 applies the principles of asymmetrical balance design for harmony. There are two more examples in the form of 2009 Chana’s E301 and 2010 CH-AUTO Lighting design can be seen in the Appendix.

### 2.1.2 The Doors

The car door design projects the idea of unity in diversity. It has two types of doors, namely the car side doors and back doors.

In the Veloster’s case, the Veloster has unusual door layout: one door on the street side, two on the curb side. The back door is much smaller, so getting in and out may be inconvenient, but tend to be more dignified. This design layout can prevent the incident that may obstruct the passengers and non passengers when opening the door on the street side.

This state of equilibrium on the opened door is a popular asymmetrical style for car body design, for instance, 1989 Ford Fiesta Urba, 2007 Mini Clubman, 2008 Mini Crossover, 2011 Renault Frenzy and 2012 Benz F700 and so forth (Fig. 2).

Design features of the Naimo concept include wrap-around windscreen, asymmetric sunroof and three-way split opening boot-lid for ‘versatile access’.

An outstanding car automobile designer, Peter Schreyer—the Chief Design Officer at Kia Motors said: “Naimo is a perfect balance of innovation, high-tech and Korean tradition, but combines this with cutting-edge technologies to deliver a truly premium experience” [2]. It is an asymmetrical balance as observed in the design of the back doors. The car features an asymmetric sunroof that has achieved



**Fig. 1** Demonstration of 2008 Fiat Phylla and 2009 Kia No3

**Fig. 2** Comparison of 2007 Mini Club man and 2008 Mini Crossover



a state of equilibrium. Another example is Kia POP concept (2010) that shows an unusual back door window.

2009 Nissan Cube explores the new form that is unbalanced in a good way. It makes an asymmetrically balanced composition. The rear end is where the Cube’s asymmetry is most evident, with a pillar on the left side only. On the right, the glass just wraps around. On the right, the glass just wraps around. The Land Rover Discovery 3 is another good example of asymmetrical design.

### 2.1.3 The Grilles

Apart from most of symmetry design in grilles such as BMW, Jeep and so on, this 1992 Ford Focus (Ghia) grilles is asymmetrical in styling and is a standout amongst the rest. It’s incredibly cool-looking and has continued to attract attention till today.

**Fig. 3** Comparisons of two types of Goodyear Eagle F1 asymmetric



### 2.1.4 The Sunroof

An automotive sunroof can be a fixed or operable (venting or sliding) opening in an automobile roof which allows light and/or fresh air to allow the entrance of the passenger. An example is the 2007 Nissan Bevel SUV concept.

### 2.1.5 The Tires and Rims

Asymmetrical tyre means a tyre which is not symmetrical with regards to the circumferential centre line of the tyre. The asymmetry may relate to the tread pattern or to the design of the tyre with regards to the tyre to rim fitment configuration. Asymmetric designed tyres are combination of comfortable and safety of specific condition such as terrible weather (raining and snowing). In addition, Hankook Ventus Prime k105 has applied asymmetrical design principles (Fig. 3).

The Goodyear Eagle F1 Asymmetric is a Max Performance Summer tire designed to be fitted for Passenger Cars. Below is data from 100 tire reviews averaging 84 % over 1,225,083 miles driven (Table 2).

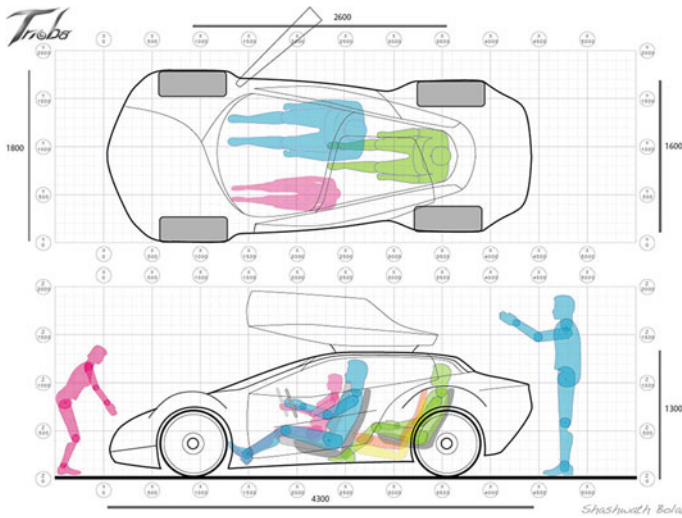
## 2.2 The Application of Asymmetry in Car Interior Design

### 2.2.1 The Configuration of Interior Space

Asymmetrical designs create active spaces which further lead to unrestricted forms of visual expression. On the negative side, if car designers overdo the degree of asymmetry, the entire design can lose its form and it can tire out the viewers' eyes (Fig. 4).

**Table 2** The reviews on the Goodyear Eagle F1 asymmetric (the multifunction asymmetric tread design ensures that each part of the tread works together to achieve maximum efficiency) [6]

Dry Grip	93%
Wet Grip	91%
Road Feedback	84%
Progressiveness	80%
Wear	73%
Comfort	84%
Buy again	83%



**Fig. 4** The demonstration of the interior design of the Trioba 2 + 1 concept. The Trioba 2 + 1 concept is an electric vehicle with a 2 + 1 seating layout aimed at enhancing interaction among passengers. It was designed by Shashwath Bolar, who graduated from Coventry University with a MA in Automotive Design [4]

### 2.2.2 Dashboard

This is the main part in car interior design. The style of interior design must match the car styling. There are a plenty of examples regarding asymmetrical design for dashboard 2011.

The all-new Hyundai Blue2 Fuel Cell Concept Car at Seoul Motor Show is an obvious example.

2005 Mazda Senku Concept Car is a ‘pioneer’ in the asymmetrical design in dashboard design.

2008 Toyota iQ’s dashboard design creates more space for the front seat passenger. Besides, 2011 Lexus CT 200 h adopts the asymmetrical balance design well.

### **2.2.3 Car Seat**

For car seat styling, there is a multitude of ways to create with asymmetrical look such as the Hyundai Blue2 Cell Concept Car.

## ***2.3 The Asymmetry in Other Aspects***

There are no rules or limits with asymmetrical balance. That does not mean that anything goes. Careful adjustments in size, shape, color and placement of the elements are required before a balance is achieved.

The attraction of asymmetrical balance to designers is due to its lack of a formula. This allows greater freedom which lends itself to more creative space. The difficulty lies in the organization of the parts. This must be overcome by careful placement of objects and the use of other organizational devices (like Gestalt principles) [3].

### **2.3.1 Materials**

When designers want to achieve harmony while applying asymmetrical design principles, they can do so by using a variety of materials. According to the engineering requirements, engineers can provide more material options to choose for car designers.

### **2.3.2 Colours**

There is no doubt that the colour plays a vital role in asymmetric harmony to some extent. For example, the 2008 Mini Crossover: The rear mirror and rims of the wheel on the car body have different colour usage (Fig. 5).

### **2.3.3 Decorative Patterns**

To decorate a car, the designers can consider various patterns on the car body to enrich the design. The Citroën C-Zero shows its distinctive style with its original design of its bonnet.

**Fig. 5** The comparison of the two sides' asymmetrical design of 2008 Mini Crossover



### 3 Conclusion

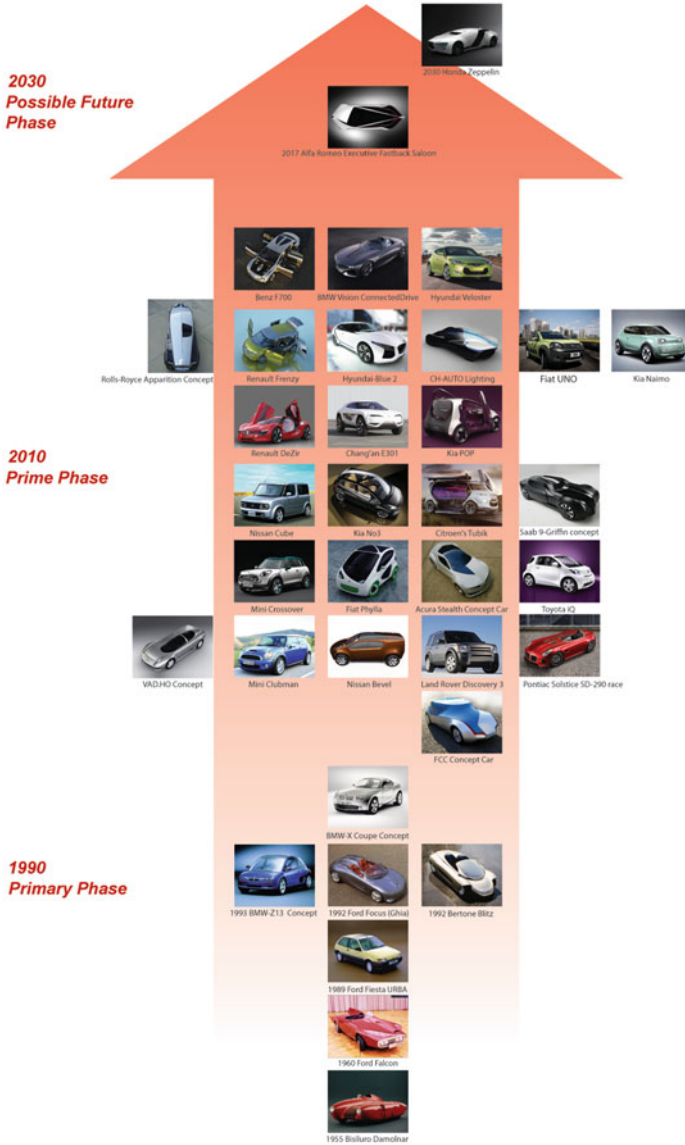
In this paper, the author has explored the influence of asymmetrical-balanced design principles on today's car body designers. In Asia, especially China, the concept of asymmetric-balanced design has been inspired, to a large extent, by the ancient Chinese philosophy of *Zhonghe*.

As part of the paper, a focus group interview was conducted amongst fellow car body designers in Northeast China. The result shows that some Chinese car designers are eager to adopt asymmetric-balanced design principles in their future works.

In summary, this paper hopes to further enrich this body of knowledge, with regards to the application of asymmetric- balanced design principle, to enlighten car designers around the world in their future creations.

# Appendix

## A Survey of the Current Trends in Asymmetric-Balanced Styling of Car Body Design



Note: This Trend Analysis shows the development of asymmetric-balanced Styling in Car Body Design. It focuses on the A, A0, A00, B, C, and D Level. It also includes MPV and SUV, and it excludes special car such as engineering car and military car etc. (concept car, show car and one off car) SN&Rain concept car designed by Liu Zhiliu as can be seen above.

## References

1. Guoqing Z (2009) The beauty of Zhonghe. Central Compilation & Translation Press, Beijing
2. [http://www.kia.bg/en/news/read/53/kia\\_naimo\\_electric\\_concept\\_stars\\_in\\_seoul/](http://www.kia.bg/en/news/read/53/kia_naimo_electric_concept_stars_in_seoul/)
3. <http://daphne.palomar.edu/design/asymm.html>
4. <http://www.carbodydesign.com/archive/2008/03/03-trioba-21-concept/>
5. McManus C (2005) Symmetry and asymmetry in aesthetics and the arts. *Eur Rev* 13(2):157–180, Academia Europea, Printed in the United Kingdom
6. <http://www.tyrereviews.co.uk/Tyre/Goodyear/Eagle-F1-Asymmetric.htm>



**Part VII**  
**New Materials and Structures**

# The Analysis of Composite Leaf Spring by Finite Element Method and Experimental Measurements

Jiashi Wang, Zaike Li and Qibin Jiang

**Abstract** The automobile industry has shown increased interest in the replacement of steel spring with E-Glass/Epoxy composite leaf spring due to the higher strength-to-weight ratio, superior fatigue strength and excellent corrosion resistance. In this work the composite leaf spring with the rectangular cross section designed for the commercial vehicle was analyzed by using the finite element software ABAQUS, and the experimental tests had been conducted to confirm the finite element analysis results. In the finite element analysis, the stress analysis and the spring rate computation have been conducted for the composite leaf spring subjected to the full load 15,000 N. The maximum compressive stress is 309.1 MPa at the middle of the composite leaf spring, and the safe factor can reach to 2.6 comparing with the material compressive strength of E-Glass/Epoxy 800 MPa. The spring rate computed from ABAQUS is 160 N/mm, and the maximum load capacity of the composite leaf spring is approximately 34,000 N. The measurements of the spring rate and the maximum load capacity were conducted on the composite leaf spring fabricated with the hot molding process method, and they are 157.5 N/mm and 34,280 N respectively. Comparing the results obtained from the finite element analysis with the experimental measurements, it can be seen that the errors are 1.56 % for the spring rate and 0.82 % for the maximum capacity load, and the main performances of fabricated composite leaf spring have the good agreement with the designed requirements.

**Keywords** Composite material · Leaf spring · Finite element analysis · Spring rate · Maximum load capacity

---

F2012-E07-004

---

J. Wang (✉) · Z. Li · Q. Jiang  
Zhuzhou Times New Material Technology Co.Ltd., Zhuzhou, China  
e-mail: wangjiashi@teg.cn

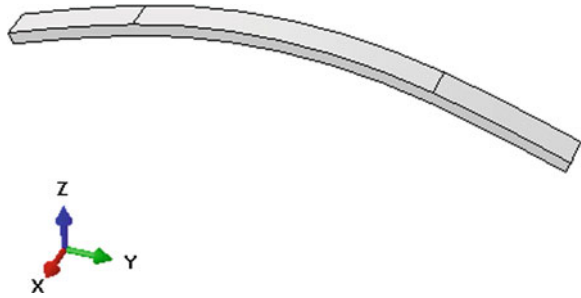
## 1 Introduction

In order to meet the needs of natural resources and economize energy, weight reduction has been the main focus of automobile manufacturer in recent years [1]. Weight reduction can be achieved primarily by the introduction of better material, design optimization and better manufacturing processes. The suspension leaf spring is one of the potential items for weight reduction in automobile. Because of the higher strength-to-weight ratio, superior fatigue strength and excellent corrosion resistance, the fiber reinforce plastics (FRP) has shown increased interest in the replacement of steel spring [2]. When the spring is made of FRP, such as E-Glass/Epoxy, the weight of the spring can reduce 60–70 %, which can leads to reduction of the unsprung weight. The elements whose weight is not transmitted to the suspension spring are called the unsprung elements of the automobile, include wheel assembly, axles, and part of the weight of suspension spring and shock absorbers [3]. The reduction of the unsprung weight could help in achieving the vehicle with improved riding qualities and increased the fuel efficiency. Therefore, the using of composite leaf spring not only leads to the weight reduction, but also improves the riding qualities.

Some works have been conducted with emphasis on the design and application of composite leaf spring, and part of them are reviewed here. Breadmore introduced the application of composite structures for automobiles [4, 5]. Moris concentrated on using composites in the rear suspension system [6]. Yu and Kim [2] designed and optimized a double tapered beam for automotive suspension leaf spring. Corvi [7] investigated a preliminary approach to composite beam design and used it for a composite leaf spring. Rajendran and Vijayarangan developed the genetic algorithms for the design optimization of light weight vehicle composite leaf spring [8], and Shiva Shankar and Vijayarangan [1] investigated the light weight vehicle composite leaf spring concentrated on the end joint analysis and testing. However, there is the limitation for the above research that the designed composite leaf spring is used for the light weight vehicle with static full load below 10,000 N for one spring. Nowadays, with the development of the automobile industrials, the composite leaf spring with more load-bearing is needed. Meanwhile, the structure, material and the fabricate process are all important. Therefore, it is necessary to investigate the composite leaf spring from simulation and experimental test, as well as verify the effectiveness and safety for the heavier load-bearing composite leaf spring.

In this paper the composite leaf spring with rectangle cross section that the constant thickness and width is  $28 \times 80$  mm is designed for the Commercial vehicle with 15,000 N full load for one spring. The finite element (FE) method is used for the analysis of stress state, computation of numerical spring rate and the maximum load capacity. Meantime, for the validity of the designed spring, the experiment is conducted on the composite leaf spring fabricated by the hot molding process. The measured spring rate and the maximum load capacity are

**Fig. 1** The 3-D structure of composite leaf spring



compared with the FE analysis results. This work develops the application of the composite leaf spring for the automobile industrial.

## 2 FE Model of the Composite Leaf Spring

According to the working and assembly conditions and considering the facility of mass production, the mono spring with constant rectangle cross section is employed for the Commercial vehicle. The geometry structure of the spring can be described as follow. The constant thickness and width is  $28 \times 80$  mm, the total length is 1,300 mm, the arc radius is 1,080 mm. Besides, the full loading is 15,000 N, and the designed spring rate is 160 N/mm. The 3-D structure can be obtained in the ABAQUS software as shown in Fig. 1, and the model is meshed with C3D8I [9] as shown in Fig. 2. The dimension of the elements is approximately 5 mm, and there are 20,000 elements. Because the composite leaf spring is mainly subjected to the moment loading, and the tensile and compressive bending stress is along the longitudinal direction. Therefore, the unidirectional fiber glass is selected to be laid up along the longitudinal direction of the spring, and the material properties of the E-Glass/Epoxy are listed in Table 1.

## 3 FE Analysis of the Composite Leaf Spring

According to the loading condition, the full load 15,000 N is applied at the middle of the composite leaf spring, and the stress along the longitudinal direction can be obtained in Fig. 3. It can be seen that the maximum stress is at the middle location, compressive stress for the outer surface and tensile stress for the inner surface. Meanwhile, the absolute value of the inner surface stress is larger than the one of the outer surface, which may be due to that the composite leaf spring is the curved beam [10]. According to the material properties as given in Table 1, the compressive strength of composite material is smaller than tensile strength, so the verify of the stress strength should be based on the compressive strength. The

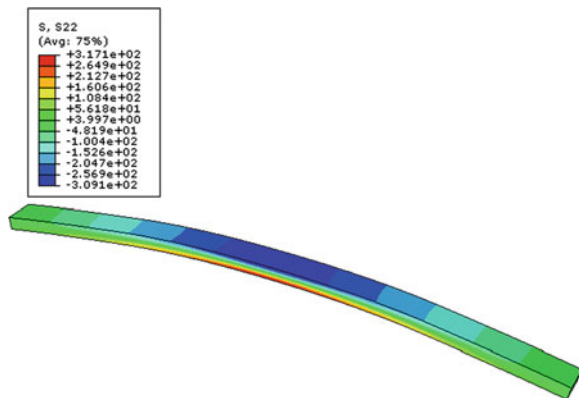


**Fig. 2** Finite element mesh of the composite leaf spring

**Table 1** Material properties of E-glass/epoxy

Properties	Value
Tensile modulus along X direction ( $E_x$ ), MPa	6,530
Tensile modulus along Y direction ( $E_y$ ), MPa	45,000
Tensile modulus along Z direction ( $E_z$ ), MPa	6,530
Tensile strength, MPa	1,100
Compressive strength, MPa	800
Shear modulus along XY direction ( $G_{xy}$ ), MPa	2,433
Shear modulus along YZ direction ( $G_{yz}$ ), MPa	2,433
Shear modulus along ZX direction ( $G_{zx}$ ), MPa	1,698
Poisson ratio along XY direction ( $\nu_{xy}$ )	0.217
Poisson ratio along YZ-direction ( $\nu_{xy}$ )	0.217
Poisson ratio along ZX-direction ( $\nu_{xy}$ )	0.366

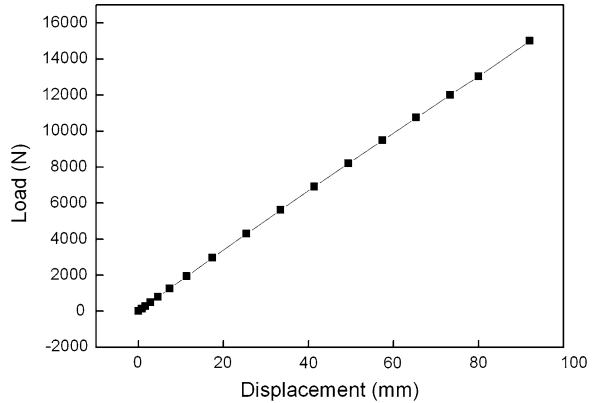
**Fig. 3** The stress contour along the longitudinal direction of the composite leaf spring subjected to 15,000 N



maximum compressive stress is 309.1 MPa at the middle of the composite leaf spring as shown in Fig. 3. Combining the compressive strength in Table 1 and the compressive stress in Fig 3, it can be calculated that the safety factor is 2.6.

Spring rate is an important parameter for the spring assembled in the vehicle suspension, and it can be computed from the FE analysis as described as follow. During the FE analysis, the variables such as the applied load and the displacement of the composite leaf spring can be recorded, and the load–displacement curve can

**Fig. 4** The load–displacement curve of the composite leaf spring obtained from ABAQUS



be plotted in Fig 4. It can be seen that the slope is almost constant during the analysis process, and the relationship of the load and the displacement can be fitted as the linear function by the origin software

$$y = 160x + 59.6 \tag{1}$$

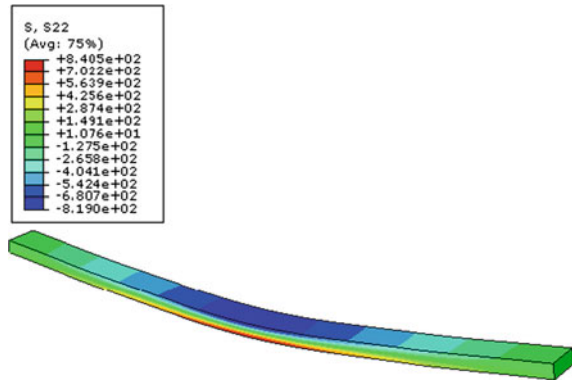
where x and y represent the displacement and load respectively, and 160 should be the spring rate. The second part 59.6 should be the deviation which is introduced by the FE simulation and the function fitting. The error can be calculated as  $59.6 / 15,000 \times 100 \% = 0.40 \%$ , and it can be neglected in the engineer application.

The maximum load capacity is another important parameter for application of the composite leaf spring. Theoretically, when the maximum compressive stress of the composite leaf spring is equal to the compressive strength, the spring will be fractured, and the load should be the maximum load capacity. During the FE analysis, the maximum load is set from 20,000 to 70,000 N, and the increasing step is set as 2,000 N. When the load is increased to 34,000 N, the stress state of the composite leaf spring can be obtained as shown in Fig. 5. The maximum compressive stress is 819.0 MPa, which is just larger than the stress strength 800 MPa. Therefore, it is suggested that 34,000 is the maximum load capacity of the composite leaf spring.

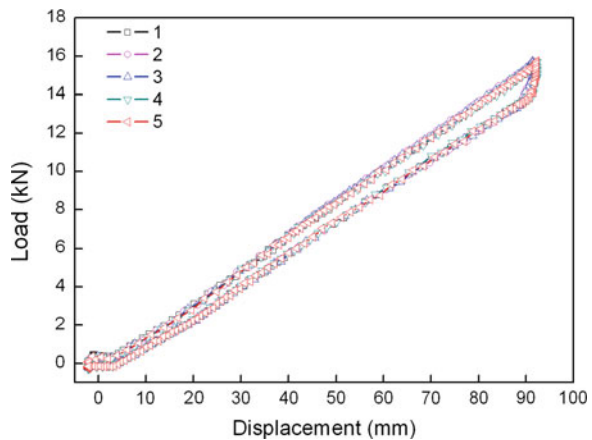
## 4 Experimental Testing

The designed composite leaf spring had been fabricated with the hot molding process method, and the three-point bending experiment is conducted to measure the spring rate. The composite leaf spring is loaded from zero to the prescribed maximum load 15,000 N and back to zero with loading speed 200 N/s. After five cycles, the load–displacement curves can be obtained as given in Fig. 6, and five spring rates were computed from the curves, listed as 160.2, 154.9, 156.2, 157.0

**Fig. 5** The stress contour along the longitudinal direction of the composite leaf spring as the maximum compressive stress close to the compressive strength



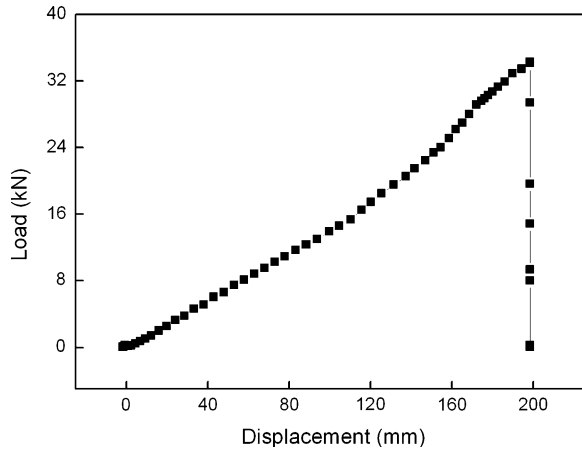
**Fig. 6** The load–displacement curves of the composite leaf spring obtained from the experimental tests



and 159.2 N/mm. The averaged value is computed and taken as the final spring rate, which is 157.5 N/mm. Comparing the experimental results with the value 160 N/mm obtained from FE analysis in Sect. 3, the error is 1.56 %, and they have the good agreement.

After the measurement of the spring rate, the maximum load is modified as 70,000 N, which is about two times of the maximum load capacity theoretically. The loading speed is set as 200 N/s, and the loading process is stopped automatically when the composite leaf spring is fractured. The recorded load–displacement curve is obtained as shown in Fig. 7, and the maximum load capacity can be extracted from the curve, which is 34,280 N. Comparing the experimental result with the value 34,000 N computed by ABAQUS, the error is 0.82 %.

**Fig. 7** The maximum load capacity test of the composite leaf spring



## 5 Conclusions

The designed composite leaf spring for the commercial vehicles is analyzed by the FE analysis and experimental test. In the FE analysis, the spring rate and the maximum load capacity are computed by ABAQUS software, and they are 160 N/mm and 34,000 N respectively. In the experimental tests, the three-point bending experiments of composite leaf spring fabricated with the hot molding process are conducted, and the tested spring rate and maximum load capacity are 157.5 N/mm and 34,280 N. Comparing the results obtained from the FE analysis with the experimental tests, it can be seen that the error is 1.56 % for the spring rate and 0.82 % for the maximum capacity load, and the main performances of fabricated composite leaf spring meet the designed requirements. In this work the delamination damage between the layers in the composite leaf spring is not considered, which will be investigated in the next step.

## References

1. Shiva Shankar GS, Vijayarangan S (2006) Mater Sci 12:220–225
2. Yu WJ, Kim HC (1988) Comp Struct 9:279–300
3. Tanabe K, Seino T, Kajio Y (1982) SAE 820403:1628–1634
4. Beardmore P, Johnson CF (1986) Comp Sci Technol 26:251–281
5. Beardmore P (1986) Comp Struct 5:163–176
6. Morris CJ (1986) Comp Struct 5:233–242
7. Corvi A (1990) Comp Struct 16:259–275
8. Rajendran I, Vijayarangan S (2001) Comp Struct 79:1121–1129
9. Simulia (2007) Abaqus user’s manual, Abaqus Version 6.7.1. Dassault Systemes
10. Hibbeler RC (2010) Mechanics of material. Pearson Education Publications, New Jersey



# Finite Element Analysis of Two Kinds of Dump Trunk

Zhi Li, Tie Wang, Jingxin Wang, Zhaohui Peng and Na Wang

**Abstract** This paper creates 3D models of U-shape trunk and square-shape trunk which are widely used in our country, compares the quality parameters of them under the same conditions. Then the stress distribution of two kinds of dump trunk are computed in full load condition and overload condition by HyperMesh. The result shows that U-shape trunk's stress distribution is worse than square-shape trunk's. It provides a reference to improve the design of the trunks.

**Keywords** Dump truck · U-shape trunk · Square-shape trunk · Finite element analysis · Optimization

## 1 Introduction

At present, dump truck is widely used, its main purpose in short freight, mining, construction site, road and bridge constructions and so on. Along with our country construction speed, the urban infrastructure construction and big engineering project implementation constantly, the demand for of dump truck grows rapidly.

The dump truck which has square-shape trunk is applied widely. Domestic U-shape trunk equipments development started later, and the use of U-shape trunk in European and American countries have more popularity. U-shape trunk has

---

F2012-E07-005

---

Z. Li (✉) · T. Wang · J. Wang · Z. Peng · N. Wang  
Department of Vehicle Engineering, Taiyuan University of Technology,  
Taiyuan 030024, China  
e-mail: lizhi2qn@163.com

many advantages, like unloading more clean, light weight and lower center of gravity, etc. This paper studied two kinds of trunk by finite element method and evaluated their respective advantages and disadvantages, providing the reference for the following design improvement.

## **2 The Finite Element Model of the Trunks**

### ***2.1 3D Models of Two Kinds of Trunk***

The shape dimension of square-shape trunk is  $5,600 \times 2,300 \times 1,600$ . It consists of fore-board, bottom board, left side board, right side board and back board. Thickness of each board is 4 mm. Every board have rib. Boards are connected by welding. The shape dimension of U-shape trunk is same as square-shape trunk's [1]. Two trunks can be exchanged on the same dump truck chassis.

U-shape trunk is produced by a piece of steel, so the side boards and the bottom board are connected into one body, does not need to be welded, thickness of board is 6 mm. The material of two trunks is Q235 steel plate, which yield strength is 235 MPa, tensile strength is 375 MPa, modulus of elasticity is 200 GPa, poisson's ratio is 0.33. Creating 3d models of two trunks in Pro/E.

Calculating the quality and volume of two trunks, the results shown in Table 1. As the table, although thickness of U-shape trunk steel plate is larger than square-shape trunk's, its mass is lighter than square-shape trunk's because of its less box rib, and the volume of U-shape trunk is smaller too. Height of gravity center of two trunks is not much difference.

### ***2.2 The Choice of Finite Element Model***

The network partition of finite element calculation model of the trunk is made in HyperMesh. Due to the structure of the dumper is typical of Shell, it is used to simulated with the side of 40 mm plate after extracting the mid-surfaces of each board. The trunk of welding uses unit (Rbar) connecting, and hinged part adopts to Rigid connection unit (Rigid) to simulate. In order to ensure the quality of the grid, geometric details (chamfering, pour round, etc.) are conducted and simplified in the part, which has small influence on the trunk of strength and rigidity. After the completion of the pretreatment, square model trunk finite element model consists of 61,708 units and U-shape trunk finite element model includes 66,644 units [2].

**Table 1** Two kinds of trunk mass and volume of the contrast

	Mass(kg)	Volume(m <sup>3</sup> )	Height of gravity center (m)
U-shape trunk	3,380	20.42	0.89
Square-shape trunk	4,220	22.66	0.91
Differ	20 %	10 %	0.6 %

### 2.3 Creating Constraints

According to stress analysis and a large number of calculation, in the lifting force moment, the stress of trunk structure is poor, so we calculate conditions by selecting the moment of lifting the trunk from the vice frame. On the bases of the working condition, constraint on the hinge joint of trunk overturning support and auxiliary vehicle frame is that restraining x,y,z direction of the translational degrees of freedom and y,z direction of the rotational degree of freedom. Constraint on the connection of trunk support before and lifting cylinder is x direction of the translational degrees of freedom and y,z direction of rotational degree of freedom [3].

### 2.4 Load to Bear

In the lifting working condition moment, the main load lifting on the trunk are lifting cylinder effect and the influence of tote on the board. The calculation process of lifting force mainly from Fig. 1, F is lifting the initial moments of oil cylinder lifting force, G for trunk with full quality, L turn over is the distance between oil cylinder bearing under and turning shaft, L is for distance of the center of gravity and the turning over after shaft before lifting. According to balance principle: lifting force  $F = G * L/L$  turn over. In this article the tip truck chassis is 6 × 4. It has three axis and its load is 18t, overload can achieve 35t, so when loading, the choice of G respectively is 180 kN, 300 kN. From the formula, it can be calculated that the lifting force of about 70 kN when full loaded, while it is about 140 kN when overloaded.

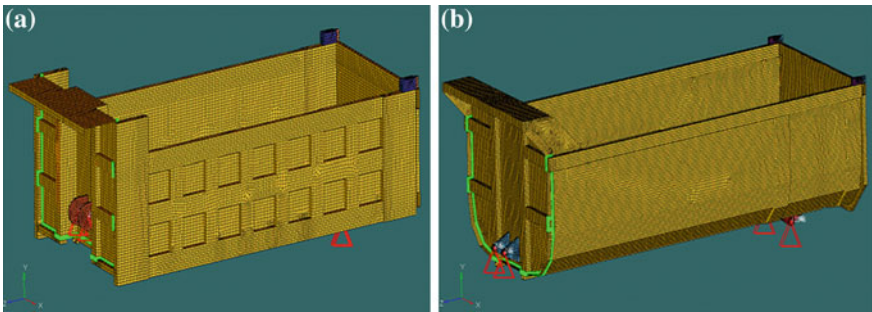
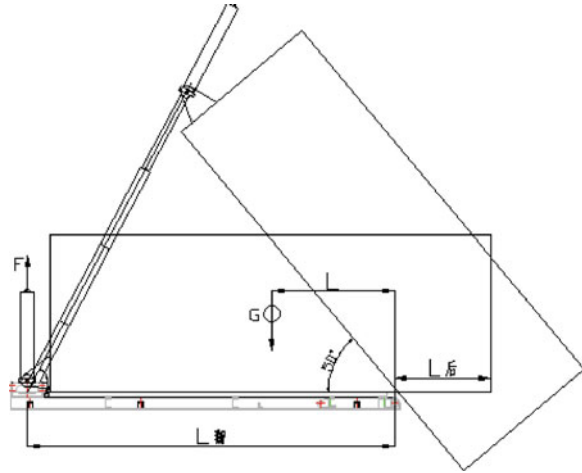
Force loading on the trunks is divided into two parts, bottom board force and four board forces. For the convenience of calculation, U-shape trunk is also considered as a bottom board and four side boards. This paper considers the load on bottom board is evenly distributed, so a uniform load is applied on the bottom board. Load on each board is changed with the height of cargo. And load in the same height is evenly distributed.

Bottom force of trunk is calculated as:

$$q = H\gamma \tag{1}$$

H is height of the cargo, m.  $\gamma$  is the bulk density of cargo, N/m<sup>3</sup>.  $\gamma$  is calculated as:

**Fig. 1** Dump truck lifting force calculation diagram



**Fig. 2** Finite element model of two trunks. **a** *Square-shape* trunk. **b** *U-shape* trunk

$$\gamma = \rho g \tag{2}$$

$\rho$  is the density of cargo, in this paper, the value of  $\rho$  is set at  $1,500 \text{ kg/m}^3$ .  $g$  is the acceleration of gravity,  $9.8 \text{ m/s}^2$ .

Pressure  $q_x$  on each board is calculated as:

$$q_x = \rho g h_x \left( 1 - \frac{2}{\pi} \beta \right) \tag{3}$$

$h_x$  is the height of the cargo correspond to  $q_x$ .  $\beta$  is the angle of repose of cargo, in this paper, the value of  $\beta$  is set at  $\pi/4$ .

Two trunks' finite element models are shown as Fig. 2.

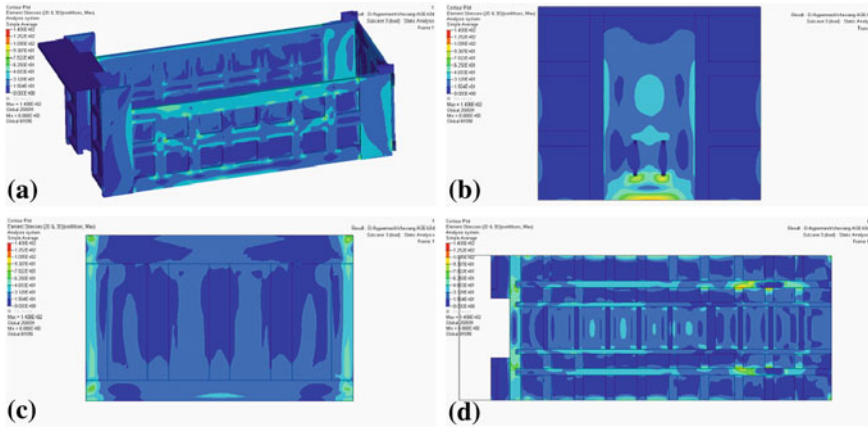


Fig. 3 Stress distribution of square-shape trunk with full load. a Whole trunk. b Fore-board. c Back board. d Bottom board

### 3 The Results of Finite Element Analysis and Comparison

#### 3.1 Trunks' Stress Distribution in Full Load Condition

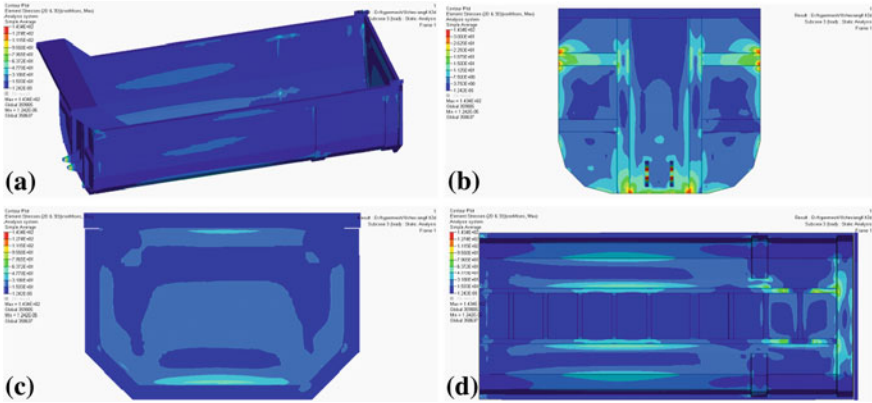
The stress distribution of two trunks with 18t load is shown in Figs. 3 and 4.

From the graph can be seen, two trunks' stress distribution at full load stress conditions is good, the max stress is smaller than yield strength of the material. The maximum stress of Square-shape trunk occurs at the bottom board's overturning support welding position, about 140 MPa; maximum stress of U-shape trunk occurs at the connector of lifting cylinder and the front board, is about 143 MPa, did not exceed the yield strength of material 235 MPa. Other parts of large stress of Square-shape trunk are that: weld connector of front board and bottom board, is about 125 MPa; connector of carling and the first beam on the bottom board, is about 109 MPa; left and right reinforcing ribs on the back board, is about 78 MPa. Other parts of large stress of U-shape trunk are that: connector of the fore-board and side boards, is about 127 MPa; carling on the bottom board, is about 111 MPa; bottom of the back board, is about 79 MPa.

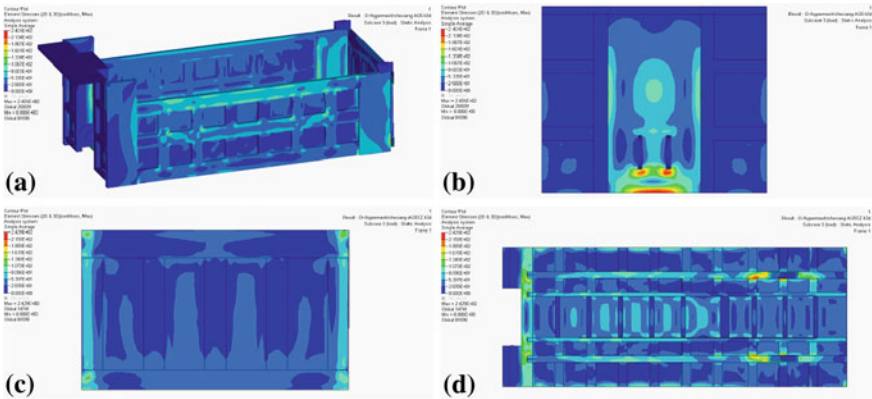
#### 3.2 Trunks' Stress Distribution in Over Load Condition

The stress distribution of two trunks with 35t load is shown in Figs. 5 and 6.

From the graph can be seen, two trunks' stress distribution at over load stress conditions is worse than the full load condition. The maximum stress of Square-shape trunk occurs at trunk's turning point, is about 240 MPa. Other parts of large stress of Square-shape trunk are that: weld connector of fore-board and

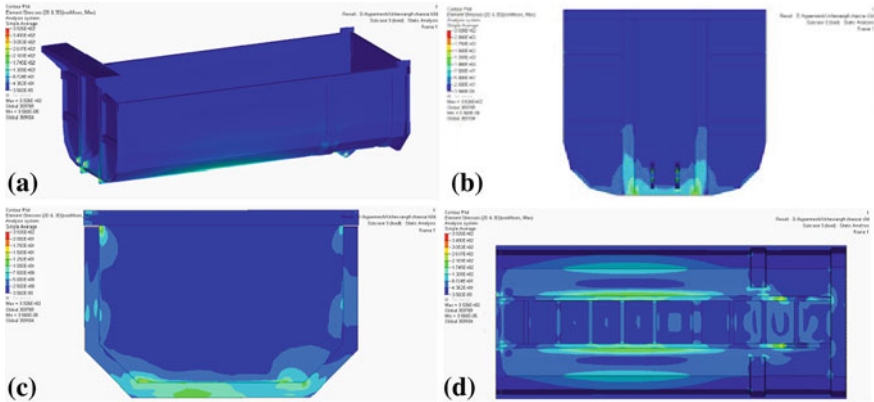


**Fig. 4** Stress distribution of U-shape trunk with full load. **a** Whole trunk. **b** Fore-board. **c** Back board. **d** Bottom board

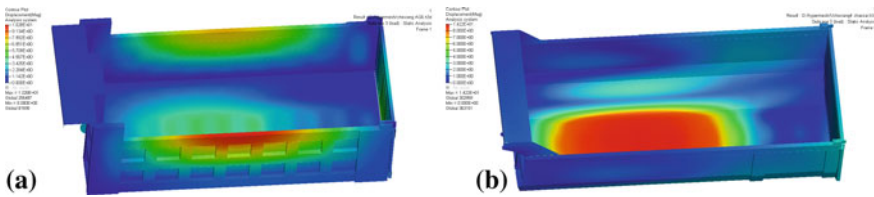


**Fig. 5** Stress distribution of *square-shape* trunk with over load. **a** Whole trunk. **b** Fore-board. **c** Back board. **d** Bottom board

bottom board, is about 188 MPa. U-shape trunk appears obvious stress concentration, stress distribution is not uniform. The maximum stress of U-shape trunk occurs at the connector of lifting cylinder and the fore-board, is about 392 MPa, exceeding the yield strength of the material. Other parts of large stress of U-shape trunk are that: carling on the fore-board, is about 306 MPa; bottom of the back board, is about 261 MPa.



**Fig. 6** Stress distribution of U-shape trunk with over load. **a** Whole trunk. **b** Fore-board. **c** Back board. **d** Bottom board



**Fig. 7** Deformation of two trunks with over load. **a** Deformation of *square-shape* trunk. **b** Deformation of U-shape trunk

### 3.3 Deformation Contrast of Two Trunks in the Overload Condition

The deformation of two trunks with 35t load is shown in Fig. 7.

In overload conditions, the maximum deformation of square-shape trunk appears on the upper middle of side boards, the maximum displacement is about 10 mm. The maximum deformation of U-shape trunk appears on the front of bottom board, is about 14 mm. Deformation of other parts is small [4].

### 3.4 The Results of Finite Element Analysis

Under the full-loaded (18t) circumstance, on account of large section modulus in bending of the U-shape trunk, its stress distribution is approximate to that of the square trunk, which illustrates the mechanical property of the U-shape trunk is in line with the square-shape trunk in Standard load conditions. Under the over-loaded (35t) circumstance, large strength of the U-shape trunk is more than yield strength

of material due to few reinforcing ribs in its bearing part. Although accretion of strength of the square-shape trunk is apparent, it is not more than yield strength of material owing to more reinforcing ribs. It is the stresses of both trunks' parts such as the joint of lift cylinder and fore-board, weld of chassis flip plate and ribs that are in adverse working conditions, which should be improved in further design [5].

Regard to the deformation of over-loaded conditions, the square-shape trunk has minor effect on the deformation, but it is evident that side boards around appear expansion. As for the U-shape trunk, its deformation mostly appear at the bottom board, meanwhile, the deformation is much more obvious, which illustrates the design of the U-shape trunk still needs updating.

## 4 Conclusions

By the finite element static analysis and comparisons of both trunks, conclusions are as follows:

- (1) As for the quality, the U-shape trunk has distinct advantages over the square-shape trunk. The shortage of the volume should be further improved.
- (2) The results of trunks' finite element static analysis show that under the over-loaded circumstances, the stress results of U-shape trunk are not as good as that of the square-shape trunk. For this reason, the square-shape trunk is much more popular than the U-shape trunk concerning most dump trucks' over-loaded conditions in China. Therefore, it should be further optimized.
- (3) By the distribution of stresses of both trunks, it can be perceived that square-shape trunks still have opportunities in reducing weight. For over-loading reasons, traditional square-shape trunks, in beefed-up design, boast excessive weight. However, the distributions of trunk materials should be more reasonable on the premise of the trunk stiffness, which is not only lighter but also more fuel-economic for dump trucks.

## References

1. Wang F (2010) Structure strength analysis of dump truck. *Manuf Inf Eng China* 2010.10
2. Gao J-L (2010) Study on light weight of heavy-duty dump truck based on structural optimization and high-strength steel application. Master degree thesis of Wuhan University of technology 2010.5
3. Chen S-Y (2010) Design and calculation of dump truck carriage and lifting device. *Spec Purp Veh Parts* 2010.7
4. Poh KW, Dayawansa PH, Dickerson AW (1999) I.R. thomas. steel membrane floors for bodies of large rear-dump mining trucks. *Finite Elem Anal Des* 32:141-161
5. Liang J-B (2010) Finite analysis of dump trunk. *Eng Mach* 2010.5(49)



# Advanced Solid Lubricant Technology Improve Engine Performance

Yupeng An, Kejin Zhang, Dan Wang, Junyan Zhang and Bin Zhang

**Abstract** The amount of oil consumed by transportation worldwide is increasing rapidly, it was predicted that the basic demand for oil world-wide will continue to grow in the future and the price fluctuations will continue. The climate problems ask for engine emission reducing substantially. Along with the requirements for engine energy saving and emission reduction, especially the restriction of the emission reduction, is harsher and harsher; many approaches have been developed to achieve the aims. Among them, to reduce the friction coefficient of engine frictional parts to save energy and reduce emission is becoming more and more important because a larger part of engine combustion work (20~45 %) is consumed to overcome friction work. Furthermore, the successful application of high pressure common rail fuel system demands low friction and high wear resistance for plunger and needle valves. The fullerene-like nanostructure hydrogenated carbon films with high hardness and high elasticity exhibit super low friction under ambient condition with 20 % relative humidity. With the application of super low friction carbon films, the friction coefficient could be reduced significantly. The bench test indicates that the super low friction carbon films is able to provide reliability for high pressure common rail fuel system, save fuel 1.5 % and reduce emission 2–5 %. It is believable that the employment of the super low friction carbon films on the frictional parts of engine is one of the economical and timely ways for engine energy saving and emission reduction. The strategy of designing robust surface technology

---

F2012-E07-006

---

Y. An (✉) · K. Zhang · D. Wang  
China FAW Group Corporation R&D Center, Changchun, China  
e-mail: mixinyan@rdc.faw.com.cn

J. Zhang · B. Zhang  
State Key Laboratory of Solid Lubrication, Lanzhou Institute of Chemical Physics, Chinese Academy of Sciences, Lanzhou, China

to reduce frictional losses may lie in our ability to learn from nature, where organic and inorganic chemistry combine to provide robust adoptable surface layers. The organic thin films chemically bond to carbon films improved the adaptability of lube to carbon films and enhanced the corrosion resistance. The results will expand and ensure the application of carbon films to most frictional parts of engine, and thus to save fuel and reduce emission much more.

**Keywords** Low friction · Solid lubrication · Engine · Friction work · Hydrogenated carbon films

## 1 Introduction

In recent years, the consuming of petroleum was rapidly increased with the increasing of the number of motor vehicles. At the same time, human living environment was also destroyed seriously by traffic jam and environmental pollution. Thus, even China has brought in a myriad of measures, including fuel-economy rules 20 % tighter than America's. The United States Department of Energy has conducted a workshop in which the focus was on industry research needs for reducing friction and wear in transportation. Reducing friction and wear in engine and drive train components could save the US economy as much as US\$ 120 billion per year. There are many hundreds of tribological components, from bearings, pistons, transmissions, clutches, to gears and drive train components.

Carbon films have been investigated because of their promising properties such as high hardness, low friction coefficient, optical transparency and high chemical inertness [1]. Numerous techniques have been employed to deposit the carbon films: magnetron sputtering [2–5], filter cathodic vacuum arc [6, 7], pulse laser deposition [8] and plasma enhanced chemical vapor deposition [9, 10]. Among the above mentioned techniques, magnetron sputtering is the most suitable technique for large-scale industrial application. Carbon films, particularly, due to the frictionless and high hardness, are supposed to reduce friction and extends system life-span of machine components. Lawes et al. have studied the tribological properties of carbon films for engine applications. In their study, the harder a-C:H film was more wear resistant than the softer WC/C a-C:H film and performed. Yutaka Mabuchi, from Nissan Motor CO., Ltd, firstly reported an application of pure carbon films onto Valve-lifter, which reduced the friction of about 40 % [11].

For years, nanostructure (hydrogenated) carbon films have received great attentions due to their excellent properties, like high hardness, high elastic recovery, low friction and chemical inertness et al. Because of such attractive advantages, carbon film can be used as protect-coated for anti-wear and -corrosion. The car industry, in particular, in order to energy conservation and emission reduction, need a new type of surface treatment, where the carbon films is the best choice of one.

FAW is very early in began to pay attention to this problem. In 2009, FAW and Lanzhou Institute of Chemical Physics (LICP) have established joint laboratory. Junyan Zhang, the team leader, have been very early on the research of diamond-like films. In 2008, Zhang reported a new kinds of carbon films-named Fullerene-like hydrogenated carbon (FL-C:H) film that hold a super low friction properties.

## 2 Design of Coated Component in Motor Vehicles

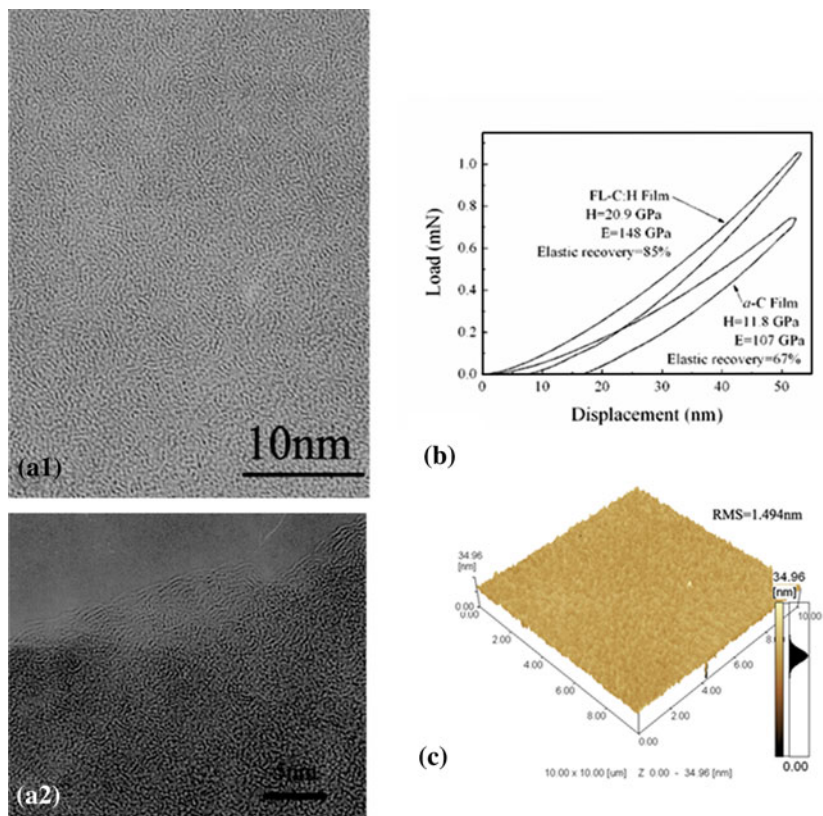
Fullerene-like hydrogenated carbon (FL-C:H) films were firstly fabricated by plasma enhanced chemical vapor deposition (PECVD) by Zhang et al., which can also be achieved by magnetron sputtering of Ti target in methane and argon atmosphere. Afterword, Buijnsters et al. showed that the films synthesized by electron cyclotron resonance CVD also had such microstructure. It's really interesting that, compared with fullerene-like carbon nitride (FL-CN<sub>x</sub>) films, FL-C:H films exhibit not only a super low friction coefficient ( $\mu = 0.009$ ) even in ambient atmosphere with 20 % relative humidity, but also no heating required in the deposition process. The unique properties are very important for industrial production and application.

Figure 1(a1) and (a2) show HRTEM images of the FL-C:H films deposited from sputtering of Ti target in methane and argon atmosphere at bias of  $-800$  V. It clearly shows that ordered domains of several nanometers in size consisting of straight and curved planes arrangements the observation of curved graphene layers indicates that odd member rings are present in the structure, which induce the curvature in the basal planes and form fullerene-like structures. Contrast with amorphous carbon (a-C:H) films, fullerene-like carbon (FL-C:H) films were proved to have high hardness, extreme high elasticity (Fig. 1b and c). The low temperature deposition process allowed the FL-C:H films to be deposited onto various material surface.

The XPS C1s spectrum of the film deposited at  $-800$  V bias is shown in Fig. 2. The decomposing results show that the sp<sup>2</sup> carbon bond content of approximately 71 %. This value was evaluated by fitting the C1s peak with the two main components, diamond represented by the sp<sup>3</sup> bond (peak at 285.2 eV) and graphite represented by the sp<sup>2</sup> bond (peak at 284.8 eV), and by calculating the area fractions under the peak. Furthermore, small contents of C-O bonds at around 286.3 eV are detected. The absence of the TiC peak in the C1s spectrum of the film indicates that no titanium atom or its carbide exists at least on the surface of the film.

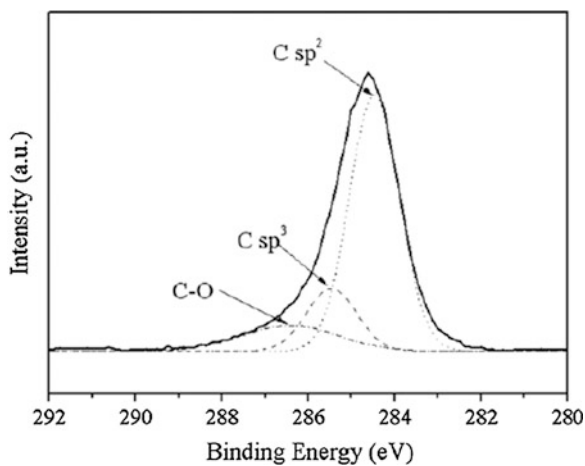
### 2.1 Grow Mechanism

During the deposition, the discharge voltage fluctuated significantly after the glow discharge ignition. The discharge voltage of sputtering titanium target in mixture of methane and argon, and for comparison, in argon, as a function of deposition

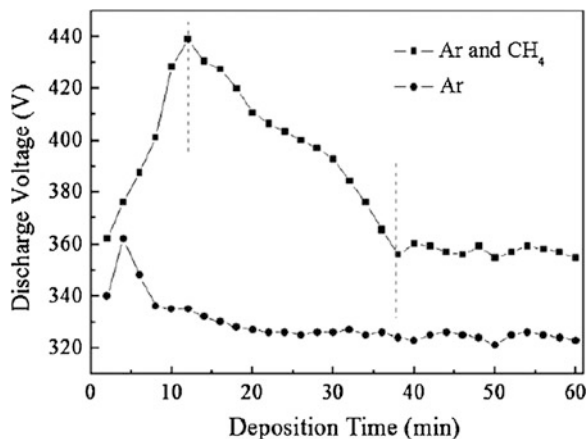


**Fig. 1** HRTEM images of the fullerene-like structures of FL-C:H films: at the center (**a1**) and edge (**a2**) of a sample, (**b**) nanoindentation load–displacement curves of the FL-C:H and a-C:H films, (**c**) AFM morphologies of the FL-C:H films

**Fig. 2** Fitted XPS C1s peak for the film



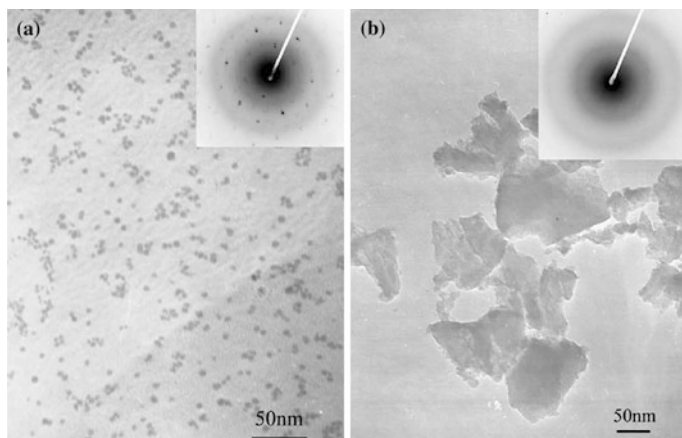
**Fig. 3** Two different TEM images (*a*, *b*) and the corresponding selected area electron diffraction patterns of hydrocarbon layer scraped off from the after-deposition target



time is shown in Fig. 3. It can be seen that the trend of change obviously distinguished in two conditions: discharge voltage of sputtering titanium in argon almost keeps constant during the whole deposition process. However, in the case of sputtering titanium target in methane and argon, the discharge voltage increases sharply after the discharge ignition and reaches a maximum value of about 440 V at 12 min. Sequentially, it decreases to a steady value of 340 V. It is well known that reactive sputtering will undergo an abrupt transition of steady stages when the reactive gas flow rate or the discharge voltage steps over a critical value. Accordingly, the initial increase of the discharge voltage in our film deposition can be ascribed to the formation of a carbide layer on the target surface, as is known as 'target poisoned'. While, an obvious decrease of discharge voltage can be observed after 12 min sputtering, this is quite different from the conditions of reactive sputtering in oxygen or nitrogen. The phenomena is explained as follows, during deposition, the CH<sub>n</sub> ion discharged from methane gas can be condensed on the substrate, as well as on the target. It can be expected that the amorphous can also deposited on the target and finally the target will be covered by an amorphous carbon layer. As such a hydrocarbon layer is loose and more electric compared with carbide, so the discharge voltage decreases after 12 min sputtering.

As the target surface was covered by a hydrocarbon layer and the sputtering actually occurred on the hydrocarbon layer rather than titanium target, it can be expected that the hydrocarbon layer plays an important role on the fullerene-like structure formation. To gain an insight into it, the hydrocarbon layer was scraped from the after-deposition target surface, TEM and Raman analyses were performed.

The result of TEM analysis indicates that two different microstructures are detected, which were seen in Fig 4a and b. One microstructure is composed of nanoparticles ranging from 5 to 10 nm. The SAD patterns of the nanoparticles indicate that the d spacings between lattice planes were consistent with those of the nano-crystalline graphite Fig. 4a. The other one consists of sheet-like particles whose SAD patterns show two broad diffuse rings, which arise from the amorphous carbon Fig. 4b. It can be concluded from TEM analysis that the hydrocarbon layer



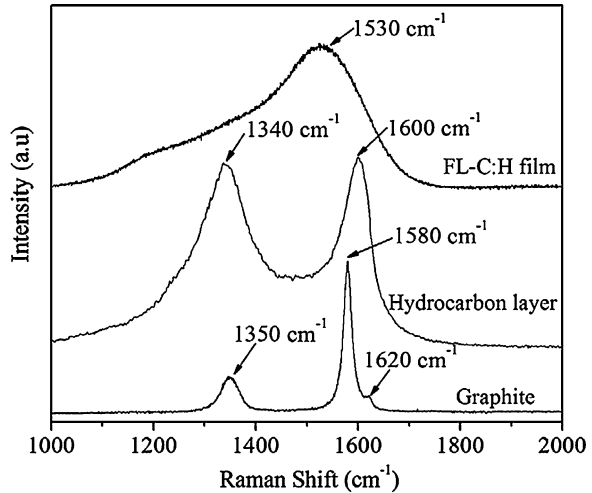
**Fig. 4** Two different TEM images (a, b) and the corresponding selected area electron diffraction patterns of hydrocarbon layer scraped off from the after-deposition target

covered on the target surface consists of amorphous carbon and nano-crystalline graphite, while fullerene-like or onion-like structures was not found in it.

The visible Raman spectrum of the hydrocarbon layer was showed in Fig. 5. The spectra of the FL-C:H film and graphite was also showed for comparison in the same figure. We can see that the Raman spectrum of the hydrocarbon layer covered on the target has two obvious peaks around  $1,350$  and  $1,600\text{ cm}^{-1}$ , respectively, and two peaks exhibit similar intensities. Comparing the Raman spectrum of the hydrocarbon layer with that of the FL-C:H film, the G peak shifts from  $1,600$  to  $1,530\text{ cm}^{-1}$ , meanwhile, the intensity of the D peak at around  $1,350\text{ cm}^{-1}$  decrease sharply and overlaps with G peak. They call the amorphization trajectory, consisting of three stages, first the  $sp^2$  groups become smaller, then topologically disordered, and finally change from  $sp^2$  ring to  $sp^3$  chain configurations.

According to this model, the formation of hydrocarbon layer on the target correlates to the stage 1, this stage corresponds to the reduction of the in-plane correlation length  $L_a$  within an ordered graphite layer, and the reduction of the grain size in the perfectly oriented graphite will induce the appearance of the D peak. The average G peak moves from  $1,580$  to  $1,600\text{ cm}^{-1}$  due to phonon confinement in smaller graphitic domains, since the phonons disperse upwards away from the center of the Brillouin zone. In this stage,  $ID/IG$  is related to the aromatic cluster size  $L_a$ , for the hydro hydrocarbon layer, its aromatic cluster size can be calculated by using Tuinstra-Koenig equation,  $L_a = 44 - (ID/IG)^{-1}$ , about  $40\text{--}50$ . This calculated result is consistent with the TEM analysis, in which we demonstrated the existence of nano-crystalline graphite with the size from  $5$  to  $10\text{ nm}$ . Obviously, no fullerene-like structures or onion-like structures was formed in this stage. When the hydrocarbon layer was sputtered out and formed the film containing fullerene-like structure, the G peak decreases to  $1,530\text{ cm}^{-1}$ , lower

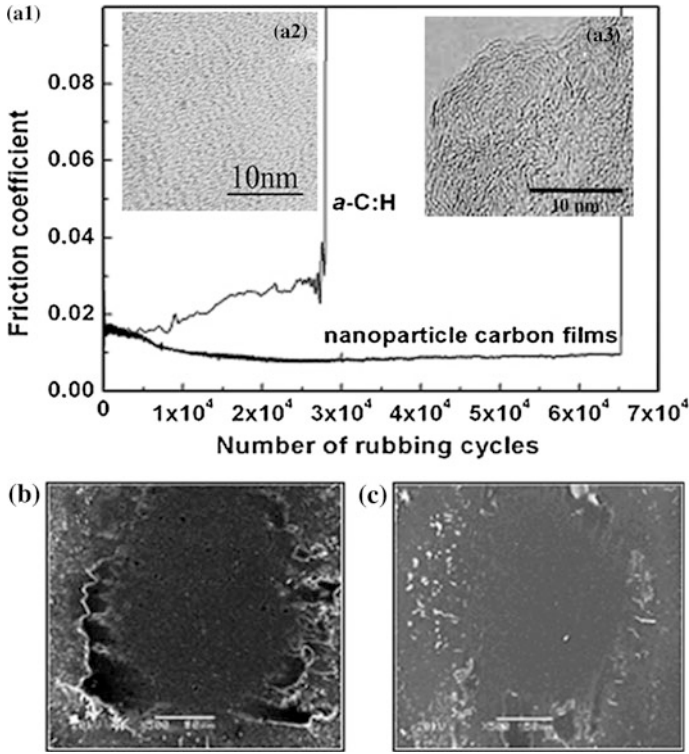
**Fig. 5** Raman spectra of the hydrocarbon layer, the FL-C:H film and graphite



than nano-crystalline graphite, and the ID/IG ratio decreases. This change accords with the second stage of the three stage model. In this regime, T-K equation is no longer valid, Ferrari and Robertson proposed a new relation to calculate the La,  $La = [(ID/IG)/0.0055]^{1/2}$ , for the FL-C:H film, the calculated result show that the aromatic cluster size in the film is about 10–15 units. From the hydrocarbon layer to the FL-C:H film, the aromatic cluster size decreases and the G peak shifts to lower wavenumber, which means topological disorders are progressively introduced into the graphite layer, bond angle distortion and other disorders cause a softening of the vibration frequencies, and the aromatic clusters become smaller and more disordered. At this stage, the film consists of mainly sp<sup>2</sup> sites in some chain-like configurations and puckered ring-like configurations. The ring-like configurations consist of five-, six-, seven-, and eight-fold disordered ring. As is well known, fullerene-like carbon films are mainly composed of mainly sp<sup>2</sup>-bonded graphene planes containing odd number rings. The odd number rings just like pentagons exist in the basal planes which give rise to the curvature of graphene planes and form fullerene-like structure. That is to say, fullerene-like carbon films can only form at the second stage. At this stage, when the hydrocarbon layer was sputtered out from target, odd number rings are introduced into perfect graphene planes. The odd number rings may prefer the formation of curvature graphene planes, as a result hydrogenated carbon films containing fullerene-like structure can be synthesized (Fig. 6).

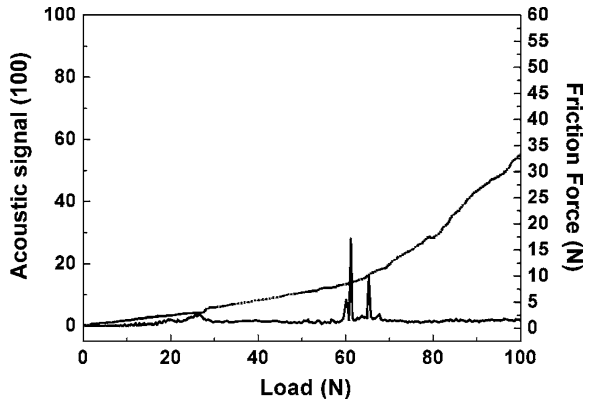
## 2.2 Triological Properties

Due to the unique structure which endow the films high hardness, extreme high elasticity, the FL-C:H films show a super low friction and super low wear properties. In order to reduce friction and wear in engine, such low friction and low



**Fig. 6** The friction properties of the FL-C:H films: **a** the friction coefficient of the FL-C:H films and a-C:H films; **b** The SEM images of the surface morphology of wear scar of the FL-C:H films and a-C:H films

**Fig. 7** The adhesion test curve of FL-C:H films on NiCr18 steel substrates under load speed of 100 N/min





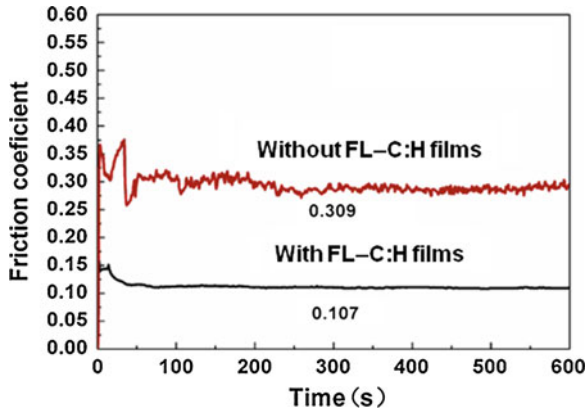


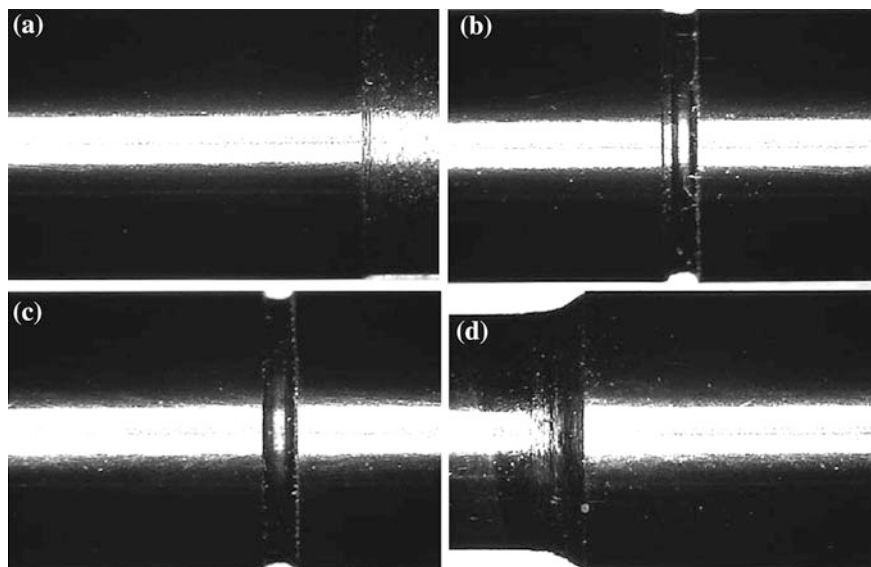
Fig. 8 The friction coefficient of the FL-C:H films in SRV-3 tests



Fig. 9 Part FL-C:H films Coated workpieces' photos

wear is very important for long life running. But there is still one key point that high adhesion on the substrates needed.

The parts of engine were made by kinds of raw materials, structure and thermal expansion coefficient are of big differences. And in that sense, Choosing a gradient transition layer is particularly important. In our study, the NiCr13 was used as substrates. Through the cross experiment, finally a Ti/TiC composition gradient layer was selected. With a metal bonding layer and a composition of graded layers, the adhesion of FL-C:H films on NiCr18 steel reached as high as 62 N (Fig. 7).



**Fig. 10** FL-C:H films coated control piston after 1250 h reliability tests, **a** the head, **b** the upper, **c** the down and **d** the tail

According to the SRV-3 tests (Fig. 8), the samples with FL-C:H films had a friction coefficient only one-third of that without FL-C:H films. It means that the FL-C:H films can very good reduce the friction coefficient. Then we deposited the so called FL-C:H films to some parts of the engine.

Figure 9 show some fullerene-like carbon coated work pieces' photos.

### 3 Bench Tests

In order to test the FL-C:H films coated parts' tolerance, the FL-C:H films coated control pistons were chosen to do reliability rig test. The results are shown in Fig. 10. It is clear seen that after 1,250 h reliability tests, the control pistons are almost no damage. The static coating return oil is about 50 %, and no coating of the piston return oil is static about 100 %.

### 4 Conclusion

Through carefully control the carbon film growth conditions, FL-C:H films can be obtained. Such films have high hardness, high elastic and low friction properties. So the films are suit to use as protecting coat, like engine key components. After

careful design the composite gradient layer, FL–C:H films' adhesion can reach 62 N on NiCr18 substrates, which can meet the needs of industry. The SRV tests indicate that the samples with FL–C:H films had a friction coefficient only one-third of that without FL–C:H films. The reliability rig test show that the designed nano-structure carbon films can meet the needs of the engine harsh running environment. The static coating return oil is about 50 %, and no coating of the piston return oil is static about 100 %.

## References

1. Robertson J (2002) Diamond-like amorphous carbon. *Mater Sci Eng R*(37):129
2. Wang Z, Wang CB, Zhang B, Wang Q, Zhang JY (2011) Effects of negative bias on the structural, topological and tribological properties of amorphous carbon films prepared by magnetron sputtering. *Surf Interface Anal* 43:1218–1223
3. Cho G, Yen BK, Klug CA (2008) Structural characterization of sputtered hydrogenated amorphous carbon films by solid state nuclear magnetic resonance. *J Appl Phys* 104:013512
4. Bui XL, Pei YT, De Hosson JTM (2008) Magnetron reactively sputtered Ti-DLC coatings on HNBR rubber: the influence of substrate bias. *Surf Coat Technol* 202:4939–4944
5. Dai HY, Jiang H, Zhan CY, Huang NK (2009) Effects of sputtering current on the bonding structure and mechanical properties of diamond-like carbon films deposited by MFPUMST. *Surf Interface Anal* 41:560
6. Zhu J, Han J, Han X, Schlaberg HI, Wang J (2008) Sp<sup>3</sup>-rich deposition conditions and growth mechanism of tetrahedral amorphous carbon films deposited using filtered arc. *J Appl Phys* 104:013512
7. Kang MC, Tak HS, Jeong YK, Lee HW, Kim JS (2010) Properties and tool performance of ta-C films deposited by double-bend filtered cathodic vacuum arc for micro drilling applications. *Diamond Relat Mater* 19:866–869
8. Rau JV et al (2010) Pulsed laser deposition of hard and superhard carbon thin films from C60 targets. *Diamond Relat Mater* 19(7):14
9. Racine B, Benlahsen M, Zellama K, Bouzerar R, Kleider JP, Von Bardeleben HJ (2001) Electronic properties of hydrogenated amorphous carbon films deposited using ECR-RF plasma method. *Diamond Relat Mater* 10:200–206
10. Yoon SF, Tan KH, Rusli, Ahn J, Huang QF (2001) Comparative study on the effects of ion density and ion energy on diamond-like carbon deposited by electron cyclotron resonance chemical vapor deposition. *J Appl Phys* 89:4830–4835
11. Mabuchi Y, Hamada T, Izumi H, Yasuda Y et al (2007) The Development of Hydrogen-free DLC-coated Valve-lifter. *SAE Tech Pap* 2007(01):1752

# Wrought Magnesium Alloy AZ31 Grain Refinement by Predeformation

Fei Xiong, Lichun Cui and Ping Wang

**Abstract** Lightweight BIW (body in white) has become one of the challenges for automotive OEM companies. Magnesium alloys become one of the options because of its high specific strength. However, the fabrication cost of wrought Mg alloys is still pretty expensive due to its coarse grained structure. Wrought magnesium alloy AZ31 as cast with an initial grain size of over 500  $\mu\text{m}$  was studied. Grain refinement is achieved by means of predeformation process at elevated temperature. It was found that predeformation process could significantly affect the mechanical properties of the final products. Predeformation made between at low temperatures and high temperatures appears to be quite different which determine the macro mechanical properties. An anisotropic structure is found after predeformation at as low as at strain of 0.05. Dynamic recrystallisation has been seen one of the effective methods to refine the grain structure of wrought magnesium alloy for better mechanical properties, which is shown strong dependence on the occurrence of twinning process. Metallographic analysis was used to explain the microstructural evolution during the deformation process.

**Keywords** Wrought magnesium · Dynamic recrystallisation (DRX) · Predeformation · Twin · Extrusion

---

F2012-E07-007

---

F. Xiong (✉) · L. Cui · P. Wang  
Anhui Jianghuai Automobile Co. Ltd. R&D Centre, Hefei, China  
e-mail: kj\_jszx@jac.com.cn

## 1 Introduction

Growing concern about the global environmental problems has made magnesium alloys a strong candidate for automotive industry. Mg alloys are currently used in relatively small quantities for auto parts, mainly in die-castings [1–4]. Wrought magnesium alloys are of great interest because of better mechanical properties and ductility in comparison with cast alloys [5, 6]. However, applications of wrought magnesium alloys are still very limited due to poor formability at room temperature due to its hexagonal close packed (hcp) crystalline structure with the  $c/a$  ratio of 1.624 [7]. Hot working of wrought magnesium alloys has been carried out to overcome this limited ductility. Modification of microstructure of wrought magnesium alloys, alternately by means of high temperature deformation, can also be achieved such as grain refinement to improve the properties as well as the formability.

It is not surprising that majority of the research work is in grain structure refinement on rolled magnesium alloys because of magnesium and its alloy's strong property dependence on grain size. Dynamic recrystallisation has been reported to be an effective method to refine grains [8–11]. Extremely fine-grained wrought magnesium alloys have been achieved by dynamic recrystallisation after fabrication processes such as extrusion, rolling and forging. However, one of the key factors affecting the dynamic recrystallisation process is the initial grain size [12, 13], which significantly affects the recrystallised grain size and the fraction of this recrystallisation. Those wrought magnesium alloys after hot-deformation such as extruded, rolled or forged have average grain size less than 50  $\mu\text{m}$  while as cast wrought magnesium alloys are in generally with average grain size over 500  $\mu\text{m}$ . Therefore, it is important to fully understand the deformation behaviour of as cast wrought magnesium alloys in order to have better mechanical properties by better-controlled processes.

The objective of this work is to study the effects of the initial grain size and the microstructure on the mechanical properties and deformation properties by means of predeformation process.

## 2 Experimental Procedures

Commercial available wrought magnesium alloy AZ31 as cast with initial grain size around 500  $\mu\text{m}$  was used for the study. Specimens were machined to rectangular cub.

Predeformation tests were carried out at room temperature (RT) and 400 °C at true strain rate of 0.01 and 0.1  $\text{s}^{-1}$  respectively. In order to study the effects of the predeformation, further tests were conducted at 400 °C and the same strain rates as in predeformation tests were applied. The further tests were tested as a function of

the orientations namely as 0 and 90° in relation with the initial applied force direction.

In order to investigate the deformation mechanism, extrudate were also used in plane strain compression tests at the same test parameters.

Specimens were all polished to 3 μm prior the tests to minimise the friction during the plane strain compression test. Microstructural examination was performed by optical microscopy. Revealing the grain structure was achieved by etching at room temperature in a picric solution. Average grain sizes were calculated from the optical micrographs by the linear intercept method.

### 3 Experimental Results

Predeformation tests were conducted at RT and 400 °C at a true strain rate of 0.01 s<sup>-1</sup>. Based on these, further tests were carried out at 400 °C with the same strain rate of 0.01 s<sup>-1</sup> at two orientations (0 and 90°) relatively to the predeformation. Figure 1 presented the flow stress of AZ31 as a result of deformation temperature and orientation effects.

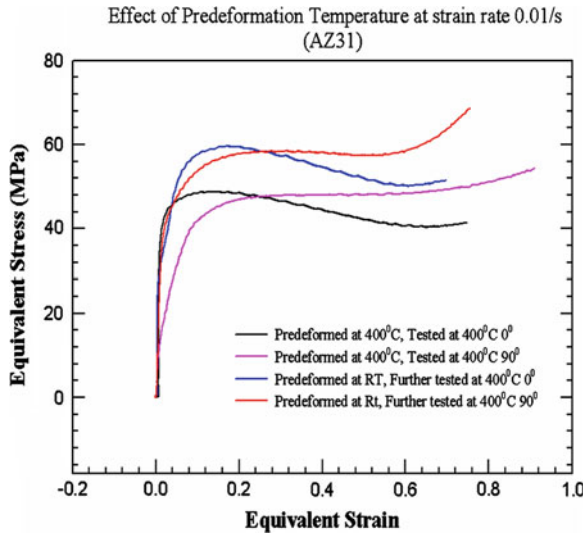
It was clearly shown that the predeformation temperature has significant impact on the material properties. Two types of the stress–strain curves can be distinguished. Flow stress with a single peak that indicates the dynamic recrystallisation took place was observed when the applied stress was along 0° (RD). A sharp increasing strain hardening was found followed by a strain softening. When the stress was applied perpendicular to the stress direction of predeformation, a steady-state strain was observed at both predeformation conditions. It is expected that the yield stress was shown decreasing with increasing temperatures.

Comparison experiments were conducted with extrudate AZ31. Tests were conducted at two orientations; extrusion direction (ED) and transverse direction (TD). Figure 2 presented the flow stress results. As reported previously, the yield stress was also shown decreasing when applied force is rotating from ED to TD as in tension. The strain rate has shown an effect of increasing yield strength in general.

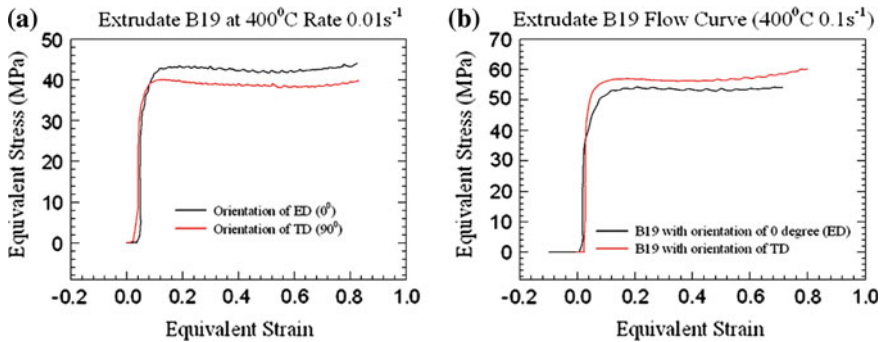
Figure 3 presented the flow curve as a result of predeformation in comparison with extrudate. It is apparent that the predeformation process has significant impact on the mechanical properties. Further details will be explored in the discussion section.

### 4 Discussion

It is known that DRX proceeds by nucleation followed by growth. Mechanism of DRX in low alloy magnesium was found to involve dynamic polygonisation in rotated lattice regions adjacent to initial boundaries. Although nucleation in cubic



**Fig. 1** AZ31 as CAST flow stress curves as a function of orientation after predeformed at RT and 400 °C with strain rate 0.01 s<sup>-1</sup>

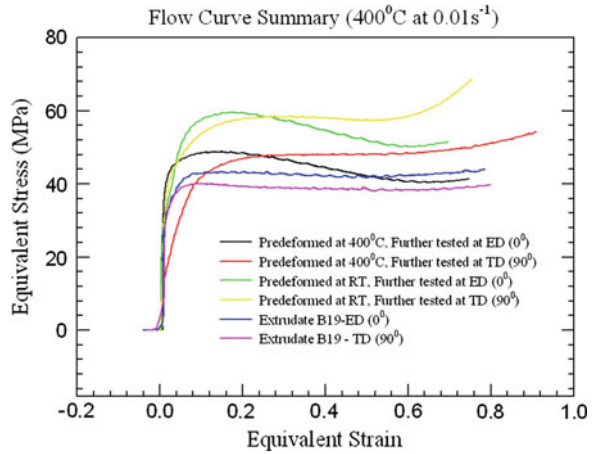


**Fig. 2** Extrudate AZ31 Flow Curve in plane strain compression; **a**at 400 °C and true strain rate of 0.01 s<sup>-1</sup>; and **b**at 400 °C and true strain rate of 0.1 s<sup>-1</sup>

metals with low to medium SFE (stacking fault energy) can occur frequently by bulging or twinning in addition to subgrain formation as reported in [14–18], it was observed that twinning is one of the essential factors for nucleation in magnesium alloy in our study.

From Figs. 2 and 3, it is clearly evident that when the material was predeformed at lower temperature (RT), a high yielding stress was obtained. The anisotropic mechanical properties were observed after predeformation which AZ31 as CAST is believed to have a homogenous structure. It seems when further deformation was carried out along the same extension as in predeformation (0°), a dynamic

**Fig. 3** Flow curve behaviour as a result of predeformation; tested at 400 °C and true strain rate 0.01 s<sup>-1</sup> at two orientations (ED and TD)



recrystallisation process was taken place which a single peak stress curve was shown. Therefore, it is convinced that the grains have been rotated during the predeformation which is rather strong temperature dependence but less strain rate sensitivities, which results were presented separately.

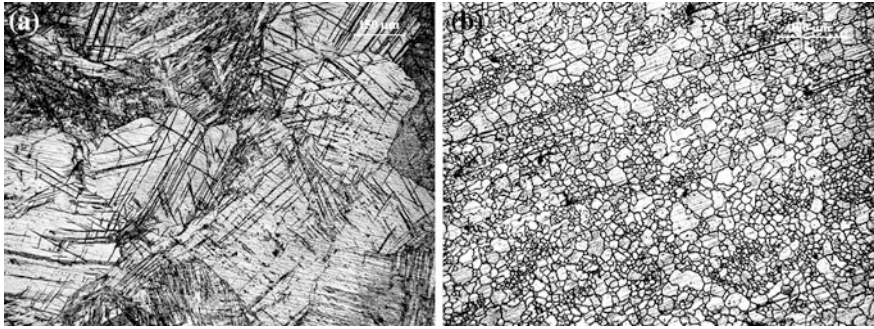
As reported, the extruded AZ31 has a texture of such that basal planes were parallel to the extrusion direction but tilted with c-axis towards the transverse direction, while the rolled material is believed its c axis tilted towards its rolling direction. As the results shown above, it is seen that predeformation process on AZ31 as cast shown a effect of rotating homogenous structures into a preferred grain structure with its c-axis pointing to its rolling directions similar to rolling materials. Consequently during further plane strain compression along its initial straining direction (0°), minimal basal slip or twins are possibly initially but (c+a) and (a) were possible and highest yield stress is expected.

Metallographic study as shown in Fig. 4(a) indicates very high fraction of twinning was seen at lower temperature at strain as slow as in 0.07, while an almost fully recrystallised structure was seen when the material was deformed at 400 °C even to a strain of 0.07. Therefore, what is to be believed responsible for this grain refining process, which grain size has been reduced from over 500 μm to less than 20 μm? To investigate the twinning effect, the same specimen deformed at RT (Fig. 4a) was annealed at 400 °C for about 20 min as shown in Fig. 5. Clearly, recrystallisation was taken place during annealing, which indicates somehow a strong influence of twins in the sake of dynamic recrystallisation.

Based on this finding, it is clearly evident that predeformation has a strong influence on its mechanical properties, which is strongly dependent on the deformation temperatures rather than strain rate as shown in Fig. 6.

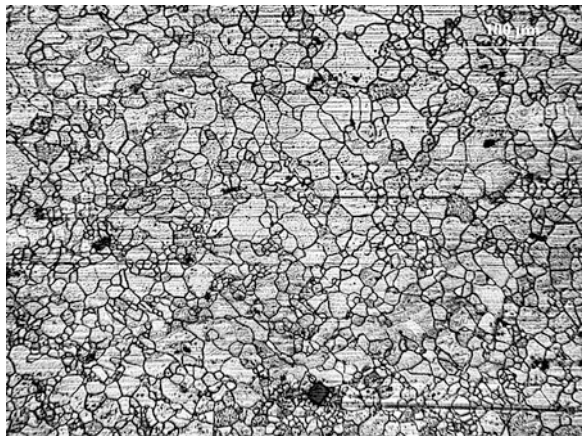
During the further plastic deformation, when stress was applied along extension direction (0°), plastic deformation is seen to result from dislocation slip and twinning because of the possible grain orientation as explained above. If we consider twinning to be an effective grain refining process, this would explain the



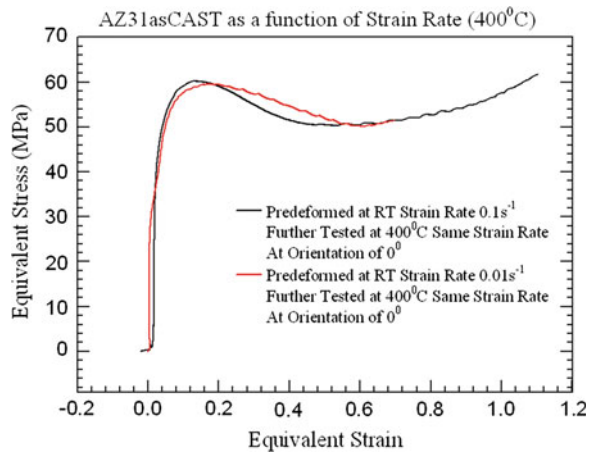


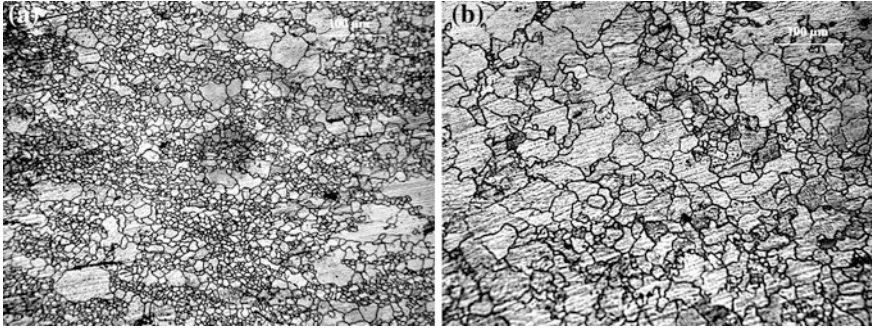
**Fig. 4** AZ31 as CAST Metallography after Predeformation; **a**predeformation was carried at RT, a true strain rate of  $0.01\text{ s}^{-1}$  and strain 0.07; and **b**predeformed at  $400^\circ\text{C}$ , a true strain rate of  $0.01\text{ s}^{-1}$  and strain 0.07

**Fig. 5** Metallography of AZ31 annealed at  $400^\circ\text{C}$  for 20 min after predeformed at RT with a true strain rate of  $0.01\text{ s}^{-1}$  to a strain of 0.07



**Fig. 6** Flow curve as a function of strain rate





**Fig. 7** Metallography of AZ31 tested after predeformation; **a** tested at 400 °C and a true strain rate  $0.01 \text{ s}^{-1}$  at orientation of 0° (RD); and **b** tested at 400 °C and a true strain rate of  $0.01 \text{ s}^{-1}$  at orientation of 90° (TD)

higher work hardening rate in the 0° orientation. Twinning induced at lower temperature or less favourable orientation for slip could be an effective or somehow necessary nucleation sites for dynamic recrystallisation. As presented in Fig. 7, finer grain structure was obtained when the stress was applied along 0° (RD) in comparison with 90°, which less favourable orientation is thought for twinning.

## 5 Conclusion

The mechanical properties of wrought magnesium alloy AZ31 as cast could be significantly improved by the predeformation process which grain size has been reduced significantly from over 500  $\mu\text{m}$  to around 20  $\mu\text{m}$ . This will significantly improve the fabrication efficiency of wrought Mg alloys. The mechanical behaviour after predeformation will exhibit similar trends to that of rolled sheet.

## References

1. 袁序弟, 镁合金在汽车工业的应用前景, 汽车科技 (2002) 3:1–4
2. 李明惠, 镁合金材料在轿车轻量化中的应用 (2002) J Guangdong Commun Polytechnic 3:44–47
3. Zhang CX, Chen P-L, Chen H-J, Shi A-J, Guang S-K (2008) Application and research progress of magnesium alloy in automobile industry. Foundry Technol 29(4):531–535
4. 陈虎, 镁合金的研究及其在汽车轻量化中的应用, 企业技术开发 (2009) 28:17–19
5. Goken J, Bohlen J, Hort N, Letzig D, Kainer KU (2003) Thermec 2003. In: Chandra T, Torralba JM, Sakai T (eds) Material science forum 426–432, Trans Tech Publications, Switzerland pp153–160
6. Xiong F, Davies CHJ (2003) Thermec 2003. In: Chandra T, Torralba JM, Sakai T (eds) Material science forum 426–432, Trans Tech Publications, Switzerland pp3605–3611

7. Roberts CS (1960) Magnesium and its alloys. In: Hollomon JH (ed) Wiley, NY pp5–6
8. Yamashita A, Horita Z, Langdon TG (2001) *Mater Sci Eng* A300:142
9. Koike J, Kobayashi T, Mukai T, Watanabe H, Suzuki M, Maruyama K, Higashi K (2003) *Acta Mater* 51:2055–2065
10. Barnett MR, Kelly GL, Hodgson PD (2000) *Scripta Materialia* 43:365–369
11. Yang X, Miura H, Sakai T (2003) *Mater Trans* 44:197–203
12. Myshlyayev MM, McQueen HJ, Mwembela A, Konopleva E (2002) *Mater Sci Eng* A337:121–133
13. Takuda H, Fujimoto H, Hatta N (1998) *J Mater Process Technol* 80–81:513–546
14. Watanabe H, Tsutsui H, Mukai T, Kohzu M, Tanabe S, Higashi K (2001) *Int J Plast* 17: 387–397
15. Agnew SR (2002) Plastic anisotropy of magnesium alloy AZ31 Sheet. *Magnesium Technol* 2002:169–174
16. Agnew SR, Duygulu O (2003) A mechanistic understanding of formability of magnesium: examining the role of temperature on the deformation mechanisms. *Mater Sci Forum* 419–422:177–188
17. Sitdikov O, Kaibyshev R (2001) *Mater Trans* 42(9):1928–1937
18. Styczynski A, Hartig Ch, Bohlen J, Letzig D (2004) *Scripta Mater* 50:943–947

# Consideration of Biomimetics in Structural Design of Vehicle Side Intrusion Bars

Yan Rui, Aleksandar Subic and Chunhui Wang

**Abstract** This paper presents the biomimetic design approach to the development of novel sustainable lightweight vehicle side intrusion bar. The new structure has increased stiffness at a significantly reduced weight while maintaining its crash-worthiness. The paper explores different biomimetic structures for vehicle side intrusion protection. Side-impact collisions are the second leading cause of death and injury in traffic accidents after frontal crashes. Side intrusion bar is an effective passive safety device for reduction of occupant injuries in a side-on crash.

**Keywords** Biomimetic · Structural design · Lightweight · Vehicle · Side intrusion bar

## 1 Introduction

Light weighting has gained increased importance in the automobile industry today. The main reasons for this are the increasingly stringent greenhouse gas regulations, reduced fossil fuels and increase price. The fuel consumption of cars is influenced by its fuel factors and in particular by weight of vehicle. Because of this, lightweight materials and structures are becoming increasingly important for the design of modern cars.

---

F2012-E07-009

---

Y. Rui (✉) · A. Subic · C. Wang  
RMIT University, Melbourne, Australia  
e-mail: s3312107@student.rmit.edu.au



**Fig. 1** a Side impact crash. b Car door with side intrusion bar installed

One of the most important requirements for automobile manufacturers is to develop vehicle structures that are crashworthy; that is they cushion impact and absorb the energy of impact over a maximum period of time and along large deformation paths with minimum acceleration [1]. The US National Highway Traffic Safety Administration (NHTSA) standards recommend use of lightweight materials and structures in vehicles for enhanced passive safety not only for the occupant but also for pedestrians or people outside the vehicle.

Notably, side impact crash is the second most common type of vehicle impacts after frontal impact. In such impacts, there is no room for large deformation of the vehicle structures; there are no other components to protect the occupant during the accidents. In United States side impacts result in injuries to occupants which account for 25 % of fatalities due to impacts between passenger cars and light trucks and approximately 30 % between passenger car crashes [2].

The manufacturers are required to meet the requirements for the side door safety by reinforcing the doors with door intrusion bar (see the example in Fig. 1). The function of the side door intrusion bar is mainly to provide the crush resistance to the occupant with high level safety. Side intrusion bar is assembled inside of the door frame and is designed to minimize the passenger compartment penetration in case of side crash accidents. The intrusion of the side door structure should be minimised and the force applied on the side door during the crash should be distributed over the door structure surface in such a way that the passenger in the cabin is protected well and is injured as little as possible.

There are many biological materials and structures in nature that exhibit excellent light weighting and high impact resistant performances. This paper explores different approaches to design of new lightweight side intrusion bars inspired by nature. This type of structure would have increased stiffness at a significantly reduced weight while maintaining its crashworthiness. The structure would be produced from lightweight metallic materials in order to maintain low cost, recyclability and conformability at our acceptable price to this section.

## **2 Materials Selection in Biomimetic Structural Design**

For material selection in mechanical design, Ashby illustrated the basic procedure, which established the links between material selection and function, shape and process [3].

### ***2.1 Function: Energy Absorber***

NHTSA standards recommend using lightweight materials and structures in vehicles for enhanced passive safety. The purpose of this new type of side intrusion bar design with biomimetics structure is to reduce the risk of serious and fatal injury to occupants of vehicles in side impacts by specifying strength requirements for side doors, limiting the forces, deflections and weight as energy absorber based on Federal Motor Vehicle Safety Standards.

### ***2.2 Shape: Sandwich Structure***

Sandwich structure is used widely in the vehicle industry for energy absorption parts, since it has comparatively higher energy absorption ability and lower weight than other traditional structures, such as hollow tube, I-beam etc. The challenge here is to find biomimetic structures that will enable comparable performances as energy absorber in those areas.

### ***2.3 Process: Sustainable***

The process determines the shape, the size, the precision and the cost. All those factors have dramatically effects on the environment since more concerns focus on the climate change effected by the CO<sub>2</sub> emission now. Cheap and less time consuming manufacturing process is the needs of the existing automotive industry and especially important for the automotive industry suppliers.

### ***2.4 Material: Lightweight Materials***

Material selection is determined by function. Shape sometimes influences the selection. Challenge here is to find the biomimetic structures that will enable less expensive more environmentally friendly materials that are available in large quantities to fulfil the requirement of the function.



**Table 1** Mass reduction potential using alternative materials

Lightweight material	Material replaced	Mass reduction (%)
Magnesium	Steel, cast iron	60–70
Carbon fibre composites	Steel	50–60
Aluminium matrix composites	Steel, cast iron	40–60
Aluminium	Steel, cast iron	40–60
Titanium	Alloy steel	40–55
Glass fiber composites	Steel	25–35
Advanced high strength steel	Mild steel, carbon steel	15–25
High stress steel	Mild steel	10–15

At present, sheet-steel panels are still the favourite material in industry for manufacturing of the body shell. Steel is competitive at an acceptable price and the process primarily involves the use of flat components. The high level of plastic deformation and absorption of energy by this material also means that currently it is unbeatable in meeting safety requirements. The potential for weight-saving relating to the material itself, materials such as aluminium, magnesium and composites all have a substantially lower specific weight than steel. From the report of Supplier Business (Table 1), using materials with a lower specific weight like aluminium and deploying modern methods of calculation in design allows engineers to achieve weight-saving over the conventional steel body [4].

The main advantage of metals compare to composites is that metals can achieve the objective of reducing weight while retaining the proven concept of the self-supporting body, cutting material costs and bringing about overall lower costs of investment. There is significant further potential for reducing weight by appropriate use of all the engineering characteristics of the metal materials in conjunction with innovative biomimetic structures and design.

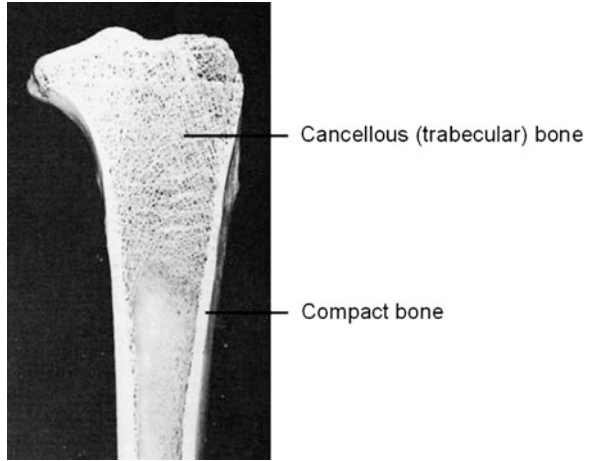
The steel has the best stiffness compared with other metals [5], but it is dense. Aluminium has one-third the stiffness of any steel, but for comparable weight, aluminium absorbs twice the energy that steel absorbs in a crash compared to steel. In this research, aluminium is chosen as the material of the newly designed side intrusion bar.

### 3 Biomimetics Cellular Structures

Nature contains some wonderful time-proven solutions in regards to impact resistant materials. Biomimetic, also known as biomimicry, is considered an abstraction of a good design of nature. This is a new field of science that studies how nature designs, manufactures and assembles/disassembles the molecules in order to produce structures with improved performances (i.e. mollusc shells, bone, skin, tendons, insect fly, eggs shell, lotus leaves) [6].

Biomimetic cellular sandwich structures inspired by nature have been used extensively in a variety of appliances for light weighting and for absorbing impact

**Fig. 2** Longitudinal section of tibia [7]



energy. The basic point is to have a dense skin and a lightweight core by appropriate choice of materials and geometry to achieve higher stiffness-to-weight ratio. Many natural materials possess internal cavities to reduce the density and improve the impact resistant ability. These include cork, bones, wood and plant stalks. Researchers have been developing lightweight structures for several decades, such as honeycomb structure, foam structure, tubular structure and others.

Bone is a structure of varying density. It has been naturally designed to provide structural support and protection of internal organs of a living body. Regions subjected to higher stress are denser. The outside surface is made of high density material and is called compact bone; the inside part of the bone has a lower density and is called cancellous bone. The average density is  $1.5 \text{ kg/m}^3$ . Figure 2 shows the longitudinal section of a tibia.

Bones such as tibia or femur are subjected to bending moments during normal loading. These create both tensile and compressive stresses in different regions of the bone. There is a large variation in measured values of both the tensile and compressive strength of bone. Different bones in the body need to support different forces, so there is a large variation in strength between them. The tensile strength of bones is 60–70 MPa; compressive strength is 70–280 MPa. Table 2 shows a comparison of bone tensile strength with some typical metals. The specific strength of bones is relatively higher than that of metals since the average density is much lower (see Table 2). Bone structure is a lightweight structure with high impact resistibility that makes it suitable for biomimetic design of a car intrusion bar.

## 4 Reconstruction of a Biomimetic Structure

The reconstruction of bone morphology is based on a stack of CT scanned slices obtained for a designated bone. The quality of the reconstructed bone structures depends on the resolution and the voxel size of the CT-scan.



**Table 2** Comparison of strength properties for bone and metallic materials

Material	Strength (MPa)	Density (kg/m <sup>3</sup> )	Specific strength (kN m/kg)
Magnesium alloy	275	1,740	158
Aluminium	240	2,700	89
Stainless steel	50–2,400	7,860	6–305
Titanium alloy	1,300	4,510	288
Bone	60–70	1.5	40,000–46,667

There are two principle ways to obtain the CT scanned slices. X-ray computed tomography or Computer tomography (CT) is a medical imaging method employing tomography created by computer processing. Digital geometry processing is used to generate a three-dimensional image of the inside of an object from a large series of two-dimensional X-ray images taken around a single axis of rotation. The other way is Magnetic resonance imaging (MRI), nuclear magnetic resonance imaging (NMRI), or magnetic resonance tomography (MRT), which is a medical imaging technique used in radiology to visualize detailed internal structures. MRI makes use of the property of nuclear magnetic resonance (NMR) to image nuclei of atoms inside the body.

After the bony structures are labelled in all slices, an automatic three-dimensional reconstruction of the bone is performed. In this approach, surface and finite element mesh are generated in commercial software Mimics. Figure 3 shows an example of the reconstruction model with finite element mesh of the rabbit femur.

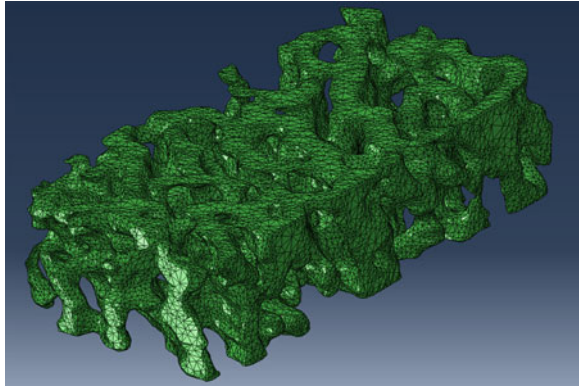
Quasi-static compression and impact tests are simulated in software ABAQUS based on the Side Impact Protection Standard FMVSS 214 (Federal Motor Vehicle Safety Standard). FMVSS 214 specifies performance requirements for protection of occupants in side impacts. Through the simulation, the forces, deflections and energy absorption ability of the new bone structure using material aluminium are obtained. The side door intrusion bar geometry is optimized using ABAQUS Topology Optimization Module (ATOM) to achieve the required requirements under specific load bearing conditions. The purpose is to specify the optimized geometry of the side door intrusion bar with bone structure, which has the highest specific energy absorption ability. This means that the newly designed intrusion bar is lightweight and crashworthy.

## 5 Selective Laser Melting Manufacturing

Selective laser melting (SLM) is an additive manufacturing process that uses 3D CAD data as a digital information source of the component design and energy in the form of a high powered laser beam (usually an ytterbium fibre laser) to create three-dimensional metal parts by fusing fine metallic powders together.

Currently there are ten materials qualified for this manufacturing method. These are high quality steels, titanium-, aluminium- and nickel-based alloys with powder

**Fig. 3** Reconstruction model with finite element mesh of rabbit femur



grain sizes between 10 and 60  $\mu\text{m}$ . The producible layer thickness is between 20 and 50  $\mu\text{m}$ . It is possible to achieve a component accuracy of  $\pm 50 \mu\text{m}$  [8]. The types of applications most suited to the SLM process are complex geometries and structures with thin walls and hidden voids or channels. Bone structure is complicated with thin walls and channels. Such structure cannot be manufactured using traditional manufacturing methods.

Although SLM or additive manufacturing is in its infancy with relatively few users in comparison to conventional methods (such as machining, casting or forging), in advanced technology applications, SLM significantly reduces the constraints on designers. This design freedom results in optimised structures and shapes that would otherwise be constrained by conventional processes or the tooling requirements for volume production. SLM helps to reduce lead times, reduce tooling costs and permits the creation of designs not previously possible. With the development of this technology, the cost of manufacturing side door intrusion bar based on bone structure geometry using SLM method will be decreased.

## 6 Process and Validations

The samples of optimized side intrusion bar with bone inner structure produced using SLM method are tested. The force, deflection and energy absorption data are collected and recorded. The tested results are statistically analysed and the data is used to validate the simulation results.

Conventional side door intrusion bar is modelled in CATIA and analysed in ABAQUS according to the requirements of FMVSS 214 as well, which is used here as a benchmark. The performance and weight of new designed side intrusion bar using material aluminium are compared with the results of conventional one.

Side intrusion bar with the same biomimetic structure using alternative metal materials are explored. The tested results are compared with the aluminium one.

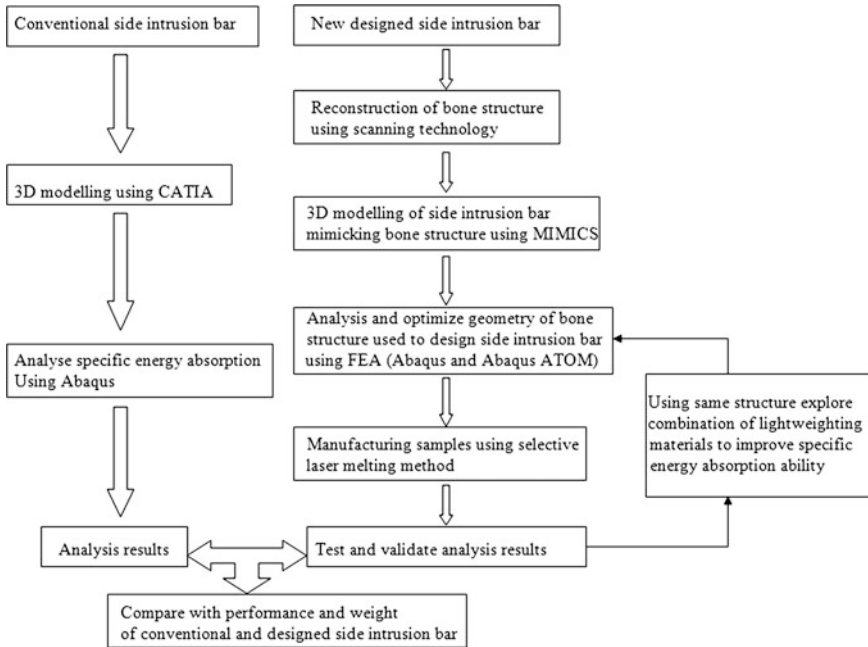


Fig. 4 Flowchart of the approaches

The purpose is to improve the specific energy absorption ability of new designed lightweight bone structure side intrusion bar with combination of different materials.

Figure 4 shows the flowchart of the approaches of the biomimetic design.

## 7 Conclusions

The paper presented the biomimetic design approach to the development of novel sustainable lightweight vehicle side intrusion bar. This lightweight vehicle structure has increased stiffness at a significantly reduced weight while maintaining its crashworthiness. To achieve these demanding requirements, the research explored biomimetic design principles inspired by concepts and solutions from nature.

The presented approach begins with the model and analysis of the current side intrusion bar as the benchmark, followed by comparison of energy absorption properties of newly designed side intrusion bar using a biomimetic structure. This process is described as follows:

1. Biomimetic structures are selected based on the similar load modes and mechanical properties between natural structures and component (side intrusion bar).

2. Conventional side intrusion bar is modelled and analysed using software CATIA and ABAQUS, and the analysis results are taken as the benchmark for further studies.
3. 3D bone structures are reconstructed from high-resolution CT images using a combination of edge extraction and CAD surface generation within the computer aided design software Mimics. New side intrusion bar is modelled based on the reconstructed bone structure.
4. FMVSS crashworthiness standard for the vehicle side door is employed to evaluate the impact resistant ability of the side intrusion bar designed based on the biomimetic structure using FEA software.
5. The geometric model is finalised using software ABAQUS and ATOM to achieve optimal performance under specific load bearing conditions.
6. Optimized car side intrusion bar design produced using the SLM method.

The new design of the side intrusion bar mimics the structures of the bone. This structure is lightweight and with high efficient energy absorption capacity, which offers a wide range of potential applications not only in the automotive sector, but also in aerospace, sports and other areas.

## References

1. Anselm D (2000) The passenger car body: design, deformation characteristics, accident repair. Warrendale, Pa., USA: SAE International
2. Basavaraju DH (1998) Design and analysis of a composite beam for side impact protection of a seaden. Mysore University, India
3. Ashby MF (2010) Material selection in mechanical design. Elsevier Science, Burlington
4. Lightweighting in automotive design and manufacturing. Stamford: Supplier Business, IHS Automotive; 2011
5. Olsen J (2006) Material assets. <http://www.caree.org/bike101framematerials.htm>
6. Borsellino C, Bella GD (2009) Paper-reinforced biomimetic cellular structures for automotive applications. Mater Des 30(10):4054–4059
7. Gibson LJ, Ashby MF (1999) Cellular solids: structure and properties. Cambridge University Press, Cambridge
8. Uhlmann E. Generative manufacturing methods: selective laser melting. Berlin: Fraunhofer-institute production systems and design technology

# Development of High Performance FRP Crush Box

## A Report of JSAE FRP Working Group Activity: Numerical Analysis of Fracture Behavior of FRP Crush Box with Tapered Trigger

**Reika Akita, Atsushi Yokoyama, Asao Koike, Kouji Kawamura,  
Yoshihiro Sukegawa and Hiromichi Oohira**

**Abstract** Activities in recent years, Fiber Reinforced Plastics (FRP) composite crush box consisting of a continuous random glass fibers and thermoplastic resin have been developed under consideration. Because of their superior mechanical properties in combination and lightweight structures, the FRP working group of The Society of Automotive Engineers of Japan (JSAE) has been considering the possibility of applying FRP crush box in a vehicle body. We have developed several FRP crush box and evaluated the energy absorption properties, expectation of impacted fracture process, manufacture cost experimentally. The structure with 45° trigger chamfer is one in the developed FRP crush box. It has the continuous force path based on the stable destruction progresses and satisfied with the requirement of high energy absorption. The initial micro-fracture of the trigger part of FRP crush box was observed by the group. Also the transition process of initial micro-fracture to a continuous and stable fracture which is called

---

F2012-E07-012

---

R. Akita (✉)  
ITOCHU Techno-Solutions Corporation, Ibaraki, Japan  
e-mail: reika.akita@ctc-g.co.jp

A. Yokoyama  
Kyoto Institute of Technology, Osaka, Japan

A. Koike  
Isuzu Advanced Engineering Center, Fujisawa, Japan

K. Kawamura  
Quadrant Plastic Composites, Yokkaichi, Japan

Y. Sukegawa  
Automobile Research Institute, Kobe, Japan

H. Oohira  
JSOL Corporation, Tokyo, Japan

'progressive crushing mode' has been found out through the experimental tests. We have analyzed the destruction mechanism of the trigger part in the early stage from the experiment. In addition, we try to make the numerical simulation model of FRP in reference these experimental results. Modeling mentioned above fracture propagation is a challenging task due to the complex nature of damage growth in composite. In this study, the numerical simulation of trigger area fracture in FRP crush box was performed with 3D finite element model based on the JSAE working group experimental specification and condition. The different composite material models of solver LS-DYNA<sup>®</sup> were tried in the analysis. The finite element model include the representation of delamination using a tiebreak contact interface and more physically based model parameters were applied. The numerical results were compared with the experimental reports. The specimens of Glass Mat Reinforced Thermoplastic (GMT) crush box with triggering form 45° chamfer were adopted in the calculation. The crush behavior and the progressive crushing mode of the trigger part were simulated with these models. It will be expected that the fracture propagation, fracture morphology and energy absorption predictions correlate well with the experimental results.

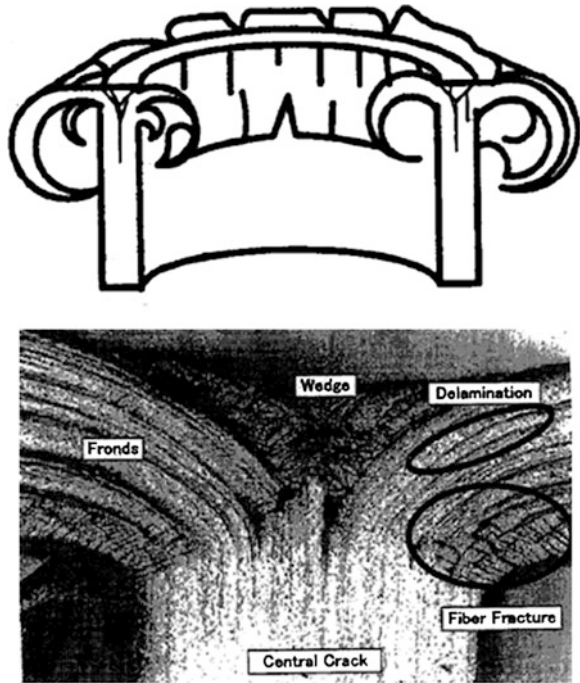
**Keywords** FRP crush box · Progressive crushing mode · Trigger · GMT · Simulation

## 1 Introduction

To reduce CO<sub>2</sub> emissions, the light weight of components is important in the automotive industry. The challenge is to replace heavy metal parts with light weight construction made from plastic and long glass fiber to enhance the strength of the material. Recently, the Fiber Reinforced Plastics (FRP) composite materials have been improved significantly. Specifically, its light weight is the major reason for the increasing application of composite materials in the automobile industry [1–5].

The crush box system is a structural component, which contributes to the crashworthiness during a front or rear collision. FRP composite crush box consisting of a continuous random glass fibers and thermoplastic resin have been developed under consideration. Because of their superior mechanical properties in combination and light weight structures, the FRP working group of JSAE has been considering the possibility of applying FRP crush box in a vehicle body. We have developed several FRP crush box and evaluated the energy absorption properties, expectation of impacted fracture process, manufacture cost experimentally. The structure with 45° trigger chamfer is one in the developed FRP crush box. When using metal material such as aluminum, the compression buckling of plastic deformation is utilized for the energy absorption. On the other hand, the fracture mode with fiber fracture and delamination are made good use of the FRP.

**Fig. 1** Progressive crushing destruction mode of a FRP tube



Specifically, such as a sample cylindrical typical structure, the continuous failure behavior form called Progressive Crushing is well known (Fig. 1). The crush zone spread the inner side and the outside towards the cylinder wall, the failure mode looks like petals.

Generally, there is up-and-down motion of the load when the metal material is during the buckling behavior. But an ideal rectangle waveform can be obtained by FRP material (Fig. 2). It has the continuous force path based on the stable destruction progresses and satisfied with the requirement of high energy absorption [6].

The FRP workgroup of JSAE focused on the trigger region of FRP crush box. Also the transition process of initial micro-fracture to a continuous and stable fracture which is called ‘progressive crashing mode’ has been found out through the experimental tests. We have analyzed the destruction mechanism of the trigger area in the early stage from the experiment [6].

## 2 Experimental Specimen of FRP Crush Box

In this study, the cylindrical tubes of FRP crush box specimen was considered with using thermoplastic GMT. GMT provides a high strength to weight ratio, chemical/corrosion resistance, and excellent impact properties both low and high speed.

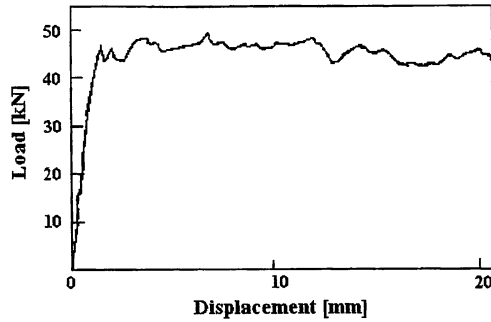


Fig. 2 Load-displacement curve of FRP tube on progressive crushing

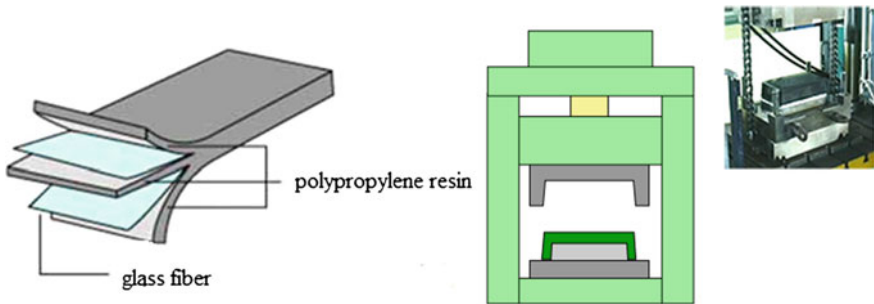


Fig. 3 GMT sheet and production machine for crush box

Compared to metals, GMT offers greater design flexibility, opportunities for structural component consolidation, and lower tooling costs.

The cylindric GMT tube was manufactured from random glass fiber prepregs (Quadrant plastic composite Japan). The matrix was polypropylene resin, and the glass fiber aspect ratio was 40 %. The production is by press-forming 6 layers GMT sheet in the state where the sheets were heated until the resin was melted, and the fibers tangled in matrix (Fig. 3).

Configuration of the cylindric GMT tube is shown in Fig. 4. The tub was made first, and then the 45° trigger chamfer is cut to size.

## 3 Experiment

### 3.1 Experimental Results

The 14 same specimens of FRP crush box were prepared, and the low speed compression examinations were carried out using difference crush strokes for every specimen. A Shimadzu AG-E10 tester was utilized in this examination. In



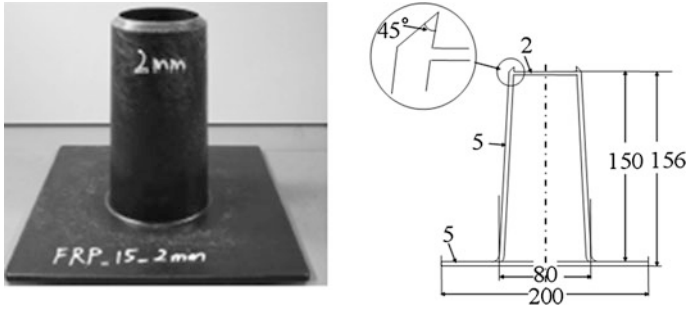


Fig. 4 FRP crush box exterior view and dimensions

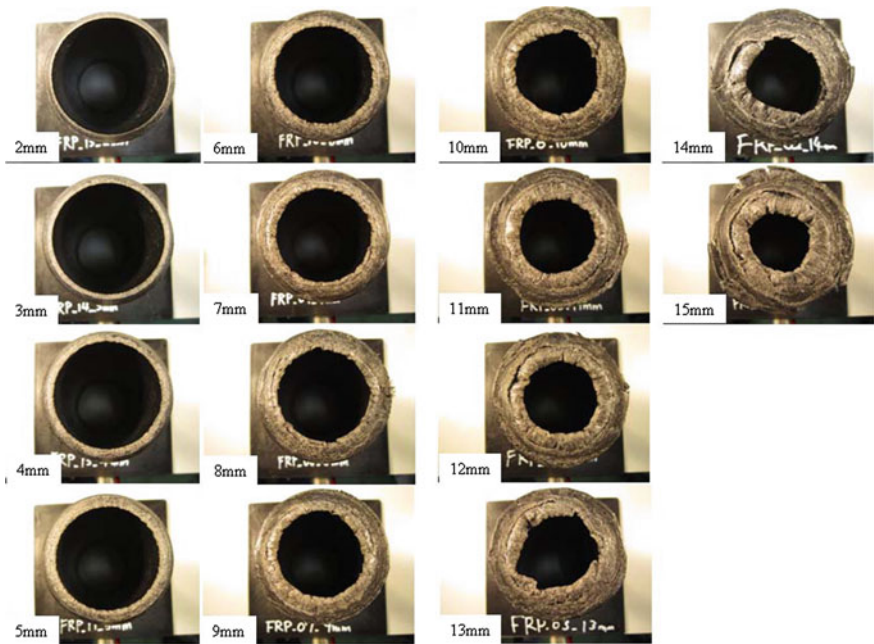


Fig. 5 After-examination appearance of the 14 specimens of FRP crush box

order to observe the destructive mode and destructive process at the tip of specimen, the movements of tester crosshead were increased 1 mm every time for every specimen from 2 to 15 mm. Total 14 examination were be done. The test speed was 10 mm/min. Figure 5 shows the after-examination appearance of the 14 FRP crush box specimen.

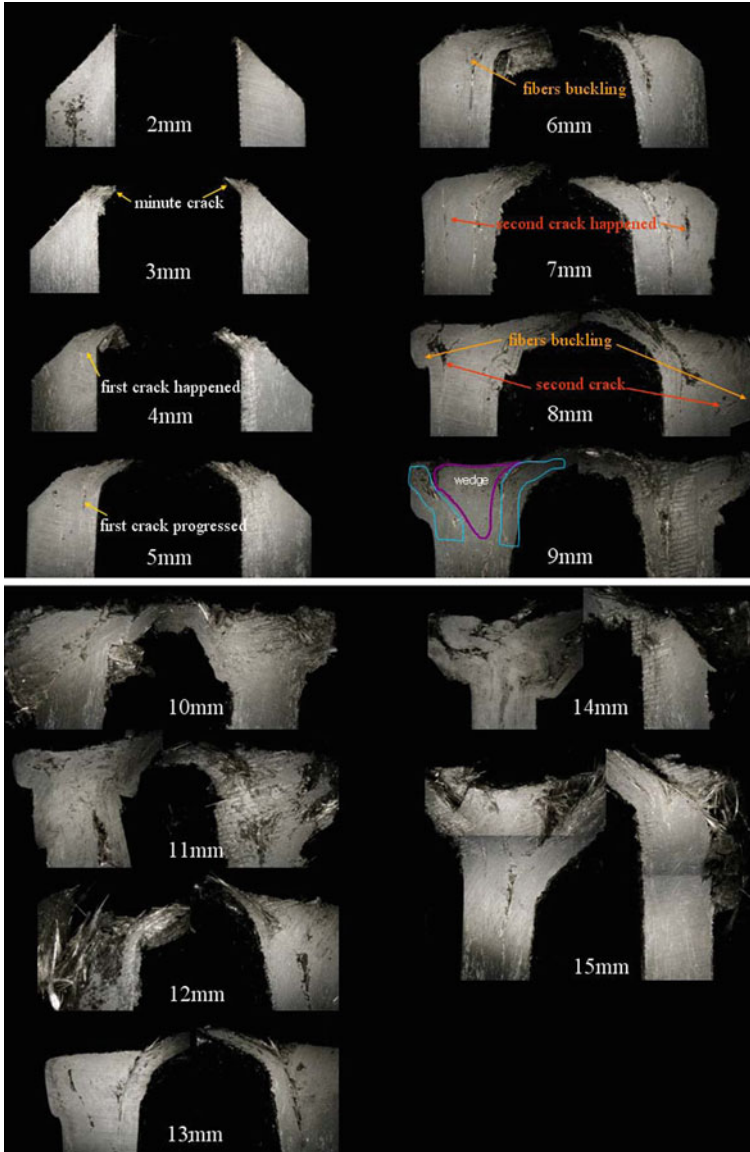


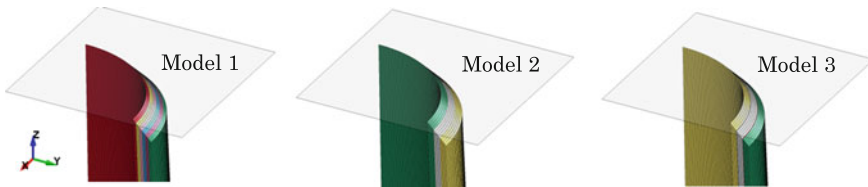
Fig. 6 Photograph of cross section of trigger area in different crush strokes

### 3.2 Destructive Mechanism Investigation

In order to observe advance of destruction about the FRP crush box specimens loaded from 2 to 15 mm in the movements of the crosshead, the after-examination

**Table 1** Investigation of trigger area in different crush strokes

2 mm	The trigger tip fell on the inner side slightly
3 mm	The trigger tip fall increasing, some minute cracks occurred
4 mm	The first crack happened on the inner side
5 mm	The first crack progressed in the cylindrical direction of an axis
6 mm	Fibers buckling occurred
7 mm	The second crack happened near the outer side
8 mm	The second crack progressed and fibers buckling occurred
9 mm	Wedge appeared and the Progressive Crushing begun
10–15 mm	Progressive Crushing mode progressed



**Fig. 7** Details of FE Models

specimens were cut in the lengthwise direction. Figure 6 and Table 1 show the photographs of cross section and investigation results from the observing sections.

## 4 Numerical Simulation

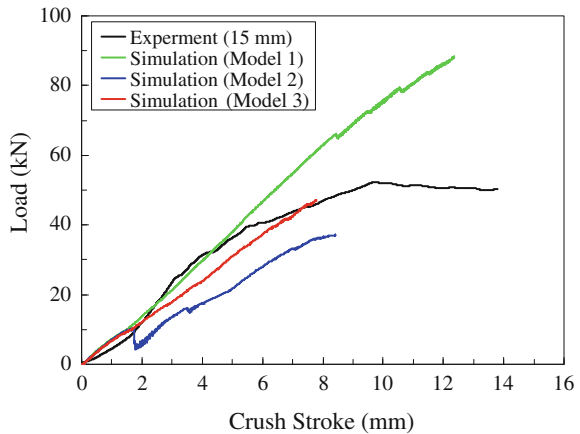
### 4.1 Details of 3D finite element model

In this study, a 3D finite element model was developed to simulate the progressive failure behaviors and energy absorption properties. Three types of FE model were considered for the cylindric FRP crush box with solid elements. Model 1 was a no failure model for conforming the material properties of GMT. Model 2 simulated the delamination with a tiebreak contact interface. Model 3 was a simple cohesive elastic model to challenge more complex delamination simulation. The tester crosshead was created using a rigid plate with shell elements. In order to shorten computation time, 1/4 model was modeled. The details of these models show in the Fig. 7. The solver LS-DYNA Ver.971d R5.1.1 was used.

**Table 2** Material properties of FRP crush box used in the FE analysis

Material property	Symbol	Values
Longitudinal young's modulus	Ea	50000 MPa
Transverse young's modulus	Eb	5800 MPa
Transverse young's modulus	Ec	5800 MPa
Poisson's ratio	$\nu$	0.3
Shear modulus	Gab	2000 MPa
Shear modulus	Gbc	2000 MPa
Shear modulus	Gca	2000 MPa

**Fig. 8** Load-Crush Stroke responses simulation versus experiment

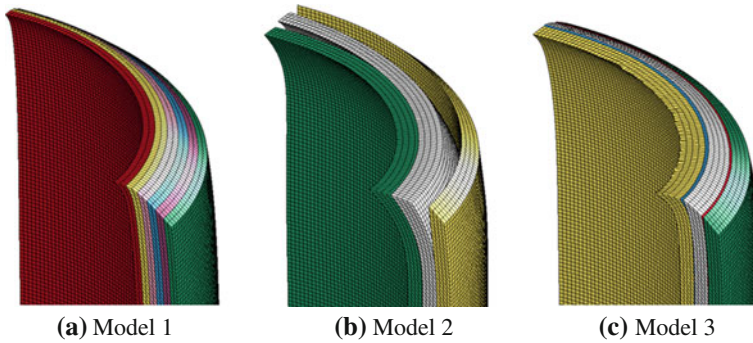


### 4.2 Boundary and Material Properties

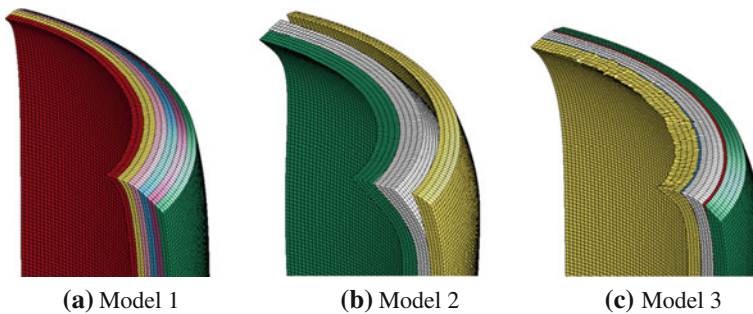
The bottom side of the models were perfectly fixed. The displacement time history was loaded to the tester crosshead. For the boundary conditions of crosshead, the displacement along the z axis downwards only permitted. The GMT material properties used for MAT\_02 in LS-DYNA are listed in Table 2. Material parameters were not measured experimentally but have been estimated on more experience. Moreover, a transversal isotropic material behavior around the fiber direction is assumed. The anisotropy definition AOPT=3 in the material definition was used to define the orientation of the fibers respectively.

### 4.3 Numerical Results

Figure 8 shows the load-crush stroke curves of FEM results for Model 1, Model 2 and Model 3. The load in the figure shows the contact force value between the crosshead and crush box from LS-DYNA calculations with three models. The crush stroke in the figure shows the displacement of crosshead.



**Fig. 9** Deformation of three models (at stroke 5 mm). **a** Model 1, **b** Model 2, **c** Model3



**Fig. 10** Deformation of three models (at stroke 7 mm). **a** Model 1, **b** Model 2, **c** Model3

The comparison of three models numerical load-crush stroke results with the experimental result is in the figure. It is seen that the comparison of the crush response behavior of Model 1 was favorable due to the crush stroke value reached 4 mm, before the first crack progressed. This means the material properties of GMT were appropriate in the analysis. But the load response behavior of Model 2 and Model 3 appeared low value than experimental results. The factors are the best failure criteria of material parameters for simulation did not been overcome at this time. Figure 9 shows the deformation of three models when the crush stroke was 5 mm. Figure 10 shows the deformation of three models when the crush stroke was 7 mm.

## 5 Conclusions

In this study, the numerical simulation of trigger area fracture in FRP crush box was performed with 3D finite element model based on the JSAE working group experimental specification and condition. The finite element model include the

representation of delamination using a tiebreak contact interface and cohesive elastic model were developed. The crush behavior and the progressive crushing mode of the trigger part were simulated with this model. The numerical results were compared with the experimental reports. It clearly demonstrated how the part of failure behavior of FRP crush box is similar between the experiment and simulation.

In this study, we considered the failure criteria of material parameters for simulation model. But there are many things remaining which cannot be carried through. In the future, we will determine the optimal material models as it applies to this simulation. To overcome these challenges, the possibility of application of FRP to vehicle body will be investigated.

## References

1. Hamada H et al (1996) Study on energy absorption structures with composite tubes—results of study on structural FRP working group-. JSAE 965:29–32
2. Thornton PH et al (1977) The interplay of geometric and materials variables in energy absorption. Trans ASME 99:114–120
3. Hull D et al (1991) A unified approach to progressive crushing of fibre-reinforced composite tubes. Compos Sci Technol 40:377–421
4. Hamada H et al (1997) Analysis of crushing mechanism on composite tube under axial load, SAE, Warrendale
5. Technical report (2002) Series No. 37, JSAE, 2002
6. Koike A et al (2011) Development of high performance FRP crush box—a report on FRP working group activity analysis of collapse mechanism of the trigger part -, JSAE 104–11: 5–8

# Development of the High Performance FRP Crush Box: A Report of JSAE FRP Working Group Activity. Analysis of Collapse Mechanism of the Trigger Part of FRP Crush Box

Asao Koike, Atsushi Yokoyama, Reika Akita, Yoshiro Sukegawa,  
Koji Kawamura and Hiromichi Oohira

**Abstract** The working group for structural use of FRP in JSAE (FRP W/G), has been considering the possibility of applying FRP in use of a crush box of a car. Compressing the vertical plane of the FRP laminate structure, a destruction of stable crack growth between layers, and rupture of the fiber occurs continuously. This mode is called “progressive crushing”, and considered to be an ideal energy absorbing form. The objective of this study is to observe the phenomenon of the initial micro-fracture of the trigger part of FRP crush box, and analyze the transition process of initial micro-fracture to the progressive crushing. The authors have observed the phenomenon of initial rupture process, the cracks due to the delamination from compression inside the crush box, and the cracks occurred outside the crush box. Also the rupture of the fibers was observed by X-ray CT scanner.

---

F2012-E07-013

---

A. Koike (✉)

Isuzu Advanced Engineering Center, Ltd, Kanagawa-ken, Japan  
e-mail: asao-koike@isuzu.co.jp

A. Yokoyama

Division of Advanced Fibro-Science Graduate School, Kyoto Institute of Technology,  
Kyoto, Japan

R. Akita

ITOCHU Techno-Solutions Corporation, Chiyoda-ku, Japan

Y. Sukegawa

Japan Automobile Research Institute, Chiyoda-ku, Japan

K. Kawamura

Quadrant Plastic Composites Japan Ltd, Yokkaichi, Japan

H. Oohira

JSOL Corporation, Chuo-ku, Japan

**Keywords** Energy absorb · FRP · Crush box · Thermal plastics · GMT

## 1 Introduction

Now a days, for the aim of reducing energy consumption, lightweight body has been demanded for a car development. In the field of passive safety, not only making a safer structure, but at the same time, reducing the weight is also been required. Therefore, in order to reduce the weight, study of vehicle body structure, material selection, and new processing technologies have been greatly under development. Since composite materials such as fiber reinforced plastics (hereinafter, FRP), has a good stiffness/weight ratio, and also the advantage of the flexibility on designs, it has begun applying to body parts. Furthermore, FRP is expected as an energy absorbing materials, since from their excellent energy absorption performance [1–4]. The working group for structural use of FRP in JSAE (JSAE FRP W/G), has been considering the possibility of applying FRP in use of a crush box of a car. Compressing the vertical plane of the FRP laminate structure, a destruction of stable crack growth between layers, and rupture of the fiber occurs continuously. This fracture morphology mode is so called “progressive crushing” (Fig. 1).

In this mode, the destruction is continuously developed, and only a little vertical movement of the load is observed, where buckling of the metal have a large movement. Therefore, progressive crushing mode has an ideal absorbing energy ability (Fig 2).

The JSAE FRP W/G has made an interest in this excellent energy absorption characteristics for the use of “crush box” which the purpose to prevent damage to the vehicle body at low speed collisions [5].

In order to generate a progressive crushing, sharp pointed edge, which is called “trigger” plays a big role before the stable progressing mode starts. But, the phenomena around this early stage were not clearly observed precisely. In order make FRP a “designable material”, the immediate goal of the activities, is to make a precise CAE model in which to describe actual crushing response in the early stage, before progressive crush begins. In this chapter, the initial micro-fracture of the trigger part of FRP crush box was observed, and the transition process of initial micro-fracture to progressive crushing was analyzed.

## 2 Previous Activities of the FRP W/G

From the past, The JSAE FRP W/G has been making study for thermoplastic FRP materials by use of car, since it is more cost effective than other FRP materials. Below, is the activity which the W/G have been working.



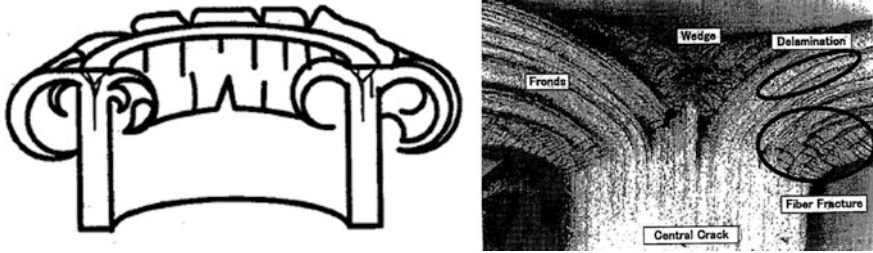
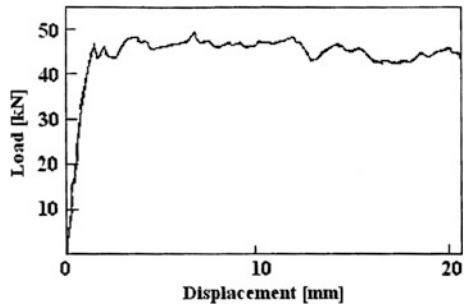


Fig. 1 Progressive crushing destruction mode of a FRP tube

Fig. 2 Load–disp. curve of FRP tube on progressive crushing



### 2.1 Survey of Basic Characteristics

A survey of basic characteristic, such as investigation of mean force, energy absorbing amount, by changing numbers of laminated sheet in manufacture, characteristics in various temperatures, angled applied force [6].

### 2.2 Effect of Discrepancies in Material Processing

Artificially a hole was made to simulate the discrepancy of material processing, and reached to a conclusion that at dynamic crash, depending on the size of the defect, it will not effect to deterioration of mechanical characteristics [7].

### 2.3 Numerical Analysis

In order to design a crush box from zero, the W/G has built a model to simulate the mechanism of destruction.

First, for the fracture axis direction, in a scope of microscopic deformation theory in static, delamination, shear failure, tensile failure, and compression failure

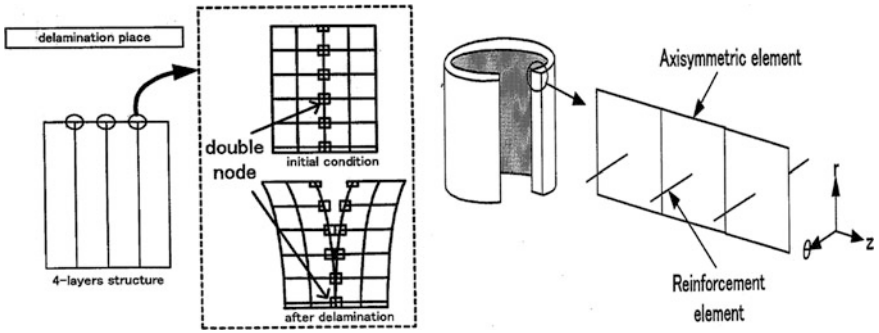
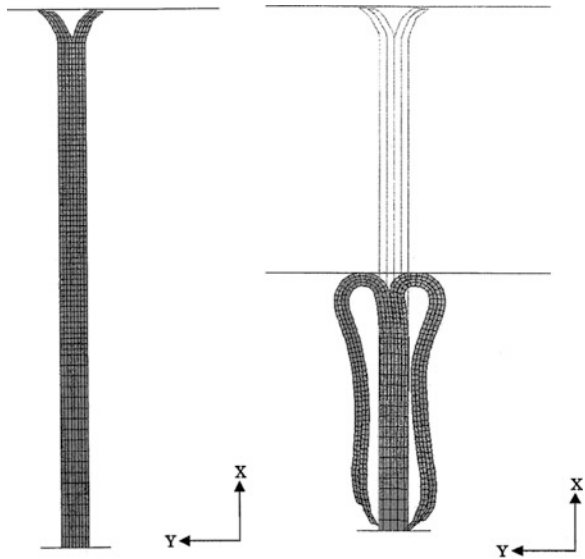


Fig. 3 A numerical simulation method used in FEM

Fig. 4 Axisymmetric finite element model and deformed shape



was considered. Then, consideration was applied for the circumferential direction, the buckling, and progress of cracks. These were then in consideration of the way to combine. Finally, the studies of combination were applied to FEM using MSC MARC (Fig. 3), and the FEM model was constructed [8].

Figure 4 is a FEM model that reflects all the results of study. This model has a good correlation in the plateau part of progressive crushing. However, this model is able only to simulate from the point of progressive crushing begins.

As a next step, the consideration of destruction from the very beginning, to the progressive crushing is demanded (Fig. 5).

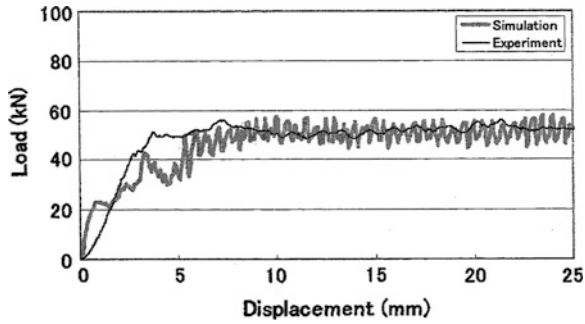


Fig. 5 Comparison of experimental and analytical results

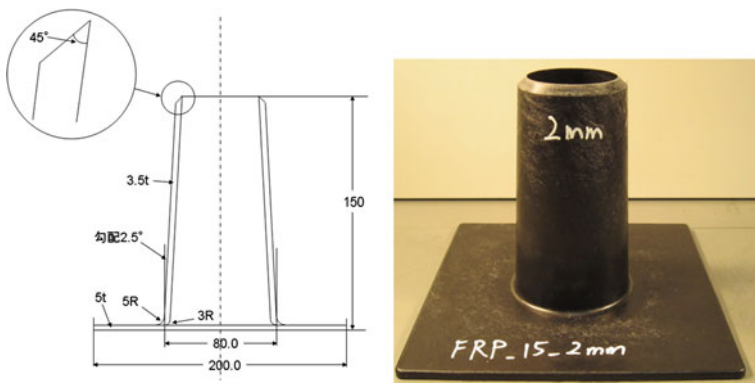


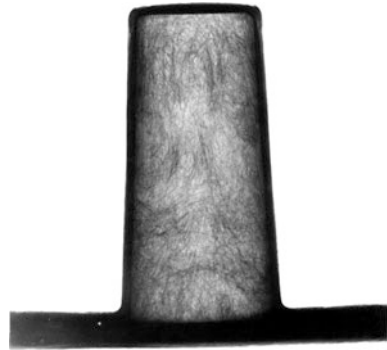
Fig. 6 FRP crush box dimensions, and exterior view

### 3 FRP Crush Box

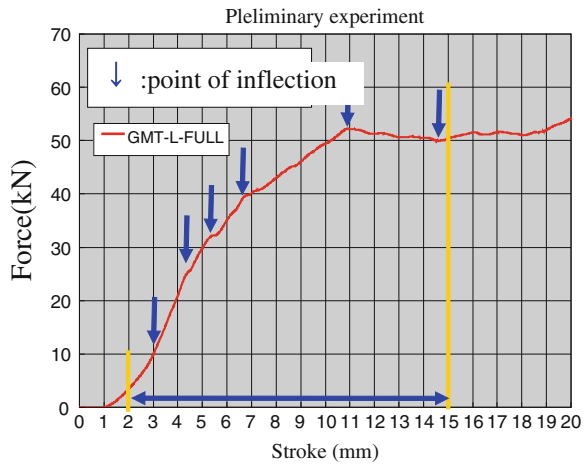
The crush box which have been evaluated was made of random continuous glass fiber reinforced poly-propylene. This was manufactured by heating the prepregged composite sheet (Quadrant Plastic Composite Japan's Unisheet) to a melting temperature of polypropylene, and be pressed. The shape of specimen is cylindrical, with a slight gradient, and a flange at the bottom. On the top, there is a 45° oblique trigger part for making a progressive crushing. The volume fraction of fiber was 40 wt % (Fig. 6).

Figure 7 shows the soft X-ray picture of the appearance. As can be seen from the soft X-ray photograph, the continuous glass fiber is widely spread, which resin rich distribution is almost not seen.

**Fig. 7** FRP crash box inner part by soft X-ray



**Fig. 8** Preliminary experiment to define transition area



## 4 Collapse Mechanism

### 4.1 Experiment

First, in order to identify the transition region, from the initial state to progressive crush fracture, preliminary test was held to investigate the transition region.

The judgment of the transition region was determined as the crushing load shows plateau load force against the stroke. Point of inflection in the diagram was also determined to be included.

As from Fig. 8, result from the preliminary test, it is roughly say that the load level is plateau from 11 mm stroke, but since a point of inflection was observed after 14 mm, the possibility of transition region has considered up to 15 mm.

Based on the results described above, 14 FRP crash boxes were prepared, and decided to carry 14 different quasi-static tests which the makes the maximum stroke 1 mm gain for every next test, and observe the fracture process.

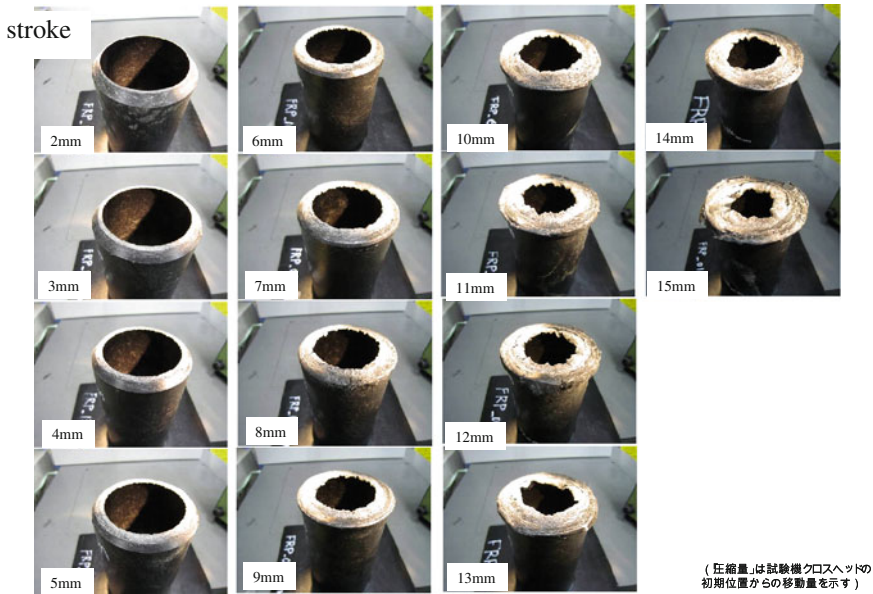


Fig. 9 14 FRP crush box after the preliminary experiments

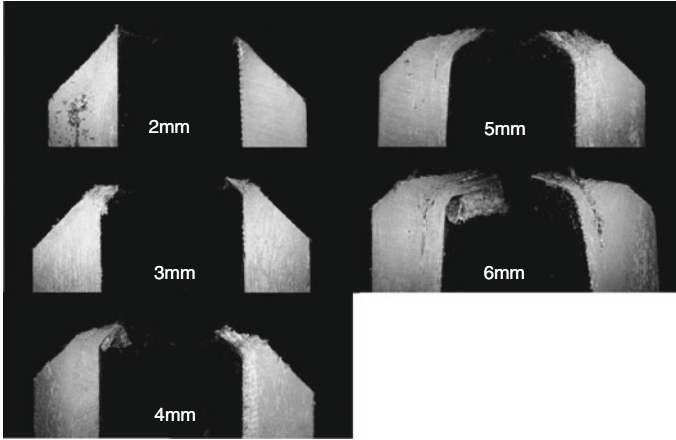
Figure 9 is the appearance of all the specimen after the test. In the case of 15 mm stroke, the progressive crushing mode is clearly observed.

### 4.2 Analysis of Destruction Mechanism

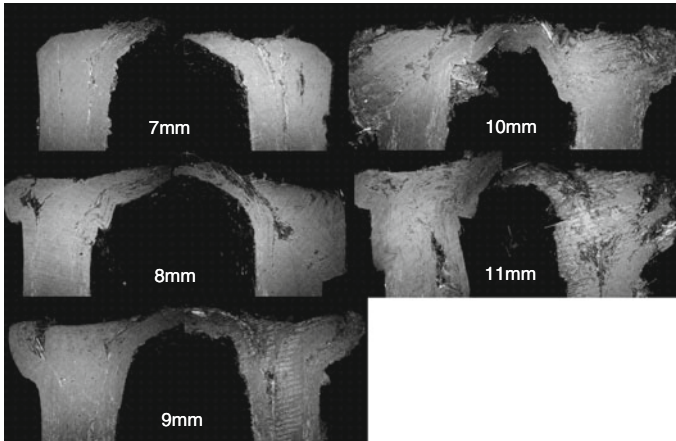
To investigate the progress of destruction from the specimen which the stroke applied from 2 to 15 mm, the specimen was cut into the vertical direction, and was polished. Also, some specimen were observed by X-ray CT scanner.

Figures 10, 11, 12 presents the cross-section of each specimen.

First, at the state of 2 mm stroke applied, trigger part tipped slightly toward inside of the cylinder, from its geometric shape. When at 3 mm stroke, tipped part was increased, and from the thought of the difference of the curvature of layers, some small cracks from delamination have occurred. In 4 mm stroke, the initiation of the first major crack has fixed from these delamination cracks. In this case, the first major crack (Crack I) has occurred near the inner side of the section. This Crack I has occurred in this location by the balance between geometrical influence, such as diameter, thickness of the crush tube, and material strength, such as mechanical strength of fibers, matrix, and inter layer strength. When the stroke of 5 mm, the development of the crack is observed clearly. At 6 mm, when the applied load form the top is increasing, some part of the trigger area is bended inside the crush tube, but outside the Crack I, by some constraint from circular way



**Fig. 10** Cross section of top trigger part of crush box in different crush strokes (2–6 mm)



**Fig. 11** Cross section of top trigger part of crush box in different crush strokes (7–11 mm)

layered fibers, the area have lost the place to go. The buckling of fibers can be observed in this remaining area.

When at 7 mm stroke, remaining area developed at 6 mm stroke was increased. The force from this area has not only applied downwards, but to the outside the cylinder. By this, second crack (Crack II) has been developed. At 8 mm, buckling of the fibers at the outer area of Crack II has begun, and the part which collapses outside has been developed. By this, the fundamental conditions to progressive crushing was generated. When at 9 mm, it can be clearly observed that, collapsing inner, outer part, and the center remaining part is separated. This remaining part will play a role as a wedge, to increase Crack I and Crack II when the stroke increases.

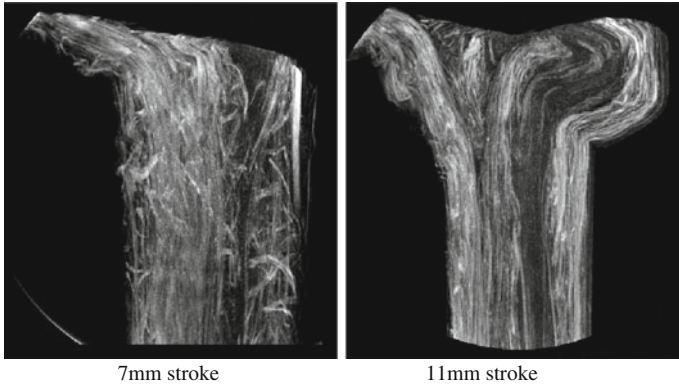


Fig. 12 Behaviour of fiber at 7 and 11 mm stroke by X-ray CT scanner

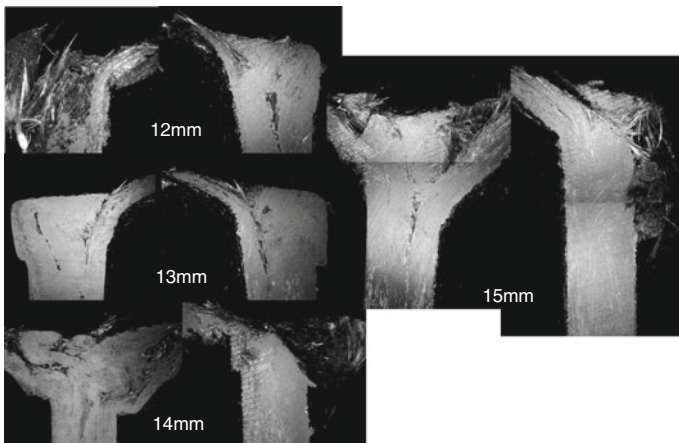


Fig. 13 Cross section of top trigger part of crush box in different crush strokes (12–15 mm)

For 10 mm stroke and later, the fracture mechanism described in 8, 9 mm has been repeated continuously, and it can say that the destruction has transit to progressive crushing.

This is supported from the preliminary experiment that the stroke-load characteristics became plateau 10–11 mm stroke.

From the X-ray CT scanner, not the crack of the matrix resin, but the behaviour of the fibers can be observed. As the 7 mm stroke case, split of the layer as the Crack II developed, and for the 11 mm stroke, the Fibers are tilted as the wedge part makes both inner and the outer part spreading the in and out like a “petal” (Fig. 13).

## 5 Conclusions

From the experiment and analysis done above, the transition process of initial micro-fracture to the progressive crushing is summarized as follows:

- Tipping of the trigger toward inside initiate small cracks, and generate first major crack “Crack I”.
- When the continuous load is applied further, some area which cannot tip inside the crush box remains. Soon from this remaining area, the outer part is squeezed out, and the secondary crack “Crack II” is generated.
- There exists a remaining area between Crack I, and Crack II. This then acts as a “wedge” to start the progressive crushing.

For future, the JSAE FRP W/G is planning to investigate the phenomena quantitative, and develop a precise expression of the transition region to the progressive crushing by CAE.

## References

1. Hamada H et al (1996) Research on energy absorbing parts by use of FRP tube—report on FRP W/G for structural use [in Japanese]. JSAE Congr Annu Proc 995:29–32
2. Thornton PH et al (1977) The interplay of geometric and materials variables in energy absorption. Transaction of ASME, pp 114–120
3. Hull D et al (1991) A unified approach to progressive crushing of fibre-reinforced composite tubes. Compos Sci Technol 40:377–421
4. Hamada H et al (1997) Analysis of crushing of fibre-reinforced composite tube under axial load. SAE
5. JSAE working group for structural use of FRP, Technical Report Series, vol 37, Japan Society for Automobile Engineers (2002)
6. Nakatani T (2005) Development of high performance FRP crush box [in Japanese]. JSAE autumn congress presentation
7. Nakatani T (2007) Development of high performance FRP crush box [in Japanese]. JSAE autumn congress presentation
8. Tateishi G (2003) Analysis of destruction behavior under an impact load on high polymer composites [in Japanese]. Doctoral thesis, Kyoto Institute of Technology



# Research of Application of Crash Durable Adhesive on a Chinese Domestic Car Body

Zhongying Yue, Xiukui Yuan, Chaoqian Gao, Liantai Yuan, Qiang Liu, Fuquan Zhao, Yufei Wang, Xiaojun Yang and Jie Xu

**Abstract Methodology:** There are several methods to evaluate the adhesive bonding performance. In this study, three categorical methods were employed. Firstly, for the adhesive location selection, the CAE analysis was used to identify the adhesive bonding effect on body stiffness improvement. Combined the simulation result with work shop assembling process, the key flanges for adhesive were optimized. Secondly, for the adhesive grade selection, the tensile lap shear, T-peel, impact peel test at high and low temperature environment, the salt spray test, humidity test and wash off test were selected. Thirdly, for the crash performance verification, the axial drop tower impact test with Dow new crash durable adhesive was simulated with explicit finite element method. Through above three technical methods, the over-all properties and detail application area in car-body were derived. **Results:** The lap shear and peel testing results show that the crash durable adhesive product could fully meet the requirement of automotive industry. The low-temperature shear strength is above 35 MPa. The axial crush testing simulation results show that the load resistant capability of Dow crash durable adhesive is superior to spot welding joining. Through the computer-aided engineering (CAE) analysis on one of Chinese domestic car with the crash durable adhesive, the bending stiffness could be increased up to 8 %. **Limitations of this study:** The study is mainly directed against cold-rolled steel sheet that a Chinese domestic OEM used. For galvanized steel, high strength steel, and other alloy like magnesium and aluminium testing are studied in other separate study. What does the paper offer that

---

F2012-E07-020

---

Z. Yue (✉) · X. Yuan · C. Gao · L. Yuan · Q. Liu · F. Zhao  
Zhengjiang Geely Automobile Research Institute Co., Ltd, Hangzhou, China  
e-mail: yuezy@rd.geely.com

Y. Wang · X. Yang · J. Xu  
The Dow Chemical (China) Co., Ltd, Shanghai, China

is new in the field including in comparison to other work by the authors? This paper presents a complete set of new adhesive bonding verification analysis and test tools, the study aimed to validate and verify the application and contribution of this new vehicle body bonding technology on Chinese domestic car body trough testing and CAE method, which has significant value on the promotion and application of new automotive materials. *Conclusions*: The new type of crash durable adhesives in this study can meet all of Chinese domestic OEM standards. And it could help to enhance body stiffness, increasing vehicle crashworthiness and durability. It is a high efficiency connection type which could be the alternative of spot welding.

**Keywords** Structural adhesive · Body structure · Stiffness improvement · Adhesive testing · CAE

## 1 Introduction

With the rising requirements of automotive lightweight, the modern body processes require the use of lighter, stronger materials to achieve higher strength requirements. Under this demand, a stable and efficient body connection becomes particularly important. At present, the conventional spot welding is still a primary connection method, while the arc welding, laser welding, riveting and bolt connections are the other useful supplement. Body structural adhesive bonding technology, beginning from the mid-1990s in some German companies, becomes reliable joining method for many the body design staffs in recent years. The Euro-car-body meeting reports show that more and more new vehicle models adopted structural adhesive connections [1–4]. The bonding length of some high-end models is even longer than 150 m [5].

Compared with the conventional connection methods, the application of structural adhesive can bring the advantages of the following aspects: (1) increase the connection strength and release the local stress concentration and improve body dynamic stiffness; (2) enhance the body NVH performance. Statistical data show that the structural adhesive can improve the body static stiffness by 10–16 % [6]. At the meantime, structural adhesive can effectively reduce interior noise and improve the car speech intelligibility; (3) the car model which uses the toughening anti-collision grade of structural adhesive, can be enhanced in crash safety and durability aspect. In the simulation study of a public model, using toughened structural adhesive—crash durable adhesive, the frontal impact and side impact occupant compartment intrusions have be significantly improved [7]. A model of the other OEMs' durability test data show that: the use of weld bonding connection, the relevant parts of the spot weld life has increased by 300 % [8]; (4) dissimilar material connections: structural adhesive connection between the dissimilar metal materials can effectively prevent the galvanic corrosion. At the same time, there are many examples of the bonding solution for the metal/plastic,

metal/composites, composites/composites connection, which laid the foundation for the future of the lightweight body work [9].

Although there are more than 10 years of experience of structural adhesive use in automotive industry, the technologies of the adhesive bulk material properties, connectivity, connection process, and application location in car body are often managed by foreign OEMs. For domestic OEMs there is very limited application case and less experience on the use of structural bonding. This study was designed to introduce the performance assessment method of crash durable adhesives and the adhesive location identification method for body performance enhancement.

## **2 Test and Simulation Method**

### ***2.1 Bulk Material Test and Coupon Test***

#### **2.1.1 Test Matrix**

In order to test the lap shear strength and corrosion strength, and other technical requirements to improve vehicle durability, crash performance and body stiffness, the following 3 groups' tests are designed with 3 grades of structural adhesives.

Group #1: Application testing, including sagging and wash-off test, used to characterize the performance of wash off resistance in the paint shop.

Group #2: Mechanical behavior test, Including: shear strength at room temperature and low temperature case, T-peel strength testing, corrosion, humidity, salt spray, aging, immersion testing, as well as room temperature and low temperature impact peel strength test.

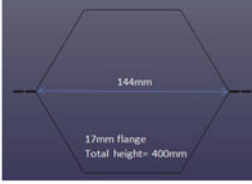
Group #3: Material physical performance test, including the material density, viscosity and solid content.

#### **2.1.2 Materials in the Test**

Three grades of structural adhesives were used in the test. Two of them are from Dow Automotive Systems (made in Dow European), crash durable grade: D1 and D2. The other one is the competitor's structural adhesive (made locally). The substrate used is the cold-rolled steel from a Chinese domestic OEM.

#### **2.1.3 Curing Condition**

All samples with adhesive used shall be cured according to 3 kinds of schedule outlined below, results shall be reported respectively: (1) Normal curing schedule: 180 °C, 30 min; (2) Minimum curing schedule: 160 °C for 20 min; (3) Over-baked curing schedule: 200 °C for 40 min.

<b>Total height</b>	= 400 mm	
<b>Flange width</b>	= 17 mm	
<b>Flange distance</b>	= 144 mm	
<b>Thickness</b>	= 0.8 mm	
<b>Spot weld diameter</b>	= 5 mm	
<b>Adhesive thickness</b>	= 0.5 mm	
<b>Material</b>	= DC04 steel	
<b>Impact Speed</b>	= 12 m/s	
<b>Drop mass</b>	= 50 kg	
<b>Solver information</b>	= LS-DYNA: ls971s R5.0, Revision 59419	
	= WINDOWS X64, Single precision (I4R4), 8 CPUs	

**Fig. 1** Axial crush specimen cross-section and parameters

### 2.1.4 Test Method and Apparatus

All the lap shear and T-peel coupon specimens and test procedures are based on ISO 4587 and ASTM D1876. Instron 5569 testing machine was used for all of the quasi-static tests. The Instron 9250 testing machine was used for the impact peel tests which are based on ISO 11343.

## 2.2 Axial Crush Simulation

In order to verify the performance of crash durable adhesive on the axial impact load, the column crush test was designed. Through the CAE analysis, the contribution of crash durable adhesive on different spot weld pitches specimens was analyzed. The cross-section of the specimen is the regular hexagon, as shown in Fig. 1, while the height is 400 mm. The specimen was made of 0.8 mm thick DC04 steel. The drop mass is 50 kg, and the impact velocity was designed to 12 m/s.

The crash durable adhesive bonding only, spot welding only (30 and 60 mm pitch), as well as hybrid bonding (crash durable adhesive with spot weld) were considered in the simulation. LS-DYNA R971 code was used in the simulation. In that code, crash durable adhesive was modeled as 3D solid element which tied to the sheet metal shell element. The stress–strain curves under different strain rates and the corresponding failure parameters are given to simulate the adhesive stress state and the cohesive failure process.

## 2.3 BIW Simulation

One of the body in white (BIW) in research stage was selected to demonstrate the structural bonding advantages in this study. The model is a compact hatchback, and the initial design of the main connection is spot welding. The body stiffness is calculated by MSC.NASTRAN software. In the bending stiffness calculations, the

front and rear shock tower suspension points were fixed, concentrated force  $F$  was applied on the front seat beam position, so that the body is under bending condition. In the post-processing, the maximum deformed node point at the bottom of rocker sill on both sides was monitored. The bending stiffness, in units of N/mm, was given by loading force  $F$  dividing the averaging vertical displacements of these two node points.

For the further optimization, Altair Optistruct solver was employed to set up a topology optimization. The target is to maximize the bending stiffness. Also, according to the actual cost requirement of the OEM, the adhesive length needs to be controlled to about 35 m. The result shows a continuous crash durable adhesive bonding line with different element density, which helps us to identify the key locations for the adhesive contributed to the enhancement of bending stiffness. Based on the result as well as the actual situation of the body shop, the final adhesive bonding line layout was determined. In calculations, the crash durable adhesive was also modeled as 3D solid element with the thickness of 0.3 mm. The adhesive width was based on body flanges' overlap. The adhesive solid elements were linked with sheet metal shell components using rigid body elements. Crash durable adhesive material parameters include the elastic modulus (1,500 MPa), density ( $1.24 \text{ g/cm}^3$ ), and Poisson's ratio (0.45).

## 3 Result and Discussion

### 3.1 Testing Result

#### 3.1.1 Application Test: Sagging and Wash-Off Result

The sagging test results at room temperature and  $170 \text{ }^\circ\text{C}$  were shown in Table 1. The crash durable adhesive D1 shows the best anti-sagging performance at both temperatures. And there is no displacement in the wash-off test either. The structural adhesive H1 performed is not good in these two tests.

#### 3.1.2 Mechanical Behaviour Test Result

Lap Shear strength

In accordance with ISO 4587, the specimens were prepared and subjected into lap shear test. The shear strength of structural adhesive had conducted the following experiment:

1. Room temperature test: curing conditions of  $180 \text{ }^\circ\text{C}$  and 30 min. After curing, the specimens were placed into  $23 \text{ }^\circ\text{C}$  and 50 % humidity conditions for 24 h. The testing shear rate is 10 mm/min;

**Table 1** Application test result

Test result	Displacement (horizontal/vertical) (mm)		
	D1	D2	H1
Adhesive grade			
Sagging (room temperature)	0/0	0/0	5/8
Sagging (170 °C)	0/0	3/3	10/10
Wash-off test (60 °C/30 min)	0	2	5

2. Minimum curing condition: curing conditions of 160 °C and 20 min. After curing, the specimens were placed into 23 °C and 50 % humidity conditions for 24 h. The testing shear rate is 10 mm/min;
3. Over-baked curing condition: curing conditions of 200 °C and 40 min. After curing, the specimens were placed into 23 °C and 50 % humidity conditions for 24 h. The testing shear rate is 10 mm/min;
4. Low temperature test: curing conditions of 180 °C and 30 min. After curing, the specimens were firstly placed into 23 °C and 50 % humidity conditions for 24 h and then placed into -30 °C for 24 h. The testing temperature is -30 °C;
5. High temperature test: curing conditions of 180 °C and 30 min. After curing, the specimens were firstly placed into 23 °C and 50 % humidity conditions for 24 h and then placed into 80 °C for 24 h. The testing temperature is 80 °C;
6. Cyclic corrosion test: Substrate is 0.8 mm steel with anti-rust oil. 1 cycle equals to 4 h salt spray plus 4 h room temperature plus 16 h 40 °C and 100 % humidity conditions;
7. Water immersion test: curing conditions of 180 °C and 30 min. After curing, the specimens were firstly placed into 23 °C and 50 % humidity conditions for 24 h and then placed into 55 °C water for 7 days.

Three samples were tested and the average strength values are recorded into Table 2 for each group testing. The failure mode is described using CF (Cohesive Failure) model. For example, 100 % CF means completely cohesive failure, while 0 % CF means adhesive failure (debonding from metal). The crash durable adhesive of D1 and D2 lap shear tests shows cohesive failure mode. Even under severe corrosion conditions, D1 and D2 also maintained more than 50 % area connecting with the metal. During the cyclic corrosion test and the water immersion test, the steel substrates of some specimens were severe corrosion and could not be put into electrophoresis, so the result table listed as N/A (Not Available). To integrate the lap shear test results can be seen that the adhesive D1 has the best performance.

### T-Peel Strength

In addition to the shear failure, there is another main failure mode for adhesives: peel. Table 3 lists the T-peel test results under the room temperature curing and minimized curing conditions. The test based on ASTM D1876 standard, the each groups used three samples and the average strength values were recorded.

**Table 2** Shear strength test result

No.	Adhesive grade	D1		D2		H1		
		Testing conditions	Shear strength (MPa)	Failure mode (% CF)	Shear strength (MPa)	Failure mode	Shear strength (MPa)	Failure mode
1	Normal test	30.02	100	29.02	100 % CF	22.96	50 % CF	
2	Minimum curing	26.22	100	27.76	100 % CF	22.00	0 % CF	
3	Over-baked curing	25.86	100	29.72	100 % CF	21.95	50 % CF	
4	-30 °C low temperature	38.31	100	43.60	95 % CF	24.81	10 % CF	
5	90 °C high temperature	23.40	100	21.66	85 % CF	17.65	50 % CF	
6	Cyclic corrosion test	0 cycle	19.9 ± 0.4	100	N/A	N/A	N/A	N/A
		60 cycles	15.8 ± 0.5	60	N/A	N/A	N/A	N/A
		90 cycles	14.6 ± 0.8	50	N/A	N/A	N/A	N/A
7	Water immersion test	21.51	50	17.93	50 % CF	N/A	N/A	

**Table 3** T-peel strength test result

No.	Adhesive grade	D1		D2		H1	
		Testing conditions	T-Peel strength (MPa)	Failure mode (% CF)	T-Peel strength (MPa)	Failure mode (% CF)	T-Peel strength (MPa)
1	Normal test	11.01	100	6.11	100	4.95	30
2	Minimum curing	10.01	100	9.34	100	7.70	100

The results showed that the peel strength of crash durable adhesive D1 is higher than others, and its failure modes are full cohesive failure.

### Impact Peel Strength

The impact peel strength can be used for the characterization of vehicle flanges adhesive failure behaviour in the high-speed collision conditions. The test was based on the ISO 11343 standard. Two groups of tests were carried out: room temperature and -30 °C low temperature. The test results are shown in Table 4. Crash durable adhesive D1 and D2 at room and low temperatures can maintain a high impact peel strength (>30 N/mm), while the room temperature impact of structural adhesive H1 is low. And the H1 peel strength at low temperatures is almost zero.

### 3.1.3 Material Physical Parameter Test Result

According to the regular density, viscosity and solid content test method, the physical parameters of crash durable adhesive D1 was given at 23 °C: Density is 1.24 g/ml; Viscosity is 46 Pas; Solid content is 99.3 %.

**Table 4** Impact peel strength test result

No.	Adhesive grade	D1		D2		H1	
		Testing conditions	Impact peel strength (N/mm)	Failure mode (% CF)	Impact peel strength (N/mm)	Failure mode (% CF)	Impact peel strength (N/mm)
1	Normal test	36.0	100	35.0	90	12.5	80
2	-30 °C low temperature	33.6	100	35.3	100	0.4	90

### 3.2 Axial Impact Simulation Result

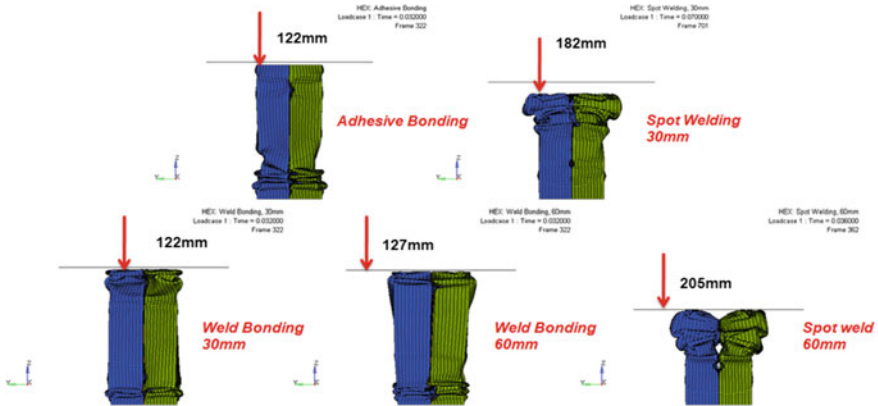
In the simulation of the axial impact test, the material parameters is based on the structure adhesive D1 in above test. Figure 2 shows the final result of the axial impact simulation in the 6 cases: adhesive bonding, spot welding (30 mm pitch), spot welding (60 mm pitch), weld bonding (30 mm pitch), and weld bonding (60 mm pitch). The final height of samples, the maximum and average load and the failure adhesive element numbers were given in Table 5.

As seen in the Fig. 2 and Table 5, the spot welding specimen with 60 mm pitch was the weakest one, and more than half of the height was collapsed, while the spot welding specimen with 30 mm pitch lost about 45 % of the total height. Using crash durable adhesive bonding can effectively increase the specimens' residual height, regardless of the existence of the spot weld. The height loss of the specimen with crash durable adhesive is only about 30 %. The average anti-load capacities of the adhesive bonding specimens are 50 % higher than the spot welding ones.

### 3.3 BIW Bending Stiffness Calculation Result

Table 6 shows the results of the calculation of the bending stiffness of the BIW. Figure 3 shows 2 patterns of the adhesive location diagram. As each car body is unique, it is difficult to identify stiffness contributed locations on a body design only based on experience. The first step to identify the key locations is to model adhesive as more as possible into the compartment component flanges. Approximately 80 m structure adhesive model was built into the original BIW model. At this point, the bending stiffness improvement due to the crash durable adhesive bonding is about 9 %. Secondly, this "full" adhesive model was input into Altair Optistruct software for topology optimization. Based on the output adhesive element density value, the adhesive pattern was adjusted to about 35 m, as shown in Fig. 3b. While the length of the crash durable adhesive is reduced by 56 %, the bending stiffness is still increased by 8.2 %.





**Fig. 2** Axial impact test simulation result

**Table 5** Axial impact test simulation result

No.	Joining type	Final height $H_{res}$ (mm)	Maximum load $F_{max}$ (kN)	Average load $F_{ave}$ (kN)	Failure adhesive element numbers
1	Adhesive bonding	278.00	99.353	29.5	273
2	Spot welding (30 mm pitch)	217.66	100.437	19.8	N/A
3	Weld bonding (30 mm pitch)	277.73	99.353	29.5	264
4	Weld bonding (60 mm pitch)	272.88	99.353	28.3	271
5	Spot welding (60 mm pitch)	194.73	100.438	17.6	N/A

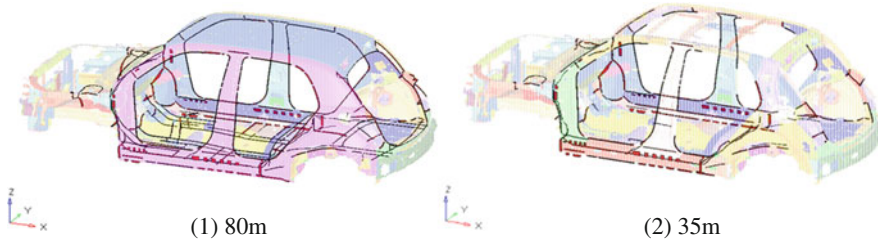
For this car body, the key area to maintain the bending stiffness is A, B-pillar, rocker sill, the cross beam under front windshield and the joining between the rear floor and rear wheel house.

### 4 Conclusion

High and low temperature lap shear test and T-peel test results show that the crash durable adhesive product can fully meet the car body running conditions. Low-temperature shear strength is up to 35 MPa. The axial impact simulation results show the anti-collision ability of the crash durable adhesive is much better than the conventional spot welding design. The CAE analysis verification on one of a Chinese domestic car model shows that the product could increase the BIW bending stiffness up to 8 %.

**Table 6** BIW bending stiffness calculation result

	The original design	Structural bonding design	Optimized structural bonding design
Structural bonding line length (m)	0	80	35
Bending stiffness (N/mm)	10,880	11854.49	11770.73
Improved percentage (%)	0	9.0 %	8.2 %

**Fig. 3** Adhesive pattern diagrams

The axial impact test simulation and CAE analysis on car body can simulate the anti-load capacity of crash durable adhesives, and figure out the effective locations for the product. The crash durable adhesive application in modern car body structure could effectively contribute to improvement of the body stiffness, impact resistance and durability. At the meanwhile, it could help to reduce the concentration force on spot weld. The structural bonding is an alternative to method to spot welding and worth to be promoted as a high efficient connection method in the OEM production line.

## References

1. Goede M, Stehlin M (2009) SuperLIGHT-car project—an integrated research approach for light weight car body innovations. International conference “innovative developments for lightweight vehicle structures”, 26–27 May 2009, Wolfsburg
2. Pfestorf M (2009) Multimaterial light weight design for the body in white of the new BMW7 series. International conference “innovative developments for lightweight vehicle structures”, 26–27 May 2009, Wolfsburg
3. Mlekusch B, Elsasser H (2011) Audi—the new A6, eurocarbody 2011. 13th global car body benchmarking conference, 18–20 Oct 2011, Bad Nauheim

4. Cha S, Seo S, Chang IS (2011) Hyundai—the new i40, eurocarbody 2011. 13th Global car body benchmarking conference, 18–20 Oct 2011, Bad Nauheim
5. Gowland S et al (2009) Jaguar-XJ-production, eurocarbody 2009. 11th Global car body benchmarking conference, 20–22 Oct 2009, Bad Nauheim
6. Symietz D, Lutz A (2007) Structural bonding in automobile manufacturing: properties, applications and performance of a new bonding technique, sv corporate media GmbH
7. Wang D, Yang E, Mansour M (2011) Structural bonding CAE practice on auto-body light weight. 2011 China auto light weighting technology symposium, Sept 2011, Chongqing
8. Cao J et al (2011) Crash-stable adhesive application on body structure connection. The 3rd Chongqing material society symposium, March 2011, Chongqing
9. Yang E (2010) Structural adhesive and auto light weighting. 2010 China auto light weighting technology symposium, Sept 2010, Wuhu

# The Study of Aluminum Alloy Application on Automotive Control Arm

Juanli Ni, Li Li, Qiang Liu, Fuquan Zhao, Yi Xu, Shijie Guo and Bowen Changhai

**Abstract** Taking the control arm of a vehicle of a Chinese domestic brand as a prototype, the material of the control arm was changed from steel to aluminum alloy (6xxx). In this study, by importing the model size and the force parameters, the force distribution of the control arm was analyzed with Finite Element Analysis (FEA) method. The structure of the arm has been optimized. The aluminum alloy control arm has been made finally and the weight has been remarkably reduced by 39 %.

**Keywords** Vehicle · Aluminum alloy · Forging · Control arm · FEA

## 1 Introduction

Nowadays, along with the development of automobile industry, saving energy and reducing gas emissions become the two major objectives. An important measure to save energy and reduce gas emissions is to reduce the weight of automobiles. The tradition steel used in automotive can't meet the requests of reducing the weight of automotive. Recently, there are two research aspects of reducing the weight of automotive. One is to develop a lightweight material with very excellent properties

---

F2012-E07-021

---

J. Ni (✉) · L. Li · Q. Liu · F. Zhao  
Zhejiang Geely Automobile Research Institute CO. LTD, Hangzhou, China  
e-mail: nijuanli@rd.geely.com

Y. Xu · S. Guo · B. Changhai  
Suzhou Nonferrous Metals Research Institute, Suzhou, China

(such as high specific modulus, high specific strength) replacing the tradition steel. Another one is to design a new lightweight structure replacing the original structure by improving and optimizing the material structure. Sang et al. [1] had analyzed the front control arm by using ABAQUS. Meanwhile, they point out a method to make lightweight control arm in order to improving capability of the bear weight and reducing the structure's weight. Wang et al. [2] analyzed and designed the control arm of one car in order to improve the structure stability and reduce the weight of the control arm. Zhang [3] had improved the structure of control arm by topology and analyzed the stiffness and the strength in order to design lightweight control arm. Dong-Chan Lee et al. [4] also improved the structure of the arm by using topology and analyzed the structure by FEA. They put forward lightweight structure of control arm made by aluminum alloy. This structure has been used in the car for years. Song et al. [5] also designed a lightweight structure of a car by using structure optimization technics and the theory of Kriging.

There are many researches on optimizing the structure but still seldom researches which combine materials and structure. Given the requirements of fatigue strength and stiffness of the control arm, aluminum alloy is the most ideal materials which can be made into control arm. It has many merits, such as lower density ( $2.7 \text{ g/cm}^3$ ), higher specific strength, higher corrosion resistance, good thermal stability, easy shaping, and recoverability, etc. This paper could mainly discuss the properties of the aluminum alloy (6xxx) developed by Chinese Aluminum Company. The structure of control arm was analyzed by Finite Element Analysis (FEA). Based on the above, the remarkable lightweight control arm was made by aluminum forging.

## 2 Materials

Figure 1 shows the contrast of the mechanical properties of several different aluminum alloys (6061 and 6082 are very familiar materials which are used very abroad. KS651 and KD610 are two merit materials which are developed by KOBELCO.), apparently, the tensile strength, yield strength and elongation of 6XXX are higher than others.

Figure 2 shows the two different forging technic of aluminum alloy control arm. Contrasting traditional technic, the new technic can improve the rate of finished product by 15–20 % and dispense with the processes of bending, extending, additional heating and forging. It is a merit technic which can reduce the cost and meet the respect of environment. However, the size and the shape of the roughcast were fixed. So the new technic just can produce the products which have fixed size and shape. In this point, the new technics was not more flexible than the traditional technic.

The forging part was cut into pieces to sampling. Then every piece was observed at low magnification. Figure 3 shows the method to cut into pieces to sampling. Figure 4 shows morphology of the forging sample at low magnification.

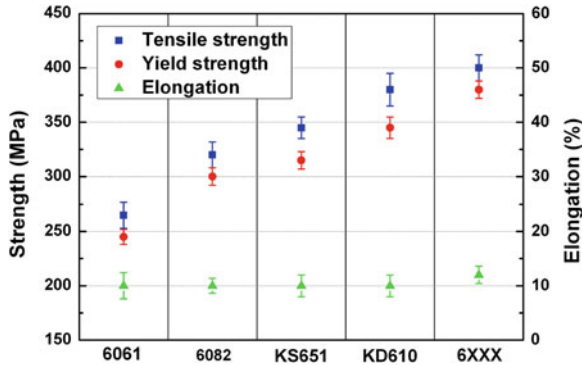


Fig. 1 Contrast of the mechanical properties of several different aluminum alloys, apparently, the tensile strength, yield strength and elongation of 6XXX are higher than others

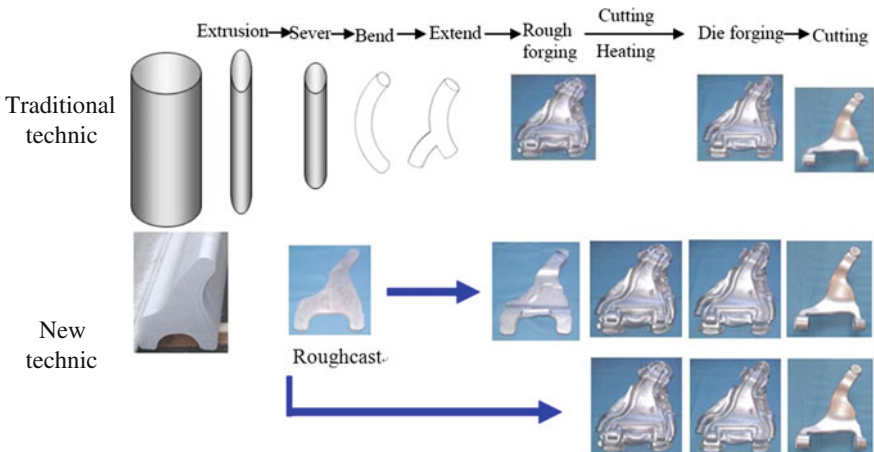


Fig. 2 Contrast of two different forging technics

Figure 5 shows the forging sample areas which were observed by EBSD and Fig. 6 shows the pictures of EBSD morphology of the forging sample. The pictures a–d of Fig. 6 are corresponding with the areas showed in Fig. 5. Both Figs. 4 and 6 show that there is no very big grain which could infect the properties of forging part.

### 3 Structure Design

Figure 7 shows the three-dimensional model of the control arm of one Chinese car. It was made of stamping steel plate joined by welding. The steel plate was made by Baoshan steel company. The steel was B380CL which has merit cold forming

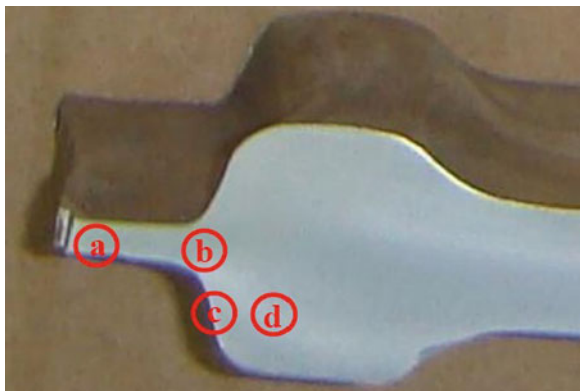
**Fig. 3** The method to cut into pieces to sampling

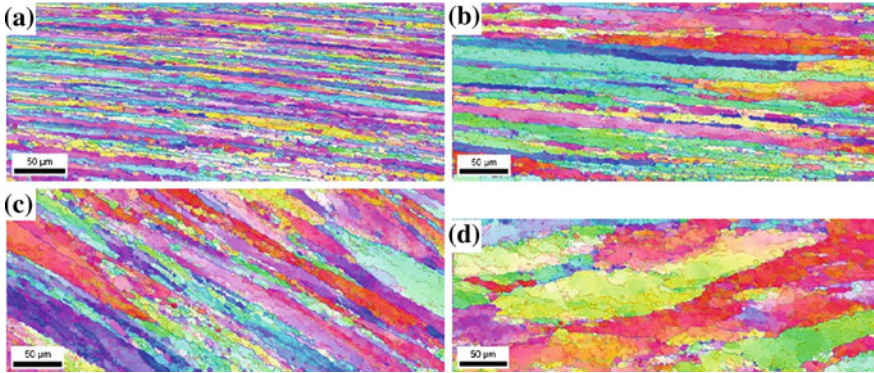


**Fig. 4** Morphology of the forging sample at low magnification



**Fig. 5** Morphology of the forging sample at high magnification





**Fig. 6** EBSD morphology of the forging sample

**Fig. 7** The three-dimensional model of the steel control arm



property ( $s_{0.2} \geq 260$ ,  $s_b \geq 380$  MPa). The main body colored blue is the part need to be made by aluminum alloy instead of steel plate. The main technical requests were as followings:

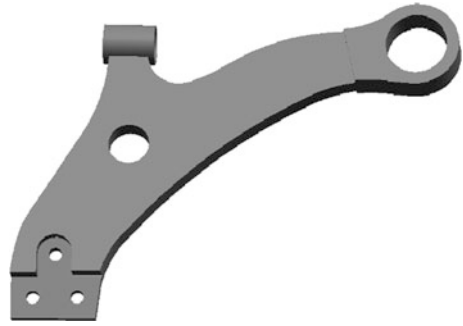
1. The size precision should be made sure.
2. The extruding strength of both front and rear linings should not smaller than the setting value.
3. The corrosion time should meet with the design time.
4. The structure strength should meet the requests of every condition the control arm worked.

The control arm was analyzed when it worked in seven familiar conditions by using ANSYS. In the FEA model, the Young’s modulus of aluminum alloy was 70 GPa. The Poisson ratio was 0.33. The density was  $2,700 \text{ kg/m}^3$ . The model was meshed by tetrahedron cell with node in the middle in order to enhance simulation precision.

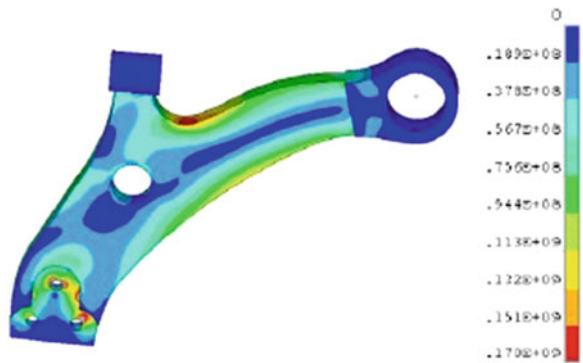
The forging part was designed based on the three-dimensional model of the control arm and it kept the size of the original part and avoided the effects of other parts. The forging part is showed in Fig. 8. The part made based the model showed



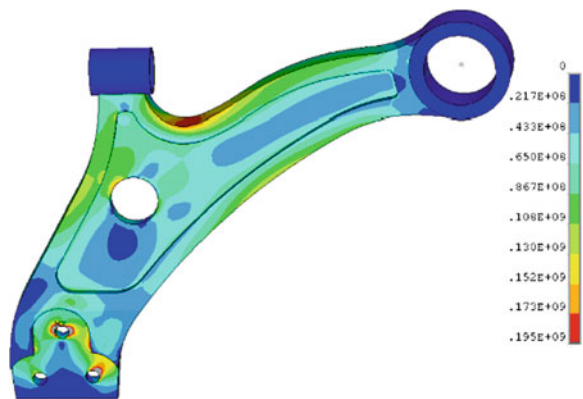
**Fig. 8** The three-dimensional model of the aluminum alloy control arm



**Fig.. 9** The condition of getting across the road with holes



**Fig.. 10** The condition of getting across the road with holes for the arm whose structure was optimized



in Fig. 8 had bear the highest force when it was simulated on the condition of getting across the road with holes as showed in Fig. 9. In this condition, the part has born the highest force and this condition is the worst condition the control arm worked. The fringe of this arm is the main area which bears the most. By contrast, the middle bears least. Given this, the shape of the arm was optimized. The fringe had been thickened and the middle had been thinned. The worst condition of the improved arm had been analyzed, as showed in Fig. 10.

**Fig. 11** The control arm made by aluminum alloy and steel respectively



Figure 10 shows that the most born of the optimized arm is 195 MPa which can meet with the properties of aluminum alloy 6xxx with high yield strength (380 MPa). The safety coefficient is up to 1.94.

Considering the requirements of the forging technics, the control arm has been made by aluminum alloy based on the optimized model, showed as Fig. 11. The weight of stamping steel arm is 2.8 kg. The weight of aluminum forging arm is 1.7 kg. By contrast, the weight of the arm has been remarkably reduced by 40 %.

## 4 Conclusion

After the testing of materials and analyzing by FEA, the aluminum alloy arm has been made. The main results are as follows:

1. The aluminum alloy (6xxx) developed by Chinese Aluminum company has very merit properties than others, like 6061, 6082, KS651, KD610.
2. There is no very big grain which could infect the properties of forging part made by 6xxx.
3. The weight of the aluminum alloy arm compared with the steel one can remarkably reducing by 39 %.

**Acknowledgments** This work was financially supported by the Supporting Program of the “twelfth Five-year Plan” for Sci & Tech Research of China [2011BAG03B00]. The authors would like to thank Aluminum Corporation of China for their support on this item.

## References

1. Sang N, Bai Y et al (2010) Lightweight design for front-swing arm of an automobile base on ABAQUS. *J Changchun Inst Technol* 2(11):79–82
2. Wang FJ, Fu YF et al (2009) A research on lightweight design for the lower-arm of suspension based on reliability theory. *Automot Eng* 11(31):1070–1073

3. Zhang ZL (2010) Lightweight design for front-swing arm of an automobile. *Beijing Automot Eng* (2):28–31
4. Lee DC, Lee JI (2003) Structural optimization concept for the design of an aluminum control arm. *Automobile Eng* (217):647–656
5. Song BC, Park YC, Kang SW, Lee KH (2009) Structural optimization of an upper control arm, considering the strength. *Automobile Eng* (223):727–735

# Using Shape Memory Alloys in Automotive Safety Systems

Viorel Gheorghita, Paul Gümpel, Joachim Strittmatter,  
Chiru Anghel, Thomas Heitz and Mathias Senn

**Abstract** In modern automobiles a lot of actuators are used to run safety systems. Nowadays these are mechanical, electromechanical, pneumatic, pyrotechnic or electromagnetic actuators. For releasing them electrical or mechanical energy is used. This paper presents a new class of actuators in safety systems using shape memory wires. They are able to replace the conventional actuators. The goal for this research work is to use shape memory elements in a clamping system of a steering column as well in safety as in comfort area. The shape memory elements control the opening and closing function that presses with maximum 5,000 N against the steering jacket. For the first prototype, called drum type, shape memory wires are used to open the system and disc springs are used for closing. The second prototype is a so-called lateral actuator, where shape memory elements are used for the opening and closing function. Tests with the drum prototype are carried out with up to 16 wires up to date. Each wire is preloaded with 50 N that corresponds to a compression of the disc springs of 800 N. When the wires are electrically activated they contract the disc springs until 1,200 N over a stroke of 1 mm. In this configuration an electrical power of 16 V and 56 A is used. The second prototype

---

F2012-E07-023

---

V. Gheorghita (✉) · P. Gümpel · J. Strittmatter  
University of Applied Sciences Konstanz, Konstanz, Germany  
e-mail: vgheorgh@htwg-konstanz.de

P. Gümpel · J. Strittmatter  
WITg Institut für Werkstoffsystemtechnik Thurgau an der Hochschule Konstanz,  
Thurgau, Switzerland

T. Heitz · M. Senn  
ThyssenKrupp Presta, Eschen, Liechtenstein

V. Gheorghita · C. Anghel  
University Transilvania, Brasov, Romania

is designed with four wires of 0.5 mm diameter for closing and two wires for opening the clamping system. To open the clamping system in less than one second an electrical power of 7 A and 12 V is necessary, while 14 A and 12 V is needed to close it within 1.5 s. At the moment the application of the first prototype is restrained through an energy limitation, because the battery of modern automobiles would not be sufficiently adequate. Anyway, in the near future more electrical cars will be on the market and therefore this prototype can successfully be implemented. One of the advantages using shape memory alloys in the design of a steering column is its lightweight. Moreover it is possible to control the energy in any time because of the electrical activation and the control of the electrical resistance of the shape memory actuators. Thereby this actuator can be activated and the steering column can even be released in special crash situations in order to create enough space for the airbag and to avoid a possible touch of the body of the driver with the steering wheel.

**Keywords** Automotive · Safety systems · Steering column · Shape memory alloy

## 1 Introduction

In spite of the increasing number of cars the number of injured or killed persons is constantly decreasing. This fact is a consequence of the increasing number of automotive safety devices and systems. The new cars have currently three types of safety systems: passive, pre-crash and active. In these safety systems shape memory alloys can act as actuators which even can respond in milliseconds. When these materials are heated the martensitic structure is changed into austenitic structure. During this phase transformation a shape memory actuator is able to contract, to bend or to rotate. The use of shape memory alloys as actuator material has some main advantages: they are smaller and easy to activate with the electrical source and therefore their use often reduces the complexity of the systems. Thereby weight and size of these systems also can be reduced.

### 1.1 Statistics in Europe About Accidents

During the time period of April 2012, the police recorded 249 deaths in road traffic in Germany; compared to the same month from last year, this number decreases with 27.2 %. The number of the injured persons also decreased with 18.3 % [1]. During the time period of 1990–2010 in Europe the number of injured persons in automotive accidents declined in the range of 8 % within this period to the total number of 242,700. In contrast in December 2010 the number of accidents without killed persons increased with 19 % to 247,800. The fatalities number decreased with 37 % and the injuries also decreased with 17 % comparable with December

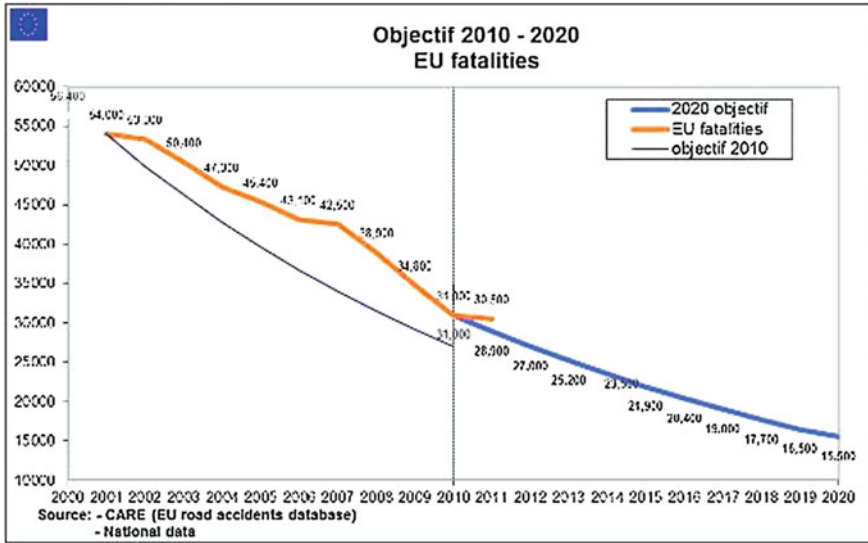


Fig. 1 Evolution of fatalities in Europe [2]

2009. As we can see in the Fig. 1 the objective for 2020 is to reduce the fatalities [2]. In parallel with them it will be reduced the number of injured persons and accidents.

In that idea EU-government searches solutions to reduce the number of accidents, deaths and injuries. The objective for 2010 was to save 25,000 lives. That means each part of a car which is used for the safety system should always be optimized. If you can anticipate the accident and if the safety systems are ready to act, you can better protect the occupant.

### 1.2 Statistics in China About Accidents

As a result of these dynamic changes in the economy, road transport infrastructure development and motorization, road traffic accidents have become a more severe problem in China. According to the annual report of the China Road Traffic Accident Statistics, the number of people who died from road traffic accidents in 2005 was 98,738, with the number of injured five times higher, and is believed to be underestimated in rural areas in China. This fatality number is about 20 % of the total traffic fatalities in the whole world each year, and the number of fatalities is expected to be even worse due to the rapidly increasing number of vehicles and novice drivers [3].

Conclusions of this statistics are that the safety systems should be updated continuously. The automotive industry should always search new device, new materiel which can perform this systems and protect better the driver.

## **2 Short Introduction About SMA**

Shape memory alloys (SMA, smart metal, memory metal, memory alloy, muscle wire, smart alloy) are alloys that “remember” their original, cold-forged shape by returning to the pre-deformed shape by heating. This material is a lightweight, solid-state alternative to conventional actuators such as hydraulic, pneumatic, and motor-based systems. Shape memory alloys are finding applications in industries including medical and aerospace [4].

In the automotive industry they can replace electrical, thermal, hydraulic and magnetic actuators from different systems, like safety systems, clutch drive, folding and setting mirror, and others by showing additional advantages (Fig. 2).

## **3 Application of SMA in Steering Columns**

### ***3.1 Introduction to the Safety Steering Column***

The main function of a steering column is to transfer the torque applied to the steering wheel by the driver via the steering shaft to the steering gear. Another important function is for crash safety. The steering column can collapse and absorb energy during the crash phase. Therefor is a crash element as well as a clamping system (3) required. The clamping system is holding the steering wheel for a reach and rake adjustable steering column in position with a clamping force between 3,000–5,000 N—depending on the steering column design respectively system. The clamping system can be opened manually by the lever. But the lever has a big disadvantage because its position could damage the knee during the crash. There is only one crash force set up due to the manually clamping system. That also can cover more or less only one specific crash situation. All the other crash situations at e.g. different speeds, different drivers weight are compromises [5].

This leads now to two important reasons to implement SMA system into the clamping systems of Steering Columns:

1. Removing the lever can reduce knee accidents.
2. Adjustable clamping force can lead to many different crash absorbing forces

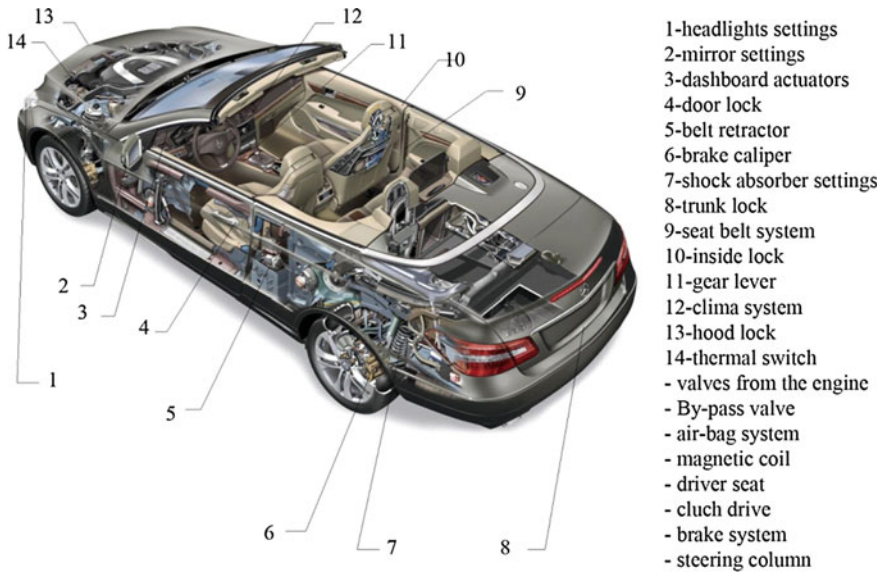


Fig. 2 Possibilities to use SMA in automotive systems [6]

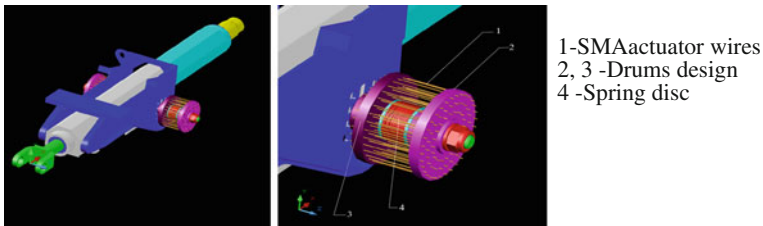


Fig. 3 Drum prototype

### 3.2 Drum Prototype

The task of this application is to open the clamping system in less than 1 s. Actuator wires are used which can react in 1 s at 3,000–5,000 N. In order to guarantee 5,000 cycles the chosen NiTi wires are loaded with 400 N/mm<sup>2</sup>. The NiTi wires have an As-temperature higher than 80 °C and a diameter of 0.40 mm. Was tested also wires with diameter 0.44 and 0.5 mm (Fig. 3).

$$\text{Power for one wire : } F_w = \sigma \cdot A = 400 \cdot \frac{\pi \cdot 0.4^2}{4} = 50.26 \text{ N} \tag{1}$$

$$\text{Maximum number of the wires : } n = \frac{F_t}{F_w} = \frac{5,000}{50.26} = 99.48 \tag{2}$$



Between the drums the disc spring is contracted at 5,000 N. The two drums are made from a special isolating material. SMA actuator wires are attached between the drums. By applying the system with electrical energy (e.g.: by pushing a button from the steering wheel), SMA wires (1) are contracted and the drum (3) will be pulled towards drum (2) and thereby the spring will be compressed.

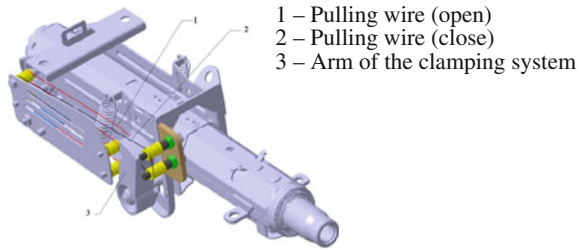
The bracket part (blue one) will be free and the driver can adjust the position of the steering wheel (steering column). During the whole adjusting process the energy for the SMA wires is controlled; otherwise the wires would be overheated. In order to contract within 1 s the SMA wires need a lot of energy. When the electrical source is off the actuator wires will cool down, change into its martensitic phase and reset the whole system into the first position, because the disc spring will push drum (3) and also part of the bracket. In this case the steering column will be blocked in the desired position. So the clamping system is opened (or activated) with SMA actuator, this means with electrical energy, and is closed with disc springs, that means with mechanical energy.

The last test was made for 16 wires; each wire should develop a force higher than 50 N. In this case the disc springs are pretensioned at 800 N. After activation the final force is 1,200 N. The tests are made to 16 V electrical tension and 56 A, current intensity. To get this mechanical output (force, displacement vs. time) at least 3.5 A/wire is necessary. For 100 wires (see formula 2), 350 A it will be necessary. In this moment the electric battery of the cars are limited and the drum prototype could be assembled in this design. The next approach is to reduce the electrical energy by using fewer wires.

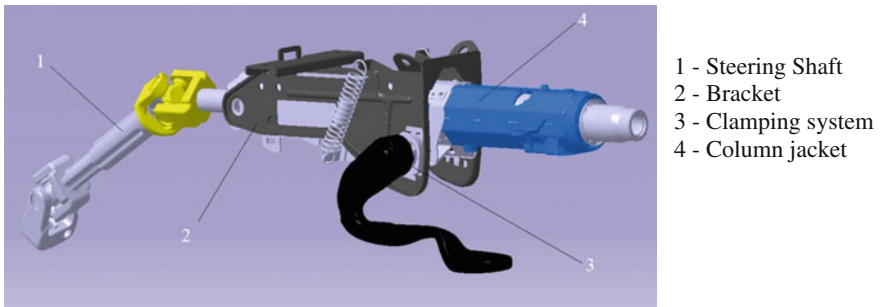
### ***3.3 Lateral Actuator***

The reaction of each safety system depends on the speed of the vehicle. So the new concept should allow activation times much faster than 1 s. The steering wheel incorporates the airbag system. So the reaction time of the airbag system is of importance for the new concept of the safety steering column. The activation of general airbag system takes place within maximum 60 ms. As a consequence the new concept of the clamping system also should be able to react within 60 ms in order to control the steering column during an accident. By means of this the airbag function could be considerably improved in order to react in the most appropriate way referred to the accident condition. But in a first step our group is focused on the mentioned reaction time of about 1 s in order to use the safety steering column for a comfortable adjustment of the steering column.

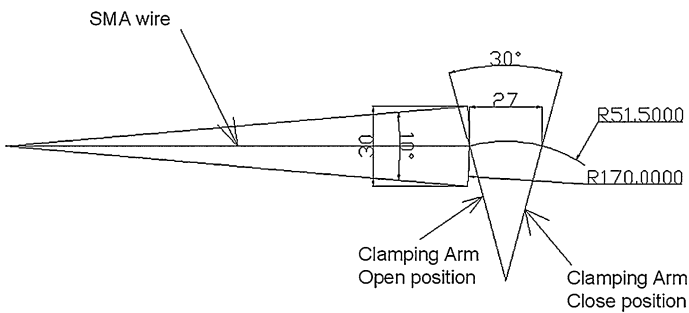
In this case we propose a second system which can open and close the steering column clamping at maximum 5,000 N ( $F_t$ ) over 5,000 cycles within 1 s. In cooperation with the industrial partner 3D models are designed in the Material Testing Laboratory of the HTWG Konstanz and are shown in the next pictures (Fig. 4).



**Fig. 4** Lateral wire actuator



**Fig. 5** Steering Column with steering shaft [5]



**Fig. 6** Arm cinematic

The bracket part (grey one from Fig. 5) was applied with a force of 5,000 N from the clamping system. In that second prototype the releasing arm of the steering column is slightly modified and SMA actuators wires are fixed directly to the arm of the clamping system.

In this case SMA wires are used to open and also to close the clamping system. Electrical energy is used instead of manual energy. The system is more comfortable by pressing a button and then adjusting the steering column. When the

source is “on” because of the activation of the button the wire (1—red one) pulls the arm until the clamping system will be opened. And when the button is released (“off”) a microcontroller will send electrical energy to the other wire (2—black one) in order to pull the arm into the other direction. In that way the clamping system is closed again. Electrical energy is used to open and close the clamping system (Fig. 6).

Open-close position is  $30^\circ$ ,  $\sim 27$  mm. The clamping system is closed by 8 Nm ( $M_t$ ) torque (this value is given by the manufacturer and was verified in own tests).

Calculation for the SMA wires force:

$$M_t = F_w \cdot b \implies 8 = F_w \cdot 0.0515 \implies F_w = 155 \text{ N} \quad (3)$$

The wire is able to contract in the range of 3–5 %, but only 3.5 % contraction is used in order to fulfill the requirements concerning the required life time cycles.

$$\text{Length of the wire: } \frac{3.5}{100} \cdot L = 27 \implies L = 771.5 \text{ mm} \quad (4)$$

Because of this calculated wire lengths, they are conducted over different deflection pulleys (yellow). NiTi alloys with a diameter of 0.44 mm was used for these prototypes. In order to contract within 1 s the wire needs a considerable amount of energy. Last tests are made with 0.5 mm wires; two wires for opening and four wires for closing the system. Active length of the wires is 650 mm. In this configuration an electrical current of 3.5 A is used for each wire.

While in the first prototype electrical energy is only used to open the system, in the second prototype electrical energy is used for both actuations: to open and close the clamping system.

## 4 Conclusions

The main idea for this new system is to use SMA for comfort reasons to remove the lever of the clamping system and at the same time it could be used as a new crash safety system for steering columns. A further positive effect of removing the lever is that the possibility of knee injury is reduced. It is known the term “in position” and “out of position” for the head of driver and body in the crash phase. In this sense, the presented system could reduce the clamping force of the clamping system during a crash in order to find the best position of the drivers head “in position” (optimal position). Optimal position for head is to contact the airbag in the middle of the bag. In accordance with European and Asian regulations to reduce the injury of the driver, this system (lateral actuator) can be used in the passive safety system of the cars.

The present results show that the shape memory alloys can do a good job in this new automotive safety system.

Some advantages using SMA are:

- Reduction of the manual force—it is comfortable, in this case the driver can always be careful at the traffic
- Avoidance of noise in car
- Miniaturization of the system compared to systems using classic actuators
- Control of the contraction of the wires in every moment and therefore information concerning the status of the clamping mechanism.

## References

1. [http://www.dvr.de/site.aspx?url=html/betriebe\\_bg/daten/unfallstatistiken144.htm](http://www.dvr.de/site.aspx?url=html/betriebe_bg/daten/unfallstatistiken144.htm). Accessed on 13 July 2012
2. [http://ec.europa.eu/transport/road\\_safety/specialist/statistics/trends/index\\_en.htm](http://ec.europa.eu/transport/road_safety/specialist/statistics/trends/index_en.htm). Accessed on 13 July 2012
3. Zhao S (2009) Road traffic accidents in china. IATSS Res 33(2):125–127
4. Gumpel P et al (2004) Formgedächtnislegierungen. Expert verlag, Renningen, p 146, ISBN 3-8169-2293-7
5. Heitz T (2010) Analysis of using CFK-material for steering column components in passenger vehicles. Brasov, CONAT, pp 245–253
6. [http://mercedes-benz-blog.blogspot.de/2010/03/new-mercedes-benz-e-class-cabriolet\\_6980.html](http://mercedes-benz-blog.blogspot.de/2010/03/new-mercedes-benz-e-class-cabriolet_6980.html). Accessed on 13 July 2012

# Study on Electro Rheological Fluid Shock Damper and Adjustable Damping Performance

Jianhua Wang, Fei Xie, Yuncheng Wang and Chunbao Guo

**Abstract** The electro rheological (ER) technology is an advanced study with so much superior advantages and applications that it has been given much attention to automotive research and application field. The paper analysed the structure ERF shock damper and the working principles, through which the methods of adjusting ERF shock damper working characteristic can be obtained. The relationship between electric field and resistance force of ERF shock absorber were described and the mathematical model was established based on MATLAB/Simulink and some important factors of ERF shock damper are discussed. Through simulation analysis, it was proved that the structure of ERF shock damper is reasonable and feasible which can produce continuous and controllable damping force which could improve vehicle ride comfort and driving stability.

**Keywords** ER technology · ERF · ERF shock damper · Damping force · Mathematical model

## 1 Introduction

Electro rheological technology is a scientific practice by successfully applying electro rheological phenomenon or effect to engineering field. It's a new technology that applies electric field to control the material of the rheological properties [1].

---

F2012-E07-024

---

J. Wang (✉) · F. Xie · Y. Wang · C. Guo  
State Key Laboratory of Automotive Simulation and Control, Jilin University,  
Changchun, China  
e-mail: xiefei620@126.com

The electro rheological effect is that, under applied electric field, the flow rheological properties of electro rheological fluids such as viscosity increases several orders of magnitude more than without electric field, and has obvious yield stress which can change reversibly and be controlled continuously and steplessly. This change can make flowing liquid thickened and even be turned into the matter of solid state in comparison to solid state. This material can keep the shape and apparent shear yield stress, and when electric field disappears, the electro rheological fluids immediately become loose and restore the original liquid state [2].

The electro rheological effect has many superior performance characteristics, such as reversible, controllable, low energy consumption, etc. These superior performances make the electro rheological materials have wide applications and great potential economic and social benefits, and can be widely used in automotive engineering, hydraulic engineering, aviation and navigation, production automation and other industrial and technical areas.

Shock damper is the damping component of automotive suspension system, of which the performance influences directly on the dynamic load of wheels, suspension dynamic displacement and the comfortability of vehicle. ERF shock damper is a kind of active shock absorber controlled by control signals; its advantages are that adjusting range is extensive and responding fast, simple structure, easy to realize computer control and antivibration and denoiser. Therefore, it has been attached more and more attentions by mechanical and electronic industry and automobile industry. With the development of electro rheological technology, ERF shock damper is considered to be a kind of new shock absorber of high performance and will get more and more wide applications.

## 2 Modelling and Structural Analysis of ERF Shock Damper

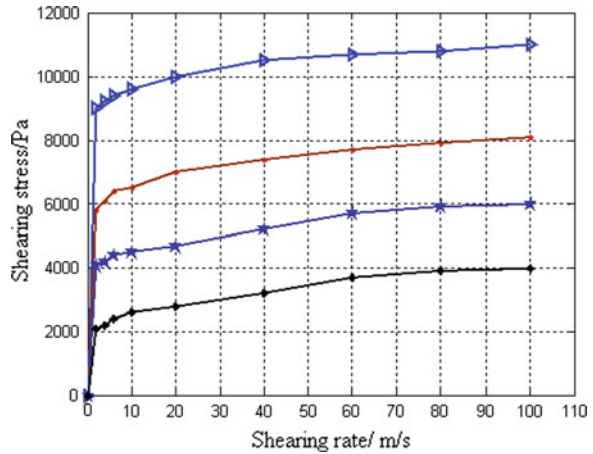
### 2.1 Analysis of ERF Mechanical Properties

The mechanics performance of electro rheological fluids is complex. For most of electro rheological fluids, when under no applied electric field and in low concentration, the electro rheological fluids is basically a Newton fluid which presents a Newton fluid characteristics that in flowing state the shearing stress is proportional to the shearing rate. When under applied electric field, the electro rheological fluids changes into visco-plastic body.

In order to study the relationship between stress and strain velocity, the mechanical properties of electro rheological fluids is necessarily to be described. It's generally considered that the constitutive equation of electro rheological fluids is in accordance with Bingham model [3]:

$$\tau = \tau_B + \eta_B \dot{\zeta} \quad (1)$$

**Fig. 1** Graph of shearing stress with shearing rate of ERF



Where,  $\tau$  is shearing stress of electro rheological fluids;  $\tau_B$  is yield stress of electro rheological fluids;  $\eta_B$  is apparent viscosity of electro rheological fluids under electric field;  $\zeta$  is shearing rate of electro rheological fluids.

Figure 1 shows the relationship between shearing stress and shearing rate of electro rheological fluids.

From Fig. 1 it can be seen that under the applied electric field, the electro rheological fluid presents as Bingham flow characteristics that with the increment of shearing rate, the shearing stress of electro rheological fluids trends to increase but variation becomes smaller, and under the same condition the shear stress is similar to the values without electric field. Thus, under the same applied electric field condition, along with the increment of shearing rate, the viscosity of the electro rheological fluid basically remains unchanged.

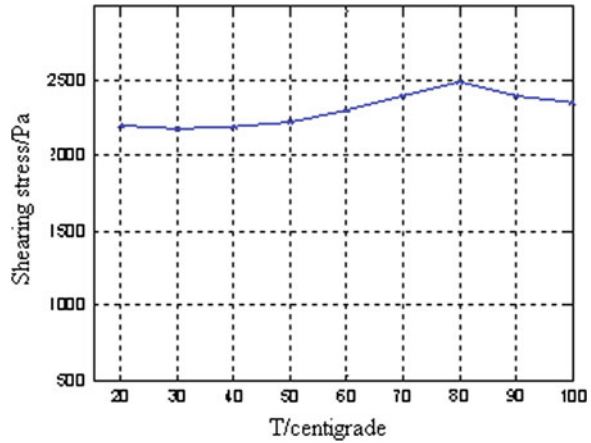
Figure 2 shows the relationship between shearing stress and temperature of electro rheological fluids.

From Fig. 2 it can be seen that the temperature of the electro rheological fluid reaches to 80 °C, the shearing stress becomes the maximum. When other conditions are the same and within the certain temperature range, the shearing stress of electro rheological fluid increases along with the rise of temperature. When the temperature exceeds this range, the shearing stress reduces slowly but still has good mechanical properties.

## 2.2 Modelling of ERF Shock Damper

As a kind of damping device of vibration system, shock damper has the characteristics of vibration energy consumption in vibration process as soon as possible to make vibration decay. Electro rheological fluid shock damper is a device that changes the electricity energy into mechanical energy with the same basic working

**Fig. 2** Graph of shearing stress with temperature of ERF



principle to the traditional liquid shock absorber; both the two kinds of shock damper are utilizing the damp force which produced by fluid flowing through some gaps to make the vibration reduced. The difference in comparison to the traditional shock damper, the electro rheological fluid shock absorber can realize the stepless adjustment of damping force through the electro rheological effect. According to the types of energy conversion devices, ERF shock damper can be divided into three types of working pattern: shear type, fluid type and extrusion type.

Based on the consideration of the three patterns, this paper decides to use the ring channel fluid type as the electro rheological fluid shock damper working mode.

Under the applied electric field, the electro rheological fluid performance presents characteristics of Bingham fluid and its constitutive relationship be described as follows [4]:

$$\begin{cases} \tau = \tau_B \text{sgn}\left(\frac{du}{dr}\right) + \eta \frac{du}{dr} & (\tau > \tau_B) \\ \frac{du}{dr} = 0 & (\tau \leq \tau_B) \end{cases} \quad (2)$$

Where,  $\tau$  is shearing stress of electro rheological fluid;  $\tau_B$  is the critical value in relation to applied electric field.

The shearing stress of ERF has linear distribution along the damping clearance, the maximum shearing stress electro rheological fluid appears close to the working chamber and piston, and the minimum shearing stress appears in the middle of symmetry plane. When the shearing stress produced by pressure difference between the two sides of damping channel, is smaller than the critical yield shearing stress which is close to the working chamber and piston, the electro rheological fluid stay motionless; When the former is bigger than the latter, the electro rheological fluid starts to flow which is close to the plate, but the electro rheological fluid in the middle of the symmetry plane changes into solid state and



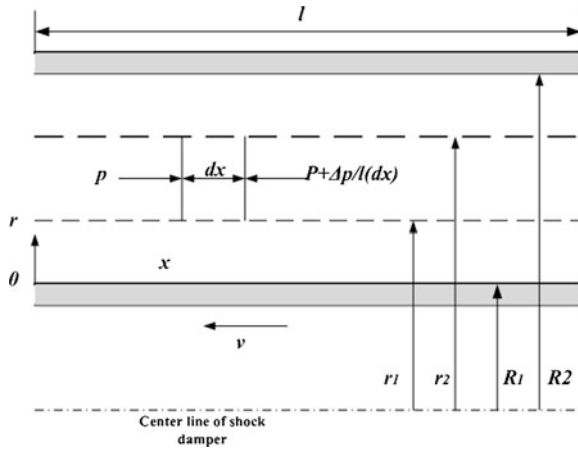


Fig. 3 Mechanical diagram of ERF element in ring form

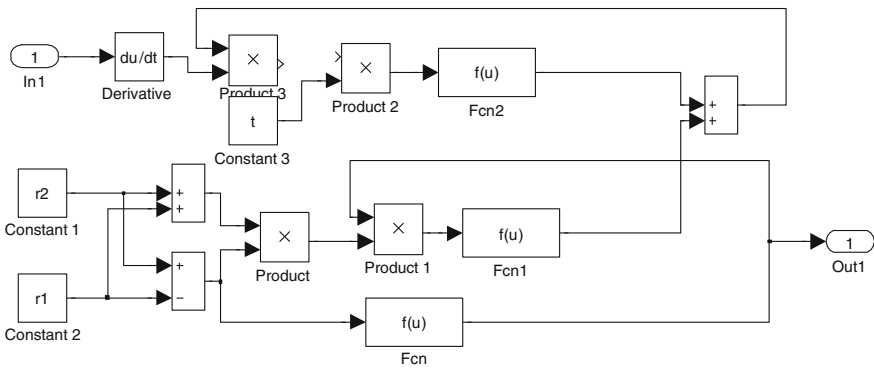


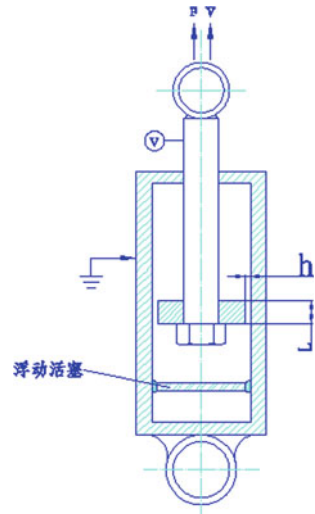
Fig. 4 Mathematical model of ERF shock damper based on MATLAB

produce a rigid flow area [5]. Figure 3 shows the mechanical diagram of ERF element in the ring form.

From the above analysis, we can conclude that for the electro rheological fluid of rigid flow area, the following ERF shock damper mathematical model is set up to [6] (Fig. 4):

$$\begin{cases} \pi(r_2^2 - r_1^2) \frac{\Delta p}{l} dx + 2\pi r_2 \tau_B dx + 2\pi r_1 \tau_B dx = 0 \\ r_2 - r_1 = \frac{2\tau_B}{\Delta p} \end{cases} \quad (3)$$

**Fig. 5** Structure of ERF shock damper



### 2.3 Structural Analysis of ERF Shock Damper

As the shock absorber displacement of car suspension is long, and in aspects of structure size and structure intensity it has strict demands, so its electro rheological fluid shock damper cannot be designed for the extrusion type. The piston of electro rheological fluid shock damper is on straight-line movement back and forth in cylinder, using the applied electric field to control the electro rheological fluid flow characteristics to change damping force which can change the pressure difference between the upper and lower chamber, so the damping force can be regulated continuously (Fig. 5).

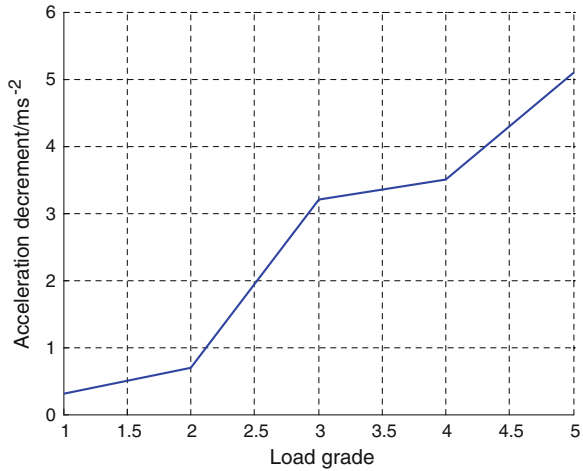
Generally speaking, the structure of electro rheological fluid shock damper demands compact size, small number of parts, low cost of manufacturing, also manufacturing process and assembly process are as simple as possible. And at the same time that the installation dimensions of electro rheological fluid shock damper and the structural strength also should be considered.

## 3 Performance Analysis of ERF Shock Damper

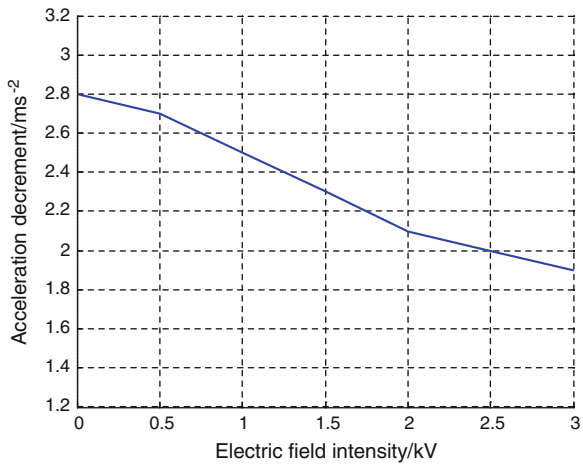
On the basis of established the model and designed structure of electro rheological fluid shock damper, this paper chose some typical factors which has great impact on the performance of ERF shock damper, such as applied load, applied electric field strength and motivating frequency, to run simulation and validate the adjustable damping performance of ERF shock damper.

Figure 6 shows the relationship between applied load and damping performance. Figure 7 shows the relationship between applied electric field strength and

**Fig. 6** Diagram of impact of load grade on acceleration decrement



**Fig. 7** Diagram of impact of electric field intensity on acceleration decrement

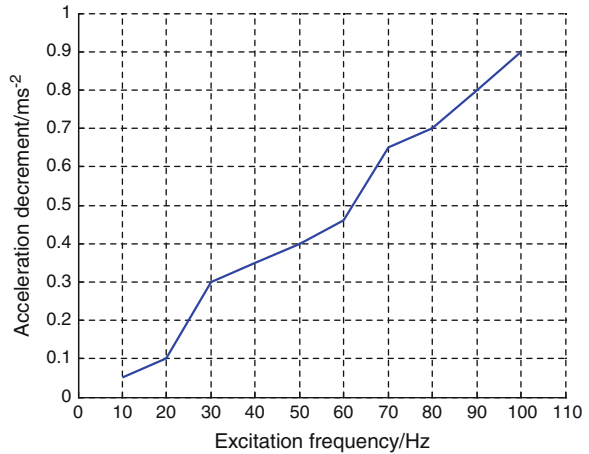


damping performance. Figure 8 shows the relationship motivating frequency between damping performance.

### 4 Conclusion

The paper analysed the typical structure of ERF shock damper and its working principle, through which the methods of adjusting ERF shock damper working characteristic can be obtained. The relationship between applied electric field strength and damping force of ERF shock damper were described and the mathematical model was established based on MATLAB and some important factors of

**Fig. 8** Diagram of impact of excitation frequency on acceleration decrement



ERF damper were discussed. Through simulation analysis, it was proved that the applied structure of ERF shock damper is reasonable and feasible which can produce continuous and controllable damping forces which could improve vehicle ride comfort and driving stability.

## References

1. Zhu H (2010) Automobile shock absorber based on electro-rheological technology. *Tractor Farm Transporter* 37(1):10–11
2. Wang G, Li D (2011) Study on electro rheological fluid (ERF) shock absorber. *Technol Dev Enterp* 30(13):77–78
3. Chenguan W (2000) *Electro rheological technology—theory, material, engineering, applications*. Beijing institute of technology press
4. Tian W, Gao J, Zou Y, Zhang M (2010) Simulation and Analysis of ER damper. *Mach Building Autom* 4:106–109
5. Shen C (2008) The application of electro-rheological fluids to shock absorber of vehicle. *Agric Equipment Veh Eng* 2:26–28
6. Xiao G (2007) Shock absorber using electro-rheological technology. *J Shandong Univ Techn (Nat Sci Ed)* 6:53–55

# Cyclic Tension–Compression Test of Mg Alloy Sheet at the Elevated Temperature

Oh Suk Seo, Heon Young Kim, Myoung-Gyu Lee, Ji Hoon Kim  
and Dae Yong Kim

**Abstract** Recently, lightweight material has been widely used in the field of automotive and electronic industries. However, some difficulties exist in characterizing the material, poor formability and abnormal stress–strain behaviour such as Mg alloy sheet. In this paper, a new cyclic tension–compression test machine, which can measure the stress–strain curves of thin sheet metals under non-monotonous condition such as tension/compression or compression/tension, was developed. And the evaluations were performed with a newly designed cyclic tension–compression test machine.

**Keywords** Lightweight material · Mg alloy sheet · Cyclic loading test · Twin · Slip

## 1 Introduction

These days, research is being focused on lightweight materials to enhance fuel efficiency and reduce emission gas in cars, and increase the mobility of mobile

---

F2012-E07-029

---

O. S. Seo · H. Y. Kim (✉)

Department of Mechanical and Biomedical Engineering, Kangwon National University,  
Chuncheon, Korea

e-mail: schoolsos@kangwon.ac.kr

M.-G. Lee

Graduate Institute Ferrous Technology, Pohang University of Science and Technology,  
Pohang, Korea

J. H. Kim · D. Y. Kim

Materials Deformation Group, Korea Institute of Materials Science, Changwon, Korea

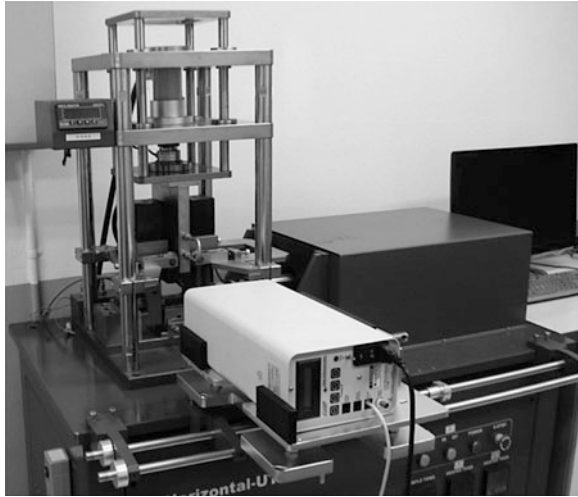
electronic devices [1, 2]. Especially, Mg alloy not only has superior lightness compared to Al alloy, an existing lightweight material, but also has high specific strength and weldability, as well as excellent corrosion resistance. It is also receiving much interest as a lightweight material because, unlike plastic materials, it is environment friendly and possesses a classy surface unique to metals.

Mg alloy has been manufactured mainly using die-casting, but recently, a stamping method that uses Mg alloy sheets is being actively studied. Kang et al. [3] conducted a formability evaluation of circle and rectangle deep drawing process using Mg sheet, and confirmed that the formability is better at high temperature. Kim et al. [4] conducted a wide scale test on Mg alloy sheets, established a database, and provided an experimental base to evaluate warm compaction characteristics. The above research, however, only applies it to a limited model and sheet forming technology research. This is because, unlike other metal sheets, a Mg alloy sheet shows asymmetric stress–strain behavior due to singular behavior such as slip, twin, and untwin at room temperature, and such singular behavior disappears at above a certain temperature. Such singular behavior is materialized by a tension–compression cyclic loading test, and research on Mg alloy sheets is being actively done in the US [5] and Japan [6] by conducting such test. Therefore, this research describes the development of a tester that considers temperature and can perform cyclic loading (tension–compression, compression–tension) to obtain the mechanical behavior of a Mg alloy sheet, which shows singular behavior. A performance evaluation of the developed tester was also conducted, and tension–compression cyclic loading data of Mg alloy sheet was obtained through the tester.

## 2 Cyclic Load Tester

The horizontal type was adopted to prevent mis-alignment and buckling, and two guide rail systems and a comb-type jig were used on the basis of several previous studies [5, 6]. It was designed to consider various test speeds in the uniaxial direction, from 0.001 to 1,000 mm/min, with the guide rails. The tester was also designed to test various load conditions at 400 °C or above, and heat cartridges were installed, 2 on the top and 3 on the bottom respectively, to maximize temperature performance. In addition, a cooling channel and heat insulators were installed to minimize heat deformation of the structure. A laser extensometer was used as a strain measurement device. It was designed to be able to control displacement and strain when analyzing behavior based on various strains, as well as to conduct load control. To control buckling that can be occurred during compression testing, a hydraulic cylinder that can create pressure of up to 1 t with vertical load (side force) was installed on the top. Also, an indicator was installed so that the vertical load's hysteresis, which appears under tension and compression, can be checked in real-time and retrieved as data (Fig. 1).

**Fig. 1** Cyclic tension–compression test machine



### 3 Performance Evaluation of Cyclic Test Machine

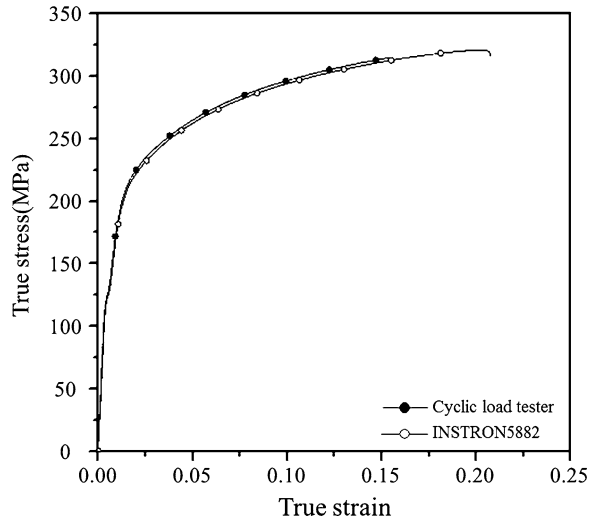
#### 3.1 Evaluation of Uniaxial Tensile Test

The test data from newly developed machine were compared with those of commercial universal test machine (INSTRON5882) to verify the reliability of the developed cyclic tension–compression test machine. The test was conducted at room temperature, the speed was 2 mm/min, and the ASTM E8 standard was used. A non-contact laser extensometer was used to measure strain. Figure 2 is the result of comparison, which shows good correspondence with each other.

#### 3.2 Evaluation of Temperature Range

The most important factor at the elevated temperature is heating performance. To maximize heating performance, direct contact heat cartridges were installed, 2 on the upper die and 3 on the lower die. To measure the temperature distribution of the sample, the temperature was measured at 5 points in the longitudinal direction of the sample, while the temperature distribution in the width direction was ignored because it was evaluated to be even [7]. The time to reach each temperature section of the tester (100, 150, 200, 250 and 300 °C) was measured to be within approximately 10 min, and the time for the sample to reach the target temperature was also within 10 min. However, the difference between the set temperature of the tester and the sample's target temperature was approximately 5:4, due to heat transmission loss in the grip region and convection loss at the sample surface.

**Fig. 2** Comparison of uniaxial tensile test using the cyclic tension–compression test machine and INSTRON5882



Measuring the temperature distribution of the sample, even temperature distribution was verified on both sides of the 15 mm section from the sample’s center, while there was approximately 30 °C difference at the 25 mm section.

### 3.3 Evaluation of Vertical Load

The important factor of the developed cyclic tension–compression test machine is vertical load (side force). Buckling occurs on the sheet under the compression load, and this can be prevented by vertical load. However, vertical load correction is mandatory for materials such as Mg alloy, which are greatly influenced by temperature.

Equation (1) is the correction equation for tension and Eq. (2) is for compression. Here,  $F_T$  is the tensible load,  $F_C$  is the compressible load,  $F_N$  is the corrected load,  $F_L$  is the load obtained from the test,  $F_S$  is the vertical load. Also,  $\mu$  is the friction coefficient. The friction coefficient was given in the references [8].

$$F_T \Rightarrow F_N = F_L - 2\mu F_S \tag{1}$$

$$F_C \Rightarrow F_N = F_L + 2\mu F_S \tag{2}$$

## 4 Conclusion

1. Horizontal type cyclic tension–compression test machine was developed, which can be done at the elevated temperature.



2. The test data from newly developed machine were compared with those of commercial test machine, which shows good correspondence with each other.
3. 2 heat cartridges were installed on the top and 3 on the bottom, which shows even temperature distribution within gauge length.
4. Vertical load was compensated by calculating frictional load under tension and compression, respectively.

**Acknowledgments** This work was financially supported by the Mg Material R&D Project for the Super-light Vehicle operating for the execution of WPM (World Premier Materials) Program funded by the Ministry of Knowledge Economy, Republic of Korea.

“This work was supported by the National Research Foundation of Korea(NRF) grant funded by the Korea government (MEST) (No.2012R1A2A2A01014141)”

## References

1. Lee BH, Lee CS (2008) Prediction of microstructure during hot-working of AZ31 Mg alloy. *KSTP* 17(2):117–123
2. Kleiner M, Chatti S and Klaus A (2006) Metal forming techniques for lightweight construction. *JMPT* 177:2–7
3. Kim HY, Choi SC, Kim HJ, Hong SM, Shin YS, Lee GH (2008) Forming limit of AZ31B magnesium alloy sheet in the deep drawing with cross-shaped die. *Int J Mod Phys B* 22:6045–6050
4. Lee MG, Kim HJ (2011) Experimental and analytical evaluation of forming characteristics for AZ31B magnesium alloy sheet. *KSTP* 20(2):146–153
5. Piao K, Lee JK, Kim HY, Wagoner RH (2009) Compression test of Mg AZ31B at elevated temperature, TMS annual meeting and exhibition, 15–19 Feb 2009, San Francisco
6. Kuwabara T, Kumano Y, Ziegelheim J, Kurosaki I (2009) Tension-compression asymmetry of phosphor bronze for electronic parts and its effect on bending behaviour. *Int J Plast* 25: 1759–1776
7. Lee MG, Kim JH, Chung K, Kim SJ, Wagoner RH, Kim HY (2009) Analytical springback model for lightweight hexagonal close-packed sheet metal. *Int J Plast* 25:399–419
8. Piao K (2011) An elevated-temperature tension-compression test and its application to Mg AZ31B. PhD thesis, The Ohio State University

# The Third Generation Auto Sheet Steel: Theory and Practice

Shanqiang Ying and Han Dong

**Abstract** Strength upgrading generally increases the contradictions between strength and ductility of steels, especially lacking of enough ductility during stamping. Nowadays, many efforts have been undertaken to improve ductility of auto sheet steels. Based on the a novel microstructure modification idea featured by Multi-phase, Meta-stable and Multi-scale ( $M^3$ ) proposed by the authors, over 30 % of ultrafine grained austenite were designed to improve ductility, balanced with remained martensite to maintain higher strength. It was resumed that the proposed  $M^3$  microstructure would result in a improvement of product of ultimate tensile strength and total elongation to over 30 GPa %. New low carbon steels alloyed with medium manganese (3–9 % Mn) developed in laboratory presented really an remarkable improvement in ductility to 40–30 % as ultimate tensile strength ranging from 800 to 1100 MPa. An industrial scale melt and stamping were taken over in the TISCO and FAW respectively. It was shown by the result that hot-rolled 6 mm thick steel sheets with ultimate tensile strength of 800 MPa presented better stamping behavior than the conventional 380 MPa grade steel sheets when they were stamped into cross beams, which means the new steel developed could be used as a potential candidate material for lightweight and cold forming components. Cold-rolled sheets annealed at intermediate temperature also showed an remarkable improvement in ductility even up to 40 % of total elongation at strength level of 800 MPa due to the same reverse austenite transformation phenomenon.

---

F2012-E07-030

---

S. Ying (✉)

China FAW Group Corporation, Changchun, China  
e-mail: yingshanqiang@rdc.faw.com.cn

H. Dong

China Iron and Steel Research Institute Group, Beijing 100081, China

**Keywords** Automobile · Sheet steel · Microstructure · Property

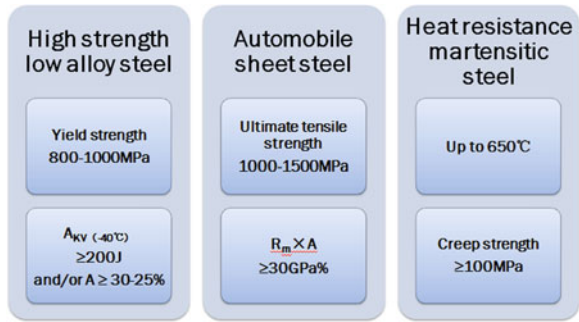
## 1 Introduction

Nowadays, steel is widely used in the human society than any other kinds of materials, both for structural and functional applications. Steel has been the materials basis of our civilization over 2000 years, and now it is still playing very important roles in the world [1]. It is well known that the performances of steel products are closely related to the constitution and morphology of microstructures. Both characterization and effective control of microstructure are now from micron scale to nano scale steadily (to be in nano order). But there still exist some aspects in ambiguous statues in steel science, in which the phenomena and laws are far from totally understanding by human beings. And thus the potentials to develop new technology still remain to be explored.

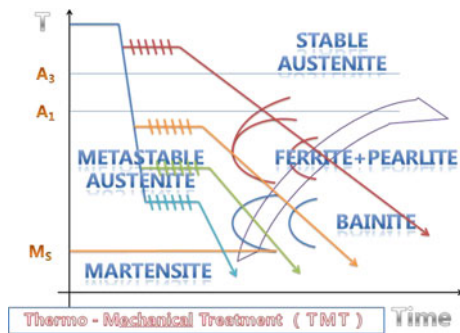
The ultimate tensile strength of perfect iron crystal was theoretically calculated to be of 21 GPa. In 1956, ultimate tensile strength of 13 GPa was achieved by Brenner in whiskers of iron [2]. But it should be pointed out that the actual steel products are strengthened by defects to resist the movement of dislocations within matrix. The steel with highest tensile strength was obtained in cold drawn pearlitic steel wire developed by Nippon Steel in 1990s. High strain resulted in tensile strength of 5.7 GPa in wire in diameter of 0.04 mm through high dislocation density and dislocation strengthening. Meanwhile, the commercial cold drawn pearlitic steel for tire presents the highest tensile strength of 4.0 GPa in the wire in diameter of 0.2 mm. The data of ultimate tensile strength of most martensitic steels are normally within the range of 600–1,800 MPa. The upper limit for martensitic steels to be applied is around 2.2 GPa. Yield strengths of commercial hot rolled HSLA steels are generally in the scale of 400–700 MPa. The highest yield strength being achieved in HSLA steel by Thermo Mechanical Treatment (TMT) is close to 1 GPa [3]. Obviously, the steel products are far from the strength of perfect iron crystal, the binding force of steel matrix. It means that there is a potential for people to improve the strength of steels.

It can be accepted that strength is raised only when there is enough energy to be absorbed during deformation and fracture. Total elongation and notch impact energy are commonly used to evaluate ductility and toughness of steels respectively. In steels, the understanding for structures to control ductility and toughness is conventionally connected with inclusions, precipitates, grains, etc. For multi-phase steel, the coordination of deformation among phases becomes important, but still need to be investigated. For clean steels, there may be a transition of cracks originated from inclusions to the defects in matrix or boundaries, which is certainly still unknown. Steels can be classified as materials composed of different components in multi-scale. It is necessary to identify the microstructure factors to control ductility and toughness in different scales.

**Fig. 1** The target of the program: performances of three steels improved remarkably



**Fig. 2** The processing proposed to obtain M3 microstructure in steels

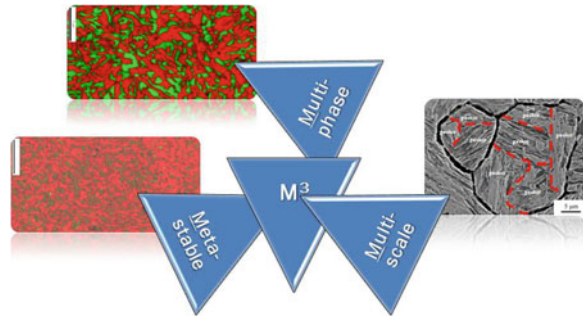


The target of the Program is to develop new generation steels for infrastructure, automobile, and boiler pipe, as shown in Fig. 1. The mechanical properties will be improved significantly, and leads to the improvements in safety and reliability of structures and equipments.

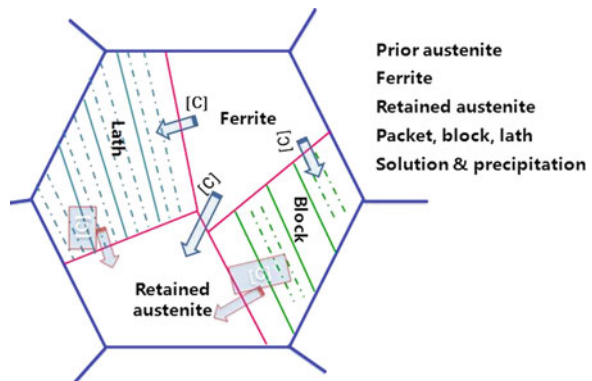
Over past 40 years, TMT has been believed to be the most remarkable progress in both physical metallurgy and processing. It is mainly related to the austenite state at high temperature and the transformations during cooling. In recent years, the attractions have been drawn to the stability of austenite and relative transformation in the elevated and lower temperature range: the transformation of meta-stable austenite, the stability of transformed phases, and the behavior of carbon during transformation, etc. The key point of new TMT in the elevated and lower temperature range is microstructure stability and carbon behavior, Fig. 2. For martensitic heat resistance steel, the stabilities of matrix and grain boundaries are supposed to be controlled to improve creep strength. The understanding of the microstructure stability and carbon behavior could certainly help us to achieve the expected multi-phase microstructure, and lead to the target of enhancement in strength, ductility and toughness.

At the turn of century, researchers in Japan, Korea, Australia, EU and China devoted their efforts on the refinement of ferrite in steels [4, 5]. Grains of 1 μ in size were believed to be the limitation in the bulk specimens processed by heavy hot deformation, which resulted in yield strength of 800 MPa. The state of austenite was thought to be controlled for the beneficitation to grain nucleation and

**Fig. 3** The microstructure characterized with  $M^3$  is target to improve performances



**Fig. 4** Schematic illustration to the potential  $M^3$  microstructure control



retardation to grain growth. From the point view of refinement, lath bainite or lath martensite are obviously the finest microstructure we have. Meanwhile, the scales to identify bainite or martensite are from austenite in dozens of microns to packet and block in microns, to lath in sub-micron, to precipitates in nano meters. The multi-scale characterization provides more choices to control microstructure, and then properties. It is still unclear in the transformation mechanism of ultra-low carbon steel. The transformed phases are quite complex, but are beneficial to toughness. It is worth to pay attention to the transformation and the microstructure in ultra-low carbon steel.

As stated above,  $M^3$  (multi-phase, meta-stability, multi-scale) microstructure control is the means to obtain steels with high performance, as shown in Fig. 3. And Fig. 4 illustrates schematically the formation of  $M^3$  microstructure during the processing.

## 2 The New Auto Sheet Steel with Improved Ductility

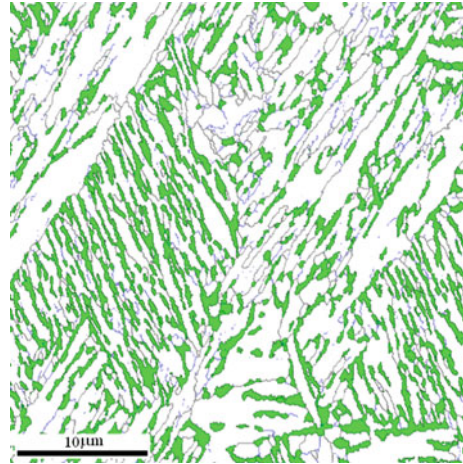
Apart from the weight-lightening, the safety standard of the automobiles was also being paid more and more attention. It was reviewed by American researcher that in 1980s the strengthening of IF steel and the galvanized steel sheets was paid

more attention for their cost and erosion properties, in 1990s the strengthening of HSLA, C–Mn, BH steels were widely applied in auto industries due to their low cost and higher crashworthiness, and in 2000s the crash properties of DP steel, TRIP steel and Hot stamped martensitic steel were mostly selected in auto industries concerning their low cost, weight-lightening and safety improvement in crash. The development of automobile steels in recent days would be mainly focused on ductility improvement at even higher strength level and at lower cost, which results in proposal for the third generation auto sheet steel to meet the requirements for weight-lightening, crash-worthiness and easy fabrications [5].

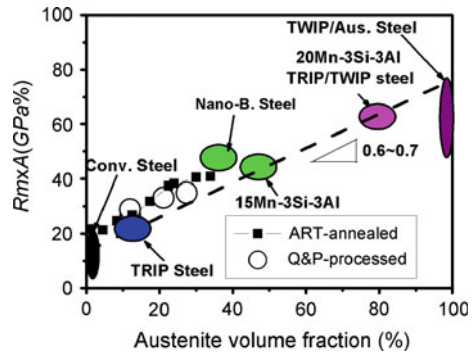
Over the last two decades a significant research effort has been put in the development of Advanced High Strength Steel grades with high strength and high ductility. As an index of formidability and absorbed energy of materials, the product of ultimate tensile strength ( $R_m$ ) and total elongation ( $A$ ),  $R_m \times A$ , has been applied to tailor the steels roughly for automobile application [6]. For the conventional steels possessing primarily ferrite-based microstructures, such as interstitial free (IF), dual phase (DP), transformation induced plasticity (TRIP), complex-phase (CP), and martensitic (MART) steels, their  $R_m \times A$  is only about  $15 \pm 10 \text{ GPa } \%$  named as the first generation auto sheet steel [7]. Contrast with this low value, the second generation auto sheet steel including twinning induced plasticity (TWIP) steels, Al-added lightweight steels with induced plasticity, and other fully austenitic steel, their  $R_m \times A$  is remarkably high up to  $50 \pm 10 \text{ GPa } \%$ . It was thought to be the best material for cold forming and energy absorption in crash but much more expensive and difficulty in processing [8]. It is clear that the advantage of the first generation steel is their cost-effective, but the disadvantage is their low ductility, comparing with that of the second generation steel. The background demonstrated above promoted worldwide study on development of the third generation auto sheet steel with high  $R_m \times A$  in between these two groups but at relatively low cost. We defined the third generation auto sheet steel as  $R_m \times A$  no less than  $30 \text{ GPa } \%$  at strength levels of 1.0–1.5 GPa, which is just in between the first generation auto sheet steel and the second generation auto sheet steel and obtained from the medium-Mn steels with ultrafine grained ferrite and austenite structure, Fig. 5.

In Fig. 6, the product of  $R_m \times A$  of different kinds of steels, such as conventional steels (IF steel, DP steel, Martensitic steel) [9], conventional TRIP steel [9], Nano-Bainitic steel [10], and TWIP steel and austenitic steel [9], is briefly summarized as a function of austenite volume fraction. It is interesting to be notice from Fig. 7b that no matter TRIP effect or TWIP effect in the steel, generally the  $R_m \times A$  linearly increases with increasing of austenite volume fraction from conventional steels to TWIP steel. The slope between  $R_m \times A$  and the austenite volume fraction is  $\sim 0.65 \text{ GPa } \%/ (1 \%)$ , indicating the strong dependence of  $R_m \times A$  on austenite volume fraction. It could be expected roughly that 20–40 % metastable austenite is essential to obtain steel with  $R_m \times A$  of 30–40 GPa %. Thus the dual phase structure with metastable retained austenite in BCC matrix may be a promising way to design the new type automobile steel with both ultrahigh strength and high ductility by means of TRIP/TWIP effects.

**Fig. 5** EBSD examined microstructure of the ultrafine grained medium-Mn steels with large fractioned austenite, in which the white phase is the martensitic laths and the green phase is austenite laths



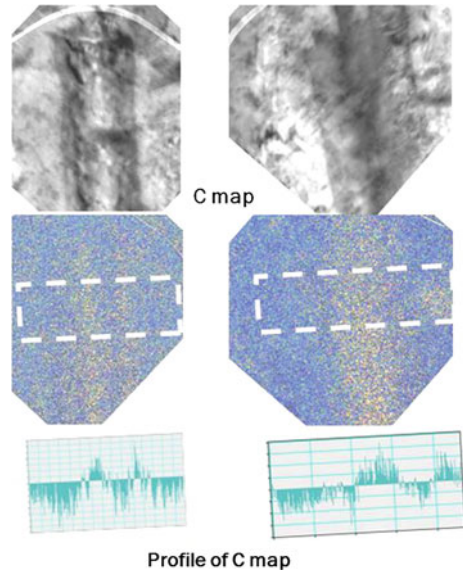
**Fig. 6**  $R_m \times A$  related with retained austenite



Another key point is the diffusion control of alloy elements during transformation, typically C and Mn distribution in different phases, which is very important for the uniform multi-phase distribution in the high performance steel. Zhou Huihua and her colleagues of Tsinghua University verified the carbon partitioning clearly in a medium carbon steel, Fig. 7.

How to control the steel microstructure with FCC and BCC phases to get both high strength and high ductility? In this study, the  $M^3$  microstructure is not only the characters of the desired microstructure but also the controlling approaches to get this structure. For example, to get the high strength, the microstructure should be controlled in multi-scales, such as prior austenite grain scale, packet, block and lath scale. These kinds of controlling of the microstructure were clearly demonstrated in ART-annealed medium manganese steel and the Q&P processed steels, which in turn gives microstructure of processed steels with  $M^3$  features [9, 11–13]. As it was demonstrated very clearly by conventional TRIP steel and Q&P processed steel, the so called “Q&P” steel as firstly proposed by Speer, multi-phase and meta-stable is crucial for the high strength and high ductility [14, 15]. Apart

**Fig. 7** Partitioning of carbon in a medium carbon steel



from this Multi-phase and Meta-stable character, the scale of the microstructure units, i.e., the Multi-scale is also one of the important characters controlling strength and ductility of steel by the coupling behavior among phases.

How to develop the  $M^3$  structure in steel by heat treatments? In light of the processing of conventional TRIP steel, isothermal holding of the austenite in the intercritical region (partial phase transformation from austenite to ferrite to develop a FCC+BCC structure) following by bainite holding of the retained austenite (partial phase transformation from the retained austenite to bainite to form a triple phase structure with ferrite, bainite and retained austenite) is the most straightforward manner to obtain BCC-FCC dual phase structure. But this process gives a rather soft large grained ferrite matrix, thus cannot be applied to get ultrahigh strength. The hard ferrite matrix and large amount of retained austenite could be obtained by austenite reverted transformation from annealing (simply called ART annealing in this study), which gives ultrafine grained matrix and large fractioned austenite phase (>20 %) [16], or the quenching and partitioning (Q&P) process, which results in a strong hard martensitic matrix and relative large fractioned austenite (5–15 %) [17].

In this research, based on the conception of  $M^3$  structure conception, the ART-annealing process was applied to produce the third generation auto sheet steel aiming at getting automobile steel with ultrahigh strength and high ductility, i.e., with excellent combination of strength and ductility. In order to obtain dual phase structure with ultrafine grained hard ferritic matrix and metastable austenite phase by ART-annealing, the chemical composition has to be specially designed to control the coarsening of both martensite lath and the newly developed austenite. It is well known that difference from the fast diffusion of interstitial elements, such



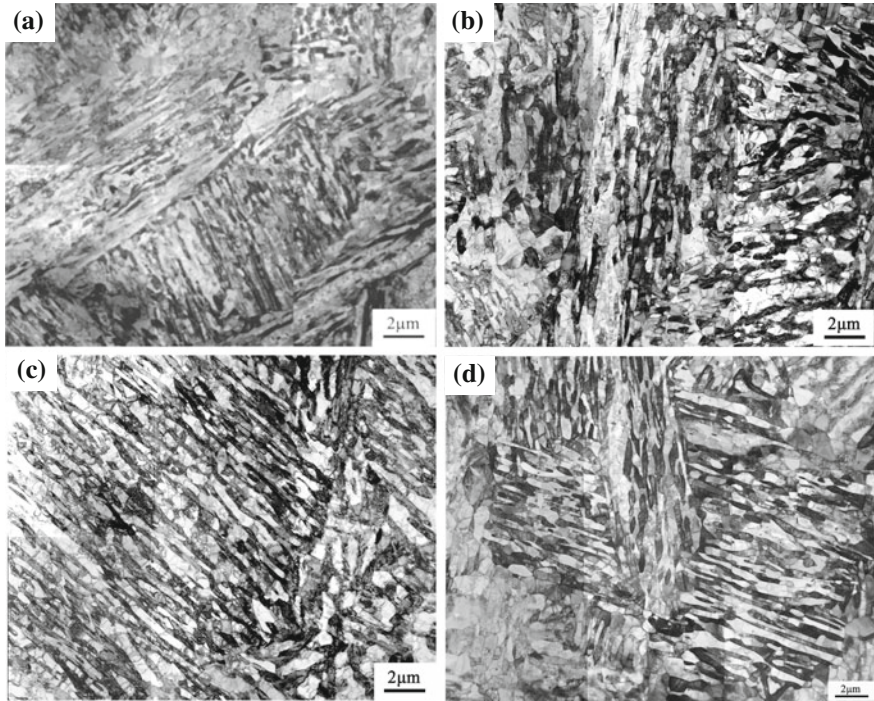
as carbon, substitutional elements can suppress the microstructure coarsening during ART-annealing at relative low temperature. Amongst the elements applied in the dual phase steel and austenite steel and TWIP steel, such as the Si, Mn, Cr, Ni, Mo and Al, Mn is not only a cheap element to enlarge the austenite region and stabilize the austenite phase, but a strong element for substitutional solute hardening.

In Lab of CISRI, Fe–Mn–C steels with 3–9 % Mn and varied carbon concentration were designed to develop BCC–FCC dual phase steels with TRIP/TWIP effects by ART-annealing. Fe–Mn–C alloys composition design was carried out based economy and solute strengthening principle and its microstructure design methodologies was carried out based on fundamental strengthening mechanisms and metastable austenite deformation stability theory. The cooling rate effect on the harden ability, the quenching temperature effects on microstructure and mechanical behavior, the ART annealing resulted microstructure and mechanical properties and the Mn replacing carbon alloying were studied in detail. Especially, ART-annealing behaviors, the microstructure evolutions and the element (Mn–C) partitioning behaviors were presented with theoretical consideration. The strengthening and ductility-enhancing mechanisms were studied based on the detailed microstructure characterization, mechanical properties examination and the analysis of the relationship between microstructure and mechanical properties.

In this section, the development of the third generation auto sheet steel at strength level of 1,000 MPa with  $R_m \times A$  of 30–40 GPa % processed by ART-annealing was reported. The ultrafine lamellar ferrite–austenite dual phase structure will be demonstrated, the substantially enhanced mechanical properties of the newly developed third generation auto sheet steel will be presented. At last the strengthening and ductility-enhancing mechanisms of the third generation automobile steel will be proposed tentatively based on the detailed microstructure characterization, mechanical properties examination and the analysis of the relationship between microstructure and mechanical properties.

### 3 The Microstructure and the Processing

As an example of the C–Mn steel processed by ART-annealing, the ultrafine lamellar ferrite/martensite structure of Fe-0.2 % C-5 % Mn steel characterized by TEM was shown in Fig. 8. After 1 h annealing at 650 °C, the dark/bright lamellar structure in the original martensite packets was clear with austenite lath parallel to the slightly coarsened martensite lath. The equiaxed austenite grains could also be found in the packet boundary or original austenite grain boundary. After 1 h annealing, the width of austenite laths is about 0.2–0.3 μm. With increasing of annealing time, the BCC–FCC duplex microstructure with parallel ferrite laths and austenite laths still remains in Fe-0.2 % C-5 % Mn steel after 6, 12 and 48 h ART-annealing at 650 °C as shown in Fig. 8b, c and d. In addition, it can be seen from Fig. 8 that increasing annealing time improves the uniformity of the

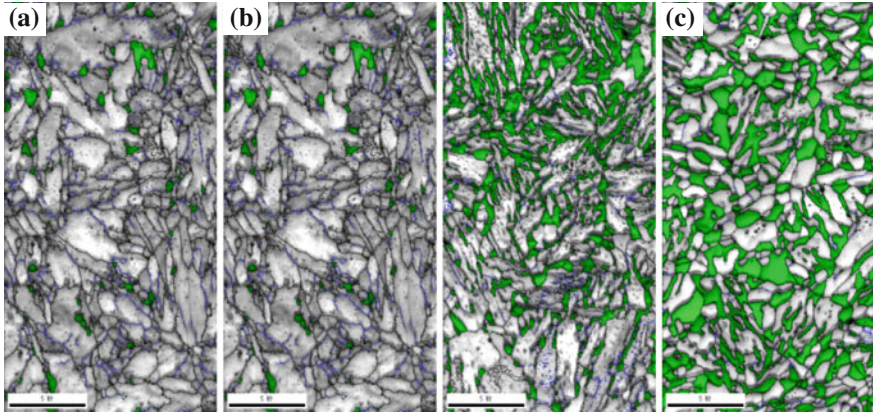


**Fig. 8** Microstructures of Fe-0.2 % C-5 % Mn steel ART-annealed at 650 °C with **a** 1 h, **b** 6 h, **c** 12 h and **d** 48 h

microstructure and decreases the precipitation of carbides, suggesting the concurrence of austenite growth by thickening, precipitation dissolve in the interface region between precipitation and the coalescence martensite laths. After 6 and 12 h annealing, the austenite width is about 0.3  $\mu\text{m}$ , slightly thicker than that of 1 h annealed specimen. Even after 48 h annealing at 650 °C, the width of both austenite lath and ferrite lath is only about 0.4  $\mu\text{m}$ , indicating the high thermal stability at this high temperature. This may need further study on the mechanism of this kind of thermal stability.

From Fig. 8, it is very interesting that the width of both austenite lath and ferrite lath is still very fine after long time annealing. It was measured the average width is about 0.5  $\mu\text{m}$  for even after 144 h annealing (not given here), which still belongs to the submicron grain sized materials, indicating the high thermal stability of Fe-0.2 % C-5 % Mn steel during ART-annealing process. Also with increasing of annealing time, no precipitation could be found in the studied regions.

The ultrafine lamellar microstructure was also observed through EBSD in FEG/SEM as presented in Fig. 9 as a function of annealing time. In this figure, the austenite phase was revealed by green color but the ferrite phase was presented by the grey color. The blue colored lines depict the low angle boundaries with misorientation lying in between 3 and 15° and the black lines present the high angle

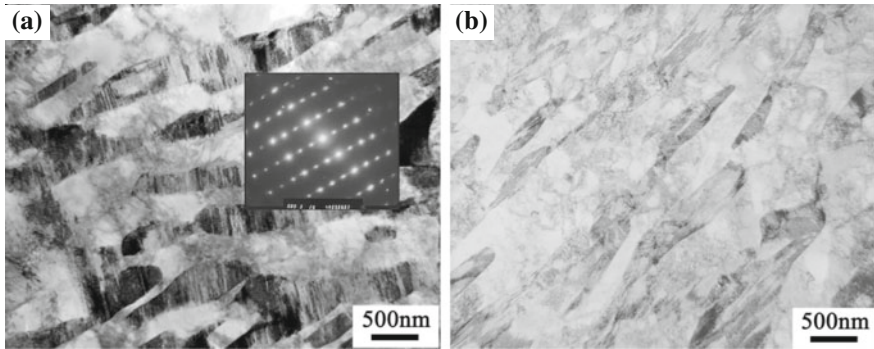


**Fig. 9** Microstructural observation of medium Mn steel ART-annealed at 650 °C with different time. **a** 1 min–4.5 %  $\gamma$ , **b** 1 h–22.5 %  $\gamma$  and **c** 12 h–33.7 %  $\gamma$

boundaries with misorientation larger than 15°. It can be seen that the austenite grains gradually developed in the initial martensite. In the short ATR-annealing time, for example annealing time lower than 30 min at 650 °C the nearly equiaxed austenite grains mainly could be found in the grain boundary or packet boundary as shown in Fig. 9a. Due to the low misorientation between martensitic laths, no clear martensitic lath structure could be identified in these shorted time annealed microstructure. When the annealing time was larger than 30 min at 650 °C, the nucleation and growth of lath type austenite grains occur in between the martensitic lath as shown in Fig. 9b. Also it can be seen that the parallel lath typed structure becomes clear in these annealed microstructure, because the austenite nucleated in between the martensitic lath highlights the lath structure. After 6 h ART-annealing, the austenite grains nucleated and grew both in the boundary regions and in between the martensitic lath slightly coarsened with increasing annealing time as revealed in Fig. 9c.

Deformation microstructure of Fe-0.2 % C-5 % Mn steel after ART-annealing at 650 °C with 6 h was characterized by TEM as shown in Fig. 10a and b. After about 37 % uniform uniaxle tension deformation, twined martensite could be distinguished from the annealed martensite. In Fig. 10, one type of martensite with twin plate direction perpendicular to the original austenite plates and another type martensite with twin plate direction parallel to original austenite lath were presented. It can be seen that in one austenite only one packet could be found, which is different from the thermal stability controlled phase transformation. High dislocation density generated in the austenite neighbored martensite was evidenced by XRD measured results of  $2.5 \times 10^{15} \text{ m}^{-2}$ . It may be expostulated that the high dislocation density in the martensite lath (ferrite) may be attributed to the volume expansion resulted from phase transformation from austenite to martensite.

Based on the above results and discussion, the annealing behaviors of the quenched Fe-0.2 % C-5 % Mn steel were studied at 650 °C with annealing time for up to



**Fig. 10** Room temperature deformation structure at maximum uniform elongation (37 %) of Fe-0.2 % C-5 % Mn steel after 6 h annealing at 650 °C. **a** One type of martensite with twin plates direction perpendicular to the original austenite plates with inserted diffraction pattern and **b** Another type of martensite with twin plates direction parallel to original austenite lath

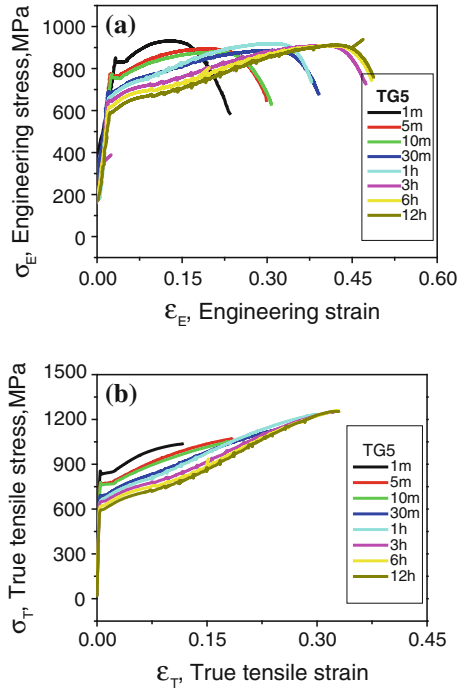
144 h. The austenite reverted transformation during annealing in the intercritical region (ART-annealing) were examined by TEM, STEM and XRD. The conclusions could be summarized that (1) ART-annealing of Fe-0.2 % C-5 % Mn steel resulted in the microstructure evolution from fully martensite structure to an ultrafine grained duplex microstructure with austenite fraction of  $\sim 34$  %. The final ultrafine lamellar ferrite/austenite duplex structure was obtained by lath scale microstructure, i.e., the ART-annealing. (2) Even after 144 h annealing at 650 °C, the width of both austenite lath and ferrite lath remains smaller than 0.5  $\mu\text{m}$ , indicating the high thermal stability of the ultrafine grained duplex microstructure of Fe-0.2 % C-5 % Mn steel, which may be attributed to the slow diffusion rate of Mn in austenite. (3) During deformation process, the austenite gradually transformed into martensite, which suggests that the deformation behavior of ART-annealed medium manganese steel were controlled by the phase transformation induced plasticity (TRIP effects).

## 4 Mechanical Properties of Medium Manganese Steel

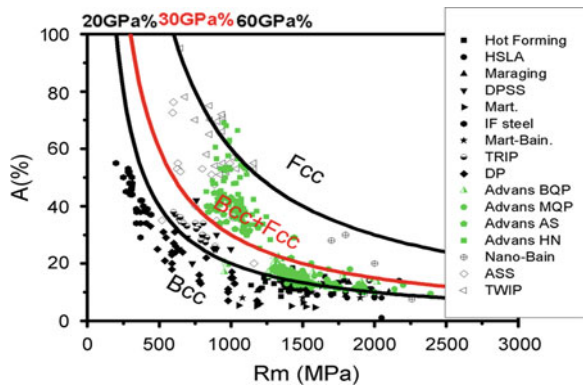
The engineering tension stress–strain curves of Fe-0.2 % C-5 % Mn after air cooling and annealing with different time were given in Fig. 11a. It can be seen from the engineering stress–strain curves that the increasing annealing time from 1 min to 12 h increases the total elongation (AT) significantly from 20 to 45 %, decreases the yield strength from 830 to 600 MPa, whereas the ultimate tensile strength remains about  $960 \pm 30$  MPa. The true stress–strain curves of studied steel were given in Fig. 11b. It can be seen from the true stress–strain curves that the ultimate tensile stress increases from  $\sim 1,000$  to 1,350 MPa with increasing annealing time from 1 min to 12 h, suggesting the increased work hardening with increasing of annealing. Interestingly, it can be seen that serrated or jerk flow feature can be observed from the stress strain curves, indicating



**Fig. 11** The stress–strain curves of Fe-0.2 % C-5 % Mn processed by ART-annealing with different annealing time. **a** Engineering stress–strain curves and **b** True tensile stress–strain curves

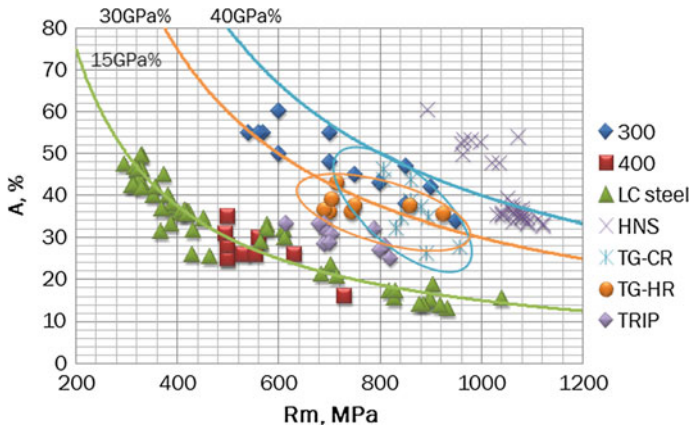


**Fig. 12** Dependence of total elongation on ultimate tensile strength of the 3rd generation auto sheet steel (green dots) developed in our program comparing with the 1st and the 2nd auto sheet steels

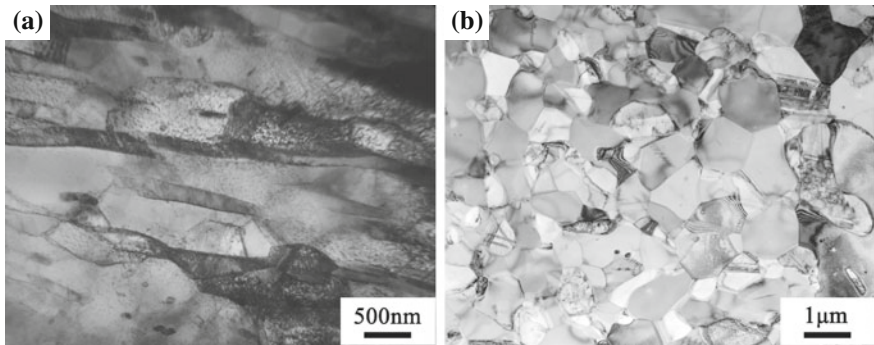


dynamic strain aging and strong localized deformation during tension test in the steel after 1 h or long time annealing at ambient temperature, Fig. 11b. Furthermore, the true stress–strain curves of the long time annealed specimens assume “S” typed shape, which may indicate the phase transformation during tension deformation process.

The mechanical properties of the medium manganese steels applied in this study were summarized in Fig. 12. It can be seen from Fig. 12 that within the range of ultimate tensile strength from 800 to 1,500 MPa the total elongation can be high up to 45–30 %. The product of ultimate tensile strength to total elongation



**Fig. 13** The balance between ultimate tensile strength and total elongation of steels (TG-HR and TG-CR represent the 3rd generation auto steel hot rolled and cold rolled in TISCO respectively)



**Fig. 14** The microstructures of (a) TG-HR steel coil and (b) TG-CR sheet respectively

in the  $R_m$  range of 800–1,500 MPa is about 40 GPa, which means that the objective of the third generation auto sheet steel can be realized and would give important role in the production in steel industry. The industrial trials have been undertaken in TISCO and  $R_m \times A$  can meet with the target of the Program for both hot rolled strip and cold rolled sheet, Fig. 13, which present lamellar structure in hot rolled strip and uni-axle structure in cold rolled sheet, Fig. 14.

## 5 Conclusions

From point of view of steel grades and quality, the steels used today are definitely different from what we have decades ago. It is worthy to pay more attentions to the circumstance and development of steels in China than ever before, especially due

to the rapid progress of industrialization and urbanization. It should be aware of the situation and co-existence of both market and steel industry at this special moment. Matching with the market demands and steel science and engineering, it is believed that more and more new steel grades with higher performances will appear. In order to meet the development of society and economy, one should apply new technologies, new processing, and new equipments to develop high performance steel products with characteristics of high strength and high ductility for auto sheet steel, high strength and high toughness and/or high ductility for HSLA steel, high creep strength for heat resistance steel. Certainly, steel is a kind of new materials changing day by day. In the future, an affordable system of steel production and applications should be constructed to meet the requirements.

The third phase of 973 Program (2010–2014) on steels has been granted by MOST to promote the occurrence of new steel technologies since 2010. As a result, the fundamentals of microstructure control featured by multi-phase, meta-stable and multi-scale ( $M^3$ ) have been established, and then the targets of high performance steels have been setting up: the third generation advanced high strength sheet steels ( $R_m \times A \geq 30 \text{ GPa \%}$  as  $R_m$  from 1,000 to 1,500 MPa) for automobiles with improved ductility and low cost. At present, the product of  $R_m \times A$  in auto sheet steels has been doubled to be over 30 GPa %, comparing with conventional auto sheet steels. It can be expected that the new generation steels developed will improve the safety and reliability of steel components in service remarkably for automobiles in the future.

**Acknowledgments** The author would like to express sincere thanks to his colleagues involved in the 973 Program for their great academic contributions. Ministry of Science and Technology is acknowledged for the financial funding of the 973 program of No.2010CB630800.

## References

1. Dong H, Wang MQ, Weng YQ (2010) Performance improvement of steels through  $M^3$  structure control. *Iron Steel* 45(7):1–7
2. Brenner SS (1956) The growth of whiskers by the reduction of metal salts La croissance de barbes par la reduction de sels metalliques Das wachsen von “whiskers” durch reduktion von metallsalzen. *Acta Metall* 4:62–74
3. Dong H, Sun XJ, Cao WQ et al (2010) On the performance improvement of steels through  $M^3$  structure control, advanced steels. In: Weng YQ, Dong H, Gan Y (eds). *Metallurgical Industry Press*, Beijing, pp 35–57
4. Dong H, Sun SJ, Hui WJ et al (2008) Grain refinement in steels and the applications trials in China. *ISIJ Int* 48:1126–1132
5. Anderson D (2008) Application and reparability of advanced high-strength steels. American Iron and Steel Institute, <http://www.autosteel.org>
6. Heimbuch R Overview: Auto/Steel partnership, [www.a-sp.org](http://www.a-sp.org)
7. Jacques P, Furnemont Q, Mertens A et al (2001) On the sources of work hardening in multiphase steels assisted by transformation-induced plasticity. *Al Phil Mag* A81(7): 1789–1812

8. Frommeyer G, Brux U, Neumann P (2003) Supra-ductile and high-strength manganese-TRIP/TWIP steels for high energy absorption purposes. *ISIJ Int* 43(3):438–446
9. Shi J, Cao WQ, Dong H (2010) Ultrafine grained high strength low alloy steel with high strength and high ductility. *Mater Sci Forum* 654–656:238–241
10. Garcia-Mateo C, Caballero FG (2005) Ultra-high-strength bainitic steels. *ISIJ Int* 45(11):1736–1740
11. Cao WQ, Wang CY, Shi J et al (2010) Application of quenching and partitioning to improve the ductility of ultrahigh strength low alloy steel. *Mater Sci Forum* 654–656:29–32
12. Wang CY, Shi J, Cao WQ et al (2010) Characterization of microstructure obtained by quenching and partitioning process in low alloy martensitic steel. *Mater Sci Eng A* 527:3442–3449
13. Wang CY, Shi J, Cao WQ et al (2011) Study on the martensite in low carbon CrNi3Si2MoV steel treated by Q&P process. *Acta Metall Sin* 47(6):720–726
14. Speer JG, Hackenberg RE, DeCooman BC et al (2007) Interface migration during annealing of martensite/austenite mixture. *Phil Mag Lett* 87:379–382
15. Speer JG, Matlock DK, Cooman BC et al (2003) Carbon partitioning into austenite after martensite transformation. *Acta Mater* 51:2611–2622
16. Miller RL (1972) Ultrafine-grained microstructures and mechanical properties of alloy steels. *Met Trans* 3A:905
17. Wang CY (2010) Investigation on 30 GPa % grade ultrahigh-strength martensitic-austenitic steels. Degree of doctor dissertation. Central Iron and Steel Research Institute, 2010